

ANL--82-62

DE83 006229

Distribution Category:  
Coal Conversion Demonstration  
Plants (UC-89)

---

ANL-82-62

CONF-820612

---

ARGONNE NATIONAL LABORATORY  
9700 South Cass Avenue  
Argonne, Illinois 60439

THE PROCEEDINGS OF THE 1982 SYMPOSIUM ON  
INSTRUMENTATION AND CONTROL FOR  
FOSSIL ENERGY PROCESSES

June 7-9, 1982

Adam's Mark Hotel

Houston, Texas

**NOTICE**

**PORTIONS OF THIS REPORT ARE ILLEGIBLE. It**  
**has been reproduced from the best available**  
**copy to permit the broadest possible avail-**  
**ability.**

Sponsored by

U.S. Department of Energy  
Office of Fossil Energy

Argonne National Laboratory  
Society for Control and Instrumentation  
of Energy Processes

September 1982

Prepared for the U.S. Department of Energy  
Task No. 49644

# **LEGIBILITY NOTICE**

**A major purpose of the Technical Information Center is to provide the broadest dissemination possible of information contained in DOE's Research and Development Reports to business, industry, the academic community, and federal, state and local governments.**

**Although a small portion of this report is not reproducible, it is being made available to expedite the availability of information on the research discussed herein.**



## ACKNOWLEDGMENTS

The U.S. Department of Energy, Argonne National Laboratory, and the Society for Control and Instrumentation of Energy Processes, sponsors of the 1982 Symposium on Instrumentation and Control for Fossil Energy Processes, thank the 1982 Symposium Committee for organizing and presenting this Symposium. The Symposium Committee members, listed on the following page, acknowledge the many persons who contributed to the success of the Symposium: speakers presenting papers, luncheon and banquet speakers, session chairs, and the organizations participating in the Show and Tell hardware display.

Special recognition and thanks are due Richard Greene of Trade Associates for presenting the commercial instrumentation exposition concurrent with the Symposium.

Funding of this Symposium by the U.S. Department of Energy - Fossil Energy is gratefully acknowledged.

The many organizations, including private industry, universities, national laboratories, and government are thanked for the numerous contributions by their employees. Their investment of time and effort led to a successful Symposium, furthering the solution of instrumentation and control problems in fossil energy processes.

Future Symposia are planned for June 20-22, 1983, in San Diego, California, and June 11-13, 1984, in Atlanta, Georgia. Additional information will be sent to people on the printed distribution list and will be available from Argonne National Laboratory, Conference Planning and Management, 9700 South Cass Ave., Argonne, IL 60439.

Proceedings of previous Symposia are also available from NTIS:

- 1977      The Proceedings of the 1977 Symposium on Instrumentation and Process Control for Fossil Demonstration Plants, held July 13-15, 1977, Chicago, IL (ANL-78-7/CONF-770729)
- 1978      The Proceedings of the 1978 Symposium on Instrumentation and Control for Fossil Demonstration Plants, held June 19-21, 1978, Newport Beach, CA (ANL-78-62/CONF-780656)
- 1979      The Proceedings of the 1979 Symposium on Instrumentation and Control for Fossil Energy Processes, held August 20-22, 1979, Denver, CO (ANL-79-62/CONF-790855)
- 1980      The Proceedings of the 1980 Symposium on Instrumentation and Control for Fossil Energy Processes, held June 9-11, 1980, Virginia Beach, VA (ANL-80-62/CONF-800602)
- 1981      The Proceedings of the 1981 Symposium on Instrumentation and Control for Fossil Energy Processes, held June 8-10, 1981, San Francisco, CA (ANL-81-62/CONF-810607)

SYMPOSIUM COMMITTEE

General Chair:

*Nancy M. O'Fallon*, Argonne National Laboratory

Program Chair:

*John V. Walsh*, Jet Propulsion Laboratory

Vice Program Chair:

*William R. Miller*, Ashland Synthetic Fuels, Inc.

Exposition Liaison:

*Herb C. March*, Procon, Inc.

Conference Arrangements:

*Miriam L. Holden*, Argonne National Laboratory

Secretary:

*June Johansen*, Argonne National Laboratory

Sponsor Liaison, DOE:

*T. K. Lau*, U.S. Department of Energy  
Combustion and Heat Systems Division

Industrial Sponsor Liaison:

*Herb Kaplan*, President, SCIEP, Inc.

Sessions and Session Organizers:

Mass Flow: Solid-Gas Streams:

*F. Don Freeburn*, U.S. DOE-Morgantown Energy Technology Center

Physical and Chemical Properties of Coal:

*Frank T. Finch*, Los Alamos National Laboratory

Temperature:

*Herb Kaplan*, SCIEP, Inc.

Mass Flow: Solid-Liquid Streams:

*E. Newt Hayes*, The Foxboro Company

Analysis: Electromagnetic and Chromatographic:

*Mary Anne H. Scott*, University of Tennessee Space Institute

Control System Design and Modeling:

*C. Thomas Carroll*, Foster Wheeler Energy Corporation

Level and Density:

*Paul Raptis*, Argonne National Laboratory

Valves and Erosion:

*James L. Powell*, U.S. DOE - Fossil Energy

Control: Experimental Results and Data Handling:

*Clayton T. Crowe*, Washington State University

Particulate Measurement and Control:

*James C. F. Wang*, Sandia National Laboratories

Analysis: Nuclear:

*Richard W. Doering*, General Atomic Company

Underground Processes:

*Ron Zielinski*, Monsanto Research Corporation

TABLE OF CONTENTS

Page

Monday, June 7

Opening Session

Session Chair: John J. Roberts (Argonne National Laboratory)

Welcome from ANL

John J. Roberts (Argonne National Laboratory)

Welcoming Address from DOE

Donald L. Bauer (U.S. Department of Energy)..... 1

Shale Oil as a Source of Jet Fuel

Herbert R. Lander (U.S. Air Force, Jet Fuels Division)

The Future of Coal Liquefaction

Paul Wellman (Ashland Synthetic Fuels, Inc.)..... 5

Master of Ceremonies for Luncheon

William R. Miller (Ashland Synthetic Fuels, Inc.)

Luncheon Speech: Oil Shale -- Present and Future

James Gary (Chemical Engineer, Colorado School of Mines)..... 6

Mass Flow: Solid-Gas Streams

Session Chair: F. Don Freeburn

(U.S. DOE - Morgantown Energy Technology Center)

Mass Flow Measurement of Solids/Gas Stream Using Radiometric Techniques

J. K. Linn, D. G. Sample (Sandia National Laboratories)..... 12 -

Solids Flow Control and Measurement in the Peatgas<sup>TM</sup> Pilot Plant Program

S. Wohadlo, R. Biljetina, R.M. Laurens, R. Bachtta (Institute of Gas Technology)..... 21 -

Magnetic Resonance Coal Flowmeter and Analyzer

J. D. King, W. L. Rollwitz, A. De Los Santos (Southwest Research Institute)..... 30

Advances in Instrumentation and Control for MHD - CDIF Update

M. L. Miller, B. B. Rogers (Mountain States Energy, Inc.)..... 41 ✓

Performance Characteristics of a Capacitive Mass Flowmeter on the ANL Solids/Gas Flow Test Facility

J. P. Bobis, W. E. Brewer, J. R. McQuinn, N. M. O'Fallon, R. J. Armani (Argonne National Laboratory)..... 50

Real Time Velocity Measurements of Airborne Solids Flow with an Industrial Correlation Flowmeter

T. E. Murphy, M. J. Post (Sybron/Taylor, Inc.), J. P. Bobis (Argonne National Laboratory), H. L. Farley (Foster Miller Associates, Inc.). 65

	<u>Page</u>
Monday, June 7 (contd.)	
Mass Flow Measurements of Gas-Solids Suspensions Using Venturimeters with Light Attenuation A. Payne, M. Werner, D. Plank, C. T. Crowe (Washington State University).....	77
<u>Physical and Chemical Properties of Coal</u>	
Session Chair: Frank T. Finch (Los Alamos National Laboratory)	
Viscous Effect on Acoustic Scattering by Elastic Solid Cylinders and Spheres W. H. Lin, A. C. Raptis (Argonne National Laboratory).....	86
The Effects of Metal Chelates on Wet Flue Gas Scrubbing Chemistry S.-G. Chang, D. Littlejohn (Lawrence Berkeley Laboratory).....	98
Transfer of Asphaltene-Coated Particulates from Model Fluids into an Aqueous Phase L. A. Khan (Illinois State Geological Survey).....	114
Coking of SRC-II Process Streams C. S. Wen (Gulf Research & Development Company).....	122
Factors Affecting the Adhesion of Coal Particles to Oil-Coated Air Bubbles L. A. Khan (Illinois State Geological Survey).....	145
Equivalent Weight Determinations of Black Acids Obtained by the Reductive Carboxylation with Bituminous and Lignite Coals R. C. Duty, M. J. Lavin, I. C. Chiri (Illinois State University)....	153
<u>Temperature</u>	
Session Chair: Herb Kaplan (SCIEP, Inc.)	
Thermometry in Coal Utilization J. F. Schooley (National Bureau of Standards).....	161
Combustor Pinhole Camera A. B. Witte, N. Gat, L. M. Cohen (TRW Space and Technology Group)...	169
Acoustic TDR Temperature Measurement N. Gopalsami, S. H. Sheen, A. C. Raptis (Argonne National Laboratory)	182
Application of Thermally-Activated Gas Canisters in MIS Oil Shale Retorts J. Ronchetto, J. Campbell, E. Frohwein, J. Clarkson, V. DuVal, W. Miller(Lawrence Livermore National Laboratory).....	190
Master of Ceremonies for Banquet John V. Walsh (Jet Propulsion Laboratory)	
Banquet Speech: Humorous Court Decisions Judge Lee Duggan (Texas Appellate Court)	

Tuesday, June 8

Page

Mass Flow: Solid-Liquid Streams

Session Chair: E. Newt Hayes (The Foxboro Company)

An Online Correlation Computer for Noninvasive Mass Flowrate Measurement in Ducts F. Lenksuz, K. G. Porges (Argonne National Laboratory).....	198
Development of Neutronic Mass Flow Meter T. Gozani, J. Esterl, J. Goodman, H. Bernatowicz (Science Applications, Inc.).....	206
Some Recent Slurry Flow Measurements with SLTF K. G. Porges, C. Kampschoer, S. Cox, W. Brewer (Argonne National Laboratory).....	226
Conductivity Probe and Data Acquisition for a Liquefaction Cold Model W. Fuchs, D. Smith (U.S. DOE - Pittsburgh Energy Technology Center).	233
Operating Experience with High Temperature Sonic Doppler Flowmeter in Coal Liquefaction Plants A. C. Raptis, H. B. Karplus, W. P. Lawrence (Argonne National Laboratory).....	247
Evaluation of Coriolis Flow Meters in Liquefaction Slurries W. Lee Smith (Micro Motion, Inc.).....	257

Analysis: Electromagnetic and Chromatographic

Session Chair: Mary Anne H. Scott  
(University of Tennessee Space Institute)

In-Situ, Real Time Measurement of NO, NO <sub>2</sub> , and SO <sub>2</sub> by Tunable Atomic Line Molecular Spectroscopy (TALMS) T. Hadeishi, R. McLaughlin (Lawrence Berkeley Laboratory).....	263 -
On-Line Composition with Laser-Based Techniques F. T. Finch, A. Hartford, Jr. (Los Alamos National Laboratory).....	270 -
Microwave Properties of Coal Derived Liquids and Coal-Recycle Solvent Slurries: Potential for On-Line Monitors I. B. Goldberg, K. E. Chung (Rockwell International Science Center).	279
Time-Domain Measurements of the Dielectric Properties of Oil Shale -- The Development of an On-Line Dielectric Probe M. F. Iskander (University of Utah).....	280
Shale Oil Separations by HPLC W. A. Dark (Waters Associates).....	291



Tuesday, June 8 (contd.)

Page

Control System Design and Modeling

Session Chair: C. Thomas Carroll (Foster Wheeler Energy Corp.)

Rapid Measurement of Asphaltene/Preasphaltene Ratios with Potential for Feedback Control in the SRC Process J. E. Mrochek, M. S. Denton, W. D. Bostick, S. R. Dinsmore (Oak Ridge National Laboratory).....	292
Instrument & Control Design Criteria for Fossil Energy Process Management R. Cunningham, C. R. Stewart, W. K. Triebel III (Honeywell, Inc.)...	305
Use of Computer Graphics to Study Binary Distillation Control Alternatives A. G. Hill, J. B. Howell (Oklahoma State University).....	318
Control Problems in Combined-Cycle MHD-Steam Power Plants: Effects of Turbine Configurations on Dynamic Response D. A. Rudberg, C. A. Heikes, J. C. Shovic (Montana State University)	329
Nonlinear Dynamic Model of the TVA 20-MW AFBC Pilot Plant V. Sumaria, K. C. Kalnitsky (JAYCOR), J. R. Byrd (Tennessee Valley Authority).....	338
A Survey of Near and Long Term Uses of Lumped Parameter Dynamic Models for Fossil Fuel Processing Facilities T. L. Greenlee, M. R. Ringham (JAYCOR).....	348

Master of Ceremonies for Luncheon  
Herb Kaplan (SCIEP, Inc.)

Luncheon Speech: Houston in Retrospect  
Jim McConn (Former Mayor of Houston)

Poster Presentations

A High Pressure Instrumented Flow Control System for Hydrogeologic Injection Testing R. G. Reeves (Sierra Pump Systems).....	365
Turbine Transducer Developed for Adverse Conditions D. R. Cooper, J. L. Edson (Idaho National Engineering Laboratory)...	366
Computer-Aided Fluctuation Analysis of an MHD Generator J. E. Barbay, Jr., S. Sami (Southern Illinois University).....	372
A Method to Deduce Char Flow to the Bi-Gas Reactor by Heat Balance E. C. Baetens, R. Frummerman (Frumerman Associates, Inc.).....	381
The X-Ray Absorption Measurement of Fluid Saturations in Oil Sand Cores E. Miles-Dixon, G. E. Sedgwick, T. R. Heidrick (Alberta Research Council, Canada).....	392

Tuesday, June 8 (contd.)

Page

Test of Laser Base Instruments on a Fixed Bed Coal Gasifier  
Allen Hartford (Los Alamos National Laboratory)

Instrumentation for Physical Properties and Solvent Quality in  
Coal Liquefaction Processes  
J. R. Hightower (Oak Ridge National Laboratory)

Fossil Energy Test Facilities at Argonne National Laboratory  
Ronald A. Scharping (Argonne National Laboratory)

Show and Tell Hardware Display

Session Organizer: T. K. Lau (U.S. DOE - Fossil Energy)

List of Show and Tell Hardware Display Participants..... 400

Wednesday, June 9

Level and Density

Session Chair: Paul Raptis (Argonne National Laboratory)

Microwave Bed-Level Detectors  
D. M. DeLauder, C. A. Balanis (West Virginia University)..... 407

Menisci Level Sensing and Surface Tension Measurement Using a Laser  
Beam Optical Lever Effect  
P. Longrigg (Solar Energy Research Institute)..... 415

Level Measurements for High Temperature Coal Slurries  
N. Gopalsami, A. C. Raptis (Argonne National Laboratory)..... 422

Quantitative Applications of Gamma Densitometry in the Coal Industry --  
A Critique  
P. Shea, R. Sher (Stanford University), T. Gozani (Science  
Applications, Inc.)..... 435

On-Line Multicomponent Mass Flow and Density Gradient Analysis in  
Slurry Pipe Lines  
G. V. Walford (Gull Engineering, Inc.)..... 446

Improved Efficiency in Coal Preparation Circuits  
M. N. Mackinnon (Kay-Ray, Inc.), G. W. Robertson (Preparation  
Sales, Inc.)..... 447

Valves and Erosion

Session Chair: James L. Powell (U.S. DOE - Fossil Energy)

Pacific Abrasive Fluid Letdown Valve  
N. J. Condon, F. R. O'Brien (MCC Pacific Valves)..... 455

Design Principles of Low Impingement Type Slurry Letdown Valves  
H. H. Illing (Kieley and Mueller)..... 461

Wednesday, June 9 (contd.)	<u>Page</u>
H-Coal Pilot Plant High Pressure and Temperature Letdown Valve Experience N. D. Bond, W. R. Miller (Ashland Synthetic Fuels, Inc.).....	469
Block Valves in Liquefaction Letdown Service -- An Update M. Beasley (Mogas Industries, Inc.), V. Ragle (Ashland Synthetic Fuels, Inc.).....	470
Acoustic System for Monitoring Pressure Boundary Wear C. A. Youngdahl, W. A. Ellingson (Argonne National Laboratory).....	477

Control: Experimental Results and Data Handling

Session Chair: Clayton T. Crowe (Washington State University)

Automated Data Qualification R. W. Brower, J. L. Anderson, L. D. Goodrich, A. D. Mackley (EG&G Idaho, Inc.).....	488
Computer Controlled Consolidation Test Results for Faraday Connected MHD Power Generation K. Marcotte, R. Johnson, S. Shink (Montana State University).....	501
The Control of Industrial Fluidized Bed Boiler Plant M. J. Virr (Johnston Boiler Company).....	509
Process Control of Multi-Solid Fluidized Bed Combustion G. Gangaram, R. D. Litt (Battelle, Columbus Laboratories), E. C. Seber (Struthers Thermo-Flood Corporation).....	522
Control System Requirements for the 20 MW TVA/EPRI Fluid Bed Demonstration Unit R. R. Dixon (Babcock & Wilcox Company), D. J. Dziubakowski (Bailey Controls Company).....	530
Hydrogeologic Testing of the E. J. Kubat Borehole, San Juan County, Utah: Utilization of a High Pressure Instrumented Flow Control System D. F. Hoexter (Woodward-Clyde Consultants).....	540

Master of Ceremonies for Luncheon  
Nancy M. O'Fallon (Argonne National Laboratory)

Luncheon Speech: Closing Remarks  
Nancy M. O'Fallon (Argonne National Laboratory)

Particulate Measurement and Control

Session Chair: James C. F. Wang (Sandia National Laboratories)

Characterization of Aerosols in Low-Btu Product Gas and Combustion Process Streams R. J. Anderson, J. J. Kovach, U. Grimm, J. O. Mapstone, Jr. (U.S. DOE - Morgantown Energy Technology Center).....	548
---	-----

	<u>Page</u>
Wednesday, June 9 (contd.)	
Particle Size Measurement Using Optical Convolution with a Double-Slit Mask	
D. A. Tichenor (Sandia National Laboratories).....	571
Atomization of Coal-Methanol Slurries	
S. J. Kim, E. Crow, C. T. Crowe (Washington State University).....	580
Particle Collection by Cyclones at High Temperature and Pressure	
J. C. F. Wang, M. A. Libkind (Sandia National Laboratories).....	587
<u>Analysis: Nuclear</u>	
Session Chair: Richard W. Doering (General Atomic Company)	
Progress and Performance of On-Line Analyzers of Coal	
C. M. Spencer, D. R. Brown, T. Gozani, H. Bozorgmanesh, H. Bernatowicz (Science Applications, Inc.), O. J. Tassicker, F. Karlson, (Electric Power Research Institute).....	619
Coal/Stone Monitoring Using Two Energy Gamma Transmission	
J. S. Wykes, G. M. Croke (National Coal Board, England).....	634
Rapid Component Analysis of Coal Samples by Means of Alpha Backscattering	
J. Eddy (Indiana University), K. G. Porges (Argonne National Laboratory).....	643
The Use of Natural Gamma Radiation in the Coal Mining Industry	
J. S. Wykes, I. Adsley, L. R. Cooper (National Coal Board, England).	663
<u>Underground Processes</u>	
Session Chair: Ron Zielinski (Monsanto Research Corporation)	
Instrumentation for Optimizing an Underground Coal Gasification Process	
P. W. Seabaugh, R. E. Zielinski (Monsanto Research Corporation-Mound)	671 -
In Situ Recovery of Bitumen from Oil Sands -- Laboratory Pilot Plant Experience	
D. M. Nguyen, T. R. Heidrick (Alberta Research Council, Canada).....	682
Multiple Tracer Gas Analyzer	
J. E. Uhl (Sandia National Laboratories).....	692 -
Measurement and Evaluation of a Simulated Underground Coal Gasification Experiment by a Microprocessor System	
K. Guntermann, G. Suhens, M. Kurth, F. H. Franke (The Aachen University of Technology, Federal Republic of Germany).....	704
List of Exhibitors.....	714



WELCOMING ADDRESS

Donald L. Bauer  
Deputy Assistant Secretary  
for Fossil Energy  
U.S. Department of Energy  
Washington, D.C. 20585

Good morning.

I am pleased to be here this morning to represent Jan Mares, DOE's Fossil Energy Assistant Secretary, in welcoming each of you. It is a particular pleasure to come down to Houston. I've tried to make this trip on several occasions in the past, primarily to visit the Exxon Donor Solvent liquefaction plant in nearby Baytown. But something always seemed to come up at the last minute to prevent it. I'm pleased that I finally made it, particularly now. With all the turmoil about budgets, deficits, interest rates, and the like -- that's the steady diet for Washingtonians these days -- it is good to escape for awhile.

It's also a particular pleasure to be back among the technical community. As many of you know, I worked for several years in the coal processing part of the Fossil Energy program. Now I'm in what they call a "policy-making" position. I don't get to rub elbows with technicians and engineers as often as I might wish. Instead, I have to deal more with lawyers and economists. Lawyers, they're the ones that if you're driving around hopelessly lost and you stop and ask one where you are, he most likely will respond, "Sir, you are in an automobile." Information? Yes. Useful? Not always.

And economists. They're the ones who have predicted four of the last two recessions.

Of course, I'm being facetious. In fact, if it's one thing we in the technical community have learned in recent times, it is that technology cannot be separated from economics. Technological change most often is driven by the potential for improved economics. And just as often, a technology can be stopped in its tracks if the economics aren't there.

I was as surprised as many of you were last month when Exxon announced it was postponing indefinitely its commercial oil shale project in Colorado. It's no secret that we in the Department of Energy believed this to be an extremely important project, not only because of the technology it would pioneer, but because it seemed destined to break the cycle of false starts that has characterized attempts to build a synfuels industry in this country. Now that it's been shut down, the debate about government involvement in commercializing new energy technologies has been rekindled. How far should this involvement go? What form should it take? Is Exxon's interest the national interest?

These are important questions. Granted, they are beyond the scope of this symposium, but how they are answered will almost certainly impact many of your organizations.

I would like to spend a few minutes bringing out some points that might have been missed in much of the debate, or I might say, the obituaries, that surfaced about the synfuels industry after the Exxon announcement.

First, the idea that it is dead. I would be the first to admit that the Exxon decision gave the synfuels industry a jolt. But it hasn't been fatal. Projects are still moving ahead. The Union shale project, albeit much smaller, is in its major construction phase leading to completion next year. Just within the last couple of months, the Great Plains coal gasification project in North Dakota passed the 33 percent completion stage, counting both engineering and construction. This project will cost in excess of \$2 billion, and those cost projections are holding steady during the construction phase.

The Great Plains plant is scheduled to be on-line beginning in late 1984, with full operation in 1985. In its core will be 14 Lurgi Mark-IV gasifiers -- 12 operating, two on standby -- each 4 stories high, weighing more than 200 tons -- converting 14,000 tons of lignite each day into 125 million cubic feet of synthetic natural gas, the equivalent of 9 million barrels of oil annually. It's an impressive undertaking. And when one recognizes that gasification is an integral part of every coal-based synthetic fuel flow scheme, the importance of the Great Plains project to this country is magnified even more.

Great Plains and Union aren't the only synthetic fuel technologies that are crossing the commercial threshold. Outside Kingsport, Tennessee, the Eastman Kodak company is constructing a coal gasification plant, with no Federal funds, no price or loan guarantees, no government involvement at all. The plant is considerably smaller than Great Plains and less expensive, but nonetheless, it represents a decision by one company that coal gasification is a sound investment. Kodak will use the synthesis gas to make chemicals for its business needs. In that market, in that geographic region, the economics justify moving forward with this first-of-a-kind technology.

Likewise, Dow Chemical apparently believes the economic potential exists for manufacturing fuel gas from coal; so it is involved in a privately-financed gasification pilot project in Louisiana.

Texaco, Southern California Edison, and several other partners are still proceeding with the Cool Water gasification project in California.

Exxon itself has evaluated the market potential in Europe for synthetic natural gas, found it substantial, and is moving ahead with a half billion dollar program to scale up an advanced catalytic coal gasification process in a large pilot plant

Westinghouse is negotiating with the SASOL firm in South Africa to supply a full-size version of their fluidized bed gasifier as a commercial demonstration. British Gas is now offering commercial versions of their Lurgi slagging gasifier. Shell-Koppers likewise is moving on their own.

The point is that industry has never shown a reluctance to invest its own R&D and commercialization funds when there was a reasonable potential to compete in the marketplace and return a profit. The pace of synfuels may have slowed in recent months, but the industry is still alive.

Another point is that the Government still has a mechanism in place to move these vanguard projects off the drawing boards and into construction. The U.S. Synthetic Fuels Corporation has more than \$14 billion to invest in loan guarantees and price supports, or perhaps, to participate in joint ventures. It is now evaluating five finalists from its first round solicitation, and last week, it received 35 more proposals in round number two. These proposals are important, because to be eligible, a firm must be willing to back its project with significant cost and risk sharing. Private financing must account for at least 25 percent of a project's cost to be eligible for a loan guarantee. For a joint venture, it's 40 percent.

A third point is that more advanced technologies are being moved into position to contribute when the investment climate is right. We recently completed the final government co-sponsored test run at the Exxon Donor Solvent pilot plant. During the last two years, more than 8600 hours of data were accumulated on both bituminous and sub-bituminous coals. This month, the plant is operating with private funding to add a third coal to the data base, a Texas lignite.

We will also conclude our involvement this year in the H-Coal liquefaction pilot plant in Kentucky. This technology forms the core of one of the first round finalists now being evaluated by the Synfuels Corporation. Just as the H-Coal technology had its roots in the Federal program, so did the U-Gas process, the basis for the Memphis coal gasification proposal, also one of the five finalists at the SFC. Outside the Department's program, TVA recently achieved the first sustained test run of its 2nd-generation gasifier in Alabama.

How about other fossil energy technologies, other than synthetic fuels? Fluidized bed combustion, for example? Based in large part on the Federal research program, nearly every major boiler manufacturer in the country is now either developing his own atmospheric fluidized bed unit or marketing one commercially. At last count, at least 30 AFB units were either in design, construction, or operation -- all privately financed.

Coal-oil mixtures are now being offered commercially, and if we can establish a sound data base and develop the beneficiation techniques necessary, coal-water mixtures could make an even larger impact. The downhole steam generator for producing deep deposits of heavy oil is now making the transition from Government research to commercial reality. And the list could go on.

So I'm convinced there has been significant technical progress in the fossil energy area. The Colony project aside, we are going to see new fossil technologies come into commercial use in the 1980s. And if they are going to be safe, reliable, economic, and environmentally acceptable, the introduction of effective instrumentation and control systems must keep pace.

As you know, previous pilot and smaller-scale testing of new fossil energy concepts has shown some inherent drawbacks in relying on equipment from other industrial processes. The unique combination of high temperature, high pressure, and the erosive and corrosive environment of many advanced fossil fuel systems places extraordinary demands on instrumentation and controls.



What many of you may not have is confidence that there is going to be a Department of Energy to listen to your ideas and if they warrant, to share the risks of proving their technical viability. Two weeks ago, as many of you read, the President formally sent to the Congress a bill to abolish the Department. But listen to what the President said:

"The legislation that I'm sending to the Hill today will not dismantle the structure of government that we need to fulfill our energy goals. I am urging that the critical defense, energy emergency and research functions be retained in the Department of Commerce." (emphasis added)

In fact, under the proposed legislation, energy is installed as a primary line function of Commerce, not relegated to a secondary role but placed at a level comparable to Commerce's mainline activities. That's how 17 of the 21 member nations of the International Energy Agency organize their government energy program. It makes sense. The industrial and business communities that routinely deal with the Commerce Department are the same communities that represent the end-points of our R&D program -- the communities that must find the research useful if our tax dollars are going to be well spent.

Regardless of whether the legislation passes, the linkage of Commerce and Energy does show one thing: that energy and energy technology in this Administration cannot be dealt with as a separate entity. Economics, environment, government, and industry -- and yes, even lawyers -- have integral roles in the development of new technologies.

That's the importance of a conference like this. It provides a forum for the cross-pollination of ideas and concepts between government and industry. It should help tell us where our program should be focused, to prevent wasteful overlap with the efforts of industry, yet to continue the high-risk research that industry is unwilling or unable to pursue. It should tell us where there are gaps in our data base. It should help us determine the proper melding between our technology centers and the national laboratories.

Most importantly, it hopefully will tell you where there are technological advances that can be picked up and moved into commercial practice. The successful transfer of technology is, after all, our most fundamental objective.

I look forward to meeting with many of you today, and I hope you find your experience here both enjoyable and worthwhile.

Thank you.

The Future of Coal Liquefaction

Paul Wellman  
Ashland Synthetic Fuels, Inc.  
P. O. Box 2166  
Houston, TX 77252

Abstract

Today is still the day of opportunity for the development of coal conversion technology. These technologies must be developed over the next 10 to 15 years.

Such development would place an upper limit on the world price of oil.

The most critical problem area is an assured supply of mobility fuels. The Middle East political instability is of great concern because of the economic repercussions of a prolonged interruption of Middle East oil supply.

Some technologies are well developed for coal liquefaction, and many others are in various stages of development.

Technology is not the constraining factor but, rather, economics. The United States government must create the economic climate necessary to assure development.

SHALE OIL - PRESENT AND FUTURE

James H. Gary  
Chemical and Petroleum-Refining Engineering Department  
Colorado School of Mines  
Golden, CO 80401

The status of the synthetic fuels industry is changing so rapidly it seems that a ticker tape similar to that of the stock market is needed to keep up with it. To put 1982 into the proper perspective, let us take a look at how things were one year ago.

In the Spring of 1981 there was a crude oil shortage, crude prices were high, and there was a large amount of buying crude for storage as insurance against future price increases. Because of these factors and the prediction by the experts that there would be a continuing shortage of crude oil through the 1980's, plans for commercial production of synthetic liquid fuels were being executed as rapidly as practical. The Colony Oil project (Exxon and Tosco) to produce 47,000 barrels per day (BPD) of syncrude from oil shale was operating at full speed with the target of 1985-87 to come on stream at an estimated capital cost of three billion dollars (\$64,000 per BPD). Union Oil Company of California was constructing a 10,000 BPD facility to start production in late 1983 at an estimated capital cost of \$550,000,000 (\$55,000 per BPD). The Cathedral Bluffs project (Occidental and Tenneco) was conducting development operations to produce shale oil by a modified in situ process (MIS) while at the same time they were conducting mining operations on federal lease tract C-b in preparation for producing about 90,000 BPD of shale oil by 1990. Paraho was operating the federal facility at Rifle and was planning a 50,000 BPD operation. Rio Blanco Oil Shale Company (Gulf and Amoco) was preparing federal lease tract C-a for a series of MIS tests. There were also a number of smaller operations under way, including Geokinetics and the Multiminerals operation on the U.S.B.M. Horse Draw site.

By Fall 1981, the situation had changed considerably. There were 160,000,000 barrels of crude oil in floating storage plus larger than usual supplies of crude in refinery and terminal storage tanks. Interest rates were near the 20% level and borrowing money had become very expensive. As a result of a world-wide recession and the high costs of money and crude oils, as well as an increase in the percentage of high-mileage cars on the road, there was a greater than predicted decrease in petroleum consumption and a softening of crude oil prices. As a result there was a dramatic turnaround in the oil shale industry.

During October and November, Multiminerals and Cathedral Bluffs announced changes in their plans. Multiminerals closed their development projects at Horse Draw and Cathedral Bluffs stopped their development operations on Tract C-b. During the first quarter of 1982, world crude purchases decreased even further because of the deepening recession and drawdowns of up to 4,000,000 BPD on crude oil in storage. This caused a further lowering of crude oil prices with some countries selling at below posted prices. Interest rates continued near the 20% level.

On May 3rd, 1982, Exxon announced the termination of the Colony project thus furloughing about 2000 workers. This was followed in a few days by Tosco announcing the sale of their 40% portion of Colony to Exxon. The reasons given by Exxon were the soft crude oil market, the high cost of money, major decreases in profits, and the rapidly estimated costs of construction. The estimated capital costs of the 47,000 BPD plant had increased from 1.5 billion (\$32,000 per BPD) in 1979 to 6 billion (\$128,000 per BPD) by the time the plant would be put on-stream in 1985-87.

Although these shutdowns were a major blow to the developing industry, there were some benefits. The pace at which development was occurring slowed and competition for skilled labor in the area was reduced. As a result, this increased the probability that continuing projects would not significantly overrun budget and would not be terminated. This turn of events also increased the possibility that political attitudes might change to be less restrictive to oil shale development.

At this writing, the only continuing major operation to produce shale oil commercially is that of Union Oil of California. To take advantage of a pool of skilled workers in the area, released when Exxon announced they were furloughing 2,000 workers, Union announced they would be hiring 400 additional workers during the summer months of 1982. Union expects to produce 10,000 BPD of syncrude by late 1983 and they still estimate the capital cost to be \$550,000,000 (\$55,000 per BPD).

Rio Blanco Oil Shale Company is on hold and they have petitioned for a five-year delay in continuing operations. At the time of the lease sale in 1974, tract C-a was leased with qualification that the shale was to be removed by surface mining and retorted above ground with adjacent land to be available for lease to store overburden and site process units. After the lease sale, the Department of Interior reversed itself and stated it did not have the authority to lease the adjacent land. Since that time, attempts have been made to pass Congressional legislation which would permit the leasing of adjacent land by Rio Blanco but these attempts have been unsuccessful. The use of surface mining would greatly decrease mining costs and increase resource recovery. About 90% of the resource can be converted to shale oil by surface mining and retorting while less than 60% can be recovered by other methods. It appears that Gulf and Amoco believe the only feasible operation is by surface mining and retorting and without the required legislation they will not proceed. They have tested MIS retorting on-site and are constructing a small Lurgi-Ruhrgas retort at their research facility at Hamarville, PA.

Other projects still active include the Paraho-Ute, Geokinetics, and White River Oil Shale projects in Utah and Chevron and Mobil projects scheduled for Colorado. With the exception of the Geokinetics process these are all in the early stages of operation and are a number of years away from commercial operation.

Paraho is seeking a loan guarantee from the Synthetic Fuels Corporation (SFC) and plans to build a 10,000 BPD retort module on their tracts near Vernal, Utah.

Geokinetics has applied for SFC support for a 2000 BPD operation on Utah oil shale lands.<sup>4</sup> This would be in the form of five 400 BPD in situ retorts. The Geokinetics retorts are best suited for shallow, thin, horizontal seams of oil shale. Explosives are used to raise the surface of the ground to create avenues of communication needed to get the heat in and the oil out.

The Defense Department has requested bids to supply 120 million gallons of jet fuel from oil shale over a four-year period (equivalent to 2000 BPD) and it is reported that Geokinetics is joining with a refinery to bid on this.

The White River Project is just getting underway. This is a joint venture owned by Phillips Petroleum, Sun Oil, and Sohio. Eventually production is planned to be about 106,000 BPD.<sup>4</sup>

Chevron is constructing a 290 BPD fluidized pilot plant at their Salt Lake City Refinery. Their long-range plans are to start commercial production in the late 1990's if all goes well.

Mobil is in the preliminary stages of an engineering design for a 50,000 BPD shale operation in the 1990's. Discussions have started with the communities on Colorado's Western Slope but it is in a very preliminary state.<sup>4</sup>

The oil shale lands of Exxon, Union, Chevron, and Mobil are all in the Parachute, Colorado area. This concentration creates additional problems with respect to socio-economic impacts on the existing communities when oil shale development occurs. This emphasizes the need for close coordination of all phases of development.

So much for the past and the present - what does the future hold for commercial production of shale oil? Political considerations (war or peace in the Middle East, OPEC unity, anti-industrial activism, etc.) affect shale oil development greater than any one other factor and these are almost impossible to predict with any degree of certainty. Instead, a look at the characteristics of the technical and economic aspects of shale oil production will give an idea of the feasibility of a shale oil industry.

Raw shale oil is not a good refinery feedstock because of its high nitrogen, arsenic and olefin contents. Because most U.S. refineries would not be able to process raw shale oil, most of the companies involved in oil shale development are planning to produce a hydrogenated shale oil called Syncrude and capital costs for oil shale plants include the equipment for hydrogenating raw shale oil to Syncrude. Therefore, the characteristics of Syncrude, rather than raw shale oil, should be compared with conventional U.S. crude oils.

Syncrude is a premium quality crude oil because it has low sulfur, nitrogen, and metals contents and very little high boiling material. In the U.S., the only high volume refinery products which sell for a profit are those boiling between 32 F and 650 F. Components boiling above 650 F are

either converted to materials boiling between 32 F and 650 F or sold for a lower price per gallon or per pound than was paid for crude oil. For many years, U.S. refineries have been using catalytic cracking processes to convert gas oils boiling between 650 F and 1050 F to gasoline but there have not been processes to convert the portion of the crude oil boiling above 1050 F (called vacuum reduced crude (VRC)), with high sulfur, nitrogen, and metals contents to profitable products economically. The cost of VRC conversion is high in terms of both capital and operating costs especially for some of the heavier Texas and California crude oils containing large amounts of sulfur and metals. These crudes contain from 30% to 50% VRC.

Syncrude has an initial boiling point of about 350 F and an end point about 1000 F. This means there is very little gasoline in Syncrude but most (about 65%) is in the diesel and jet fuel boiling ranges (350 to 650 F). Air force tests indicate that these fractions require very little upgrading to produce a satisfactory product. Union and Amoco have developed catalysts that can convert all of the shale oil directly to diesel and jet fuel by hydrogenation. Therefore, it does not have the problem of converting or disposing of the VRC.

The cost of producing Syncrude from oil shale is estimated to range from \$30 to \$42 per barrel depending on the location, the process, and the estimator. This would be competing (in 1982 dollars) with sweet crudes selling in the \$35 to \$38 range.

It is difficult, and sometimes misleading, to make comparisons between shale oil costs and crude oil costs because the costs are usually expressed differently. For example, in 1978, the cost of finding and developing a barrel of new crude oil in the U.S. was \$15.<sup>1</sup> At the same time, the cost of a barrel of shale oil was said to be \$30,000 per barrel per day (based on a capital cost of \$1.5 billion for a 50,000 BPD shale oil facility). This high front end cost was given as a major deterrent factor in shale oil development. To put them on the same basis, let us convert the cost of a barrel of new U.S. crude oil to a barrels per day figure.

The minimum life of a shale oil facility is 20 to 30 years. For a twenty-year life, it will be producing a barrel per day for 7300 days or a total of 7300 barrels of shale oil per BPD capacity. At \$15 cost per barrel of new oil, the front-end cost to find a BPD for 20 years is \$110,000 more than three times the front-end cost of a shale oil facility.

The 1981 estimated cost for finding a new barrel of oil in the U.S. was \$22 per barrel<sup>2</sup> or \$160,000 per BPD for 20 years. In 1981, Union Oil and Exxon were estimating \$55,000 and \$110,000 respectively, per BPD for a shale oil facility. Either of these look very good with respect to the cost of a BPD of new U.S. crude.

The costs of finding a barrel of new crude oil in the U.S. during the later part of the 1980's (when Exxon's Colony operation was scheduled to be in production) is estimated to cost about \$100.<sup>3</sup> This gives a front-end cost of \$730,000 per BPD for 20 years for new U.S. crude. Exxon estimated the 1985-87 cost of a 47,000 BPD Syncrude facility to be about \$6 billion

including interest costs. This is about \$128,000 per BPD for 20 years. It follows, therefore, the estimated front-end cost of a new barrel of U.S. crude is almost six times as high as that of shale oil.

These figures cannot be compared directly because the U.S. tax structure is not the same for the two facilities and benefits crude oil production when compared with production of shale oil. For example most, if not all, of the finding costs for new oil can be expensed. There is no finding cost for oil shale so it cannot benefit from this because all of its front-end costs are capitalized. This amounts to about half of the cost of a new barrel of oil (the other half is site-well drilling, collection facilities, etc.) and means that the actual cost to the company in terms of dollars output is on the average only about 50% of the actual cost. Even so, the cost of a new BPD of shale oil is considerably less than the cost of a new BPD of new U.S. crude. If the life a facility is considered to be 30 years then shale oil looks even better.

Operating costs are higher for shale oil than for new crude during the years it is free flowing, but secondary recovery costs approach the operating costs for Syncrude production, and tertiary recovery costs are higher.

Another aspect of the costs of shale oil is that during the early years of production more than half of the cost of a barrel of raw shale oil is due to depreciation and return on investment. Once the facility is built this remains a constant value and is not affected by rising operating costs or inflation; only the direct operating costs will increase. The result is the gross cost of producing a barrel of shale oil or Syncrude over the years the facility will be operated will decrease relative to conventional crude oil.

The disadvantages of shale oil as compared with crude oils are the long lead times required (about 10 years), tax discrimination in favor of conventional crude oils, the unresolved environmental issues, and the strong vocal resistance of relatively small anti-technology groups which affects all political issues.

The long lead times are due to a number of factors. One is the amount of background work that has to be done to act as a basis for environmental impact studies and the issuance of environmental permits. Another is due to the large number of permits (100 to 200) that must be obtained from federal, state, and local authorities. Some permits have to be obtained in sequence so that applications cannot be made until other permits have been granted. Also, many of these permits do not have a legal limit as to the time the issuing agency has to take action and work can be delayed by the unwillingness of an individual to take action even though there is no basis for not awarding the permit.

Unresolved environmental issues can have a major effect on costs because a facility built to conform to existing regulations may not be able to operate because of new regulations put into effect during construction or after startup. An example is the required visibility regulation which has not as yet been specified. Typical visibility on the Western

Slope is well over 100 miles and the law specifies "no significant deterioration". At this time there has been no definition of "significant deterioration" or how it is to be measured. If a specific mileage decrease is set based on Eastern U.S. standards, where good visibility is 25 to 35 miles, the results may be prohibitive to any type of industrial operation on the Western Slope. Other EPA standards have been changed so that trying to conform to standards represents shooting at a moving target.

The significant advantages of shale oil production include no finding costs, large shale resources in the Rocky Mountain Area with recoverable amounts of oil equal to the world's conventional crude oil reserves, secure access in time of national defense, high yields of middle distillates (diesel and jet fuel) which are critical for national defense, and a decrease in the federal balance of payments deficit because of displacement of purchases of foreign crude.

The development and operation of a commercial size retorting module by Union Oil of California will give economic, environmental, and technical data not heretofore available. This should give impact data on which to base future designs and greatly reduce the risk of investment in shale oil facilities and give cost data which can have significant impacts of foreign crude oil pricing policies. The history of oil shale has been a roller coaster of ups and downs mainly due to political events not under the control of industry. Now, of course, is one of the downs but it is encouraging that work is continuing although at a slower pace than may be desirable from a national security viewpoint. The 1980's may be the period of the slow emergence of a small but viable commercial shale oil industry.

#### References

1. R. E. Megill, "Problems in Estimating the Cost of Finding Oil and Gas", World Oil, May, 1981, 171-175.
2. R. McNally, Petroleum Engineer, January 1982, 21-26.
3. J. D. Haun, Presidential Lecture, American Association of Petroleum Geologists, 1980.
4. J. H. Jennrich, "Uncertainty, Cost/Price Freeze Hit Fledgling Synfuels Industry", Oil & Gas Journal, May 24, 1982, 21-25.



MASS FLOW MEASUREMENT OF SOLIDS/GAS STREAM USING  
RADIOMETRIC TECHNIQUES\*

James K. Linn<sup>†</sup> and David G. Sample  
Sandia National Laboratories  
Process Research Division 4746  
Albuquerque, NM 87185

Abstract

A mass flowmeter utilizing radiometric techniques has been designed and built for measuring flows in two phase gas/solids feed streams in coal gasification processes. The instrument combines a radiometric density measurement and a time cross-correlation velocity determination into a non-intrusive gas/solids mass flowmeter. Accuracies of 5 to 10 percent are anticipated for flow with 10% solids fraction and velocities of one to five meters per second. This paper describes the theory, the relevant radiometric cross-sectional background data, and the developed system digital data handling.

Introduction

Several advanced entrained-bed coal gasifiers utilize gas-motivated dry coal or char as the fuel stream. Lack of accurate measurement of the coal or char mass flowrate is a common problem. Real-time mass flow data are required for process control

Existing mass flow instrumentation utilizes one of several techniques, including:

1. Measurements of the cross-section density via the dielectric constant of the solids;
2. Direct measurements of the force produced during angular acceleration of the mass (Coriolis flowmeter)<sup>1</sup>;
3. Load cell measurements or auger feed rates; and
4. Pressure drop measurements through orifices.

Other techniques have been investigated with some degree of success. The problems with the techniques mentioned above are numerous. Dielectric constant measurements perform adequately up to about 7% moisture in coal/char. The change in dielectric constant due to the solids then becomes masked by the moisture. Coriolis meters do not currently exist for high temperature applications. Also, test data at low temperatures show unsteady behavior for certain flow regimes<sup>2</sup>. Load cells and auger feed

---

\* This work supported by the U.S. Dept. of Energy under Contract DE-AC04-76DP00789.

<sup>†</sup> Presenting author.

readouts in general are either too slow or too remote for most control applications. Pressure drop measurements are limited at higher solids fractions and are limited to certain coal size.

### Present Approach

In this paper, we describe a new mass flowmeter which has been developed and is currently being tested. The flowmeter measures mass flow indirectly by combining a nuclear radiation transmission-derived density measurement with a time cross-correlation velocity determination. The advantages of this technique are (1) it is non-intrusive to the flow stream, (2) it is applicable at high temperatures and high pressures, and (3) it is potentially accurate to within 5 to 10 percent. The inherent disadvantages are that the technique provides an indirect measurement of mass flow, which is dependent upon other influences, and the technique relies on natural density variations in the solids flowrate which will be somewhat unique to individual applications.

### Discussion

As stated previously, the mass flowmeter described in this work combines a density measurement via nuclear radiation transmission with a stream velocity determination via time cross-correlation of natural density variations. We will first establish the theoretical basis, and known properties of the materials. Consider the transmitted intensity of an incident beam of a high energy nuclear source through an empty steel pipe (see Figure 1):

$$I_{\text{out}}(E) = I_{\text{in}}(E) \exp \left\{ -2t \rho_{\text{st}} \left( \sum_i (\mu_i / \rho_i) \omega_i \right) \right\}$$

where  $I_{\text{in}}(E)$  is the incident intensity at energy  $E$ ,  $t$  the pipe wall thickness,  $\rho_{\text{st}}$  the volume density of the steel ( $\approx 7.9 \text{ gm/cm}^3$ ),  $\mu_i / \rho_i$  the total cross-section of the  $i$ th elemental component of the steel (energy dependent) and  $\omega_i$  the mass function of the  $i$ th component.

Table 1 lists the mass fractions,  $\omega_i$ , and subsequent elemental and total cross-sections for type 316 stainless steel (commonly used in fossil energy applications) as a function of photon energy for energies between 70 and 500 keV.

Table 2 summarizes the resulting attenuation coefficients and transmission fractions for various pipe wall thicknesses (assuming the beam diameter is significantly less than the pipe diameter). As is apparent from the data, x-ray energies above 100 keV are necessary to achieve a reasonable transmission. The pipe size selection is more important for the lower energy cases considered.

Table 1. Mass Fractions and Total Elemental X-ray Cross-Section for 316 Stainless Steel

Element	Mass Fraction $\omega_i$	Total X-Ray Elemental Cross-Section			
		E=70 keV ( $\text{cm}^2/\text{gm}$ )	100 keV ( $\text{cm}^2/\text{gm}$ )	200 keV ( $\text{cm}^2/\text{gm}$ )	500 keV ( $\text{cm}^2/\text{gm}$ )
C	.0008	*	*	*	*
Si	.0075	.002	.001	.001	*
P	.0004	*	*	*	*
S	.0003	*	*	*	*
Cr	.1900	.114	.055	.025	.017
Mn	.0200	.013	.006	.003	.002
Ni	.1400	.113	.059	.021	.013
Cu	.0050	.005	.002	.001	*
Mo	.0300	.038	.030	.007	.003
Fe**	.6060	<u>.454</u>	<u>.212</u>	<u>.085</u>	<u>.048</u>
Total		.76	.37	.14	.083

\* < .001.

\*\* Difference

Table 2. X-ray Transmission Through 316 Stainless Steel Pipe (Fraction) (Density: =  $7.9 \text{ gm/cm}^3$ )

Pipe Wall Thickness (cm)*	Energy			
	70 keV	100 keV	200 keV	500 keV
.635 (1-1/4", Sch 160)	.00049	.024	.245	.435
.555 (3/4", Sch 160)	.0013	.039	.293	.482
.485 (1-1/4", Sch 80)	.0030	.059	.342	.529
.455 (1", Sch 80)	.0042	.070	.365	.551
.391 (3/4", Sch 80)	.0091	.102	.421	.599

\* Transmission is through two wall thicknesses.

In gas-motivated-solids feed systems, coal or char (devolatilized coal) occupies up to 20% by volume of the pipe. Analogous to Table 1, elemental total cross-sections for a selected coal type are given in Table 3, and the resulting x-ray transmission factor for the coal in typical process pipe sizes is given in Table 4. In contrast to steel, the transmission through coal is considerably less energy-dependent, and greater than 50% between 70 keV and 200 keV. As corroboration of the theoretical data, experimental intensity vs. mass density using a mono-energetic x-ray beam of 70 keV has been measured for a Montana Rosebud coal sample and a pure graphite<sup>(3)</sup>. The calculated total cross-section (i.e., slope) values are slightly greater than experimentally measured for a 70 keV source. Experimental calibration of the transmission vs. the density for actual coal or char may be necessary to eliminate this uncertainty in the field.

Accuracy of the mass density measurement is dependent upon calibration accuracy and signal/noise ratio. In radiometric applications with reasonably high source intensities, the predominant noise contribution is from the statistical fluctuations

Table 3. Elemental Mass Fraction and Total X-ray Cross-Section Absorption Coefficients - Montana Rosebud Coal\*

Element	Mass Fraction ( $\omega_i$ )	Elemental Cross-Section ( $\text{cm}^2/\text{gm}$ )			
		70 keV	100 keV	200 keV	500 keV
C	.684	.109	.103	.082	.062
H	.047	.015	.014	.011	.008
N	.010	.002	.001	.001	.001
Mg	.0022	**	**	**	**
Al	.0091	.002	.001	.001	.001
Si	.0175	.004	.003	.002	.001
S	.0076	.002	.001	.001	**
Ca	.0158	.007	.004	.002	.001
Ti	.0007	**	**	**	**
Fe	.0048	.004	.002	.001	.001
O <sup>†</sup>	.201	.032	.030	.026	.017
Total		.18	.16	.13	.092

\* Bulk Density  $\approx 1.2 \text{ gm/cm}^3$

\*\* < .001

† Difference

Table 4. Transmission by Coal (20% by Volume) for Various X-ray Energies

Pipe ID (cm)	Energy			
	70 keV	100 keV	200 keV	500 keV
2.95 (1-1/4", Sch 160)	.58	.77	.91	.94
3.25 (1-1/4", Sch 80)	.55	.75	.89	.93
2.43 (1", Sch 80)	.64	.80	.92	.95

in the beam, i.e., shot noise. Shot noise is approximately equal to  $K_1 (\eta T)^{1/2}$ , where  $K_1$  is a constant, and  $\eta$  is the received count rate and  $T$  the counting period. Since a "signal" is the difference in received counts, i.e., scalable to " $\eta T$ ", signal/noise is proportional to  $(\eta T)^{1/2}$ . Given that  $\eta$  is constant for a measurement period of interest,  $T$  can be selected of sufficient duration, such that signal/noise is large, the density measured averages over the density fluctuations, and the accuracy is limited by experimental calibration, currently estimated to be in the order of 5%<sup>2</sup>.

Consider next how we determine the velocity of a solids/gas stream, Figure 1, with average velocity  $\bar{v}$ . The mass flow at location 1 is given as follows (neglecting absorption by gases):

Measured mass density (MMD) =  $\bar{\rho} d$ , where  $\bar{\rho}$  is the mean solids density,  $d$  is the tube inner diameter.

$$\bullet \bullet \text{Total Mass} \approx \bar{\rho} \frac{\pi d^2}{4}$$

where skin effects within the pipe are assumed to be compensated for in the "calibration" of the MMD. (Note: The radiometric beam diameter is much smaller (approximately one-fourth) than the pipe inner diameter.)

Natural density variations occur in coal solids feeding systems<sup>1</sup>. The relative magnitudes of the density variations have been estimated at greater than 20% of the flow, although this is not well documented due to the difficulty of real-time measurements.

The time-dependent mass at location 1, see Figure 1, can therefore be given by:

$$\text{Mass}_1(t) = \bar{\rho} \frac{\pi d^2}{4} (1 + f(t)) , \quad f(t) \approx .2$$

where  $f(t)$  is used to describe the time varying portion of the solids feed, i.e.,  $f(t)$  has zero mean.

The mass at location 2 is given by

$$\text{Mass}_2(t) = \bar{\rho} \frac{\pi d^2}{4} (1 + f(t - \frac{\ell}{v})) ,$$

where  $\ell$  is limited to separation distances such that significant mixing of the solids does not occur, i.e.,

$$f(t) \approx f(t - \frac{\ell}{v})$$

Taking the time cross-correlation of the two mass signals gives

$$F(T) = \int_p (\text{mass}_2(t-T) \cdot \text{mass}_1(t)) dt ,$$

where  $p$  is the integration period, and in practice  $10 \frac{\ell}{v} < p$ .

The separation distance,  $\ell$ , should be chosen as long as possible (to minimize the effect of measurement uncertainty in  $T$ , see below) and still maintain a recognizable correlation between the signals received. Mixing within the pipe will destroy any recognizable correlation if the separation distance,  $\ell$ , is too long. The test program underway will define limits on  $\ell$ . The cross-correlation is then given by

$$F(T) = C \int_p (1 + f(t-T-\frac{\ell}{v})) \cdot (1 + f(t)) dt$$

where  $C$  is a constant. Thus,

$$F(T) = C \int_p f(t-T-\frac{\ell}{v}) \cdot f(t) dt$$

Taking the maximum of  $F(T)$ , we have

$$\text{Max } F(T) = F(T') = C \int_p f(t)^2 dt, \quad T' = \frac{\ell}{v}$$

Given values of  $F(T)$  versus time,  $T'$ , can be found. The mass flow rate (MFR) is then given by

$$\text{MFR} = \frac{\text{MMD}}{d} \cdot \frac{\pi d^2}{4} \cdot T' = \text{MMD} \cdot \frac{\pi d}{4} \cdot \ell/T'$$

In the mass flowmeter developed by us, a programmable computer/controller, in combination with two interval counters,

is used to simultaneously store the nuclear counts received per sampling interval at both locations for a period P in two arrays (A( $\eta$ ), B( $\eta$ )). The maximum product is then found with a corresponding time delay or sample number "j".

$$\text{Max}_{j=1, \eta} \left( \sum_{i=1}^j (A(i) \cdot B(i+j)) \right), \text{ where}$$

$$B(i+j) = B(i+j-n) \text{ for } i+j > n$$

The delay, T, is then given by

$$T = \frac{j}{S}, \text{ where } S \text{ is the sampling rate.}$$

The system block diagram is shown in Figure 2.

### Design Considerations

From cost and stability considerations, radiative sources were selected over high energy x-ray generators (see Table 5). Cs<sup>137</sup> is an appropriate source due to its long half-life and energy spectrum (510 keV peak). In the time cross-correlation electronics, the design is a compromise between (1) a desirable high sampling rate (short counting interval), for accuracy, and (2) detectability of the variations in the coal feed, i.e., longer counting intervals.

Testing of the prototype flowmeter is currently in progress in a solid/gas flow test facility. The design accuracy includes anticipated uncertainties in the velocity or time delay measurement equal to the sampling interval, and in the mass determination equal to the density calibrations, Figure 3. It has been assumed uncertainties in the time delay measurement due to quantization are uncorrelated with uncertainty in the mass density measurement.

### Conclusions

We have developed a radiometric mass flowmeter for gas-motivated solids streams, specifically, coal or char feed streams for coal gasification. The flowmeter uses a radiometric technique and is applicable in high temperature, high pressure

---

Table 5. Design Characteristics

Source	100 mCi Cs <sup>137</sup>
Scintillator	BGO
Detector	PM tube
Sampling Interval	20-40 ms (selectable)
Total Sampling Period	2 s
Detector Spacing	1 meter (selectable)

---

applications where nonintrusive flow measurements are necessary. In general, no modifications to existing plant hardware are necessary to utilize the flowmeter. Laboratory measurements have been made to verify the nuclear cross-sectional data for a single coal sample, and flowmeter testing is in progress. The flowmeter has a potential accuracy of between 5 and 11 percent over a flow velocity range of 1 to 5 meters per second.

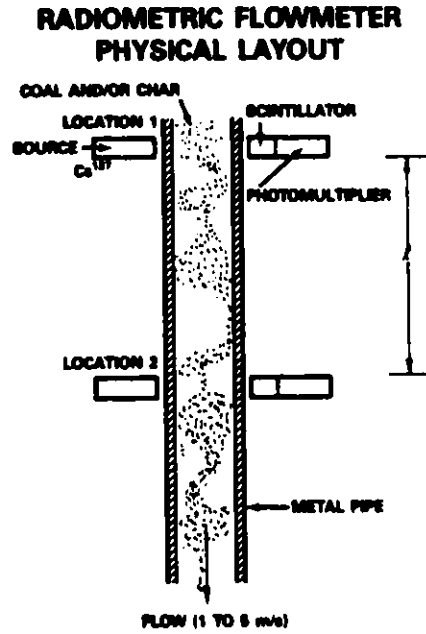


Figure 1.

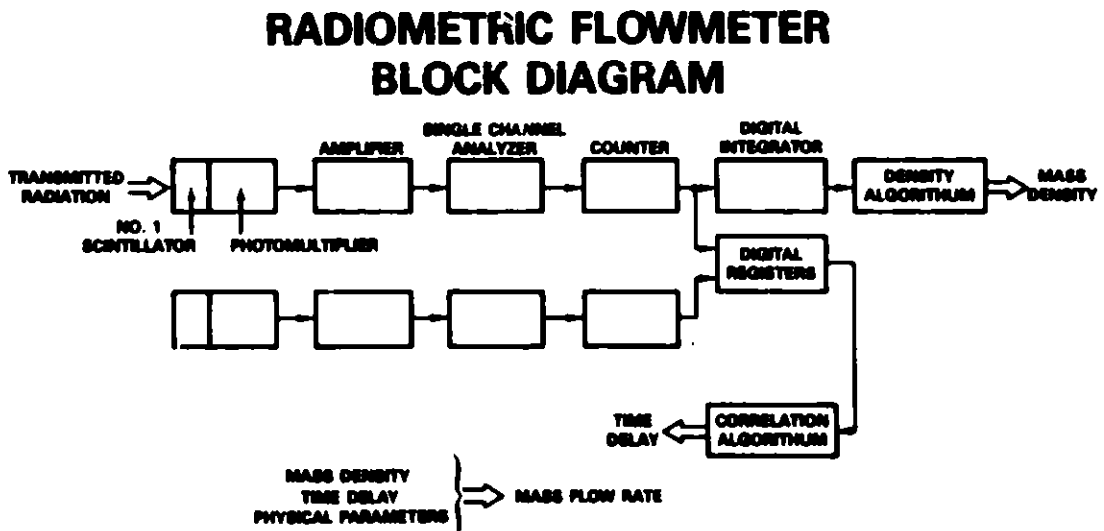


Figure 2.



## FLOWMETER DESIGN ACCURACY

### RADIOMETRIC FLOWMETER DESIGN ACCURACY VERSUS FLOW VELOCITY

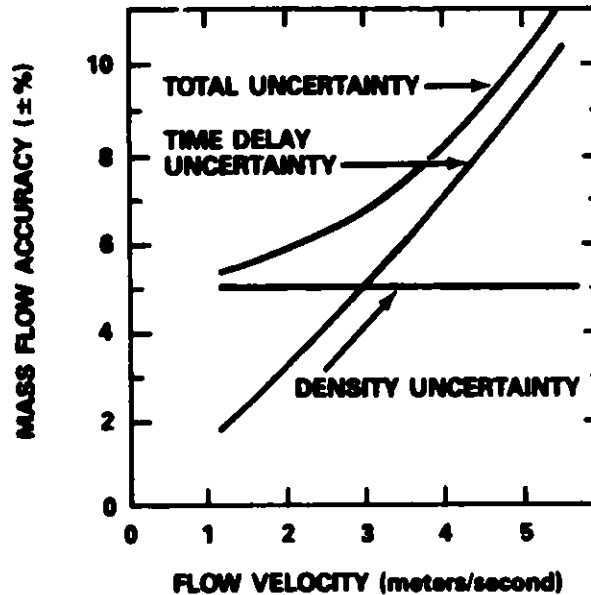


Figure 3.

### References

1. Biggs, F. and Lighthill, R., "Analytical Approximations for X-Ray Cross-Sections II, SC-RR-71-0507, December 1971.
2. Mathur, M., "Evaluation of Modified C-type Micro Motion Device," PETC Coal-Flow Test Facility, October - December 1981, pp. 4-7.
3. Castle, J. G., Stoker, G. C., Sample, D. G., Thomas, M. G., and Linn, J. K., "Preliminary Evaluation of a Radiation Gauge for Coal/Char Density Measurements for Coal Gasification Applications," Sandia National Laboratories Report SAND-81-1819, February 1982.

## SOLIDS FLOW CONTROL AND MEASUREMENT IN THE PEATGAS™ PILOT PLANT PROGRAM

S.J. Wohadlo, R. Biljetina, R.M. Laurens and R. Bachta  
Institute of Gas Technology  
3424 S. State St.  
Chicago, IL 60616

### Introduction

Peat gasification research began at IGT in 1974 under the sponsorship of the Minnesota Gas Company (Minnegasco). Sponsorship has since grown to include the U.S. Department of Energy (DOE), the Gas Research Institute (GRI) and Internorth (a parent company of Northern Natural Gas Co). In 1980 the program was expanded to pilot plant scale to further develop peat gasification technology. A large coal conversion pilot plant facility (formerly the HYGAS pilot plant) located at IGT's Energy Development Center was modified in 1981 to test IGT's PEATGAS process. A 1-year operating program was just recently completed.<sup>1</sup>

In a pilot plant program, the measurement and control of major process variables such as flow, temperature, pressure, density and level are essential to develop accurate material balance and reliable scale-up data.<sup>2</sup> Of these, solids mass flow metering and control usually present the most difficult application. Problems are encountered because of a) solids characteristics, which can cause erosion and plugging; b) measurement requirements, which are often at elevated pressures and temperatures; and c) changes in stream characteristics, such as density, viscosity and solids concentration.

This paper reviews the approaches used to measure and control solid-liquid and solid-gas mixtures and elaborates on the design, installation and operating experiences of a lockhopper dry feed system commissioned to control solids feed to the gasifier.

### PEATGAS Process

Peat is classified a geologically young coal and is currently used in Europe as a source of fuel, electric power and chemicals. In the United States, peat is found in all 50 states. Of these, Minnesota has the second largest peat reserves totaling about 16 billion tons. In some states, peat represents the only significant energy resource available.

The PEATGAS process is an alternative means for the production of substitute natural gas (SNG) using a peat feedstock. The process uses a three-zone, fluidized-bed reactor to convert the carbon and volatile matter in the peat to methane and liquid fuels by hydrogasification at operating temperatures up to 1700°F and pressures of 500 psig. Figure 1 is a flow diagram of the process.

### Solids Measurement and Control

The main area of experimental study is the PEATGAS reactor. To close the balance around the gasifier a number of process streams must be measured.<sup>2,3</sup> Three streams, composed of solids-liquid and solids-gases mixtures, entering and leaving the gasifier are particularly important and are shown in Figure 2. Methods used in measuring and controlling these multi-component streams are presented. Information describing other instrumentation applications has been published in papers pertaining to the HYGAS pilot plant.<sup>2,3,4</sup>

### Solids-Liquid Measurement and Control

The PEATGAS reactor has two solids discharge streams. Both streams exit as a solid-liquid slurry that must be let down in pressure to dispose of the solids residue.

The reactor off-gas contains entrained solids that are removed by a cyclone. Solids exit the cyclone and flow by gravity into a tank where they are cooled by mixing with water to form a slurry. The slurry level in the tank is controlled by throttling a high-pressure letdown valve. (This valve made by the Willis Oil Tool Co., is known as a Willis choke.) The choke is an M1 model and consists of two tungsten-carbide circular discs and a pair of 1/4-inch diameter orifices. With one disc fixed in the valve body, the other can be rotated 90 degrees to open or block the flow. IGT's improvements to the choke's trim design increased the valve's operating life and reduced its maintenance.<sup>4</sup>

The slurry stream consists of fine solids (95% -100 US Sieve size). Solids loading varies between 2 and 10 wt % in the slurry. The flow is measured after the pressure is reduced by a 1-inch magnetic flow meter. Since this device gives volumetric output, solids concentration and composition are obtained by automatic sampling at pre-set, timed intervals.

The second reactor outlet stream contains ash discharge from the bottom of the gasifier. Ash is automatically dropped out of the char gasifier by regulating a solids control valve. The ash is conveyed with steam into a tank where the steam is condensed and the solids cooled by mixing with water to form a slurry. Once again the slurry level is automatically controlled with a Willis choke valve. A pair of 1/2-inch diameter orifices are used for flow control in the tungsten-carbide discs.

Solids loading varies between 5 and 20 wt %. Flow is measured by a high-pressure venturi. The venturi pressure taps require water purges to prevent plugging. Solids concentration is obtained using the method previously described. In addition, a continuous, on-line gamma-radiation density detector is attached to the 1-1/2-inch Schedule 160 slurry pipe. This meter uses a Cesium 137, 100-millicurie source and is calibrated for a 0.9 to 1.1 S.G.U. span. Satisfactory results have been obtained, however, sporadic operation has been observed and is believed to be caused by trapped gas bubbles flowing in the pipeline.

### Solids-Gas Measurement and Control

Measurement and control of solids entering a high-pressure system are essential to pilot plant and future commercial operations. In the PEATGAS pilot plant program IGT installed, started-up and demonstrated operation of one such technique — a lockhopper dry feed system.

In the coal gasification program, a slurry technique was used to feed solids into the high-pressure reactor.<sup>3</sup> However, a dry feed method was preferred in the peat program because of favorable economics. Design criteria were developed for the system (Table 1).

Table 1. Design Criteria for Dry Feed Material

- Provide a continuous solids weight-rate measurement.
- Accurately measure the batch weight of solids to within +1% (of batch weight).
- Compensate weight-rate measurement for accurate and reliable operation over a range of process parameters.
- Feed solids at controlled rates between 1 and 4 tons/hr at operating pressures to 500 psig.
- Prevent bridging, ratholing or segregation in feed equipment due to variable feedstock characteristics.
- Scale-up to commercial-size plants.

After carefully evaluating state-of-the-art, dry feed systems, IGT chose Petrocarb, Inc., to manufacture the system for the pilot plant because of their experience in similar applications.<sup>5</sup>

#### Lockhopper Dry Feed System Description

The lockhopper dry feed system, referred to as a solids injection system by the manufacturer (Petrocarb, Inc.), automatically feeds peat at controlled weight-rates against pressures up to 500 psig. A simplified equipment diagram for the peat lockhopper feed system is shown in Figure 3. It consists of two specially designed vessels, the primary and storage injectors, that have nominal capacities of 5000 and 2500 pounds of peat, respectively. The storage injector, used to pressurize the peat from atmospheric to gasifier pressure, is filled from a 16-ton live-bottom bin with a scalping screen that removes the oversize. Peat in the storage injector is automatically transferred to the primary injector whenever the primary injector can accept a 2500-pound storage injector batch.

The primary injector is the system feeder and delivers a continuous flow of peat to the gasifier through a pneumatic conveying line. Peat is discharged from the primary injector under weight-rate control. Solids flow control is achieved without the use of a mechanical rate controlling device.

### Dry Feed System Instrumentation

Filling the storage injector and the transfer of material between the storage and primary injectors are automatically sequenced by hard-wired electromechanical relays. The relay logic incorporates all safety and process interlocks to ensure reliable and continuous lockhopper operation. Interfacing with the relay logic are Foxboro Spec 200 electronic analog controls, which handle all analog signals, computational requirements and automatic control functions for the feed system. Figure 4 shows a simplified schematic of the weight measurement and control portion of the system.

The storage and primary injectors are independently weighed on A.H. Emery Company hydraulic load cells. An expansion joint between the two vessels provides the freedom of movement necessary for independent weighing. All auxiliary piping and electrical tie-ins to both vessels are arranged to provide sufficient flexibility for accurate weighing. The weight signal from each injector is compensated for the pressure and spring thrust generated by the expansion joint and also for the weight of the injector and the weight of gas in the injector. The storage injector weigh instruments record the weight of each batch of peat and the total weight of peat fed during a test run. The primary injector weigh instruments control and measure the feed rate of peat to the gasifier through cascade control of the pressure differential between the primary injector and the gasifier.

The feed system uses Kamyrr ball valves for peat lockhoppering in the storage injector. Most other feed system valves in on-off service are Kamyrr valves. These valves have stainless-steel balls and seats and were tested at the factory for gas-tight sealing capability.

The injectors are enclosed in a sided structure to prevent wind loads from affecting the weight readings. The injectors are supported on a second smaller structure within but remain independent of the sided structure to prevent vibration and side loads from affecting the weight readings.

### Operating Experience

IGT began commissioning of the dry feed system in November 1981 with the shakedown of the lockhopper logic sequence. Although the electromechanical relay logic had been shop assembled and shop tested, interface problems arose when the control logic was tied into field sensors, field actuators and Foxboro controls. The problems were systematically identified and corrected.

With the logic sequence debugged, a calibration of the weighing system was attempted. Several problems became apparent. Process piping, control wiring and instrument air tie-ins to both injectors had to be reworked to increase their flexibility and minimize weighing errors. The expansion joint between both injectors was reworked to eliminate mechanical drag, which caused weighing system hysteresis. The expansion joint spring rate compensation instrumentation was reworked

because the actual spring rate of the expansion joint was higher than originally specified by the manufacturer. After solving these problems, the weigh system was calibrated.

Several additions were made to the feeding system during system start-up. Drexelbrook radio frequency level probes were added to both injectors to allow the lockhopper sequencing logic to operate under weight control or under level control. This modification increased the system's flexibility. Computerized data logging of feed system pressures, temperatures, weights and flows was added to facilitate data collection. Finally, a valve positioner was added to the pneumatic transport line differential pressure control loop to increase its response speed and provide more accurate valve positioning.

Two successful gasification tests were completed with the new dry feed system. The first test was made in December 1981 and the second in March 1982. Figure 5 shows the weight of peat versus time tracing in the primary injector for a 3-hour period during the March test. The weight of peat in the primary injector rises rapidly during solids transfer from the storage injector and falls off gradually during approximately a 1/2 hour of continued peat withdrawal. Approximately 2200 pounds of peat are added in each of these cycles giving a gasifier feed rate of approximately 2.2 tons/hr. Figure 6 shows the transport line pressure differential versus time for the same time period. The pressure differential is essentially constant. The system performance record to date is presented in Table 2.

Table 2. Dry Feed System Performance

Total Number of Cycles	335
Total Peat Fed, tons	365
Operating Pressure, psig	300-500
Feed Rate, tons/hr	1-2.5
Operating Time, hr	225
Peat Moisture Content *, wt %	10-30

\* (wet basis)

#### Summary

Accurate and reliable solids flow measurement and control was achieved during the operation of the PEATGAS pilot plant. Standard instrumentation, modified to meet process requirements, was used to measure multi-component flows of solid-gas and solid-liquid mixtures. In addition, a lockhopper feed system using an innovative solids rate control and measurement technique was installed, commissioned and operated.

IGT as a process developer will continue to look for new or improved instrumentation that might be better suited to measure important process variables such as the solids mass flow applications discussed herein.

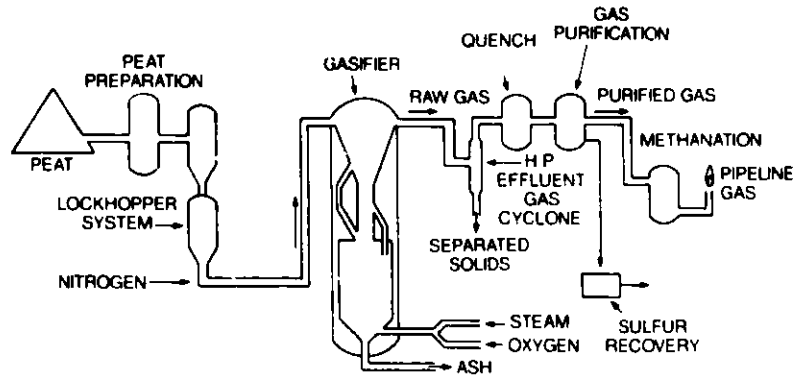


Figure 1. PEATGAS Pilot Plant Facility

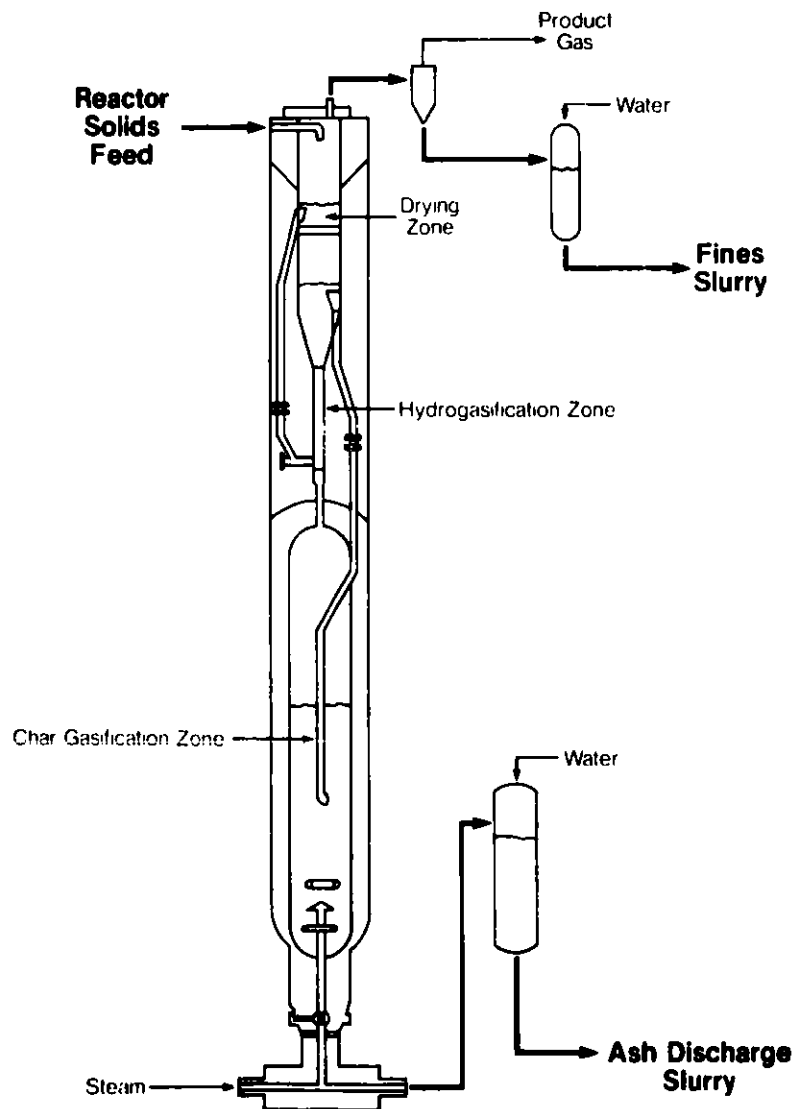


Figure 2. PEATGAS Reactor Solids Flow Measurement

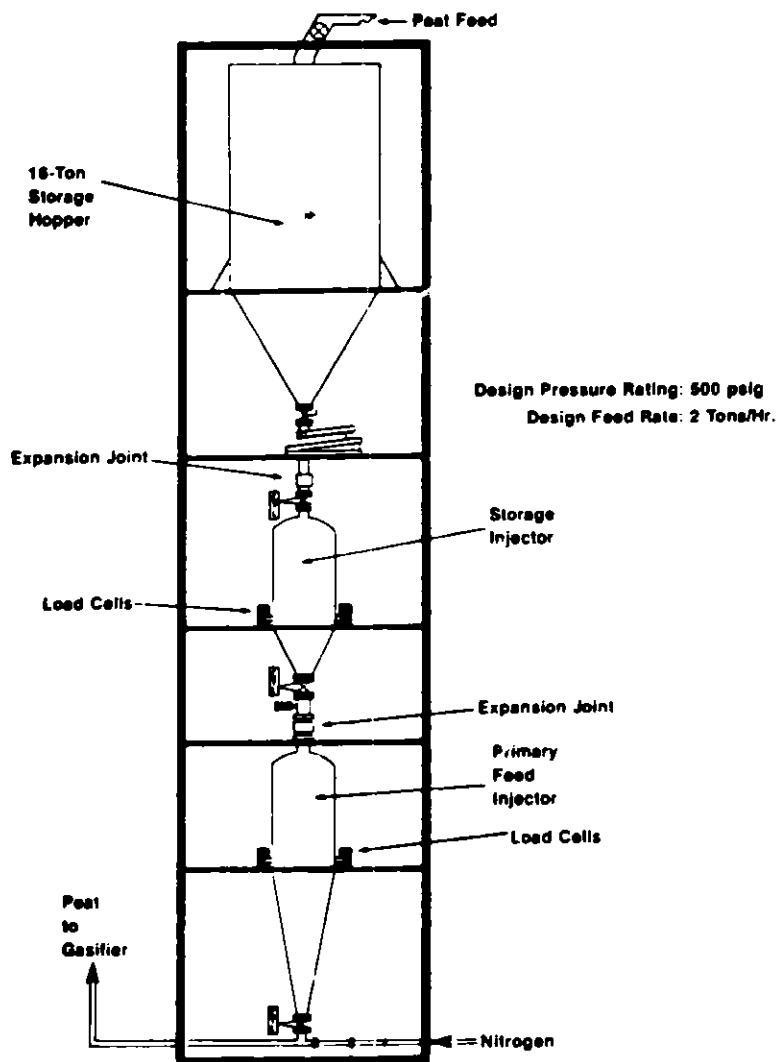


Figure 3. Lockhopper Feed System

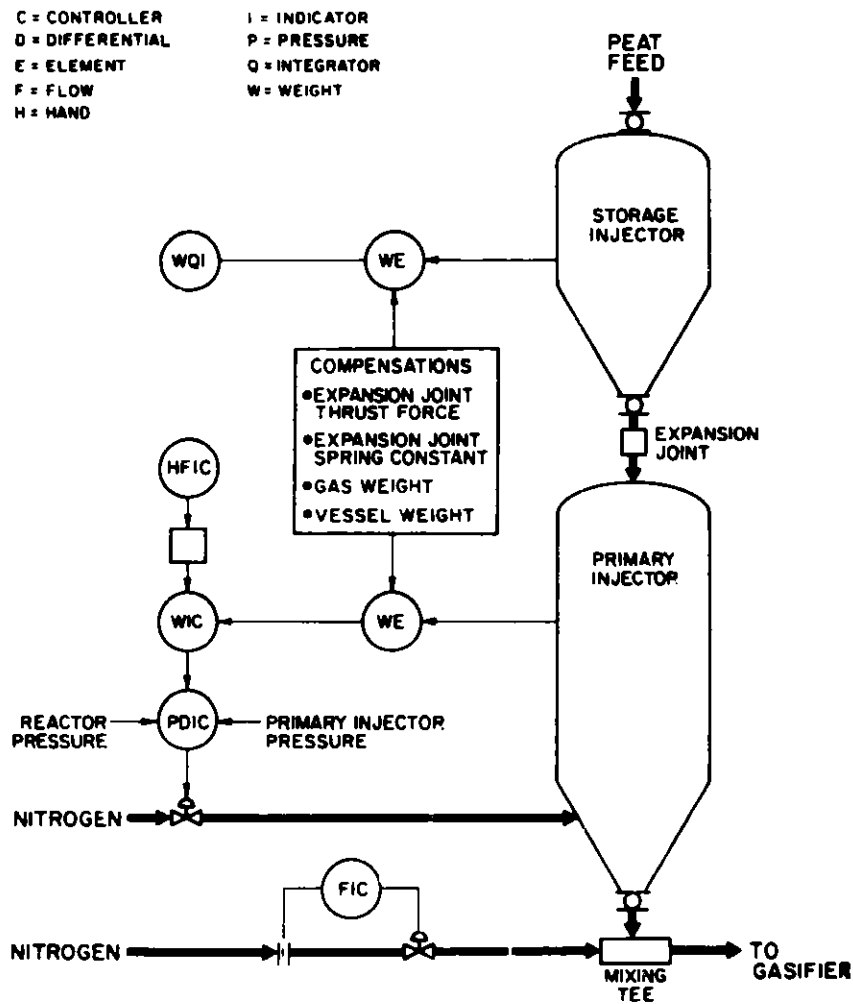


Figure 4. Peat Weight Measurement and Control Schematic



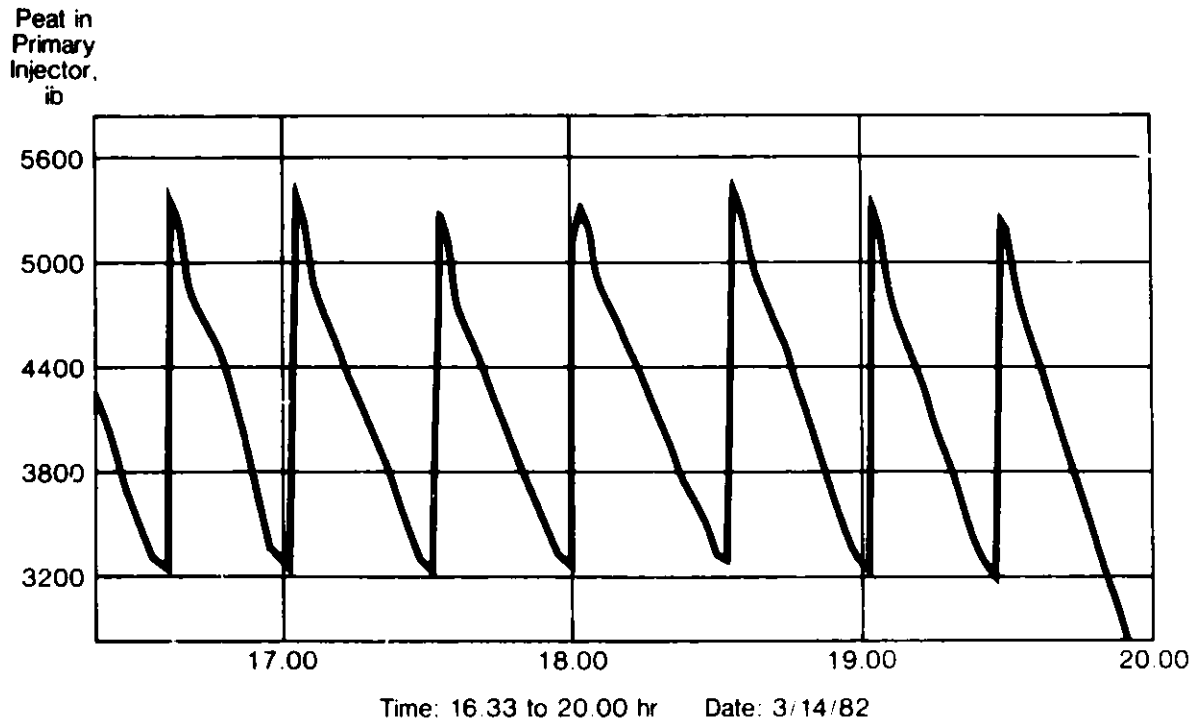


Figure 5. Peat Weight in Primary Injector Vs. Time

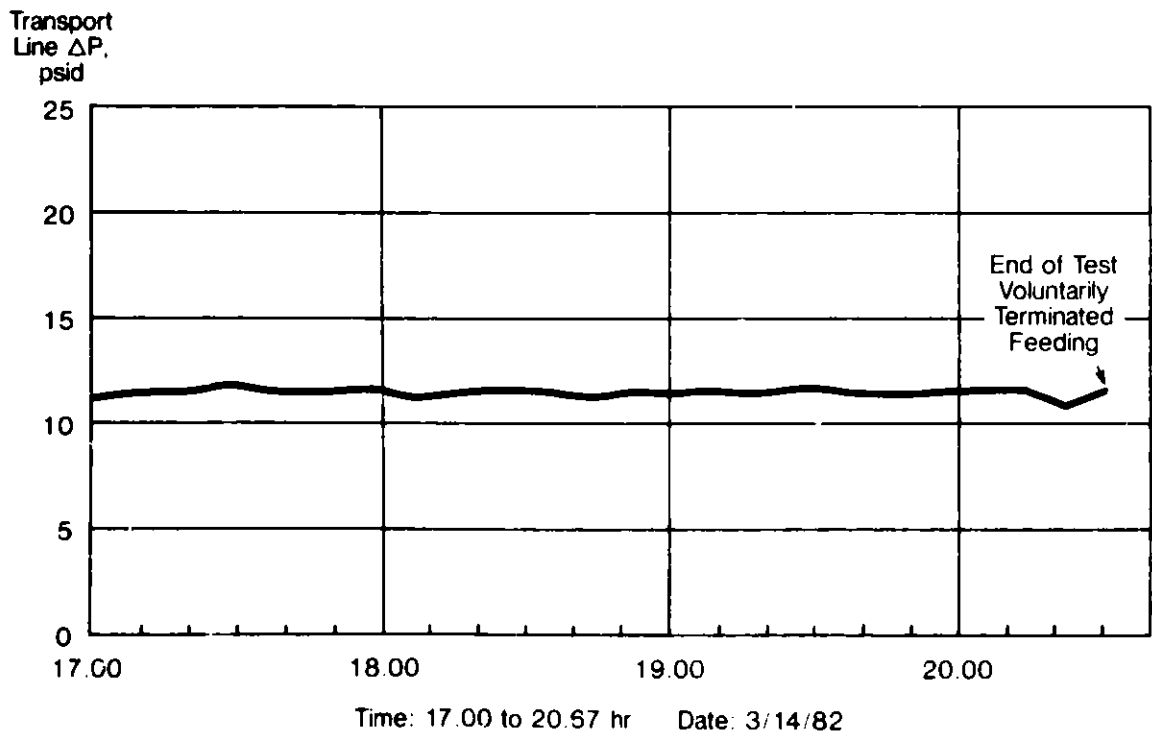


Figure 6. Peat Transport Line Pressure Differential Vs. Time

### Acknowledgement

The work presented in this paper was jointly funded by the U.S. Department of Energy and the Gas Research Institute.

### References

1. Punwani, D.V. and Biljetina, R., "PEATGAS Pilot Plant Operating Results". Paper presented at the IECEC Conference, Los Angeles, August 8-13, 1982.
2. Wohadlo, S.J., Olson, D.P. and Bair, W.G., "Instrumentation and Controls for a High-Pressure, High-Temperature, Fluidized-Bed Coal Gasification Process". Paper presented at the 85th National Meeting of the AIChE, Philadelphia, June 4-8, 1978.
3. Bair, W.G., "Instrumentation and Data Acquisition Techniques in the HYGAS Pilot Plant". Paper presented at the 1977 Symposium on Instrumentation and Process Control for Fossil Demonstration Plants, Chicago, July 13-15, 1977.
4. Anderson, J.E. and Wohadlo, S.J., "Controlling Erosion in a High-Pressure Letdown Valve". Plant Eng., June 23, 1977.
5. Reintjes, H., "The Petrocarb Pneumatic Feeding System as Applied to the Feeding of Coal in the Synthane Coal Gasification and MHD Power Generation Processes". Paper presented at the 70th Annual Meeting of the AIChE, New York, November 16, 1977.

## MAGNETIC RESONANCE COAL FLOWMETER AND ANALYZER\*

J. Derwin King, William L. Rollwitz and Armando De Los Santos

Southwest Research Institute  
Instrumentation Research Division  
6220 Culebra Rd.  
San Antonio, Texas 78284  
Phone: (512) 684-5111 Ext. 2740

## ABSTRACT

The electron spin resonance (ESR) and nuclear magnetic resonance (NMR) properties of 22 varieties of both Eastern and Western U.S. coals have been measured and related to the pertinent physical properties and compositions. This information has been applied to the development of an evaluation model of an instrument for measuring the mass flow, calorific value, and several constituents of coal delivered by dense phase gaseous flow through small pipes. The initial use of the instrument is the measurement of finely divided coal used to supply a fluidized bed combustor but other applications are believed feasible. The instrument senses flowing coal in a non-contacting manner by use of magnetic and electromagnetic fields. The electron and nuclear magnetic resonance data so obtained is processed by an integral microcomputer to provide a near real-time readout of the flow velocity, flow density, mass flow rate, calorific value (BTU/lb.), percent moisture, percent hydrogen and percent carbon for the burnable part of the coal. The mass flow rate and calorific value data are integrated to provide totalized flow and the total delivered heating value in BTU. The instrument design is discussed and performance information is provided, along with ESR-NMR data on the coals.

## INTRODUCTION

With the increased interest in new combustion and conversion processes, the requirement for accurate and continuous on-stream measurement of coal carried by pneumatic and slurry flow through pipes and by conveyor belts has become of increasing importance. Such information is needed for better control of the coal flow to insure more efficient and uniform combustion, lower emissions, and better regulation of the heat or power that is generated. To be useful a coal flowmeter should provide, as a minimum, real-time data on the flow rate. Information on the moisture level, the heating value and the composition of the flowing material are also of value for many applications. With current methods, the total flow, flow rate and flow velocity are commonly available only as relatively long time averages while composition data and moisture determinations require time consuming analyses of discrete samples. This is not adequate to meet the modern needs of coal utilization. Instead, the amount and characteristics of the burnable coal in the flow must be known and controlled instantaneously if optimum combustion or processing is to be obtained. Unfortunately neither suitable instruments nor proven techniques have been available for making such measurements. In order to satisfy this need the noninvasive techniques of electron spin resonance (ESR) and nuclear

---

\*This work was supported in part by U.S. Department of Energy under contract DE - AC21 -79ET15465

nuclear magnetic resonance (NMR) have been investigated and used as the basis for the development of the experimental coal flowmeter and analyzer<sup>1-3</sup> shown in Figure 1. This instrument measures the flow, caloric value, moisture and other properties of powdered coal delivered by pneumatic flow through a small pipe. On the basis of the findings in this development it is believed feasible and practical to apply the magnetic resonance methods to measuring coal flow in larger pipes, in slurries and to measuring less finely divided coal moving on a conveyor belt.

Electron spin resonance, is particularly well suited for making relevant measurements on flowing coal. It is basically non-contacting and responds to free electrons which are associated with the carbon content<sup>4-9</sup> and universally present in coal but rare in other natural materials. Thus, ESR will respond to the coal<sup>10</sup> but is insensitive to most rock, water, mineral matter or other materials which are present. Quantitative measurements of flowing materials which have unpaired electrons, such as coal, are also available with ESR. Nuclear magnetic resonance, like ESR, is also non-contacting and requires only that appropriate magnetic and radiofrequency fields be coupled into the material being measured. While ESR detects unpaired electrons, NMR detects the nuclei of a selected atomic specie in a material. The detection of hydrogen nuclei is the most common application of NMR and is of most interest in the measurement of coal.<sup>11-12</sup> This is particularly true since the most common isotope of carbon, C<sup>12</sup>, is not detectable by NMR and C<sup>13</sup> is of such low concentration that adequate sensitivity is only achieved at very high magnetic field intensities which are believed to be impractically high for coal flowmetering. Transient NMR can detect and measure the hydrogen contained within a material and, by appropriate techniques, the amount of hydrogen in each state can frequently be determined. In coal, the hydrogen in the moisture can be sensed along with the hydrogen in the volatiles and other components. By appropriate signal processing, the two can be separated to permit each hydrogen bearing component to be quantitatively measured. In addition to the possibility of noninvasive, noncontacting measurement of the concentration and composition of coal within a nonmetallic pipe, NMR has previously been used for liquid flow metering<sup>13-15</sup> and has been found useful for measuring the velocity of flowing coal.<sup>2,3</sup> These features made the combination of ESR and NMR attractive as the basis for coal flow metering. To further establish the utility of these methods, however, the measurable coal parameters, the range and accuracy of the measurements, and the effects of variations in the coal composition on the measurements were investigated in research performed as the initial part of the instrumentation development program.

The experimental ESR and NMR studies used samples of 22 different types of domestic coals covering almost the full range of variations found in the composition, rank and calorific values of coal from both the eastern and western regions of the United States. These samples, ranged from subbituminous C to anthracite and were selected to have a wide range of heating values and substantial variation in the relative percentages of moisture, volatiles, ash, and carbon. The coal was examined extensively using electron spin resonance and hydrogen nuclear magnetic resonance to determine what ESR or NMR signals or signal components, or signal combinations, if any, could be used to measure the composition, moisture level and heating values of the coals and to investigate the range of signal characteristics and the effects of the constituents on the design of a practical flowmeter.

### Magnetic Resonance Methods

EMR and NMR both require that the sample material be exposed to a relatively static magnetic field,  $H_0$  and detection is accomplished by sensing the effects of interactions between an applied electromagnetic field and the magnetic moment of subatomic particles of interest. These effects result in perturbation of the absorbed and re-emitted electromagnetic field as illustrated in Figure 2 that are most intense when the frequency of the electromagnetic wave coincides with the resonant frequency of the particles in the magnetic field. This resonant frequency,  $\nu_0$ , is directly proportional to the intensity of the magnetic field,  $H_0$ , and in the case of electrons is

$$\nu_0 = 2.7994 H_0 \quad (1)$$

where  $\nu_0$  is the frequency in MHz and  $H_0$  is the magnetic field intensity in Gauss. In the case of hydrogen NMR the resonant frequency is

$$\nu_0 = 4.2577 H_0 \text{ kHz} \quad (2)$$

In the coal flowmeter the hydrogen NMR frequency is 10 MHz ( $H_0 = 2349$  Gauss) and EMR is at a frequency of 2 GHz ( $H_0 \approx 714$  Gauss). These lower than usual field intensities have been employed to minimize the size, weight, power and costs of the magnet. By this approach, the magnet requirements are very modest and practical compared to those commonly used in laboratory systems.

The ESR and NMR methods are basically noncontacting and can be used to detect and measure through intervening non-metallic materials that can be penetrated by the electromagnetic field. Figure 3 illustrates the concept of the sensing head employed in the instrumentation system. The magnets provide the static field,  $H_0$ , while the electromagnetic field is produced by radiofrequency current flowing in the RF coil. Magnetic resonance response is sensed by the same coil.

### Coal Studies

In the experimental studies the properties of the 22 coals and the compositions as determined by both proximate and ultimate analyses were correlated with the hydrogen NMR amplitudes and relaxation time constants and with the ESR amplitude and line widths. Samples of the "as received" coals, as well as samples of each that were dried in a vacuum oven at 50° C., were measured. The amplitude and the line width of the ESR responses were determined at both 2.0 and 9.8 GHz and utilized for comparison with the calorific value as well as with the percentages of: moisture, ash, volatiles, carbon, hydrogen, oxygen, nitrogen, and sulphur. The hydrogen transient NMR responses from the coals were measured at a frequency of 30 MHz and analyzed to separate and measure the amplitude, the spin-lattice relaxation time constants,  $T_1$ , and the spin-spin decay time constants,  $T_2$ , of the signals. Adequate NMR and ESR signal levels for flowmetering were obtained from all coal samples. Correlation between the EMR and NMR signals and the coal parameters were determined using computer methods which calculated the coefficients and produced scatter plots relating a measured quantity to a selected coal property. The computed coefficients ranged from near zero for the ash content to as high as 0.99 for the percent water as a function of the processed NMR signal amplitude. A scatter

plot of the ultimate hydrogen content compared to the hydrogen NMR signal amplitude from the dried coal samples is shown in Figure 4. Each dot represents one of the equal weight samples of the 22 types of coal while the straight line is the best fit to all the data. The accuracy of the hydrogen NMR measurements are believed to approach an order of magnitude better than is implied by the results in Figure 4 and much of the spread is believed, on the basis of a limited verification effort, to be attributable to the actual differences between one finite sample of coal and another of the same type. This sampling problem is indicative of the difficulties in determining the accuracy of the NMR measurements compared to the standard analytical techniques.

Figure 5 shows a similar scatter plot and best straight line fit for the log of the total ESR signal (product of amplitude and linewidth) compared to the carbon content of the 22 coal samples. While somewhat more scatter is evident than in hydrogen measurements the correlation factor is 0.95.

The calorific value as determined by use of the combined NMR and ESR data is shown in Figure 6 for the 22 coal samples. Results which show errors of less than 500 BTU/lb. in most cases, were obtained by use of a common set of calibration constants for all the samples. By use of optimized constants for each type coal, substantial improvement can be realized.

The three examples are illustrative of some of the more favorable measurements of coal composition by magnetic resonance methods. Moisture content was also found to be measurable to near 1% without weighing and without calibration for the specific type of coal. Other coal composition and quality parameters showed lower correlation factors. Flow density, flow velocity and mass flow were also found to be measurable and provisions for these factors are included in the experimental flowmeter.

#### Evaluation Model

The Evaluation Model of the Coal Flowmeter and Analyzer, Figure 1, is designed for on-stream measurement of pneumatically transported powdered coal in a dense phase flow through a 3/8-inch pipe. This instrument uses both electron spin resonance and nuclear magnetic resonance to sense pertinent flow parameters and physical properties of the coal. Flow, composition and quality parameters are readout on two numerical panel meters. One meter shows the coal flow rate in tons/hour or BTU  $\times 10^6$ /hour, as selected, while the second meter may be switched to indicate any of the following:

- Moisture, %
- Ash, %
- Totalized Mass Flow
- Volatiles, %
- Flow density
- Totalized BTU
- Carbon, %
- Flow velocity

With the exception of ash, the readout data is computed from the sensed NMR and EMR signals by an integral microprocessor. Ash is not directly measurable but the average value for the type coal is manually entered to permit the quantities to be displayed in percentage. Electrical outputs of selected parameters are available in analog and digital format.

Figure 7 shows a block diagram of the Evaluation Model. The flowing coal is carried in a standard size (schedule 40) 3/8-inch pipe made of Teflon which passes through the ESR sensor and then through the NMR sensor. Both sensors

are contained within a common assembly and located in-line with the coal flow stream. This assembly also contains the microwave portion of the ESR detector, the two electromagnets and several auxiliary components.

The Electronics Assembly houses the remainder of the ESR detector circuitry, the NMR detector, a microcomputer based controller and data processor and the power supplies for the electronics and for the magnets. In addition to the two data readout meters and associated rotary switches, three push-button type switches located on the front panel of this assembly control the power on-off, the initiation of instrument operation and the reset of the computer. Other controls, test switches, and test points (connectors) are located behind an access panel on the front of the Electronics Assembly.

The ESR signal and the multiple NMR signals used in the data computations are sequentially sampled at an average rate of 60 per second. A total of 256 samples of each signal are averaged to improve the signal-to-noise ratio and to enhance the measurement accuracies. These averaged values are used by the integral MC-6800 based microcomputer to calculate the data parameters displayed on the panel meters. Each parameter is re-calculated and the readouts are simultaneously up-dated every 23 seconds.

The NMR sub-system measures the hydrogen in the flowing coal to provide data for determining the total hydrogen content as well as for separately determining the moisture content and the hydrogen in the volatiles. Measures of the flow velocity and the density of the flowing coal are also obtained from the hydrogen NMR signals. Transient NMR methods are used for detection in both the free induction decay and pulse echo modes.

The ESR sub-system uses field modulated, continuous wave methods and operates on a nominal frequency of 2.0 GHz. Using a reflecting mode cavity the 2 GHz solid state oscillator is locked to the cavity frequency to maintain low reflected power under the changing load imposed by varying amounts and characteristics of the flowing materials. The magnetic field is fixed at an intensity which provides the maximum output amplitude. The detector output, filtered by a low pass circuit with a cut off frequency of 1.0 Hz, is proportional to the number of free electrons in the flowing material. This signal provides data on carbon content and the density of the coal in the flow stream.

### Experimental Results

The Evaluation Model was tested in the laboratory using flow loops composed of lengths of thin wall Teflon tubes filled with selected types of coal. The selected flow loop passed through the sensor and was used as a belt around two pulleys which rotated at controlled speeds. The amount of coal in these tubes was equivalent to that in dense phase flow being about 15% of full pack in the 3/8-inch pipe. The loop velocity was variable over a range of 5-35 feet/second. Tests with coals of three different compositions showed the capability of the instrument to properly indicate the parameters displayed on the panel meters with a repeatability of 1-2% depending upon quantity selected for readout.

Tests to evaluate the Model under pneumatic flow conditions were conducted in the instrumented facilities of the Pittsburgh Energy Technology Center (PETC). For these tests, finely powdered Rosebud (Montana) coal of both 4% and 8% nominal moisture levels was used. The tests included five flow densities at nominal gas flow velocities of 25, 50 and 100 feet per second for each of the two coals. The long-term average flow density selected for the tests ranged from approximately 5% to 15% of full line pack but substantial instantaneous variation was present during all tests.

Results of the PETC tests showed the capability of the Evaluation Model to sense the flowing coal over the full range of flow velocity and flow density and to provide readouts of the available parameters which was in general agreement with the reference measurements. Analysis of the data to precisely establish the measurement ranges and accuracies are currently underway. The preliminary results do, however, show the capability to sense the flowing coal over the full range of test conditions with both the ESR and the NMR sub-systems. Both responded to the flow density and the NMR sub-system correctly responded to both the changes in the coal moisture and the flow velocity.

#### Conclusions

The use of ESR and NMR for on-stream coal flowmetering and analysis has been found feasible and has been implemented in an experimental instrumentation system. The results of this work show:

1. The hydrogen NMR signal from coal can be used to measure the hydrogen moisture and volatiles contents, as well as the flow density of the hydrogen bearing constituents and the flow velocity.
2. The EMR signal from coal can be used to measure the carbon content and the flow density of the carbon component.
3. The combined EMR-NMR data can be used to additionally measure the calorific value and the flow density of the burnable coal.
4. Calibration for the type coal provides highest accuracy.
5. Further analysis of the experimental data is necessary to establish the measurement ranges and the attainable accuracy under pneumatic flow conditions.

#### Acknowledgements

Many persons contributed to the success of the work reported herein. Phillip A. Hornung, Ph.D. carried out much of the work in correlating the EMR and NMR properties of the coal with the physical characteristics and Errol S. Riewerts performed most of the experimental measurements. Services of Mr. Art Hall and later Mr. Dana Hewitt of the U. S. Department of Energy, Morgantown Energy Technology Center, as the Contract Technical Project Officers were particularly important to the success of the efforts. The cooperation of Dr. M. T. Mathur and his staff at PETC was most helpful in conducting the system evaluation.



## REFERENCES

1. King, J. Derwin, Hornung, P.A. and Rollwitz, William L., "Coal Flow Meter Development, Feasibility Study" Phase A Report, U.S. D.O.E. Contract No. DE-AC21-79ET15465, April 1980.
2. King, J. Derwin and Rollwitz, William L. "Coal Flow Meter Development, Laboratory Evaluation", Phase II Report, U.S. D.O.E. Contract No. DE-AC21-79ET 15465, December 1981.
3. King, J. Derwin, Rollwitz, William L. and De Los Santos, Armando, "Coal Flowmeter Development, Evaluation Model", Phase III Report, U.S. D.O.E. Contract No. DE-AC21-79ET15465, April 1982.
4. Ubersfeld, U., Etienne, A. and Combrisson, J., "Paramagnetic Resonance, A New Property of Coal-Like Materials," Nature. Vol. 174 (25 Sept. 1954) P. 614.
5. Ingram, D.J.E. and Colleagues, "Paramagnetic Resonance in Carbonaceous Solids," Nature. Vol. 174 (23 Oct. 1954) P. 797.
6. Singer, L.S., "A review of Electron Spin Resonance in Carbonaceous Materials," Proc. of the Conference on Carbon. Vol. 2 (1961) P. 37.
7. Bennett, J.E., et al., "Paramagnetic Resonance from Broken Carbon Bonds," J. Chem. Phys. Vol. 23 (1955) P. 215.
8. Ingram, D.J.E., "Electron Resonance Studies of Heat-Treated Organic Compounds," Proceedings of the Conference on Carbon (3rd Biennial) (1957) P. 93.
9. Ubersfeld, U. and Erb., E., "Paramagnetic Resonance in Coals and Heat Treated Organic Compounds," Proc. of the Conference on Carbon (1957), P. 103.
10. King, J. Derwin and Rollwitz, William L., "Coal Thickness Gauge Using RRA Techniques", Final Report, NASA Contract NAS 8-32606, September 1980.
11. Ladner, W.R. and Stacey, A.E., "Broadline Nuclear Magnetic Resonance Measurements on Carbonized Coals," Fuel. Vol. 44 (1965) P. 71.
12. Retcofsky, H.L. and Friedel, R.A., "Room-Temperature Proton Magnetic Relaxation Times in a Bituminous Coal," Fuel. , Vol. SL VII, No. 5 (Sept. 1968) P. 391.
13. Singer, J.R., "Flow Rates Using Nuclear or Electron Paramagnetic Resonance Techniques with Applications to Biological and Chemical Processes," J. of Applied Physics, Vol. 31, No. 1 (Jan. 1960), P. 125.
14. Singer, J.R., "Blood Flow Rates by Nuclear Magnetic Resonance Measurements," Science, Vol. 30, (December 1959) pp 1652-3.
15. Gardner, C.G. and Rollwitz, W. L., "Measurement of Fluid Flow by Means of the Frequency Shift of a Spin Generator," Final Report 15-1835-01, Southwest Research Institute, 19 June (1967).

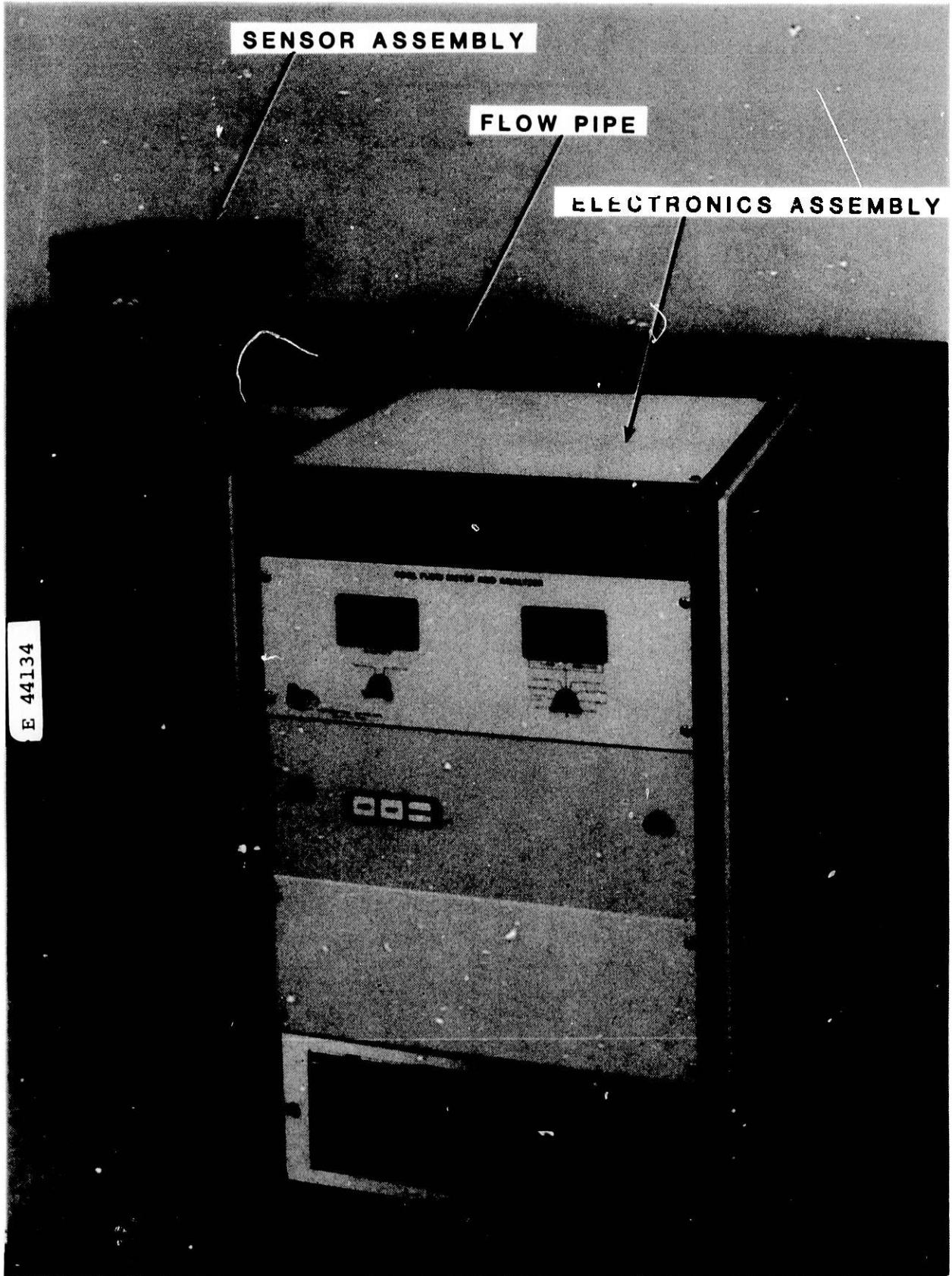


FIGURE 1. EVALUATION MODEL OF COAL FLOWMETER AND ANALYZER

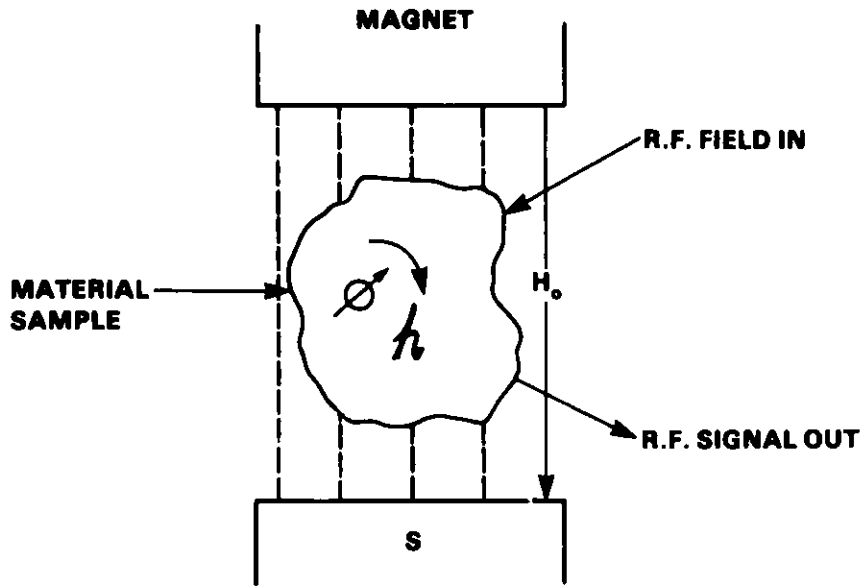


FIGURE 2. BASIC MAGNETIC RESONANCE DETECTION CONCEPT

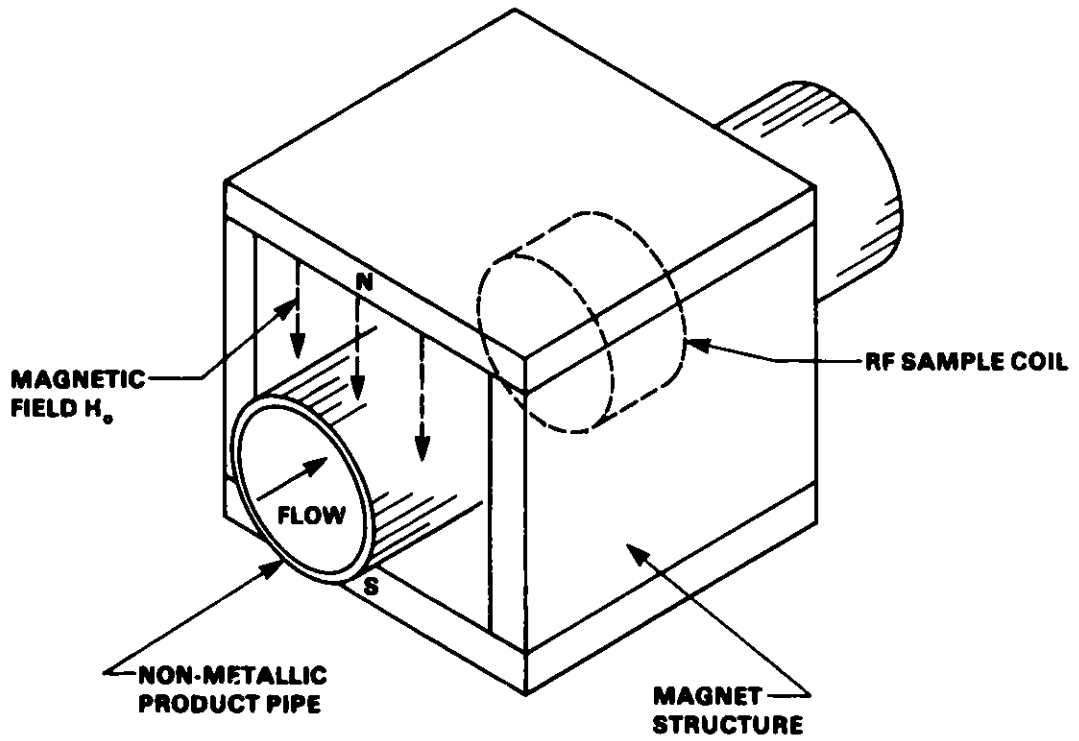


FIGURE 3. BASIC MAGNETIC RESONANCE FLOWMETER SENSOR CONCEPT

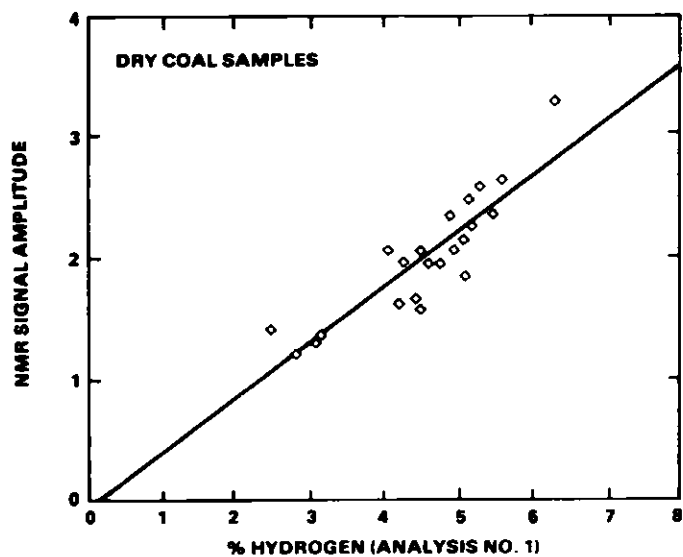


FIGURE 4. HYDROGEN NMR AMPLITUDE VS % HYDROGEN AS MEASURED BY ULTIMATE ANALYSIS NO. 1 FOR DRY COAL SAMPLES

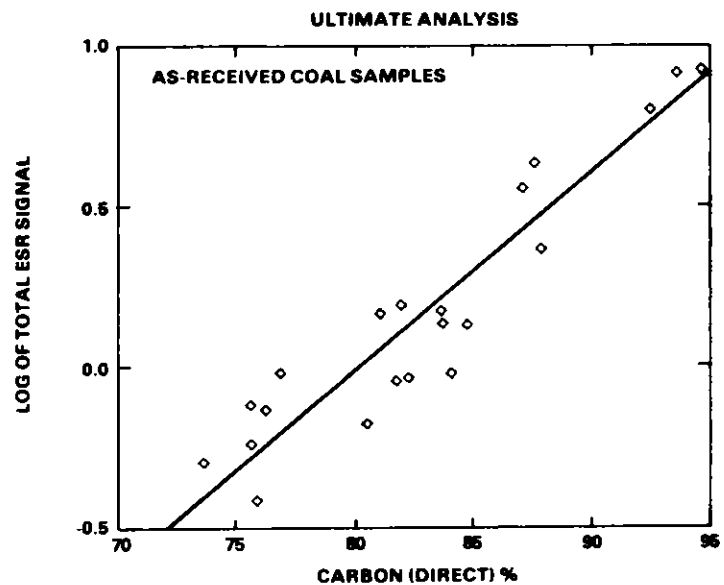


FIGURE 5. TOTAL ESR SIGNAL FROM AS-RECEIVED COAL SAMPLES COMPARED TO % CARBON BY DMMF (DIRECT METHOD

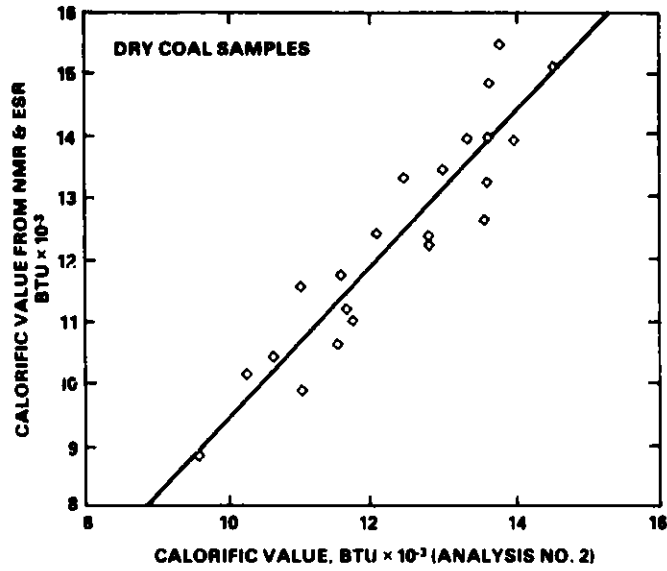


FIGURE 6. CALORIFIC VALUE CALCULATED FROM NMR & ESR DATA COMPARED TO MEASURED VALUE

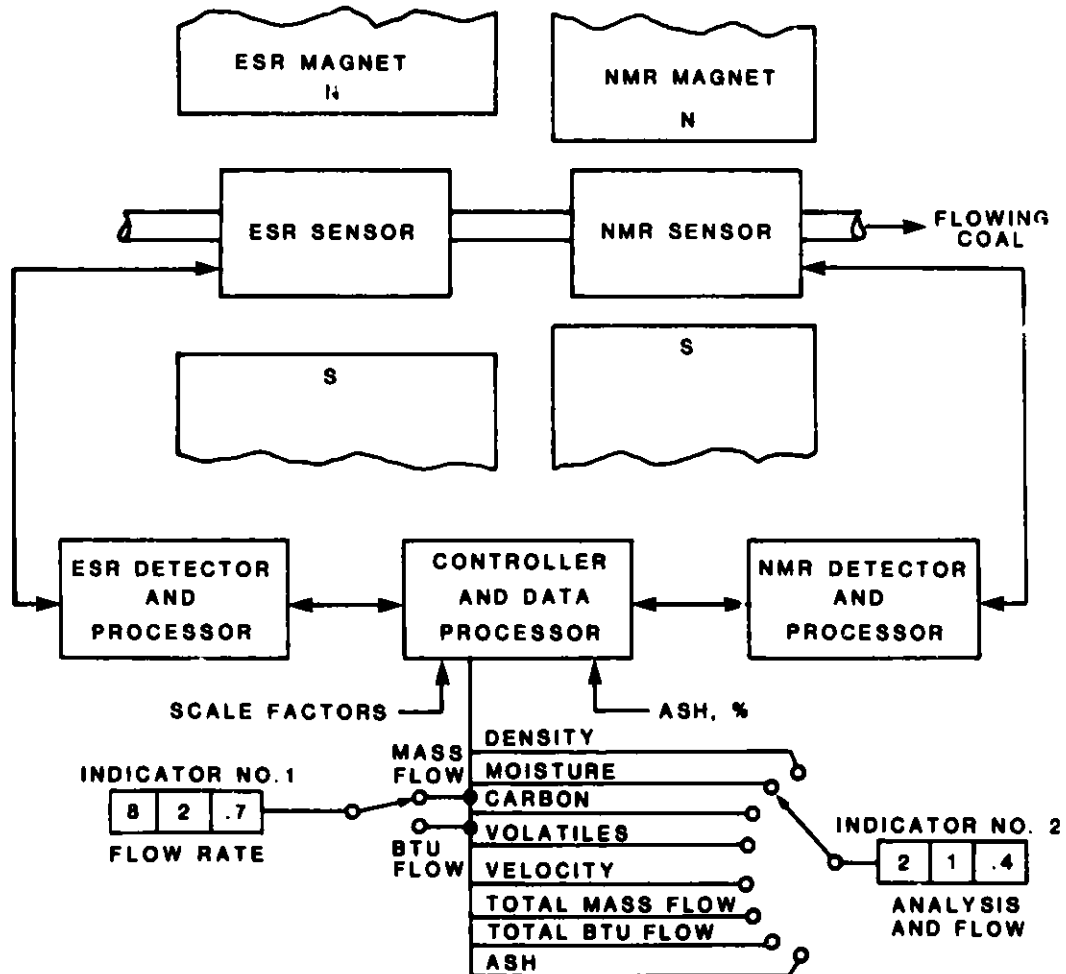


FIGURE 7. BLOCK DIAGRAM, MAGNETIC RESONANCE FLOWMETER AND ANALYZER

ADVANCES IN INSTRUMENTATION AND CONTROL FOR MHD - CDIF UPDATE

Michael L. Miller, Bradley B. Rogers\*

Mountain States Energy, Inc.  
P.O. Box 3767  
Butte, MT 59702  
Telephone (406) 494-7389  
or FTS 587-7389

Abstract

During the first 18 months of operation at the DOE MHD Component Development Integration Facility at Butte, Montana, operating problems and experience have prompted a vigorous program of original innovation and improvement in I&C systems.

Problems experienced with the pneumatic solids transport system initially provided have resulted in the development at CDIF of an original Granular Solids Supply Metering System, capable of delivering 1 to 20 lb/min of flyash to the MHD ash injected combustor.

Other original work includes a continuous pressure monitoring system for an MHD generator which resists tap slagging. Improvements have been made in accuracy, reliability and fault diagnosis in air and oxygen flow measurement systems.

Introduction

Magnetohydrodynamics, or MHD, is the process of passing an electrically conducting gas, in the form of a plasma, through a magnetic field at high velocity and thus generating electricity. This electricity is drawn off as direct current (DC) through electrodes located on the walls of the MHD channel generator. The DC is then inverted to AC and supplied to the commercial power grid.

Because of the intricate cooling system in an MHD generator, it is possible to operate at plasma inlet temperatures in the neighborhood of 5000°F. The generator outlet temperature is at least as hot as is normally seen in steam boilers, and thus it is possible to combine MHD power generation with a conventional steam power plant. The combined thermal efficiency of such a plant would be as much as 50% greater than conventional steam plants, and because of the nature of the MHD process, the pollutants delivered to the atmosphere are decreased markedly.

The U.S. Department of Energy is currently funding a nationwide MHD research program involving the production of MHD power from coal. As part of this national program, the MHD Component Development and Integration

\*Presenting Author

Facility (CDIF) has been established and is currently operating in Butte, Montana. The purpose of the CDIF is to assemble and test various components of MHD power trains, such as channel generators, combustors and magnets, provided by DOE contractors or others. The Electric Power Research Institute (EPRI) has provided in the last year an inverter, so that the DC power from the MHD channel may be converted to AC and put on the commercial power grid.

MHD power generation was first achieved at the CDIF in April 1981 and testing has been ongoing since. This paper will discuss a few of the problems which have been encountered in measurement and control in the last year, and our solutions to these problems. These problems are presented in the form of case histories. Accompanying each case history is a brief discussion of the system involved and its contribution to MHD research.

### Solids Flow Control

At the present time the CDIF is not operating with coal, but rather with a fuel oil fired combustor. It is necessary for optimum performance of the MHD channel that the walls of the channel be coated with molten slag material, as they would be with coal combustion. This slag, a form of flyash, acts as a thermal insulating barrier, reducing the heat loss from the channel and reducing erosion, thus increasing generator life. Since there is no flyash present in fuel oil, it is necessary to inject it into the combustor separately.

The flyash injection system at the CDIF begins with of a pressurized vessel filled with approximately 3000 lbs of ash. This conical vessel reduces down to a 0.1 inch diameter hole, at which point the ash is mixed with a conveying air stream and pneumatically transported approximately 300 feet to the point of injection into the combustor. The flyash system has been beset with problems since initial activation. First it was not possible to get the ash out of the injection vessel into the transport line. This was overcome by enlarging the hole size on the bottom of the vessel, but following this, ash flow from the vessel would plug the 1/4" I.D. transport line.

This problem of plugging the transport line was approached by calculating the saltation velocity of ash. The saltation velocity is that velocity below which the turbulence intensity of the pneumatic air stream is not sufficient to keep the particles in suspension and some of the particles "saltate" and collect on the bottom of the transport pipe, thus causing plugging. It was also determined from our investigations that the 1/4" transport line was too small to supply the necessary range of mass flow of ash, and it was subsequently replaced with a 3/8" I.D. line. The carrier air velocity in this 3/8" line is controlled at a point above the saltation velocity, and the line plugging problems have been eliminated.

After this, it was possible to send ash to the combustor during a test; however, there was virtually no control over the amount of ash which was sent. Ash flow could be established, but attempts to vary the flow by

changing the injection vessel pressure or carrier gas flow were not effective within a certain range; below that range the ash flow stopped entirely. This problem was overcome to some extent by replacing the mixing-tee supplied by the vendor with one of our own design, utilizing an eductor into the transport air line. With this design, the ash flowrate could be varied between 8 and 15 pounds per minute by varying injector vessel pressure, but below 8 lbs per minute ash flow would stop. The combustor and channel require 2.4 lbs per minute of ash flow at times, so it was necessary to lower the flowrate even further. This was accomplished by the redesign of the mix-tee to incorporate 5 air injection ports along its length. These ports allow the injection of jets of air into the ash flow stream and thus prevent arching, or plugging, of the ash in the mix-tee, keeping it free-flowing even at the low tank to line differential pressures necessary to achieve 2 lbs per minute of ash flow. The injection air also serves as a secondary means of metering the ash flow; it is possible to control the range of ash flow by varying the intensity of injection air.

With the development of the air-injected educting mix-tee it became possible to send the desired ash flowrates to the combustor, but there remained problems with finely controlling the ash flowrate within the 1/2 pound per minute band desired. The flowrate was extremely sensitive to any variation in the differential pressure between the carrier gas at the mix-tee and the internal tank pressure. This problem was overcome by changing from flow control to pressure control on the transport line, while assuring that the velocity was sufficient to prevent line plugging.

By incorporating all of the above mentioned changes, control of ash flowrate between 0 and 25 lbs per minute within 1/4 pound per minute was achieved. The system has operated successfully for about 50 hours of combustor testing since the modifications, without any interruption of ash flow.

Experience gained on this system has been used to design a new dry solids transport system, utilizing microprocessor control, which will control the flowrate of bulk solid materials fully automatically. This system will be operational this year.

#### Slag Resistant Pressure Tap

As was previously mentioned, the MHD channel interior is coated with a molten slag layer during operation. This slag layer makes it difficult to measure the internal pressure of the plasma stream, because the 18 pressure ports located along the length of the channel can slag over and plug. To prevent this, a continuous stream of air is passed through the pressure ports to keep them free of slag until such time as a pressure reading is desired. At this time the purge air is shut off, the line pressure equalizes, and a pressure profile measurement is attempted. This method has not proven to be successful because the rapid rate at which the ports slag over when the purge air is shut off makes it impossible to get a reliable measurement.



Because of these problems, a system is under development at the CDIF to determine channel pressures without interrupting the purge gas flow. The system is based on measurement of the purge gas flow velocity and its relationship to the channel pressure.

Consider the pressure Mach Number relationship for one-dimensional, isentropic, compressible flow of an ideal gas:

$$\frac{P_0}{P} = \left(1 + \frac{\gamma - 1}{2} M^2\right)^{\gamma/\gamma-1} \quad (1)$$

Where:  $P_0$  = Stagnation pressure (velocity = 0)  
 $P$  = Static pressure  
 $\gamma$  = The ratio of specific heats,  $C_p/C_v$   
 $M$  = Mach Number

For air,  $\gamma = 1.4$ , when the Mach Number is equal to 1 (the velocity is equal to the speed of sound) the pressure ratio between static and stagnation conditions is:

$$P/P_0 = .5283 \quad (2)$$

Now, consider the Area-Velocity relation for the same fluid:

$$(1 - M^2) \frac{du}{u} = -\frac{dA}{A} \quad (3)$$

Where:  $A$  = Area of flow channel  
 $u$  = velocity

From investigation of equation 3 it is obvious that to accelerate a subsonic flow, the channel area must decrease; the opposite is true for a supersonic flow. When the velocity is equal to the speed of sound (i.e.  $M=1$ ) the area must be constant for the relation to be satisfied. Thus it is never possible to accelerate a flow to supersonic conditions by decreasing the area of the flow channel. It is possible, however, to accelerate the flow to sonic conditions by decreasing the flow area sufficiently, then allowing the area to remain constant at the reduced size. When this is done the flow reaches its maximum attainable velocity unless the flow channel diverges and allows the flow to become supersonic. This condition is commonly referred to as "choked" flow, and this principle is the basis for the pressure measuring system design.

The pressure differential required to drive an air stream to the speed of sound is given by equation 2. If a pressure differential of .5283 or greater is applied across an appropriately shaped flow channel the flow will "choke". When a flow is choked the velocity of the air in the purge line will not be affected by an increase in purge line pressure. The pressure port on the channel will be the critical point of the flow stream. The pressure in the purge line will be raised until the point is reached where the velocity device (a hot wire anemometer) no longer shows an increase in velocity. At this time we will know that the pressure port is choked. The pressure in the line will then be lowered

until the velocity device records a change in velocity. The pressure at which this happens will be the critical pressure. Neglecting line losses, the channel pressure is then determined from equation 2, i.e.  $P_{channel} = .5283 P_{chamber}$ . Figure 1 illustrates that a velocity device capable of resolving a 2% change in velocity is capable of determining the driving pressure ratio within 3%. This performance can be improved somewhat by experimentally determining the lag of the velocity measuring device and accounting for it in the final analysis.

In the derivation presented here, many second order effects have been neglected. These effects can be investigated both analytically and experimentally. The final result will be an equation like equation 2 with a slightly modified constant.

The concept presented here has been tested at the CDIF. The results obtained verified that the concept is sound, but because of high inaccuracies involved in the testing devices, the results were not extremely useful. The channel pressures that were obtained, however, were in the expected range. Based on the encouraging results obtained from this test, more accurate instrumentation has been ordered, and development of the system will continue.

#### Combustion Air Flow Measurement Calibration

In order to achieve the high temperatures necessary in an MHD channel, the combustion air must be enriched with oxygen prior to combustion. The stoichiometry in the channel is a very important experimental parameter and thus these flows of air and oxygen must be accurately measured. In the past at the CDIF there have been serious questions raised concerning the accuracy of the vortex shedding flowmeters installed in the air and oxygen lines, as well as in the line carrying a mixture of air and oxygen. Because of the importance of these measurements, it was determined that their calibrated accuracy should be traceable to the National Bureau of Standards. In order to accomplish this, the flowmeters in the line must be calibrated against an NBS traceable device. The calibration has been done initially using an orifice plate calibrated to within  $\pm .5\%$  of scale to NBS by the Colorado Engineering Experiment Station. A significantly more accurate venturi tube has been ordered, but will not be installed until November of this year. The venturi will be accurate to approximately 1/10 of 1 percent.

The orifice plate was placed in the air line, providing a system configured as illustrated in Figure 2. Because of the principle of operation of the vortex shedding flowmeters, it was possible to carry out the calibration of the oxygen and oxidizer flows, as well as the combustion air flow. The vortex shedding flowmeters work on the aerodynamic principle known as the Von Karman vortex street. The vortex street establishes itself as the flow separates behind a blunt body, alternately shedding vortices from each side of the downstream end of the body. The intensity of the vortex street is typically characterized in a dimensionless number known as the Strouhal Number (St) defined as follows:

$$St = \frac{nD}{V}$$

Where:  $n$  = vortex shedding frequency  
 $D$  = body width  
 $V$  = flow velocity

The Strouhal Number is very nearly a constant over a large range of Reynolds numbers. Therefore, a doubling of velocity will also double the frequency of vortex shedding. By measuring this vortex shedding frequency the flow velocity is obtained. Since the Strouhal Number is independent of the Reynolds number, it is also independent of the density and viscosity, thus the meter is sensitive only to velocity. The velocity signal is fed into a flow calculator which also receives pressure and temperature inputs. The mass flow is calculated according to the formula:

$$m = \rho AV$$

Where:  $m$  = mass flowrate  
 $\rho$  = density  
 $A$  = flow area  
 $V$  = velocity

The density is calculated according to the ideal gas law. There is no way to change the density calculation once the meter is received from the factory. Since the gas constant in the ideal gas law is different for air and oxygen, or mixtures of the two, the density calculated by the flow calculator is only accurate for one substance. To correct for errors in density, the frequency signal from the vortex shedding sensor must be modified appropriately.

As an initial calibration, using the orifice, the flowmeters were all calibrated for air density. This was done by calibrating the air and oxidizer flowmeters without oxygen flowing. After this, oxygen flow was added and, based on the readings from the combustion air and oxidizer lines, the oxygen meter was calibrated. Thus all of the meters were calibrated correctly for air. In order to correct the oxygen meter for the density of oxygen as compared to air, the meter reading was raised approximately 12%. (The density ratio between oxygen and air is equal to the ratio of molecular weights, as can be easily deduced from the ideal gas law. This ratio is approximately 1.12 to 1.)

After this, the oxidizer flow element will still read correctly only for air. The instrument output is corrected for density by the data acquisition computer, based on the oxygen and air flowmeter readings, and this corrected flowrate is displayed on the CRT terminals.

After the corrections were made to the flowmeters, data was taken to determine the error band of each instrument. When the analysis was done, curves as illustrated in Figure 3 were generated. Based on the analysis we were able to establish error and uncertainty bands for each of the instruments.

### Heat Transfer Measurements

The walls of the MHD channel consist of segmented copper electrodes forming the anode and cathode walls, along with copper sidewalls

electrically isolated from the anode and cathode. These electrodes and walls are cooled by an intricate system of cooling water channels. As slag builds up inside the channel, the heat transfer decreases significantly and thus the heat transferred into the cooling water decreases. Because of this, we can infer the degree of slagging of the channel from the heat transfer away from it; for this reason, the cooling water heat transfer measurement is important.

The heat transfer measurement is based on the mass flow and temperature rise of the cooling water according to the formula:

$$Q = mc\Delta T$$

where Q = heat transferred  
 m = mass flow of cooling water  
 c = specific heat of cooling water  
 $\Delta T$  = Temperature out - Temperature in

When the CDIF was first operated, it became apparent that these measurements were greatly inaccurate. The type T thermocouples which had been installed to measure temperature rise were treated as linear devices over a wide range of temperatures, causing very significant errors in the  $\Delta T$  measurement. Also, the mass flow measurements were attempted with orifice plates that were sized incorrectly and installed with insufficient straight pipe runs upstream.

The problem of incorrect application of the thermocouples has been corrected to some degree by programming a standard type T thermocouple curve into the Data Acquisition System computer, feeding the signals from the thermocouples into the computer, and calculating the temperature rise in the computer. The corrected data is stored and may be monitored during a test.

The problem of inadequate line length for correct application of the orifice plates was resolved by replacing all of them with averaging pitot tube flowmeters called Annubars, made by Detrik Standard Corp. With tube-type flow straighteners, the Annubars have shorter line length requirements than orifice plates, and could be installed correctly within the limitations of space available. They have performed reliably.

These modifications provide a more accurate measurement of the heat transfer from the channel. In order to establish error bands and traceability on this measurement, calibration standards will be obtained. These standards will be of a quartz thermometer, capable of resolving fractions of a degree Fahrenheit, and a positive displacement type flowmeter accurate within 1/2 of 1%. These devices will be used to calibrate and establish error bands in a manner similar to that applied to the COA and oxygen calibration presented previously.

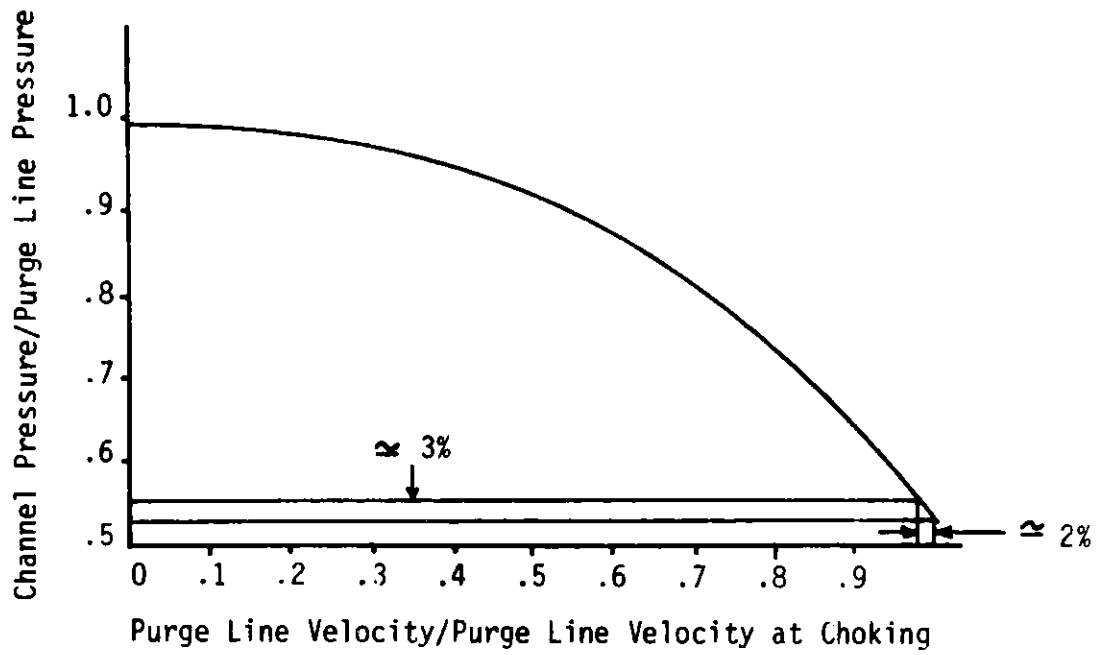


FIGURE 1 -- Velocity Device Sensitivity Curve

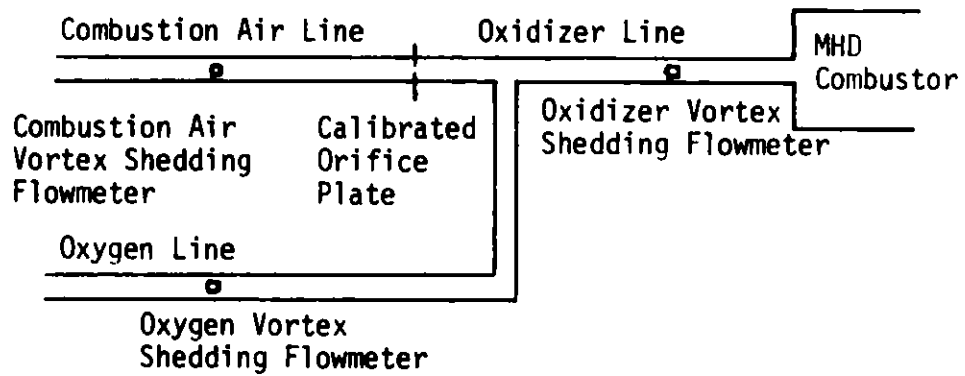


FIGURE 2 -- Combustion Gases Flow Loop

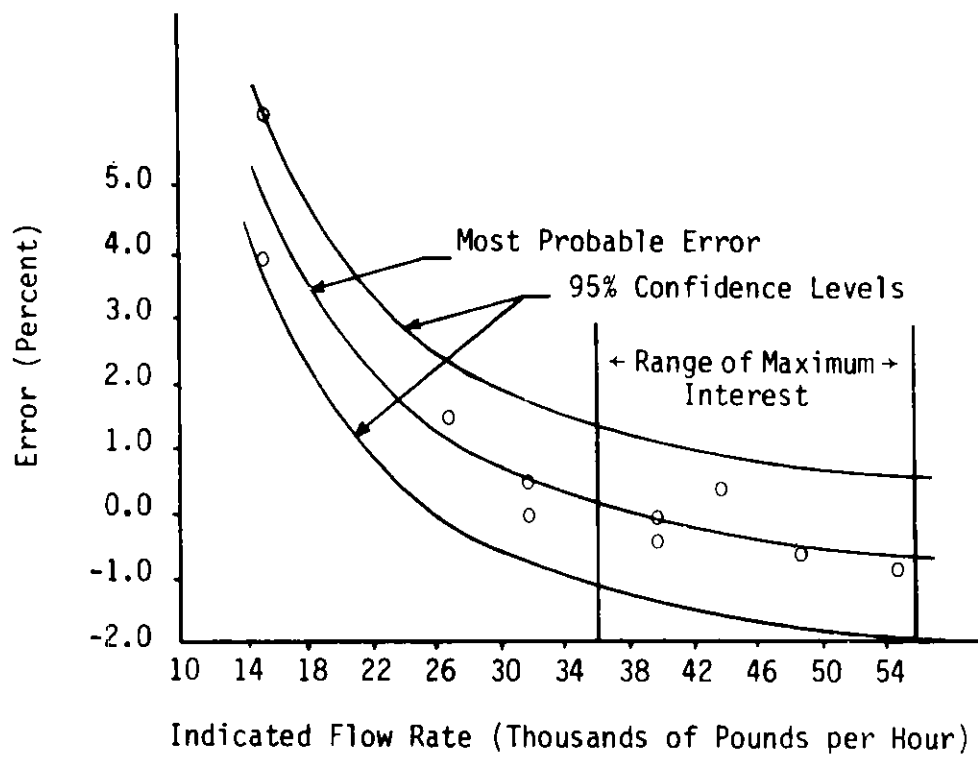


FIGURE 3 -- Oxidizer Flow Element Error Curve

PERFORMANCE CHARACTERISTICS OF A CAPACITIVE MASS FLOWMETER  
ON THE ANL SOLIDS/GAS FLOW TEST FACILITY

J. P. Bobis, W. E. Brewer, J. R. McQuinn,  
N. M. O'Fallon, and R. J. Armani  
Argonne National Laboratory  
Applied Physics Division  
Argonne, IL 60439  
312/972-6122 or 6047  
FTS: 972-6122 or 6047

Abstract

This paper describes the Argonne National Laboratory Solids/Gas Flow Test Facility (S/GFTF) and presents the results of the measurement of mass flow with the capacitive flowmeter at S/GFTF.

The capacitive flowmeter velocity measurements are compared with the gas velocity. The flowmeter's combined density/velocity measurements, which yield the mass flowrates, are compared with the time rate of change of the S/GFTF hopper weight.

For the different flow tests, instrumentation accurately monitored the air flowrate/temperature and the mass flowrate of the predominant 1-2 mm diameter limestone exiting and entering the hopper. The gas flowrate ranged from 150-350 CFM when operating at 20°C and near atmospheric conditions. The solid flowrate ranged from 0.3 to 3.0 lbs/sec as measured by hopper load cells and monitored with the data acquisition system.

Introduction

The Solids/Gas Flow Test Facility (S/GFTF) has been designed and constructed at Argonne National Laboratory (ANL) to support the development of flow instrumentation at ANL for the continuous monitoring of mass flow in the process streams of modern coal gasification systems. This need for mass flow measuring instrumentation has been documented in a state-of-the-art report.<sup>1</sup> The integrated facility with its data acquisition system is capable of providing measured and controllable flow conditions in several vertical and horizontal test regions that simulate the flow conditions in coal conversion plants.

One of the many techniques employed to measure the mass flow rate is the ANL capacitive flow instrument<sup>2</sup> where the measured capacitance varies as the dielectric constant of the material within it changes. Thus, this device yields a signal proportional to the average density or the volume fraction of solids. Several small electrodes in tandem and separated by a known distance in this capacitive flow instrument are used to give a velocity measurement by cross correlating their signals. The present study encompasses a detailed description of S/GFTF and the performance, for the measurement of mass flow, by the capacitive flowmeter on S/GFTF.

### Facility (S/GFTF) Description

The test facility, S/GFTF, is shown in Fig. 1 and schematically in Fig. 2. The S/GFTF is a closed system operating at gas temperatures up to 50°C and 5-10 psi above atmospheric pressure. The present limestone solids are conveyed with gas through 2 or 3 in. pipe and mass flows from 0.3 to 3.8 lbs/sec can be maintained in the dense and dilute phase test regions. The main elements of S/GFTF are:

1. Two storage hoppers mounted on electronic scales for direct readout of the solid's weight and where each hopper is capable of storing 900 lbs of solids.
2. Valves for varying the solid and gas flow rate.
3. Valves that can be arranged for different modes of loop operation.
4. Rotary blower powered with a 40 hp motor and capable of 320 CFM at 6 psig.
5. Sensors for measuring the gas flowrate/temperature and loop pressures.

### Typical S/GFTF Operational State

A typical operational state of S/GFTF is shown schematically in Fig. 3. A 3 in. knife valve (KV), operated from the control panel, permits variation of the quantity of solids delivered from the dense phase gravity flow section. The solid mass flows are pneumatically conveyed through the 8 ft long dilute phase test region and transparent spool pieces are located in the dense phase region and upstream of the capacitive flowmeter in the dilute phase section. The gas velocity is controlled, also from the control panel, in a manual or automatic mode by means of a bypass valve and process controller, which shunts the air from the loop. The solids/gas media is returned to hopper 2 through the dilute phase test section shown in Fig. 4 and for the unload mode, the emptying of hopper 1 lasts 5 to 50 minutes for the 0.3 to 3.0 lbs/sec range of mass flows. Upon completion of the unloading of hopper 1, the diverter valves are altered and the contents of hopper 2 are reloaded into hopper 1. Gas temperatures above 20°C can be obtained by controlling the heat exchanger and chiller following the blower.

### Solids Valve Control

A reliable method exists for reproducing the opening of the 3 in. KV controlling the amount of solids. A linear voltage differential transformer (LVDT) is coupled to the gate valve's linear stroke and it generates a dc voltage proportional to the valve position with a 3.6 V/in. sensitivity. A low mass permanent magnet core, with high retentivity, moves axially within a coil assembly and has a linear displacement of 4 in.

### Aeration Scheme for Low Mass Flows

For mass flows in the 0.3 to 0.8 lbs/sec, an effect aeration method with a whisper of the S/GFTF air exists above the 3 in. KV, at the base of the



vertical dense phase section, to successfully allow the passage of solids past the KV from hopper 1. Figure 5 shows, in a pictorial manner, the location of the six 1/16-inch aeration ports along the KV uniformly tapered 3 in. to 1.5 in. cone. Two are located near the valve seat and are aimed at a 30° angle downward. The remaining four are all aimed upward at a 30° angle, with each pair at a different elevation on the cone. The source of dry air is from the output of the rotary air blower.

### Mixing Tee Jet

For mass flows up to 4 lbs/sec, the cone is removed and it is necessary to increase the gas velocity at the solids/gas mixing tee with the gas jet shown in Fig. 6. The jet consists of a slanted wedge at the top and a venturi-shaped piece at the bottom, with both pieces capable of being adjusted for a desired gap. With a 0.188 in. jet gap, the resultant uniform mass flowrates are shown in Table 1 and the mass flowrate variation was less than 5%.

Table 1. S/GFTF Mass Flows with Gen. 2 Mixing Tee

Date	Run	Hopper 2 lbs/sec	Gas Flowrate CFM	Time Int. Sec.
3-25	8	1.05 ± 0.03	155 ± 0.8	300
		1.01 ± 0.03	205 ± 0.4	150
3-26	9	2.03 ± 0.1	163 ± 1	90
		1.97 ± 0.06	232 ± 1	160
3-26	12	2.97 ± 0.1	153 ± 1	135
4-7	10	3.26 ± 0.2	194.6 ± 0.5	50
3-24	7	3.78 ± 0.1	148 ± 2	75

### Solids Description

The solids used in this experimental study of the capacitive flowmeter on S/GFTF was 18A coarse limestone with an average density of 177 lbs/ft<sup>3</sup>. The results of a particle size analysis with a 12 compartment sieve are shown in Table 2. For the limestone loaded into S/GFTF, approximately 95% had a 0.71 to 1.4 mm diameter and approximately 80% had a 1.0 to 1.4 mm diameter. However, after 18 unloadings of the solids from hopper 1 to hopper 2, approximately 60% had a 1.0 to 1.4 mm diameter. Hence, S/GFTF was nicknamed the dolemite grinding facility (DGF).

### Hopper Weigh System Performance

The calibration of the electronic scales for hoppers 1 and 2 is performed with the static loading of eight certified 110.2 lb (50 kg) weights onto the empty hopper and the processed analog signals from the load cells are monitored with a precision digital voltmeter. Over a six month period, the weigh system sensitivity factor spanned between 233.8 to 237.2 lbs/volt. To provide an

Table 2. S/GFTF Limestone Particle Size Distribution

Mesh #	Tyler Equivalent	Opening Microns (mils)	Limestone <sup>a</sup> % by Weight Distribution	
			Virgin	18 Unloads
10	9	2000 (78.7)	1-2	0-1
14	12	1400 (55.5)	32-39	18
18	16	1000 (39.4)	41-46	41
25	24	710 (27.8)	10-15	22
35	32	500 (19.7)	1-2	7
45	42	355 (13.9)	0.5	3
60	60	250 (9.8)	0.5	2
80	80	180 (7.1)	0.5	2
120	115	125 (4.9)	0	3
170	170	90 (3.5)	0.5	0.5
230	250	63 (2.5)	0.5	0.5
325	325	45 (1.7)	0.5	0.5
		1000 $\mu$ < x < 2000 $\mu$	x = 73-85	x = 59
		710 $\mu$ < y < 1000 $\mu$	y = 10-15	y = 22

<sup>a</sup> 18A coarse limestone.

indication of the mass flow rate, the S/GFTF data acquisition system (DAS) determines the difference in hopper weight over a 5 to 20 sec time interval and calculates the solid flow rate. This maximum 1.5% variation in weigh system sensitivity factor is indicative of the mass flow accuracy and repeatability.

#### S/GFTF Data Acquisition System

For S/GFTF, the parameters being measured by the DAS illustrated in Fig. 7 are:

1. Hopper 2 weight;
2. Gas flowrate;
3. Hopper 1 weight;
4. Solid valve control position;
5. Gas valve control position;
6. Gas temperature; and
7. Capacitive flowmeter density signal.

These seven analog signals are scanned, as fast as a complete scan per sec, by a 16-channel 0 to 5 V analog to digital (A/D) converter system and stored in the computer memory. In real time, the loop operator can monitor on the computer terminal the mass flowrate of the solids in each hopper, as well as the instantaneous values of the gas flowrate/temperature. When the unloading of hopper 1 is complete, the software program, SGFTF3, for any selected time interval, generates time plots of all seven signals and calculates their mean and standard deviation.

### Capacitive Flowmeter and Measuring Electronics

The capacitive flowmeter,<sup>2</sup> as shown in Fig. 8, consists of two separate capacitive measurements -- one for density and the other for velocity. The capacitive density/velocity mass flow method has been described by a number of authors.<sup>3-6</sup> Within the spoolpiece, the short dimension electrodes, in the direction of flow, are used for the velocity signal and the long electrode is used for the density signal. A drive electrode serves as the other half of a parallel plate capacitor arrangement for the density and velocity electrodes. In December 1981, the capacitive flowmeter was located, as shown in Fig. 4, in a horizontal section of the S/GFTF dilute phase region and was approximately 6 ft downstream from the mixing tee (Fig. 6).

The schematic diagrams of the instrumentation for processing the signals from the capacitive flowmeter are shown in Figs. 9 and 10. A stable, 100 kHz sinewave oscillator is applied to the drive electrode with each sensing electrode connected to a current-to-voltage converter preamplifier, as shown in Fig. 9. Except for their gain, all preamplifiers were identical and any time delay differences were insignificant. To enhance the sensitivity of the density signal, a current buckout signal, derived from the drive signal, is introduced into the input of the density channel preamp. A null is achieved at the receiver bandpass filter output, with the amplitude and phase adjustments of the buckout current source, with only a gas flow through the capacitive flowmeter. The preamplifier output is bandpassed filtered, 100 kHz  $\pm$  5 kHz, and amplitude demodulated as shown in the Fig. 10 receiver schematic. The output of the amplitude demodulator is amplified and DC coupled to 1 sec first order low pass filter for the density signal and AC coupled to a 0-5 kHz low pass filter for the particle velocity signals. The receiver output for the density signal was measured in real time with the S/GFTF DAS, but the receiver outputs for the particle velocity measuring electrodes were recorded on a IRIG standard instrumentation magnetic tape recorder for cross correlation analysis.

The amplitude modulated phenomenon experienced by the capacitive flowmeter with a solids/gas flow is detailed in Fig. 11. With a 100 kHz voltage across the electrodes and the flowmeter experiencing a DC change of capacitance, the current sensed by the preamplifier is:

$$I = CWV_p \cos wt + \Delta CWV_p \cos wt + V_p d \left( \frac{\Delta c}{\Delta t} \right) \sin wt$$

(1)                      (2)                      (3)

where the applied drive =  $V_p \sin wt$ ,  $w = 2 \pi (100 \text{ kHz})$ , and  $C$  = the flowmeter capacitance with a gas flow. The first term is a steady state term and is cancelled with the buckout circuit. If it is assumed that the change in capacitance due to solids is  $K \sin W_s t$ , then terms (2) and (3) yield an amplitude modulated phenomena.

A block diagram of the instrumentation for performing time and frequency domain analysis on the particle velocity signals is shown in Fig. 12. Frequency domain information is obtained with a real time analyzer (RTA) and the dual channel digital signal (DSP) processor. Dual channel cross correlation

is also performed on the DSP with a 60 kHz analysis range and 64 linear averages for the pair of particle velocity electrodes 9E/10E and 9E/12E that have a 0.6 and 6.0 in. separation, respectively.

### Experimental Results

The first mass flow measurements with the capacitive flowmeter on S/GFTF were performed in December 1981. The initial measurements of particle velocity and density (particle concentration) were performed with the drive electrode at the bottom region of the dilute phase (i.e., the velocity and density electrodes were at the top) and the sensing velocity electrodes were 9E, 10E, and 12E. A comparison could be made from the 9E/10E cross correlation maximum time delay with that from the 9E/12E cross correlation. The drive signal was a 30V PK-PK, 100 kHz sinewave.

#### Particle Velocity Measurements at Low Mass Flow Rates

For each mass flow rate of 0.3 and 0.75 lbs/sec, the air flow rate was advanced stepwise from 194 to 324 CFM. A uniform mixing of solids and gas was observed entering the capacitive flowmeter, and there was no settling of the solids. With the capacitive flowmeter approximately 6 ft downstream of the mixing tee, without a jet, the particle velocity sensing electrodes yielded less than 1% amplitude modulation of the 100 kHz drive signal. This resulted in a poor cross correlation measurement of the amplitude demodulated signals from any pair of particle velocity sensing electrodes, but the spectral analysis of any preamplifier output revealed a predominant 0-2 kHz signal that the cross correlation analysis showed was related to the particle velocity. This signal, which was independent of the 100 kHz drive signal, is likely the result of an electrostatic effect in this pneumatic conveying system. This charging mechanism is well known,<sup>7</sup> but the accurate prediction of the signal characteristics is not. A typical correlogram for the 0.6 and 6.0 in. separated pairs of electrodes (9E/10E and 9E/12E) is shown in Fig. 14 and their corresponding frequency spectra in Fig. 13. The signal energy content is mostly in the 0-1 kHz range and rolls off 20 db before 2 kHz. Both correlograms have a distinct maximum and the time delay of each maximum is 0.65 ms and 6.44 ms, respectively, for the 9E/10E and 9E/12E sets of electrodes. This transforms to a 76.9 ft/sec particle velocity when the gas average velocity is 155.4 ft/sec (in 2 in. pipe). While the further separated electrode pair, 9E/12E, yields a distinguishable maximum, it shows several obvious smaller peaks. These are partially related to the particle velocity having some variation over the 6 in. electrode separation and the signals becoming incoherent.

The results of the particle velocity measurements for these two low mass flows of 0.3 and 0.75 lbs/sec are shown in Fig. 15. The particle velocity is linearly proportional to the gas velocity for each mass flow rate and a linear least square fit indicates that for the gas velocity range of 150 to 250 ft/sec, the particle velocity followed the relationship  $PV = K + 0.36 GV$ .

#### Particle Velocity Measurements at High Mass Flow Rates

The particle velocity measurements for mass flow rates of 1.2, 2.1, and 3.0 lbs/sec are also shown in Fig. 15. To achieve these higher mass flow rates, the mixing tee incorporated the jet (Fig. 6) and the 3 to 1.5 in.

tapered cone was removed from the 3 in. KV. The distinctive character of the correlogram maximum continued unchanged. The particle velocity remained linearly proportional to the gas velocity for each mass flow rate, and for the gas velocity range of 120 to 180 ft/sec, it followed the relationship  $PV = K + GV$ . It is somewhat probable that altering the S/GFTF geometry had an effect on the particle velocity, but it is important to emphasize that the particle velocity magnitude was reproducible for redundant tests.

#### Density Measurements

The results of the particle concentration measurements with the capacitive flowmeter are shown in Figs. 16 and 17. Figure 16, a time plot for a constant mass flow of 1.25 lbs/sec and an increasing gas flowrate from 160 to 210 CFM, illustrates that the measured density signal with the capacitive flowmeter decreased appropriately for each gas flowrate. Both signals (density and particle velocity) were measured with the capacitive flowmeter and are plotted in Fig. 17 for mass flowrates of 1.2, 2.2, and 3.1 lbs/sec. For each constant mass flow, the measured density decreased as the particle velocity increased and, for a constant particle velocity, the density signal increased as the mass flowrate increased. The peak-peak fluctuation of the density signals increased as the mass flowrate increased, and this could be strong evidence that at the higher mass flows, the media became less homogeneous.

#### Conclusion

The S/GFTF at ANL is now operational and can easily provide a pneumatic transport of solids for developing, testing, and calibrating flowmeter instrumentation. For the 0.2 to 3.7 lbs/sec range of solid mass flows and for the gas flowrate ranging from 150-350 CFM, a mass flowmeter can be installed in a vertical or horizontal pipe run with a DAS providing easy access of all pertinent flow and loop parameters.

The performance of the ANL capacitive flowmeter on S/GFTF has clearly shown that it is capable of measuring the particle velocity and the concentration of solids. The particle velocity was measured using the cross correlation method for a large range of mass flows and for volume fractions of solids to gas less than 1%. At present, the particle velocity signals originated from an electrostatic effect in this pneumatic conveying system. The measured density signal was shown to be proportional to the particle concentration for solid volume fractions less than 1% when a nulling scheme was used in the current sensing electronics. Also, the density signal was shown to be inversely related to the measured particle velocity for a range of constant mass flows.

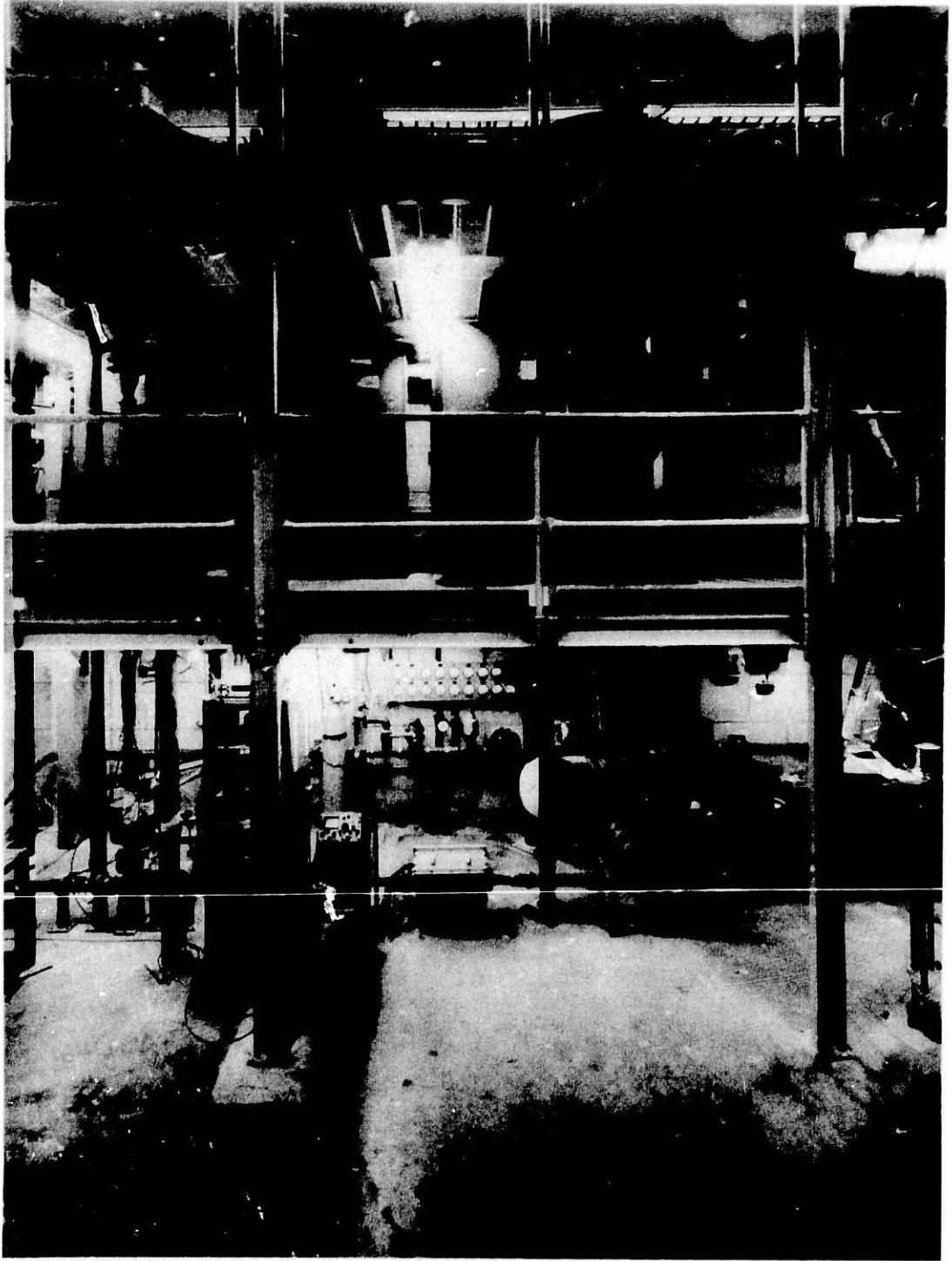
#### Acknowledgments

The authors of this report acknowledge the valuable assistance of the ANL Central Shops personnel and, in particular, the efforts of E. Lewandowski and J. Rowley in repairing the capacitive flowmeter and preparing the necessary piping elements for modifying S/GFTF. John M. Paul and William K. Brookshier provided valuable assistance in the design of the electronic instrumentation, while Joe Blahunka and Stan Koslowski performed the necessary construction of the electronic circuits. The work performed in preparation of the figures and drawings by Paul Begitschke is appreciated. Finally, the authors want to

thank Ray Grajek and Leon Dates for assisting in the coordinating of the experiments; Karl Porges and Ezzat Doss for their technical support; Holt Farley in the initial analysis of the data; and Gregory J. Bobis for timely drawing preparations.

#### References

1. N. M. O'Fallon, et al., "A Study of the State-of-the-Art of Instrumentation for Process Control and Safety in Large-Scale Coal Gasification, Liquefaction, and Fluidized-Bed Combustion Systems," Argonne National Laboratory report ANL-76-4 (Jan. 1976).
2. W. W. Managan, J. J. Eichholz, and R. W. Doering, "Field Test of a Capacitive Transducer for Density/Velocity (Mass Flow) Measurement on the HYGAS Pilot Plant Solvent/Coal Feedline," Argonne National Laboratory report ANL-78-62, pp. 193-221 (1978).
3. M. S. Beck, et al., "Measurement of Mass and Volume Flows of Slurries and Gaseous Suspensions," Process Instrumentation in the Metal Industries report IMC 1971, pp. 49-54.
4. M. S. Beck, G. Culvert, J. H. Hobson, K. T. Lee, and P. T. Mendies, "Total Volume and Component Flow Measurement in Industrial Slurries and Suspensions Using Correlation Techniques," Trans. of the Institute of Measurement and Control, Vol. 4, No. 8 (Aug. 1971).
5. M. S. Beck and A. Plaskowski, "Measurement of the Mass Flow Rate of Powdered and Granular Materials in Pneumatic Conveyors Using the Inherent Flow Noise," Instrument Review (Nov. 1967).
6. R. G. Green, S. H. Foo, and J. G. Phillips, "Flow Measurement for Optimizing the Feedrate of Pulverized Fuel to Coal-Fired Boilers," Argonne National Laboratory Report ANL-81-62, pp. 180-185 (1981).
7. S. O. Soo, "Dynamics of a Charged Suspension," Int. Rev. Aerosol Phys. Chem., 2:81-149.



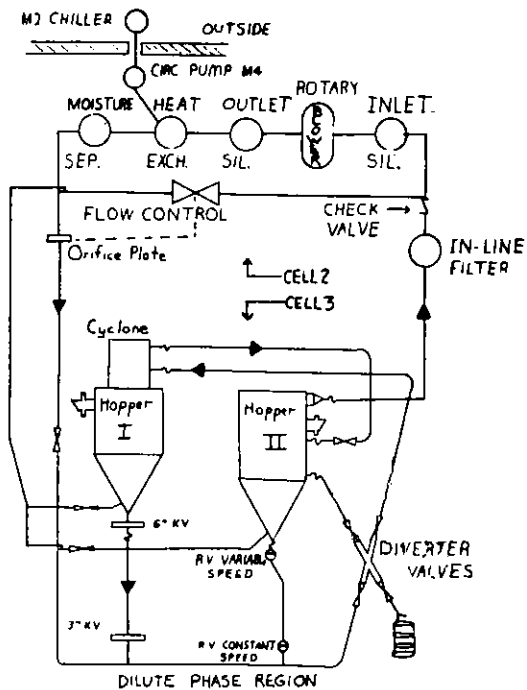


Fig. 2. Schematic of the Solids/  
Gas Flow Test Facility

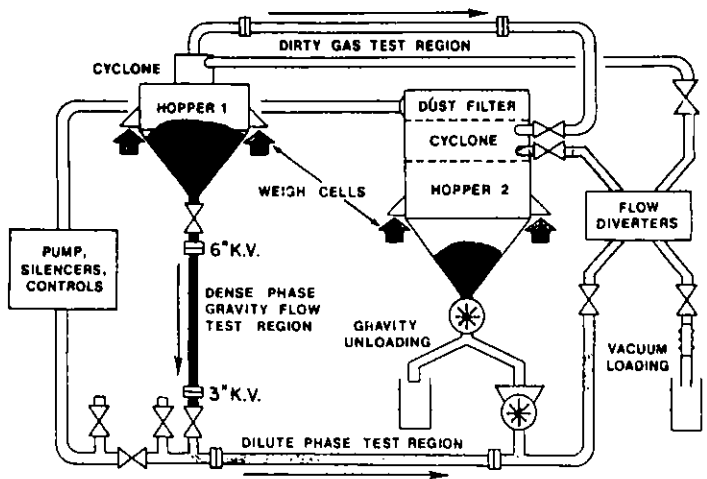


Fig. 3. Precision and Unload Mode  
for ANL S/GFTF

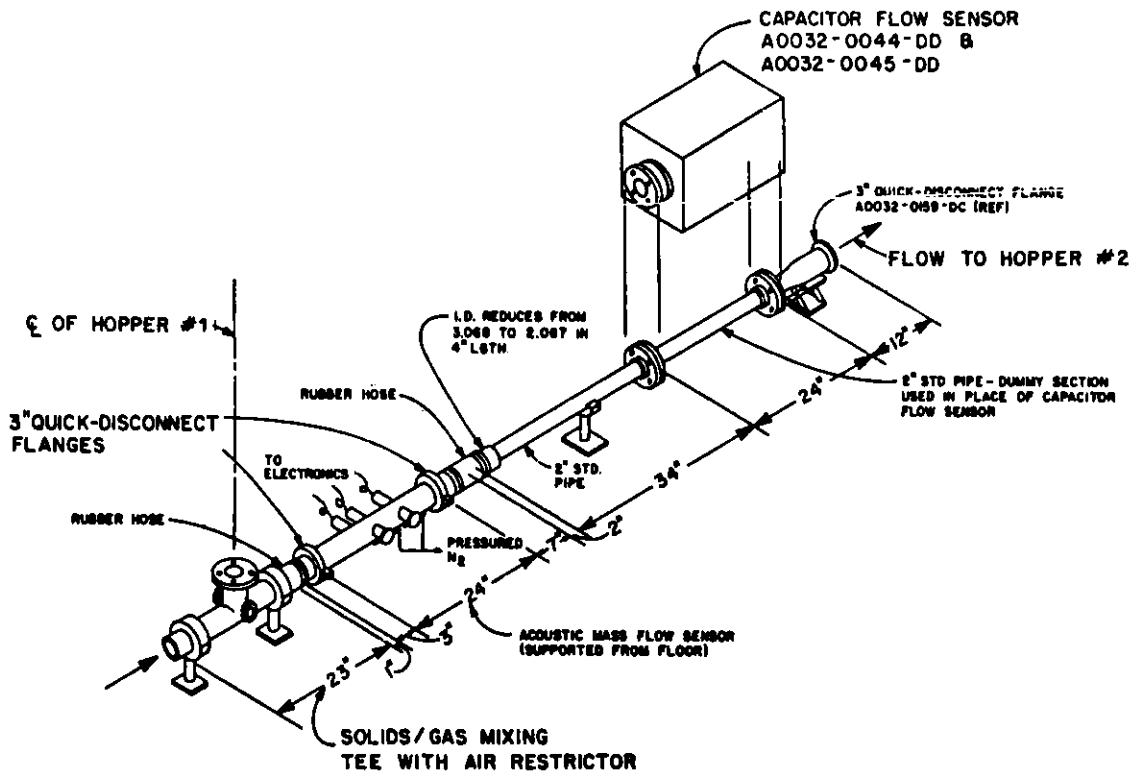


Fig. 4. Capacitive Flowmeter in Dilute Phase Region in the ANL S/GFTF



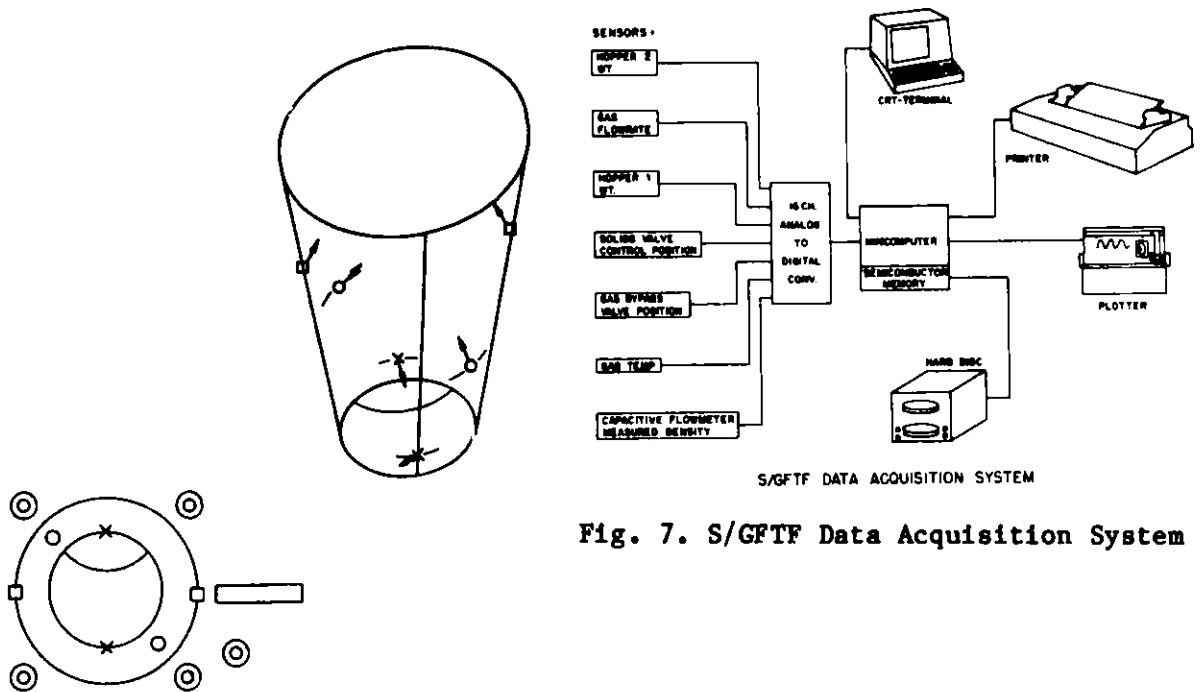
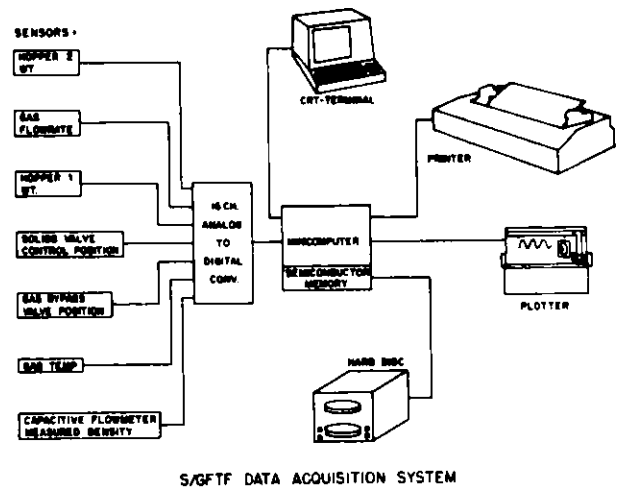


Fig. 5. Six Aeration Ports along the 3 in. KV Uniformly Tapered 3 in. to 1.5 in. Cone Located above S/GFTF Mixing Tee



S/GFTF DATA ACQUISITION SYSTEM

Fig. 7. S/GFTF Data Acquisition System

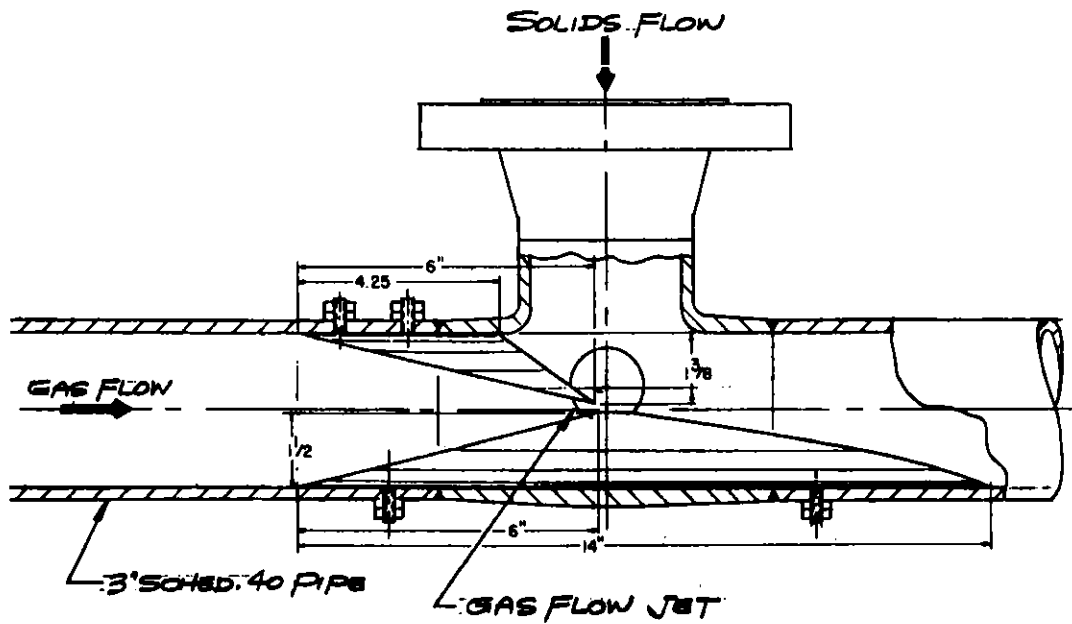


Fig. 6. S/GFTF Generation II Solids/Gas Mixing Tee

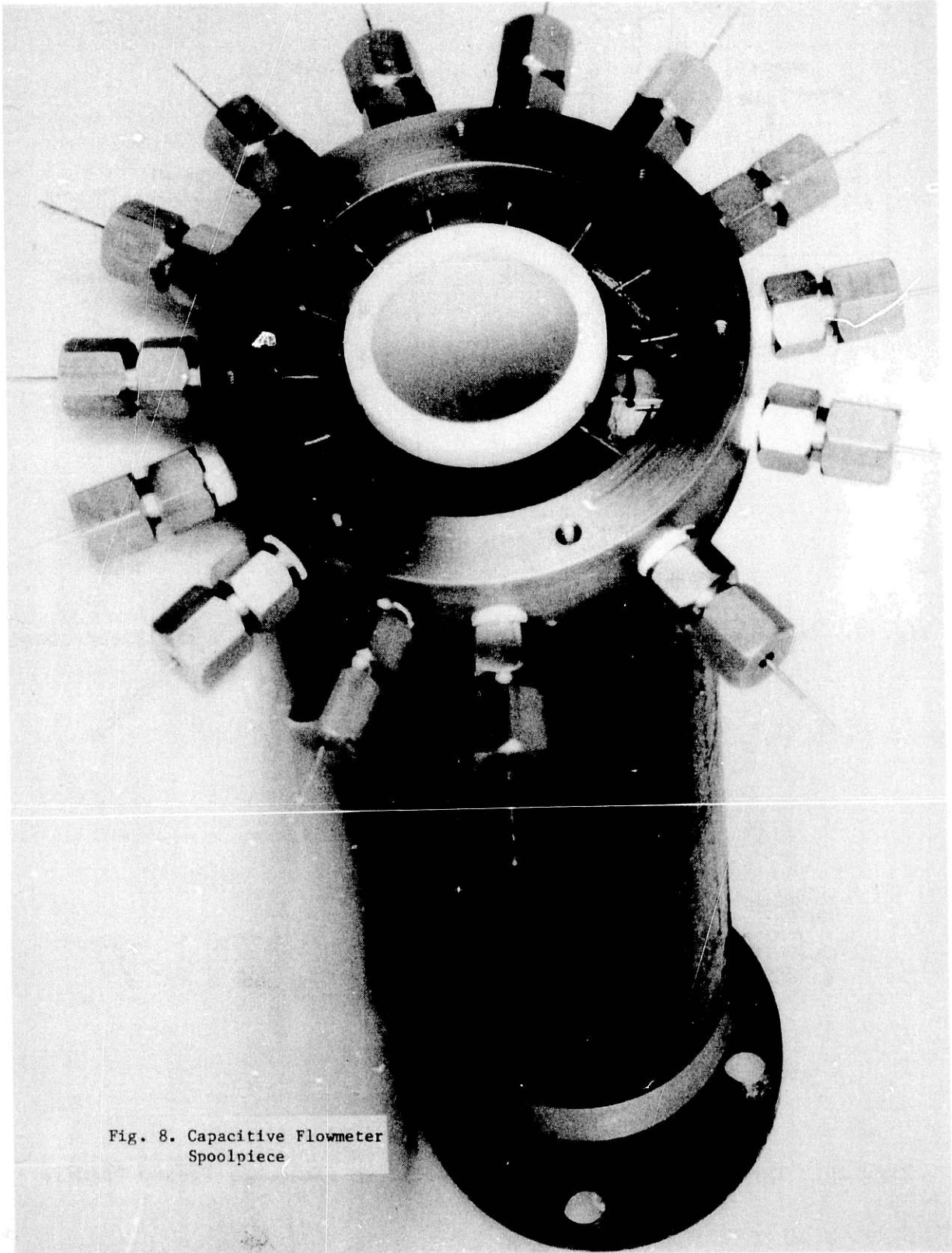


Fig. 8. Capacitive Flowmeter  
Spoolpiece

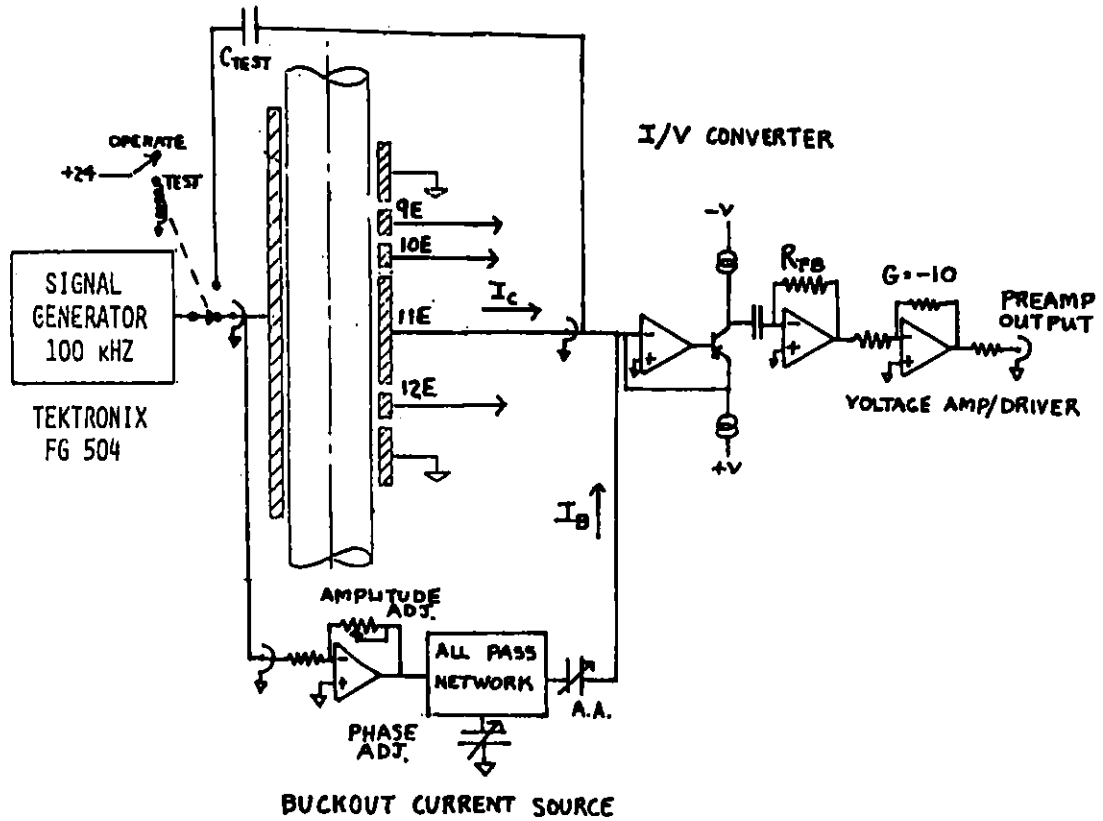


Fig. 9. Current Sensing Preamp for Capacitive Flowmeter Electrodes

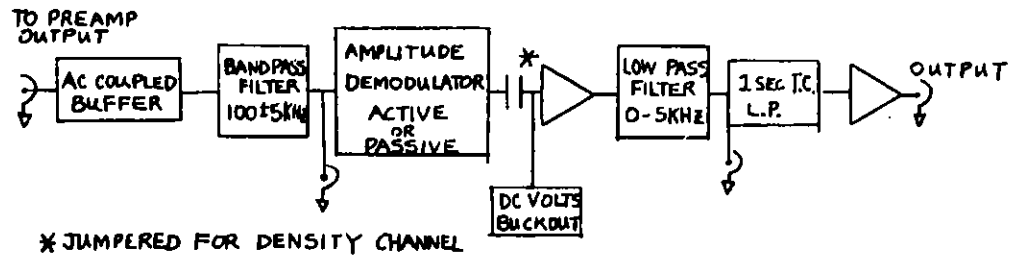
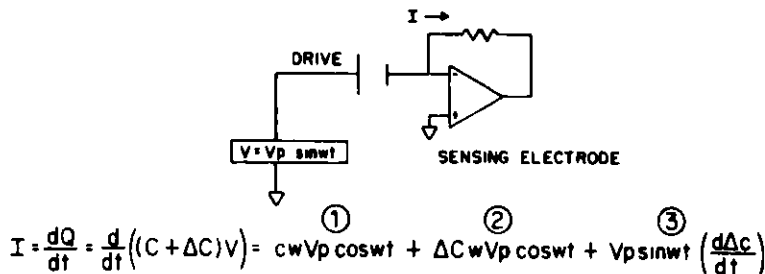


Fig. 10. Typical Receiver for the Capacitive Flowmeter Preamp Signals



1'  $cwVp \cos \omega t$  IS STEADY STATE TERM

2  $\Delta CwVp \cos \omega t = K_1 \sin \omega t \cos \omega t \rightarrow AM$   
if  $\Delta C \rightarrow \sin \omega t$

3  $Vp \sin \omega t \left( \frac{d\Delta C}{dt} \right) = K_2 \sin \omega t \cos \omega t \rightarrow AM$   
if  $\Delta C \rightarrow \sin \omega t$

Fig. 11. Basic Principle of Capacitive Flowmeter

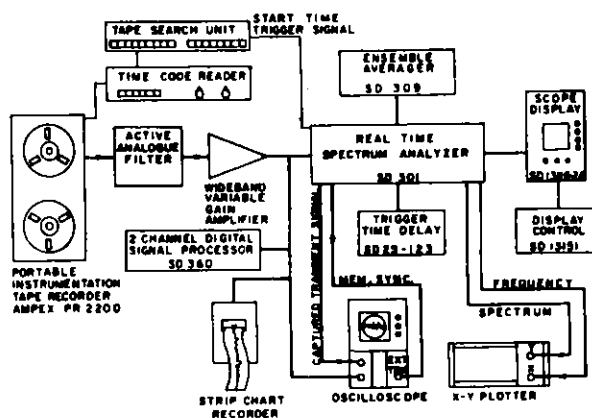


Fig. 12. Block Diagram of Data Analysis System for S/GTF Flowmeter Signals

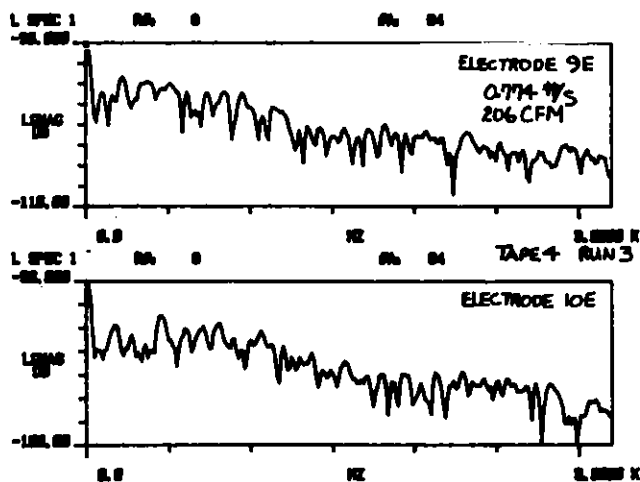


Fig. 13. Typical Amplitude Spectra for Capacitive Flowmeter Electrodes 9E, 10E at S/GTF with 0.774 V/s Mass Flow

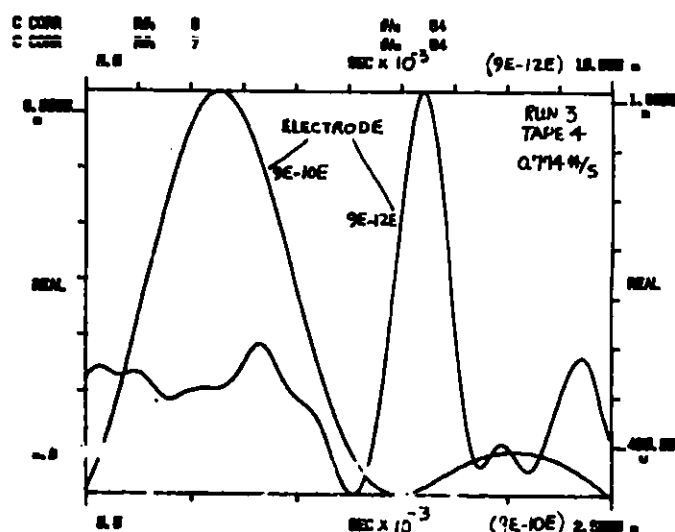


Fig. 14. Measured Cross Correlation Function for Capacitive Flowmeter at ANL S/GTF

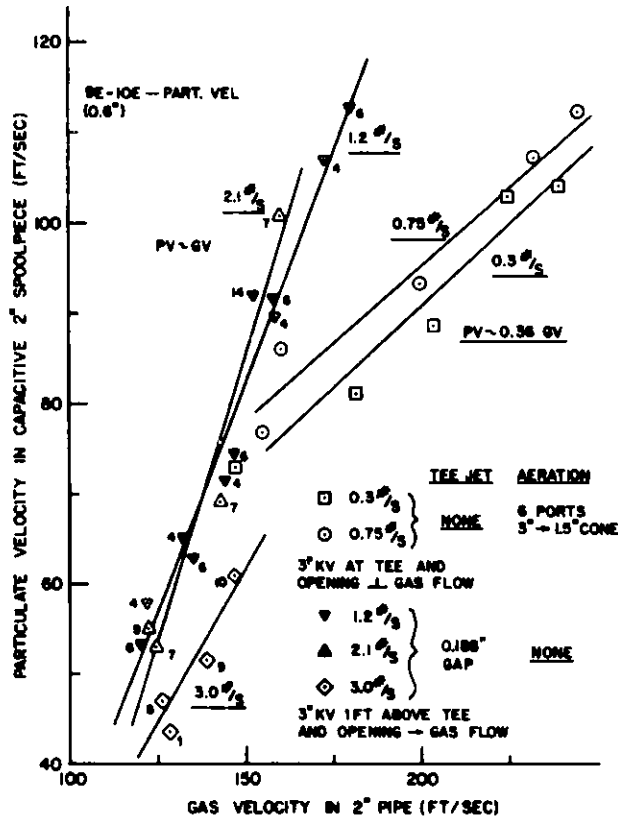


Fig. 15. Limestone Particulate Vel. vs Gas Vel. at S/GFTF

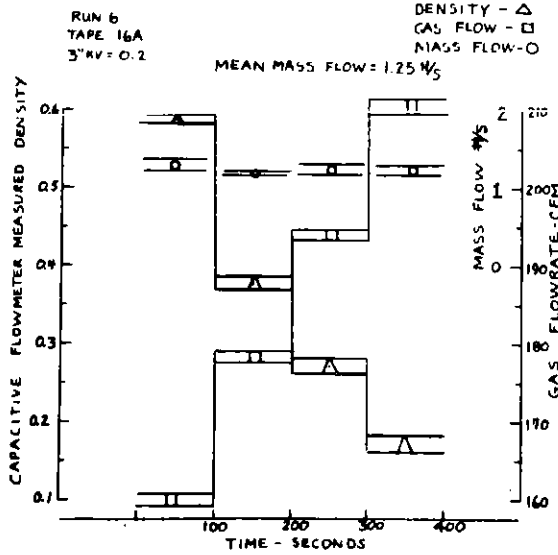


Fig. 16. Capacitive Flowmeter Measured Density for Constant Mass Flow and Increasing Gas Flowrate at ANL S/GFTF

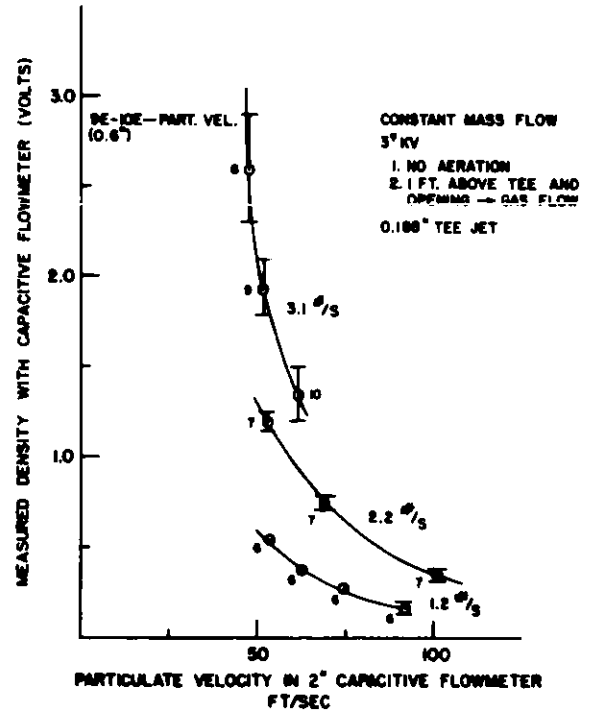


Fig. 17. Measured Density vs Measured Particulate Velocity with Capacitive Flowmeter at S/GFTF

REAL TIME VELOCITY MEASUREMENTS OF AIRBORNE SOLIDS FLOW  
WITH AN INDUSTRIAL CORRELATION FLOWMETER

Thomas E. Murphy and Melvin J Post  
Sybron/Taylor, Inc.  
P. O. Box 110  
Rochester, NY 14693  
716/235-5000

James Bobis  
Argonne National Laboratory  
Argonne, IL 60439  
312/972-6122

Holt L. Farley  
Foster Miller Associates, Inc.  
Special Programs Group  
350 Second Avenue  
Waltham, MA 02154  
617/890-3200

ABSTRACT

Flow velocity measurements of airborne limestone particles were made in the range of 65 to 110 ft/sec with mass flows in the range of 0.2 to 0.7 pounds/sec. Measurements were made on the Argonne Solids/Gas Test Flow Facility using the Argonne experimental capacitive sensors.

Flow rates were computed by the Taylor Industrial Correlation Flowmeter to provide real time velocity measurements. The real time velocity results are compared to differential pressure and commercial research-type correlation velocity estimates.

Introduction

The Taylor Instrument Company has been interested in Correlation Flow Measurement of Clean Fluids for some time. We describe here the application of a prototype correlation flow meter (CFM) to measurement of airborne particle flows. Our objective was to demonstrate that the Taylor CFM could in fact measure two phase flows given appropriate sensors for the flow.

In cooperation with the Argonne National Laboratory and Foster Miller Associates, we measured the flow of limestone particles in the Applied Physics Divisions Solids-Gas Flow Test Facility (S/GFTF) and using their experimental capacitive transducers. We have no previous experience with two phase gaseous flow. Our instrument, shown in Figure 1, normally uses ultrasonic sensors designed to measure clean liquid flows. We are, therefore, delighted to report the success of these preliminary measurements at the S/GFTF.

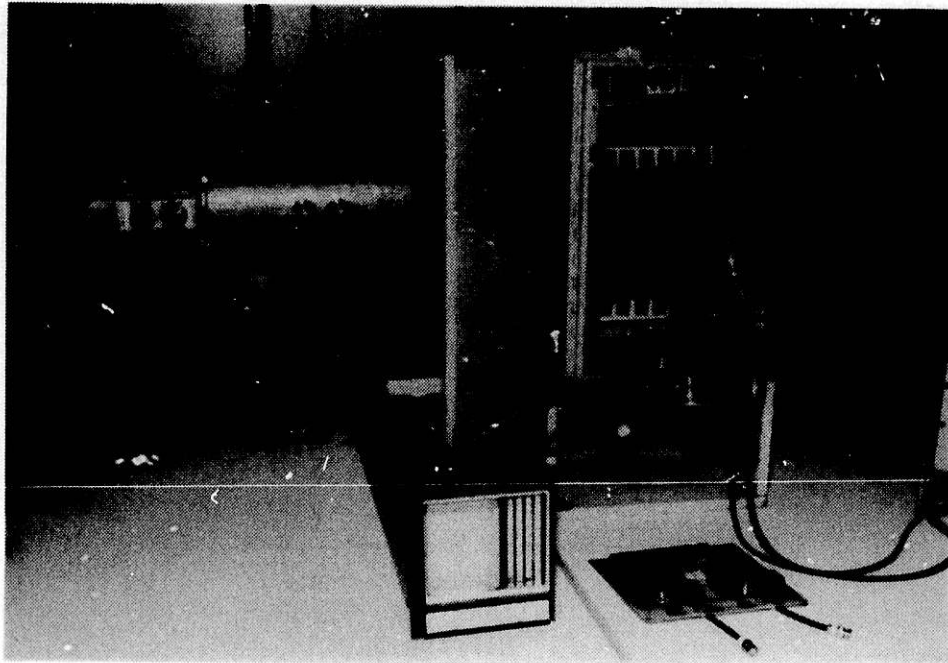


Figure 1. The Taylor prototype Industrial Correlation Flowmeter

We have been convinced for some time that the real problems in Correlation Flow Metering involve understanding the phenomena in the flow and properly designing sensors based on that understanding. These results support that conviction.

#### ANL Experimental Facilities and Sensors

The Applied Physics Division's Solids/Gas Flow Test Facility is shown in Figure 2. In our experiments limestone particles were unloaded from hopper 1 entered the flow via a 3" mixing Tee at a rate controlled by a 3" knife valve and were collected in hopper 2. The capacitive sensors were placed about six feet away from the mixing Tee where the particles mix with the air. The 3" pipe was reduced to the 2" diameter of the sensor section upstream of the sensors.

The experimental capacitive sensors are described in detail in earlier ANL reports to this symposium.<sup>1</sup> Figure 3 shows these sensors. The transducers used were spaced nominally 15 and 150 millimeters apart with an intermediate spacing of 135 millimeters also possible. A drive electrode, excited at 100 KHz, is opposite the sensing electrodes and extends the full length of the sensing region. This configuration includes shaping electrodes which provide a very uniform field in a radial plane. The field in the axial direction, however, would be less uniform due to the extended drive electrode. The ANL preamplifiers and filters were also used to obtain a demodulated signal. The S/GFTF circulated limestone particles ranging from about 3 millimeters in diameter down to fine dust. A sieve analysis showed that 70% were below 1 millimeter in diameter. However, homogeneity varied among samples making characterization more difficult.

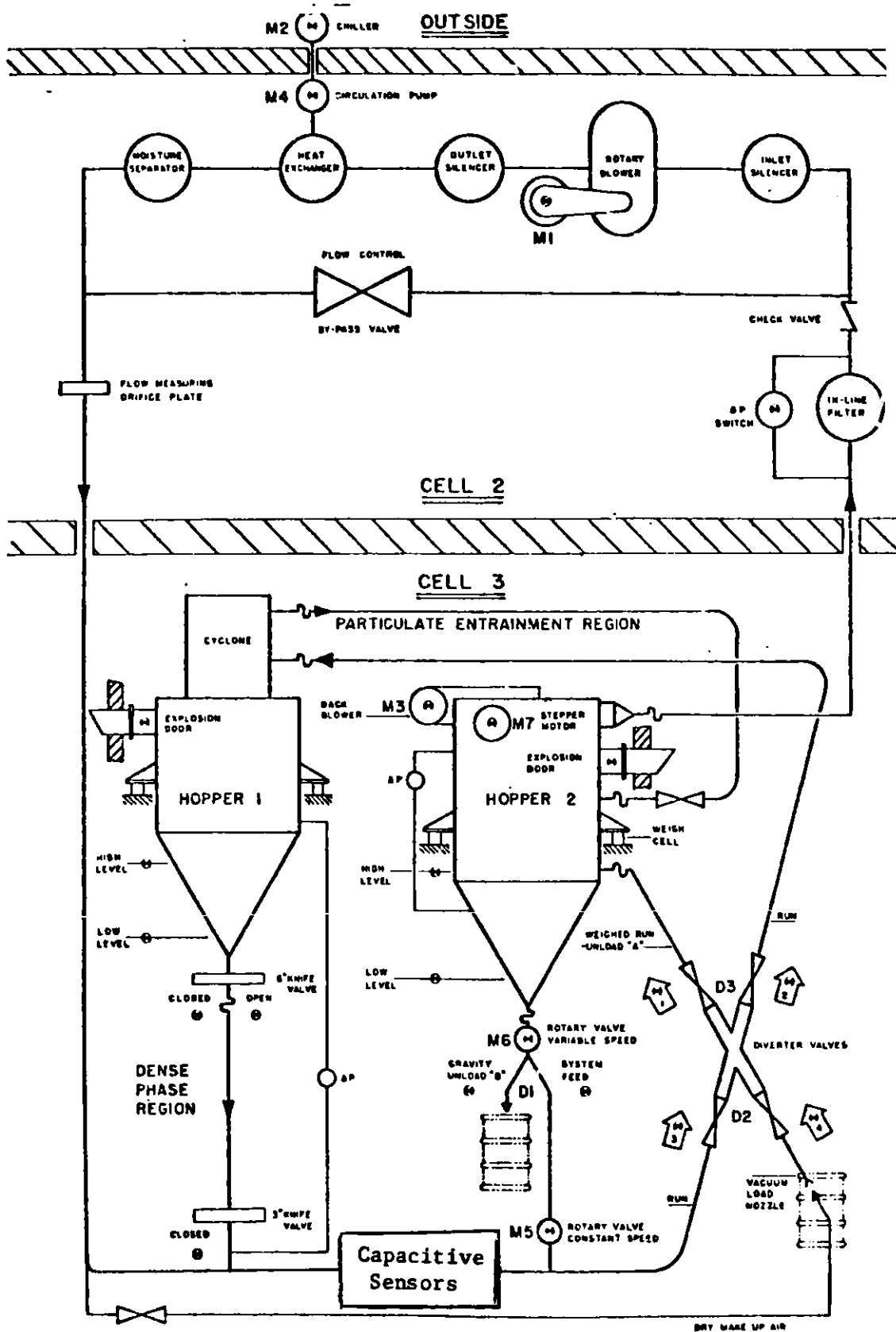


Figure 2. The Solids/Gas Flow Test Facility



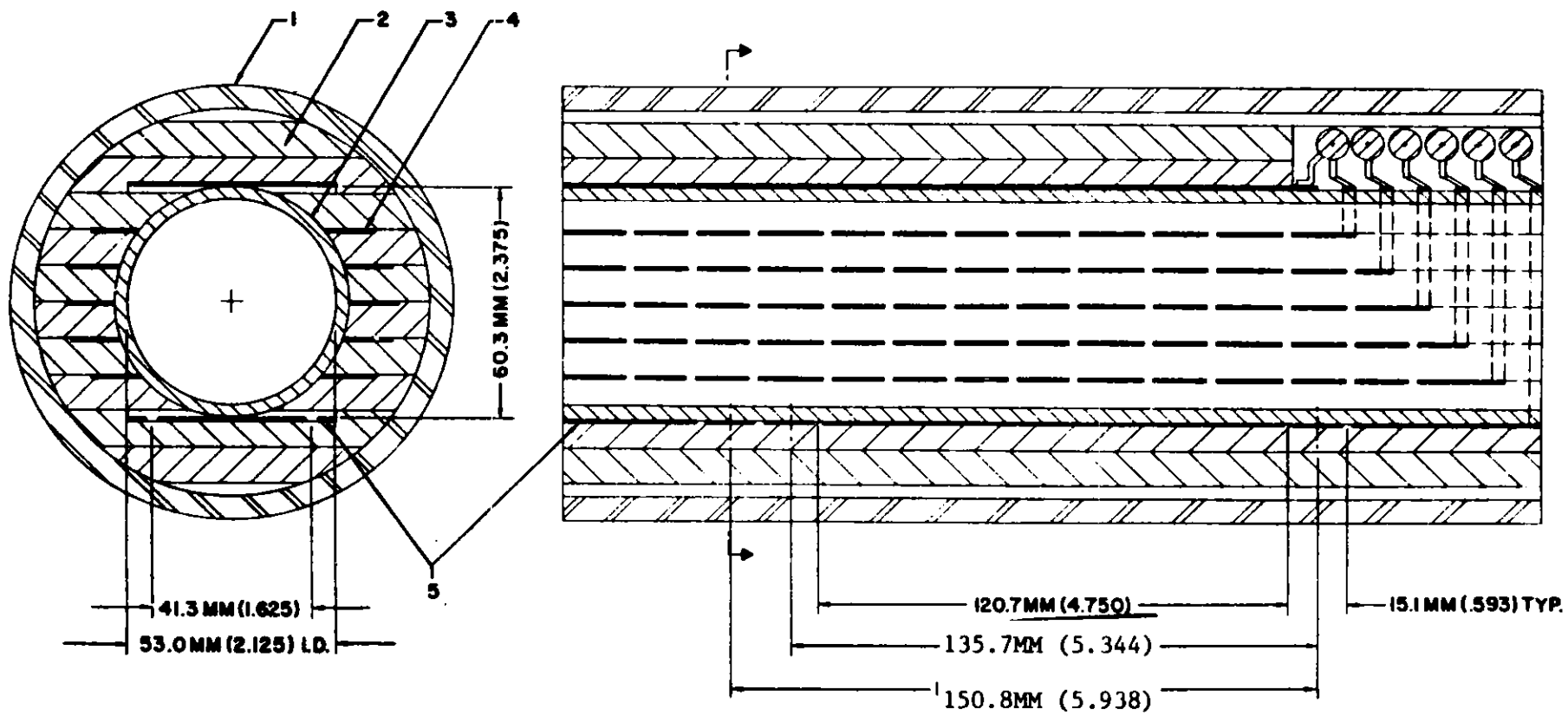


Figure 3. The ANL Capacitive Sensors

THE PROTOTYPE CORRELATION FLOW METER

A prototype correlation flowmeter (CFM) designed with industrial applications in mind was used in these experiments.

The correlation of two signals measures their similarity. A correlation flowmeter measures the similarity of signals seen at the upstream sensor to the same signals after they have progressed with the flow to the downstream sensors. There will, therefore, be a peak in the correlation vs. time delay curve. The peak corresponds to the time of flight or delay time due to the flow velocity. The physical origin of the signals differs with flow composition requiring a design match of sensor type and configuration choices to flow properties.

The Taylor CFM is a polarity/interpolated peak overflow type correlator. This means that it computes the average time of flight or delay time,  $\tau_d$ , of flow signals using the upper area of the correlation peak rather than just the highest point of the peak. If L is the distance between the sensors, the resulting velocity, computed as

$$V = \frac{L}{\tau_d} \quad (1)$$

has both improved accuracy and resolution over simple peak overflow correlators.<sup>2</sup> Accuracy is improved since 16 or more measurements of the upper area of the correlation peak are used to compute an average time of flight. This gives a reduced variability compared to a single point at the peak with the same number of time delay channels. Resolution is improved since the values of the average are not restricted to quantized increments of the time delay as a single point is.

The digital polarity correlation is performed by proprietary parallel processing chips. While there are only 168 actual channels or time delays, by using a variable sampling rate our instrument has the equivalent of over 970 channels. A much simpler instrument using an earlier version of these chips is described by Flemons.<sup>3</sup> We have extensively augmented the basic CFM functionality of the chips.

Figure 4 lists some performance specifications of the Taylor CFM. Note that some entries apply to ultrasonic sensors only while we used capacitive sensors in the work described here.

**Figure 4. Specifications of Taylor Correlation Flowmeter**

- Range of Velocity measurements:** 0.5 to 60 ft/sec.
- Measurement Spans:** Max, 3 to 60 ft/sec.;  
Min, 0.15 to 3 ft/sec.
- Output:** Current. 4 to 20 mA D.C.  
Frequency. 0 to 10 KHz  
Pulse. (frequency divided  
by 2 to 99999)
- Pipe Sizes:** 6 thru 24 inch.
- Pipe Materials:** All homogeneous metal and plastic pipes, assuming material is sonically conductive (laminated pipes are not satisfactory).
- Process Fluids:** All sonically conductive liquids, including those containing particles and minor entrapped gases.
- Reynolds Number:** Above 2000-5000.
- Accuracy:** 3% of reading, 5% to 100% of span.
- Resolution:** 0.25% of reading.
- Response Time:** 0.5 sec. on 60 ft/sec. range  
(Minimum) 10 sec. on 3 ft/sec. range
- Transducer Mounting:** Transducer must be adjusted to provide stated accuracy.
- Zero Flow:** The present circuit will "clamp" the output to zero for flow rates less than 5% of span.
- Mounting:** The electronic package must be located within 10 feet of the pipe mounted ultrasonic transducers.

The velocity range is selectable by thumbwheel switches from 3 to 60 ft/sec full scale or from 1 to 20 Meters/sec full scale. Ranges higher than 70 ft/sec are possible but were not used in the present work. On a given range the span is down to 5% of full scale with a limit of around 0.5 ft/sec due not to instrument performance but to generally poor correlation at low velocities. There is 50% overrange and underrange capability. Accuracy is specified at 3% of reading but can be improved at the expense of response time. Since response time is fastest on the high ranges and slowest on low ranges, using the highest range compatible with the expected span of velocities allows faster response.

Note that 4-20 mA current output, 0-10 KHz (full scale) frequency output and a pulse output (frequency divided by a selectable factor of 2 to 99999 for long time averaging of flow) are all available. In these experiments, frequency and 4-20 mA outputs were used.

Beyond the basics summarized in Figure 4, we expect that in a typical industrial application the operator may wish to

1. Make sure that an unreliable output (poor S/N due to poor correlation) is suppressed.
2. Speed up the response time of the meter at the expense of accuracy but without changing ranges.
3. Improve the accuracy of the output when a high signal to noise ratio exists without changing range or response time.

We have provided options to accommodate items 1-3 above. These options were not adjusted during the experiments described however. From our experience with this prototype, we expect that the options above and other CFM functions can now be redesigned to be adaptive or automated while also reducing the cost and size of the CFM.

### Velocity Measurements

A comparison of particle velocities and air velocities for different particle loadings is given in Tables 1 and 2. These results were obtained both during the actual runs and from recordings of the preamplifier signals made on an Ampex PR 2230 recorder.

Since the Taylor CFM was configured for a sensor spacing of 30 or 60 millimeters we could not make real time correlation from the sensors spaced at 15mm at the velocities used. Normalized correlation at the 15mm spacing was on the order of 0.7 but was more erratic at low loadings than the 150 and 135mm spacings tabulated. We found that data from the 135mm sensor spacings gave generally better results but with normalized correlations in the range of 0.2.

TABLE 1  
Flow Rate Measurements at Higher Loadings

L = 135mm  
(L = 150mm)  
 $\pm \% \text{ Error} = \frac{1SD}{\text{Mean}} \times 100\%$

$V_{\text{cfm}}$ (ft/sec)	$V_{\text{commercial}}$ (ft/sec)	$V_{\text{air}}$ (ft/sec)	lbs/sec
110.46 $\pm$ 0.47%	103.71 $\pm$ 2.09%	244.1 $\pm$ 0.785%	0.736 $\pm$ 3.08%
(110.03 $\pm$ 1.55%)	(105.93 $\pm$ 1.27%)		
76.01 $\pm$ 1.25%	73.45 $\pm$ 1.45%	155.4 $\pm$ 0.847%	0.774 $\pm$ 3.50%
(76.25 $\pm$ 1.11%)	(74.17 $\pm$ 0.79%)		
70.44 $\pm$ 0.56	70.80 $\pm$ 1.07%	151.4 $\pm$ 0.847%	0.608 $\pm$ 5.78%
(71.44 $\pm$ 0.97%)	(71.55 $\pm$ 2.70%)		
113.40 $\pm$ 1.09%	110.95 $\pm$ 1.77%	248.8 $\pm$ 0.818%	0.501 $\pm$ 9.98%
(112.48 $\pm$ 1.94%)	(110.96 $\pm$ 1.41%)		

TABLE 2  
Flow Rate Measurements at Lower Loadings

L = 135mm

$V_{\text{cfm}}$ (ft/sec)	$V_{\text{commercial}}$ (ft/sec)	$V_{\text{air}}$ (ft/sec)	lbs/sec
97.00 $\pm$ 0.91%	100.02 $\pm$ 1.77%	239.28 $\pm$ 0.61%	0.302 $\pm$ 9.27%
64.38 $\pm$ 2.02%	64.76 $\pm$ 4.18%	147.28 $\pm$ 2.07%	0.325 $\pm$ 5.85%
62.59 $\pm$ 0.82%	64.69 $\pm$ 3.56%	143.69 $\pm$ 1.51%	0.268 $\pm$ 14.93%
101.05 $\pm$ 0.44%	104.35 $\pm$ 1.04%	242.36 $\pm$ 0.51%	0.239 $\pm$ 12.55%

The  $V_{\text{cfm}}$  particle velocity data were obtained from the CFM frequency output with a Data Precision 5740 Frequency Counter. The ANL commercial correlator averaged  $2^6$  spectra at a 120 KHz sampling rate and the

correlation peak was found via a cursor. The air velocity data is derived from an orifice plate well upstream of the mixing tee. The pounds per second data is derived from multiple readings of the hopper weight during the experiment.

### Particle Velocity

The CFM and commercial correlator velocity readings are comparable and agree within the variability of their readings with few exceptions.

The particle velocity as measured by both the Taylor CFM and the commercial correlator is less than 1/2 the air velocity as shown in Figure 5. Since air velocity is derived from orifice plate measurements and verified by a pitot tube, we conclude that the particles are slower and are not fully mixed into the entire flow or accelerated to terminal velocity. This is most likely due to the proximity of the sensors to the mixing tee and possibly to the pipe reduction of 3 to 2 inches upstream of the sensors.

There is also a loading effect illustrated by Figure 5, the heavier loadings giving higher velocity readings. We expect that this is related to a combination of incomplete mixing, acceleration and sensor field inhomogeneity. The result is variations in power vs. frequency and signal to noise ratios for eddies at different velocities. Theoretically, higher flow rates pick up more particles but the maximum size of particles transported is limited by the density and viscosity of the air and particles. Therefore, because the capacitive electrodes sense the changes in capacitance or net charge due to the particles caught up on eddies, any nonuniformity in the particle distribution and concentration can change the way the eddies are "marked". Heavier loadings appear to "mark" the larger more rapidly moving eddies better, giving them a higher signal to noise ratio. Lighter loadings possibly deposit more particles in the outer, slower moving part of the flow where the small sensors are located.

Therefore, an additional factor may be the shape of the sensed region in the axial direction. Stronger signals may be arising near the electrodes since the field should be stronger there. That produces slower velocity readings since the flow is slower (and more noisy) there. The capacitive sensors are being relocated in the flow loop to moderate the above effects.

### Variability in Velocity Measurements

The variabilities of the CFM and commercial correlator are roughly comparable. Even though the CFM has only 168 actual channels (time delays), it operates with the equivalent resolution and accuracy of over 970 channels. We can make a rough comparison of the CFM (using peak interpolation and weighted sample clock) and the commercial correlator playing the role of a peak overflow correlator with over 1000 channels.

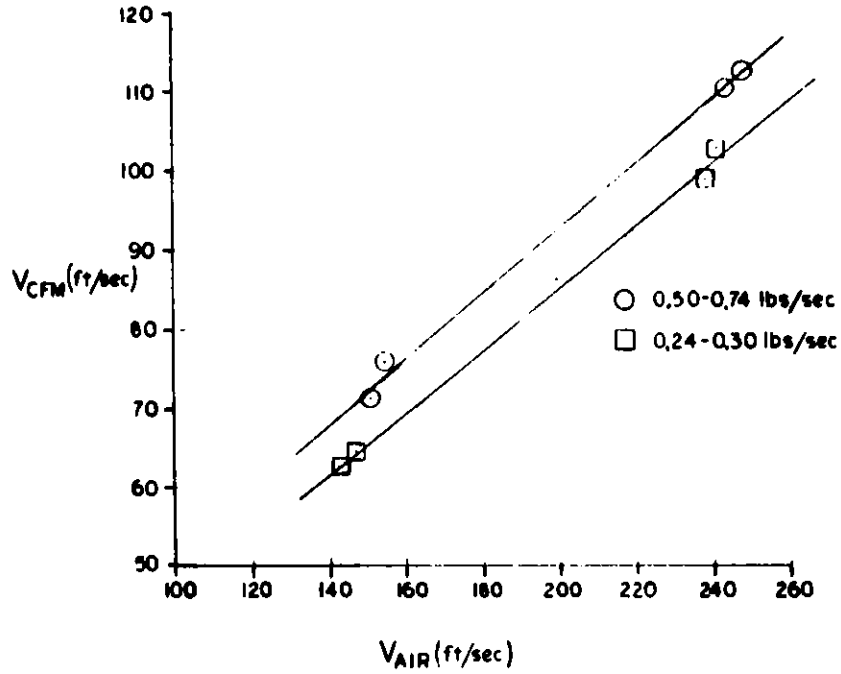


Figure 5. Comparison of Particle Velocity ( $V_{cfm}$ ) and Air Velocity ( $V_{air}$ )

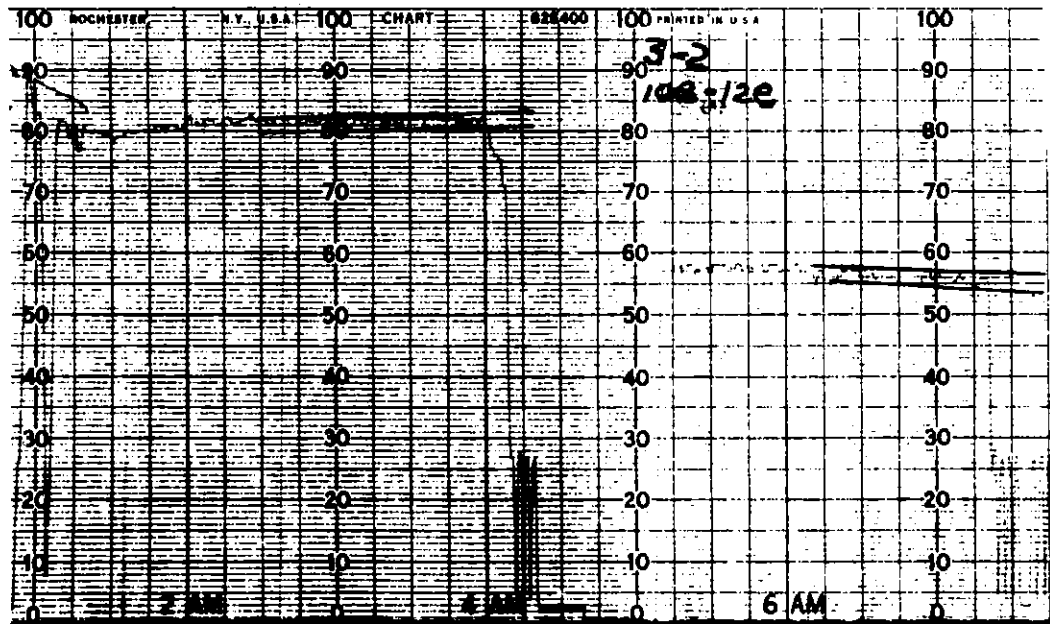


Figure 6. Taylor CFM 4-20 mA Output Recording

Notice in Figure 6, the CFM real time 4-20 mA output, that the average velocity was not stationary. We predict theoretically that the variability due to eddy flow noise would be  $\pm 1.5$  to  $\pm 2.2\%$  ( $1SD/Mean \times 100\%$ ). The variability on the recording is certainly comparable to that and has a response time of 0.5 to 1.0 second. However, taking readings over the several minutes of a run reflected the nonstationarity of the flow system as well as the flow noise itself. In general, the CFM readings covered a larger portion of the runs than the commercial correlator and were hence more affected by non-stationarity bias. On the other hand, the data from the commercial correlator was averaged over a smaller portion of the experimental runs and would be less influenced by nonstationarity. Finally, the commercial correlator performs a direct correlation as opposed to polarity correlation which decreases its variability by a factor of 0.63. We assume that all of these factors roughly cancel out.

Note also that while air velocity was reasonably steady, the loading had a considerably higher variability. As we said, the particles loading the air are what gives a signal. We, therefore, expect that a great deal of the variability in our readings really was associated with the loading variability rather than with the randomness of eddy patterns.

#### Conclusions

We conclude that the Taylor prototype Industrial Correlation Flow-meter can conveniently measure airborne particle velocities given appropriate sensors and input conditioning electronics. Further, the accuracy, response time and resolution are roughly comparable to more expensive research correlators. Finally, the major area to concentrate on in correlation flow measurement is the understanding of the flow characteristics and how to design sensors and input conditioning electronics to match and adapt to the flow characteristics.

#### Acknowledgements

The authors experienced a particularly fine cooperative effort at the S/GTF. We wish to thank Dr. O'Fallon and the ANL staff for their support and encouragement of these experiments. These experiments are an outstanding example of the benefits industry can derive from ANL facilities and expertise.

#### References

1. W. W. Managan, J. J. Eichholz and R. W. Doering, "Field Test of a Capacitive Transducer for Density/Velocity (Mass Flow) Measurement on the HYGAS Pilot Plant Solvent/Coal Feedline". Proceedings of the 1978 Symposium on Instrumentation and Control of Fossil Energy Processes, Newport Beach, California (June 19-21, 1978).
2. J. R. Jordan and R. G. Kelly, "Integrated Circuit Correlator for Flow Measurement," Measurement and Control, Vol. 9, p. 267, 1976.



References  
(Cont'd.)

3. R. S. Flemons, "A New Non-Intrusive Flowmeter", National Bureau of Standards Special Publication 484, Proceedings of the Symposium on Flow in Open Channels and Closed Conduits. NBS, Gaithersburg, Maryland (February 23-25, 1977).

MASS FLOW MEASUREMENTS OF GAS-SOLIDS SUSPENSIONS  
USING VENTURIMETERS WITH LIGHT ATTENUATION

by

A. Payne, M. Werner, D. Plank and C.T. Crowe  
Department of Mechanical Engineering  
Washington State University  
Pullman, WA 99164-2920

Abstract

Two independent measurements are needed to measure the flow rate of each phase in gas-solids mixtures. With the gas-solids flow through a venturi, two such measurements are the pressure drop between the pipe and throat and the attenuation of light across the flowing mixture. This technique is viable if the particle size is known. Another approach is the measurement of pipe-throat pressure drop and the total pressure drop across the venturi. This technique is valid for Stokes number exceeding seven and is independent of particle size.

Introduction

The need to measure the flow rates of gas-particle mixtures is encountered in pneumatic transportation systems, in combustion and reactor systems, and in coal gasification systems involving char transport by high pressure, high temperature steam. A wide variety of devices have been proposed for such measurements, ranging from acoustic and capacitive instruments to instruments utilizing cross-correlation of signals from two different stations in a line.

Studies at Washington State University have focussed on the venturimeter as a device for metering gas-solids flows. The venturimeter is attractive because of its simplicity and reliability. Also, the essential scaling parameters have been identified so the instrument can be confidently scaled up to prototype operation. Concerns specific to the venturimeter are the erosive potential of the conveying fluid and the head loss associated with a variable area duct. The erosion problem is no more severe than on other components in the line. Recent studies at Washington State University have shown that the total head loss is not excessive, in fact, much less than the head loss associated with a bend. Moreover, the total head loss provides further useful information for measuring flow rate.

Independent of the device used, at least two separate measurements are needed to determine the flow rate of each phase. For a device that measures the velocity of the particulate phase, another measurement of particle number density (or bulk density) is needed to have the flow rate of the solid phase. The flow rate of the conveying phase can be assessed by measuring the pressure and temperature and assuming velocity equilibrium between phases. This assumption becomes less reliable for decreasing pipe size.

This paper investigates the utility of laser attenuation measurements in conjunction with venturi pressure drop measurements to yield the flow

rate of each phase. The likelihood of using only pressure measurements to achieve the same purpose is also considered.

### Gas-Solids Flows in Venturimeters

The principle of operation of venturimeters with single phase flows is well-known. The pressure drop due to acceleration of the fluid through an area constriction can be related directly to the flow rate through application of Bernoulli's equation and correction factors for viscous effects. The same principle extends to gas-solids flows with pressure drop being additionally dependent on particle size and solids flow rate.

The pressure drop in a venturi with gas-solids flow, depends on the extent to which the particles are accelerated. Small particles are able to maintain near-velocity equilibrium as the mixture accelerates toward the throat. The increased force needed to accelerate the particles manifests itself as increased pressure drop in the conveying phase. In the limit of particles sufficiently small to maintain velocity equilibrium with the gas, the flow behaves as a single phase fluid with a modified density. In this case, the pressure drop is given by

$$\Delta P_{TP} = \Delta P_G (1+Z) \quad (1)$$

where  $\Delta P_G$  is the pressure drop with only gas flowing through the venturi and  $Z$  is the <sup>g</sup> loading, that is, the ratio of particulate mass flow to gas mass flow rates. This flow condition is known as equilibrium flow.

Acceleration of the particles relative to the gas (and the associated pressure drop) depends on the time available for particle acceleration and the characteristic aerodynamic response time for the particles. The aerodynamic response time is quantified by

$$\tau_A = \rho_p D^2 / 18\mu \quad (2)$$

where  $\rho_p$  is the material density of the particle,  $D$  is the particle diameter, and  $\mu$  is the dynamic viscosity of the conveying fluid. This time represents the time required for a particle, released from rest, to achieve 63% of the freestream velocity in the constant velocity flow.

The time available for acceleration is approximately the fluid residence time in the venturi, or

$$\tau_R = L/U \quad (3)$$

where  $L$  is the throat diameter and  $U$  is fluid velocity.

The Stokes number is the ratio of aerodynamic response time to flow residence time.

$$St = \tau_A / \tau_R = \rho_p D^2 U / 18\mu L \quad (4)$$

Equilibrium flow is attained when the Stokes number approaches zero.

The Stokes number represents the primary scaling parameter. Large scale systems can be modeled by smaller particles in a bench-scale experiment. The Stokes number representative of -200 mesh pulverized coal particles in a feed-line to a combustor in a coal-fired power plant is approximately 2. On the other hand, conveyance of char particles between 10 and 80 mesh in steam at 1000 psi and 700°F represents a range of Stokes numbers between 10 and 800.

Experiments with gas-particle flow through venturis indicate that the pressure drop ratio at a given Stokes number varies linearly with loading. Results of experiments with limestone particles are shown in Fig. 1. One notes that the results fall below the limiting line for equilibrium flow, but that the data tend to approach equilibrium flow conditions as the Stokes number is decreased. The linear dependence of pressure drop ratio ( $\Delta P_{TP}/\Delta P_g$ ) with loading allows one to incorporate loading into a pressure ratio parameter defined as

$$Pr = \left( \frac{\Delta P_{TP}}{\Delta P_g} - 1 \right) / Z \quad (5)$$

which is primarily dependent upon Stokes number. The pressure ratio parameter approaches unity as a Stokes number approaches zero.

The variation of pressure ratio parameter with Stokes number for coal particles in a standard ASME venturi geometry for Stokes numbers from .6 to 150 is shown in Fig. 2. One notes that, as the Stokes number decreases, the pressure ratio parameter increases toward unity. However, the most striking feature of this figure is the insensitivity of pressure ratio parameter to Stokes number for Stokes numbers exceeding four. This trend indicates that pressure drop is independent of particle size in this range. Further, if the flow rate of the conveying phase is known, ( $P_g$  known) then the loading is given directly from the two-phase pressure measurement, namely,

$$Z = \left( \frac{\Delta P_{TP}}{\Delta P_g} - 1 \right) / Pr \quad (6)$$

where  $Pr$  is the asymptotic limit of the pressure ratio parameter. The mass flow rate of the particulate phase is obtained by multiplying  $Z$  by the known flow rate of the conveying phase.

In many cases, the flow rate of the conveying phase may not be known. In this case, further measurements are needed to provide the flow rate of each phase. Two measurements are considered in this paper: laser attenuation and total pressure drop.

#### Laser Attenuation Measurements

Experiments were performed with a  $\frac{1}{2}$  mW laser directly across the throat section of the venturi. The system was designed with a beam-splitter to provide a reference beam which did not traverse the gas particle mixture. The intensity was measured with two photoresistive cells and associated electronic circuitry. Special efforts were made to insure minimum thermal drift and to eliminate stray light. The details of the experiment can be found in the reference.

Attenuation of a laser beam by a gas-particle cloud is assumed to obey Beer's law; that is, the spatial rate of decrease of intensity is proportional to the intensity or

$$\frac{dI}{d\ell} \propto -CI \quad (7)$$

where  $I$  is intensity,  $\ell$  is the beam length, and  $C$  is the proportionality constant. If the particle size is much larger than the beam wave length, a condition satisfied in this study, the particle simply serves to block (geometric limit) the incident light. By relating the proportionality constant to the blockage area provided by the particles, one finds that the intensity should vary as

$$\ln(I_0/I) \propto Z(\rho_g/\rho_p)(U_0/U_T)(L/D) \quad (8)$$

where  $I_0$  is the reference intensity,  $Z$  is the loading,  $\rho_g/\rho_p$  is the material density ratio,  $U_0/U_T$  is the particle velocity ratio between the entrance and the venturi throat,  $L$  is the total path length, and  $D$  is the particle diameter.

Results of the laser attenuation experiments plotted as a function of loading for two different coal particle sizes (mass median diameter) are shown in Fig. 3. One notes the anticipated linear variation with loading. Also, one notes the larger sensitivity to loading with decreased particle size, as expected. Currently more extensive experiments are under way at Washington State University to investigate size distribution effects and the influence of nozzle geometry.

The observed linearity of laser light attenuation with loading suggests the combination of light attenuation and pressure drop measurements to determine the flow rates of each phase. If the attenuation curve is known for a given particle size, the attenuation measurement will yield the loading,  $Z$ , directly. The pressure drop for the conveying phase,  $\Delta P_g$ , can be obtained from the measured two-phase pressure drop; that is,

$$\Delta P_g = \Delta P_{TP} / (1 + Z Pr) \quad (9)$$

The value of  $\Delta P_g$  will yield the flow rate of the conveying phase using conventional single-phase flow correlations. The flow rate of the particulate phase is the product of the conveying mass flow rate and the loading,  $Z$ . A slight correction may be needed in that the pressure ratio parameter,  $Pr$ , depends on particle size and the conveying fluid velocity. The latter may not be known, a priori. However, the initial value for the pressure ratio parameter will be estimated based on the assumed velocity and corrected once the velocity is calculated. The iteration would converge quickly because the pressure ratio parameter is a weak function of Stokes number.

#### Total Pressure Drop Measurements

A series of measurements were undertaken to establish the pressure loss across the venturimeter, from the entrance to the end of the diffuser section. The original purpose of these measurements was to establish the level of total head loss with gas-solids flows to assess if these losses were excessive. The measurements were done with a wide range of particle

sizes and exit cone angles from 2° to 8° (full angles). It was found that the long exit cones gave rise to higher pressure losses due to the frictional losses associated with increased surface area. Also, the pressure losses associated with the 8°-exit cone exhibited some unsteadiness characteristic of incipient separation. The optimum exit cone angle appeared to be 6°. The total pressure loss associated with the 6° exit cone were not excessive and were significantly less than the loss to be encountered for gas-particle flow around a bend.

The ratio of total pressure drop ( $\Delta P_{TTP}$ ) to pressure drop between the entrance and the throat ( $\Delta P_{TP}$ ), is shown in Fig. 4 as a function of loading. The Stokes numbers range between 7 and 123. One notes that the data fall very close to a single curve, implying that the total pressure drop ratio ( $\Delta P_{TTP}/\Delta P_{TP}$ ) is independent of Stokes number (and particle size) in this range. This finding parallels the discovery of constant pressure ratio parameter at high Stokes numbers reported above. This finding is very encouraging for utilizing the venturimeter to establish the flow rates of each phase at high Stokes numbers. Measuring both pressure drops ( $\Delta P_{TTP}$  and  $\Delta P_{TP}$ ) to determine the total pressure drop ratio and using the data in Fig. 4 allows one to establish the loading. Having the loading, the pipe-throat pressure drop and the pressure ratio parameter yields the pressure drop for the conveying phase alone (Eq. 9). This value yields the flow rate of the conveying phase which, together with the loading, gives the flow rate of the solid phase. This approach yields flow rates without having to know particle size provided the Stokes number exceeds seven, a condition encountered in char transport by high pressure, high temperature steam.

### Conclusions

The measurement of light attenuation and pipe-throat pressure drop can yield the flow rates of each phase provided the particle size is known.

The measurement of pipe-throat pressure drop and total pressure drop across the venturi will yield the flow rate of each phase without particle size information, provided the Stokes number exceeds seven.

### Reference

Payne, Allen L., "An Experimental and Numerical Study of Gas-Solids Mixture Flows in a Venturi," Ph.D. thesis, Washington State University, 1982.

### Acknowledgements

The authors acknowledge the support of DOE Grant DE-FG22-BOPC30212 and NSF Grant CPE-7925077.

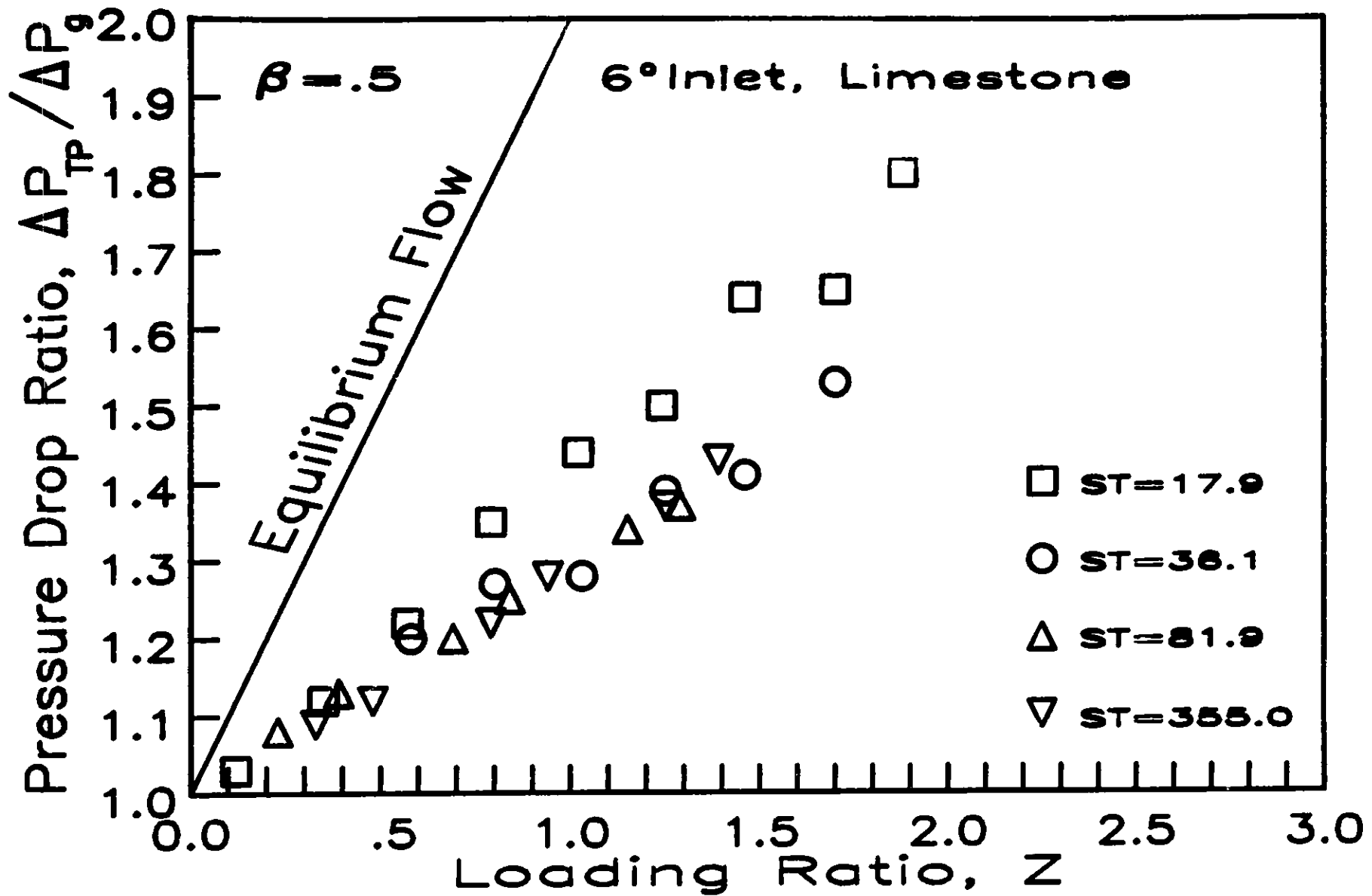


Figure 1. Pressure drop ratio versus loading for limestone particles.

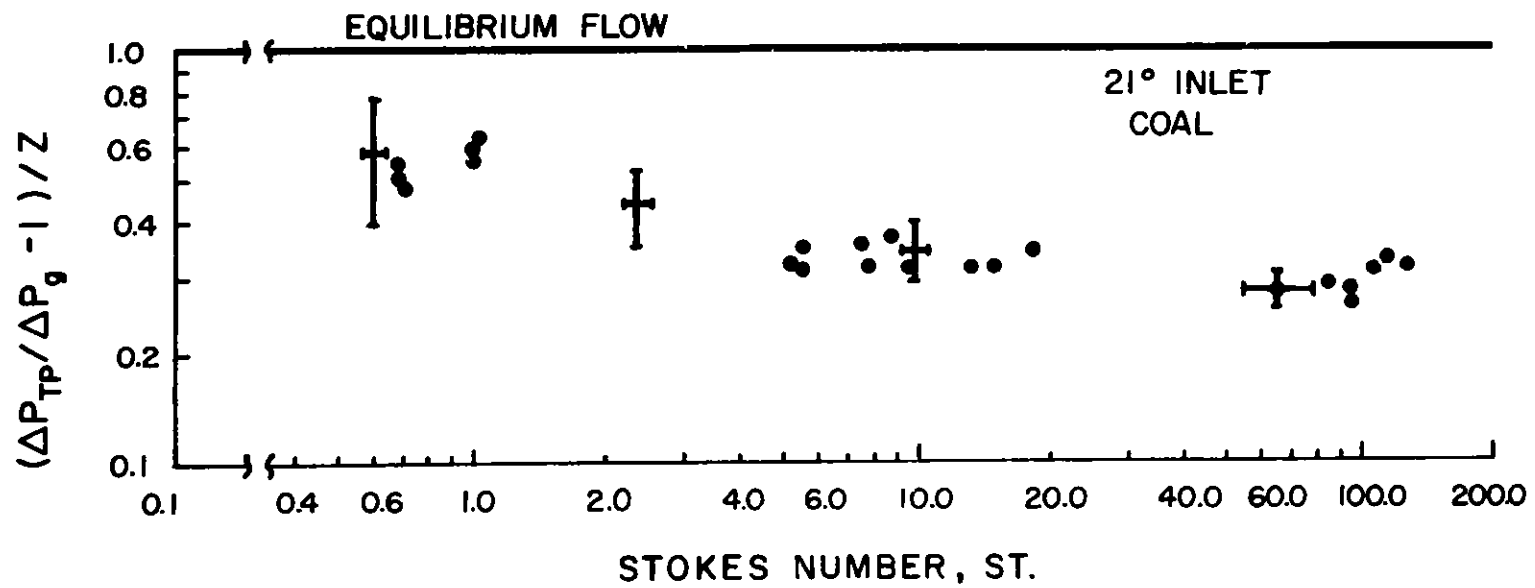


Figure 2. Pressure ratio parameter versus Stokes number for pulverized coal.



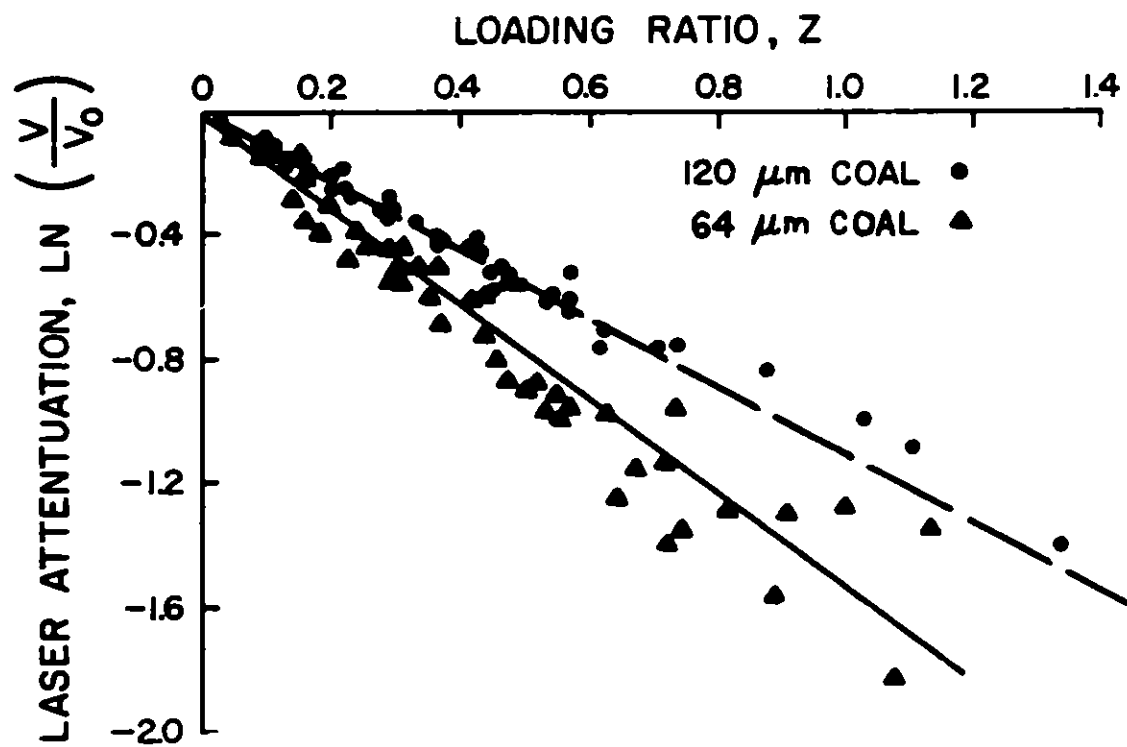


Figure 3. Laser light attenuation versus loading ratio.

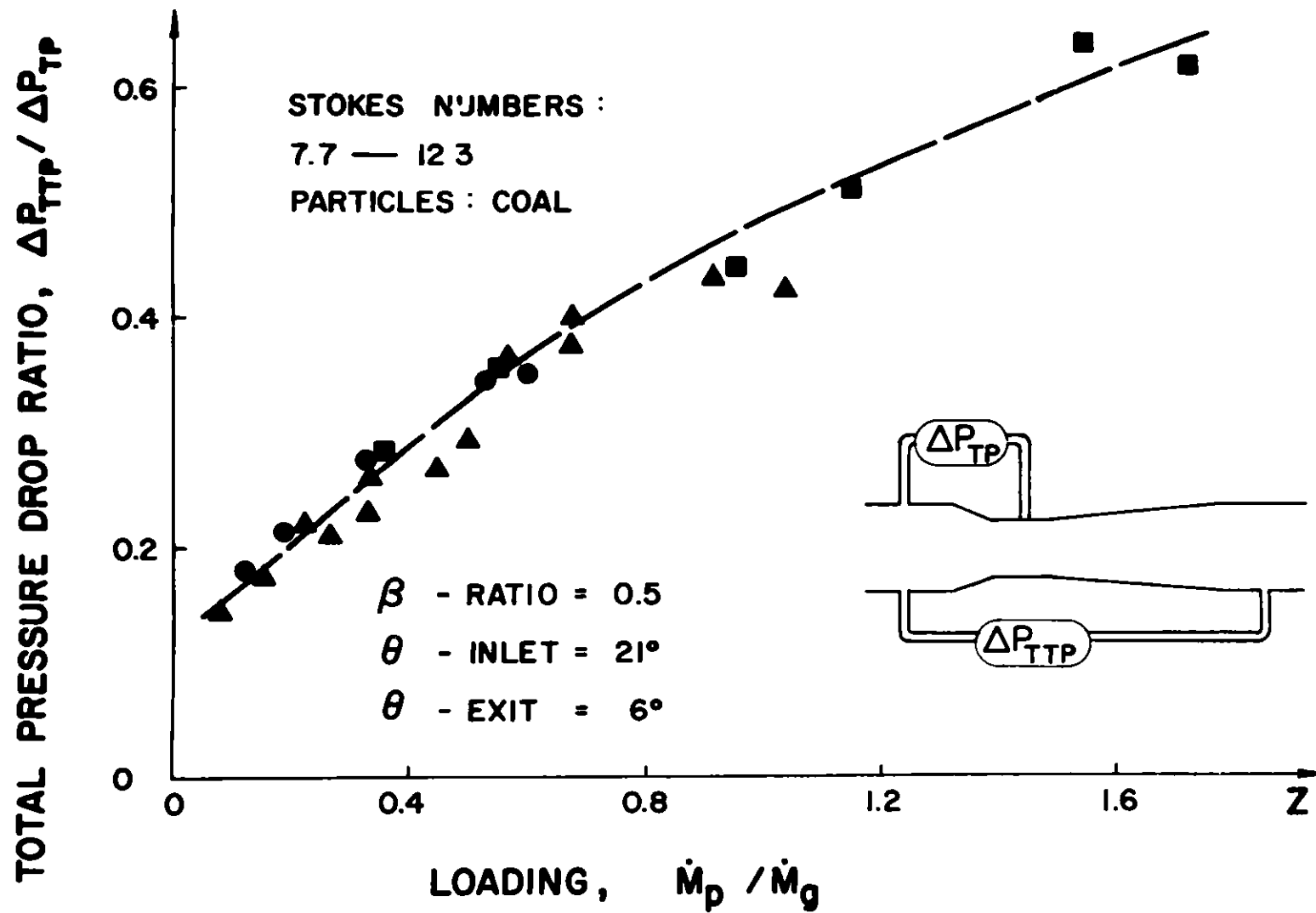


Figure 4. Total pressure drop ratio versus loading for Stokes numbers from 7 to 123.

Viscous Effect on Acoustic Scattering  
by Elastic Solid Cylinders and Spheres

by

Wen H. Lin and A. C. Raptis  
Argonne National Laboratory  
Components Technology Division - 308  
9700 South Cass Avenue  
Argonne, Illinois 60439  
Phone: (312) 972-6150  
FTS: 972-6150

ABSTRACT

This paper deals with analytic studies and numerical results of the scattering of plane sound waves from an elastic circular cylinder and from an elastic sphere in a viscous fluid. The elastic properties of the cylinder and the sphere and the viscosity of the surrounding fluid are taken into account in the solution of the acoustic-scattering problems. The associated acoustic quantities, such as the acoustic radiation forces, the acoustic attenuation, and the acoustic scattering patterns, are first derived in closed forms and then evaluated numerically for a given set of material properties.

Numerical results show that increasing fluid viscosity tends to increase the directionality of the angular distribution of the scattering patterns, especially in the forward direction. The acoustic-radiation force on the cylinder or on the sphere is in the direction of the incident wave and increases as the viscosity of the fluid increases.

1. INTRODUCTION

The fluid viscosity results in the dissipation of sound-wave energy and hence plays an important role in the analysis of sound absorption, which may occur in the process of sound-wave scattering. Sewell [1] was the first to treat sound absorption by rigid, fixed spheres and circular cylinders in a viscous gas. Later, Lamb [2] simplified the Sewell treatment and studied sound scattering by rigid, fixed, or movable spheres in viscous fluids. Epstein [3] considered three models of sound-wave scattering from a rigid solid sphere, an elastic solid sphere, and a fluid sphere to study the absorption of sound waves in suspensions and emulsions. In another general study of water fog in air, Epstein and Carhart [4] considered the scattering of acoustic waves by a fluid sphere in viscous and thermally conducting fluids. Allegra and Hawley [5] then extended Epstein and Carhart's theory to study sound absorption by elastic solid spheres in viscous and thermally conducting fluids and provided considerable experimental work as well as literature survey.

The present study concerns the scattering of a plane sound wave from an elastic, homogeneous, solid sphere and a circular cylinder immersed in an

infinite, viscous, barotropic, compressible fluid. The primary objectives of the study are to investigate the effect of fluid viscosity on acoustic-wave scattering patterns, acoustic-radiation force, and acoustic attenuation and to provide an analytical basis to enhance the experimental determination of the fluid viscosity.

The parametric study of the variations of the acoustic quantities mentioned above with the change of fluid viscosity enables one to furnish charts of the acoustic quantities for different viscous fluids. These charts (or figures) offer a possibility for determining the fluid viscosity if the corresponding experimental measurements of the acoustic quantities are compared with the analytic results. The successful application of the study to determine fluid viscosity depends much on the accurate experimental measurements of sound speed and one of the following: far-field scattering patterns of acoustic waves, acoustic radiation forces on the suspending spheres or cylinders, and acoustic attenuation.

At present, we report the analytic results of variation of the acoustic-scattering quantities with respect to fluid viscosity. Later, these results will be incorporated with the experimental measurements to determine the viscosity of coal slurries in coal conversion processes. The feasibility of the application of acoustic techniques to determine slurry viscosity will then be determined. An analytical study is also now being undertaken for the scattering of a plane sound wave from multiple elastic circular cylinders and spheres in viscous fluids to determine the effects of multiple scattering and particle interaction on the acoustic-scattering quantities.

## 2. SOUND SCATTERING FROM AN ELASTIC CYLINDER AND A SPHERE IN VISCOUS FLUIDS

Consider a plane sound wave of frequency  $f$  be incident perpendicularly upon an infinitely long circular cylinder in the  $x$  direction and upon a sphere in the  $z$  direction, as shown in Fig. 1. The cylinder and the sphere are of elastic, homogeneous materials and are immersed in an infinite, viscous, compressible, and barotropic fluid medium. All disturbances caused by the incident wave are assumed to be so small that the linearized theory is applicable.

The scattering of the sound wave from the circular cylinder is two dimensional because the cylinder is so long that the axial disturbances are negligible. However, the spherical scattering is a three-dimensional problem in strict sense. When the incident wave is approaching the sphere along the axis of  $\psi$ , there will be no dependence on  $\psi$  and the problem becomes axially symmetrical.

Because of mode conversion in the scattering process, the wave motion external to the cylinder (or the sphere) consists of the incident compressional wave, a scattered compressional wave, and a viscous wave; the wave motion inside the cylinder (or the sphere) includes a refracted compressional wave and a transverse shear wave. The acoustic equations for the wave motion in the barotropic, viscous, compressible fluid can be deduced from the linearized hydrodynamic equations and the linearized equation of state, and those for the wave motion inside the elastic, homogeneous, solid cylinder (or

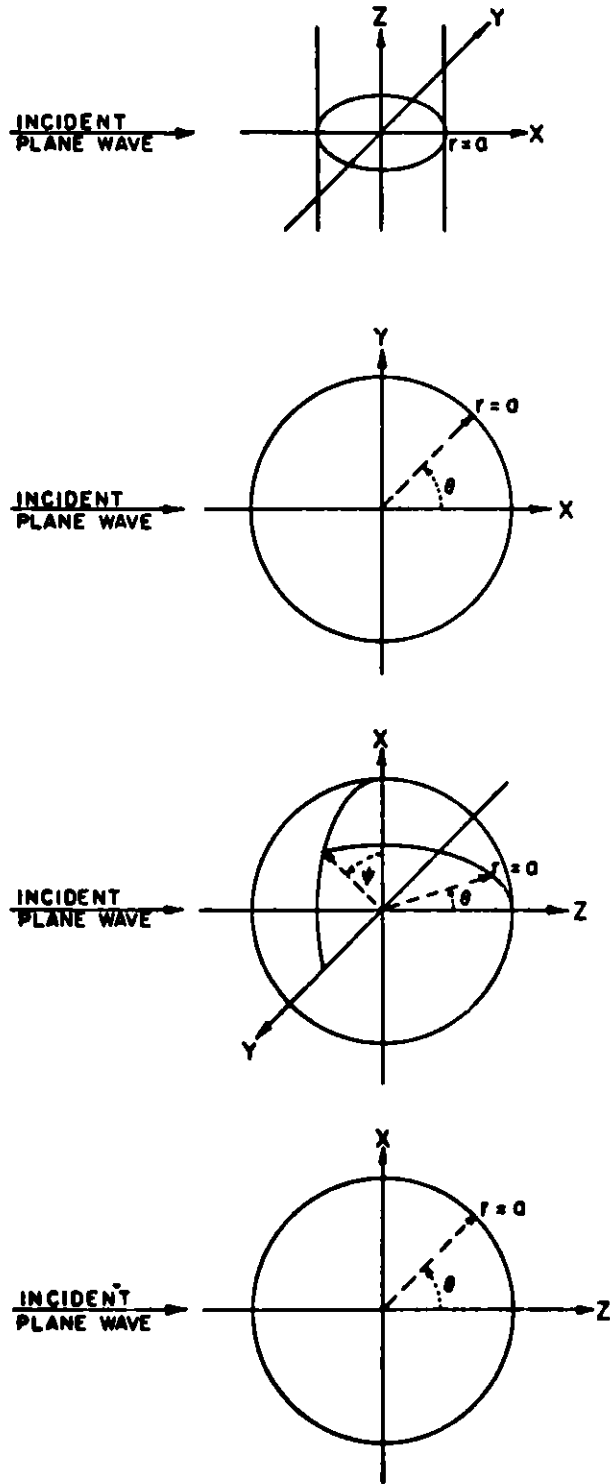


Fig. 1. Coordinate Systems for Sound Scattering by Circular Cylinder and Sphere

sphere) are obtained from linear elasticity. The details of these acoustic equations and their related parameters are shown in [6].

The appropriate boundary conditions for the acoustic scattering due to the cylinder (or the sphere) are: (1) the normal and tangential components of velocity and stress are continuous across the interface of the cylinder and the fluid (or the sphere and the fluid); (2) the scattered waves must be outgoing.

The solutions to the boundary-value problems of the acoustic scattering from the cylinder (or the sphere) are obtained in terms of unknown coefficients and circular (or spherical) Bessel and Hankel functions, respectively, for the refracted and scattered waves. The unknown coefficients are then determined from the boundary conditions, and the resulting equations of these unknown coefficients are a set of linear algebraic equations, which can be numerically solved with the use of digital computers for a given set of the material properties. Once the unknown coefficients are determined, the problems of sound scattering from the cylinder (or the sphere) are completely solved and the related acoustic quantities can be computed accordingly.

The detailed analytical expressions of the far-field scattering patterns, the acoustic-radiation forces, and the acoustic attenuation coefficients are derived in Ref. 6. In the following, we present some of the numerical calculations of the scattering patterns at a far field and the acoustic-radiation forces to illustrate the effects on them of the fluid viscosity and the scatterer size (i.e., the radius of the cylinder and the sphere).

### 3. NUMERICAL CALCULATIONS AND DISCUSSIONS

Numerical examples chosen for the parametric studies are plane sound waves incident upon a brass circular cylinder or a brass sphere in water. The density, Young's modulus, and Poisson's ratio of the brass are  $8.5 \text{ g/cm}^3$ ,  $10.4 \times 10^{11} \text{ dynes/cm}^2$ , and  $1/3$ , respectively, and the diameters of the cylinder and sphere are  $0.158750 \text{ cm}$  ( $1/16 \text{ in.}$ ). The density of water is  $1 \text{ g/cm}^3$ , and the sound speed in water is about  $1.50 \times 10^5 \text{ cm/sec}$  at  $20^\circ\text{C}$ .

Figures 2 and 3, respectively, show the angular distributions of the scattered pressures at far field for the brass cylinder and the brass sphere in water at  $20^\circ\text{C}$  ( $68^\circ\text{F}$ ) for different dimensionless wavenumbers of sound. These figures show the effect of the ratio of the cylinder (or sphere) size to the wavelength of the sound on the scattered waves.

As seen from the figures, the magnitude of the angular distributions of the scattered pressures increase as the dimensionless wavenumber of sound increases. For the dimensionless wavenumber less than 2, the magnitudes of the scattering patterns for the cylinder are larger than those for the sphere; however, the opposite trends are observed for the dimensionless wavenumber greater than two. The backward scattering is more dominant than the forward scattering for both the sphere and the cylinder when the radius of the cylinder (or sphere) is small compared with the wavelength of sound (i.e.,

$K_1 a < 1$ , where  $K_1$  and  $a$  are, respectively, the wavenumber of sound wave and the radius of the cylinder or the sphere). As the radius of the cylinder (or

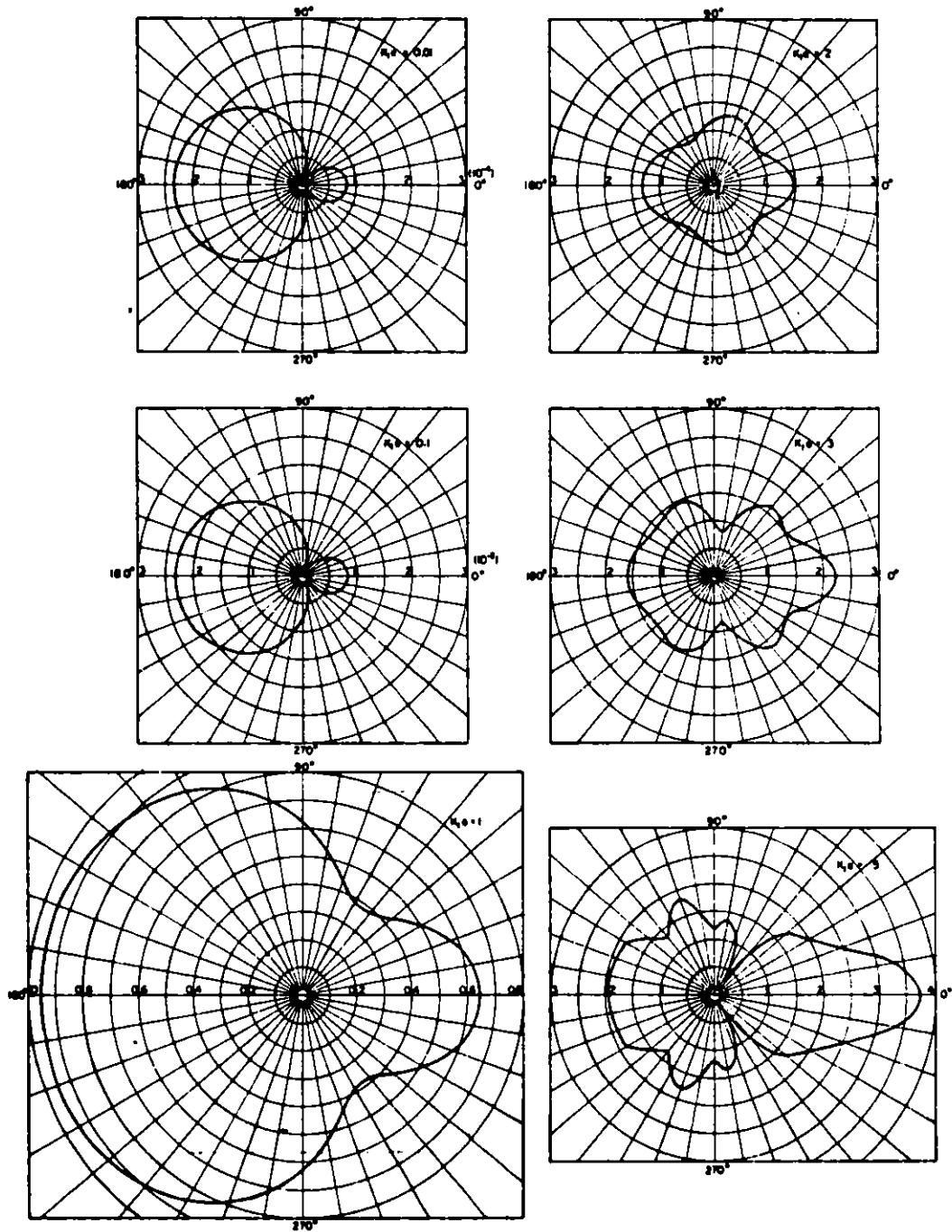


**Fig. 2. Scattering Patterns for Brass Cylinders ( $a = 0.0793750$  cm) in Viscous Water at  $20^\circ\text{C}$  ( $68^\circ\text{F}$ )**

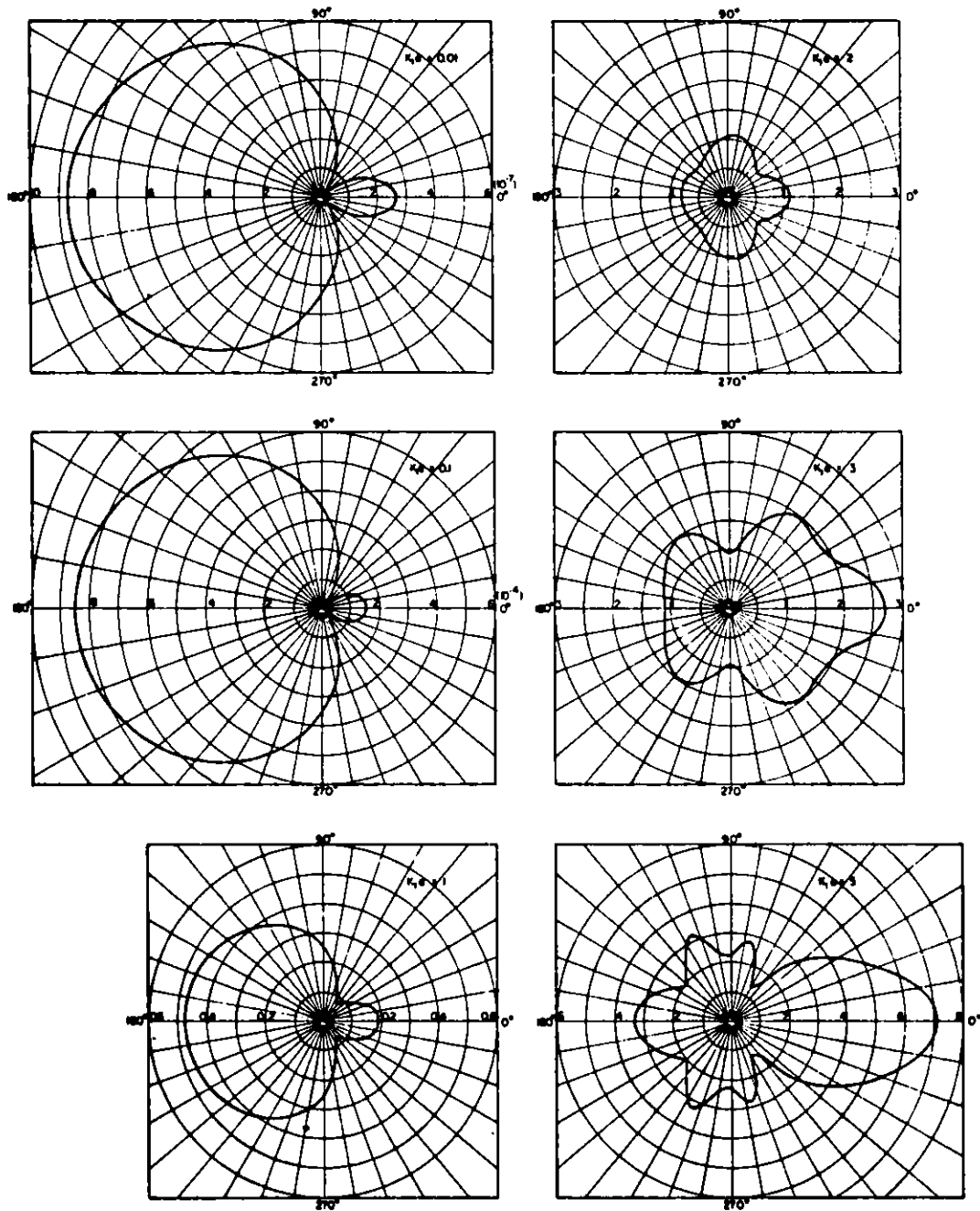


Fig. 3. Scattering Patterns for Brass Sphere ( $a = 0.0793750$  cm) in Viscous Water at  $20^\circ\text{C}$  ( $68^\circ\text{F}$ )



sphere) is large compared with the wavelength of sound (i.e.,  $K_1 a > 1$ ), the directionality of the scattered waves becomes apparent and increases with the increase of the dimensionless wavenumber, and the forward scattering is more dominant than the backward scattering.

The effect of the fluid viscosity on the scattering patterns is shown in Figs. 4 and 5. The results are obtained for the fluid medium at different viscosities associated with different fluid temperature for the same frequency of the incident wave. As seen from the figures, the more viscous the surrounding fluid is, the more dominant scattering is in the backward and forward directions for both the cylinder and the sphere. Since the viscous shear waves decay rapidly away from the solid boundary, the general patterns of the far-field scattered waves, except their magnitudes, are less dependent on the viscosity of the fluid.

Figure 6 shows the variations of the acoustic-radiation forces with respect to the dimensionless wavenumber of the incident sound wave. The acoustic-radiation forces are linearly proportional to the dimensionless wavenumber when the frequency of the incident wave is low (i.e.,  $K_1 a < 0.6$ ). The linearity then breaks down as the frequency of the incident wave increases. The acoustic-radiation force is maximum at  $K_1 a = 1$  for the circular cylinder, and at  $K_1 a = 1.35$  for the sphere. As the frequency of the incident wave further increases, the forces decrease and the rate of decreasing for the sphere is faster than that for the circular cylinder.

Table 1 shows the comparison of the present results with those obtained by Morse [7] for the acoustic-radiation force per unit length of the circular cylinder per unit pressure of the incident wave. The present results are close to Morse's results because of low viscosity of water. The fluid viscosity has some effect on the magnitude and phase of the acoustic-radiation forces.

#### 4. CONCLUDING REMARKS

This paper presents analytical solutions as well as numerical results for the boundary-value problems concerning with the interaction of a plane sound wave with an elastic cylinder and an elastic sphere immersed in a viscous fluid. The objectives of this study are to investigate the effects of the fluid viscosity and the scatterer's elasticity on acoustic scattering and its associated quantities. The interaction of the incident wave, the scattered waves, and the refracted waves is solved in terms of unknown coefficients and cylindrical (or spherical) wave functions for the circular cylinder (or sphere) to satisfy the boundary conditions. The resulting equations are linear algebraic with respect to the unknown coefficients and are numerically solved with the aid of digital computers for a given set of the material constants. Acoustic quantities are then numerically computed when the unknown coefficients are determined.

Numerical results show that the ratio of the cylinder (or the sphere) radius to the wavelength of the incident sound waves has more effect on the scattering patterns and the radiation forces than the fluid viscosity does.

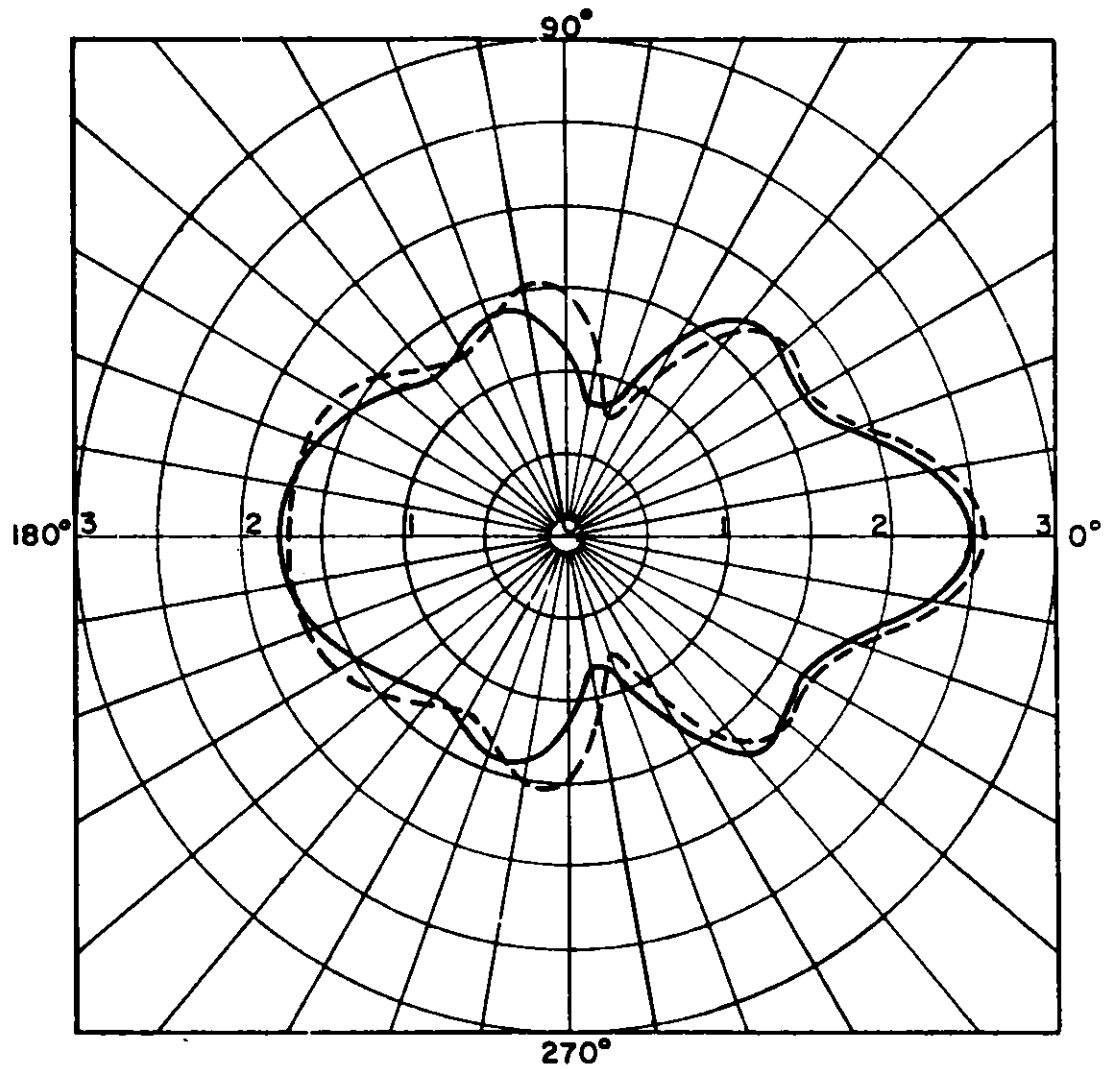


Fig. 4. Viscous Effect on the Scattering Pattern for a Brass Cylinder  
 ( $a = 0.0793750$  cm,  $1/32$  in.) in Water for  $f_{inc} = 10^6$  Hz; Solid Line  
 ( $\nu = 0.4106 \times 10^{-2}$  cm<sup>2</sup>/sec,  $K_1 a = 3.28$ ,  $k_1 a = 1.16$ ) and Dashed Line  
 ( $\nu = 1.7930 \times 10^{-2}$  cm<sup>2</sup>/sec,  $K_1 a = 3.51$ ,  $k_1 a = 1.16$ )

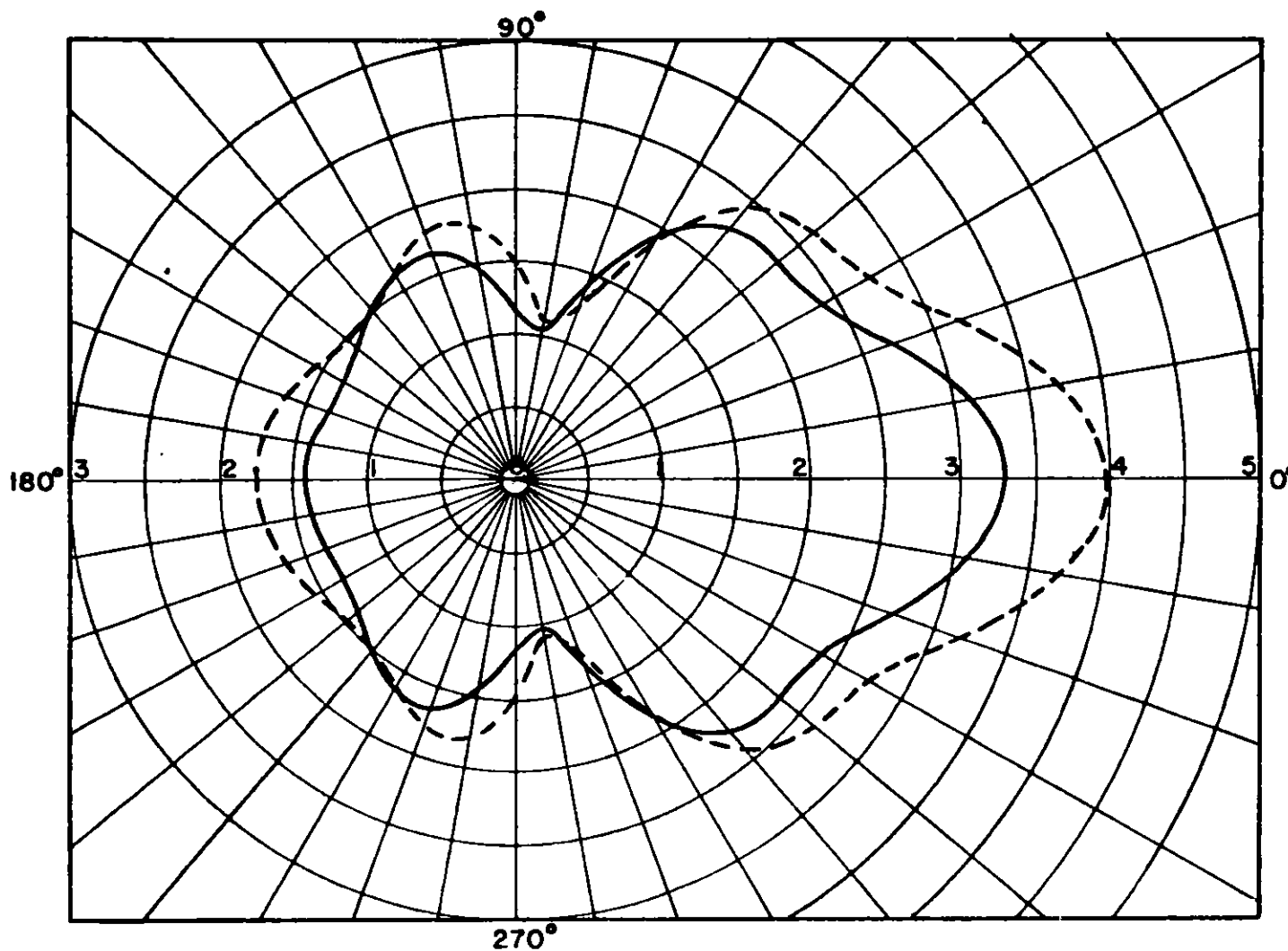


Fig. 5. Viscous Effect on the Scattering Pattern for a Brass Sphere  
 ( $a = 0.0793750$  cm,  $1/32$  in.) in Water for  $f_{inc} = 10^6$  Hz; Solid Line  
 ( $\nu = 0.4106 \times 10^{-2}$  cm<sup>2</sup>/sec,  $K_1 a = 3.28$ ,  $k_1 a = 1.16$ ) and  
 Dashed Line ( $\nu = 1.7930 \times 10^{-2}$  cm<sup>2</sup>/sec,  $K_1 a = 3.51$ ,  $k_1 a = 1.16$ )

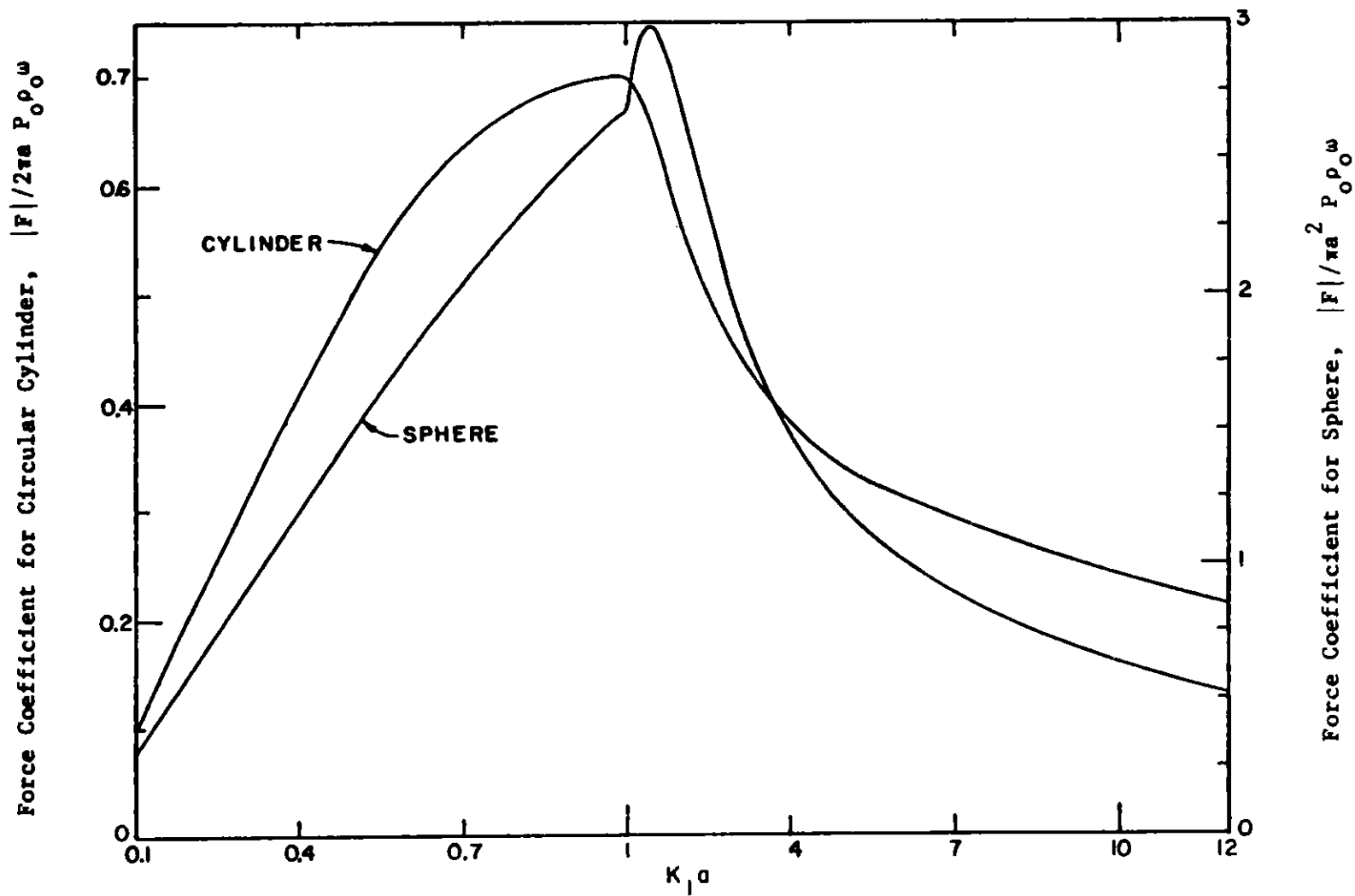


Fig. 6 Amplitude of Acoustic-Radiation Forces on a Cylinder and a Sphere of Radius  $a$ , Plotted Against Dimensionless Wavenumber ( $K_1 a$ )

The fluid viscosity has slight effect on the angular distributions of scattering patterns, specially in the angles near the forward and backward directions.

With this parametric study one can furnish a chart of angular distributions of scattered pressure fields for various viscous fluids. The chart can be used with the experimentally determined patterns of scattered pressures to identify the viscosity of the associated fluid.

Table 1

Comparisons of the Acoustic-Radiation Force  
Coefficients ( $|F|/2\pi a P_0 \rho_0 \omega$ ) for  
A Circular Cylinder in Viscous and Inviscid Fluids

$K_1 a$	Kinematic Viscosities of Fluid, $\text{cm}^2/\text{sec}$			
	$1.1026 \times 10^{-2}$	$1.0126 \times 10^{-1}$	$1.0126 \times 10^1$	0 (inviscid) [3]
0.01	0.0101	0.0104	0.0150	-
0.02	0.0202	0.0206	0.0267	-
0.05	0.0505	0.0511	0.0603	0.050
0.10	0.1014	0.1023	0.1149	0.101
0.20	0.2052	0.2065	0.2242	0.204
0.35	0.3613	0.3630	0.3852	0.356
0.50	0.5021	0.5038	0.5264	0.519
0.70	0.6342	0.6355	0.6536	0.631
1.0	0.7014	0.7017	0.7122	0.706
1.1	0.7002	0.7003	0.7093	0.705
1.2	0.6926	0.6925	0.7006	0.699
1.5	0.6511	0.6510	0.6582	0.631
1.7	0.6187	0.6188	0.6262	0.593
2.0	0.5718	0.5728	0.5809	0.563
3.0	0.4517	0.4575	0.4685	0.456
4.0	0.3829	0.3881	0.4023	0.391
5.0	0.3429	0.3469	0.3649	0.356

#### ACKNOWLEDGMENTS

This work was performed for the Office of Advanced Research in Instrumentation and Control Technology, Fossil Energy, U.S. Department of Energy. The authors would like to thank R. S. Zeno, G. S. Rosenberg, T. P. Mulcahey, and N. M. O'Fallon for their support and encouragement. Thanks are also due to Nancy Heeg for her typing of this report.

REFERENCES

1. C. J. T. Sewell, The Extinction of Sound in a Viscous Atmosphere by Small Obstacles of Cylindrical and Spherical Form, Phil. Trans. R. Soc. Lond. A 210, 239-270 (1910).
2. Sir Horace Lamb, Hydrodynamics, Dover Publications, New York, 6th Edition, pp. 511-516, 529-531, 657-659, (1945).
3. P. S. Epstein, On the Absorption of Sound Waves in Suspensions and Emulsions, Contributions to Applied Mechanics and Related Subjects in Theodore von Karman Anniversary Volume, Calif. Inst. Tech., pp. 162-188 (1941).
4. P. S. Epstein and R. R. Carhart, The Absorption of Sound in Suspensions and Emulsion I. Water Fog in Air, J. Acoust. Soc. Am. 25, 553-565 (1953).
5. J. R. Allegra and S. A. Hawley, Attenuation of Sound in Suspensions and Emulsions: Theory and Experiments, J. Acoust. Soc. Am. 51, 1545-1564 (1972).
6. W. H. Lin and A. C. Raptis, Viscous Effect on Acoustic Scattering by Elastic Solid Cylinders and Spheres, Technical Memorandum ANL-CT-82-, Argonne National Laboratory (1982). (To be published)
7. P. M. Morse, Vibration and Sound, McGraw-Hill Book Company, New York, Second Edition, pp. 347-357, (1948).

THE EFFECTS OF METAL CHELATES ON WET FLUE GAS SCRUBBING CHEMISTRY<sup>†</sup>

S.-G. Chang\* and D. Littlejohn  
Energy and Environment Division  
Lawrence Berkeley Laboratory  
University of California  
Berkeley, California 94720  
415/486-5319

Abstract

Addition of metal chelates in a wet stack gas scrubber to improve removal efficiency of both NO and SO<sub>2</sub> could provide a major new dimension to environmental control technology without requiring major capital modification to existing power plants. Criteria for an effective metal chelate additive include large absorption capacity and rapid binding rate of NO, and rapid regeneration rate of metal chelates from nitrosyl metal chelates by reaction with absorbed SO<sub>2</sub> in aqueous solutions. The thermodynamics and kinetics of chemical reactions involved are discussed. Laser Raman spectroscopy, gas chromatograph, and mass spectrometry have been employed to directly and unambiguously identify some reaction intermediates and products.

Introduction

Power plant flue gas contains several hundred ppm NO<sub>x</sub> and hundreds or thousands ppm SO<sub>2</sub>. Most NO<sub>x</sub> is in the form of relatively insoluble NO. Several simultaneous desulfurization and denitrification processes,<sup>1-3</sup> still in the development stage, are based on the addition of metal chelates such as Fe(II)EDTA in aqueous solutions to promote absorption of NO in solutions. These metal chelates can bind NO to form nitrosyl metal chelates, which can react with absorbed SO<sub>2</sub> in aqueous solution to produce reduced nitrogen species such as N<sub>2</sub>O, N<sub>2</sub>, and sulfate while metal chelates are regenerated. Identification of an optimum metal chelate for better removal efficiency of NO and SO<sub>2</sub> in a wet scrubber requires knowledge of the thermodynamics and kinetics of the coordination of NO to various metal chelates. Knowledge is also needed on the kinetics and mechanisms of the reaction between nitrosyl metal chelates and absorbed SO<sub>2</sub> in solution to calculate the regeneration rate of metal chelates and to control the products of reaction by adjusting the scrubber operating conditions. Not much of this information is available in the literature, although several ferrous and cobalt chelates have been used as additives for testing in bench-scale wet stack gas scrubbers. This paper discusses some important factors that should be considered in identifying an optimum metal chelate catalyst and in developing an efficient wet stack gas simultaneous desulfurization and denitrification scrubber.

<sup>†</sup>This work was supported by the U.S. Department of Energy under Contract No. DE-AC 03-76SF00098 and by the Morgantown Energy Research Center under Contract No. 82MC14002.

\*Presenting author, to whom correspondence should be addressed.

## Absorption Capacity of NO and SO<sub>2</sub> in Aqueous Solutions

### Absorption of NO

Nitric oxide is nonreactive in water (in the absence of oxygen), and the solubility of NO in aqueous solutions is very small. The Henry's Law coefficient is  $1.93 \times 10^{-3} \text{ M atm}^{-1}$  at 25°C and zero ionic strength.<sup>4</sup> The solubility decreases with increasing temperature; the enthalpy of solution is  $\Delta H^\circ = -2.94 \text{ Kcal/mole}$ . The Henry's Law coefficient of NO decreases with increasing ionic strength ( $\mu$ ); this decrease amounts to approximately 8% for  $\mu = 0.1 \text{ M}$ . The solubility of NO in aqueous solution was found to be independent of pH over the range 2 to 13. For 500 ppm NO in equilibrium with aqueous scrubbing solution at 50°C and  $\mu = 0.1 \text{ M}$  and gas-to-liquid ratio of 100, the fraction of NO present in the aqueous phase is only  $3.2 \times 10^{-2}\%$ .

One approach to enhance the absorption of NO is to use a water-soluble metal chelating compound to form nitrosyl metal chelates with NO.<sup>5</sup> Many studies have been done on determining the structure of these chelates, yet few have been done on determining their thermodynamic properties and reaction rates. Hishinuma et al.<sup>6</sup> and our group<sup>7</sup> have recently determined the equilibrium constants, enthalpy, and entropy for the coordination of NO to Fe(II)EDTA and Fe(II)NTA respectively. Both these groups performed their experiments by bubbling a mixture of NO and N<sub>2</sub> of known NO concentration through a metal chelate solution and then measuring the NO concentration in the outlet gas with a NO<sub>x</sub> analyzer (Fig. 1). NO absorption was carried out until the NO concentration in the outlet gas became equal to that in the inlet gas, i.e., until equilibrium was reached. The experiments were performed at several temperatures to evaluate enthalpy and entropy of the reaction. The results of this study are shown in Table 1.

Table 1. Kinetic and thermodynamic data for reversible NO coordination to ferrous chelates.

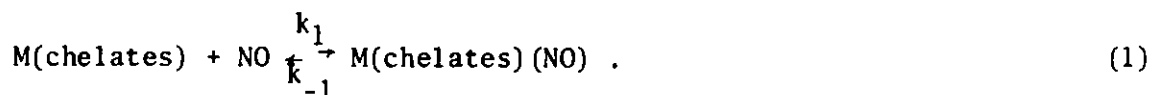
Ferrous chelates	$k_1$ $\text{M}^{-1}\text{sec}^{-1}$	$k_{-1}$ $\text{sec}^{-1}$	K $\text{M}^{-1}$ at 298°K	$\Delta H$ Kcal/mole	$\Delta S$ e.u.
Fe(II)(H <sub>2</sub> O) <sub>5</sub> (NO)	$(7.1 \pm 1.0) \times 10^5$	$(1.5 \pm 0.6) \times 10^3$	$(4.7 \pm 2.0) \times 10^2$		
Fe(II)(citrate)(NO)	$(4.4 \pm 0.8) \times 10^5$	$(6.6 \pm 2.4) \times 10^2$	$(6.7 \pm 2.0) \times 10^2$		
Fe(II)(acac) <sub>2</sub> (NO)	$(4.0 \pm 3.0) \times 10^2$	24 ± 2	17 ± 14		
Fe(II)(NTA)(NO)	$\approx 7 \times 10^7$	$\approx 35$	$2.14 \times 10^6$	-11.94	-11.0
Fe(II)(EDTA)(NO)	$\approx 6 \times 10^7$	$\approx 60$	$1.15 \times 10^7$	-15.8	-20.7

We recently determined the equilibrium constant for the coordination of NO to Fe(II)(H<sub>2</sub>O)<sub>5</sub>, Fe(II)(citrate), and Fe(II)(acac)<sub>2</sub> using a temperature-jump apparatus (Fig. 2). The source of the temperature jump is a high-voltage d.c. power supply connected to a capacitor through a solenoid switch. After the capacitor is charged, the switch is disconnected. By closing a variable spark gap, the energy stored in the capacitor can be discharged through a cell containing the reaction under study. A temperature jump of



8°C occurs within several microseconds. The temperature jump induces a change in the concentration of reactants and products as the reaction shifts to a new equilibrium. The shift is monitored by a photomultiplier that responds to changes in absorption of a nitrosyl ferrous chelate. The results are displayed on an oscilloscope, which is triggered by the closing of the spark gap.

The coordination of NO to metal chelates can be written as



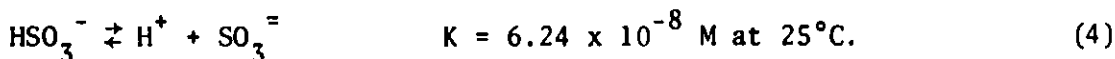
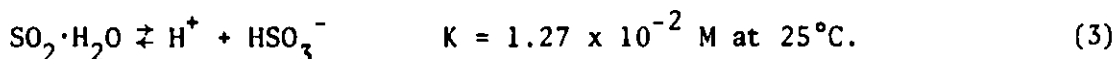
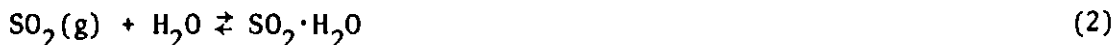
The reciprocal of the relaxation time equals the forward rate constant times the sum of the final equilibrium concentrations of M(chelates) and NO plus the backward rate constant. When the reciprocal of the relaxation time is plotted against the final concentrations of M(chelate) + NO, the slope of the curve gives the forward rate constant ( $k_1$ ) and the point of interception gives the backward rate constant ( $k_{-1}$ ). The results are summarized in Table 1.

By comparing the equilibrium constants of reactions listed in Table 1, it is obvious that Fe(II)(EDTA) and Fe(II)(NTA) have much larger absorption capacities for NO than Fe(II)(H<sub>2</sub>O)<sub>5</sub>, Fe(II)(citrate), and Fe(II)(acac)<sub>2</sub> have.

For 500 ppm NO in equilibrium with aqueous scrubbing solution containing 0.1 M Fe(II)EDTA at 50°C,  $\mu = 0.1$  M, and gas-to-liquid ratio of 100, the fraction of NO present in the aqueous phase is 94%.

### Absorption of SO<sub>2</sub>

SO<sub>2</sub> is quite soluble in water; four major S(IV) species are produced after dissolution of SO<sub>2</sub> in aqueous solutions: SO<sub>2</sub>·H<sub>2</sub>O, HSO<sub>3</sub><sup>-</sup>, SO<sub>3</sub><sup>=</sup>, and S<sub>2</sub>O<sub>5</sub><sup>=</sup>. The equilibrium concentration of these S(IV) species depends on both the partial pressure of SO<sub>2</sub> and the pH of the solution. The Henry's Law coefficient of SO<sub>2</sub> is 1.24 M atm<sup>-1</sup> at 25°C. Hydrated SO<sub>2</sub> can ionize to form bisulfite ion, HSO<sub>3</sub><sup>-</sup>, which can undergo further ionization to produce sulfite ion, SO<sub>3</sub><sup>=</sup>.



Bisulfite ion is also in equilibrium with the pyrosulfite ion S<sub>2</sub>O<sub>5</sub><sup>=</sup>:



Table 2 lists the equilibrium concentration of 4 S(IV) species with 1000 ppm SO<sub>2</sub> at various pH's and at 25°C. The equilibrium concentration of total aqueous S(IV) species increases with increasing solution pH at a given partial

pressure of  $\text{SO}_2$ ; i.e., the absorption capacity of  $\text{SO}_2$  in aqueous solution is larger at a high solution pH.

Table 2. Equilibrium concentration of sulfites (mole/liter) at  $P_{\text{SO}_2} = 1000$  ppm at  $25^\circ\text{C}$ .

Sulfites	pH 7	pH 6	pH 5	pH 4	pH 3
$\text{SO}_2 \cdot \text{H}_2\text{O}$	$1.24 \times 10^{-3}$	$1.24 \times 10^{-3}$	$1.24 \times 10^{-3}$	$1.24 \times 10^{-3}$	$1.24 \times 10^{-3}$
$\text{HSO}_3^-$	$1.58 \times 10^{+2}$	$1.58 \times 10^{+1}$	1.58	$1.58 \times 10^{-1}$	$1.58 \times 10^{-2}$
$\text{SO}_3^{=}$	$9.82 \times 10^{+1}$	$9.82 \times 10^{-1}$	$9.82 \times 10^{-3}$	$9.82 \times 10^{-5}$	$9.82 \times 10^{-7}$
$\text{S}_2\text{O}_5^{=}$	$1.75 \times 10^{+3}$	$1.75 \times 10^{+1}$	$1.75 \times 10^{-1}$	$1.75 \times 10^{-3}$	$1.75 \times 10^{-5}$

### Absorption Rate of NO and $\text{SO}_2$ in Aqueous Solutions

#### Rate of Mass Transfer

In actual packed towers, and when the rate of diffusion in the gas phase is significantly larger than that in the liquid phase, the mass transfer of gaseous species through an interface into an aqueous phase can be expressed by the equation<sup>8</sup>

$$N_a = k_a(C_i - C) \quad , \quad (a)$$

where  $N$  is the flux of the diffusing species in  $\text{mole cm}^{-2} \text{sec}^{-1}$ ,  $C_i$  and  $C$  are the concentrations of species in liquid phase at the interface and a distance from the interface in  $\text{mole/cm}^3$ . The area effect is taken into account by a combined coefficient  $k_a$ , where  $a$  is the (unknown) transfer area per unit volume of packing and  $k$  is the mass transfer coefficient of the diffusing species. In a typical wet flue gas scrubber<sup>9</sup> with packed absorption tower,  $k_a$  is on the order of  $0.1 \text{ sec}^{-1}$ .  $N_a$  is the rate of absorption per unit volume of packing.

#### Rate of Formation of Nitrosyl Metal Chelates

With a temperature-jump technique, we have directly measured the formation and dissociation rate constants<sup>5</sup> of  $\text{Fe(II)(H}_2\text{O)}_5\text{NO}$ ,  $\text{Fe(II)(citrate)NO}$ ,  $\text{Fe(II)(acac)}_2\text{NO}$ ,  $\text{Fe(II)(EDTA)NO}$ , and  $\text{Fe(II)(NTA)NO}$  (Table 1). Values for the rate and equilibrium constants for the formation of  $\text{Fe(II)(H}_2\text{O)}_5\text{NO}$  determined in this study agree well with those determined by Kustin et al.<sup>10</sup> The forward and reverse rate constants for the formation of  $\text{Fe(II)(citrate)NO}$  are somewhat smaller than the values for the  $\text{Fe(II)(H}_2\text{O)}_5\text{NO}$  complex, while the equilibrium constant is larger. The kinetics for the formation and dissociation of the  $\text{Fe(II)(acac)}_2\text{NO}$  complex are much slower than any other complex studied.

For both Fe(II)(EDTA)NO and Fe(II)(NTA)NO, the relaxation times due to the temperature jump were too fast to be measured. However, an upper limit of 10 microseconds was established for the relaxation times for both complexes. Using this value with the equilibrium constants determined for Fe(II)(EDTA)NO and Fe(II)(NTA)NO by Hishinuma et al.<sup>6</sup> and our group<sup>7</sup> respectively, the lower limits of forward and reverse rate constants were calculated (Table 1).

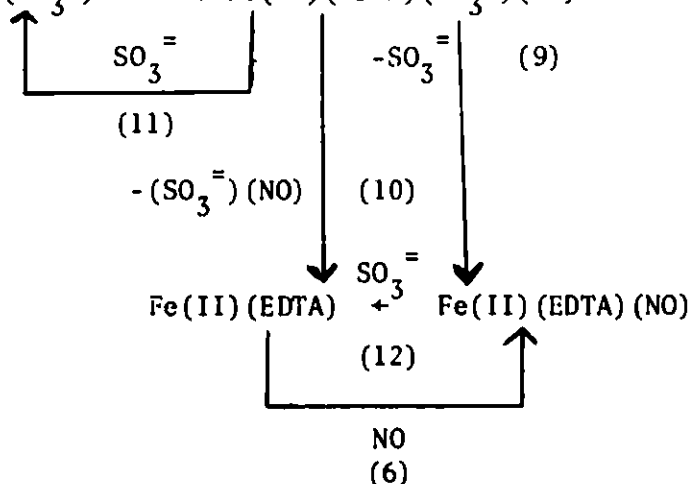
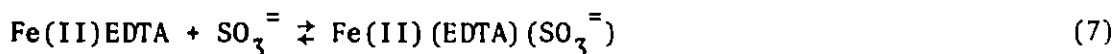
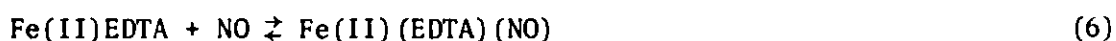
The absorption rates of NO in an aqueous solution of Fe(II)EDTA were also measured by Teramoto et al.<sup>11</sup> and Sado et al.<sup>12</sup> using a stirred vessel with a free flat gas-liquid interface. The forward rate constants of the complexing reaction were derived on the basis of the theory of gas absorption. Their results are in good agreement with ours.

### Rate of Dissociation of SO<sub>2</sub> in Aqueous Solution

Dissolution of SO<sub>2</sub> can be expressed by Eqs. (2)-(5). Reaction (3) proceeds very fast as can be seen from the rate constant (k<sub>3</sub>) and reverse rate constant (k<sub>-3</sub>) measured by Eigen et al.<sup>16</sup> using a relaxation technique: k<sub>3</sub> = 3.4 x 10<sup>6</sup> sec<sup>-1</sup>, and k<sub>-3</sub> = 2.0 x 10<sup>8</sup> M<sup>-1</sup> sec<sup>-1</sup> at 20°C.

### Regeneration Rate of Metal Chelate Catalysts

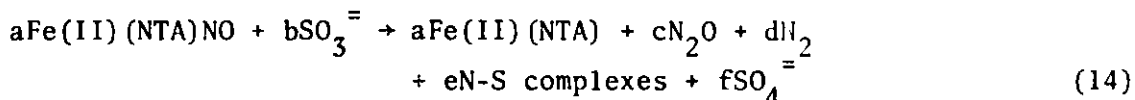
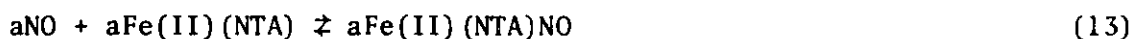
When both NO and SO<sub>2</sub> are bubbled into an aqueous solution containing metal chelates such as Fe(II)EDTA, reduced nitrogen species, nitrogen-sulfur complexes, and sulfate are produced. The kinetics and mechanisms of reactions involved in this SO<sub>2</sub>-NO-metal chelates aqueous system have not been well characterized yet. Teramoto et al.<sup>11</sup> have recently proposed the following reactions that could take place in this system:



They suggested that reactions (9), (10), and (11) are slow compared to reaction (12); and the activation energies of reactions (9) and (12) are larger

than those of reactions (6) and (8). From the absorption rate study using a stirred vessel, they derived the forward rate constant of reaction (8) to be  $1.4 \times 10^8 \text{ M}^{-1} \text{ sec}^{-1}$  at  $25^\circ\text{C}$ . The rate constants of other reactions, the rate law, and the products of all reactions involved have not yet been reported.

We have started to investigate the reaction kinetics between Fe(II)(NTA)NO and sodium sulfite/bisulfite as a model for the reactions of  $\text{SO}_2$ -NO-metal chelates in aqueous solutions. The reaction can be expressed as follows:



The experiments were performed under  $\text{O}_2$ -free conditions to avoid the oxidation of Fe(II), NO, and sulfite. The concentration of Fe(II)(NTA)NO was monitored by visible absorption spectrometry during the course of the reaction. A spectrum of Fe(II)(NTA)NO complex is shown in Fig. 3 and has been found to obey Beer's Law. The rate of disappearance of Fe(II)(NTA)NO in the presence of  $\text{SO}_3^{=}$  or  $\text{HSO}_3^-$  has been found to have a first-order dependence on the concentration of Fe(II)(NTA)NO and a first-order dependence on the concentration of  $\text{SO}_3^{=}$  or  $\text{HSO}_3^-$ . The rates can be expressed as follows:

$$-\frac{d[\text{Fe(II)(NTA)NO}]}{dt} = \left\{ k_{14}[\text{SO}_3^{=}] + k'_{14}[\text{HSO}_3^-] \right\} [\text{Fe(II)(NTA)NO}] \quad (b)$$

Tentative values for  $k_{14}$  and  $k'_{14}$  have been obtained. At pH 8.0,  $k_{14} = 0.8 \text{ M}^{-1} \text{ sec}^{-1}$ ; and at pH 3.5,  $k'_{14} = 0.05 \text{ M}^{-1} \text{ sec}^{-1}$ . These values were obtained at  $20^\circ\text{C}$ . At low pH (around 2 to 3), the apparent reaction rate decrease due to the inability of NTA to effectively bind with ferrous ions under the conditions, leading to a low concentration of Fe(II)(NTA)NO. This is caused by NTA's existing in the completely protonated form at very low pH. The ionic strength dependence of the reaction rate has been investigated at conditions near neutral pH. The results indicate that there is no dependence of the reaction rate on ionic strength under the experimental conditions employed.

The Fe(II)( $\text{H}_2\text{O}$ )<sub>5</sub>NO complex is not stable<sup>13</sup> at neutral or basic pH, so the reaction was studied under acidic conditions only. The reaction of Fe(II)( $\text{H}_2\text{O}$ )<sub>5</sub>NO with bisulfite ion at pH 2.2 was found to have a first order dependence on bisulfite ion concentration. Linear plots of 1/absorbance of Fe(II)( $\text{H}_2\text{O}$ )<sub>5</sub>NO vs. time were obtained, showing the same behavior as Fe(II)(NTA)NO. The reaction rate can be expressed as:

$$-\frac{d[\text{Fe(II)(H}_2\text{O)}_5\text{NO}]}{dt} = k_{15}[\text{Fe(II)(H}_2\text{O)}_5\text{NO}][\text{HSO}_3^-], \quad (c)$$

where  $k_{15} = 0.1 \text{ M}^{-1} \text{ sec}^{-1}$  at pH 2.2. The reaction of Fe(II)( $\text{H}_2\text{O}$ )<sub>5</sub>NO with  $\text{HSO}_3^-$  is significantly faster than the reaction of Fe(II)(NTA)NO with  $\text{HSO}_3^-$  under similar conditions.

### Identification of Reaction Products

The intermediates and products that can be formed from the reaction of  $\text{SO}_2$ , NO, and ferrous chelates in aqueous solutions have not been well characterized yet. A few compounds such as sulfate,  $\text{N}_2\text{O}$ , and some N-S complexes (sulfamate<sup>15</sup> and amine disulfonate<sup>1,2</sup>) have been found. A tedious wet chemical analytical method has recently been described<sup>15</sup> for determining N-S compounds. However, the mass balance between products and reactants of this reaction has not been made. Because it is necessary to identify intermediates and products so that reaction kinetics and mechanisms can be characterized and an optimum stack gas scrubber developed, we have begun to develop analytical techniques so that species can be directly, rapidly, and quantitatively determined and the mass balance of the reaction between nitrosyl metal chelates and  $\text{SO}_2$  in aqueous solutions can be performed.

Nitrous oxide,  $\text{N}_2\text{O}$ , has been determined to be one of the reaction products and has been measured by gas chromatographic techniques (Table 3). At low Fe(II)(NTA)NO concentrations ( $< 0.005 \text{ M}$ ), a substantial fraction of the nitrogen from the NO attached to the complex is converted into  $\text{N}_2\text{O}$ . Under basic conditions, 40 to 50% of the nitrogen is converted into  $\text{N}_2\text{O}$ . Under acidic conditions, a smaller amount, 25 to 35%, is converted into  $\text{N}_2\text{O}$ . At Fe(II)(NTA)NO concentrations in the range of .02 to .01 M, there is considerably less  $\text{N}_2\text{O}$  produced. The amount of nitrogen from the  $\text{N}_2\text{O}$  observed is  $\leq 10\%$  of the nitrogen from NO attached to the complex. The  $\text{SO}_3^-$  or  $\text{HSO}_3^-$  concentrations do not affect the amount of  $\text{N}_2\text{O}$  produced so long as they are in excess of the concentration of Fe(II)(NTA)NO. We are investigating the effect of Fe(II)(NTA)NO concentration on the amount of  $\text{N}_2\text{O}$  produced to determine why this occurs.

$\text{N}_2$  is a possible product of the reaction. Analysis of  $\text{N}_2$  with a gas chromatograph would be difficult, so it was decided to use mass spectroscopy to determine the amounts of  $\text{N}_2$  and  $\text{N}_2\text{O}$  produced by the reaction. An argon atmosphere is used as an inert buffer gas over the solution. A sample of the gas over the solution after the reaction is complete is collected in an evacuated bulb and run on a mass spectrograph. In the preliminary runs done so far, the amounts of  $\text{N}_2\text{O}$  observed are in reasonable agreement with those obtained by GC techniques.  $\text{N}_2$  has been found to be variable, although it appears to be a substantial fraction of nitrogen-containing products. The amount of NO in Fe(II)(NTA)NO that is converted into  $\text{N}_2$  ranges from about 20 to 60% in the runs done so far (Table 3).

We are also developing procedures to quantitatively identify the nitrogen and nitrogen-sulfur compounds in solution that could be produced by the reaction of Fe(II)(NTA)NO with  $\text{SO}_3^-$  or  $\text{HSO}_3^-$ . The compounds that we are developing analyses for include ammonia ( $\text{NH}_3$ ), nitrate ion ( $\text{NO}_3^-$ ), nitrite ion ( $\text{NO}_2^-$ ), hydroxylamine ( $\text{NH}_2\text{OH}$ ), hydroxylamine monosulfonate ( $\text{HONH}(\text{SO}_3^-)$ ),

hydroxylamine disulfonate ( $\text{HON}(\text{SO}_3)_2^-$ ), amine disulfonate ( $\text{HN}(\text{SO}_3)_2^-$ ), amine trisulfonate ( $\text{N}(\text{SO}_3)_3^{3-}$ ), and sulfamic acid ( $\text{H}_2\text{N}(\text{SO}_3)^-$ ).

Table 3. Product analysis of the reaction of  $\text{Fe}(\text{II})(\text{NTA})\text{NO} + \text{SO}_3^{2-}/\text{HSO}_3^-$ .

$[\text{Fe}(\text{II})(\text{NTA})\text{NO}]$	$[\text{S}^{\text{IV}}]$	pH	Measurement technique <sup>a</sup>	Species measured	Fraction of total nitrogen observed
$1.80 \times 10^{-3}$ M	$8.0 \times 10^{-2}$ M	8.65	GC	$\text{N}_2\text{O}$	0.51
$1.80 \times 10^{-3}$ M	$10.8 \times 10^{-2}$ M	7.2	GC	$\text{N}_2\text{O}$	0.36
$1.80 \times 10^{-3}$ M	$9.8 \times 10^{-2}$ M	5.8	GC	$\text{N}_2\text{O}$	0.24
$1.80 \times 10^{-3}$ M	$10.6 \times 10^{-2}$ M	3.9	GC	$\text{N}_2\text{O}$	0.25
$2.68 \times 10^{-3}$ M	$4.1 \times 10^{-2}$ M	7.95	GC	$\text{N}_2\text{O}$	0.41
$2.68 \times 10^{-3}$ M	$4.75 \times 10^{-2}$ M	6.15	GC	$\text{N}_2\text{O}$	0.22
$2.68 \times 10^{-3}$ M	$5.3 \times 10^{-2}$ M	3.2	GC	$\text{N}_2\text{O}$	0.25
$2.68 \times 10^{-3}$ M	$5.3 \times 10^{-2}$ M	2.9	GC	$\text{N}_2\text{O}$	0.19
$2.25 \times 10^{-2}$ M	0.234 M	8.0	GC	$\text{N}_2\text{O}$	0.042
$1.07 \times 10^{-2}$ M	$2.67 \times 10^{-2}$ M	6.3	GC	$\text{N}_2\text{O}$	0.026
$5.85 \times 10^{-3}$ M	$2.10 \times 10^{-2}$ M	6.9	MS	$\text{N}_2\text{O}$	0.08
$9.85 \times 10^{-3}$ M	$2.51 \times 10^{-2}$ M	7.4	MS	$\text{N}_2\text{O}$	0.09
$7.83 \times 10^{-3}$ M	0.209 M	8.0	Devarda	$\text{NO}_2^-, \text{NO}_3^-$	0.11
$2.25 \times 10^{-2}$ M	0.234 M	8.0	Devarda	$\text{NO}_2^-, \text{NO}_3^-$	0.05
$1.41 \times 10^{-2}$ M	0.122 M	6.7	Devarda	$\text{NO}_2^-, \text{NO}_3^-$	0.05
$2.02 \times 10^{-2}$ M	0.144 M	8.05	Devarda	$\text{NO}_2^-, \text{NO}_3^-$	0.085
$1.07 \times 10^{-2}$ M	$2.67 \times 10^{-2}$ M	6.3	Iodimetry	HADS	0.07
$5.85 \times 10^{-3}$ M	$2.10 \times 10^{-2}$ M	6.9	Iodimetry	HADS	0.067
$9.85 \times 10^{-3}$ M	$2.51 \times 10^{-2}$ M	7.4	Iodimetry	HADS	0.105
$5.85 \times 10^{-3}$ M	$2.10 \times 10^{-2}$ M	6.9	MS	$\text{N}_2$	0.19
$9.85 \times 10^{-3}$ M	$2.51 \times 10^{-2}$ M	7.4	MS	$\text{N}_2$	0.60

<sup>a</sup> Measurement techniques: GC = gas chromatograph, MS = mass spectrograph, Devarda = Devarda reduction analysis, iodimetry = triiodide-thiosulfate titration

<sup>b</sup> Effect of pH on  $\text{N}_2\text{O}$  production

<sup>c</sup>  $\text{N}_2\text{O}$  production at higher  $\text{Fe}^{\text{II}}(\text{NTA})\text{NO}$  concentrations

<sup>d</sup>  $\text{NO}_2^-$  not separated from  $\text{NO}_3^-$

Ammonia is determined by making the reaction mixture alkaline with the addition of sodium hydroxide and distilling 50-100 ml of the solution into standardized, dilute hydrochloric acid. The acid plus distillate is then titrated with standardized sodium hydroxide to determine the amount of ammonia. No ammonia has been detected in any of the reaction mixtures tested so far.

$\text{NO}_2^-$  and  $\text{NO}_3^-$  are routinely analyzed by colorimetric methods. The reaction solution is generally reddish or yellowish colored and consequently interferes with colorimetric techniques. It may be possible to decolorize the solution prior to analyzing for  $\text{NO}_2^-$  and  $\text{NO}_3^-$ . Both anions may be detected by reduction to ammonia by Devarda's alloy (45% Al, 50% Cu, 5% Zn) in a basic solution. The ammonia is then distilled into standardized hydrochloric acid. The remaining acid is titrated with standardized sodium hydroxide. In the reaction mixtures that have been analyzed, 5 to 10% of the nitrogen from NO

bound to the ferrous nitrosyl complex was in the form of  $\text{NO}_2^-$  or  $\text{NO}_3^-$  (Table 3).

Hydroxylamine disulfonate (HADS) and hydroxylamine monosulfonate (HAMS) were analyzed by iodimetry, as described by Sato.<sup>15</sup> The solution is first adjusted to pH 5.6 with an acetate buffer used to maintain the pH. Excess standardized triiodide solution is added and backtitrated with standardized thiosulfate solution. This allows the determination of the amount of sulfite remaining in solution and eliminates the possibility of sulfite's interfering in the iodimetric titration done at higher pH for the compounds of interest. The solution is adjusted to pH 9.8, and a borate buffer is used to maintain the pH. Excess triiodide solution is again added, and the solution is back-titrated to determine the amounts of hydroxylamine disulfonate and hydroxylamine monosulfonate. About 10% of the nitrogen in the ferrous nitrosyl complex has been converted to HADS and HAMS in the mixtures thus far analyzed (Table 3).

Wet analytical techniques are not sufficiently rapid or specific to identify all the species present in chemical systems as complex as the ones under study. We have recently started to use laser Raman spectroscopy to efficiently and unambiguously identify species present in mixes of  $\text{SO}_2$ , NO, and metal chelates.

The first step in the identification process is to acquire Raman spectra of all potential reaction products so that the relative scattering efficiencies and Raman shifts will be known. The species we have studied, along with their Raman shifts and scattering efficiencies relative to sulfate ion, are shown in Table 4. The limiting factors in Raman spectroscopy are the need for fairly high concentrations and the attenuation of the spectra by colored solution. Since some of the reaction products are present in fairly low concentrations and some of the solutions used are colored, it has been necessary to use fairly long data acquisition times to obtain useful spectra.

Laser Raman spectroscopy has been used to detect the products of the reactions of  $\text{Fe(II)(NTA)NO}$  with sulfite ion and  $\text{Fe(II)(H}_2\text{O)}_5\text{NO}$  with bisulfite ion. Solutions of potential reaction products, including nitrogen-sulfur compounds, were prepared to obtain Raman shifts and relative scattering efficiencies. Figures 4A and 4B are Raman spectra of HAMS and HADS respectively. Sulfate ion was added to the solutions as a reference so that the relative scattering efficiencies could be obtained. The HAMS peak is at  $1060\text{ cm}^{-1}$ , the HADS peak is at  $1085\text{ cm}^{-1}$ , and the  $\text{SO}_4^{2-}$  peak is at  $985\text{ cm}^{-1}$ .

Figure 4C is a spectrum of a solution with initial concentrations of  $0.037\text{ M Fe(II)(H}_2\text{O)}_5\text{NO}$  and  $0.19\text{ M bisulfite ion}$  at  $\text{pH} \sim 4$ . The  $985\text{ cm}^{-1}$  sulfate peak is from the ferrous sulfate used to prepare the solution and the sulfate created as a reaction product. The peaks due to HADS and HAMS are apparent at  $1085$  and  $1060\text{ cm}^{-1}$ . The species responsible for some of the other peaks present, such as the  $1245$  and  $1280\text{ cm}^{-1}$  peaks, have not yet been identified. The solution is colorless after the completion of the reaction. The  $488\text{ nm Ar}^+$  laser line was used to obtain the spectra.

Figure 4D is a spectrum of  $\text{Fe(II)(NTA)NO}$  and sulfite ion at  $\text{pH } 8.3$ , with initial concentrations of  $0.043\text{ M}$  and  $0.100\text{ M}$ , respectively. Additional sulfate ion was added to the solution at the time of mixing, making a total of

0.091 M sulfate added to the solution. The peak due to HADS is prominent at  $1085\text{ cm}^{-1}$ . Since the solution is basic, HADS will not be rapidly hydrolyzed to form HAMS. The reacted solution absorbs strongly in the blue region of the spectrum, so the 647 nm  $\text{Kr}^+$  laser line was used for this spectrum.

Table 4. Raman shifts and scattering efficiencies of some species relative to sulfate ion.

Compound	Raman shift	Relative scattering efficiency ( $\text{SO}_4^{2-} = 1.00$ )
$\text{SO}_4^{2-}$	$985\text{ cm}^{-1}$	1.00
$\text{SO}_3^{2-}$	$\sim 970\text{ cm}^{-1}$	0.067
$\text{NO}_2^-$	$818\text{ cm}^{-1}/1332\text{ cm}^{-1}$	0.0235/0.055
$\text{NO}_3^-$	$1050\text{ cm}^{-1}$	0.42
$\text{N}_2\text{O}$	$1285\text{ cm}^{-1}$	0.08
$\text{N}_2\text{O}_2^-$	$(1383\text{ cm}^{-1})^a$	—
$\text{HON}(\text{SO}_3)_2^-$ (HADS)	$1087\text{ cm}^{-1}$	0.63
$\text{HONH}(\text{SO}_3)^-$ (HAMS)	$1061\text{ cm}^{-1}$	0.21
$\text{NH}_2\text{OH}$	$1007\text{ cm}^{-1}$	0.09
$\text{N}(\text{SO}_3)_3^-$ (ATS)	$1100\text{ cm}^{-1}$	0.045
$\text{HN}(\text{SO}_3)_2^-$ (ADS)	$1087\text{ cm}^{-1}$	0.025
$\text{H}_2\text{NSO}_3^-$ (SFA)	$1052\text{ cm}^{-1}$	0.18

<sup>a</sup>From J.E. Rauch and J.C. Decius, *Spectrochim. Acta* 22, 1963 (1966).

Figure 4E is a spectrum of an initial concentration of 0.012 M  $\text{Fe}(\text{II})(\text{NTA})\text{NO}$  and 0.100 M sulfite ion at  $\text{pH} \sim 7$ . The  $985\text{ cm}^{-1}$  sulfate peak overlaps with the broader sulfite peak centered at  $970\text{ cm}^{-1}$ . The peaks to HADS and HAMS are weak but visible at  $1085$  and  $1060\text{ cm}^{-1}$ . While the reacted solution does absorb in the blue region of the spectrum, the absorption was sufficiently weak to allow the 488 nm  $\text{Ar}^+$  laser line to be used. The sharp spikes in the spectrum are due to noise in the laser output.

Work is currently in progress to quantitatively determine the amounts of the observed products that are produced by the reactions of ferrous nitrosyl complexes with sulfite and bisulfite ions. The observed quantities will be compared to those predicted from the known reaction rates. This will allow us to evaluate how well the chemistry of the nitrogen-sulfur compounds are known.



### Conclusions

Adding some metal chelates to a wet stack gas scrubber can improve the removal efficiency of both NO and SO<sub>2</sub>. The extent to which the amount of NO and SO<sub>2</sub> can be removed depends on the property of the metal chelate additives and the design of the scrubber. An efficient metal chelate additive should have a rapid binding rate with NO and large equilibrium constants for the formation of nitrosyl metal chelates. The removal capacity of gaseous NO as a function of the equilibrium constant of nitrosyl metal chelates is shown in Fig. 5. In this calculation, we assume that the volume ratio of flue gas to scrubbing solution is 100, the initial partial pressure of NO in flue gas is 500 ppm, and the concentration of total ferrous ion in aqueous scrubbing solution is 0.1 M at 50°C. The results of this calculation indicate that as the equilibrium constant increases, the amount of gaseous NO removed increases; and, therefore, the concentration of nitrosyl ferrous chelates in solution also increases. For Fe(NTA)NO with  $K = 4.6 \times 10^5 \text{ M}^{-1}$ , the final partial pressure of NO is 80 ppm, and the equilibrium concentration of Fe(NTA)NO is  $1.5 \times 10^{-3} \text{ M}$ .

The regeneration rate of metal chelates from nitrosyl metal chelates by reaction with sulfite/bisulfite ions depends on both the rate constant and the concentration of reactants. The results discussed previously indicate that if Fe(II)NTA is used as an additive, the rate controlling step will be the regeneration of this metal catalyst in a typical wet stack gas scrubber because the absorption rate and the mass transfer rate of NO are much larger than the regeneration rate of Fe(II)NTA. Therefore, it might be advantageous to choose a catalyst that has neither a very large NO absorption capacity nor a very rapid NO absorption rate but has a rapid reaction rate with sulfite/bisulfite ions. A slower catalyst regeneration rate requires a longer residence time and therefore larger equipment, more capital investment, and higher operating costs.

Laser Raman spectroscopy, gas chromatography, and mass spectrometry have been developed to directly, rapidly, quantitatively, and unambiguously identify reaction intermediates and products so that reaction kinetics and mechanisms can be characterized and byproducts of a stack gas scrubber can be effectively controlled.

### Acknowledgments

We thank Professors Leo Brewer, Robert Connick, and Scott Lynn for helpful discussions; and we appreciate the support and encouragement of Miss Stephanie Bialobok and Dr. Jack Halow. This work was supported by the Morgantown Technology Center, Contract No. 82MC14002, through the Assistant Secretary of Fossil Energy of the U.S. Department of Energy under Contract No. DE-AC 03-76SF00098.

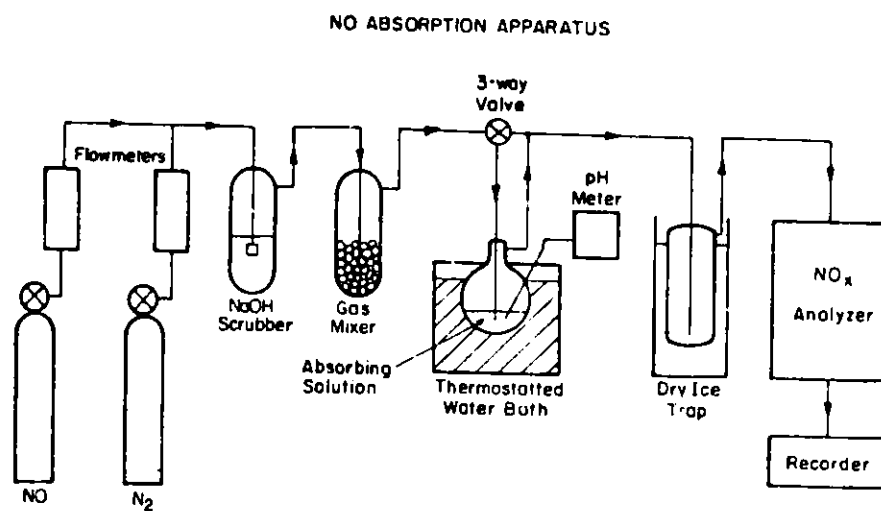


Figure 1. NO absorption apparatus. This setup is used for determining the enthalpy, entropy, and equilibrium constants for the reversible binding of NO to various metal chelates in aqueous solution.

### Temperature Jump Apparatus

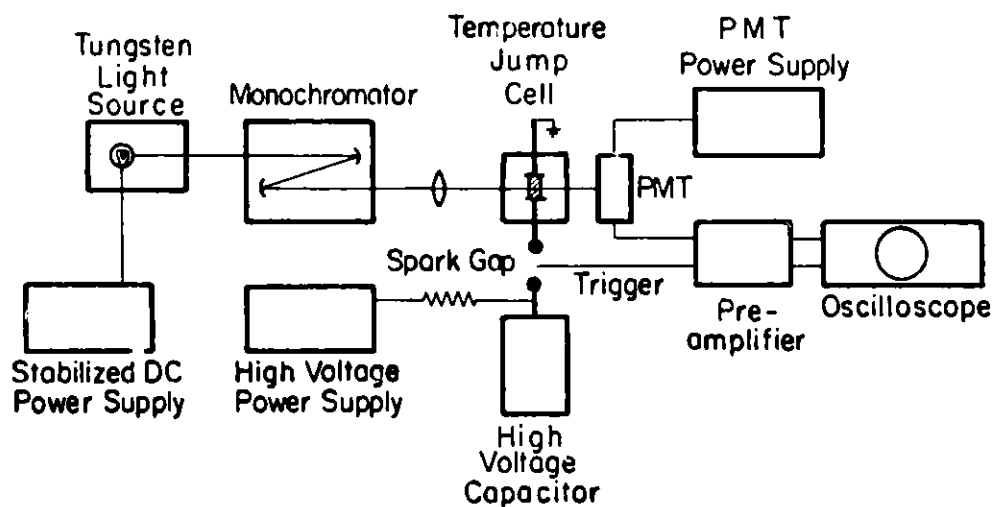
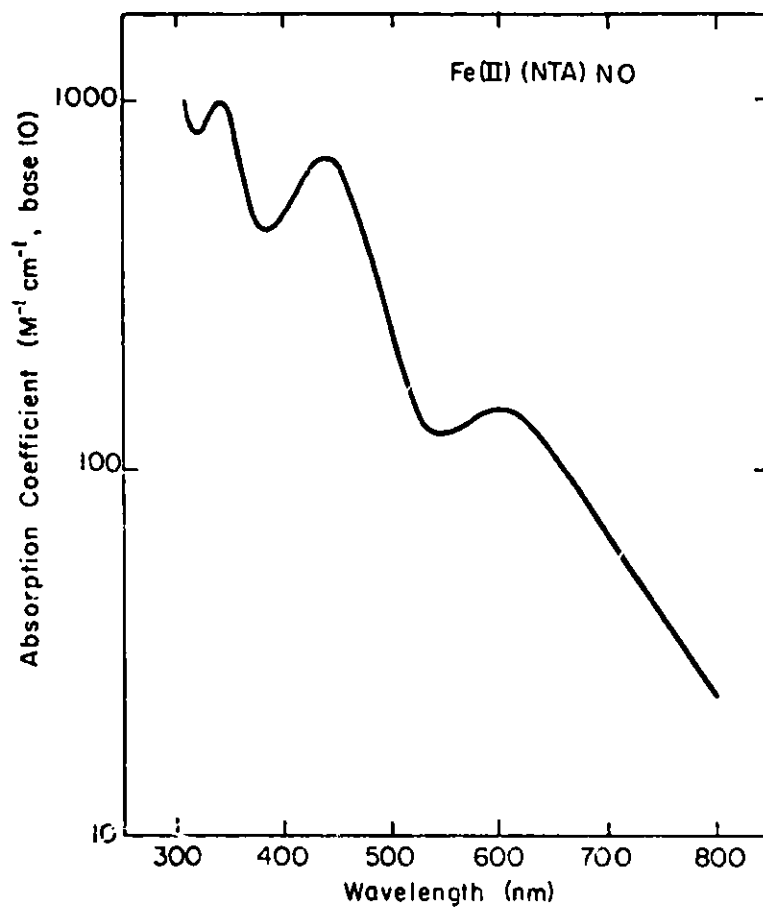


Figure 2. Temperature-jump apparatus. This setup is used for determining the formation and dissociation rate constants and equilibrium constants for the reversible binding of NO to various metal chelates in aqueous solutions.



XBL 816-5927

Figure 3. An absorption spectrum of Fe(II)(NTA)NO from 800 to 300 nm.

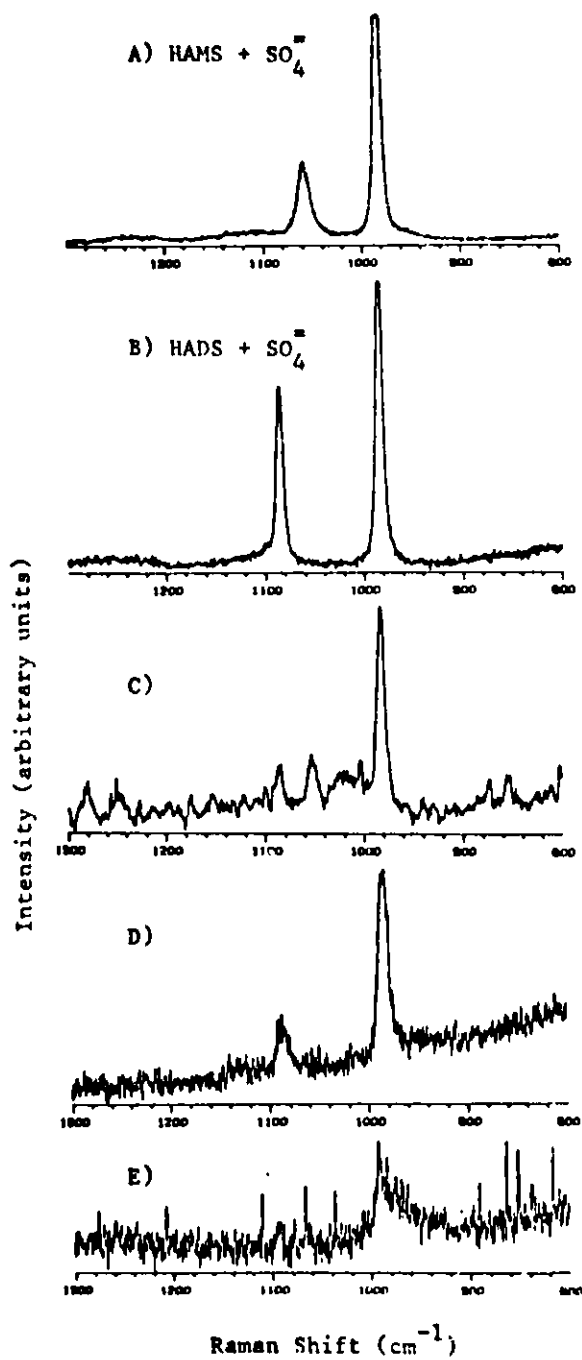
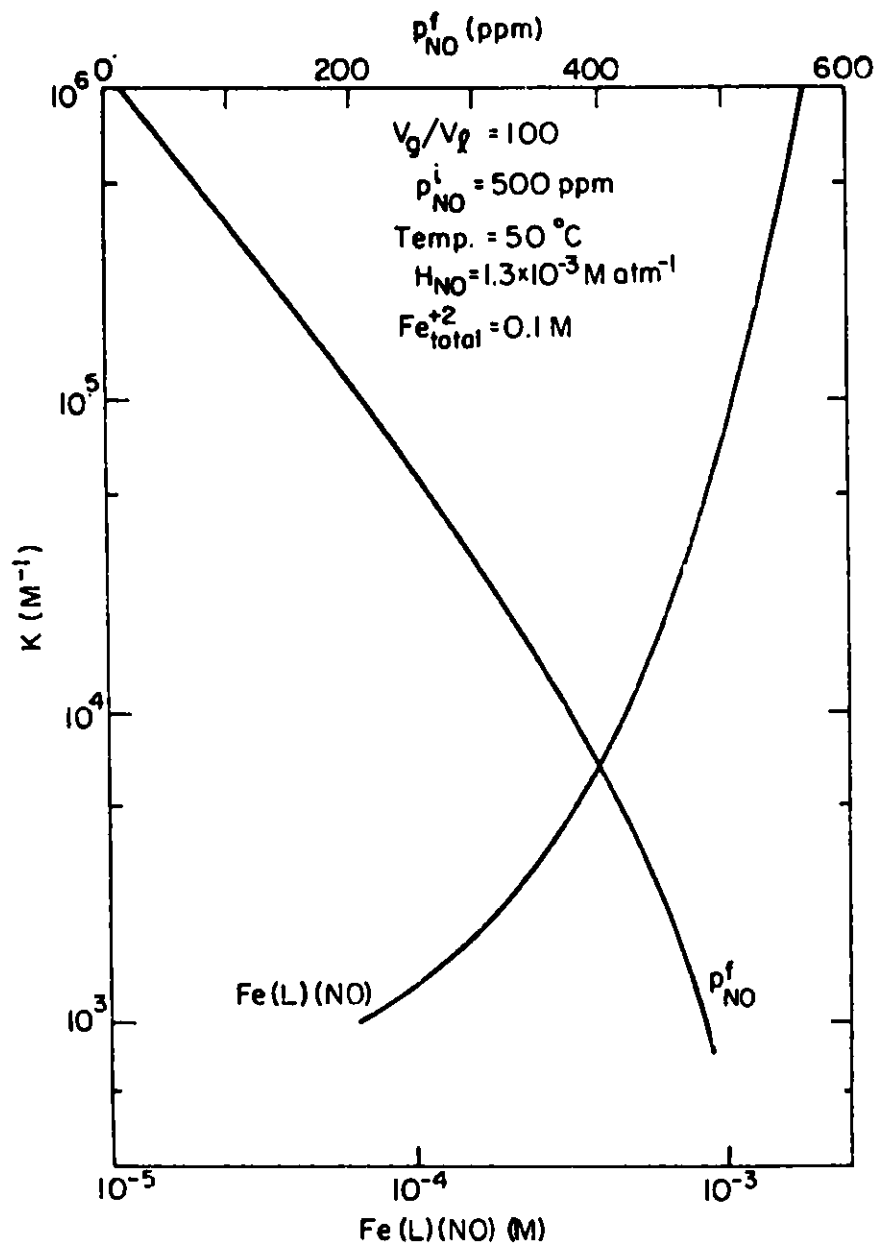


Figure 4. Raman spectra of (A) hydroxylamine monosulfonates (HAMS), (B) hydroxylamine disulfonates (HADS), and reaction mixtures of (C)  $\text{Fe(II)(H}_2\text{O)}_5\text{NO}$  with  $\text{HSO}_3^-$ , and (D) and (E)  $\text{Fe(II)(NTA)NO}$  with  $\text{SO}_3^{=}/\text{HSO}_3^-$ .



XBL 823-5456

Figure 5. The effect of the equilibrium constant of nitrosyl metal chelate in aqueous solutions on the removal efficiency of gaseous NO.  $V_g$  and  $V_l$  are the volume of the flue gas and the volume of the scrubbing solution respectively;  $p_{NO}^i$  and  $p_{NO}^f$  are the partial pressures of NO in the flue gas before scrubbing and after reaching an equilibrium condition with the scrubbing solutions.  $H_{NO}$  is Henry's coefficient of NO at 50°C, and  $\text{Fe(L)(NO)}$  is the concentration of nitrosyl ferrous chelates in the scrubbing solution.

References

1. L.H. Yaverbaum, Nitrogen Oxides Control and Removal, Recent Developments, Noyes Data Corporation, Park Ridge, N.J. (1979).
2. A.E. Martin, ed., Emission Control Technology for Industrial Boilers, Noyes Data Corporation, Park Ridge, N.J. (1981).
3. S.-G. Chang, D. Littlejohn, and N.H. Lin, "Kinetics of reactions in a wet flue gas simultaneous desulfurization and denitrification system," Symposium on Advances in Flue Gas Desulfurization, A.C.S., Atlanta, Georgia (March 30-April 3, 1981); LBL-13063 (1981).
4. J.N. Armor, *J. Chem. Eng. Data* 19, 82 (1974).
5. D. Littlejohn and S.-G. Chang, *J. Phys. Chem.* 86, 537 (1982).
6. Y. Hishinuma, R. Kaji, H. Akimoto, F. Nakajima, T. Mori, T. Kamo, Y. Arikawa, and S. Nozawa, *Bull. Chem. Soc. Japan* 52, 2863 (1979).
7. N.H. Lin, D. Littlejohn, and S.-G. Chang, accepted for publication in *I&EC Process Res. and Dev.* (1982).
8. T.K. Sherwood and R.L. Pigford, Absorption and Extraction, 2nd ed., McGraw-Hill, New York (1952).
9. Scott Lynn, private communication.
10. K. Kustin, I.A. Taub, and E. Weinstock, *Inorg. Chem.* 5, 1079 (1966).
11. M. Teramoto, S. Hiramane, Y. Shimada, Y. Sugimoto, and H. Teranishi, *J. Chem. Eng. Japan* 11, 450 (1978).
12. E. Sado, H. Kumazawa, I. Kudo, and T. Kondo, *Ind. Eng. Chem. Process Res. Dev.* 19, 377 (1980).
13. A. Ringbom, Complexation in Analytical Chemistry, Interscience, New York (1963).
14. K. Sawai and T. Gorai, *Kyusan to Kogyo*, 187 (1976).
15. Sato, "Oxidation of sodium sulfite with nitrogen dioxide," Paper No. INDE 210, American Chemical Society Meeting, Honolulu, Hawaii (1979).
16. G. Czerlinski and M. Eigen, *Z. Elektrochem.* 63, 652 (1959).

TRANSFER OF ASPHALTENE-COATED PARTICULATES  
FROM MODEL FLUIDS INTO AN AQUEOUS PHASE

Latif A. Khan\*

Introduction

When run-of-mine coal is liquefied, the mineral matter present in the feed is carried into the effluent produced by the liquefaction process. Removal of these fine particles of mineral matter from liquefied coal prior to its use would improve its potential as a future energy source.

Theoretically, particulates may be separated and removed from liquefied coal by utilizing differences of size and density; however, physical cleaning of the highly viscous effluent to remove such fine particles will not be sufficiently thorough and will necessitate a secondary cleaning of the rejected material. An alternative, physico-chemical method would utilize differences in surface properties of the effluent materials to effect a transfer of particulates to an aqueous phase. Clearly, the development of such an efficient, one-step cleaning process for the recovery of fines would be of considerable importance.

One such method may be the liquid-liquid extraction of the ultra-fine particles from one aqueous medium into another<sup>1</sup>. In order to separate the fines in the liquid-liquid extraction, it is necessary to collect them selectively on dispersed aqueous droplets so that they can be carried away by that particular medium. It has been observed that fine particles, collecting on droplets of the dispersed phase, stabilize some emulsions. Extensive work on this subject has been done by Pickering<sup>2</sup>, Briggs<sup>3</sup>, Weston<sup>4</sup>, Chessman and King<sup>5</sup>, Schulman and Leja<sup>6</sup>, and Hildebrand<sup>7</sup>. Fuerstenau<sup>1</sup> successfully utilized this phenomenon for the extraction of hydrophilic aluminum particles, with an average diameter of  $0.1\mu$ , from water into ISO-octane by using Alkyl sulfonates as surface-modifying agents. He found that an increase in surfactant concentration increased the surfactant adsorption on the aluminum particles thus making the particles more hydrophobic and facilitating their extraction into the oil (ISO-octane) phase.

In this study, we reversed the process. First, we conditioned the effluent in benzene or xylene, as a model fluid. Then we added a particular surfactant or combination of surfactants to the model fluid in order to modify the surface of the fine mineral particles. When mixed with water, these particulates separated from the model fluid and transferred to an aqueous phase. We examined the effects of the hydrophile-lipophile balance (HLB) for a combination of surfactants, the concentrations and type of surfactant, and the mixing and centrifugation time for the extraction of the particulates from the model fluids into the aqueous phase.

\* Present address is Illinois State Geological Survey, 615 East Peabody Drive, Champaign, IL 61820; 217/344-1481.

### Materials and Methods

The solvent-refined coal ash (SRC) used in these tests was obtained, first, by filtering 3:1 SRC II through a 0.45 $\mu$ -milipore filter, and then, soxhlet extraction of all benzene-soluble components from the filter cake. Reagents used were of a technical grade.

In this study, benzene or xylene was used instead of the effluent produced by liquefaction for safety and ease of handling as well as for transparency and homogeneity of the phase. Prior to the aqueous phase, particulates were conditioned in these model fluids by adding specified quantities of surfactants. The model fluid, ash, surfactants, and water were mixed for a given time by inverting the sealed tube containing the mixture in a mechanical device at the speed of 60 inversions per minute, unless stated otherwise. The mixture was then left to settle and separate into the model fluid and aqueous phases. After settlement, the phases were separated with a disposable syringe and filtered through a 0.45 $\mu$ -milipore filter to recover the ash.

The mixture was centrifuged after mixing for different time intervals whenever the resistance to distribution or the effect of external force on the distribution was being examined.

### Experimental Results and Discussion

The mineral matter loses its original surface properties when it becomes coated with asphaltenes during the liquefaction process. The physico-chemical behavior of the particulates, which is determined by the exposed external coating, can be controlled with surfactants. Whenever surfactants are added to such a system, they may adsorb not only on the surface of the solids but also at the liquid/liquid interface as an oriented film. At each site they will perform different functions. The adsorption of ionic surfactants and their surface coverage will change the wetting properties of the particles<sup>8</sup>.

When model fluids, particulates, and water are agitated together, the fluids break up into small drops that collide with each other and with the particulates. The modified surface properties of the constituents then largely determine to which phase the ash particles migrate on resolution of the phases after mixing. A surfactant may cause the dispersion of a hydrophilic phase in oil phase or the reverse, depending on the nature of the surfactant. The type of the action and the behavior that may be expected from a surfactant can be predicted from its HLB value. The effects of the HLB produced by a combination of surfactants on the transfer of asphaltene-coated particles to an aqueous phase is given in table 1. Table 1 shows that the transfer of the asphaltene-coated particles from benzene to the NaCl-solution takes place only between the HLB 9 through 11, with the maximum around 10. No transfer of the particulates was achieved below and above that HLB range.

The HLB also seems to affect the behavior of the distributed ash in the aqueous phase: figure 1 shows the increased dispersion of ash in water. In the HLB range of 9 through 11, a surfactant may produce an oil-in-water emulsion. Since in this range the ash was transferred to the aqueous phase,



Table 1. Effect of HLB on distribution of SRC II ash from benzene to NaCl-solution after mixing for 2 min.: surfactant concentration 10,000 ppm (benzene basis); benzene:NaCl-solution 27:12.5 cc.

Tween 20 to Span 80 ratio	HLB	Particulates distributed to aqueous phase (% total)
2:8	7	0
3:7	8	0
4:6	9	88.5
5:5	10	100.-
6:4	11	87.7
7:3	12	0

it is expected that any other oil-in-water emulsifying agents may be used to achieve the transfer of the ash to the aqueous phase.

The HLB figures may be used in the selection of the proper type of surfactant; however, these are just ratios between the hydrophile and lipophile portions of a molecule and indicative of neither the efficiency nor effectiveness of a surfactant<sup>8</sup>. Surfactants differ in their ability to produce the appropriate emulsions and hence also to distribute the ash. Table 2 shows the distribution of the ash from model fluid into an aqueous phase achieved with the same concentration of different trade brand surfactants. For equal concentrations, the distribution of this ash decreases successively from Hyonic PE 260 to Ninate 411 to Duponal to Miranol. If the coating on the ash particle changes, the distribution pattern may vary.

Table 2. Effect of the type of surfactant (1000 ppm) on the distribution of particulates from 25 cc xylene to 12.5 cc NaCl-solution after 30 inversions.

Surfactant	Particulates distributed to aqueous phase (% total)
Hyonic PE 260	82.0
Ninate 41 (alkylamine dodecyl benzene sulfonate)	80.4
Duponal (sodium lauryl sulfate)	56.5
Miranol C2M {-2-"Cocoyl"-1-(sodium carboxymethyl)-1- [2-(sodium carboxymethoxy) ethyl]-2-imidazolinium hydroxide}	51.2

Since adsorption of the surfactants depends on their concentration in the aqueous phase<sup>9</sup>, it was expected that the transfer of ash to water would be affected by the concentration of surfactants. Our experiments showed that there was no distribution of ash to the aqueous phase with the combination of Tween 20 and Span 80 at HLB 10 with surfactant concentrations below 3000 ppm. The effect of Nekal on the distribution of ash to the aqueous phase is shown in table 3. In this case, recovery of the ash increases with an increase in the surfactant concentration, although not proportionately.

Table 3. Effect of concentrations of Nekal on distribution of particulates from 25 cc xylene into 12.5 cc NaCl-solution after mixing for 15 minutes.

	Nekal (ppm)	Particulate distribution (wt% of total)
D 11	250	0
D 12	500	80
D 13	750	81.8
D 14	1000	83.3

Concentration of a surfactant affects not only the amount of ash, but the behavior of the particles distributed to the aqueous phase (table 3; figs. 2 and 3). At lower surfactant concentrations, the ash is pushed into water as a gelatinous mass, usually hanging from the interface. This structure is retained even after prolonged exposure to the aqueous phase (compare D 11 and D 12 of figs. 2 and 3). With an increase in the surfactant concentration, the ash particles transfer to the aqueous phase as individual particles or as small agglomerates (D 13, figs. 2 and 3). A further increase in the concentration of surfactant causes the particles to agglomerate again. When the aqueous exposure time is increased, these particles get wetted by the aqueous phase as the surfactant dissipates and the agglomerated structure falls apart (D 14, figs. 2 and 3). Large concentrations of surfactants may be, therefore, detrimental for the ash distribution as well.

Instead of changing the wetting properties directly large quantities of surfactants added to the system may cause the removal of some coating. This type of removal may be facilitated by the oriented adsorption of surfactants on adjacent layers. When the surfactants adsorb on layers of the coating with their hydrophilic groups oriented towards the water, then the hydration of these polar parts will reduce the van der Waals attraction between those layers, and also will increase the electrostatic repulsion, thus causing removal of the coating<sup>8</sup>. Such a removal reduces the amount of surfactant covering the surface of the ash particles. Removal of the adsorbed surfactant may also be caused by the hydraulic currents generated during the mixing.

This removal of the surfactant and reduction of surface coverage on the ash will adversely affect its distribution. It appears that the asphaltene-coated ash particles must overcome a resistance in order to transfer to the aqueous phase, and that the force required to overcome the resistance is provided by surfactants. With an increase in the mixing intensity, the ash distribution to the aqueous phase drops (table 4), indicating an apparent removal of the surfactant<sup>10</sup>.

If this force due to the surfactant coverage is reduced so much that the particle cannot overcome the resistance to the transfer, then an external force, such as centrifugal force, may be required to facilitate the transfer. The amount of ash distributed to the aqueous phase under the influence of this external force will be directly proportional to the amount of surface covered with surfactant. The quantity of the ash distributed to aqueous phase, and therefore, the amount of the surfactants covering the surface of

the particulates depend upon their concentration in the solution at any mixing intensity (tables 5 and 6).

Table 7 shows that the distribution of ash to water decreases with increase in the mixing intensity even at low concentrations, indicating a continuous removal of the surfactant from particle surfaces during the mixing.

Table 4. Effect of mixing time on distribution of particulates with 1500 ppm Nekal to NaCl-solution from xylene containing 100,000 ppm p-cresol.

Xylene:NaCl-Sol.	Mixing time	% Ash distribution to NaCl-Sol.
25:12.5	5	71.0
25:12.5	10	70.6
25:12.5	15	69.7
25:12.5	30	41.2
25:12.5	60	0

Table 5. Effect of surfactant concentration on the distribution of ash with Nekal under the influence of external force after mixing for 65 minutes.

Xylene:H <sub>2</sub> O (cc)	Surfactant core (ppm)	Ash distributed to H <sub>2</sub> O (%)
25:12.5	500	50.0
25:12.5	1000	83.3
25:12.5	2500	83.3
25:12.5	5000	83.3

Table 6. Effect of surfactant concentration on the distribution of ash with #822N under the influence of external force after mixing for 45 minutes.

Xylene:H <sub>2</sub> O (cc)	Surfactant core (ppm)	Ash distributed to H <sub>2</sub> O (%)
25:12.5	100	16.6
25:12.5	200	33.3
25:12.5	500	50.-
25:12.5	1000	71.4
25:12.5	2000	83.3

Table 7. Effect of mixing time on the distribution of ash with 100 ppm #822N under the influence of external force.

Xylene:H <sub>2</sub> O (cc)	Mixing time (min.)	Ash distributed to H <sub>2</sub> O (%)
25:12.5	5	83.3
25:12.5	10	81.8
25:12.5	15	77.8
25:12.5	20	75.0
25:12.5	30	66.7
25:12.5	45	16.7
25:12.5	60	9.1
25:12.5	90	1.0

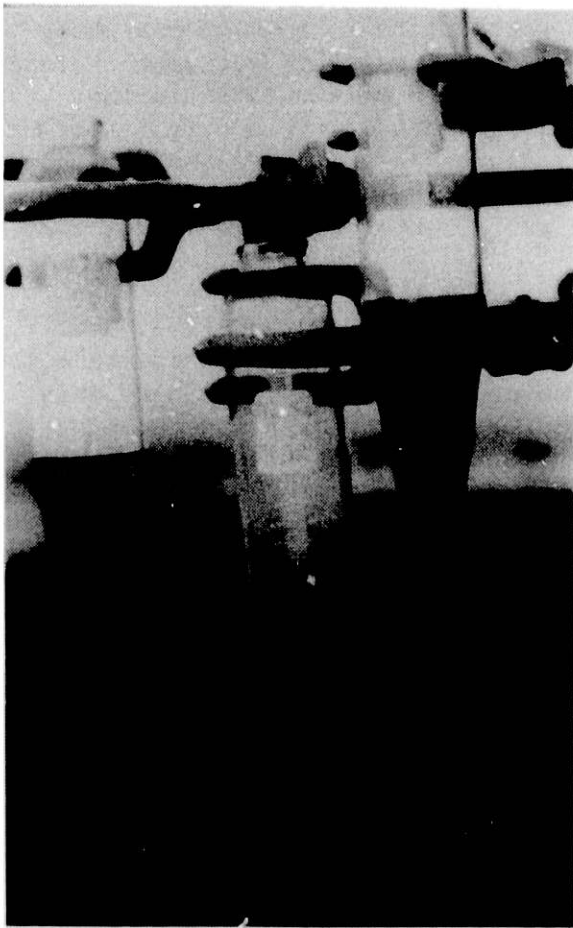
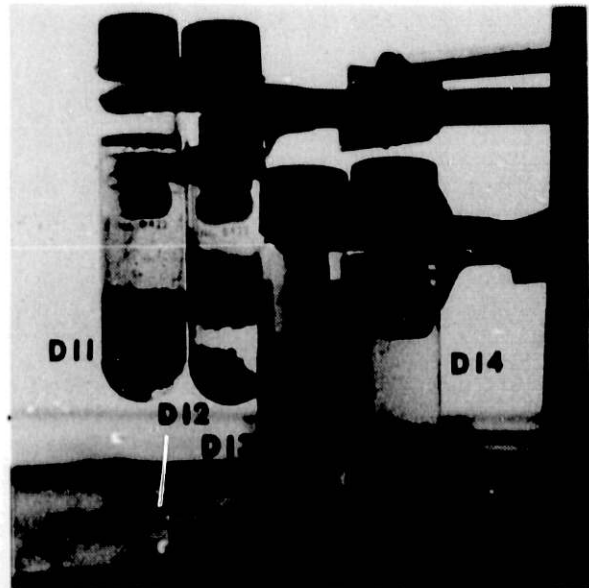
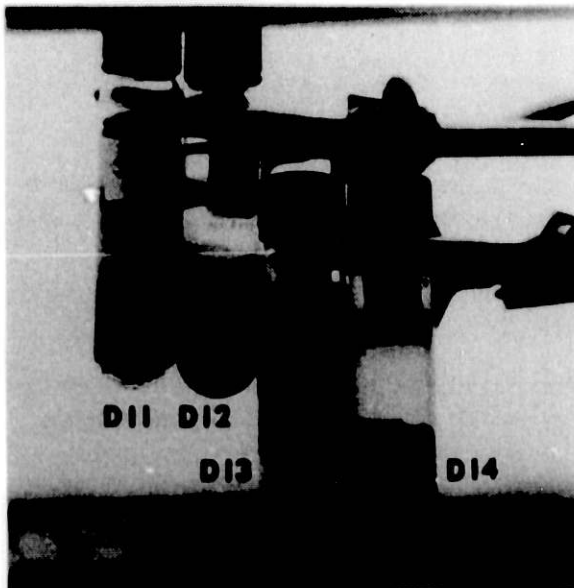


Figure 1. Effect of HLB on distribution of ash from benzene to NaCl-solution.



Figures 2 and 3. Behavior of particulates distributed to the aqueous phase with the concentrations of Nekal listed in table 3. Figure 2 is immediately after distribution, and Figure 3 is 24 hours after distribution.

During our investigations we noted that for the same amount of surfactant the distribution of the asphaltene-coated particulate to the aqueous phase from xylene containing p-cresol was more when NaCl-solution was used instead of water. This increase in the distribution of the particulates to the aqueous phase might have been caused by the increase in the adsorption of the surfactant. The presence of NaCl may have decreased the mutual repulsion of the polar groups, and this may have, in our opinion, led to closer packing of the surfactant molecules at the interface and a larger coverage of the ash particles with the surfactant.

Contact-angle measurements on the plug prepared from the SRC II ash indicated that the adsorption of the surfactants, capable of transferring the ash from the model fluid to the aqueous phase, make the ash particles more hydrophilic; the smaller the contact angle (measured through the aqueous phase), the larger is the ash distribution to the aqueous phase. With decrease in the contact angle the particles become more hydrophilic and tend to produce oil/water emulsion<sup>6</sup>. This o/w emulsion seems to be a necessary requirement for the transfer of the ash particle to the aqueous phase whereas the transfer of the hydrophilic particles to the model fluid is supported by hydrophobic nature of the particles<sup>1</sup>.

#### Summary

The transfer of the asphaltene-coated particulates from model fluids into an aqueous phase can be achieved by using surfactants of a certain HLB range. The recovery of ash in such tests depends upon the concentration of the surfactant. Below a certain concentration external force will be required to help the ash particles overcome the resistance to their transfer. The recovery of the ash under the influence of the external force depends on the surfactant concentration and the mixing intensity which is believed to reduce the surface coverage of the ash with surfactant. With the same reagents the amount of the ash transferred to NaCl solution was more than to water.

#### Acknowledgments

This work was inspired by my experience with ash distribution research in the laboratory of J. D. Henry, West Virginia University, Morgantown and was done there.

#### Disclaimer

Although the research described in this article has been funded wholly or in part by the U.S. Department of Energy to J. D. Henry it has not been subjected to the Department's and West Virginia University peer and policy review and therefore does not necessarily reflect the views of the WVU or Department and no official endorsement should be inferred. Because of the indefinable nature of the asphaltene coating, surface heterogeneity of the solids, and statistical nature of the attachment process together with experimental limitations, the results may be considered strictly qualitative. The surfactants that did not perform well in these tests may do better under other conditions.

References

1. R.W.M. Lai, and D. W. Fuerstenau, "Liquid-Liquid Extraction of Ultra-fine Particles," AIME Transaction, Vol. 241, p. 549 (1968).
2. S. U. Pickering, "Emulsions," J. Chem. Soc., Vol. 91, p. 2001 (1907).
3. T. R. Briggs, "Emulsions with Finely Divided Solids," Ind. Eng. Chem., Vol. 13, p. 1008 (1921).
4. F. E. Weston, "Colloidal Clay and the Hydrolysis of Oils and Fats," Chem. Age, Vol. 4, pp. 604, 638 (1921).
5. D. F. Chessman, and A. King, "The Properties of Dual Emulsions," Trans. Faraday Soc., Vol. 39, p. 594 (1938).
6. J. H. Schulman, and J. Leja, "Control of Contact Angles at the Oil-Water-Solid Interface Emulsions Stabilized by Soil Particles ( $\text{BaSO}_4$ )," Trans. Faraday Soc., Vol. 50, p. 598 (1954).
7. J. H. Hildebrand, "Emulsion Type," J. Phys. Chem., Vol. 45, p. 1303 (1941).
8. M. Rosen, "Surfactants and Interfacial Phenomena," John Wiley & Sons, New York (1978).
9. P. Somasundaran, and D. W. Fuerstenau, "Mechanism of Alkyl Sulfonate Adsorption at the Alumina-Water Interface," J. Phys. Chem., Vol. 70, p. 90 (1966).
10. D. J. Henry, et al., Quarterly Progress Reports to ERBA E(40-1)-5105.

COKING OF SRC-II PROCESS STREAMS

C. S. Wen  
Gulf Research & Development Company  
P. O. Drawer 2038  
Pittsburgh, Pennsylvania 15230  
Phone: (412) 665-5964

Abstract

Coking characterization of various SRC-II process streams was investigated to properly define the parameters and conditions of coke formation. Technologies such as pressure differential scanning calorimetry and thermogravimetry were used in conjunction with Fourier Transform Infrared Spectroscopy and scanning electron microscopy. Coking data from the microprocess units were correlated with data obtained from a batch autoclave, a continuous bench-scale, and a process development unit.

Introduction

It has been observed that certain streams in the SRC-II process are susceptible to coke formation. Several isolated cases of actual coke formation in pilot plant dissolvers, hot separators, preheaters, and transfer lines were reported in the past. The potential for coking within the SRC-II operation is of obvious concern, and a better understanding of the coking phenomenon is required in order to avoid conditions that could lead to coking.

The coking project, funded by DOE (during the period of January 1, 1980 to September 30, 1981) was initiated to study the parameters which initiate, propagate, and accelerate coke formation. It was intended that the work would ultimately lead to the development of criteria to avoid coking in large-scale operations and to develop test methods for monitoring coke formation. During the period of this work, a thorough and quantitative study of coke formation at various stream points in the SRC-II operation has been undertaken. Techniques such as pressure differential scanning calorimetric/thermogravimetric techniques, FT-infrared, and scanning electron microscopy were used in conjunction with batch-autoclave and bench-scale continuous runs to investigate an insight into the phenomenon of coke formation and to provide data useful in the SRC-II plant operation.

Experimental

Different P-99 process streams were investigated including coal feedstock, feed slurry, dissolver effluent, atmospheric flash bottoms, vacuum tower bottoms, process solvent, recycle slurry, and coke-like materials from dissolver and hot separator as well as a Ft. Lewis dissolver preheater outlet sample.

Methods developed specifically for characterizing/measuring SRC-II process streams and solids with respect to coke formation including solvent fractionation, pressure differential scanning calorimetry, thermogravimetry, Fourier transform infrared spectroscopy, and scanning electron microscopy.

Pressure differential scanning calorimetry and thermogravimetry with a Dupont 990 thermal analyzer system were used for the coking studies. The pressure differential scanning calorimetry (PDSC) can directly measure the heat evolution in the process reaction at high pressures. In the system, a pressure transducer and backpressure regulator were installed on-line for precise pressure control and pressure readout.<sup>1</sup> During the run, a slight flow of hydrogen gas (about 20 ml/min over the sample) was maintained through a digital flow controller. The solid or slurry samples were weighed, placed in sample pans, and heated to desired temperatures at linear heating rates or heated isothermally under various hydrogen pressures. A graphitized carbon black or a coal-inert char was chosen as the reference sample.

In a typical thermogravimetric (TGA) run, a platinum boat containing the sample was suspended from the quartz beam of the balance. A chromel-alumel thermocouple was placed in close proximity to the sample. The reactor was made of a quartz tube which was surrounded by a tube furnace. Samples were heated to desired temperatures at linear heating rates. Purge gas (e.g. N<sub>2</sub>, H<sub>2</sub>, air, etc.) at a flow rate of around 50 ml/min was constantly flowing through the apparatus during the experiments.

Batch-autoclave runs under controlled operating conditions were also carried out to verify PDSC/TGA data and to prepare controlled coke-like solids for examinations.

## Results and Discussion

### Measurement Coking Characteristics by Thermogravimetric Technique (TGA)

To develop a rapid, accurate method for determination of coking characteristics, the thermogravimetry technique (TGA) has been used for measurement of light volatile matter, heavy volatile matter, fixed carbon, and ash content. The proportions of these components of coal and of various SRC-II process streams are believed to be indications of coke formation.

A typical TGA thermogram of Powhatan coal is given in Figure 1. The TGA and the weight loss rate, DTG (differential thermogravimetry) thermograms show two major weight loss steps: the first is volatile matter (VM) and the second is fixed carbon (FC). The first weight loss occurred in a nitrogen atmosphere. Air was then introduced to burn off the fixed carbon from the sample causing the second weight loss. Between 350 and 600°C, the coal weight loss is significant because of the large aromatic layer molecule decomposition. We define this major release as light volatile matter (VM<sub>L</sub>). Above 600°C the coal weight loss is small, as only volatile matter is released from the residue char decomposition. This weight loss is referred as heavy volatile matter (VM<sub>H</sub>).

Thermogravimetric analysis of SRC-II streams indicated that there was a strong tendency for decreasing the amount of FC+VM<sub>H</sub> as the coal feedstock and feed slurry flow to the preheater outlet and the dissolver effluent (Figure 2). However, high contents, 40-85 wt%, of FC+VM<sub>H</sub> existed in solid samples, (e.g., ATB, VTB, dissolver, and hot separator cokes). The process solvent contained entirely light volatile matter.



The amount of fixed carbon plus heavy volatile matter (FC+VM<sub>H</sub>) in certain streams appears to give a good correlation with coke formation in continuous pilot plant operations. There was a greater tendency to form coke with higher FC+VM<sub>H</sub> values.

#### Fourier Transform Infrared Characterization

It is known that when coke forms during coal liquefaction large changes of chemical functionality and aromaticity occur. The infrared technique provides a method to detect the presence of chemical groups, to preclude or limit the existence of proposed structures and to demonstrate similarities and differences before and after reaction. Therefore, this technique has been applied to determine the chemistry of coke formation.

Infrared spectra of process streams taken from the Gulf Research 1 ton/day SRC-II Process Development Unit (P-99) are compared in Figure 3. The strong absorption bands arising at 3030 cm<sup>-1</sup> (the aromatic C-H stretchings) and at the region of 750-870 cm<sup>-1</sup> (the aromatic out-of-plane C-H vibrations) in solid coke-like materials suggests the degree of aromaticity increases, and carbon polymerization ensues during the coke formation.

In order to compare the degree of polymerization for various SRC-II streams, a ratio of the aromatic hydrogen to total hydrogen was measured:

$$D_p = \frac{H_{ar}}{H_{ar} + H_{al}} \quad (1)$$

The aromatic hydrogen, H<sub>ar</sub>, is computed from the intensity of aromatic C-H stretching absorption band at 3030 cm<sup>-1</sup>, whereas the aliphatic and/or alicyclic hydrogen, H<sub>al</sub>, is based on the total intensities of C-H stretching bands between 2860 and 2960 cm<sup>-1</sup>.

The values of D<sub>p</sub> for various SRC-II process streams are plotted in Figure 4. A slight increase of D<sub>p</sub> in the dissolver effluent, as compared to feed slurry, suggests that feed slurry begins to lose alkyl groups and to polymerize in the dissolver. Consequently, marked increases of D<sub>p</sub> values occurred in atmospheric flash bottoms, vacuum tower bottoms, and solid cokes, compared to coal and feed slurry. These increases of D<sub>p</sub> value indicate further polymerization.

#### Petrographic Examination of SRC-II Process Streams

Scanning electron microscopy (SEM) technique has been used to study particle size, shape, and type of coal minerals existing in solid-coke samples from P-99 Runs. SEM provides a very effective method of examination of the organic and inorganic structural changes during coke formation in the SRC-II process.

Petrographic examination indicated that the hot-separator coke consisted of smaller size particles (average particle diameter ~1.40 μm) with lower anisotropic carbon (~76.7 vol%) than those in the dissolver coke particles (average particle diameter ~2.37 μm and 93.8 vol% of anisotropic carbon) (Table I). In addition, the vacuum tower bottoms has the largest size

particles (average particle diameter  $\sim 3.23 \mu\text{m}$ ), but it consists essentially of tar-like material ( $\sim 80.1 \text{ vol}\%$ ) and less anisotropic carbon ( $\sim 2.8 \text{ vol}\%$ ).

The optical micrographic studies (Figure 5 and 6) showed that pyrrhotites present in the coke-like solids are of relatively large particle size associated with carbonaceous organic anisotropic or isotropic carbon. In contrast, pyrrhotites existing in atmospheric tower bottoms and in vacuum tower bottoms are finely dispersed, small particles which apparently remain mobile and active during coal liquefaction.

A preheater outlet sample from the Ft. Lewis 50 ton/day pilot plant operated by Gulf was also examined petrographically to determine the degree of alteration of the coal in the preheating stage. This sample is composed primarily of vitrinite, inertinite, and mineral matter. The vitrinite appears as masses with bits of inertinite, mineral matter, and some exinite randomly disseminated throughout the matrix (Figure 7). This contrasts with vitrinite in raw coal which contains linearly oriented particles corresponding to the bedding layers of the coal seam. The vitrinite particles are rounded in preheater outlet samples rather than angular as in raw coal. These features suggest that in the preheater vitrinite has reached its plastic state, vitroplast, a phenomenon which occurs at about  $305^\circ\text{C}$  in most coals. Some of the vitroplast has formed mesophase which solidified to semicoke as shown in optical micrographs.

In addition, pyrite is the predominant inorganic constituent in the preheater samples. Some of the pyrite appears to be converted to pyrrhotite as the particles are cream-colored and less reflective, and they exhibit slight anisotropy. The fine dissemination of pyrite/pyrrhotite throughout the organic matrix suggests that it became dispersed while the coal was in its plastic state. Thus, fine distribution is significant with regard to ability to catalyze liquefaction reactions.

#### Coking Investigation by Pressure Differential Scanning Calorimeter/Thermogravimetric Techniques

Typical coal pressure DSC thermograms (Powhatan LR-24924 coal) are shown in Figure 8. Upon heating, the large coal aromatic-layer molecules absorb heat and soften, causing a broad endothermic peak below  $425^\circ\text{C}$  in the PDSC thermogram. At higher temperatures, these large coal molecules begin to condense and form a liquid crystal mesophase. This carbonaceous mesophase is only a transient existence in the temperature range where coal plastic properties are evident. As the temperature is increased, the mesophase materials begin to react with hydrogen and generate a distinct exothermic peak at the temperature range of  $450\text{--}475^\circ\text{C}$ . This peak is largely dependent on the hydrogen pressure. The exothermic heat evolution involves heat generated from the dehydration reactions of the coal phenolic, hydroxyl, and carbonyl functional groups. As the temperature continues to increase, a sharp endothermic peak comes out between  $475$  and  $500^\circ\text{C}$ , indicating a considerable excess energy required to overcome the coal-entangling structure between molecules; meanwhile, the condensed aromatic molecules begin to congeal to a semicoke. Consequently, at high temperature, if the unstable part of coal molecules continues polymerization, more gas is produced and a hardened coke is formed causing another dramatic exothermic curve in the PDSC thermograms.

The pressure effect on coking of feed slurry was also investigated at a heating rate of 20°C/min. Figure 9 demonstrates the influence of hydrogen pressure on thermal behavior of feed slurry. In thermograms of low-pressure runs (below 400 psi), a series of endothermic peaks occur at temperatures between 350 to 400°C because of the vaporization of lower molecular weight constituents in the feed slurry. In contrast, this phenomenon is suppressed under high pressures. A broad endothermic peak centered at about 450°C, which represents energy required to overcome the coal structure entangling and molecular polymerization during feed hydrogenation, was enhanced under higher hydrogen pressure. At higher reaction pressure, the amount of available hydrogen (molecular or dissolved) was higher, thus enhancing reactions.

A determination of volatile matter and fixed carbon after the measurement of pressure DSC indicated that a decrease of total amount of FC+VM<sub>H</sub> occurs as the operating hydrogen pressure increased (Figure 10).

Studies of the effect of operating temperature on coking of dissolver feed slurry indicated a minimum amount of FC+VM<sub>H</sub> occurred at ~440-455°C and a marked increase of FC+VM<sub>H</sub> occurred at 475°C (Figure 11).

Studies of the effect of residence time on coking of dissolver feed slurry indicated a minimum amount of FC+VM<sub>H</sub> occurred at 40-60 min reaction time when other conditions were similar to SRC-II reactor conditions (Figure 12).

#### Coal Feedstock Correlation on Coking

As described in a report<sup>2</sup> on Process Development Unit P-99 operations, coke in amounts ranging from small to significant have been found in the dissolver. The reason could partially be attributed to coal feedstock reactivity.

Fourteen P-99 dissolver cokes have been investigated to correlate coking tendency with their original coal feedstocks. Table II summarizes coke formation in the P-99 dissolver in conjunction with operating temperature, hydrogen partial pressure, total run time, and feedstock coal.

As can be seen in the table, the operating temperatures and hydrogen partial pressures were close in these runs. Beside equipment/operating problems, coal feedstock appears to be an important factor related to the dissolver coke formation. The effect of coal feedstock on the degree of polymerization (D<sub>p</sub>) and the amount of FC+VM<sub>H</sub> found in the dissolver coke is demonstrated in Figure 14.

In another attempt to correlate microprocess data with data from continuous bench-scale runs, experiments on three vacuum bottoms samples (from Cushman vacuum distillation) were conducted to measure their coking components (FC+VM<sub>H</sub>), and to measure the degree of polymerization. Coal feedstocks in these three runs were 100% Ireland coal, 50/50 Ireland-Blacksville mixture, and 100% Blacksville coal. The runs were made in the simulated SRC-II mode of operation, and a detailed description of experimental conditions can be found in a DOE report.<sup>3</sup> Figure 13 shows the relationship between the FC+VM<sub>H</sub> values in the coal feedstocks and in the heavy products (Cushman bottoms). The

highly refractory Blacksville coal, either by itself or in mixture, produced a higher content of coking components ( $FC+VM_H$ ) and a higher degree of polymerization (Figure 13, curve d) in the corresponding Cushman bottoms. These observations are in good agreement with the yield of IOM and the hydrogen consumption in the continuous bench-scale runs (Figure 13, curves a and c). In general, the higher the amount of  $FC+VM_H$  presented in coal feedstock, the higher the tendency to form coke during coal liquefaction.

#### Summary

A summary of major results from this work is described below:

1. The amount of fixed carbon plus heavy volatile matter ( $FC+VM_H$ ) as a composition parameter measured by the thermogravimetric determination appears to give a good correlation with the coking characteristics of various SRC-II process streams. The higher the fixed carbon plus heavy volatile matter, the higher the coking tendency exists.
2. The degree of polymerization ( $D_p$ ) measured by FT-infrared showed marked increases of  $D_p$  values in atmospheric flash bottoms, vacuum tower bottoms, and solid coke samples, compared to the original coal feedstock and feed slurry.
3. Petrographic examination of SRC-II process streams by scanning electron/optical microscopy showed that a predominance of anisotropic carbon was observed in the dissolver and the hot-separator coke, indicating the coking of reactive organic constituents during coal liquefaction reactions. In contrast, a large percentage of tar-like material was found in vacuum tower bottoms and in atmospheric flash bottoms.
4. Coke formation in SRC-II streams is highly dependent on process parameters such as coal feedstock, operating temperature, residence time, hydrogen partial pressure, and heating rate. Increasing hydrogen pressure results in decreasing dissolver feed slurry coking; however, the minimum coke formation exists under certain ranges of operating temperature ( $\sim 850^\circ F$ ), and residence time (50-60 min). This temperature and time corresponds to SRC-II reactor conditions that are "normal" for processing reactive bituminous coals.
5. High concentrations of finely dispersed pyrrhotite were found to be present in atmospheric flash bottoms and vacuum tower bottoms, confirming the advantage of recycling bottoms slurry stream to SRC-II reactors.

#### References

1. C. S. Wen, "Solvent Refined Coal (SRC) Process: Coking of SRC-II Process Stream. Part I and II," September 1981, Report No. DOE/ET/10104-21.
2. H. G. McIlvried and W. Gall, "Experience with Solid Deposits in SRC-II Process Development Unit P-99, Runs P99-11 to P99-76," March 1982, Report No. DOE/ET/10104-32.
3. M. E. Prudich, "SRC-II Feedstock Screening Methods," September 1981, Report No. DOE/ET/10104-31.

Table I: PETROGRAPHIC EXAMINATION OF SRC-II STREAMS

<u>Type</u>	<u>Hot Separator Coke (P99-66-8)</u>	<u>Dissolver Bottom Coke (P99-66-8)</u>	<u>Vacuum Tower Bottoms (P99-63-8)</u>	<u>Atmospheric Flash Bottoms (P99-63-2)</u>
Average Particle Diameter, $\mu\text{M}$	1.40	2.37	3.23	--
Anisotropic Carbon (vol %)	76.7	93.8	2.8	2.0
Isotropic Carbon (vol %)	1.7	0.6	0.1	0.2
Vitrinite (vol %)	7.6	0.5	8.5	1.8
Fusinite + Semifusinite (vol %)	2.7	0.2	3.0	2.1
Micrinite (vol %)	0.5	0.3	0.6	0.0
Tar-like Material (vol %)	1.5	0.2	80.1	92.1
Reflectance (%)	1.06-3.00	~2.4	1.4-2.4	~2.2

Table II: COKES OF PDU P-99 DISSOLVER\*

<u>P-99 Run No.</u>	<u>Coal</u>	<u>Dissolver Average Temp.</u>	<u>H<sub>2</sub> Partial Pressure at Dissolver Outlet</u>	<u>Run Time</u>	<u>Amount of Coke (%Vol of Dissolver)</u>	<u>Coke FC+VM<sub>H</sub></u>	<u>Coke Dp</u>
29 Dissolver Top	Blacksville II-2	860°F	--	37 days	25 vol%	79.6 wt%	0.49
29 Dissolver Btm						86.3	0.49
39 Dissolver Top	Valley Camp	851	1308 psia	47	5	76.3	0.90
39 Dissolver Btm						84.1	0.92
48 Dissolver Top	Powhatan No. 5 (2nd Shipment)	860	1285	42	5	68.4	0.28
48 Dissolver Btm						63.7	0.29
52 Dissolver Btm	Powhatan No. 5 (3rd Shipment)	855	1298	62	3	74.0	0.26
64 Dissolver Top	Powhatan No. 5 (4th Shipment)	849	1525	20	12% (Top)	70.3	0.53
64 Dissolver Btm					4% (Btm)	74.6	0.55
66 Dissolver Top	Powhatan No.5 (4th Shipment)	855	1510	29	12.5 (Top)	77.0	0.49
66 Dissolver Btm					25 (Btm)	79.8	0.80
79 Dissolver Btm	Ireland Mine	856	--	40	2	73.0	0.28
83 Dissolver Top	Powhatan No. 6	845	--	55	1.4 (Top)	61.2	0.56
83 Dissolver Btm					3.4 (Btm)	70.3	0.52

\* Information from Reference 2.

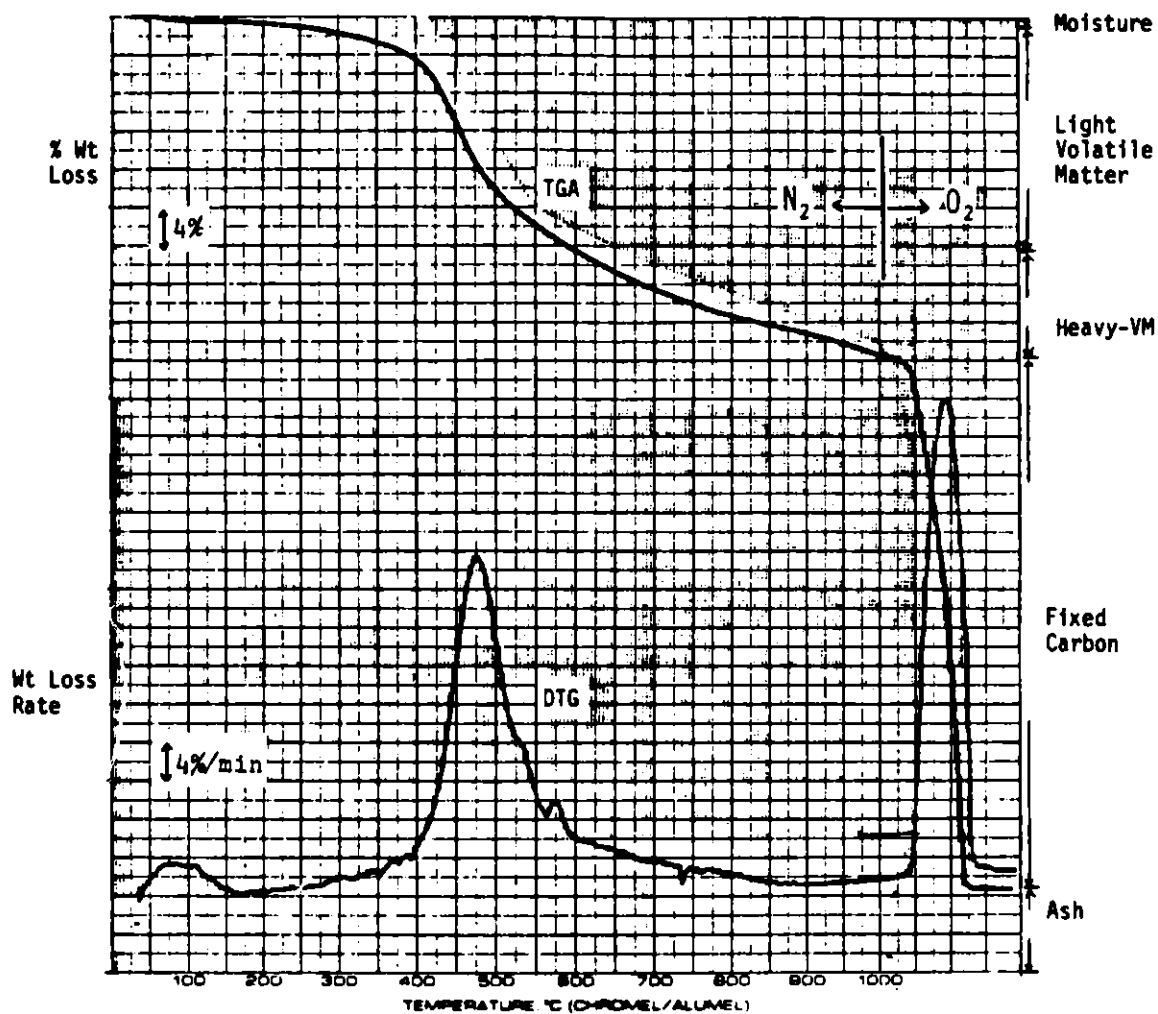
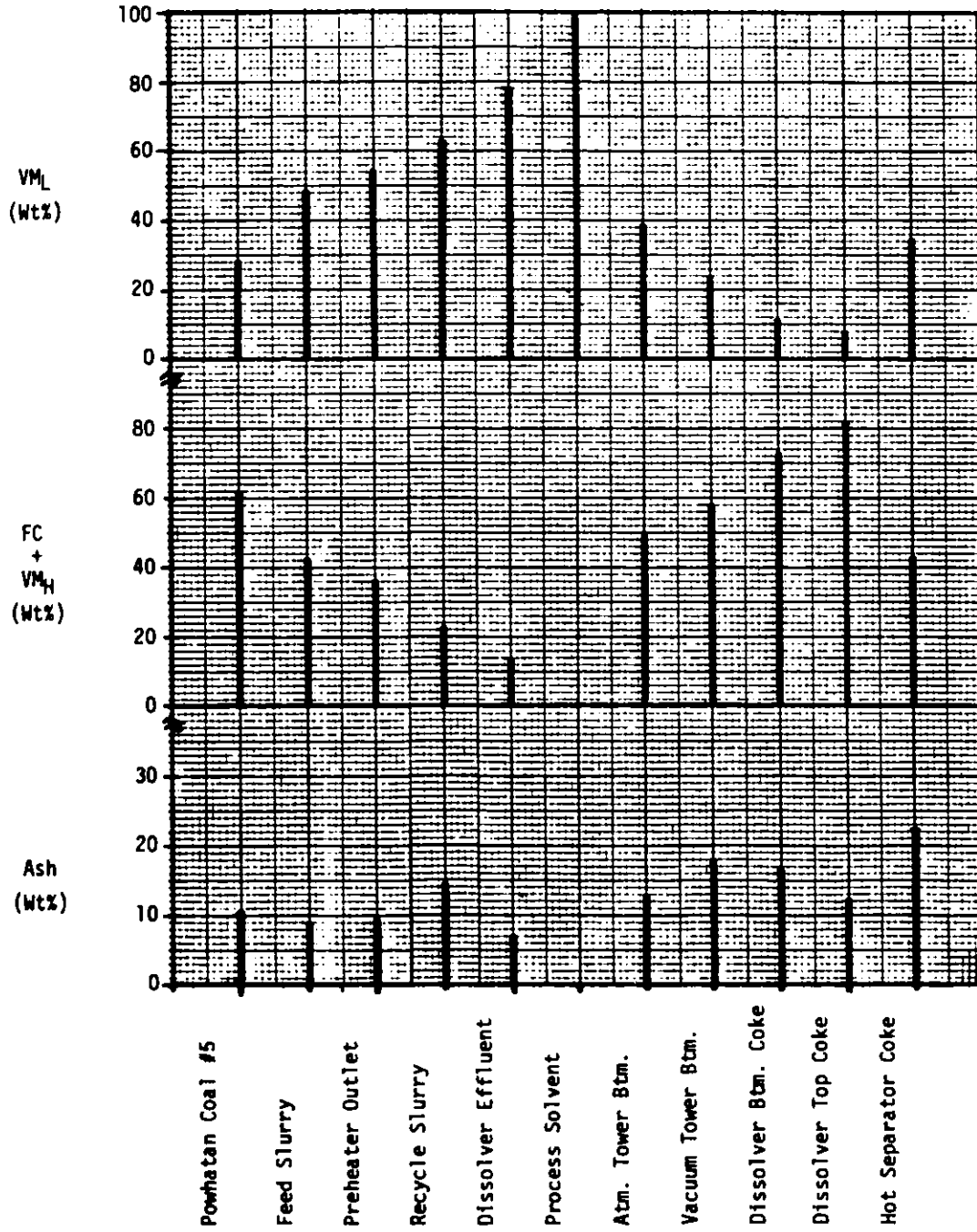


Figure 1. TGA and DTG thermograms of Powhatan coal (LR 24924).

(Coking Ability Measurement by Thermogravimetric Technique)

Figure 2. THERMAL COMPOSITION PROPERTIES OF SRC-II PROCESS STREAMS





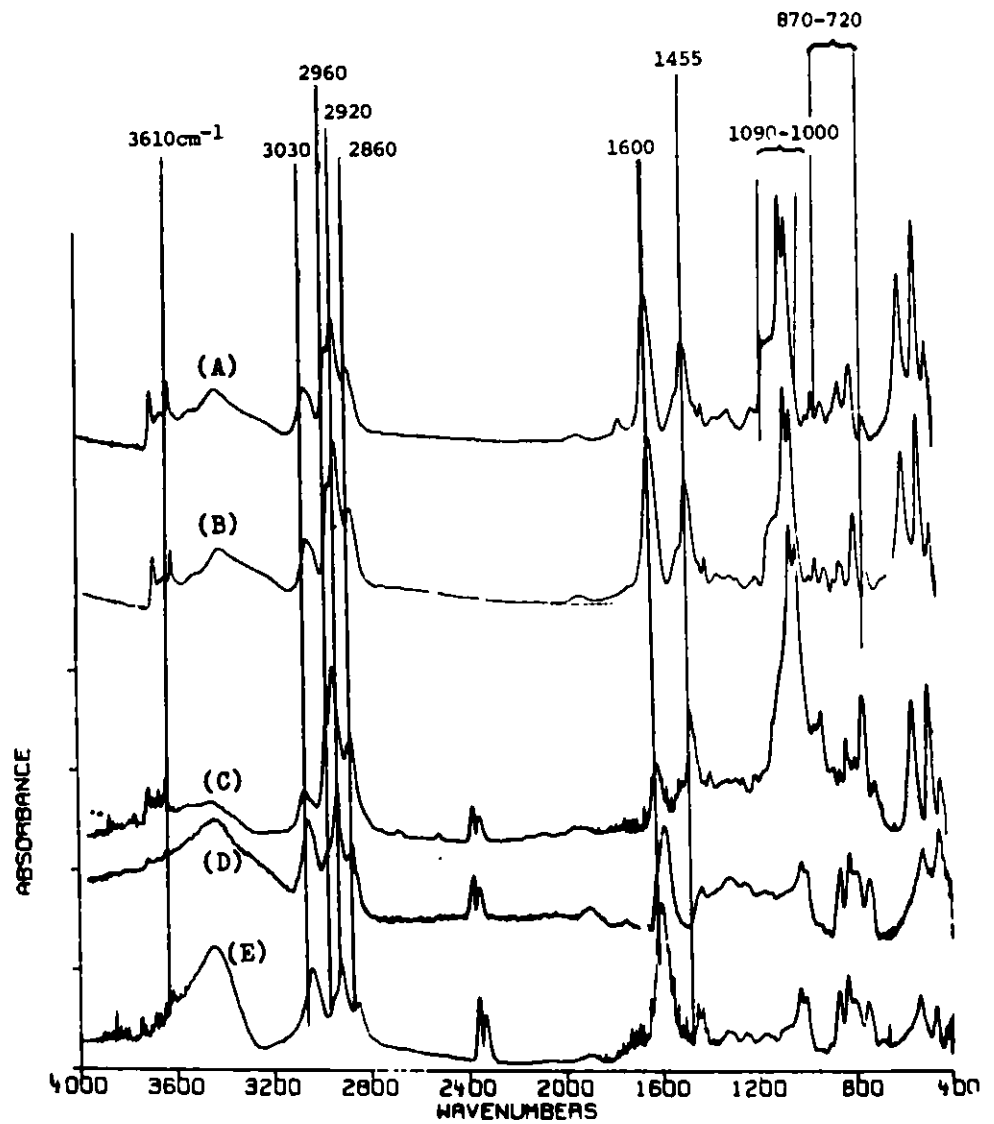


Figure 3. FT-infrared spectra of (A) vacuum tower bottoms, (B) atmospheric flash bottoms, (C) hot-separator coke, (D) dissolver-top coke, and (E) dissolver-bottom coke.

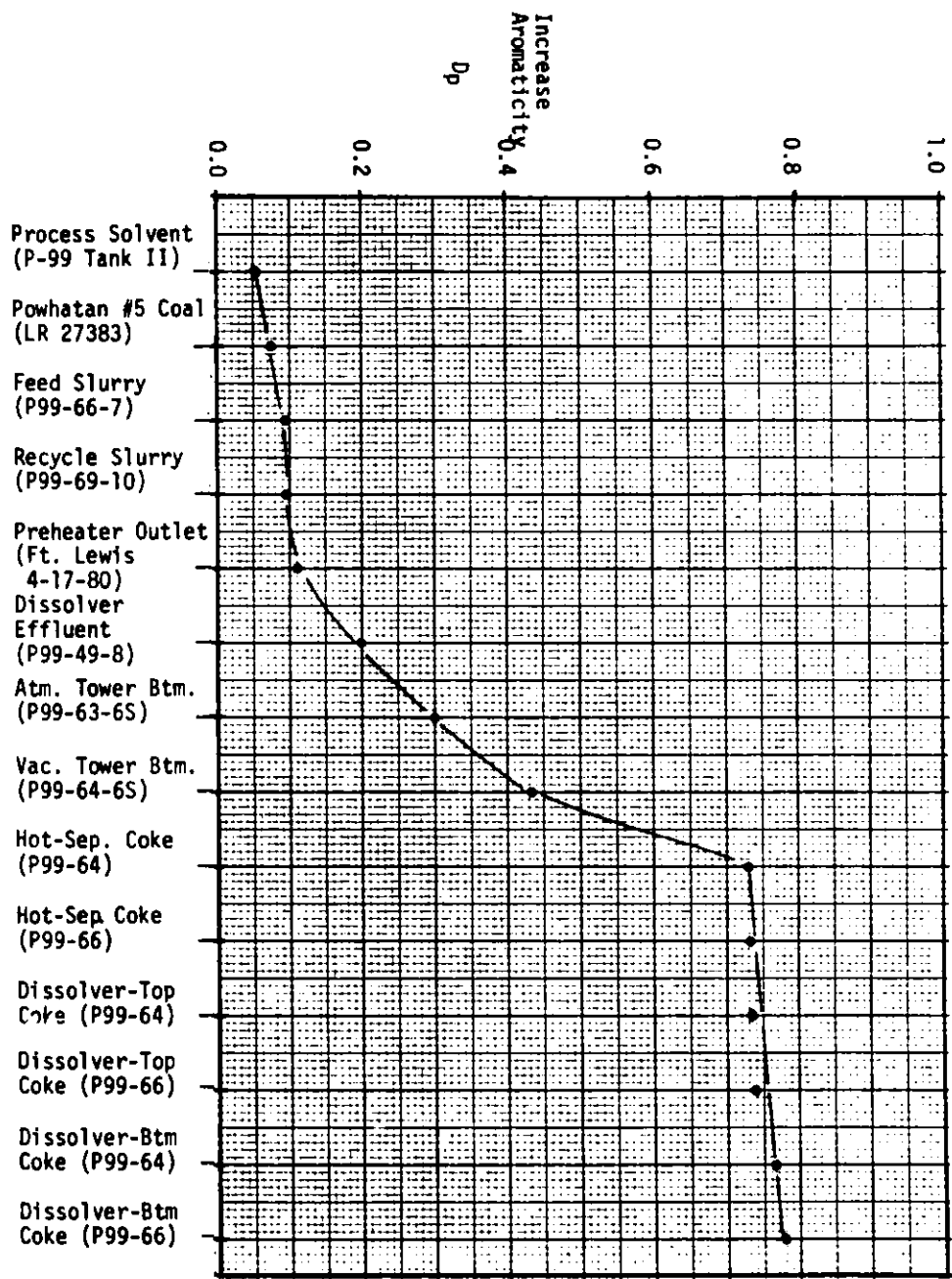
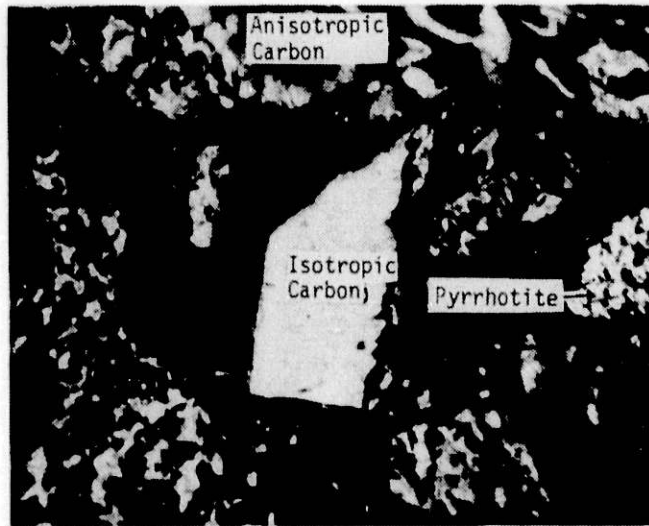


Figure 4. Degree of polymerization ( $D_p$ ) for various SRC-II process streams (Stream samples prepared for pyridine insoluble, except coal, feed slurry, process solvent, recycle slurry, and dissolver effluent)



Hot-Separator Coke  
(P99-66)

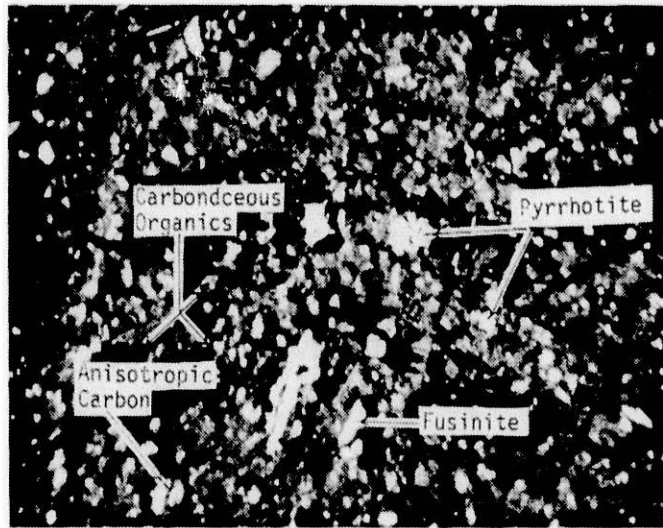
20 $\mu$



Dissolver Btm. Coke  
(P99-66)

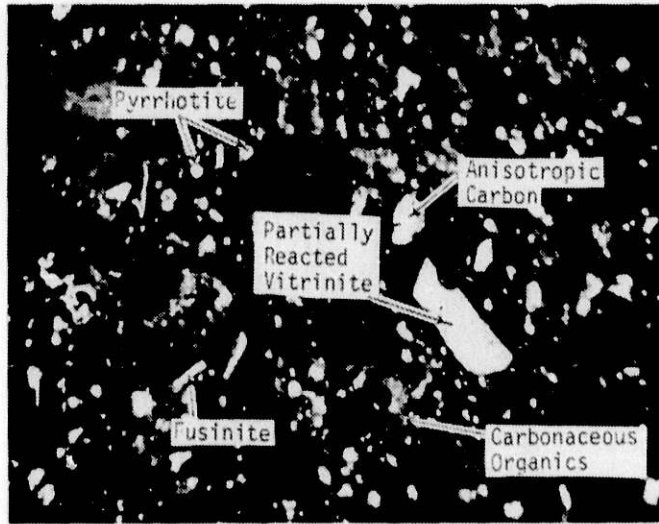
20 $\mu$

Figure 5. Optical micrographic analysis of hot-separator and dissolver bottom cokes.



Vacuum--Tower  
Bottoms  
(P99-64-5S)

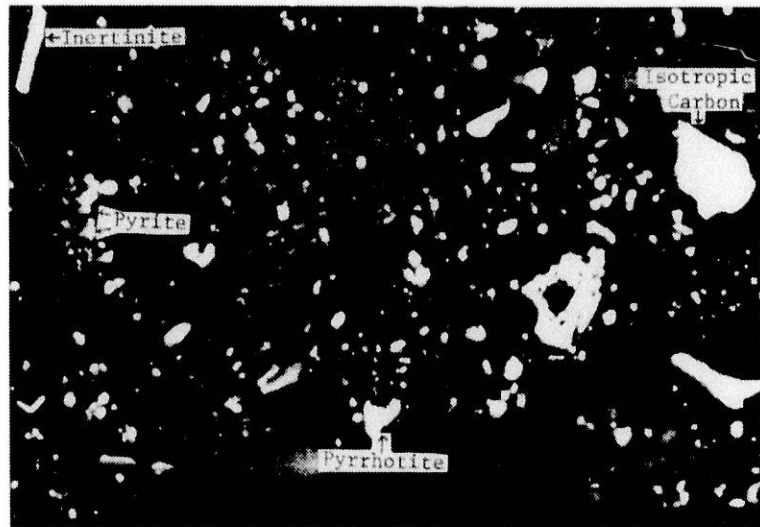
20μ



Flash-Tower  
Bottoms  
(P99-63-5S)

20μ

Figure 6. Optical micrographic analysis of vacuum tower bottoms and atmospheric tower bottoms.



62.5 μ

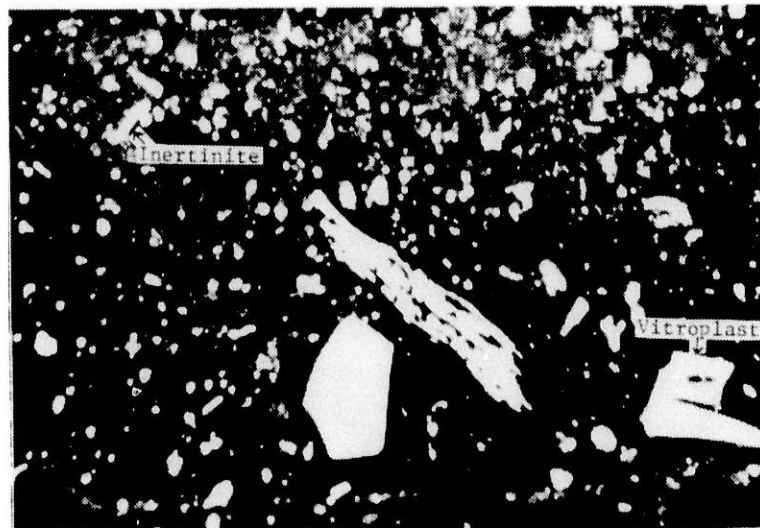
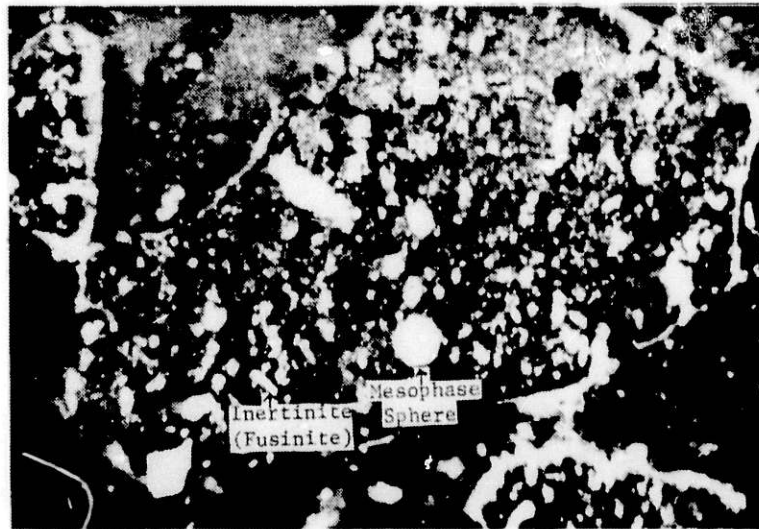


Figure 7-I, OPTICAL MICROGRAPHIC ANALYSIS OF FT. LEWIS PREHEATER OUTLET SAMPLE.



62.5  $\mu$

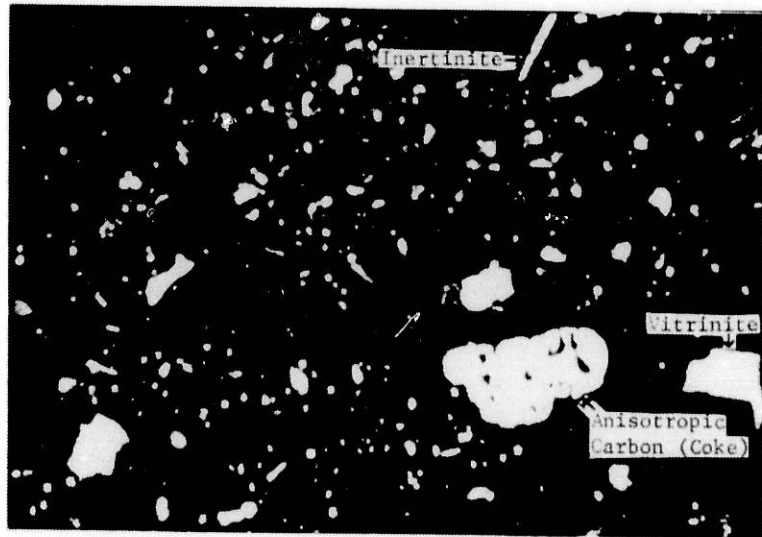


Figure 7-11, OPTICAL MICROGRAPHIC ANALYSIS OF FT. LEWIS PREHEATER OUTLET SAMPLE.

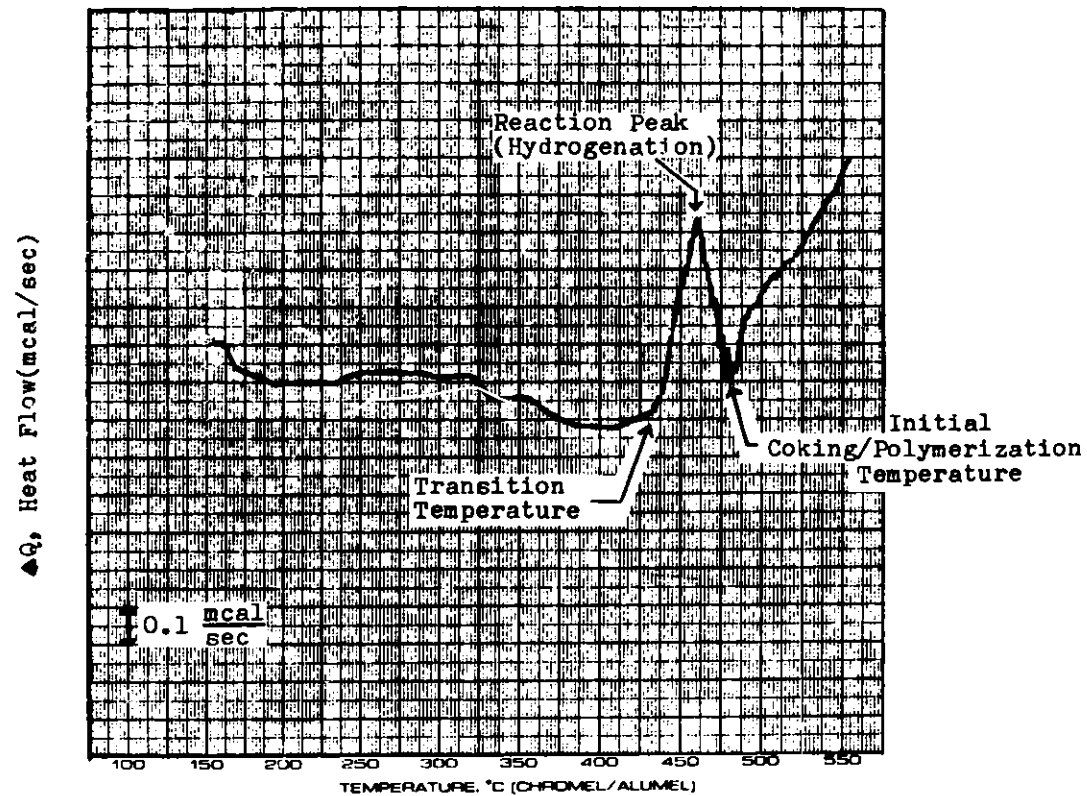


Figure 8. Pressure-DSC thermogram of Powhatan coal (LR 24924) under 900 psi H<sub>2</sub> and 20°C/min.

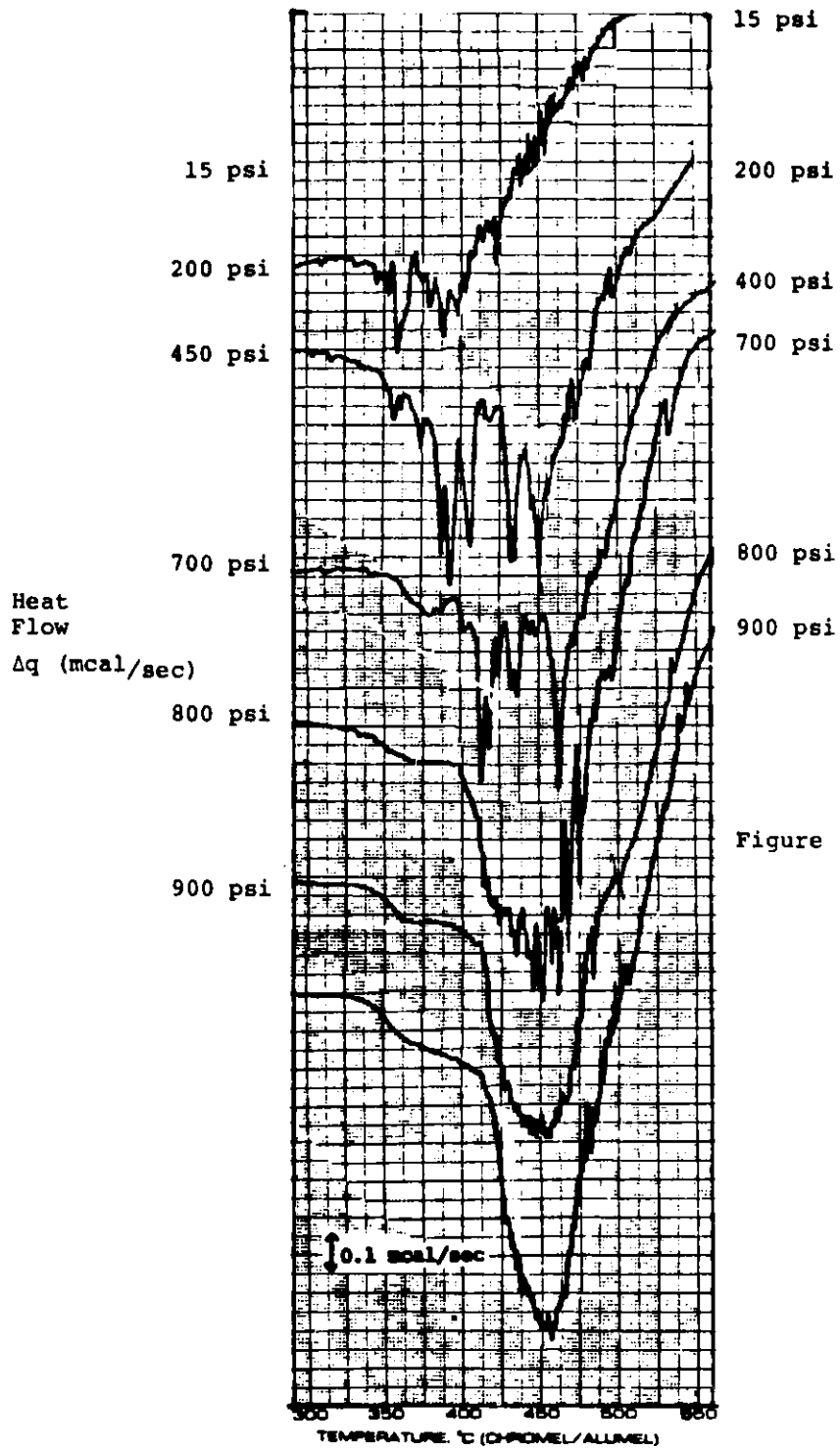


Figure 9. Hydrogen pressure effect on thermal behavior of feed slurry (P99-67-11) (PDSC = 20°C/min)



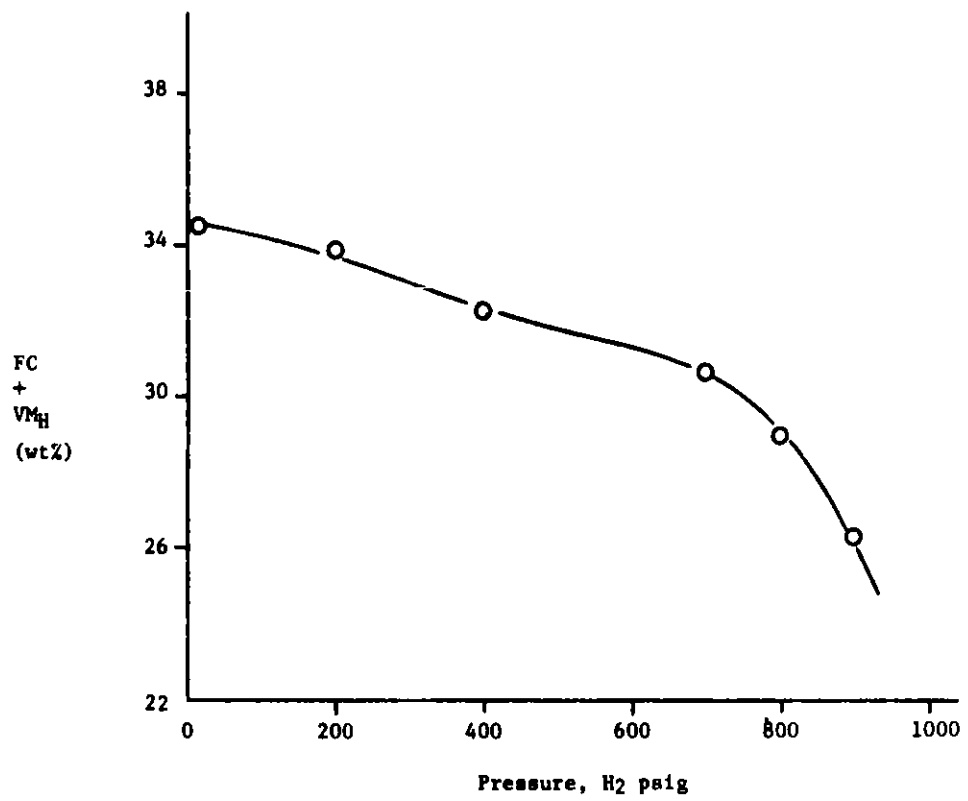


Figure 10. EFFECT OF HYDROGEN PRESSURE ON YIELDS OF FC+VM<sub>H</sub> (fixed carbon plus heavy volatile matter) USING FEED SLURRY (P99-67-11) DETERMINED BY PDSC/TGA RUNS.

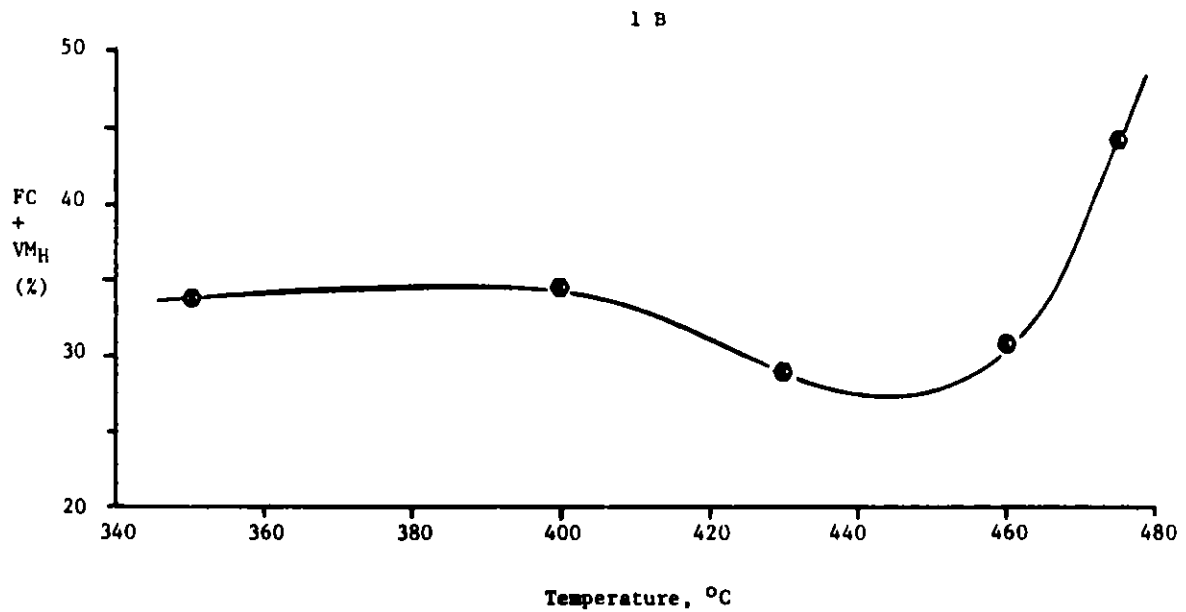
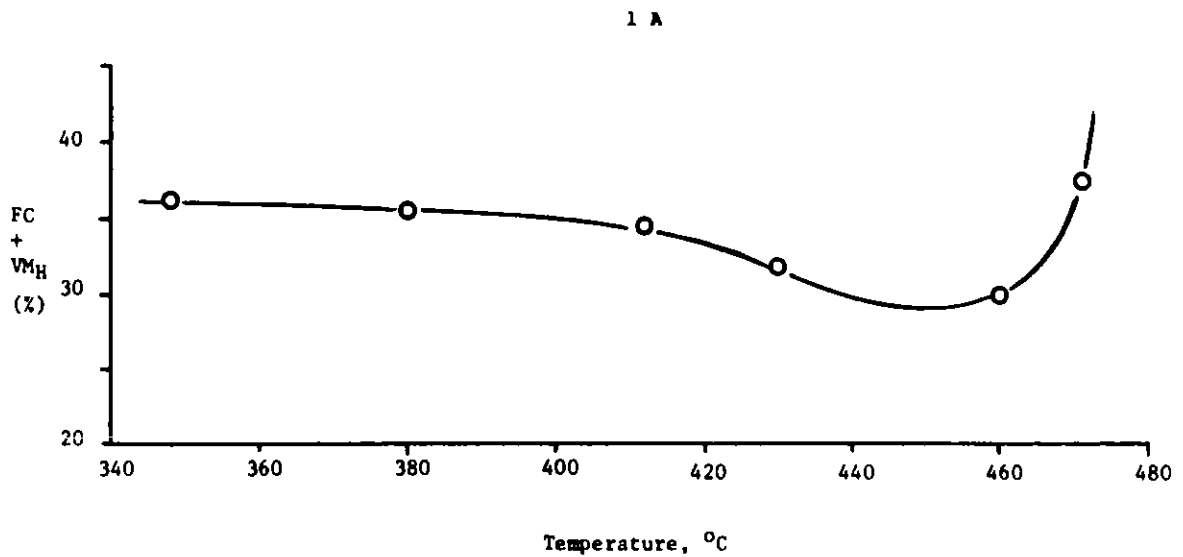


Figure 11. EFFECT OF OPERATING TEMPERATURE ON THE YIELDS OF FC+VM<sub>H</sub> (fixed carbon plus heavy volatile matter) where o: PDSC/TGA runs using feed slurry (P99-50-3S)

●: Autoclave runs using feed slurry (P99-64-8S)

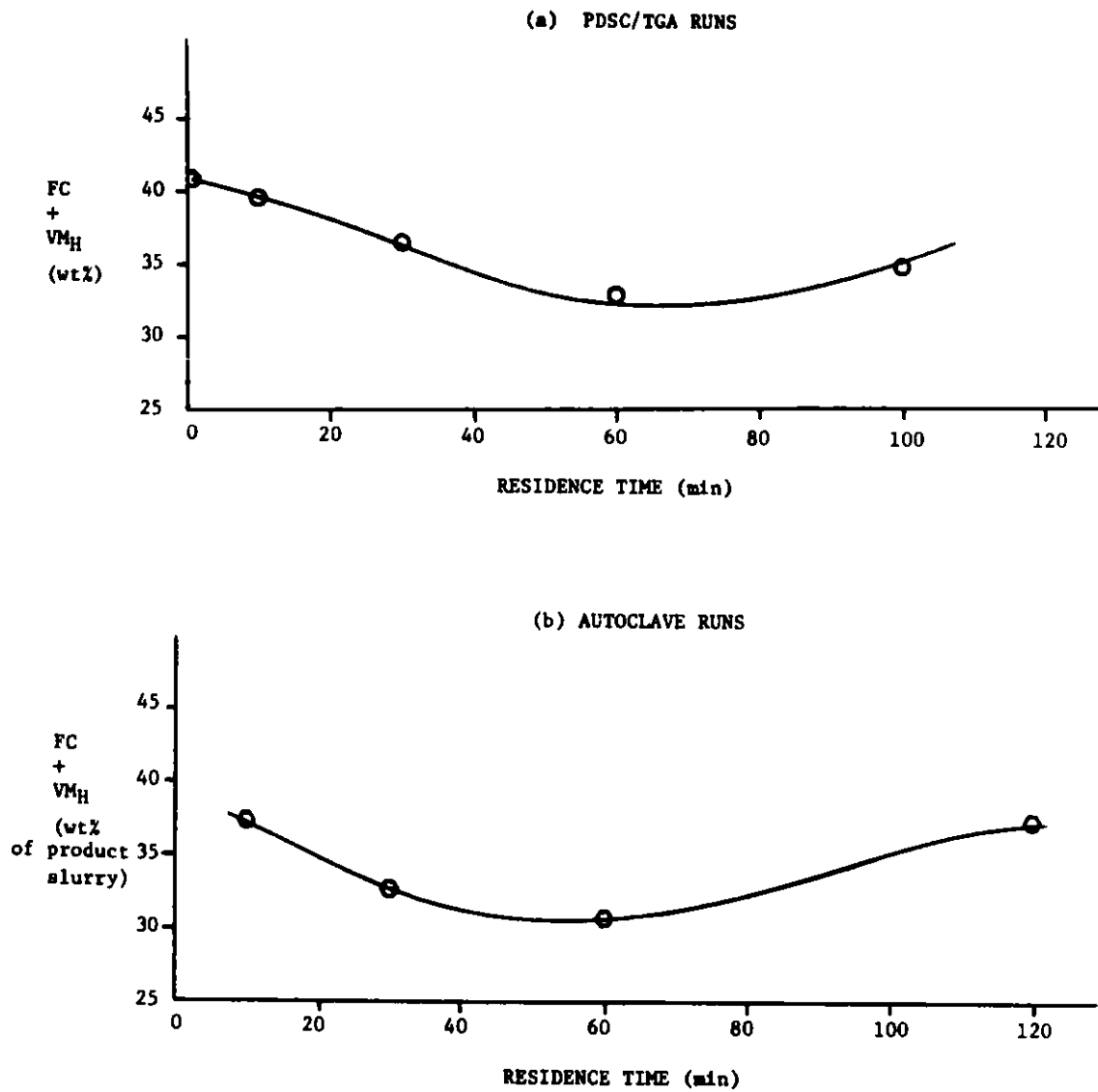


Figure 12. EFFECT OF RESIDENCE TIME ON THE YIELD OF FC+VM<sub>H</sub> (fixed carbon plus heavy volatile matter) where ○: PDSC/TGA runs at 460°C and 900 psig H<sub>2</sub>.  
 ●: Autoclave runs at 460°C and 1800 psig H<sub>2</sub>.

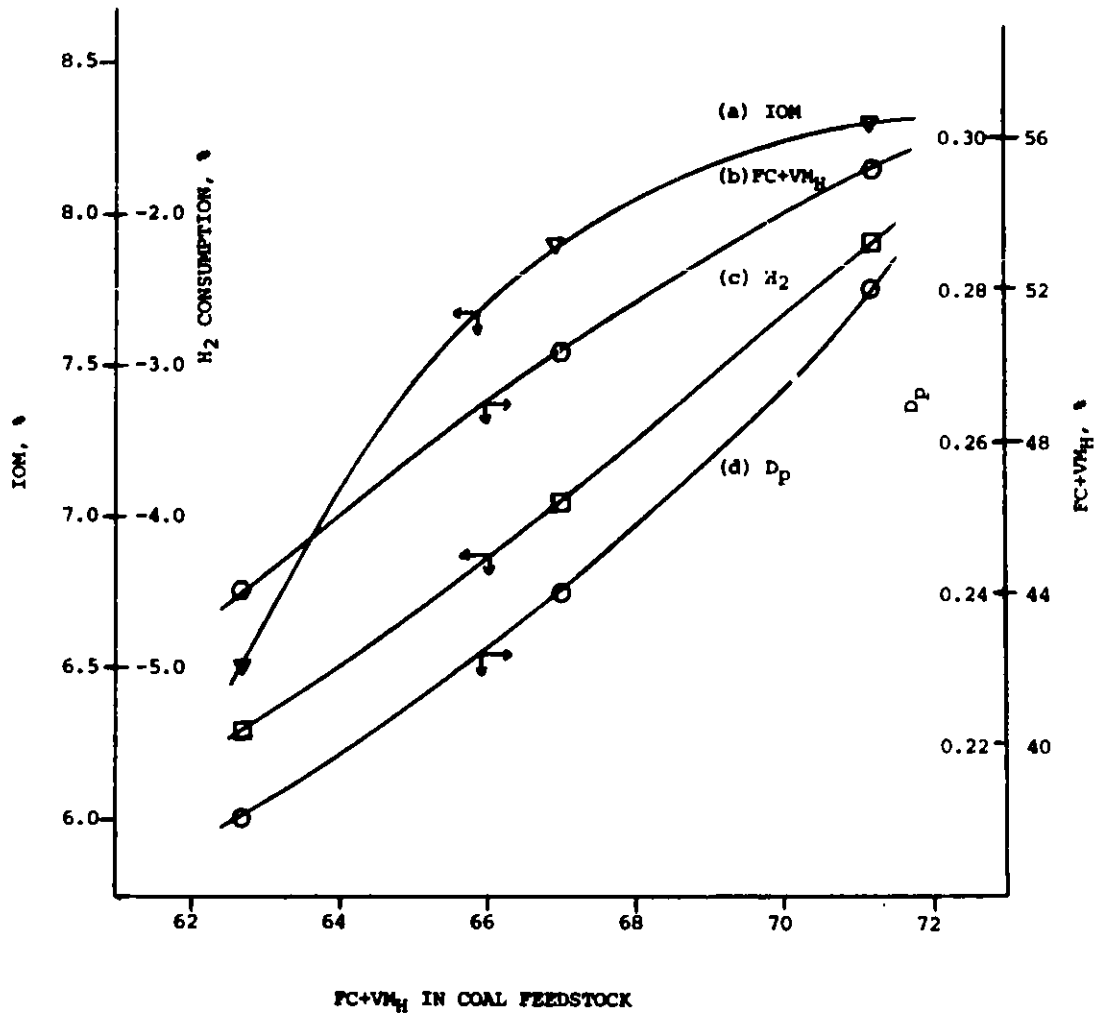


Figure 13. CORRELATION OF MICROPROCESS PDSC/TGA DATA WITH COAL FEEDSTOCK WHERE IOM (curve a) AND H<sub>2</sub> CONSUMPTION (curve c) ARE TAKEN FROM A-1 UNIT EXPERIMENTS, AND FC+VM<sub>H</sub> (curve b) AND D<sub>p</sub> (degree of polymerization, curve d) ARE TAKEN FROM PDSC/TGA DATA.

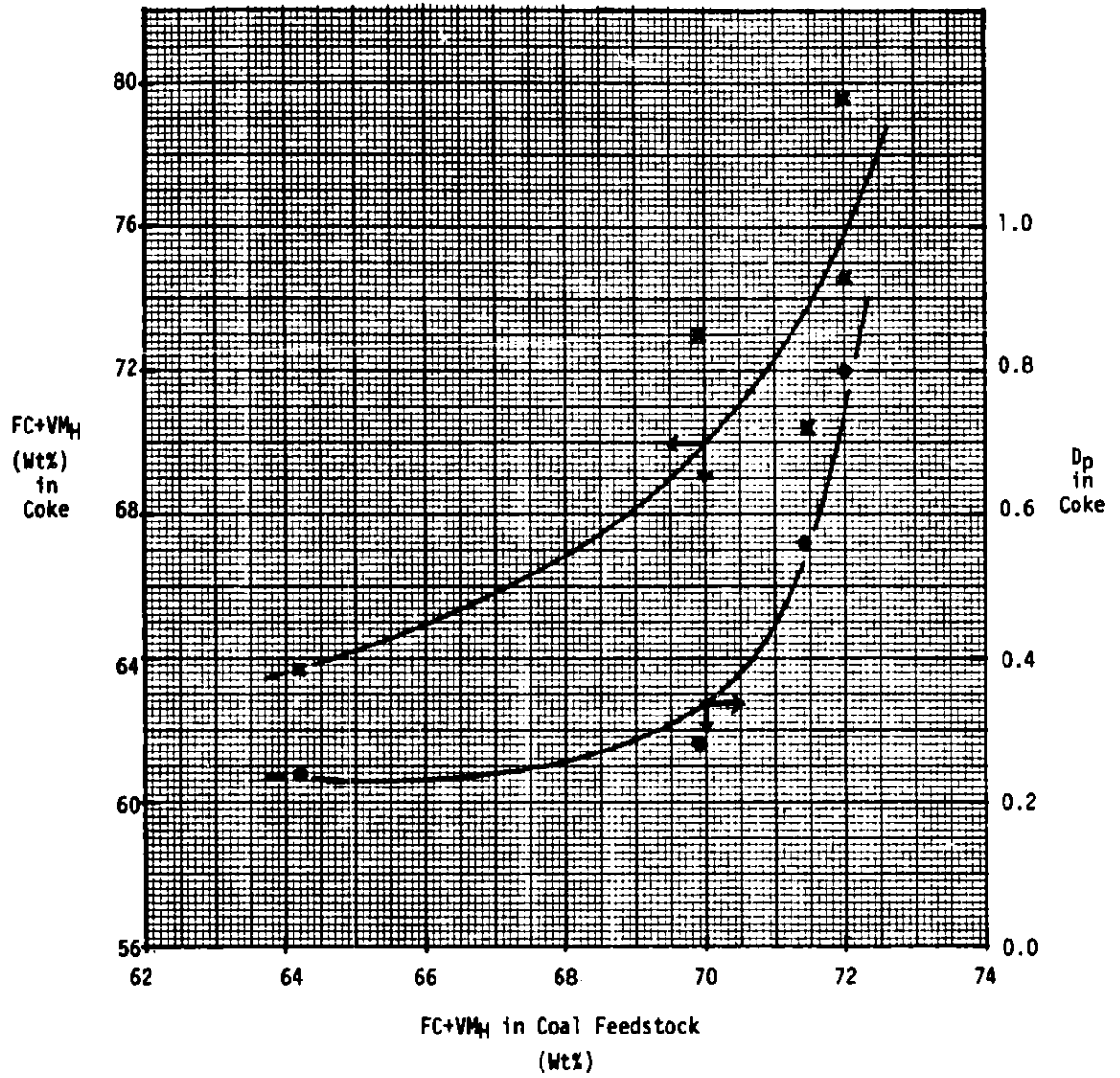


Figure 14. Effect of coal feedstock on amount of FC+VM<sub>H</sub> and D<sub>p</sub> values of P-99 dissolver coke samples

FACTORS AFFECTING THE ADHESION OF COAL PARTICLES TO OIL-COATED AIR BUBBLES

Latif A. Khan and Carl W. Kruse  
Illinois State Geological Survey  
615 East Peabody Drive  
Champaign, IL 61820  
217/344-1481

Introduction

The commercial methods for cleaning coarse coal depend upon differences in the specific gravity of coal and the gangue. The effectiveness of these gravity methods decreases as particle sizes decrease. When the diameter of the particles is a few hundred microns or less, differences in the surface properties of coal and gangue become the dominant factor for effective cleaning. Flotation and oil agglomeration are the two cleaning methods most frequently mentioned for fine coal processing. Both these processes utilize the differences in surface properties of the feed constituents for separation of combustibles from the mineral matter.

In oil agglomeration, the selective wetting of coal by a sufficient quantity of a liquid petroleum product, such as gasoline, kerosene, or fuel oil, is used to selectively agglomerate the fine coal particles into a mass large enough to stay suspended on a screen that allows the fine gangue particles to pass through<sup>1</sup>. An oil which is efficient with respect to selective wetting of coal is not necessarily the best for producing a strong agglomerate. It may be better to collect the coal with lighter oils and then use heavier oils to complete the formation of a structure strong enough for screening. On the microscopic level, this process involves a collection step in which a coal/water interface and an oil/water interface are partly replaced by a coal/oil interface.

The efficiency of the collecting process can be increased with respect to the amount of oil needed if the oil is dispersed in water before contacting it with the coal<sup>2,3</sup>. If the blending of oil and water is vigorous, an emulsion results having a larger volume than that of the components. This increase in volume is caused by the entrapment of air. The coated air bubbles that are formed exhibit the surface properties of oil globules but they are much lighter, and consequently they rise and cream out when the emulsion is left to settle. When this oil/water emulsion is mixed with a coal-water slurry, the coal particles collect on the coating around the air bubbles and are buoyed to the surface where they can be removed by skimming. In this case, the separation takes place in a relatively quiescent zone compared to a flotation cell with constant aeration.

Successful collection of coal by the pregenerated emulsion (or foam) requires first that coal particles be brought into contact with oil surfaces around the air bubbles and secondly that the coal particles attach to these surfaces. The frequency of collisions between the oil and coal particles is determined among other factors by the number of coal particles, the number of air bubbles, and the distance between them<sup>4</sup>. The present paper examines in detail the phenomenon of coal particles collecting on oil as well as some of the relationships that affect this adhesion.

### Materials

The feed coal was prepared by grinding a sample from the Herrin (No. 6) Coal Member from Macoupin County, Illinois, in a ball mill. The distribution of the particle sizes after grinding is given in table 1. A regular grade of gasoline, samples A and B, and a kerosene sample, K, were obtained from local fuel vendors at different times. Sample A was stripped of a portion of its higher volatile components to produce a residual fraction designated AH. Sample B was partially distilled to obtain a fraction of the more volatile components, designated BL, and a residue designated BH. Deionized water was used unless otherwise specified.

Table 1: Particle-size distribution of the feed.

Particle size		Finer cumulative	Particle size		Finer cumulative
$\mu$	wt%	wt%	$\mu$	wt%	wt%
88-176	3.4	100	11-16	10.8	53.6
62-88	3.9	96.6	7.8-11	10.1	42.8
44-62	7.0	92.7	5.5-7.8	8.3	32.7
31-44	9.2	85.7	3.9-5.5	9.4	24.4
22-31	12.1	76.5	2.8-3.9	7.4	15.0
16-22	10.8	64.4	2.8	7.6	7.6

### Experimental Procedure

#### Coal-Collection Experiments

Ten grams of coal was slurried in 300 ml of water and left to soak for three hours. One ml of oil was mixed with 300 ml of water for 30 seconds in a malted-milk mixer and the resulting oil-water emulsion was added without delay to the coal-water slurry. The coal slurry and the emulsion of oil-in-water were gently mixed for 30 seconds with a hand-held electric mixer. This mixture was then washed into a separating device (fig. 1). On resolution, the floating coal was separated by making a cut three inches below the floating mass. Solids in the float and the sink were separated by filtration, dried, and analyzed.

The separating device consists of two glass cylinders 18 in. long by 2 in. I.D., which were separated by a plastic ball valve. The assembly is mounted in a tiltable frame. The lower cylinder is fitted with an expandable rubber stopper which can be moved to any position in the lower cylinder. This arrangement enables the operator to make a cut at any desired level.

#### Interfacial Tension Measurement

The interfacial tensions were measured in a Fisher surface tensiometer using the standard procedure.

#### Contact-Angle Measurements

A plug of coal prepared for the contact-angle measurements was mounted in a rubber stopper and suspended in an aqueous phase for conditioning. Oil

was introduced from the side of the container with a hypodermic needle. Oil droplets of the same oil on different plugs were photographed to determine an average contact angle.

### Results and Discussion

The surface of a coal particle in a coal-water slurry and that of an oil globule or oil-coated air bubble in an oil-water emulsion are in contact only with water. When the coal particle contacts and adheres to the oil globule, water is displaced from the area of contact on the coal particle and also on the oil globule. A new interfacial area between the coal and oil is generated. These changes in the interfacial areas alter the surface free energy of the system. If  $\underline{A}$  is the area of contact between the oil and coal particle (fig. 2), then the interfacial area between the oil/coal will increase by  $\underline{A}$ , whereas the interfacial area between oil/water and coal/water will decrease by the same amount. If  $\gamma_{oc}$ ,  $\gamma_{ow}$  and  $\gamma_{cw}$  are the interfacial free energies per unit of the three interfaces, respectively, the total change in the surface free energy, due to adhesional wetting, is given by the Dupre equation (1).

$$-\Delta G_w = \underline{A} (\gamma_{ow} + \gamma_{cw} - \gamma_{oc}). \quad (1)$$

The wetting force,  $W_a$ , due to the net changes in the interfacial tension is defined by equation 2.

$$W_a = \gamma_{ow} + \gamma_{cw} - \gamma_{oc} \quad (2)$$

The oil/water interfacial tension,  $\gamma_{ow}$ , can be measured directly whereas the interfacial tensions of the solid-liquid interfaces,  $\gamma_{cw}$  and  $\gamma_{oc}$ , cannot be. Contact angles are used to determine the difference between  $\gamma_{cw}$  and  $\gamma_{oc}$ .

For the contact angle  $\theta$  between the oil and the coal (fig. 3), we may write

$$\gamma_{ow} \cos\theta = \gamma_{cw} - \gamma_{oc}. \quad (\text{Young's equation}) \quad (3)$$

Substitute  $\gamma_{ow} \cos\theta$  for  $\gamma_{cw} - \gamma_{oc}$  in the wetting force equation 2.

$$W_a = \gamma_{ow} + \gamma_{ow} \cos\theta = \gamma_{ow} (1 + \cos\theta) \quad (4)$$

From equation 2,  $W_a$  is seen to increase with an increase in  $\gamma_{ow}$  and  $\gamma_{cw}$ .  $W_a$  also increases if  $\gamma_{oc}$  decreases<sup>5</sup>. A change in the interfacial tension is caused by the change in the molecular interaction energy across the interface between the phases. The larger the resulting attraction or the larger the affinity between the phases, the smaller is the interfacial tension (fig. 4).  $W_a$  is a measure of the work required to separate a unit area of oil from the surface of the coal. An increase in  $W_a$  indicates a stronger bond between the oil and coal particle. An increased recovery of the combustible is to be expected when  $W_a$  increases provided other conditions such as the pulp density, the ratio of oil to coal, the mixing time, the mixing intensity, and the temperature remain constant. Table 2 shows the



changes in the wetting force  $W_a$  and in the recovery of combustibles achieved with different oils.

Table 2: Recovery of combustibles and interfacial properties as a function of oil types.

Hydrocarbon oil	Contact angle $\theta$	$1 + \cos\theta$	$\gamma_{ow}$ dynes/cm	$W_a$ dynes/cm	Recovery % of total
K	132	0.33	12.87	3.77	33.2
BL	120	0.5	15.04	7.52	53.2
BH	98	0.861	11.64	10.02	71.6
AH	90	1.0	10.05	10.05	72.5

Combustible recovery varies with use of different oils (table 2). Because experimental conditions were kept constant, the differences in recovery are believed to reflect only the differences in oil properties. A change in surface characteristics of any one of the three phases affects two of the three interfacial tensions. Therefore, a change in  $W_a$  can result from simultaneous changes in the two interfacial tensions that have oil on one side of the interface,  $\gamma_{ow}$  and  $\gamma_{oc}$  (equation 2). The interfacial tensions between the different oils and water were measured directly whereas the  $\gamma_{oc}$ , determined indirectly through the contact angle, decreases as the recovery of combustibles increases; however, neither the angle nor its cosine have a linear relationship with the percentage of combustibles recovered. A decreasing angle is indicative of a progression of increased affinity of the oil for coal.

A ranking of oils in order of decreasing contact angles would, for the set of oils studied, place them in an order of their increasing effectiveness; but the nonlinear way in which a change in oil type affects the two interfacial tensions suggests the need to measure both  $\gamma_{ow}$  and the contact angle  $\theta$  for prediction of oil performance. The recovery of combustibles correlates well with the wetting force,  $W_a$  (table 2). These results suggest that the measurement of interfacial tension and contact angle of an oil and coal submerged in water may be used to predict its processing behavior.

This adhesion model can be used also as a tool in forecasting the effect of an induced change in any of three interfacial energies and its subsequent influence on  $W_a$  or the recovery of combustibles.

### Conclusions

The driving force of adhesional wetting,  $W_a$ , correlates well with the collection capability of the oils tested for the recovery of combustibles from raw fine coal under controlled conditions. These data and the success of this experimental work encourage optimism that additional work will lead to the development of a good prognostic tool for estimating the effects of other variables affecting interfacial tensions and the recovery of

combustibles. One of the most important variables to pursue in the next phase of the work will be the modification of the solid surface and development of proper technique for measuring  $W_a$  under those conditions.

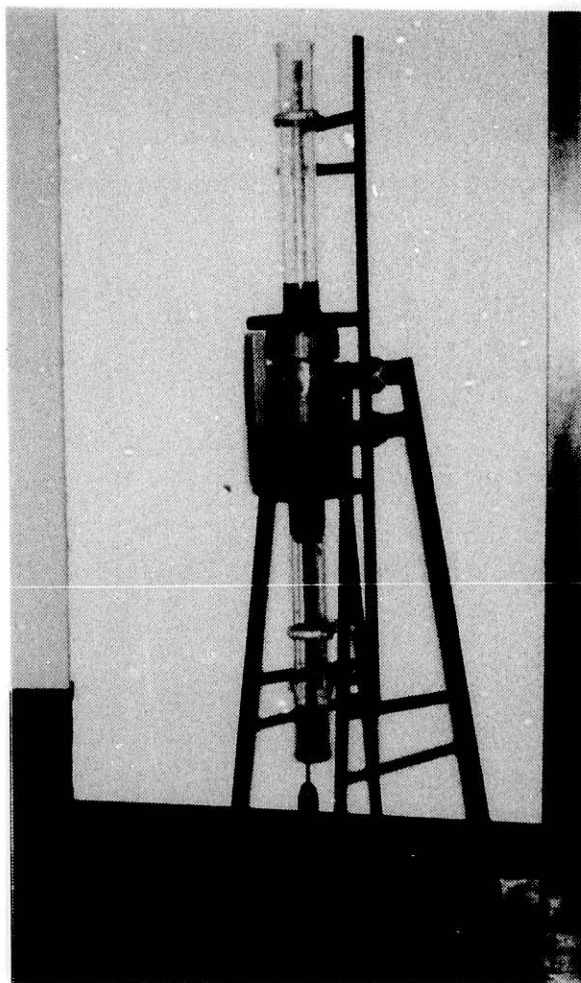
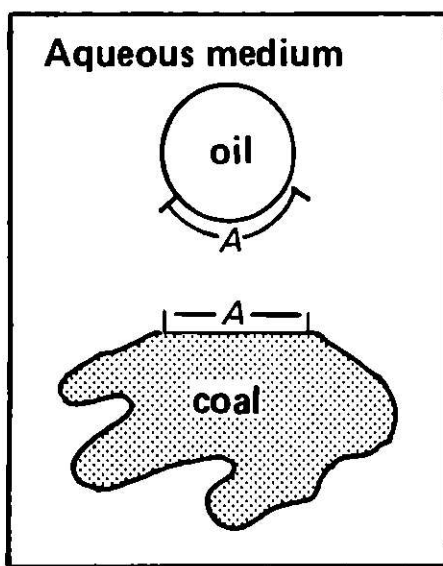
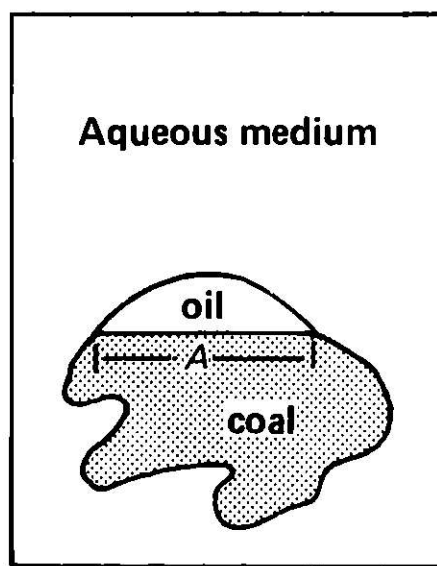


Figure 1. Separating device.



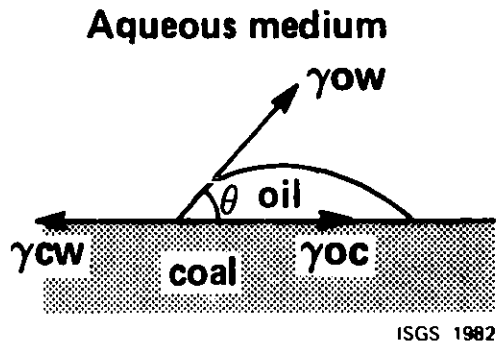
Before adhesion



After adhesion

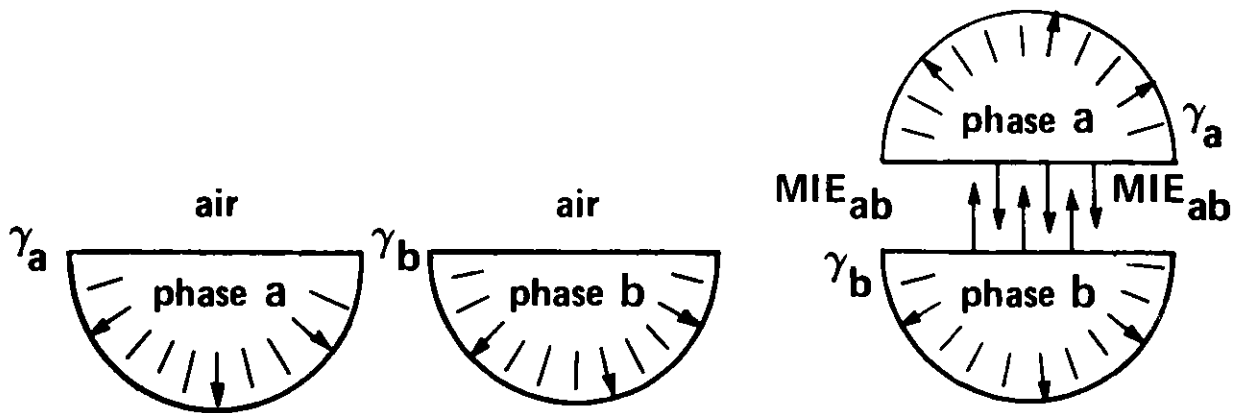
ISGS 1982

Figure 2. Adhesional wetting of coal by oil.



ISGS 1982

Figure 3. Contact angle of an oil drop on the coal surface (in water).



$$\gamma_{ab} = \gamma_a + \gamma_b - 2 MIE_{ab}$$

$\gamma_{ab}$  = interfacial tension

$\gamma_a$  and  $\gamma_b$  = surface tension

$MIE_{ab}$  = molecular interaction energy across the interface between a and b

ISGS 1982

Figure 4. Surface tension and interfacial tension of phases a and b.

References

1. V. P. Mehrotora, K.V.S. Sastny, and B. W. Morey, "Oil Agglomeration Offers Technical and Economical Advantages," Mining Engng., Vol. 32, No. 8, p. 1230 (1980).
2. R. M. Schubert, "Method for the Treatment of Coal Washery Wastes," U.S. Patent 3,856,668 (1974).
3. C. N. Bensley, T. R. Swanson, and S. K. Nicol, "The Effect of Emulsification on the Selective Agglomeration of Fine Coal," International Journal of Mineral Processing, Vol. 4 (1973).
4. L. A. Khan, and C. W. Kruse, "Analysis of the Collection Phenomena in the Oil Agglomeration of Fine Coal Particles," to be published.
5. M. J. Rosen, "Surfactants and Interfacial Phenomena," A Wiley-Interscience publication, John Wiley and Sons, New York (1978).

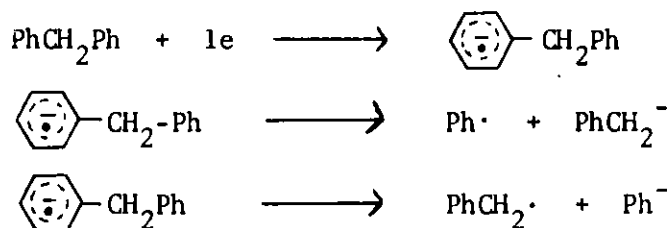
EQUIVALENT WEIGHT DETERMINATIONS OF BLACK ACIDS OBTAINED BY  
THE REDUCTIVE CARBOXYLATION WITH BITUMINOUS AND LIGNITE COALS

Robert C. Duty, Michael J. Lavin, Itayi C. Chiri  
and Duke B. Yoon  
Illinois State University  
Normal, IL 61761  
309/438-2697

Introduction

Carboxylation reactions with Illinois bituminous coal and lignite coals have been accomplished with sodium and with potassium in aprotic solvents of tetrahydrofuran (THF), toluene, naphthalene, hexamethylphosphoramide (HMPA) and triethylamine.<sup>1-4</sup> These reactions were successful in solubilizing the coals to a maximum of 83% with more than half of the soluble products isolated as black acids. Recently, reactions with potassium and a Westerholt Mine coal in glyme and triglyme solvents were reported which reduced the coal into smaller fractions with an increase in hydrogen content.<sup>5</sup> This study prompted Collins *et al.*<sup>6</sup> to examine if aromatic-aliphatic model compounds could be cleaved at the aliphatic linkages which the potassium-coal reactions in glyme-triglyme solvent had suggested.

Sternberg and co-workers<sup>7</sup> previously had successfully alkylated coal and their high solubility was attributed to the cleavage of ether linkages to form phenolate anions which subsequently could be O-alkylated. In addition, C-alkylation was proposed for the aromatic anions produced. Collins' study<sup>6</sup> unequivocally proved that aliphatic carbon-carbon bonds were cleaved at low temperature when toluene was isolated as a reaction product from both 1,2-diphenylethane and diphenylmethane. Collins' proposed mechanism suggests the formation of aromatic anions, aromatic radical anions as well as aliphatic and aromatic free radicals.



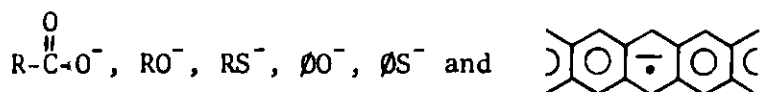
Previously, other authors<sup>8-11</sup> had claimed that 1,2-diphenylethane could not be cleaved with alkali metals, but Quest *et al.*<sup>11</sup> had found that a cesium-sodium-potassium-alloy could cleave bibenzyl. Collins' reactions with alloys of alkali metals does support Quest's experimental observations with the cesium-potassium alloy, and aliphatic carbon-carbon bond linkages indeed are broken. As Collins suggests, this may be an efficient low-temperature method for degrading coal by cleavage of aliphatic and aromatic-aliphatic bonds.

A recent study<sup>1</sup> has shown that the carboxyl group content of coal can be increased several fold by reacting coal with sodium metal and carbon

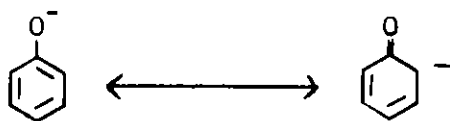
dioxide. Undoubtedly, the reaction occurs via the carboxylation of the  $\alpha$ -position of sodium phenolate sites<sup>12</sup> and the carboxylation of aromatic radical anions that are generated<sup>13</sup> from the sodium.

Recent results in this laboratory<sup>2-4</sup> indicate that potassium is a more efficient alkali metal than sodium for carboxylation reactions, and Stock's meticulous studies<sup>14</sup> with potassium in tetrahydrofuran are ample evidence to suggest this also. Stock's reactions with potassium, naphthalene and coal at ambient temperature generated  $20 \pm 1$  anions per 100 carbon atoms. Consequently, in addition to these 20 carbanion sites, the alkali metal alloys should break the macromolecular coal structure further through cleavage of the aliphatic and aliphatic-aromatic linkages to generate additional carbanion sites.<sup>6</sup>

Coal samples are known to contain the following functional groups; 1) carboxyl groups, albeit at low percentages in brown coal,<sup>15</sup> lignite,<sup>15</sup> and bituminous coal,<sup>16</sup> 2) ether linkage,<sup>15,16</sup> 3) hydroxyl groups,<sup>17</sup> 4) mercaptans<sup>18</sup> and 5) thio ethers.<sup>18</sup> Consequently when a coal sample is treated with an active alkali metal-alloy, the following basic sites would occur:



The phenolate ion acts as a precursor to carboxylation reactions through a delocalized resonance hybrid.



### Results and Discussion

Reductive carboxylation reactions of Illinois bituminous coal were run in toluene and triethylamine with potassium, carbon dioxide and biphenyl at 100°, 200° and 300°. North Dakota lignite was reacted under the same conditions with toluene as a solvent.

#### Material Balance

The material balance comparison between bituminous and lignite coal is shown in Table 1 with toluene as the solvent in each case.

One case is evident from examination of Table 1 in that a weight increase is proportional to an increase in temperature, e.g. the higher the temperature the higher the weight increase. Wachowska<sup>19</sup> had reported a similar weight increase in his alkylation study where the weight increase of alkylated coal was higher than the corresponding alkyl group content. Evidence was presented to suggest the anions of the aromatic clusters in coal were reacting with the solvent and the electron transfer agent that were

Table 1

Material Balance for Reductive Carboxylation Reactions  
with Bituminous & Lignite Coals  
(Solvent-Toluene)

Reaction Temperature	Coal Type	Weight of Reactants(g) <sup>a</sup>	Weight of Isolated Products(g) <sup>b</sup>	Weight Increase (decrease) (%)
100°	bituminous	20	18.6	(8%)
	lignite	20	19.2 ± 0.2 <sup>c</sup>	(3.9 ± 1.1%)
200°	bituminous	20	20.3 ± 0.3 <sup>c</sup>	6.0 ± 2.0%
	lignite	20	19.6 ± 0.1 <sup>c</sup>	(2.1 ± 0.2%)
300°	bituminous	20	30.6 ± 2.1 <sup>c</sup>	52 ± 11%
	lignite	20	25.4 ± 5.0 <sup>c</sup>	51%

<sup>a</sup>Weight includes 10 g coal plus 10 g biphenyl

<sup>b</sup>Weight includes the insoluble residue, the biphenyl, the black acids, the neutral compounds and the amphoteric compounds.

<sup>c</sup>two determinations

incorporated into the products. We ran a blank run with toluene, biphenyl, potassium and a catalytic amount of bituminous (0.2g) at 200° in the exact manner as previously run with 10g of bituminous coal and experienced a 47% increase in weight. A result that confirms Wachowska's observations.

#### Percent Solubility and Black Acid Yields

The percent solubility and black acid yields are presented in Table 2.

The maximum solubility occurred at 200°C with a lower solubility occurring at 300°C. The ratio of the weight of the insoluble residue to that of the original coal sample was used as a measure of the solubility. An indirect way of looking at solubility would be to compare the weight ratios of the black acids to that of the insoluble residues. One could assume that if all the high molecular weight insoluble residue had broken down during carboxylation, that it would have been totally converted into the low molecular weight black acids. Consequently, as the insoluble residues weight approaches zero, the black acid's weight should approach unity, i.e.

$$\lim_{\text{residue} \longrightarrow 0} (\text{weight fraction of black acids}) = 1.0$$

Table 2 exhibits this weight fraction increase very well because the 200°C reaction in every case has a maximum of carboxylic acids generated regardless of the solvent or the coal used.



Table 2  
Percent Solubility and Black Acid Yields

Reaction Temperature	Coal Type	Initial Weight of coal(g)	Weight Insoluble Residue(g)	Weight Black Acids(g)	% Solubility
(Solvent - Toluene)					
100°	bituminous	10.0	8.9	1.70	11.1
	lignite	10.0	5.7 ± 0.2 <sup>a</sup>	4.4 ± 0.8 <sup>a</sup>	43.4 ± 1.9
200°	bituminous	10.0	6.9 ± 0.6 <sup>a</sup>	4.9 ± 0.05 <sup>a</sup>	31.0 ± 6.0
	lignite	10.0	3.6 ± 0.3 <sup>a</sup>	4.5 ± 0.5 <sup>a</sup>	63.5 ± 3.3
300°	bituminous	10.0	15.0 ± 1.3 <sup>a</sup>	1.8 ± 1.5 <sup>a</sup>	(neg.)
	lignite	10.0	7.3 ± 0.9 <sup>a</sup>	3.8 ± 0.7 <sup>a</sup>	27.1 ± 8.1
(Solvent - Triethylamine)					
100°	bituminous	10.0	6.6 ± 0.1 <sup>a</sup>	2.2 ± 1.0 <sup>a</sup>	24.3 ± 9.0
200°	bituminous	10.0	3.2 ± 1.4 <sup>a</sup>	6.6 ± 0.2 <sup>a</sup>	68.5 ± 14.5

<sup>a</sup>Average & average deviation for two determinations

#### Equivalent Weight Determination:

Equivalent weight determinations were measured by back titrating an excess of standardized sodium hydroxide as described further in the experimental. The equivalent weights of these black acids are shown in Table 3.

The highest equivalent weights occurred for those reactions at 300°C. This, undoubtedly, results from the fact that the higher temperature promotes decarboxylation reactions to occur.

Equivalent weights are no indication of the molecular size unless one knows the number of carboxyl groups per molecule. If one assumes these black acids are the same molecular size as those generated from Mayo's hypochlorite studies<sup>20</sup> (mol.wt. 557 via VPO), the number of carboxyl groups per molecule would be approximately two. This piece of evidence is very tenuous, especially so since these acids were generated under two extremely different chemical environments. It becomes even more tenuous when one compares the carbon content for reductive carboxylation reactions (72%) with those acids from the hypochlorite study (58%).

One more direct comparison we can make is to measure the strength of the carbonyl stretching frequency and compare this to the equivalent weight measurements. If the equivalent weight size is directly proportional to the number of carboxyl groups, one should be able to show a correlation between

Table 3

## Equivalent Weight of Black Acids

Reaction Temperature	Coal	Solvent	Equivalent <sup>a</sup> Weight
100°	bituminous	toluene	258 ± 8
100°	lignite	toluene	305 ± 10
100°	lignite	toluene	258 ± 3
200°	bituminous	toluene	307 ± 19
200°	lignite	toluene	3.24 ± 8
200°	lignite	toluene	3.42 ± 32 <sup>c</sup>
300°	bituminous	toluene	335 ± 3
300°	lignite	toluene	458 ± 3
300°	lignite	toluene	500 ± 10
100°	bituminous	triethylamine	541 ± 118 <sup>b</sup>
100°	bituminous	triethylamine	395 ± 155 <sup>c</sup>
200°	bituminous	triethylamine	468 ± 129 <sup>b</sup>
200°	bituminous	triethylamine	490 ± 172 <sup>c</sup>

<sup>a</sup>two determinations

<sup>b</sup>four determinations

<sup>c</sup>six determinations

equivalent weight and strength of carboxyl peak. This correlation is shown in Table 4 for the bituminous and lignite coals run in toluene.

Table 4

## Carbonyl Group Strengths versus Equivalent Weights

Reaction Temperature	Coal	Carboxyl Peak Strength @1710cm <sup>-1</sup> (cm/mg) <sup>a</sup>	Eq. wt. of Black Acids
100°	bituminous	0.87	258 ± 8
200°	bituminous	0.55	307 ± 19
300°	bituminous	0.40	335 ± 3
100°	lignite	11.6 ± 1.7 <sup>b</sup>	282 ± 7
200°	lignite	10.4 ± 0.1 <sup>b</sup>	333 ± 20
300°	lignite	5.3 ± 0.9 <sup>b</sup>	479 ± 7

<sup>a</sup>height of carbonyl peak measured from background at 2100cm<sup>-1</sup>.

As the equivalent weight increases, the carbonyl stretching vibration decreases and this suggests there are fewer carboxyl groups present at the higher equivalent weights. The strength of the carbonyl peak was determined by measuring the height of the carbonyl peak and subtracting the background vibration at  $2100\text{cm}^{-1}$  from the carbonyl peak height.

The elemental analyses for the bituminous and lignite coals are shown in Table 5.

Table 5  
Elemental Analyses of Black Acids

Reaction Temperature	% C	% H	% N	% S	% Ash	% O <sup>a</sup>
A. Bituminous Coal - Solvent:Toluene						
100	70.71	5.26	0.87	1.83	2.26	19.07
100	70.66	5.00	0.88	1.64	1.26	20.56
200	72.93	4.54	1.66	0.92	0.97	18.98
200	72.28	4.77	1.18	1.73	0.67	19.37
300	66.99	3.66	1.71	5.89	1.66	19.96
300	69.58	3.92	1.91	1.00	1.86	21.73
B. Lignite Coal - Solvent:Toluene						
100	65.86	4.09	1.25	0.53	0.31	27.96
100	70.92	4.22	0.71	0.26	0.46	23.43
200	69.77	4.37	1.81	0.40	0.34	23.32
200	69.09	4.31	1.31	0.65	0.25	24.39
300	64.04	4.36	1.76	0.43	0.39	29.02
300	65.17	4.61	2.85	0.26	4.19	22.92

<sup>a</sup>Obtained by difference (%O=100%-%C-%H-%N-%S-%ash)

The oxygen trend in this table does not correlate well with the equivalent weight, e.g. the smaller the equivalent weight, the higher the oxygen content should be. Unfortunately, Table 5 does not exhibit this trend, however, it might be due to the way the oxygen content was determined which was by difference, i.e. the oxygen was determined by subtracting the percentage sum of carbon, hydrogen, oxygen, sulfur, nitrogen and ash from 100%. Therefore, all errors generated from any of these elements and other elements not reported will show up as an error in oxygen. One point Table 5 does make is that all black acids have a higher oxygen content than what was found in the raw bituminous or raw lignite coals.

#### Experimental Procedure

#### Materials, Reactions and Autoclave

Illinois bituminous coal and North Dakota lignite were reacted as raw coals (250-325 Tyler mesh) that had been dried at 100°. Reactions of coals were run in an Autoclave Engineers magnedrive packless, 1-liter stainless-steel autoclave equipped with a three-blade paddle wheel stainless steel stirrer that extended to the bottom of the autoclave. The autoclave was stirred at 900-1100 rpm. The temperature of these reactions was varied from 100° to a high temperature of 300°C.

The autoclave was charged with 10 g of coal, 10 g of alkali metal, and an aprotic solvent. The reactions were purged with dry nitrogen and run under nitrogen for five days, and the autoclave was pressurized with carbon dioxide for two days. After the reaction was complete, the excess alkali metal was decomposed by quenching the reaction with isopropyl alcohol.

The solvent was removed by rotary evaporation under vacuum, and the neutral compounds were extracted with an ether-benzene reflux (3/1 v/v)<sup>21</sup>. The ether-benzene layer was separated from the insoluble residue by centrifuging at 10,000 rpm with a Sorvall Model GLC-1 centrifuge and extracting with 5% potassium hydroxide to remove any solubilized acids.

The insoluble residue was refluxed with the 5% potassium hydroxide solution to extract the black acids. The potassium hydroxide solution was centrifuged, and the black acids were precipitated by acidifying the basic solutions with hydrochloric acid.

The insoluble residue from the potassium hydroxide extraction was demineralized,<sup>22</sup> and a total acidity and carboxyl group analyses were determined.

#### Infrared Analysis

Potassium bromide wafers were made in a pellet die (Beckman Model K-13) under 18,000-20,000 psi for periods of 20 min. The spectral grade potassium bromide (Fisher) was dried in a drying pistol overnight under vacuum at 100°C with phosphorus pentoxide. Approximately 6 mg. of the residue, known to the nearest mg., was weighted and mixed with 1.00 g. of potassium bromide, known to 3 significant figures. This was shaken on an automatic shaker for 90 sec. From 0.150 to 0.200 g of the mixture was placed into the press, made into a wafer and run on a Perkin-Elmer 621 Grating IR.

Table 6  
Equivalent Weight of Known Acids

	Eq. wt.	% Error
m-HO- $\phi$ -COOH	138	0.27%
2,3-Naphthalene dicarboxylic acid	108 $\pm$ 3.7 <sup>a</sup>	0.26%
1,2,4- $\phi$ (CO <sub>2</sub> H) <sub>3</sub>	68.2 $\pm$ 0.35 <sup>a</sup>	2.6%
1,2,4,5- $\phi$ (CO <sub>2</sub> H) <sub>4</sub>	63.5	2.0%
Tannic Acid	547	
C <sub>76</sub> H <sub>52</sub> O <sub>46</sub>		
F.W. 1701.23		

<sup>a</sup>average and average deviation for two determinations.

### Equivalent Weights of Black Acids

Demineralized moisture-free (dmmf) black acids were dissolved in an excess of standardized sodium hydroxide solution and stirred under nitrogen until dissolved. The excess sodium hydroxide was back titrated to pH 7, and the equivalent weight of the acids were determined from the amount of sodium hydroxide consumed. Equivalent weight of known acids were titrated to determine the accuracy of this procedure and these results are shown in Table 6.

### References

1. Duty, R.C., Hussman, G., Austin, J., Fuel, 60, 83 (1981).
2. Chiri, I., Masters Thesis, Ill. State U., 1981.
3. Lavin, M., Masters Thesis, Ill. State U., 1982.
4. Yoon, D., Masters Thesis, Ill. State U., 1982.
5. Hornback, H. P., Niemann, K. Erdoel Kohle, Erdgas, Petrochem. Brennst. Chem., Compent. 77178, Suppl. Vol. 1977, 295.
6. Collins, C.J., Hornback, H. P., Maxwell, B., Woody, M.C. and Benjamin, B.M., J. Am. Chem. Soc., 102, 851 (1980).
7. a) Sternberg, H.W.; Delle Donne, C.L.; Wender, I., Fuel, 47, 219 (1968).  
b) Sternberg, H.W.; Delle Donne, C.L.; Pantages, P.; Moroni, E.C.; Markby, R.E., ibid. 50, 432 (1971). c) Sternberg, H.W.; Delle Donne, C.L., ibid. 53, 172 (1974).
8. Conant, J.B., Garvey, B.S., J. Am. Chem. Soc., 49, 2599 (1927).
9. Willig, G., Ber. Dtsch. Chem. Ges., 64, 437 (1931).
10. Gilman, H.; Young, R.V., J. Org. Chem., 1, 315 (1936).
11. Quest, D.E., Ph.D. Dissertation, Georgia Institute of Technology, Oct. 1977 in Ref. 6.
12. Lindsey, F. and Jeskey, E., Chem. Rev., 57, 583 (1957).
13. Wawzonek, S. and Wearing, D., J. Am. Chem. Soc., 81, 2067 (1959).
14. a) Stock, L.M., Alemany, L.B. King, S.R., Fuel 53, 000 (1978). b) Stock, L.M., Alemany, L.B., and Handy, C.I., Division of Fuel Chemistry Reprints, 24, (1), 156 (1979).
15. Tucks, W. and Stengel, W., Breunstaff-Chem., 10, 303 (1929).
16. Ruberto, R.C. and Cronanek, D.C., in "Organic Chemistry of Coal", Ed. Larsen, J.W., American Chemical Society, Washington, D.C., 1978, p. 50.
17. Heathcoat, F. and Whealter, R.V., J. Chem. Soc., 2839 (1932).
18. Lissner, A. and Nemes, A., Bruenstoff-Chem., 16, 101 (1935).
19. Wachowska, H., Fuel, 58, 99 (1979).
20. Mayo, F.R. and Kirsher, N.A., Fuel, 58, 698 (1979).
21. Duty, R.C., R. Hayatsu, Moore, L.P., Scott, R.G., Studier, M., and Winans, R.E., Fuel, 59, 97 (1980).
22. Duty, R.C. and Liu, H.F., Fuel, 59, 546 (1980).

## THERMOMETRY IN COAL UTILIZATION

James F. Schooley  
National Bureau of Standards  
Washington, DC 20234

### Introduction

The importance of coal as an energy source has increased in recent years relative to that of oil and natural gas. U.S. Department of Energy data show that U.S. coal production jumped by 25% between 1978 and 1980. In relative energy units, coal thus surpassed U.S.-produced crude oil and approached within 5% of the energy contained in U.S. natural gas production. Indeed, the U.S. actually exports as much as 20% of its coal production.

There are many projects aimed at increasing the breadth and effectiveness of coal use in the U.S. Among these are the burning of coal for process heat to operate electrical generators, the gasification of coal--either in reactors or in the ground--to produce a pipeline fuel, the production of synthetic liquid fuel from coal, and the burning of coal in MHD generators for the direct production of electricity.

Each of these processes depends for its efficiency upon the reliable measurement of temperature, among other important parameters which include pressure, flow, and composition. In this paper, we discuss both present and prospective techniques for temperature measurement in these processes.

### Thermocouple Thermometry

The direct combustion of coal in boilers to produce electric power from turbo-generators is far and away the most common use of coal--a 1000 MWe generating plant uses about 10 kilotons of coal each day. The temperatures maintained in such boilers range up to 1800 °C in the burner itself, 1300-1800 °C in the furnace where the steam is produced, and on down to 250 °C in the stack<sup>1</sup>. Temperature measurement in this well-established process utilizes principally thermocouple thermometers. The major problems encountered in these measurements are the loss of calibration accuracy and the finite lifetimes of the probes.

There are seven types of thermocouple thermometers that have been given letter designations by the Instrument Society of America. These include the four base-metal types, as well as three noble-metal types. EMF vs temperature tables for each of these thermometers can be found in Ref. 2; the values listed in Ref. 2 serve as reference values both for manufacturers and for users. Upper temperature limits for their use in protective thermowells are recommended by the American Society for Testing and Materials<sup>3</sup>. This reference provides helpful discussions regarding the environmental limitations of these thermometers, too. One should note that the use of heavier gage wire will permit the use of particular thermocouple thermometers at higher temperatures or for longer service.

Currently, Type K thermometers, employed in wires as heavy as 8 Gage, predominate for the measurement of temperatures as high as 1100-1200 °C. Efforts to obtain long-term measurements of temperatures above the range covered by the standard thermocouple thermometers have led to the use of specially-prepared probes employing mineral insulation and controlled atmospheres, as well as the use of newer, high-temperature thermocouple types.

Some of these newer thermocouple systems involve platinum alloys dif-

fering from those in Types B, R, and S. The point is often raised in discussing the use of noble-metal thermocouples that they are very expensive in comparison with the base-metal types. We wish to point out that this argument usually is irrelevant. Even in so-called "routine" service, enhanced thermometer lifetime or enhanced reliability has a definite monetary value; in the case of developmental work, where the instrumentation needed to evaluate a process or to develop procedures may not exist, efforts to "save money" by using unsatisfactory thermometers rank as sheer folly.

Still other high-temperature, non-standard thermocouple thermometers are coming into more routine use.<sup>3</sup> Tungsten-rhenium alloys are used in a series of specialized thermometers that are useful up to temperatures as high as 2300 °C. Nickel-molybdenum alloy thermocouples have been developed for use in reducing atmospheres; they possess a sensitivity similar to that of Type K. More experience has been obtained with the Nicrosil/Nisil thermocouple thermometer during the past few years indicating that this system is considerably more stable than Type K to heating in air.

Table I summarizes sensitivity and range information for some of the newer thermocouple types.

Table I

Sensitivities and upper limits for newer thermocouple thermometers

Type	Ave. Seebeck Coef. V/°C	Upper Limit °C	Environment
Pt-40 Rh vs Pt-20 Rh	2.2	1800	Long-life
Pt-15 Ir vs Pd	30	1300	High-sensitivity
Pt-5 Mo vs Pt-0.1 Mo	30	1500	High-sensitivity
Ir-40 Rh vs Pt-40 Rh	5.5	1600	Combustors
Pd-31 Pt-14 Au vs Au-35 Pd	40	1260	Long-life
Ni-18 Mo vs Ni-1 Mo	45	1200	Reducing atm.
Nicrosil-vs Nisil	35	1250	High-stability
W-3 Re vs W-25 Re	15	2760	High-temperature

The properties of the Nicrosil/Nisil thermocouple as a thermometer are discussed by several authors in the recent 6th Symposium on Temperature, Its Measurement and Control in Science and Industry.<sup>4,5,6</sup>

A major problem with the use of thermocouple thermometry in developing new processes for energy production from coal is that of measurement accuracy. The EMF measured in a thermocouple circuit really represents the integral of many products of the Seebeck coefficient and the temperature gradient carried completely around the circuit as shown in Eq (1):

$$E = \oint S_j \nabla T \cdot dx \quad (1)$$

For ideal, homogeneous wires of composition A and B, Eq (1) reduces to  $E = (S_A - S_B) \Delta T$ . For real thermocouples, however, there are many accidental sources of EMF, as pointed out recently by Mossman et al.<sup>7</sup> Mossman et al. illustrate the effects of gradients and inhomogeneities arising from impurities or strains in a thermocouple circuit upon its EMF output in a figure which illustrates the occurrence of a strong maximum in a defective thermocouple circuit output when the test thermal gradient is located well away

from the target location.

R. P. Reed, of Sandia Laboratories, has pointed out the great value of branched-circuit diagnostic techniques for understanding and safeguarding thermocouple thermometry data in critical applications.<sup>8</sup> Reed has illustrated these methods for thermometry in terms of underground coal gasification; such precautions also are warranted in any expensive or isolated experiments in synthetic fuels process development.

Certainly the most difficult problem in thermocouple thermometry remains that of protecting the probe from debilitating environments. Much of the research in combustion and other corrosive, erosive systems is concerned with the development and evaluation of materials capable of withstanding these hostile environments for long periods of time.<sup>9,10</sup>

#### Velocity-of-Sound Thermometry

There are many other methods capable of providing accurate thermometry measurements in the processing of coal. Among these is the technique that relies upon the temperature dependence of the velocity of sound, usually in solids. In most applications the measurement consists of monitoring the time required for an ultrasonic pulse to travel through a probe wire, to be reflected by a discontinuity in the wire circumference or by the free end of the wire, and to return to the detector.<sup>11</sup> The technique has been used for some time in nuclear reactor thermometry.<sup>12</sup> We will say nothing further about this technique here, since Gopalsami will discuss it fully later in this session.

#### Johnson Noise Thermometry

Another thermometry method that has proved successful for high-temperature measurements under difficult conditions is that of Johnson noise. The basic equation describing this method was proposed by Nyquist:<sup>13</sup>

$$\langle V^2 \rangle = 4RkTdf \quad (2)$$

where  $\langle V^2 \rangle$  is the square of the voltage produced by thermal excitation of the electrons in a resistor of resistance  $R$ ,  $k$  is the Boltzmann constant,  $T$  the thermodynamic temperature, and  $df$  the detector bandwidth. This method is capable of quite high levels of accuracy--experiments reported during the 6th Temperature Symposium<sup>14,15</sup> reached thermodynamic uncertainties as low as a few millidegrees--and it is also useful in debilitating environments. There are several techniques in use in hostile-environment Johnson noise thermometry;<sup>16,17</sup> one of the best-developed, however, is the result of a long-standing collaboration between Blalock of the University of Tennessee and Borkowski, Horton, and Shepard at the Oak Ridge National Laboratory.<sup>18,19</sup> Their scheme utilizes separate measurements of the noise voltage  $(K4kRTdf)^{1/2}$  where  $K$  is the gain of the circuit amplifier, and of the noise current  $[(K'4kTdf)/R]^{1/2}$ . These quantities are multiplied in the circuit shown in Fig. 1 to produce the noise power

$$\langle P^2 \rangle = (K'4kTdf)^2 \quad (3)$$

which has the significant advantage that it is independent of the probe resistance. The calibration curve of the ORNL Johnson noise power thermometer shows excellent linearity at temperatures as high as 1250 °C. The ORNL



group, in a paper presented during the 6th Temperature Symposium, reported finding temperature uncertainties as small as 0.5% at temperatures up to 700 °C. This method has been used mainly for thermometry in nuclear reactors. Its natural advantages, however, ensure its success in many applications in the processing of coal.

### Radiation Thermometry

#### Planck-Law Thermometry

We turn now to radiation thermometry methods. The use of radiation for thermometry in hot systems has major advantages and major disadvantages as well. Among the advantages are its remote nature--there is no probe to corrode, erode, or melt--its speed, and its adaptability to different target species. Its chief disadvantages have been its sensitivity to errors from variation in emissivity, from reflected radiation, from degraded transmission in optical paths or in windows, and from variations in target phase compositions.

Eq (4), elucidated by Planck in 1900,<sup>20</sup> shows the relation between the spectral intensity  $L_\lambda$  of a target blackbody and its so-called "brightness temperature"  $T_b$ :

$$L_\lambda = c_1 / [\lambda^5 \exp(c_2 / \lambda T_b) - 1] \quad (4)$$

$c_1$  and  $c_2$  are the first and second radiation constants, respectively. Note that the temperature must be expressed in kelvins in Eq (4).

Eq (4) can be used in various ways to evaluate the temperature of a hot target. In principle, one could use the fact that Eq (4) yields unique curves for the spectral intensity of blackbody radiation as functions of wavelength for particular temperatures; simply evaluating the peak wavelength of the distribution through use of the Wein displacement law could yield the temperature. In practice, however, measurements of temperature are not often performed in this way.<sup>21</sup> A major drawback is the fact that most radiating systems are neither perfect blackbodies, nor even "graybodies" (for which the emissivity  $\epsilon(\lambda)$ , while not exactly unity for all wavelengths of interest, is constant throughout the measured range of wavelengths). Another problem lies in the fact that the peak in the spectral intensity varies substantially with temperature, so that the radiation detector would need to be responsive over a similarly wide wavelength range.

The Planck Law is often used in the so-called "two color" technique to produce rapid and convenient temperature measurements that rely on the uniformity of the spectral emissivity only over a limited wavelength span. In this case, Eq (4) is used to provide values of  $T_b$  from relative intensity measurements at two wavelengths.

The most common use of the Planck Law for high-precision thermometry is that recommended in the text of the International Practical Scale of 1968:<sup>22</sup>

$$L_\lambda(T) / L_\lambda(T_{ref}) = [\exp(c_2 / \lambda T_{ref}) - 1] / [\exp(c_2 / \lambda T) - 1] \quad (5)$$

The freezing point of gold, 1064.43 °C, specified for IPTS-68 thermometry, is commonly used as the reference temperature. Once again, even small deviations from blackbody conditions introduce measurement errors.

There are several methods by which thermometrists have succeeded in preserving the advantages of radiation thermometry while avoiding its major

disadvantages. Not all of these methods have been applied to temperature measurement in coal systems, but all of them could be so used.

### Line Reversal Thermometry

Zinneman and his co-workers at the Argonne National Laboratory presented a discussion of the U-25 US/USSR cooperative MHD generator experiment during the 1980 Symposium of this series.<sup>23</sup> An informative discussion of line-reversal thermometry can be found in Ref 24. Campbell and his co-workers working on the Mississippi State University MHD project, also reported successful measurements using the sodium line-reversal technique. These measurements were reported during last year's Symposium.

### Laser-based Thermometry

An area of radiation-based thermometry which has grown in recent years to become a really powerful tool for combustion and other gaseous system measurements is that of laser-based Raman scattering and fluorescence. These measurements basically address the Boltzmann population distribution of the molecular energy levels in the target gas. There are several techniques used in these measurements, in general benefitting from the use of laser light sources and spectroscopic detection. We will mention two of these which allow the measurement of temperature--in some cases with 1% accuracy--and composition, both at high data rates--potentially  $10^8$  per second--and with spatial resolution of less than 1 mm. In general, these techniques require the availability of an optical path through the target gas and they also involve a reasonably good understanding of specific states of the target molecule.

CARS. Perhaps the best-known of the spectroscopic thermometry techniques is the Coherent Anti-Stokes Raman Spectroscopy (CARS) method. In one of several papers on this topic presented during the 6th Temperature Symposium,<sup>25,25</sup> Verdick and his co-workers discussed the system shown in Fig. 2. Basically, a "pump" laser beam at frequency  $\omega_1$  and a second beam,  $\omega_2$ , are chosen to populate a Raman-active excited state of the target molecule. This state is separated from the initial state by  $\omega_v$ . This technique yields a strong, resonance-based intensity at the frequency  $\omega_3$ . Typically the Stokes beam either is scanned or used as a broadband light source. In either case, the resulting spectrum is a wavelength scan similar to that shown in Fig. 3. The intensity distributions arising from the changing populations in the molecular levels making up the target vary noticeably with temperature, allowing an evaluation of the system temperature from the spectrum profile. The Q-branch transition spectra shown in Fig. 3 were calculated for  $N_2$  as a function of temperature, and verified by CARS measurements at 2100 K.

Eq (6) shows how the level population probabilities  $P(v,J)$  depend upon the system temperature T:

$$P(v,J) = \frac{g_J(2J+1) e^{-E_v/RT} e^{-B_v J(J+1)/RT}}{Q_v Q_R(v)} \quad (6)$$

In this Eq,  $v$  and  $J$  are the vibrational and rotational quantum numbers, respectively,  $g_J$  is the nuclear spin degeneracy,  $g_v$  and  $Q_R$  are the  $v$ th level

vibrational and rotational partition functions, respectively,  $E_v$  is the vibrational energy in state  $v$ ,  $B_v$  is the rotational constant in state  $v$ , and  $R$  is the gas constant.

These workers have found it possible to obtain temperature measurements from  $10^{-8}$  second laser pulses even in sooty, highly-incandescent flames. These results agree with the conclusions of W. L. Flower, discussed during last year's Symposium, concerning the usefulness of Raman scattering measurements in particle-laden gases. More recently, Hartford has described the use of CARS for characterizing coal gasifiers.<sup>27</sup>

Laser Tomography. Semerjian and Santoro, at the National Bureau of Standards, have adapted relatively high-intensity absorption spectroscopy to a technique that they call "laser tomography".<sup>28</sup> This technique avoids the "onion peeling" problems associated with the acquisition of optical signals from regions of varying temperature. This technique appears to have good potential for specific applications in coal thermometry, in areas including non-symmetric flows; rapid, real-time measurements; and simultaneous measurements over two-dimensional or three-dimensional regions.

Eq (7) shows the ratio of the transmitted radiation intensity  $I_v$  to the incident intensity  $I_v^0$  at frequency  $v$ :

$$I_v/I_v^0 = \exp\left(-\int_0^L N_1 \cdot Q_v ds\right) \quad (7)$$

The ratio depends upon the density of molecules  $N_1$  and the absorption cross section  $Q_v$  integrated over the line of sight  $ds$ .

Since there is no way to solve for the distribution of  $N \cdot Q(T)$  along  $ds$  on the basis of one measurement, Semerjian and Santoro vary the angle of observation to localize their measurements for both temperature and concentration data.

### Summary

In this paper, we have illustrated some of the common problems that exist in thermocouple thermometry, still the workhorse for temperature measurements in coal utilization, as well as some of the progress in this time-tested technique. Furthermore, we have mentioned other contact and radiation methods that are available for these measurements, in the earnest hope of providing some guidance for innovation in thermometry for coal utilization experiments and development.

### References

1. D. R. Hardesty and J. H. Pohl, Sandia Labs Report 78-8804, 1979.
2. R. L. Powell et al., "Thermocouple Reference Tables Based on the IPTS-68", NBS Monograph 125, 1974.
3. ASTM Committee E-20, "Manual on the Use of Thermocouples in Temperature Measurement", ASTM Special Technical Publication 470B, 1981.
4. G. W. Burns, "The Nicrosil versus Nisil thermocouple: Recent development and present status", 6th Symposium on Temperature, Its Measurement and Control in Science and Industry, Vol. 5, American Institute of Physics, in press (subsequent references will be "Temperature 5").
5. N. A. Burley et al., "The Nicrosil versus Nisil thermocouple system: A critical comparison with the ANSI standard letter-designated base-metal thermocouples", Temperature 5.

6. T. P. Wang and C. D. Starr, "Oxidation resistance and stability of Microsil-Nisil in air and reducing atmospheres", *Temperature* 5.
7. C. A. Mossman et al., "Testing of thermocouples for inhomogenieties", *Temperature* 5.
8. R. P. Reed, "Diagnostics for defective thermocouple circuits", *Temperature* 5.
9. H. P. R. Frederikse et al., "Materials for Instrumentation for Fossil Energy Technologies", NBS Interim Report NBSIR 81-2348, August 1981.
10. D. R. Diercks et al., "Analysis of Components in the Grand Forks Energy Technology Center Slagging Coal Gasification Plant", DoE Materials & Components Newsletter, No. 37, April 1, 1982.
11. L. C. Lynnworth, "Temperature profiling using multizone ultrasonic waveguides", *Temperature* 5. See also J. J. Ronchetto, "Ultrasonic Thermometry in Oil Shale Retorts", Proceedings 1981 Fossil Instrumentation Symposium, ANL 81-62, p. 31.
12. H. A. Tasman, "Ultrasonic thin-wire thermometry for nuclear applications", *Temperature* 5.
13. H. Nyquist, "Thermal agitation of electric charge in conductors", *Phys. Rev.* 32, 97 (1928).
14. G. Klempt, "Errors in Johnson noise thermometry", *Temperature* 5.
15. C. P. Pickup, "A noise thermometer for the range 100-150 °C", *Temperature* 5.
16. H. B. Brixy et al., "Applications of noise thermometry in industry under plant conditions", *Temperature* 5.
17. T. R. Billeter and C. P. Cannon, "Dual high temperature measurements using Johnson noise thermometry", *Temperature* 5.
18. C. J. Borkowski and T. V. Blalock, "A new method of Johnson noise thermometry", *Rev. Sci. Instr.* 45, 151 (1974).
19. T. V. Blalock, "A decade of progress in high temperature Johnson noise thermometry", *Temperature* 5.
20. See, for example, R. P. Benedict, Fundamentals of Temperature, Pressure, and Flow (John Wiley & Sons, New York, 1977), Chapter 8.
21. However, see the paper of R. F. Leftwich, "Infrared Radiometry Applied to Critical Temperature Measurement in the Coal Gasification Process", Proceedings of the 1977 Symposium on Instrumentation and Process Control for Fossil Demonstration Plants, ANL-78-7, p. 390.
22. International Committee for Weights and Measures, "The International Practical Temperature Scale of 1968 Amended Edition of 1975", *Metrologia* 12, 7 (1976).
23. T. Zinneman et al., "Instrumentation for the U-25 MHD Generator", Proc. 1980 Fossil Instrumentation Symposium, ANL-80-62, p. 75.
24. A. G. Gaydon and H. G. Wolfhard, Flames, Their Structure, Radiation, and Temperature (The Macmillan Co., New York, 1960).
25. J. F. Verdieck et al., "CARS thermometry in reacting systems", *Temperature* 5.
26. G. L. Switzer and L. P. Goss, "A hardened CARS system for temperature and species-concentration measurements in practical combustion environments", *Temperature* 5.
27. A. Hartford, "Optical Instrumentation for On-Line Monitoring of Coal Gasifiers", Paper EC 3, March 9, 1982 meeting of the American Physical Society, Dallas, TX; unpublished.
28. H. G. Semerjian and R. J. Santoro, "Laser tomography for temperature measurements in flames," *Temperature* 5.

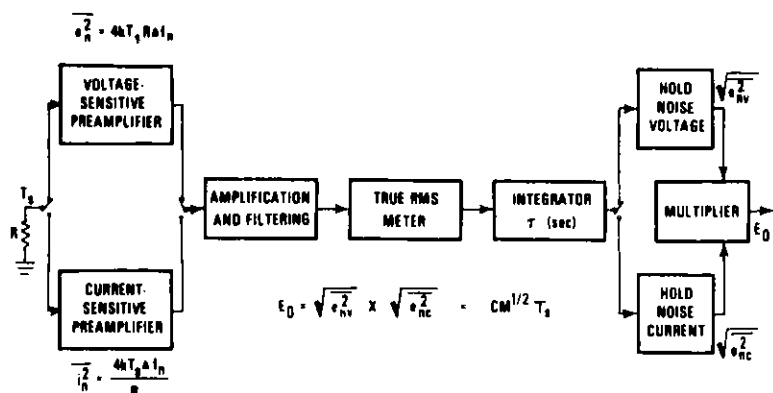
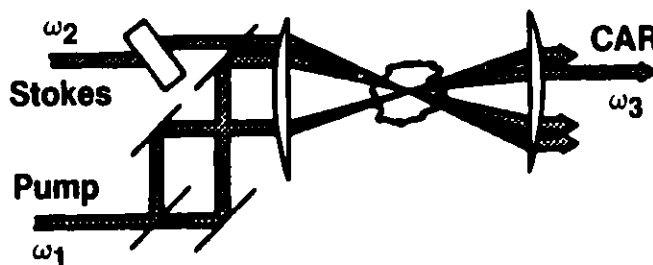
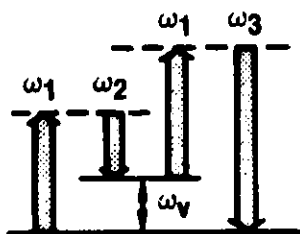


FIG. 1. A SYSTEM FOR MEASURING THERMAL NOISE POWER

• Approach



• Energy Level Diagram



• Spectrum

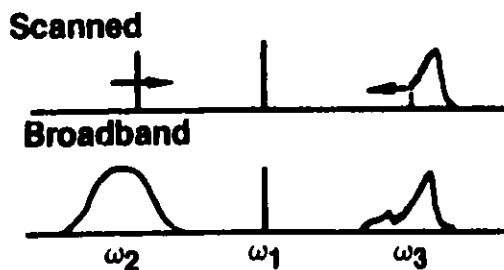


FIG. 2. Coherent Anti-Stokes Raman Spectroscopy (CARS)

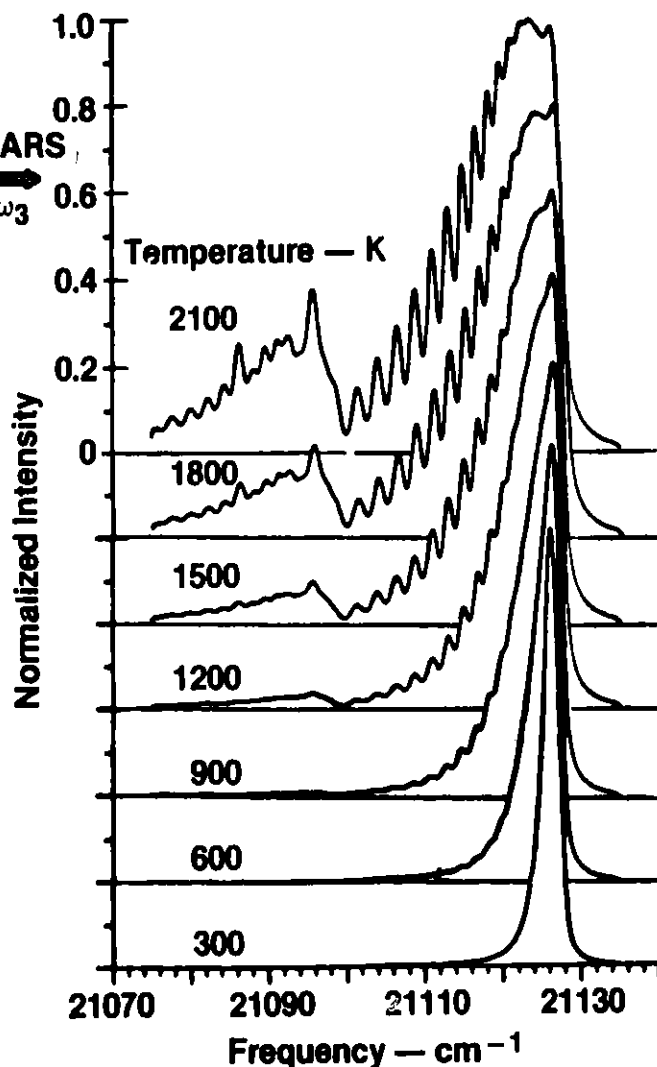


FIG. 3. Temperature Variations of the CARS Spectrum of N<sub>2</sub>

COMBUSTOR PINHOLE CAMERA\*

A. B. Witte, N. Gat, L. M. Cohen  
TRW Space & Technology Group  
One Space Park, RL/1032  
Redondo Beach, CA 90278

Abstract

Aerodynamic window and pinhole camera concepts\*\* were combined in developing a novel gas purged port to view high pressure combustion phenomena. Whereas gas purge requirements were only about 10 percent of that needed for conventional access ports, thereby minimizing flow disturbances, the window was kept free of combustion debris for hours of real-time video observation in the TRW 20MW MHD Coal Combustor. The pinhole camera has been used mainly to record slag motion on combustor walls and to observe interesting coal sheet ignition phenomena. These observations, recorded on video tape as well as displayed in real time, were used to improve our understanding of basic phenomena, operating conditions and performance. The concept has also been used for "clean" access while making spectroscopic measurements.

Introduction

This section describes the combustor pinhole camera which was developed to observe combustion phenomena inside a high pressure (6 atm) slagging, pulverized coal combustor. The instrument incorporates a conventional TV video camera, external light filters coupled to the camera automatic gain control (AGC), and an aerodynamic-window pinhole assembly which permits optical access. The pinhole assembly incorporates an innovative gas purge concept or aerodynamic window to purge the optical port. The assembly is shown in Figure 1. The pinhole is 12 cm long with a major diameter of 5 cm and a minor diameter of 2 cm. Two of the tubes circulate cooling water and the third tube feeds purge gas for expulsion through the aerodynamic window. Installation of the instrument on the head end of the TRW MHD Pulverized Coal combustor is shown in Figure 2. Only the video camera can be seen. The fields of view from the combustor head end are shown in Figure 3.

Two key features of the pinhole are that no material (glass) windows contact the combustion gases and very little gas purge is necessary to keep the optical train clear of combustion debris. Conventional glass window ports with gas purges generally cannot be kept clean in this combustion environment for test periods beyond a few minutes. The use of low purge rates minimizes the local and global aerodynamic disturbances to the observed phenomena.

---

\*This research was supported by the U.S. Department of Energy Contract DE-AC-01-79-ER10029.

\*\* Patent Documents, DoE Case S-56,353 (RL-8451), TRW Docket 11-0274.

The dynamic range of the TV camera was extended by several orders of magnitude by using an external variable density filter wheel coupled to the camera agc. This feature also provided signal saturation protection to the vidicon tube.

### Pinhole Design

#### Conceptual Design

The conceptual design of the pinhole camera is shown in Figure 4. Nitrogen gas flows through the orifice in the pinhole assembly to provide an aerodynamic window which repels particulate and condensable gases while permitting optical access for viewing or diagnostics. Both this aerodynamic window and the remote positioning of the image transfer optics ensure that the port remains clear at all times. The focused geometry of the convergent nozzle provides a large momentum flux of purge gas at the orifice to repel particles without using large amounts of gases which might otherwise dilute or disturb the combustion processes. These same purge gases help cool the pinhole assembly. Additional water cooling was also provided adjacent to the purge manifold.

The set of lenses is used to optimize the field of view and to transfer the pinhole orifice to the lens plane of a recording camera or vidicon. More on this is said later. Not shown here is an external variable density filter wheel which was adjusted automatically so as to limit saturation of the recording camera.

#### Design Requirements

At this stage, special emphasis was placed on providing pinhole hardware which could demonstrate concept feasibility rather than the subtleties of an optimum design. The subsequent operating performance of the device would serve to improve the instrument in a second generation design.

The following technical requirements were established in order to provide a basis for the pinhole design.

1. Provide a purge configuration to repel combustion particulate and gases, keep hole clear of slag, cool pinhole assembly, and minimize combustor flow disturbances.

2. Provide additional external filters to safely extend the dynamic range of the TV camera (vidicon). These filters are to be integrated into the existing agc for the camera.

#### Purge Considerations

Repulsion of Combustion Particulate. The force balance on a decelerating nonburning particle whose motion is opposed by the purge flow is

$$m \frac{du}{dt} = -C_D \frac{1}{2} A \rho_j (u - u_j)^2$$

The time to decelerate the particle to zero velocity (i.e., time to stop and hence begin to repel the particle) is

$$t = \frac{4}{3} \frac{\rho}{\rho_j} \frac{d}{C_D} \frac{\frac{u_o}{u_j}}{u_j \left(1 - \frac{u_o}{u_j}\right)}$$

where,

$\rho, \rho_j$  = particle and jet densities

$u_o, u_j$  = particle initial velocity and jet velocity

$d$  = particle diameter

$C_D$  = drag coefficient

Now for conditions here

$$\frac{\rho}{\rho_j} = 10^2$$

$$d = 50 \times 10^{-4} \text{ cm}$$

$$C_D \approx > 1$$

$$u_o = 1500 \text{ cm/sec}$$

$$u_j = 3 \times 10^4 \text{ cm/sec (assures sonic flow through pinhole)}$$

then,

$$t \leq 10^{-6} \text{ sec.}$$

The distance traveled after this short interval is

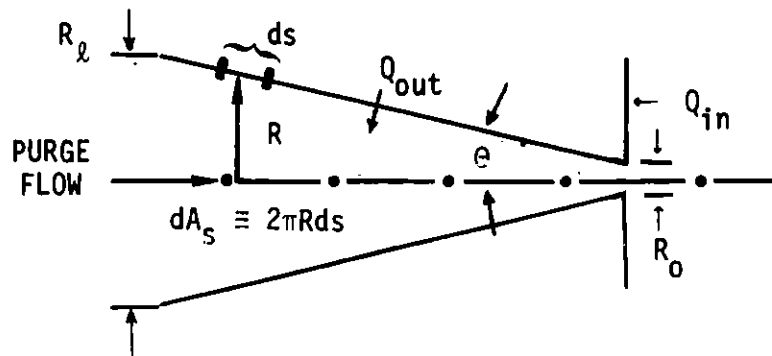
$$\begin{aligned} x &= \frac{1}{2} u_o t \\ &= 8 \times 10^{-4} \text{ cm} \end{aligned}$$

which is less than the particle diameter. Thus the purge level required to keep the pinhole sonic is more than adequate to stop combustion debris from entering the pinhole.



### Cooling of Pinhole

The pinhole is cooled to some degree by the purge. The amount of cooling has been estimated as follows to determine an equilibrium temperature



of the copper pinhole. The heat balance is

$$Q_{in} = Q_{out} = \int \underline{q} \cdot \underline{n} \, dA_s$$

where the heat flux and film coefficient are

$$q = h(T_w - T),$$

$$h = C_H \rho u c_p, \text{ and}$$

$$\rho u = \dot{m}/A.$$

One obtains

$$Q_{in} = \frac{2C_H c_p \dot{m} (T_w - T)}{\sin\theta} \int_{R_o}^{R_l} \frac{dR}{R}$$

and thus

$$(T_w - T) = \frac{Q_{in} \sin\theta}{2C_H \dot{m} c_p \ln \frac{R_l}{R_o}}$$

For our conditions...

$$q_{in} = 50 \frac{\text{Btu}}{\text{ft}^2 \text{ sec}} \frac{\pi (.9)^2}{4 \times 144} \text{ ft}^2$$

$$\theta = 15 \text{ (half angle)}$$

$$c_H = 0.003 \text{ (Re} = 5 \times 10^5)$$

$$c_p = 0.25 \frac{\text{Btu}}{\text{lbm}^\circ\text{F}}$$

$$R_\ell = 7 \text{ mm}$$

$$R_o = 1 \text{ mm}$$

$$\dot{m} = 0.02 \text{ lbm/sec}$$

The temperature difference becomes

$$(T_w - T) = 1000^\circ\text{F}$$

To insure that the assembly operates at a lower wall temperature, a water coolant passage was added to the pinhole assembly to provide additional cooling.

#### Purge Level for Slag Rejection

Continuous molten slag flow on the wall of the combustor would cover the pinhole unless the purge were adjusted to keep it clear.

The slag density and velocity are assumed to have the following values

$$\rho_{sl} = 1.5 \text{ g/cc}$$

$$u_{sl} = 1 \text{ cm/sec}$$

The gas purge conditions already specified for the jet emerging from pinhole exit plane are

$$\rho_j = 1.2 \times 10^2 \text{ g/cc}$$

$$u_j = 3 \times 10^4 \text{ cm/sec}$$

The condition to be satisfied to separate the slag flow at the orifice is indeed satisfied, i.e.,

$$\rho_j u_j^2 \gg \rho_{sl} u_{sl}^2$$

#### Decay of Purge Disturbance

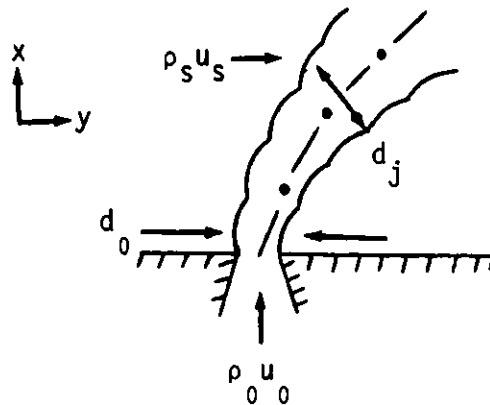
Disturbances to the combustor flow by the purge gases near the pinhole will now be estimated. Although the jet momentum flux to cross stream momentum flux ratio is quite large,

$\rho_o u^2 / \rho_s u_s^2 = \lambda$  of several hundred, the ratio of forces decays

rapidly with jet length

$$\frac{\lambda d_o^2}{d_j^2} \sim \frac{1}{x^2}$$

This follows from two key features of the jet: (1) linear growth,  $d_j \sim x$ , and (2) constant total momentum flux,  $\rho_o u_o^2 d_o^2$ . Thus, not only does the jet velocity decay as  $1/x^2$ , but the jet is also turned away into the cross stream direction.



A correlation by Keffer and Baines of the jet penetration is shown in Field.<sup>1,2</sup> At large extent, one obtains

$$\frac{y}{d_o \lambda} = 5.5 \left( \frac{x}{d_o \lambda} \right)^{2.175}$$

where  $y$  and  $x$  are the distances from the orifice in the cross flow and downstream directions, respectively. From the above correlation, the jet is swept out of the pinhole line of sight by  $y \sim 2 d_o$  at a downstream distance of  $x \sim 10 d_o$ . For this pinhole,  $d_o = 2$  mm. Downstream disturbances should be small for  $x > 2$  cm.

### Pinhole Optics

Spatial Resolution. The resolution of a pinhole camera is essentially determined by the aperture and the distance to the object. For a pinhole, the Rayleigh resolution,  $\delta$ , is

$$\delta = 1.22 \lambda f\#$$

where

$$f\# = \frac{L}{d_o}$$

L is the objective distance, 100 cm, and  $d_o$  the aperture diameter, 0.2 cm. Choosing the wavelength in the red (.6 microns) the resolution becomes

$$\delta = 1.22 (.6) 500 = 366 \text{ microns.}$$

Since we do not expect to see microscopic detail, such resolution is acceptable provided that an 0.2 cm aperture can be purged to keep the slag clear.

Next, field of view needs to be considered. The port body is a 6.6 cm length of tube with a diameter of 22.8 mm. The pipe aspect ratio limits the field of view. To solve this problem a set of field lenses is provided to relay the combustor pinhole aperture to coincidence at the iris (aperture) of the vidicon. This is shown in the optical scheme in Figure 4.

The lens nearest the combustor aperture is located a focal length from the pinhole. This lens accepts semi-paraxial rays from the object within the field of view and relays them through the lens to a focal point between the first and second lens. Because the rays are paraxial they are brought to a focus at a distance equal to the focal length of the lens. Note, however, that the directions of the received rays from an extreme off axis angle are collimated somewhat parallel to the axis of the centerline of the system. All rays entering the pinhole are generally made to go parallel to the axis.

The second lens then takes the rays, collimated from the first lens, and converges them to an image of the combustor pinhole. Note that the rays passing through the image of the pinhole have now become paraxial because they have been taken from a place at the focal length of the second lens. Thus, lens No. 1 is located a focal length's distance from the pinhole. Lens No. 2 is separated from lens No. 1 by twice the focal length, and finally, the imaged pinhole is located at one focal length from lens No. 2 (assuming lens No. 1 and No. 2 are identical). This scheme then provides a wide field of view although it suffers a loss of resolution due to the pinhole. Although the camera is located external to the combustor wall, the camera focus is set for the distance from the combustor wall to the region of interest.

To protect the vidicon from overexposure, a neutral density filter wheel was placed between the vidicon and the pinhole assembly. It was integrated electronically with the automatic gain control to adjust the intensity for the best picture. The details of the electronics circuit can be found in the reference, Coal Combustion Aerothermochemistry Research Final Report.<sup>3</sup>

Estimates of peak radiation into the optical train were made including losses to specify vidicon requirements. Based on these estimates a black and white vidicon (Javelin Model

SC821) was selected. After the first test it was obvious that a less sensitive color vidicon unit would also work. Successful tests were made with a color vidicon (JVC Model G-71) which is now used continuously in several locations.

## Results

### Calibration Photograph

A checkout photograph, shown in Figure 5, was taken through the pinhole assembly. The pinhole was located 1 meter from an eye chart illuminated by a 120 watt flood lamp. A five second exposure was required using Type 52 Polaroid film (ASA 400). The field of view observed is 37 cm which corresponds to a total angle of about 22°.

### Combustion Videotapes

The use of the pinhole camera, once installed in either the combustor head end or slag tank, was highly successful. In the head end, a clear picture of the slag motion on the walls was observed while only the preheater was in operation. When the coal flow was initiated, obscuration of the pinhole occurred very rapidly (with 1 to 2 seconds) as the flow transients decayed. A very interesting coal ignition sequence was recorded while purging the coal pintle of the 325 Mesh coal used in one of the test series.

Six polaroid pictures taken from the video replay screen are recorded in Figure 6. The picture quality resulting from this first attempt at transfer is disappointing, but this penalty is, of course, small compared to the benefit of having real-time video coverage of these combustion phenomena. Each photograph records a view taken from the head end toward the slag baffle. In photograph (a), only the 2900 F air preheater is in operation, the coal not yet being injected. The dark cylindrical object on the left side is the coal pintle, the light background, hot slag and the dark right side, the slag baffle. Slag motion on the wall is easily observed on the video tape. The white splotches on the slag baffle are actually protuberances of molten slag moving circumferentially by air shearing forces. In photograph (b), a very small amount of coal has been injected while in (c), ignition has occurred and in (d), the flame has encompassed the perimeter of the coal sheet. In photograph (e) the flame front has advanced along the sheet toward the pintle and in (f) the flame appears to be attached to the pintle exit. After this sequence, the burning coal sheet appeared to be convected back toward the camera and head end of the combustor. Subsequent viewing was obscured by a uniform bright background, apparently that of a uniform volume of burning particles. Besides this problem, another one which limited viewing of the combustor processes, was that the slag motion built a "streamlined" bridge over the pinhole orifice, blocking the view but not plugging the

orifice itself. This problem can probably be minimized by using a re-entrant rather than flush mounted pinhole assembly so that the slag can flow around, rather than over, the device.

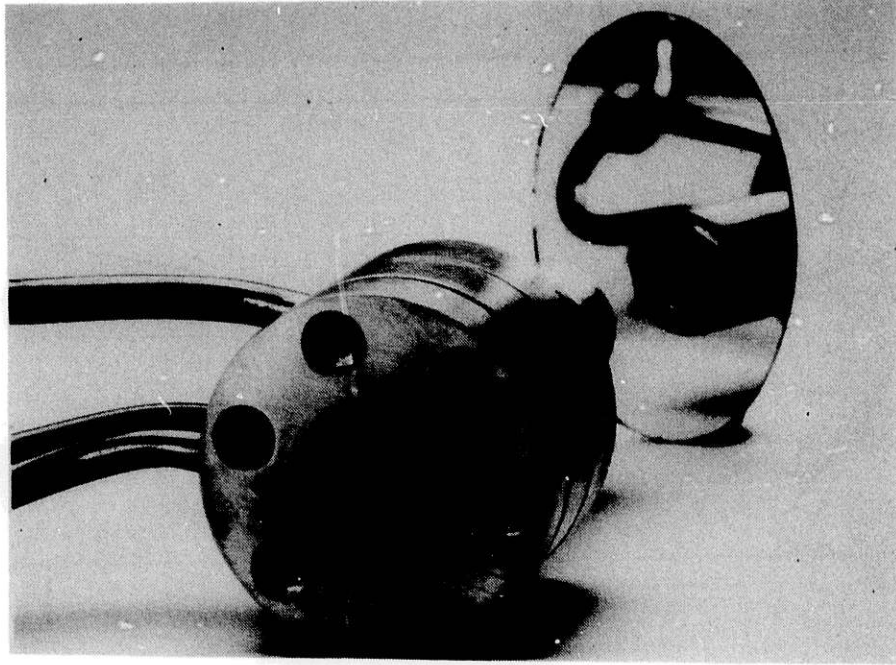


Figure 1. PHOTOGRAPH OF PINHOLE ASSEMBLY

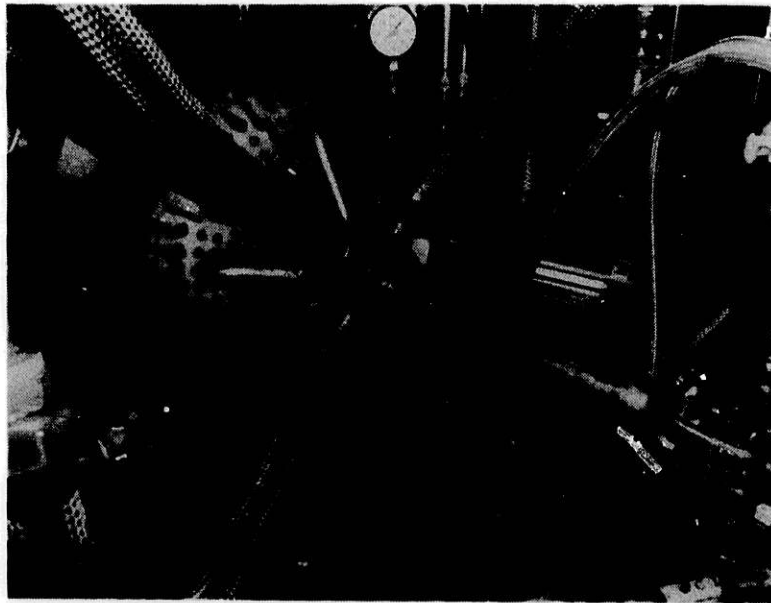


Figure 2. PINHOLE CAMERA INSTALLED ON  
HEAD END OF TRW COMBUSTOR

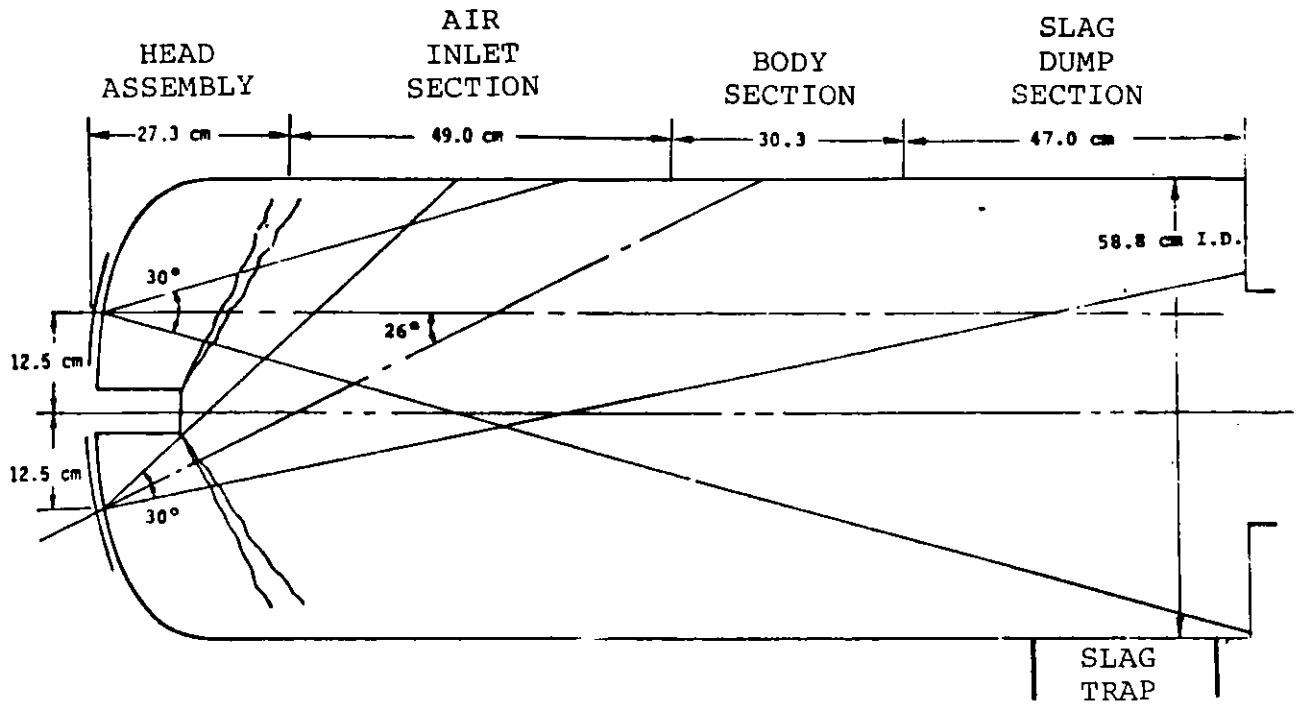


Figure 3. FIELD OF VIEW FROM PINHOLE PORTS IN HEAD END

Pinhole Camera Port Conceptual Design

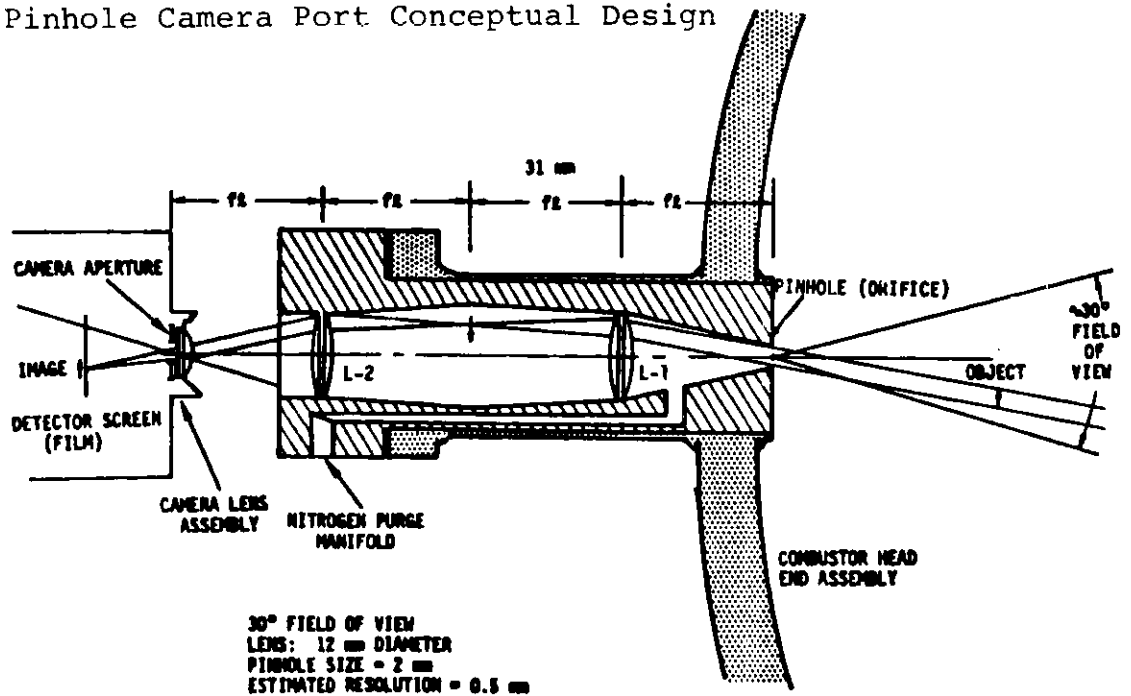
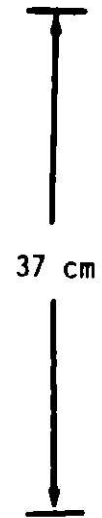
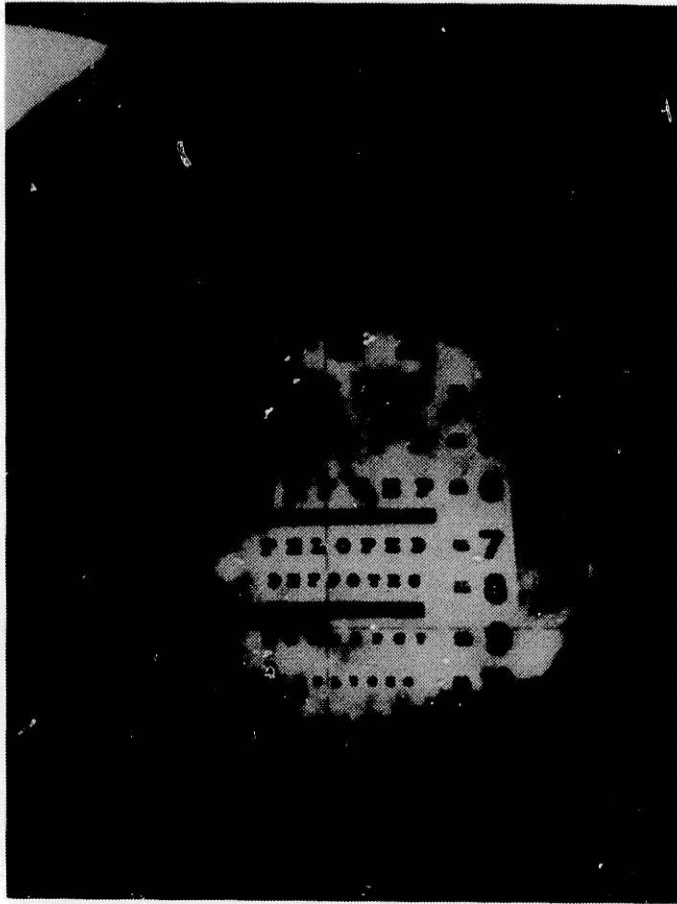


Figure 4. CONCEPTUAL DESIGN OF PINHOLE CAMERA



Pinhole located 1 meter from eye chart. Five second exposure type 52 Polaroid (ASA 400) chart illuminated at one meter with 120 watt flood lamp. Smallest letters 5 mm wide.

Figure 5. PINHOLE CAMERA PHOTOGRAPH



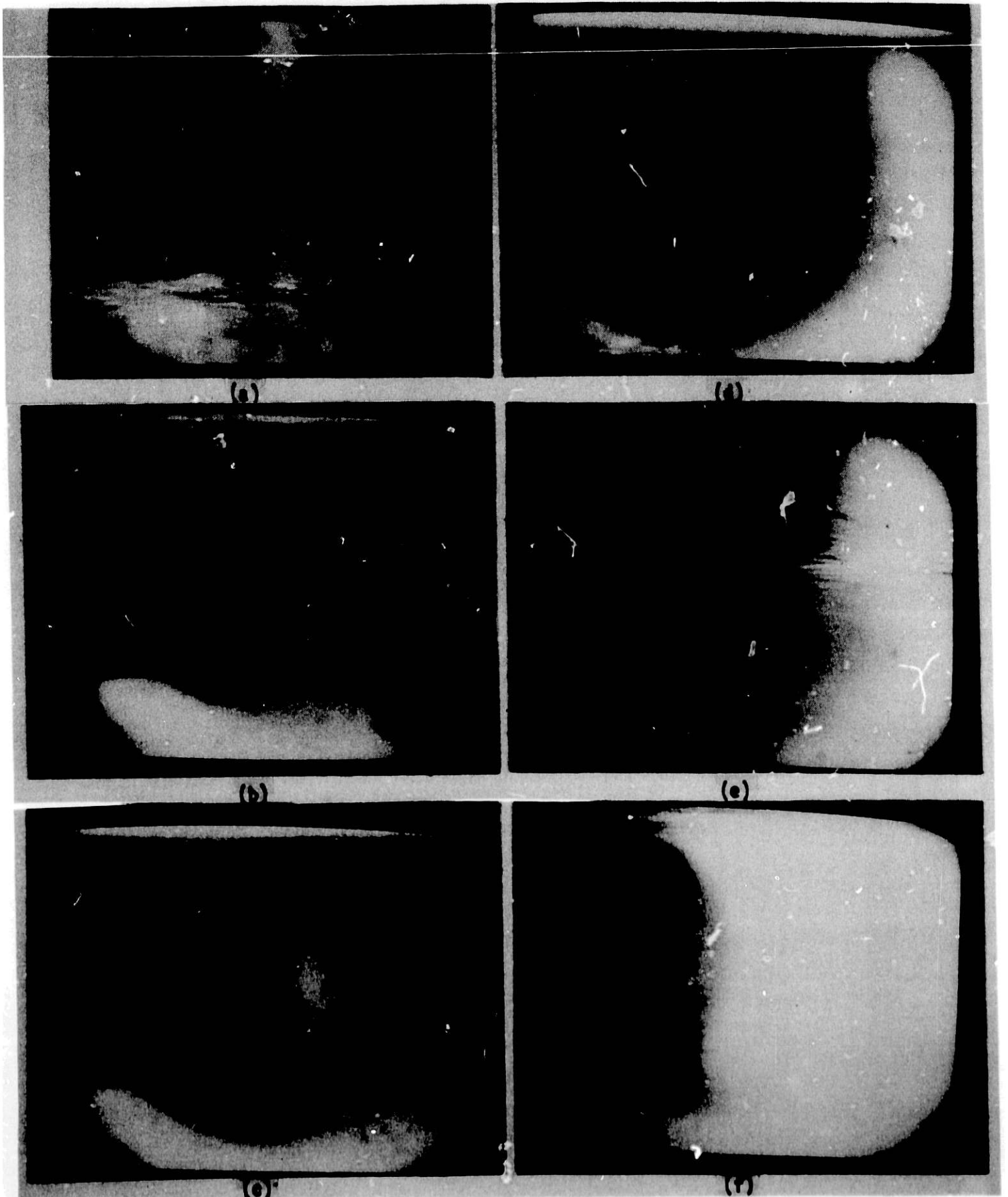


Figure 6. PHOTOGRAPHS OF VIDEO SEQUENCE OF COAL IGNITION AT INJECTION PINTLE

References

1. Keffer, J. F. and Baines, W. D., 1963, J. Fluid Mech. 15, pp. 481-496.
2. Field, M. A., Gill, D. W., Morgan, B. B. and Hawksley, P. G. W., "Combustion of Pulverized Coal," The British Coal Utilisation Research Association, Leatherhead, 1967.
3. Witte, A. B., Gat, N., Denison, M. R. and Cohen, L. M., "Coal Combustion Aerothermochemistry Research - Final Report," S/N 34731, 15 December 1980.

ACOUSTIC TDR TEMPERATURE MEASUREMENT

N. Gopalsami, S. H. Sheen, and A. C. Raptis

Argonne National Laboratory

Components Technology Division, Bldg. 308

Argonne, IL 60439

312/972-5925

FTS: 972-5925

Abstract

This paper presents some of the preliminary results on the fabrication and testing of an acoustic Time Domain Reflectometer (TDR) system targeted for temperature measurements in coal conversion systems.

Acoustic thermometry is based on the dependence of sound velocity on temperature. The technique consists of transmitting short pulses of sound waves in a thin rod with notches made at certain intervals along its length. The time interval between each pair of echoes, reflected by the notches, is measured and related to the average temperature of the corresponding segment.

A feasibility study performed at Argonne National Laboratory concluded that acoustic TDR is feasible for temperature measurements and profiling in coal conversion systems. This study, however, pointed out that the success of the thermometer in the hostile environment of a coal conversion plant will depend on the choice of sensor materials and on the development of appropriate electronics for isolating the echoes from the noise background.

The sensor materials to start with are tested in a laboratory furnace. Future work will involve testing the materials in a pilot plant and developing the time-interval measurement electronics. The main features of the proposed data processing system will be discussed.

## INTRODUCTION

Acoustic Time-Domain Reflectometry (TDR) is a method of temperature measurement based on the principle that almost all materials exhibit a change in sound velocity with temperature. The method consists of transmission of an acoustic pulse through a thin wire in which several impedance discontinuities (notches) are incorporated; acquisition of the reflected signals from the discontinuities; and the measurement of time intervals between successive reflections, which are then related to the average temperatures of the corresponding segments by calibration.

The thin-wire acoustic temperature sensor was first envisaged by Bell in 1957 [1]. Since then, several improved versions of acoustic sensors have been developed and tested in many applications due largely to the efforts of Lynnworth and his coworkers[2]. A major application has been in the nuclear reactor fuel pin temperature measurements where high temperatures and lack of visual access preclude the use of conventional thermometers. Temperature profiling of up to sixteen zones using a single waveguide has been reported [3].

In light of its great potential for high temperature applications, Argonne National Laboratory investigated the feasibility of using ultrasonic thermometry in coal conversion processes [4]. Thermocouples and other conventional thermometers proved to be inadequate because of the adverse environments prevailing in the reactors or combustors. The success of the ultrasonic thermometry, as the study concluded, is critically dependent on two factors: one on finding a good sensor material which will show good sensitivity to temperature and at the same time will withstand the hostile environment; and the other on developing appropriate electronics that will isolate and detect the echo peaks from the noise background. The noise sources are due to particle impingement and other mechanical perturbations inflicted on the sensor wire. The echo detection electronics of the available systems, based on zero crossing or on direct peak detection, will not perform adequately in a noisy situation.

This paper presents some of the preliminary results pertaining to the fabrication and testing of the thermometer and to the testing of sensor materials. A brief outline of the proposed signal processing system is also presented.

### THE ULTRASONIC THERMOMETER

A bench type of ultrasonic thermometer was designed, fabricated and tested in the laboratory. It consists of a transducer attached to a waveguide by which acoustic waves are propagated and interrogated for temperature measurement.

The transducer, as shown in Fig. 1, is basically a nickel wire around which a coil is wound about half-wavelength long. A ferromagnetic material such as nickel changes (contracts) in length on the application of a magnetic field, called magnetostrictive property [5]. A permanent magnet is placed adjacent to the coil for producing a d.c. magnetic field (bias) which enables the transducer to be operated in the linear and highly sensitive range of the magnetostrictive curve. Exciting the coil with an alternating current sets up an alternating field superimposed on the d.c. field, thus producing an alternating type of strain (acoustic wave) in the nickel wire.

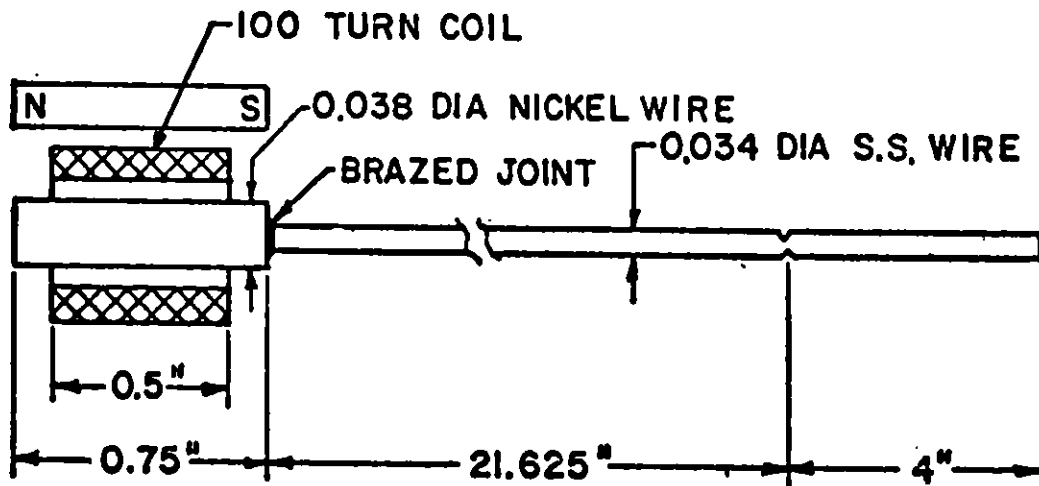


Fig. 1. Magnetostrictive Transducer.

The nickel wire is brazed to a stainless steel wire which has a notch at 4 inches from the end. The coil is excited by a Panametrics pulser/receiver with an electrical pulse of about 150V and 70 ns wide. Fig. 2 shows the received echo waveforms in which the first echo corresponds to the notch, the second to the end reflection and the third due to reverberation. The center frequency of the echo signal is around 100 kHz.

For comparison, a 100 kHz piezoelectric transducer (Dunegan/Endevco, 0.5 inch dia.) was tested by epoxy joining a stainless steel rod of 0.15 inch diameter and 4 inch long reflection zone. Fig. 3 shows the received echo waveforms for an input excitation that is similar to the magnetostrictive case. Evidently, the magnetostrictive transducer provides sharper echoes than the piezoelectric type. This is generally true since the former has relatively a low Q-factor and broad bandwidth.

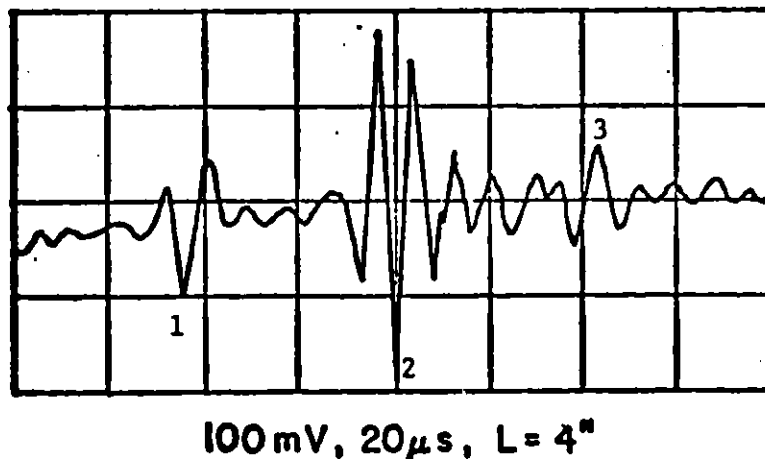


Fig. 2. Magnetostrictive Transducer Performance.

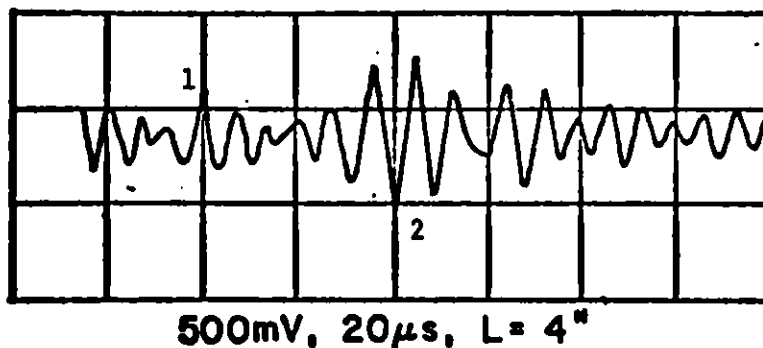


Fig. 3. Piezoelectric Transducer Performance.

### TESTING OF SENSOR MATERIALS

The experimental setup for the materials testing is shown in Fig. 4 which consists of the ultrasonic thin wire sensor, a pulser/receiver, delay gate, time interval counter, oscilloscope and oven. The purpose of the delay gate is to isolate and output a desired pair of echoes for time interval measurement. The time interval counter (HP model 5370A) is capable of providing  $\pm 20$  ps resolution. Its start and stop channels may be triggered at predetermined voltage levels by positive or negative going signals. It has

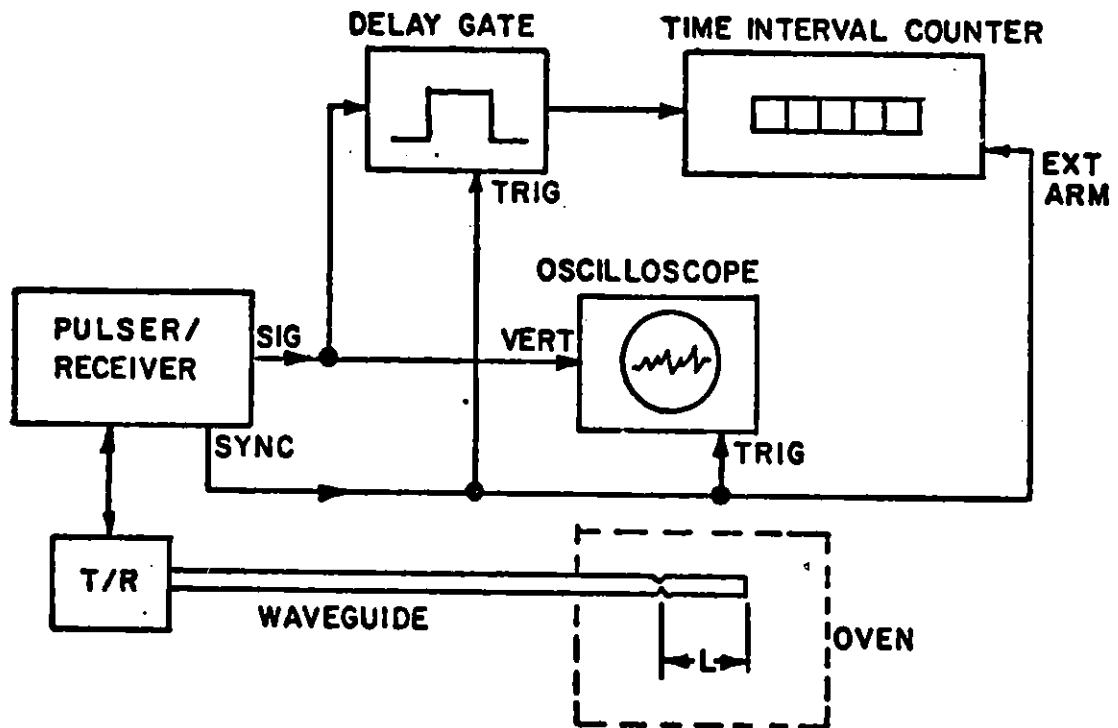


Fig. 4. Experimental Setup for Materials Testing.

statistical averaging features such as mean and standard deviation.

Two in-house materials, namely stainless steel 308 and an alloy of tungsten and 25% rhenium, were tested for sensitivity over a temperature range from ambient to 1100°F (limited due to the use of brazing joints). Fig. 5 shows the transit time (normalized to its value at the ambient temperature) versus temperature curves for the two wires. The values were reproducible after a few cycles of heating and cooling. The temperature in the oven was measured by means of a chromel-alumel thermocouple.

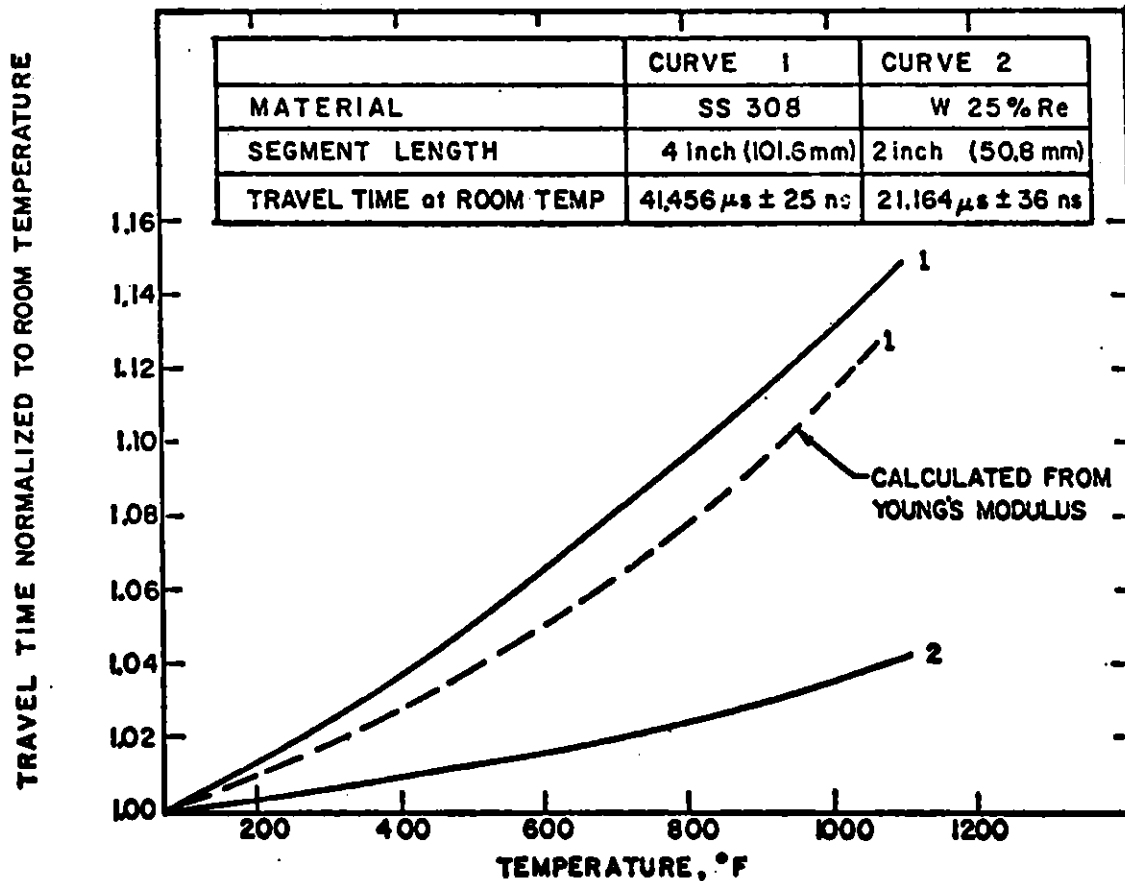


Fig. 5 Acoustic Temperature Sensitivities of Materials.



The dotted line in Fig. 5 shows for comparison the transit time values for stainless steel 304, calculated from the formula for velocity of sound:  $v = \sqrt{E/\rho}$ . The values of Young's modulus, E, and density,  $\rho$ , at various temperatures were obtained from a Handbook [6]. The deviation of the experimental values from the calculated ones maybe due to the use of different types of stainless steel (308 and 304).

The temperature sensitivities of stainless steel and tungsten-rhenium alloy are respectively 15% and 4.3% for 1000°F change. Their melting points are correspondingly 2600°F and 5666°F. Pending further tests, the tungsten-rhenium alloy is hence potentially useful for high temperature application despite its low sensitivity.

#### PROPOSED SIGNAL PROCESSOR

A generalized correlator was proposed for echo detection and time delay estimation in the ANL feasibility study [4]. The generalized correlation is defined as the inverse fourier transform of (frequency) weighted cross-spectral density function. It was shown by computer simulations that sharp correlation peaks can be produced by using appropriate weighting function in the generalized cross-correlation of the received echo signal and a reference (noise-free) echo. The choice of weighting function is based on the knowledge of noise statistics. For example, a weighting function based on the reciprocal of the noise spectral density was shown to provide good results.

#### CONCLUSION

A magnetostrictive type acoustic TDR system was fabricated and tested in the laboratory. Its performance towards the targeted thermometric application was found to be satisfactory and in fact superior to a similar piezoelectric system. Two in-house materials, namely stainless steel and a tungsten-rhenium alloy, were tested for acoustic temperature sensitivity. The stainless steel has a better sensitivity than the tungsten-rhenium alloy. But the latter has a high melting point and is a proven high temperature thermocouple material in nonoxidizing atmospheres. Further materials testing is, however, required and it will include ceramic materials as well as refractory metals and their alloys. After evaluating the materials in the laboratory, they will be field-tested to assess their performance capabilities in the hostile environment of coal conversion systems.

**REFERENCES**

1. J. F. W. Bell, "The Velocity of Sound in Metals at High Temperature," *The Philosophical Magazine*, Vol. 2, 1957, pp 1113-1120.
2. L. C. Lynnworth and E. P. Papadakis, "Ultrasonic Thermometry," Proc. 1970 Ultrasonics Symposium, San Francisco, CA, October, 1970.
3. K. E. Kneidel, "Advances in Multizone Ultrasonic Thermometry Used to Detect Critical Heat Flux," *IEEE Trans. on Sonics and Ultrasonics*, Vol. SU-29, 1982, pp. 152-156.
4. N. Gopalsami, A. C. Raptis and T. P. Mulcahey, "Monitoring Temperatures in Coal Conversion and Combustion Processes via Ultrasound," Argonne National Laboratory Report, ANL-FE-49622-TM09, 1980.
5. J. Blitz, Fundamentals of Ultrasonics, London: Butterworths, 1967.

APPLICATION OF THERMALLY-ACTIVATED GAS CANISTERS IN MIS OIL SHALE RETORTS\*

J. Ronchetto, J. Campbell, E. Frohwein,  
J. Clarkson, V. DuVal and W. Miller  
Lawrence Livermore National Laboratory  
P.O. Box 808, L-207  
Livermore, California 94550  
Phone: (415) 422-6450  
FTS: 532-6450

Abstract

We have developed and field tested thermally-activated gas canisters for use as temperature sensors during modified in-situ (MIS) oil shale retorting. These instruments allow one to determine when known retort bed positions reach a predetermined temperature. From this information, the degree of flow uniformity through the bed can be determined. The main advantage of this concept is that the thermal sensors need no physical connection to their respective data acquisition instruments.

The construction and emplacement of these sensors is quite simple and inexpensive. In brief, a metal canister is filled with compressed freon (or other easily detectable gas) and sealed with a temperature sensitive cap. This cap is designed to open at a specific temperature. The released gas is then detected by analyzing the retort offgas using conventional gas chromatographic methods. The canisters are emplaced in the retort during construction. For the field test described here, we simply lowered them downhole onto the rubble pile. They are ruggedly designed to survive subsequent blasting operations.

Introduction

The successful operation of any modified in-situ (MIS) retort depends upon a number of key factors; but two of the most important are the sweep efficiency and the degree of oil destruction by burning, coking and cracking. We use the term sweep efficiency to refer to that fraction of the rubble pile that actually reaches retorting temperature.<sup>1</sup>

The sweep efficiency is a strong function of the fluid flow through the retort (i.e., the porosity and permeability distribution). In general, the sweep efficiency can be expected to be less than 100% and, in cases of severe channeling (e.g., Occidental Oil Shale Company, Retort 5),<sup>1</sup> less than 50%.

We have field tested a set of thermally-activated freon canisters that can map the shape of the flow field in an operating MIS retort. From this

-----  
\*Work performed under the auspices of the U.S. Department of Energy by the Lawrence Livermore National Laboratory under contract number W-7405-ENG-48 for presentation at 1982 Symposium on Instrumentation and Control for Fossil Energy Processes, June 7-9, 1982, Houston, Texas.

information, the process engineer can identify regions of nonuniform flow and, if necessary, take corrective action to maximize the sweep efficiency--i.e., oil recovery.

The freon canisters, which were ruggedly constructed to survive blasting, are emplaced in the retort during bed preparation. Later, during the retorting phase each canister releases its gas when a thermal front causes it to reach a preset temperature. The released gas is then detected in the retort offgas via normal gas chromatographic techniques. By using different freons, one can identify which canister, and therefore which location in the retort, reached the release temperature. By plotting the release times for the various canisters, a map is generated showing the shape of the flow field in the bed.

The principal advantages in using these canisters as thermal detectors are the low cost and the lack of a physical connection to the detector. In commercial-scale retorting operations it is often economically impractical to emplace thermocouples in the retort. Thus, these canisters provide an inexpensive means for determining the approximate shape of the retort front.

#### Principle of Operation

The freon canisters are activated by the steam/condensation front that travels through the retort ahead of the retorting front (Figure 1). The shape of the steam front has been found to closely match that of the retorting front,<sup>2</sup> however, it moves through the bed at a velocity 5 to 10 times faster.

There are two major advantages to activating the canisters with the steam front:

1. Because the steam front precedes the retorting front, it provides a predictive capability. This allows the process engineer more flexibility (and time) for developing and implementing a suitable control strategy.
2. The low temperature of the steam plateau (approximately 60-80°C) allows the use of a wide range of freon-type gases without concern for possible thermal degradation. (Many freons degrade above 150-200°C.) Freons have the advantage of being inexpensive, readily available and easily detected in trace concentrations in the offgas, and have moderate vapor pressures at the release temperatures.

#### Canister Construction/Gas Detection

The main canister body was constructed from two-inch-diameter schedule 80 steel pipe with welded closures at each end (Figure 2). One closure is machined to accept a standard freon gas-fill valve while the other contains a thermally-activated plug. The thermal plug consists of a brass cap soldered in place using a bismuth-based alloy having a eutectic point of 47°C (117°F). The canister closures are protected by two screw-on caps; one is modified and contains vent holes (to allow the freon to

escape) and also a lift ring used to lower the canister down the well bore to the rubble bed.

We used SF<sub>6</sub> and a total of four different freons in the canisters: F11, F12, 13B1 and F114. Each canister contained a total of approximately 600 cm<sup>3</sup> of liquified freon, either as a single compound or a mixture of two.

The released gases were detected using an automated gas-chromatograph system with an electron capture detector. The chromatograph used was a Varian model 3700 with a Hewlett Packard model 3388 integrator. The chromatograph operating conditions were:

Column:	1 meter x 3 mm stainless steel.
Packing:	Poropak Q, 100/120 mesh.
Carrier gas:	nitrogen, ultra high purity.
Detector temperature:	200°C.
Oven temperature program:	80°C hold two minutes, 80°C-140°C @ 20°C/minute, 140°C hold, total run time 10 minutes.

Prior to the field test the system was calibrated with SF<sub>6</sub> and freon standards.

#### Retort Emplacement

The freon canisters were field tested in the Rio Blanco Oil Shale Company (RBOSC) experimental Retort 1. The retort was nominally 60 x 60 feet square and 400 feet high; further details of its construction and operation are given elsewhere.<sup>3</sup> In brief, the rubble bed was created by successively blasting layers of shale into a void space mined at the base of the retort.

During construction of the retort we installed an array of 13 canisters at two levels in the shale bed, for a total of 26 canisters (Figure 3). The canisters were lowered onto the rubble bed through wells drilled from the surface (the wells were drilled for purposes other than emplacing the canisters). The actual layout pattern is shown in Figure 4; except for canister 11, the patterns for the two levels were identical.

After an array of canisters was emplaced and the subsequent layer of shale blasted, we analyzed the retort vent gas for freon to determine if any cans had failed; no freons were detected. Therefore we were confident that no canisters failed.

#### Results and Discussion

The results obtained from the canisters are summarized in Table 1 and Figures 5 and 6. The data are expressed in terms of the normalized steam front velocity. Velocities were calculated from the straight-line distance from the retort top to the canister, and the elapse time (days) from retort ignition to detection of the canister gas. The velocities have been normalized to the maximum value determined for all canisters at a given level.

Table 1. Summary of experiment results for freon canisters in RBOSC Retort 1.

<u>Canister No.</u>	<u>Gas Species</u>	<u>Front Velocity (Normalized)</u>	
		<u>Upper Array</u>	<u>Lower Array</u>
1	SF6	0.47	0.98
2	F11	1.0	1.0
3	F12	--	0.64
4	13B1	--	0.76
5	F114	0.164	--
6	SF6, F11	0.444	--
7	SF6, F12	0.651	0.87
8	SF6, 13B1	--	0.89
9	SF6, F114	--	--
10	F11, F12	--	0.81
11	F11, 13B1	0.122	0.82
12	F11, F114	--	0.74
13	F12, 13B1	--	--

A total of 15 of the canisters emplaced in the retort were detected, six out of 13 at the upper level and nine out of 13 at the lower level. The seven cans missed at the upper level resulted from chromatograph failure caused by a power outage, whereas the four at the lower level were triggered during the period when operating personnel were no longer in the field.

Despite these operating difficulties, the velocity data from the detected canisters provide a fairly good map of the flow field in the retort. Two features can be readily observed in the data shown in Figures 5 and 6. Note that the array view is approximately the same as Figure 4. First, in the upper region of the retort (between the top of the rubble bed and the first canister array) a higher permeability region appears to exist in the western half of the bed, and specifically in the southwest corner (Figure 5). Note that the canisters in the eastern portion (of the upper array) were triggered during the chromatograph outage, implying the steam front velocity in this region was lowest.

Secondly, the data from the lower array of canisters show the velocity distribution to be fairly uniform across the bed. Thus the apparent nonuniform flow in the upper region of the retort did not persist into the lower part of the bed. A least-squares fit of a plane to the velocity data shows a slightly higher gas flow near the western side of the bed. However, in general, the flow is remarkably uniform, implying a nearly flat, but slightly tilted, retorting front near the bottom of the bed. Such a uniform front signifies a good sweep efficiency for this retort.

#### Acknowledgments

The authors gratefully acknowledge the cooperation of the Rio Blanco Oil Shale Corporation, particularly Mr. Roy Hutson, for their assistance in conducting this work. The assistance of Dr. Stanley Grotch in preparing the three-dimensional plots is also deeply appreciated.

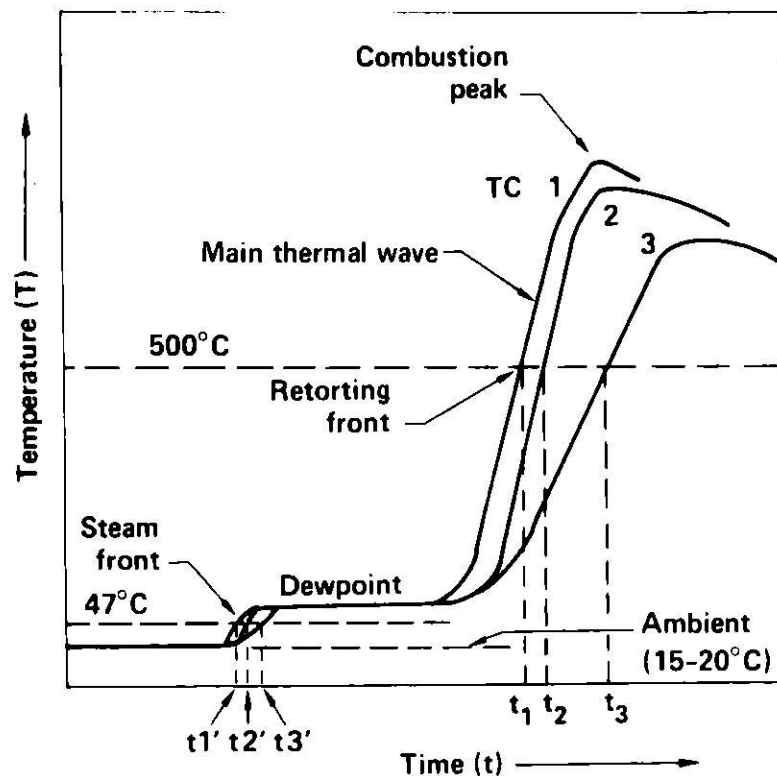


Figure 1

Hypothetical time-temperature history as measured by an array of three thermocouples in an oil-shale rubble bed. Note that a steam/condensation front precedes the main thermal wave. The shape of the steam front (47°C) and retorting front (500°C) are quite similar since both are mainly governed by the fluid flow (permeability) distribution in the bed.

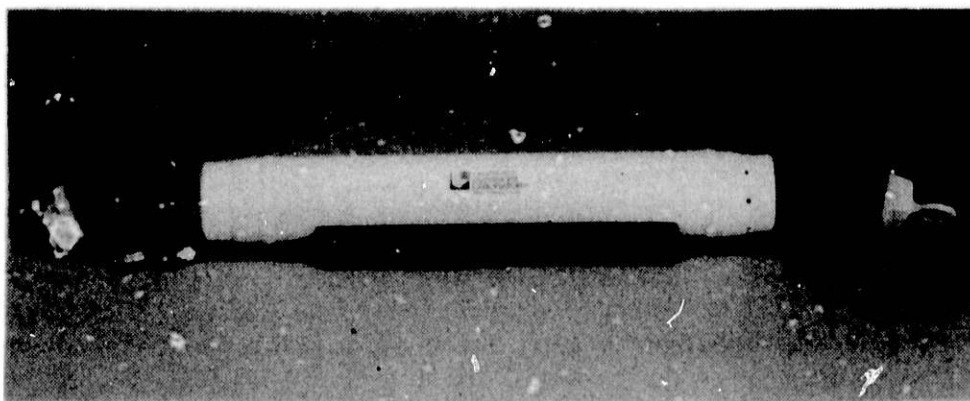


Figure 2

Exploded view of thermally-activated freon canister.

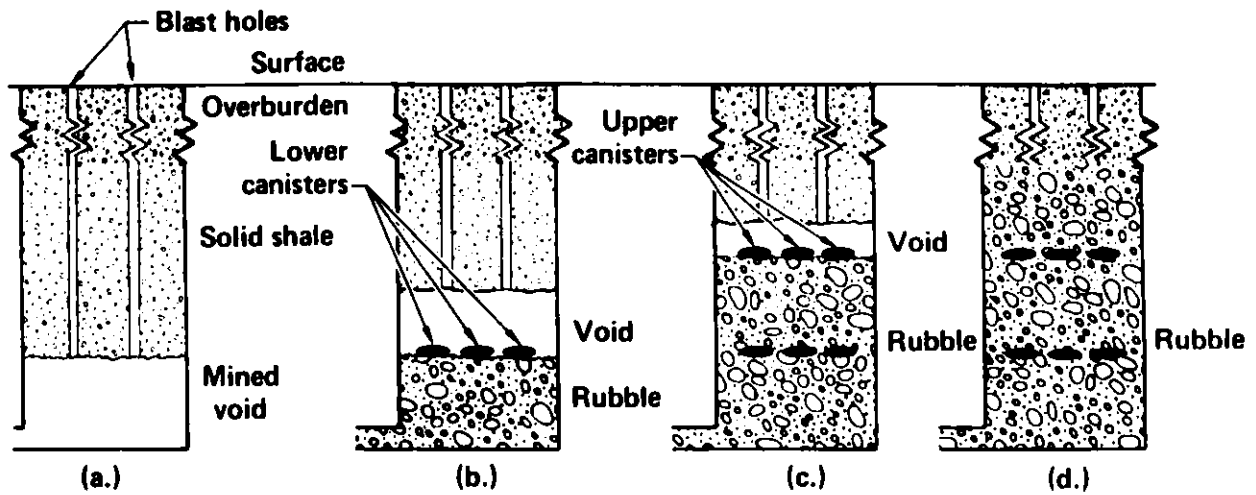


Figure 3

Schematic diagram of RBOSC Retort 1 showing: (a) the initial mined cavity with wells drilled from the surface, emplacement of the (b) first and (c) second array of canisters during retort blasting operations, and (d) the final rubble bed.

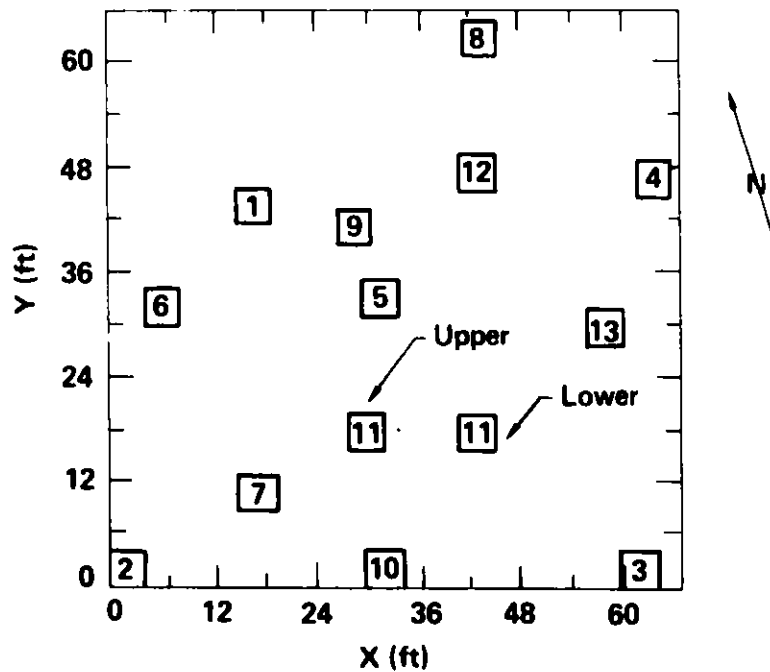


Figure 4

Plan view showing the layout of freon canisters across the rubble bed. With the exception of canister 11, the layout was the same for both the upper and lower arrays.



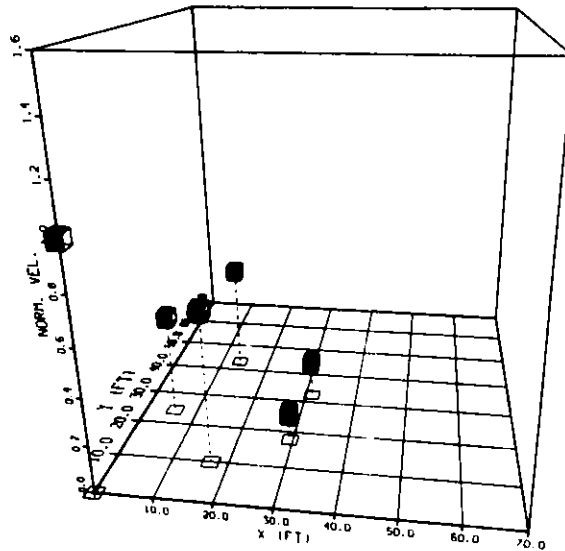


Figure 5

Normalized steam front velocity determined from gas release from freon canisters in the upper-level array as viewed looking approximately north. Only six of the 13 cans were detected (due to the effects of a power outage on the chromatograph.)

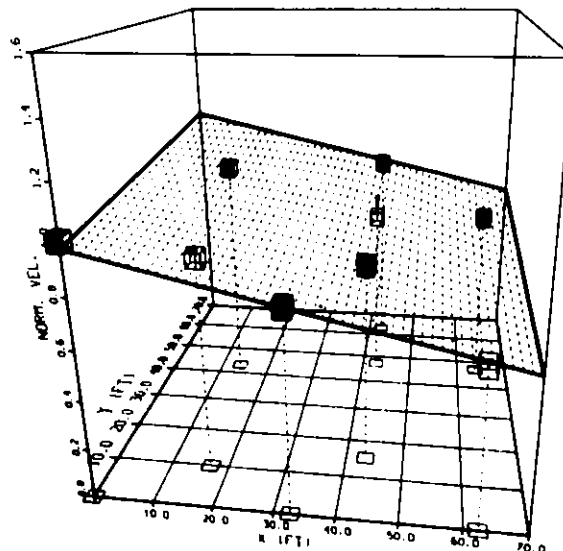


Figure 6

Normalized steam front velocity determined from gas released from freon canisters in the lower-level array as viewed looking approximately north. Nine of the 13 cans were detected. The plane represents a least-squares fit to the data and shows the approximate shape of the front.

References

1. M. L. Gregg and J. H. Campbell, "Sweep Efficiency Modeling of Modified In-Situ Retorts," in the Thirteenth Oil Shale Symposium Proceedings, Colorado School of Mines Press, J. Gary, Ed., (1980) p. 87.
2. W. A. Sandholtz, "Some Relationships of Thermal Effects to Rubble Bed Structure and Gas Flow Patterns in Oil Shale Retorts," in the Thirteenth Oil Shale Symposium Proceedings, Colorado School of Mines Press, J. Gary, Ed., (1980) p. 114.
3. K. L. Berry, R. L. Hutson, J. S. Sterrett and J. C. Knepper, "Modified In-Situ Results of Two Field Retorts," in the 15th Oil Shale Symposium Proceedings, Colorado School of Mines Press, J. Gary, Ed. (1982).

## DISCLAIMER

This document was prepared as an account of work sponsored by an agency of the United States Government. Neither the United States Government nor the University of California nor any of their employees, makes any warranty, express or implied, or assumes any legal liability or responsibility for the accuracy, completeness, or usefulness of any information, apparatus, product, or process disclosed, or represents that its use would not infringe privately owned rights. Reference herein to any specific commercial products, process, or service by trade name, trademark, manufacturer, or otherwise, does not necessarily constitute or imply its endorsement, recommendation, or favoring by the United States Government or the University of California. The views and opinions of authors expressed herein do not necessarily state or reflect those of the United States Government thereof, and shall not be used for advertising or product endorsement purposes.

AN ONLINE CORRELATION COMPUTER FOR NONINVASIVE  
MASS FLOWRATE MEASUREMENT IN DUCTS

F. Lenkszus and K. Porges  
Argonne National Laboratory  
Applied Physics Division, Bldg. 316  
Argonne, IL 60439  
312/972-6091  
FTS: 972-6091

Abstract

The technique of flow velocity measurement by correlation of the readout delivered by paired sensors has been known for 40 years and repeatedly demonstrated, with a number of sensor types, in homogeneous and two-phase flow. Hardware "correlators" based on parity correlation have been designed in several laboratories; more recently, parity correlator chip circuits have come on the market.

However, to obtain a reading of the mass flowrate in multiphase flow, the velocity readout must still be combined with a determination of the medium density. To accomplish this task, a microprocessor system is indicated, which then can also provide data display and storage, flow stoppage warning, and similar programmable functions.

With recent advances in microprocessor speed and price reductions, it has become practical to dispense with the hardware parity correlator and implement a fully functional covariance computer and peak locator, using commercial chip and board hardware in lieu of special chips and boards. This considerably improves reliability and accuracy of the velocity measurement while bringing down the cost.

A prototype unit will be described that can employ acoustic or radiation beam transmission, dielectric or conductivity sensor pairs for the velocity measurement, as well as any of these sensors for the medium density measurement, and delivers a mass flowrate readout at 0.1-2 second intervals. The system is based on an 8086/8087 microprocessor board, an analog-to-digital conversion board, and a bit-slice (2900) high-speed computing board that incorporates a Multiplier-Accumulator chip. The 8086 can be programmed in high-level language, allowing program improvements, with a standard commercial development system; a number of somewhat different programs, specifically designed for some flowmeter task and installation site, can thus be provided in EPROM, as plug-in chips or cards.

When one sets out to design an instrumentation system, it pays to define at the outset as clearly as possible the detailed tasks for each subsystem and the manner in which these must interact to make the whole perform in a certain way, determined on one hand by its intended use and operating environment and, on the other hand, by cost and availability of electronic hardware.

With regard to the first category, it is clear that much more is needed for industrial installations than for laboratory use. The ideal industrial instrument provides a single function readout and autonomously adjusts and aligns whatever component needs such services, including startup as well as restart after, say, a power failure. It should detect abnormal conditions in the measurand and announce these, upon a negative outcome of one or several tests; very incidentally, it would also provide those functions usually delivered by a "datalogger": information display and storage. In contrast, a laboratory instrument can replace all adjustment/alignment subsystems with manual controls, and may replace on-line computation with immediate off-line computation in addition to datalogging.

As concerns the electronic state-of-the-art, it is the immediate future that must be considered, which imposes a need for continuous and reasonably knowledgeable surveillance of the chip and board industry. What we are talking about is, nowadays, a dedicated subspecies of microcomputer in which specific functions are realized in software and firmware, in preference to a wired solution. This choice not only reduces unit cost but also makes the system adaptable, allowing changes indicated by practical operating experience without having to replace parts of the wired circuitry. On the other hand, the software can be transferred to another and improved system, as such systems become available, while hardware tends to become obsolete in a few years.

These general remarks apply especially to the field of robotics or the design of assembly and fabrication automata. In their simplest form, such machines have existed since the early 19th century -- the Jacquard loom of 1803 comes to mind -- whereas interactive devices which, e.g., can sense the position of the workpiece are a development that had to wait for the microcomputer, which now can provide the necessary complex feedback between sensing, computation, and machine displacement at speed.

The subject of this report, a correlation flow velocity meter, also goes back some time -- 40 years. During the first 25 years, this scheme could provide single measurements in a particularly difficult situation by recording with two or more sensors for a certain time and then digitizing and processing the data. The first simple correlator, using vacuum tubes, made its appearance in the 1950s. More capable correlators, with considerably faster action, were produced when discrete-component transistor circuitry was in its heyday. In the late 1960s, the first on-line correlator-equipped flow velocity meter was designed at Karlsruhe Technical University; soon thereafter, a similar, more elaborate instrument was built at Delft University (Netherlands) and at almost the same time, in England. The history of these on-line instruments paralleled the development of correlators intended for laboratory (off-line) use, where speed was less important than quality of performance. To achieve the needed speed at the then state-of-the-art, the on-line correlators had to sacrifice

some quality by resorting to parity correlation (in which the magnitude of fluctuations is discarded and only the sign is kept). Multiplication can thus be implemented in Boolean Exclusive/Nor circuitry which is both fast and cheap enough to allow deployment in many parallel units.

This kind of circuitry was later incorporated into a special chip, fabricated at the University of Edinburgh electronics laboratory from designs submitted by Bradford University staff. The chip design includes an ingenious means of peak location (which unfortunately discards information as it develops and thus does not allow comparison with other full-process correlators except for the final outcome). Following the early lead provided by the Karlsruhe group, the covariance peak is tracked by feedback steering the sampling rate which, in this feedback system, is proportional to the flow speed. This allows a theoretically unlimited velocity range. Practically, however, a sudden change in velocity can throw it out of tracking altogether -- a problem widely encountered with this type of first-order Servo system in other applications. The variable sampling rate also eliminates the possibility of noise reduction and antialiasing by Nyquist filtering of the input.

When our group at ANL first considered the project of building a special correlation processor for on-line use, this chip was available, as were a number of sophisticated laboratory-type correlators. Through study of techniques and algorithms used by laboratory instruments to compute the covariance, evaluation of parity correlation, scrutiny of the circuitry provided for robotics, together with a survey of the latest available chips and chip manufacturers' announced future plans and prognoses by experts, the conclusion was reached that it may no longer be unavoidably necessary to sacrifice quality by parity correlation. Multiplication rates of 100-200 kHz were projected for the new 16-biters about to be offered, and special multiplier chips were becoming available to deliver a product to an accumulator built into the chip in about 0.1  $\mu$ s. This suggested a design based on one of the new microprocessors, with speed enhancement just for the correlation task. The manner of routing samples could be set up in such a way as to cover a large time span with relatively few sample points, and tracking could thus be provided by a direct peak location scheme that could be running during the computation process and thus terminate further acquisition when the peak had been located. Further routines would be needed to guard against false peaks, and additional programs would cover startup and channel adjustment -- all these being tasks for which skilled technicians are used in laboratory correlation work, but which needed to be automatized for industrial deployment -- in almost exact analogy to robotics design.

In the meantime, a number of these programs have been fully detailed. A speed-enhancer and associated DMA was designed and built in prototype, based on bipolar (bit slice) circuitry and incorporating a multiplier-accumulator (MAC) chip. The speed of the bit slicer keeps the rate to five multiplication-addition sets per microsecond. As chip technology advances, this could be doubled; for the present, a complete scan over about one second maximum transit time, say, a "turndown ratio" or velocity range of about 50, takes less than 30 ms, whereas acquisition of 1024 sample pairs for a new processing run takes

100 ms at a 10 kHz sampling rate. A number of additional programs can be run within the 70 ms thus available, and a readout rate of 10/sec can be achieved. This rate is adequate for a gas/solid line (typical speed: 3 cm/ms; sensors separated by one pipe diameter, say, 5-6 cm, thus yield a transit time or covariance peak offset of 20 samples). For slurry flow, sampling at 1 kHz is indicated (by similar considerations) and the correlation processing time thus becomes trivial -- 3% of the acquisition interval. These considerations suggest that, except perhaps for special situations, present processing speed may be adequate for any flow-metering application. They also emphasize one of the design goals of this undertaking: since a variety of noninvasive correlation sensors have worked in laboratory loops and test rigs which used a wide range of media flowing at various speeds through pipes of various sizes, a great deal of flexibility was called for in the processor. With this remark, we may now briefly describe some detailed functions of the system, illustrated in Fig. 1, which is a functional (rather than specific) block diagram.

Analog signals from a pair of sensors enter at top left. Analog channels separate AC and DC components; AC signals are digitized in ADC units and passed on to the unit labeled  $C_t$ , which checks samples for overflow and trims the gain in the analog channels, as indicated by the arrows. Thus, the gain is automatically set to optimum upon start-up by means similar to other applications of feedback gain control, e.g., in nuclear surveillance channels.  $C_t$  also sends data to the memory M and initiates DMA transfer of data to the speed enhancer board, as well as pickup of computed covariance point blocks from that board. The format of speed enhancer input words is 1 byte, whereas the computed covariances are digitized in 2-byte words.

Now the computation unit  $C_t$  produces a trial transit time  $t_{ud}^*$  which must be verified and corrected. (For a variety of reasons, correlation velocity systems tend to produce a meter factor, deviating from the true mean velocity by as much as 30%.) Confirmation involves a comparison of location and shape of the latest sample with preceding memory-stored covariance peak locations and widths -- a simple type of pattern recognition. If the test fails, then a fresh batch of data may be called while certain statistical tests are applied. The time scan is widened so as to catch a coast-down situation. If renewed computation and tests fail again, a flow failure is announced. These tracking routines are shown as a function box  $R_t$ . A somewhat different routine is specified for start-up, when all programs are brought into action until the peak is found, and for normal running which may use a shortened routine. The provisional transit time being accepted, it is corrected for meter factor (box CORR) from a table T that can store factors appropriate to different situations.

Return now to the top of the diagram. On the right side, signals from additional sensors deliver analog signals from which the medium density or its equivalent can be computed. Still more sensors, used for correcting the density signal for temperature or moisture effects, are indicated. As the density measurement is fully as important as the velocity measurement if mass flowrate readout is needed in a situation where density can change, i.e., in two-phase flow, it pays to go to some trouble, including feedback stabilization, etc., to make this channel work. Tracking is clearly needed where the

density may change fairly drastically, and a correction (which, in this case, may make use of temperature, etc., information) is provided, together with a table that will have to be prepared by laboratory measurements, including both bench tests and loop runs.

Corrected velocity and density measurements now can be combined to read the flowrate, or perhaps the solid feedrate. This information is turned over to the datalogger which provides storage and regular, as well as demand display functions.

The left and right sides of Fig. 1 thus have similar functional features. To be sure, the velocity program (left side) can be exactly specified, whereas programs indicated on the right side are necessarily specific for a number of available sensors (such as capacity or conductivity sensing, beam transmission sensing, etc.). Moreover, the accuracy of the density readout depends on the sensor, choice of type, and detailed geometry, much more than on the algorithm (straightforward for most sensor types), while the accuracy of the velocity reading clearly depends in large measure on the program. For those reasons, rather than from a wish to emphasize the importance of this sub-program, some practical details will now be described.

Figure 2 shows the system as a hardware (rather than functional) block diagram. The correlation channels share an ADC that is equipped with several Nyquist filters so as to permit different sampling rates up to 10 kHz. A faster version is readily implemented with more expensive ADC arrangements or chips. Samples are temporarily stored on a board based on an 8085 CPU, with capacious memory and I/O functions. This board provides the feedback channel gain adjustment discussed earlier. In addition, it could compute sample variances as an aid in determining loss-of-flow, if a faster CPU chip (such as an 8088/8087) could be provided. Samples are trimmed to the 7-bit plus sign format required by the speed enhancer system and transferred in DMA mode via the 501 board in blocks. Sampling continues during the various computation routines discussed above, hence the memory is continuously refreshed.

The master CPU board, based on an 8086 with 8087 arithmetic enhancement, communicates with all peripherals through its I/O facilities. It performs peak tracking, acceptance testing, and decision routines. The density channel uses a voltage-to-frequency converter so as to integrate over density fluctuations during the time the velocity sensors pick up 1024 samples each. Use of a VFC also eliminates the possible need for a Nyquist antialiasing filter in this channel. Density samples are directly transferred to the master CPU board. For diagnostic purposes, a graphics display has been incorporated, receiving blocks of computed data points and other information by DMA transfer on the system bus.

The speed-enhanced covariance computer is shown in Fig. 3. The micro-code that runs this operation uses words of 40-bit length that are cycled in various loops to fetch certain sequences of data words from the U-store and D-store directly to the two input ports of the multiplier/accumulator. Every 1024 multiplications, the accumulator contents are transferred, shifting down three times, to the sum-of-products store. An offset of one

sample is introduced for the first 40 product sums, then an offset of two for another 20, then 4, 8, and finally 16 for the last 44 points, covering a total delay of 1,024 sampling intervals with a quasi-logarithmic time scale. As already indicated, this complete coverage takes about 30 ms.

This direct computation of the covariance can be compared with a Fourier Transform routine, used in many of the laboratory correlators. Because of the greater complexity of the program, which involves 10 butterfly cycles for a 1024 by 1024 FFT, one would estimate a speed of an average of one complete operation per ms, yielding 10 ms for a complex FFT, or 20 ms for both channels. A convolution, requiring another ms, is followed by the computation and weighted averaging of the slope of the phase associated with the complex cross-power spectrum. All this might take about the same time, 30 ms, but requires a more complex speed enhancement board. For off-line analysis, this method, known as "Cepstrum" analysis, has found increasing applications in the last few years as it exploits the available information somewhat more efficiently than the straightforward covariance computation in the time regime.

As a final topic, we would like to point out an instructive analogy between the covariance computation at increasing offset between two sample sets, i.e., a shift in time, and the operation of a target-seeking automaton. Considering a type of target-seeking in which the general direction of the target is known but changes continuously, one might change the orientation of the "pointer" in a series of discrete steps and check after each step whether the cosine of the angle between the target direction and the pointer is increasing. In correlation processing, on the other hand, one computes the convolution

$$\text{cov}(u,d)_k = \sum_{j=0}^{N-1} d_j u_{j+k} \quad ; \quad k = 0, 1, \dots, K-1$$

from a set of N samples d and N+K samples u. The above equation also, as it happens, denotes a set of scalar products of N-space vectors  $\vec{U}$  and  $\vec{D}$ ,

$$\vec{U} \cdot \vec{D} = |U| |D| \cos \theta$$

and thus expresses something closely similar to a successive rotation of the U-vector by 90° in N-space (the analogy would be exact for a cyclic rotation of d-samples). As this stepwise rotation brings the vectors closer to alignment, the cosine evidently will increase until at some point it is a maximum or, for a situation where the correlation is 100%, unity. The two vectors also could point in opposite directions, in the case of anticorrelation. Finally, when there is no correlation at all in two sets of samples, then the average angle between the corresponding N-space vectors amounts to 90°, whence the scalar product converges towards zero.



In a practical sense, this specific analogy suggested the modus operandi of the correlation processing routine adopted in the ANL design. In lieu of building the entire covariance span slowly, sample-by-sample, upon the arrival of each new sample pair, as is the established route of the described parity correlation schemes, the covariance is run up, point-by-point, from zero delay until the cosine peaks.

There is also another more general message conveyed by robotics: cost-effective design of any such system should maximize software and supplement this only where necessary with speed enhancement; the latter again should make use of available chips and/or boards rather than proprietary chips. A recent development could modify this strategy somewhat: uncommitted logic arrays with potentially high speed are appearing on the market, and such chips could allow specific hardware design at an attractive cost -- a single charge for mask production, allowing unlimited replication. At present, arrays are still modest in size and scope, but will indubitably grow larger as a market for this kind of device develops. Other future developments would be a version of the system that relegates the sample management task to a microcontroller chip such as the INTEL 8096, providing on-chip program and data memories, an enhanced arithmetic, and programmable I/O. A master CPU based on INTEL 80268 plus matching floating point (when available) would allow routine processing at 5 to 10 times faster rates through pipelining and additional internal register capacity.

The system we have described thus shares a problem which has been quite general in the field: when the work has been finished and the package is ready for production, the specific hardware has become somewhat obsolete. While this may be annoying to the designer, the user is more likely to be gratified if something is offered which works, and works better and faster than anything previously available, which has been the aim of this project.

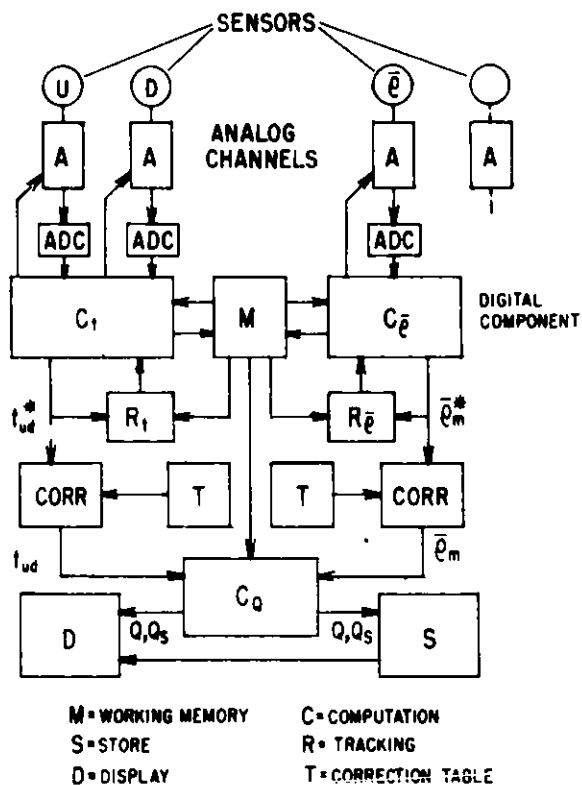


Fig. 1. Systems Block Diagram, On-Line Correlation Velocity/Density Computer (CVDC)

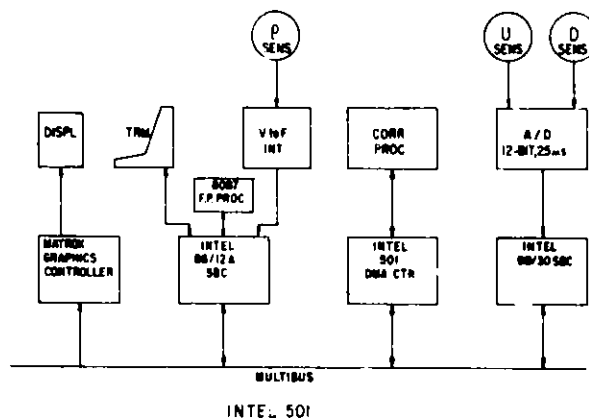


Fig. 2. Hardware Block Diagram, CVDC

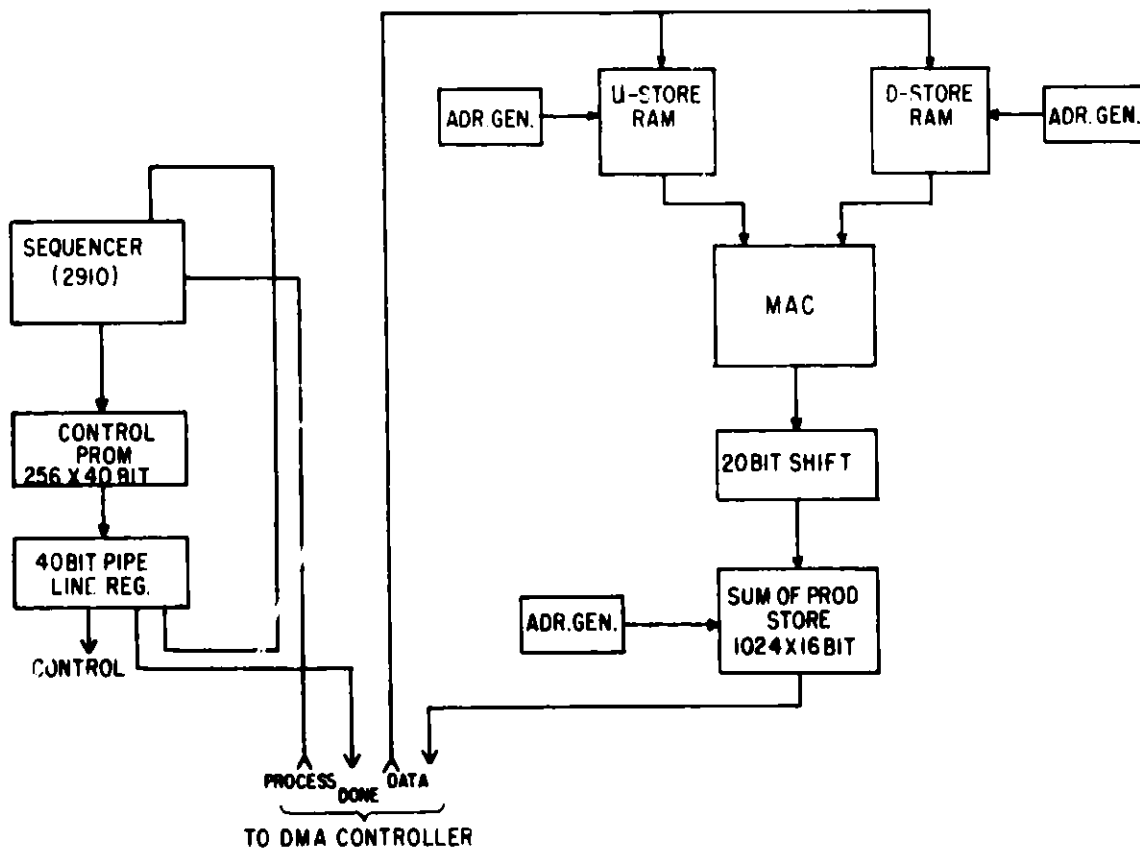


Fig. 3. Speed Enhancer Board, Velocity Computation

DEVELOPMENT OF NEUTRONIC MASS FLOW METER\*

T. Gozani, J. Esterl, J. Goodman, and H. Bernatowicz  
Science Applications, Inc.  
5 Palo Alto Square  
Suite 200  
Palo Alto, CA 94304

Abstract

The development of a truly non-intrusive neutronic mass flow meter for measurement of mass flow rates in very harsh environments such as exist at coal liquefaction plants is described.

The state-of-the-art in the 14 MeV two-phase flow measurements is briefly reviewed, along with the principles of the measurement techniques. A conceptual system is discussed delineating all its main components. A theoretical model is developed that allows analysis of the experimental data and extrapolation to plant conditions. The results of experiments performed using a liquid/solid loop are described. These experiments demonstrated that two-phase flow velocities can be readily measured to precisions better than 1% using commercially available and reliable components.

---

\*Work supported by the U.S. Department of Energy, Pittsburgh Energy Research Center

DEVELOPMENT OF NEUTRONIC MASS FLOW METER\*

T. Gozani, J. Esterl, J. Goodman, and H. Bernatowicz

Science Applications, Inc.  
5 Palo Alto Square  
Suite 200  
Palo Alto, CA 94304

Introduction

This paper describes the development of a non-intrusive neutronic mass flow meter for continuous measurement of mass flow rates in environments where more conventional intrusive or non-intrusive devices could not perform.

The main objective of the overall program is to research, develop, and build a pulsed neutron mass flow meter capable of measuring the mass flow rate of coal liquefaction plant vacuum bottoms and other streams, which are both corrosive and erosive and are at high temperature and pressure.

Background Review

Instrumentation currently being used for two-phase mass flow rate measurements has generally evolved from single-phase measurement techniques. An extensive review of the state of the art techniques for two-phase flow measurements is given in References (1-4). Methods for measuring the various thermal and hydraulic parameters associated with two-phase flow phenomena are surveyed in these references. These evaluations identify the known and potential difficulties associated with the experimental procedures and the potential gains that might be achieved with more research and development effort, and thus provide insight as to which techniques appear to deserve further consideration and development.

In general, the adaptation of single-phase mass flow rate measurement techniques to two-phase flows has not been completely successful because of the unusually severe operating conditions of the two-phase flows and the complex analytical modeling required to relate the instrument response to the flow phenomena. For steam-water flows encountered in simulation experiments of nuclear reactor accidents, various combinations of instruments have been used to calculate the total mass flow rate. They are a gamma densitometer, a turbine meter, and a drag body. The latter two devices are intrusive type instruments whereas the gamma densitometer measurements are made completely outside the fluid carrying pipe. For the particle-liquid flows at the pressures and temperatures of interest for

---

\* Work supported by the U.S. Department of Energy, Pittsburgh Energy Research Center.

coal liquefaction plants, these intrusive type instruments are highly undesirable since their useful lifespan in a harsh operating environment, such as the coal-solvent slurry, would be severely limited. There is, therefore, a strong incentive to develop a truly non-intrusive mass flow rate measuring technique that is unaffected by the thermodynamic conditions inside the pipe, and the environment outside it.

Recently Kehler and co-workers<sup>(5-8)</sup> have published data from their pulse neutron analysis (PNA) velocity measurements. The feasibility of PNA techniques for the measurement of two-phase steam-water velocities and mass flows was shown experimentally in tests at the Idaho National Engineering Laboratory and at the PKL facility operated by KWV at Erlanger, Germany.

In these tracer measurements the oxygen in the water molecules was tagged (activated) by the  $^{16}\text{O} (n,p) ^{16}\text{N}$  reaction. This reaction results in a radioactive tracer of short half life (7.13 seconds) that emits highly energetic gamma radiation of 6.13 MeV. The fast neutrons required for the activation of oxygen were produced by the  $d(t,n)\alpha$  reaction in a portable pulsed neutron generator that emits no radiation except when it is being operated. The bulk of Kehler's work has focused on two-phase steam-water flows related to nuclear reactor safety analysis experiments. Other researchers<sup>(9-11)</sup> have studied the PNA technique in various flow geometries also related to nuclear reactor safety analysis experiments. That work also demonstrated the fundamental feasibility of the PNA technique to measuring gas-liquid flows. Porges and co-workers<sup>(12)</sup> have studied the feasibility of using PNA in the measurement of particle-liquid flow velocities. Their results were very promising in that mass flow rate accuracies of less than 1%, compared to a timed diversion weigh tank mass flow rate measurement, were achieved.

While there are other methods to measure two-phase mass flow rates, none other appear as promising, as non-intrusive, and as flexible as the nuclear one. As discussed above, there is a significant amount of background data that lent confidence to the practicality of designing, building, and successfully using such a device in a coal liquefaction plant. The goal of the work discussed in this paper is to integrate prior knowledge and experience into a practical, field, working instrument.

#### Mass Flow Measurement by Nuclear Technique

The mass flow rate measurement is determined from the product of slurry density,  $\rho$ , slurry velocity,  $V$ , and slurry flow cross sectional area,  $A$ . Thus, the mass flow rate,  $M$ , is given by:

$$\dot{M} = \rho AV \quad (1)$$

In this respect, the slurry mass flow rate is a calculated quantity and is not measured directly such as in the weigh tank-time determination which is a true mass flow rate measurement. However it is quite often beneficial to know separately the velocity and especially to monitor continuously the total stream density. The slurry flow cross sectional area

is easily calculated from the internal pipe diameter. The mean slurry density is determined by conventional and accurate gamma transmission densitometry. The mean slurry velocity is determined by a time-of-flight measurement using the pulsed neutron activation (PNA) tracer technique.

In measuring fluid velocity by the time-of-flight tracer technique, a fluid element is tagged at some distance upstream of a detection station, usually by the injection of a detectable tracer. Time-of-flight velocity is calculated as the ratio of the distance between the injection and detection locations to the time lapse between the time of injection and detection. In applying the PNA technique, a fluid volume element is activated by a neutron source. The induced activity is measured downstream and the time delay between the activation pulse and the arrival of the induced activity downstream gives a direct measure of time-of-flight velocity. Thus, with the PNA tracer technique, problems associated with tracer injection are eliminated, however, other problems such as tracer dispersion possibly causing a degraded time-of-arrival should be addressed.

The key feature of the mass flow measurement method studied here is the use of the pulsed neutron technique. The pulsed neutron activation (PNA) technique uses neutrons from a commercial neutron generator to produce, in the slurry material, radioactive products with half lives long enough to be subsequently measured. Commercial neutron generators use the  $d(t,n)\alpha$  reaction to produce pulses of 14 MeV neutrons with controllable pulse width and frequency. When these neutrons bombard a substance, they interact with its atomic nuclei in several ways, including: inelastic scattering,  $(n,p)$ ,  $(n,\alpha)$ ,  $(n,2n)$  and  $(n,\gamma)$  reactions. Some of these reactions lead to radioactive products with half-lives long enough to be subsequently measured. The three most abundant elemental constituents of coal, or coal derived liquids, that can be activated are C, O, and Si. Unfortunately, the half lives of the products of the neutron reaction on carbon are too short to be used for velocity determination. The  $(n,p)$  reactions on  $^{16}\text{O}$  and  $^{28}\text{Si}$ , and thermal neutron capture in aluminum, leading also to the same tracer as silicon, create radioactive products with half lives of 7.13 seconds and 2.27 minutes, respectively; these elements represent the best choices for tagging in the present application of coal liquefaction plants. Both tracers can be measured simultaneously, as is shown in Figure 2. However, the oxygen provides, by far, the most effective activated tracer.

#### Conceptual Nuclear Mass Flow Rate Meter

A schematic of a conceptual nuclear mass flow meter, as shown in Figure 1, delineates all the main components of the system, namely:

- Pulsed 14 MeV neutron source (with variable pulse widths, e.g., 0.1 to 1 second and repetition rates of 0.05 to 5 pulses per second).
- Composite shielding, to provide biological shielding against radiation, to reduce background radiation at the detector, and to maximize useful neutron flux across the pipe.

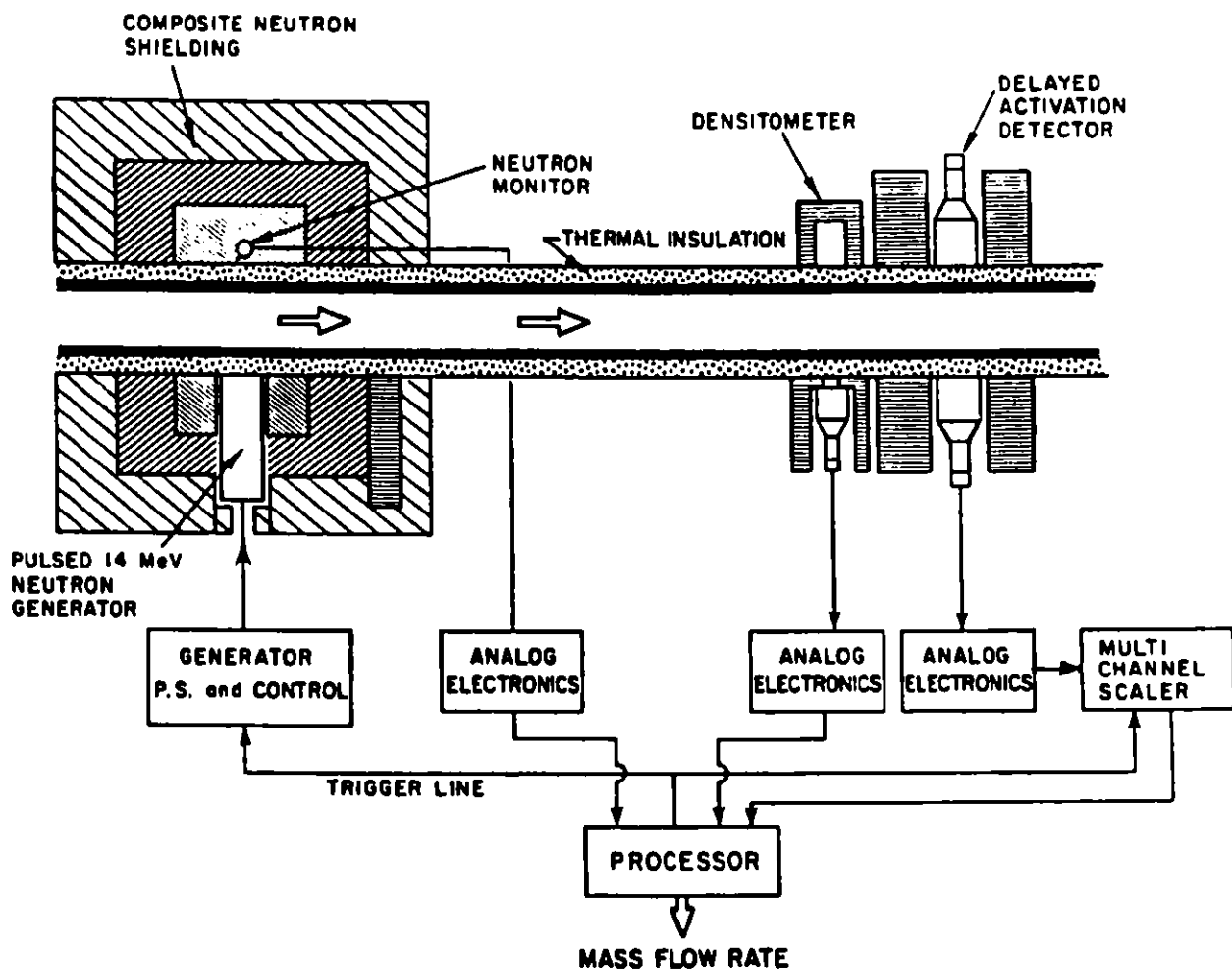


Figure 1. Schematic of Neutronic Mass Flow Meter

- Fast neutron detector to monitor the 14 MeV neutron production by the accelerator.
- Gamma ray densitometer to determine independently the density of the flow.
- Gamma ray detection system to measure the activity of the tagged elements, consisting of efficient gamma ray detector (BGO, NaI) with proper shielding.
- Analog electronics to process the signals from the various detectors (neutron detector, densitometer detector, and the scintillation counter for the activation detection).
- Multi-channel time analyzer to determine the arrival time of the activity and its time distribution.
- Data processor and control unit to trigger the pulse sequencer, to acquire data from all sensors, to process them and yield mass flow rate and other quantities of interest.

### Theoretical Modeling

In this section we discuss the theoretical tools that allow us to interpret the experiments reliably and permit us to extrapolate the data to conditions prevailing in the coal liquefaction plant.

A PNA velocity measurement entails the following: a short burst,  $t_n$ (sec), of neutron activates a slug of the stream with an effective length  $l_n$ (cm). The activity is measured  $t$  sec later with an appropriate gamma ray detector. The detector has an effective length  $l_d$ (cm) and is located  $Z$ (cm) down stream. The radioactivity time constant is  $\lambda$ . Thus after time  $t$  the initial activity decayed by  $e^{-\lambda t}$ . If the activated or tagged slug and the effective detector length were very narrow, and no dispersion of the tagged tracer occurred, the velocity is determined simply from the relationship:

$$v = \frac{Z}{t} \quad (2)$$

In reality the irradiation profile is finite because of the difficulty of collimating the neutron beam and the loss of activity associated with such a collimation. Similarly the detector has a finite sensitive length. Both quantities can be varied over a limited range in order to possibly maximize the precision of the velocity measurement. The finite spatial resolutions of the irradiation zone and the detection zone along with tag dispersion, inherent to the stream and its flow regime, create a distribution of detected activation as a function of time -  $C(t)$  counts per unit time. The velocity can be determined unambiguously from this counts vs. time distribution if the flow regime of the stream is known. However, relationships between the count distribution and flow velocity were derived<sup>(6)</sup> that depend only weakly on the specific flow regime. The basic



definitions and equations relating count-rate distributions, velocities, error propagation due to counting statistics, and their relationship to the system parameters, were derived elsewhere<sup>(13)</sup>.

The main equations used in the analysis reported in this paper are given below:

$$V_j = Z(I_j/I_{j+1}) \quad (3)$$

where  $V_j$  is the velocity based on the  $j$ -th time moment.  $V_{-1}$  applies mainly to turbulent flow,  $V_{-2}$  applies to laminar flow and others with strong dispersion, and  $V_0$  applies to slug flow.  $V_{-2}$  is the least sensitive quantity to the flow regime.  $Z$  is the distance between the source and the detector;  $I_j$  is the  $j$ -th time moment of the accumulated count of the tracer as a function of time,  $C(t)$ , corrected for the radioactive decay during the flight time

$$I_j = \int_0^{\infty} C(t) e^{-\lambda t} t^j dt \quad (4)$$

The relative error in the velocity is given by

$$\frac{\sigma}{V} \approx \frac{V}{Z} \frac{\sigma_t}{\sqrt{I_0}} \quad (5)$$

where  $\sigma_t$  is the width of the time distribution, and hence it represents the uncertainty of the individual values of time of flight.

Using a simple model which was corroborated by experiments,  $\sigma_t$  and  $I_0$  are related linearly to  $1/V$ . Using the latter, one can relate the velocity uncertainty to all of the important system parameters:

$$\frac{\sigma}{V} = \frac{\sqrt{V}}{2} \frac{1}{\sqrt{K}} \frac{(\lambda_n + \lambda_d) + Vt_n}{[(\lambda_n + Vt_n)\lambda_d t_n]^{1/2}} \quad (6)$$

where  $\lambda_n$  and  $\lambda_d$  are the effective length of the irradiation zone and the detector, respectively,  $t_n$  is the irradiation (pulse width) time, and  $K$  relates to the nuclear properties (14 MeV neutron cross-section, radioactivity decay constant of the tagged element, the neutron flux, and the detector efficiency).

Eq. (6) is a useful guide in designing the neutronic mass flow meter. If  $\lambda_n \approx \lambda_d \gg Vt_n$ , the equation becomes independent of the former and is proportional to  $t_n^{-1/2}$ .

Another useful result of Eq. (5) or (6) is that there is a distance  $Z = Z_{\min}$  where  $\sigma/V$  is a minimum

$$Z_{\min} = 2 V/\lambda$$

which is equal to 21V for oxygen and 393V for silicon activation. The minimum in the error of V is, however, very shallow, allowing a wide range of values for the selection of Z.

### Experimental System

The experimental system assembled for this study consisted of the following:

- constant head liquid loop
- conventional single-phase liquid flow meter (venturi type) and proper tank and valves for simple time diversion management
- pulsed 14 MeV drift-tube type neutron generator
- shielding tank
- gamma ray scintillation detectors (NaI and BGO)
- nuclear electronics and computerized multi-channel and scaler analyzer

These components are described in more detail in Ref. (13). Suffice to state here that the time of flight measurements were done in a geometry that very closely simulates pipe sizes (e.g. 2" diameter) and other geometrical details of actual configurations in a coal liquefaction plant. Different geometries, for example large pipe diameter, can readily be accommodated with the neutronic mass flow meter.

The measurements were conducted with water (89% oxygen) to simulate turbulent flow and a water-sugar mixture (about 50% concentration) to simulate near laminar flow. The solid phase in these runs was made of fine sand ( $\text{SiO}_2$ ). However, the amount of it retained in suspension, and hence in the flow, was very small. Therefore, the time of flight response of silicon was determined by measurement of a solid slurry containing sand (53% O and 47% Si).

### Experimental Results

The experimental portion of this investigation covered many topics to define uncertain effects, substantiate assumptions, and corroborate calculations in order to optimize a prototype neutronic mass flow meter. Gamma ray spectra of various materials, irradiated under different conditions, were obtained in two types of detectors. Several different velocity measurements were taken over a factor of 10 range in velocity. Very high precision was obtained for the velocity determinations. The irradiation (activation) profile of the neutron generator was investigated. The effects of collimation and absorbers on the detectors were determined. Steady state experiments determined that silicon is detectable under realistic conditions. A brief discussion of the results of the various measurements follows.

### Activation Profile

The initial profile of the tagged elements, or distribution of the neutron activation, was measured at two positions of the 14 MeV source: flush with the pipe and 2" back. The distribution is characterized by the quantity FWHM (full width at half maximum), which describes the effective width of the irradiation zone (equal roughly to  $\lambda_n$  (see Eq. (6)). For the "flush" position, the FWHM is 11 cm and for the second position it is 15.5 cm.

### Detector Resolution

The detector spatial resolution describes the ability of the detector to detect the radiation emitted by the tracer as a function of distance from the detector axis along the pipe axis. This characteristic, like the activation profile, can affect the accuracy of the time of flight determination. The FWHM of the detector spatial resolution (roughly equivalent to  $\lambda_d$  used in Eq. (6)) was determined to be approximately 14 cm.

### Count-Rate Vs. Source-Pipe Distance

Next, the decline in count-rate as a function of the increase in source to pipe distance was measured. This distance may have to change to accommodate different pipe sizes and other spatial constraints. By moving the source 3" away from the pipe, the count-rate decreased by a factor of four.

### Gamma Ray Detectors

Two gamma ray scintillation detectors, NaI(Tl) and BGO, were studied. Both of them have fair energy resolution (the former a factor of two better than the latter) and high efficiency for high energy (the latter higher than the former). The main advantages of the BGO for the application at hand is its high peak to Compton ratio and its high efficiency per unit volume. The spectrum of activated  $\text{SiO}_2$  in both detectors is shown in Figure 2. The irradiation time was 10 sec., followed by a 5 sec. delay and a 10 sec. counting period. These times were chosen to represent a realistic situation which neither enhances nor suppresses the long-lived  $^{28}\text{Al}$  ("tagged Si") activity versus the short-lived isotope  $^{16}\text{N}$  ("tagged O"). BGO is more advantageous in this case. However, because of cost consideration and availability in large sizes, it is quite possible that NaI would be adequate in many applications.

### Solid Slug Measurements

Two quantitative solid slug experiments provided estimates of count rate of fluid flows. The first experiment involved irradiating a 2" diameter slug of lucite, 32 weight percent oxygen. After counting the activated lucite and making various corrections for decay, observation time, etc., counting rates for  $^{16}\text{N}$  were predicted for various combinations

of fluid flow speed and irradiation time. The results were consistent with the counting rates observed in water flow experiments. This provides confidence in the second set of predictions made from the second solid slug experiment using sand. After an irradiation time of 30 seconds and a five-second delay, a gamma ray energy spectrum was obtained for 30 seconds. The spectrum was similar in quality to the BGO spectrum of Figure 2. The net <sup>28</sup>Al counts were obtained and estimates of Si activation counting rates were calculated. The results are shown in Table 1. As is shown in the next section, reasonable precision in the silicon, e.g., solid phase, velocity can be achieved even with these relatively low count-rates.

Table 1  
PREDICTED COUNTING RATES IN A SLURRY  
CONTAINING 2.5 Wt% SILICON

Irradiation Time (sec)	Flow Velocity (m/sec)	Counts/100 Cycles
.1	0.1	120
.1	0.5	25
.1	1.0	12
.1	2.0	6
.05	0.1	60
.05	0.5	12
.05	1.0	6
.05	2.0	3

### Velocity Measurements

Completion of an extended series of velocity measurements showed excellent internal agreement between analysis models and excellent agreement with external checks. The latter is, of course, vital to acceptance of the basic technique. This section discusses the data obtained and their analysis using the methods discussed in the section entitled "Theoretical Modeling." Several different methods were examined to determine their potential utility in a mass flow meter and to look at other results which might be useful to a flowmeter user, such as a possible determination of ash content in the process stream.

Velocity measurements in water under turbulent flow conditions spanned the range from .3 m/sec to 3 m/sec. Some of the raw data is shown in Figure 3. The peak on the far left is the "gamma-flash" and represents the

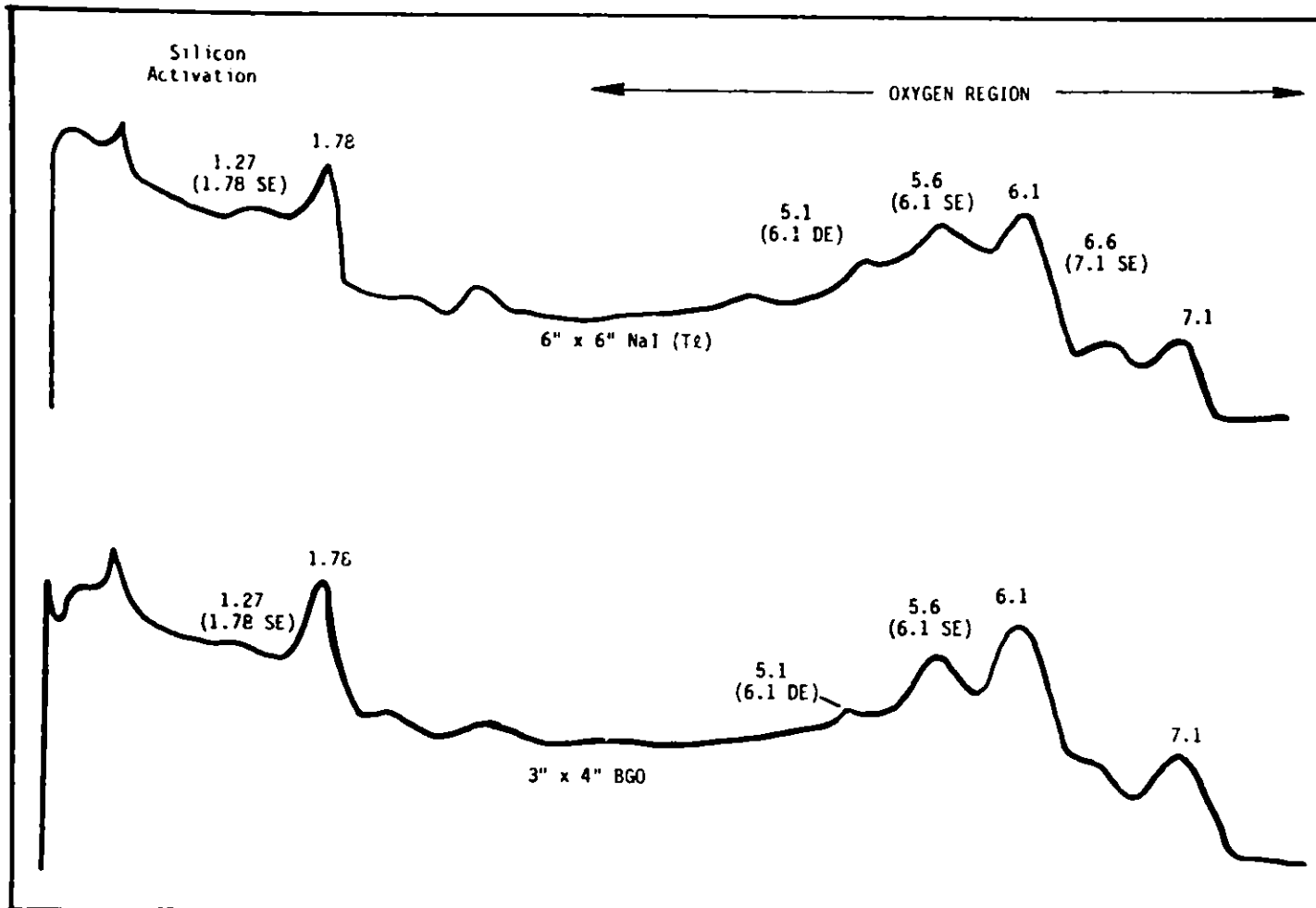


Figure 2. Comparison of Bismuth Germanate (BGO) and NaI Detectors with 14-MeV Neutron Activated Sand. All Gamma Ray Energies are in MeV.

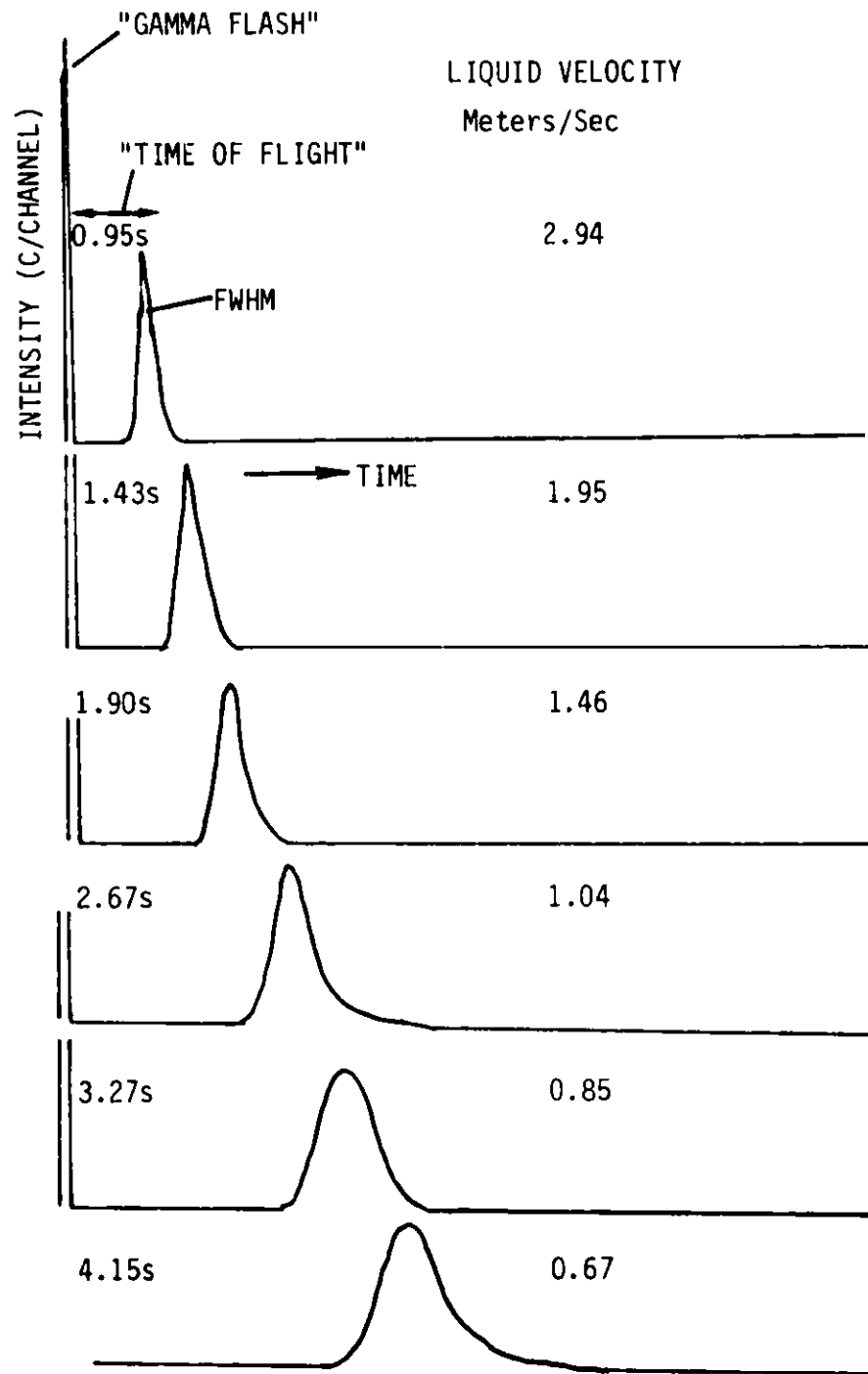


Figure 3. Neutronic Mass Flow Meter - Activation Time Profile

prompt, degraded gamma rays produced by the neutron burst. Visual peak-centroids are readily identifiable in the data. However, the tail toward longer times which grows more prominent at lower speeds clearly indicates the need for more sophisticated analyses than just locating the peak maximum.

Table 2 compares the results of computerized analyses using different models with the visual approach. Note the very high precision of the results. It is also noteworthy that in this flow regime, the results are model-independent to within 1 to 2 percent, probably sufficient for a commercial instrument. Table 3 shows the precision achievable using a single beam pulse. A single pulse (about 100 total counts) achieves a precision in velocity of 1.5% and is in agreement with a longer run.

Table 2  
LIQUID VELOCITY COMPARISONS  
(Meters/Sec)

$V_0$	$V_{-1}$	$V_{-2}$	$\sigma_V^{***}$	V (Visual Peak)
*2.92	2.95	2.97	$\pm .01$	3.00
*1.91	1.93	1.95	$\pm .005$	1.95
*1.43	1.44	1.45	$\pm .003$	1.45
*1.020	1.030	1.039	$\pm .002$	1.030
** .843	.850	.858	$\pm .001$	.893
* .846	.853	.861	$\pm .001$	.866
** .671	.677	.682	$\pm .001$	.695
** .549	.554	.558	$\pm .001$	.576
** .449	.452	.445	$\pm .0004$	.470
** .373	.376	.379	$\pm .0003$	.393
** .335	.337	.340	$\pm .0004$	.349
** .299	.300	.302	$\pm .0004$	.306

\* 200 pulse cycles, 100 msec irradiation time, 5 msec wide time channels, 2 to 5.5 seconds per cycle.

\*\* 100 pulse cycles, 100 msec irradiation time, 5 msec wide time channels, 11.08 seconds per cycle.

\*\*\* The calculated errors for  $V_0$ ,  $V_{-1}$ , and  $V_{-2}$  were identical to one significant figure.

Table 3  
COMPARISON RESULTS OF SINGLE PULSE TO MULTIPLE PULSES  
(Velocity in meters/sec)

No. Cycles	$V_0$	$V_{-1}$	$V_{-2}$	V (All) Error	Visual
100	.335	.337	.340	$\pm .0004$	.349
1	.330	.333	.336	$\pm .004$	-

\* Both sets of data taken with 100 msec irradiation time, 5 msec wide time channels, and 11.8 seconds per pulse.

The overall accuracy of the time-of-flight  $^{16}\text{O}$  velocity measurement was checked against a venturi placed upstream of the point of neutron activation. Pressure drop across the venturi was measured with a Celesco Model P70 differential pressure transducer set up with a 0-5 psid diaphragm. The venturi was calibrated by simultaneous measurements of the venturi flowrate and timed diversions. The net weight of the diverted water could be weighed with an accuracy of 0.1%; however, the overall diversion flowrate is estimated to be accurate only to within  $\pm 2\%$  because of the manual operation of the diversion valves. This accuracy is far poorer than that of the neutronic mass flow meter, but sufficient for the purpose of this study.

Several tests of time-of-flight velocity by  $^{16}\text{O}$  activation were made with simultaneous venturi- $\Delta P$  measurements. For these tests, the flow was turbulent with Reynolds Numbers in the range of approximately 30,000 and 180,000. Results of these velocity measurements are shown in Figure 4. A linear regression fit to the data is also shown. The fit is extremely good and shows that the  $^{16}\text{O}$  velocity measurement is identical to the velocity measured by the venturi. This result indicates that the neutronic measurement is a highly accurate technique for absolute velocity determination.

The analysis of the experimental data has shown that other data parameters vary with velocity in modelable ways. Two of these are the time distribution width ( $\sigma_t$ ) and the total number of counts ( $I_0$ ). The product of the velocity with width was shown to vary inversely with the velocity, as predicted by the theoretical model. A similar result was obtained with the total number of counts. In this case, the net counts were normalized to the gamma-flash to account for beam intensity fluctuations. A similar normalizing technique is applicable to a field instrument, eliminating the need for a separate neutron monitor if total oxygen or silicon content information were desired as additional information. The fact that the data



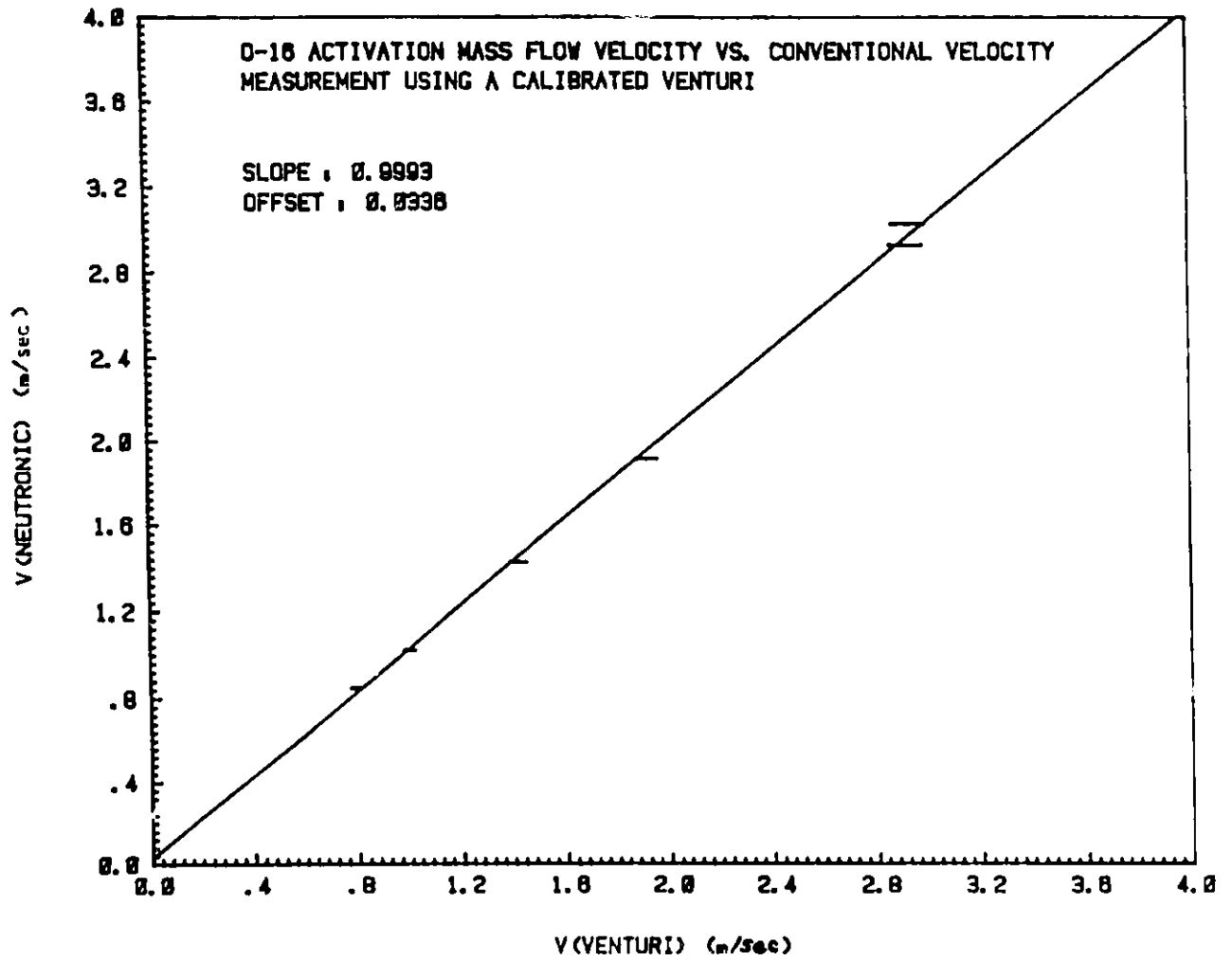


Figure 4. Comparison of Velocities Measured by Neutronic Flow Meter to Venturi

for the width and the intensity fit the theoretical model reinforces the model. More importantly, though, it permits optimization of the parameters and specifications of a neutronic flow measuring device.

Finally, neutronic mass flow velocity measurements were done in the laminar and near-laminar regime. The measurements were performed with a 50% water solution of sugar, in the velocity region covered previously by the experiments in pure turbulent flow. The results are shown in Table 4.

Table 4  
VELOCITY MEASUREMENTS IN THE TURBULENT/LAMINAR FLOW TRANSITION REGIME

$V_0$ (m/sec)	$V_{-1}$ (m/sec)	$V_{-2}$ (m/sec)	$\sigma_v$ (m/sec)	V (Visual) (m/sec)	Reynold's No.	$V_{-2}/V_{vis}^{\dagger}$
2.08	2.14	2.19	$\pm .01$	2.30	10,000	.95
1.12	1.15	1.18	$\pm .005$	1.29	* 6,900	.91
** 1.18	1.22	1.25	$\pm .005$	1.38	5,700	.91
** .691	.759	.818	$\pm .005$	.989	3,800	.83
** .396	.431	.468	$\pm .005$	.644	2,100	.73
** .320	.329	.339	$\pm .001$	.405	1,600	.84

<sup>†</sup>The mean  $V_{-2}/V_{vis}$  ratio for several turbulent flow runs is .98.

\* A 46.6% sugar solution, all other runs were 49.2%.

\*\* The shape of the activity time distribution is not characteristic of turbulent flow.

Figure 5 clearly shows the qualitative difference between laminar and the turbulent flows. The time scale is identical for the two time spectra shown. The near Gaussian shape for turbulent flow is quite different from the decaying ramp, indicative of laminar or near-laminar flow. Table 4 contains numerical results for various velocity prescriptions in the transition region. The velocity definitions are those contained in the Theoretical Modeling section. As expected, the velocities calculated by the different models vary more, circa 12 percent in the laminar region versus 1 percent in the turbulent domain. The proper velocity value for this regime is  $V_{-2}$ . The measurement precision (less than 1 percent) remains excellent. The Reynold's numbers indicate that the data shown span the transition region. Fully developed laminar flow occurs at a Reynold's number of about 2000. The  $V_{-2}/V_{vis}$  ratios clearly show the change from near turbulent to laminar conditions. The theoretical ratio for perfect laminar flow is .5.

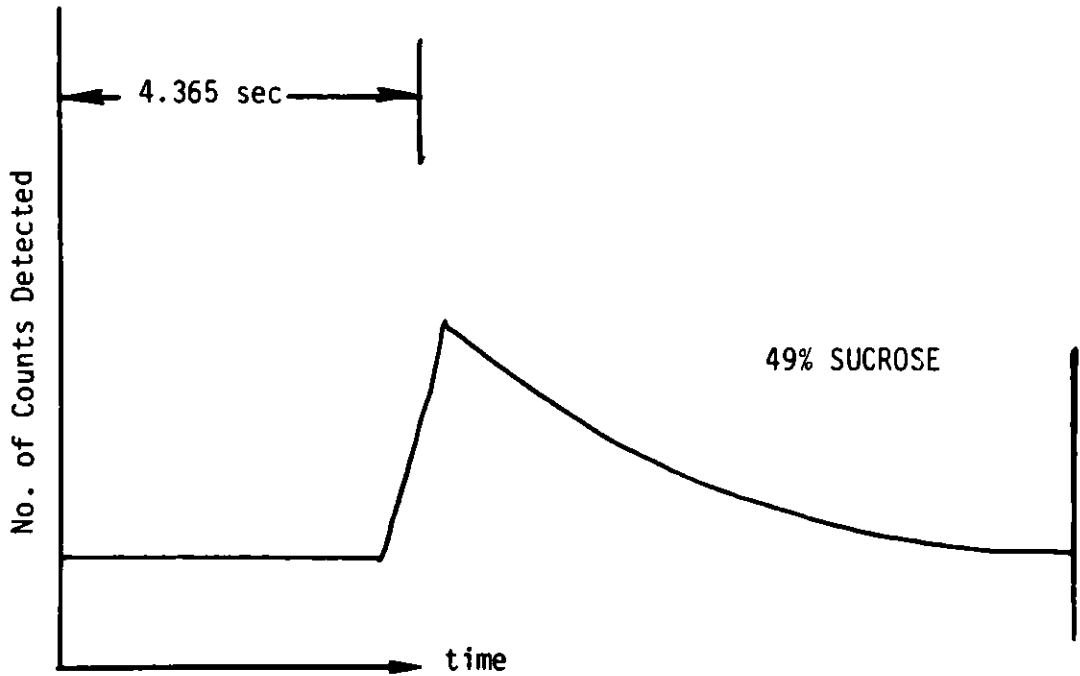
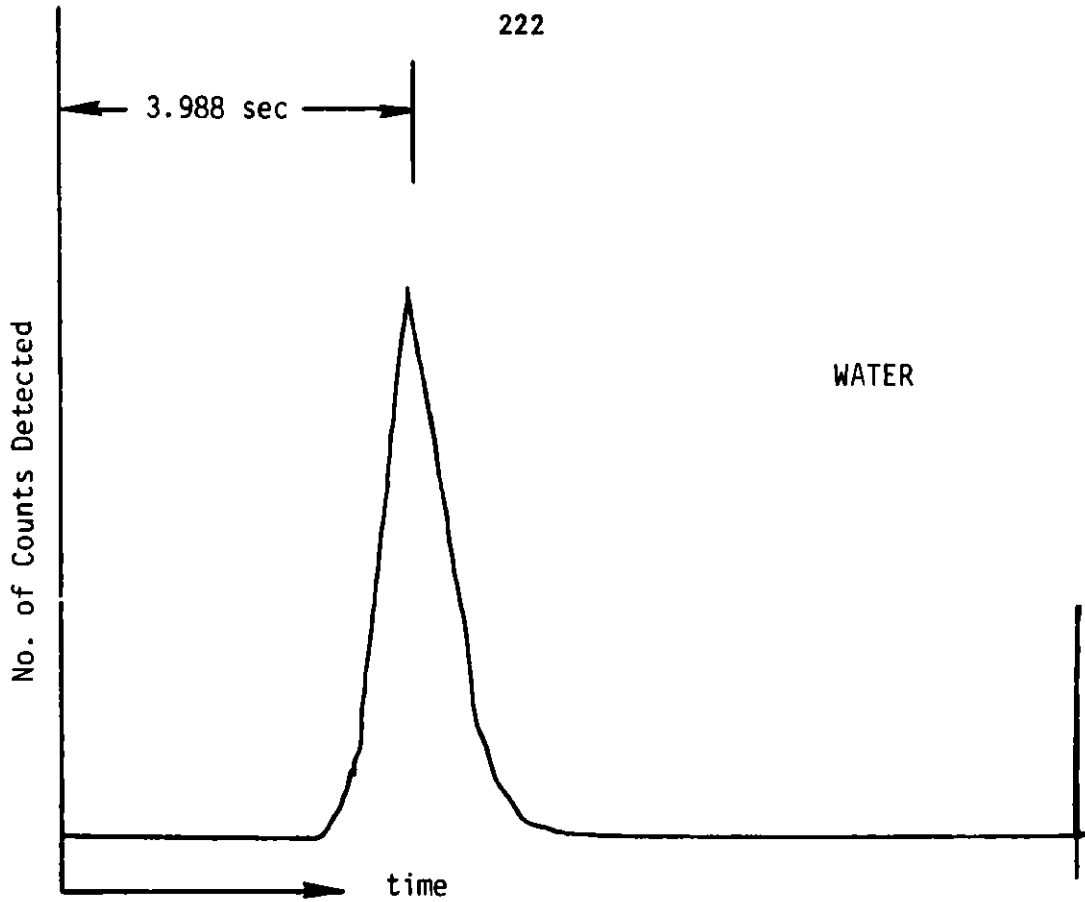


Figure 5. Comparison of Laminar and Turbulent Flow Activity Profile

Further experiments at higher sugar concentrations (greater viscosity) would have lower Reynold's numbers and may exhibit more fully developed laminar characteristics.

### Summary and Conclusions

This paper described the development of a non-intrusive neutronic mass flow meter, for applications to harsh environments like those in a coal liquefaction plant.

The main features of such a meter that make it attractive for coal conversion, power, and other industrial plants, are enumerated below:

- Truly non-intrusive
- Independent of environment
- Applicable to pilot plants as well as commercial size plants
- Applicable to small (1"-2" diam) as well as large (10"-15" diam.) pipes
- Independent of flow regimes
- Measures directly liquid/solid flow-velocity
- Measures continuously total density of multi-phase stream
- Has demonstrable high accuracy
- Can be optimized or tailored for specific applications and plant layouts
- In two-phase flow, it can distinguish between liquid and solid phases
- Can provide composition information
- Velocity measurement is absolute (does not require calibration)

The study described in this paper tested and demonstrated experimentally many of the above features in a laboratory set-up. Systematic study of the main parameters of the system was conducted in order to assess their impact on the system's design and performance and to allow a reliable extrapolation of results obtained in laboratory tests to realistic plant situations.

The experimental results described in the paper corroborated, and often exceeded, all the expectations from the neutronic mass flow meter. Noteworthy among them is the high precision with which the flow velocity can be determined. The ability to measure the solid phase in the flow, though with longer measurement time, was also illustrated.

A simple theoretical model was developed that identifies the roles of the different system parameters such as irradiation profile, detector resolution, source-detector distance, activation time, etc.

A relatively compact neutronic mass flow meter concept has emerged from this study. Such a device could be readily incorporated in any desirable measurement location.

#### Acknowledgement

The authors would like to acknowledge the help provided through discussions and information by Messrs. S. Lee and T. Simpson of the U.S. DOE, Dr. K. Porges of ANL, and M. Turgeon and P. Wilkinson of Catalytic, Inc.

### References

1. Hewitt, G. F. and Lovegrave, P. C., "Experimental Methods in Two-Phase Flow Studies," EPRI NP-118 (March 1976).
2. Brockett, G. F. and Johnson, R. T., "Single-Phase and Two-Phase Flow Measurement Techniques for Reactor Safety Studies," EPRI NP-195 (July 1976).
3. Gay, R., Brockett, G. F., and Johnson, R. T., "Two-Phase Measurement Techniques in Nuclear Safety Research," Two-Phase Flow and Heat Transfer Symposium Workshop. Fort Lauderdale, Florida, (18-20 October 1976).
4. Delhaye, J., et al., "Metrology of Two-Phase Flow-Different Methods," USNRC Light Water Reactor Safety Technical Exchange Program, Report No. CEA-R-4457, (September 1973).
5. Kehler, P., "Two-Phase Flow Measurements by Radioactive Tracer Techniques," Presentation at the Fifth Water Reactor Safety Research Information Meeting, Gaithersbury, Maryland, (November 1977).
6. Kehler, P., "Accuracy of Two-Phase Flow Measurement by Pulsed Neutron Activation Techniques," p. 2483, Vol. 5, Multiphase Transport Fundamentals, Reactor Safety Applications (Hemisphere Publishing Corp., Washington, D.C., May 1980).
7. Kehler, P., and Solbrig, C., "Measurement of the Emergency Core Coolant Bypass Flow on the LOFT Reactor," NUREG/CR-0208, (Rev. 1, June 1980).
8. Kehler, P., "Measurement of Slow Flow Velocities by the Pulsed Neutron Activation Technique," Presentation at the USNRC Review Group Conference on Advanced Instrumentation for Reactor Safety Research, Oak Ridge, Tennessee, (July 1980).
9. Percy-Griffo, M., Black, R. C., and Lahey, R. T., "Basic Two-Phase Flow Measurements Using <sup>16</sup>Tagging Techniques," NUREG/CR-0014, Vol. 2, p. 923, 1980.
10. Lin, T. and Gay, R. R., "Measurement of Droplet to Liquid Film Mass Exchange Rates in Annular Flow Using Neutron Tagging," Transactions, ANS, p. 746, Vol. 38, Miami, Florida, June 1981.
11. Perez-Griffo, M., Black, R. C., and Lahey, R. T., "A Mechanistic Analysis of LOFT Pulsed Neutron Activation Data," Transactions, ANS, p. 750, Vol. 38, Miami, Florida, June 1981.
12. Porges, K. G., et al., "Calibration of Flow and Feedrate Meters in Sites by Means of Pulsed Neutron Activation," Proceeding of the 1980 Symposium on Instrumentation and Control for Fossil Energy Processes, Virginia Beach, Virginia. ANL-80-62, p. 577.
13. Gozani, T., Esterl, J., Goodman, J., and Bernatowicz, H., "Neutronic Mass Flow Rate Meter for Continuous Mass Flow Rate Measurements," Science Applications, Inc. Report SAI-315-82-PA, (July 1982).

SOME RECENT SLURRY FLOW MEASUREMENTS WITH SLTF

K. G. Porges, C. Kampschoer, S. A. Cox, and W. E. Brewer  
Argonne National Laboratory  
Applied Physics Division, Bldg. 316  
Argonne, IL 60439  
312/972-6091  
FTS: 972-6091

Abstract

The Slurry Loop Test Facility (SLTF) at Argonne National Laboratory (ANL) was designed to provide a set of three independent measurements from which the liquid and solid mean flow speed, as well as the effective solid volume fraction in the medium, can be computed. This further yields a measurement of the solid transport rate, as well as the solid velocity drag, in slurries featuring large solid grain size and/or low viscosity liquid, as found in many coal transport and utilization plants and facilities.

Inasmuch as the solid delivery rate, rather than total mass flowrate, is the variable whose measurement is needed to optimize operation of such facilities, these measurements are intended to provide calibration for various mass flowmeters that can be installed in either a vertical or a horizontal leg of the loop.

The measurement cycle includes a direct mass flowrate measurement by timed diversion of the mainflow into a weighing tank, then a volumetric flowrate measurement in a level-sensing standpipe and, finally, a measurement of the solid component velocity by Pulsed Neutron Activation. In conjunction with analysis of the solid in terms of oxygen content, which makes use of the same neutron generator deployed on the loop, the solid feedrate can alternatively be determined by exploiting both the intensity and time rate of the observed PNA signal.

Preliminary data show velocity drag for a range of medium velocities, as well as for different solid volume fractions. Considerably more data, for different types and grain size of solids, will be needed to develop a semi-empirical model, now lacking, of this practically important parameter.

Description

The Slurry Test Loop Facility (SLTF) which is discussed in the present report is one of hundreds, perhaps even thousands, of test flow loops in operation today. Other test loops are constructed for specific experimental setups and usually dismantled after the measurements have been made. However, relatively few test facilities are specifically designed for slurry flow. Of the latter, only a few are intended for performance evaluation and calibration of flowmeters rather than for mechanical component wear testing.

In a system intended for meter calibration, the principal requirement is some highly accurate means of comparison or, even better, several such means. For slurry and similar two-phase media, the only reliable comparison is a

direct flow rate (mass/volumetric) test or sample measurement obtainable through an accurately timed diverter into a weighing/volume reading tank. This has been provided in the SLTF through a diverter shown schematically in Fig. 1. A preliminary description of this and other special features has been published.<sup>1</sup> The present report brings that description up to date and considers in more detail the underlying rationale of the details in relation to non-Newtonian two-phase flow behavior. In addition to measurements under steady flow conditions, the SLTF can provide pulsed flow and thus calibrate meter error on a typical industrial high-pressure slurry feedline (where pressure is usually generated with a piston pump that inevitably introduces pulsing).

For relatively coarse, dilute slurries, a velocity slip must be expected. In a single particle approximation,

$$v_s (dv_s/dz) = A(v_l - v_s) - Bv_s^2 \quad (1)$$

where A is a viscous drag coefficient while B represents wall-interaction (as well as particle-particle interaction) effects through which energy is lost. At equilibrium,

$$v_l - v_s \doteq (B/A)v_l^2 \quad (2)$$

Preliminary measurements with such a coal slurry indicate velocity slip of the order of 5%. For this purpose, the solid component velocity  $v_s$  is measured by means of pulsed neutron activation (PNA) together with diversion measurements of  $\dot{V}$ , the volumetric, and  $\dot{M}$ , the mass flow rate, which yields

$$fv_s = (\dot{M} - \rho_l \dot{V})/S(\rho_s - \rho_l) ; \quad (3)$$

$$\alpha = (v_l - v_s)/v_s = (Q-1)^{-1} , \quad (4)$$

$$Q = \rho_s (\dot{V}\rho_s - \dot{M})/(\rho_s - \rho_l)(\dot{V} - Sv_s) \quad (5)$$

in terms of the duct cross sectional area S, solid and liquid intrinsic densities  $\rho_s$  and  $\rho_l$ , component average velocities  $v_s$  and  $v_l$ , and solid volume fraction f,  $\alpha$  is the velocity slip factor.

As a result of velocity slip, the apparent density  $\rho_m^*$  of the medium obtained by grab-sampling and the actual mean density in the flowing medium  $\rho_m$  differ by a certain amount:

$$\rho_m - \rho_m^* = (\rho_s - \rho_l) \alpha f (1 - f)/[1 + \alpha (1 - f)] \quad (6)$$

Measurement of the intrinsic densities  $\rho_s$  and  $\rho_l$  is done by straightforward volumetric methods, noting that considerable care is needed to make sure that solid samples have come into the same equilibrium with the liquid in the volumetric sample and in the flowing loop. Like other determinations with slurry, this takes a number of separate sets of measurements whose individual



results exhibit a certain scatter. Some of this can be attributed to nonuniformity of coal, even from the same barrel (as delivered by a coal grinding plant). Similar scatter is found in sieving and in proximate analyses.

The flow regimes over which the current series of tests extends range from slug flow to quasi-laminar. Particle size  $d_p$ , solid fraction  $f$ , and applicable models are summarized in Table 1.

Table 1. Solid-Liquid Flow

$d_p$	$f$	Flow Regime	Model
Coarse	Small	Separate-Phase	Single particle in Newtonian liq.
Fine	Medium	Quasi-Homogeneous	Bingham, Pseudoplastic non-Newton. liq.
Various	Large	Paste Flow	Slug (extreme Bingham model)

The table illustrates, in a qualitative way, how varied conditions can be in slurry flow, from a suspension of large particles at low loading where the two phases would be expected to exhibit considerable independence, to paste-flow characteristic for dense loadings of particles distributed over a large range of sizes. This variability defeats conventional flow measurement through the insertion of obstacles (orifice plates, nozzles, wedges, etc.) and a measurement of the pressure difference across the obstacle, even if problems of pressure tap plugging can be coped with. Another observation, applying specifically to separate-flow, follows from Eq. (1): since the second energy-dissipative term depends on wall-interaction, a change in boundary conditions such as a pipe bend or diameter change will upset the equilibrium relation between solid and liquid mean flow speeds. Hence, the solid component will accelerate or decelerate for some distance downstream from this feature until the normal or equilibrium velocity slip has been reestablished. It then further follows that any external means of measuring the medium velocity, whether PNA or two-sensor correlation, must be sited far enough downstream from a pipe feature to sense the equilibrium velocity. As this is not always possible in an industrial installation, a "meter factor" may have to be determined by duplicating the measurement site in a test loop. For comparison purposes, a reasonably long (200-300 pipe diameter) straight horizontal leg is needed. Such a leg is provided for the PNA measurement in the SLTF, where it serves also to establish a base for a standard pressure gradient measurement. To make this measurement, taps on the top of the 2-in. Sch. 40 SS 304 pipe lead to sightglasses within which the slurry level is adjusted to equal height, upstream and downstream, through individual air pressure and vent cocks. The two sightglasses are interconnected through a manometer and differential pressure sensor of variable reluctance type.

Some additional remarks should be made regarding the PNA velocity measurement. This is, in effect, a tagging scheme much like salt or dye-tagging, used for more than 50 years in flow characterization. Somewhat more recently, tagging with short-lived activities has become established. Nevertheless, a controversy appears to have developed regarding data processing, specifically for PNA tagging. This controversy has split tagging practitioners into two camps according to preference of formula A or B for velocity computation. Let

$$M_k = Z^k \sum_{j=1} C_j e^{-\lambda t_j/t_j^k} \quad (7)$$

where  $C_j$  is the  $j$ th gamma count sample, delivered by the downstream station at time  $t_j$ , and  $\lambda$  = decay constant,  $Z$  = neutron source detector distance, then formula A asserts that

$$\bar{v}_A = M_2/M_1 \quad (A)$$

whereas formula B claims

$$\bar{v}_B = M_1/M_0 \quad (B)$$

In practice, there is little difference under slug-flow conditions (typically encountered when PNA has been used for on-line calibration of other flowmeters at ducts flowing low-viscosity media). However, for low-Reynolds' number turbulent flow, one finds  $\bar{v}_A$  noticeably larger than  $\bar{v}_B$ . In typical laminar or quasi-laminar flow,  $\bar{v}_B$  fails altogether. This apparent problem can be cleared up by referring to an observation made as long ago as 1911 to the effect that under certain circumstances, the tag ceases to represent the flow. What one then observes is the tag velocity distribution and not the medium velocity distribution. Both share the same mean transport velocity but the medium flow velocity necessarily has a fixed distribution, while tag velocity distribution varies with the downstream location of the counter. The tag ceases to represent the medium to the extent to which radial transport by diffusion rivals transport along the duct; consequently, formula B applies in turbulent flow as well as in capillary flow (when axial transport speed is artificially reduced to make radial diffusion more effective), while formula A applies in normal laminar or quasi-laminar flow. For coal slurried in hydrocarbon liquid, only the solid component accepts a tag through 14-MeV neutron irradiation; it is thus clear that in that case, formula A, which assumes the tag to represent the motion of the tagged medium, should apply, whether the slurry appears to run in quasi-turbulent mode or in any other mode.

To make effective use of a PNA system, it pays to provide two detector stations and to compare shapes of the count rate versus time plots produced by each. For illustration, Fig. 2 shows a set of such plots, produced by systematically displacing a traveling detector along the duct in increments of 1 m. The data were taken with water flowing in the turbulent regime and indicate a definite shape change, pointing to formula B as being the correct one for obtaining the true mean medium velocity; this was confirmed by repeated diversions.

PNA acquisition is organized by an on-line sequencer/computer and a T/N 1710A multiscaler with 4-input capability, connected through RS-232 to a post-acquisition computer with local interactive terminal. This arrangement permits inspection of the acquisition as it develops, with immediate computation of the mean velocity. Various diagnostic programs are in preparation.

The test loop has now been operating with coal slurry charge of various solid fractions for about six months. Currently, three flowmeters are installed at diverse test locations and a set of meter factors is being produced for both velocity (correlation) and density readout.

For purposes of flowmeter evaluation/calibration, the loop can be used to derive a "meter factor." Typical prototype capacitive and acoustic beam transmission flowmeters sample the duct within a narrow beam or defined strip centrally laid across the duct. If the solid component velocity is radially symmetric, which one would suppose a good approximation in a vertical duct, then the center flow is more effectively sampled than the peripheral flow by such a strip. The apparent velocity as determined from the location of the covariance peak on the time axis is invariably somewhat higher than that determined by PNA, presumably the true (whole-duct) average. This agrees with the supposition of more efficient center flow sampling; however, another effect partly cancels this: what the covariance peak actually determines is the mean reciprocal velocity or transit time,

$$v' = Z\sqrt{t}$$

whereas

$$v_{ave} = \overline{Z(1/\sqrt{t})} = (Z\sqrt{t}) = (Z\sqrt{t})(1 + \text{var}(t)\sqrt{t}^2 \dots)$$

hence

$$v'(\text{read from covariance plot}) = v_{ave} / (1 + \text{var}(t)\sqrt{t}^2 \dots)$$

but

$$v_{ave} = v_{true\ ave} (1+K) = v'_{covar\ plot} (1+K) / (1 + \text{var}(t)\sqrt{t}^2 \dots)$$

The variance of the transit time depends on a number of factors, such as cluster strength, cluster fading, cluster typical length, and geometry of the sensing stations. The factor K, on the other hand, depends on the ratio of the sensing region width to the duct diameter, as well as the flow velocity distribution, and should thus be particularly strong in the quasi-laminar flow regime.

This points to a program of redesign of spool pieces so as to minimize the sampling bias, together with a computation program that can evaluate the transit time variance; the result should then agree with the solid component velocity within 1-2%.

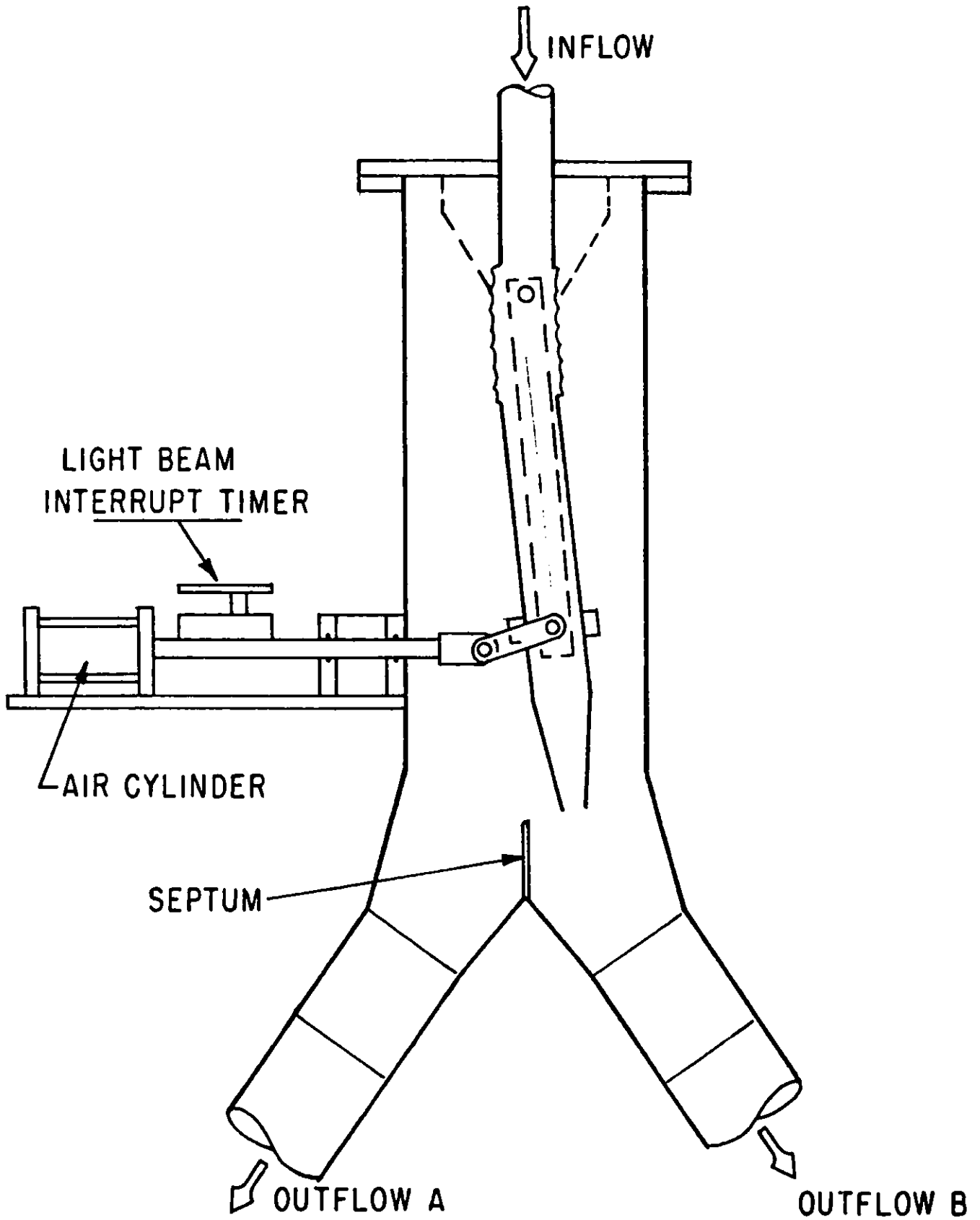


Fig. 1.

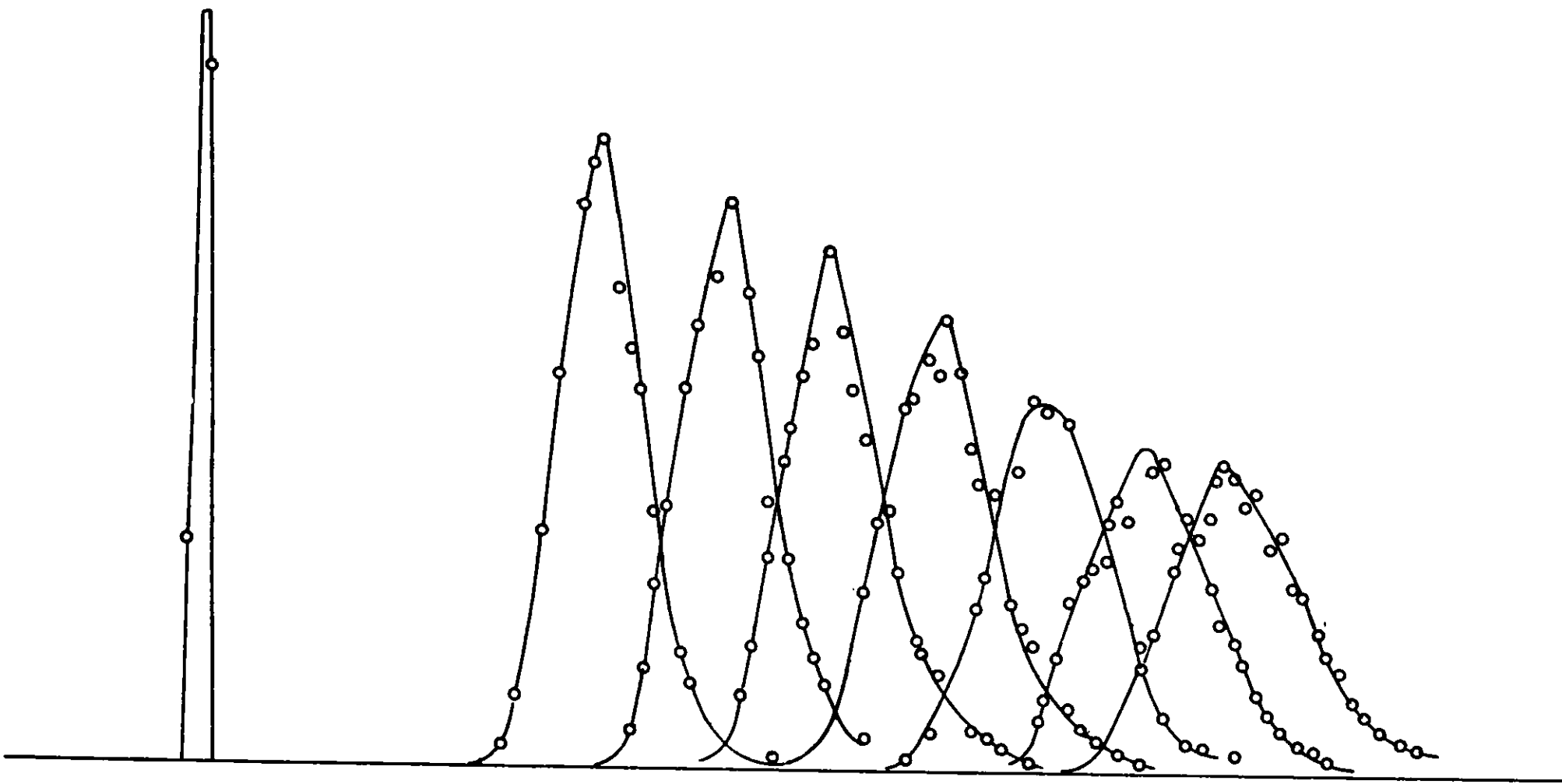


Fig. 2.

CONDUCTIVITY PROBE AND DATA ACQUISITION  
FOR A LIQUEFACTION COLD MODEL

W. Fuchs , D. Smith  
Pittsburgh Energy Technology Center  
U. S. Department of Energy  
P.O.Box 10940  
Pittsburgh, Pa. 15236

Abstract

A device has been developed to measure local bubble size and velocity of the gas-phase in a three-phase slurry bubble column operated at coal liquefaction flow conditions. An in situ electrical conductivity twin probe (0.3-cm gap) detects the difference in conductivity of the gas and slurry phases. The analog signal from each probe is rapidly digitized and stored on a waveform recorder and subsequently transmitted and analyzed on a minicomputer. Measured bubble length and velocity are computed from the measured response time interval between probes and the dwell time of a bubble on each probe. A probabilistic model is used to derive actual bubble sizes and velocities.

Introduction

Slurry bubble columns are typically used as coal liquefaction reactors in which high throughputs, good slurry mixing, and high heat transfer coefficients are desirable. Recent published work by Satterfield and Huff (1980) has drawn attention to the importance of gas absorption resistance of Fischer-Tropsch reactions occurring in a three-phase slurry reactor. Thus, global rates of reaction will be influenced by the gas/liquid surface area, gas void fraction, bubble size, and gas absorption coefficients. Previous investigations of gas liquid surface area [Akita and Yoshida (1974), Quicker and Deckwer (1981)] have largely employed photographic techniques to obtain relevant parameters such as bubble size and bubble size distribution as well as estimations of the gas/liquid surface area. This method of measuring bubble size is limited to short distances from the wall, and resolution of the bubbles is further diminished in the presence of solids. Ueyama et al. (1980) measured bubbles in a 0.6-m-ID bubble column and found that a large bubble size gradient occurs in the radial direction from the center to the wall. The bubbles near the center of the column were found to be a factor of 2 to 8 times greater than the bubble size near the wall. This observation demonstrates the necessity of measuring bubbles over the cross section of the column in order to obtain an average bubble size.

Another important parameter, local gas void fraction, has been measured by several investigators [Neal and Bankoff (1963), Hills (1974)], and the various techniques used to study local void fraction have been reviewed by Hewitt (1972), Serizawa et al. (1975), and Jones and Delhaye (1976). Buchholz et al. (1981) recently reviewed, among other devices, the use of twin-electrode conductivity probes for the determination of bubble size parameters. The use of twin-conductivity probes for measuring properties of bubbles is a relatively new technique [Serizawa et al. (1975), Buchholz and

Schugerl (1979)]. This type of detector is employed in our present investigation of gas-phase characteristics in a slurry bubble column operated at coal liquefaction flow conditions. An integral data acquisition system is also described. The gas phase characteristics that are measured by the conductivity probes include bubble length, velocity, and frequency, in addition to the gas void fraction.

### Experimental

A schematic diagram of the bubble column apparatus is shown in Figure 1. The bubble column is a transparent plastic cylinder having an inside diameter of 10.8 cm and a length of 194 cm. A single bubble cap distributor located at the bottom of the column is used to introduce the slurry and gas phases. Several ports are located along the axis of the column to allow insertion of the probe as well as slurry sampling valves and differential pressure gages.

#### Probe System

A depiction of the conductivity probe inserted into the slurry bubble column is given in Figure 2. The twin-electrode conductivity probe consists of two teflon coated wires with a diameter of 0.13 mm (0.005"). The teflon coating serves as a good moisture-repellent surface as well as an electrical insulator. This probe characteristic is essential to obtain rapid response of the bubble shedding water from the probe. The chromel wire has proven to be a good compromise between strength and electrical conductivity in a slurry environment. The pair of wires are threaded through the tubing, and a Conax fitting with teflon seals is fitted over the tubing. The ends of the tube are sealed with epoxy to hold the wires in place and provide a waterproof seal. One of the insulated wires extending from the epoxy seal is then bent in a j-shape such that the tip of the wire is perpendicular to the stainless steel tubing. In a similar manner, the other wire is bent approximately 1 mm past the bend in the first wire and terminated approximately 3 mm past the end of the first wire. The radial gap between wires avoids a liquid film buildup as a result of capillary attraction, and the vertical gap serves as a fixed reference for bubble travel after striking the upstream probe. The chromel wires are exposed at the tips of each wire with a scalpel to insure a minimal exposed area. The radial placement of the probe is accomplished during the operation of the bubble column by loosening the Conax fitting and moving the probe to the desired position with the aid of a calibrated ruler and a reference point located outside of the column.

The probe circuit consists of a power supply, probe, waveform recorder, junction box, and double pole - double throw switch. The power supply (HARRISON 2102A) is a variable DC supply nominally operated at 5 volts. Each electrode of the probe is in parallel with the power supply and waveform recorder. The waveform recorder (Biomation 2805 M) measures and stores the electrical conductivity signals over a known time interval, and subsequently the stored information can be transferred to a computer, visual display, or chart. A depiction of the probe circuit and data acquisition system is given in Figure 3.

A junction box is used to select any one of three probes installed in the slurry bubble column. A double pole - double throw switch is used to reverse

current occasionally to dispose of any charge that may be acquired on the probe tip.

### Data Collection System

The waveform recorder, or digitizer, is an analog-to-digital converter with a solid-state memory that stores the digital equivalent of an analog electric signal. The model that was used in our test facility, a BIOMATION model 2805M, provides for the simultaneous recording of two channels with sampling frequencies of up to 5 MHz; this means that each channel can be read and digitized every 200 ns. The solid-state memory provides space for 2048 numbers for each channel, with a resolution of 1 part in 256.

The trigger mechanism allows for delayed recording as well as pretriggering. Figure 4 demonstrates the difference between these two modes. The pretrigger feature, together with an adjustable trigger level control, permits the definition of a precise recording window with respect to a given or a detected trigger event. The trigger signal can be taken from either channel or can be supplied externally. In our application, a peak signal from the first channel was used, i.e., the signal caused by the probe that sees the bubble in the column first.

The contents of the memory, representing the recorded traces, are displayed on a CRT monitor. In addition, the collected information is transmitted to a computer for analysis via a digital output connection. This transmission is accomplished in asynchronous fashion; each number is transmitted on an 8-bit parallel line after a handshake signal has been established. The transfer rate is controlled by the computer; in our case it is approximately 150 data points per second. The selection of the sample speed and the arming of the trigger mechanism can be achieved manually or remotely by the computer. The interface with the computer consists of 27 lines. Of those lines, 12 are output lines, i.e., they send data or status information to the computer: 8 lines for data transmission, one line each for remote time select mode, recording status, digital output mode, and word ready flag. Fifteen (15) lines are used to send instructions to the waveform recorder: one line to enable the remote control of the instrument in general, one line to enable the remote control of the sampling speed, 7 lines for the selection of the sampling speed, one line for remote arming, 3 lines for the channel selection, one line to enable digital output, and one line for requesting a new data word. The diagram in Figure 5 illustrates the handshaking sequence.

For a typical run, a series of scans under identical conditions are taken in order to obtain a reasonably large statistical sample. The sampling interval for most tests is 0.5 or 1.0 ms per point. Figure 6 shows a plot of the data generated with one scan.

### Results and Discussion

The signal amplitude or intensity is obtained as a function of time from the probe measurements and can be related to the bubble characteristics. A computer program has been developed to read and interpret the data so that bubble velocity, bubble size, and gas void fraction are derived. In order to



interpret the conductivity probe signals, the following computations are made.

A threshold signal intensity that is slightly above the minimum baseline intensity is assigned to each recording at a level corresponding to 5 percent of maximum peak height. All signal intensities below the threshold value represent the conductive (liquid) phase, and all intensities above the threshold represent the gas phase. The dwell time,  $\tau$ , of a bubble corresponds to the duration of time in which the probe is immersed in the bubble and can be calculated from the time interval in which the signal amplitude is greater than the threshold intensity. The lag time,  $\Delta t$ , between a pair of signals corresponding to the passage of a bubble is computed from the time interval during which the centroid of a pierced bubble travels from the upstream to the downstream probe. Let us indicate the coordinates associated with the downstream and upstream probes with the suffixes 1 and 2, respectively, and let us define the time,  $t$ , at which the signal intensity exceeds the threshold intensity as the instant at which a bubble is pierced by one of the two probes; then the following expression is obtained for the lag time.

$$\Delta t = (t_2 - t_1) + \frac{1}{2} (\tau_2 - \tau_1) \quad (1)$$

From Equation 1, the lag time,  $\Delta t$ , approaches the time interval for a bubble to be pierced by each probe as the dwell time of a bubble on each probe approaches the same value. The effect of taking the centroid of the pierced bubble as the reference frame for the computation of lag time is to average small deviations in dwell time due to the deflection or nonvertical travel of the bubble, and due to the offset of the top probe with respect to the bottom probe. Figure 7 shows the relationship of the probe signal as a function of time and the measured dwell and lag time.

The matching of a signal pair representing a bubble passing through both probes requires several conditions to be satisfied. An error may result from the fact that a bubble pierced by the downstream probe is not always preceded by a bubble pierced by the upstream probe. A discussion of the scenarios for such an occurrence has been given by Serizawa et al. (1975). In one case, a bubble penetrated by the upstream probe may be deflected and not strike the downstream probe. In another case, a bubble pierced by the upstream probe may not be deflected; but before it can reach the downstream probe, another bubble that missed the upstream probe touches the downstream probe. In addition to the cases mentioned above, a slight deflection of a bubble striking the upstream probe may result in a different dwell time of the bubble on the downstream probe. Any combinations of the conditions mentioned above can occur simultaneously.

The ascending velocity,  $U_b$ , and length,  $L_b$ , of each bubble passing vertically upward through the column can now be calculated from the lag time, the dwell time, and the vertical gap ( $h$ ) between the twin probes.

$$U_b = h/\Delta t \quad (2)$$

$$L_b = h\tau/\Delta t \quad (3)$$

In order to avoid improper matching of a signal pair, the following constraints are placed on the matching process. A minimum velocity and a maximum velocity corresponding to the smallest and largest bubble observed in the bubble column are assigned to each recording. The minimum bubble velocity is assigned the value of 10 cm/s, which corresponds to a bubble size less than 1.6 mm (1/16 inch) as calculated by Stokes Law.

$$V_{min} = \frac{gD^2}{18\nu_l} \quad (4)$$

The maximum bubble velocity is calculated from the relationship given by Knicklin (1962) for the slugging flow regime.

$$V_{max} = 1.2 (U_g + U_l) + 0.35 (gD_t)^{1/2} \quad (5)$$

The acceptable velocities obtained from the probe measurements are considered to be within the limits of Equations 4 and 5. A further restriction on obtaining a signal pair is given by the similarity of the dwell time of a bubble on each probe. If the dwell time differs by more than 10 percent from each probe, then the bubble is considered to be deflected and is ignored in the analysis of bubble size and velocity.

The gas void fraction can be calculated from the ratio of the total time the signal intensity is above the threshold intensity to the total sampling time.

$$\epsilon_g = T_g/T_s \quad (6)$$

Average bubble velocities are calculated as suggested by Ueyama et al. (1980).

$$\bar{U}_b = \frac{1}{n} \sum_{i=1}^n U_{bi} \quad (7)$$

The standard deviation of the bubble velocity spectrum is given as

$$\sigma = \left[ \frac{1}{n} \sum_{i=1}^n (\bar{U}_b - U_{bi})^2 \right]^{1/2} \quad (8)$$

A typical data set that is analyzed for the gas phase characteristics consists of at least 20 matched signal pairs for a given run condition. These data sets are obtained for 8 radial positions from the center of the column to the wall. The minimum sample population to obtain statistically significant parameters for the gas-phase characteristics is being investigated. The interpretation of bubble size from measured bubble length is being developed from a probabilistic model given by Tsutsui and Miyauchi (1980).

### Conclusions

A conductivity probe and data acquisition system have been successfully developed to measure gas-phase characteristics in a slurry bubble column model operated at coal liquefaction flow conditions. The response time of the probe signal is adequate to observe the probe piercing the bubble and to establish a lag time corresponding to the gap between the twin probes. Further calibration of the probe will be made to determine the smallest detectable bubble.

### Nomenclature

D = diameter  
 g = gravitational acceleration  
 h = vertical distance between twin probes  
 L = measured bubble length  
 n = number of bubble signals that are matched  
 t = time at which probe pierces bubble  
 T = total time interval  
 U = superficial velocity  
 V = rise velocity

### Greek Symbols

$\Delta t$  = lag time  
 $\epsilon$  = void fraction  
 $\sigma$  = standard deviation of bubble velocity spectrum  
 $\tau$  = dwell time  
 $\nu$  = kinematic viscosity

### Subscripts

b = bubble  
 g = gas  
 l = liquid  
 max = maximum  
 min = minimum  
 s = total sample  
 t = tube

### Superscripts

$\bar{\quad}$  = average

### Disclaimer

Reference in this report to any specific commercial product, process, or service is to facilitate understanding and does not necessarily imply its endorsement or favoring by the United States Department of Energy.

### References

1. Akita, K. and Yoshida, F., "Bubble Size, Interfacial Area, and Liquid-Phase Mass Transfer Coefficient in Bubble Columns," *AIChE J.*, Vol. 9, No. 4, 490-494, 1963.
2. Buchholz, R., Zakrzewski, W., and Schugerl, K., "Techniques for Determining Properties of Bubbles in Bubble Columns," *Int. Chem. Eng.*, Vol. 21, No. 2, 180-187, 1981.
3. Hewitt, G.F., "The Role of Experiments in Two-Phase Systems with Particular Reference to Measurement Techniques," *Progress in Heat and Mass Transfer*, Edited by Hestroni, G., Sideman, S., and Hartnett, J.P., Vol. 6, 295-343, 1972, Pergamon, England.
4. Jones, O.C., Delhay, J.-M., "Transient and Statistical Measurement Techniques for Two-Phase Flows: A Critical Review," *Int. J. Multiphase Flow*, Vol. 3, 89-116, 1976.
5. Neal, L.G., and Bankoff, S.G., "A High Resolution Resistivity Probe for Determination of Local Void Properties in Gas-Liquid Flow," *AIChE J.*, Vol. 9, No. 4, 490-494, 1963.
6. Nicklin, D.J., Wilkes, J.O., Davidson, J.F., "Two-Phase Flow in Vertical Tubes," *Trans. Inst. Chem. Engrs.*, Vol. 40, 61-68, 1962
7. Quicker, G., and Deckwer, W.D., "Gas Holdup and Interfacial Area in Aerated Hydrocarbons," *Ger. Chem. Eng.*, Vol. 4, 363-370, 1981.
8. Satterfield, C.N., and Huff, G.A. "Effects of Mass Transfer on Fischer-Tropsch Synthesis in Slurry Reactors," *Chem. Eng. Sci.*, Vol. 35, 195-202, 1980.
9. Serizawa, A., Kataoka, I., Michiyoshi, I., "Turbulence Structure of Air-Water Bubbly Flow - I. Measuring Techniques," *Int. J. Multiphase Flow*, Vol. 2, 221-233, 1975.
10. Tsutsui, T., and Miyauchi, T., "Fluidity of a Fluidized Catalyst Bed and Its Effect on the Behavior of the Bubbles," *Int. Chem. Eng.*, Vol. 20, No. 3, 386-393, 1980.
11. Ueyama, K., Morooka, S., Koide, K., Kaji, H., Miyauchi, T., "Behavior of Gas Bubbles in Bubble Columns," *Ind. Eng. Chem., Process Des. Dev.*, Vol. 19, 592-599, 1980.

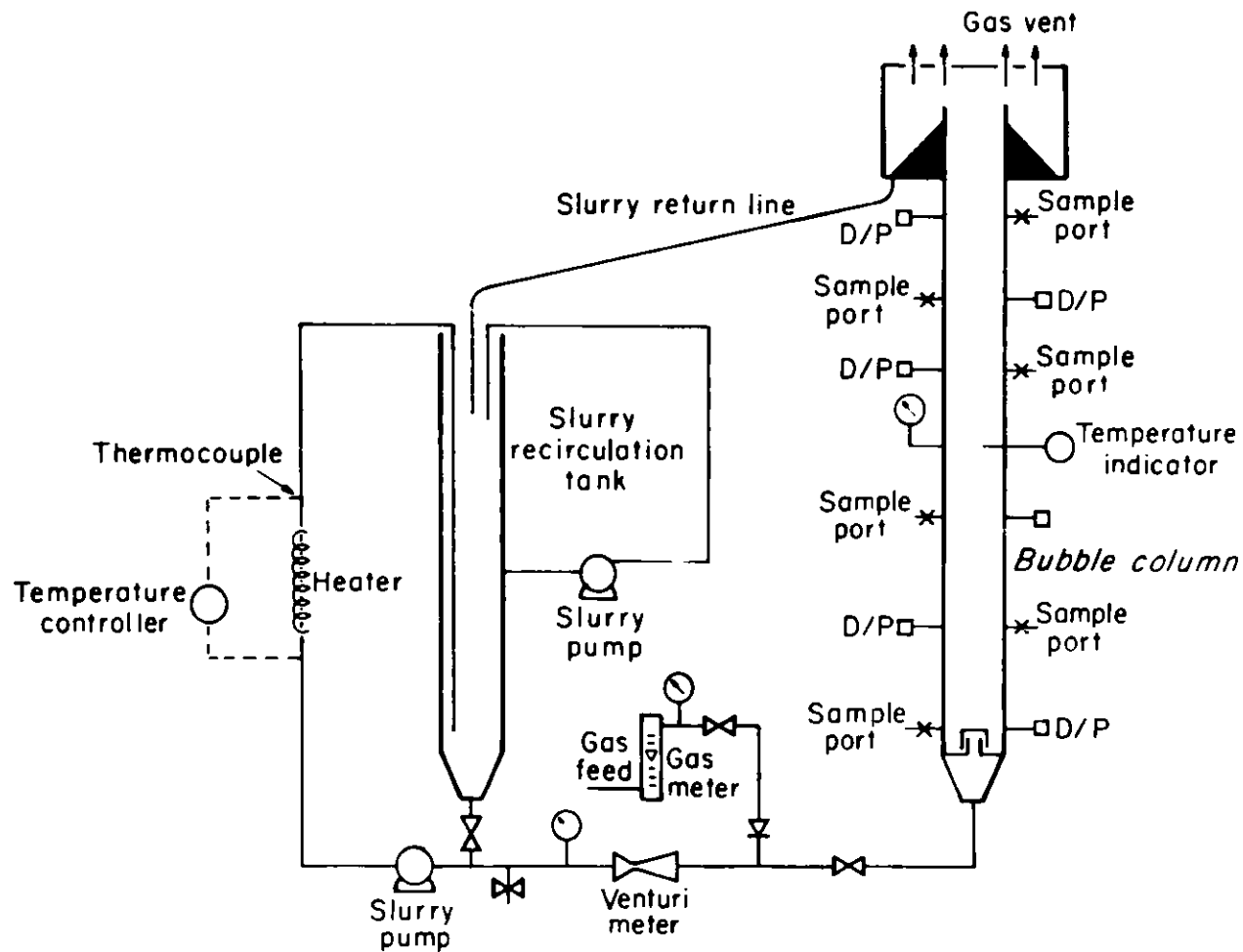
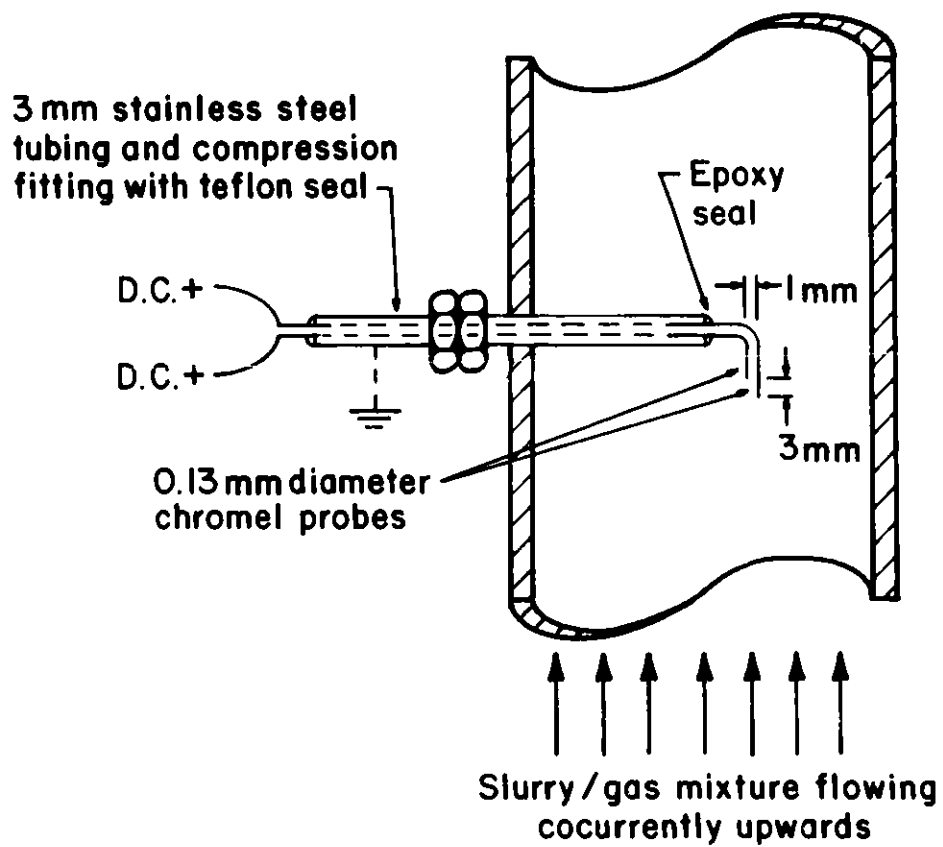
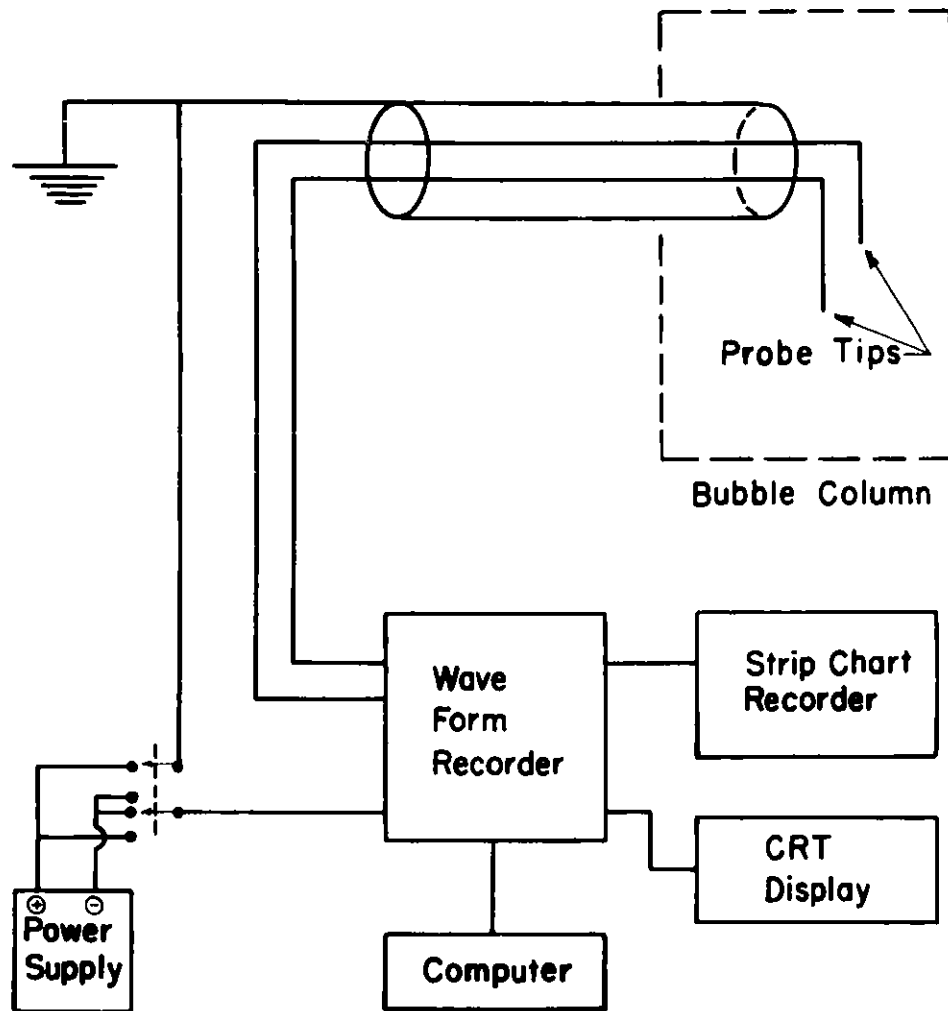


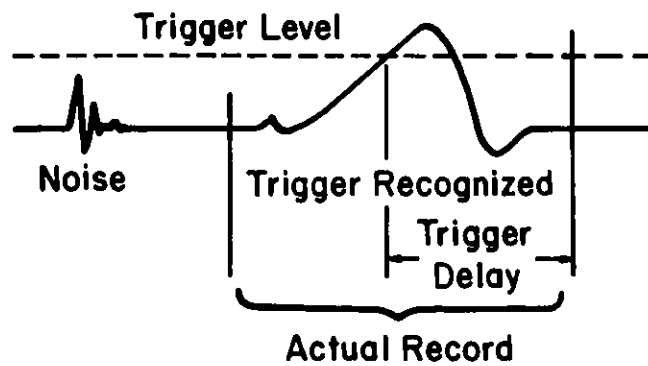
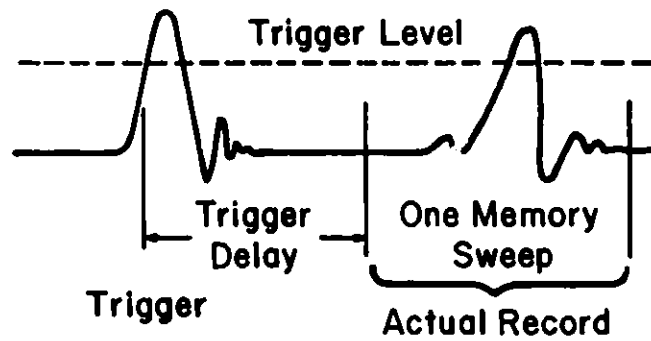
Figure 1-10.8 cm ID slurry bubble column apparatus



**Figure 2 - Probe configuration for conductivity measurements in 10.8 cm I.D. slurry bubble column apparatus.**



**Figure 3-Two point electrical conductivity probe circuit and data acquisition system.**

***Pretrigger Mode******Delayed Mode***

**Figure 4 - Scanning modes of digital waveform recorder .**



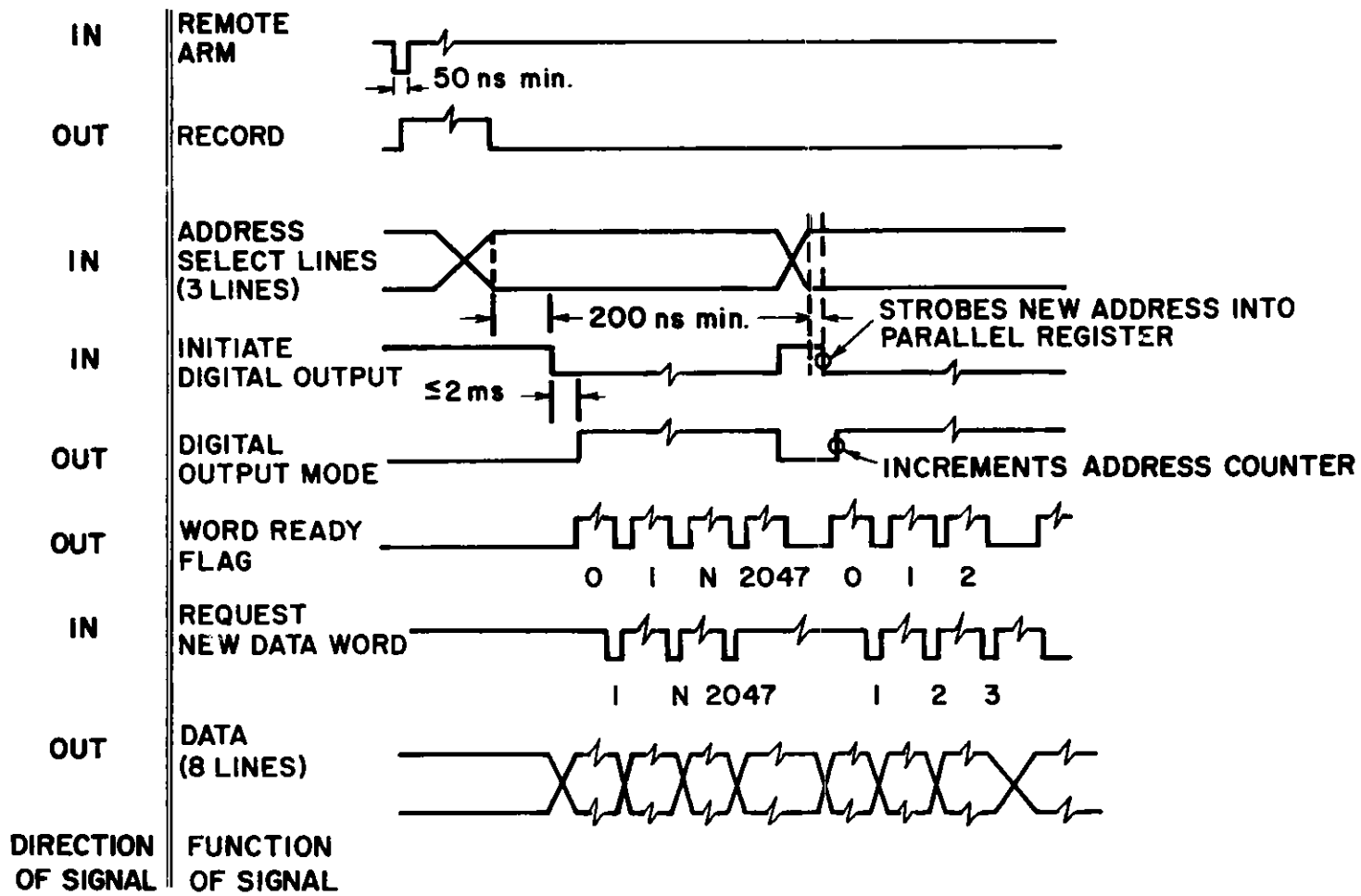


Figure 5 - Digital interface timing diagram for biomation 2805 m .

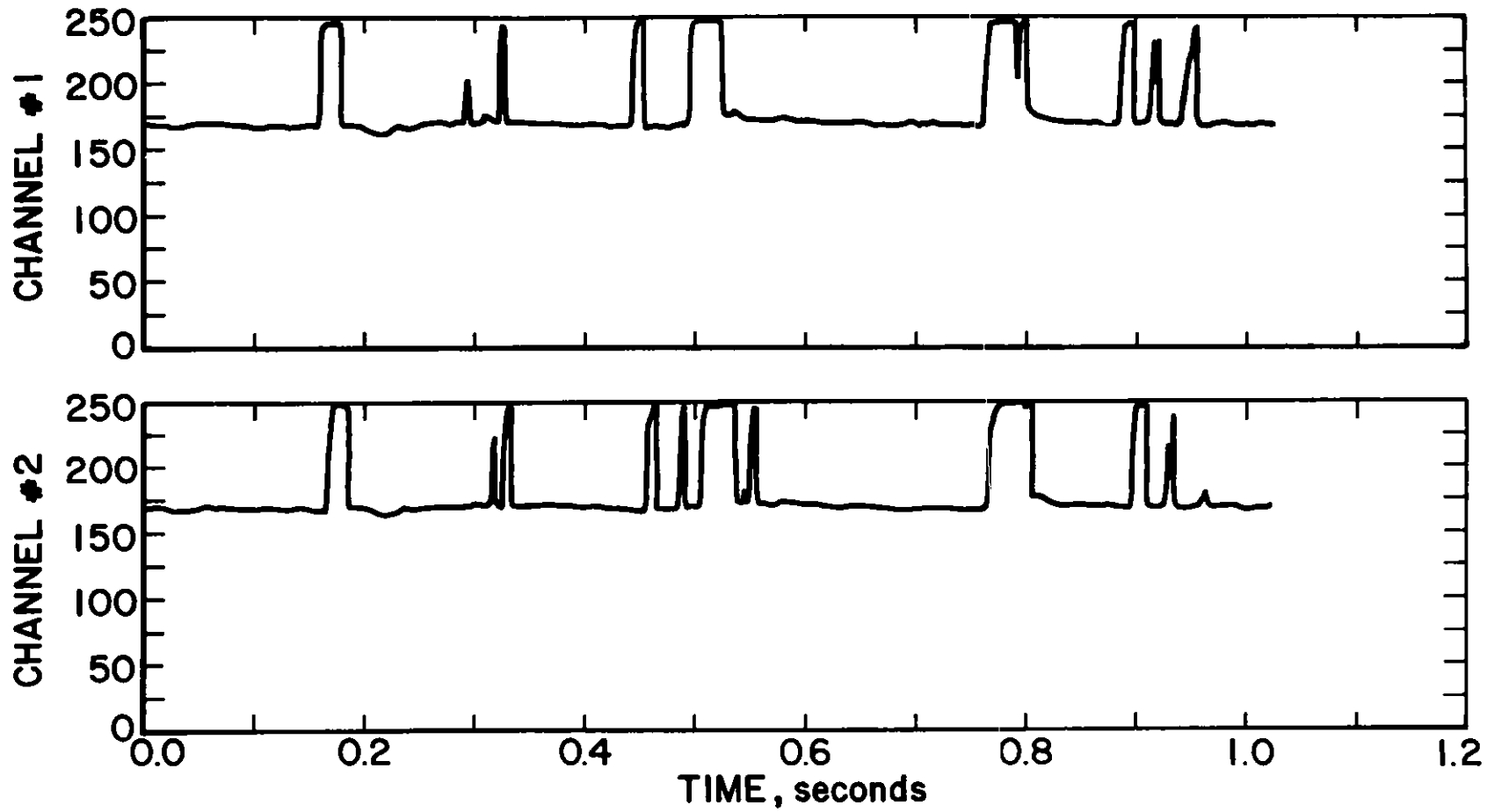
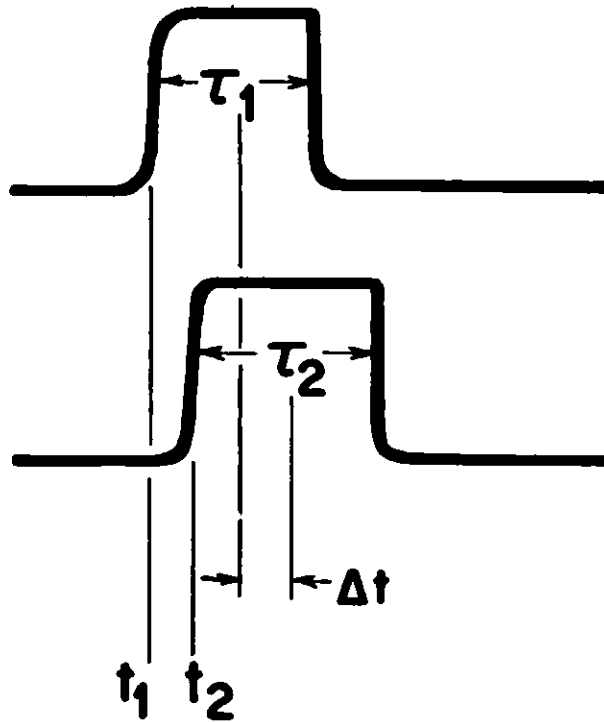


Figure 6 - Biomat data from 19 Mar - 82 08:26:24  
File : [117.2] PC025. Dat:5



Dwell Time :  $\tau_1, \tau_2$

Lag Time :  $\Delta t$

$$\Delta t = (t_2 - t_1) + \frac{1}{2} (\tau_2 - \tau_1)$$

Figure 7 - Relationship between probe signals and bubble dwell and lag time.

OPERATING EXPERIENCE WITH HIGH TEMPERATURE  
SONIC DOPPLER FLOWMETER IN COAL  
LIQUEFACTION PLANTS

by

A. C. Raptis, H. B. Karplus, and W. P. Lawrence

Abstract

The high temperature ultrasonic Doppler flowmeter\* is a non-intrusive device that was installed and tested on the high pressure slurry feed line to the preheater and the recycle line of the SRC-II pilot plant. The measurements from the ultrasonic Doppler flowmeter were compared with measurements from existing meters. The recycle line Doppler flowmeter readings were compared with those of a Venturi meter in the line, while the high pressure feed line Doppler measurements were compared with inferred flow measurements based on a materials balance concept. A consistent calibration was obtained.

---

\*H. B. Karplus, A. C. Raptis, and D. R. Canfield, ANL/FE-81-64

### INTRODUCTION

The ANL high temperature acoustic Doppler flowmeter was installed in two locations at the SRC-II pilot plant in Fort Lewis, WA<sup>1,2</sup>. A partial schematic diagram of the plant indicating the location of the ANL installed meters is shown in Fig. 1. Flowmeter  $M_1$ , is located in the high pressure slurry line that feeds the preheater, while flowmeters  $M_2$  and  $M_3$  are located in the recycle line of the plant. (The advantages, construction, and operation of the ANL meter have been discussed elsewhere<sup>1,2</sup>). The dominant features of the installed meters are the capability to operate at high temperature, and the handling of the very broad band signals obtained in laminar flows. Two types of installation for the transducers were used, while the signal processing electronics remained the same for all three meters. Flowmeters  $M_1$  and  $M_2$ , located in the preheater inlet and recycle slurry lines respectively, were installed by using conventional 500 kHz NDT transducers (Panametrics A413S) which were coupled through mode conversion plastic wedges to 8" steel wave

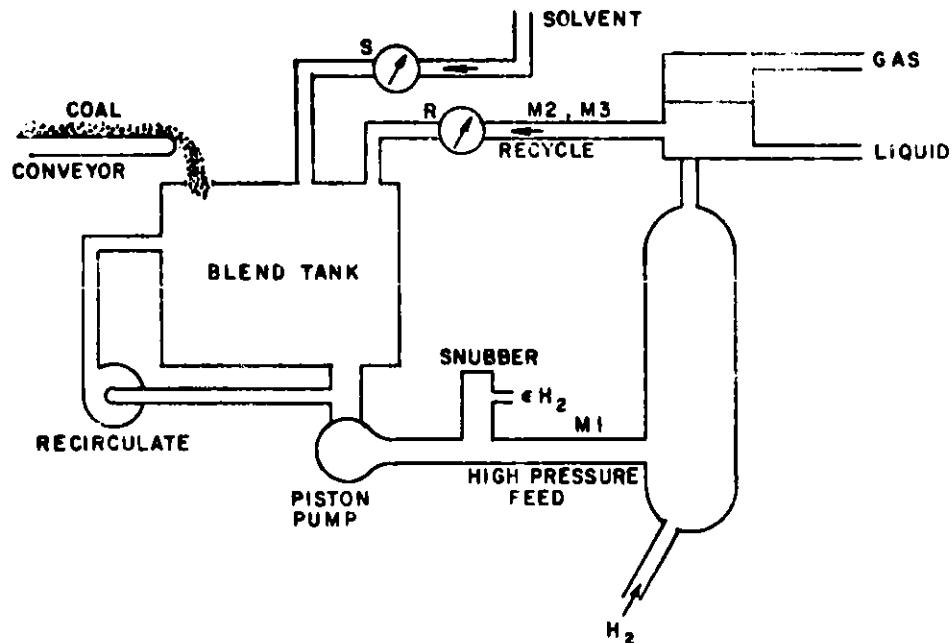


Fig. 1. Schematic of Flowmeter Location

guides, one end of which is brazed to the pipe. The sound wave is injected into the pipe at a 45° angle, scattered by the coal particles, and received by a duplicate arrangement installed on the other side of the pipe. (This received signal is processed by a set of ANL developed electronics discussed in references 1, 2). Flowmeter M<sub>3</sub>, located in the recycle line, was installed by using a pair of Lithium niobate transducers clamped directly to the pipe. Good contact with the pipe was obtained by means of spring sustaining contact pressure between optically flat surfaces. These transducers were designed originally for a different application and are resonant at 3 MHz. They are very broad band, however, and have sufficient response at the 0.5 MHz frequency used by the ANL flowmeter to be useable on the small one inch recycle line pipe. The sound wave is injected at an angle of 27°, with the pipe axis by one transducer reflected from the particles and received by the other transducer installed on the other side of the pipe. The signal is processed with the same electronics as M<sub>1</sub> and M<sub>2</sub>.

#### MEDIA

The media in the preheater inlet slurry line is oil/coal and varies in concentration from a few percent (1-3%) up to 45% by weight and particle size of 1/8" to 80% through 200 mesh, while the recycle slurry line media is oil/ash, with less than 1% ash concentration and particle size finer than can be retained by standard screens (to 200 mesh).

The recycle slurry probably contains some gas bubbles also. (A complete description of the test conditions is given in Table I). The origin of the gas bubbles and the amount of gas entrainment in the line is not known; there is also no mechanism available at the present time to determine them. Figure 1 shows that the liquid and gas are separated after the coal is heated, but traces of gas are likely to be entrained at all times. Evidence that supports the presence of gas bubbles in the recycle line can be inferred from the observations: (1) In the absence of coal feed, the media in the recycle and inlet slurry lines are the same, (2) the flowmeters M<sub>1</sub> and M<sub>2</sub> are located in the recycle and inlet slurry lines respectively, (3) under the condition of no coal feed, there are no scattering particles in either line, and (4) the

Doppler signal from  $M_1$  is too low to be detected, while the Doppler signal from  $M_2$  is detected. The fact that  $M_1$  flowmeter was not operating in the absence of coal feed led to the tentative hypothesis that the ash content particles in the recycle line, where flowmeter  $M_2$  is located, were too small

Table 1

## Specifications

Meter	$M_1$	$M_2$	$M_3$
Location	High Pressure Feed	Recycle	
Fluid	Oil/Coal	Oil/Ash	
Temperature °C(°F)	180(350)	260(500)	
Specific Gravity $g\ cm^{-3}$	1.15	1.02	
Viscosity cP	200*	12	
Max Flow lb/hr	10000	5000	
g/s	1250	630	
Max Velocity cm/s	98	136	
Pipe Radius (nom) cm(in)	2.0 (.8)	1.22 (.48)	
Reynolds Number	100	1400	
Angle of Sound Beam	45°	45°	27°
in pipe wall to pipe axis	by standoff	by standoff	direct coupled

---

\*Variable depends on residence duration in blend tank.

to scatter adequately at 500 kHz and that in fact the recycle line flowmeter was operating on bubble scatter. These bubbles would be compressed and forced into solution in the high pressure pump, shown in Fig. 1 in front of the

preheater inlet slurry line. Confirmatory experiments, such as use of high frequency excitation (1-10 MHz) on the high pressure feed line during a no coal feed operation could not be scheduled prior to the SRC-II permanent shutdown.

## RESULTS

Two versions of the ANL Doppler flowmeter were tested. The difference in these two versions is in the type of transducers and in the way the transducers are attached to the pipe; the electronics are the same for both. Flowmeters  $M_1$  and  $M_2$ , located in the high pressure slurry inlet line to the preheater and the recycle line respectively, have their transducers (Panametrics A413S) on stand off isolators, while flowmeter  $M_3$ , located on the recycle line, has the high temperature transducers (ANL-lithium niobate) close coupled to the pipe<sup>1,2</sup>.

Flowmeter,  $M_1$ , located at the preheater inlet slurry line, in the absence of any other flow measuring device in the line, is compared to a complex mass balance method used by SRC-II engineers to infer flow in the line. In accordance with the material balance method the flow in this line is equal to the rate volume change due to the drop in level in the blend tank added to the flow of all lines feeding the tank. These lines are the solvent feed, the recycle and the solid conveyor as shown in Fig. 1. The voltage output of the Doppler flowmeter and the velocity obtained by the materials balance method are plotted in Fig. 2. It can be seen that the two measurements agree very closely. In fact, they are within 2% of each other. The advantage of the Doppler method over the materials balance method is that it gives a continuous on-line measurement, while the materials balance method depends on measurements from other lines and is not on-line.

The readings from flowmeters,  $M_2$  and  $M_3$ , are compared with the readings obtained from a Venturi flowmeter located in the recycle line. Figure 3 shows the results from this comparison. In this figure the output of the Doppler flowmeter  $M_2$ , is plotted against the reading obtained by the Venturi meter.



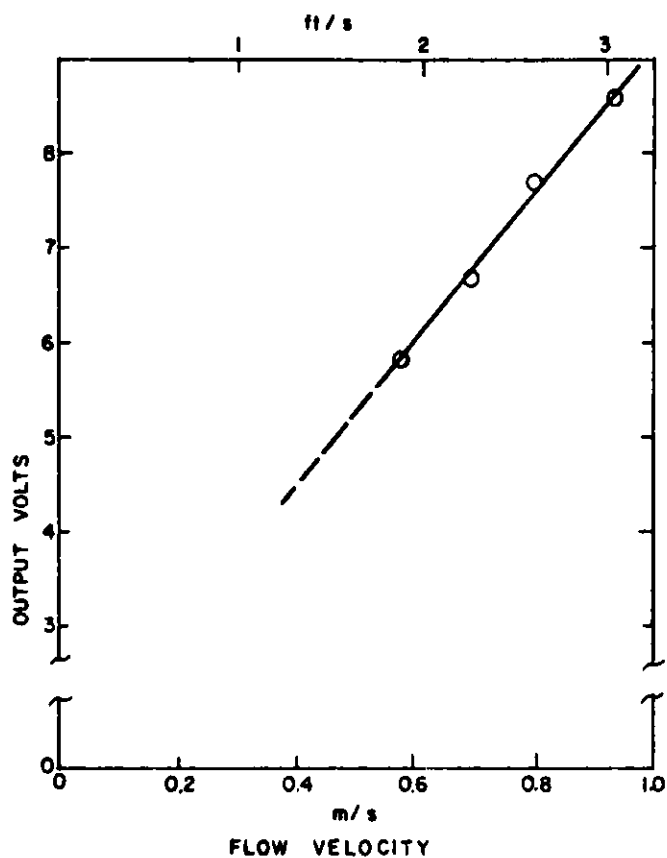


Fig. 2 Calibration of Meter M<sub>1</sub> On Pressure Feed Line

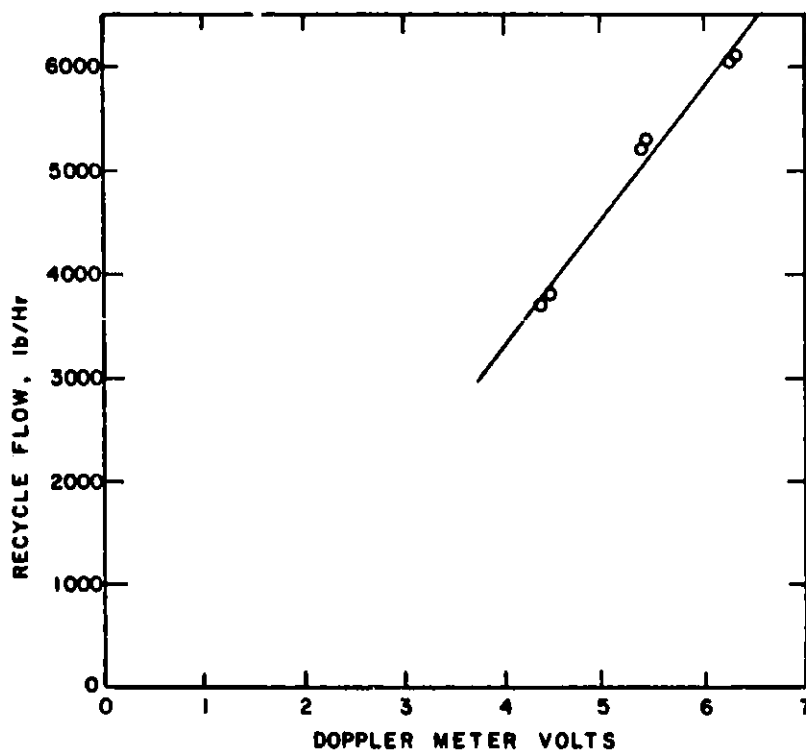


Fig. 3 Calibration of Doppler Flowmeter on Recycle Line Using Standoff Waveguides

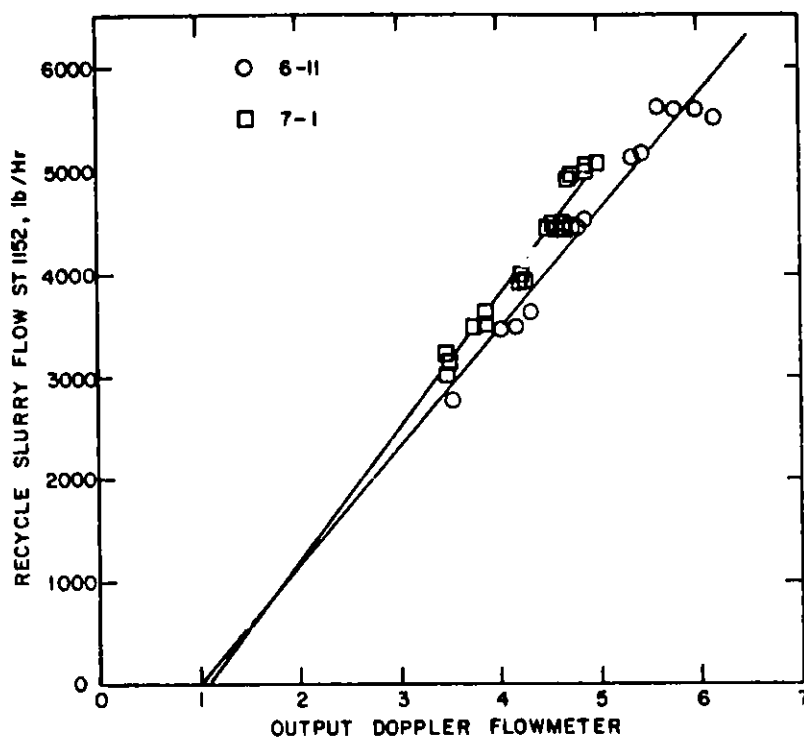


Fig. 4 Calibration of Doppler Flowmeter on Recycle Line  
Using A Close Coupled Transducer

Again, the results agree very closely and in fact are within 3% from each other. The regression coefficients obtained from Figs. 2, 3, and 4 are calculated and listed in Table 2. Figure 3 shows the comparison of the Venturi flowmeter output and the close coupled Doppler flowmeter.

After the above comparisons were made, only flowmeter  $M_3$  on the recycle line was left operating for the duration of plant operation from 6/1/81 to 7/14/81 and hourly average readings were recorded. During this period stable operation was observed until 7/4/81. Occasional non-random departures indicate the possibility of a zero shift or sensitivity change in the order of 5-10%. The relative stability of the Doppler flowmeter with regard to the reference Venturi meter was not determined because sufficient data was not available prior to the permanent shutdown of the SRC-II plant.

The electronics of the flowmeters were calibrated before installation by using white noise with sharp cutoff frequency  $f_c$ . This white noise was injected between the mixer and the internal automatic gain control (the electronics of the meter were discussed in references 1, 2). The calibration curve that resulted from this test is shown in Fig. 5.

Table 2

## Regression Formulae

V = Flowmeter output      Volt  
 Q = Flow rate              lb/hr  
 r = Coefficient of determination  
 (1) = for perfect linear functions)

$$Q = AV + B$$

<u>Date</u>	<u>System #</u>	<u>A</u>	<u>B</u>	<u>r<sup>2</sup></u>
6/1	2 Standoff	1236	1590	.99
6/11	3 Close Coupled	1208	1406	.95
7/1	3    "        "	1206	1880	.97
7/11	3    "        "	1286	1803	.97

#1 Pressure feed line      45° sound from waveguide  
 #2 Recycle line            45° sound from waveguide  
 #3 Recycle line            27° sound direct coupled

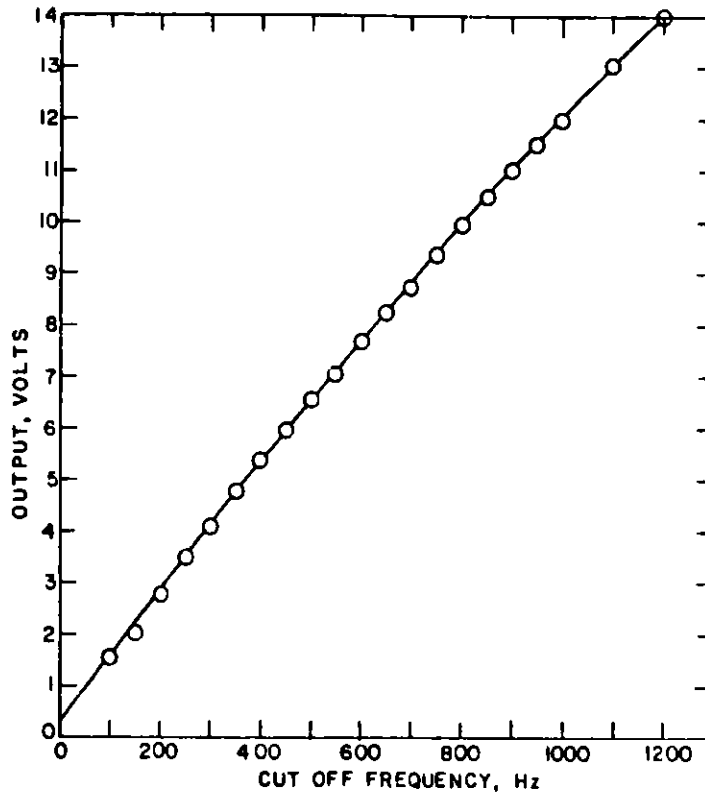


Fig. 5. Output of Doppler Meter for Band Limited White Noise Input (10V Output Limiter Disconnected).

#### DISCUSSION AND CONCLUSIONS

The high temperature acoustic Doppler flowmeter is non-intrusive and this feature is its greatest advantage over the orifice type meters that require frequent attention. At this point, however, additional work is needed to determine the following: (1) optimum operating frequency, (2) the effects of bubbles on the optimum operating frequency, (3) a mechanism that automatically observes and rejects data contaminated by the presence of excessive amounts of gas, and (4) examination of the effects of temperature, viscosity, concentration, particle size and particle size distribution on the measurement.

Acknowledgment

We would like to thank T. K. Lau and T. Simpson of DOE, and R. S. Zeno, G. S. Rosenberg, T. P. Mulcahey, G. A. Forster, and N. M. O'Fallon, all from ANL, for their support and encouragement in this work. We would also like to thank SRC-II personnel, especially D. R. Canfield and Ed King of P&M for their help and cooperation. And special thanks are due to Howard Eisenbrandt for preparation of drawings and Nancy Heeg for the typing of this report.

References

1. H. B. Karplus, A. C. Raptis, D. R. Canfield, "Development and Testing of a High Temperature Acoustic Doppler Flowmeter," ANL/FE-81-64, Sept. 1981.
2. H. B. Karplus, A. C. Raptis, D. R. Canfield, "The Sonic Doppler Flowmeter" 1981 Symposium on Instrumentation and Control for Fossil Energy Processes.

EVALUATION OF CORIOLIS FLOW METERS IN LIQUEFACTION SLURRIES

W. Lee Smith  
Micro Motion, Inc.  
12400 North Freeway, Suite 100  
Houston, Texas 77060

Roy O. Nicholson  
Monsanto Research Corp. - Mound Laboratories  
P. O. Box 32  
Miamisburg, Ohio 45342

Introduction

The solvent refined coal pilot plant at Wilsonville, Alabama, is a six ton per day coal liquefaction facility operated by Catalytic, Inc. since 1974. The unit acquires coal from various eastern mines for testing. The coal is then pulverized and blended with solvent, resulting in a 38 1/2% coal slurry, which is then pumped by a positive displacement triplex pump to the preheater for heating to process temperature of 850°F. It was determined to evaluate a Coriolis mass flow meter at this point in the process. In order to operate successfully in this application, the meter would need to be able to accurately measure the mass flow of a viscous slurry over a range of rates and temperatures without being affected by the pulsations developed by the triplex pump.

The need for the measurement of mass flow as an element of process control or revenue metering is not new. But until recently, these measurements could not be made directly; they were made by batch weighing or, in continuous processes, by inference from volumetric flow measurements. The derivation of mass flow from measured volumetric flow is complex, requiring correction for fluid density variations with temperature and, in gases and some liquids, pressure. Volumetric meters are, in general, also sensitive to variations in fluid viscosity which varies with temperature and, in many cases, flow rate. Slurries display increasing viscosity with flow rate while inks, tars and soaps display decreasing viscosity with flow rate. Direct mass flow measurement can now be made independent of the physical properties of the fluid using the Micro Motion mass flow meter.

Theory of Operation

The flow meter consists of a U-shaped sensor tube through which the fluid passes (see Figure 1). The tube is vibrated by a magnetic driver and counter balance assembly. Magnetic position sensors transmit the flow signal to electronic circuitry housed in a separate enclosure. A linear output, compatible with most display and control equipment, is produced. Components are housed in a NEMA 4 enclosure suitable for installation in industrial environments.

To understand the operation of the flow meter, let us focus on the sensor tube assembly as shown in Figure 2. A magnet attached to the tube moves inside a coil attached to the counter balance. The assembly moves

like a tuning fork; that is, the two parts move in opposing directions at a natural spring frequency. The magnet-coil pair reinforce this natural movement, operating the whole system as a low power oscillator. This is the only function of the counterweight and drive assembly. Note that the U-tube sensor is secured firmly to the meter case at a point near the process fittings. The case and the mounting surface serve as the "handle" of the tuning fork. As the tube is forced downward by the driver, it is in effect rotated about a horizontal axis through the base. At the bottom of the cycle, the spring resistance of the tube overcomes the driver and the tube slows, stops and reverses its motion. The tube rotates upward past its neutral position until the upward motion slows, stops, and reverses. This movement is repeated as an oscillation between 70Hz and 130 Hz (depending on meter size) of a few millimeters amplitude. This is the only movement of the flow meter and is an important factor in its reliability.

Fluid passing through the U-tube follows the path shown in Figure 3. As the fluid particles move down the inlet leg of the tube, they experience increasing vertical velocity or acceleration due to the tube rotational velocity. The particles experience a deceleration as they move down the outlet leg of the tube. The particle acceleration and deceleration are equal in magnitude but opposite in direction, as shown by "a" in Figure 4. The fluid resists this acceleration and exerts forces ("F" in Figure 4) equal in magnitude, but in the opposite direction from the accelerations. These forces are linearly proportional to the mass flow rate of the fluid. A study of the equations relating to these forces will show that the physical properties of the fluid do not influence the forces. As a result, the simple U-tube becomes a flow meter, able to measure mass flow without fluid property compensation and without in line sensing equipment.

The endview in Figure 5 illustrates the force couple acting on the tube resulting in the tube twist. This twist is most pronounced as the tube moves through its rest position. The angle,  $\theta$ , at this point is proportional to the magnitude of the force couple which is proportional to mass flow rate. When the tube direction is reversed, the accelerations, forces, and angle of twist are also reversed. The full cycle of tube oscillation can be seen in Figure 6.

#### Experience at SRC-1

Prior to the installation of the Micro Motion meter, the coal solvent feed rate to the reactor preheater was achieved only with great difficulty as the fluid properties varied with coal properties, temperature, recycle rates and other factors. With Micro Motion, instantaneous mass flow measurements have replaced time consuming rigorous calculations with accuracies never before achieved.

A series of tests run on the meter on 3 April, 1982 show a worst case error of 0.6% when compared to platform scales. As these scales were not certified, there is no reason to suspect the Micro Motion meter does not fall in the published accuracy of  $\pm 0.4\%$  of reading. See Figure 7.

### Future Developments

Micro Motion is currently manufacturing meters for flow rates as low as 0.5 lb/hr and as high as 200,000 lb/hr. The company is employed in the development of larger meters to handle flows up to 1mm lb/hr. The current temperature limits available are +400°F. Engineering is developing, with this SRC process in mind, the technology to allow us to accept applications in the 900-1000°F area. Current estimates indicate development will be complete by December 1982.

### Acknowledgments

#### Illustrations

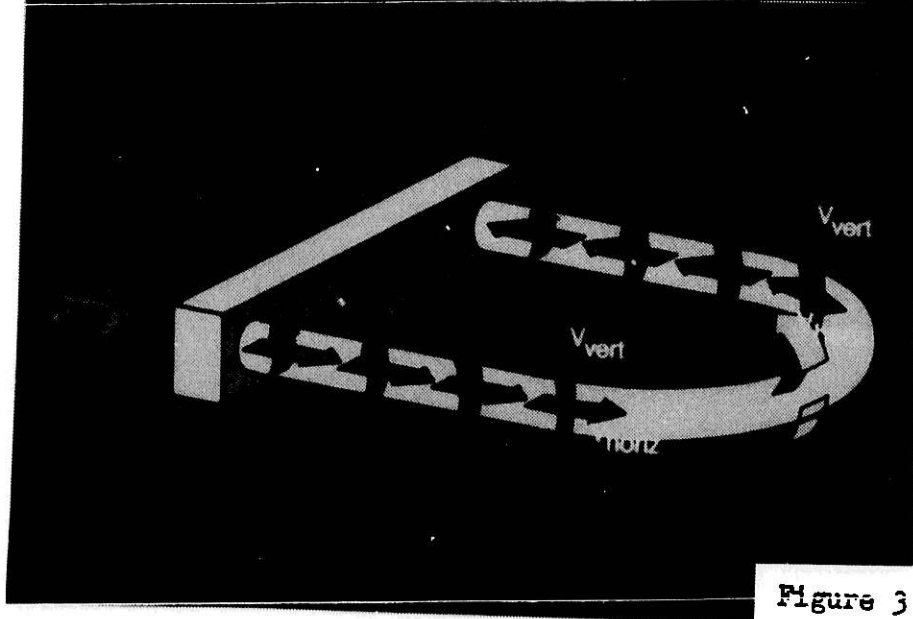
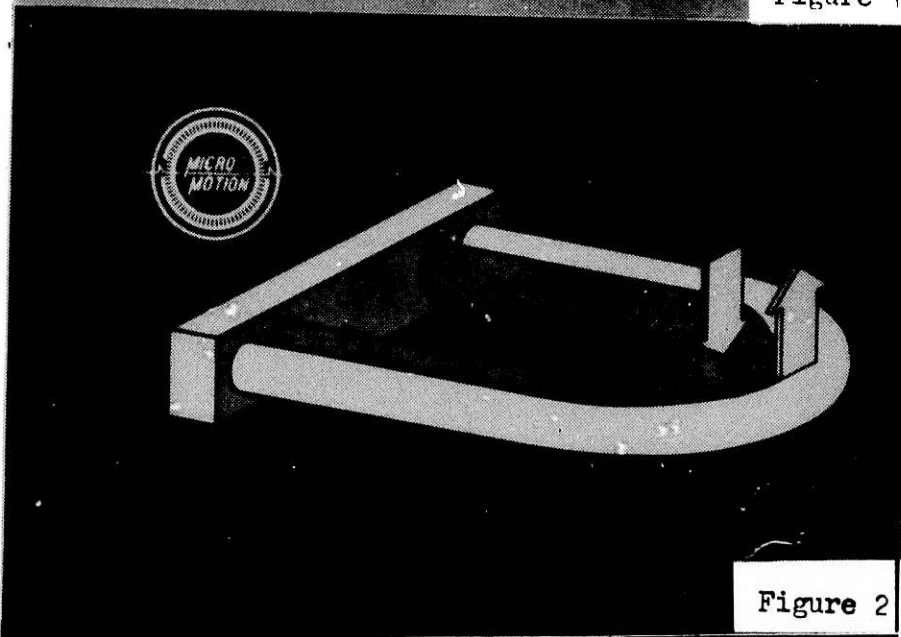
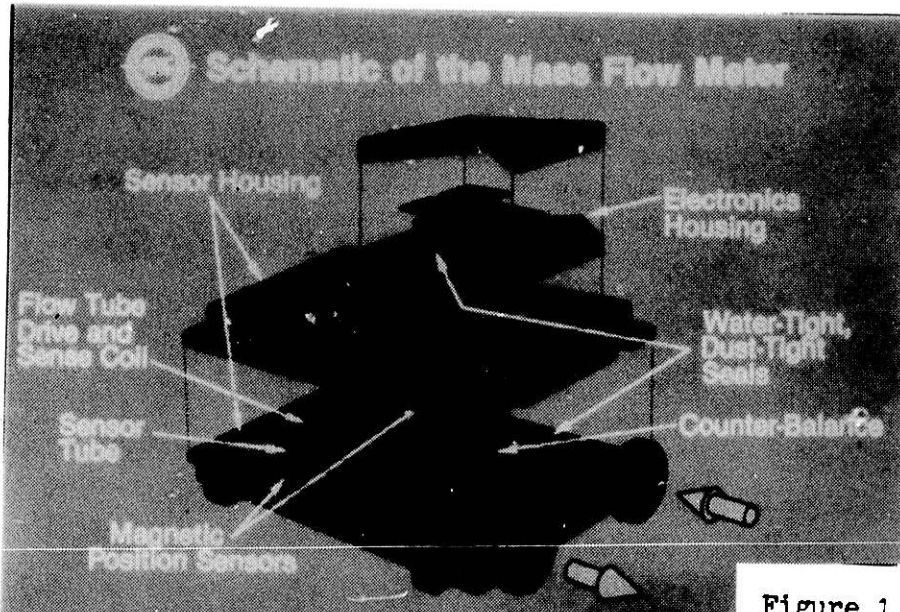
Micro Motion, Inc., 7070 Winchester Circle, Boulder, Colorado 80301

#### Photographs and Test Data

Mr. Maurice Turgeon, Catalytic, Inc., Wilsonville, Alabama

Dr. Roy Nicholson, Monsanto Research Corp.





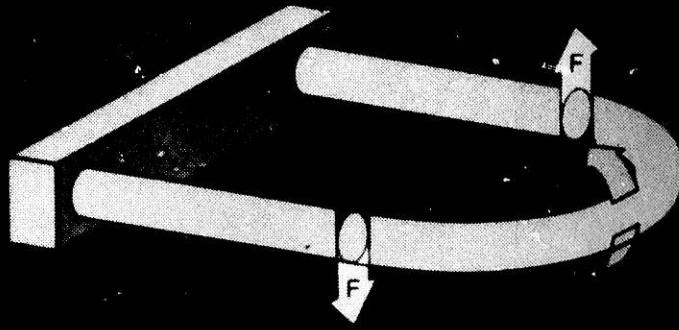


Figure 4

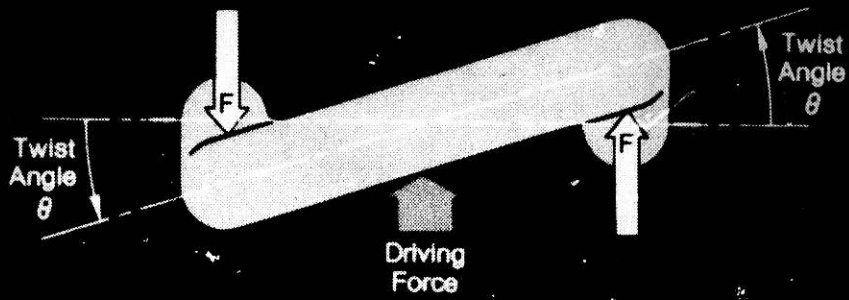


Figure 5

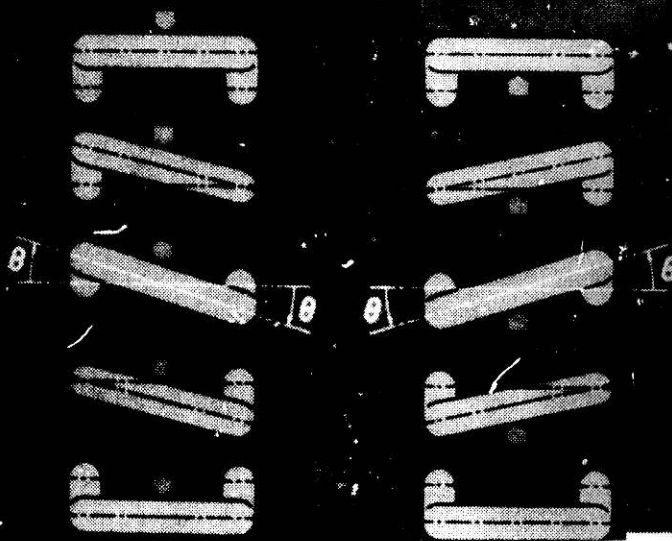


Figure 6



Figure 7

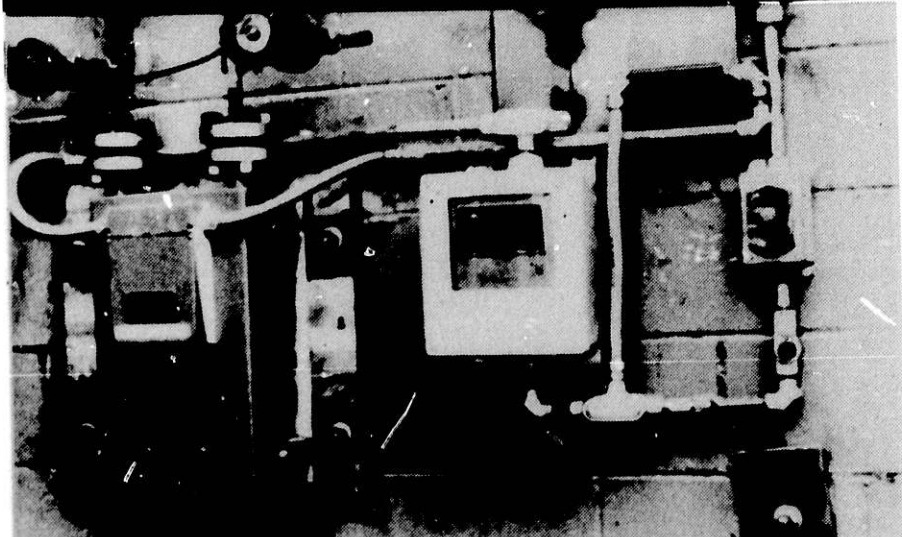


Figure 8  
The Micro Motion meter installation

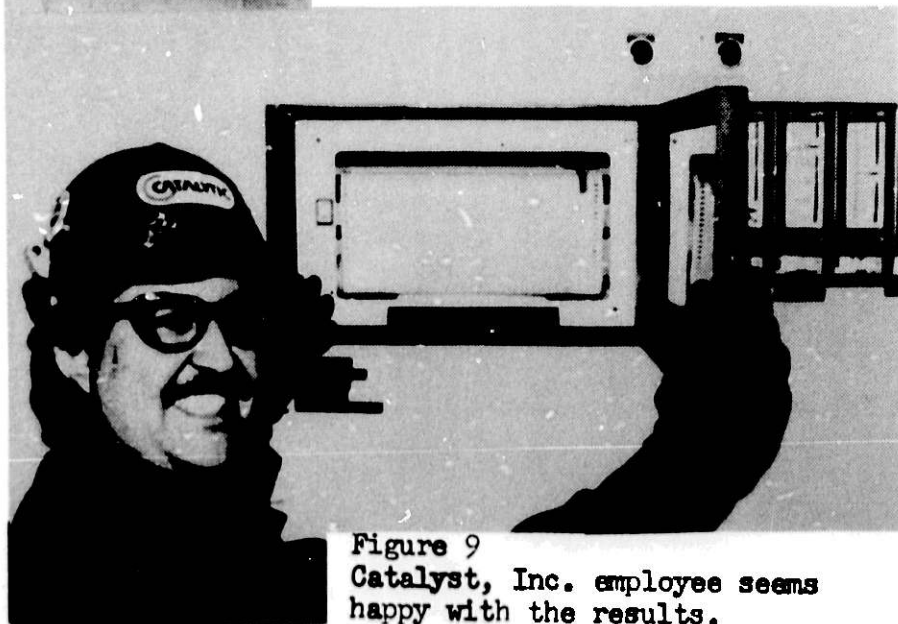


Figure 9  
Catalyst, Inc. employee seems happy with the results.

IN SITU, REAL TIME MEASUREMENT OF NO, NO<sub>2</sub>, AND SO<sub>2</sub> BY  
TUNABLE ATOMIC LINE MOLECULAR SPECTROSCOPY (TALMS)

Tetsuo Hadeishi and Ralph McLaughlin  
Lawrence Berkeley Laboratory  
University of California  
Berkeley, California 94720  
Phone: (415) 486-5734  
FTS: 451-5734

Tunable Atomic Line Molecular Spectroscopy (TALMS) is a newly developed technique for detection of molecules (as well as atoms) which is highly specific and sensitive even in the presence of high levels of background interference. The ideal analytical instrument would consist of a black box, through which a sample is transported, or is pointed to the sample to be measured, and without coming in contact with a surface that would cause alteration, would point out the level of all species in a specified concentration range. Of course, no such instrument exists today. The properties of such an ideal instrument are:

- No interference
- High sensitivity
- No matrix effect
- Inexpensive
- Precise
- Absolutely accurate
- Easy to use

TALMS is one of our attempts to construct an instrument that approaches this ideal.

TALM spectroscopy consists of splitting a source atomic emission spectral line by means of a magnetic field (Zeeman effect) and making a differential absorption measurement between one Zeeman component that has been magnetically tuned to match an analytic absorption line and unmatched Zeeman reference component. The difference in polarization between Zeeman components permits the matching and non-matching wavelengths to be alternately selected and the differential absorption measured very rapidly with an electro-optical device called a current controlled retardation (CCR) plate.<sup>1</sup> This process is illustrated in Fig. 1. The line with label  $\Delta M = +$  (lower tracing) is tuned with the magnetic field to exactly match the electronic-vibrational-rotational line of a specified molecule (upper tracing) in the sample. The TALM spectrometer detects the difference between  $\Delta M = +1$  and  $\Delta M = -1$  reference Zeeman components and the differential absorption is proportional to the concentration of molecules in the sample.

The components of the TALMS system are pictured in Fig. 2. The light from a light source placed in the electro-magnet is passed through the hole drilled in the magnetic core, then through an absorption cell, a variable phase retardation plate, a linear polarizer, and finally focused on a small monochromator. Right and left circularly polarized light, hence the higher and lower Zeeman wavelength components, are selected by CCR and a linear polarizer combination.

For in-situ measurement, the absorption cell is replaced by a real system such as combustion or combustion chamber. These components, which utilize features of Zeeman effect, form the heart of the TALM spectrometer. This simple device is capable of a surprising resolving power (in excess of 500,000) with a large acceptance angle. To determine the shape of the absorption features, a plot is made of ratio of intensities ( $I/I_0$ ) with the sample in and out of the optical path as a function of magnetic field.

Cd II at 214.2 nm at 10 KG and Zn at 213.8 nm at 20 KG magnetic field can be used to detect NO molecules by TALM spectrometer.<sup>2,3</sup> Figures 3 and 4 show, respectively, NO line absorption profiles scanned by a Cd II 214.2 nm and a Zn 213.8 nm atomic emission line.

Figure 5 shows one example of NO signals obtained with a 20 cm cell.

By means of similar technique, NO<sub>2</sub> and SO<sub>2</sub> can be measured. Figure 6 shows a line profile of NO<sub>2</sub> by means of TALMS magnetic scanning of a Cu 249.2 nm line. Figure 7 shows differential absorption line profile of SO<sub>2</sub> using a Zn 213.8 nm line magnetic scanning.<sup>4</sup>

#### Acknowledgment

This work was supported by the Director's Office of Energy Research, Office of Health and Environmental Research of the U.S. Department of Energy under Contract No. DE-AC03-76SF00098.

#### References

1. B.D. Zak, B. Chang, and T. Hadeishi, Appl. Opt. 14, 1217 (1975).
2. H. Koizumi, T. Hadeishi, R.D. McLaughlin, Appl. Physics Ltrs. 34, 382 (1979).
3. H. Koizumi, T. Hadeishi, R.D. McLaughlin, Anal. Chem. 52, 500-504 (1980).
4. H. Koizumi, T. Hadeishi, R.D. McLaughlin, Spectro. Chem. Acta 36B, 483-485 (1981).

TABLE 1. Small Molecules Measured With TALMS

Molecule	Atomic Line	Wavelength (nm)	Transition
NO	Cd(II)	214.4	$^2S_{1/2} - ^2P_{3/2}$
		226.5	
OH	Zn	213.8	$^1S_0 - ^1P_1$
	Bi	306.8	$^4S_{3/2} - ^4P_{1/2}$
I <sub>2</sub>	Zn	307.2	$^3P_2 - ^3P_1$
	Hg	546.1	$^3P_2 - ^3S_1$
S <sub>2</sub>	Mg(II)	279.6	$^2S_{1/2} - ^2P_{3/2}$
		280.3	$^2S_{1/2} - ^2P_{1/2}$
SO <sub>2</sub>	Zn	213.8	$^1S_0 - ^1P_1$
	Cd	228.8	$^1S_0 - ^1P_1$
NO <sub>2</sub>	Cu	249.2	$^2S_{1/2} - ^4P_{3/2}$
	B	249.7	$^2P_{1/2} - ^2S_{1/2}$
		249.8	$^2P_{3/2} - ^2S_{1/2}$
CH <sub>2</sub> O	Ag	338.3	$^2S_{1/2} - ^2P_{1/2}$

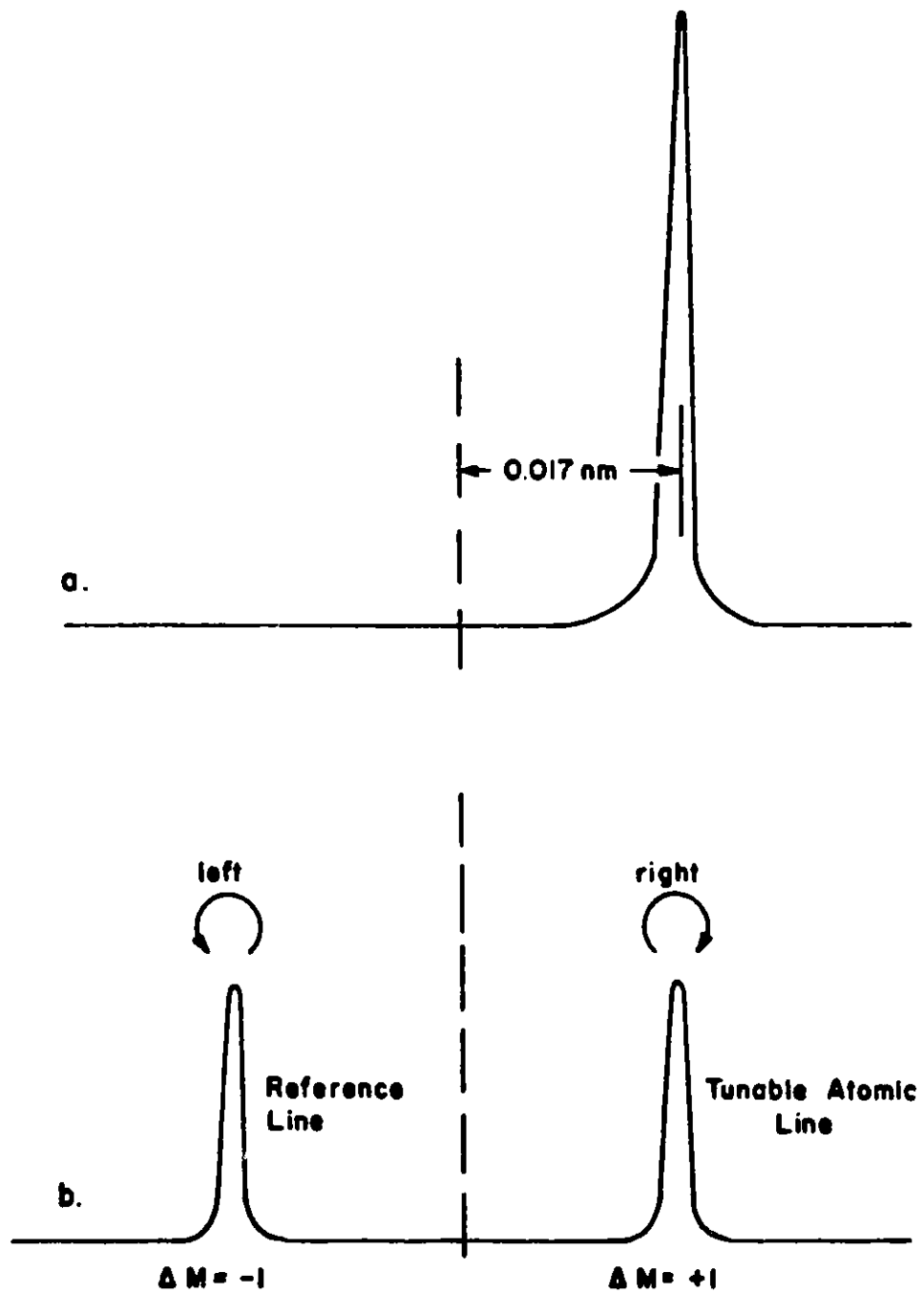


Fig. 1 Tunable Atomic Line Molecular Spectroscopy

- a) Molecular absorption line
- b) Zeeman split atomic emission line

Note: the  $M = +1$  line is right-circularly polarized and the  $M = -1$  line is left-circularly polarized.

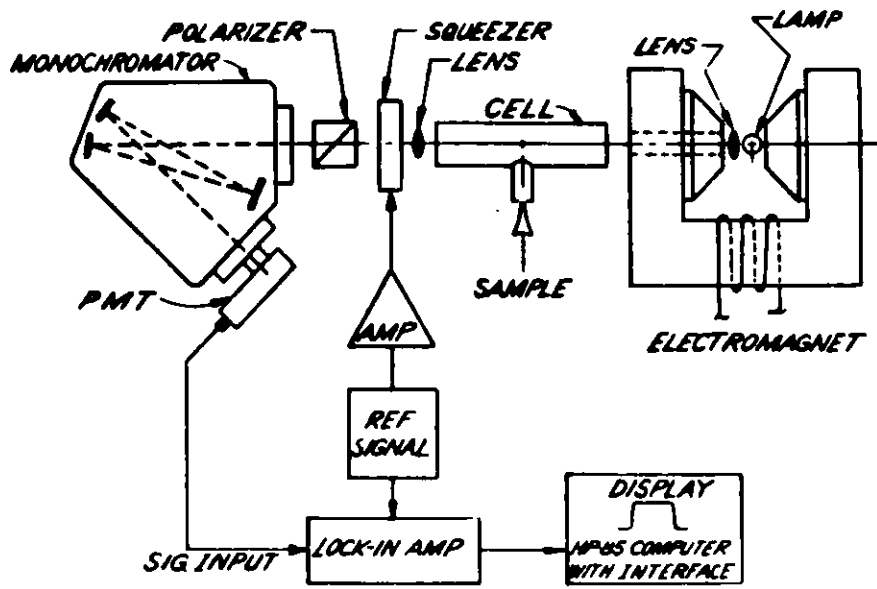


Fig. 2 Block diagram of TALMS instrumentation



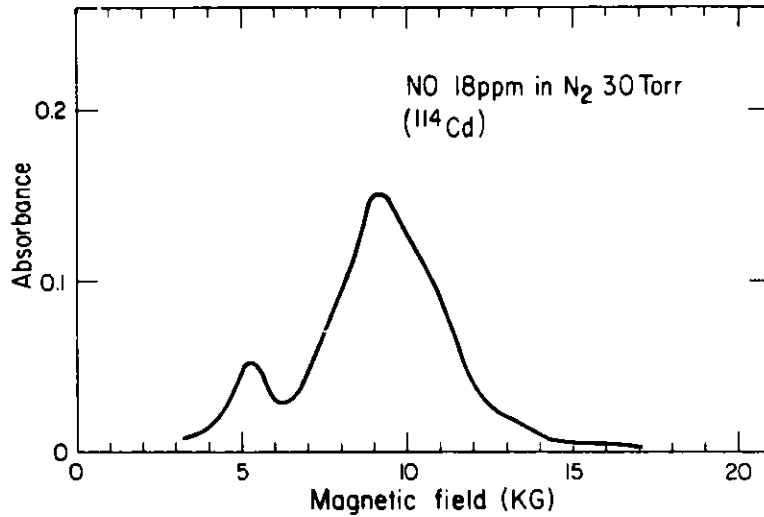


Fig. 3 Relation between the magnetic field strength and the differential absorption caused by NO for the Cd(II) line at 214.4 nm.

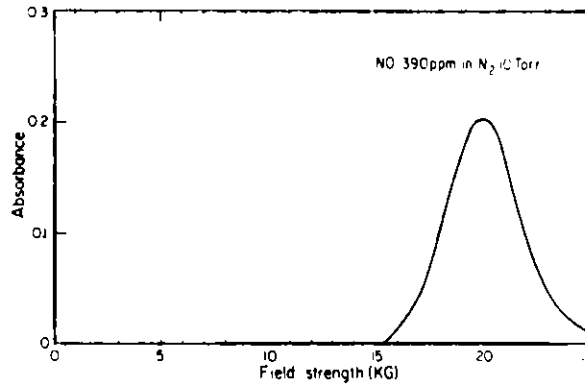


Fig. 4 Relationship between the field strength and the differential absorption caused by NO for the Zn line at 213.9.

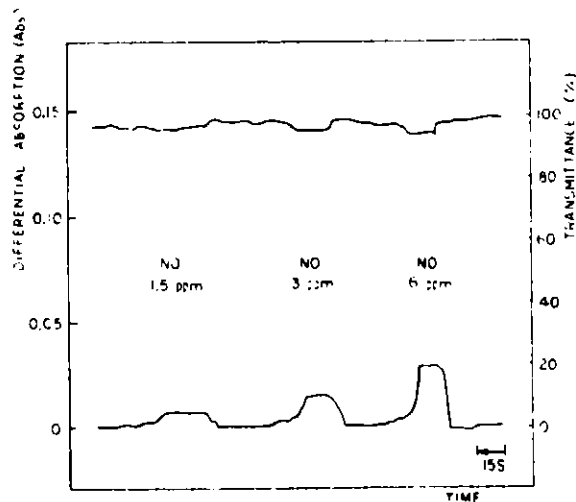


Fig. 5 NO signal with the present technique. Lower trace: differential signal; upper trace: transmittance of light through the cell.

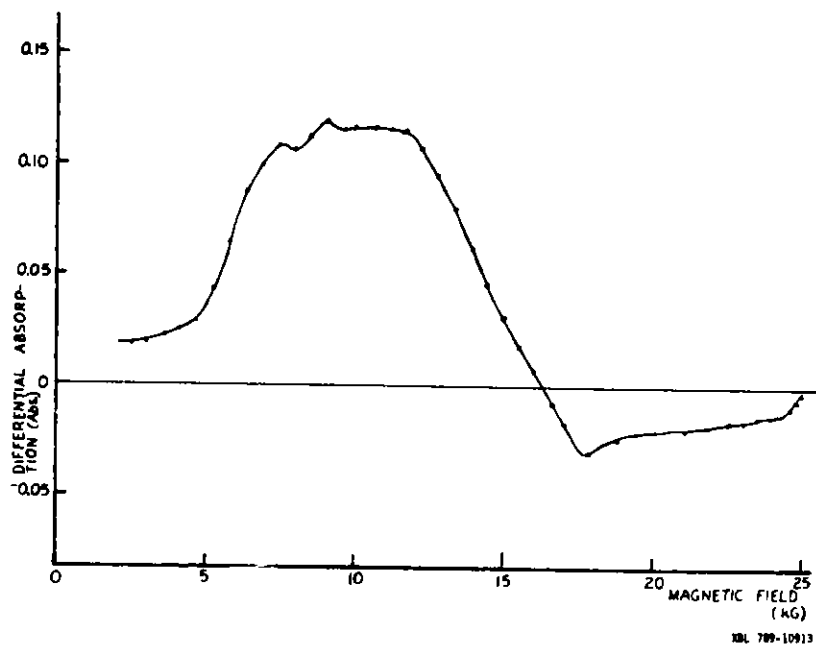


Fig. 6 High resolution absorption of  $\text{NO}_2$  obtained by TALMS measurement.

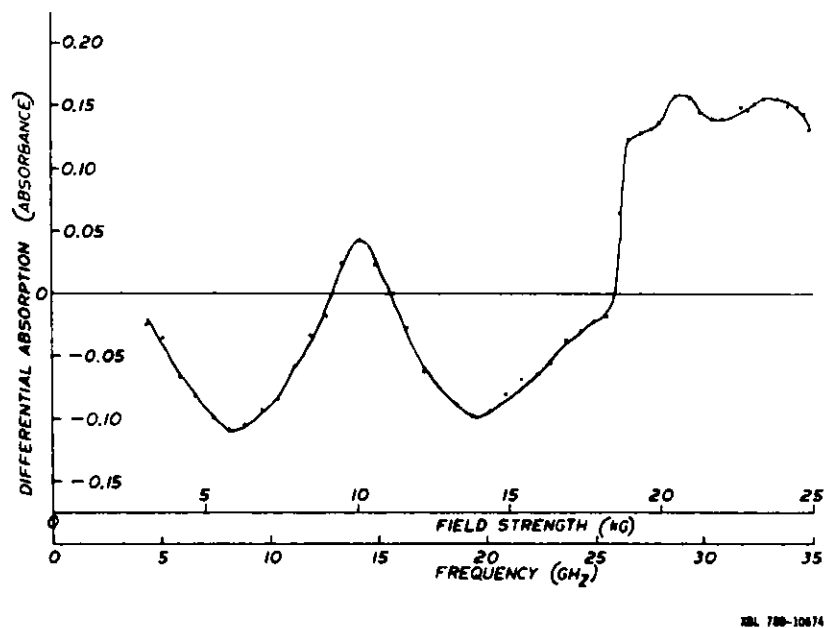


Fig. 7 Relation between magnetic field strength (shift of  $\sigma^+$  and  $\sigma^-$  components) and differential absorption of  $\sigma^+ - \sigma^-$  ( $\text{SO}_2$  0.46 torr, 10 cm cell).

ON-LINE COMPOSITION WITH LASER-BASED TECHNIQUES\*

F. T. Finch and A. Hartford, Jr.  
Los Alamos National Laboratory  
P. O. Box 1663  
Los Alamos, NM 87545

Abstract

Current methods for determining the composition of coal gasification streams generally involve sampling, some treatment, and inherent delay times prior to analysis. Optical instrumentation, on the other hand, provides the potential for on-line, rapid-response monitoring of gasifier streams. Among the optical techniques that appear quite promising for this application are coherent anti-Stokes Raman scattering (CARS), laser-induced breakdown spectroscopy (LIBS), Fourier transform infrared spectroscopy (FTIR), laser-induced fluorescence (LIF), and synchronous detection of laser-induced fluorescence (SDLIF).

Introduction

The technical risks associated with developing and operating advanced coal conversion facilities, whether for the production of liquid or gaseous fuels or for electrical generation, can be substantially reduced by the development and application of improved sensors and instruments. There is, in particular, an identified need for on-line real-time measurements of composition.

Electromagnetic radiation in the optical region of the spectrum can be utilized in a variety of ways to detect and measure concentrations of atoms, ions, radicals and molecular species in coal-conversion process streams. The use of lasers as optical energy sources provides the potential for very fine spectral resolution and short response times. Several optical techniques for on-line composition analysis are under investigation currently at the Los Alamos National Laboratory (Fig. 1). Each has its own characteristic limitations and advantages. With all the techniques data can be accumulated rapidly, allowing gasifier conditions to be monitored continuously. Inherent in most optical techniques is high spatial resolution, permitting various regions of a gasifier to be probed. Additionally, the unique spectral signatures of molecular or atomic species provide specific identification of particular materials. All the techniques being pursued can be applied to gas and vapor streams. In addition, several may be used with liquids.

Laser-Induced Breakdown Spectroscopy (LIBS)

It is well-known that the intense electric field which is generated at the focal point of a laser beam can create an ionized plasma. Particles or molecules in the plasma are reduced to highly excited ionic or neutral atomic species. The characteristic spectral emission from these excited species allows positive identification of particular elements, while the emission intensity permits quantification.

\* Work performed under the auspices of the U.S. Department of Energy

The emission from the plasma volume is initially dominated by a broad background continuum on which ionic atomic lines are superimposed. Both the continuum and the ionic atomic emission decay with time, while spectral lines from neutral atoms become more dominant. These characteristics of the plasma have led to using time-resolved LIBS (TRELIBS) to obtain the optimum detection sensitivity.

Laser-Induced Breakdown Spectroscopy can be used to measure composition of aerosols in the gas stream as well as gas phase constituents. The technique may also be applied to the surfaces of both solids and liquids.

The breakdown phenomena is only weakly dependent on laser frequency, allowing a relatively free choice of laser. The laser can be selected for low cost and reliability. A pulsed Nd:YAG laser is being used by Los Alamos.

This technique has been used under laboratory conditions at Los Alamos and under field conditions at the gasifier at Brigham Young University to detect and measure trace amounts of sodium and potassium. The ability to monitor Na and K in real time is important in combined cycle electrical power plants with hot gas cleanup in order to minimize turbine blade corrosion. Other applications where on-line real-time measurements of trace impurities is of value include monitoring of catalytic reactors or fuel cell plates for lifetime determination and of emissions for environmental control.

Total elemental analysis may also be achieved with LIBS. In measurements made with LIBS on the experimental coal gasifier at the Morgantown Energy Technology Center (METC) in March 1982 spectroscopic data on the major constituents of the gas stream and some minor constituents were obtained. The major constituents were positively identified. Oxygen and hydrogen were monitored as a function of time.

Although attempts were made to detect sodium and potassium, the noise level in the gasifier experiments degraded the detection limits for these species to the point where it was not possible to detect them in the field. It is clear that the origin of the noise in the field experiments must be understood. Noise can come from actual transient fluctuations in the stream properties, such as temperature and pressure, which would change the index of refraction in the medium and hence deflect the light output off the spectrometer slit. These fluctuations could also perturb the spark properties leading to increased noise. Visual observations of the spark and preliminary measurements with a HeNe laser indicate that these effects are very small. Noise can also arise from the vibration of the floor, which would be translated to oscillations of the optical components. The first cause cannot easily be remedied, because it is inherent in the nature of the gas stream. The second could be alleviated by a more rugged and vibration-isolated mounting of the optics, laser, and spectrometer.

#### Coherent Raman Diagnostics

Coherent Anti-Stokes Raman Spectroscopy (CARS) is a nonlinear optical spectroscopic technique based on four-wave mixing in the molecular species of interest. This technique requires two input laser wavelengths called the pump and Stokes frequencies. The output signal is a laser-like beam

at a frequency directly correlated with the pump and Stokes frequencies. Both species concentrations and temperatures can be derived via CARS.

Field measurements of the trace contaminant hydrogen sulfide have been made with CARS at both the BYU and METC gasifiers. A comparison of H<sub>2</sub>S concentrations achieved by CARS and by gas chromatographic analysis in field tests at BYU showed a good correlation. The concentration of H<sub>2</sub>S in a field test at METC was calculated to be 0.22% using room temperature parameters. Application of proper high-temperature parameters is expected to yield a higher value for H<sub>2</sub>S. This value can be compared with GC measurement during the same period of H<sub>2</sub>S = 0.35%.

Time-resolved measurements of N<sub>2</sub> and CO were also made at METC. The CO spectra show what are apparently true concentration fluctuations in real time with a two second resolution. In addition, the temperature was inferred from the N<sub>2</sub> CARS spectrum.

### Infrared Spectroscopy

Fourier Transform Infrared (FTIR) spectroscopy has been used at Los Alamos to detect minority species in the presence of coal gasifier majority species. As an example, OCS has been detected in the presence of CO. The transition of interest for OCS is obscured by the 0-1 transition of CO. However, by subtracting a reference spectrum of CO from the spectrum of CO + OCS, the OCS vibrational feature is clearly resolved. Detection limits via FTIR spectroscopy for various coal gasifier minority species are summarized in Fig. 2. The spectroscopic interferences due to majority species are also indicated.

### Laser-Induced Fluorescence

Laser-Induced Fluorescence (LIF) is a widely used technique for measuring minute concentrations of molecules and free radicals in the liquid and gaseous phases. This technique is quite sensitive. For strongly fluorescing molecules in the liquid phase, detection of parts-per-billion levels of contaminants is easily attainable, with parts-per-trillion levels achievable under certain conditions.

When a molecule is excited to an upper electronic state by a single, narrow-band laser frequency, one of the principal decay mechanisms is spontaneous emission to the ground electronic state. For most molecules in the condensed phase (liquids, aerosols, gels, etc.) this spontaneous emission takes place from the lowest vibrational level of the excited electronic state to many vibrational levels of the ground electronic states. The resultant fluorescence emission spectrum covers a wide wavelength interval (more than 100 nm in some cases). The overlap of these broadband emission spectra is the chief problem with LIF. Even in the case where the molecule of interest is in abundance, the ability to detect this molecule in a given setting is diminished by the unavoidable presence of other fluorescing molecules which may obscure any characteristic fluorescence peaks. Thus, the detection of the fluorescence from a carcinogenic molecule may be obscured by the fluorescence from other similar yet benign molecules which fluoresce in the same wavelength region.

There is, fortunately, a way to distinguish between the fluorescence from a particular molecule and the fluorescence arising from other species in the presence of the substance of interest. This technique is called Synchronous Detection of Laser-Induced Fluorescence (SDLIF). This process results in an artificial narrowing of the fluorescence width of each of the molecules excited by the laser, so that the fluorescing components of a complex mixture can be resolved and identified.

Synchronous detection of fluorescence is a well-characterized technique that has been used by forensic researchers, oil-spill analysts, and others in analytical chemistry to provide spectral "fingerprints" of complex mixtures of large organic molecules such as crude oil samples.

For multicomponent systems, the effect can be dramatic. Fig. 3a shows the conventional fluorescence spectrum of a mixture of naphthalene, phenanthrene, anthracene, perylene, and tetracene over the wavelength interval 300-500 nm. Note that there is significant overlap of the spectra of these five compounds, making it difficult to determine the relative concentration of each. Fig. 3b shows the synchronous spectrum of the same mixture. Clearly, each component can be distinguished without resorting to any complicated and time-consuming spectral subtraction algorithms. We have developed a system that will improve this technique by substituting a tunable laser for the usual xenon arc lamp source. This will greatly increase the detection sensitivity of the technique (by greater than three-orders-of-magnitude) and allow for a remote-sensing capability due to the collimated nature of the coherent laser source.

Tetracene was chosen for the initial SDLIF studies at Los Alamos, partly because the frequency of the emission-absorption band overlap matched the dye laser gain characteristic in a convenient manner. As a point of comparison, we first took the normal LIF spectrum of tetracene in benzene pumping the molecule at 470 nm with a fixed laser output. The tetracene emission spectrum is more than 90 nm wide.

On the other hand, the SDLIF spectrum of tetracene in benzene is shown in Fig. 4. In this case, both the dye laser and the spectrometer are scanned at the same rate. The result is that the tetracene fluorescence occupies no more than 7 nm (FWHM) of the spectrum. This leaves room on either side for the detection of other fluorescing molecules whose LIF spectra overlap the tetracene spectrum, but whose SDLIF spectra are completely resolvable. Note that a  $2 \times 10^{-5}$  M solution of tetracene in benzene is equivalent to two parts-per-million. Thus, extending this detection technique to the parts-per-billion regime will be relatively straightforward. The problems that arise in the use of this technique are generally the same as those found in ordinary fluorescence spectroscopy. Effects such as quenching and nonradiative losses cause spectral distortion and limit the detection sensitivity. Solvent or component filter effects may also cause distortion of the synchronous spectrum.

### Conclusions

A number of optical techniques are being developed which have the potential for on-line real-time composition in a variety of applications. These techniques are aimed at measuring the full range of constituents

which may be present in process streams, including majority, minority and trace molecular species, selected trace metals, and total elemental analysis. Limited field testing of two of the techniques has been conducted with apparent success.

Thus far in the Laboratory experimental program and field testing the optical interfaces with the process gas streams have caused less of a problem than was originally feared when the program began. Rather simple window purge techniques have been generally adequate. More elaborate techniques for interfacing the optical beams and signals with the process streams have not yet been required.

#### Acknowledgments

The authors are heavily indebted to Dr. T. R. Loree, Dr. R. F. Holland, Dr. D. J. Taylor, Dr. L. J. Radziemski, and Dr. D. A. Cremers for the experimental efforts reported in this paper. The support and cooperation of the staffs at BYU and METC during the field tests are gratefully acknowledged.

# OPTICAL ON-LINE COMPOSITION MEASUREMENT TECHNIQUES CURRENTLY UNDER INVESTIGATION AT LOS ALAMOS

TECHNIQUE	PRINCIPLE	APPLICATION	SPECIES MEASURED BY LOS ALAMOS
LIBS	ATOMIC EMISSION	TRACE CONTAMINANTS, TOTAL ELEMENTAL ASSAY	Na <sup>‡</sup> , K <sup>‡</sup> S*, O*, N, H, CN
CARS	RAMAN SCATTERING	MAJORITY, MINORITY AND TRACE SPECIES	N <sub>2</sub> <sup>*</sup> , CO <sup>*</sup> , H <sub>2</sub> S <sup>*‡</sup>
FTIR	ir ABSORPTION	MAJORITY, MINORITY AND TRACE SPECIES	COS, SO <sub>2</sub> , N <sub>2</sub> O, NO <sub>2</sub> , NO, NH <sub>3</sub> , HCN
LIF	FLUORESCENCE	MOLECULES AND RADICALS	HS
SDLIF	FLUORESCENCE	MIXTURES OF COMPLEX ORGANICS	SEVERAL POLYNUCLEAR AROMATICS

\* OBSERVED IN FIELD TESTS AT METC

‡ OBSERVED IN FIELD TESTS AT BYU

Fig. 1



## FTIR ANALYSIS FOR COAL GAS MINORITY SPECIES

<u>SPECIES</u>	<u>BAND</u>	<u>FREQUENCY (cm<sup>-1</sup>)</u>	<u>INTERFERENCE</u>	<u>DETECTIVITY (300 psi, 200 °C)</u>
COS	$\nu_3$	2058	CO (20%)	100 ppm
SO <sub>2</sub>	$\nu_1$	1149	CH <sub>4</sub> (10%)	100 ppm
N <sub>2</sub> O	$\nu_3$	2222	CO (20%), CO <sub>2</sub> (20%)	500 ppm
N <sub>2</sub> O	$2\nu_1$	2561	CH <sub>4</sub>	(200 ppm)
NO <sub>2</sub>	$\nu_3$	1615	H <sub>2</sub> O	-----
NO	(0-1)	1875	H <sub>2</sub> O (39%)	(500 ppm)
NH <sub>3</sub>	$\nu_2$	950	CO <sub>2</sub> (17%), H <sub>2</sub> O (30%)	30 ppm

PARENTHESES INDICATE ONLY ROOM-TEMPERATURE MEASUREMENTS.

Fig. 2

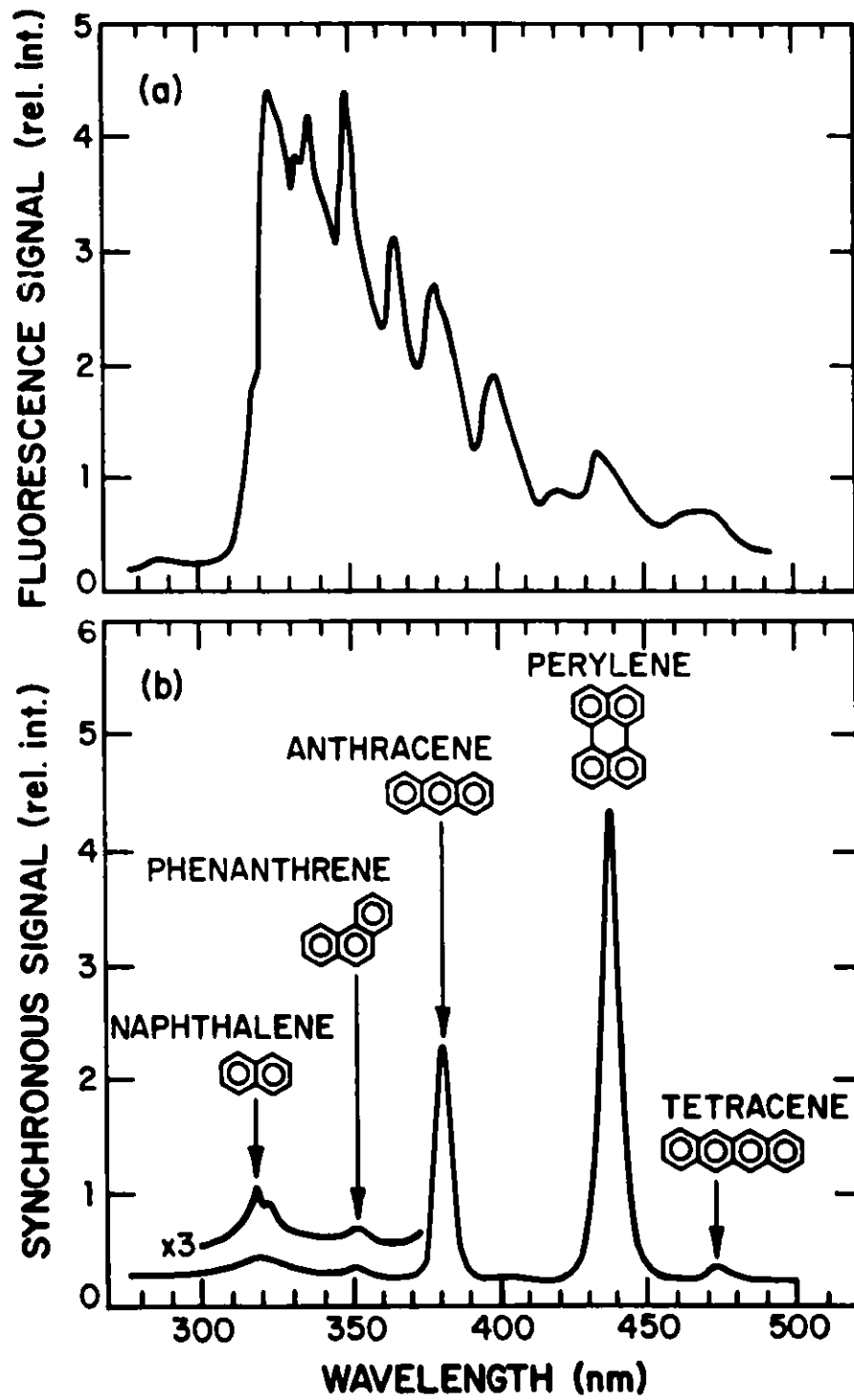


Fig. 3

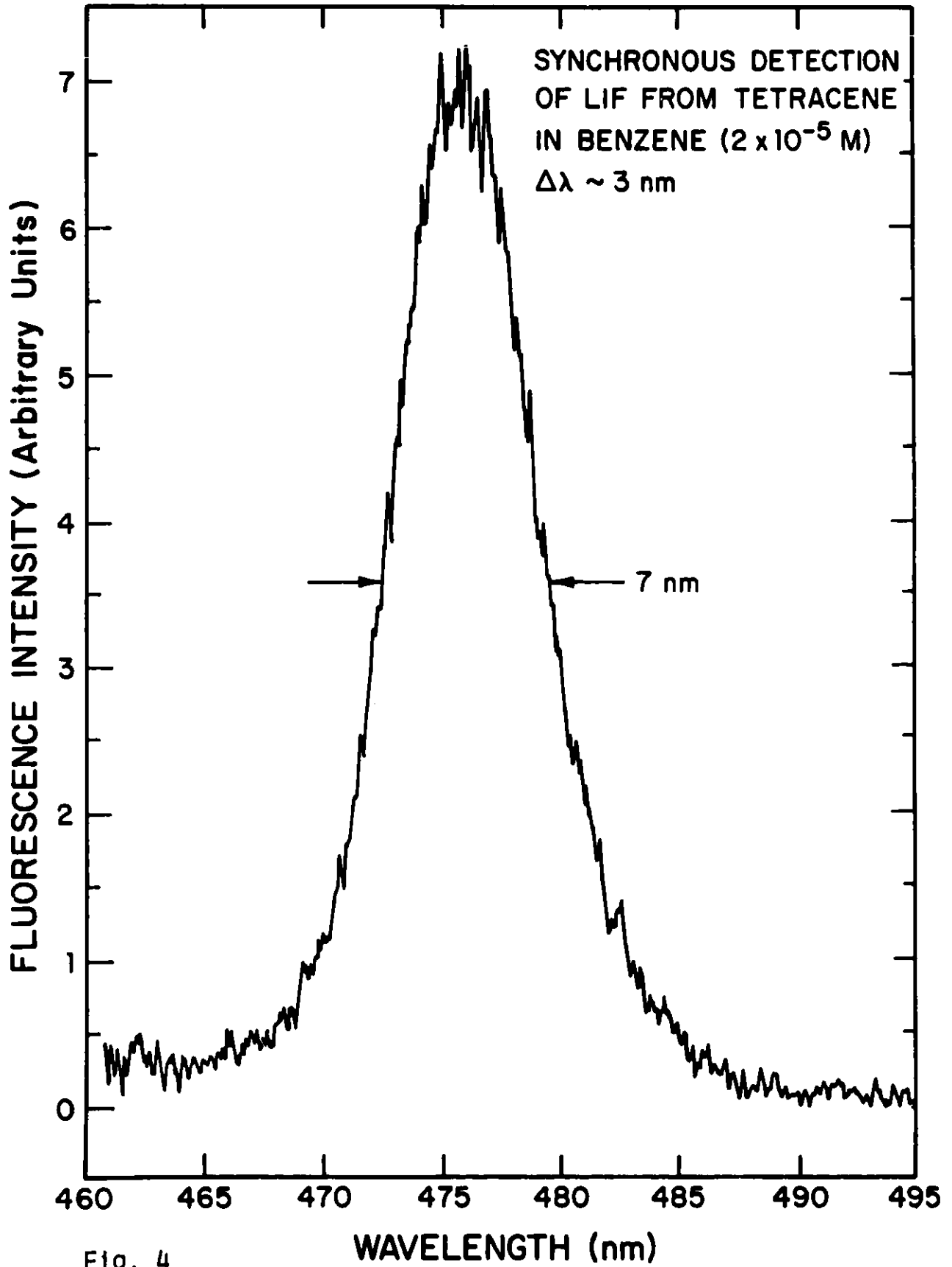


Fig. 4

MICROWAVE PROPERTIES OF COAL DERIVED LIQUIDS AND COAL-RECYCLE  
SOLVENT SLURRIES: POTENTIAL FOR ON-LINE MONITORS

I. B. Goldberg\* and K. E. Chung  
Rockwell International Science Center  
1049 Camino dos Rios  
Thousand Oaks, CA 91360  
805/498-4545

Abstract

The real part of the complex dielectric constant of SRC-I recycle solvent, SRC-II naphtha, middle distillate and heavy distillate, and tetralin were measured at 750 MHz over the temperature range of 23 to 140°C. These values were found to be strongly temperature dependent, generally increasing with temperature, and increasing in the sequence naphtha < heavy distillate < recycle solvent < middle distillate. These values were also found to be related to the phenolic contents of the liquids. The temperature dependence was attributed to the viscosity which, in turn, affects the relaxation behavior of the electric dipoles. In addition, evidence is presented which indicates that association-dissociation equilibria of the polar components also influences the dielectric constant. Measurements of slurries of the SRC-I recycle solvent with coal show that the dielectric constant,  $\bar{\epsilon}'$ , is given by the Looyenga equation:

$$\bar{\epsilon}' = [\epsilon_2'^{1/3} - \phi_1 (\epsilon_1'^{1/3} - \epsilon_2'^{1/3})]^3$$

where  $\phi_1$  is the volume fraction of the coal and  $\epsilon_1'$  and  $\epsilon_2'$  are the real parts of the dielectric constant of the coal and the solvent. Analysis of these results was carried out to determine whether a microwave monitor could be used for measurements of coal concentration.

TIME-DOMAIN MEASUREMENTS OF THE DIELECTRIC PROPERTIES OF OIL SHALE --  
THE DEVELOPMENT OF AN ON-LINE DIELECTRIC PROBE

Magdy F. Iskander  
Department of Electrical Engineering  
University of Utah  
Salt Lake City, Utah 84112

Abstract

A time-domain technique for measuring the dielectric properties of oil shale is described. This technique provides complete dielectric characterization of the oil shale over a broad frequency band from a single measurement. A small shunt capacitor terminating a coaxial transmission line is used as a sample holder. For high temperature measurement the sample holder was constructed of Kovar to minimize the measurement errors due to the differential thermal expansion of the 50-ohm coaxial transmission line and the sample holder. A procedure to determine the optimum value or values of the capacitance of the sample holder is also discussed. The development of the on-line dielectric probe which utilizes an open-ended section of the transmission line as a sample holder is described. The on-line probe has an extended center conductor which is embedded in the dielectric volume under test. It is shown that although the initial results from the on-line dielectric probe are encouraging, further work is still required to fully develop the probe for in-situ measurements.

1. Introduction

In direct and indirect ways, the thermophysical properties of oil shale influence every stage of the shale oil extraction process from exploration and resource definition to mining, retorting, and upgrading. Among the most commonly measured thermophysical properties are the thermal conductivity, thermal diffusivity, and specific heat, all of which are of well recognized importance in understanding the heat processing of oil shale. Measurement of the dielectric properties has also become an integral part of the thermophysical analysis, in view of its extreme sensitivity to the chemical and physical composition of the shale as well as to their changes during heating.

For complete dielectric characterization of oil shale, however, a large number of measurements over a wide frequency band are required. This process is obviously time consuming and may require more than one laborious measurement technique. Therefore, the adequacy of the frequently used point-by-point frequency-domain measurements to track fast (or abrupt) chemical changes, such as those occurring during rapid heating of oil shale (say, using RF energy), is severely limited. We have, therefore, developed a time-domain technique to measure the complex permittivity of oil shale. This technique provides broadband information on the frequency characteristics of the oil shale from a single time-domain measurement. In section 2, we will briefly describe the time-domain measurement system. Although various sample-holder arrangements could be utilized in these measurements, we used a small shunt capacitor terminating a coaxial transmission line as a sample holder. A simple procedure to determine the optimum value of the

test capacitance in a given frequency range will be discussed in section 4.

Finally, since the efficiency of the process of oil shale retorting and the quality of the obtained products critically depend on the ability to control the key process variables, we have developed an on-line dielectric probe for assaying and the in-situ process control of oil-shale retorting. This probe is basically an open-ended section of transmission line with an extended center conductor embedded in the oil-shale volume. A brief description of the probe as well as experimental results illustrating the feasibility of using it for oil shale measurements are given in section 5.

## 2. Time-Domain Measurement

It is generally known that for complete characterization of dielectric materials, their properties should be measured over a broad frequency band. Therefore, if point-by-point frequency-domain measurements are used, the process of complete characterization becomes time consuming and may require more than one measurement technique.<sup>1, 2</sup> Furthermore, these frequency domain measurements are simply inadequate to track the fast chemical changes that occur during rapid heating. This is because the time required for the swept frequency dielectric measurements sets a natural limit for the heating rate that can be used.<sup>3</sup> For these reasons, we have developed a time-domain technique to measure the complex permittivity of oil shale over a broad frequency band.<sup>4</sup> In this technique the permittivity behavior over a wide frequency range is obtained in only a fraction of a second using a pulse which simultaneously contains all the frequencies of interest. The accuracy of these time-domain methods is at present comparable to that of standard swept-frequency methods. Their striking advantages, however, include simplicity of the procedure, relatively cheap equipment needed, and the considerably shorter time required to do the measurements.<sup>5</sup> At present, the frequency range covered by these methods is from 10 kHz up to about 15 GHz.

A block diagram of the measurement system is illustrated in Fig. 1. The four essential parts of the system are the subnanosecond step-function generator, broadband sampling oscilloscope, temperature-controlled sample holder, and a minicomputer for the data processing. Although we started our measurements using the HP-1415 time-domain reflectometer, with a step function of rise time approximately equal to 150 picoseconds, we are presently using the Tektronix 7S12 system with a rise time of approximately 45 ps. The new system with shorter rise time has distinguished advantages in providing more accurate measurements, particularly at the higher frequencies, as will be described in the following sections.

Beside the commercially available time-domain reflectometer, the other important part in the measurement system is the sample holder. As indicated earlier, although many sample holders can be used in these measurements, we used a small lumped capacitor terminating a coaxial line section as a sample holder. This sample holder has the advantage of bridging the gap between the low frequency measurements where lumped parallel plate capacitors are usually used and the high frequency measurements where distributed elements such as a section of transmission line are used. The capacitance is formed at the end of the transmission line by reducing the

length of the center conductor by about 0.006" with respect to the length of the outer conductor of the transmission line. When a cap is placed (screwed in) on the outer conductor, there will be a gap between the end of the cap and the center conductor, thus forming a small capacitor terminating the transmission line. A schematic diagram of the sample holder as well as its equivalent circuit is shown in Fig. 2. The measurement technique follows closely the procedure we developed in earlier measurements.<sup>6</sup> A reference signal from a short circuit placed at the location of the sample holder and the reflected signal at the sample interface are recorded, digitized, and the Fourier transforms of both signals are calculated. This procedure determines the frequency dependence of the reflection coefficient, which can then be used to calculate the real and imaginary parts of the relative permittivity as described elsewhere.<sup>6,7</sup> The feasibility of the procedure was first evaluated by measuring the dielectric properties of known materials such as Teflon and mica. The obtained results which are generally in good agreement with the data available in the literature are described elsewhere.<sup>6,7</sup> The dielectric properties of several oil shale samples are then measured and the results are shown in Fig. 3. These results show good agreement with the frequency domain data obtained using the ever-slow slotted transmission line technique.<sup>8</sup> They also bridged the gap between the low- and high-frequency techniques (i.e., the results between 1 to 100 MHz) where no data were previously available.<sup>4</sup>

### 3. High-Temperature Measurements

The same sample holder geometry was used for high temperature measurements. To minimize the differential thermal expansion of the different parts (i.e., inner and outer conductors) of the sample holder and the 50-ohm transmission line, we constructed a new sample holder made of a material of very small thermal expansion coefficient. We first examined the expansion coefficients of many of the available conductors suitable for constructing a transmission line (see Fig. 4) and decided to construct the new sample holder of Kovar. Suitable outlets were also provided to permit dynamic gas analysis during heating. Once again to check the adequacy of the new sample holder for high temperature measurements, we measured the dielectric constant of mica as a function of temperature. The experimental results are shown in Fig. 5, where it is clear that the significant errors due to the differential thermal expansions between the different portions of the stainless steel sample holder are minimized by using the Kovar one. Efforts are now under way to measure the dielectric properties of oil shale as a function of temperature as well as the grade.

### 4. Optimum Capacitance of the Test Capacitor

In these dielectric measurements, it is extremely important to determine the optimum value of the capacitance that can be used for measurements over a specified frequency band. Unfortunately, there is no easy procedure to determine such a value since the optimum capacitance depends on:

- a. The value of the complex permittivity under test.
- b. The specific frequency band of interest.

We, however, have devised a procedure to calculate the optimum value of the

capacitance that can be used for a given dielectric (i.e., approximate value of the complex permittivity is required) and in a given frequency range. The procedure is based on the uncertainty analysis described in an earlier paper.<sup>6</sup> Based on these earlier analyses, it is easy to show that the calculated errors in measuring the real and imaginary parts of the complex permittivity, i.e.,  $\Delta\epsilon'$  and  $\Delta\epsilon''$ , due to uncertainties in determining the characteristic impedance of the transmission line  $\Delta Z_o$ , the capacitance of the test capacitor  $\Delta C_o$  and the magnitude and phase  $\theta$  of the reflection coefficient  $\Delta|\rho|$  and  $\Delta\theta$ , are given by:

$$\Delta\epsilon' = \left[ \left( \frac{\partial\epsilon'}{\partial Z_o} \Delta Z_o \right)^2 + \left( \frac{\partial\epsilon'}{\partial C_o} \Delta C_o \right)^2 + \left( \frac{\partial\epsilon'}{\partial |\rho|} \Delta |\rho| \right)^2 + \left( \frac{\partial\epsilon'}{\partial \theta} \Delta \theta \right)^2 \right]^{1/2} \quad (1)$$

$$\Delta\epsilon'' = \left[ \left( \frac{\partial\epsilon''}{\partial Z_o} \Delta Z_o \right)^2 + \left( \frac{\partial\epsilon''}{\partial C_o} \Delta C_o \right)^2 + \left( \frac{\partial\epsilon''}{\partial |\rho|} \Delta |\rho| \right)^2 + \left( \frac{\partial\epsilon''}{\partial \theta} \Delta \theta \right)^2 \right]^{1/2} \quad (2)$$

We utilized Eqs. 1 and 2 to determine the uncertainties  $\Delta\epsilon'$  and  $\Delta\epsilon''$  as a function of the capacitance of the test capacitor  $C_o$  for given values of  $\Delta Z_o = 0.1 \Omega$ ,  $\Delta C_o = 5 \times 10^{-14}$  F, and  $\Delta|\rho| = 1.4$  percent and  $\Delta\theta = 0.8^\circ$ .

These calculations are repeated at the lowest and highest frequencies in the desired frequency band, and the value of the capacitance  $C_o$  that is found to satisfy given allowable errors  $\delta\epsilon'$  and  $\delta\epsilon''$  in the measured  $\epsilon'$  and  $\epsilon''$  in the specified frequency band is chosen to be the optimum value of  $C_o$ . In other words, the uncertainties  $\Delta\epsilon'$  and  $\Delta\epsilon''$  are calculated from Eqs. 1 and 2 as a function of  $C_o$  at both the lowest and highest frequencies of interest. The value or values of  $C_o$  that would provide adequate accuracy, i.e.,  $\delta\epsilon'/\Delta\epsilon' > 1$ ,  $\delta\epsilon''/\Delta\epsilon'' > 1$ , is considered optimum for the given dielectric in the specified frequency range. To further illustrate this procedure, consider a dielectric material with  $\epsilon^* = 3.4 - j1.0$  (organic liquid -- Aromatic -- Arodor 1232<sup>9</sup>). Setting the allowable tolerance limit at  $\delta\epsilon' = \pm 0.5$  and  $\delta\epsilon'' = \pm 0.25$ , we see from the results shown in Fig. 6 that a capacitance of 9 pF can be used while the calculated uncertainties are less than the specified tolerance limits (i.e.,  $\delta\epsilon'/\Delta\epsilon' > 1$ ,  $\delta\epsilon''/\Delta\epsilon'' > 1$ ) in the frequency band from 100 MHz to 1 GHz. It is also clear that the major limitation is due to the uncertainties in  $\epsilon''$  since any value of  $C_o$  between 4 pF to 21 pF satisfies the selection criterion (i.e.,  $\delta\epsilon'/\Delta\epsilon' > 1$ ) while it is only difficult to satisfy the selection criterion in  $\epsilon''$ . For the same dielectric material, Fig. 7 shows curves for tolerance limits at  $\delta\epsilon' = \pm 0.5$  and  $\delta\epsilon'' = \pm 0.3$ . From the results of Fig. 7, it is clear that by relaxing the tolerance on  $\epsilon''$  (i.e., making  $\delta\epsilon'' = \pm 0.3$  instead of  $\pm 0.25$  for the results of Fig. 6), there is a range of values of  $C_o$  between 8 pF and 11 pF that can be used in this case. It is interesting to note that larger values of capacitances are generally required at lower frequencies (which is expected since lumped circuit elements are usually used at these frequencies) and smaller values of capacitances are preferable at higher frequencies, which once again agrees with our expectations since smaller capacitances in form of distributed circuit elements are usually used at higher frequencies.



### 5. On-Line Dielectric Measurements

As indicated earlier the recovery of shale oil from oil shale by above-ground and in-situ retorting schemes is a large-scale chemical process which occurs under a variety of conditions. The efficiency of the process and the utility of the products obtained are strong functions of the ability of the operator to analyze and control key process variables. Since shale rock is a complex heterogeneous material that undergoes a variety of chemical and physical transformations on application of heat, the on-line monitoring of the retorting process is crucial to improving the retort yield. For the on-line monitoring of the dielectric properties, we have developed a new dielectric probe which is basically a section of a coaxial transmission line with an extended portion of the center conductor embedded in the dielectric volume under test. By maintaining the dimensions of the transmission line, and in particular the extended portion of the center conductor, small compared to the wavelength of the highest frequency of interest, the probe can conveniently be represented by a simple shunt capacitor terminating the transmission line. The geometry of the dielectric probe as well as its low frequency equivalent circuit are shown in Fig. 8. At these lower frequencies where the shunt capacitor equivalent circuit can be assumed to be adequate, we investigated the feasibility of using the on-line probe to measure the dielectric properties of oil shale. Measurements using the frequency-domain network analyzer to determine the reflection coefficient of the sample holder with and without the sample were made.<sup>10</sup> The obtained results are shown in Fig. 9 where it is clear that reasonable accuracy is achieved at higher frequencies, while larger deviation from the results available in the literature are observed at lower frequencies. This might be due to the small value of the sample-holder capacitance, the matter which significantly limited the accuracy of the results at the lower frequencies. In an attempt to overcome this problem, one might suggest extending the length of the center conductor further to increase the value of the input capacitance of the sample holder. Under these circumstances, however, the input impedance of the sample holder cannot any longer be approximated by a capacitance terminating the transmission line. Instead, the input impedance at any angular frequency  $\omega$  will be given by:<sup>11</sup>

$$Z(\omega) = A\omega^2 + \frac{1}{j\omega C} \quad (3)$$

where A and C are two constants which can be determined from the physical dimensions of the dielectric probe. It should be noted that the first term in Eq. 3 represents the frequency dependent radiation resistance of the antenna which was neglected under the low-frequency approximation when the extended length of the center conductor was significantly shorter than the wavelength. Using the input impedance expression given in Eq. 3, the measurement procedure would involve the solution of nonlinear equations similar to those described elsewhere.<sup>12</sup> These as well as other extensions of the measurement system, including modifying the dielectric probe for high temperature measurements, are presently under investigation. Also the use of the 45 ps time-domain reflectometer for the on-line dielectric measurement is presently in progress and the obtained results will be reported soon.

## 6. Conclusions

In this paper we described the on-going efforts in our laboratory to measure the dielectric properties of oil shale using the time-domain technique. This technique provides a rapid and sensitive means of tracking reactions as they proceed and offers an exciting possibility of developing increased insight into the reaction mechanisms. In addition to providing a process-control means for maximizing and improving the quality of the re-tort yields, the dielectric properties measurements are also known for their sensitivity to changes in the organic and water contents of the material under test, and hence provide valuable information about the grade of the oil shale.

For high temperature measurements we described a sample holder made of Kovar, a metal of small thermal expansion coefficient, to minimize the differential expansions in the 50-ohm coaxial transmission line and the sample holder. For on-line dielectric measurements, on the other hand, an open-ended coaxial cable with the extended center conductor embedded in the dielectric under test was used as a dielectric probe. Although the initial experimental results obtained using this dielectric probe are encouraging, further work is still needed to fully develop this probe for low-frequency, high-temperature, and in general for in-situ time-domain measurements.

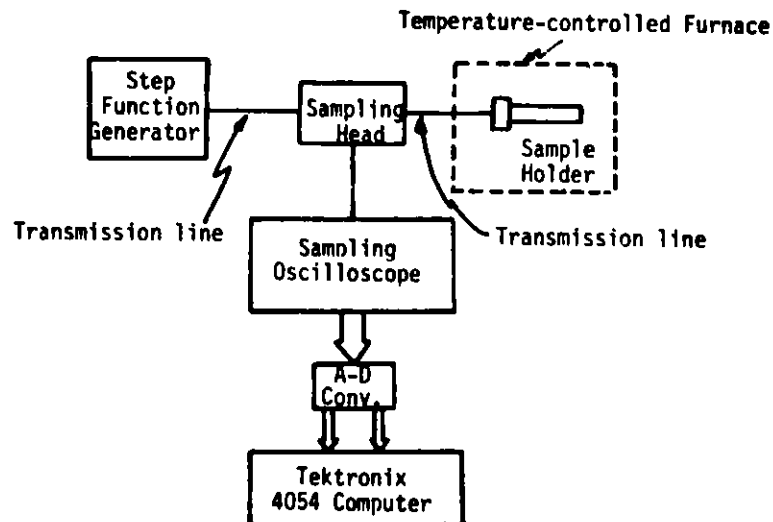


Fig. 1. Experimental setup for the time-domain measurements.

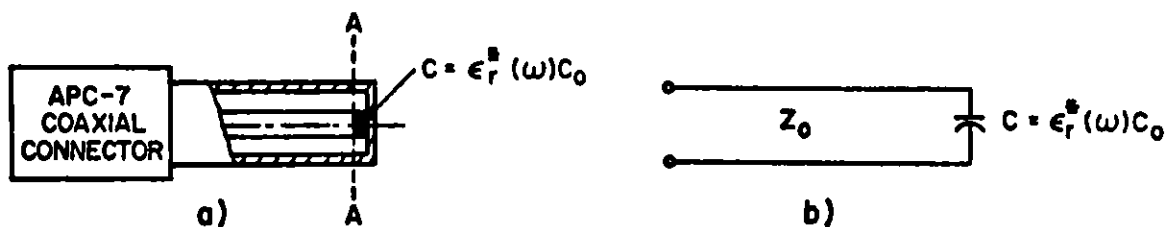


Fig. 2. The sample holder. (a) APC-7 coaxial sample holder, and (b) its equivalent circuit.

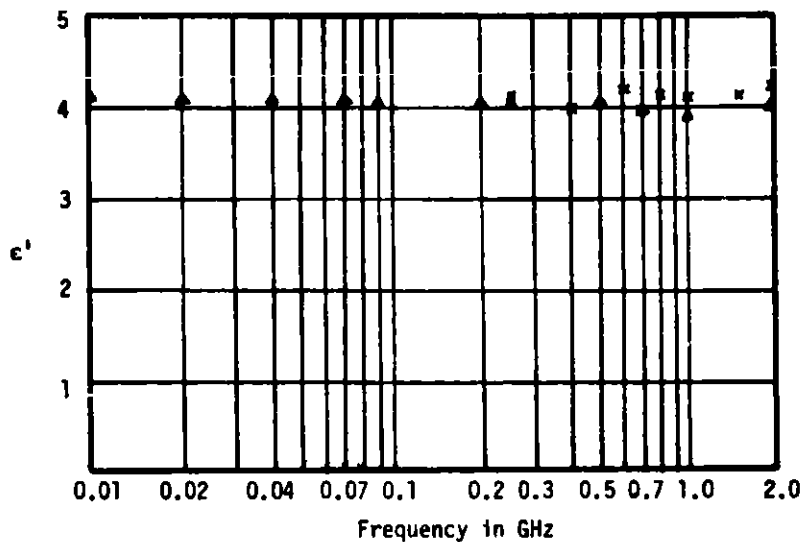


Fig. 3a. The dielectric constant of oil shale as a function of frequency at 25°C. ▲ Experimental values calculated from time-domain measurements; × point-by-point frequency domain measurements using slotted transmission line.<sup>8</sup> The capacitance of the test capacitor  $C_0 = 2.8$  pF.

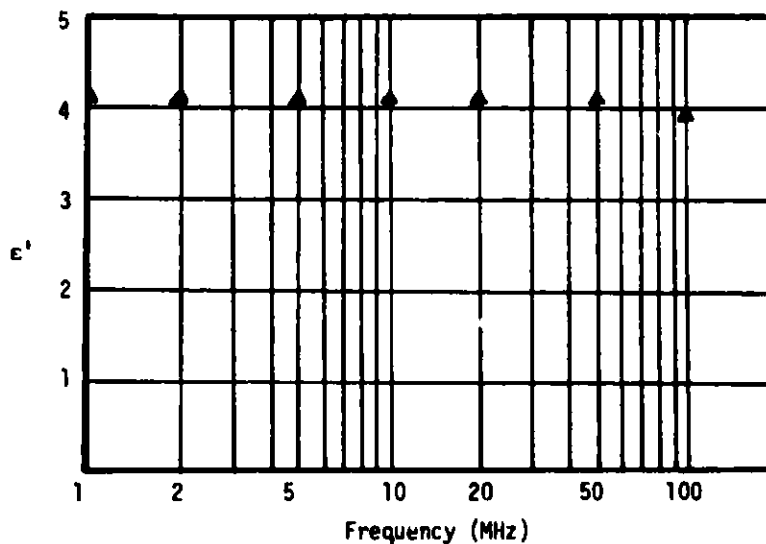


Fig. 3b. The dielectric constant of oil shale at 25°C. Estimated yield of shale -- 65 gal/ton, and the capacitance of the test capacitor  $C_0 = 5.5$  pF.

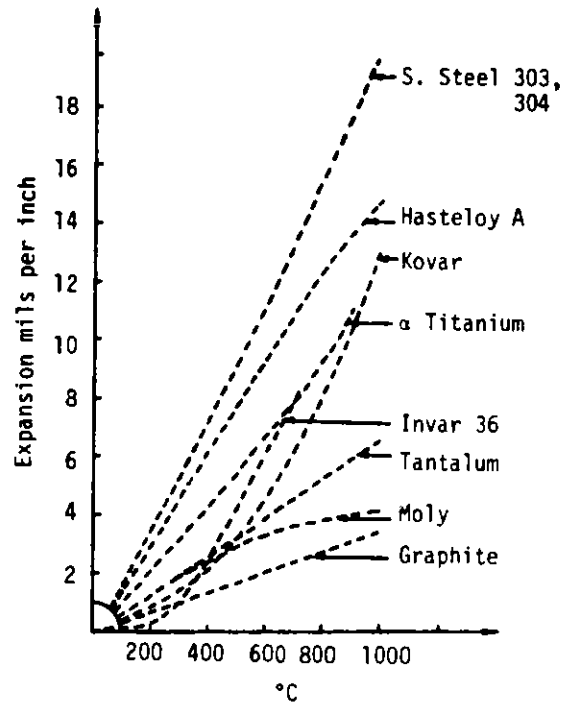


Fig. 4. Thermal expansion of conductors as a function of temperature.

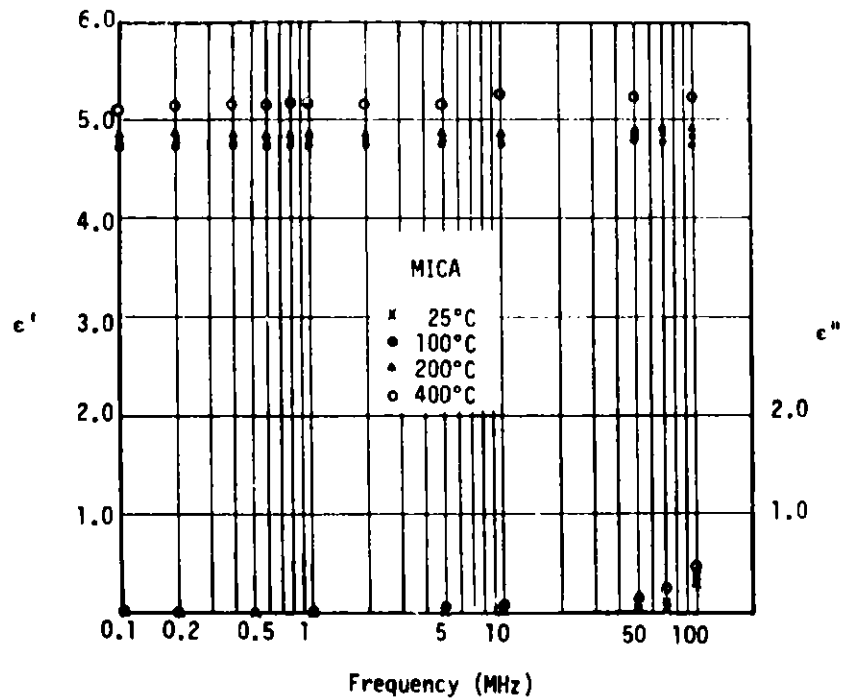


Fig. 5. The complex permittivity of mica over a broad frequency band as a function of temperature.

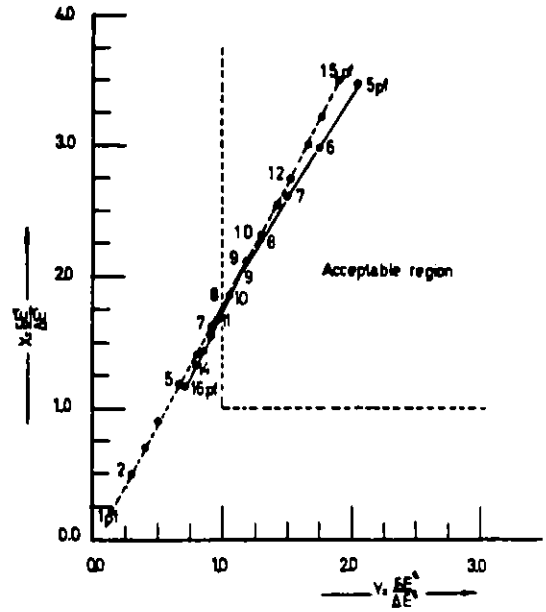
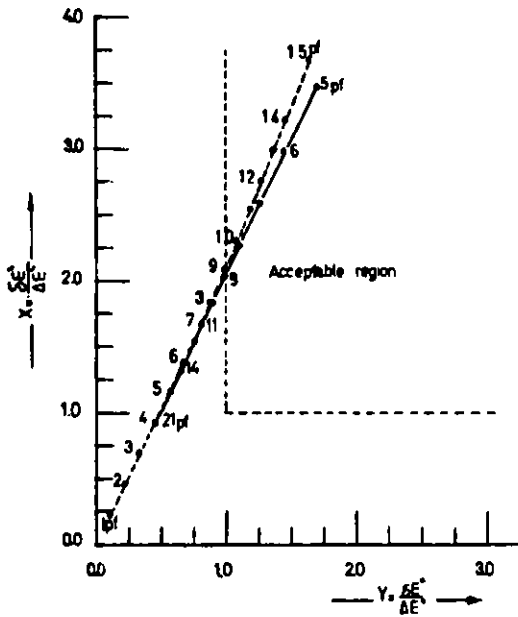


Fig. 6. Optimum value of capacitance for a dielectric with  $\epsilon^* = 3.4 - j1.0$ . ( $\delta\epsilon' = \pm 0.5$  and  $\delta\epsilon'' = \pm 0.25$ .) --- = 10 MHz and \_\_\_\_\_ = 1 GHz.

Fig. 7. Optimum value of capacitance for a dielectric with  $\epsilon^* = 3.4 - j1.0$ . ( $\delta\epsilon' = \pm 0.5$  and  $\delta\epsilon'' = \pm 0.3$ .) --- = 10 MHz and \_\_\_\_\_ = 1 GHz.

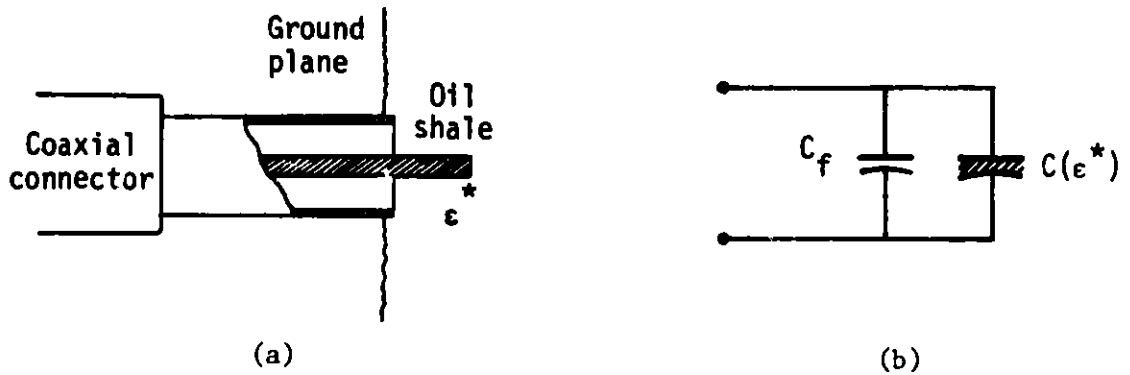


Fig. 8. (a) The on-line dielectric probe for measuring the dielectric properties of oil shale; (b) its low-frequency equivalent circuit.

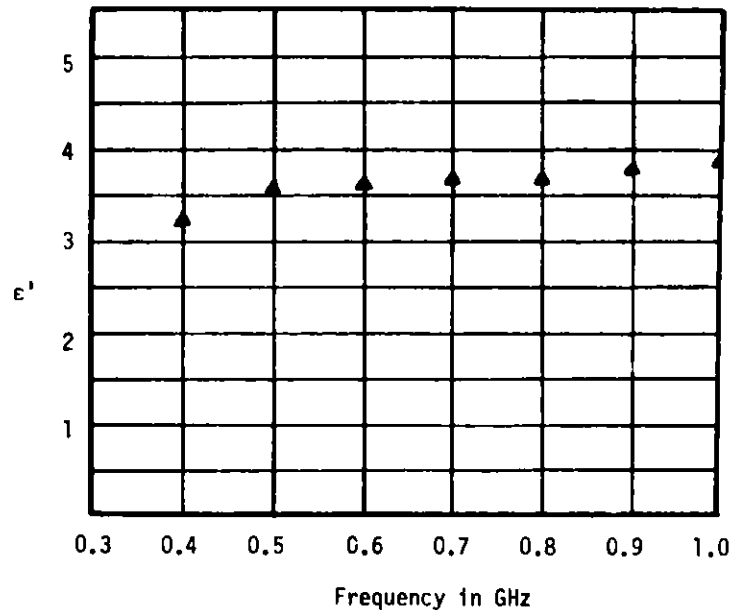


Fig. 9. The dielectric constant of oil shale at 25°C obtained using the on-line dielectric probe. The shale grade is estimated at 30 gal/ton.

#### References

1. H. E. Bussey, "Measurement of RF Properties of Materials: A Survey," Proceedings of the IEEE, Vol. 55, pp. 1046-1053, 1967.
2. M. A. Stuchly and S. S. Stuchly, "Coaxial Line Reflection Method for Measuring Dielectric Properties of Biological Substances at Radio and Microwave Frequencies -- A Review," IEEE Transactions on Instrumentation and Measurement, Vol. IM-29, pp. 176-183, 1980.
3. K. Rajeshwar, R. Nottenburg, and J. DuBow, "Thermophysical Properties of Oil Shale: Review," J. Mat. Sci., Vol. 14, pp. 2025-2052, 1979.
4. M. F. Iskander, A. L. Tyler, and D. F. Elkins, "A Time-Domain Technique for Measurement of the Dielectric Properties of Oil Shale during Processing," Proceedings of the IEEE, Vol. 69, pp. 760-762, 1981.
5. M. J. C. Van Gemert, "High-Frequency Time-Domain Method in Dielectric Spectroscopy," Philips Res. Rep., Vol. 29, pp. 530-572, 1973.
6. M. F. Iskander and S. S. Stuchly, "A Time-Domain Technique for Measurement of the Dielectric Properties of Biological Substances," IEEE Transactions on Instrumentation and Measurement, Vol. IM-21, pp. 425-429, 1972.
7. M. F. Iskander, "Permittivity Measurements in Time-Domain," M.S. thesis, University of Manitoba, Winnipeg, Manitoba, Canada, 1972.

8. A. Judzis, Jr., "Assaying Green River Oil Shale with Microwave Radiation," Ph.D. dissertation, University of Michigan, Ann Arbor, Michigan, 1978.
9. A. Von Hippel, Dielectric Materials and Applications, MIT Press, Cambridge, Massachusetts, 1954.
10. S. S. Stuchly, M. A. Rzepecka, and M. F. Iskander, "Permittivity Measurements at Microwave Frequencies Using Lumped Elements," IEEE Transactions on Instrumentation and Measurements, Vol. IM-23, pp. 56-52, 1974.
11. C. T. Tai, "Characteristics of Linear Antenna Elements", in Antenna Engineering Handbook, H. Jasik, Ed., McGraw-Hill, New York, Ch. 3, 1961.
12. J. Toler and J. Seals, "RF Dielectric Properties Measurement System: Human and Animal Data," NIOSH research report, DHEW (NIOSH) publication No. 77-176, July 1977.

SHALE OIL SEPARATIONS BY HPLC

William A. Dark\*  
Waters Associates  
34 Maple Street  
Milford, MA 01757  
617/478-2000, ext. 2673

Abstract

In the characterization of syncrudes from alternate fossil sources, there is a need for the rapid separation into hydrocarbon groups. Separations on an analytical scale, where microgram quantities of sample are required, and preparative separations on multigram scale such that additional characterization and testing can be done.

Using samples of shale oil from Utah and Thailand, HPLC techniques are shown that will accomplish these aims.

The use of a mixed bank of normal phase analytical columns for the automated separation into saturates, neutral aromatics by the number of rings, and polar aromatics in 45 minutes.

Separation of multigram quantities of shale oil into major hydrocarbon groups; saturates, aromatics, and polar aromatics, in 30 minutes. And the additional characterization of these fractions for additional compositional detail.



RAPID MEASUREMENT OF ASPHALTENE/PREASPHALTENE RATIOS WITH  
POTENTIAL FOR FEEDBACK CONTROL IN THE SRC PROCESS\*

J. E. Mrochek, M. S. Denton,<sup>†</sup> W. D. Bostick,  
and S. R. Dinsmore  
Oak Ridge National Laboratory  
Oak Ridge, Tennessee 37830

Abstract

The economics of the SRC-I process are sensitive to product recovery from the Kerr-McGee Critical Solvents Deashing (CSD) unit, and its optimal operation is, in turn, dependent on the asphaltene/preasphaltene (ASP/PASP) ratio of the feed. The ASP/PASP ratio may be modified to some extent by controlling treatment severity in the dissolver, providing that the operator has timely access to meaningful measurements of this ratio. The Chemical Technology Division of Oak Ridge National Laboratory (ORNL) is developing a rapid, automated method to determine ASP/PASP ratios of feed material to the CSD unit which is amenable to near-on-line operation. Procedures being studied employ an inert sand column with either three- or two-solvent (hexane, benzene, and pyridine or benzene and pyridine) elution to effect a separation of CSD feed into oil, ASP, and PASP or oil + ASP and PASP fractions in approximately 15 min. Weight percent (WP) and WP ratios determined from these various fractions correlated well with tabulated SRC recovery data for the Wilsonville Pilot Plant. However, a more rapid means of monitoring is required since the time involved in solvent removal and determination of the dry weight of fractions is unacceptably long and too complex for a useful process control method. A simple in-line optical detector, employing broadbanded energy (300-400 nm) and a photoconductive detector, was employed together with an integrator/plotter to rapidly measure peak areas associated with the elution of individual fractions. Correlations of individual peak areas and peak area ratios determined for 11 CSD feed samples were quite reasonable, considering the difficulty in obtaining a representative small sample from the top of a drum of SRC and showed the feasibility of an automated system for near-on-line measurement.

Introduction

The solvent refined coal (SRC-I) pilot plant at Wilsonville, Alabama, is a 6-ton/day coal liquefaction facility that desulfurizes coal by reacting a slurry of coal and process solvent with hydrogen at elevated temperatures and pressures. The low-sulfur SRC product is further processed to remove ash and unreacted coal solids in a Critical Solvent Deashing (CSD) unit by means of a proprietary process of the Kerr-McGee Corporation, and then it may be upgraded catalytically in a hydrotreater.

\*Research sponsored by the Division of Fossil Energy Research, Oak Ridge Operations, U.S. Department of Energy, under contract W-7405-eng-26 with the Union Carbide Corporation.

<sup>†</sup>Currently with Chemical Separations Corp., One Technology Drive, Knoxville, TN 37922.

The three-stage extraction process produces ash concentrate from the first stage (bottom), deashed SRC from the second stage (bottom), and a light SRC at the bottom of the third stage. The overhead product from the third stage is deashing solvent (DAS) which is recycled; the light SRC from the bottom of the third stage is recycled as a component in the process solvent stream of the SRC unit.

The economics of the SRC-I process are sensitive to SRC recovery from the Kerr-McGee CSD unit, which is in turn dependent on the quality of the SRC feed to the unit. Several controllable parameters have been found to correlate with SRC recovery. Among the more promising is the ratio of asphaltenes to preasphaltenes\* (ASP/PASP) in the feed material. Recently, pilot plant data on solvent quality (microautoclave conversion tests) have been correlated strongly with PASP content in the feed to the CSD unit.<sup>1</sup> The ASP/PASP ratio may be controlled to some extent by controlling severity of treatment in the dissolver and, perhaps, by controlling solvent quality to the SRC reactor. Measurement of solvent quality in a timely fashion to make these data available for feedback process control is, of course, not possible under current technology; however, ORNL is currently developing a solvent quality monitor that employs electron spin resonance (ESR) spectrometry.

The objective of this work is to develop a rapid measurement of CSD feed quality with primary emphasis on the ASP/PASP or a related ratio. The analytical system to perform this measurement should have three major attributes: (1) simplicity, (2) rapid measurement capability, and (3) capability for on-line or near-on-line operation by relatively untrained personnel.

#### Developmental Studies

This development effort has been pursued in two phases. The initial phase involved a rigorous fractionation of the SRC feed to the CSD unit by means of automated, preparative-scale sequential elution solvent chromatography (SESC).<sup>2</sup> This system performs the separation of large (<5-g) samples of coal or coal-derived materials into ten relatively clean fractions, which can be weighed after solvent removal. The data obtained from this detailed characterization of a few samples would serve as the basis for investigations and ultimate design of an on-line or near-on-line system. This manuscript details results on the first phase and describes progress toward developing a simple system to satisfy the ultimate objective - namely, on-line or near-on-line measurement of ASP/PASP ratios.

#### Characterization of Varying Quality CSD Feed by SESC

The separation of coal-derived materials by SESC, pioneered by the Mobil Research and Development Corporation, has been described adequately in the literature.<sup>2,3</sup> Briefly, the technique uses nine organic solvents

\*Asphaltenes are insoluble in hexane or pentane and soluble in benzene; preasphaltenes are insoluble in benzene and soluble in pyridine or tetrahydrofuran.

to elute similar chemical functionalities in series from a silica gel column which has been partially deactivated with 4% water. The sample is solubilized in tetrahydrofuran (THF) with the aid of ultrasonication, mixed with sea sand, the solvent evaporated, and the sample-laden sand packed into a precolumn for frontal elution onto the silica column. Approximately 2 L (20 mL/min) of each of the solvents is pumped through the precolumn-silica column; solvent switching is performed by a programmable rotary valve. Samples are collected with an automated fraction collector and are weighed after the solvent is removed by means of a spinning band still. Recoveries of coal samples have generally been within the range 99 to 102% of theoretical.

Three samples of SRC feed to the Wilsonville CSD unit were received from Catalytic, Inc. These samples were associated with SRC recoveries\* of 75.3% (poor), 84.4% (intermediate), and 90.5% (good). The results of fractionating these three samples by SESC are shown in Table 1 and are illustrated graphically in Fig. 1. Combining the ten fractions into three fractions more useful in process development - oils, asphaltenes, and preasphaltenes - clearly differentiates these three samples as indicated in Table 1. Note that major differences among the samples are primarily due to differences in the content of the oil and preasphaltene fractions since changes in the ASP fraction are comparatively small. The oil content increases by almost 300%, whereas the preasphaltenes decrease by 28% in going from the poor (75.3% SRC recovery) to the good (90.5% SRC recovery) CSD feed material. Illustrated in Fig. 2 are reasonably linear correlations of the respective ratios (oil + APS)/PASP and ASP/PASP with SRC recovery. This rigorous separation furnished a sound basis for proceeding to the development of a rapid method to determine these ratios on feed material to the CSD unit.

#### Solvent Extraction Studies to Simplify the System

As a first step in simplifying the system, a series of solvent extractions employing benzene, benzene-pyridine, and hexane-benzene-pyridine were performed on these three defined CSD feed samples. Weight fractions and weight fraction ratios (Fig. 3) both correlated well with SRC recovery. Even the single-solvent (benzene) extraction shown in Fig. 3 correlated well. The most linear and sensitive correlation was obtained with a two-solvent (benzene-pyridine) extraction where the weight fractions were determined after freeze-drying to volatilize the solvent.

#### Fractionation by Weight Employing Elution from a Sand Column

After having verified the feasibility of separations based upon two or three solvents, we attempted to devise a separation system that would be amenable to automation and on-line or near-on-line operation. To withstand the extreme temperature conditions anticipated, an inert sand column was employed, and the sample was applied to the column as described

\*CSD recovery of soluble coal based on cresol solubility.

Table 1. SESC Separation of CSD Feed Samples Associated with Good (217), Intermediate (220), and Poor (211) Kerr-McGee SFC Recovery

Fraction	Elution Solvent	Major Compounds	Wt %			Composite Wt %		
			217	220	211	217	220	211
Oils	1	Hexane	2.7	0.5	0.4	10.7	4.7	2.7
	2	Hexane/15% Toluene	8.0	4.2	2.3			
Asphaltenes	3	Chloroform	30.1	26.3	13.4	52.5	51.2	46.5
	4	Chloroform/10% ET <sub>2</sub> O	13.7	17.6	23.3			
	5	ET <sub>2</sub> O/3% ETOH	8.7	7.3	9.8			
Preasphaltenes	6	MEOH	7.2	5.0	5.3	36.7	44.1	50.7
	7	CHCl <sub>3</sub> /3% ETOH	5.3	4.2	4.5			
	8	THF/3% ETOH	11.9	16.4	24.9			
	9	Pyridine/3% ETOH	9.5	15.5	13.2			
	10	Pyridine/3% ETOH Backflush	2.8	3.0	2.8			

previously for the SESC system. Three solvents (hexane, benzene, and pyridine) corresponding to oil, ASP, and PASP fractions and two solvents (benzene and pyridine) corresponding to oil + ASP and PASP fractions were selected for testing. Here the mode of fractionation is one of solubility as opposed to dual modes of solubility and adsorption affinity in the SESC separation. The sand column merely serves to present a uniformly distributed sample to the solvents. Recently, Boduszynski, Hurtubise, and Silver<sup>4</sup> have described separations of SRC on an inert support (Fluoropak) using hexane, toluene, and pyridine solvents. Sample sizes of 2 to 5 g were used to enable measurement by weight because we had not yet tackled the difficult monitoring problem that would have to be solved in order to make the measurement truly rapid and automated. The same three CSD feed samples were analyzed using three- and two-solvent elution with the results illustrated in Figs. 4 and 5. The correlations of (oil + ASP)/PASP and ASP/PASP ratios with SRC recovery were good for three-solvent elution and excellent for the two-solvent elution (ASP/PASP ratio only). Replicate runs performed on two of the CSD feed samples using three-solvent elution resulted in precisions on WP measurements of  $\pm 1.2$  to 2.5%.

#### Optical Monitoring

Having achieved a simple and rugged separation system, we approached the difficult problem of a suitable in-line detector since determination of weight fractions was not amenable to rapid automated measurement. We realized from the outset of this work that accomplishment of the objective would require not only routine, rapid separations (currently about 20 min) but also determination of simple peak areas and their ratios instead of time-consuming dry weight fractions. Conventional ultraviolet, fluorescence, and infrared detectors were tested to no avail on the heterogeneous fractions eluted from the sand column. What was needed was a detector of limited sensitivity to both sample and solvent. Testing of an ORNL-developed\* optical detector using a tubular straight-through flow cell showed promise. Broad-banded light energy in the near-ultraviolet region (300 to 400 nm) and a photoconductive detector were employed with an adjustable electronic reference. Coupling this detector to an electronic integrator/plotter completed a prototype automated separations system to monitor the previously developed two- and three-solvent fractionations of CSD feed material.

#### Testing of Prototype System

In order to evaluate the prototype analytical system in a configuration suitable for on-line or near-on-line operation, a sample injection valve with calibrated loop was incorporated into the system. Weighed samples of about 0.5 g were dissolved in pyridine with the aid of sonication and were diluted to 100 mL. A constant volume, containing about 3.3 mg of sample, was loaded into the sample loop and displaced onto the sand column (50 x 1.3 cm) by the first solvent (hexane for three-solvent and benzene for two-solvent elutions), and elution of each fraction proceeded at a flowrate of 20 mL/min.

\*Courtesy of L. J. Thacker, Instrumentation and Controls Division, ORNL.

A total of 11 CSD feed samples\* were analyzed on a prototype system employing optical detection and both the two- and three-solvent elution sequences. Results obtained by two-solvent elution are illustrated in Figs. 6 and 7. An estimate of precision for multiple analyses of the same sample (a single sample dissolution only) yielded a relative standard deviation of 2.1% for the ratio (oil + ASP)/PASP. We have not yet performed multiple analyses of the same sample where multiple sample dissolutions were employed. However, we have analyzed four different samples having a narrow range of SRC recoveries (79.0 to 80.2%). The relative standard deviation ( $100 \cdot \delta / \text{mean}$ ) for the (oil + ASP)/PASP ratios of these four samples was 1.5%. The precision implied by these relative standard deviations belies the scatter depicted in Figs. 6 and 7 and indicates the need for additional work to determine its cause. For two-solvent elutions, the (oil + ASP)/PASP ratio provides a more sensitive correlation compared to either PASP or (oil + ASP) peak areas alone. The scatter in either case is about the same.

The results of three-solvent elutions are illustrated in Figs. 8 through 11. Multiple analyses of the same sample (again employing a single sample dissolution) yielded a relative standard deviation of 2.4% for (oil + ASP)/PASP. These results appeared to indicate that somewhat poorer precision was associated with three-solvent elution, and this was apparently borne out by somewhat greater scattering in the plotted data, especially that associated with the ASP fraction. Analyses of the four samples having SRC recoveries ranging from 79.0 to 80.2% resulted in relative standard deviations for oil/PASP, ASP/PASP, and (oil + ASP)/PASP of 6.9, 6.9, and 6.8%. These data are again indicative of poorer precision than that obtained by two-solvent elution. Increased scatter associated with ASP measurements was not noted here. In general, the scatter observed in ASP/PASP ratios for three-solvent elution was reduced for the ratio (oil + ASP)/PASP. The scatter was about the same as illustrated for oil/PASP in Fig. 11; however, the correlation was more sensitive to changes in SRC recovery.

### Conclusions

These measurements employing an optical detector must only be considered as a preliminary analysis of the overall feasibility of such a detector in monitoring the respective soluble fractions. Difficulties were encountered in obtaining CSD feed material with defined SRC yields; the suite of 11 samples discussed here was received only 2 weeks ago, so the samples and the method have yet to be subjected to vigorous statistical testing. Nonrepresentative sampling of CSD feed from the top of drums of material is always a danger and can only be overcome by analyzing a large number of samples. Considering those qualifications, however, some preliminary conclusions can be drawn:

1. Two-solvent elution appears to offer the potential for more precise measurement (this was also demonstrated in the early work when weight fractions and ratios were determined).

\*Samples courtesy of R. C. Janka, Kerr-McGee Corporation.

2. Three-solvent elution suffers from the disadvantage of a baseline shift when changing the eluent from hexane to benzene; however, this is somewhat offset by the fact that the oils (hexane soluble) are monitored.

Our early work demonstrated that the oil content increased by 300% in going from a poor (75.3% SRC recovery) feed to a good (90.5% SRC recovery) feed to the CSD unit. Separation of the oil and ASP fractions by three-solvent elution does not seem to be very clean as evidenced by the fact that precision improved when these two fractions were recombined.

There is little to choose between the two- and three-solvent elutions based upon time required for analysis. Turnaround time for two-solvent elution is 12 min and is 13.5 min for three-solvent elution. Final choice between the two must await additional experience and correlations associated with more samples. This decision should not delay the design of a suitable system for on-line or near-on-line operation since the only difference is the addition of one solvent.

#### References

1. SRC-I Solvent Refined Coal Process, Quarterly Technical Progress Report, April-June 1981, FE-10154-96 (March 1982).
2. M. Farcasiu, Fuel 56, 9 (1977).
3. Coal Liquefaction, The Chemistry and Technology of Thermal Processes, D. D. Whitehurst, T. O. Mitchell, and M. Farcasin (eds.), Academic Press, New York (1980).
4. M. M. Boduszynski, R. J. Hurtubise, and H. F. Silver, Anal. Chem. 54, 372 (1982).

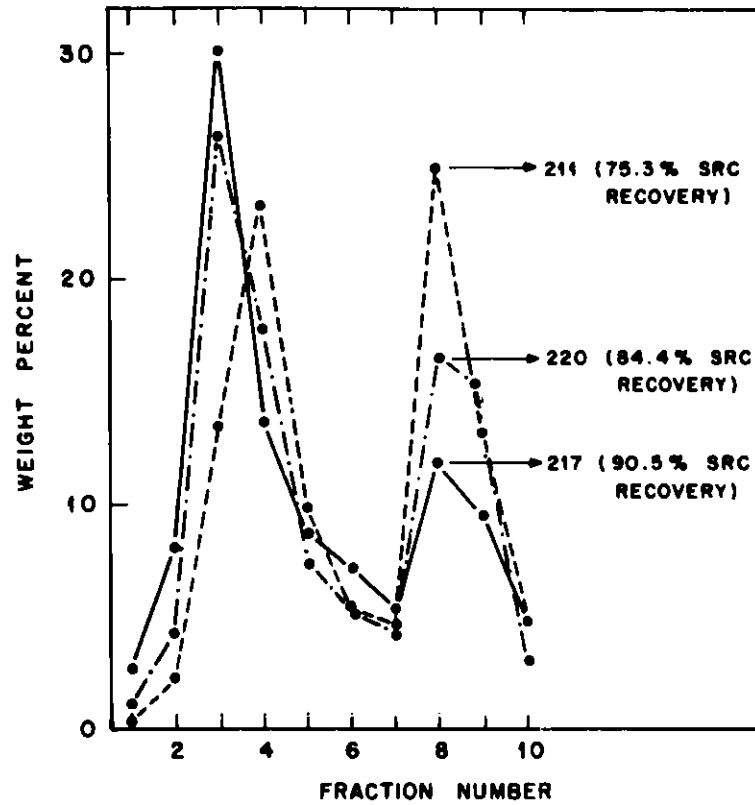


Fig. 1. Separation by SESC illustrating the differences between CSD feed material resulting in poor, intermediate, and good SRC recoveries.

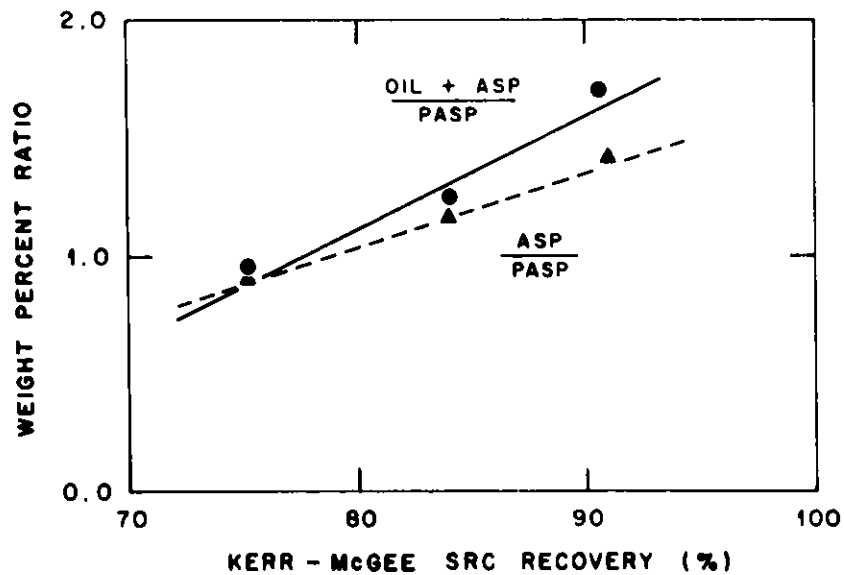


Fig. 2. Linear correlations for weight fraction ratios obtained from SESC separation data.



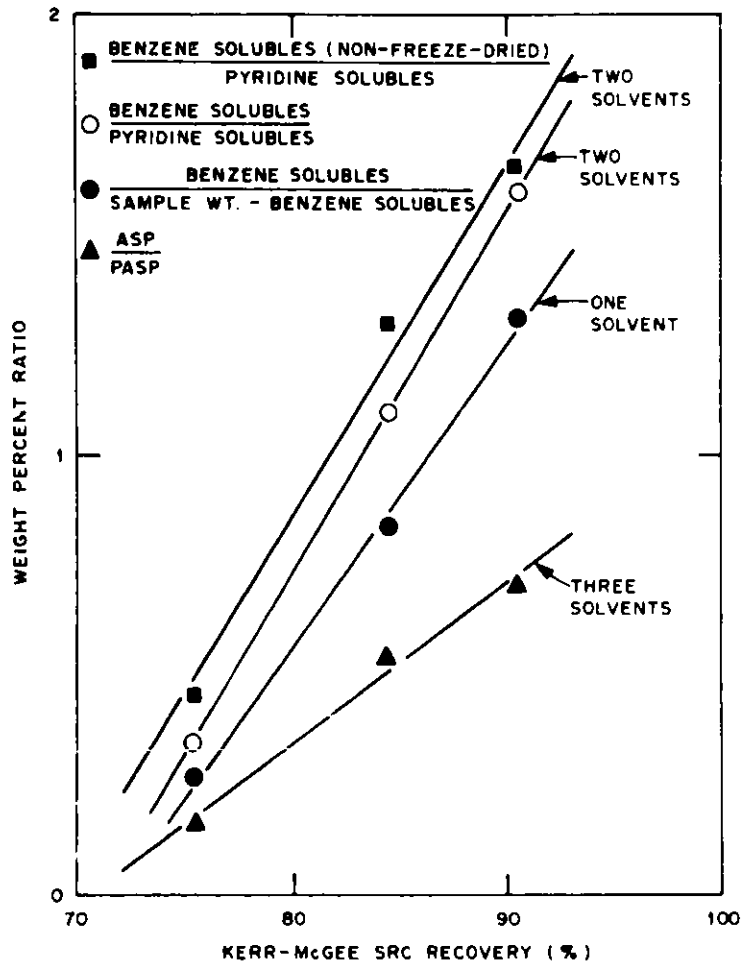


Fig. 3. Solvent extraction separation of poor, intermediate, and good (75.3, 84.4, and 90.5% SRC recovery) feed samples to the CSD unit.

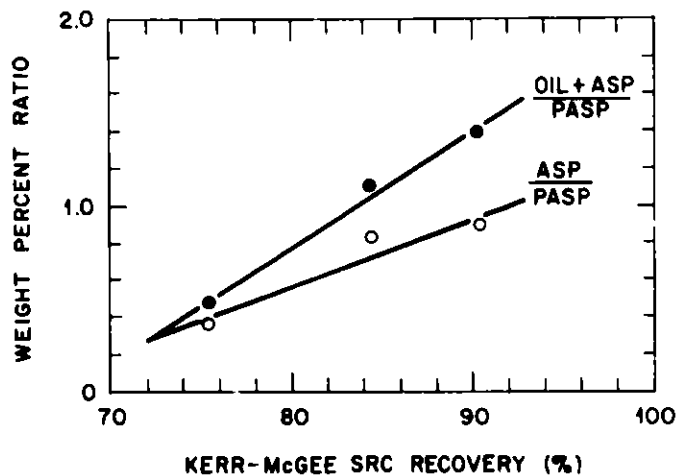


Fig. 4. Weight fraction ratios determined by three-solvent (hexane, benzene, pyridine) elutions of poor, intermediate, and good (75.3, 84.4, and 90.5% SRC recovery, CSD feed samples from a sand column.

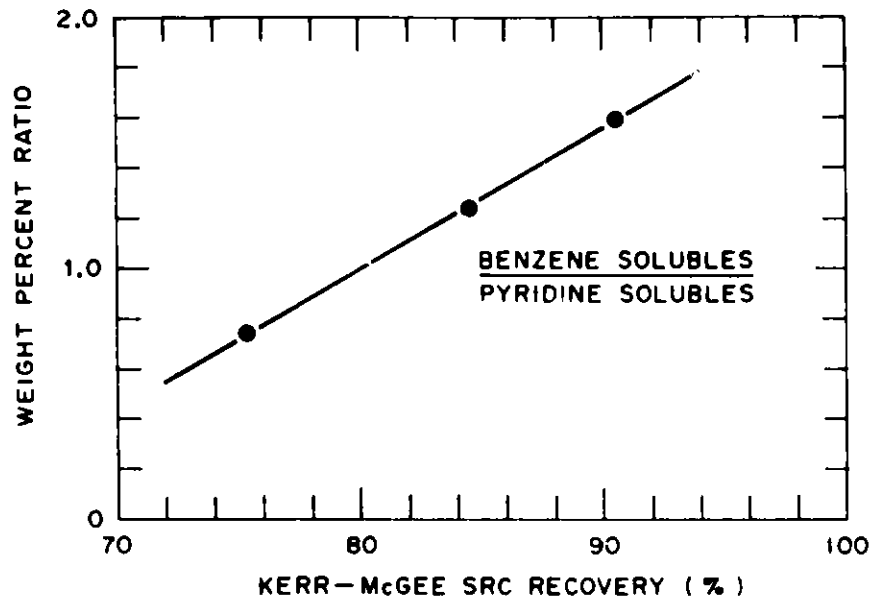


Fig. 5. Weight fraction ratios determined by two-solvent (benzene, pyridine) elutions of poor, intermediate, and good (75.3, 84.3, and 90.5% SRC recovery) CSD feed samples from a sand column.

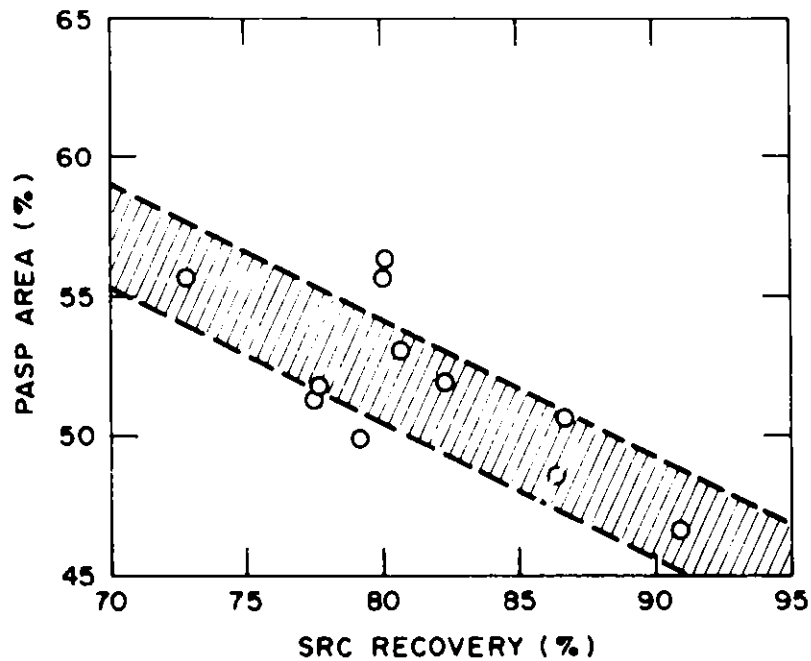


Fig. 6. Optical monitoring of PASP peak areas for two-solvent (benzene, pyridine) elution of CSD feed samples from a sand column.

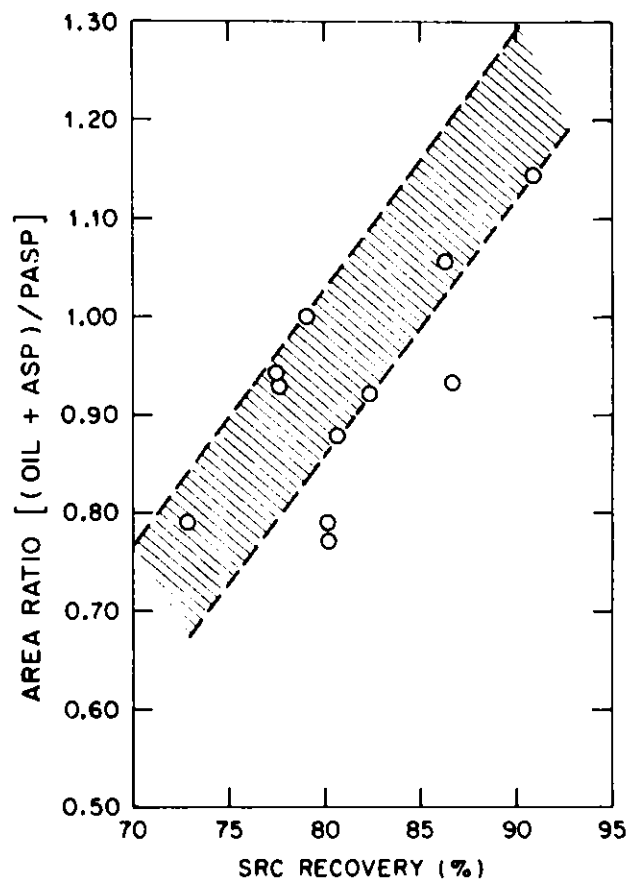


Fig. 7. Optically monitored peak area ratios for two-solvent (benzene, pyridine) elution of CSD feed samples from a sand column.

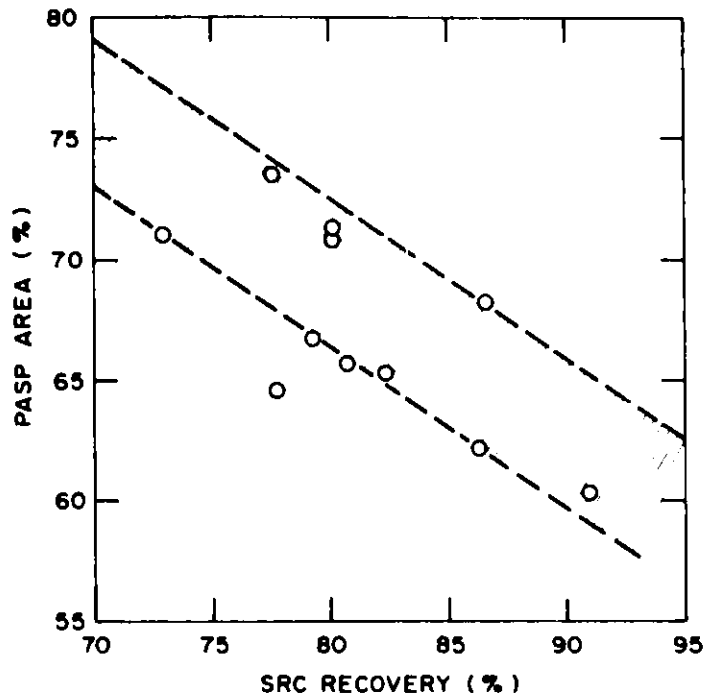


Fig. 8. Optical monitoring of PASP peak areas for three-solvent (hexane, benzene, pyridine) elutions of CSD feed samples from a sand column.

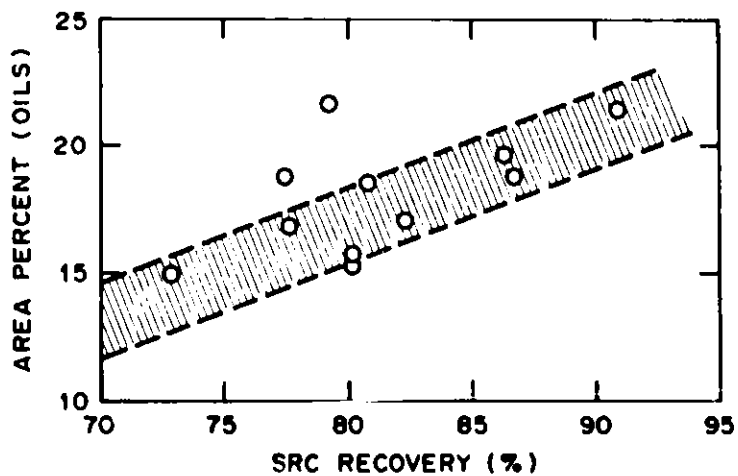


Fig. 9. Optical monitoring of oil peak areas for three-solvent (hexane, benzene, pyridine) elutions of CSD feed samples from a sand column.

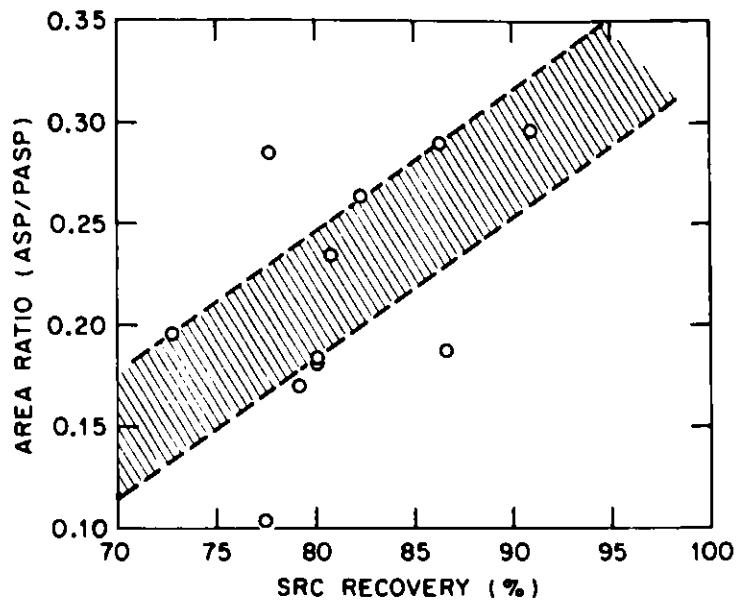


Fig. 10. Optical monitoring of ASP/PASP peak areas for three-solvent (hexane, benzene, pyridine) elutions of CSD feed samples from a sand column.

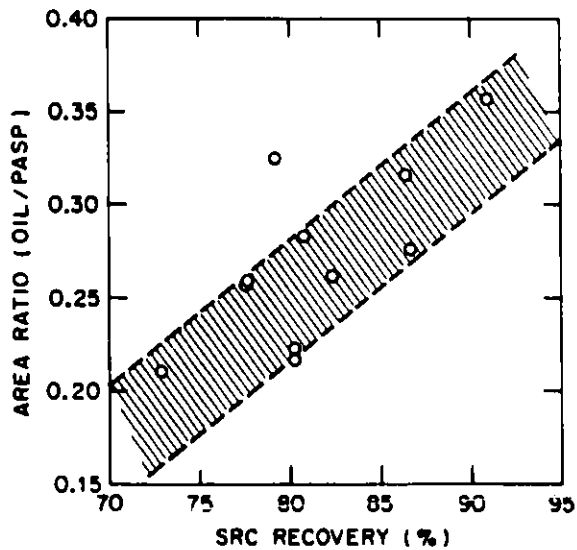


Fig. 11. Optical monitoring of oil/PASP peak areas for three-solvent (hexane, benzene, pyridine) elutions of CSD feed samples from a sand column.

Instrument & Control Design Criteria  
For Fossil Energy Process Management

R. Cunningham, \*C. R. Stewart, W. K. Triebel III  
Honeywell, Inc.  
Process Management Systems Division  
1100 Virginia Drive  
Fort Washington, PA 19034  
Phone (215) 641-3000

ABSTRACT

This paper describes a disciplined approach to Instrumentation and Control Systems applications for large and complex multi-unit process plants as are required in the conversion of fossil resources to alternative fuels. This disciplined approach we refer to as a Design Criteria.

The Design Criteria is both a document and a design technique which address project technical specifications and can resolve Control System philosophy issues at the overall plant level prior to the start of detail design. The discipline is a top-down approach which addresses the overall plant operating objectives and provides the framework within which to complete the detail design. It can reduce the number of iterations required to finalize systems specifications and provides significant reductions in the engineering design effort of those responsible for specific processes. Where multiple process licensors/contractors are involved, the Design Criteria acts as an overall project control systems specification, coordinating and clarifying the development of integrated and compatible control systems for each of the various processes.

## INTRODUCTION

Process plants, particularly the synthetic fuel plants, are becoming larger and more complex and their control systems are the key to maximizing profits. It is becoming increasingly critical to move controls from the "last items bought" to a position more appropriate to their importance in the design cycle. One proven way to accomplish this is for the plant owner and the managing contractor to schedule the development of an instrumentation and control systems design criteria in conjunction with the plant functional layout.

The design criteria is both a document and a design technique which addresses project technical specifications and resolves control system philosophy issues at the overall plant level prior to the start of detail design. The discipline is a top-down approach which both addresses the overall plant operating objectives and provides the framework within which to complete the detail control systems design. It reduces the number of iterations required to finalize system specifications and causes significant reductions in the engineering design effort of those responsible for specific processes. Where multiple process licensors/contractors are involved, the design criteria acts as an overall project control systems specification, coordinating and clarifying the development of integrated and compatible control systems for each of the various processes.

Even relatively simple synthetic fuel plants can have four or five process areas with proprietary processes. Large plants, such as SASOL II and III, can have more than a dozen process contractors or licensors involved, each with their own preferred approach to control systems. If control system integration is not addressed early in the project cycle, a plant can end up with massive integration problems, many last minute changes, spare parts interchangeability problems and training difficulties. All of these problems will add significantly to not only the engineering but the start-up and operating costs as well.

To illustrate the magnitude of the problem, let's consider a relatively straightforward twenty-thousand barrel per day coal to methanol to gasoline plant as shown in Figure 1. This plant will have approximately 2,000 control loops, 4,000 additional measured variables, 1,000 logic or start-up points, 7 to 9 control rooms and will occupy an area of a square mile. The control systems will be engineered by 8 to 10 process licensors and possibly 2 or 3 turnkey contractors for areas such as water treatment, steam and oxygen plants. Without a design criteria, we might expect to see the types of relationships as shown in Figure 2.

Obviously, the controls systems supplier is subject to the differing, and perhaps conflicting, philosophies, specifications, and designs of a multitude of process licensors and contracting engineers, while, from the owners standpoint, all of the plant control systems should appear as though designed by the same people to the same specifications. The design criteria is used to solve these problems and insure design similarity by creating the type of relationships as shown in Figure 3 where control requirements for all parties are focused through the design criteria. The design criteria reflects plant operating requirements and establishes the framework in which detail design can be completed. It, therefore, involves process and operations staff, in addition to project and/or instrument engineers. Utilizing the design criteria approach, we can define four specific areas of the control systems specification development effort:

1. The design criteria, which specifies the control system in terms of plant operating requirements.
2. Instrument specifications, which define the control equipment hardware to be supplied.
3. Application guidelines, which supplement the design criteria showing how to interpret P&ID requirements in terms of hardware and provide ground rules for any deviations from the design criteria.
4. Instrument data sheets, which contain the details of the specific control requirements for a unit as represented on the P&I drawing or mechanical flow diagrams.



There is also the parallel effort of process engineering, which results in the generation of the control loop detail for the process units. This generates the information necessary to develop the instrument data sheets, Figure 4.

Our interest today is with the mechanics of area one, development of the design criteria. The starting point for developing the design criteria is immediately following control systems vendor selection. Therefore, the capability of the vendor to take a major role in the development of the design criteria should be strongly considered during the task of selecting the control systems vendor. The first step is to make some very general outlines of the control system requirements. For example, this might mean a decision that an operator would work from a CRT console with four CRT screens and be responsible for no more than 200 valve outputs. A similar decision might be one to locate control equipment in satellite houses in or adjacent to the unit and have only the control consoles located in the control house itself. Since the details in the later stages tend to be vendor specific, it is much easier to proceed through the detailed design stages with the selected vendor without the need to prepare multiple specifications to recognize philosophy and/or vendor equipment differences.

We continue to develop our preliminary specification by partitioning the plant into operating areas as we have shown in Figure 5. Coal preparation which extends from the unloading area through washing, crushing and storage; steam generation; air separation; gasification; acid gas removal; phenol recovery and sulfur recovery; methanol synthesis and methanol to gasoline; and storage and shipping.

Our preliminary specification is next tested against the various plant areas. By reviewing the operating requirements of each of the units against our spec, we can establish the preliminary specification for each individual process control system. In our example, we know from experience that an operator can handle three large coal fired boilers from a console and so our steam plant will have two consoles, one for the boilers and one for utilities (and power generation). Similarly, an operator can handle four

1,500 T/D air separation trains from a console. In the gasification area, an operator can handle three KBW gasifiers from a console. The Lurgi gasifiers will be split into two trains and each train will require a console. The partial oxidation reactor will also require a console, although the detail review that takes place during the final stage will probably reduce this console to 3 CRT's. The acid gas removal unit will probably be a Rectisol unit or similar process arranged in two trains. Again, we know from experience that one operator can handle two Rectisol trains at steady state, but two operators are required to handle large load changes, so we will probably add a fifth and sixth CRT to this console at the detail design stage to accommodate the second operator. The phenol and ammonia recovery units require one console and these can be located in the same control building with the acid gas removal unit since the units will all be physically adjacent to each other. The methanol synthesis and methanol to gasoline units will each require a console and these will be in a common control building. Storage and shipping will have a blending control room but will not have a console since most of the control will be a part of the blending package. The water treatment area will have a console. The resulting layout is shown in Figure 6.

Our preliminary specification has survived the test against the plant unit's functionality and it can now be detailed into a completed design criteria. This does not necessarily mean generation of a detail specification. Rather, it is a conceptual design for the overall control system based on the plant operating philosophies. It must include operations input to be successful and should be a mutually developed result of a joint venture between client, contracting engineer and the control systems vendor. In almost all cases, the end result is a design criteria document issued as a project specification either by the client or through the contracting engineer.

The conceptual design should include descriptions of what the control rooms will look like, the location and role of any computers, definition of a communications network joining the systems together, installation practices and environmental conditions.

It is worth noting that, at this point, we still have not had to address point counts or specific loop functions in terms of our specification, however, we can still be proceeding at the detailed P&ID level with design. What we have done, to this point, is establish discipline under which work will be done and raised and clarified any system level issues affecting control systems. We can now add detailed hardware specifications outlining the features of the equipment to be used and also start the final stage of detailing the controls in each area.

We now review each of the units in detail and incorporate the detail control requirements from the P&ID. This review is extremely detailed and requires input from the operating staff, the process designers and the contractors start-up department. This procedure is the definitive step in designing the control system and generates a hardware configuration that can be released to the control systems vendor for construction. It is at this stage that the specific details of the hardware must be addressed. Because of the design criteria development, hardware issues resolve themselves very nicely since they are subordinated to operating requirements. If we have no design criteria and ask, for example, "how many data hiways will we need for this plant?", we can argue for months without resolving anything. If, on the other hand, our design criteria says "our plant has seven control centers with the following operating consoles --- ", the number of data hiways to be provided is a function of the number of consoles and their location and the resolution becomes straightforward as shown in Figure 7.

Obviously, this one example is overly simplistic and, perhaps, the question would have been resolved amongst the project participants in a timely manner without a design criteria, however, there are literally thousands of questions on every project the size of a synfuels plant requiring plantwide consideration. The development of a design criteria has proven to be a cost effective, organized approach towards their resolution.

# 20,000 B/D COAL-TO-METHANOL-TO-GASOLINE PLANT

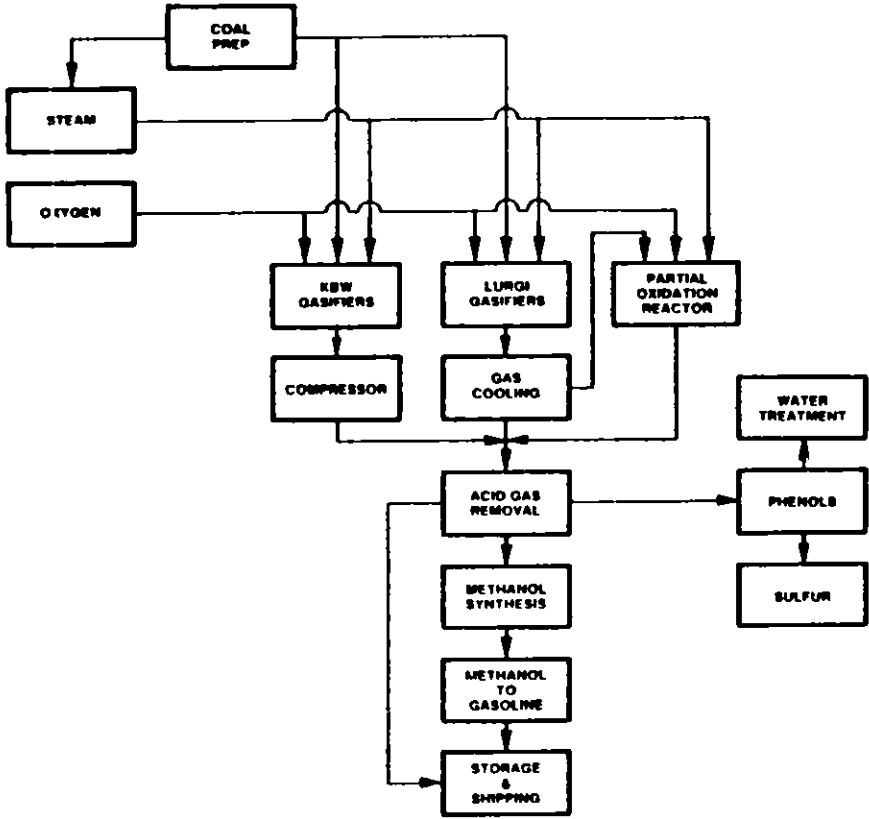


FIGURE 1.

05374-1

# POTENTIAL MULTIPLE CONTRACTOR RELATIONSHIPS

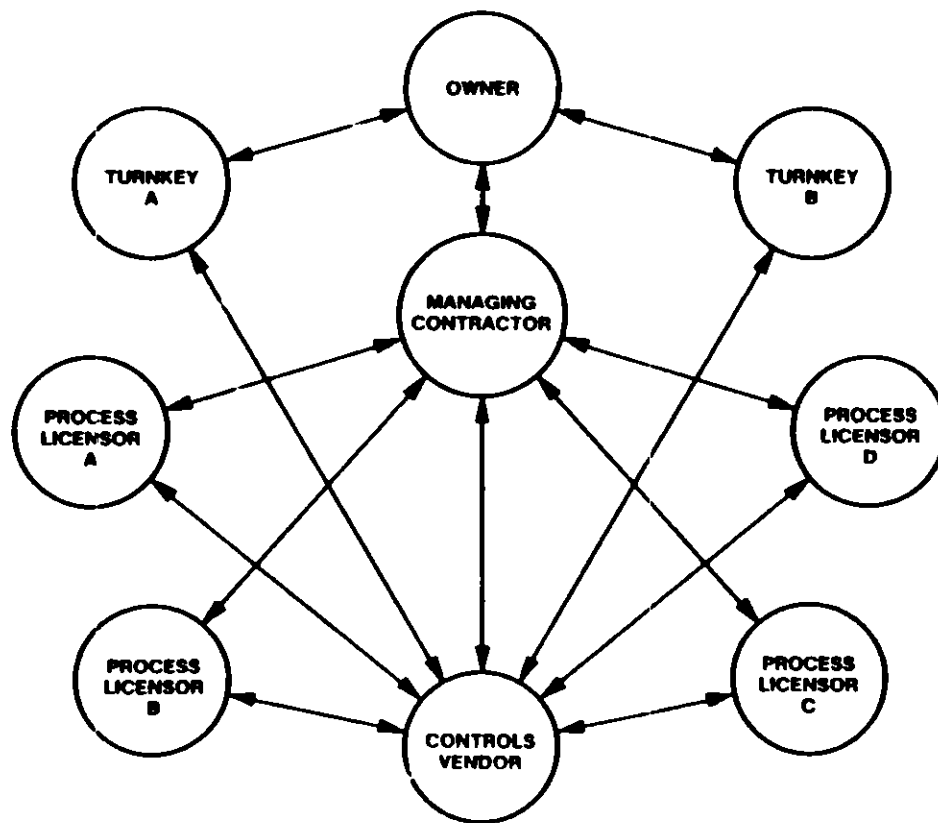


FIGURE 2.

05374-2

# DESIGN CRITERIA FOCUS

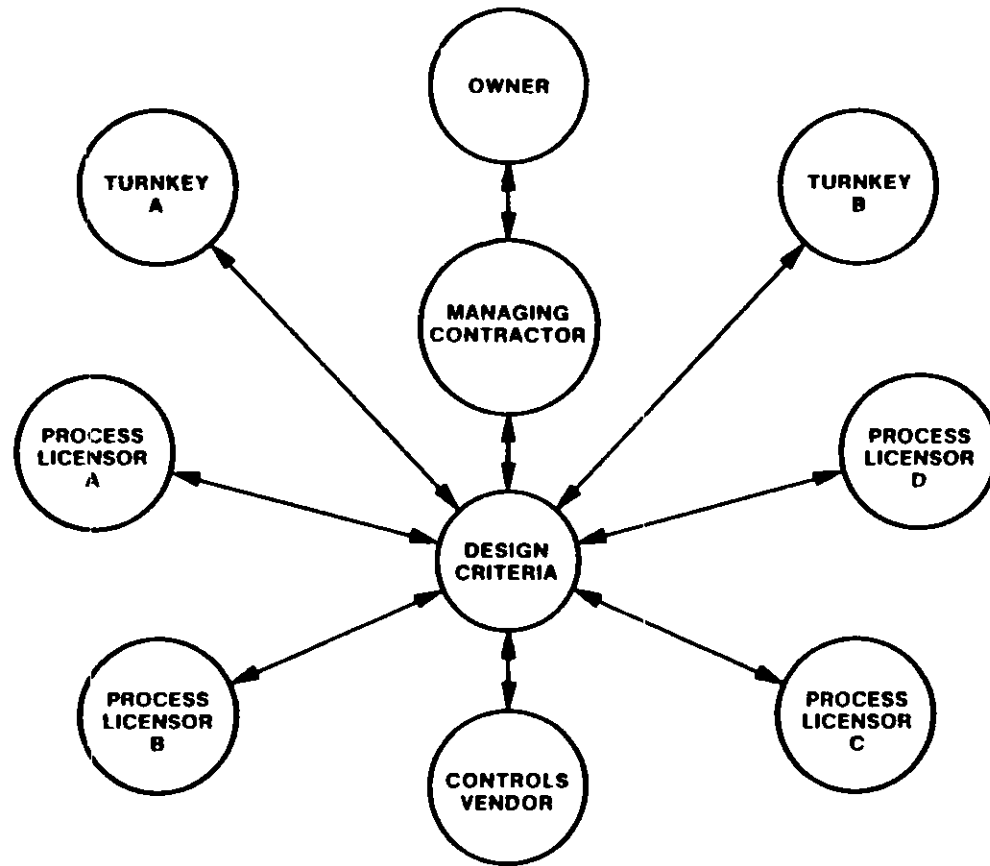


FIGURE 3.

05374-3

# SPECIFICATION DEVELOPMENT

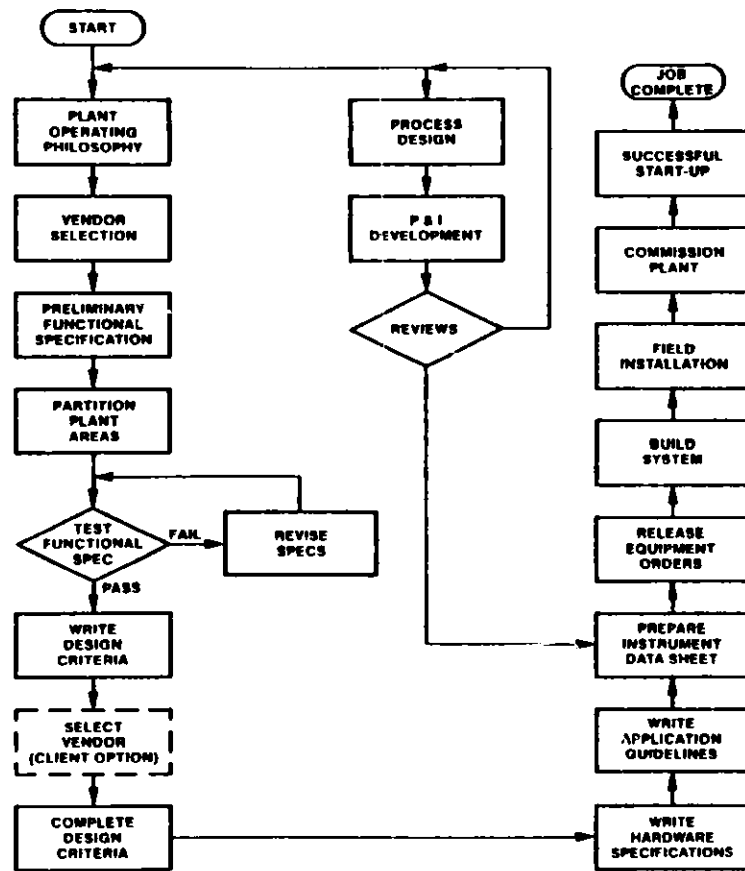


FIGURE 4.

# PLANT OPERATING AREAS

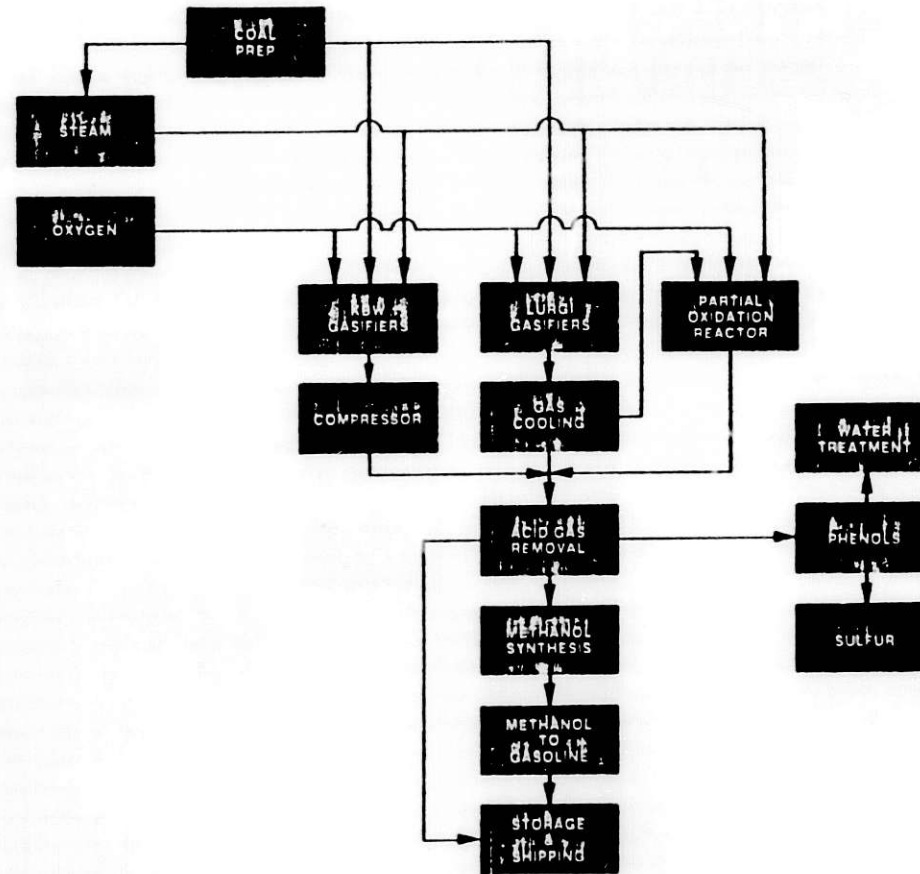


FIGURE 5.

05374 5



# PRELIMINARY CONTROL ROOM LAYOUT

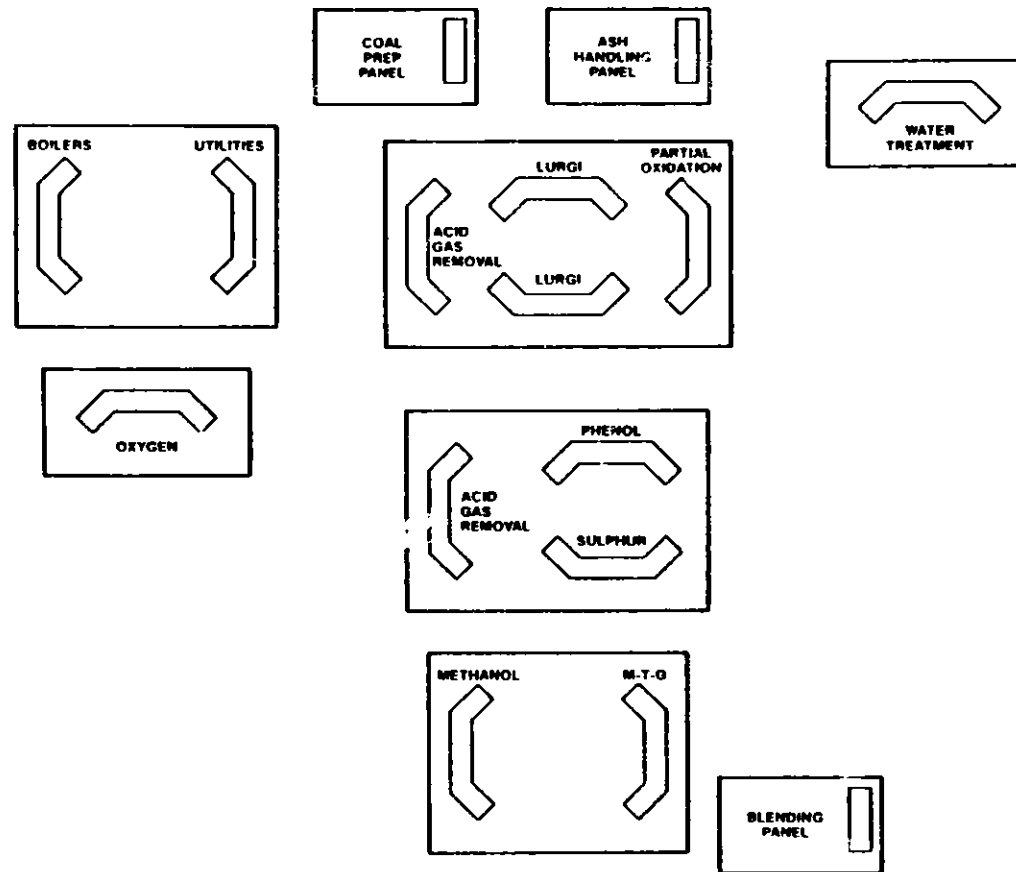


FIGURE 6.

05374-6

# SYSTEM ARRANGEMENT & DATA HIWAY LAYOUT

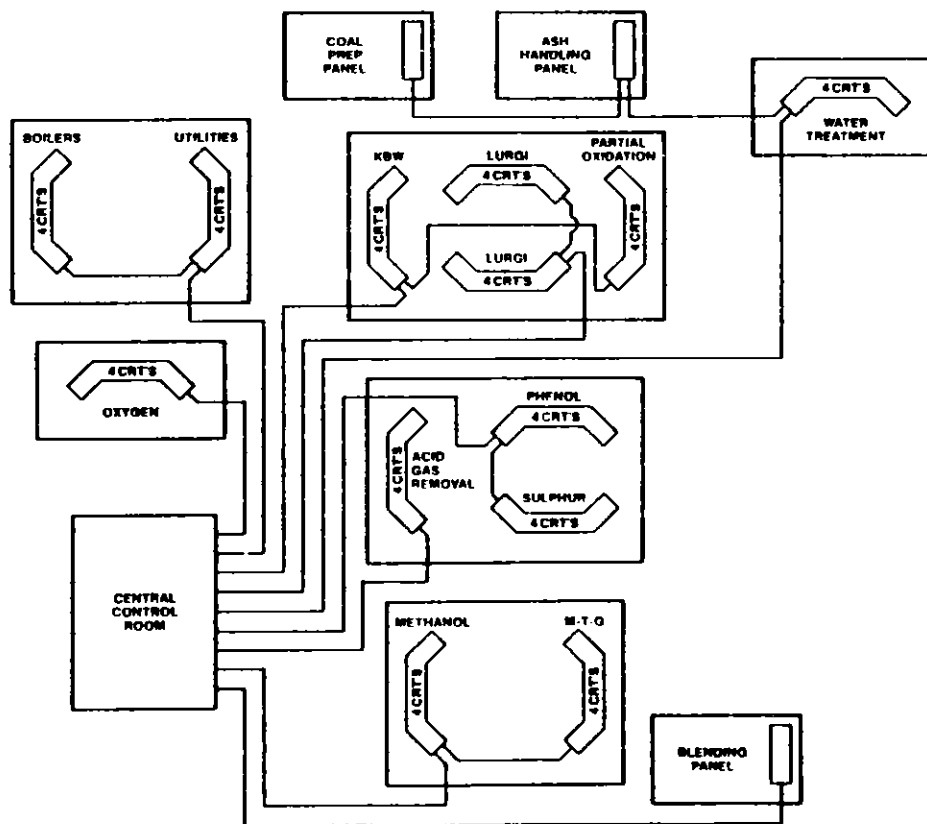


FIGURE 7.

05374-7

USE OF COMPUTER GRAPHICS TO STUDY  
BINARY DISTILLATION CONTROL ALTERNATIVES

Archibald G. Hill and John B. Howell  
School of Chemical Engineering  
Oklahoma State University  
Room 423 Engineering North  
Stillwater, Oklahoma 74078  
405/624-5280

Introduction

Distillation is the separation process most widely used by the fossil energy refining industries. Previous studies have shown that using advanced control systems can conserve up to 20 percent of the energy traditionally required by this process. However, the multivariable nature of distillation control complicates the selection of the best control strategy. This paper describes a Fortran program that is able to simulate the performance of a binary distillation column as it responds to changes in "disturbance" variables and/or "manipulated" variables. Disturbance variables considered include feed flow rate, composition, and enthalpy, and reflux enthalpy. Manipulated variables considered include reflux flow rate and vapor boilup. The following control options may be compared: feedback control of one or both control point compositions, feedback control with decoupling, and feedback control with feedforward. Alternative control strategies may be compared in two ways: 1) on the basis of cumulative error and 2) by visual comparison of response diagrams. The ability to prepare a graphical output illustrating the results of dynamic calculations is a key feature of this program.

Program Description/Capabilities

Design Portion

The calculations performed in the program are of two basic types: steady state design and dynamic response. The steady state design portion of the program makes use of the McCabe-Thiele column design technique. The operator specifies feed composition, flow rate, and enthalpy; overhead and bottoms composition; reflux ratio (as a multiple of minimum reflux); and reflux enthalpy. Feed and reflux enthalpy values are entered as a quality (i.e., the fraction of the stream that is vaporized). From this data, mass and component balances give overhead and bottoms flow rates, and liquid and vapor rates within the column. The McCabe-Thiele design technique makes the assumption of equimolar overflow. If the molar heats of vaporization of the two components are about the same, whenever a mole of vapor condenses, it vaporizes a mole of liquid. Also it is assumed that heat losses up the column and the sensible heat effects of temperature changes from tray to tray are negligible. These assumptions mean that the vapor and liquid rates through the stripping and rectifying sections will be constant under steady state conditions. The "operating lines", which relate rising vapor composition

to the liquid composition leaving the tray above, are shown as straight lines on the McCabe-Thiele diagram.

Equilibrium data for the physical system is generated as follows: column operating pressure, boiling points, Antoine equation coefficients, and Van Laar's constants for the two components are read into the computer as data. For each of 101 evenly spaced liquid compositions (from 0.00 to 1.00 mole fraction of light component) a flash calculation is performed to determine the equilibrium vapor composition, as well as relative volatility, and bubble point temperature. Thereafter, whenever the program requires the vapor composition that is in equilibrium with a particular liquid composition, a simple interpolation between the two nearest data points is used to provide a correlation.

With the equilibrium data and operating lines calculated, the computer analytically steps off trays from the bottoms composition to the overhead composition. Each vapor composition calculated (except for that leaving the reboiler) is corrected by a Murphree efficiency factor supplied as data, so that the vapor compositions are based on "real" rather than "ideal" trays. For each operating line point in the stripping section of the column, both upper and lower operating lines are used in turn. As long as the lower operating line equation gives a better separation, that equation is used to calculate operating line points. When the upper operating line gives a better separation, the tray below is identified as the feed tray, and the upper operating line is used for the rest of the trays. As soon as a vapor composition is reached that equals or exceeds the overhead product specification, the last tray is reported as the top tray.

The program will accept optimum feed tray location anywhere from the reboiler to the top tray. The operator cannot however, establish an arbitrary feed tray location.

After the initial McCabe-Thiele analysis, the program works to eliminate the "overshoot" in the overhead composition. This is accomplished by reducing the reflux ratio and performing the McCabe-Thiele analysis again, using the same total number of trays. This is done repeatedly, using an interval halving search routine, until the overhead is within 0.0002 mole fraction of the original overhead specification. In this process, the optimum feed tray location may change, but the total number of trays is held constant. The result of the above iteration procedure is the "exact reflux" value. The method used is similar to that of Buckley, et.al.<sup>1</sup> At the end of the "exact reflux" procedure, plate compositions and column flow rates are reported as the final steady state design.

A graphics section of the program may be optionally used to prepare the McCabe-Thiele diagram for the final design. This diagram may be viewed on a graphics-type CRT compatible with the Tektronix Plot 10 "Calcomp Plot Previewing" software package.

Included with the steady state design portion of the program are calculations to determine the temperature and pressure on each tray, and the minimum column diameter. Tray temperature is determined by interpolation between equilibrium data points. Pressure is determined by adding the pressure drop across each tray to the operating pressure of the top tray (both data values supplied by the user). Estimation of column diameter is done by using the vapor flow rates within the column, the ideal gas law, and  $K_V$  - an empirical constant that relates the maximum allowable superficial vapor velocity  $V_m$  to the density of the vapor  $\rho_g$  and liquid  $\rho_l$  by the formula:<sup>2</sup>

$$V_m = K_V \left( \frac{\rho_l - \rho_g}{\rho_g} \right)^{\frac{1}{2}}$$

When  $V_m$  has been determined, the minimum allowable diameter can be calculated. This is then rounded to the next higher standard size and reported as column diameter.

This is the final calculation made for design purposes. The program may be optionally ended at this point if further dynamic calculations are not required.

### Dynamic Portion

The dynamic portion of the program has been prepared to operate in a choice of operating modes: 1) to calculate the dynamic response to a step change in one or more "disturbance" variables (with or without control action) and 2) to calculate the dynamic response to a step change in one of the "manipulated" variables. Both operating modes depend upon the same dynamic process model that is similar to the one described by Luyben.<sup>3</sup>

In Luyben's original dynamic model the following assumptions are used: equimolar overflow; constant holdup of liquid in the reflux drum and column base; negligible dead time in the vapor line leading from the top of the column to the reflux drum, and in the reflux line back to the top tray; vapor boilup is generated in a thermosiphon reboiler with the assumption that liquids in the reboiler and in the column base are perfectly mixed together and have the same composition and total holdup; the holdup of vapor is assumed negligible throughout the system; the liquid rate leaving a particular tray can be related to tray holdup (in moles) by a linearized version of the Francis' weir formula; and lastly it is assumed that the dynamics of the condenser and reboiler are negligible in comparison to the response of the column itself.

All of these assumptions that were present in Luyben's original dynamic model have been retained. Together with the above has been added: the capability to have greater flexibility in column operating conditions such as feed enthalpy and product compositions; and also the ability to use an approximation of the number of "real" trays through the employment of a Murphree tray efficiency factor. In Luyben's original process model a constant value of relative

volatility was used. Here, the same table of equilibrium values calculated during the design portion of the program is used for the dynamic portion of the program. Therefore, non-ideal binary mixtures may be considered.

The digital simulation of the binary distillation column involves the simultaneous solution of a large number of ordinary differential equations and algebraic equations. The simulation logic employed is as follows:

1. Calculate vapor compositions on all trays.
2. Calculate all liquid flow rates.
3. Evaluate derivatives.
4. Integrate with Euler and start again at step 1 above.

When operating in the "disturbance" variable transient response mode, the operator sets the controller settings (gain and integral time) for the overhead and bottom product feedback controllers. For either controller, the control point can be composition on any tray, the overhead product, or the bottom product. Wherever the control point is, the setpoint of the controller becomes the original design composition at that point. Either or both controllers can be eliminated by setting the gain to zero. The reset feature can be eliminated by setting the reset time to a large number.

In addition to simple feedback control it is possible to use either feedforward action or decoupling as an incremental bias to the manipulated variable value calculated by the feedback controllers. In feedforward control, the input to both feedforward calculations is the deviation in the feed flow rate. In decoupling control, the input variable to each decoupler is the deviation of the manipulated variable, at the opposite end of the column, that is caused by the feedback control action. Thus if VP and RP represent the feedback control action for vapor boilup and reflux, respectively, then the input variable of the overhead decoupler is VP and of the bottoms decoupler is RP. The transfer function of the feedforward/decoupling element used in this program is the digital equivalent of the following expression:

$$G(s) = K_{ff}/d_0 \left( \frac{\tau_1 s + 1}{\tau_2 s + 1} \right) e^{-DT s}$$

where:

$$\begin{aligned} K_{ff}/d_0 &= \text{feedforward/decoupling gain} \\ \tau_1, \tau_2 &= \text{lead/lag time constants} \\ DT &= \text{net dead time} \end{aligned}$$

Complete descriptions of the methods of calculating feedforward and decoupling control action are given by Wood and Berry<sup>4</sup> and Wood and Pacey<sup>5</sup>

At the same time that controller settings are established, the user establishes the differential time element for Euler integration, the total time period over which dynamic response will

be observed, and the time interval at which data will be recorded and stored.

Next the nature of the disturbance is entered into the computer as a step change in either feed conditions (flow rate, composition, or enthalpy) or reflux enthalpy. Any of these values may be different from the initial design values.

Once the dynamic calculation has begun the program records and stores sixteen items of information each time the "print interval" is attained. This will usually be once every 10, 50, 100, etc. iterations. It would be impractical to store all data calculated, since a typical iteration interval of 0.001 hr would generate 16,000 items of data for each "hour" the dynamic performance was observed.

At the conclusion of the dynamic run calculations a number of graphs may be prepared which will be described by example in the next section of this paper.

The other mode of operation of a dynamic run, responding to a step change in one of the "manipulated" variables, is used primarily to calculate tuning constants for the various control actions.

### Sample Results

Several runs were performed to compare alternative control strategies for a distillation column separating a methanol/water binary mixture. Steady state design parameters for this column are given below:

Column pressure	= 1 atm (absolute)
Feed rate	= 100 lbmoles/hr
Feed composition	= 0.30 mole fraction MeOH
Feed quality	= 0.0 fraction vaporized
Overhead composition	= 0.96 mole fraction MeOH
Bottoms composition	= 0.04 mole fraction MeOH
Reflux ratio (L/D)	= 1.033 (= 1.28 x minimum)
Overhead flow	= 28.3 lbmoles/hr
Bottoms flow	= 71.7 lbmoles/hr
Reflux flow	= 29.2 lbmoles/hr
Vapor boilup	= 57.5 lbmoles/hr
Murphree efficiency	= 0.43
Total number of trays	= 24
Feed tray	= 7 (numbered from bottom)
Column diameter	= 2 ft
Tray holdup above feed	= 1.09 lbmoles
Tray holdup below feed	= 1.91 lbmoles
Reflux drum holdup	= 15.0 lbmoles
Reboiler holdup	= 3.00 lbmoles

The McCabe-Thiele diagram prepared for this case is illustrated in Figure 1.

In order to establish controller settings, runs were performed for +1% step changes in the "manipulated" variables: reflux and vapor boilup. The dynamic response of the column to these step changes was approximated according to a first order plus dead time model as shown below:

$$\frac{X_D(s)}{R(s)} = 0.0087 \frac{e^{-0.34 s}}{1.38 s + 1}$$

$$\frac{X_B(s)}{V(s)} = -0.0106 \frac{e^{-0.056 s}}{0.66 s + 1}$$

Note: deadtime = 10% of  
time constant

Process transfer functions necessary for single point feedback control are shown above. Other transfer functions necessary for feedforward and decoupling control were found in a similar manner. In cases where the process response gave a very small dead time, the dead time was approximated as 10% of the first order time constant. Dead time and first order time constant are given in units of hours. Process gain is given in units of mole fraction/ (manipulated flow in lbmoles/hour).

The process transfer functions were used to calculate proportional/integral controller settings according to a method described in the text of Murrill.<sup>6</sup> This tuning relation was designed to minimize the integral of the absolute value of the error for a system responding to a load disturbance. Calculated settings for the feedback controllers are given below:

<u>Controller</u>	<u>Gain (Engr. units)</u>	<u>Reset time (hr)</u>
Overhead composition by reflux flow	450.1	0.843
Bottoms composition by vapor boilup	-905.6	0.213

Feedback control and other alternative control strategies were compared during several dynamic runs. The disturbance for all of these runs was a 10% step increase in feed flow rate. Alternative control strategies were compared by the integral of the absolute value of the error (IAE) at each control point, observed during 10 hours of column simulation time. The IAE was normalized to the case of single point feedback control. For example, the IAE in the bottoms composition when the column was under feedback control on bottoms only, was given a value equal to one. The error in the bottoms composition ( $X_B$ ) observed during runs with all other control strategies is listed as a multiple of the error observed in this run.

The results of the dynamic runs are given on the following page:



<u>Control strategy</u>	Normalized IAE	
	<u>X<sub>D</sub></u>	<u>X<sub>B</sub></u>
Feedback on V only (to control X <sub>B</sub> )	149.3	1.0
Feedback on R only (to control X <sub>D</sub> )	1.0	264.2
Two point feedback (FB) control	6.57	1.35
Two point FB + feedforward on both R & V	7.93	0.90
Two point FB + feedforward on V only	6.57	0.86
Two point FB + decoupling on both R & V	6.14	1.90
Two point FB + decoupling on R only	2.51	1.48

The dynamic response of the first run listed above (feedback control on bottoms composition only) is shown graphically in Figure 2. The computer generated diagrams show that in this case the overhead composition stabilizes at a concentration of 0.946 mole fraction MeOH while the bottoms concentration returns to the setpoint value of 0.04 mole fraction MeOH.

The best control strategy for two point composition control appeared to be obtained in the last run listed above (two point FB + decoupling on R only). The dynamic response for this run is shown graphically in Figure 3. In this case both compositions return to setpoint values. Note however, that the best run with two point control does not control either composition as tightly as when only single point control is used.

The dynamic portion of the program will prepare two additional graphs which are not shown here. One of these graphs shows product compositions together with the composition on four intermediate trays, as a function of time. The other graph shows the values of the flow rates of reflux, vapor boilup, bottoms, and overhead as a function of time.

Future work on this program will include the addition of bottoms flow and overhead flow as alternative manipulated variables in order to examine the "material balance" approach to binary distillation control.

References

1. Buckley, P.S.; Cox, R.K., and Luyben, W.L.: "How to Use a Small Calculator In Distillation Column Design," Chemical Engineering Progress, June, 1978, pp. 49-55.
2. Peters, M.S.; and Timmerhaus, K.D.: Plant Design and Economics for Chemical Engineers, McGraw-Hill Book Company, New York, 1968, pp. 626-627.
3. Luyben, W.L.: Process Modeling, Simulation, and Control for Chemical Engineers, McGraw-Hill Book Company, New York, 1973, pp. 148-151.
4. Wood, R.K.; and Berry, M.W.: "Terminal Composition Control of a Binary Distillation Column," Chemical Engineering Science, 1973, Vol. 28, pp. 1707-1717.
5. Wood, R.K.; and Pacey, W.C.: "Experimental Evaluation of Feedback, Feedforward, and Combined Feedforward-Feedback Binary Distillation Column Control," Canadian Journal of Chemical Engineering, Vol. 50, June, 1972, pp. 376-384.
6. Murrill, P.W.: Automatic Control of Processes, International Textbook Company, Scranton, Pennsylvania, 1967, pp. 358-363.

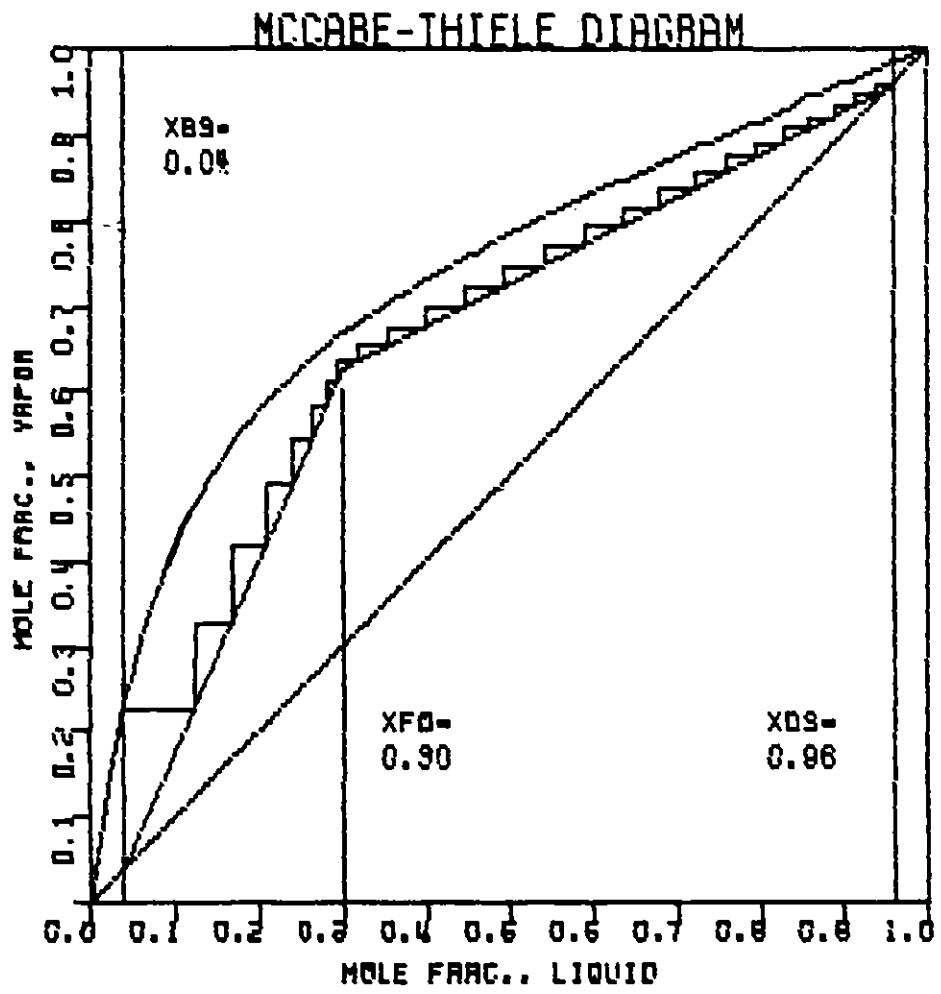


Figure 1

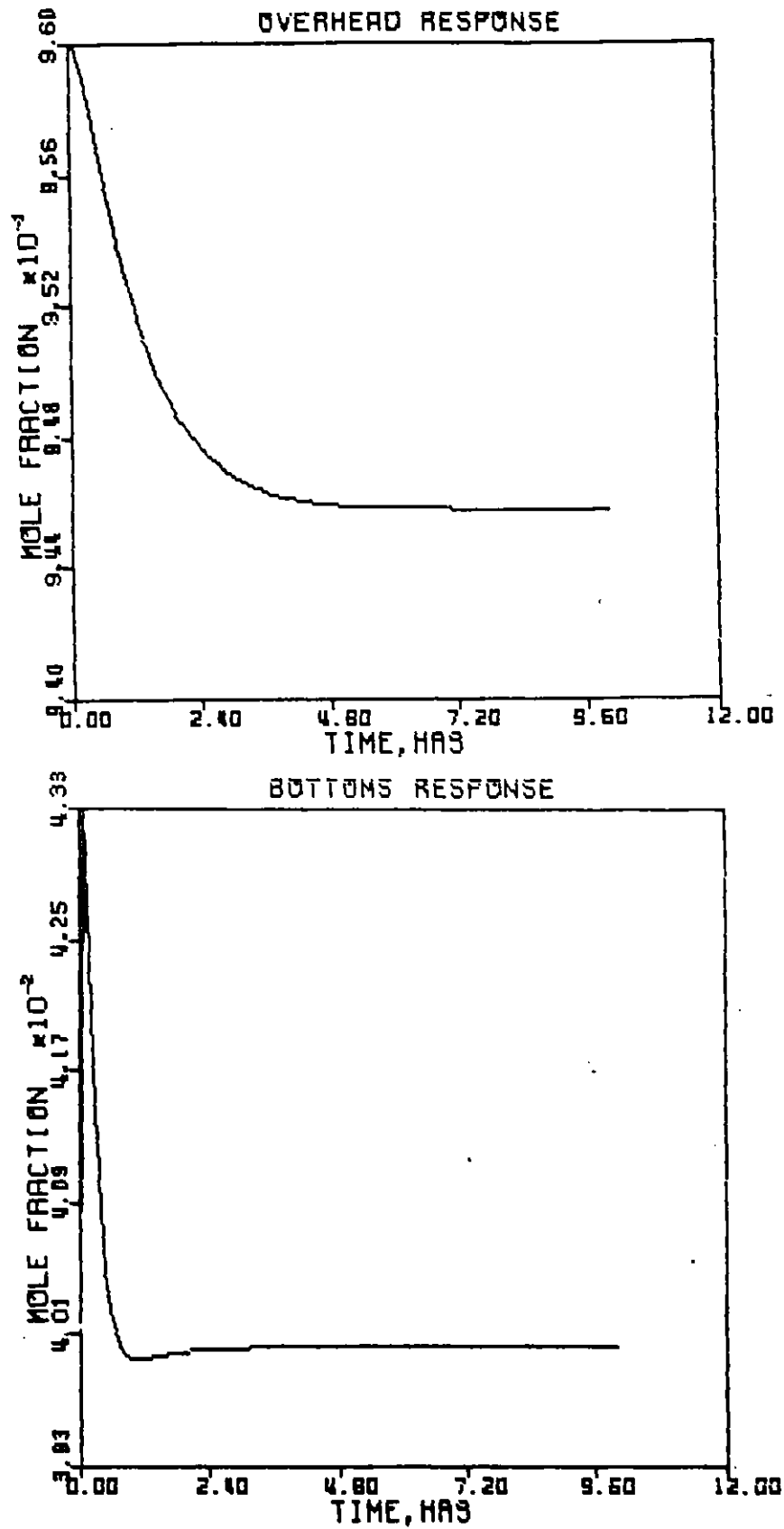


Figure 2

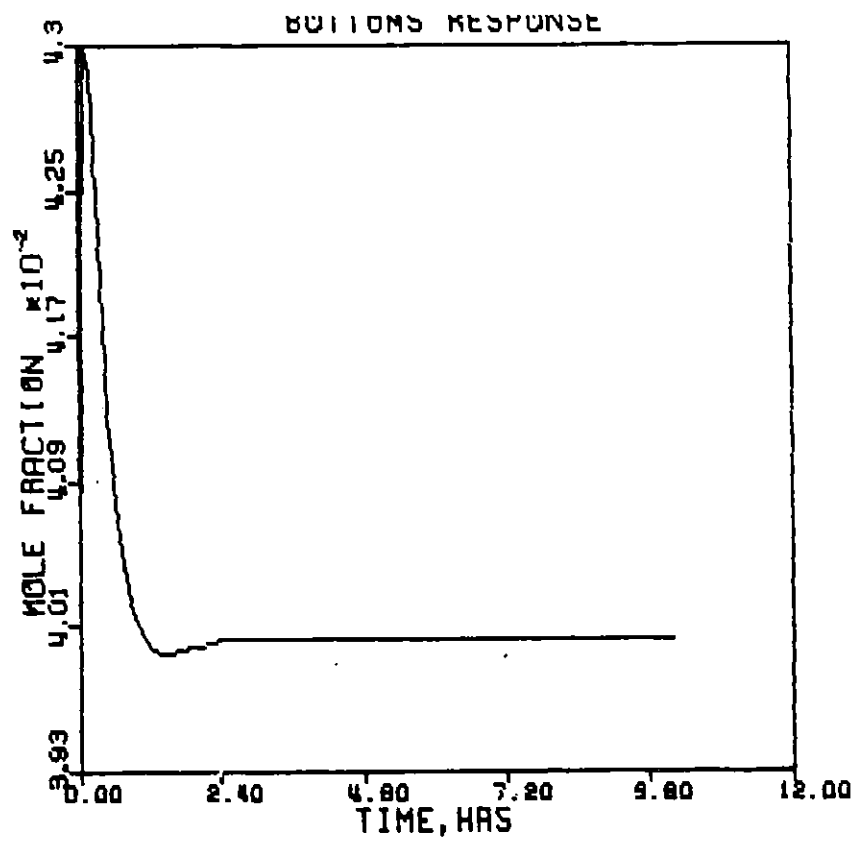
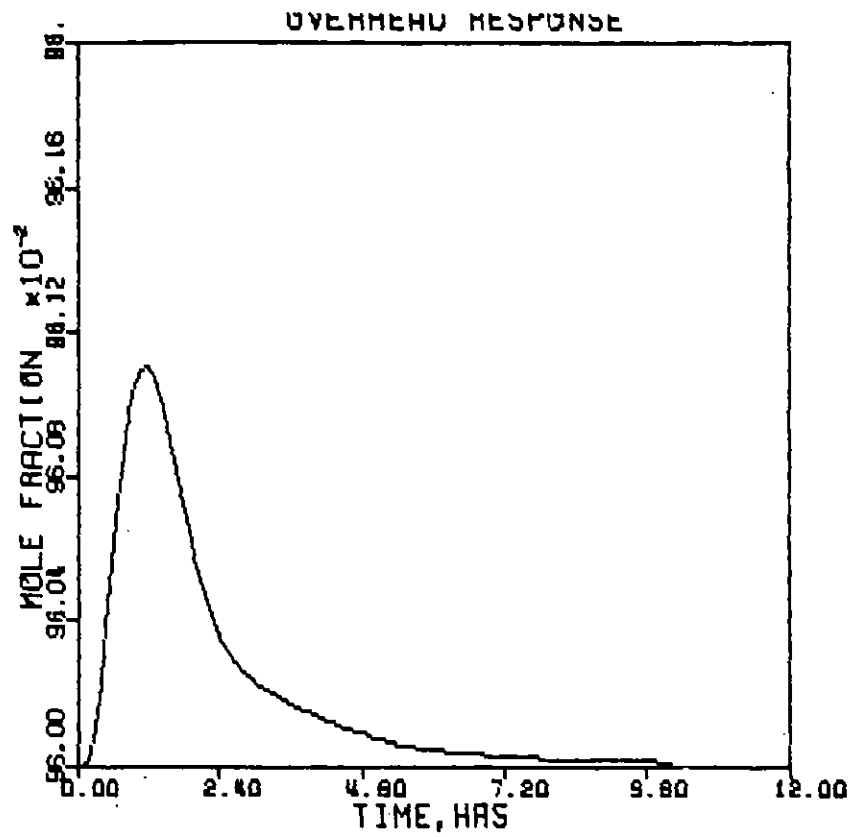


Figure 3

CONTROL PROBLEMS IN COMBINED-CYCLE MHD-STEAM POWER PLANTS:  
EFFECTS OF TURBINE CONFIGURATIONS ON DYNAMIC RESPONSE

D. A. Rudberg, C. A. Helkes, and J. C. Shovic\*  
Department of Electrical Engineering and Computer Science  
Montana State University, Bozeman, MT 59717  
(406) 994-2505

Abstract

Dynamic control has been applied to first-principle models of two 210 MWe combined-cycle MHD-steam power plants. Both plants are reheat turbine configurations, operating with shell-and-tube oxidant preheaters which deliver air enriched to 30 percent oxygen. Their distinguishing differences are the manner in which the blend air compressor (BAC) turbine is connected to the steam generator.

Simulations show that conventional driving of the BAC turbine with steam from the hot reheat header yields a system that can follow a ramp-up demand change of 1 percent per minute without significant effect on main steam pressure and with quite acceptable error of power generation. However, such a plant has difficulty in following a 10 percent per minute ramp-up demand change. Significant errors in either power generation or in main steam pressure result, depending on the mode of control that is applied. No control has been found that can reduce both errors to low levels at the 10 percent per minute demand change rate.

A plant version with the BAC turbine driven from main steam and exhausting into the cold reheat line is quite different in response and controllability. An exceptionally fine balance between steam generation and consumption is struck (especially in smaller, more oxygen-enriched units), yielding plants that follow a 10 percent per minute ramp-up of power demand with insignificant error in both power generation and main steam pressure. It is suggested that current plant configurations be reviewed in light of these findings.

1. Combined-Cycle MHD-Steam Plant Modeling and Control

A rapidly-changeable modeling system has been developed at Montana State University for purposes of predicting dynamic response of various combined-cycle plant configurations under various control policies. All current plant models are characterized by reheat turbine configuration, and oxygen enrichment of primary oxidant. Nominal steam conditions are 12.514Mpa/811K/811K (1815psi/1000F/1000F) with water spray temperature control of both main steam and reheat steam. The oxidant is ambient air, blended with the output of an air separation unit whose product is oxygen of 70 percent purity. The result is an oxidant enriched to nominal 30 percent mole

\* J. C. Shovic is currently with American Microsystems Inc., Pocatello, ID

fraction oxygen. Oxidant is preheated for combustion with a shell-and-tube recuperative oxidant preheater designed for operation at 867K (1100F) output when the plant is at full load (compared to 1922K (3000F) output of the indirectly-fired ambient-air preheater of earlier plant designs [1]). Actual preheat temperature is uncontrolled, varying somewhat with load. All models are flexible, being suitable for a range of plus-or-minus five percent oxygen enrichment about design center. They are also responsive to variations of combustor pressure, coal flow, oxygen flow, blend air flow, oxidant preheat temperature, channel loading parameter, diffuser outlet pressure, and secondary combustion air flow and enthalpy. Seeding level is held fixed at 1.0 percent mass fraction potassium throughout.

The nonlinear dynamic models of the steam turbines are based on a development by Ray [2] and include governor valves, nozzles, impulse stages, and reaction stages. The transition from subsonic to choked flow is modeled, as are the dynamics of pressure through the turbine as loads and flows vary. A similar development has been used by the Philadelphia Electric Company for simulation of a generic electric generating station [3]. Modeling of the steam generating units is done through first principles [4,5,6], thus making their descriptive equations easy to understand and modify. Also, all heat transfer is temperature-driven, thus avoiding violation of the second law of thermodynamics.

Major control for any plant configuration is applied through the governor valves of the main HP turbine and the governor valves of the BAC turbine. Numerous other control loops exist, but their effect on plant response is of a secondary nature by comparison. Typical of such loops are the spray attenuator controllers for steam temperature, the gas recycle controller for thermal quenching at the seed condenser furnace exit (which is quenched at 1350K, just above the freezing point of potassium sulfate), and the drum water level controller (which is a very important loop from the viewpoint of plant integrity). Figures 1 and 2 show the structure of controllers for governor valves of both the main turbine and the BAC turbine. Direct control of governor valve area is implied in the diagrams, whereas in practice a valve management program would be employed. Error signals are derived from the difference between power demand (QE1) and net plant output (QE4), and from the difference between main steam pressure (CIN11) and actual main steam pressure (PS5). An additional control exists for limiting channel electrical output when actual channel output (QE3) exceeds a preset limit (CMAX). For the simulation results presented here, this limit control is not activated.

When BAC turbine control is asserted solely through power generation error ( $K60 > 0$  and  $K61 = 0$ ), and main turbine control is asserted solely through main steam pressure error ( $K1 = 0$  and  $K56 < 0$ ), the control mode is called MHD-leading since increased channel firing (and subsequent steam generation) leads increased main generator output. When BAC turbine control depends solely on main steam pressure error ( $K60 = 0$  and  $K61 > 0$ ), and main turbine control depends solely on power generation error ( $K1 > 0$  and  $K56 = 0$ ), the control mode is called MHD-following since channel firing follows the errors of main steam pressure created by main generator output changes. If the turbines depend on a combination of error signals for their control, the mode is called co-ordinated control. These control modes are summarized in Figure 3.

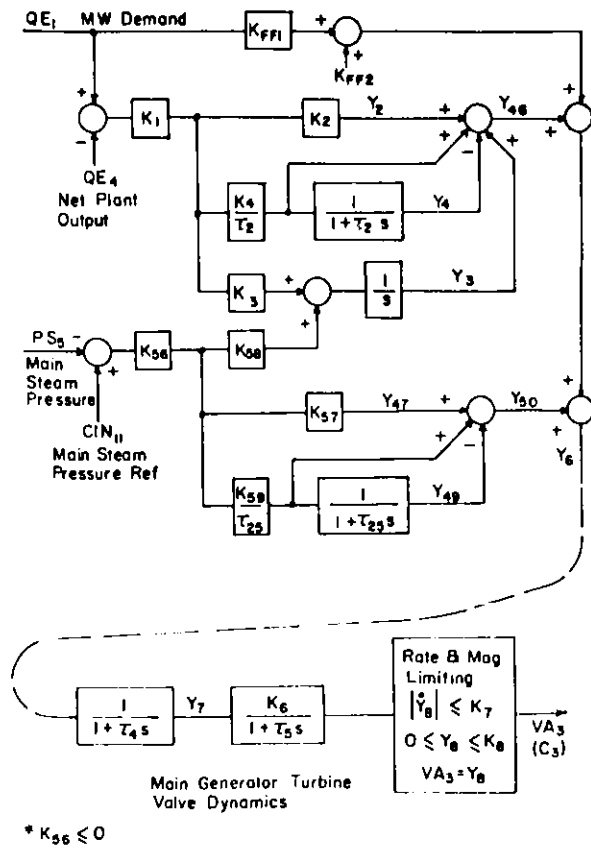


Figure 1. High-Pressure Turbine Governor Valve Controller.

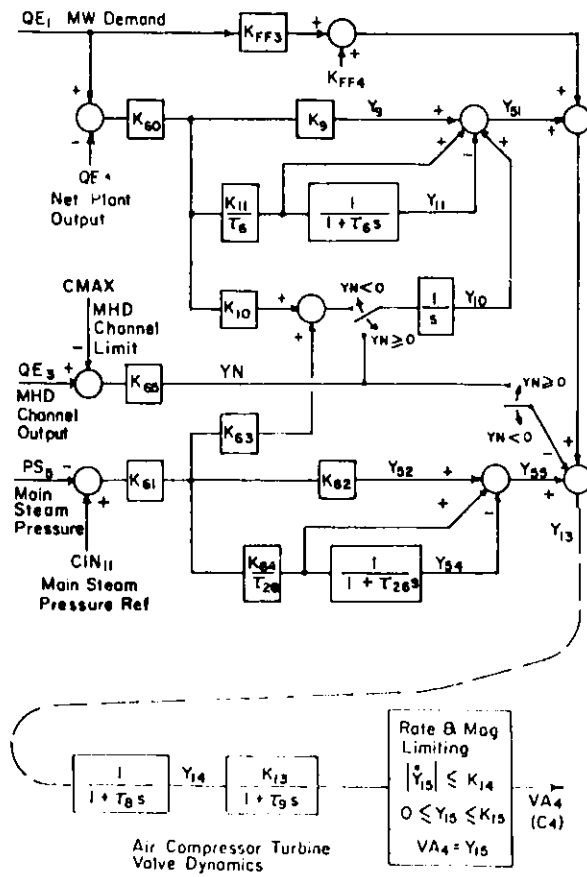


Figure 2. Blend-Air Compressor Turbine Governor Valve Controller.

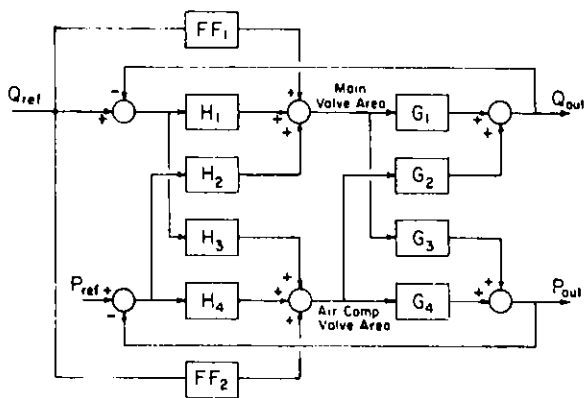


Figure 3. High-Pressure Turbine Governor Valve and Blend-Air Compressor Governor Valve Control Structure. Plant functions represented by G; Controller functions represented by H. MHD-leading when H2 and H3 non-zero; H1 = H4 = 0. MHD-following when H1 and H4 non-zero; H2 = H3 = 0. Feed-forward may be present in either mode.

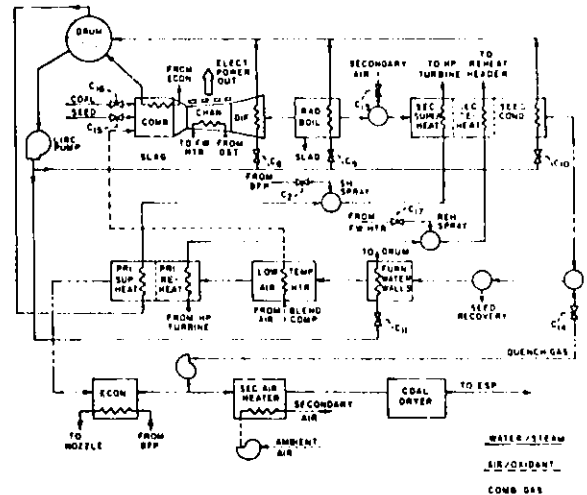


Figure 4. Oxygen-Enriched MHD-Steam Plant: Topping Plant and Steam Generator.



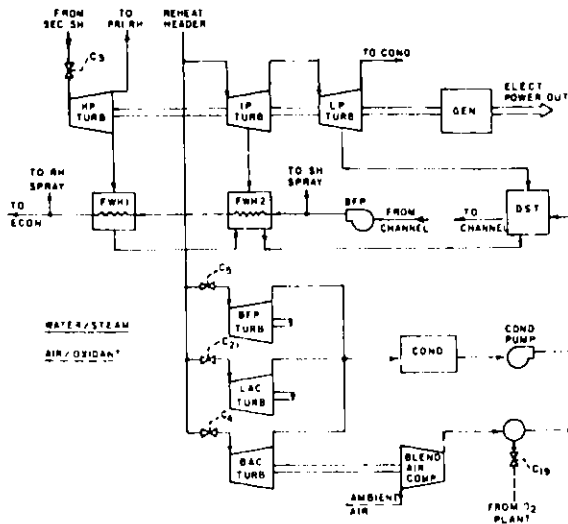


Figure 5. Oxygen-Enriched MHD-Steam Plant; Turbines and Pumps. Blend-Air-Compressor Turbine on Hot Reheat Header.

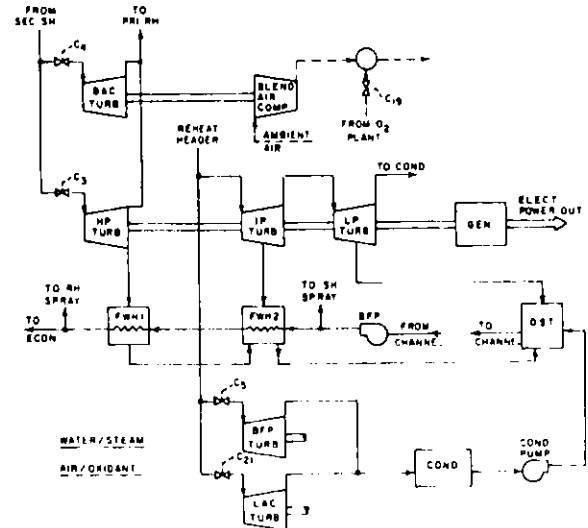


Figure 6. Oxygen-Enriched MHD-Steam Plant. Turbines and Pumps. Blend-Air-Compressor Turbine on Main Steam.

In the first version of the plant, the BAC turbine operates in the often-proposed manner on steam from the hot reheat header (whose temperature is tightly regulated but whose pressure is a function of plant load), exhausting into a condenser at the same pressure as the main turbine set (.00677Mpa (2.0"Hg)). This general configuration is shown in Figures 4 and 5, with control points as indicated. For modeling purposes, feedwater heaters have been lumped into a single heater on the HP turbine and a single heater on the IP turbine. The appearance of the deaerator-storage tank prior to the extraction-flow feedwater heaters is intentional since topping plant cooling supplants early low-temperature feedwater heating in a combined-cycle power plant.

The second version of the plant is shown in Figure 6. The BAC turbine is driven from the main steam supply at regulated high pressure and it exhausts into the cold reheat header. Thus the defects associated with variations of steam-supply pressure vanish. In fact the BAC turbine is similar to the HP turbine, being larger by a factor of about 1.4 (24.7 MW<sub>mech</sub> vs 17.2 MW<sub>mech</sub>).

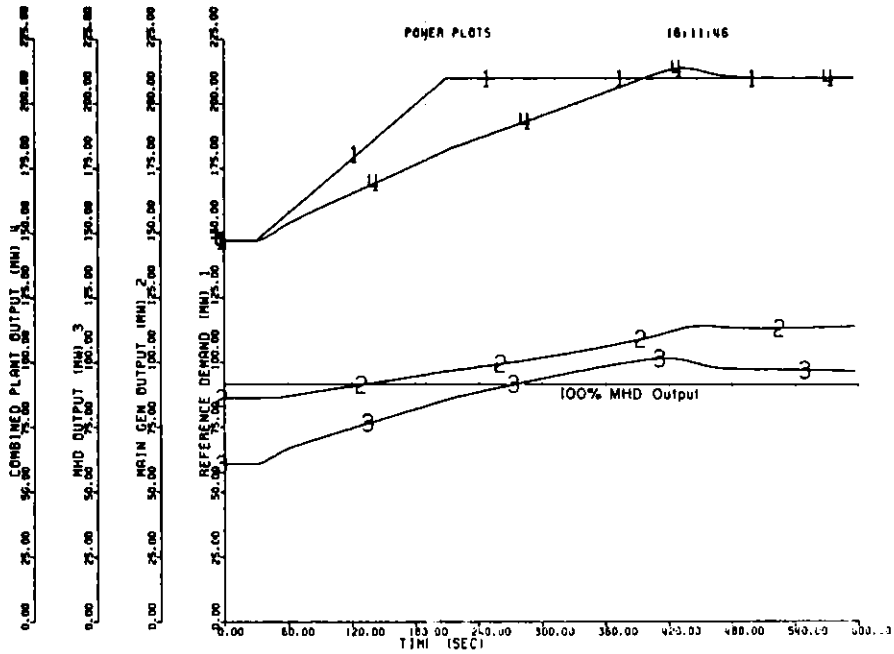
The major operational defects related to connecting the BAC turbine to the hot reheat header are that all steam for MHD channel firing (and hence system firing) must pass through the HP turbine, and that the BAC turbine supply is not pressure regulated. Indeed, the problem of supply pressure regulation for the BAC turbine is exacerbated by the existence of the intermediate-pressure and low-pressure (IPLP) turbine set, both of which are purely reaction turbines without governor valves. They present a large drain on the hot reheat header steam flow, making it quite troublesome to maintain adequate steam pressure to drive the BAC turbine, especially under rapid power demand increases. Therefore system firing capability is strongly affected by power generation control applied to the main turbine.

## 11. Dynamic Simulation Results

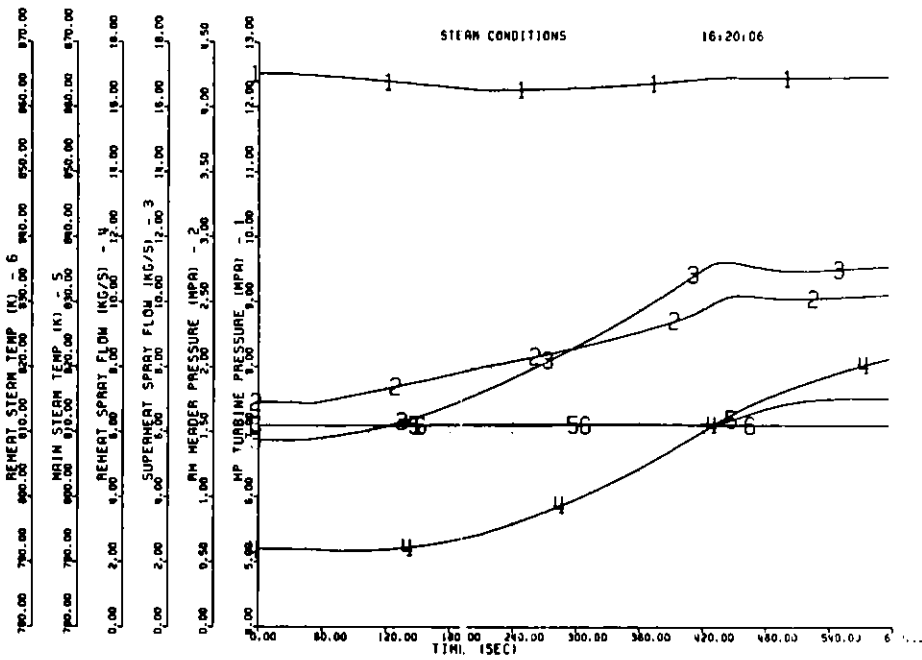
All responses for operation of the plant with the BAC turbine supplied from the hot reheat header were obtained with co-ordinated control of both the BAC turbine and the HP turbine, since pure MHD-leading and pure MHD-following control policies were not satisfactory. As a baseline test, the system was subjected to a demand increase from 70 percent of rated output to 100 percent of rated output (147 Mw to 210 Mw) at the conservative rate of 1 percent per minute. Oxygen enrichment is fixed at 30 percent throughout. The plant followed such a slow demand change without difficulty, which corroborates the results of Gilbert Associates [7] regarding such a configuration and demand slope. Results are not identical since the GA1 plant is enriched to 35 percent oxygen and control policies are not identical. Small errors occurred in demand following and main steam pressure during the simulation but they are not of consequence. The basic conclusion is that at 1 percent per minute demand change, the plant followed demand and no significant decline of main steam pressure occurred.

Figure 7 shows response of the same system to a demand increase which is also from 70 percent of rated output to 100 percent of rated output, but at the higher rate of 10 percent per minute. The BAC turbine again is connected to the hot reheat header. Oxygen enrichment is fixed at 30 percent, and control parameters are set to most tightly maintain steam pressure, which results in a failure to follow load. In Figure 8, a change in control parameters to emphasize load-following led to an excessive decline in main steam pressure. Several other control parameter sets were tried in quest of a reasonable compromise between generation error and main steam pressure error. Both errors could be reduced from the extremes shown, but not to acceptable levels simultaneously.

As shown in Figure 9, when the BAC turbine is driven from main steam, the difference in plant behavior is striking, both in demand following, which indicates plant suitability as a power grid element, and in regulation of main steam pressure, which indicates internal plant stability and integrity. The dynamic plots for operation of the BAC turbine from main steam were obtained with MHD-leading control of the BAC turbine and co-ordinated control of the HP turbine. The system was not especially sensitive to variations in controller gains, with a 2:1 range causing little change in response. These simulations show it to be advantageous, from the viewpoint of plant stability and integrity under load following, to operate the BAC from the main steam supply rather than from the hot reheat header. As explanation, any topping plant firing increase appears twice, first as increased MHD channel output and again as increased IPLP turbine output. Thus, any decrease in HP turbine output is doubly countered by increased firing. Finally, the BAC turbine steam supply is much better regulated than when reheat steam is used. Indeed, other factors, such as maximum thermal stress in the rotor bore or response of coal feeding mechanisms, may limit the dynamic response. Of course, considerations such as start-up and shut-down procedures, advisable turbine sizing, capital costs, air compressor placement, etc., must also enter into plant configuration decisions.

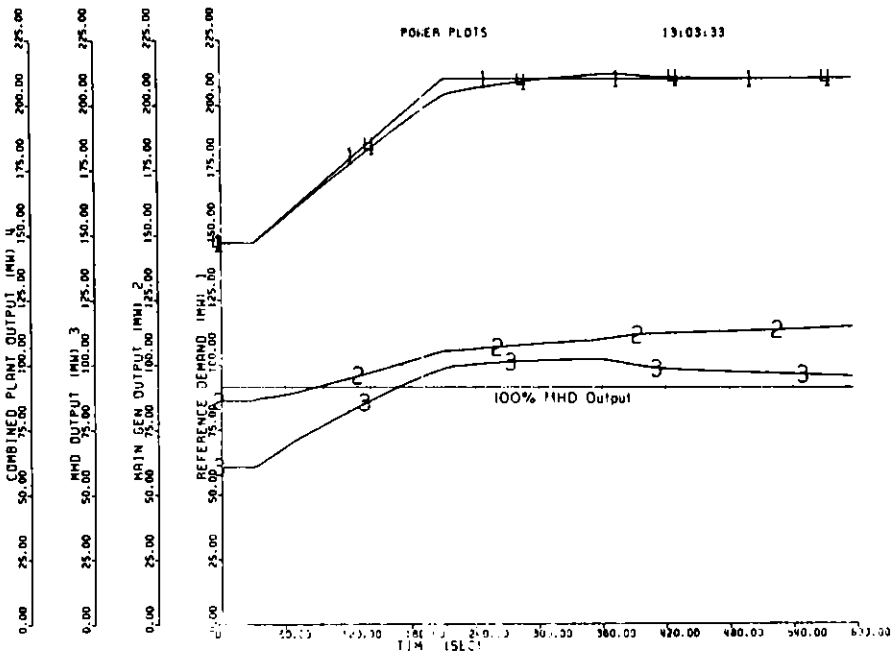


(a) Power Plots

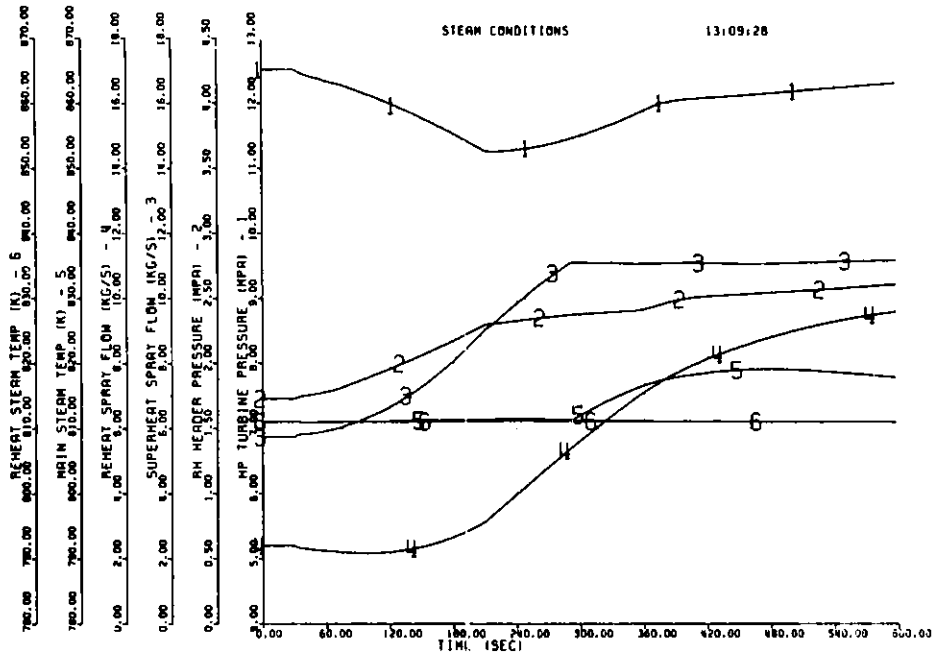


(b) Steam Conditions

Figure 7. 210 Mwe plant. 70 percent to 100 percent power demand ramp-up at 10 percent per minute. BAC turbine on hot reheat header. Oxygen enrichment at 30 percent. Control parameters set for main steam pressure control.

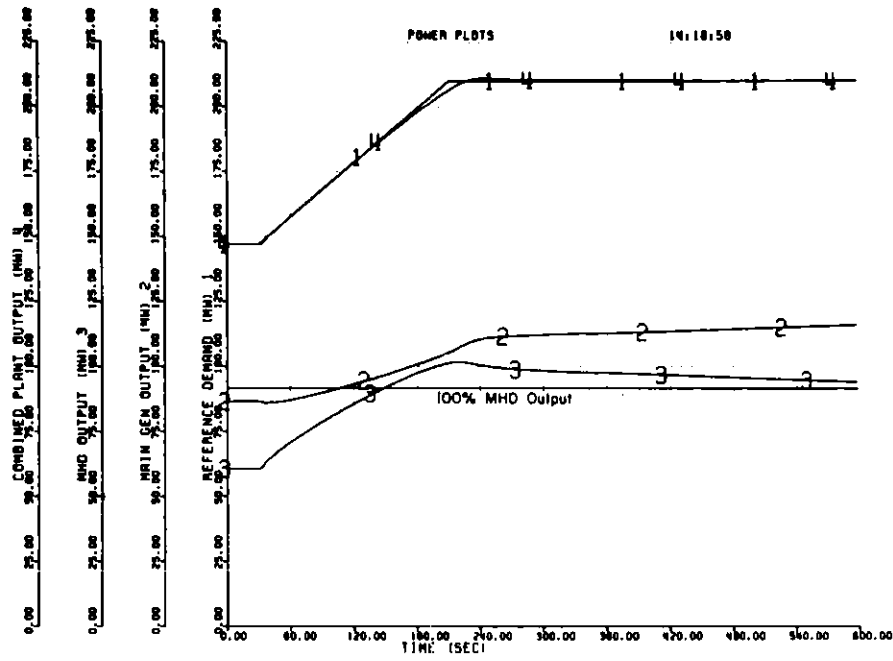


(a) Power Plots

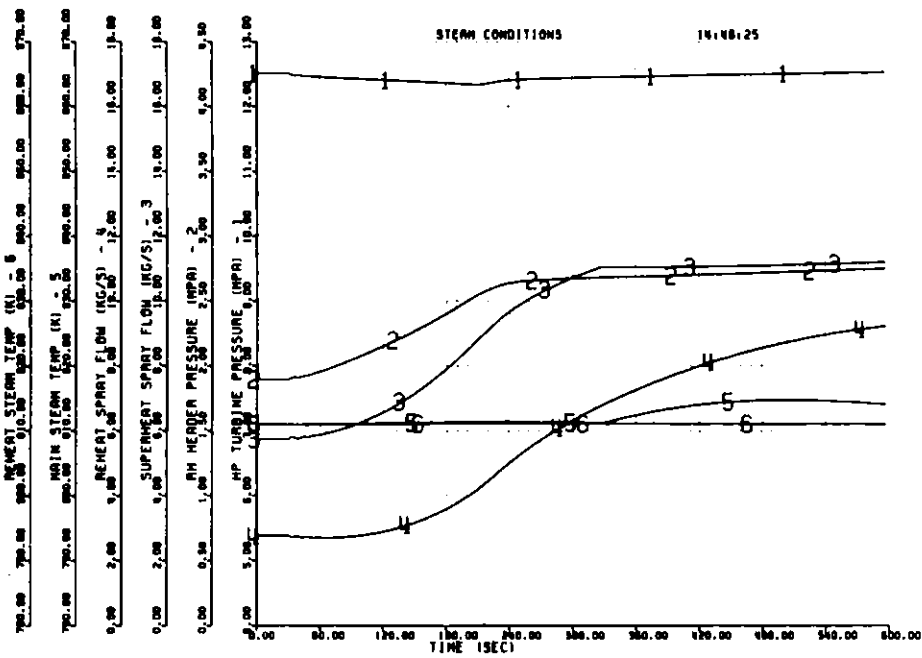


(b) Steam Conditions

Figure 8. 210 MWe plant. 70 percent to 100 percent power demand ramp-up at 10 percent per minute. BAC turbine on hot reheat header. Oxygen enrichment at 30 percent. Control parameters adjusted for load following.



(a) Power Plots



(b) Steam Conditions

Figure 9. 210 MWe plant. 70 percent to 100 percent power demand ramp-up at 10 percent per minute. BAC turbine on main steam. Oxygen enrichment at 30 percent.

### III. Conclusions

Simulations indicate that placement of the BAC turbine on the hot reheat header yields a plant that will follow a one percent per minute ramp-up of power demand, in agreement with earlier work of GAI. Such connection and operation of the BAC turbine are typical of preliminary designs for combined-cycle process demonstration units in the United States. However, the plant is not well-balanced with regard to steam generation and consumption, and it will not follow a ten percent per minute change. No control policy has yielded an acceptable main steam pressure variation while also exhibiting suitable load-following capability. Compromise policies may allow a five percent per minute change.

In comparison, using main steam to drive the BAC turbine in parallel with the HP turbine results in a remarkably fine balance of steam generation and consumption, which easily allows following of the higher demand slope. The BAC turbine is an essential part of the steam generation-consumption subsystem, and the entire system is constrained dynamically if it is treated as an ordinary auxiliary to be operated from an unregulated steam supply. It appears that combined-cycle plants should not be designed as straightforward extensions of conventional steam power plants. It is suggested that current plant configurations be reviewed and that consideration be given to repositioning the BAC turbine in the flow path.

#### References:

1. Engineering Test Facility Conceptual Design, Final Report, AVCO Everett Research Laboratory, Inc., DOE FE-2614-2, June 1978
2. Ray, Asok, "Dynamic modelling of power plant turbines for controller design", Appl. Math. Modelling, Vol. 4, April 1980
3. Sauk, P.L., Clælland, P.J., and Fagnan, D.A., "Development of a Model of a Generic Coal-Fired Power Plant", Proceedings, Joint Automatic Control Conference, June 1981
4. Kwatney, H.G., McDonald, J.P., and Spare, J.H., "A Nonlinear Model for Reheat Boiler-Turbine-Generator Systems, Parts I and II", Proceedings, 1971 Joint Automatic Control Conference, August 1971
5. Astrom, K.J., and Eklund, K., "A simplified Nonlinear Model of a Drum-Boiler Turbine Unit", International Journal Control, Vol. 16, No. 1, 1972, pp. 145-169
6. Goldsworthy, D.L., Rudberg, D.A., and Pierre, D.A., "First-Principle Dynamic Modeling and Automatic Control of an MHD-Steam Coupled Power Plant", Proceedings, Symposium on Instrumentation and Control for Fossil Energy Processes, June 1980
7. Boulay, R.B., Weinstein, R.E., and Cutting, J.C., "A Simulation of the Dynamics of a Magnetohydrodynamic/Steam Power Plant", Proceedings, 19th Symposium Engineering Aspects of MHD, Tullahoma, Tenn., June 1981

NONLINEAR DYNAMIC MODEL OF THE TVA 20-MW AFBC PILOT PLANT

Veni Sumaria, Kenneth C. Kalnitsky  
JAYCOR  
300 Unicorn Park Drive  
Woburn, Massachusetts 01801  
617/933-6805

James R. Byrd  
Tennessee Valley Authority  
1020 Chestnut Street Tower II  
Chattanooga, TN 37401  
615/751-7440

Introduction

A transient model of the TVA 20-MW atmospheric fluidized bed combustion (AFBC) pilot plant is being developed to provide a basis for: (1) understanding interactive process dynamics, (2) verifying design parameters, (3) predicting effects of subsystem changes on the entire process, (4) evaluating overall system (process and controller) performance, (5) evaluating alternate operating philosophies, and (6) designing multivariable controllers.

System Description

Figure 1 is a simplified solids/gas flowsheet for the AFBC pilot plant, and Figure 2 is a schematic of the water/steam system. The underbed air plenum (windbox) and the fluidized bed are divided into five compartments denoted as S, A, B, C, or D; compartment S is for startup only. Partitions separate the five windbox compartments, but the bed divisions are conceptual since no physical walls exist between them. The convective region is divided into three passes which are separated by waterwalls.

The steam generating arrangement is a drum-type circuit with forced circulation through the furnace waterwall enclosure and through the in-bed boiling tubes which are immersed in compartments A and B of the bed. Both the economizer and the primary superheater consist of three sections connected in series - one section for each of the three parallel convection passes. The secondary superheater, immersed in bed compartments C and D, has two sections in series with an attemperator between the sections.

Raw solids are received, crushed, screened, and dried as required. Downstream from this initial handling and preparation equipment are separate feed trains for each bed compartment (A, B, C, D, and S). Solids are pneumatically transported into the bed by the primary air system. The combustion air/gas system is a balanced draft arrangement. Combustion air from the regenerative air heater may enter the AFBC either as secondary air (fluidizing air) or overfire air. The secondary air is controlled by nine dampers (two dampers for each of bed compartments A through D and one damper for compartment S), and the overfire air is controlled by a single damper.

### Development of Model Equations

In the most general form, the phenomena occurring in an AFBC steam plant are expressed by nonlinear, partial differential equations. However, the purpose of the 20-MW dynamic model is to describe overall system performance and component interaction rather than to describe microscopic process details. Consequently, the detailed formulations were reduced to ordinary differential equations by using lumped-parameter approximations. Therefore, the dynamic model of the 20-MW pilot plant is a nonlinear, deterministic, lumped-parameter model arranged in state-space form. Equations for state variables are derived by applying the fundamental conservation laws and supporting empirical correlations within specified control volumes. The adequacy of this approach has been demonstrated in simulation of other power plants.<sup>1-8</sup> Since detailed derivations are too extensive for presentation here, only key relationships are included. These should be sufficient to illustrate the modeling philosophy and the level of approximation which have been employed.

#### Water/Steam Loop Component Models

The following water/steam loop components are modeled: boiler feed pumps, feedwater valve, economizer, drum, evaporators, waterwalls, primary superheater, secondary superheater, attemperator, attemperator spray valve, final steam header, final steam throttle valve, steam bypass valve, auxiliary steam valve, desuperheater, desuperheater spray valve, and condenser. All constants appearing in the equations are developed from design data, from heat and material balances, and from correlations obtained from open literature.<sup>9</sup> Descriptions of selected component models are presented below:

Feedwater Valve. It is assumed that during a simulation feedwater density changes negligibly. The feedwater valve model combines the resistance across the valve and the resistance in the feedwater line to compute flow through the economizer to the boiler drum.

$$W_{ec} = K_{fw} A_{fw} ((P_{fw} - P_{dr}) \rho_{fw})^{1/2} \quad (1)$$

Economizer. The economizer model predicts the energy transfer from the gas side to the water side and computes the economizer outlet water temperature and enthalpy. Each section of the economizer is separately represented by an individual state variable (metal temperature). This allows simulation of closure of one or two of the parallel convection passes. The water flow rate in each section is identical and is computed in the feedwater valve model. The outlet water conditions (temperature and enthalpy) of one economizer section are the inlet conditions to the next section, and the outlet conditions of the last section are the inlet conditions to the boiler drum. Mathematical equations that govern each economizer section are presented below. Equation 8 was derived from the ASME Steam Tables.

$$dT_{mo}/dt = (Q_{mo} - Q_{mi}) / (M_m C_{pm} + M_f C_{pf}) \quad (2)$$



$$Q_{mo} = A_o h_o (T_g - T_{mo}) \quad (3)$$

$$Q_{mi} = (K_m^* h_i A_i / (h_i A_i + K_m^*)) (T_{mo} - T_w) \quad (4)$$

$$K_m^* = K_m A_m / X_m \quad (5)$$

$$H_{ec} = H_i + Q_{mi} / W_{ec} \quad (6)$$

$$H_{avg} = Y_{ec} H_i + (1 - Y_{ec}) H_{ec} \quad (7)$$

$$T_w = C_1 H_{avg} + C_2 \quad (8)$$

Drum. The primary relations used in the drum model are the mass and energy balances as described by equations 9 and 10, respectively. In addition, a drum-level controller is provided. The drum model includes the drum, evaporators, waterwalls, recirculation pumps, and associated headers. It is assumed that the entire drum fluid path is in thermodynamic equilibrium at all times during the simulation, and that the drum fluid is at saturation conditions. Consequently, all thermodynamic variables in equations 9 and 10 are expressed in terms of steam density using steam-table curve fits. The resulting expressions are then solved to get the final working equations for the drum state variables (saturated steam density and total volume of liquid water in the drum).

$$d((V_{dr} - V_w) \rho_s + V_w \rho_w) / dt = W_{ec} - W_{psh} - W_{bd} \quad (9)$$

$$d((V_{dr} - V_w) \rho_s U_s + V_w \rho_w U_w) / dt = W_{ec} H_{ec} - W_{psh} H_{psh} - W_{bd} H_{bd} + Q_{dr} \quad (10)$$

Primary Superheater. The primary superheater model function and formulation is similar to the economizer model. Radiation from the gas/solids mixture to the tube wall is considered, and steam flow is proportional to the pressure drop between the drum and the outlet of the last primary superheater section. The primary superheater outlet pressure is based on the pressure drop between the drum and the steam header as shown below:

$$P_o = P_{dr} - Y_{psh} (P_{dr} - P_{sh}) \quad (11)$$

Secondary Superheater. Steam flows through the secondary superheater sections are computed algebraically using the steam bypass flow and the attemperator water flow. Otherwise, the function and formulation of the model for the secondary superheater is similar to the primary superheater and economizer models.

Final Steam Header. The final steam header model computes pressure, temperature, and final steam flow. The state equations shown below are derived from the dynamic mass and energy balance equations. The partial derivative terms in equation 13 are obtained by differentiating polynomial curve fits of the steam tables.

$$d\rho_{sh} / dt = (W_{ss} - W_{tv}) / V_{sh} \quad (12)$$

$$dH_{sh} / dt = (W_{ss} (H_{ss} - H_{sh}) + (W_{ss} - W_{tv}) (\partial P_{sh} / \partial P_{sh})) / (V_{sh} (\rho_{sh} - (\partial P_{sh} / \partial H_{sh}))) \quad (13)$$

### Solids/Gas Side Component Models

The following component models comprise the solid/gas side mathematical description: air/gas path, regenerative air heater, fluidized bed, freeboard, convection pass, and cyclone. Selected components are discussed below.

Air/Gas Path. The air/gas path is broken into two control volumes. The first control volume extends from the FD fan discharge to the top surface of the bed. The second control volume extends from the top of the fluid bed to the inlet of the ID fans. The mass balance nodes which define the density in the control volumes are located at the outlet of the air heater (secondary air duct) for the first volume and in the freeboard for the second volume. The differential equations that represent the flow balance about the two nodes are shown below.

$$d\rho_{sa}/dt = (G_{fd} - \sum G_{wdj} - G_{oa} - G_{ah})/V_{cv1} \quad (14)$$

$$d\rho_{fr}/dt = (G_{oa} + G_{bo} - G_{fr})/V_{cv2} \quad (15)$$

Fluidized Bed. Each of the four operating bed compartments (A, B, C, and D) is modeled independently to reflect its uniqueness and to study compartment interactions. One can study transients by perturbing any, or all, of the compartments. The model can predict the influence of one compartment on adjoining compartments for various amounts of bed interaction. The expanded bed height of each compartment, the overall sulfur capture efficiency, and the mean particle diameter of the bed char are assumed to be constant during a simulation. Additional simplifications include ignoring formation and destruction of CO and nitrogen oxides and assuming that all volatiles are released and burned in the bed. The dynamics of each compartment are modeled by four state variables - temperature, total solids mass, average bed particle diameter, and carbon mass.

The bed mass balance is expressed by equation 16. The equation was derived under the assumption that gas flows contribute negligibly to total bed mass changes. The elutriate flow rate is calculated using an algebraic equation derived from heat and material balance information. Net mass exchange between adjoining compartments is assumed to be proportional to differences in bed height.

$$dM_b/dt = F_c + F_l + F_r - F_d - F_e - \sum F_{ij} - F_{sg} \quad (16)$$

Equation 17 is the final equation for the bed energy balance. The term  $\sum F_{jCPj}(T_j - T_{ref})$  represents the algebraic sum of all solids and gas streams entering and leaving the compartment, excluding the intercompartment mixing flows. Heat transfer to the submerged surfaces is governed by algebraic equations. Intercompartment heat transfer takes place due to the net solids movement described earlier. In addition to the net mass movement between compartments, significant solids mixing is caused by the rise of bubbles. This mechanism is modeled as the product of a pseudo transport coefficient and the temperature difference between the respective compartments.

$$dT_b/dt = \sum F_{jCPj}(T_j - T_{ref}) + H_{rxn} - Q_{ws} + \sum Q_{ij} - C_{pb} T_b (dM_b/dt) / (C_{pb} M_b) \quad (17)$$

The char combustion rate for a specific coal is primarily a function of bed temperature and total surface area available for reaction. This model calculates char combustion on the basis of an average particle. Since the surface mean particle diameter of the char in the bed is considered constant during a simulation, the rate of char combustion becomes a function of char mass. Bed char mass is defined by an equation similar to equation 16. The rate of char combustion is expressed as an Arrhenius form using bed temperature and carbon mass.

A regression equation for steady-state values of bed mean particle size was developed. In order to approximate dynamics, a residence time approach was selected.

Freeboard. It is assumed that char combustion and heat transfer are the major influences on system dynamics. All other phenomena are neglected. Average freeboard gas temperature is the state variable that describes the dynamics of the one common freeboard that serves all bed compartments. The freeboard energy balance is similar to the bed energy balance.

### Model Results

Figures 3 through 6 show open-loop transient response curves for perturbations in the firing rate and the throttle valve area. Disturbances were applied to the open-loop process at zero minutes after a period of steady-state operation. Following firing rate perturbations, the evaporator bed (compartment A) temperature moves smoothly to a new value. Superheat (compartment D) temperature behavior illustrates the coupling between bed conditions and the superheat steam conditions. Drum pressure and final steam pressure respond to the changes in the steaming rate caused by the firing rate disturbance. The final steam flow responds to the changes in the final steam pressure, and the steam flow rate affects the final steam temperature. Changes in both the steam flow and temperature interact with the bed temperature.

Disturbing the throttle valve opening has little overall effect on bed temperature. The response of the superheat compartment is more pronounced than, and is different from, the response of the evaporator compartment, due to the strong coupling between steam side and bed side. The steam flow responds immediately to the change in the throttle area and causes the final steam pressure, temperature, and the drum pressure to change. After about 30 seconds, the effects of the final steam pressure overcome the effects of the throttle valve area, and the steam flow reverses its direction of change. The final steam flow is eventually re-established to a value close to the original steady state, although with a different temperature and pressure.

### Conclusions

This is a first-generation model which deals in simple fashion with the fluidized bed, splash zone, and freeboard. However, the current model is detailed enough to produce useful transient information. It can be used now to aid transient test planning and to preview open- and closed-loop plant behavior.

Work is underway to incorporate model improvements, which will result in a more realistic emulation of AFBC phenomena. The improved model will be used to analyze the 20-MW open-loop transient test data in order to establish confidence in the validity of model simulations. Once validated, the model will be a valuable tool to use for evaluating competing control strategies, load following and cycling scenarios, and design modifications. In summary, the validated model will provide a sound and consistent basis for prediction and analysis of overall system performance.

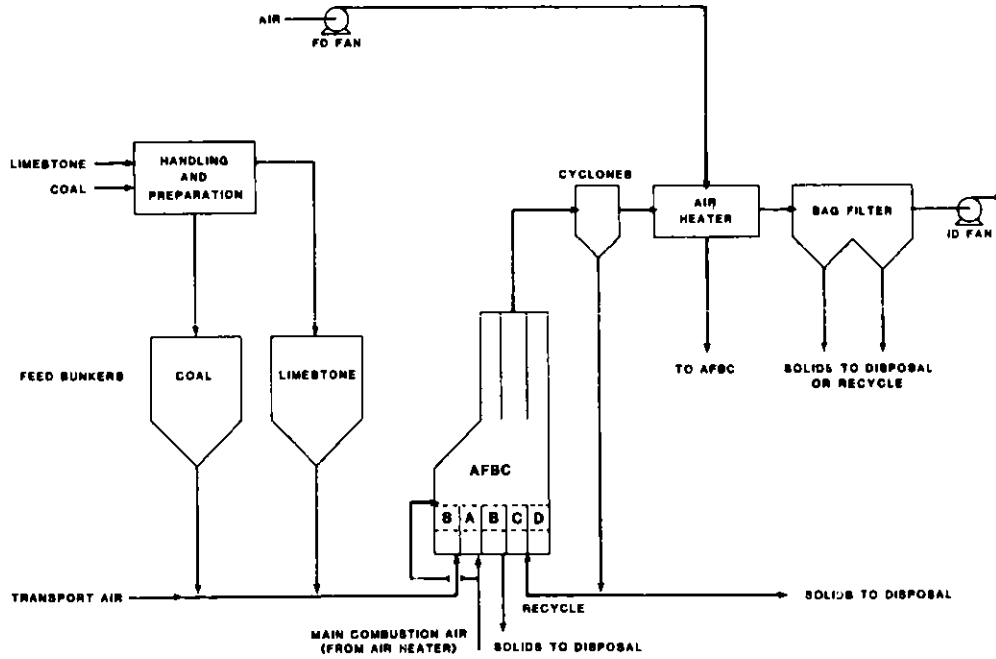


FIGURE 1 SOLIDS/GAS FLOWSHEET

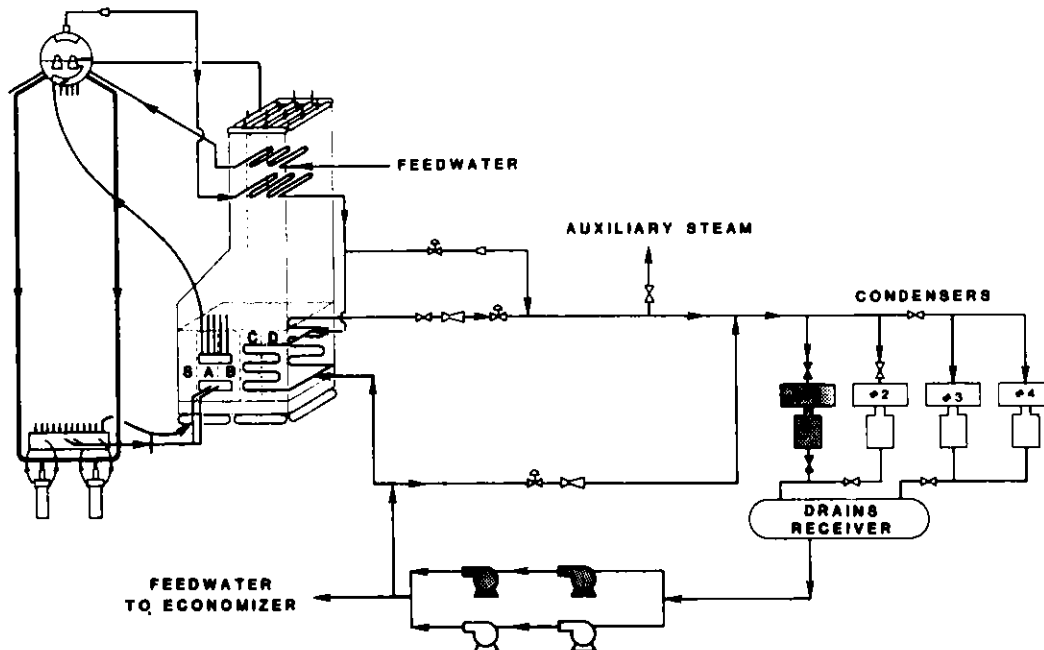


FIGURE 2 WATER/STEAM SYSTEM

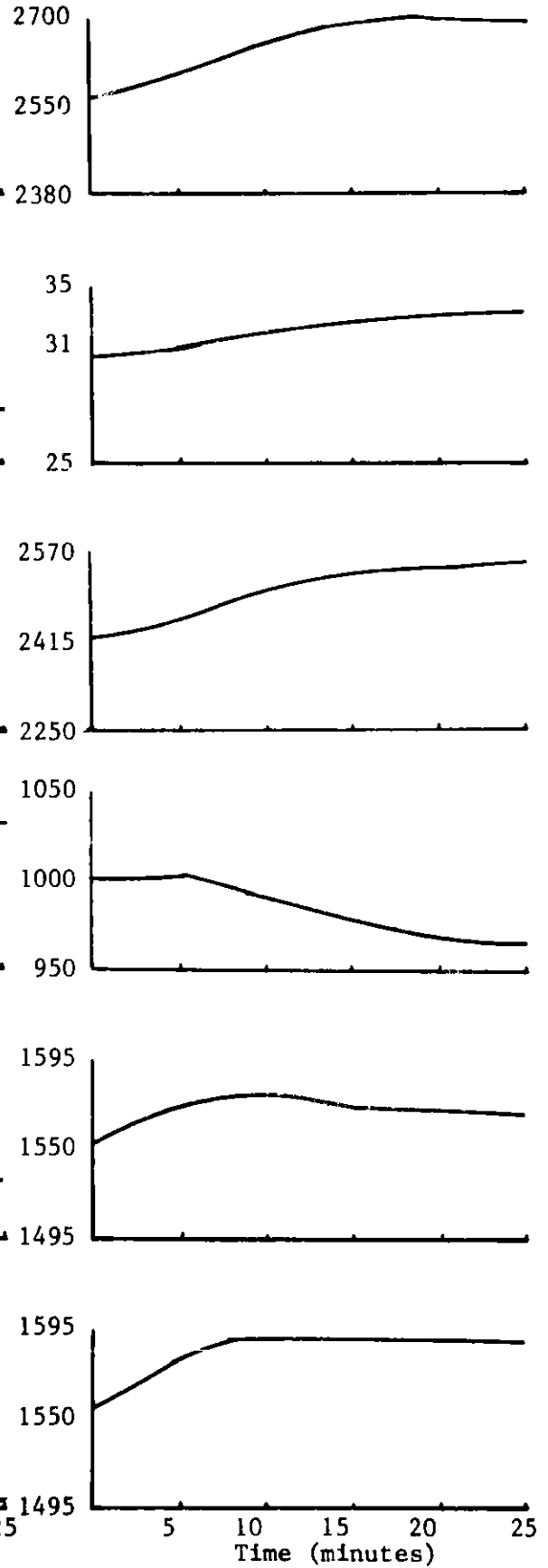
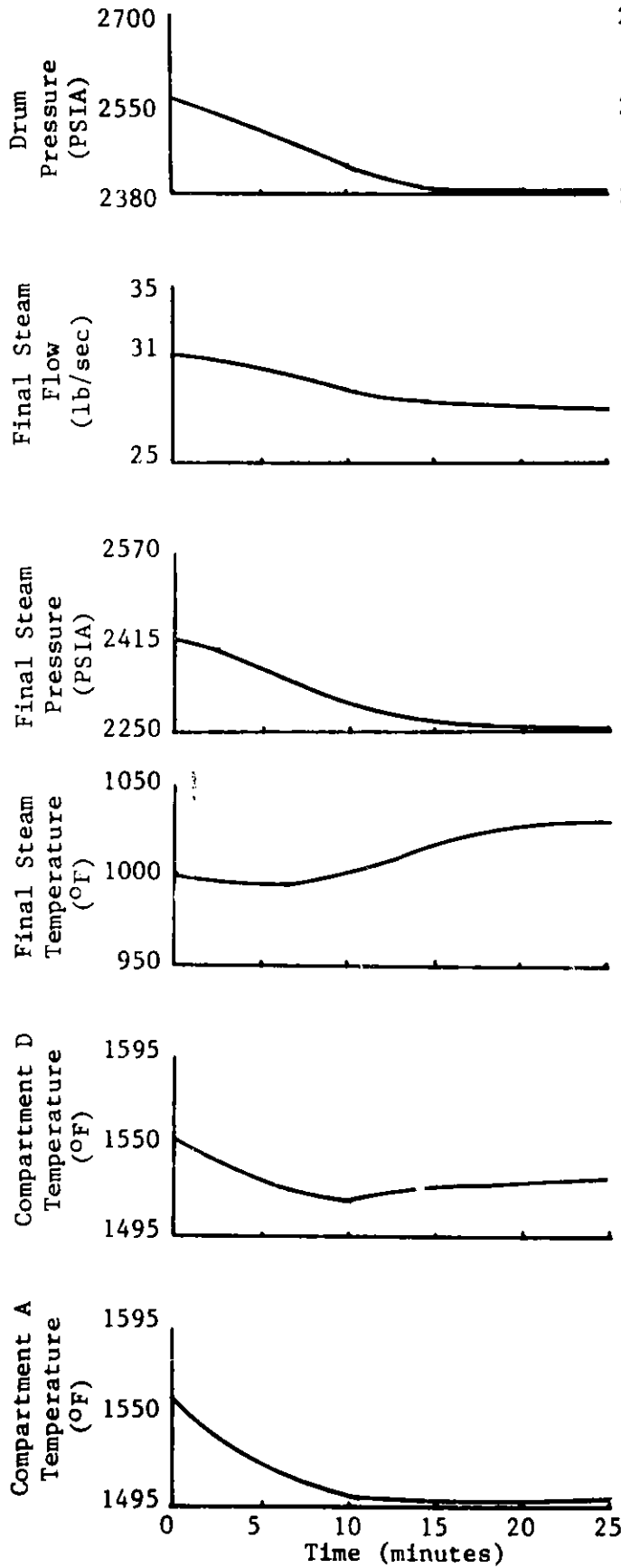


Fig. 3 -5% Firing Rate Step

Fig. 4 +5% Firing Rate Step

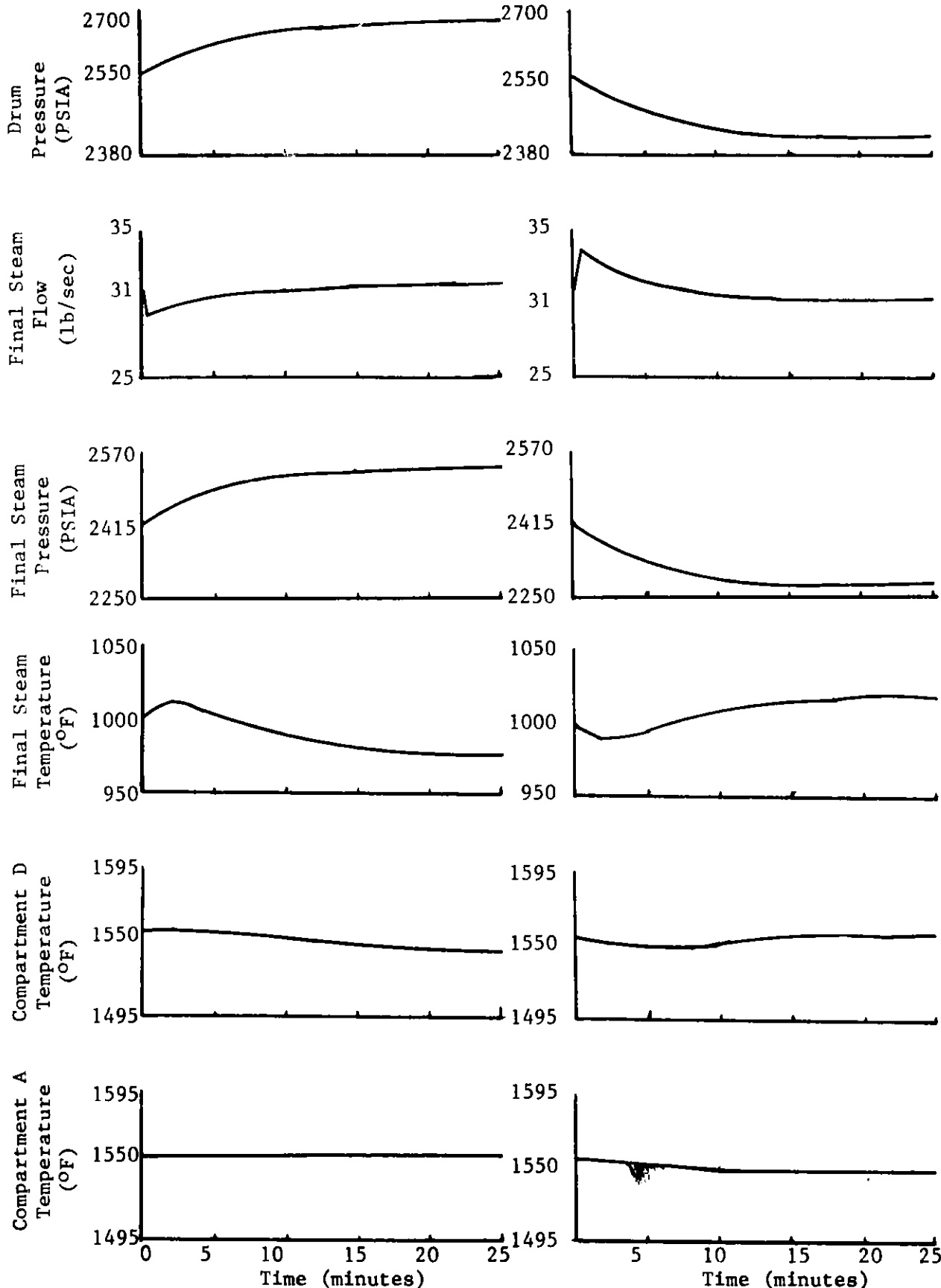


Fig. 5 -5% Throttle Area Step

Fig. 6 +5% Throttle Area Step

Nomenclature

Afw = feedwater valve area	Psh = steam header pressure
Ai = tube inside surface area	Qdr = total heat absorbed by boiling circuitry
Am = logarithmic tube surface area	Qij = intercompartment heat exchange
Ao = tube outside surface area	Qmi = heat transfer from tube to fluid
C1, C2 = regression coefficients	Qmo = heat transfer from gas to tube wall
CPb = specific heat of bed solids	Qws = heat transfer to water/steam loop
CPf = specific heat of fluid	Tb = bed temperature
CPm = specific heat of metal	Tg = gas temperature
d = derivative operator	Tmo = outside tube wall temperature
Fc = coal feedrate	Tref = reference temperature
Fd = bed drain rate	Tw = average fluid temperature
Fe = elutriate rate	t = time
Fij = intercompartment mass flow	Us = steam internal energy
Fl = limestone feed rate	Uw = water internal energy
Fr = recycle feed rate	Vcv1 = total volume of air path control volume
Fsg = solids converted to gas	Vcv2 = total volume of gas path control volume
Gah = air heater leakage flow	Vdr = total volume in drum
Gbo = gas leaving bed	Vsh = steam header volume
Gfd = air through FD fan	Vw = volume of water in drum
Gfr = gas leaving the freeboard	Wbd = blowdown rate
Goa = overfire air	Wec = economizer water flow rate
Gwdj = secondary air flow through damper	Wpsh = flow rate of steam in primary superheater
Havg = average enthalpy	Wss = steam flow rate in secondary superheater section 2
Hbd = blowdown enthalpy	Wtv = steam flow rate through throttle valve
Hec = enthalpy of water leaving economizer	Xm = tube wall thickness
Hi = inlet enthalpy	$\partial$ = partial derivative operator
Hrxn = heat of reaction	$\gamma_{ec}$ = economizer enthalpy averaging factor
Hsh = enthalpy of steam in steam header	$\gamma_{psh}$ = steam line pressure averaging factor
Hss = enthalpy of steam leaving the secondary superheater	$\rho_{fr}$ = freeboard gas density
hi = inside heat transfer coefficient	$\rho_s$ = steam density in drum
ho = outside heat transfer coefficient	$\rho_{sa}$ = air density in secondary air duct
Kfw = feedwater flow constant	$\rho_{sh}$ = density of steam in steam header
Km = metal thermal conductivity	
Mb = total bed mass	
Mf = mass of fluid	
Mm = mass of tube metal	
Pdr = drum pressure	
Pfw = feedwater pump discharge pressure	
Po = pressure at outlet of primary superheater	

References

1. J. P. McDonald, H. G. Kwatny, and J. H. Spare. "A Nonlinear Model for Reheat Boiler-Turbine-Generator Systems; Part II - Development," Proc. 12th Joint Automatic Control Conference, 219-226 (1971).

2. A. Ray, D. A. Berkowitz, and V. H. Sumaria. "Nonlinear Dynamic Model of a Fluidized-Bed Steam Generation System," Journal of Engineering for Power, Vol. 102, No. 1, January 1980, pp 202-208.
3. A. Ray, D. A. Berkowitz, and V. H. Sumaria. "Modeling and Simulation of a Multicell Fluidized-Bed Steam Generator," Journal of Energy, Vol. 2, No. 5, September-October 1978, pp 269-278.
4. M. R. Ringham and A. J. Spurgeon. "Development and Use of a Low-Power Start-up Model of the Fort St. Vrain HTGR," Proc. 18th Joint Automatic Control Conference, 332-337 (1977).
5. W.T.F. Broer, K. O. Jaegtne, J. P. McDonald and R. W. McNamara. "Fulton Station Dynamic Simulation," Paper C74-503-9, Joint IEEE/ASME Power Generation Technical Conference, September 1974.
6. J. P. McDonald. "Fulton Station: Plant Dynamic Simuations," Chap. 2 in Boiler Modeling, D. A. Berkowitz, ed., The MITRE Corporation, Bedford, MA (1975), pp. 31-52.
7. Q. B. Chow and W. Kitscha. "Design and Dynamic Performance of a New Two-Damper Pulverizer Air Flow and Temperature Control System," Proc. ISA National Symposium, 99-107 (May 1977).
8. Q. B. Chow and S. N. Chen. "A Simulation Study of Deaerator Control for CANDU Nuclear Power Plants," Proc. IEEE Power Industry Computer Application Conference, Toronto. (May 1977).
9. J. W. Wells, M. H. Culver and R. P. Krishnan. "Tennessee Valley Authority Atmospheric Fluidized-bed Combustor Simulation Interim Annual Report, January 1 through December 31, 1980," Oak Ridge National Laboratory Report No. ORNL/TM-7847, (September 1981).

#### Legal Notice

This report was prepared by the Tennessee Valley Authority (TVA). Neither TVA nor any person acting on its behalf:

a. makes any warranty or representation, express or implied, with respect to the use of any information contained in this report, or that the use of any information, apparatus, method, or process disclosed in this report may not infringe privately owned rights; or

b. assumes any liabilities with respect to the use of, or for damages resulting from the use of, any information, apparatus, method, or process disclosed in this report.

This report does not necessarily reflect the views and policies of TVA.



# A SURVEY OF NEAR AND LONG TERM USES OF LUMPED PARAMETER DYNAMIC MODELS FOR FOSSIL FUEL PROCESSING FACILITIES

## ABSTRACT

T. L. Greenlee and M. R. Ringham

JAYCOR

11011 Torreyana Road, P.O. Box 85154, San Diego, CA 92138

This paper reviews the uses that can be made of nonlinear lumped parameter dynamic models in performing system engineering analyses of processing facilities. A series of near and long term systems engineering uses are outlined in terms of scope, lumped parameter model based technical approach, and the nature of analysis results.

Particular emphasis is placed on (1) evaluation of process stability, (2) analog/digital control system design, (3) data analysis/test planning, and (4) use of the model as a basis for training simulator development. A low order fluidized bed gasifier model is used to illustrate these points.

### 1. Introduction

Synfuels processing facilities are currently being developed in an effort to reduce dependence on foreign fossil resources. Many of the facilities are new, one of a kind designs that have not been assembled or operated in the configurations being considered. This lack of operating experience coupled with the newness of certain configurations provides a strong incentive for the use of dynamic computer models/simulations in the early check-out of process designs. In Reference 1 an approach to the development of such models/simulations is outlined for a proposed TVA coal gasification facility.

The approach, which is based on first principles, results in a model that is mathematically characterized by a system of first-order nonlinear ordinary differential equations. These equations, representing the entire facility with a balanced level of detail in each subsystem, are suitable for developing digital and hybrid simulations. The resulting simulations, which may run several times faster than real-time, can be used for systems engineering tasks such as (1) determination of component/system dynamic performance characteristics of baseline facility designs, (2) determination of plant operating profiles (3) analysis of system interactions, (4) determination of measurement and control strategies, (5) analysis of performance margins (6) investigation of failure responses and propagation, (7) development of test plans, and (8) operator training. In this paper we further elaborate on these uses by discussion and examples.

### 2. Lumped Parameter Dynamic Model Uses

Table 1 lists the results of a thorough study of near and long term uses of system level dynamic models. Column one lists the systems engineering functions that can be performed with a lumped parameter model. The second and third columns describe the typical near and long term uses of such models in terms of scope, results, and the approach for accomplishing that function.

### 3. Examples of Lumped Parameter Model Usage

To make the system engineering functions in Table 1 more concrete a simple nonlinear lumped parameter fluidized bed gasifier model was developed and several of the system engineering functions were exemplified. The examination of process stability using this model is illustrated first. The second example indicates the use of such models

Table 1.

## Near- and Long-Term Uses of System-Level Dynamic Models

Systems Engineering Function of Dynamic Model	Near-Term Uses (0-12 months)	Long-Term Uses (12-'N' months)
Evaluate dynamic adequacy of static-based design & determine system*/component dynamic specification	<p><b>Scope:</b> Determine dynamic performance characteristics of static-based design provided by A.E. Analyze transient responses and infer system/component dynamic specifications (to be included in A.E. spec) that will result in optimal facility response.</p> <p><b>Results:</b> A comprehensive understanding of transient behavior of entire facility as it responds to disturbances in process inputs/outputs. Specification for system/component transient response requirements for optimal facility response to disturbances.</p> <p><b>Approach:</b></p> <ul style="list-style-type: none"> <li>• Utilize simulation with A.E.-proposed control structure. Subject simulation to input/output disturbances at various operating points.</li> <li>• Numerically compute linear dynamic models and use eigenvalue information to analyze facility transient response with respect to               <ul style="list-style-type: none"> <li>• sources of dominant modes,</li> <li>• parameter sensitivity of dominant modes.</li> </ul> </li> <li>• Determine system/component range of values for parameters affecting dominant modes that will result in optimal facility response to applied disturbances.</li> </ul>	<p><b>Scope:</b> Consider impact of design modifications or facility reconfiguration for this facility or future designs.</p> <p><b>Results:</b> Same.</p> <p><b>Approach:</b> Same.</p>
Determine startup/shutdown and operating point	<p><b>Scope:</b> Determine startup/shutdown sequences &amp; operating point transition strategies that are optimal with respect to operating objectives (25%-75% minimum time, minimum H<sub>2</sub>S in MBC) &amp; facility design constraints (metal temperature limits, catalyst over temperature, etc.).</p> <p><b>Results:</b> Schedules for control variables (flows, valve positions) that produce desired operating profiles (paths). Basis for preliminary operating policies.</p> <p><b>Approach:</b></p> <ul style="list-style-type: none"> <li>• Simulation runs investigate/refine proposed schedules.</li> <li>• Formulate nonlinear optimization problem &amp; solve using simulation as representation of constraints.</li> </ul>	<p><b>Scope:</b> Refine operating strategies as configuration of facility &amp; operating objectives change.</p> <p><b>Results:</b> Same.</p> <p><b>Approach:</b> Same.</p>
Analyze system interactions and stability	<p><b>Scope:</b> Determine nature &amp; strength of dynamic coupling between systems of facility.</p> <p><b>Results:</b> Transient response plots &amp; linear analysis results (A-matrix &amp; eigenvalues) will indicate the nature and strength of coupling between dynamic modes in systems of facility. Sign of eigenvalue indicates stability.</p> <p><b>Approach:</b></p> <ul style="list-style-type: none"> <li>• Transient response of simulation to step inputs in control variables will be analyzed in terms of its dominant time constants.</li> <li>• Linear models generated directly from simulation will be used to determine source of dominant time constants and interaction between systems.</li> </ul>	<p><b>Scope:</b> Analyze impact of design modifications on coupling/stability.</p> <p><b>Results:</b> Same.</p> <p><b>Approach:</b> Same.</p>

**Table 1.**  
**Near- and Long-Term Uses of System-Level Dynamic Models**

Systems Engineering Function of Dynamic Model	Near-Term Uses (0-12 months)	Long-Term Uses (12-'N' months)
Evaluate proposed measurement/control strategy & determine alternate strategy	<p><b>Scope:</b> Determine adequacy of proposed measurement/control strategy. Provide a means to determine alternate measurement/control strategy.</p> <p><b>Results:</b> Analytically justified measurement/control strategy that accomplishes facility operating objectives in the presence of facility disturbances and constraints.</p> <p><b>Approach:</b> Use nonlinear dynamic model for frequency- &amp; time-domain-based measurement/control strategy analysis and synthesis computer programs.</p>	<p><b>Scope:</b> Determine or assess alternate control structures required to cope with design modifications, variations in feedstock, or variations in demand character.</p> <p><b>Results:</b> Same.</p> <p><b>Approach:</b> Same.</p>
Analyze performance margins	<p><b>Scope:</b> Determine limits of facility's dynamic performance with respect to component, environmental, demand, and safety constraints.</p> <p><b>Results:</b> Knowledge of where facility operating profiles lie within constraint envelopes.</p> <p><b>Approach:</b> Utilize simulation with optimized control structure and investigate distance between facility operating profile &amp; constraint envelopes.</p>	<p><b>Scope:</b> Reevaluate performance margins affected by design modifications or changes in operating profiles.</p> <p><b>Results:</b> Same.</p> <p><b>Approach:</b> Same.</p>
Failure responses and propagation	<p><b>Scope:</b> Determine &amp; analyze dynamics of failure in facility. Include failure of sensors, actuators, and other components whose function is crucial to satisfaction of demand, environmental, safety, &amp; equipment constraints.</p> <p><b>Results:</b> Detailed knowledge of dynamic effects of crucial component/system failures on facility performance (includes failure of parallel trains).</p> <p><b>Approach:</b></p> <ul style="list-style-type: none"> <li>• List failures crucial to performance.</li> <li>• Construct dynamic models with failure switches &amp; degradation parameters so that failure can be initiated and degradation can be scheduled.</li> <li>• Utilize simulation to investigate dynamic propagation of failure through facility.</li> </ul>	<p><b>Scope:</b> Evaluate failure responses for failures that occur during normal operation. Determine stress applied to system as consequence of these failures; use this information to modify original maintenance operating plans.</p> <p><b>Results:</b> Same.</p> <p><b>Approach:</b> Look at specific failures that occur during normal operation.</p>
Develop test plan	<p><b>Scope:</b> Define a comprehensive test plan that will confirm predictions of static and dynamic facility performance. This effort would include specification of:</p> <ul style="list-style-type: none"> <li>• appropriate input test signals,</li> <li>• appropriate response variables to be recorded.</li> </ul> <p>It will provide a functional description of tests to be run on components, systems, and the facility.</p> <p><b>Results:</b> Specified dynamic tests &amp; thorough analysis of resulting data, using dynamic model predictions for comparison, will result in a validated dynamic model, whose existence implies confirmation of performance predictions.</p> <p><b>Approach:</b></p> <ul style="list-style-type: none"> <li>• Perform transient analysis on component, system, or facility model at selected operating points. Analyze response to steps in input variables in</li> </ul>	<p><b>Scope:</b> Utilize model to develop new test plans as need arises to investigate design changes or replaced components.</p> <p><b>Results:</b> Same.</p> <p><b>Approach:</b> Same.</p>

Table 1.  
Near- and Long-Term Uses of System-Level Dynamic Models

Systems Engineering Function of Dynamic Model	Near-Term Uses (0-12 months)	Long-Term Uses (12-'N' months)
	<p>terms of eigenmodes excited and sensitivity of these modes to parameter variations.</p> <ul style="list-style-type: none"> <li>• Using results from above, specify a set of input test signals and corresponding responses that must be recorded in a test run. Include update rate for measurement observations.</li> <li>• Analyze transient test data with respect to data gathered from dynamic model. Adjust model parameters to induce coincidence of responses.</li> <li>• Itemize differences between model predictions &amp; test data, and define further testing or analyses required to resolve these differences.</li> </ul>	
Operator training tools	<p>Scope: Utilize dynamic model as a tool for investigating impact of operator actions on facility performance.</p> <p>Results: Preliminary/candidate operating policies required to achieve facility performance objectives can be investigated with respect to their adequacy. Refined policies can be determined.</p> <p>Approach: Utilize dynamic model/simulation as a representation of entire facility. Input candidate operator policies as functions of time and analyze resulting transient responses. Adequacy of proposed operating policies can be judged by examining the nearness of process variables to desired operating profiles.</p>	<p>Scope: Utilize systems engineering dynamic model as baseline for developing specification for training simulator.</p> <p>Results: Develop a "real-time" version of systems engineering dynamic model and implement in on a simulator.</p> <p>Approach: Integrate streamlined form of system engineering dynamic model in a digital or hybrid computer that will permit interactive stimulation of model by operator.</p>

in analog and digital control system design. The value of lumped parameter models in test planning and data analysis is shown next. Finally, the use of lumped parameter models as a basis for training simulator development is shown.

### Gasifier Model

The model utilized in the following examples is described in detail in Reference 2. The following sentences summarize its assumptions and content. The underlying assumptions for the fluidized-bed gasifier dynamic model are:

1. The interior of the gasifier is lumped into an isothermal, isobaric zone and treated as a well stirred reactor.
2. Reacting gases ( $\text{CO}_2$ ,  $\text{O}_2$ ,  $\text{H}_2$ ,  $\text{H}_2\text{O}$ , and  $\text{CO}$ ) are assumed in thermochemical equilibrium.
3. Coal is assumed to devolatilize instantly within the gasifier. In devolatilization, it is assumed that nitrogen and sulfur are released as  $\text{N}_2$  and  $\text{H}_2\text{S}$ , respectively. Methane,  $\text{N}_2$ , and  $\text{H}_2\text{S}$  are treated as inert products of devolatilization.
4. Gasification of carbon in the char is governed by the combustion reaction (with  $\text{O}_2$ ), the Boudouard reaction (with  $\text{CO}_2$ ), and the water-gas reaction (with  $\text{H}_2\text{O}$ ). Each of these reactions proceeds at a finite rate determined by a global kinetic expression, with displacement from equilibrium as the driving force for reaction. Hydrogasification (with  $\text{H}_2$ ) reaction is neglected because of its relatively slow rate compared to the other three. The composition and thermodynamics of graphite are attributed to char.
5. The gas stream is assumed free of solid particulates.
6. Ash and unburned char are assumed to be removed from the gasifier in the form of solid agglomerates. Variations in ash content within the gasifier are neglected.

The state equations represent conservation of mass for the char.

$$\frac{dM_c}{dt} = \beta F_{fc} - \lambda M_c - R(T)M_c$$

$M_c$  = char mass - moles

$F_{fc}$  = coal flow rate - lbs/hr

$\beta$  = moles of fixed char/lb coal

$\lambda$  = rate constant for removal of char with agglomerates -  $\text{hr}^{-1}$

$R(T)$  = reaction rate (total due to  $\text{O}_2$ ,  $\text{CO}_2$  and  $\text{H}_2\text{O}$  reactions) moles/mole char

and conservation of energy for the reactor

$$\begin{aligned} (C_{pc}M_c + C_{pa}M_a) \frac{dT}{dt} = & F_{fc}H_{fc} - \lambda M_c H_c(T) - F_{ad}H_{ad}(T) \\ & + \sum_i F_{gi}H_{gi} - \sum_i F_{gx}H_{gx}(T) - Q \end{aligned}$$

where enthalpies  $H$  of the inlet streams are evaluated at inlet temperatures, enthalpies of the exit streams are evaluated at reactor temperature and

$M_a$  = ash mass in moles

$Q$  = reactor energy losses through walls, etc.

$F_{gi}$  = inlet flow of  $i$ th gas species

$F_{gx}$  = product flow of  $i$ th gas species

The gas model is the algebraic equivalent of that given in Reference 2.

### Process Stability

The nonlinear model just described can be linearized about an operating point using numerical differentiation. This process converts the state and measurement equations from the general non-linear forms,

$$\dot{x} = f(x,u,t) \quad y = g(x,u,t)$$

to the linear forms

$$\delta \dot{x} = \left( \frac{\partial f}{\partial x} \right) \delta x + \left( \frac{\partial f}{\partial u} \right) \delta u$$

$$\delta y = \left( \frac{\partial g}{\partial x} \right) \delta x + \left( \frac{\partial g}{\partial u} \right) \delta u$$

The partial derivatives in these expressions are computed for a steady state triple  $(x_{ss}, u_{ss}, y_{ss})$  that satisfy

$$\dot{x}_{ss} = 0 = f(x_{ss}, u_{ss}) \quad y_{ss} = g(x_{ss}, u_{ss})$$

The nonlinear fluidized bed model described above has been converged to a steady state operating point corresponding to:

$$x_{ss} = \begin{bmatrix} MC \\ T \end{bmatrix} = \begin{bmatrix} 68.10 \text{ moles} \\ 1799^{\circ}F \end{bmatrix}$$

$$u_{ss} = \begin{bmatrix} FCOAL \\ F20 \end{bmatrix} = \begin{bmatrix} 1850.0 \text{ lb/hr} \\ 1922.6 \text{ lb/hr} \end{bmatrix}$$

$$Y_{ss} = x_{ss}$$

The linearized model for this triple is given in matrix form in Table 2. These equations can be used to directly evaluate process stability and the small perturbation transient response character of the nonlinear model in the neighborhood of this operating point. Since we intend to utilize the transfer functions associated with this system in the next section we will compute them directly from this matrix form.

The transfer function of most use for the remainder of our analyses is the matrix  $G(s)$  where

$$\delta y(s) = G(s) \delta u(s)$$

where:

$$G(s) = \left( \frac{\partial g}{\partial x} \right) \left[ sI - \left( \frac{\partial f}{\partial x} \right) \right]^{-1} \left( \frac{\partial f}{\partial u} \right) + \left( \frac{\partial g}{\partial u} \right)$$

substituting from the linear model of Table 2 and simplifying we have,

$$G(s) = \begin{bmatrix} \frac{1.46E-5(s+2.06E-2)}{d(s)} & \frac{-4.65E-6(s+.085)}{d(s)} \\ \frac{-4.31E-4(s+1.05E-3)}{d(s)} & \frac{2.31E-3(s+2.86E-4)}{d(s)} \end{bmatrix}$$

$$d(s) = (s+1.67E-2)(s+3.45E-5)$$

$$\begin{bmatrix} \delta \dot{M}C \\ \delta \dot{T} \end{bmatrix} = \begin{bmatrix} -2.38E-4 & -1.39E-4 \\ -2.41E-2 & -1.65E-2 \end{bmatrix} \begin{bmatrix} \delta MC \\ \delta T \end{bmatrix} + \begin{bmatrix} 1.46E-5 & -4.65E-6 \\ -4.31E-4 & 2.31E-3 \end{bmatrix} \begin{bmatrix} \delta FCOAL \\ \delta FO2 \end{bmatrix}$$

STATE EQUATION

$$\begin{bmatrix} \delta y_1 \\ \delta y_2 \end{bmatrix} = \begin{bmatrix} 1 & 0 \\ 0 & 1 \end{bmatrix} \begin{bmatrix} \delta MC \\ \delta T \end{bmatrix}$$

MEASUREMENT EQUATION

Table 2. Linearized Model

Referring to our earlier definitions of  $\delta Y(s)$  and  $\delta U(s)$  we have

$$\begin{bmatrix} \delta MC(s) \\ \delta T(s) \end{bmatrix} = G(s) \begin{bmatrix} \delta FCOAL(s) \\ \delta FO2(s) \end{bmatrix}$$

For the affect of  $\delta FO2(s)$  on  $\delta T(s)$  we can write directly.

$$\delta T(s) = \frac{2.31E-3(s+2.86E-4)\delta FO2(s)}{(s+1.67E-2)(s+3.45E-5)}$$

The transient response of  $\delta T$  for a 1.0% step increase in FO2 is given by the inverse Laplace transform of

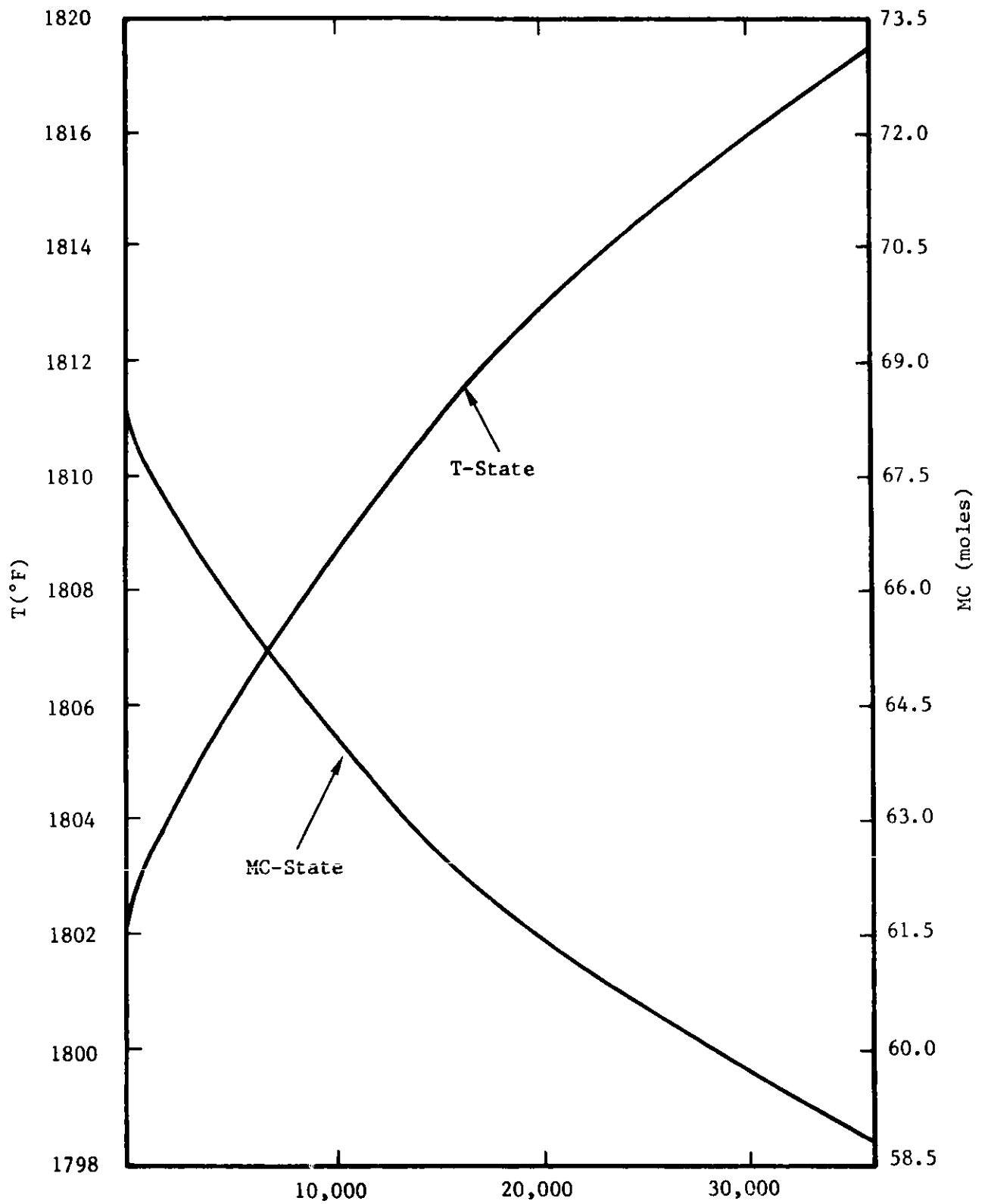
$$\delta T(s) = \frac{2.31E-3(s+2.86E-4)(19.226)}{s(s+1.67E-2)(s+3.45E-5)}$$

This inverse can be computed by partial fraction expansion as

$$\delta T(t) = 22.0 - 2.60e^{-(1.67E-2)t} - 19.4e^{-(3.45E-5)t} \quad t > 0$$

This response is seen to consist of a constant and two weighted exponential functions. The first exponential with exponent (eigenvalue)  $\lambda_1 = -1.67E-2$  corresponds to the temperature state and represents the characteristic value of the bed energy balance. The corresponding time constant is  $\tau_1 \cong -1/\lambda_1 = 59$  seconds. The second exponential has an exponent (eigenvalue) of  $\lambda_2 = 3.45E-5$  which corresponds roughly to the char mass state. This eigenvalue corresponds to a time constant of  $\tau_2 = -1/\lambda_2 = 28,986$  seconds or 8.05 hours. The weights (residues) associated with each exponential indicate the response of  $\delta T(t)$  will be dominated initially (for approximately  $5\tau_1$  seconds) by the first exponential, but the second exponential will dominate the majority of the response. The fact that each of the exponentials has a negative exponent indicates the process is stable.

Figure 1 shows the 'open loop' transient response of the nonlinear model for a 1.0% step increase in FO2. Note that the transient is made up of the exponential terms shown above. This example illustrates how the linear model allows analysis of nonlinear transients into exponential (or modal) components. The insights gained from this approach to transient analysis are valuable when one wishes to relate process parameter



Time (seconds)  
1% Step in Oxygen Feed

Figure i.



values to dominant exponential components.

### Analog and Digital Control System Design

The lumped parameter models discussed above together with their linear forms at operating points can serve as a representation of the process in control system analyses. Figures 2(a) and 2(b) show analog and digital temperature control loops using oxygen feed FO<sub>2</sub>. These loops can be thoroughly analyzed using the process transfer functions from the matrix  $G(s)$  and standard linear analysis techniques such as s-plane root locus or z-plane root locus.

### Data Analysis/Test Planning

The use of lumped parameter dynamic models in data analysis and test planning is quite common in several aerospace applications (such as aircraft stability derivative determination). In this context, the data to be analyzed consists of transient plots and there is some a priori dynamic model that supposedly provides the structure that is consistent with the observed transient data. The problem is typically one of determining parameter values in the a priori model such that the model predictions and the transient data agree while accounting for measurement and process errors/disturbances. Once this point of view is reached the next question that often arises is how can a test be conducted (what input signals, what measurements, etc.) so the determination of parameters is most accurate. This causes the topics of (1) optimal inputs for parameter determination and (2) parameter/state observability to be raised. In the discussion that follows we attempt to clarify the meaning of these terms by utilizing the simple gasifier model discussed above.

Assume we operate the gasifier so it can be represented by the linear state equations for MC and T given earlier. Suppose the measurements made on the gasifier consist of samples of MC and T taken every  $\Delta T$  seconds. Suppose further that these measurements are corrupted by gaussian white noise. For this example we imagine that three parameters ( $\theta_1$ ,  $\theta_2$ ,  $\beta$ ) are left unspecified in the linear model and we need to estimate their values to complete the data analysis task. Let the reaction rate  $R(T) = R$  so the linear model now reflects no forward coupling from T to MC. Suppose the form of the linear model in  $\theta_1$ ,  $\theta_2$ ,  $\beta$  is just

$$\dot{\delta MC} = -\theta_1 \delta MC + (1.46E-5) \delta FCOAL - (4.65E-6) \delta FO_2$$

$$\dot{\delta T} = \beta \delta MC - \theta_2 \delta T - (4.31E-4) \delta FCOAL + (2.31E-3) \delta FO_2$$

The variables  $\theta_1$ ,  $\theta_2$ ,  $\beta$  can obviously be related to unknown parameters in the nonlinear model equations. Let the measurements corrupted by noise be represented by

$$\delta Y_1 = \delta MC + V_1$$

$$\delta Y_2 = \delta T + V_2$$

where  $V_1$  and  $V_2$  represent stationary gaussian random processes such that for each measurement  $V_1(t_i)$ ,  $V_2(t_i)$  are a sequence of independent gaussian random variables. We now have a problem statement of the form:

#### Parameter Estimation Problem Statement:

Suppose a process is represented by the linear state equation

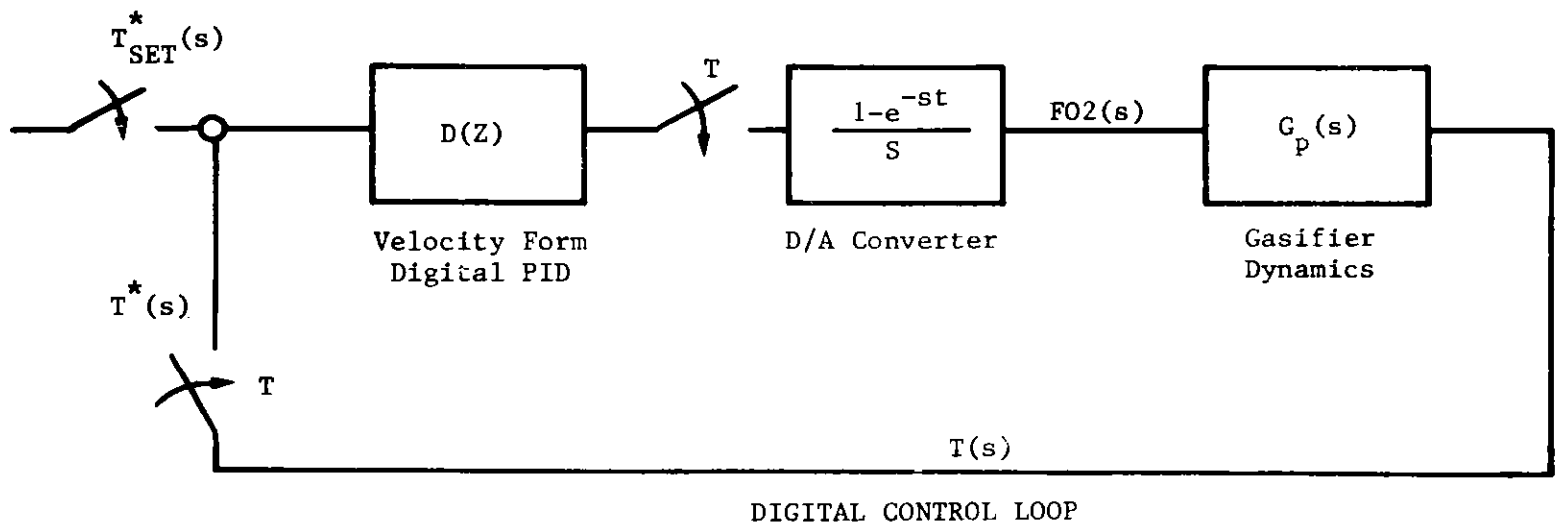
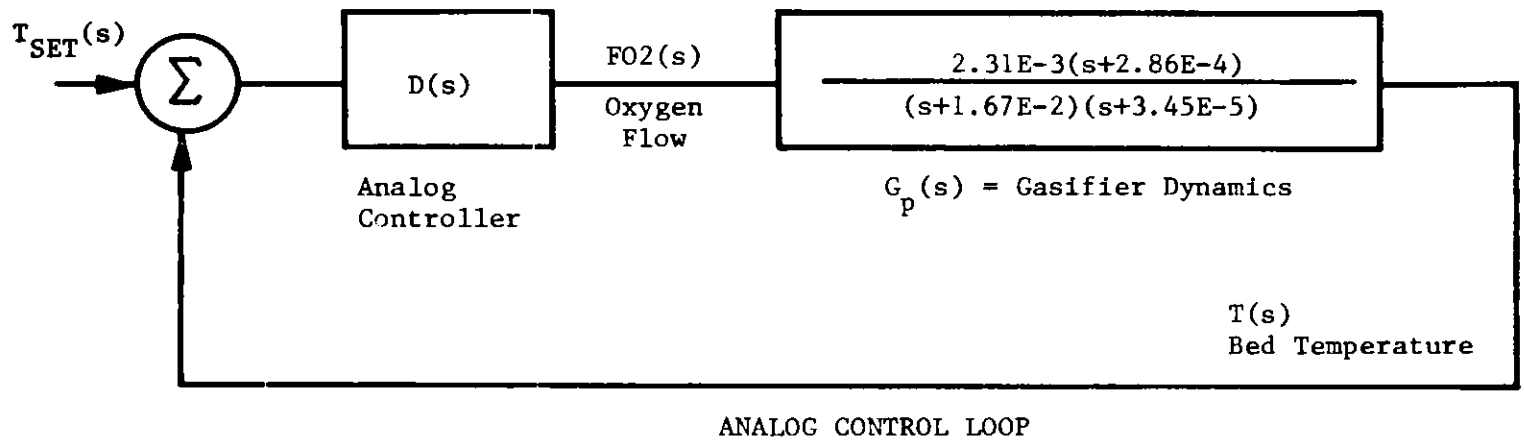


Figure 2. Idealized Analog and Digital Temperature Control Loops.

$$\dot{x} = Fx + Gu$$

where  $x$  is a vector of gasifier state variables,  $F$  is a matrix of unknown parameters in the form

$$F = \begin{bmatrix} -\theta_1 & 0 \\ \beta & -\theta_2 \end{bmatrix}$$

$G$  is a matrix of known parameters scaling the input vector. Let the measurements of  $x$  be given at discrete time points  $i$  by the vector

$$y_i = x_i + V_i$$

where  $V_i$  is a sequence of independent gaussian random vectors

$$E[V_i] = 0 \quad E[V_i V_j^T] = R_1 \delta_{ij}$$

Take the initial state as also unknown. We wish to estimate the parameters in  $F$  and the initial condition vector  $x_0$  so as to minimize (in some sense) the parameter estimation error.

An often successful approach to the solution of this problem is based on Bayesian scheme known as maximum likelihood parameter estimation. For the problem statement the maximum likelihood estimates of parameters in  $F$ , and  $x_0$  can be obtained by maximizing the conditional probability density of  $Y_i, i=1, \dots, N$  given  $F$ , and  $x_0$ . Formally, this density is

$$f(Y_1, \dots, Y_N / x_0, F) = f(v_1, \dots, v_N)$$

The likelihood function  $L$  is given by

$$\begin{aligned} L(F, x_0) &= \ln f(v_1, \dots, v_N) \\ &= -\frac{1}{2} \sum_{i=1}^N \|Y_i - x_i\|_{R_1}^2 \\ &\quad - \frac{N}{2} \ln |R_1| \end{aligned}$$

where  $\|\cdot\|_{R_1}^{-1}$  denotes the  $R_1$  weighted norm of the residual and  $|R_1|$  denotes the determinant of  $R_1$ . The parameter estimates we seek are obtained by maximizing  $L$  with respect to  $F$ , and  $x_0$  subject to the constraints defined by the linear differential equation in the problem statement. Various numerical schemes (conjugate gradient, Newton-Raphson) can be used to accomplish this constrained maximization. In either case, the covariance of the resulting parameter estimates are obtained from the inverse Hessian matrix of  $L$ . This Hessian matrix is also known as the Fisher Information Matrix. It is instructive to consider this estimator for the homogeneous portion of our gasifier state equations and the stated measurement relations. We will assume  $x(0)$  is an input of our choosing. For this simplification the system equations are represented in Figure 3 and can be written as:

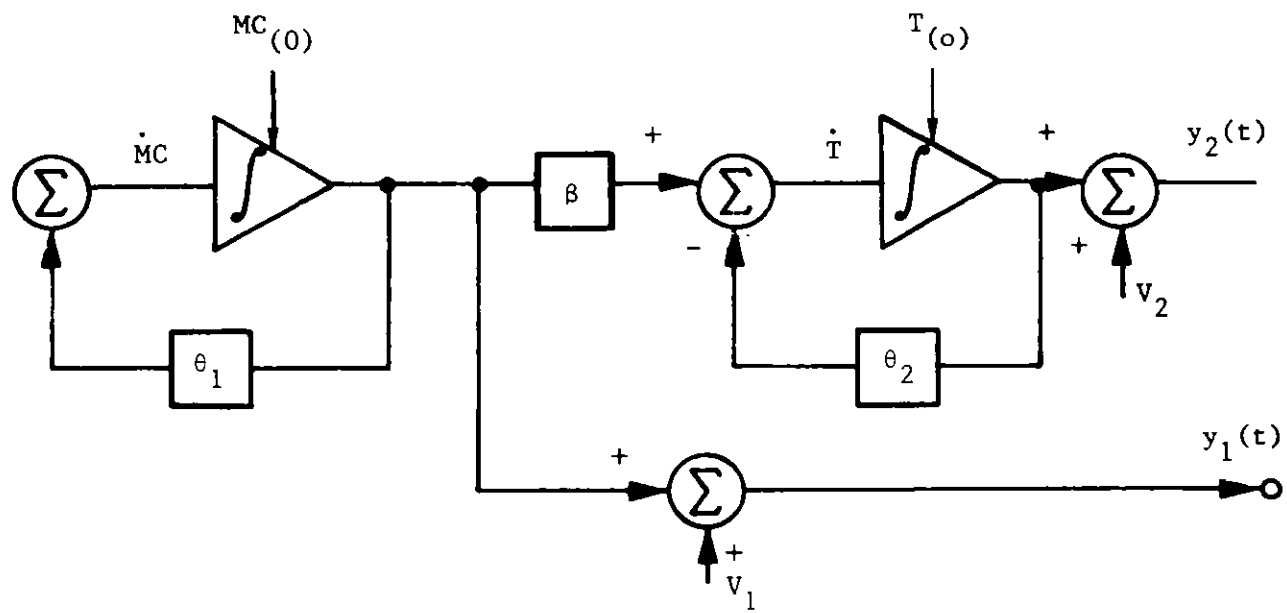


Figure 3. Example System

$$\begin{aligned} \dot{\underline{x}}(t) &= F(\underline{\theta}) \underline{x}(t) & \underline{x}(0) &= \begin{bmatrix} x_1 \\ x_2 \end{bmatrix}, & \underline{\theta} &= \begin{bmatrix} \theta_1 \\ \theta_2 \\ \beta \end{bmatrix} \\ \underline{Y}(k) &= \underline{x}(k) + \underline{\eta}(k) & k &= \Delta t, 2\Delta t, \dots, N\Delta t. \end{aligned}$$

$\eta(k)$  is a Gaussian independent identically distributed white noise sequence

$$E[\underline{\eta}(k) \underline{\eta}^T(j)] = R \delta_{kj} \quad R = rI$$

The discrete time solution to the state equation can be written down directly as:

$$\underline{x}(k) = e^{kF(\underline{\theta})\Delta t} \underline{x}(0)$$

The log likelihood cost function can be written

$$\begin{aligned} J(\underline{\theta}) &= -1/2 \sum_{i=1}^N (\underline{Y}(i) - \underline{x}(i))^T R^{-1} (\underline{Y}(i) - \underline{x}(i)) - \frac{N}{2} \ln(\det R) \\ &= -1/2 \sum_{i=1}^N (\underline{Y}(i) - e^{F(\underline{\theta})i\Delta t} \underline{x}(0))^T R^{-1} (\underline{Y}(i) - e^{F(\underline{\theta})i\Delta t} \underline{x}(0)) \\ &\quad - \frac{N}{2} \ln(\det R) \end{aligned}$$

It is shown in Reference 3 that the Fisher Information Matrix can be simplified and for this problem expressed as

$$FIM = \sum_{i=1}^N \left( \frac{\partial}{\partial \underline{\theta}} [e^{F(\underline{\theta})i\Delta t} \underline{x}(0)] \right)^T R^{-1} \left( \frac{\partial}{\partial \underline{\theta}} [e^{F(\underline{\theta})i\Delta t} \underline{x}(0)] \right)$$

To evaluate the FIM, we first need the state transition matrix. This is given by

$$e^{F(\underline{\theta})t} = \begin{bmatrix} e^{-\theta_1 t} & 0 \\ \frac{\beta(e^{-\theta_1 t} - e^{-\theta_2 t})}{(\theta_1 - \theta_2)} & e^{-\theta_2 t} \end{bmatrix}$$

The state vector as a function of time is

$$\underline{x}(t) = \begin{bmatrix} e^{-\theta_1 t} x_1 \\ \frac{\beta(e^{-\theta_1 t} - e^{-\theta_2 t})}{(\theta_1 - \theta_2)} x_1 + e^{-\theta_2 t} x_2 \end{bmatrix}$$

The partial derivative matrix for the FIM can be computed as

$$\frac{\partial}{\partial \theta} [e^{F(\theta) i \Delta t} \underline{x}(0)] = \begin{bmatrix} -i \Delta t e^{-\theta_1 i \Delta t} x_1 & 0 & 0 \\ \frac{-i \Delta t \beta e^{-\theta_1 i \Delta t} x_1}{(\theta_1 - \theta_2)} & \frac{-i \Delta t \beta e^{-\theta_2 i \Delta t} x_1}{(\theta_1 - \theta_2)} & \frac{x_1 (e^{-\theta_1 i \Delta t} - e^{-\theta_2 i \Delta t})}{(\theta_1 - \theta_2)} \\ -\gamma & +\gamma & \\ & -i \Delta t e^{-\theta_2 i \Delta t} x_2 & \end{bmatrix}$$

$$\gamma = \frac{\beta (e^{-\theta_1 i \Delta t} - e^{-\theta_2 i \Delta t}) x_1}{(\theta_1 - \theta_2)^2}$$

For purposes of discussion define

$$\frac{\partial}{\partial \theta} e^{F(\theta) i \Delta t} \underline{x}(0) = \begin{bmatrix} a_i & 0 & 0 \\ b_i & c_i & d_i \end{bmatrix}$$

Then the FIM can be expressed as

$$\text{FIM} = \sum_{i=1}^N \begin{bmatrix} \frac{a_i^2 + b_i^2}{r} & \frac{b_i c_i}{r} & \frac{b_i d_i}{r} \\ \frac{b_i c_i}{r} & \frac{c_i^2}{r} & \frac{c_i d_i}{r} \\ \frac{b_i d_i}{r} & \frac{c_i d_i}{r} & \frac{d_i^2}{r} \end{bmatrix}$$

Now we can make some observations about the FIM:

1. Since each term in the sum is a positive definite matrix, more terms (i.e., more data points) will increase the information. However, the norms of the successive matrix components of the FIM form a monotone decreasing sequence. In fact, the rate of decrease is approximately twice the rate of decrease of the modes (due to the products of terms). The total information is also scaled by the inverse noise covariance matrix.

2. Each term of the FIM is a singular matrix (column 3 equals  $c_i/d_i$  times column 2). However, the sum may have rank 3 as long as  $c_i/d_i$  is not constant for all  $i < N$ . We may in fact be able to identify all the parameters with as few as two measurements. (The quality of the estimates may not be good enough for our purposes.)

3. If the wrong input initial conditions are used (e.g., an eigenvector of the system) the FIM may remain singular for all time. Consider the input  $x_1=0$  and  $x_2=1$ . Then  $a_i$ ,  $b_i$ , and  $d_i$  are all zero resulting in the FIM having rank 1 for all time. For this problem, that

this is a bad input for parameter estimation is obvious from the block diagram in Figure 3.

4. In the case of widely spread eigenvalues (i.e.,  $0 \gg \theta_2$ ), the elements of the FIM decay at different rates. This leads to the conclusion that data must be taken at a high frequency for fast modes and at a lower frequency for slower modes. This is exactly what intuition (and the sampling theorem) tells us.

Notice also that the gradient of the log likelihood function is also a function of the matrix used to construct the FIM.

$$\frac{\partial J}{\partial \theta} = \sum_{i=1}^N \left[ \frac{\partial}{\partial \theta} (e^{iF(\theta)\Delta t} \underline{x}(0)) \right] R^{-1} [Y(i) - e^{-iF(\theta)\Delta t} \underline{x}(0)]$$

This is also a function of data. Qualitatively, at least, the dependence on actual data,  $Y(i)$ , is more pronounced for small  $N$ . For large  $N$ , statistical smoothing will take over and make the gradient more well behaved.

Clearly, the information just revealed shows the coupling between dynamic model structure, parameter observability, measurement errors, input signal requirements, sample rates, and parameter estimation error covariance. Insights regarding these couplings can be used to guide test plans so as to maximize the usefulness of collected data.

### Training Simulator Development

Training simulators are often required for operator training and control hardware testing. Often a simplified dynamic model of the process can be useful as a basis for such a simulator. Such a model can be made to have reasonable fidelity and short solution times. One approach to the development of this type of model/simulator is illustrated in Figure 4.

The discrete time linear forms in the process block of this figure are written as

$$\delta x(k+1) = \Phi(k+1, k) \delta x(k) + \Gamma(k+1, k) \delta u(k)$$

$$\delta y(k) = H(k) x(k)$$

where the matrices  $\Phi, \Gamma$ , and  $H$  are discretized forms of the corresponding continuous matrices integrated over the time interval  $(t_{k+1}, t_k)$ . A major advantage of this form is that it gives exact solutions to the state and measurement equations at the sample instants and all integration problems can be taken care of "off-line". To be more specific, the state transition matrix for the linear system in continuous time is

$$\Phi(t, \tau) = e^{F(t-\tau)}$$

For the discrete model this is just

$$\Phi(k+1, k) = e^{F(t_{k+1}-t_k)} = e^{F \Delta t_k}$$

which can be computed off-line to any desired accuracy. Once this matrix is known dynamic propagation of the state is accomplished by simply multiplying the current state vector by it.

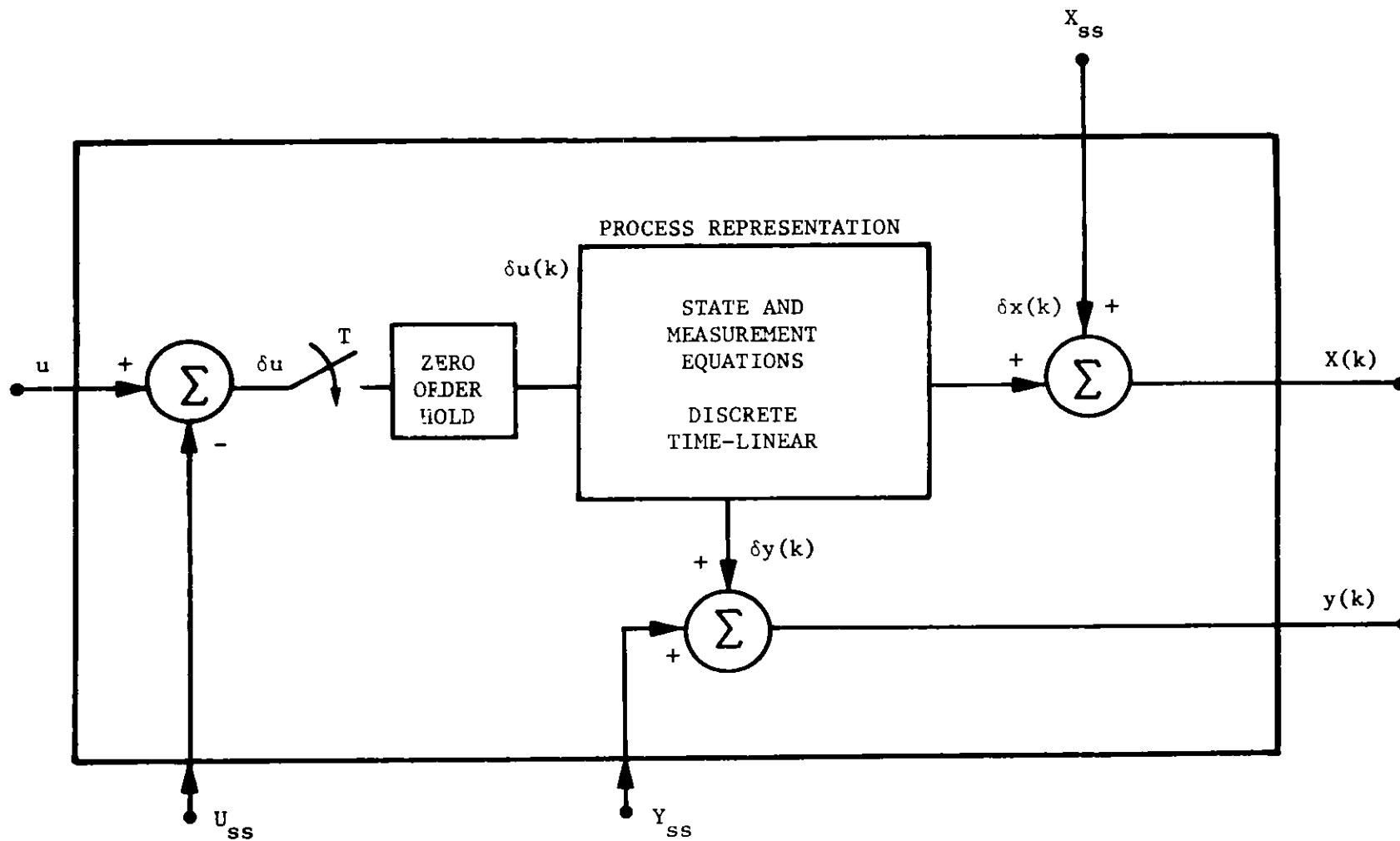


Figure 4. Process Simulator Schematic



#### 4. Conclusions

This paper has given an overview of the uses of lumped parameter models in systems engineering analyses. Examples have illustrated certain of these uses in more detail via use of a simple gasifier model.

#### References

1. Greenlee, T.L., et.al., "A Systems Level Dynamic Modeling Approach for the TVA 20,000 TPD Coal Gasification Facility", Proceedings 1981 SCIEP, CONF-81067, June 8-10, 1981.
2. Ringham, M.R., et.al., "A Low-Order System Level Model of a Fluidized-Bed Gasifier", Proceedings 1981 SCIEP, CONF-81067, June 8-10, 1981.
3. Goodwin, G.C. and R.L. Payne, Dynamic System Identification: Experiment Design and Data Analysis, Academic Press, New York, 1977.

A HIGH PRESSURE INSTRUMENTED FLOW CONTROL SYSTEM FOR  
HYDROGEOLOGIC INJECTION TESTING

---

Robert G. Reeves  
Sierra Pump Systems  
P. O. Box 4179  
Incline Village, NV 89450  
702/832-0220

Abstract

High pressure water was produced by air driven, pilot operated, reciprocating, piston, liquid pumps at 12:1 compression; that is a working drive area of about 12 times the hydraulic area to produce 1000 psi hydraulic pressure at 15 GPM with an air drive pressure of 83 psi. Inlet water of 22% NaCl concentration was filtered via 200 micron filters. Discharge hydraulic pulsations were dampened with hydropneumatic accumulators. Accurate flow of high pressure water was achieved with a self-contained, direct acting, diaphragm sensing, externally gas loaded dome pressure reducing regulator. This is designed to provide high downstream flows while maintaining accurate control of primary pressures. Pressure relief was a spring-loaded externally adjusted relief valve. Hydraulic flow was measured at the low and high flow ranges with NBS calibrated turbine flow meters. Pressure was measured with both a bourdon tube gauge and a calibrated pressure transducer. A high pressure control valve dead-ended the system during acceptance testing. System maintained constant pressure at  $\pm 0.5\%$  linear full scale while varying flow, and maintained constant pump rate of  $\pm 5\%$  while varying pressure, per specifications of user.

TURBINE TRANSDUCER DEVELOPED FOR ADVERSE CONDITIONS

D. R. Cooper  
J. L. Edson  
Idaho National Engineering Laboratory  
EG&G Idaho, Inc.  
P. O. Box 1625  
Idaho Falls, Idaho 83415

Abstract

This paper reviews the latest developments that the Idaho National Engineering Laboratory (INEL) has made on a turbine transducer used in measurement of two-phase flow. It is operated in a modular configuration with a drag transducer to provide mass flow data. Current configurations allow its use in single modules or in multiples to provide flow profile information. The turbine can also provide mass flow data when used with associated instrumentation such as a densitometer. The transducer, which is the product of long investigations and test series, is subject to high vibration loading and high temperatures as well as a borated liquid environment; flow conditions range from all liquid to all steam and from ambient temperatures to over 600°F at pressures up to 2200 psig. In the past, the long soak times in borated water led to corrosion and subsequently, short lifetimes. This new design, however, uses materials that were chosen carefully to inhibit corrosion and provide maximum life. Graphite bearing and carbide shaft materials were selected to provide this corrosion resistance along with mechanical integrity and resistance to wear. The new turbine design has met all operational requirements in actual use and in extended lifetime tests.

Introduction

The Idaho National Engineering Laboratory (INEL) uses turbine transducers to help measure mass flow at the Loss-of-Fluid Test (LOFT) reactor. These operating conditions include severe mechanical and flow induced vibrations and a variety of flow conditions, ranging from all liquid (borated water) to all steam, and from ambient temperatures to 600°F at pressures up to 2200 psig. Rapid temperature change is another condition experienced during the performance of a LOFT experiment where cold (approximately 80°F) borated water is injected into a system that is operating at about 600°F. The turbine is also required to restart after long periods of remaining idle in water with a high amount of dissolved air. Furthermore, the turbine functions in a radioactive environment, so repair is not feasible and a long lifetime is essential. Finally, all parts must be positively locked and contained to prevent the loss of parts into the reactor system.

These unique operational and geometric requirements precluded the use of off-the-shelf commercially available turbines, so commercial vendors known to do custom design were asked to consider designing a turbine to meet these adverse environmental conditions. But, for various reasons none expressed an interest. Subsequently, we initiated in-house efforts to design, build, test, and deliver a turbine transducer. The product of these efforts

(Figure 1) is a modularly constructed turbine transducer, designed to mate with a drag-disc module, while also allowing for use in other mounting configurations. The turbine consists of a bearing-rotor assembly with a non-rotating shaft supported by two post assemblies; a pickup coil is contained in the module body.

### Design Considerations

The design of the turbine transducer required solving two problems: selecting suitable materials and designing the rotor-bearing assembly. Operating experience from an earlier, unsuccessful design and advice from material vendors provided insight to specific problem areas and required the following design features to be incorporated:

1. Bearing and shaft materials
2. Surface finish of the bearing and shaft
3. Rotor-bearing configuration
4. Bearing-shaft clearance (tolerance)
5. Self-aligning shaft supports
6. Dynamic balance of the rotor.

We chose a graphite bearing and a carbide shaft because of a combination of tests, experience, and vendor application recommendations. The graphite bearing was the best choice as the borated water eliminated the possible use of all metallic bearings because of corrosion problems. Ball bearings are universally 440 stainless steel, which are subject to corrosion. Gold journal bearings running on stainless shafts ran free during tests, but were subject to crevice corrosions and deposits during nonrunning time and then failed to restart.

We chose the tungsten carbide shaft over a variety of other possibilities for two reasons. First, vendor tests indicate that the combination of the graphite bearing and the carbide shaft, with each having a surface finish of eight or better, results in lifetimes significantly longer than stainless steel shafts. Vendors recommended avoiding stainless steel shafts for this application. Second, long lead times in material procurement and fabrication difficulties prompted selecting tungsten carbide over silicon carbide, which has been manufactured and used with even longer lifetimes expected. Thus far, tungsten carbide shafts have been used in most units and operating experience has been satisfactory.

Rotor-bearing configuration is determined by the selection of the graphite bearing material. Since graphite does not have great structural tensile strength, the material must be held in compression, which necessitates a journal configuration that is held in the rotor. A shouldered configuration was not used in order to eliminate high stress areas and to simplify machining. Bearing retention is also an important consideration because of the 600°F temperature range. Retention by an interference fit is accomplished by inserting the bearing in the rotor that has been heated to 900°F. The bearing is manufactured in two parts with an internal retainer key to prevent its displacement by the thrust if it were to loosen.

In addition, the use of tight tolerances between the bearing and shaft and dynamically balancing the rotor to 10,000 rpm were recommended to help extend the lifetime.

Operational experience from an earlier design dictated the requirement for self-alignment of the shaft. This alignment feature is required to avoid an axial misalignment of the two posts which results from the relief of work stresses at elevated temperatures. The forces could break a brittle shaft made of silicon carbide. In addition, this misalignment along with the tight tolerances could distort the shaft, causing the rotor to freeze. The final shaft support configuration (Figure 2) has ball ends that mate with compression spring sockets in the supporting parts. The ball ends have integral thrust surfaces that mate with the graphite bearing. This feature provides self-alignment capability of greater than 5 degrees.

#### Test and Operational Experience

The final design was tested in a flow loop to provide actual operating experience. The flow loop was operated at the design conditions of temperature (525°F), pressure (2200 psig), flow (15.2 m/s), and water chemistry to provide realistic test conditions. The turbine operated in these conditions in excess of 2000 hours and showed no evidence of wear or degraded performance.

The turbines were calibrated and satisfactory calibration characteristics have been produced. Turbines designed for 15.2 m/s full scale have exhibited a linear ratio of greater than 10 to 1 and are repeatable to 0.15 m/s. A typical calibration curve is shown in Figure 3.

Subsequently, the turbines operated without failure in the LOFT facility; three turbines have successfully operated for greater than 600 hours, over a period of 6 months and 5 complete test cycles. We have examined these turbines, and no evidence of wear or degraded performance was observed.

#### Conclusion

The development efforts have resulted in a turbine design that operates in adverse conditions and has a long lifetime.

The following factors are considered to be key requirements for the successful design and operation of the turbine:

1. Graphite journal bearing held in compression, operating on a hard, highly finished shaft
2. Dynamically balanced rotor-bearing assembly
3. Maintenance of close tolerances
4. Self-aligning shaft-support configuration.

Each of these factors addressed a specific problem encountered during earlier testing and operation. Each eliminated or corrected a problem that had led to failure of the previous turbine design. The product is a highly rugged, dependable turbine that operates reliably in the LOFT system.

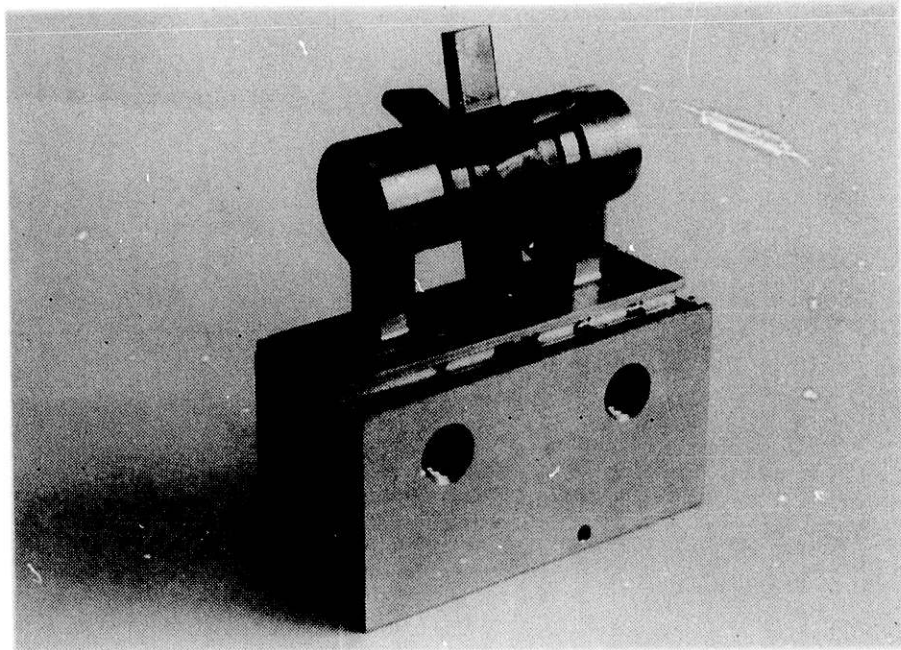


Figure 1. Turbine transducer.

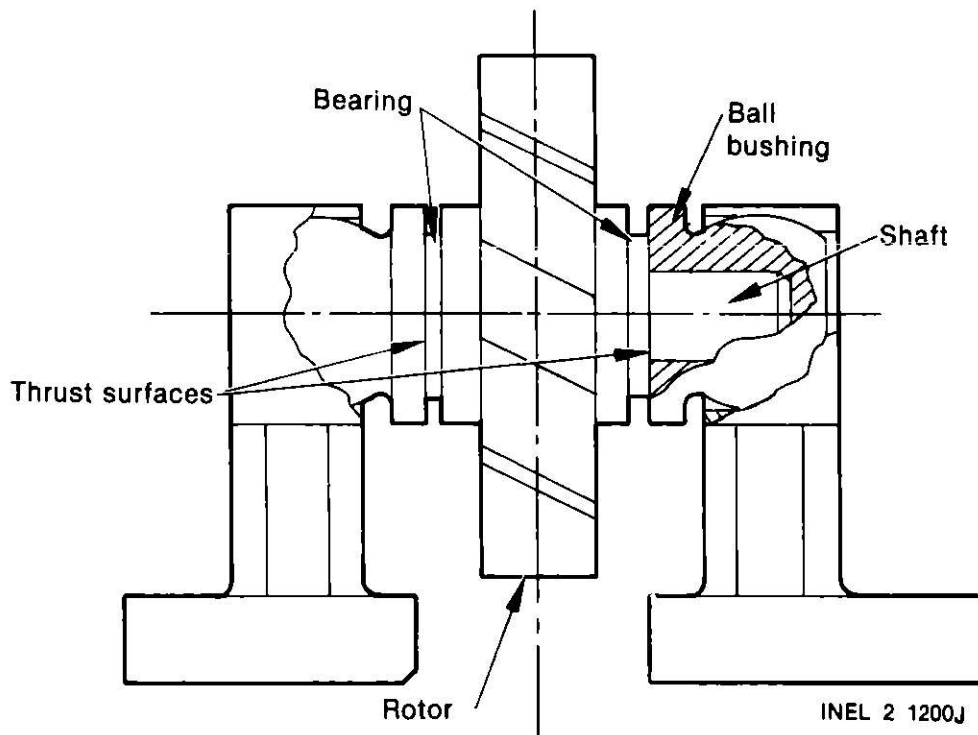


Figure 2. Turbine rotor and shaft support detailing self-alignment features.

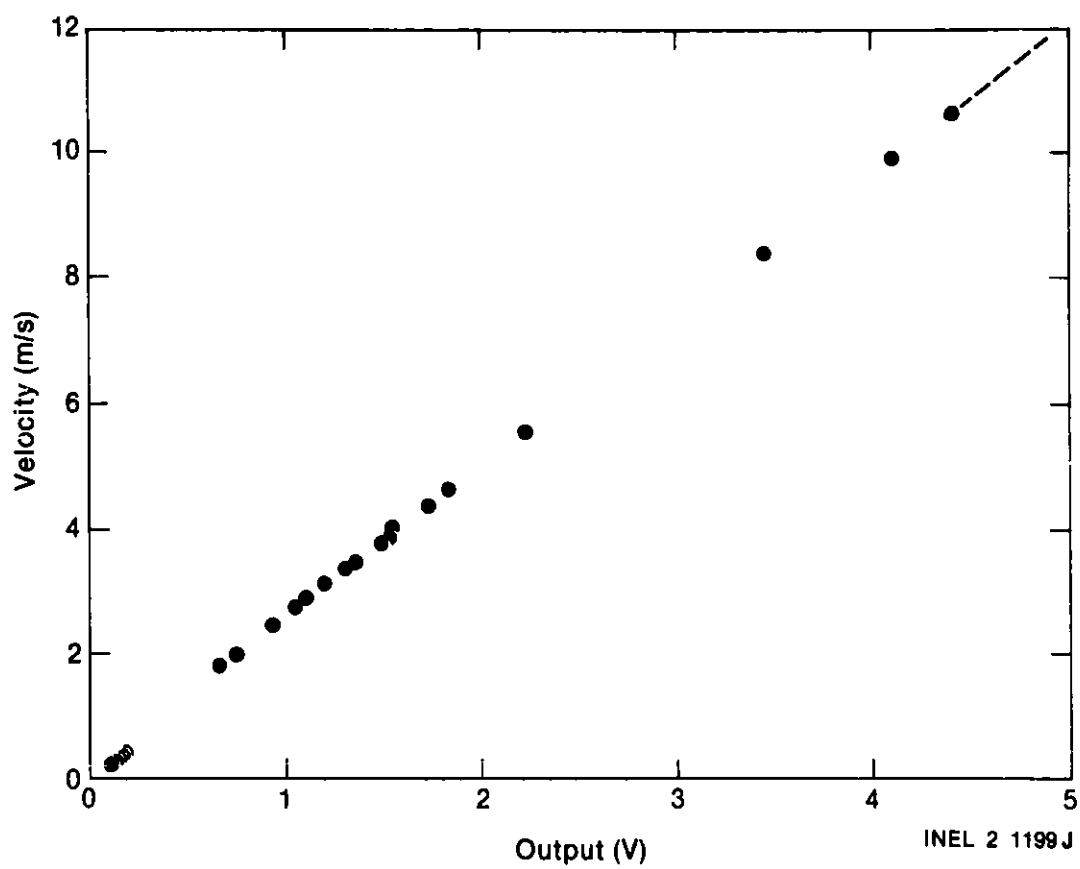


Figure 3. Flow calibration.

Acknowledgements

Many people provided supporting efforts in this task, each of which contributed to the successful design. Specific mention must be made of the efforts of four people. R. C. Peel of Design Engineering and W. W. Weichel of Instrument Assembly provided the extra effort required in their areas. R. P. Evans and M. R. Donaldson provided expert assistance in directing the task.

Work supported by the U.S. Nuclear Regulatory Commission, Office of Nuclear Regulatory Research under DOE Contract No. DE-AC07-76ID01570.

Notice

This report was prepared as an account of work sponsored by an agency of the United States Government. Neither the United States Government nor any agency thereof, or any of their employees, makes any warranty, expressed or implied, or assumes any legal liability or responsibility for any third party's use, or the results of such use, of any information, apparatus, product or process disclosed in this report, or represents that its use by such third party would not infringe privately owned rights. The views expressed in this paper are not necessarily those of the U.S. Nuclear Regulatory Commission.

Copyright

The submitted manuscript has been authored by a contractor of the U.S. Government under DOE Contract No. DE-AC07-76ID01570. Accordingly, the U.S. Government retains a nonexclusive, royalty-free license to publish or reproduce the published form of this contribution, or allow others to do so, for U.S. Government purposes.



COMPUTER-AIDED FLUCTUATION ANALYSIS  
OF AN MHD GENERATOR

J. E. BARBAY, Jr., and S. SAMI, College of Engineering and Technology, Southern Illinois University, Carbondale, Illinois 62901, (618)-536-3396

ABSTRACT

Three channels of data recorded during tests conducted jointly in the USSR by ANL and their Soviet counterparts on an MHD channel were analyzed with the aid of a micro-computer. The recorded signals were from the main inverter and two voltages from different segments of the channel. A Z80/S100 based computer with an 8 bit A-to-D convertor, a two port RS232 card with a 64 microsecond clock and a Hi-Point plotter were used to (1) plot the data and (2) make some basic measurements (e.g., RMS, mean). Using the definition of the correlation coefficient a FORTRAN program was written and used to evaluate the coefficient. This required the writing of an assembly language subprogram to read data from the disk to an integer FORTRAN array.

Using results from the multiple runs with the correlation coefficient, plots were made in an effort to gain some information about the transient time of the plasma in the channel. A coherence and cross spectral estimation program was adapted for use on the microprocessor. Modifications of the program were necessary in order to select different frequencies from the spectrum for time delay studies.

1.00 INTRODUCTION

A series of tests have been made by a joint US/USSR cooperative program in open-cycle MHD electrical power generation. These tests were made in the Soviet Union at the U-25b facility using the Soviet MHD Channel No. 2 and a superconducting magnet supplied by the United States. Extensive instrumentation of the combustor and channel was in place for the test series. In Test No. 6, provisions for the measurement of the "power-take-off currents" for frames 12-23 (inverters 12-23) and currents 132-143 (inverters 132-143) were made as for currents for frames 57, 93, and inverters 17, 19, and 21 were monitored using the same instrumentation that had been used in Test No. 5. Most of

the measurements were made by a digital data acquisition system. The system was based on an HP 2100 computer that sampled the various transducers. Digital readings were then stored on magnetic tapes for later use. Such a large collection of data was accumulated that a computer-based data bank and sophisticated set of programs that allow access to the data was written by programmers at Argonne National Laboratory. The information in the data bank that represented digitized data taken by the HP 2100 computer was readily available to researchers in the MHD program at Argonne.

In order to better study the fluctuations associated with some of the electrical quantities during the on going tests, arrangements were made to record continuous analogue data using a four channel TANDBERG analogue tape recorder. One of the four channels was used as a reference channel to be used internally for a zero reference. The remaining three channels were used to record two of the interframe voltages and one inverter current. Unlike the data from the digital acquisition system, the data on the analogue tapes was not readily available to MHD researchers at Argonne. No provisions had been made to provide access to this data. There was no convenient means of transferring the measurement to Argonne's computer for analysis.

Arrangements were made to have faculty from the College of Engineering and Technology use some of the computer resources of the Technology Department to digitize the continuous data from the test tapes. The tapes that were loaned to SIU-C were from tests 5 and 6. These tapes contained measurements of the voltages at frames ED24, ED51, and inverter current 17 for test 5. The tapes for test 6 recorded voltages ED28, ED51 and the current for inverter 17. Original plans called for the data to be read from the analogue tape by a Cromemco System Three micro-computer onto floppy disks. Then it was planned to move the digitized data to the University's IBM 370. Correlation studies of the data were to be made, to determine if plasma transient time information could be obtained from the data.

## 2.00 SIU-C's FACILITIES FOR ANALYSIS

Initial arrangements were made by the administrative staff of the College of Engineering and Technology for the resources of the College to be used to capture the data on the analogue tapes and then analyze the recovered data. Originally, the plan called for the use of an old mechanical recording oscillograph in conjunction with an HP cross correlator to view and analyze the data. Indeed, both the oscillograph and the cross correlator were on the University inventory list, and in fact were on their appointed spot in the equipment closet. The unfortunate reality was that neither was serviceable. Old age, and lack of maintenance had taken it's due. The project budget would support only the personnel for the summer, there was no possibility of obtaining equipment with the limited funds on

hand. In short, the SIU-C staff appeared to be sitting on the wrong side of the saw, sawing away at the tree limb. If the talented people at Argonne National Laboratory with their extensive resources had not gotten the information they required how could it be done with little or no equipment at SIU-C?

Fortunately, there was one piece of new equipment available for use by the SIU-C staff. A small microprocessor based computer was available. This computer was being used by the College's off-campus Industrial Technology Military programs for instructional purposes in a beginning programming course. The on-campus machine was to be used for the development of instructional material and to gain a working knowledge of the capabilities of the computer in general engineering applications. In addition to the Cromemco System Three microcomputer, an eight bit A-TO-D board for the S100 bus was available. The A-TO-D card was from a Cromemco System Three whose owner planned to write COBAL accounting programs and found that the A-TO-D function was not really required for an ACCOUNTS RECEIVABLE program package. At that time the capabilities of the very new microcomputers were not known. No software existed for using the A-TO-D board, and none of the staff had any experience dealing with a computer in a real time application, or with assembly language programming. There were even a few doubting Thomases around that thought the new microprocessor based computers were little more than toys with no real capabilities.

The Cromemco System Three is a S100 bus microprocessor based computer that makes use of 4 MHZ 280 processor chip. The available system had a full 64k bytes of 250 nanoseconds memory on a single board. A 280 Macro Assembler that utilized the 158 instruction set of the 280 to its fullest and a FORTRAN IV compiler complete with every FORTRAN feature except complex numbers, were included with the system. A CP/M like operating system (CDOS, Cromemco Disk Operating System) developed by the manufacturer loaded programs, moved data on and off the floppy disk, and other system jobs. A dual 277 single sided, single density drive served as the system's mass storage unit. Each drive had a capacity of 250 kbytes of storage (now up to 1.2 meg for new machines). A digital interface card (TU-ART) provided the system with two duplex data channels along with two parallel ports in addition to the single RC232 port used by the system console and the parallel printer output port. This card also provided ten interval timers that are accessible by the programmer both from assembly language programs and FORTRAN programs. One such timer was used to support variable sampling rates by the A-TO-D card. For flexibility the address of the fourteen I/O ports used by the card are switch selectable. Interrupt mode selection was accomplished by switches on the card. One has the choice of the 8080 interrupt mode using "Restart" instructions which are forced onto the bus or 280 mode 2, (vector interrupts). The sample rate of the A-TO-D card was

controlled by using the interval timer on the TU-ART card to generate interrupts at the desired sample rate and to instigate the operation of the A-TO-D card by causing the computer to transfer from a segment of do nothing code to the A-TO-D driver and then back to the do nothing code after a reading was taken by the A-TO-D card. By using the Z80 mode 2 interrupts the program had control over the location which the Z80 would jump to when interrupted by the timer. The source of the TU-ART was the same as that of the A-TO-D card, the computer that was to run an accounting package. (An accountant should never let an engineer specify a computer system for an account function.)

The eight bit A-TO-D card played a key roll in removing data from the tapes. This card had seven analog input ports with an input voltage range of from -2.56 to +2.54 volts. The input impedance was 20 megohms plus a 0.001 microfarad input capacitance measured at a sample rate of 1 kHz and 10 kHz. The resolution of the card was eight bit. This meant that the measured range of voltage, between -2.56 and +2.54 volts could be represented with a scale having 256 divisions, not an excessive number. Conversion time for one reading was 5.5 microseconds with an accuracy of plus or minus 20 millivolts. No use was made of the seven D-TO-A output ports that the card supplied. The card was connected to the outside world by means of a multiple conductor cable from the top of the board to the back of the computer case. This cable had a tendency to interfere with the top of other computer boards plugged into the bus.

The documentation that was available for the Cromemco System Three was excellent, and provided a foot hold for beginners. This was especially true if one compared the documentation available for other comparable computers at that time. System documentation that came with CDOS provided programming information needed to understand the portion of the operating system used to read and write files on the floppy disks. The documentation that was provided with the Z80 Macro Assembler package was complete and clean enough so that a beginner could learn assembly language programming to the point where the software required to drive the TU-ART board, and the software required to run the A-TO-D board could be written. Several examples of assembler language programs were provided in the packages that accompanied the A-TO-D card and the TU-ART card. A metronome example program that caused the bell on the system console to ring at a measured rate served to illustrate the exact principle that was required to control the sample rate of the A-TO-D card. The available computer was not a large machine, but it did offer one advantage over the larger IBM 360/370 on campus. Sometimes it is far better to have a little computer with full control over the entire machine than to have a small part of a large machine for short periods of time.

### 3.00 ADDING TIMING TRACK

After the project was started and it was realized by all that the mechanical oscillograph and the cross correlator were not going to work, the direction of the effort shifted to that of utilizing the small micro-computer to perform the desired task. The first step in this direction was to develop a means of reviewing the data on the tape. Since there were several hours of data present on the tapes, it was obvious that each track of the tape would not be sampled every 64 microseconds for the entire length of each tape. The tapes were copied using a second tape recorder. Then a timing track was added to the copy to make three channels of data and one of timing information. The timing track consisted of one second pulses that carried individual pulse identification. Thus any of the unique timing markers could be used as a trigger point to start the sampling sequence. In this way the data from a small segment of tape could be repeatedly located and sampled. Data at any of these marked locations could then be sampled a single channel at a time, and hopefully with no built-in delay between channels due to the time required to serial access data from several ports. If the data was to be collected by making a single pass at one point on the tape and sampling all three channels of information simultaneously, there would be a built in delay due to the sampling time required for each channel and the sampling rate maximum would have been reduced by a factor of three. One possible drawback to making multiple pass measurements was that an error could be introduced if the sampling process could not be exactly restarted at the same point on the tape for the multiple runs.

A test tape was recorded using a signal generator to produce a sine wave, a square wave, and a triangle wave on three separate channels. Using the Cromemco System Three, a timing track was added to the test tape. Every second, a ASCII bell (DEC 07) was recorded onto the tape. Each of the ASCII bell characters also had a count number recorded on the tape just before the bell character. When the tape was played back, one would receive first a second count and then an ASCII bell character. The timing track was recorded directly from pins 2, 3 and 7 of the RS232C serial output port of the computer with a 4800 baud rate. By connecting the output of the tape recorder to the RC232C input of a CRT terminal the timing marks could be read while reviewing the other three channels on an oscilloscope. This test tape was used to test the multiple sampling run techniques for the introduction of possible timing errors due to inconsistent start up of the sampling program on multiple runs. The sampling program was designed to read the second count from the timing track and start sampling on the reception of the first ASCII bell character after the desired count had been reached. This test showed that no timing errors were added to the data by multiple sampling runs. Multiple runs of the same data produced the same readings for each run. To be sure of the entire process, the sample tape was then copied onto a second

tape recorder in the same manner that the actual data was to be handled. By comparing the phase relation of signals from different channels on both the original test tape and the copy it was determined that the copying process had introduced timing errors between the various channels of data on the tape. This unexpected source of errors was eliminated by recording the timing track on the fourth channel of the tapes and thereby not using the internal zero reference feature of the TANDBERG tape recorder. In addition to the timing track added to the data tape, a known one volt dc signal was recorded on unused portions of the tape. This known one volt signal level served as a calibration signal when the sampling runs were made. After the addition of the timing channel and the calibration voltage, the original tapes were ready to be sampled.

#### 4.00 FIRST SET OF MEASUREMENTS

The TANDBERG came equipped with a small four channel monitor oscilloscope on which the magnitude of the signal output from each of the four channels of recorded data could be viewed. A preview of the tape from Tests 5 and 6 was made by looking at the signal from the three data channels on the small monitor and using the fourth channel, the timing track, to send a timing count to a CRT terminal through the RC232C serial input of the CRT. Times were noted for time periods of sizable fluctuations for all three channels of data, two voltages and one inverter output current. Only those time periods where a reasonable level of fluctuation could be seen with the monitor were selected. Many portions of the original tape contained signal fluctuations of much less than one volt peak-to-peak. An ideal range would have been from -2.565 to +2.54, thus using the full range of the A-TO-D card. At best, only a resolution of 256 could be had. When the fluctuation signal was less than one volt peak-to-peak the ability of the A-TO-D card to numerically characterize the signal significantly reduced.

An assembly language program was written to sample the data from the tapes. This program used the timing track to locate the desired starting point on the tape for each sampling run. The starting point count was controlled by the operator from the keyboard along with the number of samples and the time between each sample. The minimum sampling time was 64 microseconds. An interval timer on the TU-ART card served as the time base for determining the sampling interval using a program that was similar in operation to the sample metronome program provided by Cromemco. To maximize the data that could be stored in each run, an effort was made to minimize the size of the sampling program in order to leave as much of the 64k of memory free for data as possible. The data area of the program was declared at the very end of the sampling program and the capacity deliberately set very short. By intentionally writing over the data buffer, all of the 64k RAM memory up to the operating system, could be used to store data. Approximately 48k of

memory could be used for data storage. CDOS subroutines were used to dump the data to the disk once collected. Fourteen floppy disks, each with a storage capacity of more than 250,000 bytes were filled with sample data. At that point a new problem developed.

Originally, the plan was to transmit the raw data to the University's IBM 370 over a telephone link. One look at the number of bytes to be transmitted versus the transmission rate and it was decided that it would be more convenient to process the data using the Cromemco System Three to run FORTRAN. Programs to plot the data; find average, mean, and rms values, and to perform cross-correlation coefficient were written. The main calling program was written using RATFOR, a FORTRAN preprocessor program. This set of programs calculated the auto-correlation and cross-correlation coefficients using the text book definitions. Large amounts of computer time were consumed to analyze just a few samples of data from a number of different test runs with the channel.

The results of the computer analysis runs were a disappointment. The plots of voltages and currents, the auto and cross-correlation plots all showed that the fluctuations were related to the 50 hz frequency of the local power grid. The fundamental frequency found was 300 hz ( $2 \times 3 \times 50$  ... from the three phase dc to ac inverter). Only a hint of plasma transient time could be found by the most optimistic review of the data plots and correlation plots.

#### 5.00 SPECTRAL ANALYSIS

If plasma time transient information was to be obtained from the reading of voltages and current collected on an analogue tape, several improvements in the technique were obviously required. Before any measurements were made, a timing track should be prerecorded on one of the existing channels. At the time of the experiment, a known calibration voltage should be recorded on each of the channels after each run has been made, using the same input amplifier gain as was made during the run. The input gain of each channel should be adjusted so that the fluctuations have a peak to peak range as near five volts as possible. Doing this would make the best use of the A-TO-D card's input range and result in the best possible resolution of the data. Using a simple CRT terminal, the timing track count could be monitored and the test log for the tape could then reference the timing markers. As the tests were already completed, none of the above improvements could be made. One more improvement in the technique was possible. That was to rewrite the analysis programs so that the unwanted noise from the power inverters could be removed.

A listing of "COHERENCE AND CROSS SPECTRAL ESTIMATION PROGRAM" written by G. C. Carter and J. E. Ferrie from the NAVAL

UNDERWATER SYSTEM CENTER, NEW LONDON, CONNECTICUT was obtained. The backbone of the program was a Fast Fourier pair of subroutines used to transform data from the time domain to frequency and back. Also included are subroutines for six generalized cross correlation functions. The program was quite extensive, and required fairly large array space (for a microprocessor based computer). At the time there was no way of knowing if the program would fit on the Cromemco System Three. An additional problem was that the single byte words used to represent the data could not be read by the FORTRAN programs compiled by the compiler that was supplied.

Both FORTRAN and the assembler had a COMMON statement. This common feature of both languages was used to write a FORTRAN callable subroutine in assembler language that read data into an eight bit data array that had the same starting location as an array of an eight bit FORTRAN integer variable. The eight bit integer variable could then be converted to full size integers for the purpose of calculation. The main program was entered into the computer from the listing, along with a sample data for testing. After many hours of hunting for some obscure typing errors the program output results almost agreed with that of the listing. The difference between the two results was attributed to the manner in which a small microprocessor based computer and a larger machine performs calculations, even if both machines use 32 bit words for floating point numbers. A subroutine was added to the main program that gave the operator a chance to suppress any desired frequencies that appeared in the spectrum of the data after the Fast Fourier transformation had been made. Transforming the waveform to the frequency domain improved the ability of the system to analyze the data. Correlation runs that had previously taken 50 minutes or so, ran in approximately 5 minutes using the Fast Fourier techniques. Using the simulated test data a known delay could be detected from data that had been "contaminated" with 300, 600 900,.... hz noise. Unfortunately funding for the project ran out before the actual data was analyzed with the second set of programs.

## 6.00 CONCLUSIONS

An S100 bus, 280 based microprocessor was successfully used to sample, digitize, collect and store a large number of readings from data stored on an analogue tape recorder. To get the best results one needs to make careful advanced preparation to provide means for a timing track, calibration signals, and fully utilize the input range of the A-TO-D card. Meaningful analysis of the data can be done using a small microprocessor based computer such as spectral analysis and cross correlation and available FORTRAN compilers. Low cost computers, such as the Cromemco System Three and others will be a welcome addition to many laboratories. These small computer will greatly expand the measurement and analysis capability of these laboratories.



## REFERENCES

1. U.S./U.S.S.R. Cooperative Program in Open-cycle MHD Electrical Power Generation, Joint Test Report No. 4, Test No. 4 and 5, Argonne National Laboratory, Argonne, Illinois, 1981.
2. Programs for Digital Signal Processing, Edited by the Digital Processing Committee, IEEE Acoustics, Speech, and Signal Processing Society, IEEE Press, 1979.
3. S. Mason and Zimmerman, Electronic Circuits, Systems and Systems, John Wiley & Sons Inc., New York, 1960.

A METHOD TO DEDUCE CHAR FLOW TO THE  
BI-GAS REACTOR BY HEAT BALANCE\*

E. Charles Baetens and Robert Frummerman  
Frummerman Associates, Inc.  
218 South Trenton Avenue  
Pittsburgh, PA 15221

Abstract

A thermal balance method to measure char flow to the BI-GAS reactor is proposed to eliminate the need to provide supplemental fuel gas to Stage I of the reactor and to achieve better process control. The safety requirements of the BI-GAS system demand accuracy, quick response, and reliability in a char flow measurement system. A conceptual design of the measurement system and an assessment of how the system meets BI-GAS safety requirements is provided.

Potential obstacles to char flow measurements by thermal balance, such as incomplete thermal equilibrium between char and steam and the effects of purge gas in the char leg, are discussed. Hardware considerations are also discussed. All hardware used by the system is commercially available making thermal balance the fastest, surest method for achieving char flow measurement.

Introduction

Safety has been the prime mover for the development of a means of measuring char flow to the BI-GAS reactor. Concern that a loss of char flow may result in deflagration or detonation within the gasifier vessel or oxygen in significant quantities downstream from the gasifier made it very difficult to demonstrate that the BI-GAS process is entirely safe under all operating conditions. This doubt can be removed by employing a char flow measurement system with rapid response and a sufficient degree of reliability and accuracy. Several systems using developmental hardware are currently being tried; the heat balance method requires only commercially available hardware.

While testing and development of char flow measurement schemes goes on, theoretical work is demonstrating that BI-GAS safety issues may have been overstated. Work at Science Applications, Inc. and Sandia National Laboratories suggests that the potential is good for demonstrating theoretically and empirically that no reasonable scenario can result in either a detonation within the reactor vessel or significant amounts of oxygen downstream of the gasifier. Also deflagrations, still a threat, cannot damage the reactor vessel if the vessel is adequately vented. Nonetheless, safety remains a strong point in favor of development of char flow measurement for BI-GAS. Further, dilute solids flow measurement is a generic need for pressurized entrained gasification, and the BI-GAS process is more controllable with char flow measurement.

---

\* Work sponsored by Morgantown Energy Technology Center under DOE Contract #DE-AC21-80MC14220.

### Conclusion

Char flow measurement via a thermal balance can achieve performance requirements necessary to insure safe pilot plant operations without supplemental methane. Char measurement via a thermal balance employs hardware which is readily available to industry. It is therefore the fastest, surest route to achieving char flow measurement for the BI-GAS process.

To assure safety of operation without the use of a supplemental gaseous fuel in Stage I, the char measuring system must sense char flow and cause the flow of oxygen to adjust proportionately. Specifications have been derived for accuracy, speed, and reliability in a three-leg system.

An accuracy of measurement (defined as three times the standard deviation of measurements) of  $\pm 30\%$  for each leg of a three-leg char feed system is sufficient to meet safety requirements and to provide reasonably smooth pilot plant process control of the char/oxygen ratio. The thermal balance system is expected to achieve an accuracy of  $\pm 20\%$ . Not only would this exceed the requirements for safety, but it would significantly stabilize plant operations by limiting the standard deviation for Stage I flame temperature to less than 6%. The elimination of large, sudden changes in gasifier temperatures will tend to reduce mechanical problems.

The system must be able to correct for a sudden loss of char flow in a char leg within ten seconds. Using fast-responding, compacted ceramic thermocouples, this response time is definitely achievable. The system must respond to a loss of char flow in a given leg at least 99.9% of the time. The thermal balance system consists of numerous components, and the durability of most of the components is established by industrial usage. The overall reliability of the system cannot be predicted, although adequate reliability can almost certainly be designed into the system. However, this must be proven by field experience.

The system described herein is for the BI-GAS pilot plant at Homer City, Pa. The char flow measurement system is more effective and safer on a large-scale gasifier. Doubling the number of char burners on the gasifier increases safety by a factor of more than one thousand and improves the overall accuracy of ratio control in the gasifier by 30%. The accuracy of the system will improve in any case because: (1) heat losses are better controlled in larger pipes, (2) thermal equilibrium for the char and steam mixed stream can be assured, and (3) purge gas flow rates will be less important.

### Specifications

The frequency of char flow failure for each of three legs has been less than one in a hundred hours of BI-GAS pilot plant operations. If the molar feed ratio of carbon to oxygen is set at above 2.5, the loss of char feed to one leg can almost never lead to excess oxygen in Stage I if the accuracy of char flow measurement in the other two legs is  $\pm 30\%$  or better. If the response time of the char flow measurement is ten seconds or less and the system effectively responds 99.9% of the time, the probability of multiple char feed flow failures and the consequences thereof are shown in Table 1.

### Theoretical Considerations

Thermal Equilibrium of Char and Steam. If the temperature measurement in the mixed char and steam is to be meaningful, the char and steam must approach a common temperature by the point of measurement. FAI has calculated that thermal equilibrium occurs rapidly.

For a particle size distribution with 9.8% of particles by weight larger than 20 mesh, a 92% approach to equilibrium can be expected three feet downstream of the eductor (Figure 1). If the piping can be arranged to allow the measurement to be taken six to eight feet downstream of the eductor, thermal equilibrium can be expected to be essentially complete, and non-equilibrium will be a minor source of error in the char measurement system.

Char Leg Temperature. The char leg feeding the eductor contains both char and gas from two sources--purge gas and gas from the cyclone. Unfortunately, it is not possible to determine whether the gas and char are in thermal equilibrium, partly because the total amount of gas coming through with the char cannot be measured. An attempt to account for differences in temperature readings between the top and bottom of the char legs by thermocouples currently in service has not been successful. The upper leg temperature is much higher than the lower leg. Most of the temperature difference seems to have resulted from inequality of the gas and char temperatures. It is reasonable to assume that a meaningful temperature measurement of char in the char leg can be made, and that the effect of gas in the char leg can be neglected or allowed for in the heat balance. This may require: (1) pre-heating purge gas to the temperature of the upper char leg before injecting it, (2) demonstrating that the unmeasured flow of gas from the cyclone has a consistent or negligible effect on the accuracy of the heat balance, and (3) minimizing the flow of purge gas so that it has little effect on temperature readings.

Superheating Steam. The accuracy of the char flow calculation is a function of the initial temperature difference between the char and steam. To maximize this difference, the steam to the eductor needs to be heated to as high a temperature as practical. Given the materials of construction, this is about 900°F. Figure 2 shows the relationship between measurement accuracy and the temperature of the steam at expected operating conditions.

Steam Eductor. Since the temperature of the steam after expansion through the eductor nozzle and just before it begins to transfer heat to the char can not be measured, its enthalpy must be derived from a knowledge of its pressure and temperature just upstream from the eductor. A good assumption is that the enthalpy of the steam which is interchanged with the char is the same as the steam upstream from the eductor nozzle.

Steam flow through the eductor nozzle can be characterized as very nearly isentropic. Following this path on a temperature-entropy diagram for steam shows that an isentropic expansion is accompanied by a reduction in enthalpy. This is due to the conversion of some of the original pressure head to velocity. However, if the velocity is subsequently dissipated without doing work--such as by inelastic impact between molecules of steam and char, or by internal friction which reduces the jet velocity to a low value, say, less than 100 ft/sec,

at a substantially constant pressure--the steam may be assumed to have undergone a transformation from high to low pressure at nearly constant enthalpy.

Specific Heat of Char. The specific heat of the char must be determined by laboratory tests of a number of char samples at temperatures in the 700 - 800°F range. The heat balance equation can be modified to permit the specific heat of char to vary with temperature if laboratory results show the specific heat to vary considerably with temperature.

Heat Losses in Pipes. The total surface area of the piping between any two temperature sensing points is less than 10 sq. ft. If at least R-30 insulation is provided, the heat loss will be less than:

$$900^{\circ}\text{F} \times 10 \text{ sq. ft.} \times 30^{-1} \text{ Btu}/^{\circ}\text{F sq. ft./hr} = 300 \text{ Btu/hr}$$

which is insufficient to reduce the temperature of the material in any of the pipes 1°F. This would render heat loss effects negligible.

Heat Balance Equation. A heat balance equation derived from steam tables is given in Table 2. The enthalpy versus steam relationship was linearized using exponentials rather than power expressions because exponential algorithms are more readily available to microprocessor-based control systems. The precision of the equation was tested to be better than  $\pm 1\%$ .

### Hardware

Thermocouples. Temperatures will be sensed with compacted ceramic thermocouples having grounded junctions. Such thermocouples with 30 gage wires have a step change time constant of a half second and an accuracy of  $\pm 2.8^{\circ}\text{F}$  at the temperatures read. The anticipated life of an unprotected thermocouple of this size in the mixed char and steam is about thirty days. Using a larger gage permits longer life at the expense of longer response time. For example, a unit with a 16 gage wire would last about five months but would have a time constant of four seconds.

Of course, placing the sensor in a thermowell would extend the life considerably, but the response time would be unacceptable. It may, however, be possible to shield the tip of the thermocouple from impingement of char particles by welding a piece of metal to the jacket of the thermocouple or to the pipe. Again, this increases response time, but possibly in a more favorable way than increasing wire size. In any case, compacted ceramic thermocouples can provide a sufficiently fast response time and will last a reasonable length of time in the environment. Experience in using these elements will help to determine the optimum size and whether or not the tip should be shielded from particle impingement.

Microprocessor-Based Control System. The char flow will be computed and the char-to-oxygen ratio will be controlled by a system like the Max I proposed by Leeds and Northrup. The heart of this system consists of two card files called controllers. Each controller accepts up to 30 analog signals from the field by way of an analog terminal board. In this application, the required capacity is for 9 signals: 4 from temperature transmitters, 3 from pressure transmitters, and 2 from flow metering sections. These signals are linearized and converted to digital signals with 13-bit resolution. The signals are also

given upper and/or lower limits to insure that a valid signal is received, and they can also be equipped with an alarm to indicate when a process variable is such that a risky situation exists. Conditioned signals are fed to one or more of sixteen available computational slots. Each slot can be assigned one of thirty-nine algorithms by keying in a code number at the ministration. The sixteen slots are then analogous to sixteen pieces of conventional instrumentation. Each slot can receive inputs from other slots or from the field as described above. Only eight of the slots, called primary slots, can deliver analog outputs to control the process.

In this application, seventeen slots are required to compute char flow, control the char-to-oxygen ratio, and to allow eight alarm conditions to cause hardware activity such as a horn sounding or a valve closing. Since each controller has sixteen slots, a second controller is required, but fifteen additional slots are available in case other variables are introduced or more control capability is required.

Thirteen of the seventeen slots are required to solve the heat balance equation including a slot to compute mass flow of steam, 5 dividers, 3 multipliers, 2 exponentials, and 2 summers. The configuration is shown in Figures 4 and 5. This is a "soft" configuration produced by relatively simple keyboard operations. The configuration can be immediately changed if other variables have to be considered. More important, the constants which are based on reference temperatures and pressures of steam into and out of the eductor can be changed to accommodate process changes such as changes in reactor pressure. Again, this involves simple keyboard operations. With a conventional system, changing the constants for this type of configuration would be almost impossible. Indeed, calibrating such a large number of relays would be extremely difficult.

The ratio controller slot has one input which is the computed flow of char and another input from a slot which computes the flow of oxygen. The output of the ratio controller modulates the oxygen control valve to provide control.

The execution of each algorithm takes 1/32 of a second, so the 16 slots (sometimes called "time slots") are serviced in sequence every half second. The analog outputs are held constant for the half second intervals during each control cycle. In addition, the process variable inputs and the controller hardware are diagnosed for hardware malfunctions and process alarm conditions each half second. These conditions are displayed on the video display of the ministration. Circuit failures within a process card also cause an LED to light up on the edge of the card. Each slot can be backed up by the corresponding slot of another controller, so that problems diagnosed in the controller circuitry result in the function of that slot being taken over by the backup slot. This may be used in the char flow system if it is found that the additional reliability is required.

### Performance

Response Time. A fast response time to loss of char flow to one char leg minimizes the excess oxygen delivered to Stage I by that leg. Figure 3 shows the spike of excess oxygen which results from total loss of char to one of three eductors during a period of one second if the time constant of the

thermocouple is 1.5 seconds. There is about a two-second delay before any control action begins. One second is an assumed time for travel to the thermocouple, the rest of the time is for the hardware to act. The excess oxygen spike maximizes at about the total flow of oxygen to that leg, i.e., char flow is totally lost before response begins. Corrective action is very rapid thereafter and takes three forms: (1) the control action throttles down the oxygen in about three seconds; the time required is directly proportional to the time constant of the thermocouple; (2) a deviation alarm can shut off oxygen in about two seconds--the time, again, being proportional to the time constant of the thermocouple; and (3) a derivative alarm, if one can be effectively employed (depending on the fluctuations in typical char flow), can shut off the oxygen valve in about one second.

Reliability. A reliable heat balance system requires reliable measurements of temperatures, pressures, and flows and a reliable microprocessor-based control system. The former can be achieved by providing redundancy of measurement backed by field testing. Reliability of the control system is normally easier to achieve than reliability of measurements. Microprocessor-based systems are more reliable than conventional systems for this application, because they perform diagnostics, eliminate potential wiring errors, employ "locked-in" digital constants, are readily backed up if necessary, and are quickly repaired by replacement of faulty process cards. A high degree of reliability is therefore anticipated for a heat balance system. In the final analysis, however, reliability will have to be demonstrated by field operation.

#### Accuracy

The accuracy of the char flow measurement system was estimated using the Monte Carlo method. For each parameter, an accuracy is specified based on manufacturers' data for hardware or on conservative estimates of the accuracy of such parameters as the specific heat of char. Next, a set of values is specified for each parameter for each of five trials. For each trial, a computer generates 2500 normally distributed random numbers for each parameter, computes char flow 2500 times, and computes the average value and standard deviation of the computations. The results are shown in Table 2. The 3  $\sigma$  accuracy varies from about 16% to about 23% and averages 20%.

#### References

Wilson, Albert L., Safety Assurance Study of High Btu Coal Gasification Pilot Plants, FE-2240-8, C. F. Braun Company, for the U.S. Department of Energy, Washington, D.C., August 1976.

Solids Feeding, Metering, and Control at the BI-GAS Pilot Plant, FE-1207-T9, Bituminous Coal Research, Inc. and Phillips Petroleum Company, for the U.S. Department of Energy, Washington, D.C., October 1979.

Factored Estimates for Eastern Coal Commercial Concepts, FE-2240-31, Interim Report Joint Department of Energy, Gas Research Institute, and Coal Gasification Program, C. F. Braun Company, for the U.S. Department of Energy, Washington, D.C., September 1978.

TABLE 1. PROBABILITY AND CONSEQUENCES OF MULTIPLE FLOW FAILURES IN CHAR LEGS

EVENT	RESULT	FREQUENCY
THREE CHAR LEGS LOSE FLOW AT ONCE.	RAPID BUILDUP OF OXYGEN IN VESSEL.	SHOULD NOT BE ALLOWED TO HAPPEN - PREVENTABLE.
CHAR LOST IN TWO LEGS - O <sub>2</sub> BEING CORRECTED FOR BOTH LEGS SIMULTANEOUSLY.	INCONSEQUENTIAL (<5%) BUILDUP OF OXYGEN IN STAGE I FOR SEVERAL SECONDS.	EVERY 680,000 HRS.
CHAR LOST IN TWO LEGS - ONE SYSTEM FAILS TO RESPOND.	SIGNIFICANT BUILDUP OF OXYGEN IN STAGE I FOR SEVERAL SECONDS.	EVERY 10,000,000 HRS.
ENTIRE SYSTEM FAILS. CHAR LOST IN TWO LEGS.	SIGNIFICANT BUILDUP OF OXYGEN FOR AN INDEFINITE PERIOD OF TIME.	EVERY 189,000,000 HRS. MAY BE PREVENTABLE.

ACCURACY OF CHAR FLOW MEASUREMENT SYSTEM VIA THERMAL BALANCE BY MONTE CARLO METHOD

HEAT BALANCE EQUATION USED

$$F_c = \frac{F_s(88.8 - .0418(P_s - 1800)) + .0621(P_m - 750) + .0251(T_s - 900) + .0002008(T_s - 900) + .0002008(T_m - 700) - .0051(T_m - 700)}{.33(T_m - T_c)} - 260$$

ACCURACIES OF VARIABLES\*

- F<sub>s</sub> = FLOW OF STEAM ±3%
  - P<sub>s</sub> = PRESSURE OF STEAM ±1/4%
  - T<sub>s</sub> = TEMPERATURE OF STEAM ±3/8%
  - T<sub>m</sub> = TEMPERATURE OF MIXED STREAM ±6/8%
  - T<sub>c</sub> = TEMPERATURE OF CHAR ±3/8%
  - C<sub>p,c</sub> = SPECIFIC HEAT OF CHAR ±3%
  - 260 = CORRECTION FACTOR FOR GAS IN CHAR ±10%
  - 88.8 = CONSTANT FOR BASE ENTHALPIES OF STEAM ±3%
  - P<sub>m</sub> = PRESSURE OF MIXED STREAM ±1/4%
- \*INSTRUMENT ACCURACIES FROM VENDOR

COMPUTED ACCURACY OF CHAR (3σ) FOR DIFFERENT VALUES OF VARIABLES

F <sub>s</sub>	P <sub>s</sub>	P <sub>m</sub>	T <sub>s</sub>	T <sub>c</sub>	T <sub>m</sub>	C <sub>p,c</sub>	Q	h <sub>1</sub>	F <sub>c(Set)</sub>	F <sub>c(Avg)</sub>	σ	3 σ %
660	1660	600	690	690	780	.33	280	88.8	3428	3440	268.4	22.0
660	1700	775	675	710	740	.33	260	88.8	3301	3314	416.8	22.7
660	1900	725	625	730	780	.33	260	88.8	308.6	309	64.8	20.6
660	1660	700	660	700	780	.33	260	88.8	2644	2649	188.1	16.0
660	2000	1000	1000	700	680	.33	260	88.8	374.4	375	23.22	16.0

TABLE 2



FIGURE 1  
 APPROACH TO THERMAL EQUILIBRIUM DOWNSTREAM OF EDUCATOR

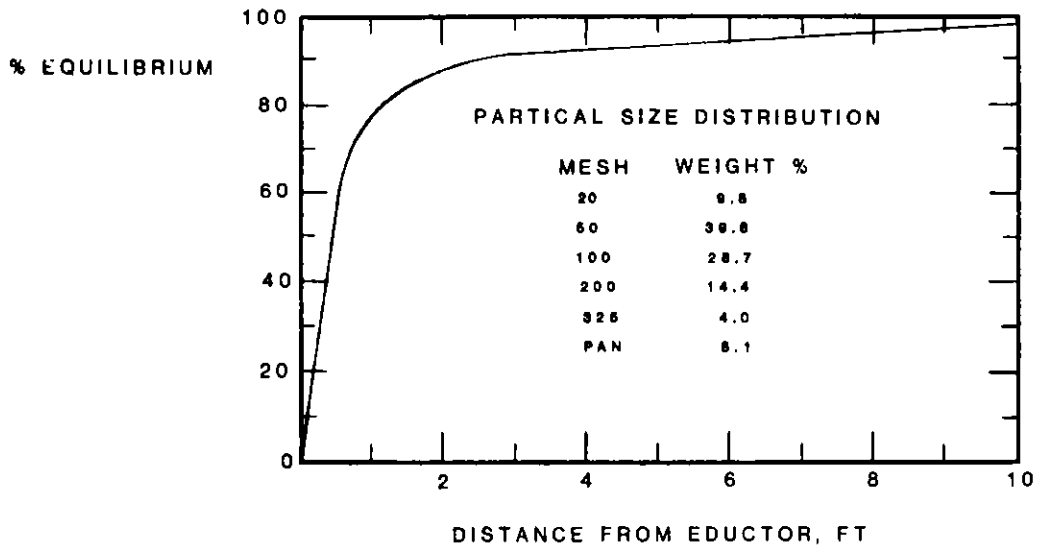
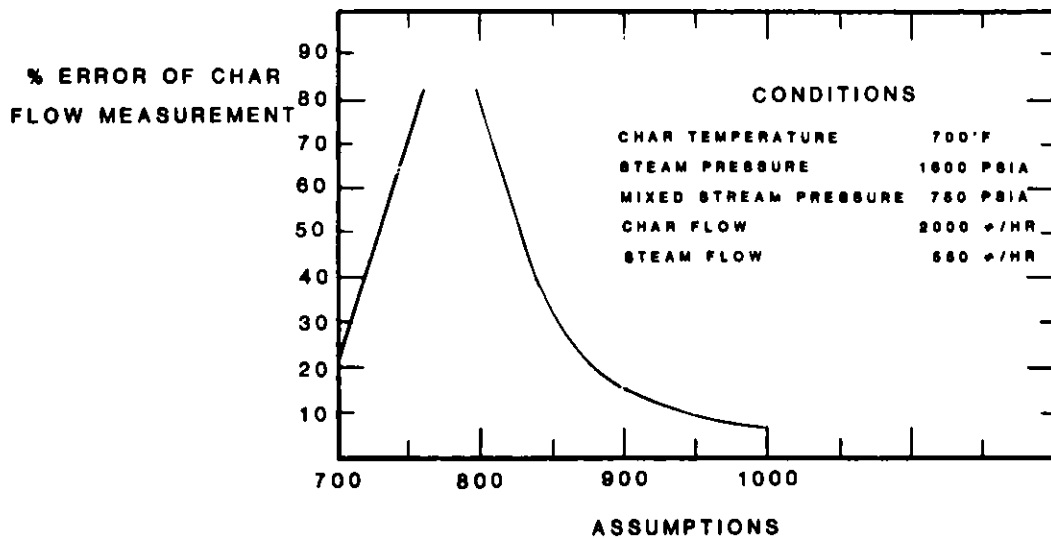
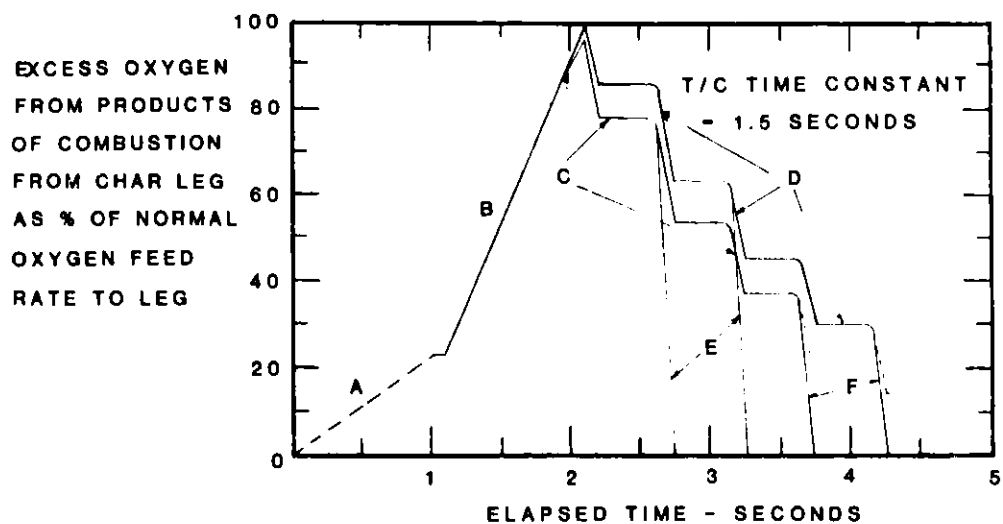


FIGURE 2  
 EFFECTS OF STEAM SUPERHEAT ON ACCURACY OF CHAR FLOW MEASUREMENT



ISENTHALPIC EXPANSION THROUGH EDUCATOR  
 ACCURACY OF MEASUREMENT OF TEMPERATURE OF STEAM, CHAR, AND MIXED  
 STREAM ±2.5°F AND THIS IS SOLE SOURCE OF CHAR FLOW MEASUREMENT ERROR

FIGURE 3 RESPONSE OF THERMAL BALANCE CONTROL SYSTEM TO A SUDDEN LOSS OF CHAR FLOW



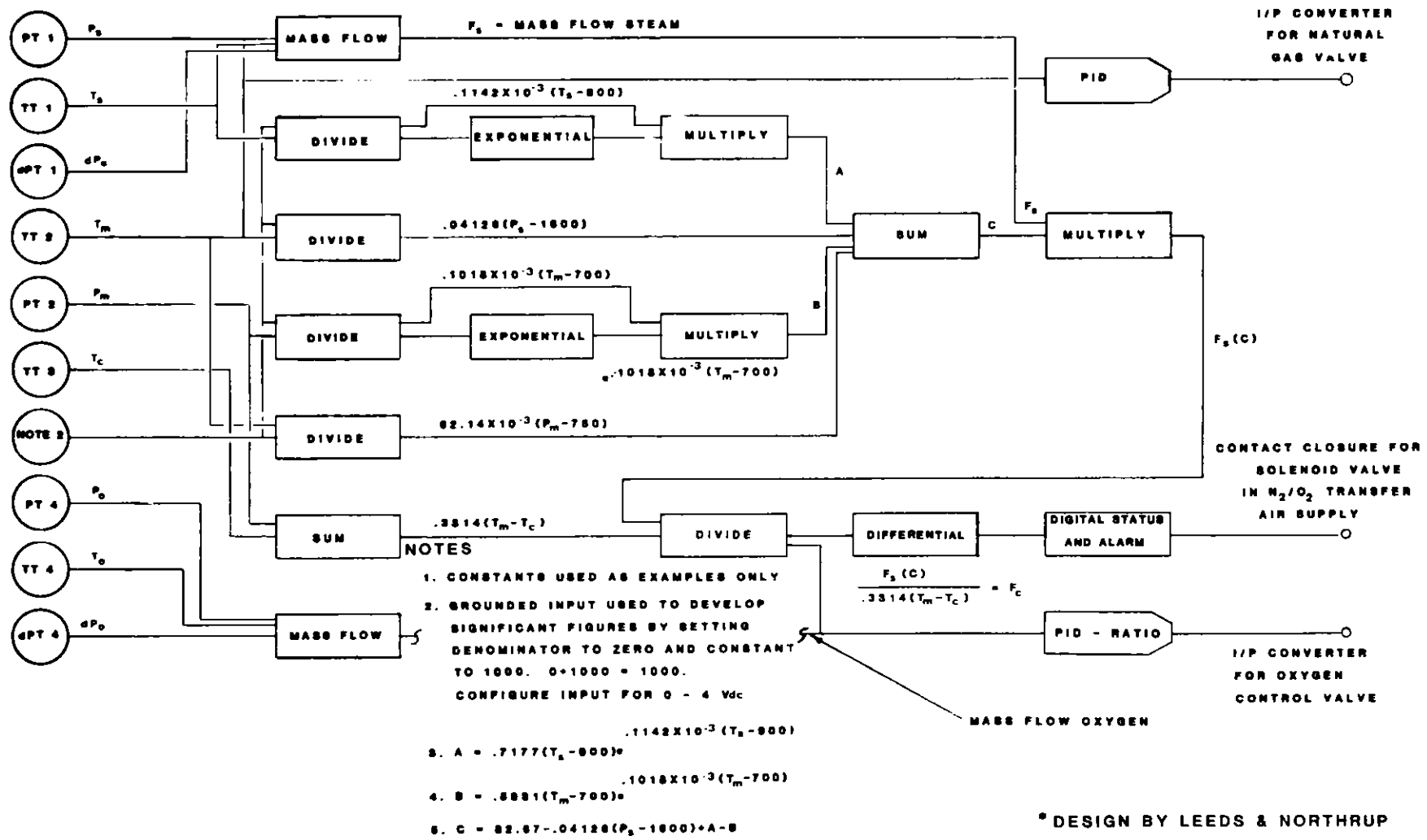
#### ASSUMPTIONS

PURGE GAS  $\propto$  CHAR  
 PURGE GAS VOLUME SIGNIFICANT  
 COMPARED WITH VOLUME OF STEAM

#### LEGEND

A - REDUCED FLOW TO EDUCTOR CAUSES  
 LOSS OF CHAR FLOW TO BURNER TIP  
 B - REDUCED FLOW REACHES CURNER TIP  
 C - CONTROL ACTION (STARTS AT 1.8 SECS)  
 D - CONTROL ACTION (STARTS AT 2.1 SECS)  
 E - DERIVITIVE ALARM SHUTS DOWN  $O_2$  IF APPLICABLE  
 F - DEVIATION ALARM SHUTS DOWN OXYGEN

FIGURE 4. MAX I CONFIGURATION FLOW SHEET FOR EVALUATION OF MASS FLOW COAL CHAR\*



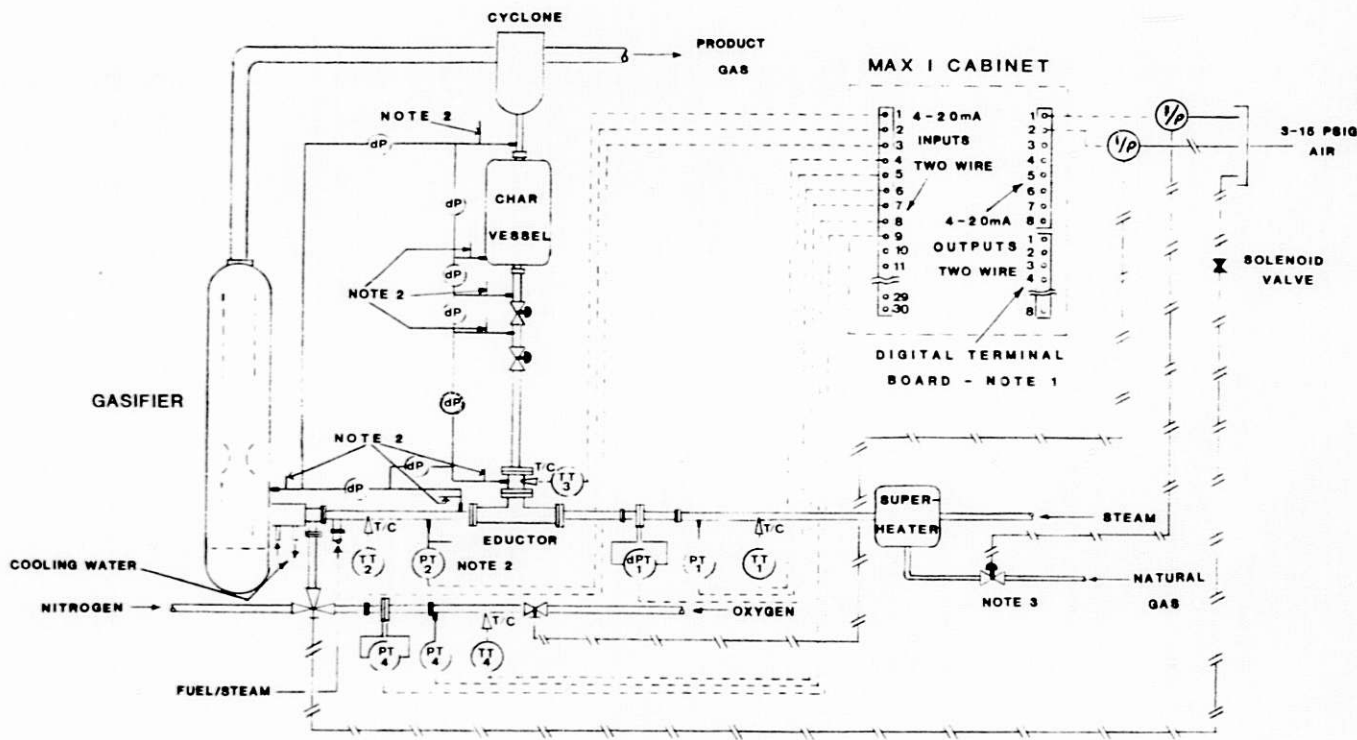
\* DESIGN BY LEEDS & NORTHRUP

FIGURE 5.

P&I DIAGRAM FOR THE MASS FLOW MEASUREMENT OF COAL CHAR\*

NOTES

1. DIGITAL OUTPUTS ARE CONTACT CLOSURES. THERE ARE EIGHT INPUTS AVAILABLE ALSO.
2. IMPULSE LINE PURGE GAS ENTRY POINTS.
3. NATURAL GAS VALVE REGULATES STEAM TEMPERATURE AS MEASURED AT TT1 THROUGH PID CONTROL ACTION.
4. FLOW SECTIONS ARE 36" LONG FOR ONE INCH PIPE.



\*DESIGN BY LEEDS & NORTHRUP

THE X-RAY ABSORPTION MEASUREMENT OF FLUID SATURATIONS  
IN OIL SAND CORES

E. Miles-Dixon, G.E. Sedgwick, T.R. Heidrick  
Alberta Research Council  
Oil Sands Research Department  
11315 - 87th Avenue  
Edmonton, Alberta T6G 2C2  
Phone: (403) 467-8861

Abstract

The Alberta Research Council has embarked on a major program of physical and numerical simulations to investigate the in situ recovery of bitumen from the Province's large oil sands deposits. One such process uses steam heating to extract the bitumen directly from the unconsolidated sands. Mathematical modelling of this process, which is based on experimental results, requires a knowledge of physical properties of porous media, such as the relative permeability to various types of fluid flow. This permeability depends on the relative amount of each fluid flowing in a multicomponent mixture during the experiment. A number of techniques are being explored to accurately measure these component fractions at the required high temperatures and pressures. These include X-ray and  $\gamma$ -ray absorption, computerized tomography, radiotracers, and neutron activation.

In this paper data are presented for sand packs with varying saturations of bitumen and aqueous solutions of sodium iodide. Sodium iodide was selected to increase the absorption contrast between the bitumen and water phases. Data are also included for longitudinal scans of cylindrical sand packs showing the variations of chordal average absorption with length during a flooding or displacement process. Scans are shown for both miscible and immiscible displacement fronts.

Introduction

In the present context, in situ bitumen recovery refers to processes which are applied to oil sands formations buried at sufficient depth to be rendered non-economic through surface mining. The oil sand in these formations consists of fully compacted unconsolidated water-wet sand with the pore space filled with varying amounts of bitumen and water. The bitumen and water total approximately 17% by weight while the pore volume or porosity is of the order of 35%. The bitumen component is extremely immobile having a specific gravity near 10° API and a viscosity of  $5 \times 10^6$  centipoise at a reservoir temperature of 10°C.

This high viscosity necessitates an increase of formation temperature to mobilize the bitumen sufficiently to effect practical recoveries. Of the number of potential recovery techniques, the Alberta Research Council has concentrated on the injection of steam mixed with various solvents and gaseous additives to extract bitumen from the porous sand.

The oil sands program includes large physical simulators<sup>1</sup>, numerical

simulations,<sup>2</sup> and basic parameter measurements.<sup>3</sup> Various non-intrusive analytical techniques are being investigated for support of the basic parameter studies. X-ray absorption represents one such method.<sup>4</sup>

### The X-Ray Absorption Technique

In the X-ray absorption method samples are placed in a beam of X-radiation with the resulting attenuation or absorption giving a measure of the intervening density and material properties. The intensity of the transmitted beam is given by Beer's Law:

$$I = I_0 e^{-\mu \rho d}$$

where I is the measured flux in counts per second;  $I_0$  is the incident flux;  $\mu$  is the mass absorption coefficient;  $\rho$  is the density of the absorbing material, and d is the thickness of the absorber. For an oil sands core sample the coefficient-thickness product is the summation of the individual products for sand, bitumen, water and possibly a tracer additive.

The above relationship is strictly valid only for a monoenergetic beam. The mass absorption coefficient however is a function of both the material and the incident photon energy. Consequently, for a polychromatic beam and sufficiently thick cross-sections, the spectrum of the beam is modified as it passes through the absorbing material. The longer wavelength photons are absorbed more readily with a resulting spectral shift to shorter wavelengths (beam hardening). Beam hardening effects are monitored by generating log-linear plots of transmitted intensity as a function of absorber thickness. Significant spectral shift manifests itself in an upward curvature with increasing thickness reflecting the lower mass absorption coefficients for higher beam energies.

The mass absorption coefficients for water and bitumen are nearly equal consequently an absorbant tracer is required to increase the contrast between the oil and water phases. Various compounds are available for addition to either of the phases. The results reported here are based on the addition of sodium iodide to the water.

### Measurement Apparatus

The data presented were obtained from prepared cores of either Ottawa sand (70 - 120 mesh) or repacked oil sands. For low temperature and pressure displacement experiments the cores were packed in acrylic and teflon tubes to give cores of 5 cm diameter and 15 to 40 cm length. The tubes were fitted to a positioning mechanism for the point by point scanning of chordal X-ray transmissivity along the length of the cores, Figures 1 and 2.

The source of radiation consisted of an X-ray tube with a tungsten target and driven by a well regulated high voltage supply. The beam was collimated to a 3 mm by 10 mm cross-section. Measurements were taken at a tube setting of 35 KV and 25 mA. Transmitted intensity was measured with a NaI scintillation detector. Counting periods of 10 seconds were sufficient

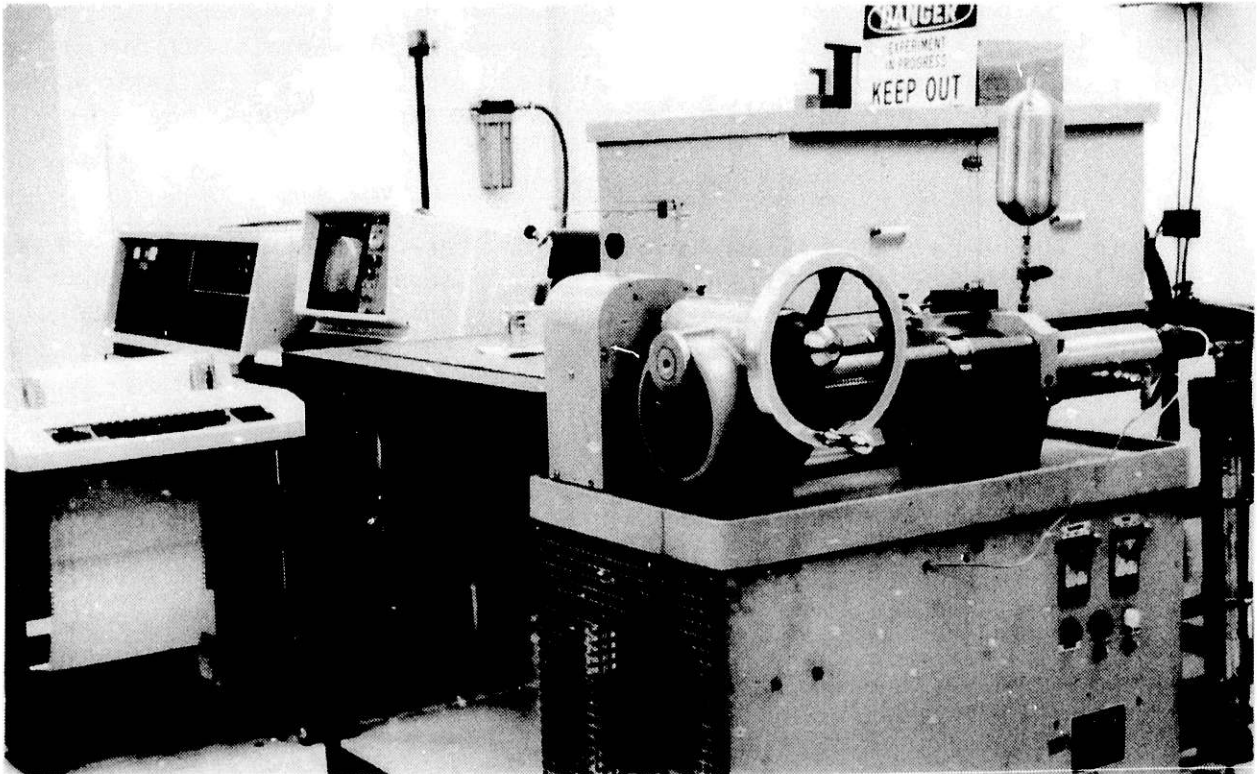


Figure 1 (a). Apparatus for X-ray Absorption Analysis of Oil Sands Cores.

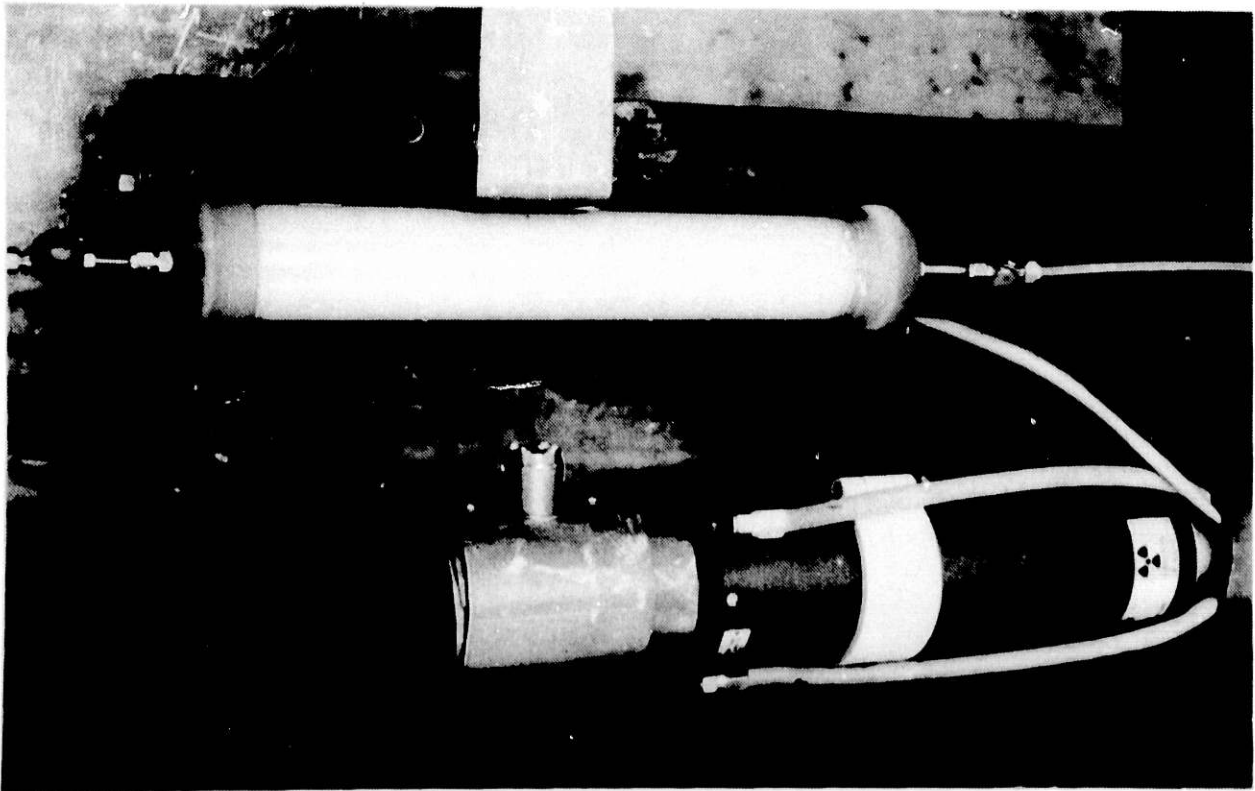


Figure 1 (b). Test Section Showing Packed Core, X-ray Tube, and Detector.

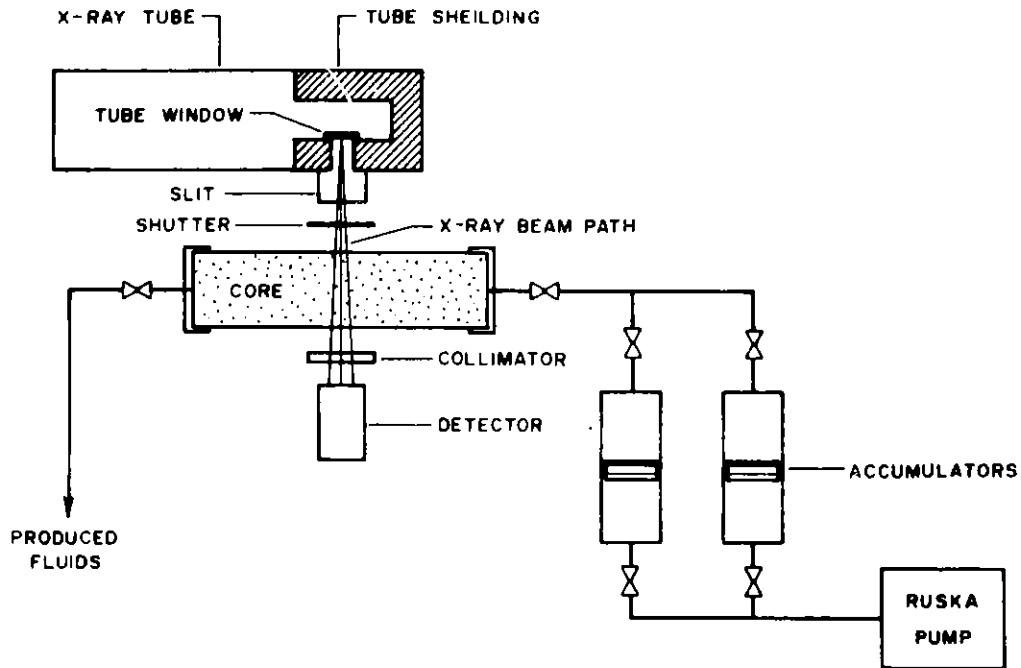


Figure 2. Schematic of X-ray Absorption Measurement System Configured for Displacement Experiments

to avoid significant errors due to the statistical variations of photon flux.

A constant injection rate (Ruska) pump and accumulators were used to flood the cores at rates varying from 25 to 250 cm<sup>3</sup> per hour. As mentioned earlier NaI tracer was added to the water phase to increase the contrast between the water and the oil. The concentration of NaI was typically 120 grams per liter. Log-linear plots of beam intensity versus thickness of sand saturated with aqueous solutions of NaI were used to verify that the above concentration did not produce appreciable beam hardening.

Calibration data were required for the quantitative calculation of the porosity and the various fluid saturations. This was provided by inserting varying thicknesses of the relevant absorbing materials into the beam path. From these readings absorption coefficients were determined at the tube voltage and current used for the core scans.

### Core Fluid Saturation Measurements

#### Miscible Displacement

The first series of runs represent a miscible displacement process wherein a core of Ottawa sand saturated with distilled water was flooded with a 0.8 molar solution of NaI tracer and water. Prior to saturation with water an initial reference scan was taken and is shown as the upper curve of Figure 3. Some packing variation is apparent. Next the core was fully saturated with distilled water and another scan taken. The core was then flooded with the water/NaI solution. The displacement front is shown



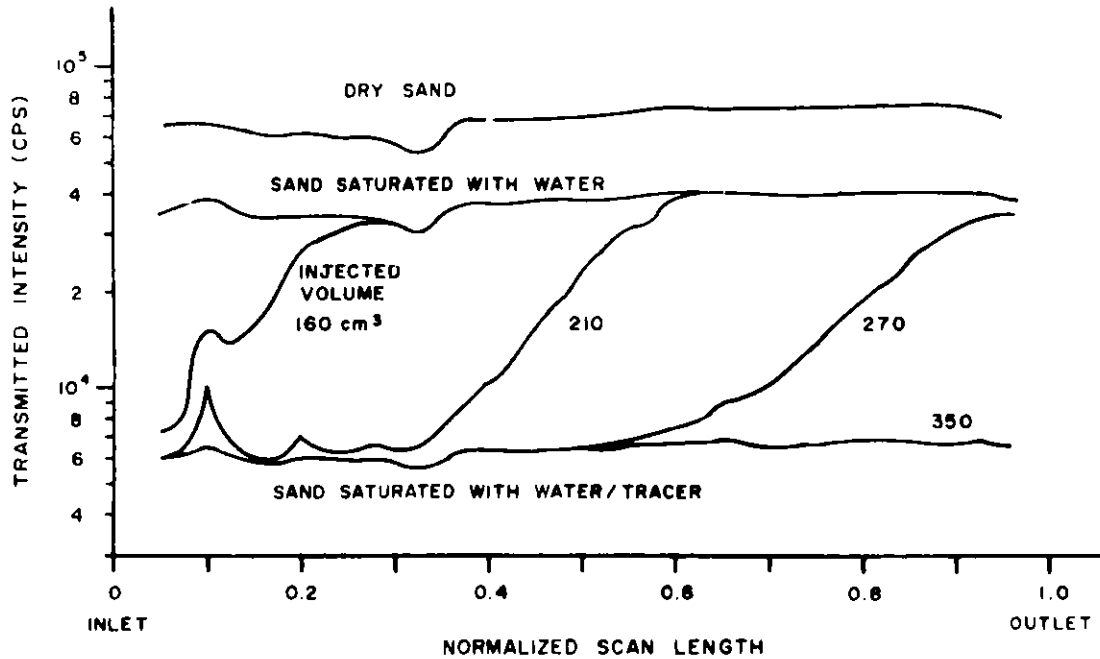


Figure 3. Miscible Flooding of Prepared Sand Core.

Ottawa sand core matrix; displaced phase-distilled water; displacing phase-water with NaI; scan length 20 cm.

for various injected volumes. The lower curve traced out by these scans gives the signal for a core fully saturated with the water/NaI solution. Using the ratio of the intensities for water saturation with and without the tracer, a porosity of 38% was calculated for the sand.

#### Immiscible Displacement - Water by Oil

In the second series of scans the core from the previous miscible displacement process was used for an immiscible displacement. The core now fully saturated with water/NaI was injected with an hydraulic oil simulating the viscosity of bitumen at 125°C, Figure 4. As the core was injected with oil the measured intensities increased as the water/NaI was displaced. The final (upper) curve traced out by these scans gives the response for a core saturated with oil and residual water/NaI. The curve for dry sand is repeated for comparison. The intensity ratio and measured values for the absorption coefficients were used to calculate a residual water/NaI saturation of 10% after flooding.

#### Immiscible Displacement - Oil by Water

The third series of runs involved the reflooding of the above oil saturated core with the water/NaI solution, Figure 5. In this case, however, an adverse viscosity ratio existed between displacing phase (water/tracer) and the displaced phase (oil). As expected the pronounced frontal displacement of previous runs was essentially non-existent. A number of scans are shown for various injected volumes. Curves for the cases of dry sand and sand fully saturated with water/tracer are also shown for

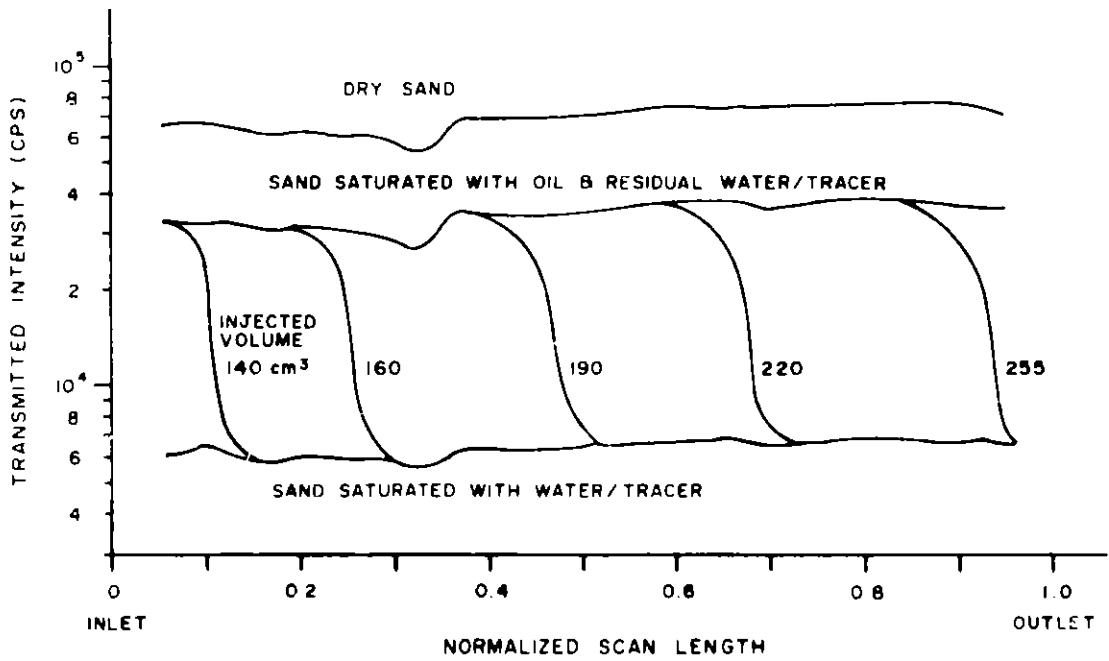


Figure 4. Immiscible Flooding of Prepared Sand Core. Ottawa sand core matrix; displaced phase - water with NaI; displacing phase - hydraulic oil; scan length 20 cm.

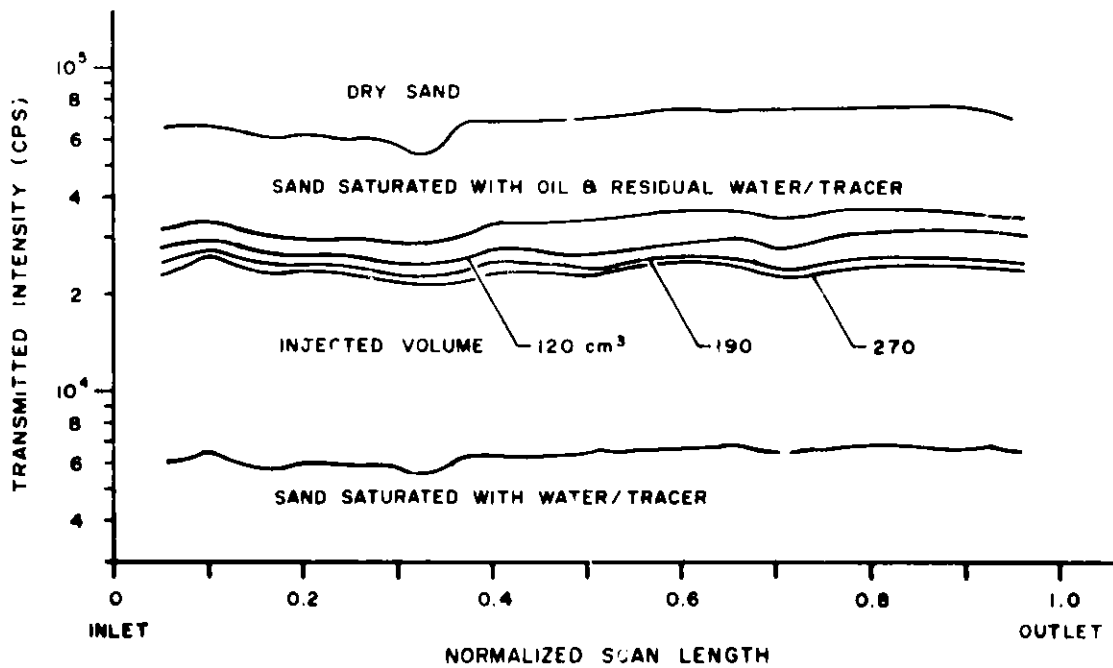


Figure 5. Immiscible Flooding of Prepared Core. Ottawa sand core matrix; displaced phase - hydraulic oil; displacing phase - water with NaI; scan length 20 cm.

comparison. Only a small fraction of the contained oil was produced. The oil saturation decreased asymptotically to a calculated residual of approximately 60%.

#### Immiscible Displacement - Bitumen by Water/Tracer/Polymer

The final series is for a repacked oil sands core subjected to water/polymer flooding, Figure 6. The water phase again contained NaI tracer at

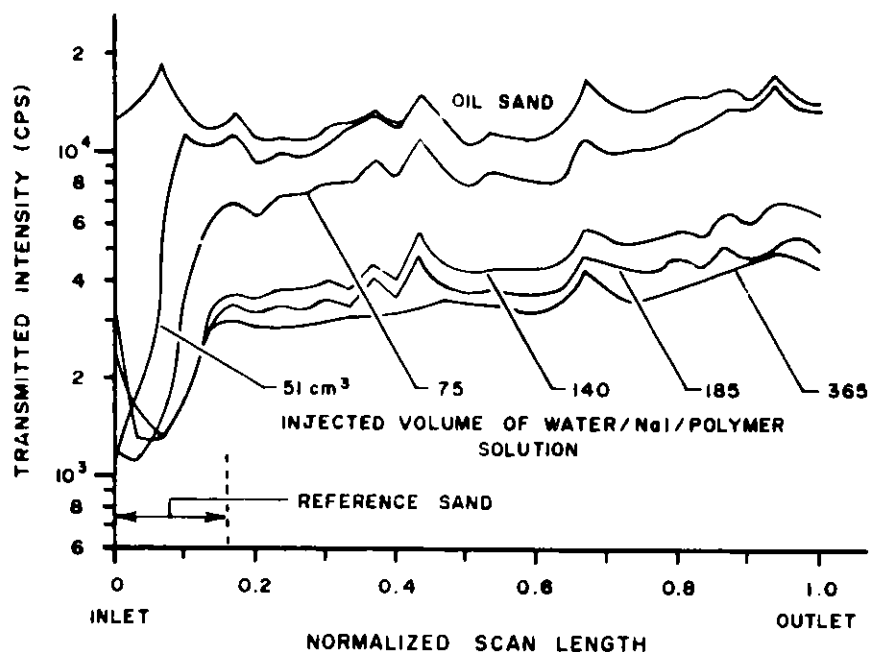


Figure 6. Immiscible Flooding of Repacked Oil Sands Core. Repacked oil sands core with 14% by weight bitumen; displacing phase-water/polymer mixture with NaI; scan length 16 cm.

a concentration of 120 g/l. A non-ionic polymer was added to the water to provide a more favourable viscosity ratio. The previous acrylic tube was replaced by one of teflon with a 5 cm internal diameter. To increase the mobility of the viscous bitumen an external heating coil was wrapped around the core to maintain the temperature between 72 - 75°C. At this temperature the viscosity ratio of displaced fluid to displacing fluid was near 0.7. A 2.5 cm length of Ottawa sand was inserted at the injection end. This appears to be useful as a reference during the flooding process in that when the reference sand is fully saturated with the displacing fluid (water/NaI/polymer) a gauge is provided for the saturations encountered during the displacement process. A calculated porosity of 40% was obtained for the reference pack.

The initial scan, upper curve of Figure 6, shows density variations prior to injection. These variations are attributed to the method of packing the oil sand. Studies are continuing on techniques for providing a more uniform pack.

The lower curves of Figure 6 are for increasing volumes of the displacing fluid. The lowest curve, taken after injection of 365 cm<sup>3</sup> (approximately 3.5 pore volumes), represents the case of residual bitumen saturation. The residual saturation obtained from the ratio of the upper and lower curves indicated a much higher recovery than that inferred from actual produced bitumen. This was explained by entrained air due to the packing process. The void space created by the trapped air was deduced knowing the density of the oil sands pack and the bitumen content. By using this as a correction for the absorption curves of Figure 6, close agreement was then obtained for the residual bitumen saturation.

#### Summary

The X-ray absorption technique has been used to measure fluid saturations and to study the dynamics of fluid flow in oil sands cores at low temperature and pressure. Work continues on the application of this technique at the high temperatures and overburden pressures encountered in the recovery of bitumen from oil sands formations. The technique has demonstrated utility in the packing of oil sands test cores.

#### Acknowledgements

The authors wish to acknowledge the Alberta Oil Sands Technology and Research Authority for funding assistance and the permission to publish this paper. The authors further wish to acknowledge the technical advice of F. Louman, M. Polikar, C. Reichert and A. Sacuta and the technical assistance of K. Forshner and B. Wiwchar all of the Alberta Research Council. Acknowledgement is also given to W. Harbert of AMOCO for advice during the initial planning stages of this project.

#### References

1. D.M. Nguyen and T.R. Heidrick, "In Situ Recovery of Bitumen from Oil Sands - Laboratory Pilot Plant Experience," 1982 Symposium on Instrumentation and Control for Fossil Energy Processes, Houston Texas (June 7 - 9, 1982).
2. G.S. Reddy, D.R. Prowse and D.A. Redford, "Physical Modeling and Numerical Simulation of In Situ Recovery of Bitumen from Oil Sands by Steam Injection," 31st Annual Meeting of the Petroleum Society of CIM, Calgary, May 25 - 28, 1980.
3. D.A. Redford, D.E. Exall, J. Boon and C. Reichert, "In Situ Research at the Alberta Research Council," 29th Chemical Engineering Conference, Sarnia, Ontario, September 30 - October 30, 1979.
4. F. Morgan, J.M. McDowell, and E.C. Doty, "Improvements in the X-ray Saturation Technique of Studying Fluid Flow," Petroleum Transactions, AIME vol. 189 (1950) 183 - 194.

List of Show and Tell Hardware Display Participants

K. R. Carr  
Oak Ridge National Laboratory  
Bldg. 3500, M.S. 6  
P. O. Box X  
Oak Ridge, TN 37830

Prototype Magnetically Coupled Drives  
for Instrumentation Impulse Lines  
Clearing and Sealing, Plug Detection,  
and Viscosity Measurement

Lawrence Cohen  
TRW Space & Technology Group  
One Space Park, M.S. R1-1028  
Redondo Beach, CA 90278

Combustion Diagnostics -- Pin Hole  
Camera, Enthalpy Probe, Sodium D-Line  
Reversal Hardware

Jasper Jackson  
Los Alamos National Laboratory  
M.S. C-335  
P. O. Box 1663  
Los Alamos, NM 87545

Nuclear Magnetic Resonant Logging  
Tool

Paul Raptis  
Argonne National Laboratory  
Bldg. 308  
Argonne, IL 60439

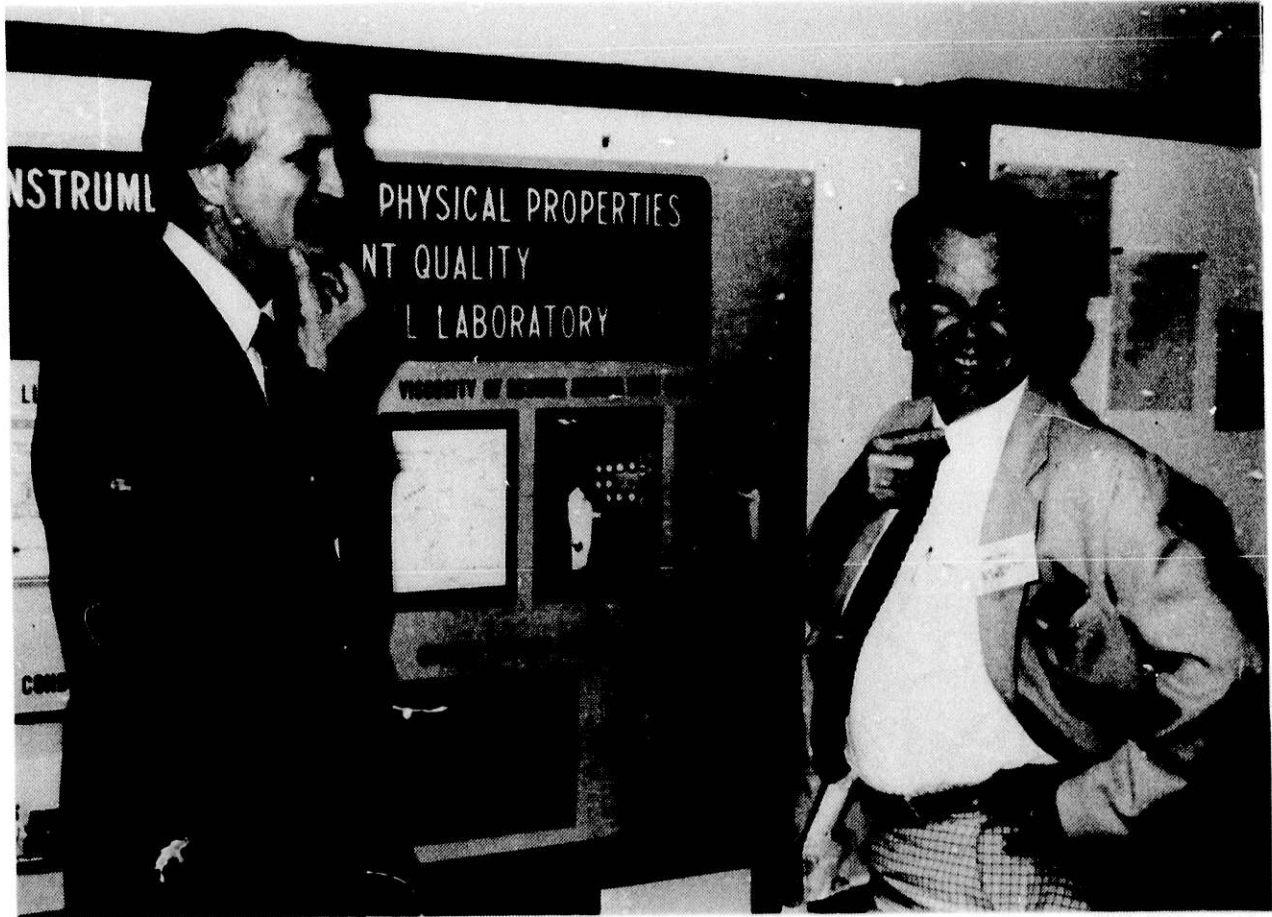
TDR for Temperature Profile Measurement

Stefan Jeglinski  
Mississippi State University  
Mississippi State, MS 39762

Laser Transmissometer/Two-Color  
Pyrometer System

James Joyce  
Harry Diamond Laboratory  
U.S. Army  
Powder Hill Road  
M.S. DELHD-RT-CD  
Adelphi, MD 20783

- (1) Fluidic Mud Pulser for Offshore  
Drilling
- (2) Fluidic Gas Concentration Sensor  
for Process Control
- (3) Fluidic Capillary Pyrometer for  
High Temperature Processes



Oak Ridge National Laboratory  
Oak Ridge, Tennessee

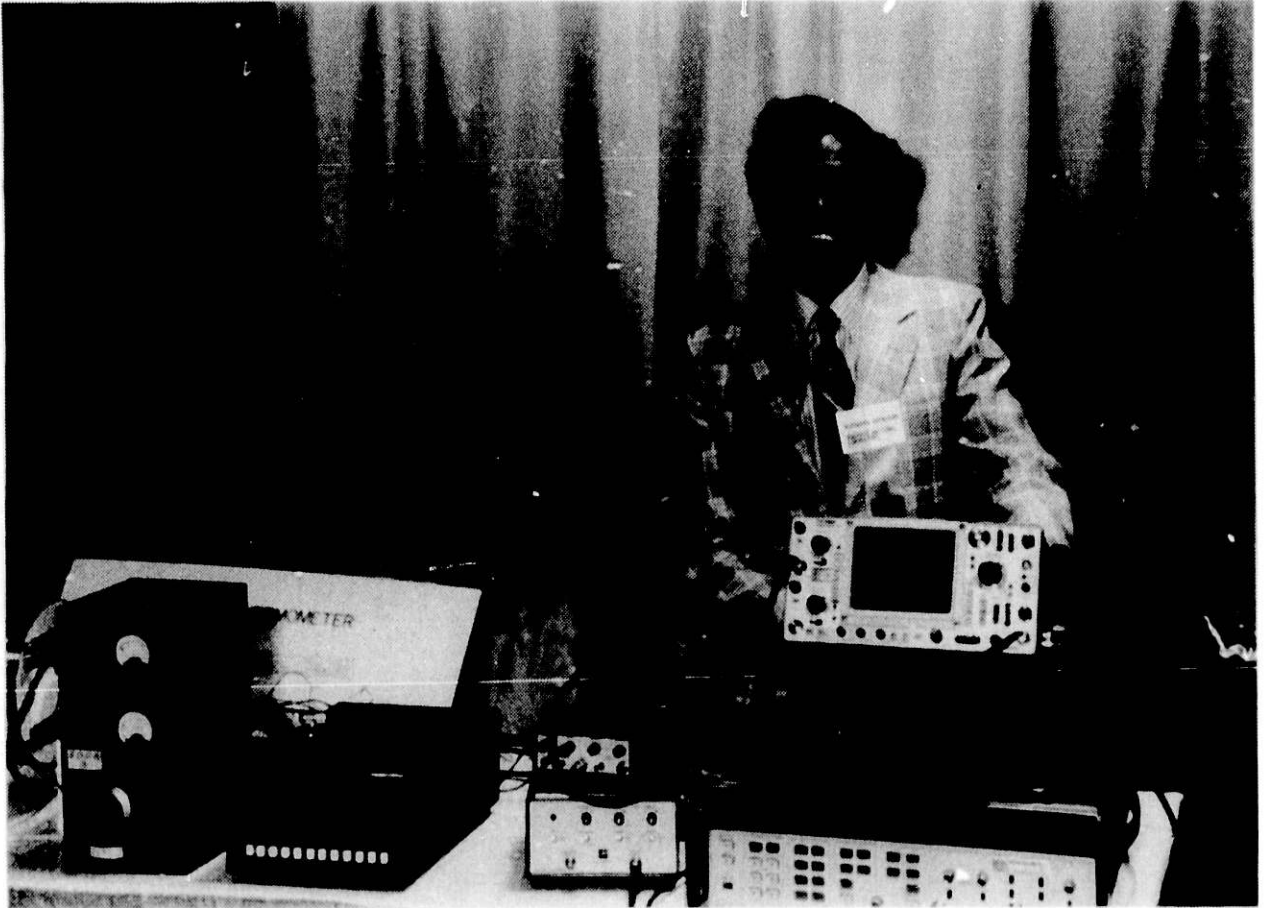


TRW Space and Technology Group  
Redondo Beach, California

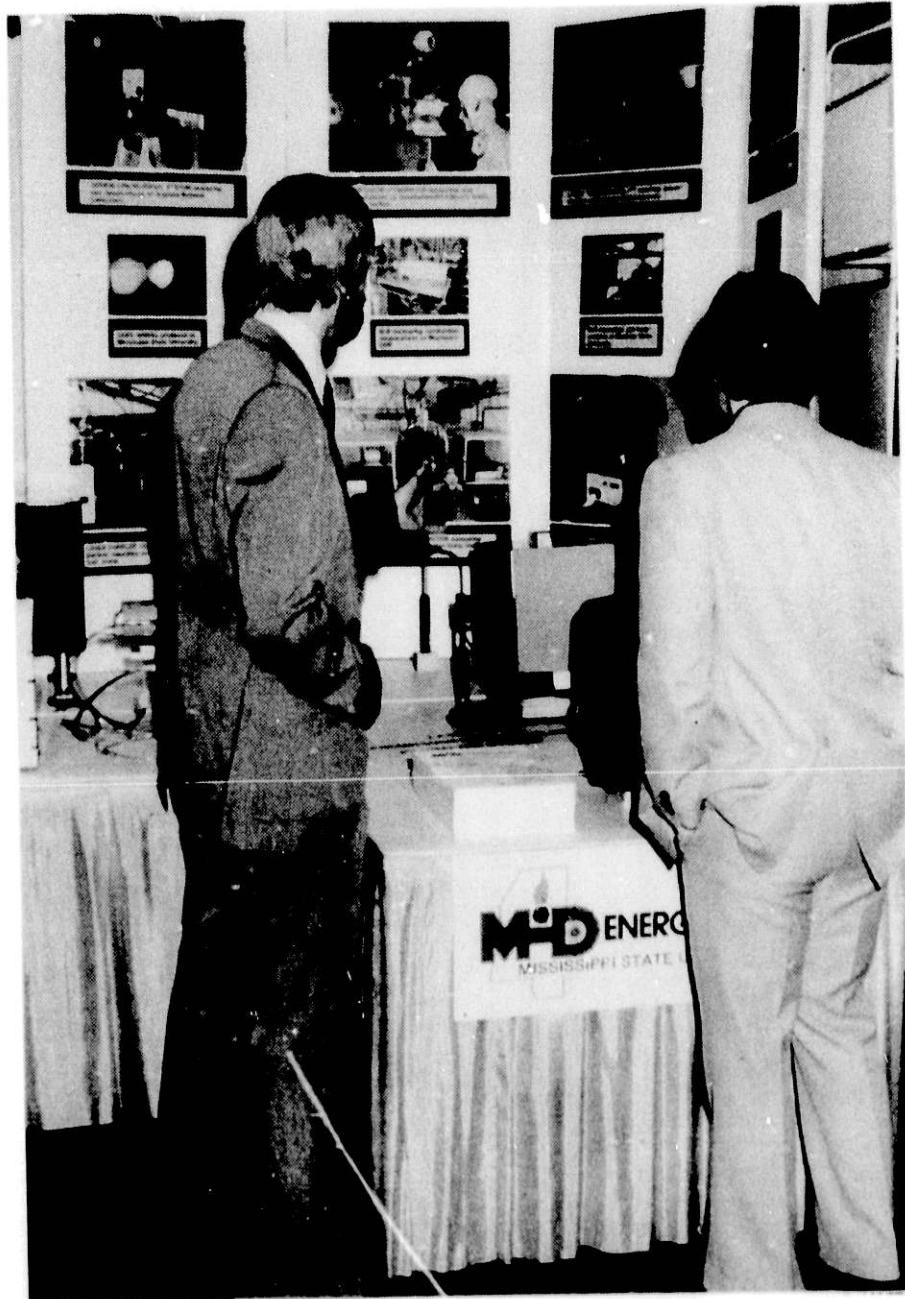


Los Alamos National Laboratory  
Los Alamos, New Mexico

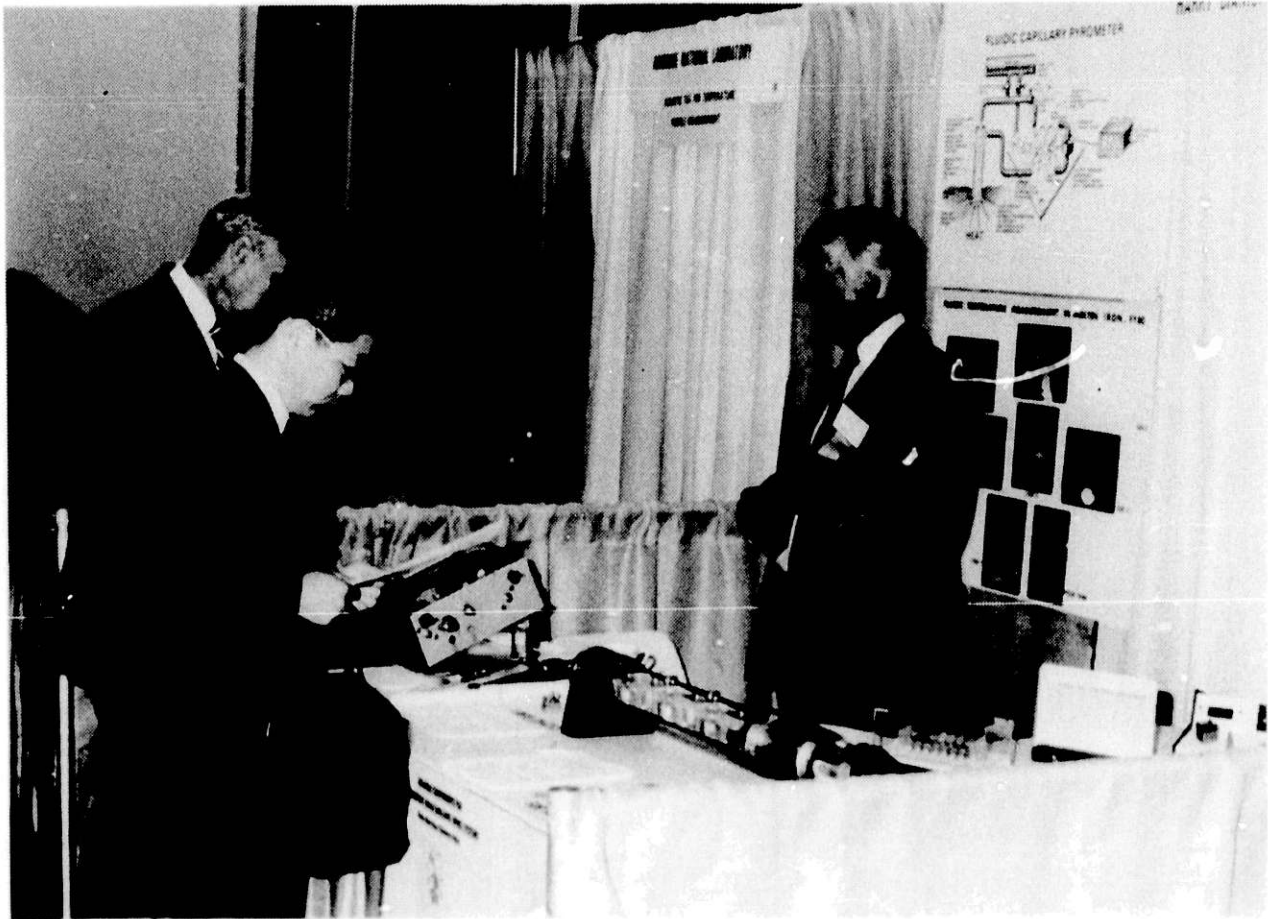




Argonne National Laboratory  
Argonne, Illinois



Mississippi State University  
Mississippi State, Mississippi



Harry Diamond Laboratory  
Adelphi, Maryland

## MICROWAVE BED-LEVEL DETECTORS

Donald M. DeLauder and Constantine A. Balanis  
Department of Electrical Engineering  
West Virginia University  
Morgantown, W.Va. 26506

### Abstract

This paper describes the design, testing, and evaluation of two candidate microwave systems for detection of bed-levels in fluidized-bed combustors. While both systems are microwave radars, two different schemes of operation are used: frequency-modulated continuous wave(FM-CW) and short-pulse time-domain methods. Testing was performed in a laboratory environment on static targets of metal, limestone, and coal.

### Introduction

The process of fluidized-bed combustion is a technique for burning coal which is high in sulfur content without releasing excessive pollutants into the atmosphere. The fluidized-bed combustion system also presents certain economic advantages over conventional combustion and power generation schemes<sup>1</sup>. The fluidized-bed combustor is essentially an upright, enclosed chamber which allows for the introduction of granular solid fuel and air into the bottom of the chamber. The granular solids are typically high-sulfur coal and limestone(mixed). These solids rest initially on a perforated plate. During operation, air is blown through the perforations creating a turbulent mixture of air and granular solids which behaves as a fluid.

Two major constraints limit the design of a radar level detector for fluidized-bed combustors. First, the temperature within the chamber during operation can reach levels of about 800°C. Clearly, any instrumentation must be protected from this hostile environment. Secondly, the combustors can be as small as 0.1 m<sup>2</sup> in cross-sectional area and two meters in depth. To remain unobtrusive, the level detector must be considerably smaller than these dimensions.

The objective of this effort is to investigate a frequency-domain system and a time-domain system for bed-level detection in a fluidized-bed combustor. The results of a wide range of laboratory measurements are presented.

### System Design

The system designs are presented in this section along with the equations required to determine the measured target range for each of the radar schemes.

#### Frequency Modulated - Continuous Wave(FM-CW) Radar

An FM-CW system uses a continuous signal which is swept in frequency<sup>2</sup>. The target will reflect some of the signal which is incident upon it. Since

the radar signal is frequency modulated, the frequency of the transmitted and reflected signals at the detector will be different at a given instant. Therefore, if these two signals are mixed and detected, the resulting beat frequency will be proportional to the target distance. If the signal is modulated linearly, the range equation is<sup>2,3</sup>

$$R = \frac{cf_b}{2f_s} \quad (1)$$

where

$R$  = target range(m)

$c$  = speed of light(m/s)

$f_b$  = beat frequency(Hz)

$f_s$  = sweep rate(Hz/s)

In Figure 1, the design of the FM-CW radar is shown in block diagram form. The signal source operates in the range of 7.0-12.4 GHz. A three port circulator is used to couple the output of the signal source to the horn antenna through ports 1 and 2. From the antenna the frequency-swept signal is transmitted toward the fuel bed where it undergoes a reflection (and transmission). Part of the reflected signal which is directed toward the antenna is coupled to the mixer through ports 2 and 3 of the circulator. At the mixer, the reflected waveform is heterodyned with the reference signal. The reference signal is obtained through a 10-dB directional coupler and variable attenuator combination. The variable attenuator is adjusted so that very strong reference signals do not mask very weak returns. The bandpass filter rejects signals with beat frequencies outside the range of interest.

In making measurements, the actual target distances are referenced to the antenna aperture. The range equation given previously, however, references the target distance to the difference in path lengths for the reference and reflected signals. To reference the bed distance to the aperture, the following modified range equation is used

$$h = R + (\ell_3 - \ell_1 - \ell_2)/2 = R - \ell_{FM} \quad (2)$$

The reference lengths are shown in Figure 1. Since the actual target distances are small, it is rather important to correctly account for these distances.

### Short-Pulse Radar

Another method for bed level detection which has been studied is the short-pulse radar system. This scheme uses the time separation between transmission and reflection of a short microwave pulse as a measure of the distance to the target<sup>4,5</sup>.

To measure small distances with a short-pulse radar, the width of the pulse must be small to maintain resolution and the pulse repetition rate must be chosen to prevent range ambiguity. The pulse generator was designed using a step-recovery diode circuit<sup>6,7</sup> which achieved a pulse width of 1.8 ns with a 50 MHz repetition rate (this repetition rate allows for distance measurements of up to about three meters). The short-pulse generator is used as the input device to the radar system. The block diagram of the entire system is shown in Figure 2. The pulses are amplified by a traveling wave tube (TWT) amplifier with a 7.0-12.4 GHz passband. A single horn antenna is used for both transmission and reception. Some of the power in the transmitted pulse leaks through the circulator and is used as the time reference. The reference and reflected pulses are sensed by a square-law detector and displayed on a sampling oscilloscope, since it is designed to accurately measure time differences. For this system, the target distance is related to the round-trip travel time by<sup>5</sup>

$$R = \frac{c\Delta t}{2} \quad (3)$$

where

$R$  = target range (m)

$c$  = speed of light (m/s)

$\Delta t$  = time separation of reference and reflected pulses (s)

Once again, to reference the target range to the aperture, the range equation must be modified to include the reference lengths (as shown in Figure 2). The range equation then becomes

$$h = R + (\ell_1 - \ell_2 - 2\ell_3 - \ell_4)/2 = R - \lambda_{SP} \quad (4)$$

### Results

To initially assess the performance of the two radar systems, measurements were made in a laboratory environment using metal, limestone, and coal targets. The metal targets were flat plates of aluminum, while the others were boxes of limestone sand or coal chunks. Further measurements were made with rough (corrugated) surfaces and with each bed enclosed by a simulated chamber. Additionally, the operation of the two systems was tested with the antenna covered by a thermal protective dielectric material. The results of these tests are described separately for the two systems.

#### FM-CW System

Results of measurements on limestone and coal beds, for both smooth and rough surfaces are shown in Table 1. The FM-CW system appears to perform well for any of the targets shown here. Similar results were obtained at other target distances. An example of the display of the beat signal is shown in Figure 3. The distance is determined by averaging the frequency of the beat signal for up to 30 cycles to provide some immunity from unwanted

signals.

In addition to testing on open beds, enclosures were built to simulate the walls of a fluidized-bed combustor. The enclosures were made of metal with square cross-sectional areas of 1' x 1' (0.91 m x 0.91 m), 2' x 2' (1.82 m x 1.82 m), and 3' x 3' (2.73 m x 2.73 m). The use of the enclosures did not appear to significantly degrade the accuracy of the measurements, regardless of the enclosure size, as shown in Table 2.

To provide thermal protection for the radar system antenna, the aperture was covered with a high grade dielectric material, which is transparent electrically at the radar frequencies up to about 2192°C. The material used was 1.11 cm thick All Silica (LI-1500), manufactured by Lockheed<sup>8</sup> as a candidate thermal protector for the NASA Space Shuttle. The average error using this cover with the FM-CW system was 1.4%, which is within the typical error range of the system without the cover.

#### Short-Pulse Radar System

Measurements using the short-pulse radar system concentrated primarily on metal and limestone targets, as the return from the coal targets proved to be too weak to be detected with the available equipment. In Figure 4 a typical display of the reference and reflected pulses for a metal target is shown. The strength of the response from limestone beds was always at least 4 dB below the intensity of the metal reflected signal. Data from measurements of smooth metal and limestone targets are shown in Table 3. These measurements were taken over a range of distances from 0.66 m to 1.49 m and indicate an average error of about 2%. Surface roughness did not appear to increase the measurement error as long as the surface provided a signal reflection which was strong enough to be displayed on the oscilloscope.

Experiments were also performed with the short-pulse radar system using targets surrounded by the metal enclosures. Results of these tests are shown in Table 4 and indicate that the enclosures have very little effect on the accuracy of the target range measurement. It was also noted that for the smallest enclosure the intensity of the reflected signal was larger than that from the same surface when it was not enclosed. This may be attributed to a waveguiding effect created by the metal enclosure.

The dielectric cover was also used in conjunction with the short pulse radar system. For this system the cover had no noticeable influence on the reflected pulse, thereby causing no change in the range accuracy.

#### Conclusions

Two microwave radar systems have been designed and tested for use as bed-level detectors in a fluidized-bed combustor. The systems were evaluated in the laboratory using static metal, limestone, and coal beds as experimental targets. Results of the experiments indicate that the FM-CW system achieves an average measurement error of 1.8%, which is slightly better than the 2.0% average error for the short-pulse radar. Furthermore, the returns from coal targets and from some rough limestone targets were not intense enough to be detected by the short-pulse radar, as it is presently

configured. Additional signal strength is needed to achieve detection. Tests using metal enclosures to simulate chamber walls indicate that the performance of both systems is not significantly changed by the enclosures. Also, the dielectric thermal protector placed over the aperture of the antenna did not degrade the performance of either radar scheme.

#### Acknowledgement

This work was supported by the Department of Energy, Morgantown Energy Technology Center under Contract No. DE-AC21-79ET15158. The authors would like to thank Mr. Dana Hewitt, Technical Project Officer, and Mr. Arthur Hall, both of Morgantown Energy Technology Center, for their interest and support of the project.

TABLE 1. FM-CW Average Measurement Errors

	COAL		LIMESTONE	
	Smooth	Rough	Smooth	Rough
Actual height(m)	1.917	1.917	1.829	1.829
Measured height(m)	1.890	1.862	1.803	1.839
% error	-1.41	-2.87	-1.42	0.55

TABLE 2. FM-CW Measurements with Enclosures

enclosure	actual range(m)	measured range(m)	% error
0.91m x 0.91m	1.524	1.487	-2.43
1.82m x 1.82m	1.524	1.481	-2.82
2.73m x 2.73m	1.829	1.785	-2.41

TABLE 3. Short-Pulse Average Measurement Errors

a. Metal Target

actual distance(m)	measured distance(m)	% error
0.660	0.658	-0.30
0.749	0.732	-2.27
0.846	0.808	-4.49
0.953	0.912	-4.30
1.011	1.011	0.00
1.077	1.062	-1.39
1.125	1.107	-1.60
1.168	1.153	-1.28
1.207	1.153	-4.47
1.260	1.227	-2.62
1.318	1.273	-3.41
1.356	1.346	-0.74
1.397	1.392	-0.36
1.445	1.438	-0.48

b. Limestone Target

actual distance(m)	distance(m)	% error
0.775	0.793	2.32
0.826	0.823	-0.36
0.892	0.897	0.56
0.963	0.958	-0.52
1.052	1.046	0.57
1.100	1.092	-0.73
1.143	1.138	-0.44
1.214	1.227	1.07
1.252	1.273	1.68
1.303	1.318	1.15
1.361	1.361	0.00
1.420	1.406	-0.92
1.486	1.511	1.68



TABLE 4. Short-Pulse Measurements with Enclosure Effects

enclosure	target	actual range(m)	measured range(m)	% error
none	metal	1.537	1.511	-1.69
0.91mx0.91m	metal	1.537	1.511	-1.69
none	limestone	1.537	1.542	0.33
0.91mx0.91m	limestone	1.537	1.542	0.33
none	metal	1.092	1.062	-2.75
1.82mx1.82m	metal	1.092	1.077	-1.37
none	limestone	1.092	1.046	-4.21
1.82mx1.82m	limestone	1.092	1.046	-4.21
none	metal	1.257	1.242	-1.19
2.73mx2.73m	metal	1.257	1.242	-1.19
none	limestone	1.257	1.242	-1.19
2.73mx2.73m	limestone	1.257	1.242	-1.19

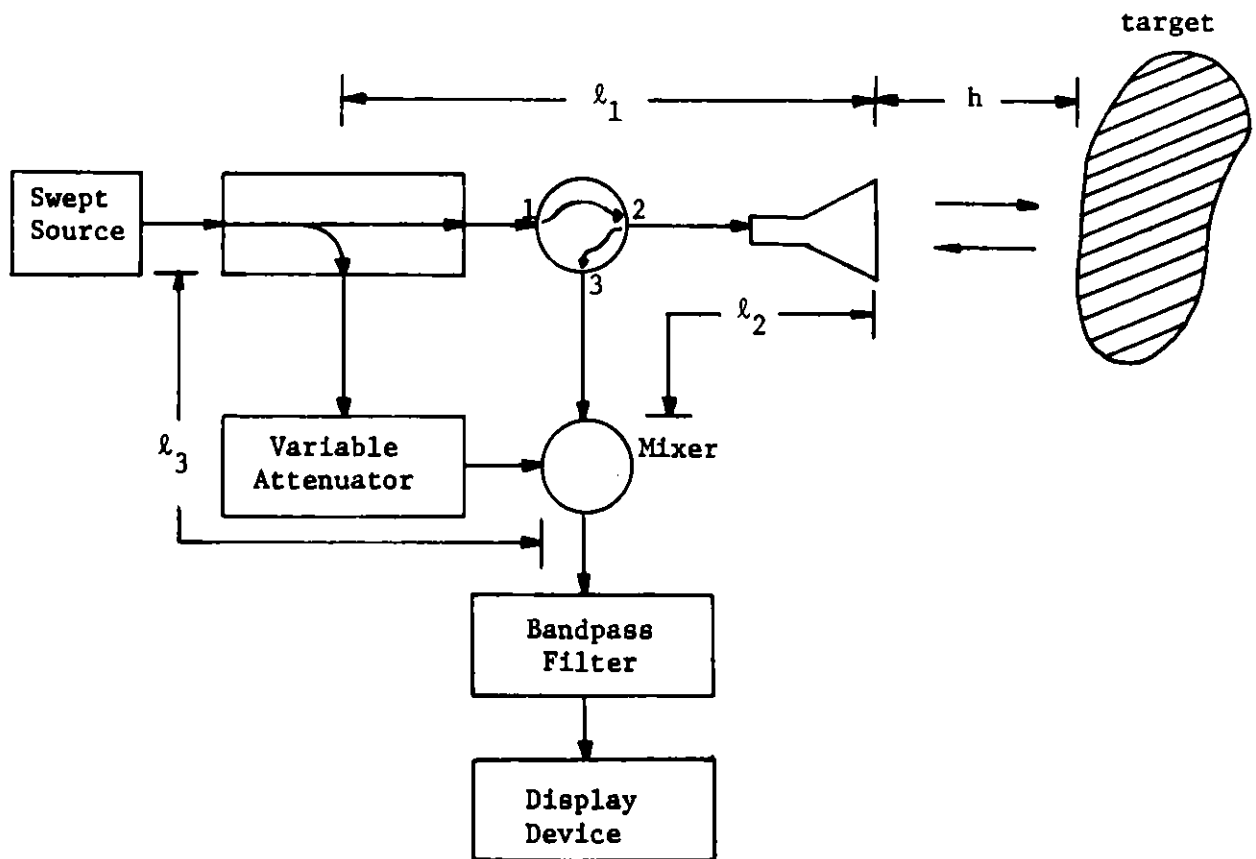


Figure 1. Block diagram of FM-CW radar

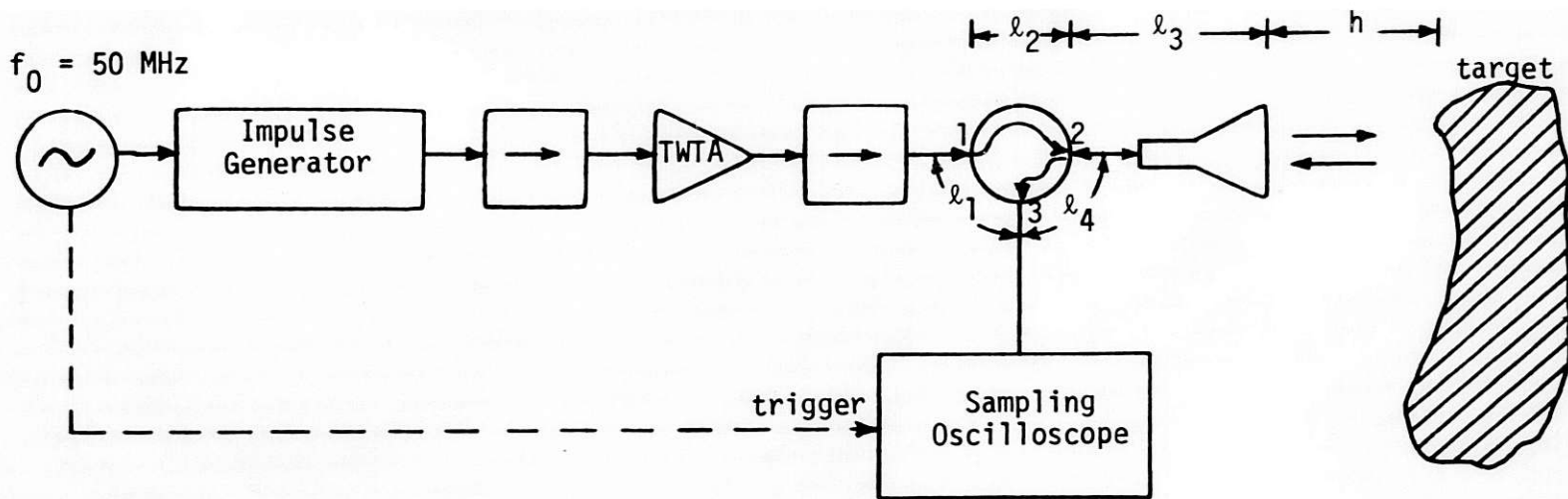


Figure 2. Block diagram of short-pulse radar



Figure 3. Typical FM-CW display

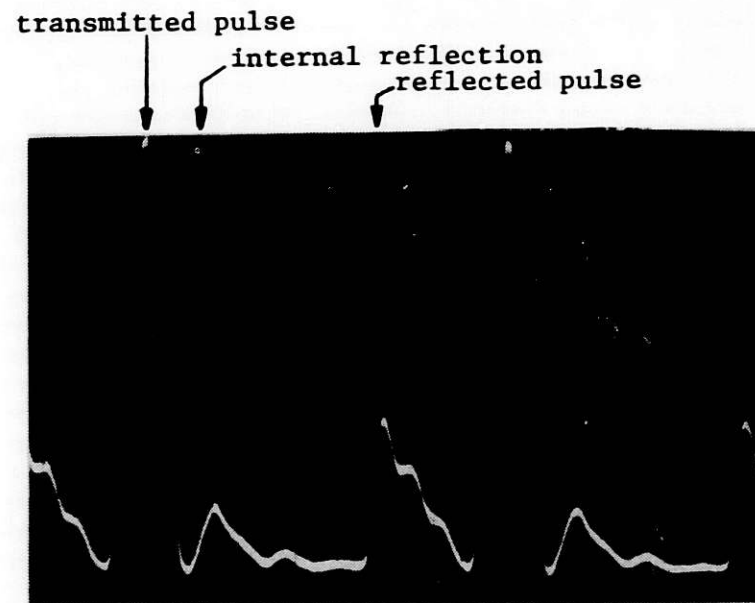


Figure 4. Typical short-pulse display

References

1. Fenelly, P.F., D.F. Durocher, H. Klemm, and R.R. Hall, "Preliminary Environmental Assessment of Coal-Fired Fluidized-Bed Combustion Systems," Contract No. 68-02-1316, Task No. 15, Prepared for the U.S. Environmental Protection Agency, Washington, D.C.
2. Skolnik, M.I., Introduction to Radar Systems, McGraw-Hill, New York, 1962.
3. Balanis, C.A. and J.R. Powell, "Fluidized-Bed Microwave Monitoring System," Annual Report 1980, Contract No. DE-AC21-79ET15158, prepared for the U.S. Department of Energy, Washington, D.C.
4. Chudobiak, W.J., R. Gray, and J.S. Wight, "A Nanosecond Impulse X-Band Radar," Proc. IEEE, vol. 66, no. 4, pp. 523-524, April 1978.
5. Balanis, C.A. and D.M. DeLauder, "Microwave Short-Pulse Bed-Level Detector," Annual Report 1981, Contract No. DE-AC21-79ET15158, prepared for the U.S. Department of Energy, Washington, D.C.
6. Hamilton, S. and R. Hall, "Shunt-Mode Harmonic Generation Using Step-Recovery Diodes," Microwave Journal, vol. 10, no. 4, pp 69-78, April 1967.
7. Siegal, B., "Simpler Digital Circuits in a Snap," Electronics, pp. 105-108, June 9, 1968.
8. Gilreath, M.C., and Castellow, S.L., Jr. "High Temperature Dielectric Properties of Candidate Space Shuttle Thermal-Protection and Antenna Window Materials," NASA TND-7523, National Aeronautics and Space Administration, Washington, D.C.

MENISCI LEVEL SENSING & SURFACE TENSION MEASUREMENT USING ALASER BEAM OPTICAL LEVER EFFECT

Paul Longrigg

Solar Energy Research Institute

Golden Colorado 80401

303/231-1000

Abstract

This paper describes the use of a laser beam optical lever effect to calibrate scientific volumetric glassware, thereby eliminating the use of mercury for this purpose.

The paper also discusses the use of the optical lever effect to make non-contact surface tension measurements of liquids.

Mercury Substitution in Calibration of Scientific Volumetric Glassware

Up until fairly recently mercury was used as the production calibration medium for scientific glassware. It was used because it afforded the calibration operator a conspicuous meniscus by which to mark the glassware. A typical manual calibration operation using mercury would initially involve a metered quantity of mercury being inserted into the 'ware. The operator would then mark, invariably with a small paint brush, the level at which the mercury resided.

Mercury, with its low vapor pressure and known handling and containment difficulties, resulted in one glassware plant losing about 300 pounds of the element annually to the general environment.

With the well known and proven hazards of mercury to all life, a substitute for this element in the glassware calibration role has been sought. This has almost universally come down in favor of water, or a mixture of water and alcohol.

But there is a problem in the use of water for this purpose, particularly where a large number of vessels have to be calibrated manually. The water meniscus lacks the conspicuity of the mercury meniscus, and as a consequence can cause eyestrain and loss of accuracy. Coloring pigments cannot be used because of solubility problems, and menisci distortion.

The recommended N.B.S. method of meniscus level determination is shown in Figure 1, and their procedure using a trained 'eyeball' is given as follows:

"On some graduated neck vessels the lines are very short indeed, extending less than one-fourth the way around the neck. Under these circumstances, there is no reference line behind the meniscus to help the operator in

estimating the vertical position of the horizontal index plane. When faced with this problem, it is necessary for the operator to place his eye in his best estimate of the horizontal index plane while observing the meniscus. With experience, an operator should be able to judge the position of this plane to within one or two centimeters. The operator's eye will be (perhaps) twenty-five centimeters in front of the short index line while the center of the meniscus will be only one centimeter behind this line (for a two centimeter neck on the vessel). The geometry of this situation dictates that the vertical position error of the meniscus will be only one twenty-fifth of the operator's error in estimating the position of the horizontal index plane." Ref. 1.

With all due respect to the N.B.S., this 'eyeball' method of calibration is hardly conducive to accuracy in a production situation involving perhaps thousands of vessels daily. In such an environment, the technique outlined above could easily lead to operator eyestrain, fatigue, and a loss of all important accuracy.

#### Helium-neon Laser

The technique described in this paper uses the excellent collimation properties of helium-neon (He-Ne) visible laser light, and the bending of that light at the meniscus. In this way, it is possible to sense incremental volume changes of liquid in a small vessel (<100 ml) or container to the order of 0.001% or better accuracy. Menisci located by the laser must be concave in shape; that is, the liquid must wet the inside surface of the container vessel, which in this case is borosilicate KG-33 glass.

Before proceeding to the meniscus-seeking position, the calibration operator accurately charges the vessel with deionized water. Metering of the water is done by a precision liquid dispenser, with exit tips fabricated from either teflon or vinyl, to eliminate the wetting-adhesion problem.

When laser light propagates through a homogeneous (translucent liquid) medium, it does not normally deviate from a straight-line path. However, the two-phase (liquid-air interface) fluid meniscus allows bending of the light beam. This gives rise to what may be termed an optical level effect. Figure 2 shows an analytical diagram of the effect.

The ray of red, collimated laser light directed into the curved upper segment of the concave meniscus will bend toward the bulk fluid for much the same reason that light is bent toward the thicker regions of a convex lens. Bending also depends on the fact that the laser-beam diameter is smaller than the meniscus height. Also, the effective refractive index of a curvilinear profiled surface increases with progression into the thicker regions of a material; and light tends to move in this direction when going from one homogeneous medium to another. Figures 3 and 4 show the optical lever effect propagating in lubrication oil. Oil is used for photographic effect, and the beam bending is seen much better in color reproduction.

#### Voltage Signals Liquid Level

The output from a silicon photovoltaic cell is used to sense the

meniscus. This signal is a steep voltage change that is generated when the He-Ne laser beam is deflected out of the sensor field-of-view by the meniscus. This signal is shown in Fig. 5.0.

The sensor is arranged to traverse vertically with the lower part of a folding mirror on the laser-beam director.

In terms of optical simplicity, it is better to sense the meniscus with the laser held stationary while the glassware is moved in a vertical traverse. However, because of the problem of water movement, a laser-beam director was devised which allows both the laser and the glassware to remain in fixed positions while sensing is carried out. The director consists of a motorized array of mirrors, on lead screws, shown in Fig. 6.0.

When the meniscus detection signal is received, the traversing motor is stopped. This mirror-scanning system is of critical design, and heavy negative feedback is employed to reduce overshoot problems.

Once the lower edge of the meniscus has been located in the vessel, it is necessary to mark the glassware for subsequent scaling, if required. Two laser-marking techniques can be used. The first employs a CO<sub>2</sub> laser. The alternative method employs an aerosol-soluble plastic that is sprayed onto the outer surface of the glassware.

The use of CO<sub>2</sub> lasers, which produce infrared light, is predicated on the fact that glass is opaque to 10.6 micron radiation, the wavelength at which the CO<sub>2</sub> laser radiates. The laser beam is directed by infrared mirrors that automatically move into position on the motorized director when the meniscus is located. The laser beam makes indents or round marking holes in the glass. Permanent glassware marking of this type is a critical procedure, for the glassware must have the minimum of material removed, yet at the same time have a readily visible mark.

### Surface Tension Measurement

#### Surface Tension, Capillary and Gravitation

The calculation of surface tension  $\sigma$  from capillary rise measurements is generally made via the capillary constant 'a' defined--- Ref. 2, 3, 4.

$$a^2 = bh = 2\sigma / (g\Delta\rho)$$

Where b is the value of both principal radii of curvature ( $R_1$  &  $R_2$ ) at the base of the meniscus above a plane liquid surface directly connected to the capillary, g is gravitational acceleration,  $\Delta\rho$  is the difference in density of the two fluid phases, and h is the meniscus height.

At a non - horizontal gas - liquid interface, at point y cms below the highest point of the interface, the hydrostatic pressure is -:

$$P_H = g \cdot \rho \cdot y \quad (g \text{ cm}^2 \text{ sec}^{-2}) \quad (1)$$

where, g is the acceleration due to gravity, and  $\rho$  is the difference between the two densities of the two liquid phases. Ref. 5.0

This hydrostatic pressure is counteracted by a capillary pressure -:

$$P_c = -P_c' + \gamma(1/R_1 + 1/R_2) \quad (2)$$

where  $P_c'$  is the capillary pressure acting at the summit of the liquid phase,  $R_1$  and  $R_2$  are the major and minor axis of the menisci,  $\gamma$  is the surface tension.

The resulting equation,  $g \cdot \rho \cdot y = P_c$ , can be solved if one of the magnitudes  $R_1$ ,  $R_2$  is infinitely great. An example is shown in Fig. 7.0.

At the left of Fig. 7.0 is a vertical solid wall. At the extreme right the liquid surface is horizontal, thus here  $P_c' = 0$ . At any intermediate point such as  $P_2$  then -:

$$g \cdot \rho \cdot y = \gamma/R \quad (3)$$

$R$  being the radius of curvature in the plane of the paper in Fig. 7.0. The other radius is infinite because the profile of the surface perpendicular to the drawing is a straight line at any value of  $y$ ; in other words, the wall is flat!!

Let  $\theta$  be the angle which the liquid profile  $P_1.P_2.P_3$ , makes with the vertical at any point, as depicted in Fig. 7.0.

The radius of curvature at this point makes an angle  $\phi = \theta - (\pi/2)$  with the vertical. When this angle decreases by  $d\phi$ , the length of the curve  $P_1, P_2$  and  $P_3$ , starting at  $P_1$  must inevitably increase by  $dS$ ,  $S$  being the incremental length of the menisci profile, and  $dS/d\phi$  is equal to  $-R$ . However,  $-dS \cdot \sin\phi = dy$ , see Fig. 7.0. The minus sign is evident because  $y$  increases downward, while  $S$  increases upward. Ref. 6 & 7.

Hence, -:

$$g \cdot \rho \cdot y = \gamma \cdot \sin\phi \cdot d\phi/dy \quad (4)$$

On definite integration of the above equation between  $y = 0$  and  $y = y$  (for  $\phi = 0$  &  $\phi$  respectively), the following results:-

$$g \cdot \rho \cdot y^2 = 2\gamma \cdot (1 - \cos\phi) \quad (5)$$

If the gas liquid interface is tangential to the solid wall along the line of contact, that is, the left hand extremity of the liquid - gas profile in Fig. 7.0, is vertical, then the greatest value of  $\phi$  is  $\pi/2$  and similarly the value of  $\theta = \pi$ . Since then  $\cos\phi = 0$ , Eq5 can be transposed thus:-

$$y = (2 \cdot \gamma / g \cdot \rho)^{0.5} \quad (6)$$

$y$  being the vertical distance between the horizontal and vertical liquid surfaces.

The ratio  $2 \cdot \gamma / g \cdot \rho$  is called the Laplace capillary constant,  $a^2$ . Thus, if the value of  $y$  can be determined experimentally, then the surface tension of a liquid can be readily found.

The high collimation properties of laser light allows an accurate determination of  $y$ , and this will now be discussed.

### Measurement of Surface Tension Using Laser Light

Because surface tension influences every shape and every motion of liquid surfaces, many phenomena can be and have been used for its determination.

The more popular methods can be categorized into four main classes, namely, i) static methods independent of any solid, ii) static methods involving a solid, iii) dynamic methods involving a solid, and iv) dynamic methods independent of any solid.

In theory and in practice those of class, (i), are preferable to the rest, and coincidentally the laser light method is best suited to this technique.

Fig. 8.0, like Fig. 7.0, represents a liquid meniscus. If a horizontal beam of light  $L_1P_1$  strikes the liquid surface, it will be reflected along a line  $P_1.O_1$ . If  $\phi_1$  is the angle (at point  $P_1$ ) between the horizontal and the radius of curvature, the angle  $L_1.P_1.O_1$ , will be  $2\phi_1$ .

If now the laser light beam is raised, but remains truly horizontal to its previous position, i.e., maintains parallelism, by  $z$  cm., the new angle  $L_2.P_2.O_2$  will be equal to  $2\phi_2$ .

Let  $h$  be the (unknown) depth of point  $P_1$  below the horizontal surface, then the depth at  $P_2$  is  $h - z$ .

As each angle  $\phi$  here is equal to  $\pi/2 - \phi$  in Fig. 7.0, it follows from Eq 5 that:-

$$y^2 = a^2 (1 - \cos\phi_1) \quad (7)$$

and -:

$$(y - z)^2 = a^2(1 - \sin\phi_2) \quad (8)$$

From these two equations #s 7 and 8, the two unknowns,  $y$  and  $a^2$ , can be determined, and from  $a^2$ , Laplace capillary constant, surface tension can be calculated.

This curvature profile method has been little used because the value of  $y$ , is difficult to measure with any precision using polychromatic light sources.

The total height of a meniscus is usually less than  $a$ , which for water is about 0.37cm, thus  $y$  will be less than 0.1 cm. To measure this, with say a precision of  $\pm 0.5\%$ , the vertical thickness of the light beam needs to be less than 10 microns thick.

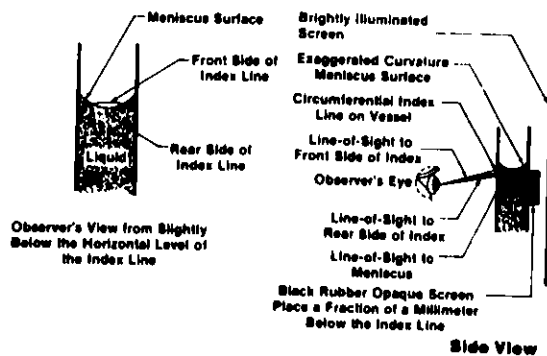
This is difficult and expensive to do with polychromatic sources but relatively easy with lasers operating at visible wavelengths.



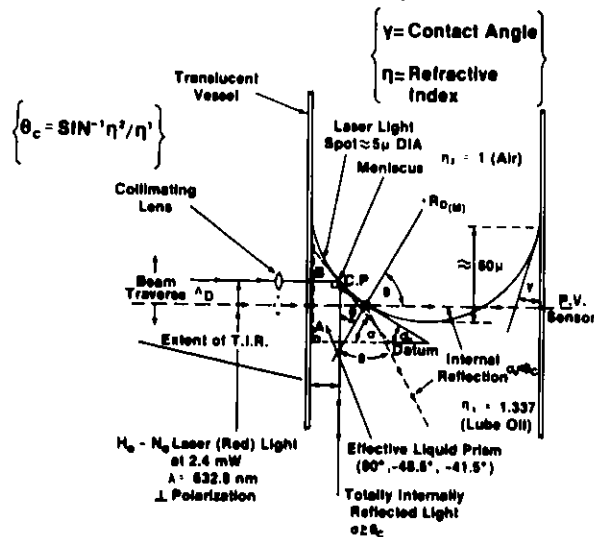
## References:

1. Lembeck, J. "The Calibration of Small Volumetric Laboratory Glassware" N.B.S. Overlap. October 1974. No. 7.
2. Sugden, S.J. Journal of the Chemical Society. 119,1483.1921.
3. Adam, N. K. "The Physics and Chemistry of Surfaces" 3rd Ed. pp. 363-372 Oxford University Press. Oxford 1941.
4. Adamson, A.W. "Physical Chemistry of Surfaces" 2nd Ed. pp. 9-18. Interscience Publishers. New York. 1967.
5. Matijvić, E. "Surface & Colloid Science" Vol. 1, Wiley Interscience. 1969. pp. 113.
6. Princen, H.M. Contact Angles & Transition Region's in Soap Films. J. Phys. Chem. Vol. 72 No. 9. Sept. 1968. pp. 3344.
7. Biery, J. C. "Some Mathematical Characteristics of Menisci and Their Use in Determination of Surface Tension" J. Am. Institute of Chemical Engineers, Vol. 16, No. 5. Sept. 1970. pp. 787.

**Figure 1. N.B.S. Method of Menisci Position Determination**



**Fig. 2. Oil and Air Meniscus Acting as a T.I.R. Prism**



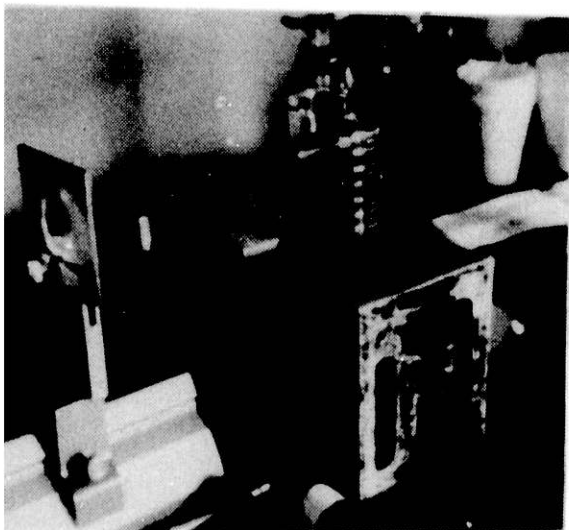


FIG. 3.

FIGURE 1. MENISCI SEEKER SIGNAL

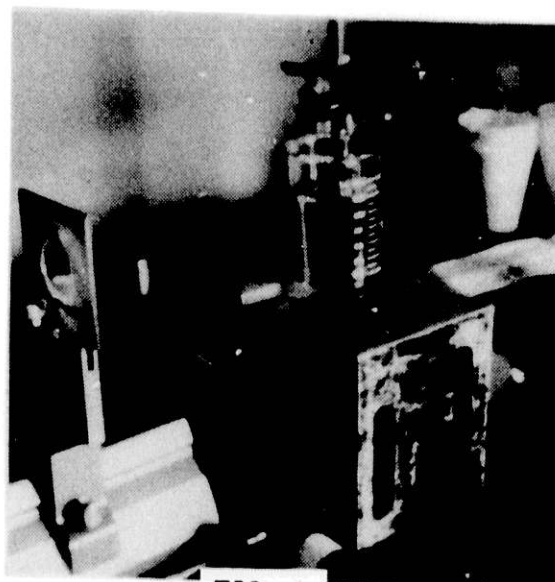


FIG. 4.

Figure 6. Laser Beam Director

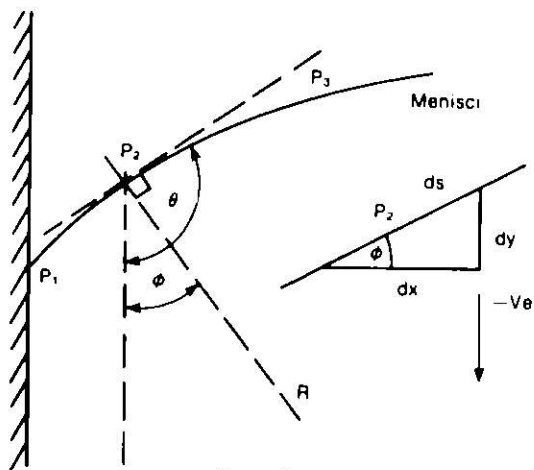
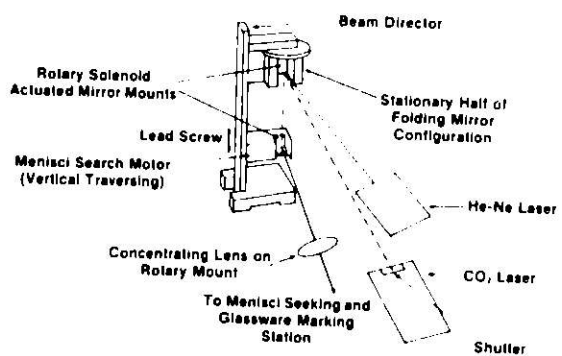
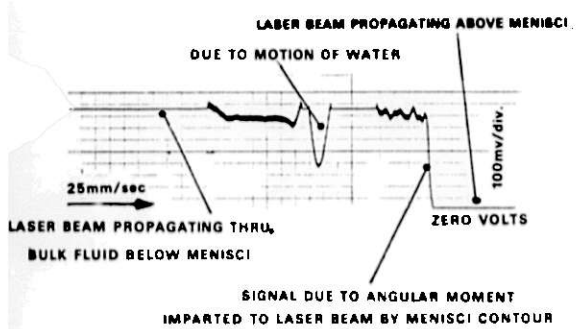


FIG. 7

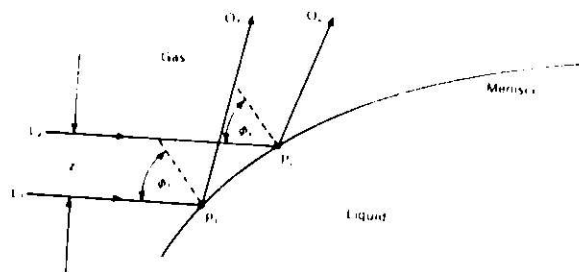


FIG. 8

LEVEL MEASUREMENTS FOR HIGH TEMPERATURE COAL SLURRIES

N. Gopalsami and A. C. Raptis

Argonne National Laboratory

Components Technology Division, Bldg. 308

Argonne, IL 60439

312/972-5925

FTS: 972-5925

Abstract

The problem of slurry level measurement in the high pressure separators of coal liquefaction systems is addressed in this paper. Besides high pressure, the separator vessel environment is hostile and at high temperature. A survey is made of the level measurement methods and devices that may be applicable to continuous slurry level service. The survey includes displacement, differential pressure, capacitance, electrical TDR, microwave, nuclear, and acoustic devices. Judging from the capabilities and limitations of these devices, the acoustic sensor holds promise in meeting the application requirements since it is nonintrusive, intrinsically safe, easily adaptable to high pressures and temperatures, and fairly accurate.

The method of acoustic pulse-echo measurements is further investigated with regard to its feasibility in slurry level service. This entails the computation of attenuation in the slurry and vapor (gas) spaces of the separator vessel and estimation of the possible measurement ranges. With limited data available on the density, viscosity, etc. of slurries from the SRC-I pilot plant at Wilsonville, Alabama, the estimated measurement range using 100 kHz in 25 wt% coal slurry is about 2.5m. Much higher ranges are found to be possible with vapor or gaseous media. Finally, a measurement scheme is proposed for echo-ranging from the top of the vessel.

## INTRODUCTION

Instrumentation deficiency has been reported for high temperature slurry level measurements in coal liquefaction systems [1]. The instrumentation need is in particular greater in the high-pressure separator vessels, where high pressures (1500 psig) and temperatures (550°F) together with plugging, corrosive and coking nature of slurries create problems for the use of conventional level sensors.

Figure 1 shows a flow diagram of the high pressure separator stage. The primary liquefaction reaction occurs in the reactor or dissolver where coal particles are dissolved in a process solvent in the presence of hydrogen at elevated temperature and pressure. The dissolver effluent consisting of coal slurry, gases and vapors goes to the high pressure separator. At this vessel, the entrained gases and vapors are separated from the slurry.

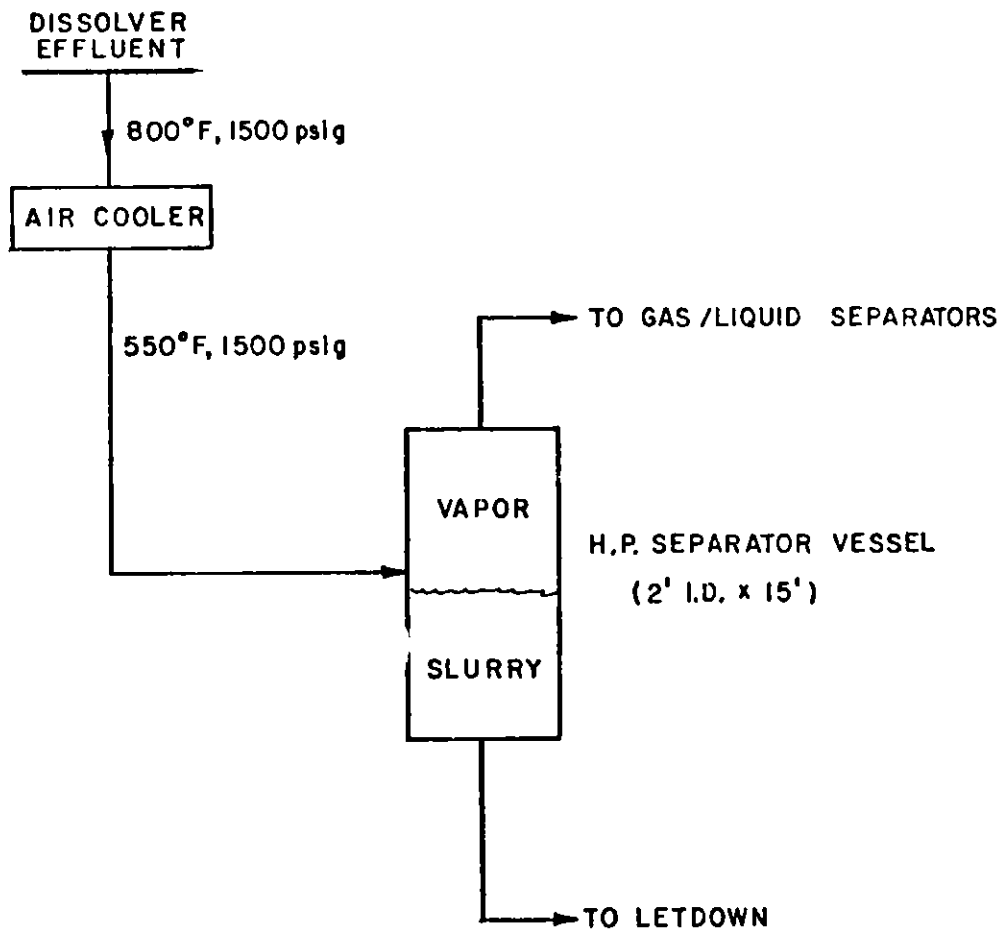


Fig. 1. Flow Diagram of the High Pressure Separator Stage.

The measurement and control of slurry level in the separator vessel are critical to the safe and efficient operation of the process and can significantly enhance product quality. This paper makes an assessment of the applicable slurry level measurement methods and further evaluates the feasibility of a promising acoustic pulse-echo system.

#### SLURRY LEVEL MEASUREMENT METHODS

A wide variety of level measuring devices is available to meet the diverse level requirements of the process industries. These devices range from simple mechanical types such as dipsticks, sight glasses and floats to the more sophisticated types such as microwave, nuclear and ultrasonic sensors. An overview of various level sensors and their applications can be found in some recent survey articles [2,3].

Table I gives the various measurement methods that are applicable to hot slurry level service, together with their working principles, capabilities and limitations. These methods can be classified as either intrusive or non-intrusive types. Among the intrusive types are the displacement, differential pressure, capacitance, electrical time-domain reflectometer and some versions of acoustic sensors. These intrusive sensors in general suffer the disadvantages of plugging, corrosion, etc., caused by the measuring materials. On the other hand, the nonintrusive sensors as the name implies are best suited to intractable materials and hostile environments. Microwave, nuclear and most acoustic sensors belong to the nonintrusive types. Among them, nuclear devices are rather expensive but largely used in applications where standard techniques prove to be inadequate. Acoustic devices are less expensive, more accurate and intrinsically safe. Other advantages which are not necessarily unique to acoustic devices include: no moving parts, easy to install and fast response times. In view of these potentials, the feasibility of acoustic sensors for the slurry level measurements is next investigated.

Table I

## Level Measurement Methods for Slurries

SENSOR TYPE	PRINCIPLE	CAPABILITIES	LIMITATIONS
Displacement	Archimedes	Good for clean liquids and interface level of liquids	Intrusive; not suitable for dense slurries
Differential Pressure	Hydrostatic Head	Widely used in cont. level applications; useful for large level changes, corrosive, viscous materials & slurries	Contacting; sensitive to density
Capacitive	Dielectric Change	No moving parts; compatible with vast range of liquids, powders and slurries	Intrusive; sensitive to temperature, particle size & moisture content
Electrial	Time-of-Flight	Insensitive to density, particle size, conductivity, permittivity of the measuring material	Intrusive; uneven coating of electrode can cause spurious reflections
Microwave	Attenuation Change	Nonintrusive; not affected by thermal gradients, dust, smoke, high-temp & press	Not suitable to water-based fluids or fluids with low dielectric values
Nuclear	Absorption Change	Nonintrusive; can be mounted on the vessel walls suitable to handle intractable materials	Sensitive to density changes
Acoustic	Time-of-Flight or attenuation	Nonintrusive Noncontacting fast response; fairly accurate	Not suitable to turbulent conditions and fluids containing foam; measurement range limited

### FEASIBILITY OF ACOUSTIC SENSORS

The most common technique for continuous level measurements is based on echo-ranging, in which the transit time of a sound pulse to and from the material surface is used as a level indication. The underlying principle is that when a traveling sound pulse encounters an abrupt change in the medium such as in the case of a vapor/slurry interface, part of the sound energy is reflected back. The success of the technique, however, depends on the feasibility of receiving the reflected pulse at sufficient strength so as to be detected. In other words it depends on the extent to which sound is attenuated in the vessel media. Hence, it is necessary to compute the attenuation values in the slurries and vapors and from which to estimate the possible measurement ranges in each medium for a given source power.

### ATTENUATION OF SOUND IN COAL SLURRIES

Attenuation of sound in solid-particle/liquid suspensions has been investigated in the past [4]. The absorption of sound in such a two-phase medium is attributed to four different mechanisms; 1) intrinsic absorption in the liquid, 2) viscous-drag, 3) thermal diffusion, and 4) scattering. Of these mechanisms, viscous-drag and scattering losses are generally dominant in dilute suspensions. For such cases, an explicit expression of attenuation is given by [4]:

$$\alpha = \frac{\epsilon}{2} \left[ \frac{k^4 a^3}{3} + k(\sigma-1)^2 \frac{s}{s^2 + (\sigma+\tau)^2} \right] \quad (1)$$

where,

$$s = \frac{9}{4\beta a} \left( 1 + \frac{1}{\beta a} \right), \quad \tau = 1/2 + \frac{9}{4\beta a}$$

$$\sigma = \frac{\rho'}{\rho}, \quad \beta = \left( \frac{\omega\rho}{2\eta} \right)^{1/2}$$

$$k = 2\pi/\lambda$$

The parameters in the above equations are defined as:

$\alpha$  = attenuation,  $\epsilon$  = particle concentration by volume,  
 $k$  = wave constants,  $\lambda$  = wavelength,  $a$  = particle radius,  
 $\rho'$  = particle density,  $\rho$  = liquid density, and  
 $\eta$  = shear viscosity of the liquid.

The main parameters of interest that affect the attenuation are frequency of sound, particle size, and temperature. The terms corresponding to frequency and particle size appear explicitly in Eq. 1, while the temperature variation affects attenuation implicitly through density, viscosity and sound velocity terms. Table II gives data on the temperature variations of density and viscosity of 25wt % slurry [5]. For a lack of data on sound velocity, its temperature variation is calculated from the relationship:

$$c = \frac{c_0}{(T/T_0)^{1/2}}$$

Table II

Variation in Density and Viscosity of Coal, Solvent  
 and 25 WT% Slurry with Temperature

TEMP (°F)	SP. GR COAL	SP. GR SOLVENT	VISCOSITY SLURRY (CP)	VOL. FRACTION OF COAL
100	1.4	1.0	63.1	0.183
200	1.4	0.955	19.05	0.176
300	1.4	0.912	8.71	0.169
400	1.4	0.870	6.31	0.163
500	1.4	0.820	12.6	0.155
600	1.4	0.772	39.8	0.147
700	1.4	0.720	4.5	0.139



where  $c$  is the sound velocity,  $T$  is the absolute temperature and the subscript  $o$  denotes some reference value.

Based on these data, the changes of attenuation on frequency, particle size and temperature are computed and plotted in Figs. 2a, b, and c. It can be seen that there are attenuation peaks at about a particle size of 0.001 cm and at temperature of 600°F. The attenuation loss increases with frequency and becomes dominant (with fourth power dependency) when the ratio of particle radius-to-wavelength is small. Using the worst case values, the maximum attenuation loss at 100 kHz is 0.26 dB/cm.

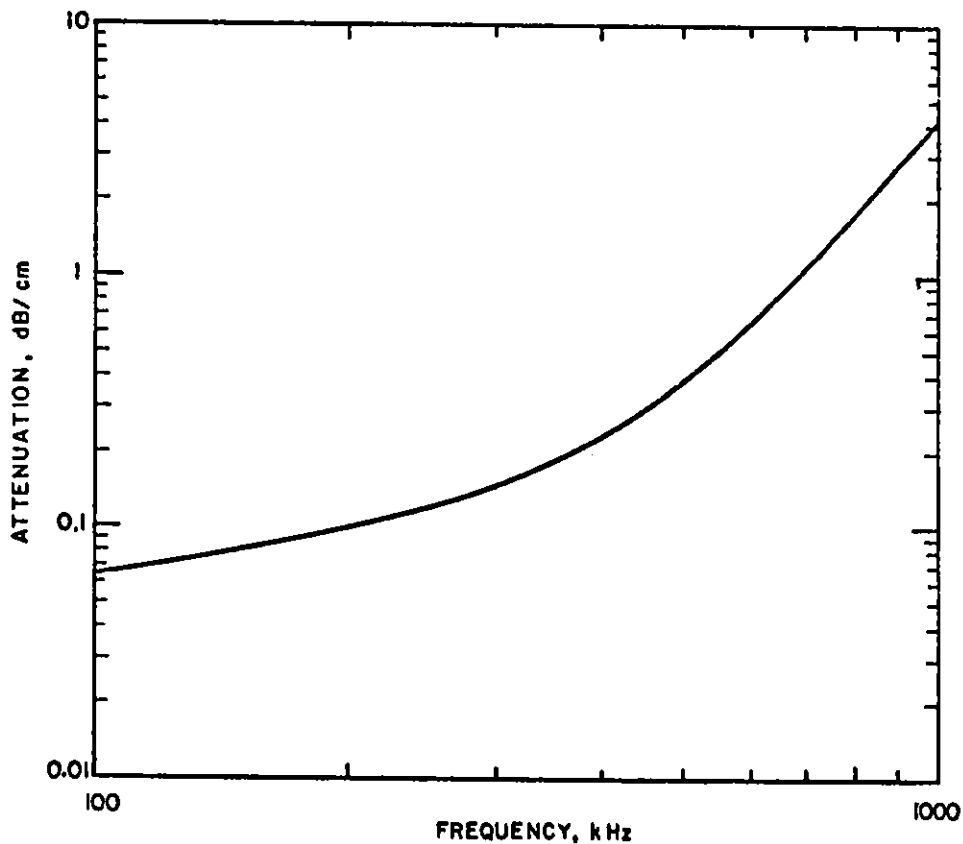


Fig. 2a. Variation of Attenuation with Frequency.

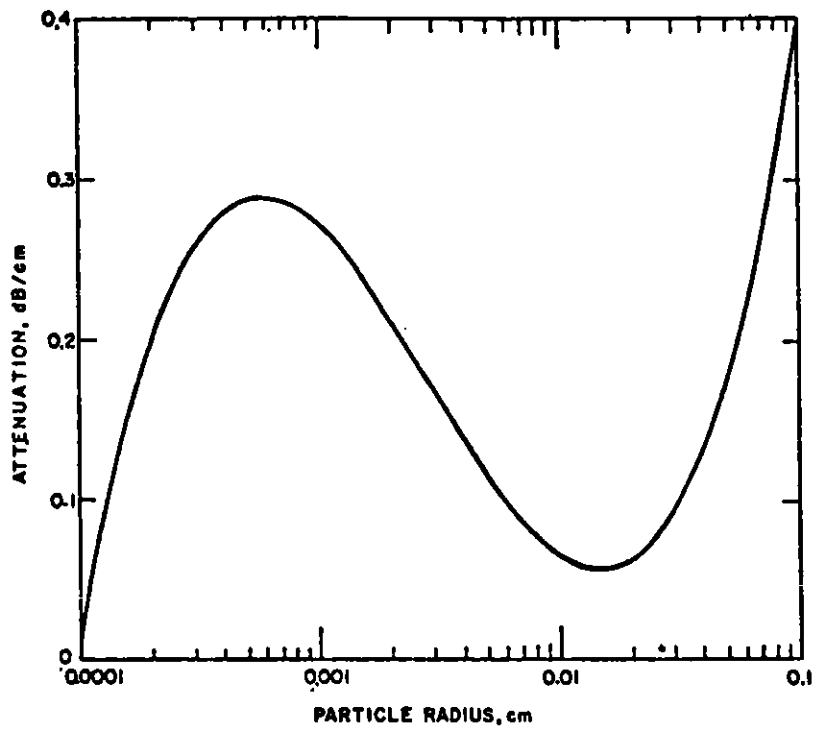


Fig. 2b. Variation of attenuation with Particle Size.

Fig. 2b. Variation of attenuation with Particle Size.

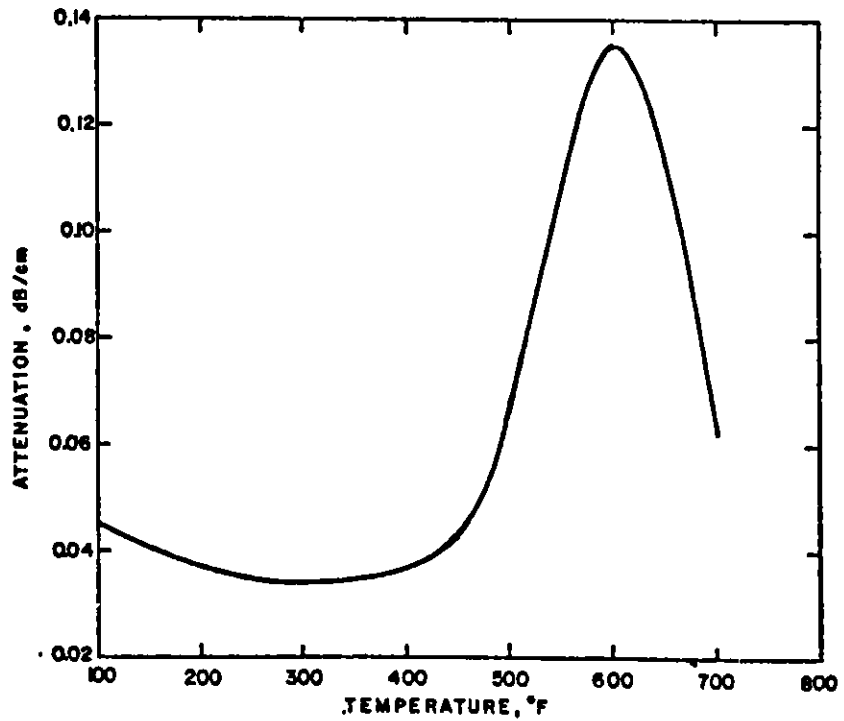


Fig. 2c. Variation of Attenuation with Temperature.

ATTENUATION OF SOUND IN VAPORS AND GASES

The attenuation of sound in vapors and gases is attributed to three factors: 1) viscosity, 2) thermal conduction, and 3) thermal relaxation. The first two factors (classical absorption) closely approximate the sound absorption in monoatomic gases. Additional losses are found to occur due to relaxation in polyatomic gases and gas-vapor mixtures particularly at high frequencies. The relaxational loss is known to have a major bearing on the frequency-to-pressure ratio [6]. Since this ratio is small at the measurement conditions (100 kHz and 1500 psig), the relaxational losses in this case may be low. Considering therefore only the classical terms of absorption, the expression for attenuation in pure gases or vapors is given by:

$$\frac{\alpha}{f^2} = \frac{8 \pi^2}{3 c_o^3 \rho_o} \left[ \mu_o + \frac{3}{4} \left( \frac{\gamma-1}{c_p} \right) k \right] \quad (2)$$

where,

$c_o$  = sound velocity,  $\rho_o$  = density of the gas,  $\mu_o$  = absolute viscosity of the gas,  $\gamma$  = the ratio of specific heats at constant pressure and temperature,  $c_p$  = specific heat at constant pressure, and  $k$  = thermal conductivity of the gas.

For a lack of data on gas-vapor mixtures, we shall consider only air for which data on the physical constants at various pressures and temperatures are given in Table III [7]. Using these values in Eq. 2,  $\frac{\alpha}{f^2}$  is computed and tabulated for each case. It is seen from Table III that there is a small increase in attenuation with an increase of temperature from 80°F to 1340°F; but a marked decrease in attenuation is seen with an increase of pressure from 14.5 psi to 1450 psi. The attenuation in air corresponding to the temperature and pressure at the separator vessel is about  $0.15 \times 10^{-3}$  dB/cm. This value is three orders of magnitude less than the attenuation estimate for the 25 WT% slurry.

Table III  
Physical Data and the Attenuation Computation  
In Air

AIR								
PRESS (PSI)	TEMP (°F)	C <sub>p</sub> CAL/G. °C	C <sub>v</sub> CAL/G. °C	SOUND VELOCITY x 10 <sup>4</sup> cm/s	DENSITY (x 1.29 x 10 <sup>-3</sup> ) g/cm <sup>3</sup>	ABS VISCOSITY (x 10 <sup>-6</sup> ) POISE	TH. CONDUCTIVITY (x 10 <sup>-6</sup> ) CAL/S. CM. °C	$\frac{\alpha}{F^2}$ dB. (H7) <sup>-2</sup>
14.5	80.3	0.240	0.171	3.4735	0.9102	180	62.61	0.12 x 10 <sup>-11</sup>
	440	0.246	0.175	4.4843	0.5458	260	97.35	0.14 x 10 <sup>-11</sup>
	1340	0.272	0.204	6.3418	0.2481	420	156.5	0.16 x 10 <sup>-11</sup>
145	80.3	0.244	0.172	3.4735	9.125	182	63.53	0.12 x 10 <sup>-12</sup>
	440	0.247	0.177	4.4843	5.441	262	98.05	0.14 x 10 <sup>-12</sup>
	1340	0.273	0.204	6.3418	2.474	422	157.8	0.16 x 10 <sup>-12</sup>
1450	80.3	0.277	0.175	3.4735	91.61	192	75.01	0.14 x 10 <sup>-13</sup>
	440	0.256	0.180	4.4843	52.53	272	103.5	0.15 x 10 <sup>-13</sup>
	1340	0.275	0.204	6.3418	24.1	432	162.7	0.17 x 10 <sup>-13</sup>

ESTIMATION OF MEASUREMENT RANGES

The measurement ranges are estimated from the maximum allowable transmission losses for a given source power. The following equation relates the various parameters of a sonar system [8].

$$SL - TL + PG + DG = NL + MR \quad (3)$$

where,

SL = Source power, TL = Transmission Loss, PG = Processing Gain,  
 DG = Directional Gain, NL = Background Noise Level, and  
 MR = Measurement Requirement.

The transmission loss, TL is given by:

$$TL = [2 \alpha R + 20 \log R] \text{ dB}$$

where  $\alpha$  is the attenuation coefficient and R is the measurement range. A typical set of values at 100 kHz for the various parameters in Eq. 3 based on water and air media are given in Table IV. Using these values in Eq. 3, the possible measurement range at 100 kHz in the 25 WT% slurry is 2.5 m, while much higher ranges are possible in the air.

Table IV

Typical Values for the Parameters in Equation 3

PARAMETER	IN-WATER	IN-AIR
SL	211.6 dB re 1 $\mu$ Pa at 1 cm	175 dB re 1 $\mu$ Pa at 1 cm
DG	24 dB	24 dB
PG	5 dB	5 dB
NL	50 dB re 1 $\mu$ Pa	50 dB re 1 $\mu$ Pa
MR	15 dB	15 dB

### MEASUREMENT SCHEME

The pulse-echo method of level measurement centers around the fact that the velocity of sound in a medium remains constant. In practice however, any changes in the temperature, materials composition, etc. would cause variations of sound velocity, and must be compensated for.

A measurement scheme that practically eliminates the dependence on sound velocity is proposed in Fig. 3. A reflector, placed inside the vessel at a known distance,  $L_1$  from the vessel top, serves to provide a reference velocity. (Alternately, another transducer on a side of the wall may be used to obtain a reference echo from the diagonally opposite side of the wall.) If  $\tau_1$  and  $\tau_2$  are the transit times from the top of the vessel to the reflector and the slurry surface respectively, then the slurry level  $L_2$  is given by  $(\tau_2 / \tau_1) L_1$ . The method of cross-correlation is used for measuring echo delays, since it is efficient under noisy conditions.

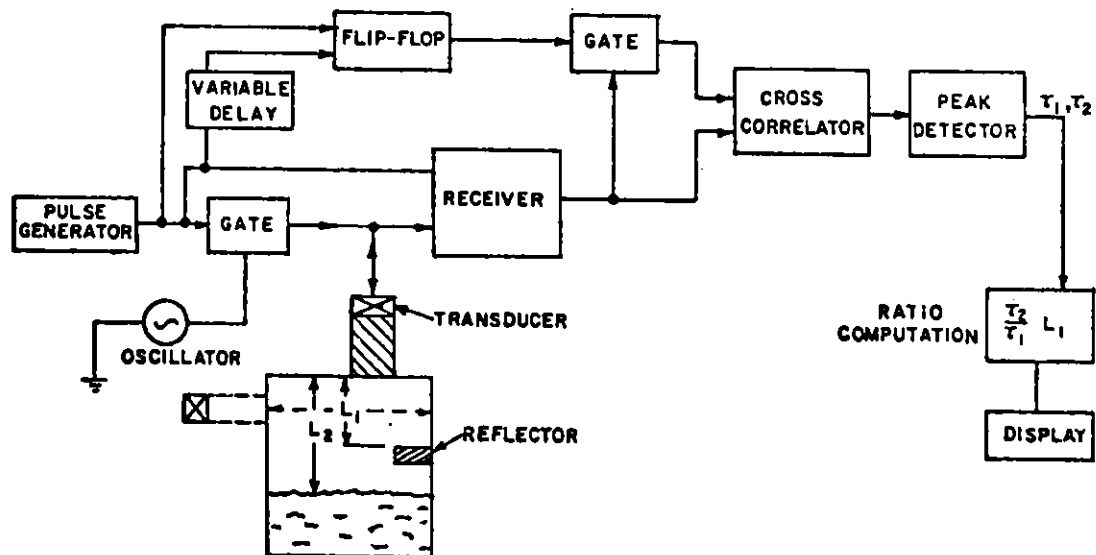


Fig. 3. Proposed Measurement Scheme.

## CONCLUSIONS

An assessment of the applicable slurry level measurement methods has been made. Among the various methods, acoustic devices are advantageous for high temperature slurry level measurement because they are non-intrusive, inherently safe, easily adaptable to high pressures and temperatures, fairly accurate and provide fast response times.

A feasibility study of an acoustic pulse-echo system has been carried out. This entails the computation of the attenuation losses in slurries and vapors and from which the estimation of possible measurement ranges in each medium. It is found that "in-slurry measurement" is feasible for dilute slurries and/or for small ranges (2.5 m at 25 WT% slurry), while higher measurement ranges are possible with "in-vapor measurements." However, the acoustic feasibility must be tested under actual conditions of the separator vessel since the presence of foam, turbulence, or a thick layer of coke coating inside the vessel can cause excessive attenuation of sound.

## REFERENCES

1. N. M. O'Fallon, "Overview of Instrumentation Needs for Advanced Fossil Energy Processes," The Proc. of 1981 Symposium on Instrumentation and Control for Fossil Energy Processes, San Francisco, CA, June 1981.
2. C. A. Belsterling, "A Look At Level Measurement Methods," Instruments and Control Systems, pp. 37-45, April 1981.
3. B. Lazenby, "Level Monitoring and Control," Chemical Engineering, Vol. 87, pp. 88-26, 1980.
4. J. R. Allegra and S. A. Hawley, "Attenuation of Sound in Suspensions and Emulsions: Theory and Experiments," J. Acoust. Soc. Amer., Vol. 51, pp. 1545-64, 1972.
5. IGT, Preparation of a Coal Conversion Systems Technical Data Book, EX-76-C-01-2286, FE-2286-32, 1976.
6. J. Blitz, Fundamentals of Ultrasonics, London: Butterworths, 1967.
7. A. C. Raptis, et al., "A Feasibility Study of Acoustic/Ultrasonic Flowmeters for Solid/Gas Systems," Argonne National Laboratory, ANL-FE-49622-TM01, 1978.
8. R. J. Urick, Principles of Underwater Sound for Engineers, McGraw-Hill, New York, 1975.

QUANTITATIVE APPLICATIONS OF GAMMA DENSITOMETRY  
IN THE COAL INDUSTRY - A CRITIQUE

Patrick Shea  
Rudolph Sher  
Stanford University  
Tsahi Gozani  
Science Applications, Inc.  
5 Palo Alto Square, Suite 200  
Palo Alto, CA 94304  
415/493-4326

Introduction

This paper discusses the use of gamma densitometry to quantitatively assay bulk samples of coal on a continuous basis. Devices using these principles to determine mass flows are on the market, and work is progressing in several countries on instruments to determine ash content. The theoretical limits of applicability and inherent assumptions of these techniques will be discussed, primarily as applied to dry bulk coal, but with some discussion of the more complicated problems of slurried coal.

The associated technique of X-ray fluorescence (XRF) will not be analyzed. While XRF has the potential to identify many individual elements, the X-rays do not penetrate more than a few millimeters of coal, and are thus not really a bulk measurement. XRF is, however, useful in lab analysis, and is thus complimentary to the methods discussed here.

Gamma rays are generated by "sources," usually a single radioactive element. These have several advantages over XRF, the main one being that no power is required to generate gammas. However, there are a limited number of gamma sources with useful energies, long enough half-lives to be economically useful, and 'clean' spectra (that is, relatively few energies emitted by the source in question).

Basics of Gamma Interaction With Matter

Gamma rays are relatively high energy electromagnetic waves that originate in the nucleus. In general, gamma rays have higher energies than X-rays (which originate in the electron shells of the atom), although there is some overlap. For a well-collimated beam of gammas passing through a thin target, it can be shown that the transmission is given by:

$$I = I_0 \exp[-\mu \rho t] \quad (1)$$

where

- I = transmitted beam intensity
- I<sub>0</sub> = source beam intensity
- μ = mass attenuation coefficient in cm<sup>2</sup>/g
- ρ = bulk density of material, g/cm<sup>3</sup>
- t = thickness of material the beam passes through, cm.



The attenuation coefficient  $\mu$  is both element and energy dependent, as shown in Figure 1. While the nonlinear behavior in the figure is the key to the multi-energy techniques to be discussed below, it can also be a source of error. For a mixture of elements, the attenuation coefficient  $\mu_{mix}$  is given by:

$$\mu_{mix} = \frac{\sum_i w_i \mu_i}{\sum_i w_i} \quad (2)$$

where  $w_i$  is the weight % of element  $i$

$\mu_i$  is the attenuation coefficient of element  $i$ ,  
and the sums are over the elements in the mix.

The ratios  $w_i / \sum w_i$  determine the composition of the mix. Since all gamma densitometry systems make some assumption about the value of  $\mu_{mix}$  at the time of measurement, this is equivalent to comparing the measured coal to a calibration coal with a composition giving  $\mu_{mix}$ .

There are several sources of error that are peculiar to nuclear processes. The first of these is the so-called "counting statistics" problem. The emission of a gamma ray by a nucleus is a random event; thus, the number of gammas emitted by a source per unit time will fluctuate. Thus, the relative error in measuring a count rate goes as (square root of the number of counts)<sup>-1</sup>. Since all the instruments discussed herein interpret changes in observed counts as changes in some coal property, this can cause errors in the instrument's reading. High source intensities, high detector efficiencies, and longer measurement times can, separately or together, reduce these errors by increasing the observed number of counts. As a practical matter, instabilities in the gain of any part of the system, e.g., those caused by temperature changes, will also show up as deviations of the measured count rate from "true". These problems of system stability are much more difficult to control.

A gamma densitometry system may be sensitive to variations in geometry, such as changes in the profile of coal on a conveyor belt or the size of the lumps of coal. This is because, as shown by equation (1), gamma attenuation is an exponential process, while physical properties are averaged linearly. For example, fewer gammas get through an amount of material evenly distributed across the beam than get through the same material covering only half of the beam by twice the thickness.

Finally, there are the problems relating to the variation of the  $\mu$ 's with energy and material. Sources used may emit gamma rays at more than one energy; and, through scattering processes, gammas can lose energy on their way to the detector. These gammas are, of course, attenuated differently than the primary energy gammas, and can greatly affect the signal from a detector without energy resolution. Variations in composition of the coal (which affects the  $\mu$  of the coal as in equation (2)) are more serious because they are more difficult to correct for. Significant variations in composition can occur even between seams in a single mine.

### Single Energy Transmission

The single-energy transmission gauge is the simplest system to analyze. With only one piece of information, only one parameter can be determined. Typically, this parameter is the  $\rho t$  (density times thickness) product; when coupled with a measurement of belt speed, this gives the mass flow rate. Several manufacturers make this type of meter. Figure 2(a) shows a typical transmission gauge.

The equation for this system can be obtained by rewriting equation (1):

$$\rho t = \frac{\ln I_0 - \ln I}{\mu} \quad (3)$$

Using the standard formulas for error propagation (and assuming no error in determining  $I_0$ ):

$$\delta(\rho t) = \frac{1}{\mu} \left[ (\rho t)^2 (\delta\mu)^2 + \frac{1}{I} \right]^{1/2} \quad (4)$$

For a typical case (say the 660 keV  $C_{s137}$  gamma through 10" of coal),  $1/\mu \approx 12$  and  $\rho t \approx 24$  in consistent cgs units. If there was assumed to be no error in the composition ( $\delta\mu = 0$ ; in practice, the measured composition is the same as the calibration sample), then the counting statistics error  $1/\sqrt{I}$  is amplified by a factor of 12. Fortunately,  $I$  can be increased by longer measurement time or stronger sources. If counting statistics are negligible, then the relative error in  $\mu =$  relative error in  $\rho t$ .

The other source of error in (4) comes from composition variations; the composition of the coal being measured may not be the same as the composition of the calibration sample. If this is true, the  $\delta\mu$  term (which is not a random error) in (4) is not zero. Equation (2) shows that  $\mu$  changes when the mass distribution of elements in the coal changes; because  $\mu$  depends on energy, the effect on  $\delta\mu$  of changes in the  $W_i$ 's depends on energy. Figure 3 shows the variation in  $\frac{\delta\mu}{\mu}$  with energy; note that if  $I$  is large enough (the error due to counting is negligible) then this is also the relative error in  $\rho t$ . Note the decrease with increasing energy; while this suggests using a high energy, it should be pointed out that sensitivity to counting statistics errors increase.

One common source of compositional error is from changes in moisture content. Above about 100 keV, hydrogen has roughly twice the attenuation coefficient of any other element. Fortunately, only one ninth of water (by weight) is hydrogen, so the sensitivity of gamma densitometry systems to moisture variations is not necessarily too great.

Another assumption, not readily apparent in equation (3), is that the path length of the gamma rays through the coal is constant across the beam. In many commercial weigh scales, a "gamma lens" is used. This is an attenuator placed in the beam near the source, which is shaped so that the equivalent path length through both the lens and the coal is constant across the beam. This means that this device is sensitive to some extent to changes in the profile of the coal on the belt. As the lens is thickened, the meter

becomes less sensitive to profile changes, but also requires stronger sources to get the same count rate. The profile of material on the belt can be changed by a change in the top size of pieces of coal on the belt, changes in moisture, and, of course, amount of material on the belt. Errors due to changes in profile depend on the source-detector geometry used, and are thus difficult to quantify.

Finally, there is the problem of "in-scattering." Gammas initially directed away from the detector can be scattered by the coal into the detector. The observed number of counts, which is assumed in equation (1) arise only from the uncollided beam, is greater than that expected based on the theoretical value of  $\mu$ . Thus,  $\mu$  appears to have a smaller value; as seen in equation (4), this translates into a larger error in  $\rho t$ . To some extent, a detector with good energy resolution can ameliorate this effect, since the scattered gammas are lower in energy than the unscattered ones and will therefore not be detected. For practical applications, however, high resolution systems are less rugged, more prone to temperature effects, and more expensive.

It should be mentioned that some attempts have been made to measure ash content by measuring density. This is based on the fact that ash has a higher intrinsic density than the "coal" matter, about 2.4 to 1.2. This is a very unreliable method of measuring ash, as the gamma densitometer measures bulk density, which is, in addition, dependent on particle size and moisture content.

#### Single Energy Backscatter Gauges

An example of this type of gamma gauge is the ash meter described in Ref. [1] and shown in Figure 2(b). In this type of device, the source and detector are situated on the same side of the coal, and the detector doesn't see the source directly. The detector sees only the gammas that are scattered back from the coal bed. Typically, lower energy gammas than those in transmission gauges are used, which means that the scattered gamma has nearly the energy of the initial gamma; the lower energy also means that the coal bed is 'infinitely' thick. In addition, the lower the gamma energy, the more gamma rays, relative to higher energies, are scattered backwards.

This type of gauge is not as amenable to theoretical analysis as the transmission gauge. The scattering of the source gamma can occur at any depth in the coal. The scattering probability is not strongly dependent on the type of material present, but the attenuation of the gammas before and after scattering is, as discussed above. Thus, the backscatter measurement is essentially a transmission measurement, but with a source distributed non-uniformly in the upper part of the coal bed.

The configuration described in Ref. [1] is relatively insensitive to variations in density and moisture, due to the choice of angle between the source and detector, and the shape of their collimators. In addition, the distance between the source-detector assembly and the coal must be set based on the ash content of the calibration coal. The coal being measured must be relatively fine (25 to 30 mm top size), and is moved through the beam by a worm drive. These two things not only tend to produce a constant bulk density in the measurement region, but also serves to make the coal bed more homo-

geneous. One requirement for homogeneity in gamma densitometry is that the gamma rays travel (on average) through more than one particle between collisions. The average distance between scatterings at the energy used (60 kev) is about 50 mm; it is considerably less for lower energy gammas. This rather short "mean-free-path" also implies that only the top portion of the coal is interrogated. Thus, the insensitivity of this particular system to moisture and density changes comes about due to the delicate balance between a number of complex phenomena.

Again, composition changes are an important source of error. It has been estimated [2] for the ashmeter described that an 0.1% change in iron content leads to a 1% change in ash reading.

Counting statistics problems are of about the same level of difficulty as in the transmission case. However, because the "source" seen by the detector is the result of one scattering, the  $I_0$  in equation (3) is much less for the same source strength than in the transmission case. This means that larger sources are required for the same count rate.

In some applications (mostly lab-scale), a correction for iron content is made by counting the fluorescent X-rays from the iron. Again, this correction is gained by making the system usable over a small range of ash contents. This is because this correction method requires a filter to cut down the iron X-ray intensity to the point where the additional count rate from more iron due to the iron X-ray just balances the loss in count rate of the backscattered gammas due to the higher attenuation of the iron. One other fault of this system is that the iron X-rays have a very limited range in coal, and thus this corrects based on the iron content of the very upper layer of the coal, and may not be representative of the iron content of the rest of the coal.

### Multi-Energy Systems

A variety of multi-energy systems have been reported. The usefulness of such systems is that with  $M$  energies,  $M$  properties can be determined. For example, with three energies, it should be possible to determine  $\rho t$ , the weight of ash, and the weight percent of elements with high atomic numbers, i.e., iron.

It should be pointed out that the "ash" measured by a gamma densitometer is not quite the same as the ash determined by the usual ASTM procedure. Gamma densitometry determines the amount of material with an atomic number ( $z$ ) greater than or equal to that of sodium, in a typical application. The ASTM ash includes the oxides of those elements, excepting sulfur and chlorine.\* Since the ratio between the weight of an ash element and its oxide is fixed, a multiplicative correction for the oxygen can be gotten. This correction is, of course, slightly composition dependent. However, relative errors in ash content determined by gamma densitometry turn out to be approximately the same as the relative error for the ASTM ash.

---

\*Some small amount of the other elements in the ash, for example sodium, are also volatile and not included in the ASTM ash.

A general methodology for analyzing M energy systems will be presented. Because the backscatter technique is formally the same as a transmission measurement on a distributed source, this general formulation will be presented in the framework of a transmission measurement.

The elements in the coal are broken up into M groups of neighboring elements,  $W_1, W_2, \dots, W_m$ . Corresponding to each group of elements  $W_i$  is the attenuation coefficient  $\mu_i$  averaged over the group as in eq. (2). Since there are M energies, there are M equations of the form of eq (3) above. There is one additional equation, that the sum of the  $W_i$ 's is 1. Finally, there is the additional unknown,  $\rho t$ . This M+1 system of equations in M+1 unknowns can be written:

$$\begin{pmatrix} \ln(I_0/I)_1 \\ \vdots \\ \ln(I_0/I)_M \\ 0 \end{pmatrix} = \begin{pmatrix} \vec{U}_1^T & 0 \\ \vdots & \vdots \\ \vec{U}_M^T & 0 \\ \vec{1}^T & -1 \end{pmatrix} \begin{pmatrix} \rho t w_1 \\ \vdots \\ \rho t w_M \\ \rho t \end{pmatrix} \quad (5)$$

$$\vec{T} = \begin{pmatrix} \Omega & \vec{0} \\ \vec{1}^T & -1 \end{pmatrix} \vec{R}$$

where  $\ln(I_0/I)_i$  is that function evaluated at energy i,

$\vec{U}_i^T$  is the transpose of the column vector whose elements are the M group attenuation coefficients at energy i, and

$\vec{1}^T$  is the transpose of a vector of M ones.

To get an estimate of  $\vec{R}$  based on the measurements  $\vec{T}$ , it is necessary to solve equation (5):

$$\hat{R} = X^{-1} \vec{T} = \begin{pmatrix} \Omega^{-1} & 0 \\ \vec{1}^T \Omega^{-1} & -1 \end{pmatrix} \vec{T} \quad (6)$$

Thus the whole question of whether or not the system will work is determined by whether or not  $\Omega$ , the matrix of attenuation coefficients, has an inverse. The matrix  $\Omega$  will be nearly singular ("ill-conditioned") when two of the energies used are close enough that the attenuation coefficients are the same (or one is merely a constant multiple of the other. Even with energies fairly well separated, the matrix  $\Omega$  is poorly conditioned, as will be seen.



$$\frac{\delta W_i}{W_i} = \left[ \left( \frac{\delta \rho t w_i}{\rho t w_i} \right)^2 + \left( \frac{\delta \rho t}{\rho t} \right)^2 \right]^{1/2} \quad (9)$$

where  $\delta x$  signifies the error in the term  $x$ .

This function (9) was evaluated for an Eastern U.S. coal analyzed by a hypothetical three energy system. The low and high energies were chosen to be 40 and 660 keV, respectively, and the middle energy was varied from 45 to 80 keV. The minimum error occurred when the middle energy was between 55 and 60 keV. Also, in excess of a million counts at each energy were necessary to get any kind of reasonable accuracy. Clearly, the error amplification is enormous. Very large count rates or long counting times are needed. Note also that eq. (9) only presents the errors due to counting statistics. Variations due to composition may be evaluated as a bias due to a  $\delta\Omega$  term.

#### Special Problems of Slurry

Gamma densitometry measurements of slurried coal have additional difficulties above and beyond those presented above. Most of these problems are related to the fact that in dilute slurries there is little coal relative to water. Thus, the bulk density of the mix varies from 1 to 1.1; to be useful, then, a density measurement must be very accurate (on the order of 0.1% to determine percent solids to 1%). The same sort of difficulty applies to measurement of ash (or any other group of elements); if the slurry is running at 10% solids, the ash content in the mix is only 1/10 of the ash fraction in the coal. Obviously, the ash content in the slurry must be measured to 10 times the accuracy desired in the coal ash content.

It is also possible to have a non-uniform distribution of coal particles in the slurry. In much the same way that profile changes in the dry coal case caused errors, these non-uniformities can cause error. Problems with voids (bubbles) can generally be eliminated by high pressure.

If low energy gammas are used, the piping section near the source and detector must be replaced with a low  $z$  material (plastic or glass). In backscatter measurements of slurry, gammas scattered from the piping or water may be more numerous than those scattered from the coal. In this case, the count rate observed will behave as a transmission through the slurry from a distributed source (the wall of the tube). It seems that in that case, it makes more sense to do a straight transmission measurement and save on required source strength.

#### Summary and Conclusions

Gamma densitometry measurements by single and multiple-energy transmission and backscatter measurements were discussed. A general formalism for analyzing multiple-energy systems was presented. While multi-energy systems can, in principle, pick out as many groups of elements as energies used, the matrices involved are ill-conditioned and thus require accurate measures of count rate (i.e., long counting times or high source intensities) to achieve

acceptable errors. Changes in coal composition and profile of coal composition and profile of coal on a belt were also seen to be important sources of error.

Transmission measurements are more amenable to analysis than backscatter, which are essentially transmission measurements made on a distributed source. In addition, transmission measurements are not restricted to low energy gamma sources, and can survey the entire bulk of coal rather than just the upper portion.

The special problems of slurried coal measurements were briefly discussed.

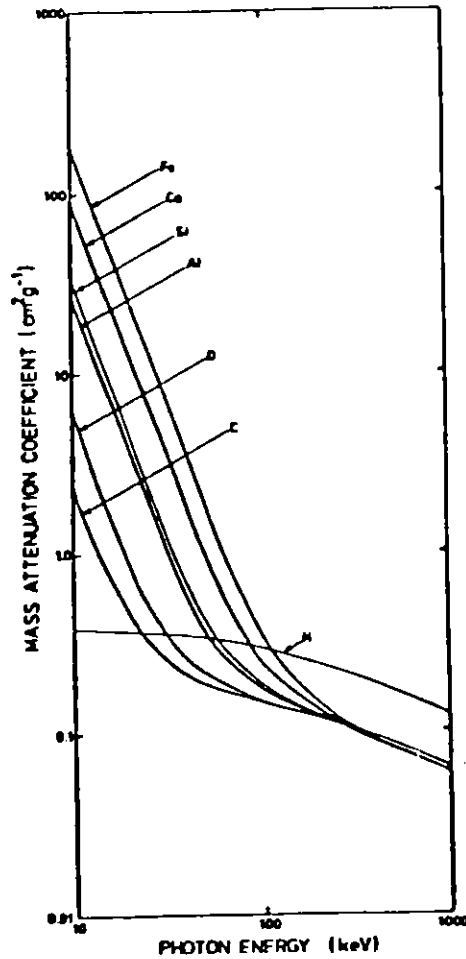
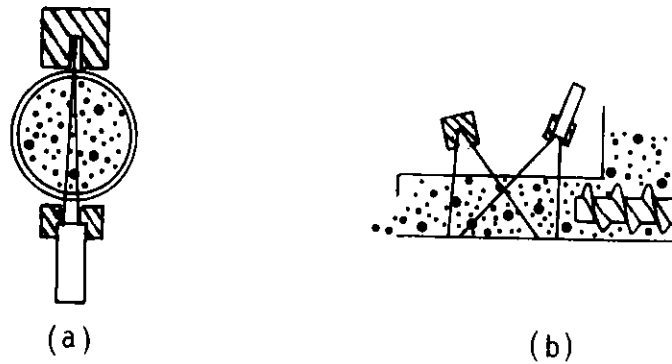


Figure 1. Variation in mass attenuation coefficient with photon energy for major coal elements, 10 to 1000 keV.

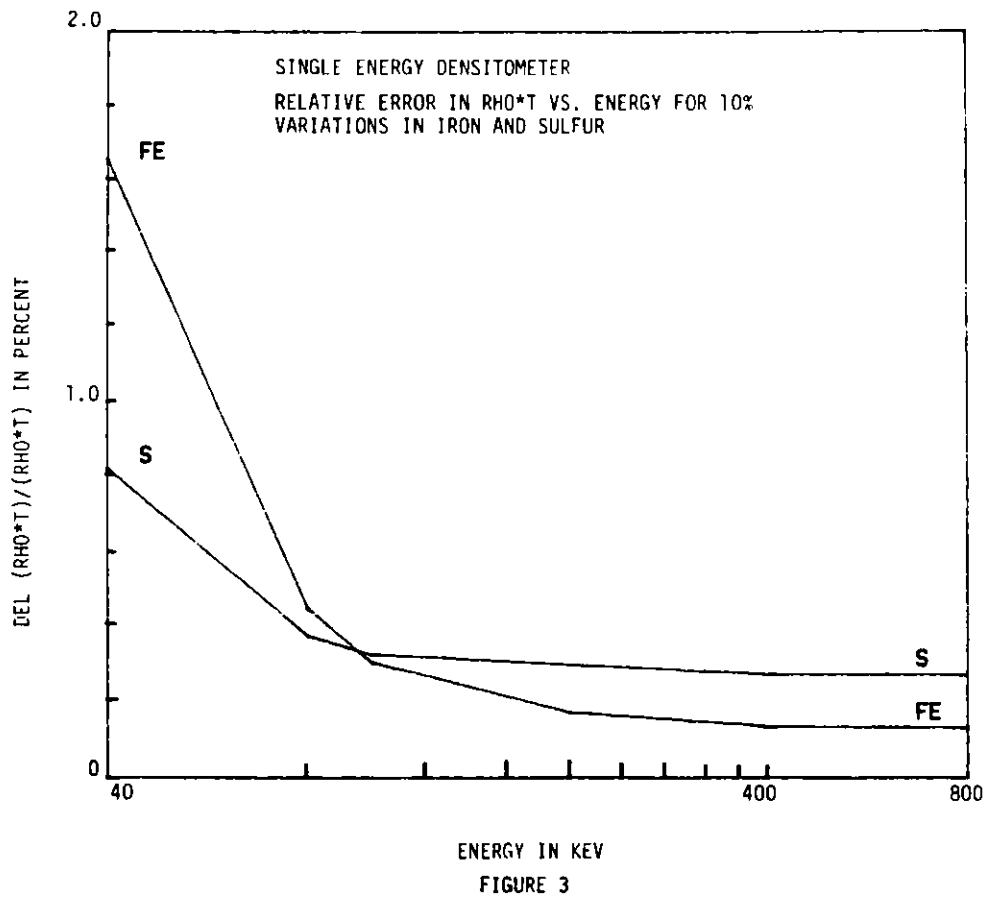




Transmission

Backscatter

Figure 2: Gamma Densitometer Systems



References

1. Trost, A. "Determination de la teneur en cendres de fines et mesure de l'epaisseur de verre, des matieres plastiques et des metaux au moyen des rayons gamma de l'americium-241," in Radioisotope Instruments in Industry and Geophysics, IAEA, Vienna, 1:435, 1966.
2. Lyman, G.S "On-line Measurement of Ash Content of Coal," Aus. I.M.M. Conference, Queensland April, 1981.
3. Clayton, C.G. "Application of Nuclear Techniques in the Coal Industry," in Nuclear Techniques and Mineral Resources, IAEA, Vienna, p 85. 1977.

ON LINE MULTICOMPONENT MASS FLOW AND DENSITY GRADIENT  
ANALYSIS IN SLURRY PIPE LINES

---

Graham V. Walford  
Gull Engineering, Inc.  
975 W. Outer Drive  
Oak Ridge, TN 37830  
615/483-4787

Abstract

The use of nuclear techniques is common for a variety of on line measurements. However, their application is often restricted to gross counting techniques, thereby achieving limited measurement performance. This paper describes techniques incorporating energy spectrum analysis to permit on line multicomponent evaluation of pipe line coal slurries and density gradient analysis. The techniques utilize gamma ray sources, typically  $^{137}\text{Cs}$  or  $^{60}\text{Co}$  and carefully placed NaI(Tl) detectors working on pipe lines up to 7.0 inches diameter with 1/4 inch steel wall. The source and one detector are placed in a transmission mode across the diameter of the pipe. The transmitted beam is attenuated by the pipe contents depending upon the total mass and the elemental makeup of the slurry. Since many of the gamma ray interactions occurring in the slurry will be Compton scattered events, then collimated detectors carefully placed will measure these events. The scattering of gamma rays is dependent upon the mean electron density (related to mass) of the slurry. The relationship of the measurement of radiation scattered at specific angles in the slurry with the measurement of the transmitted beam yields the slurry density gradient and the slurry content. Data are presented for water based coal slurries in which unwanted rock aggregates are also quantified.

IMPROVED EFFICIENCY IN COAL PREPARATION CIRCUITS

Mark N. Mackinnon  
Kay-Ray, Inc.  
516 West Campus Drive  
Arlington Heights, IL 60004  
312/259-5600

G. W. Robertson  
Preparation Sales, Inc.  
213 Coiner Street  
St. Albans, WV 25177

The most important parameter to be maintained in a coal preparation plant is the specific gravity of the plant's circuits. The closer each circuit can be kept to its set specific gravity, the more profitable the preparation plant will be. This profitability can mean anything from additional coal yield to a more efficient refuge thickener line.

A large coal preparation plant may need to monitor specific gravity in more than a dozen locations. Typical places to measure specific gravity include: heavy media lines, magnetite thickener underflows, refuge thickener underflow, froth flotation feeds, and cyclone circuits.

The most common application for a specific gravity sensor is the monitoring of the feed to a heavy media washer. The float-sink data from a washability study will show where the specific gravity should be kept in the heavy media vessel. A variance of even 0.001 SGU from the set specific gravity, or cut-point, can cause a significant loss in coal yield or coal quality. This is why a highly accurate specific gravity sensor is imperative in a coal preparation plant.

One method of measuring specific gravity in a coal preparation plant is through the use of a differential pressure cell. Figure One depicts a typical set-up for a DP cell in coal preparation.

In this example, all of the connecting piping and the meter body are filled with inert gas or air. The gas or air is purged back through the sample box by the two connecting lines whose ends are separated by a calculated distance (H). Both lines must be continuously submerged in the slurry. The flow rate of the purge units is set at about one SCFH. The difference in air pressure between the two tubes is directly proportional to the specific gravity of the medium.

There are several disadvantages with using a DP cell. Since it does not allow for an on line measurement of the specific gravity, the reading must be taken downstream in the sample box. This allows for the introduction of several extraneous variables.

An underflow and overflow must be provided to insure a homogeneous mixture inside the sample box. If the underflow or overflow plug up, the measurement will be erroneous. Any plugging inside the purged tubes will

also dramatically throw off the accuracy. In addition, any variation in the purge will induce error.

For these reasons, several coal preparation plants have become dissatisfied with the DP cell method of specific gravity measurement.

A highly accurate and reliable device for monitoring specific gravity in coal preparation plants is the gamma density sensor. This paper examines the use of the 3600 system manufactured by Kay-Ray, Incorporated, Industrial Process Control Equipment, Arlington Heights, Illinois.

The gamma density sensor operates on the principle that gamma energy will penetrate all materials but is absorbed in proportion to the mass of material it passes through. Thus, there is an inverse relationship between the amount of energy passing through a slurry pipeline and the density of that slurry. This inverse relationship is shown in Figure Two.

A schematic diagram of a Kay-Ray system is shown in Figure Three. The heart of the system is a small gamma source that is safely housed in a lead shielded holder. When a shutter mechanism on the source holder is opened, a highly collimated beam of gamma energy is emitted. This beam is directed through the slurry pipeline and into a detector mounted directly opposite the holder. The detector generates an electrical signal which is proportional to the slurry density. This electrical signal is then transmitted to remote electronics for amplification, scaling, and calibration into specific gravity units or percent solids.

The system easily bolts around any existing pipe, without any downtime or pipe modification. This eliminates the need to create a sample box and install air purges that are necessary for the DP cell. Since the Kay-Ray sensor is completely noncontacting, problems with plugged sample box tubes and underflow drains are eliminated. Because of this, maintenance on the Kay-Ray sensor is minimal, making it an extremely reliable density sensor.

Location of the density sensors within the coal preparation circuit vary from heavy media lines to refuge thickener underflows. One large Appalachian plant currently utilizes fourteen Kay-Ray sensors. Seven sensors are in Circuit A and seven are in the identical Circuit B.

The first sensor is located just after the primary coarse heavy media sump, which pumps magnetite and water into the heavy media vessel. The second sensor is just after the intermediate coal heavy media sump, which leads into the intermediate coal classifier. The fines circuit has one gauge just after the fine coal heavy media cyclone feed sump. This sump feeds the fine coal heavy media cyclones. The minus 150 mesh coal reports to two froth flotation cells. The feed to each of these cells uses a Kay-Ray sensor to monitor percent solids. The sixth unit is mounted on the magnetite thickener underflow, and the seventh is on the refuge thickener underflow. Combining Circuit A with B makes a total of fourteen sensors.

The most obvious advantage with a Kay-Ray sensor is that it is a non-contacting, direct, and on-line measurement of the slurry. The DP cell introduces several additional variables by using an indirect, down-line measurement. This is the main reason why accuracy levels of  $\pm 0.0001$  SGU can sometimes be obtained with a Kay-Ray sensor. The accuracy of a Kay-Ray sensor was found to be ten times greater ( $\pm 0.005$  to  $\pm 0.05$  SGU) than that of a DP cell in a report by the National Coal Board.

In April 1982, a coal preparation plant in West Virginia retrofitted five Kay-Ray systems in place of DP cells. Circle chart recorder data from before and after this retrofit is shown in Figures Four through Six. It is readily apparent how much more accurate the Kay-Ray was than the DP cell.

The end result of using a more reliable, accurate, low maintenance density sensor is the eventual increase in clean coal yield. A 3% yield increase has been found to be a conservative average. This would mean that a preparation plant could expect to produce 3% more clean coal by using a Kay-Ray density sensor, rather than a DP cell. At current coal prices, an average preparation plant of 600 TPH could expect to produce \$1,080,000 more coal with this 3% increase in yield.

In conclusion, it has been shown in this paper, with circle chart recorder data, that a Kay-Ray gamma density sensor can produce a more accurate and repeatable specific gravity reading. The Kay-Ray sensor only requires a fraction of the maintenance necessary with a DP cell. Because of its high accuracy and reliability, the Kay-Ray sensor can produce yield increases of more than 3%. This can result in an increase of more than one million dollars in clean coal revenue.

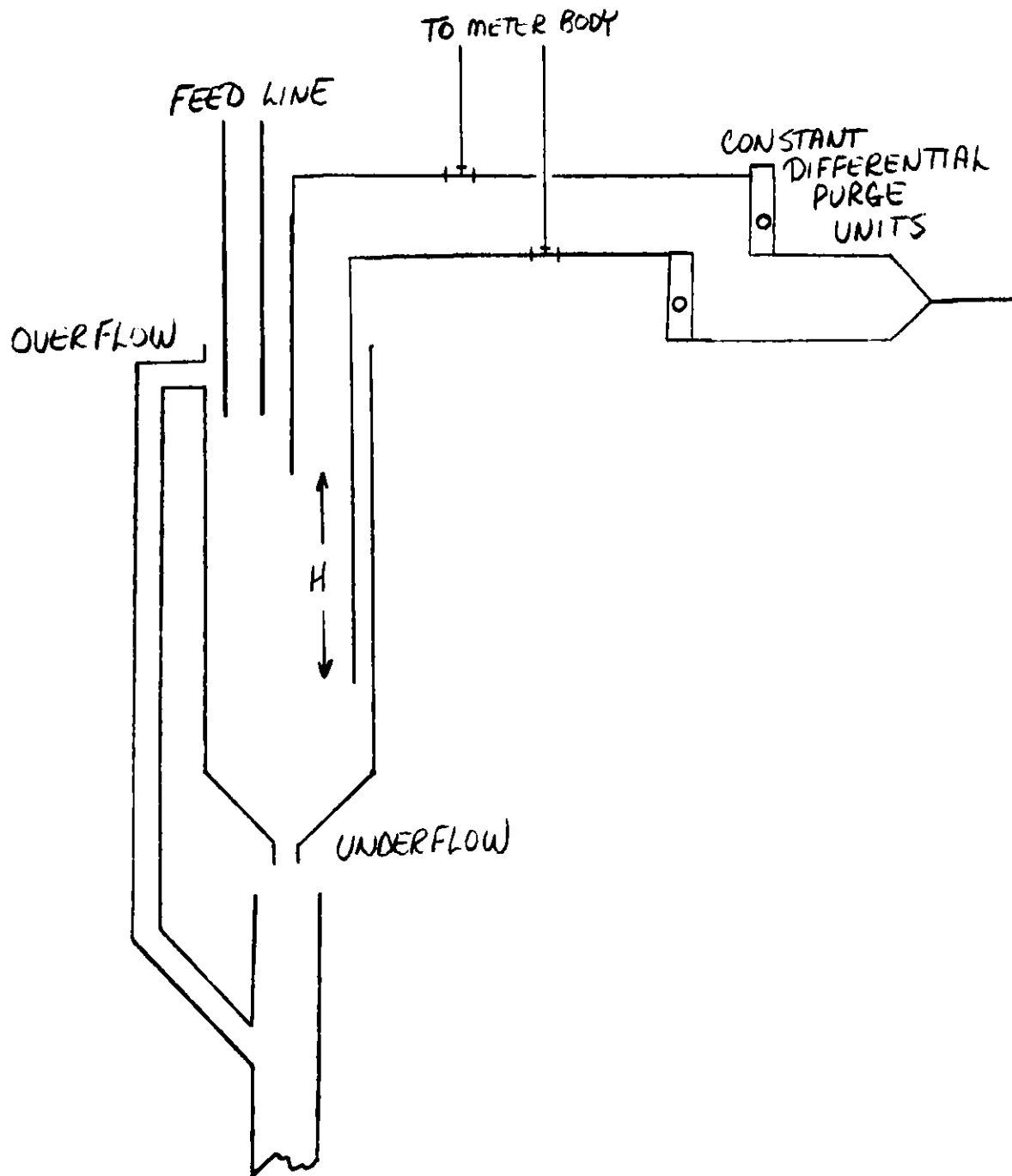


Figure One: The DP Cell

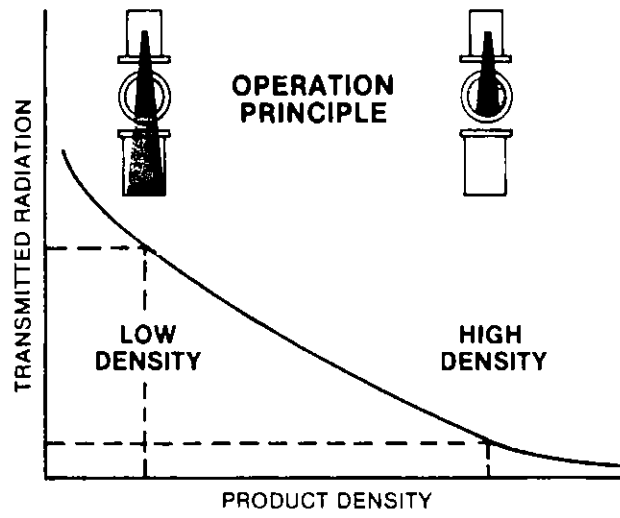


Figure Two: Radiation Absorbption

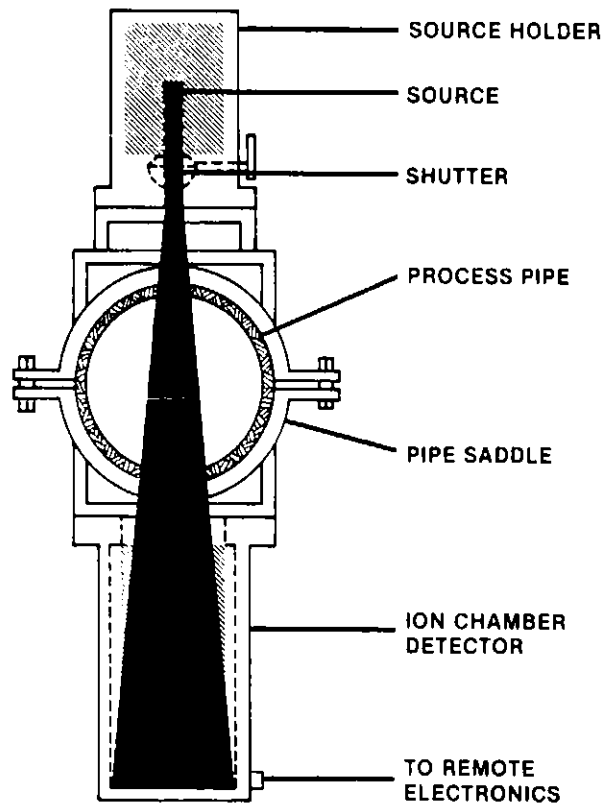


Figure Three: Kay-Ray System



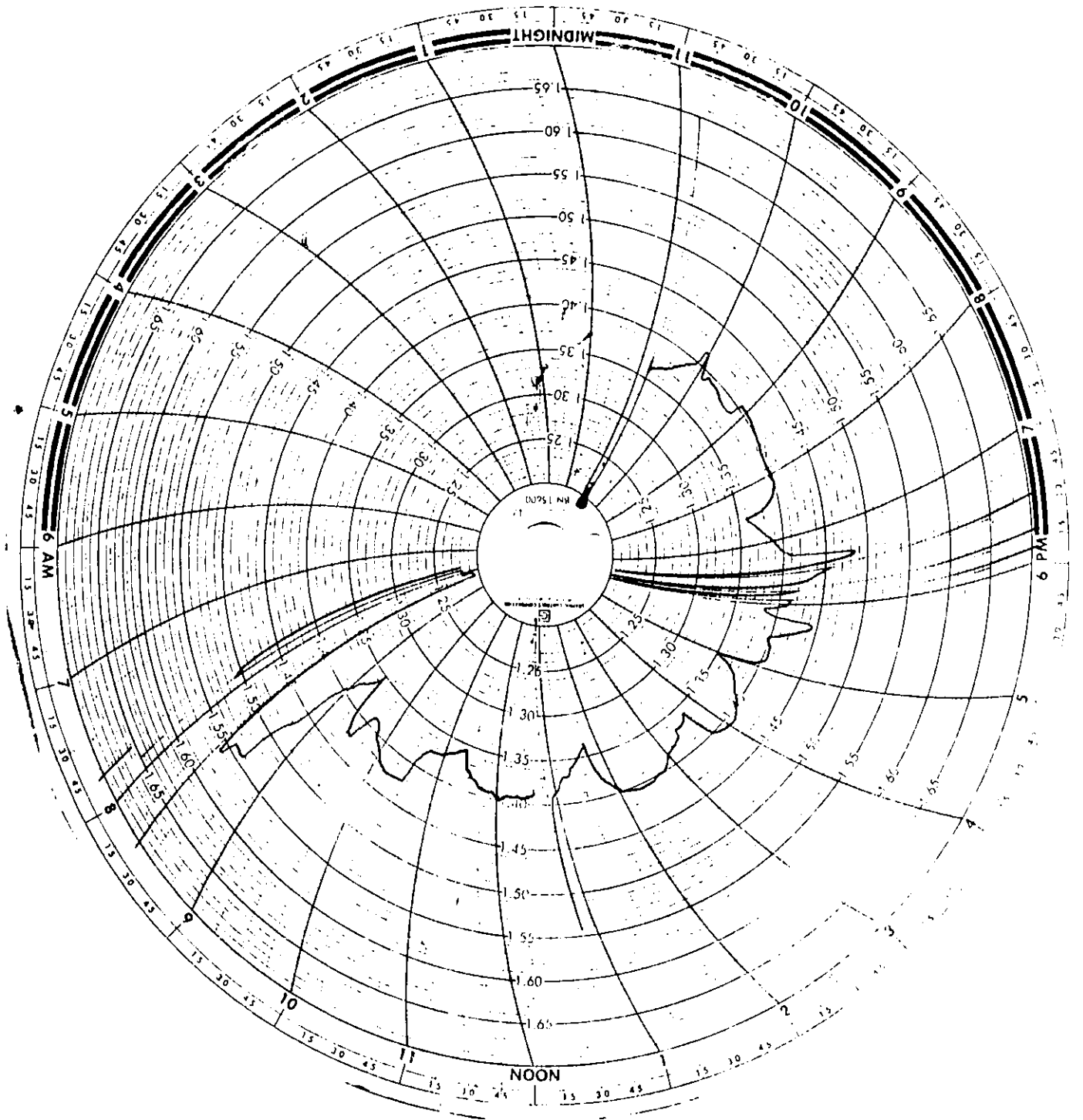


Figure Four: With DP Cell

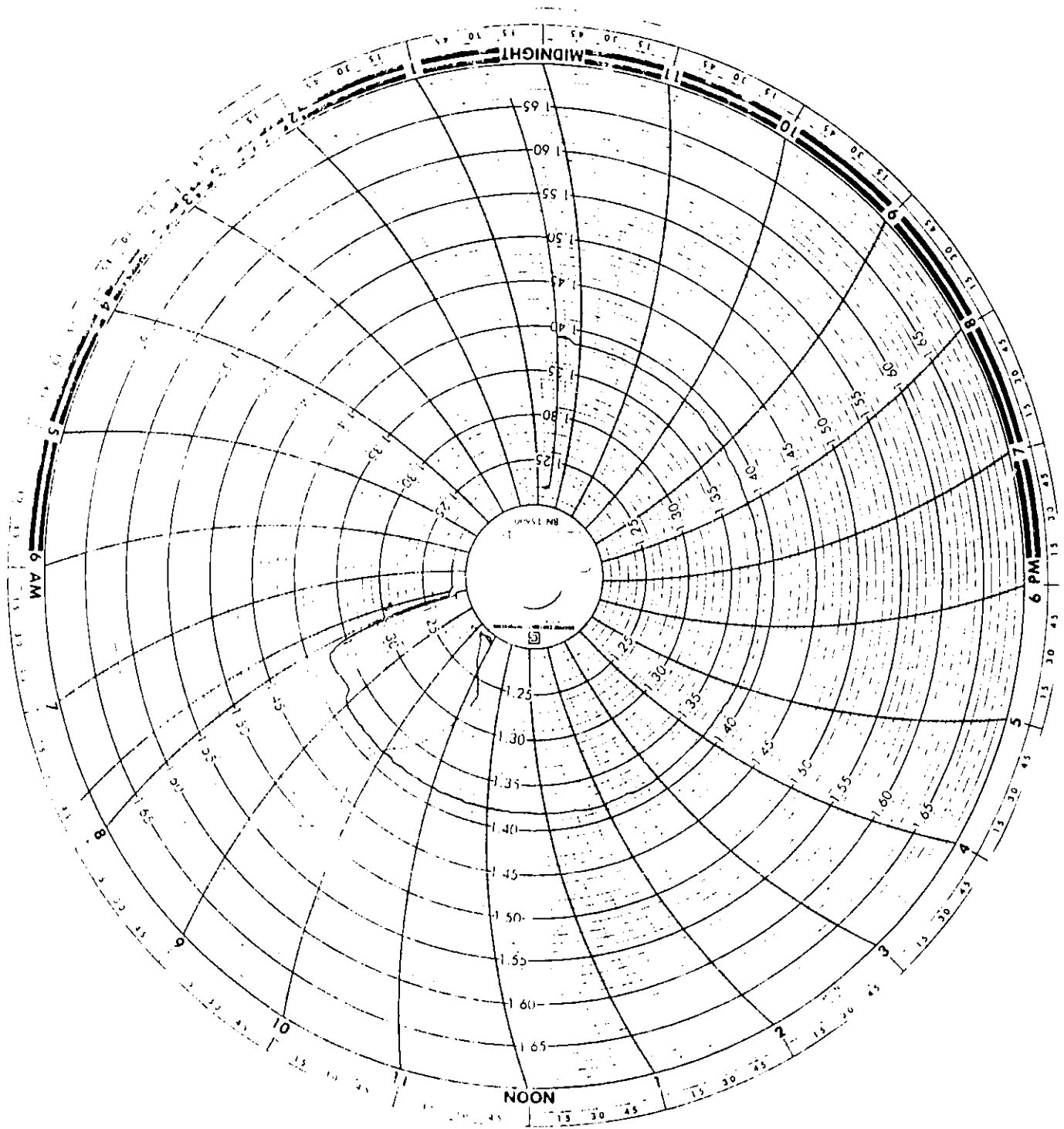


Figure Five: With Kay-Ray

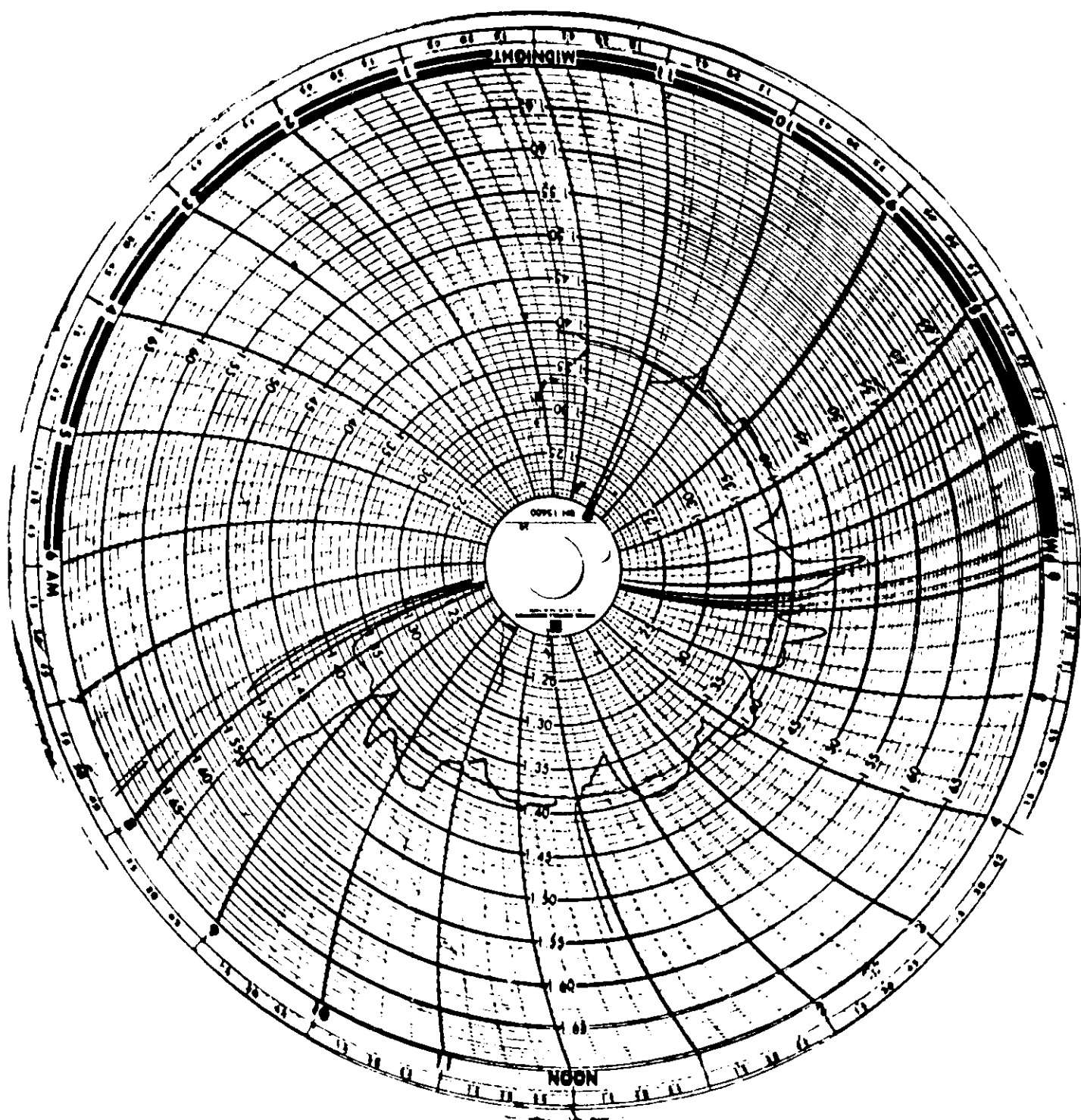


Figure Six: Kay-Ray/ DP Cell

## PACIFIC ABRASIVE FLUID LETDOWN VALVE

N.J. Condon, F.R. O'Brien  
MCC Pacific Valves  
3201 Walnut Avenue  
Long Beach, California 90807

### Abstract

Control of high pressure, high temperature abrasive fluids is the objective of a new valve from Pacific Valves. The key design feature in this control component is energy dissipation through self impingement of opposing fluid streams. Both fluid velocity and erosion are thereby effectively mitigated. To further promote durability, other valve features include a two stage letdown, reusable trim and wear resistant trim materials. Typical service conditions for the valve are 2000 psi differential pressure letdown at 900°F. Abrasive slurries from coal, oil shale, diatomaceous earth or other processes can be handled.

Flow tests (80 psig water) conducted on a laboratory prototype have shown a linear Cv response and good rangeability for the design. Pilot plant testing is now recommended to characterize valve performance under actual service conditions.

### Introduction

Control of high pressure, high temperature abrasive fluids is the objective of a new valve developed by Pacific Valves. This valve has evolved through several years of design and development directed toward meeting the need for a reliable, durable high pressure abrasive fluid control component. Difficulties encountered with modified globe valves, as well as other proprietary high pressure letdown devices, are well documented and configurations having functions that would be rapidly destroyed through erosion have been avoided.

Typical service conditions for the Pacific valve are 2000 psi differential pressure and 900°F. with abrasive fluids from coal, oil shale, or other industrial processes. Higher pressures and temperatures (e.g., 4000 psi, 1000°F) are considered readily attainable. A patent is currently pending on the Pacific design. No difficulties are envisioned in scaling up to commercial sizes. Larger trim is readily available and operating forces should remain virtually unchanged, since the only unbalanced force is due to the differential pressure acting on the stem area.

### Valve Features

The heart of Pacific's valve is the unique trim design which makes use of the principle of self-impingement to reduce the areas subject to high velocity erosion. Two stages of pressure letdown are employed (Figure 1). The first consists of two cylindrical elements which control pressure drop in the primary letdown region. A fixed inner element, the orifice plug, contains two slots located 180° apart to direct two opposing flow streams into the plug cavity, where collision of the streams dissipates most of the kinetic energy of the high pressure fluid being controlled.

A movable outer element, the orifice sleeve, is attached to the stem and partially covers the slots. The sleeve may be adjusted to increase or reduce the exposed area of the slots and thereby modulate flow through the valve.

The second pressure letdown stage consists of a back pressure orifice located downstream to further dissipate kinetic energy. It features a separately replaceable element. As presently configured, the Pacific valve is not designed to shut off flow completely. This function must be accomplished by a separate upstream shutoff valve.

In operation, flow enters the orifice plug through the two opposed slots which are open to the outlet. The effective length of the slots is varied by means of the external close-fitting sleeve attached to the stem. It is recognized that the slots and the edge of the sleeve will, in time, depending on material, erode to a degree that will make control of the flow impossible. At this time it will not be necessary to dismantle the valve and replace the trim. A second set of slots (normally covered) may be put into operation by turning the valve stem  $50^\circ$  and exposing the new slots, thereby extending trim life by as much as 100%. Eventually, however, this second part of the trim will no longer control flow and it will then be necessary to replace the orifice plug and possibly the back pressure orifice. The orifice sleeve, however, is reversible and ready to serve another period. It requires replacement only every other time that the plug is replaced.

With ease of maintenance in mind, the valve has been designed such that all trim parts may be replaced when necessary without removing the valve from the line and without removing the actuator from the valve. Furthermore, in order to prevent damage to the hard trim parts during assembly or disassembly, the bonnet incorporates a skirt to guide it in the body as long as the orifice sleeve and plug are engaged. The orifice sleeve is retained in such a manner that it has freedom to move laterally to avoid side loading the orifice plug due to concentricity tolerances.

The orifice plug is retained with a nut having two parallel flats over which only a special tool will fit. This tool is guided in the body and consequently cannot touch the orifice plug. The orifice sleeve, in turn, is of sufficient thickness to tolerate a substantial amount of erosion without losing structural strength. The part of the stem exposed to the line fluid is short and in an area of the flow stream where severe erosive velocities are minimal.

The body-bonnet joint uses a pressure energized soft stainless steel seal ring retained by a four piece segment ring located in a groove near the top of the body. Three screws are used to provide initial sealing. Thereafter, internal pressure provides the sealing force. The seal ring is reusable.

To prevent migration of solids into clearances, an elevated temperature grease with a high nickel content will be applied to all internal parts and the cavity below the stuffing box will be entirely filled.

Positioning of the plug during operation is accomplished by a hydraulic or pneumatic actuator. For pneumatic operation, a conventional diaphragm actuator is used. It is opposed by a standard compression spring which acts directly on the stem and holds the valve in the closed position with no pressure on the actuator. This arrangement permits the use of a simple bell crank between the diaphragm and the spring and eliminates the need for a close tolerance, low hysteresis linkage which would be necessary if the spring were incorporated in the actuator. The actuator illustrated in Figure 1 is sized for operation with a 3 to 30 psig pressure. A positioner (not shown) is incorporated to provide the sensitivity required for accurate flow control. An angle configuration was chosen for the body to permit removal of the bonnet for trim replacement without disturbing the actuator. It also permits straight line exit of high velocity erosive flow.

When removing the valve for servicing, it is not necessary to disconnect air lines and conduit. The actuator accessories package can be easily detached from the valve and, if so desired, left at the site. The letdown valve shown employs standard Grayloc<sup>1</sup> hubs for inlet and outlet connections. Other connections are readily adaptable.

#### Materials

Materials for the letdown valve were selected to maximize resistance to elevated temperature, wear and thermal shock. The valve body is comprised of ASTM A182 F300 series stainless steel. Trim components for the primary and secondary letdown areas (i.e., sleeve, orifice and plug) are available in several material types: tungsten carbide, treated tungsten carbides (e.g., diffusion coated with titanium diboride) or high performance ceramics (e.g., silicon carbide or sintered silicon nitride), depending on service conditions and customer preference.

Valve stem packing consists of die formed graphite rings (e.g., Grafoil<sup>2</sup>, Graphlock<sup>3</sup>) and is fully adjustable during service. The body/bonnet joint employs a reusable chrome plated stainless steel seal ring.

#### Valve Performance

A laboratory prototype of the Pacific letdown valve was constructed to study its flow behavior. Valve materials were chosen to satisfy ambient temperature conditions with 80 psig water as the fluid medium, and included a carbon steel body with precision machined nylon trim parts. Valve size was 2" with the trim exactly duplicating the internal configuration of Pacific's letdown valve design for 2" through 6" sizes.

Results of the flow test (Figure 2) indicate a smooth, generally linear change in flow coefficient (Cv) with increasing flow rate for the self-impingement design. Maximum measured Cv was 1.15 in these tests. Rangeability, defined as the ratio of maximum to minimum controllable flow, was determined to be 19 to 1. Further testing performed under actual service conditions will be required to evaluate the abrasion resistance and durability of the proposed trim components.

### Summary

In conclusion, Pacific's valve for control of abrasive fluids combines a unique energy dissipation design with practical maintenance features and erosion resistant materials. Longevity of trim parts is enhanced by two stage pressure letdown and renewable trim surfaces. Flow tests have confirmed the ability of this valve to demonstrate a linear Cv response. Pilot plant testing is now recommended to characterize valve performance under actual service conditions.

### References

1. Registered trademark, Gray Tool Company.
2. Registered trademark, Union Carbide Company.
3. Registered trademark, Garlock Div., Colt Industries.

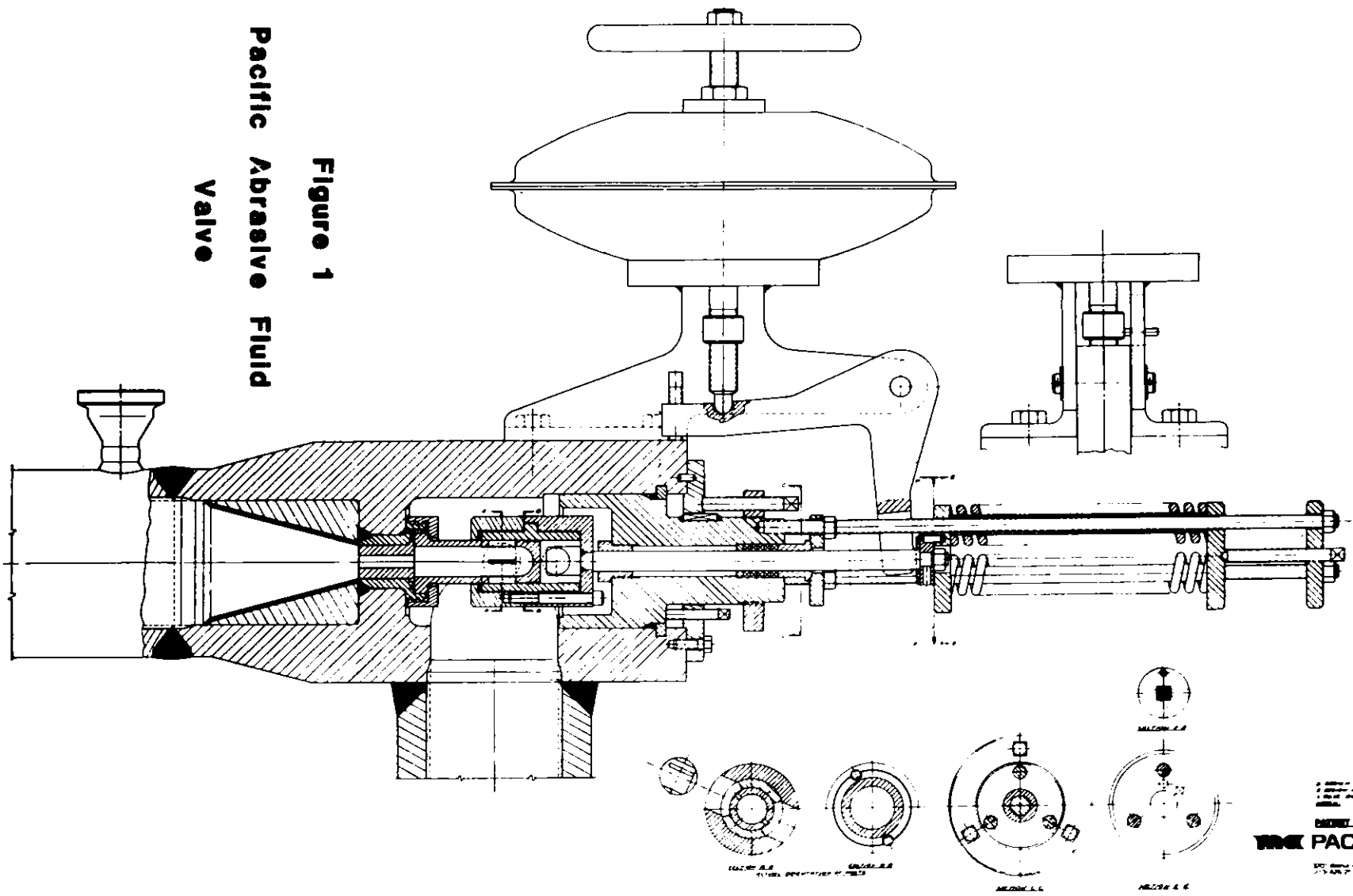


**Figure 1**  
**Pacific Abrasive Fluid**  
**Valve**

1. Material: Cast Iron  
 2. Material: Steel  
 3. Material: Brass  
 4. Material: Bronze  
 5. Material: Aluminum  
 6. Material: Inconel
   
**WRITE ADDRESS FOR**  
**PACIFIC VALVES**  

 1000 W. 10th St., Portland, Ore.  
 U.S.A.



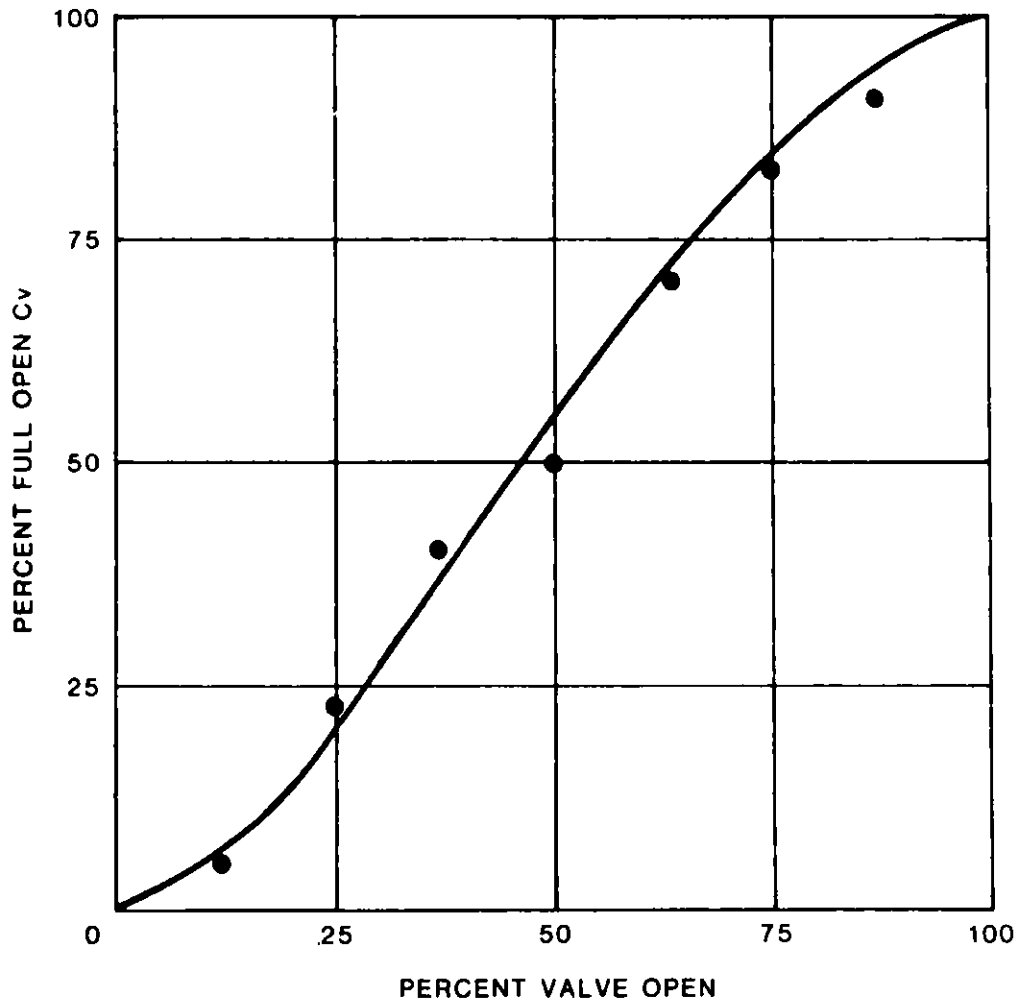


**FIGURE 2. FLOW PERFORMANCE OF  
PACIFIC ABRASIVE FLUID VALVE**

DESIGN PRINCIPLES OF LOW IMPINGEMENT TYPE SLURRYLETDOWN VALVES

Henry H. Illing  
Kieley & Mueller  
P. O. Box 907  
64 Genung St.  
Middletown, NY 10940

Many versions of slurry valves are in use and have evolved over years of development for many kinds of two and three phase service. This discussion will be limited to requirements for throttling valves exposed to a combination of high temperature and high pressure fluid with extremely hard particulate entrainment. In a few hours of throttling service, this combination can destroy many types of valves that would operate for years in less hostile service.

Probably the worst combination of elements for slurry valves exists in throttling letdown service in the synfuels industry. Here the problems of erosion are compounded by corrosion, cavitation, coking, differential expansion, thermal shock, and mechanical vibration.

Since erosion is the most significant in this list, the obvious answer would seem to be velocity control. A conventional cascade trim valve is shown in Figure 1. However, where pressure drops as high as 2,000 psi are encountered, the number of stages required to reduce velocity within reasonable limits for particle erosion control would grow from the eight shown here to fifteen or more. The proportional sizing to these stages in addition to solids accumulation, maintenance problems, and carbide costs appear to eliminate these types at this time.

Another possibility for this type of service would be the friction type, drag style trim shown in Figure 2, were it not for the particle size and concentration. In liquifaction processes, size can be as large as 1/8 inch and concentration as high as 30% by weight. Since this type trim depends on a combination of wall friction from extremely small hydraulic radii and multiple direction changes, the plugging problem is insurmountable.

Elimination of both staging methods and friction principles brings us to the flow to close high recovery (low  $F_L$ ) streamlined angle valve for this service. Figure 3 shows one of these.

In this type valve, we allow trim velocities to reach extremely high values. Now the so-called high recovery valve that exhibits recovery coefficients as low as .25 becomes a very inefficient, low recovery device. This is because the flow velocity in the vena contracta becomes sonic and shock waves are generated. Each shock wave is an irreversible, pressure-reducing

mechanism and by allowing a concentration of these to exist downstream, velocities are reduced to acceptable values at the exit plane. Figure 4 attempts to show this schematically. This can be confusing to those who do sizing because the so-called venturi angle valve with its streamlined passages is considered to be the ultimate in high Cv, high recovery valves. However, it is important to realize that the recovery coefficient is a number that is picked from data taken up to the point where choked flow begins. (10% pressure drop change with less than 2% flow change). In liquifaction service we are far beyond this point in a region where flow is no longer obeying the simple square root law. So paradoxically, the high recovery angle valve now becomes a very low recovery device.

Referring to Figure 3 and beginning at the inlet, the body I.D. is sized to give velocities that are adequate to carry the slurry but low enough to keep body erosion at a negligible value, (5 to 10 ft. per second). The bowl area acts as a miniature receiver to allow some distribution of particles that would otherwise tend to centrifuge to the outside of the curve.

Next, the stream is led to the seat and plug by tapered surfaces to minimize the angles of impingement.

Stepping of the seat ring removes the seat ring from the primary throttling area except for very low stroke positions. At greater strokes the shoulder forms the main restriction and erosion that takes place here does not affect seat leakage. This tight shut off capability can be extremely important in the event of block valve failure. Also, it can be used to extend the life of block valves by sharing their function with them. There is also a slight cascade effect that is derived from this geometry if the plug is required to operate near the seat. It is in this local area of the trim that we have maximum velocity and erosion. Static pressures in this area are near zero and gross amounts of liquid change their state to vapor.

It is also in this area that severe exciting frequencies exist that can cause resonant lateral vibrations of the plug. This type of vibration can be extremely damaging to the plug and stem and must be controlled by close clearances in a rigid guide. These clearances must be maintained at operating temperature and therefore careful selection of materials with near equal expansion coefficients is essential. The guide is not restrained by the body bore in the lateral direction but is clamped at the shoulder by a Belleville spring stack. This allows clearance to be used between the body and guide for easier disassembly with the spring pressure on the shoulder maintaining the required rigidity against lateral vibration. As indicated earlier, vapors are forced to supersonic velocity by the plug restriction. This is evidenced by choking of the flow stream. (Flow remains unchanged for changes in downstream pressure).

Referring to Figure 4, we know from long experience on valves used for clean cavitating liquids that without armor protection in the recovery area, body erosion in the areas where shock diamonds are indicated will be excessive. Carbide is used in the upstream cone where turbulence is most intense and stellite is placed in the downstream cone where much of the energy has already been dissipated. Running flow to close is the only known way of providing this protection in the downstream recovery area.

Shrink fits are needed at the interfaces of stainless steel to carbide and stainless steel to stellite to insure that differential expansion does not open clearances that would cause vibration.

Where tungsten carbide is being retained by stainless, it is extremely important to use positive retention in addition to the shrink fit. Experience has shown that, although theoretically it is possible to retain a plug by shrink alone, in reality, the quality cannot be sufficiently controlled to yield good reliability. Figure 5 shows one method of doing this. The sleeve retains the carbide by a small shoulder and a pin retains the sleeve to the post. The sleeve is shrunk on both the carbide and the post to eliminate clearance at high temperature.

The carbide diffuser and the tailpipe diffuser are also both shrink fitted and retained by a shoulder in the parent material.

Very large flats are necessary on the post O.D. to avoid packing of solid material between the plug and bonnet.

Stellite is considered the best material for the guide because of its toughness and anti-galling characteristics.

After even a short time in coal liquifaction letdown service, valve disassembly can be a problem due to bonding of parts with solidified coal. Use of heat and adequate wrenching are the most direct solutions to this. Other things that help are gold plating of thread surfaces, metal "o" rings to prevent migration of coal to threads, and openings to allow high temperature grease to be pumped into cavities that are problems. Retention of the seat ring so that an adequate ring-to-body seal is maintained is another important consideration. Here again, adequate wrenching cannot be overemphasized. Thread design is a compromise between a thread that is fine enough to give adequate squeeze to the graphoil gasket but coarse enough to offer generous clearances for removal without bonding or galling. Gold plating of threads should always be considered when finer pitches are used.

In a flow to close configuration such as this, an adverse negative gradient can cause stem positioning problems. With a spring loaded actuator, the rate of change of stem load can be-

come equal to the rate of change of the spring system. If it is opposite in sign then the spring rates cancel and air pressure changes cannot find equilibrium. To protect against this possible instability, it is necessary to use a viscous damper. This is shown in cross-section in Figure 6 and is normally located between the diaphragm casing and the spring chamber. This is an oil filled, double-acting cylinder with a bypass connected to both ends. A needle valve is installed in the bypass to allow adjustment for the required damping and slew rate.

One further consideration in designing for slurry letdown service for coal liquifaction is scaling feasibility. Most present designs have been sized for pilot plant operation. Problems in scaling up for demonstration plant size are minimized by relatively simple streamline construction. As long as impingement angles, diffuser cone angles, and clearances are maintained, a reasonably good scaling job should be achieved.

Another aspect that is worth mentioning is noise. In this type of service there is no existing noise attenuating trim that would be capable of both withstanding the erosion and remaining open (unplugged). Present plans to make full scale plants using modules from demonstration plants will keep the operating Cvs relatively low. This, in combination with the extremely heavy pipe walls that are used, should keep the estimated DB levels under 100. Loose or worn plug guides can allow mechanical vibration that will create substantially higher levels.

In the present state of the art, the flow to close streamlined angle valve is the only configuration capable of controlling both trim erosion and body erosion by means of low impingement angles and hardened downstream diffusers. The displaced seat seal offers tight shut off after prolonged running.

Until some sort of breakthrough occurs in either materials of construction or valve geometry, it appears that the type of configuration shown here will continue to be the most prominent contender for this type of service.

#### References:

N. D. Bond, "H-Coal Pilot Plant High Pressure and Temperature Let Down Valve Experience".

T. L. Dahl, "Coal Liquifaction Valve Operating Experience at Coal Liquifaction Pilot Plants".

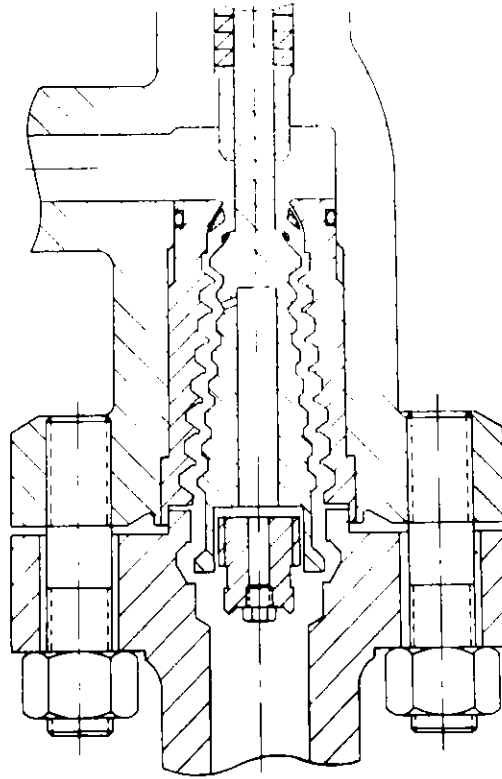


FIG 1

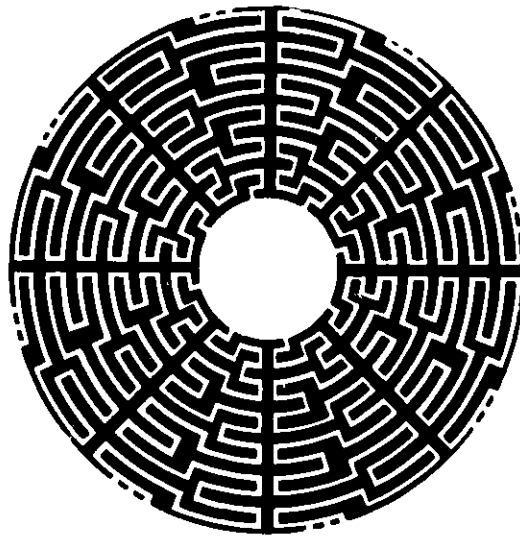


FIG 2

---

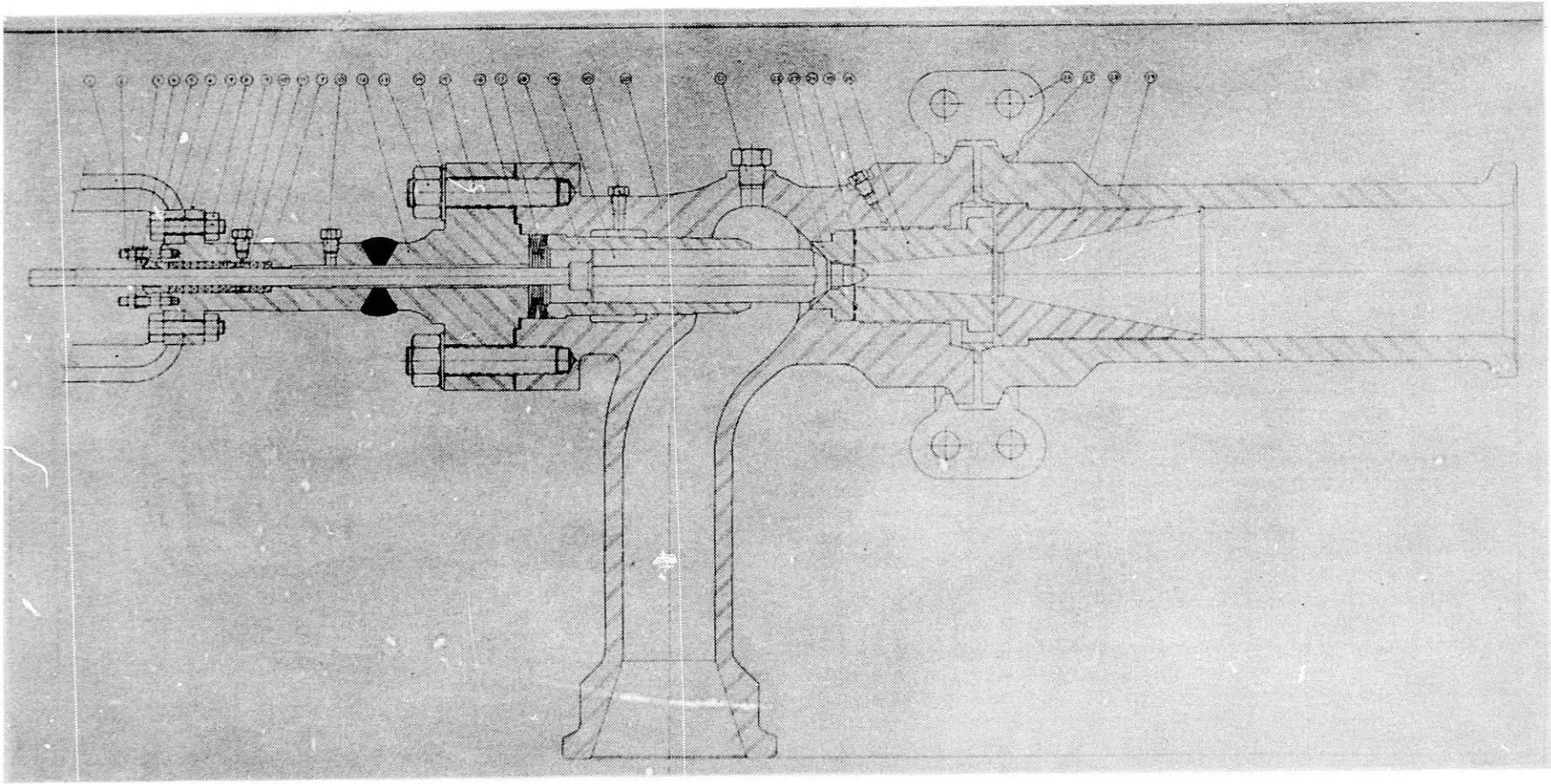


FIG 3

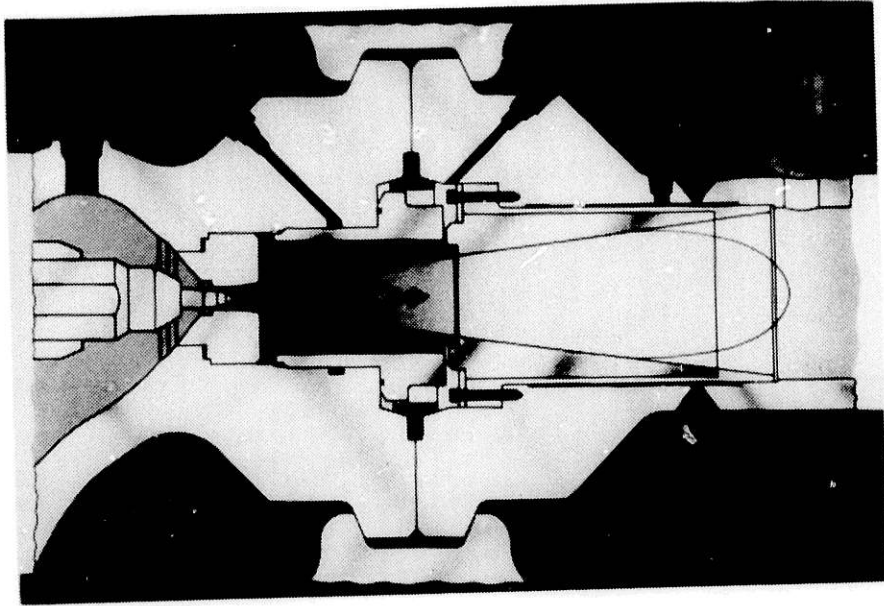


FIG 4

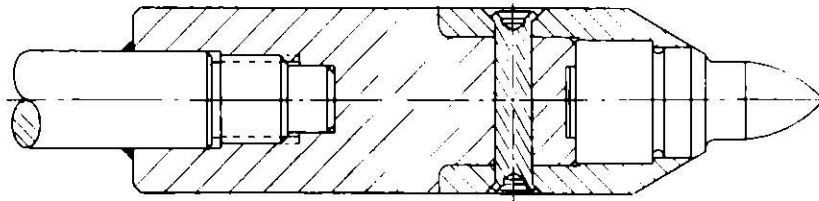


FIG 5



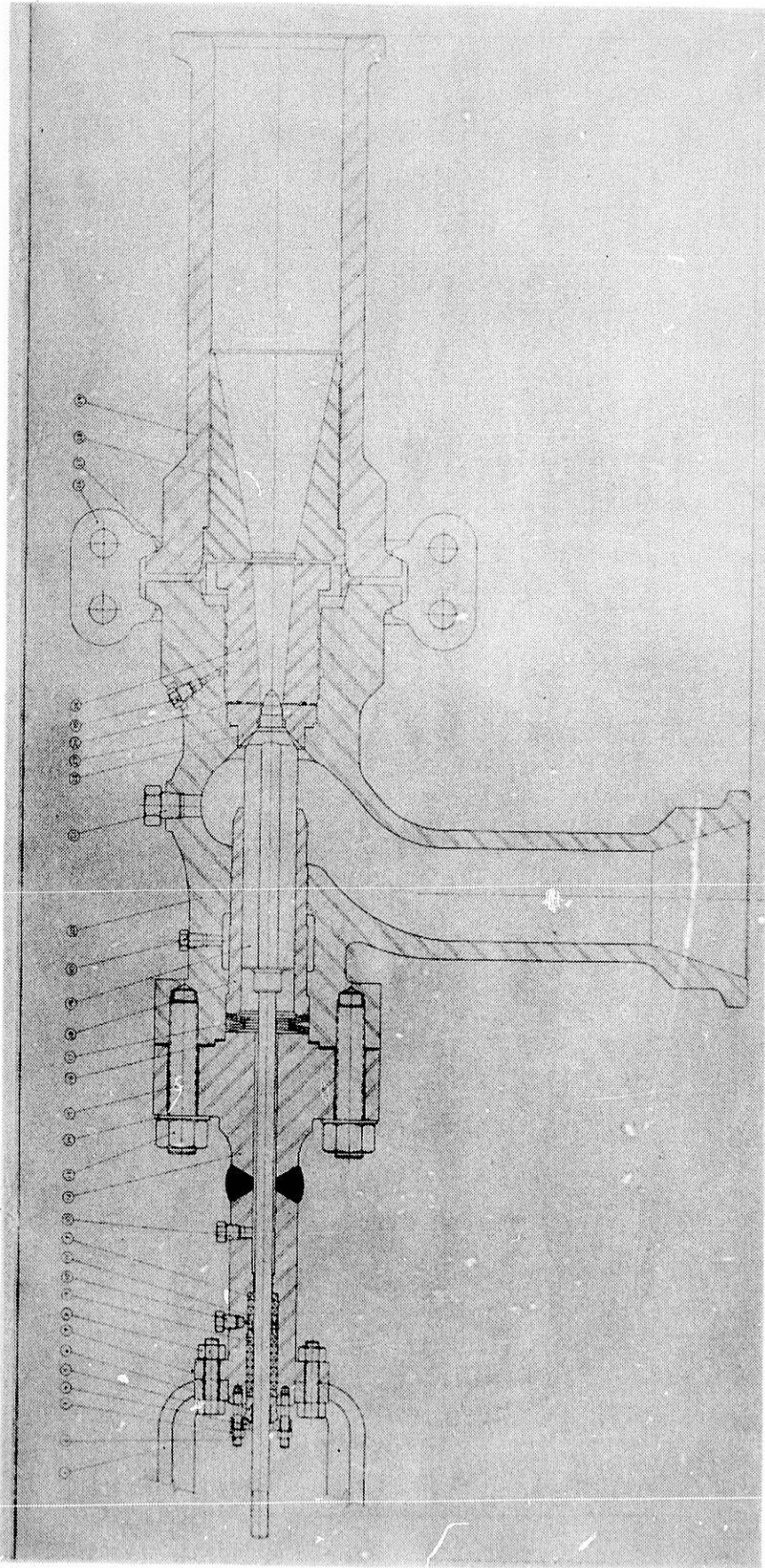


FIG 3

H-COAL PILOT PLANT HIGH PRESSURE AND  
TEMPERATURE LETDOWN VALVE EXPERIENCE

N. D. Bond and W. R. Miller  
Ashland Synthetic Fuels, Inc.  
P. O. Box 391  
Ashland, KY 41101  
606/739-8621

Abstract

This report will cover the development of the various letdown valves used for the two-stage high pressure and temperature coal slurry letdown system as used at the H-Coal Pilot Plant. The period covered in this report will be from Coal Run #6 through Coal Run #8. The valves discussed are the Cameron, Hammel-Dahl, Kieley & Mueller, and two different Masoneilans.

BLOCK VALVES IN LIQUEFACTION LETDOWN SERVICE  
-AN UPDATE

Marvin Beasley  
Mogas Industries, Inc.  
P.O. Drawer 11529  
Houston, TX 77293  
713/449-0291

Verne Ragle  
Ashland Synthetic Fuel, Inc.  
P.O. Box 391  
Ashland, KY 41101  
606/739-8621

Introduction

In June, 1981 a report was made on the status of block valves in coal conversion processes.<sup>1</sup> Since that time, additional operating experience has allowed reflection on the design features, materials and concepts presented. It is the purpose of this paper to update the information gained from this and to present recommendations for future actions.

Background

The H-Coal Pilot Plant in Catlettsburg, Kentucky is a direct catalytic hydro-liquefaction process developed by Hydrocarbon Research, Inc. to convert coal to liquids. The 600 T/D Pilot Plant is the largest capacity direct liquefaction plant in the world.

The basic process consists of the reactor, vapor-liquid separator, dual letdown trains and flash drums as shown in Figure 1. The details of the process have been previously reported.<sup>2</sup> The block valves to be discussed are those isolating the letdown valves shown in Figure 1.

The block valves in the letdown area are considered to be some of the most severe service valves in the plant. They must operate under a variety of operating and fluid conditions. They are either open or closed and when required they must perform in order to prevent plant shutdown.

Since the last report which covered the period through May 1981, operating experience has been gained on two different types of coal.<sup>1</sup> Coal run #8 lasted 131 days using Illinois #6 coal of which 90 days were on coal.<sup>3</sup> Run #9 on Wyodak coal was 26 days of which 19 days were on coal.

In general, the Mogas C-1 Block Valves performed under plant conditions; however, several problems related to design, materials and operation were evident. The results of these findings were presented below including the logical reasons for these problems.

Valve Inspection

In January 1982, and May 1982, several Mogas C-1 Ball Valves were removed from service and inspected. Figure 2 lists the valves involved along with a brief description. See Figure 1 for valve location and Figure 3 for valve construction details. Reference (1) should be consulted for a thorough description of the Mogas C-1 valve design. It cannot be overemphasized how easily these valves were to disassemble, refurbish and return to service. Unlike other valve designs, this feature of maintainability is important for block valves in this type of service.

The method used in this inspection was a joint effort by Mogas and Ashland Synthetic Fuels, Inc. As Valves were removed from service, orientation and position were marked. During dis-

assembly, all features were carefully documented and photographed for future investigation efforts. Orientation of parts, condition at removal and special features were recorded. The amount of data was voluminous, but in general the following key facts should be noted:

- (1) Two significant types of failures were found. These rendered two valves inoperable and caused two others to leak. Detailed followup investigation produced reasons for these failures which are explained below.
- (2) The proper selection of ball and seat material for wear is important. By far, the best combination has proven to be Chromium Carbide LC-1 coating (applied by the Linde d-gun<sup>®</sup> process of Union Carbide) on the ball and Stellite #3 seat rings. Both TMT<sup>®</sup>-5 (packed diffused surface modification by Turbine Metal Technology) and Stellite #6 weld overlay for ball coatings did not stand up as well.
- (3) Minor body gasket and stem seal leakage was evident. These caused no operational difficulties and can probably be corrected with design and manufacturing modifications.
- (4) The double arcuate cut in the ball does indeed work in minimizing erosion.<sup>1</sup> By accident, an actuator was hooked up incorrectly to cause clockwise rotation to open the valve. This put the arcuate cut on the side of the ball port which was opposite the initial opening point. Normally, the arcuate cut is on the side of the ball port which opens first. As shown in Figure 4, this produced erosion on the ball that has previously been eliminated by the arcuate cut.

#### Discussion of Two Valves

The valves which were found to be inoperable were B3 and B7. In both cases the postulated scenarios for failure are as follows:

- (1) Operational factors produced conditions conducive to high torque loads. The most significant was thermal transients of 500 to 600 degrees Fahrenheit that occurred when placing the valves in service and which caused severe stress conditions in the valve. Other contributing factors may have been coking and solids blockage.
- (2) Actuator oversizing provided the power source to continue to rotate the ball until failure occurred.
- (3) Stellite #3 seat ring breakage, which was a common denominator on all failed valves, compounded the situation and contributed to total lockup.
- (4) Material deficiencies contributed to failure and valve inoperability.
- (5) With the balls locked in an intermediate position, subsequent erosion damage to balls and body resulted.

Valve B3 was found to have a sheared stem extension (that item above the stem used to extend the stem for an actuator). A metallurgical analysis of the stem extension showed that the yield strength was below that specified as it was supplied with a temper at too high a temperature. The stem extension then became the weak link which sheared when actuator overtorque resulted from ball and seat lockup.

A detailed metallurgical analysis of the ball, seats and stem extension was performed by the

Institute for Mining and Minerals Research<sup>4</sup> (IMMR). See Reference (4) for full details. Their analysis suggests that impact loading of the seat ring could have caused it to break. They attribute valve lockup to seat breakage as well as TMT-5 coating wear and break-through. This sequence probably occurred over several cycles of operation.

Valve B7 had a portion of the ball sheared. A review of quality records at Mogas verified the findings of IMMR that the ball material was too hard.<sup>5</sup> This material was supplied in the incorrectly heat treated condition. Being hard, it easily initiated and propagated a crack when actuator overtorque resulted from ball and seat lockup.

The IMMR report indicates the propagating crack created an uneven stress distribution in the seat ring causing it to break. It is equally possible that seat breakage caused lockup which resulted in ball overtorque and cracking. In any case, operational transients produced shock loads and contributed to the valve's inoperability. As above, this sequence probably occurred over several cycles of operation.

Two of the valves that were inspected in May 1982, B-1 and B-4, showed striking similarity to those previously described. Both had one or more broken seats and stem extensions which had twisted in varying amounts. The valves are known to have experienced thermal transients of several hundred degrees when being put into service. This resulted in lockup of the ball and eventual stem extension failure. It is not known if the cracked seats were caused by the thermal shock or by the extreme forces exerted on the seats by the ball in the locked up condition.

### Recommendations

Based on the two significant types of failures plus other operating data, several general and specific comments are applicable. While valve failures are never acceptable, the severity of the operating conditions must always be considered when judging a valve's performance. In addition, both operators and manufacturers must learn from the failures so that both can attempt to make changes which will eliminate future problems.

As regards operations, two factors are felt to have been direct contributors. The first involves operational thermal and pressure transients. These can never be predicted, nor eliminated; however, operators must continually strive to minimize their impact by observing sound operation procedures. *Valve manufacturers must also review and modify their designs as necessary to accommodate a larger range of operational transients.*

The second factor relates to actuator specifications. Valve actuators must be sized to produce the necessary torques for actuation, but must not be oversized. Proper operating safety features such as pressure regulators on actuator air supplies must be effectively used to minimize valve damage.

Valve manufacturers must also ensure that their designs will withstand a reasonable amount of overtorque. The valve design must be based on this torque value not only when the actuator is positioned in its stops, but also for any possible intermediate position. Plant operators and the valve manufacturers must agree on a torque value and then work together to assure that the proper torque is available. The two significant failures reported above were compounded by having actuators which could deliver torques well in excess of maximum recommended levels.

As reported in Reference (1), correct material is crucial to proper valve operation and performance. Chemical compositions must be correct and physical properties must be within specified minimum and maximum values. In addition, because of characteristics of materials, certain compromises may be required. In the case of seat rings, it has become evident that Stellite #3 has superior wear resistance to many other materials as evidenced by the excellent condition of most of those removed from service. However, the ductility and impact resistance properties of Stellite #3 are much lower than desired. The latest experience would indicate that pressure and temperature transients must be considered in valve design. This may necessitate using an alternate material for seat rings which will give better impact resistance and ductility even at the expense of reducing wear resistance to some extent.

It is apparent that the conditions a block valve is subjected to in coal liquefaction service are severe. Much knowledge has been gained by both successes and failures over the past two

years. Current long run times, as compared to two years ago, are due to a cooperative effort between manufacturer and user and resulted when operating experiences were used as a learning tool. By eliminating weaknesses and building on the strong points, a valve that is suitable for coal liquefaction service has evolved.

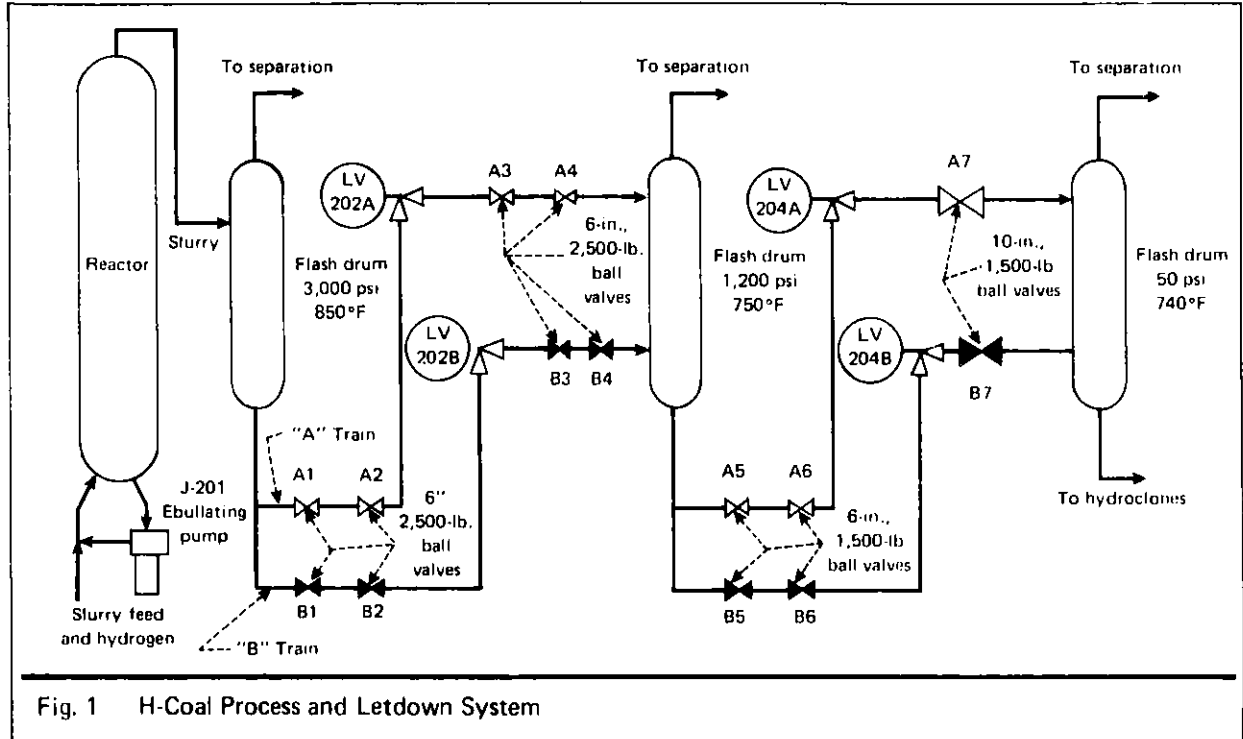


Fig. 1 H-Coal Process and Letdown System

VALVE NUMBER	SIZE	INSPECTION DATE	COMMENT
B1	6" 2500#	January, 1982	Installed January, 1981
B2	6" 2500#	January, 1982	Installed January, 1981
B3	6" 2500#	January, 1982	Installed January, 1981
B4	6" 2500#	January, 1982	Installed January, 1981
B5	6" 2500#	January, 1982	Installed January, 1981
B6	6" 2500#	January, 1982	Installed January, 1981
B7	10" 2500#	January, 1982	Installed January, 1981
B1	6" 2500#	May, 1982	Reworked, January, 1982
B4	6" 2500#	May, 1982	Reworked, January, 1982
A1	6" 2500#	May, 1982	Installed January, 1982
A4	6" 2500#	May, 1982	Installed January, 1982

Fig. 2

Table on Block Valves

PARTS LIST		TRIM SPECIFICATIONS	
Item	Quan	Description	55 · Full SS Valve ·20°F to 1000°F
1	1	Assembly, Ball and Seat Ring	
2	1	Ball	AISI 410 Stainless St. Chrome Carbide Coating
3	2	Dog	Stellite #6
1C	2	Clip, Dog	Inconel X-750
1D	2	Ring, Seat	Stellite #3
2	1	Body	ASTM A182 Gr. F316 Stainless Steel
3	2	Connection, End	ASTM A182 Gr. F316 Stainless Steel
5	2	Gasket, Body	18-8 Stainless St. Asbestos Filled
6	1	Indicator, Position	AISI 1020 or Equal
7	AR	Nut	ASTM A194 Gr. 2 Cad. Plt.
8	1	Nut, Operating Wrench	AISI C-1213 or equal
11A	2	Spring, Load	AISI 316 Stainless Steel
12	1	Gland, Packing	AISI 1020 or equal
13	1	Ring, Splined Stem Stop	AISI 4130 or equal
14	1	Ring, Lower Stem Packing	AISI 1020 Aerocoat 4 Coating or Impervious Graphite
15	1	Ring, Upper Stem Packing	Impervious Graphite
16	2	Screw, Load	SAE Grade 5
17	1	Stem	AISI 660 Stainless Steel
18	AR	Stud	ASTM A193 Gr. B7 Cad. Plt.
19	AR	Stud	ASTM A193 Gr. B7 Cad. Plt.
20	1	Washer, Load	AISI 1020 or equal
21	2	Washer, Lock	AISI 1020 or equal
25	1	Bushing	Impervious Graphite
26	1	Pin, Locating	AISI 316 Stainless Steel

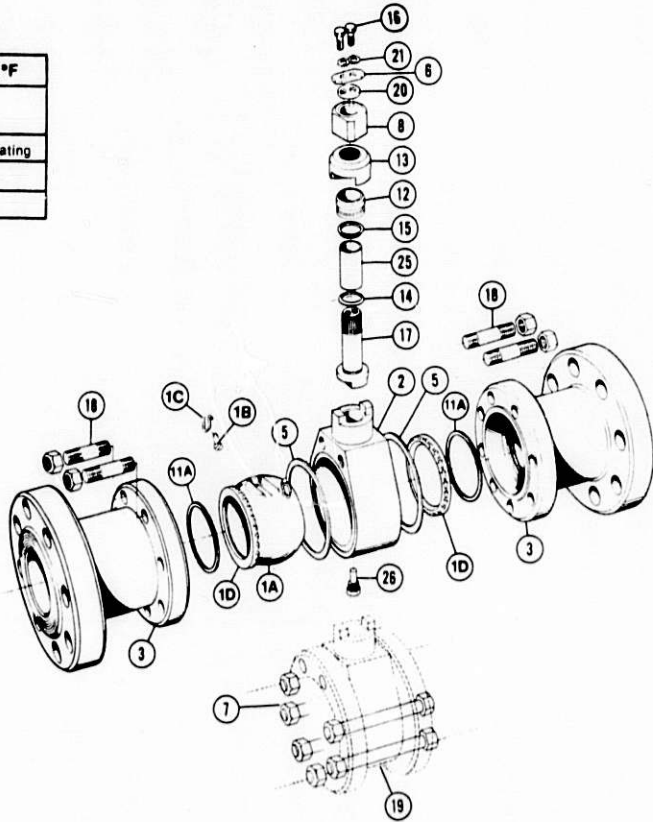


Fig. 3

Exploded View of Synthetic Fuels Block Valve

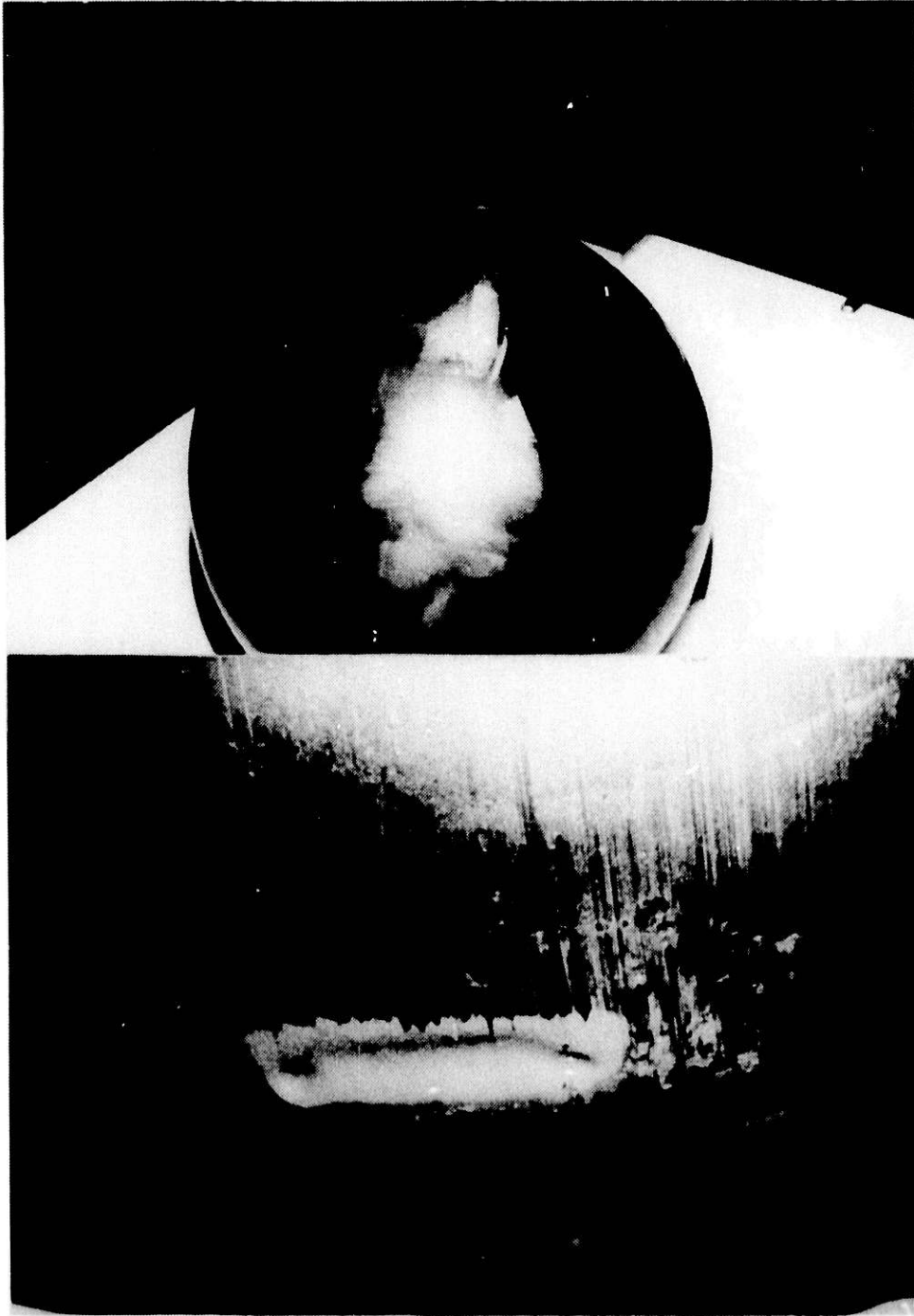


Fig. 4 Valve B6 Ball Erosion With No Arcuate Cut



References

- (1) "Current State-of-the-Art of Block Valves for Synthetic Fuel Plants", V. L. Mogas and M. E. Beasley, The Proceedings of the 1981 Symposium on Instrumentation and Control for Fossil Energy Process, 6/81.
- (2) "Designers Find Answers for Synfuels Processing", L. J. Ricci; pp 29-35, Chemical Engineering, July 27, 1981.
- (3) "H-Coal Pilot Finishes Illinois No. 6 Run", Synfuels Week, December 28, 1981.
- (4) "Failure of the Ball From Mogas Ball Valve B7" by V. Sethi and A. Sagues, IMMR report ME-MM-82-4, dated February 10, 1982.
- (5) "Failure of Valve B3" by V. Sethi and A. Sagues, IMMR report ME-MM-82-6, dated February 26, 1982.

## ACOUSTIC SYSTEM FOR MONITORING PRESSURE BOUNDARY WEAR\*

C. A. Youngdahl and W. A. Ellingson  
 Materials Science Division  
 Argonne National Laboratory  
 9700 S. Coss Ave., Bldg. 212  
 Argonne, IL 60439

An ultrasonic pulse-echo instrumentation system employing specially designed acoustic waveguides has been developed to monitor pressure boundary thickness at high temperatures.<sup>1-3</sup> The automatic equipment and techniques have been applied for on-line assessment of erosive wear of coal conversion process equipment operating at up to  $\sim 540^{\circ}\text{C}$  in liquefaction and gasification pilot plants. This report describes the waveguides and transducers, electronic instruments, and computer that make up the system. Also discussed are some of the results obtained in on-going field tests.

## ACOUSTIC WAVEGUIDES AND TRANSDUCERS

The acoustic waveguides in this system are solid metal rods utilized to thermally protect conventional PZT transducers while maintaining acoustic contact with the high-temperature component being monitored. The waveguides are typically mounted in groups, as shown in Fig. 1, at sites of anticipated erosive wear. The ultrasonic system described here interrogates the waveguides sequentially and can accommodate multiple groups of guides at sites each up to  $\sim 150$  m from the pulser-receiver.

Waveguide Design. Waveguide design considerations include material, dimensions, method of attachment to pressure boundaries, and sidewall treatment.

Austenitic stainless steel (SS) is favored for low thermal conductivity, and wrought material (ASTM grain size  $\sim 6$ ) is used to avoid excessive ultrasonic attenuation encountered in large-grained SS. All waveguide material stocks are screened for acceptable acoustic transparency before fabrication of guides. Additionally, a test piece of each rod stock is used to ultrasonically determine the optimal ratio between the cross-sectional areas of the neck and shoulder (see Fig. 2), because of differing radial microstructural variation between material lots. The typical neck diameter of 7 mm provides a suitable sampling area with small depression of local temperature.

Three sizes of waveguides have been developed and extensively tested. Medium-knurled, 130-mm-long, 9.5-mm-diam Type 304 SS waveguides are most frequently employed (Fig. 2); these are attached by electric arc stud welding to the components being monitored, as discussed in Ref. 2. For attachment by pressure coupling rather than welding, waveguides of 5/8-11 threaded Type 304 SS rod up to 200 mm long are utilized (Fig. 3). These longer waveguides do not require the convection-cooling fins employed by the shorter guides but do require greater clearance from nearby components and are more susceptible to mechanical disturbances. Finally, waveguides of 0.6-m length,<sup>5-6</sup> tapered in diameter from 16 to 13 mm over the length, have been developed and tested. These were equipped with support struts (Fig. 4) to preserve orientation and straightness in the environment of open flames through which they passed to the

\*Work supported by the U.S. Department of Energy, Office of Advanced Research and Technology and Office of Coal Processing/Division of Gasification.

pipng in a slurry preheater. (A ceramic cement coating and refractory wool insulation were added to each guide.) Inertial welding was used to produce a joint of low attenuation between a SS stud at the pipe and a waveguide extension (fabricated from ASME 193-B16 alloy, a strong material of lower acoustic attenuation but higher thermal conductivity than Type 304 SS). Cooling fins were attached to the opposite end of each composite waveguide outside the preheater.

To suppress trailing pulses generated within the guides, various sidewall treatments are employed, including knurling, threading, and  $4-\lambda$  diametral tapering. These treatments are discussed in Ref. 5.

Transducers. A dedicated (recoverable) transducer is bonded to the outer end of each waveguide with 5-min. epoxy and clamped in place. The preferred transducer has a nominal diameter of 3/8 in. and a frequency of 7.5 MHz -- either resonant or moderately damped longitudinal wave ( $\lambda = 0.76$  mm in steel).

Waveguide Ultrasonic Response. The ultrasonic response through a waveguide stud-welded to a specimen component is typified in Fig. 5, a video display produced on a Krautkramer-Branson 303B pulser-receiver without use of damping or zero suppression. Automatic timing by a time-analog gate (TAG) is made between echoes produced by the waveguide reference shoulder and the specimen backwall, thus eliminating any transducer-to-shoulder thermal gradient error.

The fine structure of the echoes is, however, a source of offset error unless accounted for by data reduction (see below); effort to eliminate the fine structure effect in waveguides through use of a modified triggering pulser is in progress. Figure 6 shows unambiguous multiple echoes obtained by direct contact to a plate sample with a highly damped 7.5-MHz (alpha) transducer used with the inverted preamplifier pulser-receiver mode. This technique is applicable for low-temperature surveying and calibration but is not effective through waveguides and is not ideal for erosion-channeled backwall surfaces where phase shifts are produced within echoes. Echoes such as those of Fig. 5, altered by use of instrument damping and zero suppression when needed, are therefore used in the monitoring system described here.

#### ELECTRONIC INSTRUMENTATION

The electronic data acquisition instrumentation utilized in the scanner is illustrated in Figs. 7 and 8. The waterproof cabinet containing the instruments is flushed with air from the instrument-air supply of the plant.

The KB 303B pulser-receiver with TAG is modified for use with the automatic system. A digital automatic gain control (AGC) card developed by Argonne is installed within the pulser-receiver, and rear panel controls and connectors are added for access to the AGC and to the CRT sweep-delay circuit. The AGC is utilized to compensate for the differing signal-amplitudes among multiple monitoring points and for signal-amplitude variation with transducer temperature changes.

The channel controller contains a clock of adjustable rate and a binary counter that produces a five-wire channel identity code for the system. (Each waveguide-transducer unit is identified by assignment to a specific channel number.) The controller also displays the decimal equivalent of the current

count (0-31) and provides a reset signal to the AGC with each change of count (typically one per 15 seconds).

A 32-channel trimming module permits the setting of an optimal AGC threshold level for each channel and also provides two sweep-delay time alternatives to the time set at the pulser-receiver, in order to accommodate various lengths of waveguides.

The site selection unit (upper left in Fig. 7) contains reed relay switches that sequentially connect the pulser-receiver to the remote switching stations one at a time through the associated RG58 coaxial signal cable. Although in less extensive configurations of the scanner the branches of the RG58 network have been successfully operated in parallel, they were isolated for the system shown in order to ensure adequate signal strength and to avoid echo broadening caused by reflections from parallel branches of great length. The site selection unit also contains a separate, adjustable source of regulated power for each of the remote stations, which require +5 V to operate decoders and reed relays.

Thermocouple switching, temperature-signal amplification, and compensation for cold-junction temperature are done electronically by means of commercially available circuit cards located in the site selection unit. For previous configurations of the system in which analog data were simply recorded and/or processed by the plant's data acquisition system, thermocouple switching was done by reed relays or within the plant system and without amplifiers.

For the system depicted in Fig. 7, a stand-alone data-reduction computer was developed and programmed by Argonne utilizing the commercially available enclosure and printer shown and including the internal motherboard and power supply of the STD BUS system.

Each waterproof remote enclosure (Figs. 1 and 8) contains a circuit board capable of serving up to 16 monitoring points. The active elements include one Gordos 835C-2 plug-in reed relay for each point actually utilized locally. This relay was chosen for its high open-contact voltage rating as well as for its sealed construction and compatibility with the five-volt operating system.

For use with piping having direct electrical heating, the central wire and shield of each transducer cable are effectively blocked to low frequencies by 0.015  $\mu$ f capacitors (and waveguides are individually insulated electrically except at the process piping).

#### DATA-REDUCTION COMPUTER

The data-reduction computer receives analog temperature and shoulder-to-backwall distance values as well as binary data for channel identification (Fig. 8) from the scanner and analog reference voltages from internal sources. A date and time-of-day clock card is contained in the computer, and detailed information on each monitoring point is stored on a conveniently replaceable EPROM in the unit. In its operating cycle the computer stores digital values from the reference voltage sources and, when channel #00 is available, begins storing digital voltage values of the temperature and distance associated with each channel. A 10-s delay is used between the time of change of channel and the time of reading values, in order to allow values to stabilize for high

accuracy. The channel controller external to the computer is thus set for >10 s (typically 15 s) between channel changes. After 8 min. the scan of 32 channels is completed, and a ~5-min. computing and printing cycle begins. As preliminary steps the computer determines the A-D converter calibration function based on the reference voltage values, and the pulser-receiver calibration function, using the values of the (~mid-scan) Type 304 SS reference specimens after correction for their ambient temperature. The computer then calculates and prints the 25°C wall-thickness value ( $\ell_w$ ) at each monitoring point, according to the following equation:

$$I = K_{304} \ell_{Sh-FW} + K_c \ell_c m_c + K_w \ell_w m_w + n \lambda/2$$

where I is the composite shoulder-to-backwall distance value indicated on a pulser-receiver calibrated for Type 304 SS at 25°C;  $K_{304}$  is the acoustic transit time ratio for a specimen of Type 304 SS at the measured temperature vs the transit time at 25°C (and thus includes the combined effects of thermal expansion and change of acoustic velocity with temperature);  $\ell_{Sh-FW}$  is the 25°C distance from the waveguide shoulder to the first (front) surface of the monitored wall;  $K_c$  and  $K_w$  are the temperature functions for a couplant foil (if present) and for the monitored wall, respectively;  $\ell_c$  and  $\ell_w$  are the 25°C thicknesses of couplant foil and wall, respectively;  $m_c$  and  $m_w$  are the 25°C velocity ratios for the couplant and wall materials compared with Type 304 SS; and  $n \lambda/2$  is a correction for offset error present because of the fine structures and relative sizes of the ultrasonic echoes. In this work, the value of  $\lambda/2$  is 0.38 mm (15 mils) at 7.5 MHz;  $n$  is the number of offset increments known to be present (usually 0, +1, or -1).

The values of the constants needed for each point and the coefficients of the temperature-correction equations are included on the EPROM noted above. Three switch-selectable modes of automatic operation are provided in the computer program: three complete scans per day (4 a.m., noon, and 8 p.m.), one complete scan on demand, and continuous scanning.

#### RESULTS OF MONITORING

Precision of +0.05 mm is achieved with steady temperatures. Under varying temperatures and changing ambient conditions (e.g., wind velocity) a similar precision can be realized if results from eroding areas are compared with results from a location that does not wear but is otherwise representative of the points considered. The latter approach was employed to obtain the results shown in Fig. 9. Continuous monitoring showed that the wear rate was extremely low except during brief intervals which were correlated with certain operating practices.

Figure 10 illustrates the automatic tracking of a large change of wall thickness over a substantial time. Again, the rate variations can be correlated with process operating conditions.

Figure 11 is an example of results conveniently obtained by the scanning system from multiple sites widely separated in an operating plant.

Field tests also demonstrated that coking within piping did not affect measured wall thickness and that the presence of coal-solvent slurry in piping reduced backwall echo amplitudes only ~8% without significant direct effect

on wall-thickness results. A  $\sim 0.07$ -mm-thick, hard corrosion film composed of Cr, Fe, S, and O within austenitic SS piping conveying  $430^{\circ}\text{C}$  coal-solvent slurry inhibited erosion and was included in the thickness measurements but contributed  $<0.07$  mm because of relatively high acoustic velocity in the film. Similarly, diffusion-bonded  $\text{B}_4\text{C}$  hardfacing on carbon steel was included in measurements, and wear of the  $\text{B}_4\text{C}$  was tracked (with correction for its acoustic velocity). Wear of Stellite weld overlaid hardfacing has been successfully followed ultrasonically through SS substrate. Additionally, it has been demonstrated that acoustic noise generated, e.g., by a pneumatic impact wrench used directly on the monitored component or by large particles impinging at high velocity directly at the monitored sites, does not disturb measurements when transducers resonant at 7.5 MHz are used for monitoring wall thicknesses typical of coal conversion equipment.

#### CONCLUSIONS

The automatic monitoring system and the techniques described can be used for continuous monitoring of pressure-boundary thicknesses at high temperatures. Measurement precision of  $\pm 0.05$  mm can be achieved under steady temperatures, or when the local temperature distribution is well known or compensated, by use of acoustic waveguides of up to 0.6 m in length. Instrumentation and techniques suitable for use in operating plants have been developed through laboratory and field tests. Real-time erosive wear results are of substantial value in the assessment of material/design choices in pilot plants. The remote scanning system can also be utilized in full-size plants with confidence and convenience to help avoid unexpected failures of components.

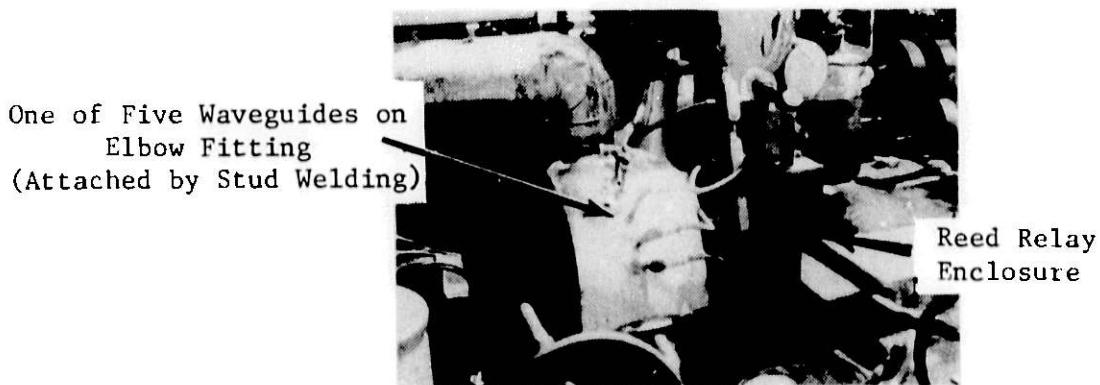


Fig. 1. Series of Five Threaded Waveguides on Thermally Insulated Elbow Fitting on  $410^{\circ}\text{C}$  Slurry Line at Exxon Coal Liquefaction Pilot Plant. Flexible conduit protects RG174 coaxial cables connecting transducers to relay enclosure.

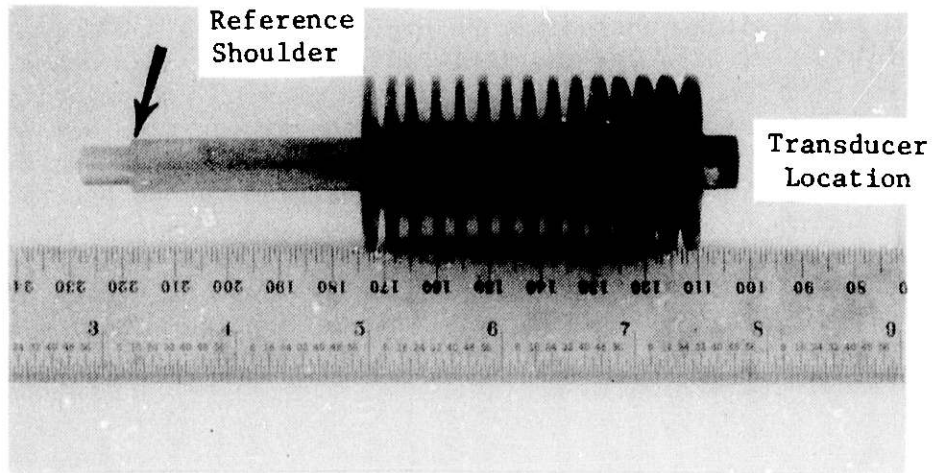


Fig. 2. Knurled SS Waveguide with Cu Cooling Fins, Reference Shoulder, and Tip for Stud Welding.

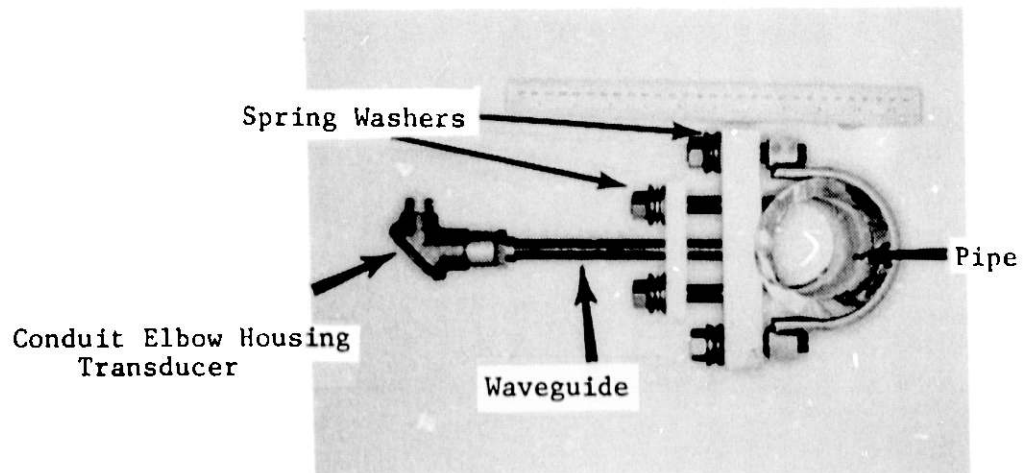


Fig. 3. Threaded SS Waveguide and Clamp on 3-in.-nom-diam Pipe. Cu or Au foil couplant is used at waveguide-pipe pressure-contact interface.

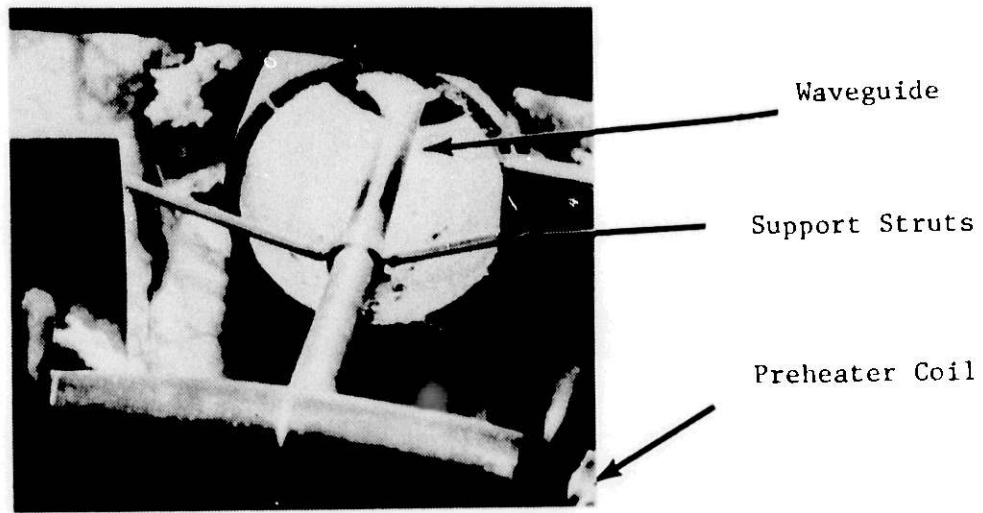


Fig. 4. 600-mm-long Waveguide with Taper and Lightly Threaded Sidewall. Struts from monitored piping in slurry preheater provide support.

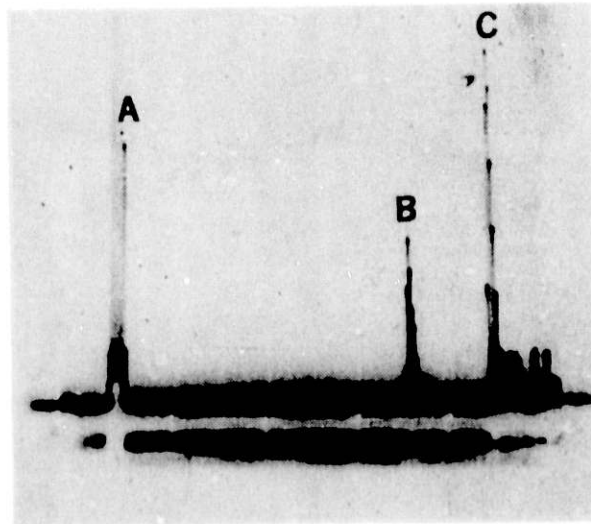


Fig. 5. Video Display of Ultrasonic Response from Waveguide Stud-welded to Specimen. Display shows transducer-triggering pulse (A), waveguide shoulder echo (B), and specimen back surface echo (C).



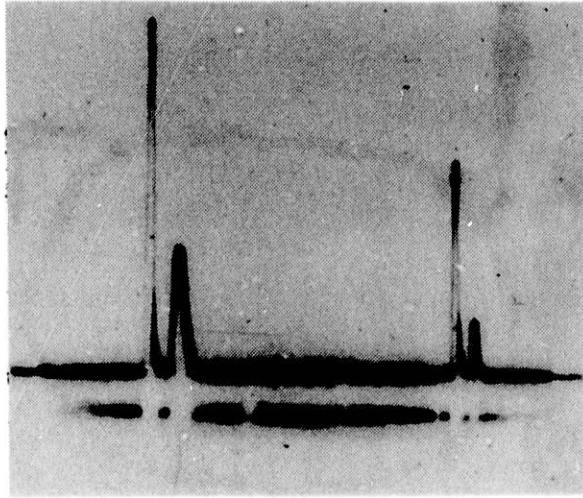


Fig. 6. Unambiguous Ultrasonic Echoes Produced by Damped (Alpha) Transducer on Plate Specimen, with Inverted Preamplifier Mode Employed.

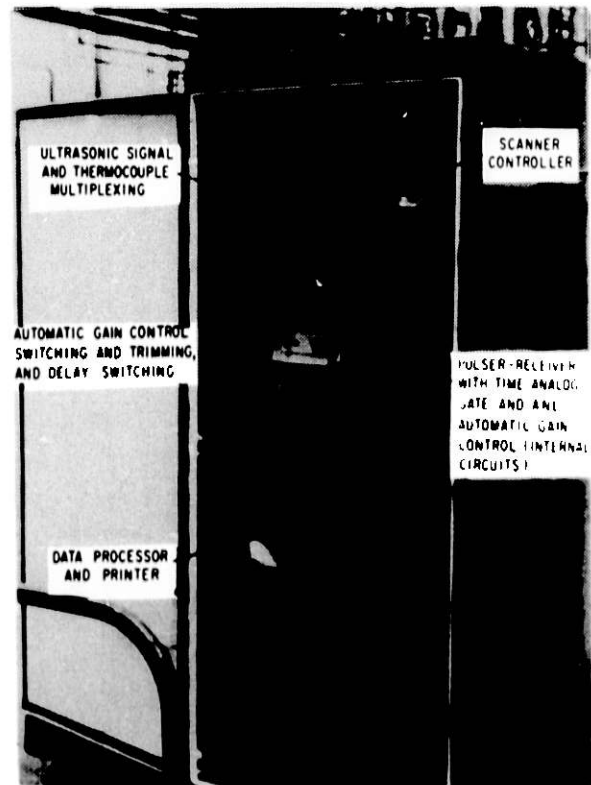


Fig. 7. Cabinet and Instruments for Scanning System Diagrammed in Fig. 8.

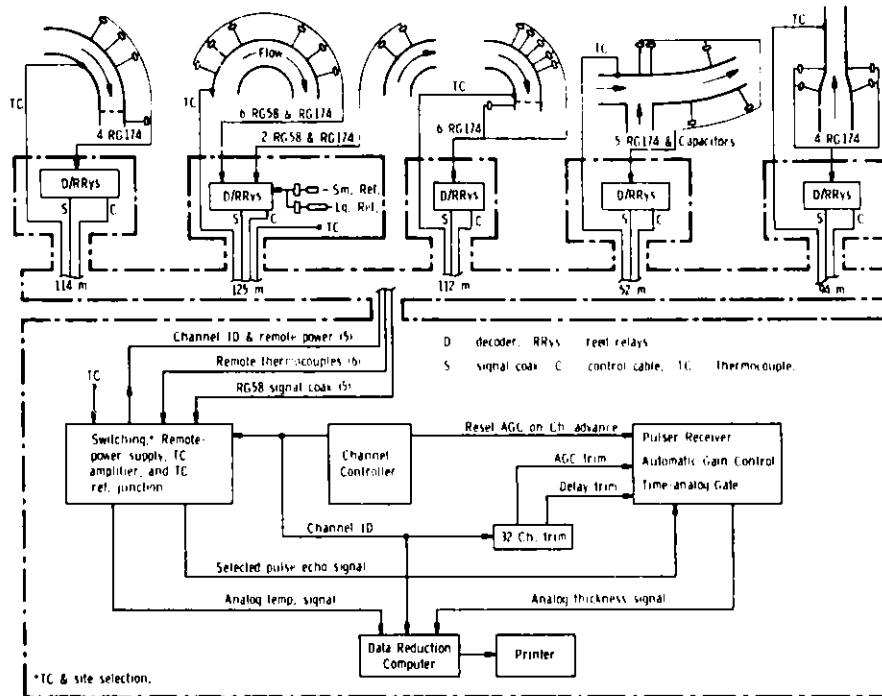


Fig. 8. Ultrasonic Scanning System for Automatic Surveillance of Thicknesses of Pressure Boundaries to Monitor Erosive Wear at Selected Sites in Exxon Coal Liquefaction Pilot Plant (ECLP). Waveguides, transducers, and ECLP process line fittings are indicated at the top of the diagram. The cooperative ECLP-ANL project produces automatically corrected results daily from 27 points located throughout the Baytown, TX, facility.

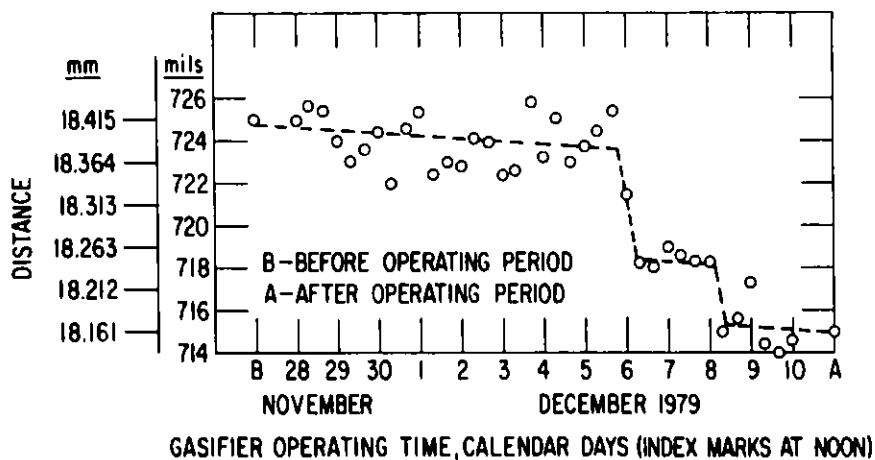


Fig. 9. Erosive Wear at Selected Site on 540°C Type 316 SS Cyclone Separator During Operation in Coal Gasifier Effluent System at Morgantown, WV, Energy Technology Center.

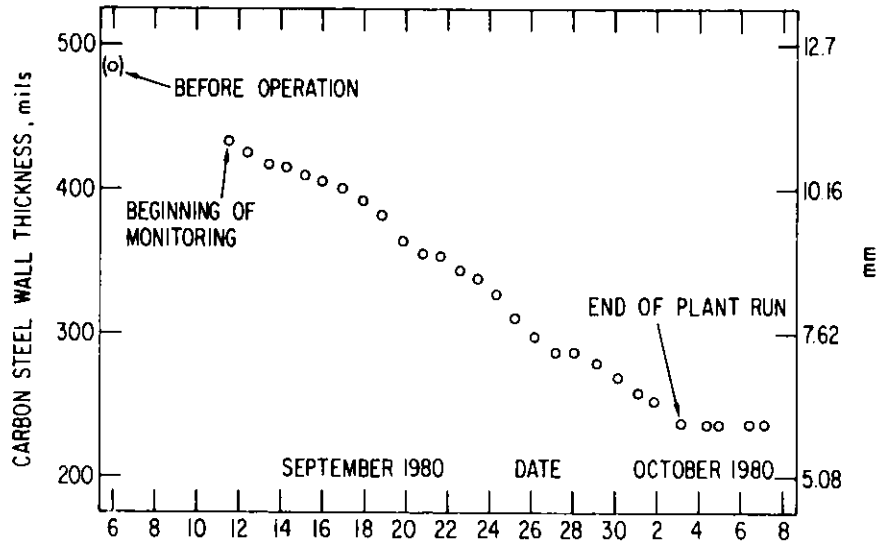


Fig. 10. Wall-thinning of Experimental Tar-separating Cyclone Operated at Temperatures up to 250°C in Effluent Gas Cleanup System of Fixed-bed Coal Gasifier at Morgantown Energy Technology Center. Results were reduced from ultrasonic data obtained automatically by ANL scanning system from site of greatest erosion-corrosion wear.

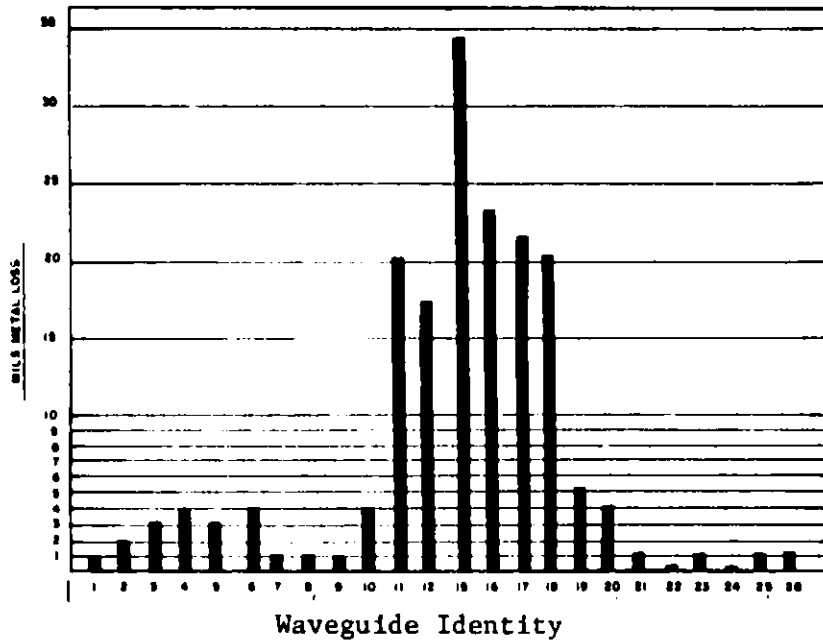


Fig. 11. Changes in Thickness of Piping at Multiple Sites in Coal Liquefaction Process Line at Solvent Refined Coal Pilot Plant (Ft. Lewis, WA) During One-month Period of Plant Operation. Greatest changes in thickness occurred at bends where slurry-flow velocity was greatest in a piping section installed by SRC personnel to study erosive wear. Results were from the SRC computer, interfaced to the ANL ultrasonic scanning system.

## REFERENCES

1. Stanton, G. C. and Ellingson, W. A., "System for Ultrasonic Monitoring of Pipe Wall Thinning (Erosive Wear) in Coal Gasifiers," Mater. Eval. 35 (4), 46-51 (1977).
2. Youngdahl, C. A. and Ellingson, W. A., "Development of Ultrasonic Techniques for Remote Monitoring of Erosive Wear in Coal Conversion Systems," Proc. of 1978 Ultrasonic Symposium, IEEE Cat. #78CH1344-1SU, pp. 305-310.
3. Youngdahl, C. A. and Ellingson, W. A., "Long-Term Erosion Monitoring of Metallic Conduits by Ultrasonic Pulse-Echo Techniques," Proc. of 12th Symposium on Nondestructive Evaluation, April 1979, Southwest Research Institute, San Antonio, TX, pp. 282-291.
4. Caines, M. J. and Youngdahl, C. A., "A High-Temperature Pressure-Coupled Ultrasonic Waveguide System," Fall 1981 ASNT Paper Summaries, pp. 318-321.
5. Youngdahl, C. A., Ellingson, W. A., Caines, M. J., Canfield, D. R., and Fiore, N. F., "Long Bimetallic Waveguides for Ultrasonic Thickness Monitoring at High Temperatures," Spring 1981 ASNT Paper Summaries, pp. 90-95.
6. Ellingson, W. A., Youngdahl, C. A., Reimann, K.J., and Syed, N. A., "Materials Technology for Coal-Conversion Processes, Progress Report for April-June 1981," Argonne National Laboratory Report ANL/FE-81-53, pp. 3-17.
7. Youngdahl, C. A., Pater, K., and Gorski, M. J., "Erosive Wear and Design Evaluation of a Stainless Steel Cyclone on the Coal Gasification Pilot Facility at Morgantown," Proc. of 1979 Conference on Properties and Performance of Materials in the Coal Gasification Environment, ASM, pp. 709-734 (1980).
8. Canfield, D. R., King, E. E., and Youngdahl, C. A., "High-Temperature Erosion Monitoring at the SRC Coal Liquefaction Pilot Plant," to be submitted for publication by NACE.

AUTOMATED DATA QUALIFICATION

Ronne W. Brower, James I. Anderson,  
Lorenzo D. Goodrich, and Arthur D. Mackley  
EG&G Idaho, Inc.  
P.O. Box 1625  
Idaho Falls, ID 83415

Abstract

Rapid advancements in measurement systems technology and the widespread applications of digital computers has separated those who control equipment systems from the physical processes involved. As a result, methods of validating information prior to its use in decision making at the control and/or man-machine interface are required. EG&G Idaho at the Idaho National Engineering Laboratory has identified some techniques which can be used to solve this problem through automated data qualification in real-time and batch modes. Pilot projects have demonstrated the feasibility to economically qualify quiescent and transient data with resulting high confidence in processed results.

Introduction

Improvements in measurements technologies and widespread application of computers for signal processing now make it feasible to collect and analyze vast quantities of data for real-time as well as historical purposes. One price paid for this capability is that users are typically isolated from the physical processes; they may accordingly lose complementary information that otherwise helps in deciding on data validity. The validation (qualification) of such data is important, since measured results (data) are influenced not only by the system or physical phenomena of interest, but also by various extraneous environmental and instrumentation factors, including instrumentation failures. In some cases, such factors or failures can corrupt the data and make them useless or misleading if they are inadvertently used to evaluate performance, or to assess operation.

Examples which illustrate undesirable consequences of accepting measurement data without adequate qualification include:

Item--During the nuclear reactor accident at Three Mile Island (TMI), attempts were made to determine the history of the water level in the core using self-powered neutron detectors. In subsequent analyses, it was determined that these measurements had failed early in the accident, and that signal interpretation had provided fictitious results.

Item--A night operator at a power plant observed an indication (panel light) of low oil level in a day storage tank, and initiated fill. The low-level light did not clear, and a day operator subsequently took the same action despite an immediate high-level indication as he started his fill procedure. The resulting spillage cost >\$2 million when the oil contaminated a yacht basin.

Item--While anesthetizing a small boy in preparation for surgery, the anesthetist received incorrect indication of anesthetic flow. Operating on this false information, he administered increased amounts of anesthetic. By the time body-function monitors disclosed the error, the boy had received a lethal dose.

These incidents demonstrate need for data qualification in instrumentation systems of widely varying complexity and application--ultimately everyone shares in the cost of these accidents. It is time that those of us in the instrumentation community develop a measurement qualification technology which can be incorporated to prevent such losses. Responsibility should further be assumed to establish a basis upon which the instrumentation user can perform cost/risk/benefit analyses to define optimum application of these techniques to his individual application.

#### Historical Summary of ADQ Development at EG&G Idaho

EG&G Idaho operates the Loss-of-Fluid Test (LOFT) facility<sup>1</sup>, a 50-MW(t) pressurized water reactor (PWR), at the Idaho National Engineering Laboratory (INEL) for the Department of Energy.<sup>a</sup> The purpose of this plant is to provide data from experiments simulating postulated accident conditions in commercial PWRs. These data are then used to develop and to assess the ability of thermal-hydraulic computer codes to predict the PWR accident behavior. Following each LOFT experiment and before the data can be used for analyses, some 300 to 500 digitally recorded experimental measurements need to be qualified. Manual postexperiment performance of this qualification task represents a significant investment which provided the incentive to develop computer based algorithms that could do automated data qualification (ADQ).

EG&G Idaho's concept of qualifying data consists of producing a high confidence that the measurement system is performing as specified and measuring the desired physical parameter within the required accuracy. In reviewing methods which have been pursued by various researchers, it was noted that they deal with instrument fault detection and identification<sup>2-15</sup> and reactor surveillance methods.<sup>16-22</sup> Mostly, these techniques consider very specific or individual aspects of a measurement characteristic rather than measurement quality.

The objectives of EG&G Idaho research efforts were to develop ADQ techniques and provide a general methodology<sup>b</sup> for validating measurements from instrumented systems in an automated manner. Although ADQ can be done via hardware and/or software techniques, funding availability and the

---

a. Work supported by the U.S. Nuclear Regulatory Commission, Office of Nuclear Regulatory Research under DOE Contract No. DE-AC07-76ID01570.

b. Methodology of automated data qualification is defined as: A structural framework with guidelines under which the potential user, based upon his individual data qualification needs and available resources, can design and develop an ADQ system for his particular application.

expertise of the personnel assigned to the project dictated that the techniques, after definition, be implemented and tested on general purpose digital computers.

The course which has been pursued by the ADQ project team at the INEL includes development of the following types of tests.

1. Individual measurement tests--These tests check the distinguishable attributes of the time series data, from an individual channel, against known system characteristics. These tests include such checks as range, signal-to-noise ratio, noise analysis in the frequency domain, and response time characteristics.
2. Comparative analysis tests--These tests are powerful tools in validating measurements. Care must be exercised to insure the test conditions sufficiently discriminate between measurement problems and recorded differences due to true physical parameter variations. At EG&G Idaho, we have chosen to think about comparisons in the following ways:
  - a. Direct redundancy--comparisons of multimeasurements of the same physical phenomena. Direct comparison tests are limited by factors such as physical system state, measurement environment, spatial proximity of sensors, transducer response characteristics, etc. As an example of direct redundancy, consider that in an enclosed system under isothermal conditions, all temperature measurements, regardless of position, can be directly compared.
  - b. Functional redundancy--At times, similar measurements which do not satisfy direct redundancy constraints may be compared through application of a system model. To illustrate this, consider use of known power distribution within a reactor core to provide a regression model wherein fuel cladding temperatures throughout the core can be compared during normal operations.
  - c. Analytical redundancy--Dissimilar measurements can be compared when data transformations into a common reference frame are possible. An example is the comparison of differential pressure and fluid velocity data after their conversion to mass flow rate.
  - d. Historical redundancy--Past performance of individual or groups of measurements under given operating conditions is a powerful asset in identifying anomalous system performance.

#### Discussion of ADQ Techniques

To perform an automated data qualification requires characterization of the measurement system from the sensor through the processing which occurs prior to data presentation at the man-machine interface (see Figure 1). Each ADQ application has its own unique set of technical/operational/economics considerations and variables. In practice, an ADO

system provides the computational and decision algorithms necessary to assess data quality through testing given aspects of time-series data against known physical parameters of the facility and measurements from which the data were obtained. The ADQ processor interfaces with data bases containing system reference information (including historical performance) and processed results. Outputs (qualifications) of the processor may be sent to analysis and/or plant control modules as well as be presented at the man-machine interface. Components of an ADQ system, which would be installed between the data processing and display functions of Figure 1, are shown in Figure 2. A brief discussion of the elements shown in this functional diagram is provided in the following sections to help clarify EG&G Idaho's ADQ concepts.

### ADQ Processor

The ADQ processor contains the necessary test functions; we have chosen to group these into three categories: data stream manipulation (DSM) function, information quality function (IQF), and estimated data quality (EDQ) function.

Data Stream Manipulation Functions. DSM functions perform any data transformations which might be necessary or advantageous in subsequent ADQ processing. Examples of such transformations include signal/noise separation, decimation, interpolation, time shifting, sampling rate modification, smoothing, differentiation, integration, data compression, and times-series data modeling.

Care should be taken to select time invariant formulations to perform these transformations whenever possible; otherwise, the filtering effects of operations such as determining mean, variance, etc., should be clearly understood.

Since a basic ADQ requirement involves the ability to use time-series data to recognize and discriminate between changes in the phenomena, measurement instrument, recording system, etc., another category of DSM functions is used to define the nature of time-series data streams. These functions are used to establish the deterministic and random properties (usually mixed) of the signals.

Information Quality Functions. IQFs basically test some detectable attribute of time-series data against known system parameters. Figure 3 illustrates the concept of IQF processing; three outputs with respect to the test are possible: pass, fail, or does not apply.

Several different IQFs might be constructed to treat a particular aspect of time-series data. An objective might be to consider the "noise" present in measured data. Various variability criteria such as variance, data range, and successive differences could be used to define variability IQFs. One might choose to treat variability by considering variance in either the time or frequency domains. Other noise criteria such as counting zero crossings, performing run tests, and characterizing probability could also be considered in variability IQFs. Single or multiple data stream inputs can be required based upon each IQF test to be performed.



The "does not apply" result is based on failure to recognize an applicability condition which may be determined from the data stream(s) being processed or from processing one or more control data streams.

Estimated Data Quality Functions. The determination of EDQ requires combining IQF outputs in some meaningful way in order to obtain an overall measure of data quality. Such an EDQ combinatorial rule requires specification of the functional relationship for combining IQFs, which includes a method of weighting individual IQF output results to a common scale of measurement (that is, units of EDQ) and also provides a measure of the relative importance of the individual IQF output results.

Computing the weighted average of IQF outputs illustrates a simple type of EDQ function. Also, data from a set of IQF evaluations might be combined in some series parallel fashion to produce the desired EDQ result. For instance, knowledge that data from a measurement channel are "out-of-range" might be sufficient to declare them invalid without further IQF processing. The information of an EDQ can be very applications specific. Appropriate IQF weights need to be assigned that reflect the importance each IQF has in terms of the data interpretation and decision activities which take place at the man-machine interface.

#### Results Data Base

Information in the ADQ results data base can be stored in compressed form to save disc space. For example, where batch processing occurs and disc space utilization is an economics consideration, only the transitions in IQF determinations (2-bit entry plus repetition count) need be saved in packed form. Similarly, EDQ evaluations can be stored as integers between 0 and 100 in packed form.

#### Reference Data Base

The reference data base of the ADQ system provides knowledge which is required by the ADQ processor for qualification of the data. This data base can contain an analytical system description to be used for manipulation of multiple data streams, historical information to be used for characterizing the measurement system and determining long-term trends, and information needed by certain types of IQFs and the EDQ. Information contained in the data base, along with the size of the data base, will be dependent on the specific application of the ADQ system.

#### System Analysis

This block contains the algorithms for detailed analysis of the system, including identification of bias errors and calibration shifts. Identification of measurement failures and degradation of measurements is provided for in this section. Where appropriate, analyses will provide corrections to the data. It is envisioned that computationally intensive, and subsequently slow, evaluations of measurement systems will be performed in the analysis section. This structure would allow the fast data qualification algorithms in the ADQ processor to be run more frequently in a real-time application, while still providing for comprehensive data qualification using the more complex techniques. Examples of analysis techniques

which would be included in the analysis section are Box-Jenkins autoregressive integrated moving average (ARIMA) models, Kalman filtering techniques, and noise analysis in the frequency domain.

### Data Presentations

ADQ processing adds new dimensions to time-series data. This additional information can be available to:

1. Trigger execution of analysis routines which might detect measurement faults, provide calibration correction, predict failure, perform common mode failure analysis, schedule maintenance, etc.
2. Provide feedback control or plant status monitoring systems with measurement health information upon which appropriate actions can be taken/recommended.
3. Present system operators and/or analysts with alarms, corrective/preventive instructions, data displays, etc., which alert him as to measurement problems.

### Applications

ADQ development at EG&G Idaho is being pursued on both batch and real-time modes. A pilot program for ADQ has been implemented at the LOFT facility and is summarized in this section.

#### Batch Mode

The pilot project defined at EG&G Idaho was to process approximately 300 channels of temperature and pressure data from LOFT loss-of-coolant accident experiments on the INEL CDC Cyber-176 computing system. Principal objectives were (a) to compare the sensitivity of ADQ methods to the manually obtained qualification results, and (b) to demonstrate potential time/cost savings of using ADQ in postexperiment qualification of transient data.

The work involved testing measurement channel limits, signal variation or "noise", and comparing measurements in functional<sup>a</sup> and direct redundancy tests. Test criteria for these IQFs were based upon known system parameters for the range (established measurement limits) and redundancy (published measurement uncertainties); the noise test criterion had its basis in empirical evaluation of healthy signals when the plant was in isothermal and isobaric conditions.

The IQF results were combined as a weighted product to form an EDQ estimate. These estimates were then summed, and ratios of the sums to the

---

a. A regression model which fit cladding temperature measurements as a function of height and radius was necessary to compare data when the reactor was at power.

number of points processed were formed. For comparison to manual results, an arbitrary scale was established for these ratios (with 100% representing a condition wherein all data tested passed each IQF):

EDQ  $\geq$  95% was labeled "accepted"

95% > EDQ > 30% was labeled "intermediate"

30%  $\geq$  EDQ was labeled "rejected."

In all cases, the ADQ evaluations processed a section of data prior to LOFT experiment initiation, the transient record during the experiment, and a brief period of quasi-quiescent data following the experiment. Without exception, those traces tagged "accepted" by ADQ received a "qualified" label when manually reviewed by the LOFT Data Integrity Review Committee (DIRC). During these evaluations, some 3% (for two experiments) to 20% (for one experiment) had EDQ values in the "intermediate" range basically due to redundancy differences. Approximately 90% of these were determined "qualified" by DIRC review, sometimes with constraining remarks. Identification of regions of low-redundancy acceptance was useful in detecting thermal-hydraulic phenomena of significance in interpretation of experiment results. The signals "rejected" by ADQ were classified as failed by the DIRC.

Results of the pilot project were encouraging. The automated process received favorable recognition by the DIRC. It was determined that a cost savings in qualifying LOFT temperature and pressure data of a factor of 3 existed, plus reduction of 2 in wall clock time. ADQ overlay displays were developed for the DIRC, wherein ADQ results were color coded into the signal (green implied EDQ  $\geq$  95%, yellow for EDQs in the intermediate range, and red for EDQ  $\leq$  30%).

On the basis of these successes, development began on a batch ADQ processor, with construction as shown in Figure 2. LOFT flow (differential pressure, drag discs, turbine meters, venturis, etc.) and nuclear (self-powered neutron detectors, reactivity meters, etc.) instrumentation are being added to the ADQ processor. Incorporation of historical information (calibration tests, noise signatures, etc.) is scheduled to be developed following completion of a LOFT large break experiment in mid-June 1982.

### Real-Time Applications

The primary purpose of the real-time ADQ pilot project initiated by EG&G Idaho at the LOFT facility was (a) to verify that the ADQ techniques which have been developed could be realistically applied in a real-time situation, and (b) to evaluate the computer resource requirements of a real-time ADQ system. The LOFT system uses three MODCOMP computers tied together in a distributed system for recording about 800 channels of experimental and process measurements. For the pilot project, it was decided to qualify and display 20 core cladding thermocouples which are used by the LOFT emergency control system (LECS). These thermocouples are located at 10 different elevations in the center fuel bundle. The technique used to qualify these measurements was intended for use during relatively long duration (50 to 2000 s) transient experiments, and had several phases as follows:

1. Data were acquired (usually at the rate of 50 samples per second) on one MODCOMP computer and transferred across a data link to a data processing computer, since the first computer had a number of higher priority functions to perform in addition to its data acquisition function.
2. The ADQ processor was designed to process the data in blocks of 100 data samples per measurement. The processing consisted of the following steps:
  - a. The data were filtered using a low-pass digital finite impulse response filter (pass frequency of 1.5 Hz and stop frequency of 2.5 Hz) and subtracted from the original data stream on a point basis. This was intended to remove the nonstationary mean of the signal, so that the signal noise could be examined. As a simple procedure for the pilot project, a root-mean-square (rms) value of the noise was calculated to provide an indication of the noise level on the signal. If the noise level was below a nominal value, the measurement was either saturated or had failed; if the noise level was greater than some other nominal value, the measurement had electronics problems or had failed.
  - b. To check for range validity of the measurement, the mean of the 100 data points was calculated and compared to the valid range of the measurement.
  - c. A redundancy check of the 20 thermocouples was performed by least squares fitting the 20 measurements to a quadratic curve (elevation was the independent variable) which approximated the axial power distribution in the reactor. The standard deviation of the measurements from the fit was calculated. Any measurement in which the deviation from the fit was greater than twice the standard deviation was flagged as a redundancy failure.
3. When the ADQ processing was completed, the data and the qualification flags were displayed in color on a Ramtec 6200 monitor. Prediction of the maximum fuel cladding temperature at a selectable future time was added to assist in experimental control.

The real-time ADQ system has been successfully operated for the past three LOFT experiments and has proven that data can be qualified during a variety of transients in a real-time environment. A fully implemented real-time ADQ system for a stationary process system could qualify several hundred measurements to the desired confidence level. Advantages of this type of system include:

1. Increased confidence in measurements used for process control
2. Detection of failed or degraded measurements for instrumentation maintenance.

### Conclusions

The "data revolution" which has occurred in the past few decades by virtue of rapid advancements in measurement systems technology and the widespread applications of digital computers has definitely separated those who control equipment systems from the physical processes involved. Methods of qualifying information prior to its use in decision making at the control and/or man-machine interface are required.

Automated data qualification, as it is being developed at the INEL, has attempted to identify some techniques which can be used to solve this problem in real-time and batch modes. Pilot projects have demonstrated feasibility to economically process quiescent and transient data with resulting high confidence in processed results. These efforts have, however, just scratched the surface of a badly needed technology.

The future of data qualification is limited only by one's imagination. Real-time bias error detection and removal, correction of calibration errors, and measurement degradation with failure prediction are certainly within capabilities of current technology. Current efforts at the development of "smart" or self-checking transducers need to be expanded to include other measurement system components so that the data displayed to the user have undergone single channel qualification analyses. Where computers are involved, comparative analyses and systems modeling algorithms may be added to increase our understanding of system status.

Those of us involved in instrument and control systems must begin to incorporate qualification technologies in the design and application of measurement systems. We need to educate the consumer to understand that the increased costs of qualification will be repaid to him many times in increased system availability, improved understanding of anomalous behaviors, and reduced risk of catastrophic action based on bad data.

### Notice

This paper was prepared as an account of work sponsored by an agency of the United States Government. Neither the United States Government nor any agency thereof, or any of their employees, makes any warranty, expressed or implied, or assumes any legal liability or responsibility for any third party's use, or the results of such use, of any information, apparatus, product or process disclosed in this paper, or represents that its use by such third party would not infringe privately owned rights. The views expressed in this paper are not necessarily those of the U.S. Nuclear Regulatory Commission.

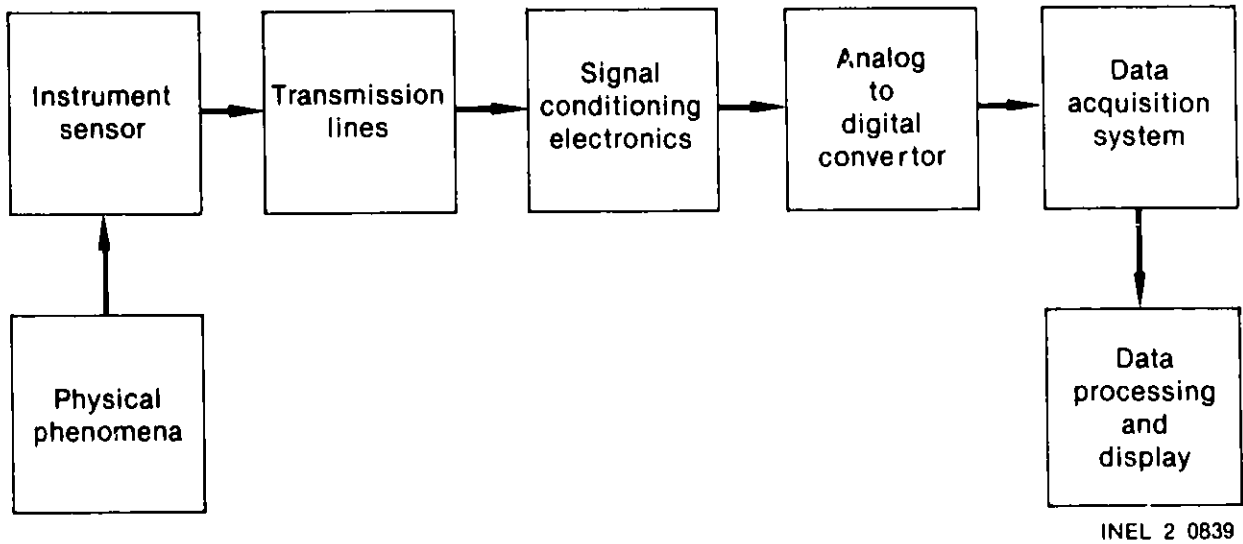


Figure 1. Typical measurement system.

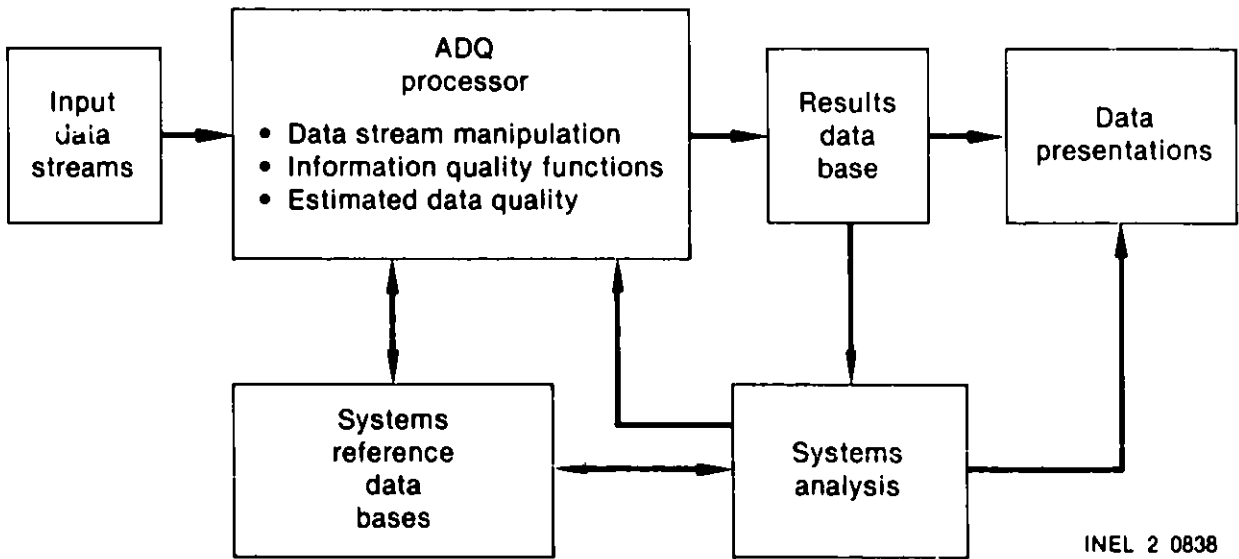
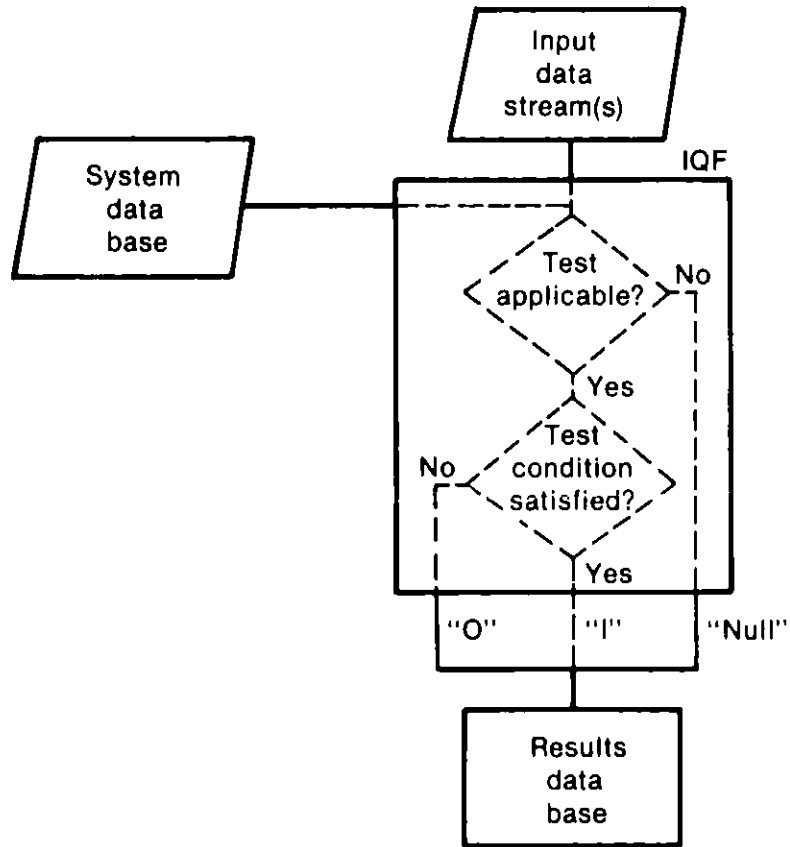


Figure 2. Major components in a unified ADQ system.



INEL 2 1219

Figure 3. Basic IQF processing.

References

1. D. L. Reeder, "LOFT System and Test Description (5.5-ft Nuclear Core 1 LOCEs), "NUREG/CR-0247, TREE-1208, July 1978.
2. R. N. Clark et al., "Detecting Instrument Malfunctions in Control Systems," IEEE Tran. Aerospace and Electronic Systems, AES-11 (1975) pp. 465-473.
3. A. S. Willsky, "A Survey of Design Methods for Failure Detection in Dynamic Systems," Automatica, 12 (1976) pp. 601-611.
4. J. C. Deckert et al., "F-8 DFBW Sensor Failure Identification Using Analytic Redundancy," IEEE Tran. Aut. Cont., AC-22 (1977) pp. 795-803.
5. J. E. Potter and M. C. Suman, "Thresholdless Redundancy Management with Arrays of Skewed Instruments," Integrity in Electronic Flight Control Systems, AGARDOGRAPH-224 (1977) pp. 15-1 to 15-25.
6. R. Onken and N. Stuckenberg, "Failure Detection in Signal Processing and Sensing in Flight Control Systems," IEEE Conf. on Dec. and Cont. (1978) pp. 449-454.
7. R. N. Clark, "Instrument Fault Detection," IEEE Tran. Aerospace and Electronic Systems, AES-14 (1978) pp. 456-465.
8. R. C. Montgomery and D. Tabak, "Application of Analytical Redundancy to Shuttle Crafts," IEEE Conf. on Dec. and Cont. (1978) pp. 442-448.
9. K. C. Daly, E. Gai, J. V. Harrison, "Generalized Likelihood Test for FDI in Redundant Sensor Configurations," AIAA Journal of Guidance and Control, 2, 1 (January-February 1979) pp. 9-17.
10. R. N. Clark, D. C. Fosth, V. M. Walton, "Detecting Instrument Malfunctions in Control Systems," IEEE Trans. Aerospace Electronic Systems, 11, 4 (1979) p. 465.
11. M. Kitamura, "Detection of Sensor Failures in Nuclear Plants Using Analytic Redundancy," Tran. Am. Nucl. Soc., 34 (1980) p. 581.
12. B. R. Upadhyaya, M. Kitamura, T. W. Kerlin, "Signature Monitoring of Nuclear Power Plant Dynamics-Stochastic Modeling and Case Studies," Proc. 19th IEEE Conf. on Dec. and Cont., 1 (December 1980) pp. 121-126.
13. M. Desai and A. Ray, "A Fault Detection and Isolation Methodology," 20th IEEE Conf. on Dec. and Cont., San Diego (December 1981) p. 1408.
14. R. N. Clark and B. Campbell, "Instrument Fault Detection in a Pressurized Water Reactor Pressurizer," Nucl. Tech., 56 (January 1982) pp. 23-32.
15. K. R. Piety and J. C. Robinson, "An On-Line Reactor Surveillance Algorithm Based on Multivariate Analysis of Noise," Nucl. Sci. Engrg., 59 (1976) pp. 369-380.



16. "Increasing Availability of Power Stations Through Advanced Surveillance," ANS Tran., 27 (1977) pp. 936-943.
17. R. C. Gonzales and L. C. Howington, "Machine Recognition of Abnormal Behavior in Nuclear Reactors," IEEE Tran. Sys. Man. Cyber., SMC-7 (1977) pp. 717-728.
18. T. W. Kerlin, G. C. Zwingelstein, B. R. Upadhyaya, "Identification of Nuclear Systems," Review Article, Nucl. Tech., 36 (1977) pp. 7-39.
19. B. R. Upadhyaya and T. W. Kerlin, "Estimation of Response Time Characteristics of Platinum Resistance Thermometers by the Noise Analysis Method," ISA Transactions, 17 (1978) pp. 21-38.
20. B. R. Upadhyaya and T. W. Kerlin, "Sensor Response Monitoring in Pressurized Water Reactors Using Time Series Modeling," Proc. IEEE Conf. on Dec. and Cont. (January 1979) pp. 878-883.
21. B. R. Upadhyaya, M. Kitamura, T. W. Kerlin, "Multivariate Signal Analysis Algorithms for Process Monitoring and Parameter Estimation in Nuclear Reactors," Anal. of Nucl. Energy, 7 (1980) pp. 1-11.
22. T. W. Kerlin, E. M. Katz, B. R. Upadhyaya, "Model Validation Necessary Only for Imperfect Modelers," Proc. Conf. on Simulation Methods for Nuclear Power Systems, Tucson, Arizona (January 1981).

COMPUTER CONTROLLED CONSOLIDATION TEST RESULTS FOR  
FARADAY CONNECTED MHD POWER GENERATION

K. MARCOTTE, R. JOHNSON, AND S. SHINK  
Department of Electrical Engineering and Computer Science  
Montana State University  
Bozeman, MT 59717

ABSTRACT

MHD topping cycles of coal-fired MHD/steam combined cycle produce direct current (d.c.) power. This d.c. power must be converted to alternating current (a.c.) power for distribution over utility power systems. Reduction of the number of inverter systems required in a Faraday connected system for conversion from d.c. to a.c. is desirable because of cost. This reduction can be accomplished by consolidating many of the MHD generator electrode outputs before inversion between d.c. and a.c. takes place.

This paper presents experimental test results for a four-electrode pair consolidation unit. The consolidation unit is computer controlled using a microcomputer and the output is supplied to a force-commutated three phase inverter system which is also under microcomputer control. The consolidation system presented is an inductively coupled circuit first proposed by R. Rosa. In the series of tests described, the four Faraday voltages are simulated with 7.5 horsepower d.c. motor generator sets and the Hall voltages were simulated using six low-voltage high current power supplies. The overall operation of the consolidation/inverter system is under LSI 11/03 computer control and is discussed briefly.

The test results presented indicate the electrode and Hall current sensitivity to load variations and frequency of consolidation switching.

INTRODUCTION

The problem of consolidating the d.c. power from a MHD topping cycle has received considerable attention<sup>1-3</sup>. If the generator is of two-terminal diagonal configuration, a single inverter system will suffice and the general problem of consolidation does not exist. Such a system has been built and tested by Avco for use on the Mark VI MHD system<sup>4</sup>. If it is desired to operate the MHD system over a fairly wide level of power output, the wider range of operational flexibility of either the multiple-diagonal or general Faraday connections is preferred.

At Montana State University (MSU), a small, four-electrode-pair consolidation system feeding a force commutated inverter system has been constructed and tested. The MSU system is under complete computer control so that all operational characteristics can be varied; these characteristics include, at a minimum: commutation frequency, notch-filtering of waveforms for harmonic suppression, and individual control of each silicon-controlled-rectifier (SCR) in the network. The MHD Faraday voltages of the system were simulated by a set of four programmable power supplies which are under computer control. The Hall voltages between adjacent electrodes were simulated with storage batteries.

The programmable power supply usage raises the question of the realism of generator simulation since the power supplies are voltage and current limited. It was decided to test the system on an actual MHD generator if possible. Scheduling problems complicated by channel failure and academic responsibilities have prevented such tests. It is presently planned to test the system on the CDIF system in 1982 using test channel 1A1. It was decided in the meantime, to drive the network with ordinary d.c. generator sets. This permits loading the consolidation/inverter network nearer its design specifications, and is more representative of MHD electrical behavior. If results can be correlated with those arising from a later channel test, further experimental development on such systems may be performed using generators alone.

### EXPERIMENTAL SETUP

The small consolidation/inverter (C/I) system tested is shown in Figure 1. Overall control of the C/I system is provided by a DEC LSI 11/03 microcomputer with floppy and hard disk storage. The LSI 11 provides system control using four Zilog Z80 microcomputers which reside inside the LSI 11 chassis. Figure 2 shows the details of the four-electrode pair consolidation network. A single Z80 is used to control the consolidation network by switching SCR's A,B,C, and D as illustrated. The SCR firing sequence is (A,C), (B,D), (A,C), (B,D), (A,C), etc. The electrode interconnection shown provides zero average flux in the transformer cores. The polarized connection of the various transformer windings causes the flux generated by one half-cycle to be cancelled by the flux generated by the alternate half-cycle. The other Z80's are used to control three single-phase inverter circuits used to form a three-phase, force-commutated inverter unit. By use of four Z80 slaved microcomputers, independent and coordinated control of the inverter and consolidation systems is achieved with reserve processor speed remaining for detection and control of faulty operation.

The experimental setup to simulate four electrode pairs using four separate 7.5Kva d.c. motor/generator sets is also shown in Figure 2. The four d.c. generators, rated at 120 vdc were connected to provide the Faraday voltages while six low-voltage, high current d.c. supplies were used to simulate the Hall field.

### TEST RESULTS

Elements in the consolidation network were designed for 120 vdc input and 5 amps electrode current. Tests were conducted for various load conditions, 20 and 30 volt Hall voltages, and 5-20KHz combining frequency. Typical circuit waveforms for current and voltage are shown in Figures 3,4,5, and 7. Proper network operation for a load current of 20 amps can be seen in Figures 3 and 7.  $V_1$ ,  $I_{R1}$ ,  $V_2$  and  $I_{R2}$  are the consolidating waveforms of the least positive pair of positive electrodes at transformer T1.  $V_5$ ,  $I_{R5}$ ,  $V_6$  and  $I_{R6}$  are the consolidating waveforms for the most positive pair of positive electrodes at transformer T2.  $V_9$ ,  $I_{R9}$ ,  $V_{10}$  and  $I_{R10}$  are the combined waveforms of all four electrodes at T3. Similar inverted waveform sets for the negative electrode connections are viewed diagonally across the consolidation network. Load data presented in Figure 6 indicates that the Rosa consolidation network is load sensitive with respect to the current balance of the electrodes.

$I_{HN}$  is the current associated with the respective Hall voltage supply,  $V_{H1}-V_{H6}$ .  $I_{KN}$  is the current from the Faraday supplies,  $V_{F1}-V_{F4}$ , as measured using current shunts  $S_{K1}-S_{K4}$ . However, if one assumes that the operational range for normal operation of the generator is between half load and full load, the operation of the network is satisfactory with respect to current balance. The results of the tests also indicate that heavier loading, (greater than design full load) of the system tended to perform quite well with respect to electrode current balance. Total input currents,  $I_1^+ - I_4^+$ , to the consolidation system are shown in Figure 7. An inverted set of current waveforms,  $I_4^- - I_1^-$ , exist on the negative electrode side. The network was designed for an operating frequency in the range of 5-10KHz. Tests were run as low as 5KHz and as high as 20KHz. Best, and quite satisfactory network performance was obtained of the 5KHz to 10KHz range.

In an attempt to extend the range of circuit balance operation, computer simulations of the mutual coupling design were performed. This simulation suggested that perhaps an unbalance coupling design might extend the range of operation to very light loadings. Preliminary test data do not confirm this suggestion.

#### REFERENCES

1. R. Rosa, "Voltage Consolidation and Control Circuits for Multiple-Electrode MHD Generators," 17th SEAM, Philadelphia, 1976.
2. A. Lowenstein, "A Comparative Analysis of Load Circuits for MHD Generators," 19th SEAM, University of Tennessee Space Institute, Tullahoma, Tennessee, June 1981.
3. K. Crisafulli, K. Marcotte, R. Johnson, and B. Jordan, "A Computer Controlled Electrode Consolidation/Force-Commutated Three Phase Inverter System for MHD Power Generation," 19th SEAM, University of Tennessee Space Institute, Tullahoma, Tennessee, June 1981.
4. A. Chaffee, et. al., "Design, Construction and Initial Operation of an Inverter System for the Mark VI Generator," 18th SEAM, Butte, Montana, June 1979.
5. R. Johnson, K. Marcotte, K. Crisafulli, and B. Jordan, "Microcomputer Control of a Consolidation/Inverter System for Combined Cycle MHD Power Generation," 1981 Symposium on Instrumentation and Control for Fossil Energy Processes, June 1981.

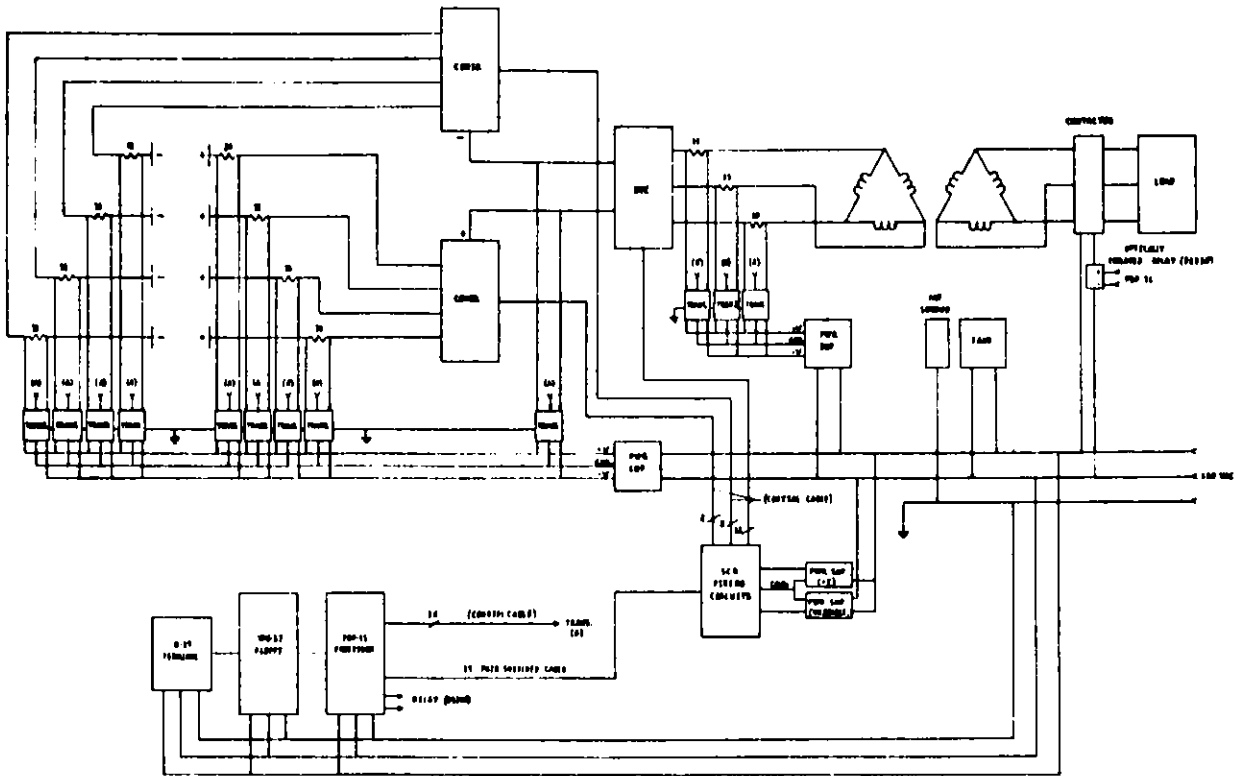


FIGURE 1  
MHD POWER CONVERSION SYSTEM DIAGRAM

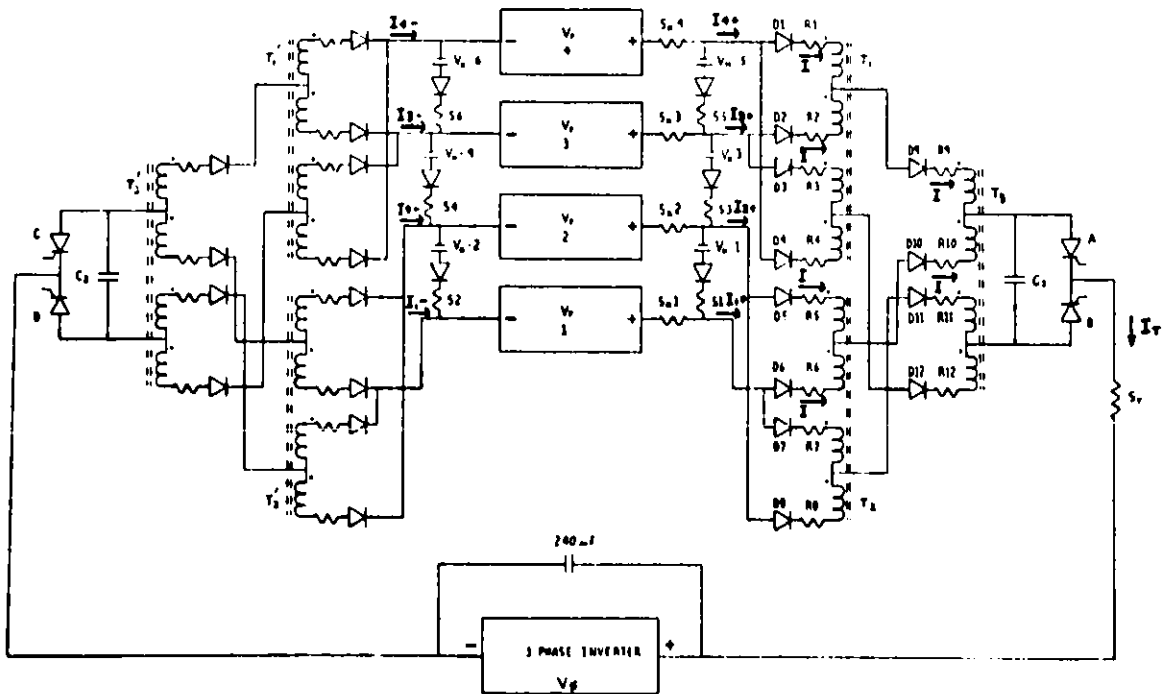
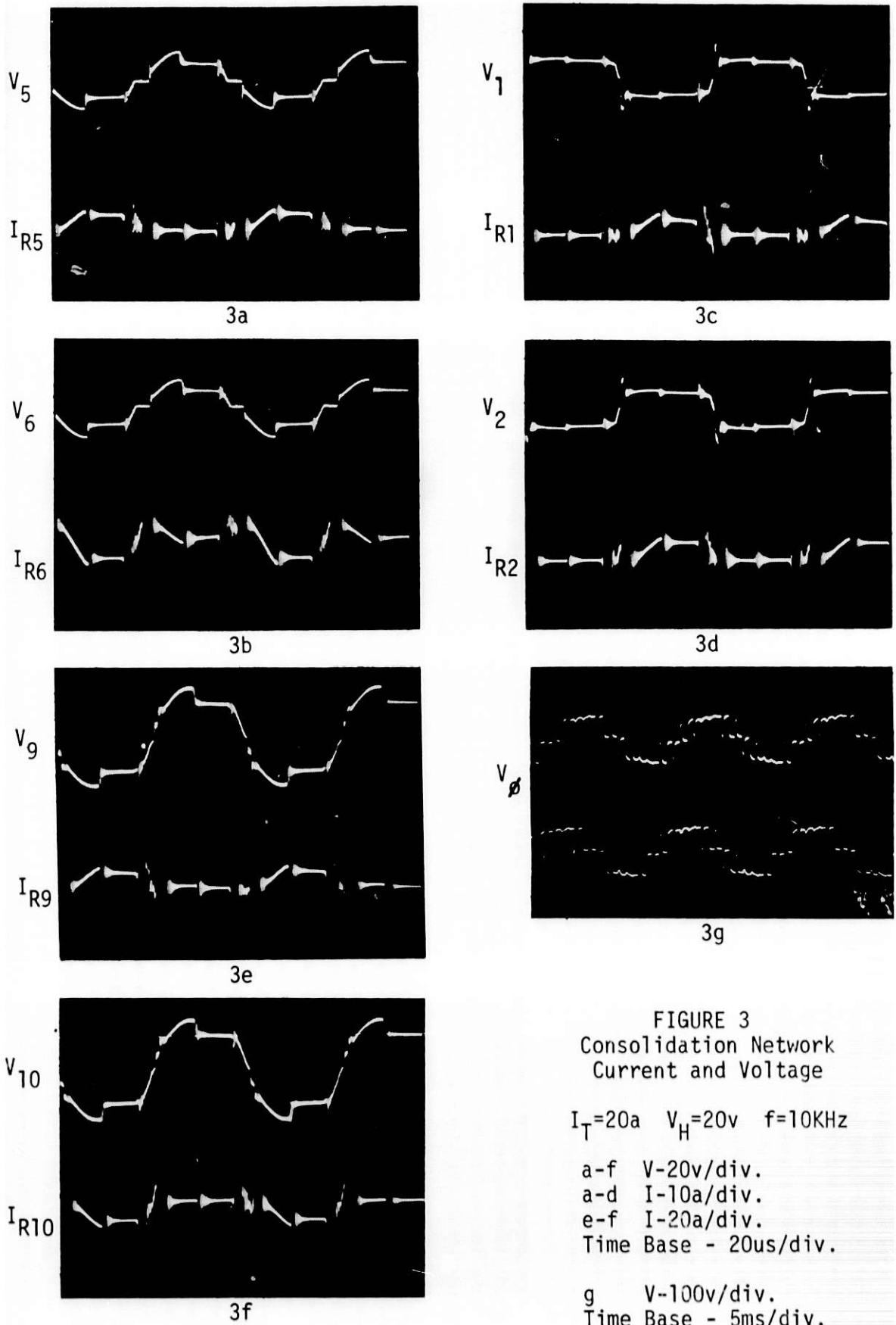
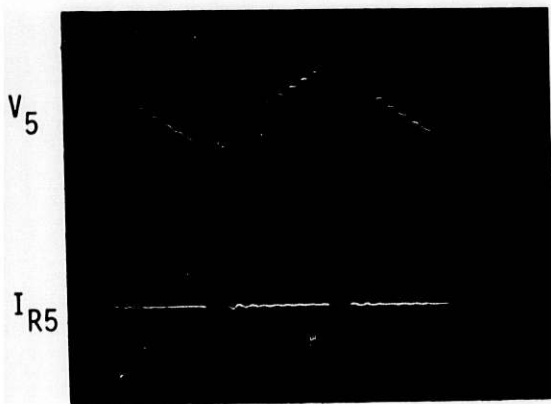
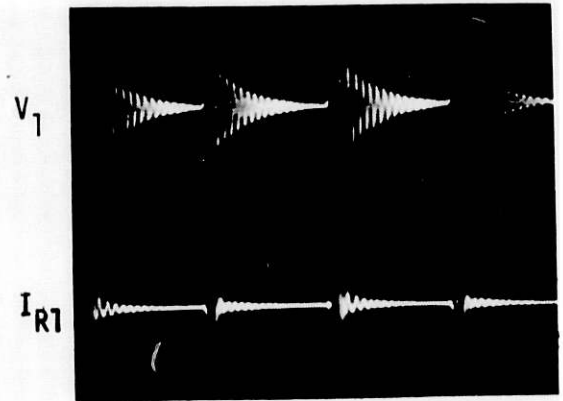


FIGURE 2  
FOUR ELECTRODE CONSOLIDATION SIMULATION

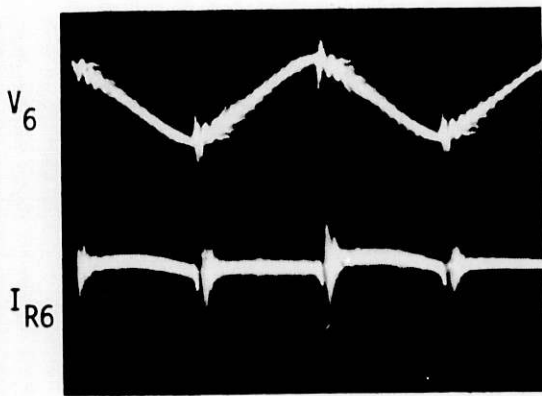




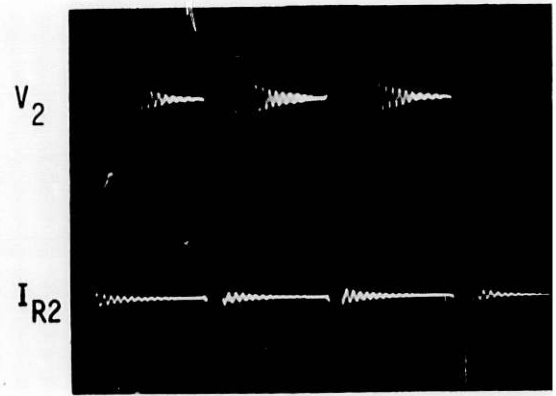
4a



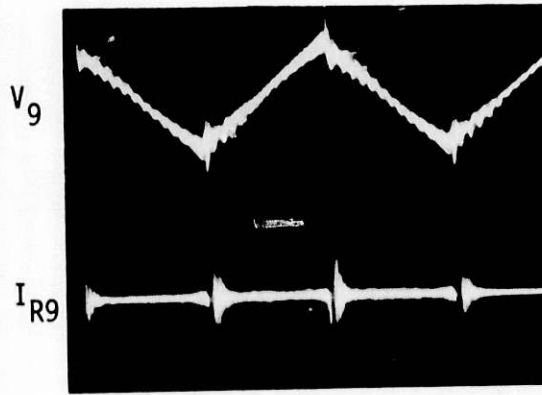
4c



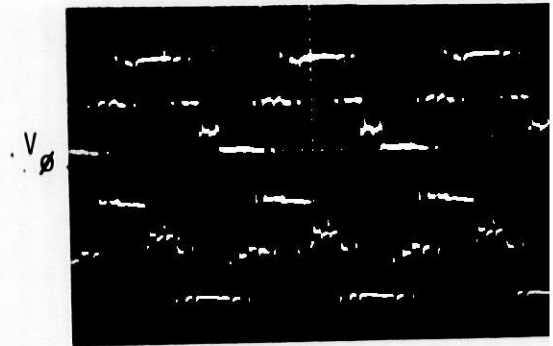
4b



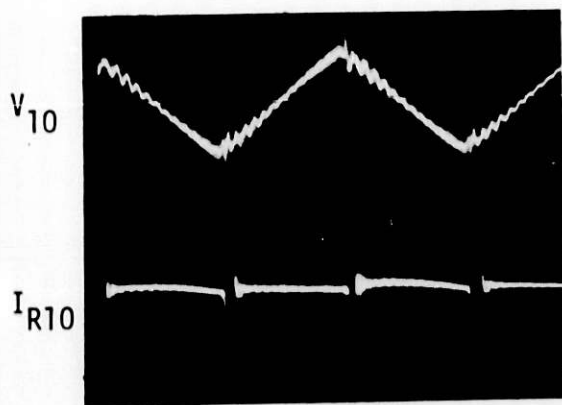
4d



4e



4g



4f

FIGURE 4  
Consolidation Network  
Current and Voltage

$I_T = 5.2a$   $V_H = 20v$   $f = 10KHz$

a-f V-20v/div.

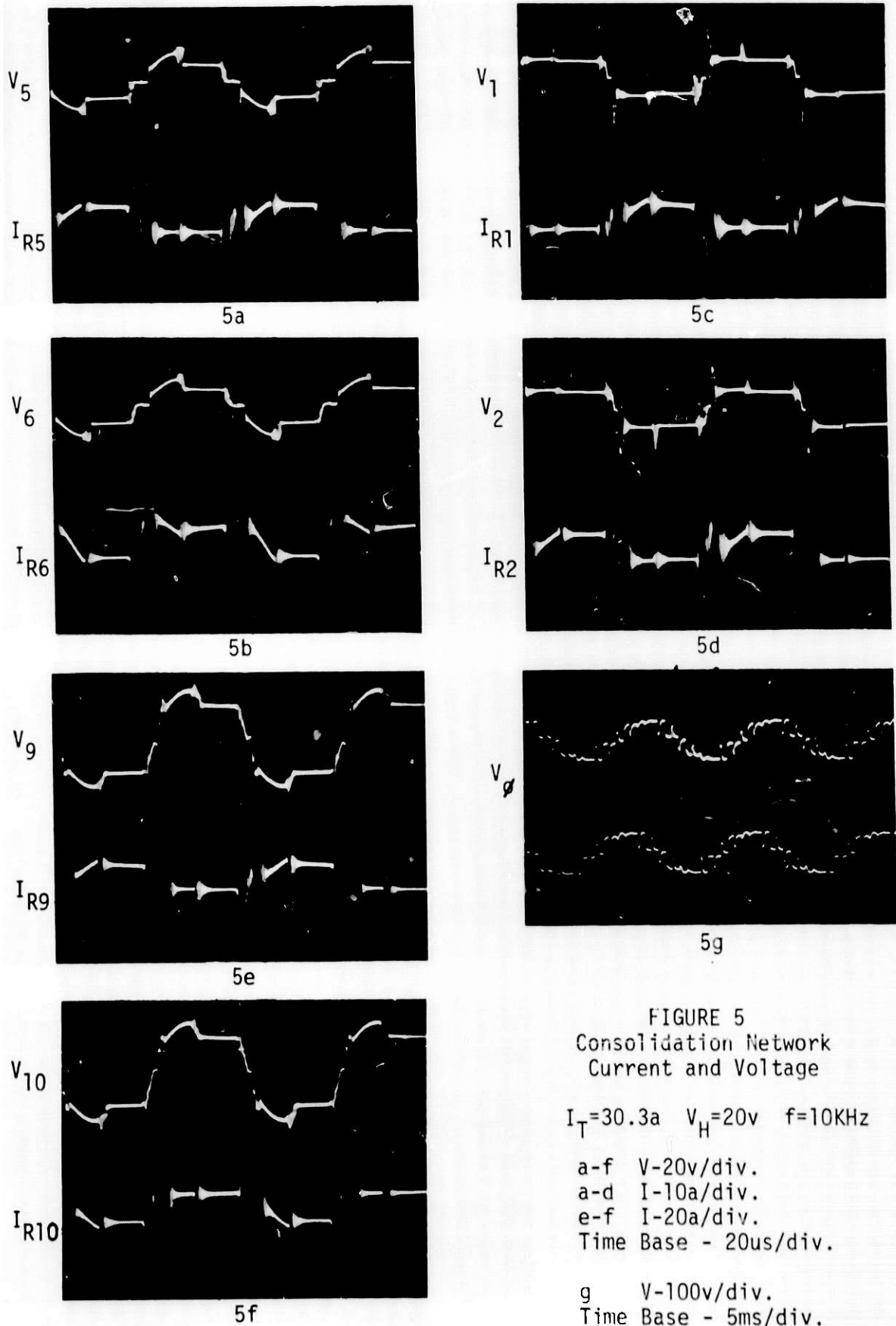
a-d I-4a/div.

e-f I-8a/div.

Time Base - 20us/div.

g V-100v/div.

Time Base - 5ms/div.





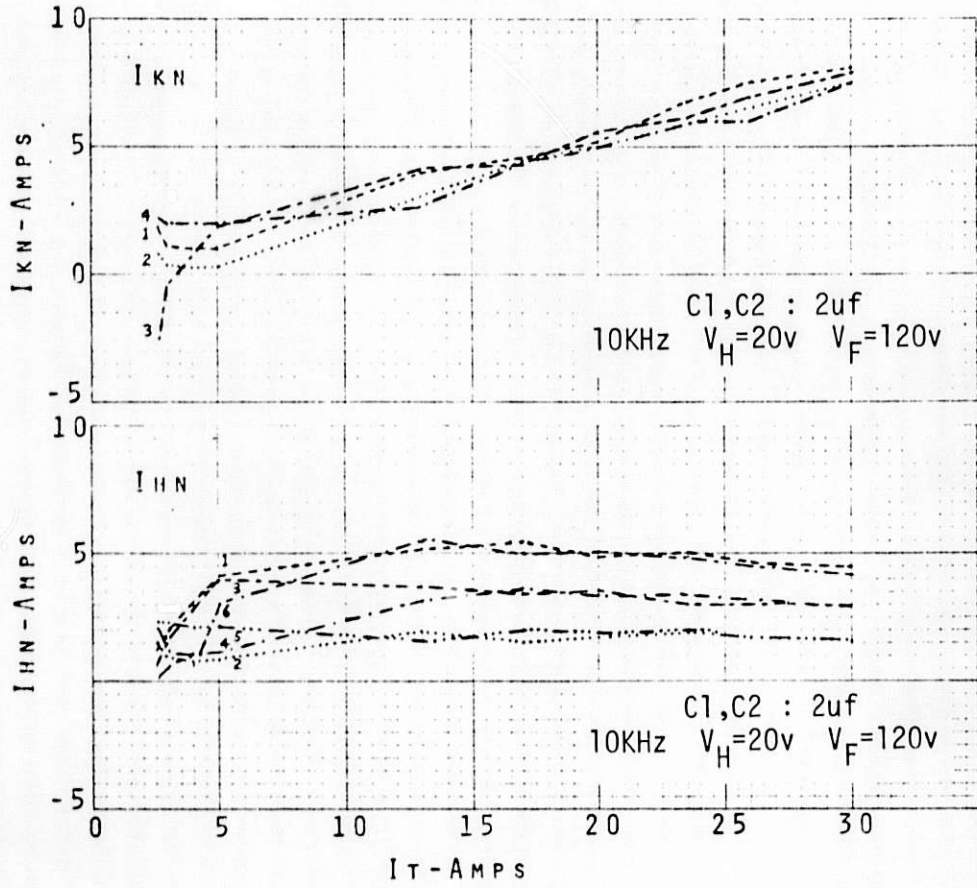


FIGURE 6 Cathode ( $I_{KN}$ ) and Hall ( $I_{HN}$ ) Current vs Load Current ( $I_T$ )

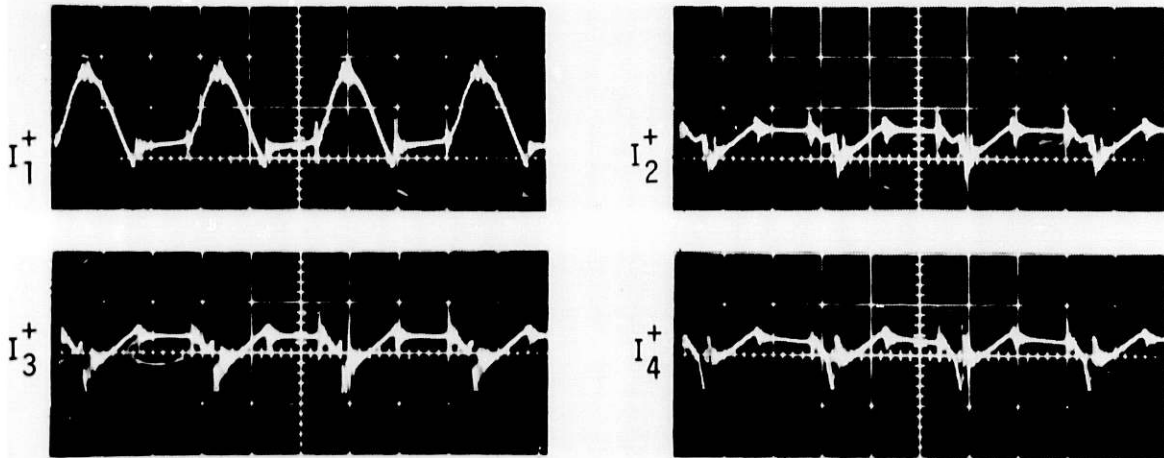


FIGURE 7 Consolidation Network Current  $f=10\text{KHz}$   $I_T=20.7\text{a}$   
 $V_H=20\text{v}$   $I-15.5\text{a/div.}$

THE CONTROL OF INDUSTRIAL FLUIDIZED BED BOILER PLANT

Michael J. Virr, Senior Vice President Technology  
Johnston Boiler Company  
300 Pine Street  
Ferrysburg, Michigan 49409  
616/842-5050

While the development of industrial fluidized bed boilers and furnaces has been underway for more than ten years, it has naturally posed some interesting control problems which have had to keep pace with the technology. Market demand for the boilers has grown because of its ability to burn coal efficiently and cleanly - in short, its ability to meet high emission standards for  $SO_2$  and  $NO_x$  while maintaining high efficiencies.

Approach to fluid bed boiler design control for industrial applications is very different from that adopted for utility boilers. Industrial boilers must be simple to install but at the same time must be capable of operating on automatic control while providing low energy consumption. The basic criterion in development therefore was to adapt the new fluidized bed combustion technology to the traditional concept of the industrial packaged boiler, which is manufactured to near-completion at the boiler plant, incorporating an integrated control system which was relatively simple from the point of view of plant operation. This is basically very different from the approach taken with utility boilers which usually have controls of considerable sophistication which are operated by carefully trained personnel.

The boiler is compactly arranged by taking a typical solid fuel fire-tube boiler or D-shaped watertube boiler and "packaging" these designs so that they adapt the combustion chamber for fluidized bed firing. The advantages of the fluidized bed can be readily utilized because it results in a relatively small combustion chamber with very high heat transfer coefficients that occur within the fluidized bed itself. It is actually possible for the relatively few "in-bed" tubes to generate over 50 percent of the output of the boiler. In this manner, a relatively compact, ship-pable boiler design can be achieved; capacities extend from 2,500 lb to 50,000 lb per hr for firetube units and 70,000 lb per hr for watertube units.

Simplicity of operation, while resulting in automatic startup, is achieved by using a through-bed or in-bed burner for startup using gas (in one case, alcohol), which eliminates the need for a separate startup burner.

High boiler efficiency is achieved by using the fluidized bed itself to get complete combustion of fines by enveloping the incoming coal in a circulation of hot solids, ensuring that even fine particles are burned. This eliminates the need for a carbon burnup cell and ensures long residence time and good sulfur retention.

The sulfur in the coal is retained within the bed by using a particulate bed of limestone, which converts the calcium carbonate to calcium sulfate ash. This material is inert at ambient temperature, and there are no restrictions on its disposal as landfill.

Very low oxides of nitrogen are also achieved compared to conventional boilers because of the low combustion temperature, which need not exceed 1650°F. The resultant NO<sub>x</sub> amounts to less than 300 ppm (the order of 0.55 lb/M RTU input).

Particulate discharge from the boiler is controlled by the use of multiple cyclone dust collectors followed by a baghouse. The highest standards of particulate emission can thus be achieved and are normally below 0.025 lb/M BTUs input. Operating boilers in sizes ranging from 2500 to 50,000 lb per hr of steam are currently providing efficiencies greater than 80 percent when burning coal. Their fuel savings, over plants using conventional coal burning technology, are substantial.

Both firetube and watertube fluidized bed boilers have been operating in a number of industrial plants for more than two years, and experience with them shows that these high technology boilers can be operated and controlled with confidence.

#### Firetube FBC Boiler Control

The packaged firetube boiler capable of multifuel firing, transportation by rail, economical installation, and stable and efficient operation is shown schematically in Fig. 1. The combustion chamber of this boiler is extended downward and tapered to form a full water cooled chamber for the fluidized bed. The bed is divided for control purposes into three parts by closely pitched bed divider tubes. This is because a single fluid bed can only be turned down by 2:1 in itself. To make the unit a multifuel burner, distributors incorporate injection nozzles that can take air/gas mixture for startup and also oil/air nozzles.

The control system of the firetube boiler is shown in Fig. 2. The start sequence is initiated by the startup programmer which lights the pilot gas burner on No. 1 bed. When that has been detected as proven by the UV head, the programmer allows gas to go into the nozzles on No. 1 bed. The bed temperature control senses the increase in temperature of that bed and initiates coal feed to the bed when the temperature has gone over 1300°F.

The startup sequence, having been gone through, provided the boiler output master control has further demand on the boiler, the bed selection logic may then demand either the second or third bed to operate sequentially. In each case, those start on gas through the startup programmer, changing over to coal as the temperature increases over 1300°F.

In order to make the unit of truly multifuel type, selection switches are fitted so that either oil or gas, besides coal, can be selected as the main fuel, in which case they are connected to the master controller to control the total output from the boiler by regulation of their flow valves.

In addition to these main control loops, subsidiary control exists to trim the air flow for oxygen content against a remote set point which may be set for operation of 1, 2 or 3 beds. This is normally set so that when there are three beds in operation on high boiler load, set point is at 5 percent O<sub>2</sub>. With just two beds in operation, a set point of 6 percent would be used, and with number one in operation, set point of 7 percent respectively. The O<sub>2</sub> is measured in the flue gas duct by means of a zirconium probe type of instrument which will thereby automatically trim for variations in air and/or coal flow to the beds to maintain a constant O<sub>2</sub> according to the remote set points mentioned above.

Further subsidiary control controls the furnace pressure in the combustion chamber freeboard to minus half an inch water gauge by variation of the ID fan inlet damper as shown on Fig. 2. The control of the boiler water level follows conventional practice; variation of the boiler feedwater regulator based on boiler water level sensing adjacent to the boiler gauge glass. This is not shown as it follows conventional practice.

#### Watertube Boiler Control

The arrangement of the packaged watertube boiler is based on the traditional D-shaped configuration of which thousands have been built for gas and oil firing. This design differs from the traditional by incorporating a concave bed within the combustion chamber, as shown in Fig. 3. This is a "second generation" design whereby the combustion part of the bed has been separated from heat transfer and control part of the bed, making these functions to a great extent independently variable. This gets away from the traditional problems of early fluidized beds where bed division is necessary as described in the firetube control system in order to achieve reasonable control of 2:1 or over.

The shape of the combustion chamber induces the fluidized solids to flow down in the center, where the fuel is fed in, returning to the surface at the sides. Fuel being delivered below the surface in the center of the bed so that the hot downward moving solids envelop the fresh solid fuel and cause it to circulate. The resulting substantial residence time for fuel particles below the surface is sufficient to achieve high combustion burnout efficiencies and thus prevent the carryover of unburnt fuel to the cyclones. This eliminates the need for the burnout cell which has been associated with early fluidized development and has been found to be required for large, flat-bottomed fluidized beds, typical of some utility boiler designs.

The unit has more than 6 ft of freeboard within the combustion chamber, thus allowing volatiles to burn out completely before entering the convective surface. If high sulfur coals are being burned, a dolomite or limestone feed may be incorporated to achieve an 80 to 90 percent absorption within the body of the fluid bed. This causes the formation of inert calcium sulfate in the ash, which is taken out automatically through the dashing system below the bed and flue gas clean-up system, and lowers the sulfur dioxide requirements. The long residence time within the bed greatly aids this absorption process.

The watertube boiler achieves natural circulation through the primary heating surfaces in the combustion chamber, which are in the form of nose tubes on each side of the bed, and the secondary convective surface between the drums and the back end of the boiler. In the power version of the boiler, requiring superheat, a convective superheater replaces the first four tubes in the convective bank of the boiler.

Another feature accommodates high ash coals and industrial refuse containing stone or other tramp materials that do not fluidize when they enter the bed. These materials fall into a de-ashing trough in the bottom of the furnace, which is occasionally fluidized, causing heavy waste material to pass through a large ash valve and water cooled screw at the base of the boiler. This operation can be carried out while the unit is in operation, and initiated from bed differential pressure between the surface and the bottom bed. The stone or tramp material is extracted by water cooled screw feeders.

The boiler control system shown on Fig. 4, as on the first unit that was installed at Haywood Tylers' factory at Keighley in England, startup sequence is initiated from a time clock. This initiates a pilot burner for startup which when proven ignites the gas which is let through premix burners which form the distributors for the combustion chamber. During this initial startup phase, the outer panels are not fluidized; the pneumatic valve being closed. This isolates the combustion part of the bed which quickly heats up, burning the fluidizing gas and air, and when a temperature of about 1100°F has been reached, the gas/coal changeover is initiated, starting the coal feeder, gas also being held on for a period of about 15 minutes on a timer in order to build up coal inventory within the bed itself. From then on the boiler output controller controls both the coal and air quantity into the bed, measuring the rate of demand on the differential from the steam flow signal generated on the boiler steam outlet pipe mounted orifice plate.

The boiler is now being controlled in output by both the coal and air rate to the boiler, and the fluidization of the wing panels which have a rapid response effect as the red hot bed material is being used as a "thermal flywheel" from which heat can be extracted rapidly by opening the air to the wing panels.

This rapid response is achieved by boiler pressure controlling the rate of air to these wing panels. Any deviation from set point has a rapid remedial effect opening or closing of the pneumatic valve positioner to these wing panels. This is demonstrated by Fig. 5 which shows a time against boiler steam output and fluidized bed temperature graph that was attained during load response tests in July of last year. Rapid variation of the load could be achieved because a steam dump condenser was fitted to the factory heating surface so that artificially large loads could be put onto the boiler in a matter of second by merely opening the valve to the dump condenser. Unfortunately, as the tests were in the summer, the dump condenser was not big enough to take full boiler output and swings in the order of only 30 percent could be artificially induced. Fig. 5 is reproduced from a three point chart recorder which indicated that a load swing in the

order of 30 percent could almost instantaneously be achieved both in the upwards and downwards direction. Such a sudden, large demand of heat output from the combustion chamber full of fluidized solids naturally caused a reduction of bed temperature. This was normally not more than 80°F, and the bed temperature would recover within 15 to 20 minutes, and therefore would not impair the boiler operation in any way. As a watertube boiler has about one-fourth of the water content of a firetube boiler, one cannot rely on the inherent heat release that one can achieve by slight lowering of boiler pressure in order to achieve steam output which is inherent in the firetube boilers described earlier.

As the wing panel boiler tubes can generate up to 60 percent of the boiler output, it is necessary to arrange a trim on this boiler pressure control circuit such that in the event of the bed temperature being depressed excessively, which would be by over 100°F, the control signal can be slowed down with respect to the rate of response on the pneumatic valve positioner, thereby assuring that the fluidized bed temperature does not get below the order of 1500°F at which temperature combustion reaction rate becomes seriously impaired compared to the correct combustion temperature of 1580°F-1600°F.

In the main boiler control circuit, two trims are incorporated - one on the coal feeder rate being trimmed by bed temperature as naturally the bed inventory of coal only changes relatively slowly. This is necessary for instance to prevent overfeeding the bed with coal which would have the temperature moving rapidly upwards because the boiler output controller was demanding a greater boiler load. In addition, the air to the boiler is trimmed on an O<sub>2</sub> signal generated from an oxygen probe in the flue gas exit to the boiler in a similar way to the firetube boiler to again ensure that the oxygen setting, which is normally a constant 4.5 percent representing 25 percent excess air, is achieved throughout the whole control range on this boiler.

We have found that, under automatic control, this boiler control system will readily give a 4:1 turndown and with careful trimming of controls under manual supervision, a turndown of just over 5:1 has been achieved using the system on Hayward Tylers' plant.

The general layout of the boiler and control panel is shown in the photograph Fig. 6. The control panel is reasonably straight-forward reading from right to left we have first the FD fan air pressure under the fluidized bed, the boiler's flue gas exit temperature (normally about 392°F), the bed temperature trim controller, the boiler pressure controller, boiler output controller, oxygen air trim, gas/coal changeover controller, and finally two auto/manual stations for the coal feeds.

This boiler is normally left unsupervised and switches itself on with the time clock initiating the startup sequence as already described. The boiler is visited once in the morning by the plant's maintenance department and once in the evening to fill in the log and carry out such operations as initiating boiler blowdown and pneumatic ash removal system, moving ash from the day bins. In the event of the boiler failing to a safe condition for any reason, a gong sounds in the maintenance department and

on the panel (which can be seen on Fig. 6). There is a series of ten lights which indicate where a fault has occurred such as low drum water level or a screw feeder blockage. The boiler is capable of operating at up to 70 percent load on only one screw feeder. Therefore, the plant does not come down in the case of a single screw blockage.

This boiler plant has now done two complete heating seasons and has shown high availability of some 98 percent. As it is the only boiler on this site, such dependability is a necessity.

### Conclusions

In conclusion, I would like to comment that the systems described have basically been of the electrical/pneumatic boiler type which is largely conventional. However, the control systems lend themselves admirably to a micro-computer controller, and we now have a project underway to incorporate such a device both on the demonstration firetube FBC boiler in our plant and on an overseas installation of one of the watertube boilers now that the control arrangement has been proven with conventional control technology.

Boiler tests on both these types have indicated that efficiencies of 80 percent or over are achieved on full-load, and the carbon and ash losses are of the order of 5 percent or less. Load response is excellent for both boiler types with loads in the order of 30 to 40 percent can be instantaneously met in the control system described.

As the excess air is controlled throughout the load range at a relatively low figure, excellent part-load efficiencies are achieved and figures as high as 79 percent have been confirmed during tests at half-load.

Where fuel supplies have become questionable, industrial plants require insurance against lack of supply of any single fuel and this a fluidized bed boiler can assure, the controls being arranged so that only a flick of a switch is necessary. At the same time, they must meet EPA and local regulations covering emissions. This has led to the rapid acceptance of fluidized bed boilers over the last two years. This is illustrated by some 34 orders we have received; 14 of these plants are already in service.

These units can not only burn high sulfur coal to within EPA standards but can also have separate feeders for conveying waste materials into the fluid bed to be burned as makeup fuel, such as, mushroom compost or lacquer.

The watertube boilers are adaptable to high pressures and cogeneration systems and, therefore, can be expected to meet a wide variety of industrial needs in the coming years.

The United States has the largest reserves of coal in the world, and there is no reason why plant managers should have to rely on imported fuels to ensure the supply of electricity and steam to their plants.

This paper is presented by the kind permission of the Directors of Johnston Boiler Company and Stone FluidFire, Ltd.

References

1. Fluidized Bed Boiler - an industrial application at Central Soya Company Inc., Marion, Ohio. A. N. Vince, R. D. Barnhart. 20th Annual Kentucky Industrial Coal Conference, University of Kentucky, April 29, 1981.
2. Industrial Fluidized Bed Boiler. Energy Management. April-June 1980. M. J. Virr.



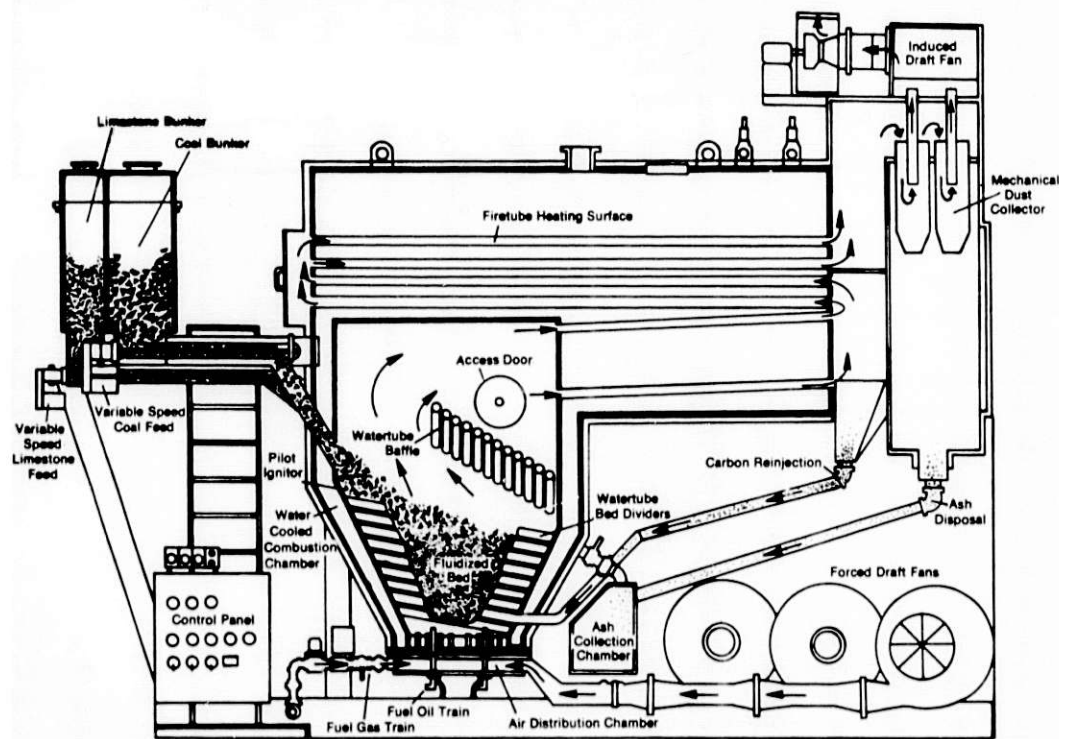
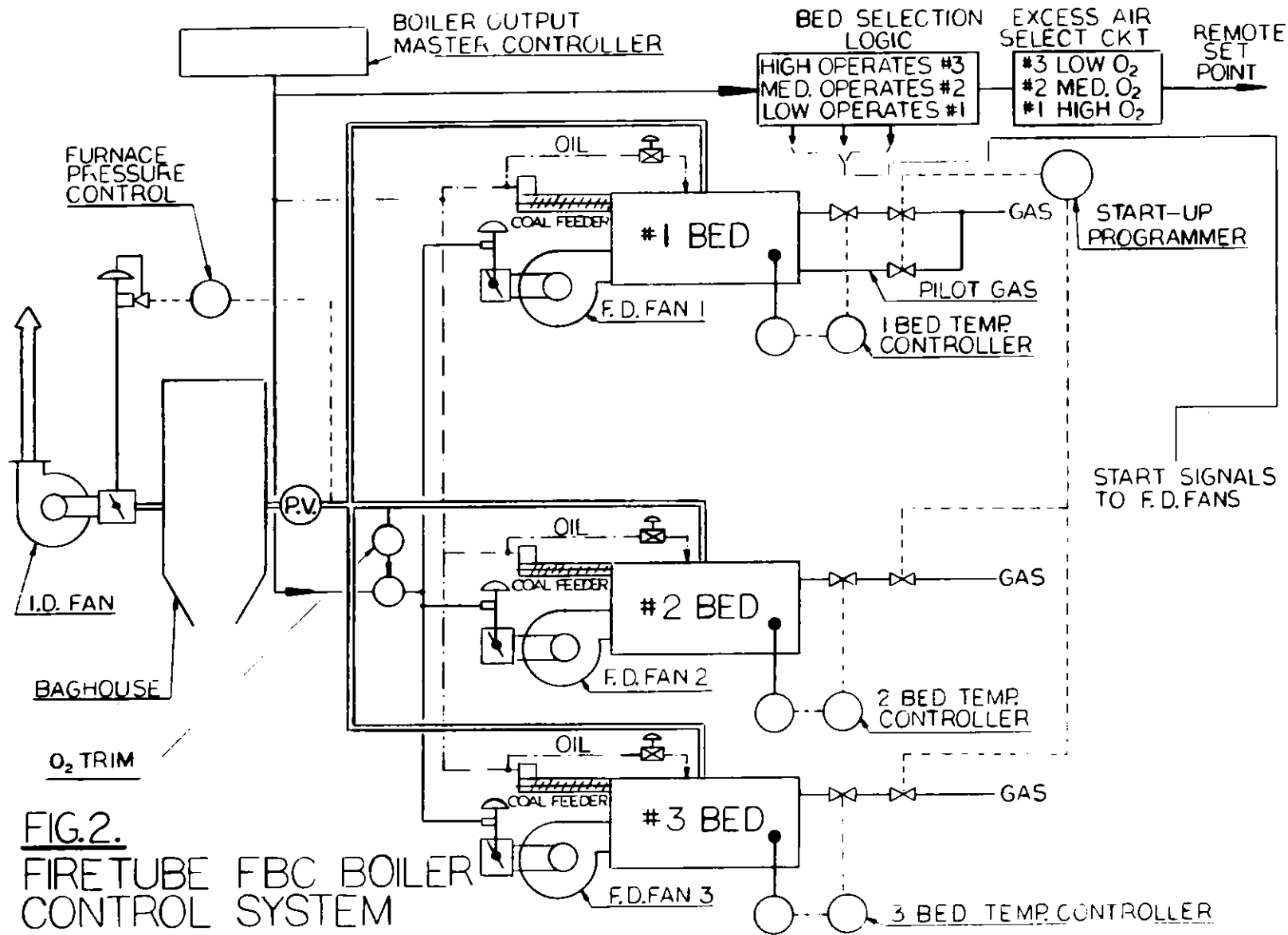


Fig. 1. Firetube Fluidized Bed Boiler



**FIG.2.**  
**FIRE TUBE FBC BOILER**  
**CONTROL SYSTEM**

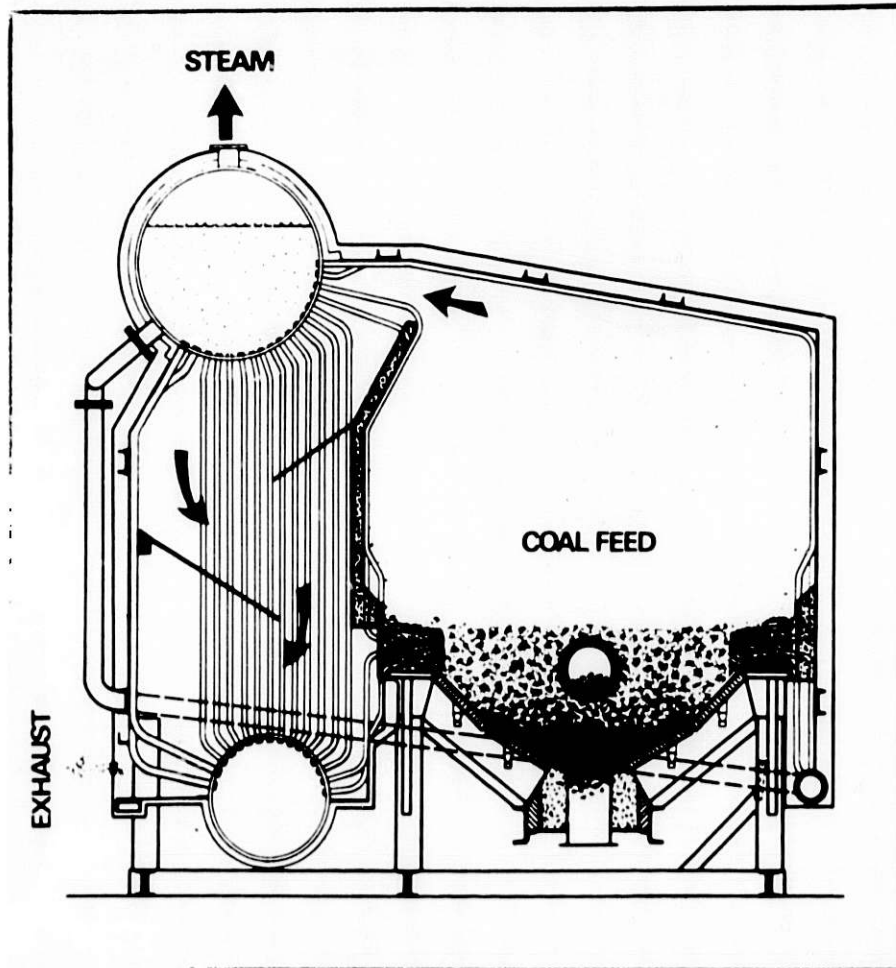
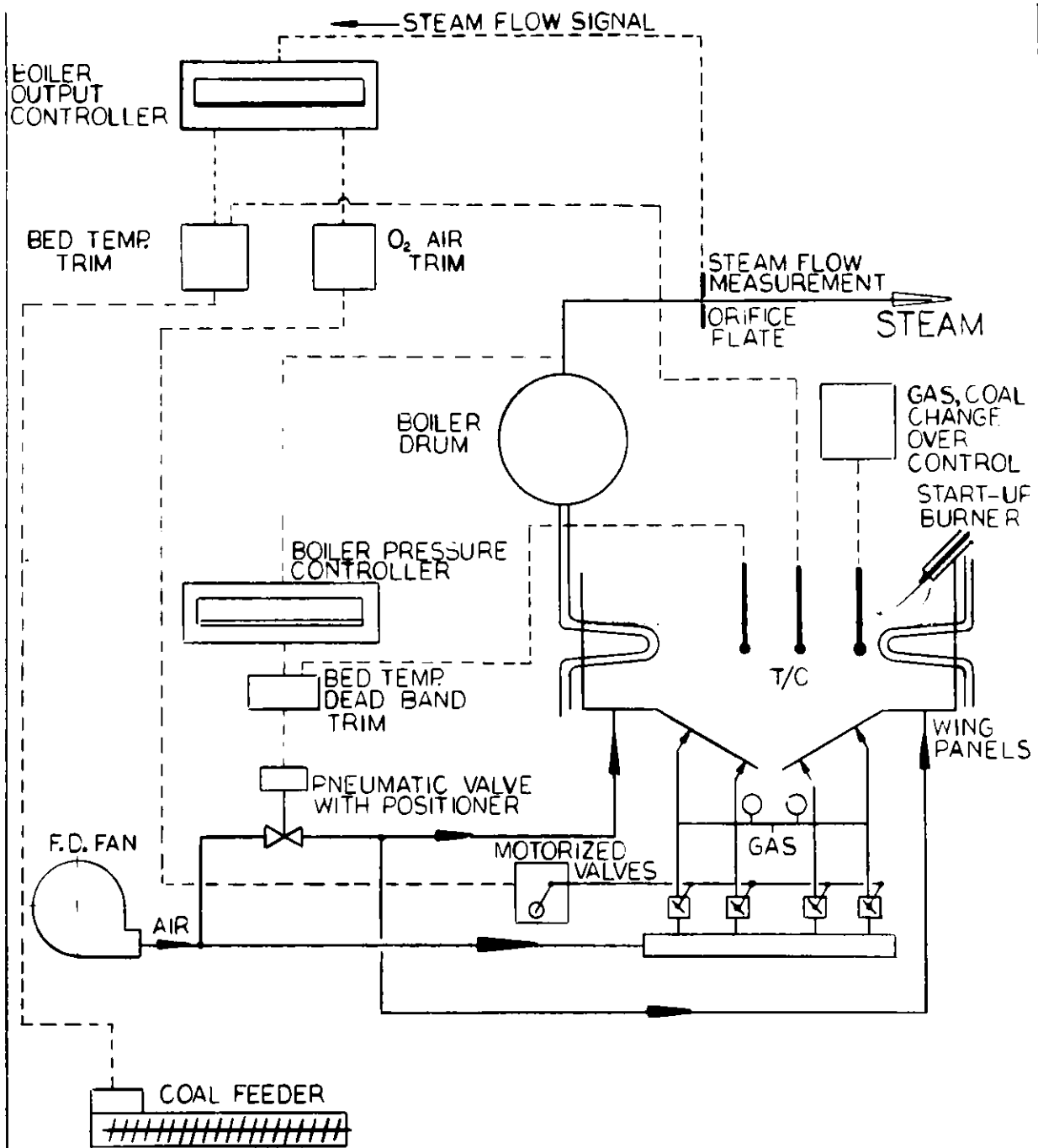
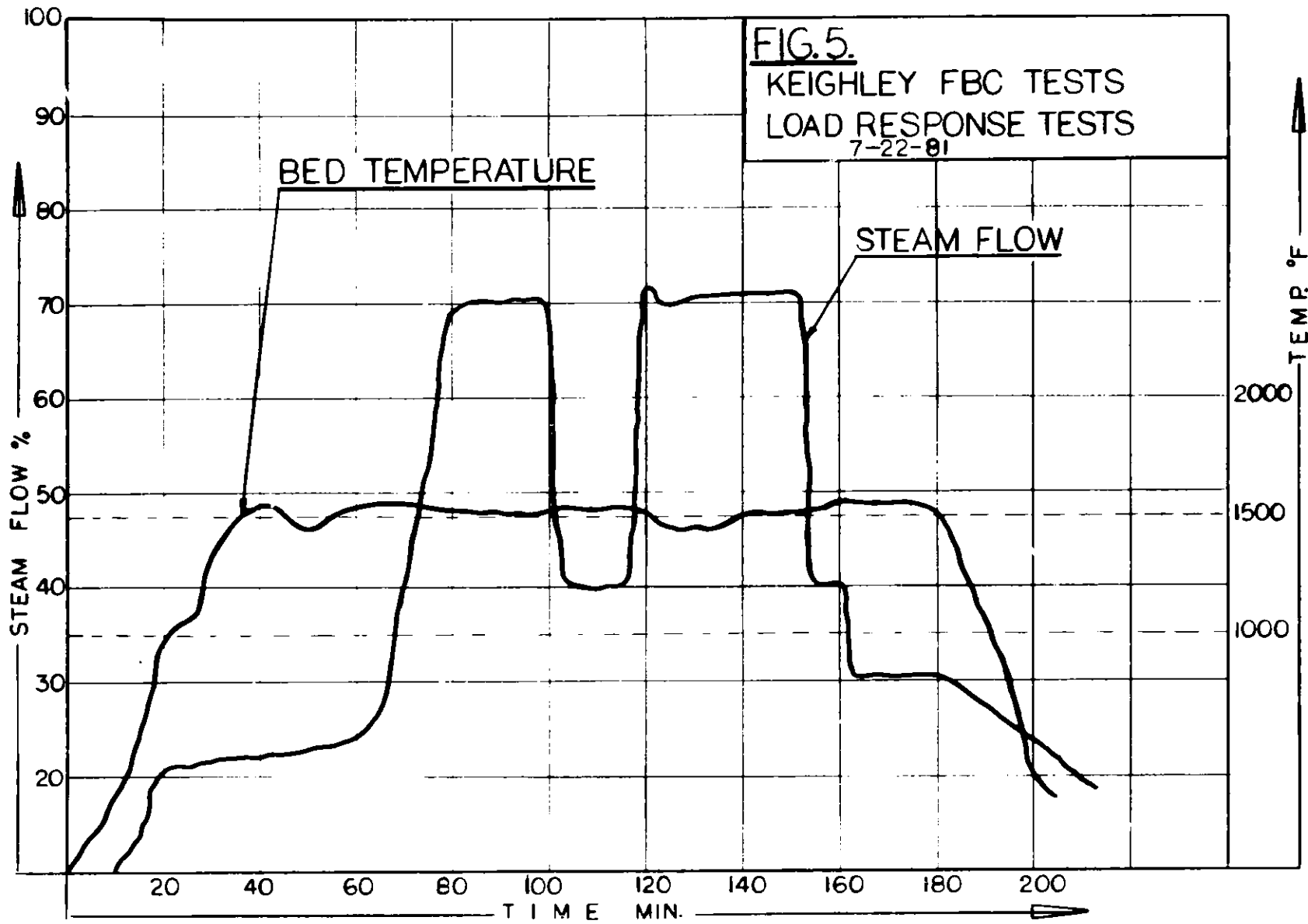


Fig. 3 Fluidfire Package Watertube Boiler Design



**FIG. 4.**  
**WATERTUBE FBC BOILER**  
**CONTROL SYSTEM**



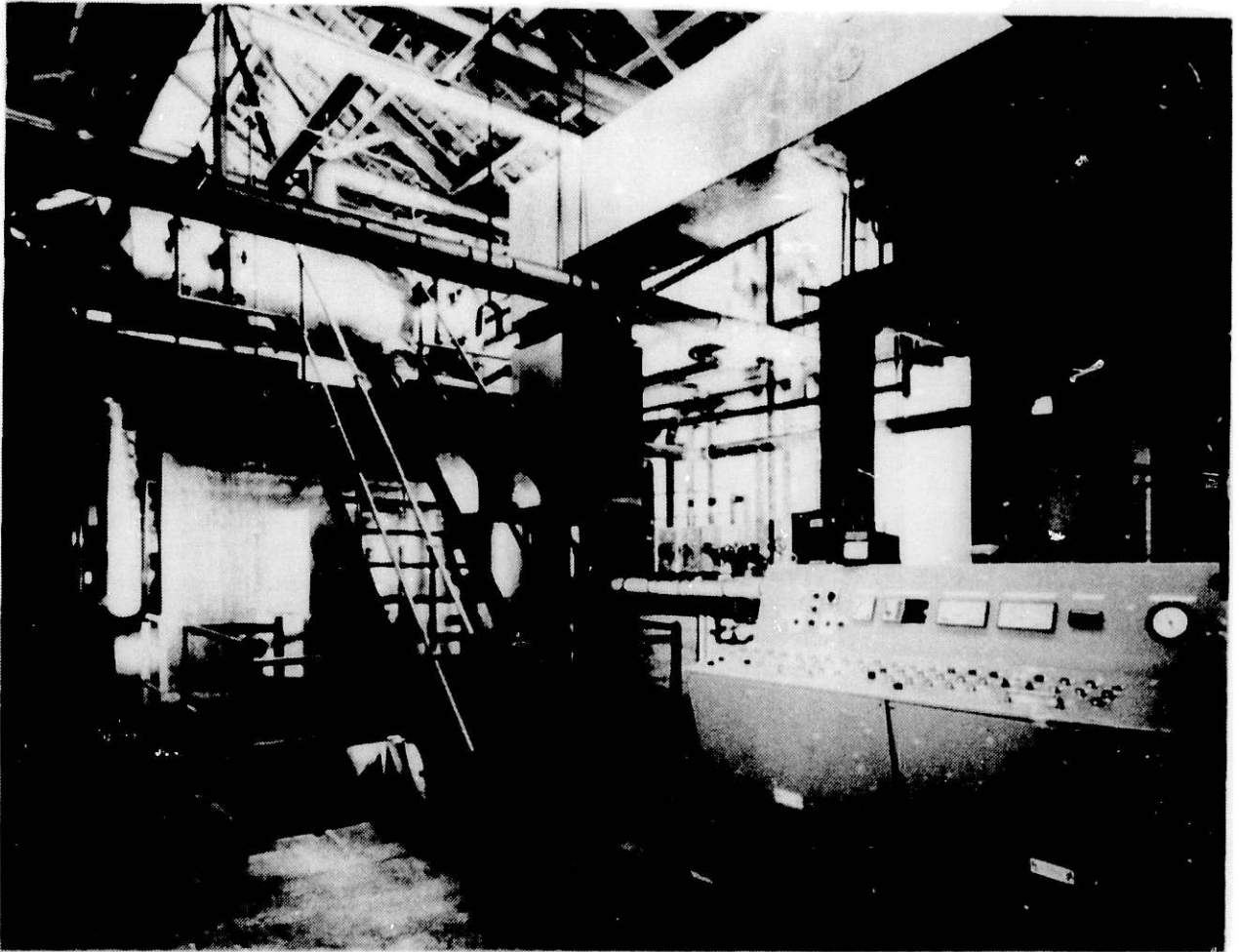


Fig. 6. Watertube Fluidized Bed Installation at  
Haywood Tylers' Keighley Factory England  
Showing Control Panel.

PROCESS CONTROL OF MULTI-SOLID FLUIDIZED BED COMBUSTION

G. Gangaram, R. D. Litt  
Battelle, Columbus Laboratories  
505 King Avenue  
Columbus, Ohio 43201

E. C. Seber  
Struthers Thermo-Flood Corporation  
P.O. Box 753  
Winfield, Kansas 67156  
316/221-4050

Introduction

As the Multi-Solid Fluidized Bed Combustion (MSFBC) process moves into commercial applications, the experience gained in process control can be applied to other fossil energy processes. Problems of temperature measurement and control, solids flow control, and turndown are common to fluidized bed combustion, gasification and oil shale or tar sands processing. The application of process control to multi-solid fluidized bed technology has included the process requirements, hardware limitations, scale-up uncertainties and pilot plant experience. Process control features for MSFBC which are being developed include on-line steam quality analysis, combustor temperature control, solids circulation control, and operator initiated automatic turndown capability. Before addressing these features, a brief description of the MSFBC process is presented.

MSFBC Process Description

MSFBC is gaining commercial acceptance because of its outstanding performance and versatility. The concept of MSFBC is illustrated in Figure 1. Combustion and heat exchange take place in separate units so that each can be optimized without adversely affecting the other's operation. Fuel is burned in the combustor while heat exchange is accomplished in the External Heat Exchanger (EHE) and the convection section which are external to the combustor. (Approximately 55% of the heat is transferred in the EHE.) This decoupling is accomplished by the circulation of a bed of fine solids consisting of sand, limestone, and ash between the combustor and the EHE. Two important functions result from this arrangement: (1) the control of combustor temperature and (2) the transfer of heat in a mildly fluidized bed heat exchanger. The former assures high carbon combustion efficiency, high sulfur capture and low  $\text{NO}_x$  emissions; the latter assures a high heat transfer coefficient and minimal tube erosion.

The combustor has another important and unique feature: a bed of large fluidized solids, referred to as the dense bed, is located at the bottom of the combustor above the air distributor. Its functions are to increase the residence time of the circulating solids, promote more gas-solids and solids-solids contact, improve carbon combustion efficiency, enhance sulfur capture, and facilitate above bed feeding. Extensive tests have demonstrated the effectiveness of the dense bed in these areas, especially for

less reactive solid fuels such as fluid petroleum coke.<sup>1</sup> The dense bed of large particles, which do not leave the combustor, is a key to the MSFBC system's superior performance. The large particles in the dense bed "stabilize" a bed of the fine particles at superficial velocities far above their entrainment velocity. The optimum interaction of dense bed and entrained bed leads to the excellent performance obtained with MSFBC while operating at higher velocities than would otherwise be possible.

The versatility of MSFBC is demonstrated by the ability to use staged combustion as an effective means of drastically lowering NO<sub>x</sub> emissions to less than 100 ppm.<sup>2</sup> Testing has demonstrated the capability to meet or exceed the very stringent California standards for NO<sub>x</sub> emissions without sacrificing other performance criteria such as sulfur capture and carbon combustion efficiency.

#### Process Control

Again the control features that have evolved with the MSFBC system are: steam quality analysis, combustor temperature control, solids circulation control, and operator initiated automatic turndown capability. Steam quality control is particularly important for the oil field steam flood application while combustor temperature control, solids circulation rate control, and turndown capability are important to all MSFBC systems. Each of the controls are discussed below:

Steam Quality Analysis. In the steam flood generator application, the objective is to maintain the desired steam flow rate and steam quality at the oil well. The steam flow rate is set by the operator. Pressure is maintained by a pressure control valve or back pressure from the steam distribution system. Steam quality is monitored by an on-line steam quality analyzer (See Figure 2). If the steam quality is not in the range of 70-80%, the operator changes fuel to water feed rate ratio to bring the steam quality back into range. The on-line steam quality analyzer is a dedicated, pre-programmed microprocessor used to calculate steam quality based on the water flow rate, the steam pressure and temperature and the differential pressure drop of the steam across a known orifice restriction. The analyzer's output can be used to indicate, record, alarm or initiate corrective action as needed.

Combustor Temperature Control. Combustor temperature can be controlled by changing the circulation rate of solids between the EHE and the combustor. This rate of circulation depends on a thermal balance around the combustor. The temperature of the combustor reduction zone is controlled by circulating solids from the EHE directly to the dense bed region (See Figure 3). When adding secondary air to the combustor, the temperature in the oxidation zone is controlled by circulating solids from the EHE to the freeboard region. Transport air is used to pneumatically transport the solids to overcome the vertical lift required.

Solids Circulation Control. The ability to circulate solids between the combustor and EHE at controlled flow rates and at high temperatures ( $\leq 1650^{\circ}\text{F}$ ) has been provided by non-mechanical valves which are referred to



as "L" valves. The flow path of the solids is from the EHE bed down through the vertical leg (See Figure 3). The solids movement through the horizontal leg of the "L" valve into the combustor is accomplished by introducing a very small quantity of aeration air. The solids flow rate has been found to be proportional to the amount of air injected; therefore controlling the amount of air injected into the "L" valve automatically controls the circulation rate.<sup>3</sup> However, the amount of air is small, (20,000 PPH of sand can be moved through a 4" diameter "L" valve by 1 SCFM of air) so very close regulation of the air flow is required in order to maintain control throughout the range of the circulation rate.

Figure 3 shows an approach to control of the air injection rate where the aeration air is controlled by cascading the combustor temperature controller to the air flow controller. An alternate approach eliminates the flow sensor relying on a digital control valve for finite air flow control.

Operator Initiated Automatic Turndown Capability. Turndown of an enhanced oil recovery steam generator is accomplished by adjusting the feed-water flow rate. Primary and secondary air flow controls and fuel and limestone feed rate control are part of the automatic turndown control capability. As shown in Figure 4, the water flow rate sets the fuel feed rate. Limestone is fed in ratio to the fuel to maintain a constant calcium to sulfur ratio for sulfur capture. The ratio can be adjusted for increased sulfur capture or for economy. As the combustor's firing rate is adjusted, the combustor exit temperature is maintained at the desired level by controlling the rate of entrained bed circulation. This changes the heat input to the EHE and hence the heat transferred to the water/steam circuit. The heat input to the convection section changes with the flow rate of gas from the combustor.

The combustor air flow is also established by the fuel feed rate so that the desired balance of fuel and air is maintained throughout the operating range (See Figure 5). A low flow limit is imposed upon the primary air rate so that the dense bed region is always above the minimum acceptable fluidization velocity. The ratio of primary to secondary air is maintained in a proper range for NO<sub>x</sub> emissions control.

#### Steam Flooding Application

Struthers Thermo-Flood Corporation, a subsidiary of Struthers Wells Corporation, has designed and manufactured a 50 MM BTU per hour steam generator for Conoco North American Production as an enhanced oil recovery application. This is the first commercial application of MSFBC and the first solid fuel fired steam flood generator (See Figure 6). The escalating price of crude oil makes it desirable to substitute less expensive solid fuels for the crude oil which is presently the primary fuel for steam flood generators. Solid fuel firing is also important because of the substantial amounts of petroleum coke available from the processing of heavy crude oil.

Steam flood generators present several special requirements which are addressed in the Struthers Thermo-Flood design. Eighty percent quality steam is generated at high pressure in a once through heating circuit from high TDS (total dissolved solids) water. Steam quality must be controlled,

along with flow and pressure, to avoid scale buildup in the tubes.<sup>4</sup>

The Process Flow Diagram, Figure 7, for the steam flood generator shows the MSFBC in addition to the auxiliary equipment. Struthers has designed and built a 5 MM BTU per hour test facility (See Figure 8) at their Winfield, Kansas manufacturing site. This test unit provides an effective means of equipment development, controls development, and fuels testing for a range of future applications.

#### Conclusion

MSFBC has moved from the pilot plant into commercial application. Plans to build a more integrated control system for future units will be based upon current experience and known process control techniques. Future possibilities include the use of flue gas oxygen concentration to trim the air flow, and the use of flue gas sulfur dioxide concentration to trim the limestone feed rate. These and other optimization steps will further increase the economic incentive and reliability of this new technology. These lessons also apply to other fossil energy processes as they move into commercialization.

#### References

1. Curran, L. and Nack, H., Battelle's Multi-Solid Fluidized Process - "An Advance Concept in Energy Conversion Processes" The International Congress on Technology and Technology Exchange, May 1982.
2. Nack, H., Liu, K. T., Lyons, C. J., "Control of Sulfur Dioxide and Nitrogen Oxide Emissions by Battelle's Multisolid Fluidized-Bed Combustion Process", The Proceedings of the Sixth International Conference on Fluidized Bed Combustion, Vol. 3, pp 979, August 1980.
3. Knowlton and Hirson, "L-Valves Characterized for Solids Flow", Hydrocarbon Processing, March, 1978.
4. Fanaritis, J. P., Nack, H., Lyons, C. J., "Application of the Battelle Multi-Solid Fluidized Bed Combustion System to Oil Field Steam Generators:", The Proceedings of the Sixth International Conference on Fluidized Bed Combustion, Vol. 3, pp 365, August, 1980.

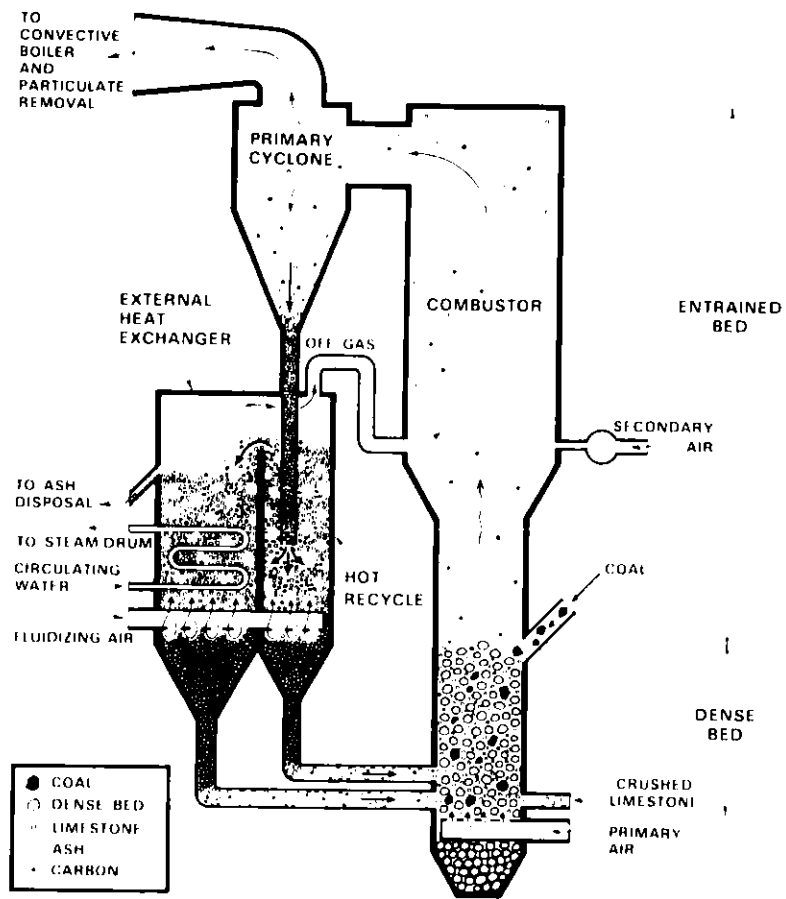


FIGURE 1 BATTELLE MULTISOLID FLUIDIZED-BED COMBUSTOR

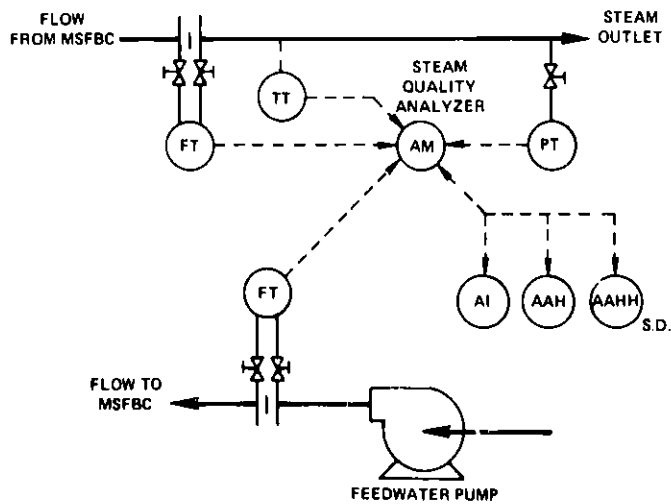


FIGURE 2. STEAM QUALITY ANALYZER

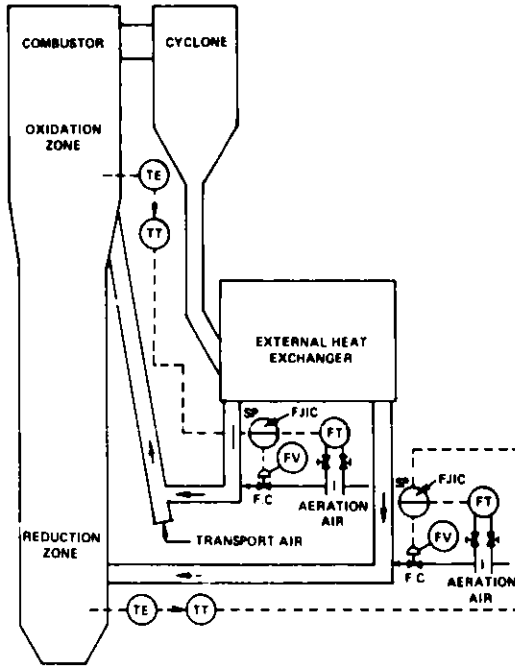


FIGURE 3. COMBUSTOR TEMPERATURE/SOLIDS CIRCULATION CONTROL

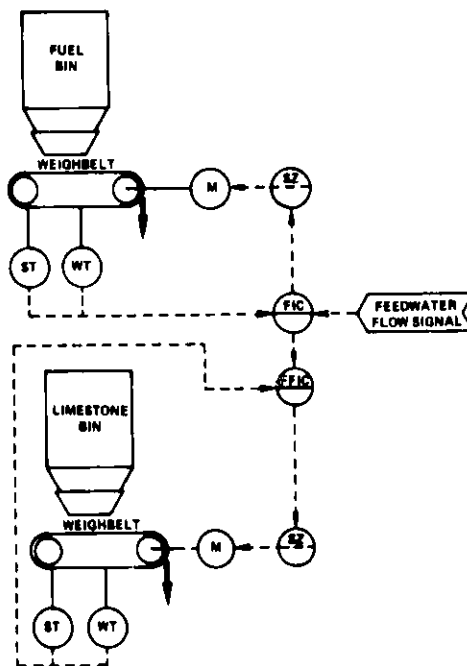


FIGURE 4. FUEL/LIMESTONE FEED CONTROLS

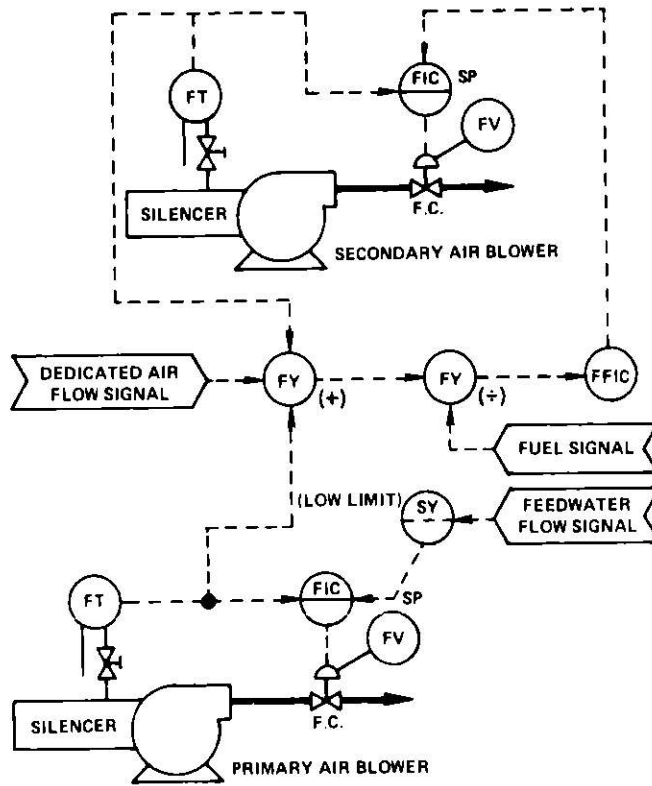
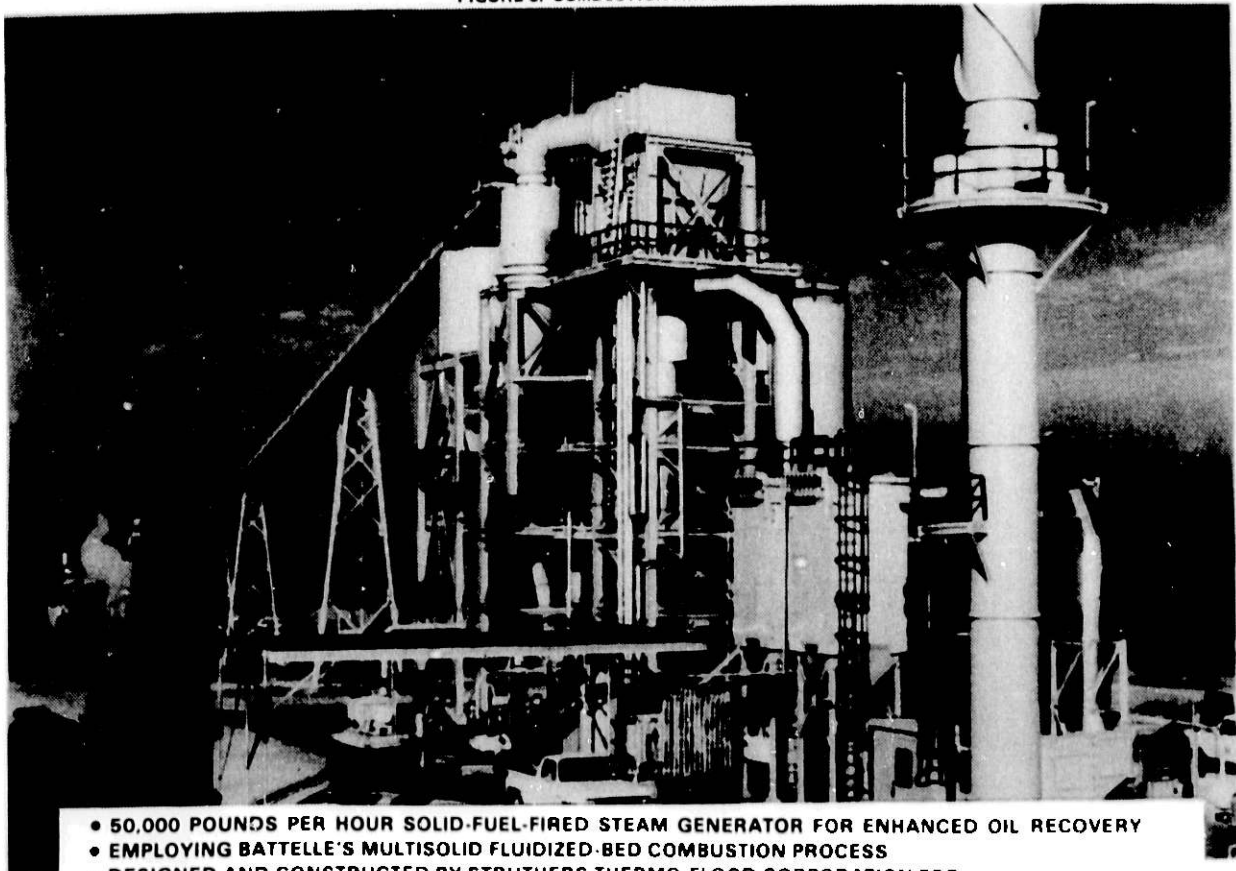


FIGURE 5. COMBUSTION AIR CONTROL



- 50,000 POUNDS PER HOUR SOLID-FUEL-FIRED STEAM GENERATOR FOR ENHANCED OIL RECOVERY
- EMPLOYING BATTELLE'S MULTISOLID FLUIDIZED-BED COMBUSTION PROCESS
- DESIGNED AND CONSTRUCTED BY STRUTHERS THERMO-FLOOD CORPORATION FOR CONOCO INC., NORTH AMERICAN PRODUCTION OPERATIONS

FIGURE 6. MSFBC-50

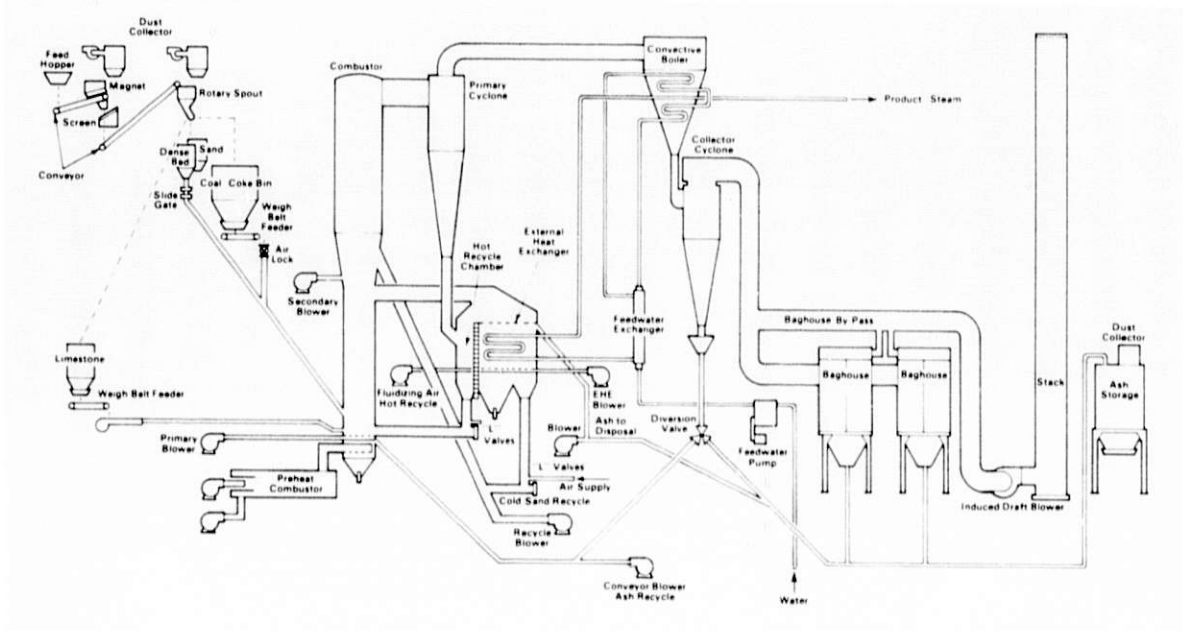


FIGURE 7. STRUTHERS THERMO-FLOOD CORP MULTISOLID FLUIDIZED-BED COMBUSTION STEAM GENERATOR

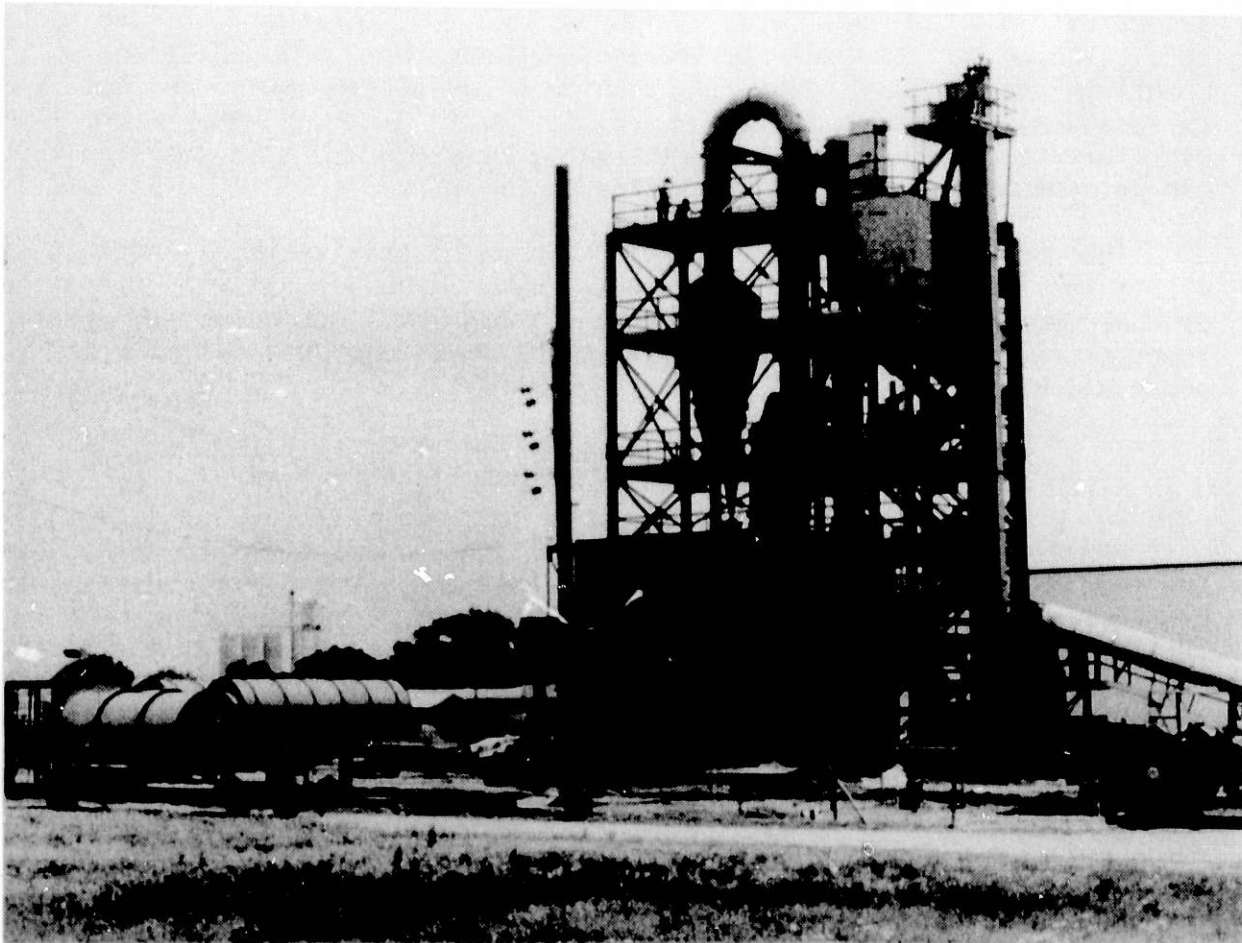


FIGURE 8. MSFBC-5

CONTROL SYSTEM REQUIREMENTS FOR THE 20 MW EPRI/TVA  
FLUID BED DEMONSTRATION UNIT

Ronald R. Dixon  
Babcock & Wilcox Company  
Lynchburg Research Center  
P. O. Box 239  
Lynchburg, Virginia 24505

Don J. Dziubakowski  
Bailey Controls Company  
29801 Euclid Avenue  
Wickliffe, Ohio 44092

Introduction

The information presented in this paper is the results of a preliminary review of process requirements for the TVA 20-MW AFBC pilot plant. Many of the pilot plant control requirements are based on experience with conventional boilers, test results of a smaller experimental unit at B&W's Alliance Research Center, or on a theoretical understanding of process dynamics. These will be under investigation during the coming year of testing at the pilot plant and therefore are not firm at this point. The objective of the preliminary review was to provide a fundamental understanding of control requirements before they were obscured by the inability to measure some of the key variables, such as hot spot temperatures. This is discussed in more depth later. These basic level requirements provide a means of developing an analytical cost function which can be used to evaluate control system performance.

The scope of interest here is limited to multivariable interactions within the boiler during on-line operations. Therefore, startup operations or the many single variable control loops such as component bearing temperatures, damper and valve positioners, and condenser controls are not addressed here.

Plant Description

The 20 MW pilot plant is designed to test various means of controlling the process. Consequently it contains some mechanisms for maneuvering and controlling the process that would not necessarily be available in a full scale plant. Figure 1 shows the steam and gas flow circuits in the boiler. The feedwater enters the economizer at approximately 530° F from a condensate storage tank. The economizer steam path is divided into three cascaded sections. Depending on the particular configuration being investigated, dampers will allow gas flow over one, two, or all three sections.

The feedwater is then fed to a conventional design drum. Forced circulation is used in the boiling region (A) to assure minimum flow is met under all test conditions. Saturated steam from the drum is input to a primary superheater in the convection pass which is also divided into three

cascaded sections. The primary superheater is followed by two banks of in-bed secondary superheat surface. Between the two banks is a desuperheater which is used to control steam temperature. Desuperheat spray is drawn off the feedwater line.

The combustion region is divided into five beds. The startup bed (F) does not contain any in-bed heat transfer surface and is located at the front of the furnace. The boiling region and superheat regions are each divided into two beds. There are no physical dividers in the furnace region thereby making distinct bed boundaries obscure. However, each region is separately controlled by a divided secondary air windbox under the distributor plate. The start up ducting is unique in that it includes a duct burner which is capable of raising the start up air temperature above 1000° F. A secondary superheater bypass is also provided for startup and additional control if necessary to achieve superheat temperature.

The coal and limestone feed system is set up for either overbed or underbed feed. Figure 2 was extracted from an EPRI report prepared by Jaycor which shows the pilot plant equipment arrangement. The overbed feed is achieved via conventional coal spreaders and a separate limestone feed system. The under-bed feed system mixes the limestone and coal at the gravimetric feeders and transports the mixture up through the distributor plate pneumatically.

#### Control Variables

The primary control variables for normal operation are listed below:

- Feedwater flow
- Steam flow
- Desuperheat spray
- Air flow to each bed
- Limestone feed rate
- Coal feed rate
- Recycle feed rate

In addition, a bed material removal conveyor is provided which can be used to control bed height. However, this is very slow and is not a normal control mechanism. The use of bypass flow is also not considered a normal control mechanism except during start up.

#### Key Instrumentation

There are many similarities between fluid bed boilers and conventional boilers and, consequently, much of the instrumentation is conventional. Main steam conditions and auxiliaries are all monitored and controlled as in other type units. Two variables unique to fluid bed control operation is the bed temperature and bed height. Both are measured by using conventional thermocouples and static pressure instrumentation, but the ultimate value is determined from several measurements and the mode of operation.



Each of the four bed regions have three thermocouples monitoring bed temperature. When all four beds are fully operating, each bed temperature is determined by a simple averaging of the three measurements and an overall bed temperature is derived from these averaged temperatures. When one or more beds are slumped (shut down), the slumped beds cause a bias on the thermocouple in that region. In this mode, the affected thermocouple readings are removed from the averaging calculation. This is particularly useful when operating on the overbed feed system where half a bed can be slumped independently. Since bed temperature is kept between 1450° F and 1650° F, standard thermocouples are employed.

Bed level is defined as the break point of the static pressure profile along the gas flow path. The static pressure is greatest at the distributor plate and changes almost linearly with distance above the plate up to the top of the bed. At the top of the bed, the slope of the pressure change with distance changes markedly because of the large difference between bed density and flue gas density. Hence, bed height can be determined using many static pressure taps. In practice, bed height is determined using three pressure measurements and one temperature measurement.

Limestone and recycle feed are also key control variables. However, measurement of these flow rates are made the same way as coal flow rate using gravimetric feeders. Hence the accuracy of these measurements are equally as poor as the coal flow measurement.

### Control System Requirements

#### Definition

The phrase 'control system requirements' is so general, and so widely used it is necessary to define the phrase in context. 'Control system requirements' is used herein to describe the collection of desired process conditions and hard operational constraints derived from a fundamental understanding of the process and its mechanical limitations. Control system requirements are expressed in terms of measurable process variables such as temperatures, pressures, and flows. Requirements are not 'specifications' and do not dictate a control strategy, configuration, or hardware.

All control requirements descend from five basic sources:

- I. Physical process constraints
- II. Economic operating conditions
- III. Regulatory requirements
- IV. Operating objectives
- V. Company policies and practices

Company policies and practices include specific hardware arrangements, modes of operation, and performance objectives. Since these are imposed on the first three basic requirements, and are peculiar to each utility, they will not be considered here.

By establishing the link between these requirements and the control system requirements, a control strategy can be developed placing appropriate weight on each requirement as interactions and compromises arise. Developing a control system design from pre-ordained control requirements obscures the purpose of each requirement and frequently results in excess emphasis on relatively soft or flexible constraints. To assist in establishing the correct emphasis, each requirement is classified as either a 'hard' (component failure will result if violated) requirement or a 'soft' requirement (only temporary degradation of performance will result).

### Physical Process Limitations

Physical process limitations are derived from the failure mechanisms of the process design. In the general case, failure mechanisms are as listed below:

1. Fracture
2. Creep rupture
3. Oxidation/corrosion
4. Erosion
6. Frictional wear

### Metal Temperatures

Design limits are established by ASME pressure vessel codes, operating experience, and laboratory experiments. For the pilot plant, oxidation and rupture are the two major concerns that set physical limits. To determine the numerical value of these limits, upset flow conditions are assumed along with maximum expected calculational errors of temperature and heat transfer coefficient. These upset values are then used to calculate the most severe conditions the material will undergo. Once these values are determined, the tube materials and dimensions can be calculated.

This type calculation is performed for each heater bank, header, and support member. From this large set of numbers, limits are determined based on 'weakest link' values.

The design temperature limits are based on a design pressure. For the pilot plant, the design pressure is 2700 psi. Since the operating pressure is expected to be about 2400 psi at the throttle, the temperature limits have an added margin under most conditions. However, despite the added margin, unit alarm limits are based on the calculated values. Consequently, these must be regarded as hard limits for control system performance. Most often, however, these limits are much higher than other control requirements and will not be challenged.

Besides steam/water pressure parts, the furnace/air duct limits are calculated in a similar manner. Since the pilot plant has both FD and ID fans, positive and negative limits are required to avoid buckling or implosion.

### Steam Separators

A second type of physical limitation is imposed by the steam separator cyclones in the drum. If drum level rises above the separators, the possibility of wet steam carryover is increased. This could lead to high heat fluxes downstream in tubes that were not designed for metal to liquid heat transfer. The result would be high risk tube failure.

Wet steam carryover is a condition that can exist for a short time and to a minor degree without serious damage. However, as the level increases further, the potential for damage is increased. This can be considered a soft limit and, consequently, the pilot plant will allow a high drum level for 20 seconds before tripping the unit. The 20 second delay also reflects the uncertainty of level conditions due to shrink and swell.

A low drum water inventory will ultimately lead to uneven flow in waterwall tubes and tube rupture. Again, the condition (low level) can exist for a short time without severe damage. Hence, the unit trip occurs only after the level has been low for 20 seconds. Again, shrink and swell effects cause some uncertainty in the level measurement which is somewhat accommodated by the 20 second delay.

### Turbine Requirements

Although the pilot plant does not have a turbine, full scale plants will. Therefore, it is necessary to demonstrate that turbine demands on main steam conditions can be met. This reduces to the requirement to avoid wet steam and avoid temperature transients. Wet steam will erode turbine components while temperature transients cause rotor stresses due to thermal expansion and contraction. Since the turbine typically employs its own protection system which will trip the unit under severe deviations, this is both a soft and hard constraint. These limits are typically the most demanding and provide the primary control system requirements.

### Economic Operating Conditions

The two major controllable factors that affect the operating economics of the AFBC pilot plant are the combustion efficiency and heat transfer efficiency. For both factors, the design objective is to maximize the efficiency. Clearly this is a soft limit and can be violated substantially during upset conditions. However, it is not definitive and must be redefined in terms of measurable variables to be stated as control requirements.

Heat transfer is maximized simply by keeping all the in-bed heating surface within the bed. This means bed height control. The heat transfer coefficients within the bed are an order of magnitude larger than the convection pass heat transfer. Therefore, the in-bed surfaces should be used to capture as much heat as possible within other limits.

Combustion efficiency is measured in terms of the amount of original combustible material consumed. Because the pilot plant uses a recycle feed, the combustion efficiency is strongly determined by the recycle rate. Increasing recycle increases combustion efficiency. To be competitive with

PC units, combustion efficiencies have to be near 99%. The pilot plant testing will determine if this is practical to achieve.

#### Regulatory Requirements

The two major regulatory agencies influencing conventional boiler operation is the NFPA and EPA. However, the role of NFPA is unclear to this author at this time since their regulations apply to PC units while the pilot plant is a crushed coal unit. Furthermore, NFPA has not addressed fluid bed standards due to higher priorities.

On the other hand, one of the major advantages of the AFBC is its ability to reduce  $SO_2$  emissions without additional flue gas cleaning. The EPA requirement is expressed as 90% of original fuel sulphur content must be removed from the flue gas. Depending on local enforcement and penalties, this may be regarded as a hard or soft limit. Sulphur capture is affected by several variables: bed temperature, gas velocity, recycle rate, and limestone to sulphur ratio. It has been determined experimentally that for given Ca/S ratios and coal/recycle ratio, a bed temperature of  $1550^\circ$  provides optimum sulphur capture. Hence, the EPA requirement converts to control requirements of bed temperature, Ca/S ratio, and coal/recycle ratio. The optimum values will be determined experimentally.

#### Operating Objectives

Operating objectives are most easily expressed in terms of desired load swing capability. Base loaded plants have no significant swing requirements while peaking units have severe swing requirements. Since the pilot plant does not produce electricity, it has no load swing requirements. However, testing is planned to determine its load swing capability which will provide the basis for swing requirements on future units.

#### Requirements Summary

The requirements discussed above are summarized in Table 1. A control system design should address and attempt to satisfy each requirement, but it is important to notice that conflicts will occur. For example, if load is changed by changing bed temperature, this will conflict with the optimum bed temperature for sulphur removal. Changing bed temperature will also change superheater absorption and upset steam temperature. Hence, the individual control requirements must be compromised to achieve the best total system performance possible. By understanding the source of the control requirements, each requirement can be properly weighted. This collection of weighted control requirements becomes the basis for measuring the performance of alternative control system designs. As testing on the pilot plant progresses, the interaction between process variables will be quantified. This will lead to a better understanding of the controllability of the AFBC process and a better dynamic performance from commercial full scale plant.

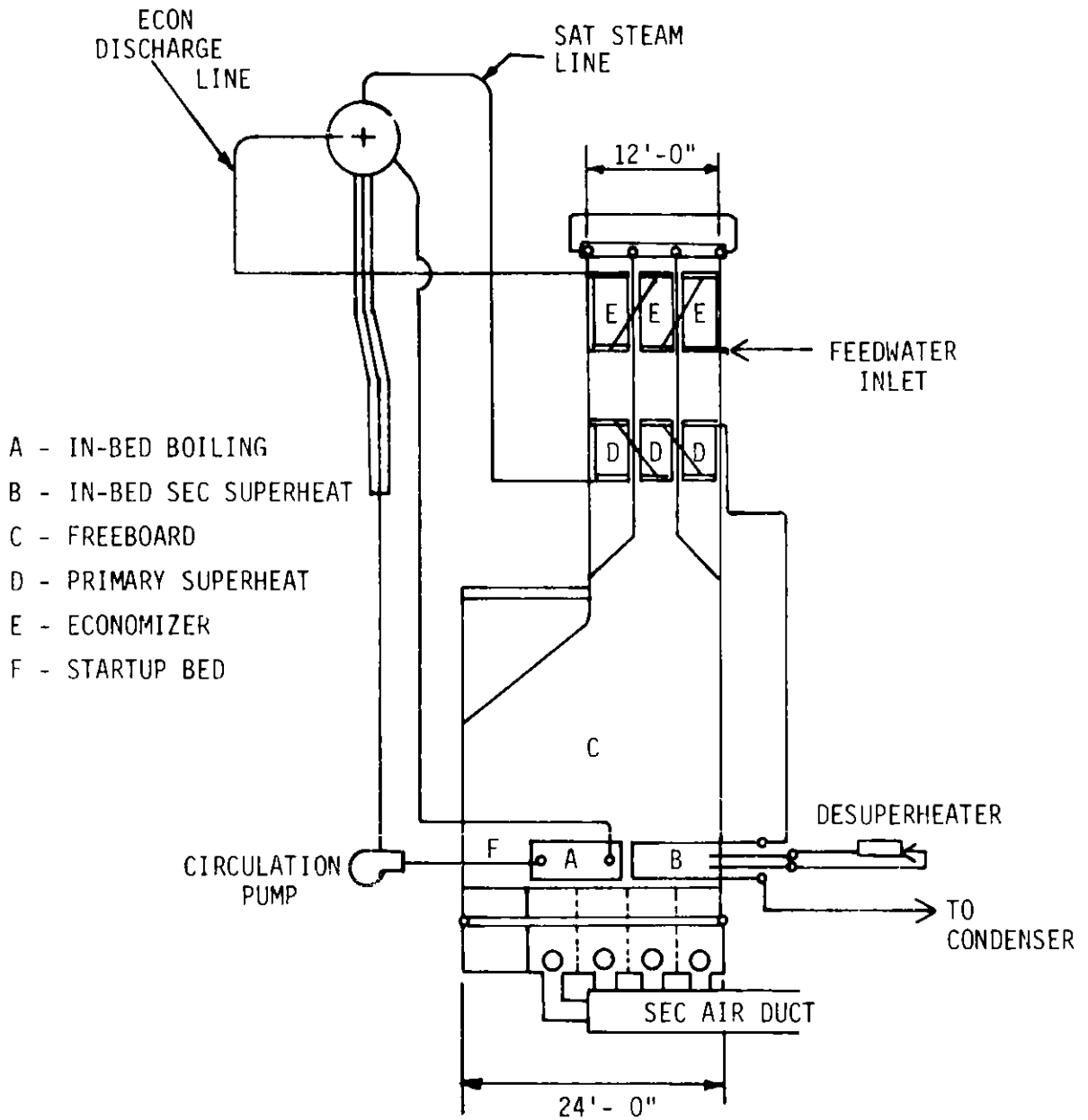
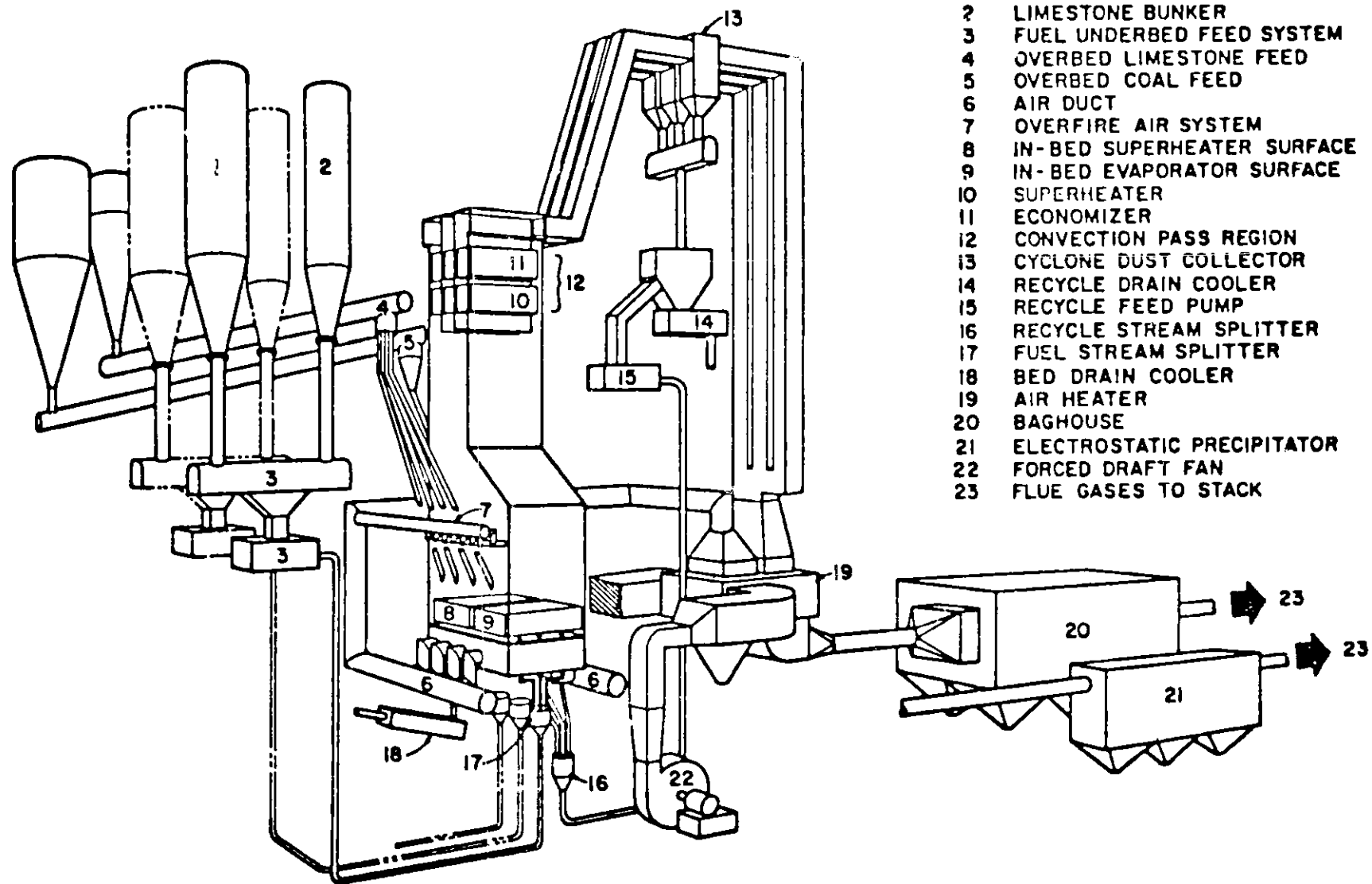




Figure 1. TVA Pilot Plant Boiler Schematic



- 1 COAL BUNKER
- 2 LIMESTONE BUNKER
- 3 FUEL UNDERBED FEED SYSTEM
- 4 OVERBED LIMESTONE FEED
- 5 OVERBED COAL FEED
- 6 AIR DUCT
- 7 OVERFIRE AIR SYSTEM
- 8 IN-BED SUPERHEATER SURFACE
- 9 IN-BED EVAPORATOR SURFACE
- 10 SUPERHEATER
- 11 ECONOMIZER
- 12 CONVECTION PASS REGION
- 13 CYCLONE DUST COLLECTOR
- 14 RECYCLE DRAIN COOLER
- 15 RECYCLE FEED PUMP
- 16 RECYCLE STREAM SPLITTER
- 17 FUEL STREAM SPLITTER
- 18 BED DRAIN COOLER
- 19 AIR HEATER
- 20 BAGHOUSE
- 21 ELECTROSTATIC PRECIPITATOR
- 22 FORCED DRAFT FAN
- 23 FLUE GASES TO STACK

Figure 2. Pilot Plant Arrangement

TABLE 1  
REQUIREMENTS SUMMARY

<u>Process Constraints/Requirements</u>	<u>Numerical Value</u>		<u>Control System Requirements</u>
	Lower Limit	Upper Limit	
<b>I. PHYSICAL PROCESS CONSTRAINTS</b>			
a) Metal Temperatures			
● 1st SSH Inlet Header	-	Vary depending on configuration 	Steam Temperature Alarm Limits 
● 2nd SSH Inlet Header	-		
● 1st SSH Outlet Header	-		
● 2nd SSH Outlet Header	-		
● Boiling Inlet/Outlet Headers	-		
● In Bed Tubing	-		
● Economizer Headers	-		
● Primary SH Inlet Header	-		
● Primary SH Outlet Header	-		
● Primary SH Tubes	-		
● Economizer Tubes	-		
b) Steam Pressure	H 2700		Steam Pressure Trip Limit 2700 psi

c) Furnace Pressure/Draft	-7" H <sub>2</sub> O 10" H <sub>2</sub> O (> 2 second duration)	Trip Unit at Specified Values
d) Drum Water Inventory	-7" +7" (> 20 second duration)	Trip Unit at Specified Values
e) Turbine		Trip at Turbine Controller Set Points
● Erosion	Pressure 2400 psi	Avoid Wet Steam
● Rotor Stress	Steam Temperature = 1003°	Avoid Temperature Transients
<b>II. ECONOMICS</b>		
a) Combustion Efficiency	Maximize (> 99%)	Maintain Recycle Rate/Coal Flow = 1.5
b) Heat Transfer Efficiency	Maximize	Keep Bed Height Above In-Bed Heating Surface (4 ft)
<b>III. REGULATORY REQUIREMENTS</b>		
a) NFPA Codes	?	?
b) EPA	90% of Original Fuel Sulphur Content	Bed Temperature at 1550° Ca/S Ratio Control Recycle/Coal Ratio Control
<b>IV. OPERATING OBJECTIVES</b>		
● Load Swing	To Be Determined	<ul style="list-style-type: none"> <li>● Bed Temperature Control Between 1450-1650 (Firing Rate Control - Coal, Air, Limestone, Recycle)</li> <li>● Bed Slumping</li> <li>● Bed Height Control</li> </ul>



HYDROGEOLOGIC TESTING OF THE E.J. KUBAT BOREHOLE,  
SAN JUAN COUNTY, UTAH:  
UTILIZATION OF A HIGH PRESSURE INSTRUMENTED FLOW CONTROL SYSTEM

David F. Hoexter  
Woodward-Clyde Consultants  
3 Embarcadero Center  
San Francisco, CA 94111  
(415) 956-7070

Abstract

Hydrogeologic injection tests were performed on a borehole in southeastern Utah to determine the potentiometric level and permeability of the Leadville Limestone. An injection pump system was specifically designed for the tests. Designed to rigid specifications, it performed well, with only minor problems. Calculated permeability values from five tests were remarkably consistent, varying from 21 to 37 millidarcies (md), with three tests from 26 to 28 md.

Introduction

The E.J. Kubat borehole, located in San Juan County, Utah, in the SW 1/4, Section 23, T37S, R19E, was drilled in 1958 as a petroleum exploration (wildcat) well (Figure 1). Drilling records and geophysical logs were examined as a part of the Paradox Basin Project, a feasibility and siting study for a high-level nuclear waste repository to be located in bedded salt deposits in the Utah portion of the Paradox Basin. This project is part of the Department of Energy National Waste Terminal Storage Program, and is being conducted by Woodward-Clyde Consultants under subcontract to Battelle Memorial Institute, Office of Nuclear Waste Isolation.

The geophysical logs of the Kubat and nearby wells showed that salt cycles potentially suitable as a possible repository horizon existed within the Pennsylvanian-age Paradox Formation in the area. Thus, it was decided to re-enter the well and extend it deeper into the Mississippian Leadville Limestone, the major water-bearing formation underlying the repository horizon.

A series of hydrogeologic tests was conducted to evaluate hydrogeologic properties of the Leadville Limestone. These tests provided data on potentiometric level, transmissivity and permeability of the test interval. Although testing of relatively highly permeable formations is common, obtaining reliable data from formations of low permeability is more difficult, and is a special aspect of the Paradox Basin Project.

Injection Pump System

An injection pump system, intended to test relatively impermeable, deep-lying formations, was designed by project personnel and built by Sierra Pump Systems, Incline Village, Nevada, to specifications set by Woodward-Clyde Consultants. The major requirements of the system were to operate at

injection pressures ranging from 0 to 1,000 psi, and to generate flows of from 0.1 to 15 gpm. The system was to inject fluid at variable, decreasing, low rates, while maintaining constant, high pressure ( $\pm$  0.5 percent linear full scale) for a test duration of up to 24 hours, in order to test low-permeability formations. It was also to maintain a constant pump rate ( $\pm$  5 percent of actual reading) at a variable, increasing pressure of from 0.0 to 1,000 psi for 24 hours, in order to test higher permeability formations. Precise flow rate and pressure control, and the virtual absence of pulsations, were necessary in order to provide reliable data, where even small variations in flow or pressure could mask the anticipated low permeability of the test interval. Additional requirements were that the system be portable and skid mounted and no larger than 4 x 10 feet, and that it be capable of pumping a brine injectate fluid of up to 300,000 ppm salt. A discussion of how this was accomplished can be found in a companion paper by Robert G. Reeves, "A High Pressure Instrumented Flow Control System for Hydrogeologic Injection Testing."

Because of long lead times for delivery of several components, construction of the pump system took approximately six weeks to complete. Because of the delays in delivery of some components and of time constraints in the field schedule, the final stipulated acceptance test was delayed until after the Kubat testing. Had this delay not occurred, minor operational problems would have been discovered prior to utilization in the field.

#### Borehole Completion

The Kubat borehole (Figure 2) was completed as an 8-3/4 inch open hole. A 2-7/8 inch tubing string was hung to 3,400 feet below kelly bushing (KB), and the test interval was capped by two inflatable packers. The test interval ranged from 3,358 to 3,575 feet KB. Formation pressures during testing were monitored by a downhole quartz crystal transducer, and conducted to a computer system at the surface by an armored cable. A shut-in valve within the tubing string controlled flow to the test interval.

#### Testing

##### Calibration and Set-Up

All instruments used during testing on the Paradox Basin Project must be precisely calibrated prior to their utilization. The rate meter was calibrated to read flow to an accuracy and resolution of 0.01 gpm; the pressure transducer had an accuracy of 2.5 psi full scale and a resolution of 0.01 psi. The computer system, capable of recording temperature and pressure data at a rate of up to 60 readings per minute, was set up on site.

##### Testing

A series of hydrogeologic tests (Figure 3) was run on the Kubat borehole during September, 1981. A static formation pressure was initially held for approximately 82 minutes, and was utilized to calculate the potentiometric level. A slug test was performed, in which the tubing was filled with the downhole shut-in valve closed, and the fluid was then

released to flow by gravity to the formation. Following this test, a constant rate injection test was initiated. After 183 minutes, however, one of the two pumps failed, causing a reduction in flow from 15 to 12 gpm. After a total of 793 minutes, pumping was discontinued, and recovery (pressure fall-off) began.

Later tests included two additional slug tests, a short-term (three minute) injection test followed by closing the shut-in valve, and an additional constant rate injection/pressure fall-off test. No constant pressure tests were run because of the relatively high permeability of the test interval.

### Test Results

An example of a data plot is shown on Figure 4, Injection Test No. 2. The pressure-time data yielded four slopes. The first two slopes, from 0-1 and 1-10 minutes, are indicative of well-bore storage and "skin", or damage, effects. The third slope, from 10 to 230 minutes, is representative of the test interval. The fourth slope, from 230 to the end of injection, is steeper, and is indicative of an apparent decrease in permeability. The reason for this decrease is unknown; it could result from facies change, decrease in the frequency of fractures away from the well bore, fault gouge, or juxtaposition of less permeable beds distant from the well bore against relatively more permeable beds near the well bore, by faulting. Other tests also indicate this apparent "barrier".

The results of the five tests analyzed are shown in the following table. They are remarkably uniform.

Test	Permeability				Comments
	gpd/ft <sup>2</sup>	ft/dy	md	m/dy	
1. Injection #1	0.6	0.1	27	0.02	15 gpm*
2. Short-Term Injection with Shut-In	0.8	0.1	37	0.03	3 minute flow
3. Injection #2	0.6	0.1	28	0.02	8 gpm; most representative test
4. Recovery #2	0.5	0.1	26	0.02	
5. Slug #3	0.4	0.1	21	0.02	Storage coefficient = $7.3 \times 10^{-4}$

\*gpm = gallons per minute

The range of the three longer duration tests (1, 3, 4) is within less than 2 md, and results in an average permeability of 27 md.

### Pump System Performance Summary

During utilization at the Kubat well and the acceptance test, two problems were encountered. While testing, one of the two parallel air-driven pumps failed. One pump was utilized for the duration of testing. It was later determined that the cause of failure was a faulty stem on the high

flow air valve assembly. Modification of the stem solved the problem. The second problem occurred during the acceptance test, conducted in Oakland, California. At high pump outputs, the pump exhaust air was as much as 50°C colder than entering air. During continuous duty the exhaust mufflers froze, necessitating removal and thawing. This problem had not occurred in relatively arid Utah during the Kubat testing. Injection of a small amount of alcohol downstream from the water filters would probably alleviate this problem.

With the exception of these two occurrences, caused by equipment malfunctions, the pump system performed completely to specifications. Additional minor "problems" include a significant amount of pump vibration, requiring considerable bracing of piping, and a high system noise level.

The pump system will again be utilized during Summer, 1982. At this time, variable rate, constant pressure tests, and tests similar to those conducted on the Kubat well are planned for another borehole drilled as part of the Paradox Basin Project.

#### Conclusions

Despite minor initial malfunctions, the pump system performed to specifications. The importance of a back-up pump and the usefulness of a compliance test were demonstrated. The pump system is a valuable, versatile tool for hydrogeologic investigations of relatively low permeability, deep formations, in which flow and injection rates must be maintained within narrow limits. The test results were accurate and remarkably uniform.

#### Acknowledgements

I wish to thank the following individuals for their advice and assistance in preparing this paper. J. Blum, C. Levine, R. Reeves and J. Thackston reviewed the text, which was edited by V. Chernock. O. DeLeon and E. Grace drafted the figures; C. Droge typed the manuscript. The hydrogeologic testing was carried out under the direction of T. Grant and F. Conwell, the assistant project manager and project manager, respectively, of the Paradox Basin Project, and J. Thackston, hydrogeology activity leader.

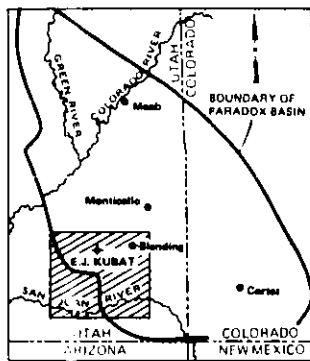
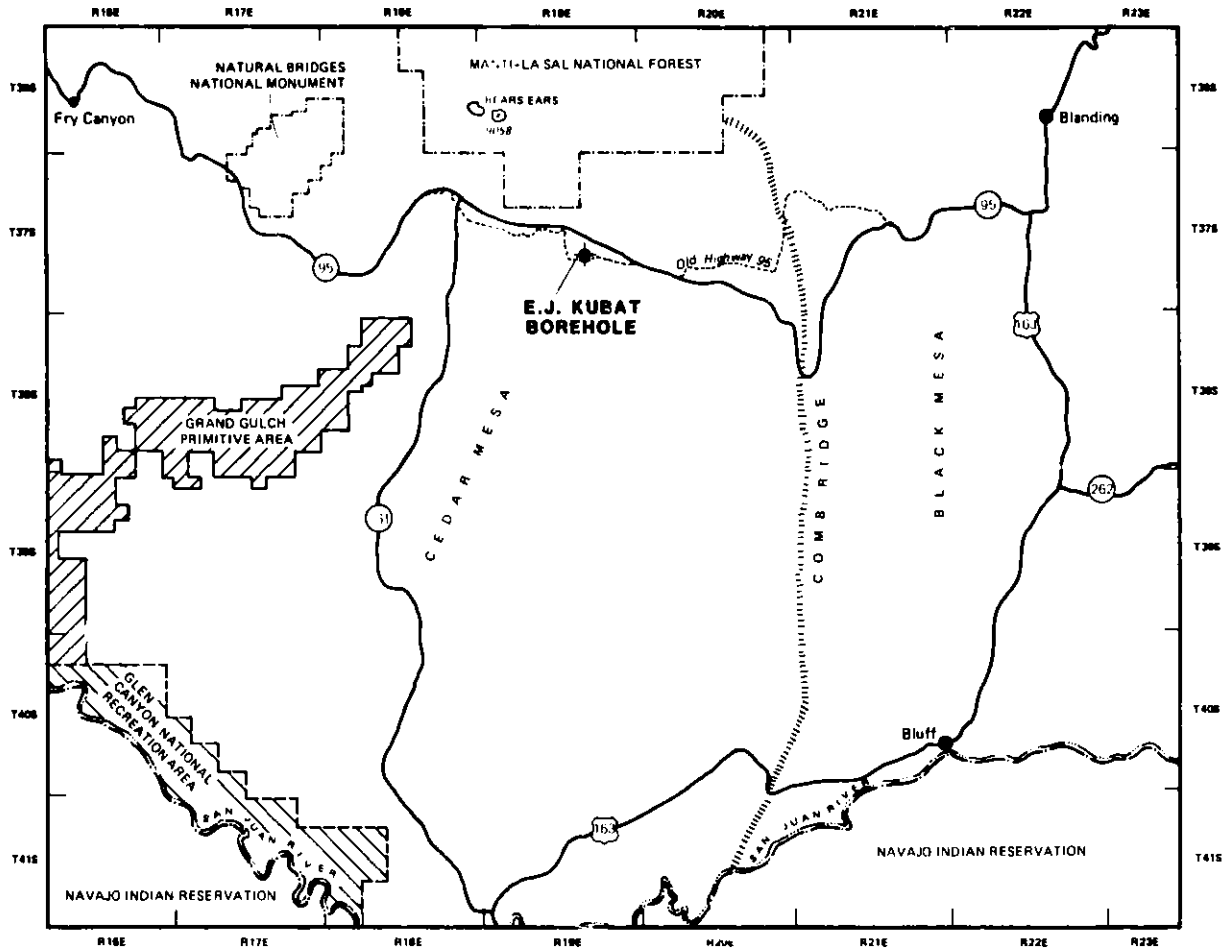
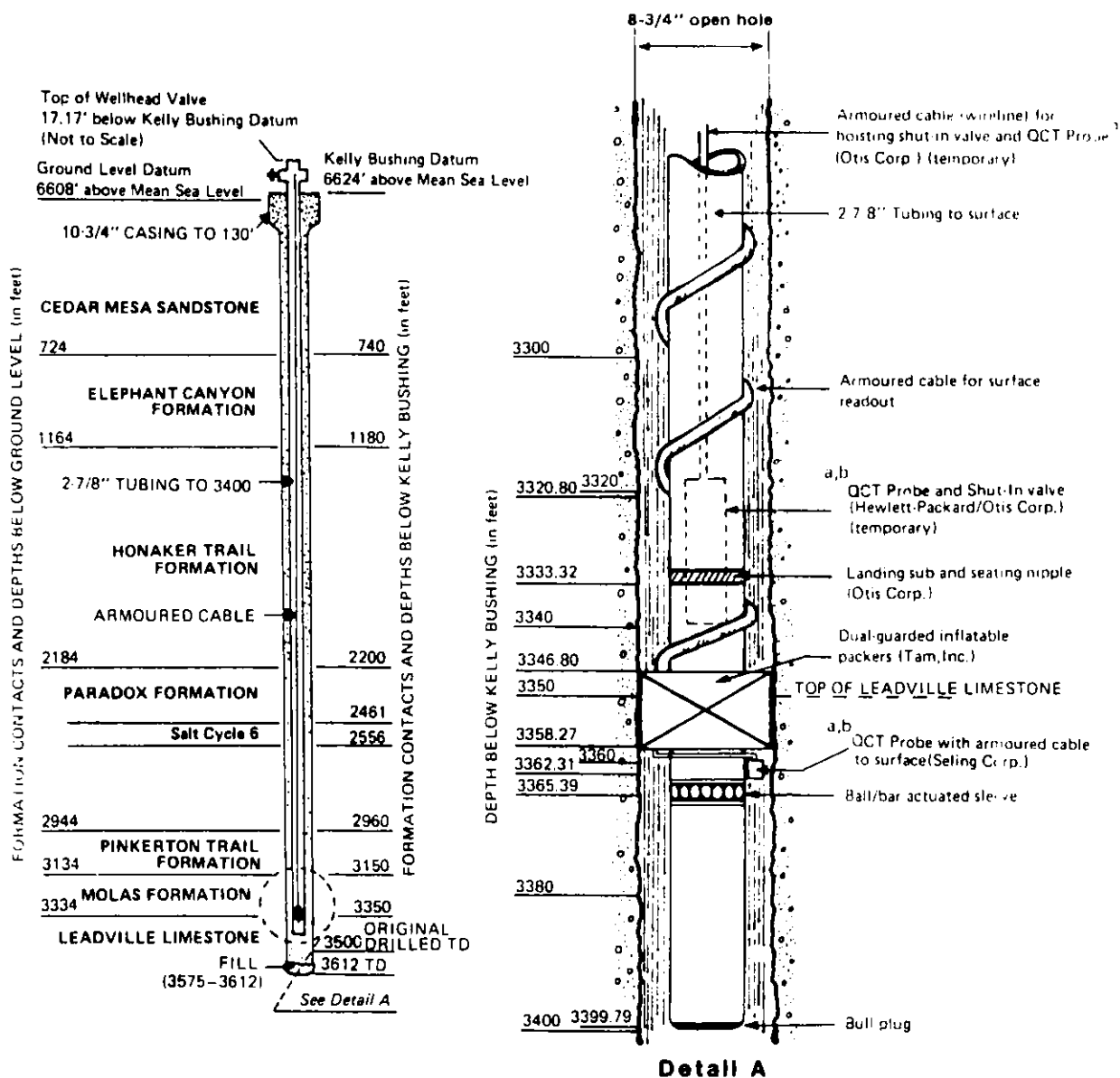


FIGURE 1 – LOCATION MAP, E. J. KUBAT BOREHOLE



- a OQT—quartz crystal transducer
- b Hewlett-Packard OQT, Otis wireline and shut-in valve temporarily installed for hydrogeologic testing; Seling OQT and armoured cable permanently installed on tubing

FIGURE 2 — BOREHOLE COMPLETION DIAGRAM E. J. KUBAT BOREHOLE

FIGURE 3 - PRESSURE-TIME HISTORY, E. J. KUBAT TEST SERIES

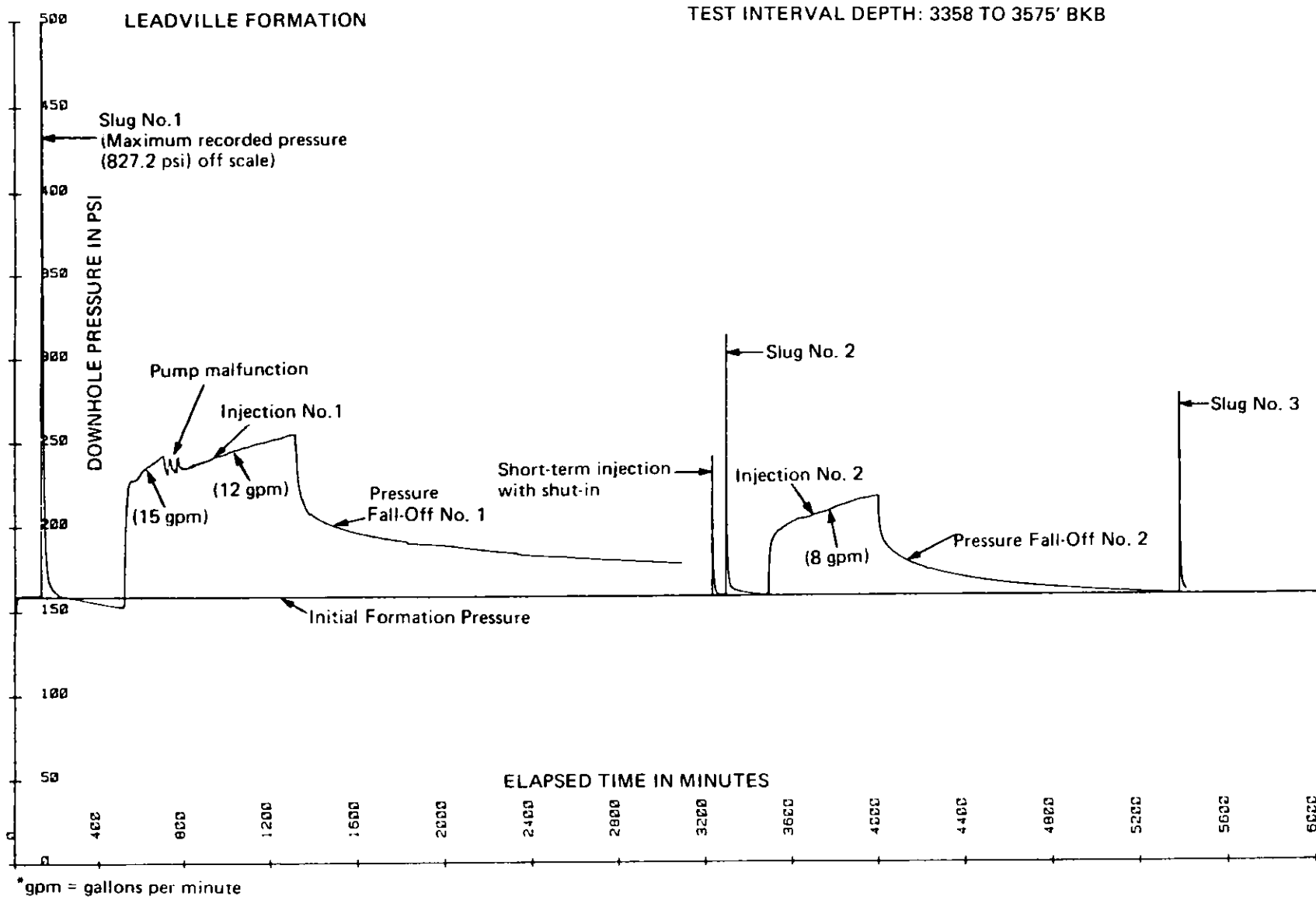
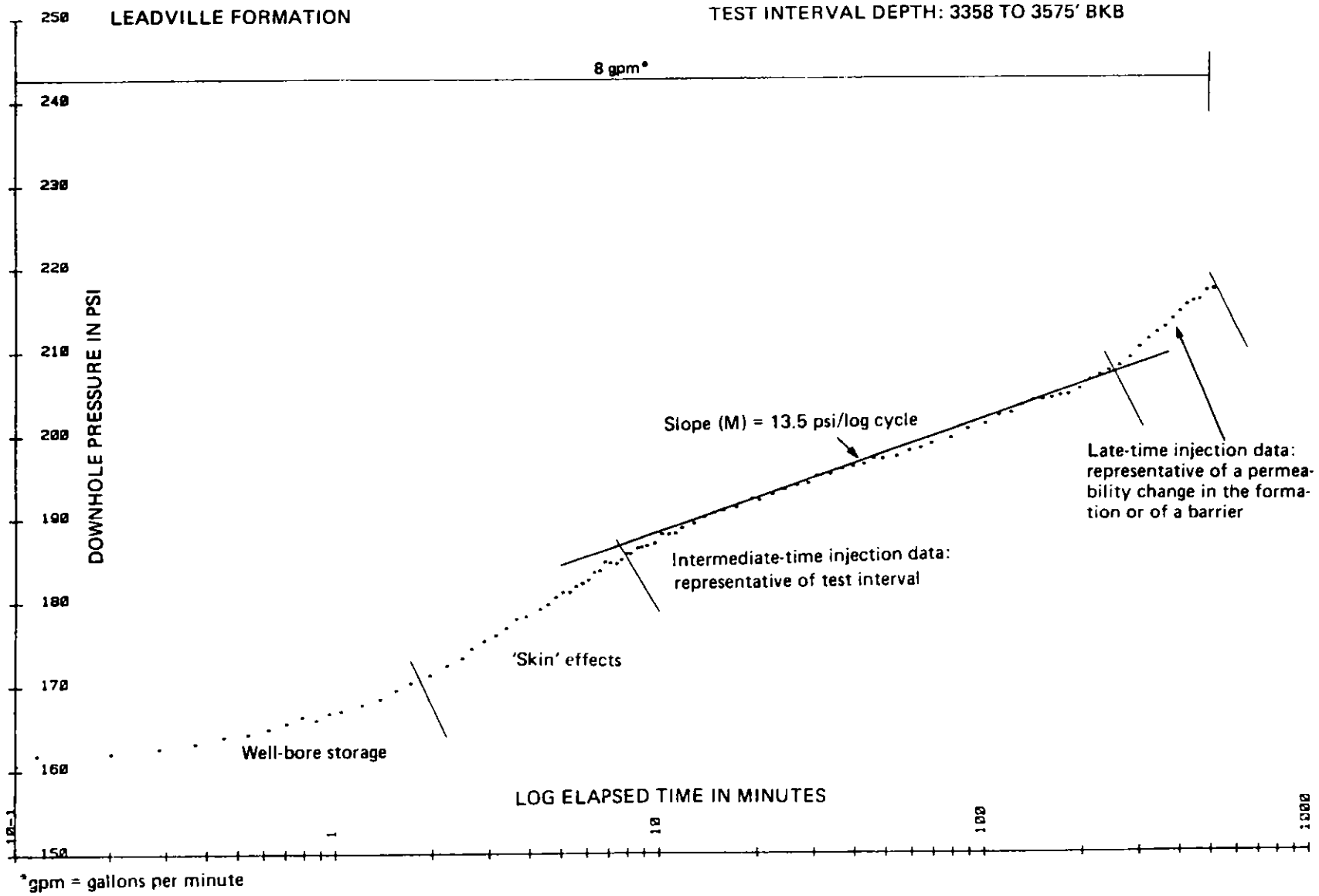


FIGURE 4 - INJECTION TEST NO. 2, E. J. KUBAT TEST SERIES





CHARACTERIZATION OF AEROSOLS IN LOW-BTU PRODUCT GAS  
AND COMBUSTION PROCESS STREAMS

Rodney J. Anderson, John J. Kovach,  
Ulrich Grimm, and Jesse O. Mapstone, Jr.  
Morgantown Energy Technology Center  
P.O. Box 880  
Morgantown, WV 26505  
304/291-4709

Summary

This report summarizes the results of the study of the aerosols generated during the combustion of a cleaned low-Btu gas. The gas was produced in the METC 42-inch, stirred fixed-bed gasifier then cleaned in the full-flow cleanup system. The clean, low-Btu gas was combusted in a large refractory-lined 6 million Btu/hr combustor and in a small stainless steel, Meker-type laboratory burner.

Reported data was obtained from Run No. 98 of the gasifier. Run No. 98 differed from the previous runs in two significant aspects: (1) the Holmes-Stretford sulfur cleanup system was not used, resulting in higher H<sub>2</sub>S levels in the producer gas, and (2) Pittsburgh seam high volatile A bituminous (HVAb) coal, which had been used in the gasifier, was replaced initially with a 3:2 (by weight) blend of Pittsburgh and anthracite coals and finally by Middle Kittanning, another HVAb coal, which was relatively low in sulfur.

Aerosol measurements were taken not only of the products of combustion (POC) from both burners, but also from the gas and air fed to the burners. Aerosol loadings of about 1 mg/m<sup>3</sup> were found in both the gas and the POC from the lab burner. These aerosol loadings were about an order of magnitude greater than that of the previous gasifier run. POC from the dynamic burner also showed an increase in mass loading. The higher mass loadings of both sources of POC aerosols were correlated to increased H<sub>2</sub>S concentrations in the clean producer gas. Higher aerosol loadings in the clean gas resulted from the presence of particles usually removed by the sulfur cleanup system.

Electrical Aerosol Analyzer (EAA) data showed that the geometric mean diameters of the lab burner aerosols were somewhat smaller than those of the gas. Large concentrations of small particles were found in the POC of both burners. Assuming unit aerosol density, integration of the particle size distributions measured in the POC of the small burner indicated mass loadings of between 3-10 mg/m<sup>3</sup>, about the same as that measured directly with filter samples. Chemical analysis of the filter samples showed the aerosols to consist primarily of sulfur oxides with some alkali and ferrous metals. No carbon was found on the POC filter samples, although graphitic carbon was detected on a plate from the Sierra impactor used to sample the dynamic burner POC.

Introduction

Low-Btu gas such as that produced by the gasification of coal is becoming increasingly important as an alternative to natural gas and petroleum products.

In order to better assess its potential application and limitations, studies are under way to characterize the POC of various qualities of low-Btu gas. One important aspect of low-Btu gas combustion is the possibility for generation of very fine aerosols that may pose a materials and environmental problem. This study was an attempt to address the measurement of these aerosols and to develop experimental techniques for their characterization.

### Experimental Procedures

The object of this study was to investigate aerosols detected in the POC of low-Btu gas obtained from the METC 42-inch stirred, fixed-bed gasifier and associated cleanup train.<sup>1</sup> The gasifier was operated on bituminous coal. Two separate combustors of the gas were studied: a 6 million Btu/hr combustor lined with refractory (dynamic facility)<sup>2</sup> and a small stainless steel laboratory burner. Both combustors were fueled with low-Btu gas (~175 Btu/scf) and were maintained with a sufficiently large air/fuel ratio (~2/1) to provide excess oxygen. The temperature in the combustion chamber of the dynamic facility was fixed at about 1400°C while the temperature of the small burner was not specifically controlled (but was maintained at a constant level by a fixed air/fuel ratio).

Daily averages of the major gas components of the clean producer gas as measured by on-line gas chromatographs are presented in Table 1. These data indicated a relatively constant gas composition with low concentrations of H<sub>2</sub>S. About the only change in the gas analysis data from previous gasifier runs is the increase of up to one order of magnitude in the H<sub>2</sub>S concentration, a result of the absence of the Holmes-Stretford sulfur removal unit from the gas cleanup system.

The aerosol data consisted of filter samples (to determine mass loading and provide material for chemical analysis) and the determination of aerosol size distributions using a commercially available Electrical Aerosol Analyzer (EAA). A Model 260 Sierra impactor was used to complement the filter data from the POC from both burners. The higher temperature POC aerosol samples (approximately 110°C at the filter) were collected on spectro-grade glass fiber filters (Gelman No. 64878-47 mm) and on 1.2 and 5.0 μm pore size silver metal membrane filters (Selas No. FM47). Aerosol samples of the burner air and low-Btu gas were collected at room temperature on spectro-grade glass fiber filters (Gelman No. 64878-47 mm) and polyvinyl chloride-membrane filters (Gelman No. 64515-47 mm), as well as silver membrane filters. Sample interval, volumetric sample rate, and changes in filter weight provided measures of the aerosol loading in each location. These filter samples were stored for subsequent chemical analysis. The sample flow rates were measured with rotometers. Frequent monitoring and manual adjustments of the flow rates provided for a steady sample rate.

An illustration of the large burner facility and available sampling ports is presented in Figure 1. Specific sampling ports utilized for this series of samples were No. 4, POC-dynamic cell; No. 5, combustion air-dynamic cell; and No. 7, producer gas sampling port. As noted in Table 2, sample rates were typically about 60 scfh with the exception of the sample from the POC. In each sampling port, the necessary size stainless steel tubing to obtain near-isokinetic flows was inserted into the middle of the process stream pipe in the direction opposing the stream flow. The sample tubing was extended at

TABLE 1

Major Gas Analysis of Cleaned Producer Gas  
Average Volume Percent by On-Line Process GC

Date	H <sub>2</sub>	CO <sub>2</sub>	C <sub>2</sub> H <sub>6</sub>	H <sub>2</sub> S	O <sub>2</sub>	N <sub>2</sub>	CH <sub>4</sub>	CO
7/18/81	15.52	8.00	0.09	0.12	0.79	50.88	1.16	23.78
7/19/81	15.91	10.31	0.10	0.17	0.76	50.99	1.36	20.35
7/20/81	17.44	9.50	0.11	0.21	0.73	49.00	1.49	22.11
7/21/81	16.56	10.82	0.12	0.21	0.76	50.60	1.46	19.43
7/22/81	16.04	9.75	0.16	0.20	0.77	50.55	1.65	20.76
7/23/81	17.17	8.51	0.29	0.22	0.72	47.67	2.74	22.44
7/24/81	17.65	8.31	0.26	0.17	0.72	47.08	2.60	23.19
7/25/81	17.07	9.17	0.25	0.16	0.73	48.47	2.56	21.45
7/26/81	17.54	8.36	0.27	0.17	0.72	47.18	2.69	23.07
7/27/81	17.59	8.00	0.27	0.17	0.71	46.73	2.70	23.61
7/28/81	17.65	7.94	0.30	0.16	0.70	45.38	2.82	22.80
7/29/81	16.82	8.36	0.27	0.15	0.74	46.42	2.66	21.43
7/30/81	17.36	7.93	0.28	0.19	0.69	45.21	2.73	22.94
7/31/81	17.57	7.69	0.28	0.18	0.68	45.01	2.72	23.42
8/07/81	16.72	8.51	0.27	0.20	0.68	47.38	2.40	21.38
8/08/81	16.98	8.21	0.28	0.19	0.68	46.93	2.46	21.89
8/09/81	17.08	8.24	0.28	0.18	0.67	46.80	2.49	21.99
8/10/81	17.48	8.05	0.29	0.19	0.66	46.29	2.59	22.45
8/11/81	17.58	8.05	0.28	0.20	0.67	46.13	2.63	22.52
8/12/81	17.82	8.07	0.31	0.19	0.65	46.43	2.68	22.89
8/13/81	17.62	8.15	0.28	0.18	0.67	46.46	2.54	22.63
8/14/81	17.59	8.15	0.28	0.18	0.66	46.37	2.49	22.57
8/15/81	17.46	8.55	0.28	0.19	0.67	47.19	2.45	21.99
8/16/81	16.86	8.76	0.27	0.18	0.68	47.98	2.39	21.25
8/17/81	16.70	8.50	0.27	0.18	0.68	48.42	2.38	21.71
8/18/81	17.12	8.33	0.28	0.19	0.69	47.82	2.39	22.00
8/19/81	16.85	8.60	0.34	0.18	0.72	48.82	2.71	21.61

least 20 inches upstream of the process stream elbow through which it was inserted to penetrate to a relatively "plug flow" region of the stream. The sample flow rate was measured by a rotometer located downstream of the filter, between the filter and the vacuum pump (when necessary). The flow rate was monitored frequently to assure that the prescribed sample rate was maintained. It was not necessary to rigorously maintain isokinetic sampling conditions because of the absence of large particles ( $>1 \mu\text{m}$  diameter). The producer gas was sampled at the pressure used to feed the burner, 15 psig, and also after the pressure was reduced to ambient with 0.5 cfm critical orifice. Dual filters, in series, were used to sample the POC from the dynamic burner.

A schematic of the small laboratory burner used for these tests is presented in Figure 2. The burner was fabricated of 1 1/2-inch stainless steel pipe. During tests, the small burner was constantly fed low-Btu gas (from the same line as the dynamic facility) at a rate of 35 scfh. Aerosol-free sheath air was provided at a rate of 400 scfh to minimize flame turbulence and to prevent contamination of the flame zone with room air. The 6-inch I.D. stack surrounding the burner was extended 24 inches above the burner plate. Sampling for both filter samples and aerosol characterization devices were performed near the top and in the center of the extended stack.

Aerosol size distributions were primarily measured with an electrical aerosol analyzer (TSI Model 3030) over the range from 0.01 to 1  $\mu\text{m}$  diameter. Characterization of the burner air for the dynamic facility was performed by sampling directly from port No. 5. Since the EAA operated only near room temperature and pressure, characterization of the producer gas (available at 15 psig at the dynamic facility) and POC (high temperature and  $-40^\circ\text{C}$  dew point) required sample pretreatment prior to ingestion by the EAA. An atmospheric pressure sample of producer gas was obtained with a 0.5 cfm critical orifice. Immediately following the orifice, the gas sample stream was expanded into a 2-foot long section of 0.5-inch pipe where it was allowed to equilibrate. A fraction (4 lpm) of this total 0.5 cfm gas sample was used by the EAA to characterize producer gas aerosols. The remainder of the producer gas was exhausted to appropriate vents to eliminate the hazard of CO to personnel. Alternate filter samples collected upstream and downstream of the orifice yielded similar particle mass loading data, indicating that the orifice did not significantly modify the producer gas particles.

In order to prevent condensation of water vapor in POC samples for measurements of aerosol size distributions, the sample was diluted with warm ( $\sim 65^\circ\text{C}$ ) dry air as near the sampling location as possible. Dilution ratios of almost 3/1 by volume (aerosol-free, dry air plus sample/sample) were required to prevent condensation. The dilution technique was further utilized to reduce the aerosol concentration to measurable levels and to minimize aerosol coagulation in transit between the sample port and the EAA. Typical values of the dilution ratio necessary to prevent condensation and provide concentrations of POC aerosols within the operational range of the EAA were 15/1 for the small laboratory burner and 80/1 for the dynamic facility. The dilution probe used to establish the necessary dilution is shown in Figure 3. The necessary clean, dry air was provided by a cleanup system (Deltech-900 CFH), applied to available instrument air. The air was heated prior to dilution with a 5-foot long temperature-controlled tube (Technical Heaters Model No. 352-5-5). Dilution air flow was precisely controlled with an in-line mass flow controller (Tylan No. FC-260). Since the entire diluted sample was

ingested by the EAA, dilution ratios were determined by the difference between the fixed sample rate of the EAA (4 lpm) and the set flow of dilution air (1-4 lpm). Dilution ratios as high as 10/1 were accurate; however, dilution ratios approaching 100/1 were expected to have an uncertainty of about  $\pm 10$  percent. The diluted sample was transmitted to the EAA via a 6-foot length of 3/8-inch polyflow tubing.

### Results

Table 2 shows the aerosol data obtained from the filter samples. Separate sections of the table show the mass loadings obtained for the burner air, producer gas, and POC from both the lab burner and the dynamic combustor. Producer gas samples were taken in parallel: those labeled "full flow" were taken at the pressure (15 psig) used to feed the combustor; those labeled "orifice" were taken after the pressure was let down through a critical orifice. Also, filter samples from the dynamic burner were collected on serial filters to monitor for possible filter breakthrough. The dynamic POC tandem filters are labeled "front" for upstream samples and "back" for downstream. Filter holders and impactors were heated to about 300°F to minimize acid mist formation and condensation during characterization of POC aerosols.

Aerosol mass loadings of 10-20  $\mu\text{g}/\text{m}^3$  were typically found in the burner air while the producer gas showed loadings approaching 1  $\text{mg}/\text{m}^3$ , about an order of magnitude greater than those measured during previous gasifier runs which utilized the Holmes-Stretford sulfur removal system. Loadings exceeding 1  $\text{mg}/\text{m}^3$  were seen in the POC samples taken from both the lab burner and the dynamic combustor. The rather large increase in mass loading of the gas and POC can be attributed, at least in part, to the absence of the Holmes-Stretford sulfur cleanup unit during this gasifier run. The main effect of the removal of the Holmes-Stretford unit was to increase the  $\text{H}_2\text{S}$  in the fuel gas by up to an order of magnitude (Table 1). As will be discussed later, the primary constituent of the POC aerosols was sulfate, which was related to the sulfur ( $\text{H}_2\text{S}$ ) concentration in the combustion gas.

Aerosol size distributions and mass loadings of the POC from both burners were measured using a Model 260 Sierra impactor (Table 3). The impactor was attached to the POC sample port in place of the filter. Loadings were determined by the impactor to be about 170 and 2  $\text{mg}/\text{m}^3$  for the dynamic combustor and lab burner, respectively. These mass loadings were similar to those obtained using filters.

In support of EAA analyses, impactor data indicated a large portion of the aerosols were less than 1  $\mu\text{m}$  in diameter. The size and concentration data of the burner air, producer gas, and POC from the lab burner are shown in Table 4. Information on the ambient air is included for comparison. These aerosol data were obtained using an Electrical Aerosol Analyzer (EAA) over the size range<sub>3</sub> between 0.01 and 1.0  $\mu\text{m}$  diameter and smoothed using a numerical technique. Unfortunately, no EAA data could be obtained from the dynamic combustor POC due to the extreme fluctuations in concentration. Manual scans with the EAA indicated that the particles were about 1  $\mu\text{m}$  in diameter.

The aerosol concentration in the producer gas was about two orders of magnitude greater than that measured in the previous gasifier run, and an order of magnitude greater than that of the air fed to the burners. Again, this

TABLE 2  
Aerosol Filter Sample Data

Burner Air							
Filter (No.)	Date	On	Off	Time (hr)	Wt Gain (gm)	Flow (scfh)	Loading ( $\mu\text{g}/\text{m}^3$ )
GF-29	7/21/81	1554	0812	16.30	0.000578	60	20
GF-30	7/22/81	0837	0816	23.65	0.000501	60	12
GF-37	7/23/81	0903	0745	22.70	0.001005	60	26
GF-44	7/24/81	1013	1446	4.55	0.000273	60	35
Ag-32 <sup>1</sup>	7/30/81	0856	1520	6.40	0.000051	60	4

<sup>1</sup>(5.0  $\mu\text{m}$ )

Laboratory Burner							
Filter (No.)	Date	On	Off	Time (hr)	Wt Gain (gm)	Flow (scfh)	Loading ( $\mu\text{g}/\text{m}^3$ )
GF-57	8/10/81	1253	1423	1.50	0.006405	10.4	14,493
Ag-45 <sup>2</sup>	8/11/81	0815	1015	2.00	0.004758	10.2	8,233
GF-59	8/11/81	1255	1525	2.50	0.005584	10.2	7,730
Ag-46 <sup>2</sup>	8/12/81	0835	1335	5.00	0.009849	10.2	6,817
Ag-47 <sup>2</sup>	8/13/81	0808	1508	7.00	0.008088	10.2	3,998

<sup>2</sup>(1.2  $\mu\text{m}$ )

TABLE 2 (Continued)  
Aerosol Filter Sample Data

POC Dynamic Burner								Location (Filters in Tandem)
Filter (No.)	Date	On	Off	Time (hr)	Wt Gain (gm)	Flow (scfh)	Loading ( $\mu\text{g}/\text{m}^3$ )	
Ag-6 <sup>1</sup>	7/22/81	0925	0935	0.167	0.012035	14.1	180,420	Front
Ag-7	7/22/81	0925	0935	0.167	0.005386	14.1	80,743	Back
DM-8	7/22/81	0949	0959	0.167	0.007686	12.0	135,387	Front
DM-9	7/22/81	0949	0959	0.167	0.008950	12.0	157,652	Back
Ag-23 <sup>1</sup>	7/27/81	1025	1320	2.92	0.048561	11.4	51,496	Front
Ag-24 <sup>1</sup>	7/27/81	1025	1320	2.92	0.025057	11.4	26,571	Back
Ag-20 <sup>1</sup>	7/29/81	0914	1334	4.33	0.076551	10.2	61,183	Front
Ag-25 <sup>1</sup>	7/29/81	0914	1334	4.33	0.026867	10.2	21,473	Back

<sup>1</sup>(5.0  $\mu\text{m}$ )

TABLE 2 (Continued)  
Aerosol Filter Sample Data

Filter (No.)	Date	Producer Gas		Time (hr)	Wt Gain (gm)	Flow (scfh)	Loading ( $\mu\text{g}/\text{m}^3$ )	Location
		On	Off					
GF-23	7/21/81	0821	1527	7.10	0.003385	60	280	Full Flow
GF-24	7/21/81	0820	1527	7.12	0.004400	60	363	Orifice
GF-27	7/21/81	1539	0812	16.55	0.007752	60	275	Full Flow
GF-28	7/21/81	1539	0812	16.55	0.005785	60	205	Orifice
GF-31	7/22/81	0840	1537	6.95	0.002077	60	175	Orifice
GF-35	7/22/81	1553	0816	16.38	0.008158	60	293	Orifice
DM-12	7/23/81	0903	1028	1.42	0.001489	48	771	Orifice
GF-38	7/23/81	1047	1424	3.62	0.001729	60	281	Orifice
Ag-9 <sup>1</sup>	7/24/81	1013	1445	4.53	0.000978	60	127	Orifice
Ag-10 <sup>1</sup>	7/24/81	1013	1445	4.53	0.001538	60	199	Full Flow
Ag-21 <sup>1</sup>	7/27/81	1015	1520	5.08	0.003296	60	381	Orifice
Ag-22 <sup>1</sup>	7/27/81	1015	1520	5.08	0.005700	60	660	Full Flow
Ag-26 <sup>1</sup>	7/29/81	0848	1338	4.83	0.002516	60	306	Orifice
Ag-27 <sup>1</sup>	7/29/81	0848	1338	4.83	0.004207	60	512	Full Flow
GF-51	7/29/81	1356	0830	18.57	0.014235	60	450	Orifice
Ag-28 <sup>1</sup>	7/30/81	0856	1520	6.40	0.002000	60	183	Orifice
GF-55	8/05/81	1112	1507	3.92	0.003196	60	479	Orifice
GF-56	8/10/81	1014	1429	4.25	0.002050	60	283	Orifice
GF-58	8/11/81	0823	1523	7.00	0.007953	60	668	Orifice
GF-60	8/12/81	0840	1340	5.00	0.007094	60	834	Orifice
GF-61	8/13/81	0812	1512	7.00	0.001507	60	126	Orifice
GF-62	8/14/81	0812	1142	3.50	0.010239	60	1721	Orifice
GF-63	8/17/81	0810	1540	7.50	0.018219	60	1429	Orifice
GF-64	8/18/81	0803	1533	7.50	0.022176	60	1739	Orifice

GF: Glass Fiber

DM: Polyvinyl Chloride

Ag: Silver

<sup>1</sup>: 5.0  $\mu\text{m}$

<sup>2</sup>: 1.2  $\mu\text{m}$



TABLE 3

## Inertial Impactor Data of POC Aerosols

Sample: Dynamic POC		Flow Rate: 7 lpm	
Collection Stages	Date: 8/14/81	Date: 8/17/81	
	Duration: 1 hour	Duration: 7.5 hours	
	Temp: 175°F	Temp: 155°F	
Stage*	EAD* (µm)	Weight (g) Increase	Weight (g) Increase
1	21.0	0.002534	0.002991
2	13.0	0.001514	0.001388
3	5.0	0.001146	0.001028
4	3.0	0.000926	0.000995
5	1.9	0.000761	0.001018
6	1.0	0.000479	0.001492
Final Filter	--	0.065567	--
TOTAL = 0.072927		TOTAL = --	
Aerosol Loading = 0.173 g/m <sup>3</sup>		Aerosol Loading = --	

Sample: Lab Burner POC		Flow Rate: 7 lpm	
Collection Stages	Date: 8/14/81	Date: 8/18/81	
	Duration: 2 hours	Duration: 7.5 hours	
	Temp: 155°F	Temp: 165°F	
Stage*	EAD* (µm)	Weight (g) Increase	Weight (g) Increase
1	21.0	0.000497	0.001267
2	13.0	0.000319	0.000746
3	5.0	0.000194	0.000521
4	3.0	0.000119	0.000355
5	1.9	0.000065	0.000340
6	1.0	0.000001	0.000336
Final Filter	--	0.000697	0.003793
TOTAL = 0.001892		TOTAL = 0.007358	
Aerosol Loading = 0.002 g/m <sup>3</sup>		Aerosol Loading = 0.002 g/m <sup>3</sup>	

\*Effective Aerodynamic Diameter.

TABLE 4  
Particle Size Characterization Using EAA

Sample	Date	Time	Concn. (No/cm <sup>3</sup> )	Diameter ( $\mu$ m)	$\sigma_g$	Dilution Ratio
Room Air 1 (B-4)	8/05/81	1010	$2.52 \times 10^4$	0.0489	1.90	1.0
Room Air 2 (B-4)	8/05/81	1015	$2.77 \times 10^4$	0.0403	2.57	1.0
Burner Air 1	8/05/81	1030	$3.84 \times 10^4$	0.0334	1.81	1.0
Burner Air 2	8/05/81	1035	$2.79 \times 10^4$	0.0416	1.79	1.0
Producer Gas 6	8/05/81	1100	$3.09 \times 10^5$	0.0438	1.81	1.0
Producer Gas 7	8/05/81	1105	$3.18 \times 10^5$	0.0425	1.72	1.0
POC: Lab Burner 1	8/05/81	1415	$8.07 \times 10^6$	0.0151	1.06	17.8
POC: Lab Burner 2	8/05/81	1425	$2.53 \times 10^6$	0.0166	1.19	17.8
POC: Lab Burner 3	8/05/81	1430	$1.01 \times 10^7$	0.0199	1.16	14.2
POC: Lab Burner 4	8/05/81	1433	$3.35 \times 10^6$	0.0284	1.14	14.2

increase was attributed to the bypassing of the Holmes-Stretford sulfur cleanup system. Aerosol mass loadings in the POC from the lab burner were about an order of magnitude greater than those measured in the previous run.

Aerosol size distribution data are presented graphically in Figures 4-7, showing number distribution as a function of particle diameter. While particle concentrations may have changed, there is little difference between the most recent size distributions and those obtained earlier. The lab burner POC aerosols have a somewhat smaller geometric median diameter than those of the gas or air. Although the producer gas shows an increase in aerosol mass loading from before, the relative particle size distribution is essentially unchanged.

Selected silver filter samples were subjected to energy dispersive X-ray (EDX) analysis, wavelength dispersive X-ray (WDX) analysis, and X-ray diffraction. Scanning electron microscopy (SEM), Auger electron spectroscopy (AES), and electron spectroscopy for chemical analysis (ESCA) also were used to examine selected filter samples and impaction plates from the Sierra impactor.

WDX analyses are presented in Table 5. Aerosols from the burner air contained trace quantities of sulfur and calcium, typical of ambient air. Sulfur was the primary constituent of the POC from both burners, particularly on the upstream filter of the dynamic facility burner. Diffraction patterns confirmed the presence of silver sulfate ( $\text{AgSO}_4$ ) on filters from both burners. This indicates that the silver membrane reacted with the sulfuric or sulfurous acid aerosol which was formed in the combustor. Chlorine was present in both of the POC filter samples as well as in the gas. Silver chloride was also identified by diffraction on one of the dynamic POC filters. About the only other elements to be detected were ferritic in nature, such as one might find from steel. Little alumina or silica was detected. Examination of selected plates from the Sierra impactor yielded similar results.

SEM and EDX analyses of producer gas samples showed traces of iron which was likely an artifact of the system, probably due to pipe scale or rust. The sample collected on the back-up filters was attributed to condensation and gas phase reactions with the filter rather than breakthrough from the upstream filter. Upstream POC (dynamic burner) filters showed some traces of ferrous-type metals such as iron, chromium, and nickel along with the ubiquitous sulfur and chlorine. Downstream (backup) filters contained only sulfur and chlorine, both of which appeared to be rather evenly distributed across the surface. Filter samples taken from the POC from the lab burner showed only the now familiar, widespread distribution of sulfur and chlorine. No carbon ( $<100 \mu\text{g}$ ) was detected on any of the POC filters by a combustion/titration method.

The final stage plates of the Sierra impactor, which was used to sample POC from both burners, were also subjected to SEM and X-ray analysis. Figure 8 shows two views, at magnifications of 20x (8a) and 50x (8b), of the plate from the impactor sample of the dynamic POC. The prominent feature is a blister which corresponds with the slit from the previous stage, i.e., the area of maximum impact. EDX analysis of this blister (Figure 8c) showed only sulfur, the other lines correspond to elements such as iron which are representative of the stainless steel plate. AES (Figure 9) and ESCA indicated the presence of carbon in a graphic structure, along with what was probably

TABLE 5  
 Qualitative Elemental Analysis (WDX)  
 of Aerosol Filter Samples

Element Sample	Al	Si	P	S	Ca	Ti	Fe	Cl	Cr	Ni	Cu
Burner Air/Ag-32	ND <sup>1</sup>	ND	ND	T <sup>2</sup>	T	ND	T	ND	T	ND	ND
Producer Gas - Orifice/Ag-9	ND	ND	ND	T	T	ND	ND	T	T	ND	T
Producer Gas - Full Pressure/ Ag-10	ND	ND	ND	Mi <sup>3</sup>	Ma <sup>4</sup>	ND	ND	Mi	T	ND	ND
Producer Gas - Orifice/Ag-22	ND	ND	ND	T	T	ND	ND	T	T	T	T
Producer Gas - Full Pressure/ Ag-27	ND	ND	ND	T	T	ND	ND	T	ND	ND	T
POC - Dynamic <sup>5,6</sup> - Front/Ag-23	ND	ND	ND	Ma	Mi	ND	T	ND	T	ND	ND
POC - Dynamic - Back/Ag-24	ND	ND	ND	T	T	ND	T	T	ND	T	T
POC - Dynamic - Front/Ag-20	ND	T	ND	Ma	T	ND	T	Ma	T	ND	ND
POC - Dynamic <sup>7</sup> - Back/Ag-25	ND	T	ND	Mi	T	ND	ND	Mi	T	ND	T
POC - Lab Burner/Ag-46 <sup>2</sup>	ND	ND	ND	Ma	Mi	ND	Mi	ND	T	ND	ND

<sup>1</sup>Not Detected.

<sup>2</sup>Trace

<sup>3</sup>Minor

<sup>4</sup>Major

<sup>5</sup>Ag<sub>2</sub>SO<sub>4</sub> diffraction pattern found.

<sup>6</sup>Possible trace of selenium.

<sup>7</sup>AgCl diffraction pattern found.

aluminum oxide. Figure 10 is a photomicrograph of the last stage impactor plate from the lab burner POC. The material scattered about the surface was determined by EDX to be large isolated particles of sulfur and silicon. The amount of silicon observed was not considered a significant fraction of the total aerosol mass loading.

#### Instrumentation Requirements

This study utilized commercially available instruments to provide a physical characterization of the particles contained in a gasification process stream and in the POC of the low-Btu gas. Simple extractive techniques were also used to obtain particulate samples for subsequent chemical analysis. In order to utilize the commercial instruments, it was necessary to condition the sample to provide conditions within the operating range of the instruments (i.e., reduce pressure, reduce temperature, dilute aerosol concentration, etc.). The conditioning of the gas sample increased the probability that the sample was not representative of the gas stream. In order to minimize this uncertainty, in-situ particle characterization is preferred.

The development of several optical particle monitors (OPM's) by the Department of Energy (DOE) has represented an attempt at addressing this problem. Current OPM's are limited to particle concentrations less than about  $10^5/\text{cm}^3$  and particle sizes larger than about 0.1  $\mu\text{m}$  diameter. This range is appropriate for the clean gasification process stream, but not for uncleaned gas and POC's. METC is currently involved in a laboratory and field evaluation of these and commercially available units to determine their limitations and the need for development of advanced OPM's.

Some instrumentation is presently under development to address the characterization of particles in the "dirty" portion of the process stream. This instrumentation includes two on-line mass monitors, both of which are based on automated, extractive sampling and provide a limited measure of size information. The design of one system is centered on a virtual impactor. Those particles which are captured by the virtual impactor are collected on a moving filter tape. The particulate mass on the filter tape is subsequently measured by a beta gauge and displayed on a microprocessor monitor. Evaluation of this system is being performed on the METC gasifier. The second system involves a high-temperature/high-pressure cyclone train. The particles collected by each cyclone are deposited into a tapered-element oscillating microbalance (TEOM). The resultant particulate mass is determined by the frequency change of the TEOM. This system is currently undergoing testing at the Curtiss-Wright PFBC.

Additional research funded by DOE is addressing various methods for improving the representativeness of extractive samples and providing a better understanding of particle-particle interactions and modifications to the physical properties of particles both inside and outside the process stream. Specific projects include probe development, dense-phase sampling, and the effects of temperature and concentration gradients on volatile particles.

#### Conclusions

The dynamic burner POC contained about an order of magnitude more aerosol material than the lab burner POC. The higher aerosol loading of the dynamic

POC versus that of the laboratory burner was attributed primarily to the reduced nucleation of sulfuric acid droplets in the lab burner due to the dry sheath air around the flame. Aerosol size characterization measurements using the EAA showed little change from those obtained on previous runs. Good agreement in the aerosol loadings of the POC was obtained from both impactor and silver filters. Because of difference in substrates, additional chemical analysis could be applied to impactor samples (Auger and ESCA).

Loadings of POC aerosols from both burners were increased over the previous gasifier run. Chemical analyses of POC aerosol samples indicated that the majority of the aerosols were composed of sulfur or sulfur compounds. Increased levels of  $H_2S$  in the producer gas resulting from bypassing the sulfur removal unit were believed primarily responsible for the higher POC aerosol loadings of this run. Another commonly observed element on the filter samples was chlorine, probably present in the form of  $AgCl$  (due to reactions with the  $Ag$  filters).

While some contribution to the dynamic burner's POC aerosol loading was anticipated to be caused by degradation of the refractory liner, chemical analyses did not detect significant quantities of refractory in the aerosol samples.

Aerosol mass loadings of the producer gas were found to be about an order of magnitude greater than those found during the previous run. This increase was attributed to the presence of particles usually removed from the process stream by the sulfur cleanup system. These producer gas aerosols contained some traces of sulfur, chlorine, and ferric compounds but were primarily composed of water and dissolved organic compounds. Since no carbon was detected in the POC aerosols, the producer gas aerosols had no apparent influence upon the POC aerosol loading (i.e., soot formation).

In three separate studies of the combustion of low-Btu gas, the gasifier and cleanup train have undergone numerous physical as well as operational modifications (i.e., various coals have been used and the system has been operated with and without the sulfur removal system). Our studies of both the producer gas and the POC of this gas indicate that the single most important parameter in determining the level of contaminants in the producer gas is the operation of the cleanup system. The most significant contaminant, in terms of POC aerosol formation, is sulfur or  $H_2S$ . The proposed mechanism of the resultant aerosol formation is the nucleation or condensation of sulfuric acid/water droplets.

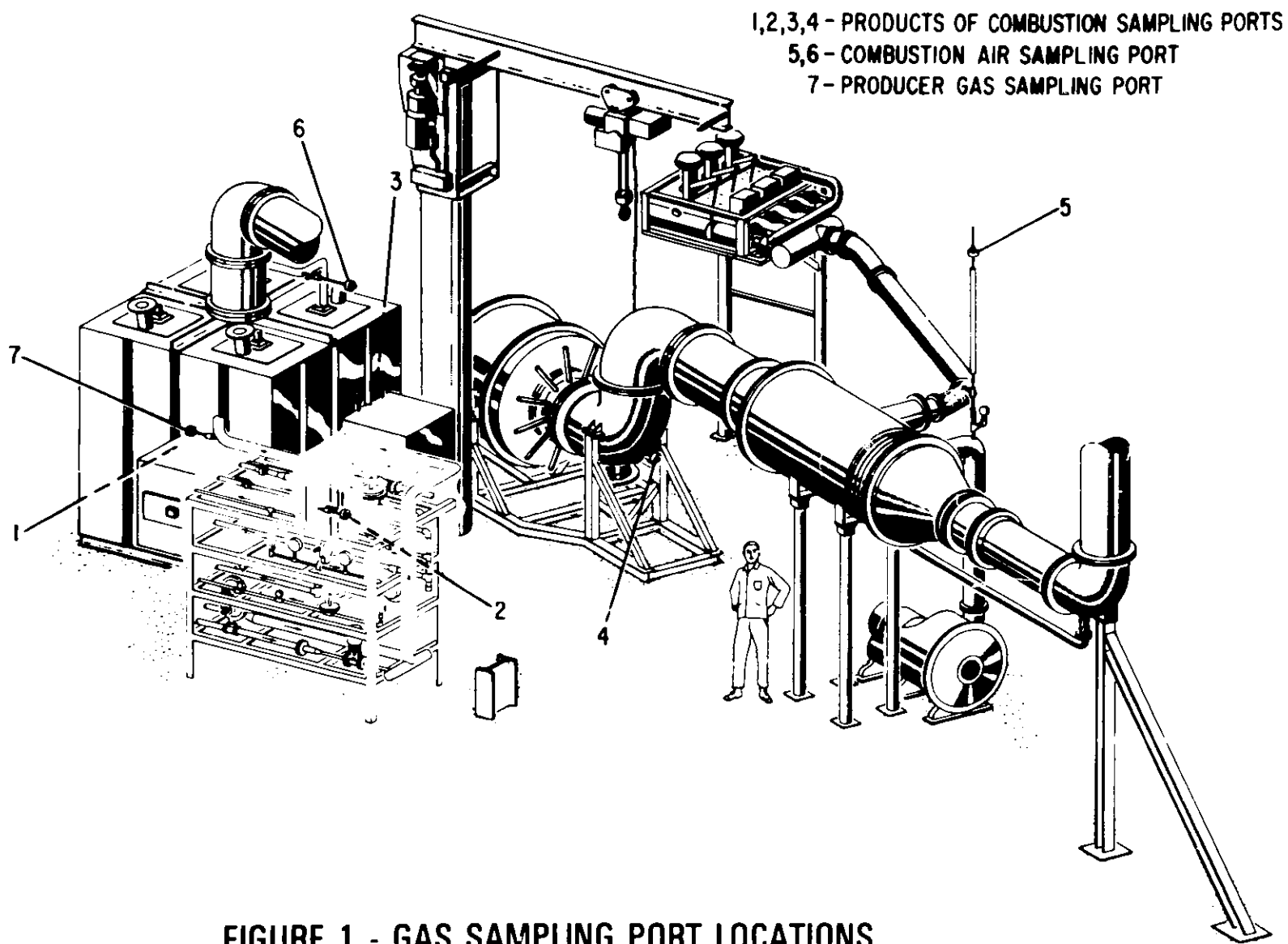


**FIGURE 1 - GAS SAMPLING PORT LOCATIONS**

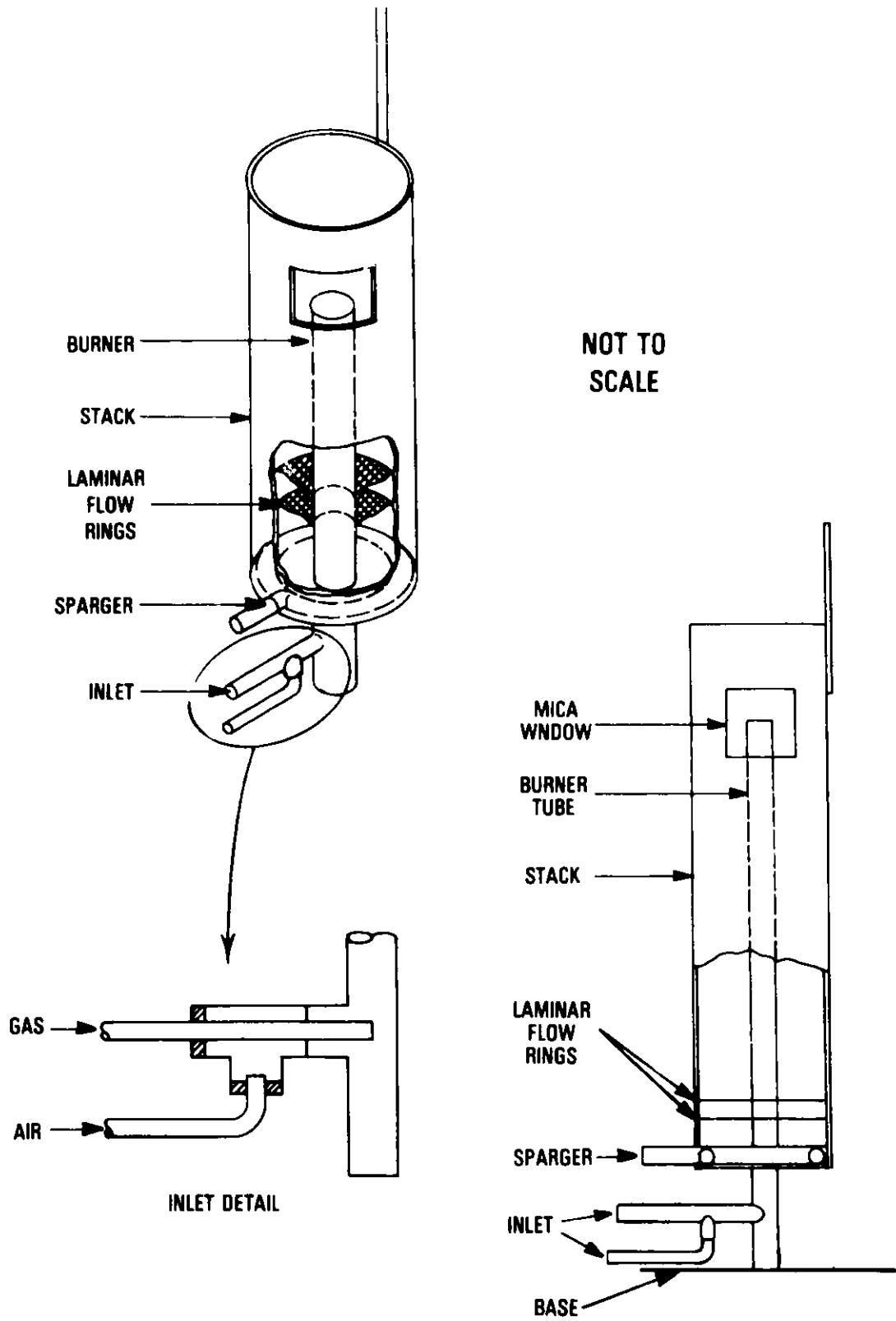
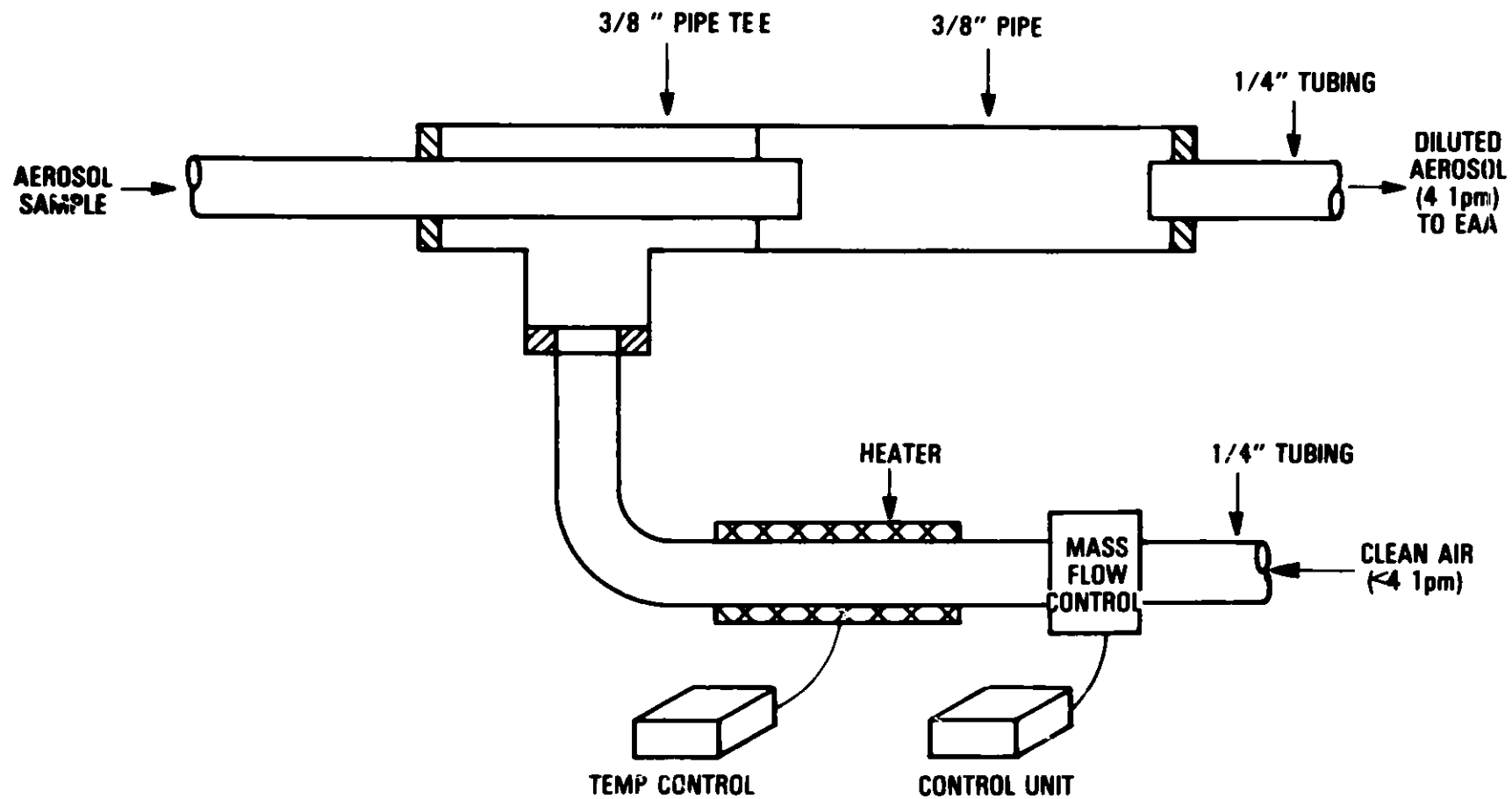


FIGURE 2 - LABORATORY BURNER FOR COMBUSTION STUDIES





564

FIGURE 3 - AEROSOL DILUTION SYSTEM

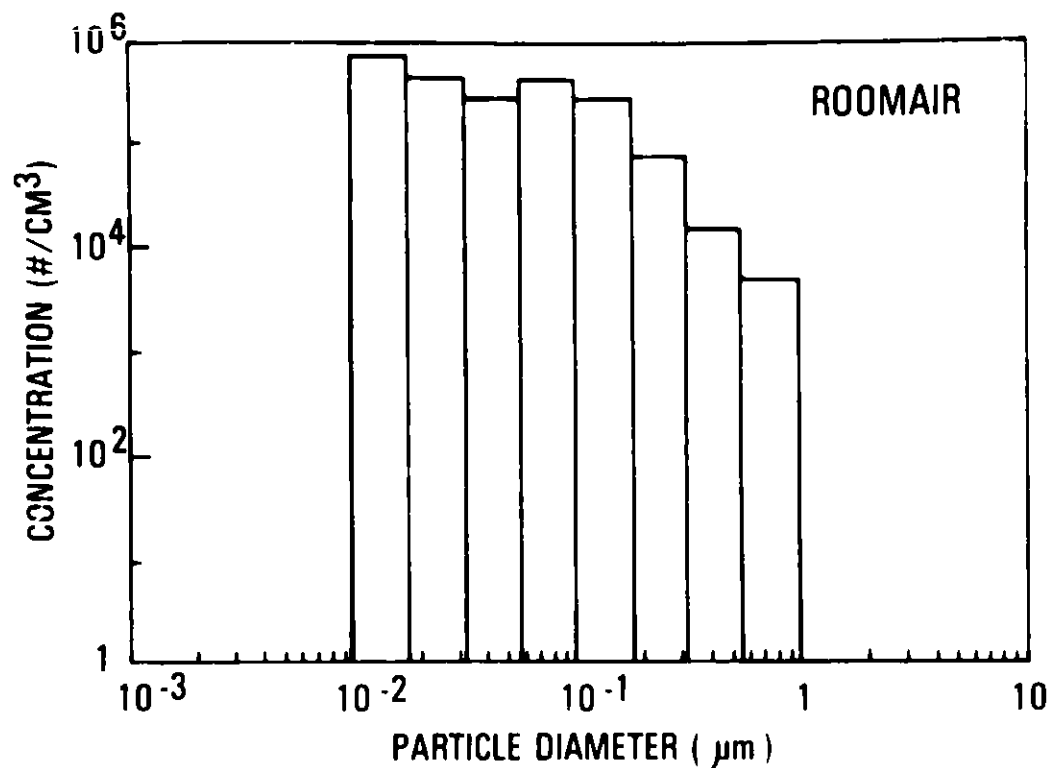


FIGURE 4 - AEROSOL SIZE DISTRIBUTION OF AMBIENT AIR AEROSOLS

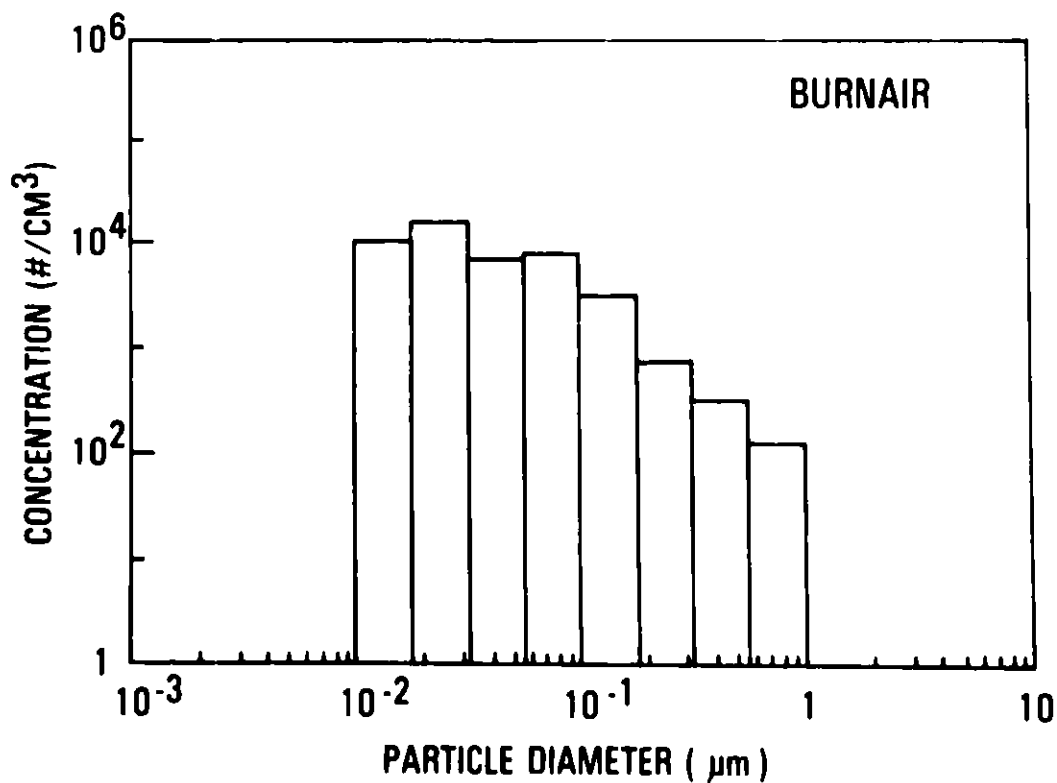


FIGURE 5 - AEROSOL SIZE DISTRIBUTION OF BURNER AIR AEROSOLS

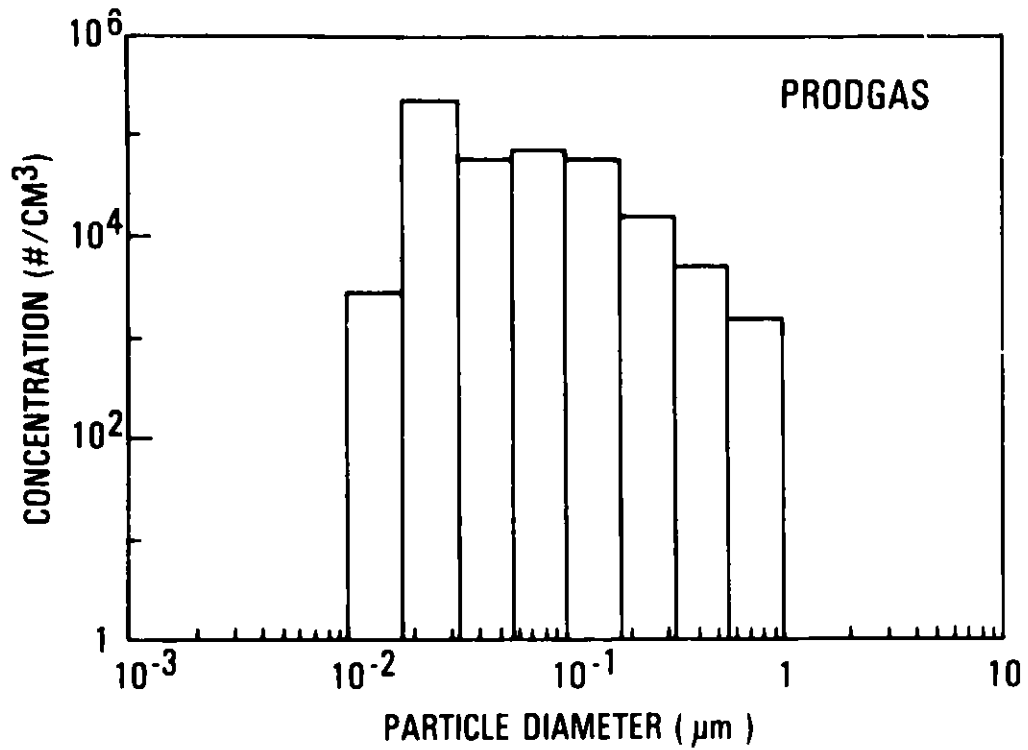


FIGURE 6 - AEROSOL SIZE DISTRIBUTION OF PRODUCER GAS AEROSOLS

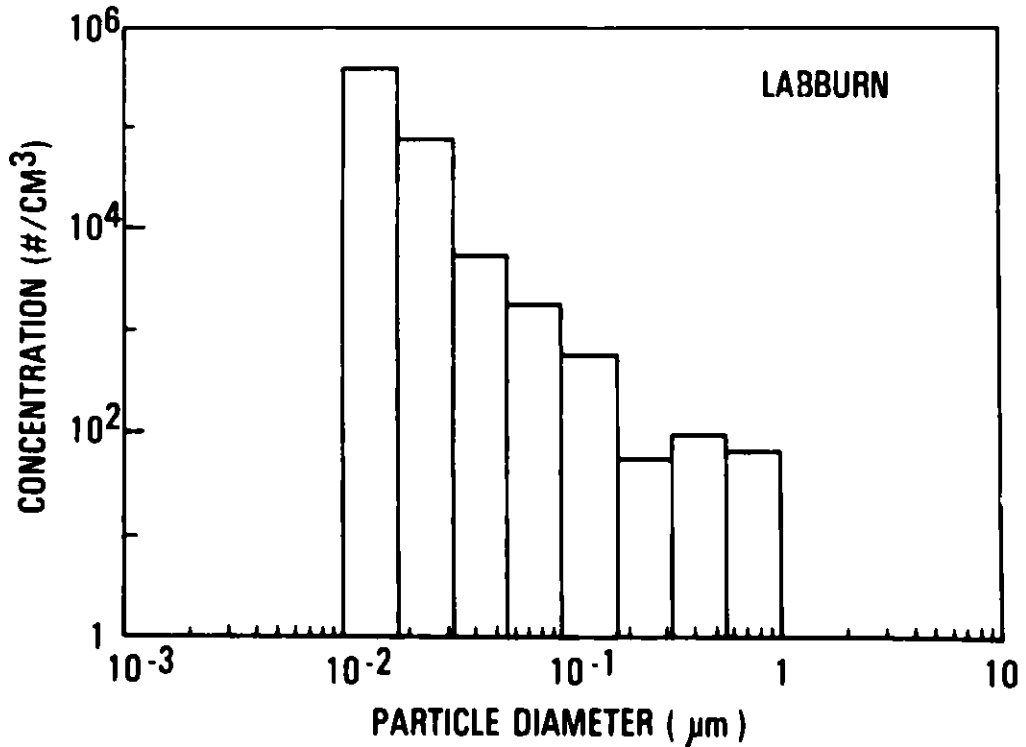


FIGURE 7 - AEROSOL SIZE DISTRIBUTION OF POC AEROSOLS FROM THE LABORATORY BURNER



**FIGURE 8a.** Low Magnification (20x) Electron Micrograph of Sample Collected on a Heated Impactor Plate from the Dynamic POC.



**FIGURE 8b.** Higher Magnification (50x) Electron Micrograph of Sample Collected on a Heated Impactor Plate from the Dynamic POC.



**FIGURE 8c.** EDX Spectra of Impactation Plate Sample from the Dynamic POC. Prominent Peaks Include the Stainless Steel Substrate and Sulfur.

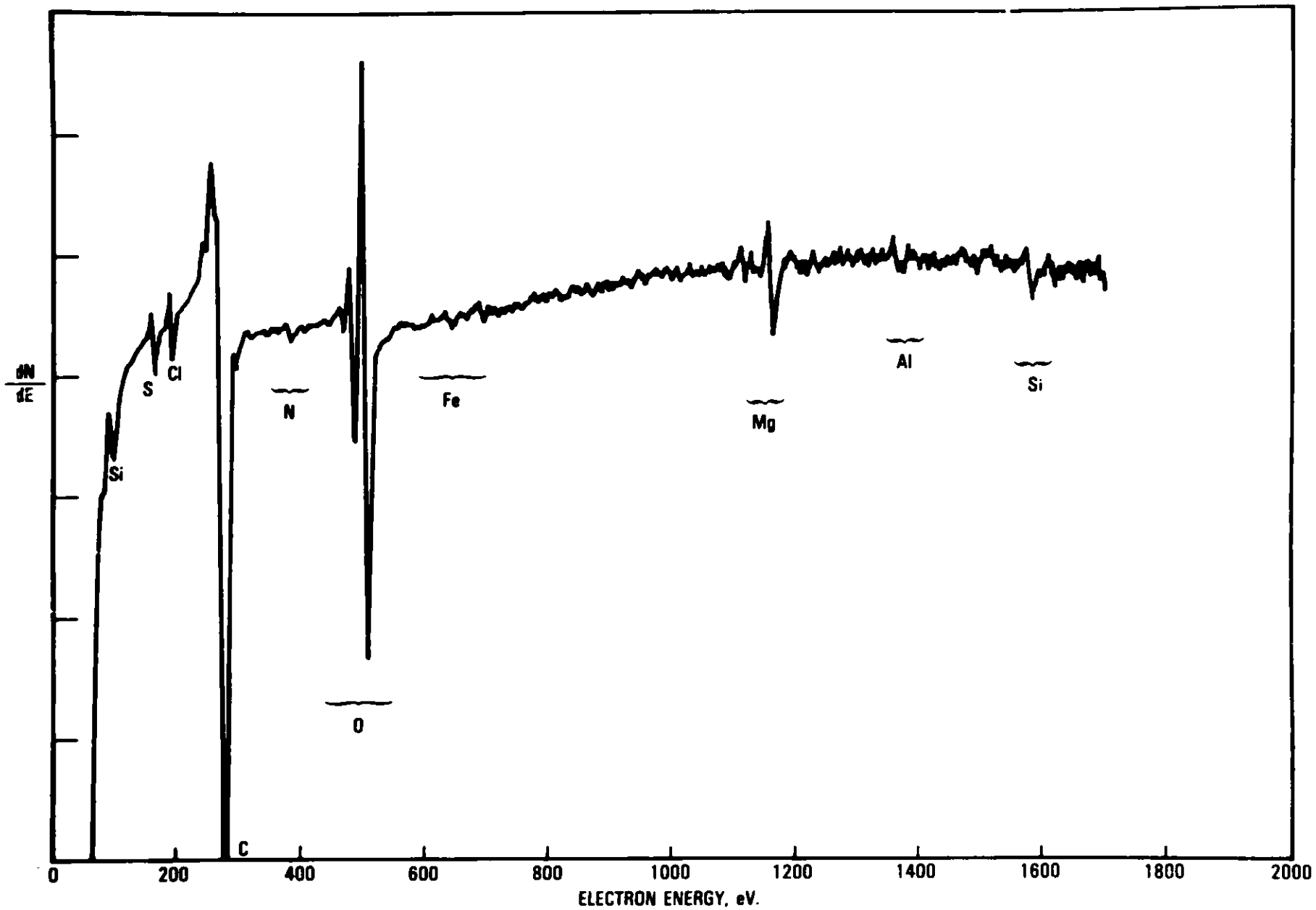


FIGURE 9 - AUGER ELECTRON SPECTROSCOPIC ANALYSIS OF DYNAMIC POC SAMPLES COLLECTED ON IMPACTION PLATE



FIGURE 10a. Electron Micrograph of Sample Collected on a Heated Impact Plate from Laboratory Burner I

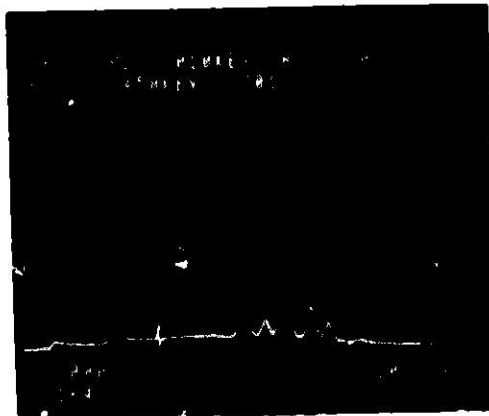


FIGURE 10b. EDX Spectra of Impactation Plate Sample from Laboratory Burner POC. As with Dynamic POC, Prominent Peaks Include the Stainless Steel Substrate and Sulfur.

References

1. "Fixed-Bed Gasification," Topical Report, DOE/METC/SP-184, 1981.
2. C. V. Nakaishi and L. K. Carpenter, "Ceramic Corrosion/Erosion Project Description," DOE/METC/SP-111, 1981.
3. Kapadia, A., Ph.D. Thesis, Mechanical Engineering Department, University of Minnesota, Minneapolis, MN, 1979.

Acknowledgments

The authors wish to acknowledge the efforts of Curtis Nakaishi, Jim King, Mike Paris, and the Analytical Sciences Branch at METC in providing direct support for this project.

PARTICLE SIZE MEASUREMENT USING OPTICAL CONVOLUTION WITH A DOUBLE SLIT MASK

D. A. Tichenor  
Combustion Research Division 8521  
Sandia National Laboratories, Livermore

Abstract

A one-dimensional convolution of the particle image with a known transparency is performed optically. When the transparency is chosen to be a specially-designed double-slit mask, the particle size can be easily extracted from the resulting output signal. The system can be operated as a single particle counter to generate particle size distributions in applications where the particle size range of primary interest is 10  $\mu\text{m}$  or larger and the number density does not exceed  $10^5/\text{cm}^3$ . In high temperature environments, the light source is provided by the particle incandescence.

I. Introduction

A variety of methods have been developed for in situ measurement of particle-size distributions.<sup>1,2</sup> The optical methods employed include Mie scattering,<sup>3</sup> interferometry<sup>4</sup> and imaging.<sup>5</sup> However, no particular instrument satisfies all requirements desired in a single particle counter. The method described here is based on imaging and is therefore fundamentally limited by the resolution of optical microscopy to particle sizes of 1  $\mu\text{m}$  and larger. For practical in situ measurements the method is limited to applications in which the size range of primary interest is 10  $\mu\text{m}$  and larger.

The double-slit method shares most of the characteristics of the variable frequency grid<sup>5</sup> (VFG) method such as insensitivity to particle shape and refractive index and the capability to function in a high temperature environment using the particle incandescence as the light source. In addition to these shared features, the double-slit method offers a significantly smaller sample volume and a less complex signal from which the particle size is extracted. The smaller sample volume increases the upper limit on number density in which this system can operate. Like most other single particle counters the double-slit method can measure velocity distributions and the joint distribution of size and velocity. Using the known sample volume the particle number density and flux can also be determined.

II. Principle of Operation

The optical configuration is similar to that of the VFG system except that the variable frequency grid is replaced by a double-slit mask.<sup>6</sup> The sample volume is illuminated with either a monochromatic or white light source as shown in Figure 1 for the 90° illumination case. An image of the moving particle is cast onto a double-slit mask and the transmitted light is measured by a photo detector. With proper design of the mask the size information becomes encoded in the double-pulsed output signal.



Stated in a general way this system extracts image information, such as particle diameter, from a time signature  $S(t)$  generated by convolving the particle image  $P(x,y)$  with a mask described by the transmittance function  $M(x,y)$ ,

$$S(t) = \iint_{-\infty}^{\infty} M(x,y) P(x,y - vt) dx dy, \quad (1)$$

where  $v$  is the particle velocity. In principle  $S(t)$  contains the size information for almost any choice of the mask. However, the mask should be chosen to simplify the process of obtaining size information from the resulting signal. In addition the  $y$  dimension of the mask should be limited to minimize the sample volume.

These considerations resulted in the double-slit mask design shown in Figure 2. The slits of widths  $W_1$  and  $W_2$  are separated by an opaque region of width  $W_1$  such that  $W_1$  is equal to the largest particle diameter of interest and  $W_2$  is equal to the smallest particle diameter of interest. When the image of a moving particle scans across the mask perpendicular to the slits, the transmitted light is represented by a double-pulsed signal.

If we assume the surface of the particle is Lambertian, the particle size can be extracted from the peak values of the two pulses. Let us first consider the back scatter configuration in which the illumination and viewing directions are approximately aligned. In this case the particle image is uniformly bright throughout the projection of the particle onto the image plane. Since the large slit is wider than the particle dimension, the first signal peak,  $I_1$ , is proportional to projected area. The second pulse height,  $I_2$ , is proportional to  $W_2$  times the horizontal dimension of the particle. For a spherical particle of diameter,  $d$ , where  $W_2 < d < W_1$ , the ratio  $I_2/I_1$  is a monotonic function of  $d$ ,

$$\frac{I_2}{I_1} = \frac{4}{\pi} \frac{W_2}{d} \sqrt{1 - \frac{W_2^2}{d^2}} + \frac{1}{\pi} \left[ \sin^{-1} \frac{W_2}{d} - \frac{W_2}{d} \right]. \quad (2)$$

This equation can be solved numerically for  $d$ . When  $W_2 \ll d$  the approximate solution is

$$d \approx \frac{4}{\pi} W_2 \frac{I_1}{I_2}. \quad (3)$$

For non-spherical particles the value obtained from equation (2) is approximately equal to the dimension of the particle measured in the direction perpendicular to the narrow slit.

A similar analysis can be performed for an arbitrary illumination angle. In the  $90^\circ$  illumination arrangement of Figure 1 a spherical particle generates a half-moon image on the mask, and the resulting relationship between the pulse-height ratio and the particle diameter is also described by equations (2) and (3). In general this relationship depends on illumination angle.

This technique can be applied in two additional arrangements that do not require particles with Lambertian surfaces. In one configuration the sample volume is illuminated with a collimated source opposite the imaging lens. The transmitted beam is eliminated with a stop at the focal point of the imaging lens, thereby casting a schlieren image of the particle onto the mask. The simple geometrical analysis of equations (2) and (3) does not apply in this case. Although we have not analyzed this configuration in detail at this time, it appears that the size information is preserved in the double-pulsed signal.

The second arrangement applies to high temperature environments in which the particles are incandescent. An external light source is no longer required, nor is it necessary for the particle to have a Lambertian surface. If the emissivity of the particle is uniform over the surface, the system response to a spherical particle is again described by equations (2) and (3).

In all of the arrangements the velocity can be determined by measuring the time between the leading edges of the two pulses and dividing that value into the known distance,  $2W_1$ . This measurement yields both the velocity distribution and the joint distribution of size and velocity.

### III. Error Estimates

Like other single particle counters, the double-slit method is subject to errors if the particle passes through the edge of the sample volume. Two types of errors occur in the double-slit system. First, when a particle is out of focus, the measured diameter is greater than the true value. In the other case the particle passes across the ends of the slits and may be oversized or under-sized as a result.

Out-of-focus errors can be eliminated when off-axis illumination is used by simply confining the illumination beam to the in-focus region. In the other arrangements an external method of defining the focal region must be used, unless of course the particle beam itself is confined to the focal region. These errors can be eliminated by illuminating the focal region with a monochromatic light source at right angles to the viewing direction. This wavelength is separated from the remaining light and detected by a second photo detector. The resulting signal provides a coincidence check that allows only those particles passing through the in-focus region to be included in the histogram.

Edge effect errors can be handled in one of two ways. First, these errors can be corrected by aligning the coincidence detector to be sensitive only to particles that pass through the center of the mask. On the other hand, if the length,  $L$ , of the slits is sufficiently large, edge effects are not severe. A geometrical analysis of a spherical particle passing at right

angles to the slits yields the following expression for the measured diameter,  $d$ , normalized by the true diameter:

$$d = \frac{1 - \frac{1}{2\pi} (\theta - \sin \theta)}{1/2 + \frac{x}{d}} \quad (4)$$

where  $\theta = 2 \cos^{-1} (2 x/d)$  and  $-d/2 < x < d/2$ .

The parameter,  $x$ , is the position of the center of the particle relative to the edge with negative values representing a center outside of the slits. These equations apply to the back-scatter and the self-luminous arrangements in which a full disc is imaged onto the mask.

Edge effects are more severe for larger particles, since they have a greater probability of engaging the edge. Equation (4) predicts that for positive values of  $x$  (particle centered within the slits) the particle is oversized by a maximum of 7.3%. For negative values of  $x$  the particle is undersized such that severe errors occur only for a small range of  $x$ . In all cases the edge-effect errors decrease with increasing slit length. As an example, assume the slit length  $L$ , is given by  $L = 2W_1$ , and assume particles of maximum size ( $d = W_1$ ) are uniformly distributed in the flow. For 80% of these particles the edge effect errors are less than 16% of the true diameter. In the case of smaller particles an even larger fraction of the population is sized to this accuracy.

#### IV. Experimental Results

An initial experiment was carried out using a 50 milliwatt He-Ne laser as the light source. Size-classified C bituminous coal particles (PSOC 98) were injected into an air stream and imaged onto the mask using  $f/10$  optics. A coincidence detector was used to eliminate edge effects. After allowing for the magnification (5x) the width of the narrow slit,  $W_2$ , was 10  $\mu\text{m}$  and  $W_1$  was 100  $\mu\text{m}$ . The signals (Figure 3) were detected by a photomultiplier tube, log transformed electronically, digitized using a Nicolet Explorer III oscilloscope and processed in a VAX 780 computer. The two peak values  $I_1$  and  $I_2$  were determined and equation (3) was used to obtain particle size. This procedure was applied to 245 double-pulsed signals to generate the histogram of Figure 4. The histogram is in good agreement with an analysis of the same batch of coal particles using the Leeds and Northrup Microtrac analyzer.

In conclusion the double-slit technique appears to be a useful method for in situ measurement of particles in the range of 10  $\mu\text{m}$  and larger. Preliminary experimental results indicate that the system is especially promising in high temperature environments where the sizing signal is generated by using the particle incandescence.

### Acknowledgments

The author would like to thank J. Wang and K. Hencken for many helpful discussions, A. Salmi for the experimental setup, and D. Beard for the Microtrac Analysis. This work is supported by United States Department of Energy/Fossil Energy.

### References

1. D. J. Holve, D. A. Tichenor, J. C. F. Wang and D. R. Hardesty, "Design Criteria and Recent Developments of Optical Single Particle Counters for Fossil Fuel Systems," Optical Engineering 20, 529 (1981).
2. E. D. Hirleman, "Laser - Based Single Particle Counters for in situ Particulate Diagnostics," Optical Engineering 19, 854 (1980).
3. A. L. Wertheimer and W. L. Wilcock, "Light Scattering Measurements of Particle Distribution," Applied Optics 15, 1616 (1976).
4. W. D. Bachalo, "Method for Measuring the Size and Velocity of Spheres by Dual-Beam Light-Scatter Interferometry," Applied Optics 19, 363 (1980).
5. J. C. F. Wang and D. A. Tichenor, "Particle Size Measurement Using an Optical Variable Frequency Grid Technique," Applied Optics 20, 1367 (1981).
6. D. A. Tichenor, J. C. F. Wang and K. R. Hencken, "Optical Double-Slit Particle Measuring System," DOE patent application filed March 1982.

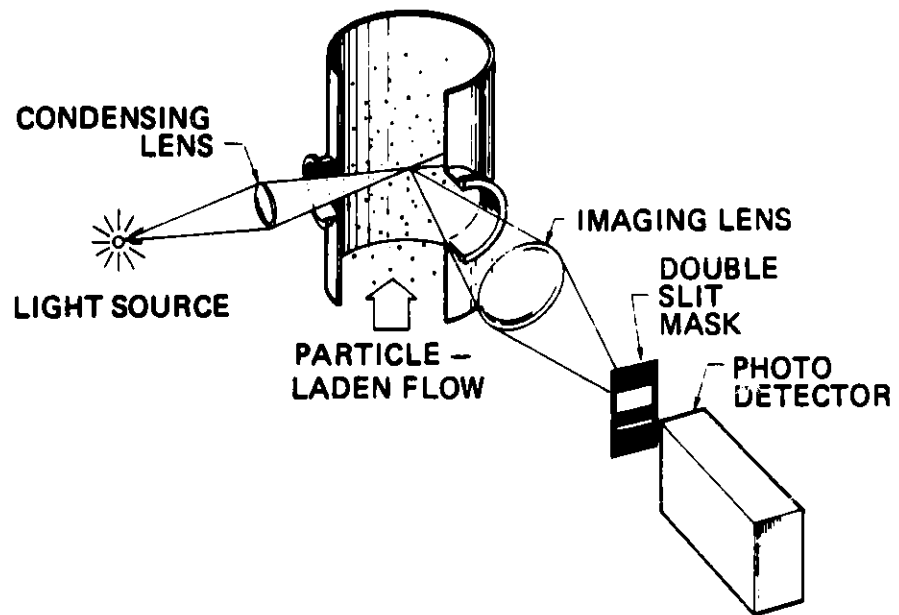


Figure 1. Double-slit system for particle sizing (90° illumination arrangement).

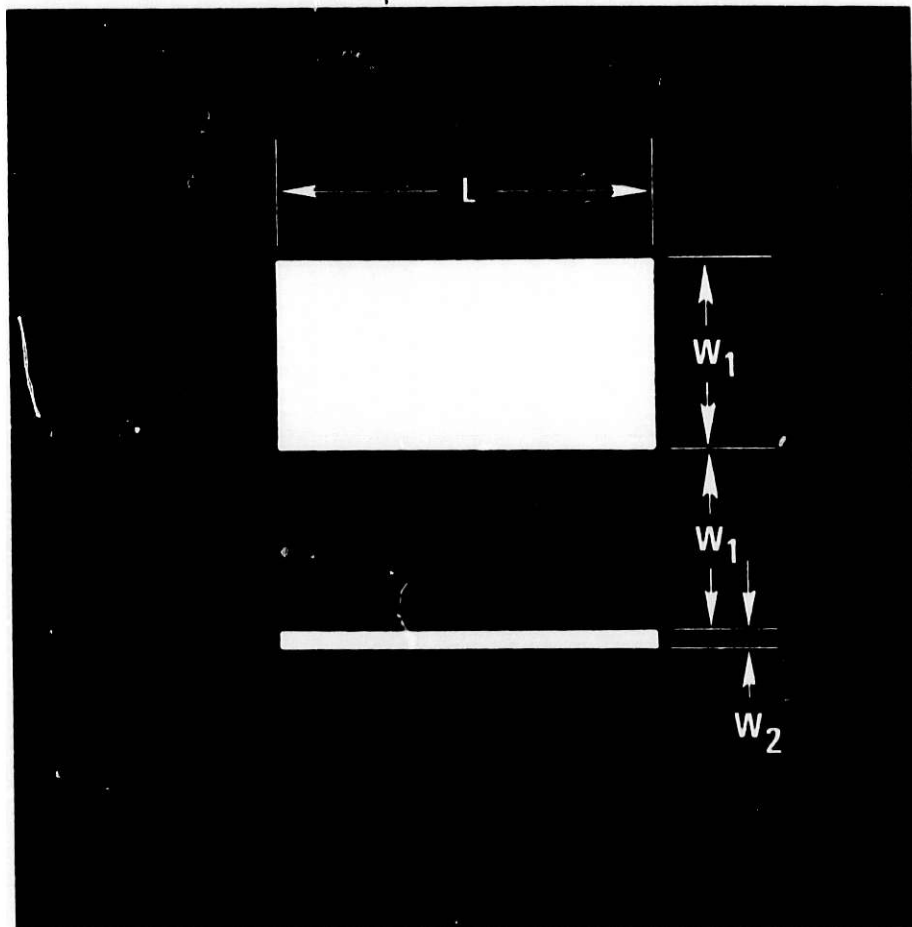
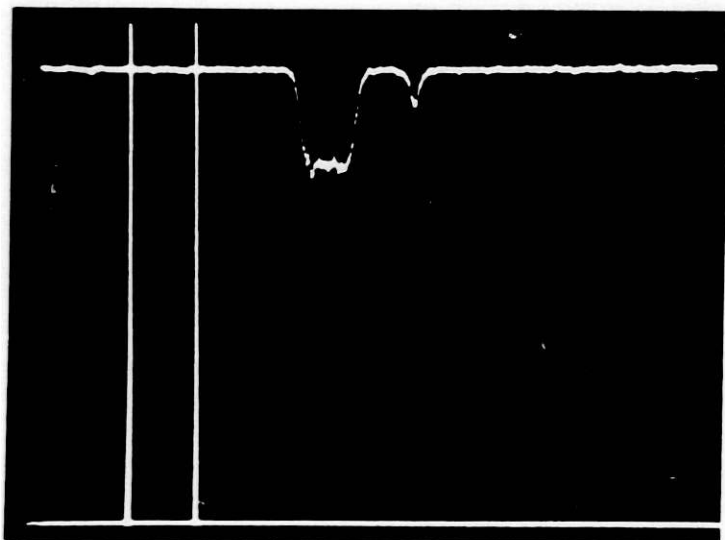
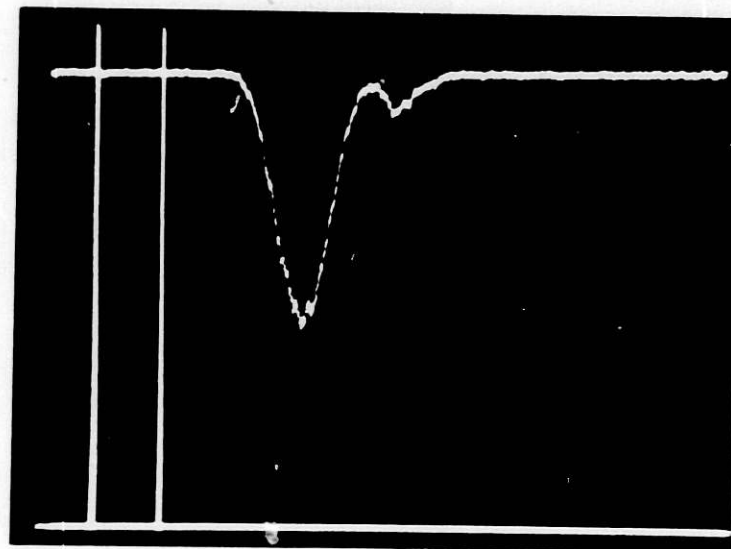


Figure 2. Double-slit mask for particles in the size range  $W_2 < d < W_1$ .

100  $\mu$ s



38  $\mu$ m



79  $\mu$ m

Figure 3. Double-slit signals from coal particles. The sizes are calculated from equation (3).

NORMALIZED VOLUME DISTRIBUTION

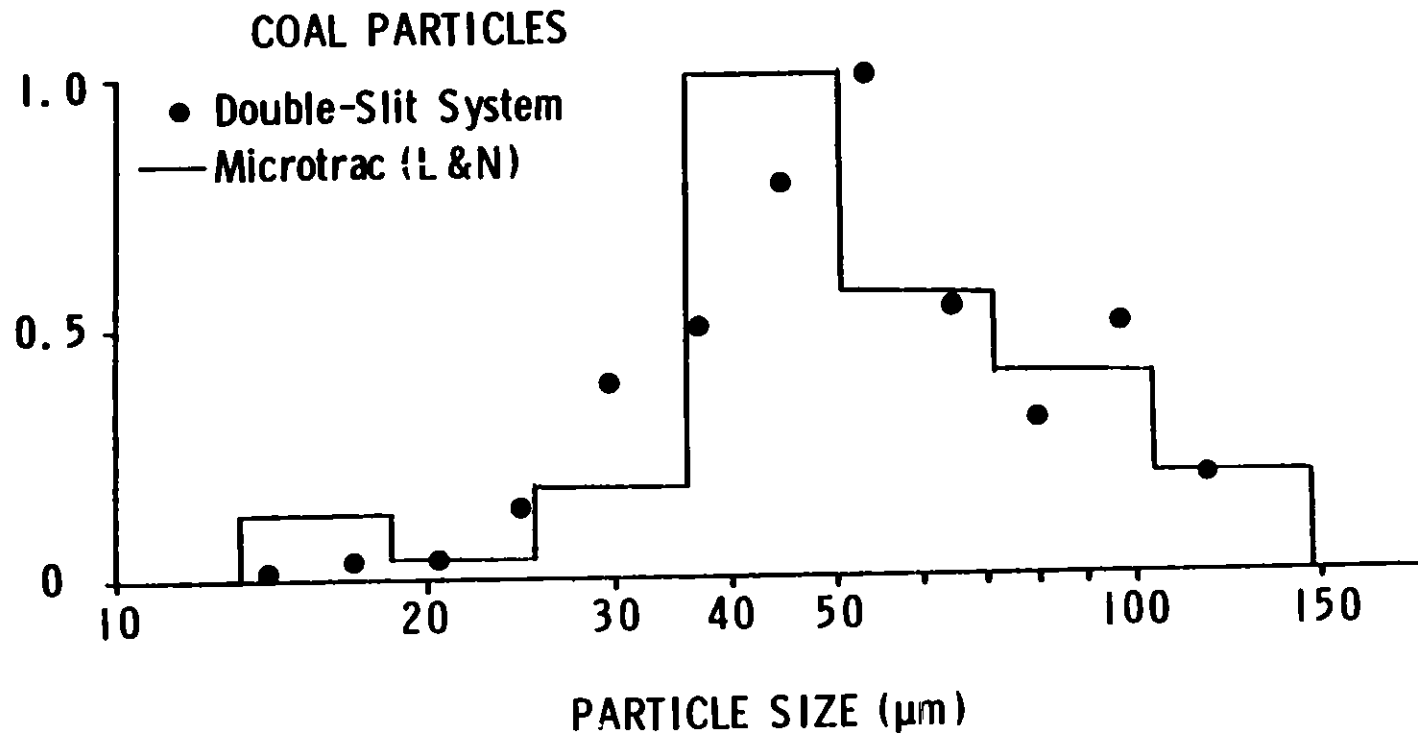


Figure 4. Size distribution of coal particles measured by the double-slit system and the Leeds and Northrup Microtrac analyzer.



ATOMIZATION OF COAL-METHANOL SLURRIES

S.J. Kim, E. Crow and C.T. Crowe  
Department of Mechanical Engineering  
Washington State University  
Pullman, Washington 99164-2920

Abstract

Experiments have been conducted to measure the drop size produced by atomization of a coal-methanol slurry with a two-fluid atomizer. The data show that the presence of the coal particles at concentrations up to 30% does not significantly affect the droplet size.

Introduction

With the increased need for energy and the dwindling supply of petroleum, there is no doubt that a greater reliance will be placed upon the use of coal. Even with the current usage growth rate, it is estimated that the coal reserves in the United States would last for 350 years. However, there are an abundance of technical problems which will accompany the increased usage of coal, these problems stem from excavation, refining, transportation and utilization.

Liquifaction and gasification are two means of utilizing the coal resources. A third, and a very promising means, is the direct mixing of solid coal particles with liquid fuels. By this means, the coal can be transported at a reasonable cost and, perhaps, can be used directly in oil-fired industrial furnaces with a minimum of modification.

Before an assessment can be made of the feasibility of this scheme, one must know more concerning the effects of the presence of coal particles on the liquid fuel combustion process. A specific concern is the effect of coal particles on the atomization of the coal-oil slurry, especially by the fact that the size of coal particles may be close to the nominal size of the droplets produced by atomization of the fuel alone.

It is common practice in the spray drying industry to atomize slurries. The primary concern is the size of the dried product. There is a scarcity of data in the literature pertaining to the effect of particle size and particle loading on the composition and size of the droplets produced by atomization. The two nozzle types commonly used for atomization of slurries are nozzle and wheel atomizers. With the wheel atomizer, atomization occurs upon discharge of the fluid from the periphery of a spinning disk. An atomizer possibly suitable for coal slurries is the two-fluid (slurry/air) or, more correctly, three-fluid (coal/liquid/air) nozzle. There is an abundance of information in the literature concerning the droplet size produced by two-fluid atomizers for single phase fluids, although there appears to be no information on the atomization of a coal-oil slurry using a two-fluid atomizer.

This paper presents some preliminary data on droplet size produced by atomization of coal-methanol slurries.

### Experimental Set-up

A schematic of the experimental set-up is shown in Figure 1. The primary objective of the set-up is to provide a continuous mixing of the slurry and to deliver this slurry to the two-fluid atomizer. The mixing tank consisted of a 50 gallon propane tank capable of withstanding pressures up to 250 psi. The mixing was accomplished by a recirculation of the slurry through the propane tank fitted with pipes which discharged the fluid along the periphery of the tank. A separate circuit with a gear pump was built to provide continuous mixing in the tank. Initially, a second circuit with a gear pump was installed to deliver the slurry to the atomizer. It was found, however, that such a delivery scheme did not function at all because the gear pump was incapable of supplying the slurry at the pressure required for the two-fluid atomizer. At this point, the design was changed and the mixing chamber was connected to a high pressure nitrogen bottle to move the slurry through the system by pressurizing the tank. After discharge through the nozzle, the spray was collected in a tank and returned to the mixing tank.

The two-fluid nozzle chosen for this study was a Delavan model 32668, an in-line swirl atomizing nozzle. This particular nozzle is capable of delivering four gallons per minute. In that that tests were conducted for four minutes, the amount of slurry in the tank had to exceed 16 gallons. The secondary air to the Delavan nozzle was supplied by 100 psi house air.

Originally it was intended to monitor the slurry flow rate by using a rotameter in the line. However, it was found that the slurry was so opaque that the float in the rotameter could not be seen. The system was modified to put a rotameter on the high pressure line supplying the tank, and the flow through the high pressure line was monitored to yield the slurry rate out of the tank and into the system.

Several initial checks were done on the system to assess such items as steadiness of the spray, uniformity of the spray in the test section, and the consistency of the slurry loading delivered to the nozzle. Samples of the spray were collected at several locations around the spray pattern and collected over different periods of time. It was found that the delivery rate of the slurry was steady. Also, the spray pattern was found to be uniform within a variation of 30 percent. The concentration of the slurry was measured from samples gathered at different times. It was found that the slurry concentration varied by less than 2 percent over the run time.

The original plan was to use photography to measure droplet size. Optical access to the chamber was provided by windows purged with a high velocity air stream issuing from a nozzle at the top of the window. The photographic system consisted of a camera mounted on a stereoscopic microscope to provide magnifications of ten or more. The light source consisted of a short-duration, high-intensity EGG light source coupled with a condensing lens. After many trials, no suitable photographs were obtained. It was felt that the difficulty arose from the low concentration of droplets in the region of measurement. The large magnifications severely restrict the field of view and the likelihood of locating a droplet.

After many futile attempts, photography was abandoned in favor of direct sampling. With this scheme, a slide is exposed to the spray for a short period of time. The slide was coated with magnesium oxide by burning magnesium ribbon beneath a glass microscope slide. By exposing the slide to the spray for a short period of time, the impinging droplets made impressions upon the magnesium oxide which were later photographed and analyzed to determine size. The direct sampling mechanism consisted of a cylinder with a hole on one side as shown in Figure 2. The coated microscope slide was inserted in the cylinder while the hole was positioned at the bottom; that is, away from the injector. When ready, the cylinder was rotated once, exposing the slide to the spray for a short period of time. It was found after some trial runs that, by adjusting the size of the hole, a representative sample with distinct droplets could be obtained. Microscope slides were then photographed and analyzed to determine the size distributions. A photograph of the magnesium oxide layer after exposure to the spray is shown in Figure 3.

### Results

The initial experiments were done with pure methanol in order to establish a baseline for the slurry experiments. Two air pressure levels were used; 30 and 60 psi. The coal particles used in the slurry had a nominal mass median diameter of 50 microns and coal concentrations of 15 percent and 30 percent (by weight) were tested. The flow rate of liquid/slurry was two gallons/min.

The results in terms of number median diameter for pure methanol and the two slurries are shown in the table below.

Fluid	Number Median Diameter (microns)	
	Air-Atomizing Pressure	
	30 psi	60 psi
Pure methanol	62	46
15% coal-methanol	65	55
30% coal-methanol	65	56

Table. Number mean diameter for methanol and coal-methanol sprays.

The expected decrease in droplet size with increased injection pressure is evident. One notes that the droplet sizes were increased but not changed significantly by the presence of the coal. It was also noted in analyzing the photographs that, in some cases, some droplets contained no coal particles at all. Also, at times there appeared to be some coal particles separated completely from the methanol which suggests some separation of the methanol from the coal in the atomizing process. One also notes from these data that the concentration of the slurry did not seem to have an appreciable effect.

One of the difficulties with these data is the fact that the droplet sizes for pure methanol are larger than would be expected from the manufacturer's data for a pure liquid. The reason for this trend is presently not known. It is anticipated that the droplet sizes were measured quite far

from the atomizing nozzle and it is likely that there could have been some agglomeration of the droplets before reaching the measuring station.

Another difficulty with the experimental set-up has been the effect of the gear pump used in the mixing circuit on particle size in the slurry. After several tests, possibly a total operating time of an hour, it was found that the particle size was measurably decreased. This reduction was attributed to the action of the gear pump.

A new system has been designed, fabricated and currently is in operation. The new system allows direct photography of the spray without the encumbrance of windows. Also, a radial flow pump is used in the mixing circuit to avoid crushing the particles. The data from these tests will be available soon.

#### Acknowledgements

The authors acknowledge the support of DOE grant No. DE-FG22-80PC30216.

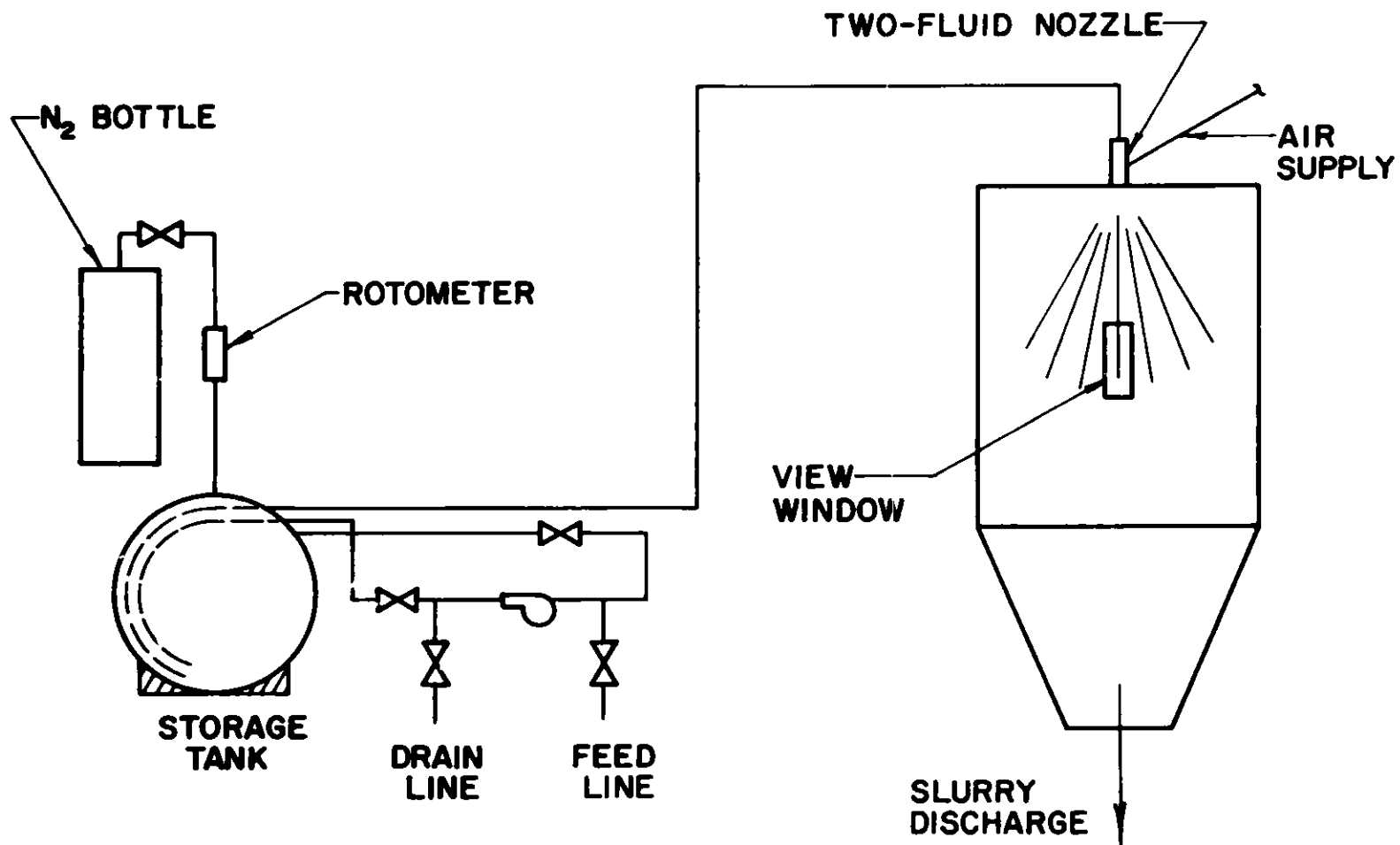


Figure 1. Schematic diagram of experimental set-up.

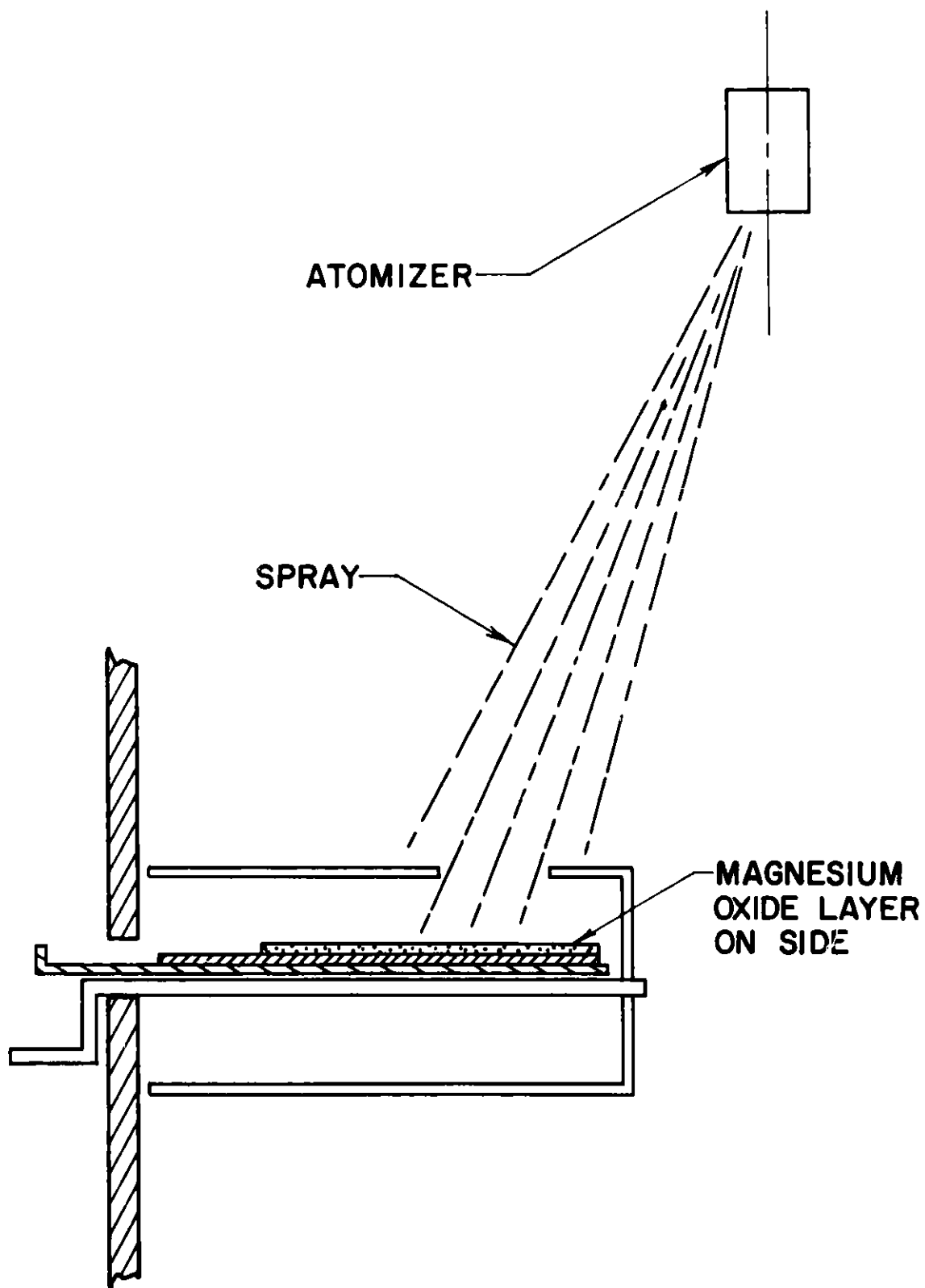


Figure 2. Direct sampling system.

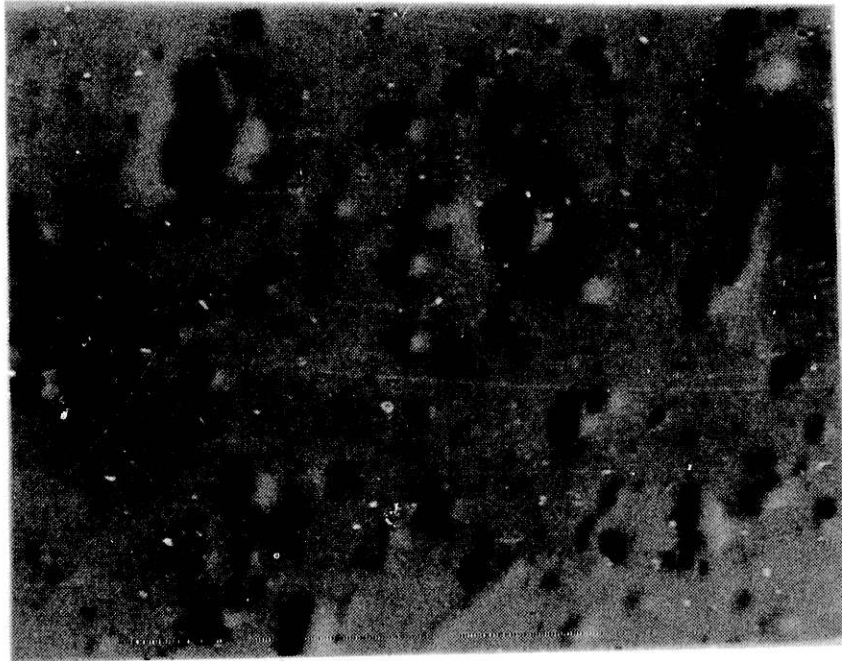


Figure 3. Photograph of exposed MgO layer

SAND82-8611  
Unlimited Release  
Printed August 1982

PARTICLE COLLECTION BY CYCLONES  
AT HIGH TEMPERATURE AND PRESSURE\*

James C. F. Wang  
Combustion Research Division  
and  
Marcus A. Libkind  
Combustion Engineering Division  
Sandia National Laboratories  
Livermore, California 94550

ABSTRACT

We have completed an experimental study using cyclones as a part of a particulate sampling system at temperatures up to 1100 K and pressures up to 11 atm. The particle collection efficiency of three different cyclones at a fixed cyclone inlet velocity was found to decrease as temperature increased or pressure decreased. This effect cannot be explained by the existing cyclone models. The 50 percent particle cut-size of each cyclone appears to correlate well with a nondimensional parameter related to the Reynolds number and the square root of the Stokes number. This correlation suggests that the cyclone efficiency depends on the viscosity and density of the sampled gas. Our results are compared with those of other investigators.

---

\*Sponsored by the U.S. Department of Energy/Morgantown Energy Technology Center. Presented at the 1982 Symposium on Instrumentation and Control for Fossil Energy Processes, Houston, Texas, June 7-9, 1982.



## INTRODUCTION

The pressurized fluidized bed combustor (PFBC) is an advanced system for the direct combustion of coal in an environmentally acceptable manner. The combustion gases from a typical PFBC contain significant quantities of erosive coal ash and attrited bed material, as well as corrosive alkali metal compounds. Thus, a key technical objective in the commercialization of the PFBC is to achieve acceptable combustion gas composition with reliable gas turbine operation. Definition of gas components is needed to guide the development of suitable hot-gas cleanup equipment and improved turbine materials.

Hot-gas cleanup components are designed to control mass loading and size distribution of particulate emissions from a PFBC. Commercially available instruments for particle detection are either optical devices that do not measure particle mass directly or sampling devices that do not provide real-time measurements. Recently we demonstrated the feasibility of using the tapered-element oscillating microbalance (TEOM) for real-time particle mass measurements at room temperature.<sup>1</sup> The objective of the current program, which is sponsored by Morgantown Energy Technology Center, Department of Energy, is to develop a real-time particle mass monitor for applications in PFBC streams. This particle mass monitor has been designed to (1) collect samples under high temperature and high pressure PFBC environments, (2) classify particles aerodynamically, (3) measure the particle mass of each size-fraction in real time, and (4) clean the

particle collectors automatically for prolonged continuous operation. In this paper, we describe our efforts to identify means of classifying particles aerodynamically and calibrating the size classification.

Although particles have been classified in many applications with a set of cyclones, their collection efficiency has been found to depend on the operating conditions. Each cyclone is designed to have a specific collection efficiency curve with respect to the size of the particles. Ideally, the efficiency curves of these cyclones should not overlap; thus, particles collected in each cyclone belong to a certain size range related to the cut-size of the cyclone. In practice, however, the collection efficiency curves of these cyclones do overlap and vary with respect to the temperature, pressure, and velocity of the sampled gas stream, the types of particles, and the number density of the particles. In order to obtain real-time measurements on the particle size-fraction from these cyclone catches, we need to know their collection efficiencies a priori at their designed operating condition. The objective of our test was to obtain the efficiency of each cyclone in the cyclone train at the PFBC exhaust conditions so it could be used as calibration data for the real-time particle size-fraction measurements.

#### PARTICLE MASS MONITOR SYSTEM

Figure 1 shows a schematic diagram of the real-time particle mass monitor system developed at Sandia National Laboratories at Livermore (SNLL). The sampling probe and cyclone train are heated electrically to 1100 K to keep the

sampled gas from cooling. The cyclone train and the real-time mass detectors (TEOM) are housed inside a pressure vessel and both are kept at the PFBC pressure. The combination of electrical heaters and the pressure vessel allows the sampled gas to be at the PFBC exhaust condition, thus minimizing the measurement biases encountered in other sampling arrangements from dilution, cooling, and depressurization. The sampling nozzle is designed to satisfy the isokinetic sampling requirements and the fixed inlet velocity requirement for a consistent cyclone operation. Different sampling nozzles are needed for process streams at different velocities.

The cyclones, which are used to classify sampled particles, are a set modified from an Acurex Source Assessment Sampling System (SASS). They were redesigned with flanges and thicker material for high-temperature and high-pressure operation. The inside geometry of these cyclones is identical to that of the original SASS train. Figure 2 shows a picture of the three SASS cyclones connected in series. The collection cup at the bottom of each cyclone would be replaced by the TEOM detector for real-time measurements. However, during our cyclone calibration test, these cups were used.

We made other modifications on the SASS train to interface each cyclone to a TEOM detector. Figure 3 shows a schematic diagram of a typical cyclone arrangement. Added to the bottom of the cyclone is a funnel that has a slope closely matching that of the cyclone body. The purpose of this funnel is to reduce the diameter of the opening of the dust outlet to less than 2.5 cm, which is the dimension of the dust collector of the TEOM detector. A second modification is the addition of a swirl baffle at the bottom of the funnel. The swirl baffle is a crossed baffle whose length

dimension is aligned with the axis of the cyclone, as shown in Figure 4. This swirl baffle is designed to break up any cyclic motion of the cyclone flow before the flow reaches the TEOM detector and introduces noise to the real-time mass measurements. Table 1 lists the geometric data of the cyclone arrangements. The notation used in the table also appears in Figure 3.

According to the manufacturer, the original SASS train cyclones have particle cut-sizes around 10, 3, and 1  $\mu\text{m}$  at room temperature. Because the gas turbine manufacturers and environmental groups have interests in particles at these sizes, we selected the SASS train as the particle classifier for the mass monitor system. For this paper, these cyclones have been designated as 10, 3, and 1  $\mu\text{m}$  cyclones.

In our test, the sampled gas from the cyclone train is cooled in a condenser, then passes the metering valve and flow meter before exhausting to the atmosphere. The sampling velocity is manually controlled by the metering valve and is measured by the flow meter. An HP85 computer and HP-3497A data logger are used to record all temperature, pressure, and flow-rate information on the monitor.

The critical component in this monitor is the real-time TEOM detector. Since the development of the TEOM detector is not related to the present test, it is not described here. References 1 and 2 provide detailed descriptions on the TEOM for interested readers.

## EXPERIMENTAL SET-UP AT WESTINGHOUSE

The calibration test for these modified SASS cyclones was conducted at the Westinghouse Waltz-Mill facility in Madison, Pennsylvania, in September 1981. This facility was designed, constructed, and operated by Westinghouse with the support of both the Department of Energy and the Environmental Protection Agency for evaluating particle removal equipment at temperatures up to 1150 K and pressures up to 15 atm. It is, however, not a PFBC. Hot-gas flows up to 5.5 kg/s, or 4.25 m<sup>3</sup>/s, can be provided. Equipment up to 1.37 m in diameter and 2.44 m in length can be mounted within an insulated pressure vessel for testing. Figure 5 shows a simplified schematic of the Westinghouse test facility (Test Passage 5) which comprises a pressure chamber, dust injection system, dust sampling and classification system, and interconnecting piping. Other equipment (not shown in the figure) includes air compressors, preheaters, fuel supply, combustor, muffle chamber, and controls.

During the SNLL sampling cyclone test, Acurex's ceramic bag filter was tested at the same Westinghouse test passage. The Acurex filter was housed inside the pressure chamber and was tested simultaneously with our test. The SNLL sampling system was located at the inlet pipe to the Acurex filter. Grab samples were periodically taken by Westinghouse at both the inlet and outlet of the Acurex filter with impactors. The particle loading measurements by the inlet grab sampler were used as references to the SNLL sampling cyclone tests.

Fly ash from a hot-gas cleanup cyclone at Curtiss-Wright Small Gas Turbine PFBC was injected in the test stream via the Westinghouse dust injection system at

an average rate of 2.3 g/s. The size distribution of the fly ash in the injection system has a number mean of 3  $\mu\text{m}$  and an upper limit at 40  $\mu\text{m}$  (in Figure 6). Table 2 shows the operation conditions of the cyclone test at the facility. The sampling rate was varied to keep the sampling velocity constant and matched to that of the process stream for isokinetic sampling operation.

#### CYCLONE CALIBRATION TEST

The objective of the cyclone test conducted at the Westinghouse Waltz-Mill facility was to obtain calibration information on the particle collection efficiency of individual cyclones in the SASS train. To achieve this objective, we decided that we needed to test each cyclone with inlet particles of a known size distribution. By comparing the size distributions of the inlet particles and the cyclone collected particles, we could determine the particle collection efficiency of that particular cyclone. Samples of the inlet particles entering the cyclones were obtained by replacing the test cyclone with a filter which collects all particles larger than 0.5  $\mu\text{m}$ . A schematic diagram of the test arrangement is shown in Figure 7. The sampling nozzle, heated probe, pressure vessel, condenser, metering valve, and flow meter were the same as those in the complete real-time particle mass monitoring system. Only one cyclone or filter was tested inside the pressure vessel at one time. The real-time mass detector TEOM was replaced by a regular dust collector supplied by Acurex Corp. The funnel and swirl baffle were installed at the bottom of each cyclone dust outlet port.

For each cyclone, four process-stream flow conditions were tested (Table 2).

The sampling system was pressurized and heated to the process-stream condition before the sampling nozzle was inserted into the process stream. Each sample was collected for about 30 minutes before the sampling system was withdrawn from the process stream. A dust sample was collected from the cyclone collection cup and stored for off-line size analyses.

Particle samples collected by the cyclones and the filter were analyzed by an impactor, a Coulter counter and a Quantimet image analyzer, to obtain size distribution measurements. The particle collection efficiency of the cyclones was obtained by comparing the fractional size distributions of the cyclone-collected samples with those of the positive filter at the same condition. Because particle size measurements at  $1\ \mu\text{m}$  or smaller from the impactor and Coulter counter analyzers were too poor to yield reasonable cyclone efficiency data, all cyclone efficiency data reported here are based on results from the Quantimet image analyzer. The lower limit on particle size measurements from the Quantimet is about  $0.5\ \mu\text{m}$ . Accuracy in size measurements for particles less than  $1\ \mu\text{m}$  is deteriorated as they approach this lower limit.

Each sample was counted at two magnifications: 360x and 1000x. The field size at each magnification was adjusted to count not more than 500 particles. Ten thousand particle counts were obtained to form a size-distribution histogram at each magnification. A combined histogram was obtained from the histograms at these two magnifications based on their field sizes. Figure 8 shows typical combined histograms of the cyclone-collected samples. The size distribution of the sample from the  $1\ \mu\text{m}$  cyclone closely resembles that from the positive filter. Less small particles

are found in the sample from the 10  $\mu\text{m}$  cyclone, as expected. For particles larger than 10  $\mu\text{m}$ , slopes of both distributions should be similar because those large particles are collected by both devices with inlet dust of similar size distributions. For data comparisons, we normalize the particle size distributions of the cyclone samples by matching the slopes of these distribution curves at the large particle side.

Figure 9 depicts how the cyclone efficiency data are obtained. The thick curve, which shows a normalized size distribution of particles collected on the positive filter, is used as the reference data. The thin-line curves represent the size distributions of the particles collected in the three cyclones tested. The slopes of these cyclone curves at the large particle side are matched to that of the reference size distribution curve from the filter. The measurement transfer function of the Quantimet analyzer at each particle size is assumed to be a constant. The particle collection efficiency of a cyclone (e.g., the 3  $\mu\text{m}$  cyclone in Figure 9) at a specific size ( $d_j$ ) can be obtained by

$$\eta(d_j) = \frac{n_j}{N_j}$$

where  $\eta(d_j)$  = cyclone efficiency at particle size  $d_j$

$n_j$  = modified particle number density of the cyclone sample  
at size  $d_j$

$N_j$  = particle number density of the filter sample at size  $d_j$



"Modified particle number density" means that the vertical scale of the size distribution of the cyclone sample has been adjusted to match the slope for the large particles to the normalized reference size distribution from the positive filter sample at the same operating temperature and pressure conditions.

#### TEST RESULTS

Figure 10 shows the particle collection efficiencies of all three SASS cyclones tested at a typical PFBC exhaust condition, i.e., 1100 K and 6.44 atm. Lines have been drawn between data points to aid visual interpretation. (Similar shapes on efficiencies are obtained for these cyclones at other test conditions.) The fact that these efficiency curves are separate from each other makes the real-time particle size-fraction measurements feasible: The real-time particle mass monitor is designed to have these three cyclones connected in series. On the basis of the data in Figure 10, the 10  $\mu\text{m}$  cyclone will collect nearly 100 percent of those particles larger than 20  $\mu\text{m}$  and 50 percent of those particles at 10  $\mu\text{m}$  at this PFBC exhaust condition. Downstream from the 10  $\mu\text{m}$  cyclone, the 3  $\mu\text{m}$  cyclone will collect particles with sizes between 3 and 20  $\mu\text{m}$ , and particles larger than 10  $\mu\text{m}$  with 100 percent efficiency. The 1  $\mu\text{m}$  cyclone, the third cyclone in series, will collect particles with sizes between 0.3 and 10  $\mu\text{m}$ , and particles larger than 1.5  $\mu\text{m}$  with 50 percent efficiency or greater. With simultaneous measurements of the

particle mass collected on these cyclones in series, one can estimate the relative particle population in sizes larger than 10  $\mu\text{m}$ , between 6 and 10  $\mu\text{m}$ , and between 1.5 and 6  $\mu\text{m}$  based on the 50 percent cut-size of each cyclone. The total particle mass or the dust loading density can be obtained by adding the measurements from all three cyclones.

Figures 11 through 13 show the particle collection efficiency of each cyclone at four temperature and pressure conditions. These results indicate that the efficiency of the cyclones tested at a fixed cyclone inlet velocity decreases as the temperature of the carrier gas increases. Conversely, the efficiency decreases as the pressure of the sampling system decreases. The latter cannot be explained by the existing cyclone models, which predict that the cyclone efficiency should be independent or only weakly dependent on pressure.

In fact, it is well known that, in practice, cyclone performance does not follow any existing model. Empirical correlations have been used by many cyclone designers or researchers.(4,5) The popular correlation parameters are the Reynolds number and the Stokes number. Figure 14 shows plots of the 50 percent particle cut-size of each cyclone versus the nondimensional product of Reynolds number and the square root of the Stokes number. These nondimensional parameters are defined with the nomenclature used in Reference 5 as follows:

$$N_{\text{Re}} = \frac{D u \rho_G}{\mu_G} = \text{Reynolds number,}$$

where  $D$  = cyclone diameter, cm

$u$  = average cyclone inlet velocity, cm/s

$\rho_G$  = gas density, g/cm

$\mu_G$  = gas viscosity, g/(cm·s)

and

$$N_{Stk} = \frac{C' d_p^2 \rho_p u}{9 \mu_G d_H} = \text{Stokes number,}$$

where  $C'$  = Cunningham slip correction factor

$d_p$  = particle diameter,  $\mu\text{m}$

$\rho_p$  = particle density, g/cm

$d_H$  = hydraulic diameter of the cyclone inlet, cm.

Good correlations were obtained for the 10  $\mu\text{m}$  and 3  $\mu\text{m}$  cyclones, suggesting that the cyclone efficiency depends on the viscosity and density of the sampled gas. A similar correlation was also reported in the literature. However, based on our limited test data, results from different cyclones do not correlate with each other. The fact that the data appear to be parallel

to each other indicates that cyclone size is also an important parameter. Data from the 1  $\mu\text{m}$  cyclone are not aligned on a straight line, but spread along the general trend of the data from other researchers. Further tests are needed to establish an empirical scaling law on cyclone performances.

Recently, Dietz(6) developed a cyclone model which is a modification of that of Leith and Licht.(3) When we attempted to correlate our data to Dietz's model, limited success was obtained. Good agreement was obtained between the theory and data for the 10  $\mu\text{m}$  cyclone performance. For the 1  $\mu\text{m}$  cyclone, fair agreement was obtained between the theory and data. However, no agreement was obtained for the 3  $\mu\text{m}$  cyclone. Further R&D effort is needed in developing cyclone models and in performing tests so that the cyclone behavior can be understood and better predictions can be made.

### CONCLUSIONS

At the Westinghouse Waltz-Mill facility, we achieved our test objectives of obtaining particle-collection-efficiency calibrations for the modified SASS cyclones at the PFBC exhaust conditions. These calibrations allow us to measure particle mass and size-fraction distribution at critical size ranges, namely larger than 10  $\mu\text{m}$ , between 3 and 10  $\mu\text{m}$ , and between 0.3 and 3  $\mu\text{m}$ .

The particle collection efficiency of the cyclones tested at a fixed inlet velocity was found to decrease as temperature increased or pressure decreased. Limited success was obtained when we correlated our data with an empirical parameter,  $N_{Re} (N_{Stk})^{1/2}$ , and a recent cyclone model. It is evident from our

test that further cyclone tests are needed to assess the cyclone models and to establish empirical scaling laws for cyclone performance in general.

#### ACKNOWLEDGMENTS

The authors would like to thank the following persons: E. Porter of SNLL for assembling the cyclone hardware and assisting with the test; B. Frazee of Butler Service Group for designing the hardware; R. O'Rourke, D. Ciliberti, and B. Turner of Westinghouse for conducting the tests and performing the impactor and Coulter analyses; M. Perry and P. Dietz of General Electric for computing the cyclone performance from their model; C. Slettevold and T. Quick of Lawrence Livermore National Laboratory for performing the Coulter and Quantimet analyses; and M. Shackleton and J. Sawyer of Acurex for allowing us to perform our test jointly with their experiment at Westinghouse.

#### REFERENCES

1. J. C. F. Wang, H. Patashnick and G. Rupprecht, "A New Real-Time Isokinetic Dust Mass Monitoring System," JAPCA, 30, p. 1018, September 1980.

2. J. C. F. Wang, H. Patashnick and G. Rupprecht, "Recent Developments on a Real-Time Particulate Mass Monitor for Stack Emission Applications," JAPCA, 31, p. 1194, November 1981.
3. D. Leith and W. Licht, "The Collection Efficiency of Cyclone-Type Particle Collectors--A New Theoretical Approach," AICHE Symposium, Series 1972.
4. J. M. Beechmans, In Aerosol Measurement, ed. by D. Lundgren, University of Florida Press, Gainesville, FL, 1979.
5. R. Parker, R. Jain, S. Calvert, D. Drehmel, and J. Abbott, "Particle Collection in Cyclones at High Temperature and High Pressure," Environmental Science and Technology, 15, p. 451, 1981.
6. P. W. Dietz, "Collection Efficiency of Cyclone Separators," General Electric Internal Report No. 79CRD244, 1979.

TABLE 1  
CYCLONE DIMENSIONS (cm)

Notation	10 $\mu\text{m}$ Cyclone	3 $\mu\text{m}$ Cyclone	1 $\mu\text{m}$ Cyclone
S	4.6	6.99	1.59
$R_C$	7.64	4.09	1.82
$R_t$	3.33	0.64	0.56
h	7.62	8.26	2.22
H	12.86	15.24	7.0
a	4.76	1.28	1.12

TABLE 2  
OPERATING CONDITIONS

	Run #1	Run #2	Run #3	Run #4
Pressure (atm)	6.44	6.44	11.1	11.1
Temp. (K)	700	1100	1100	700
Air Density (Kg/m <sup>3</sup> )	3.2	2.0	3.5	5.6
Sampling Volume Flow Rate (m <sup>3</sup> /min)	0.5754	1.0	0.3525	0.6128
Particle Mass Density (Kg/m <sup>3</sup> )	1.5 ~ 2.5 $\times 10^3$	1.5 ~ 2.5 $\times 10^3$	1.5 ~ 2.5 $\times 10^3$	1.5 ~ 2.5 $\times 10^3$
Gas Viscosity (g/S.cm)	$3.45 \times 10^{-4}$	$4.42 \times 10^{-4}$	$4.42 \times 10^{-4}$	$3.45 \times 10^{-4}$

## FIGURE CAPTIONS

- Fig. 1. Schematic diagram of the SNLL real-time particle mass monitor system.
- Fig. 2. Picture of the SASS cyclone train.
- Fig. 3. Schematic diagram of the cyclone, funnel, and swirl baffle arrangement.
- Fig. 4. Picture of the funnel, swirl baffle, and dust collection cup.
- Fig. 5. Schematic diagram of the test facility at Westinghouse Waltz-Mill site.
- Fig. 6. Particle size distribution of the fly ash used at the Westinghouse test facility.
- Fig. 7. Schematic diagram of the test arrangement at Westinghouse test facility.
- Fig. 8. Typical particle size distributions from samples collected at 1 and 10  $\mu\text{m}$  cyclones.
- Fig. 9. Data reduction procedure for obtaining particle collection efficiency of the cyclones.



Fig. 10. Calibration results of SASS cyclones at 1100 K and 6.44 atm.

Fig. 11. Calibration results of 10  $\mu\text{m}$  cyclone.

Fig. 12. Calibration results of 3  $\mu\text{m}$  cyclone.

Fig. 13. Calibration results of 1  $\mu\text{m}$  cyclone.

Fig. 14. Correlation of cyclone 50 percent cut-size with respect to  $(N_{Re})(N_{Stk})^{0.5}$ . A.P.T. and Exxon data are duplicated from Reference 5.

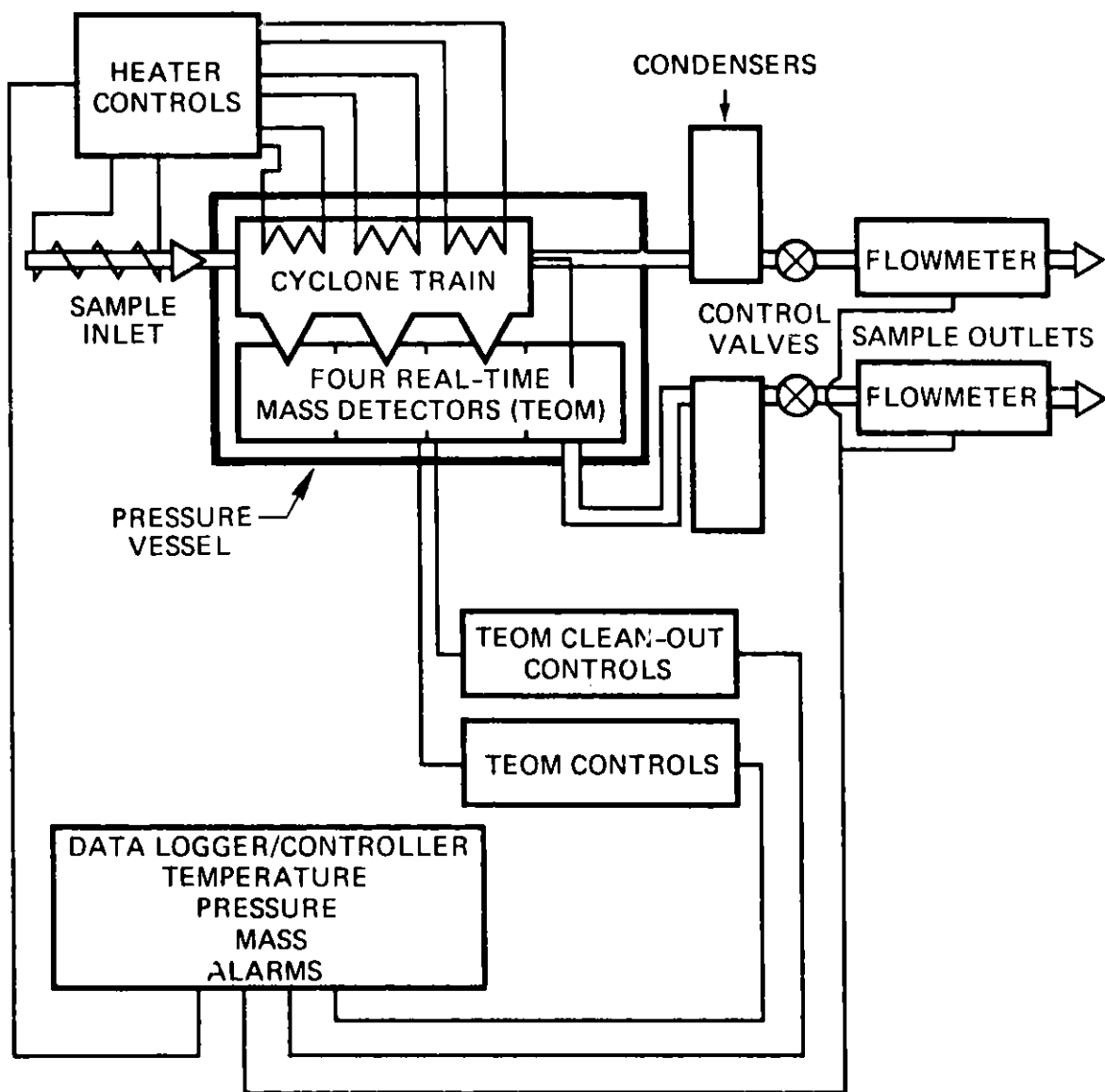


Figure 1. Schematic diagram of the SNLL real-time particle mass monitor system.

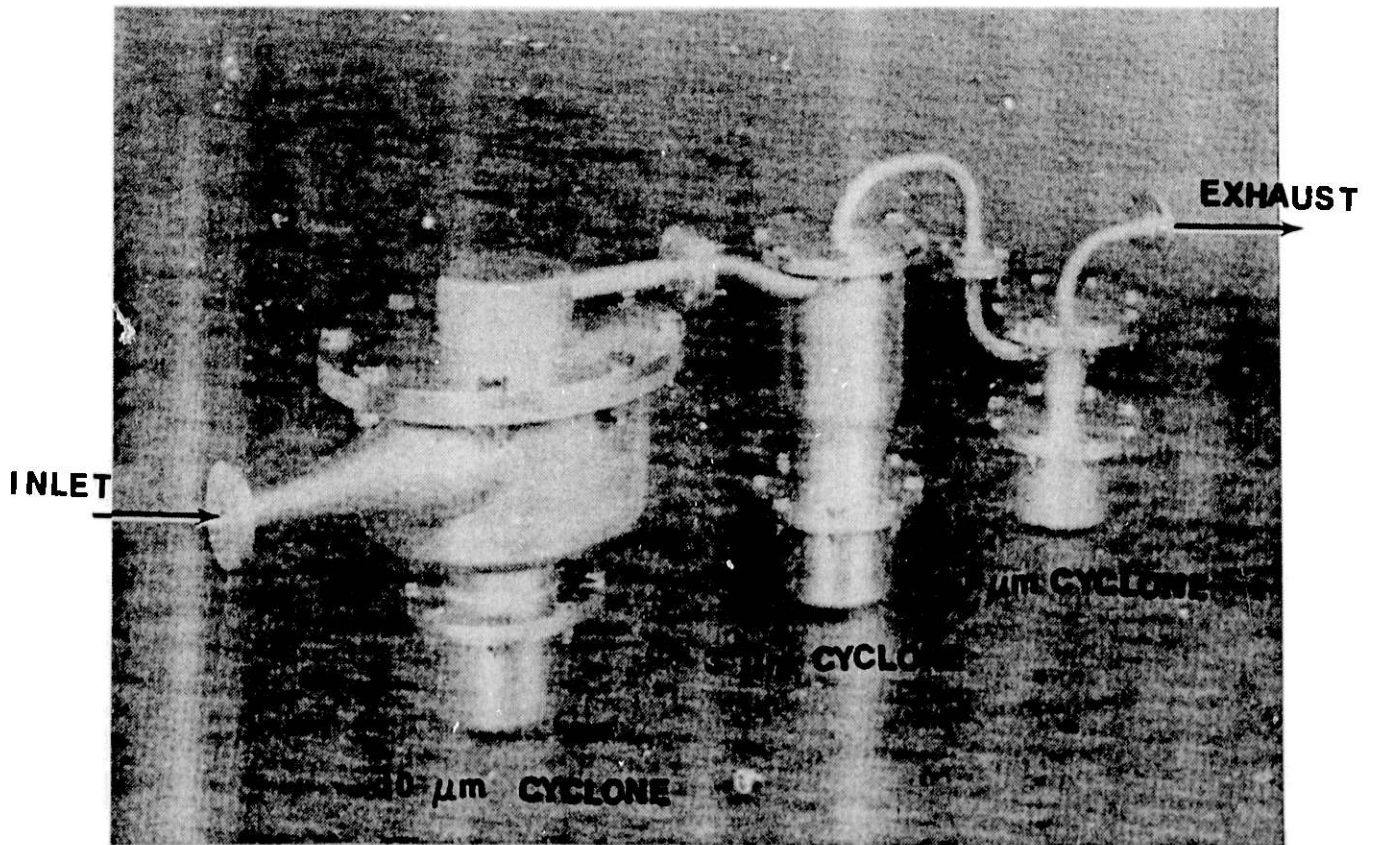


Figure 2. Picture of the SASS cyclone train.

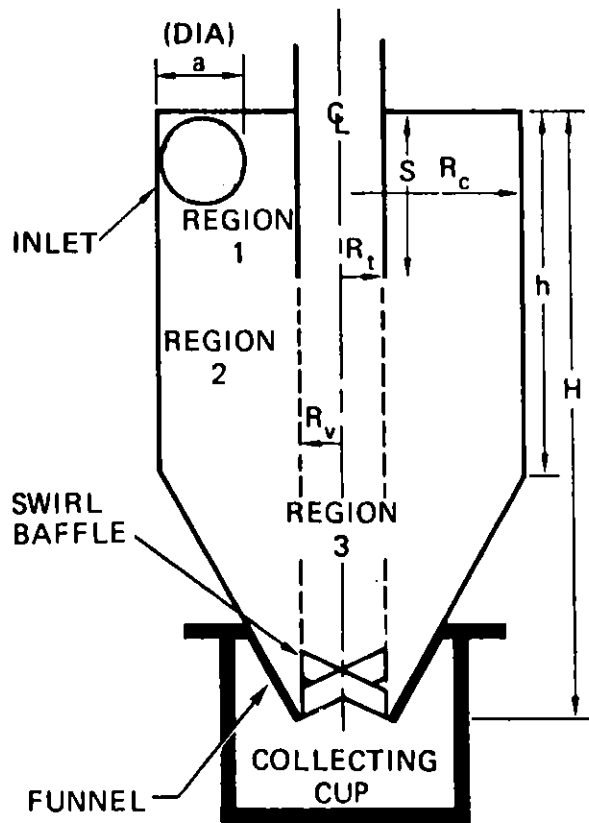


Figure 3. Schematic diagram of the cyclone, funnel and swirl baffle arrangement.

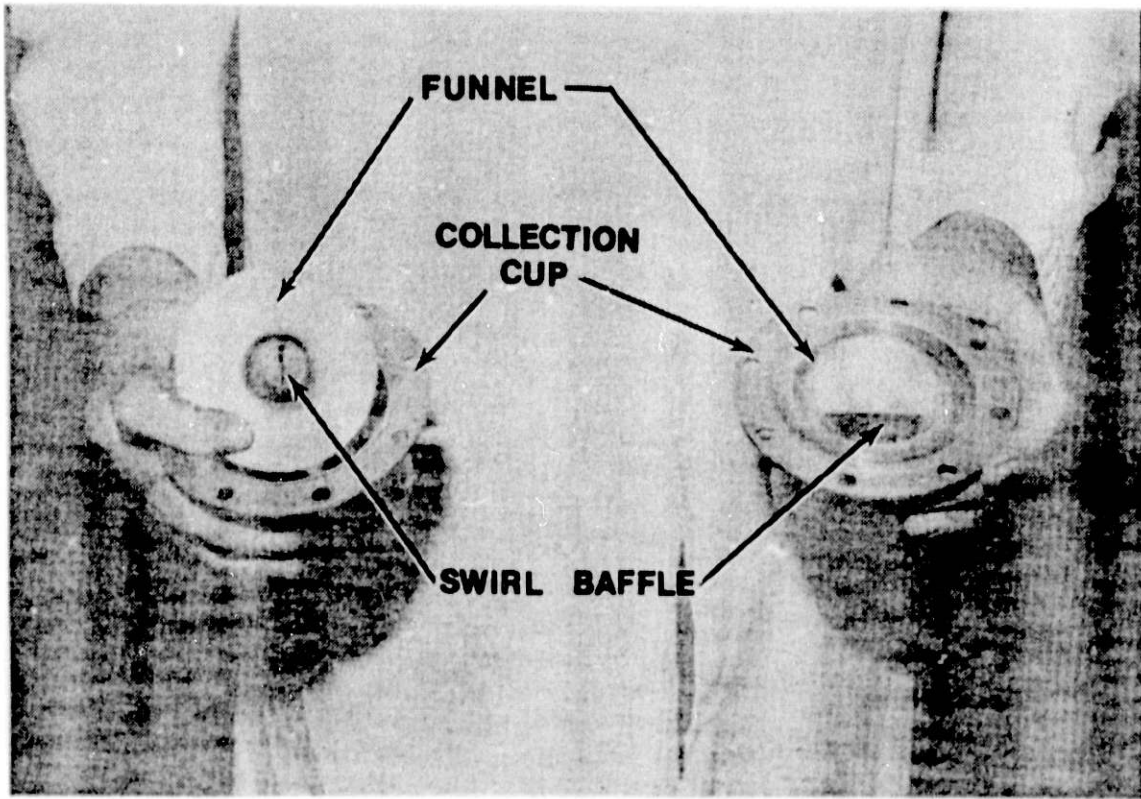


Figure 4. Picture of the funnel, swirl baffle and dust collection cup.

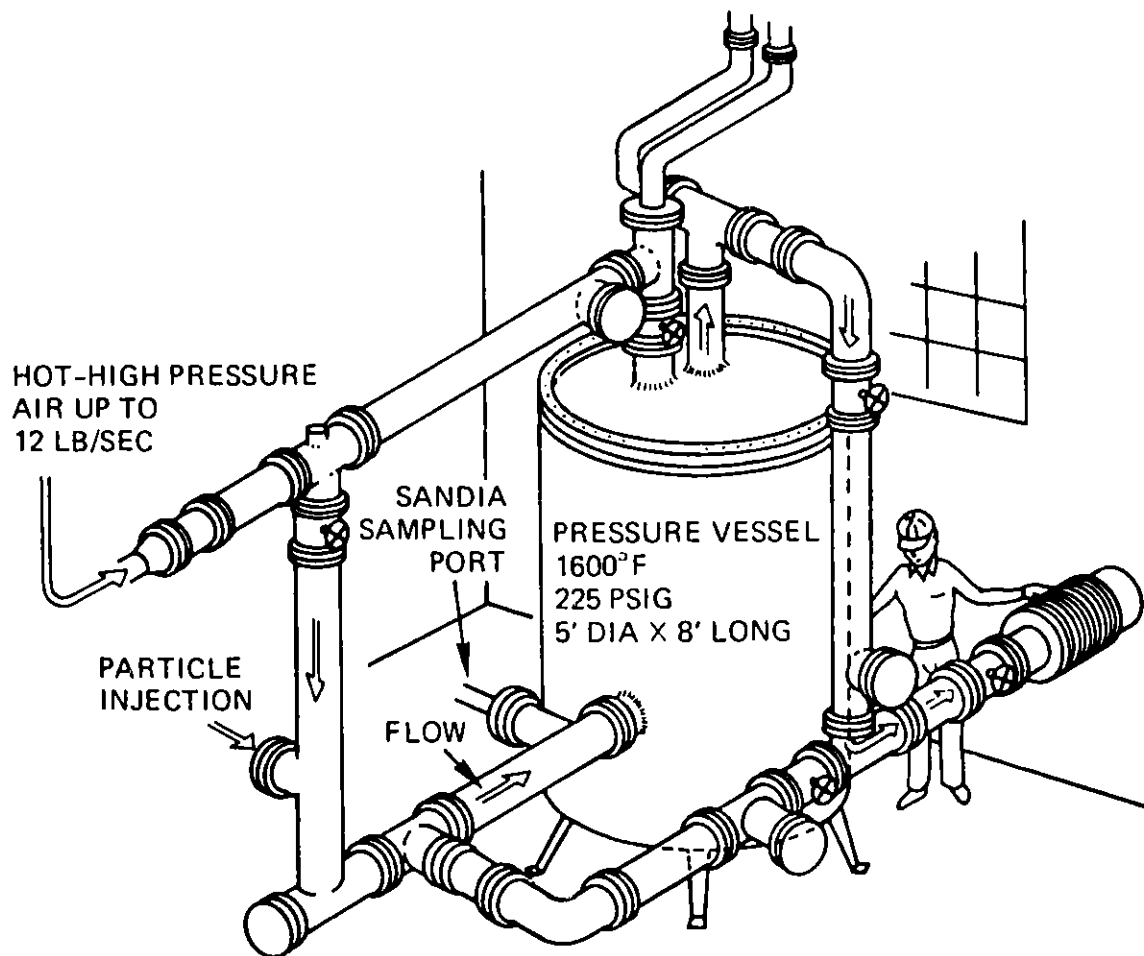


Figure 5. Schematic diagram of the test facility at Westinghouse Waltz-Mill site.

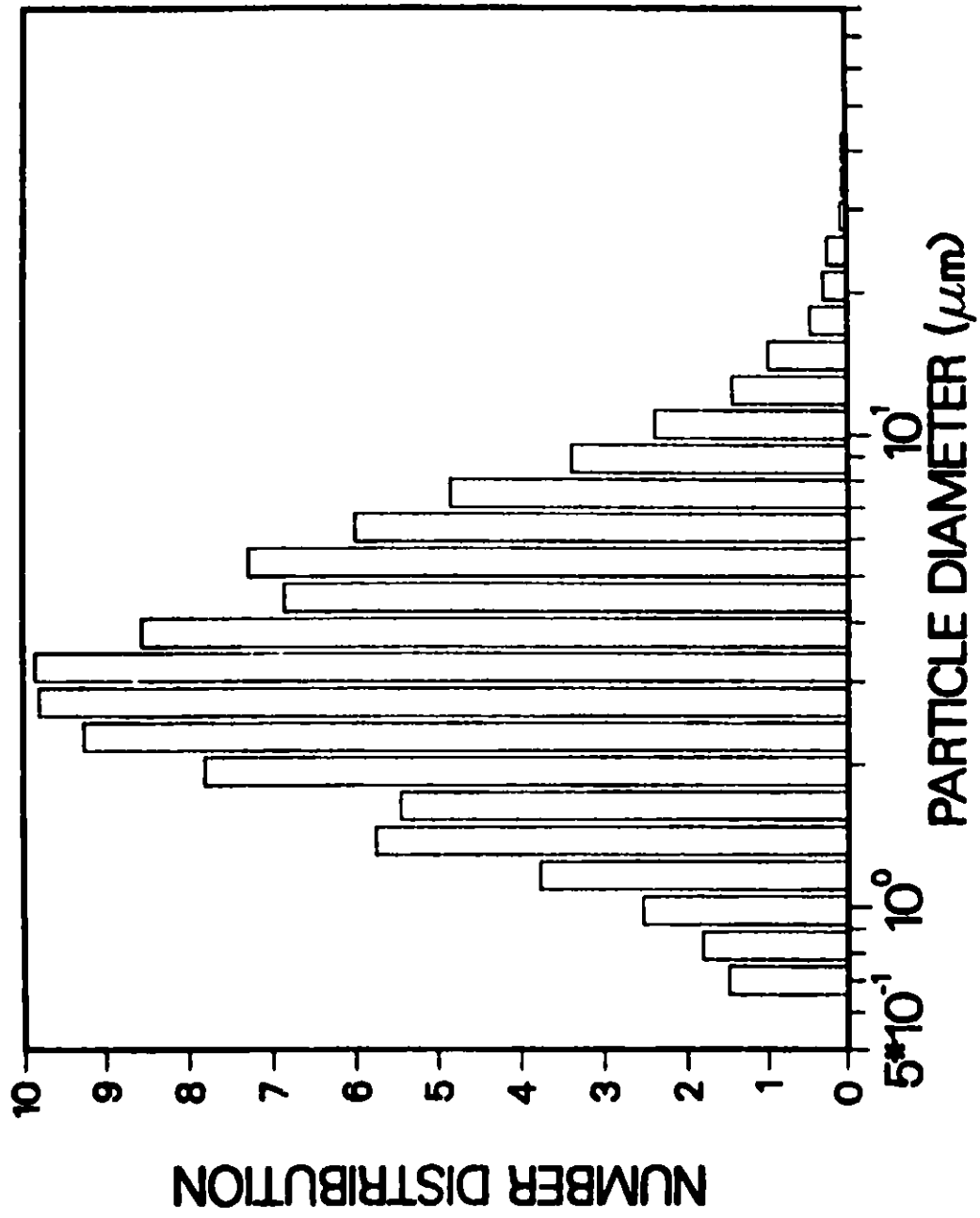


Figure 6. Particle size distribution of the fly ash used at the Westinghouse test facility.

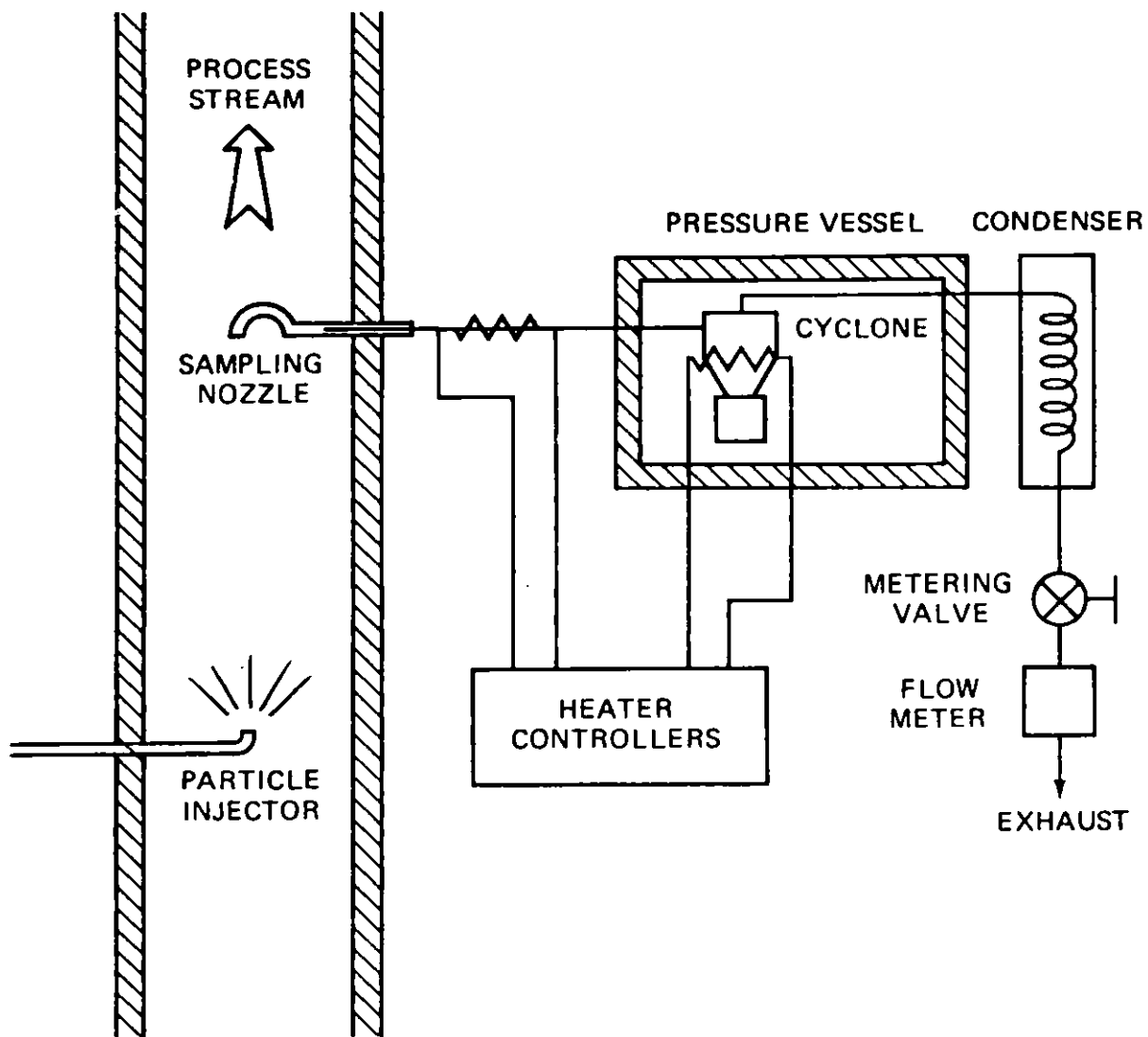


Figure 7. Schematic diagram of the test arrangement at Westinghouse test facility.



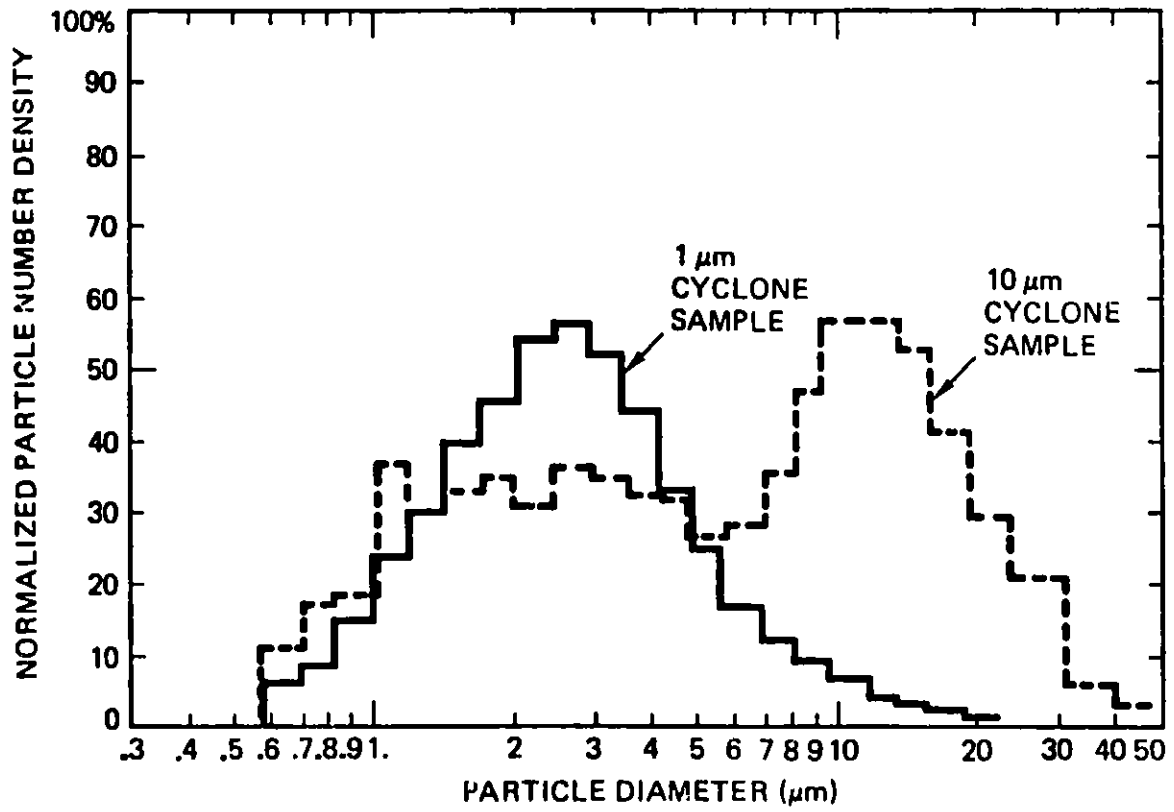


Figure 8. Typical particle size distributions from samples collected at 1 and 10 μm cyclones.

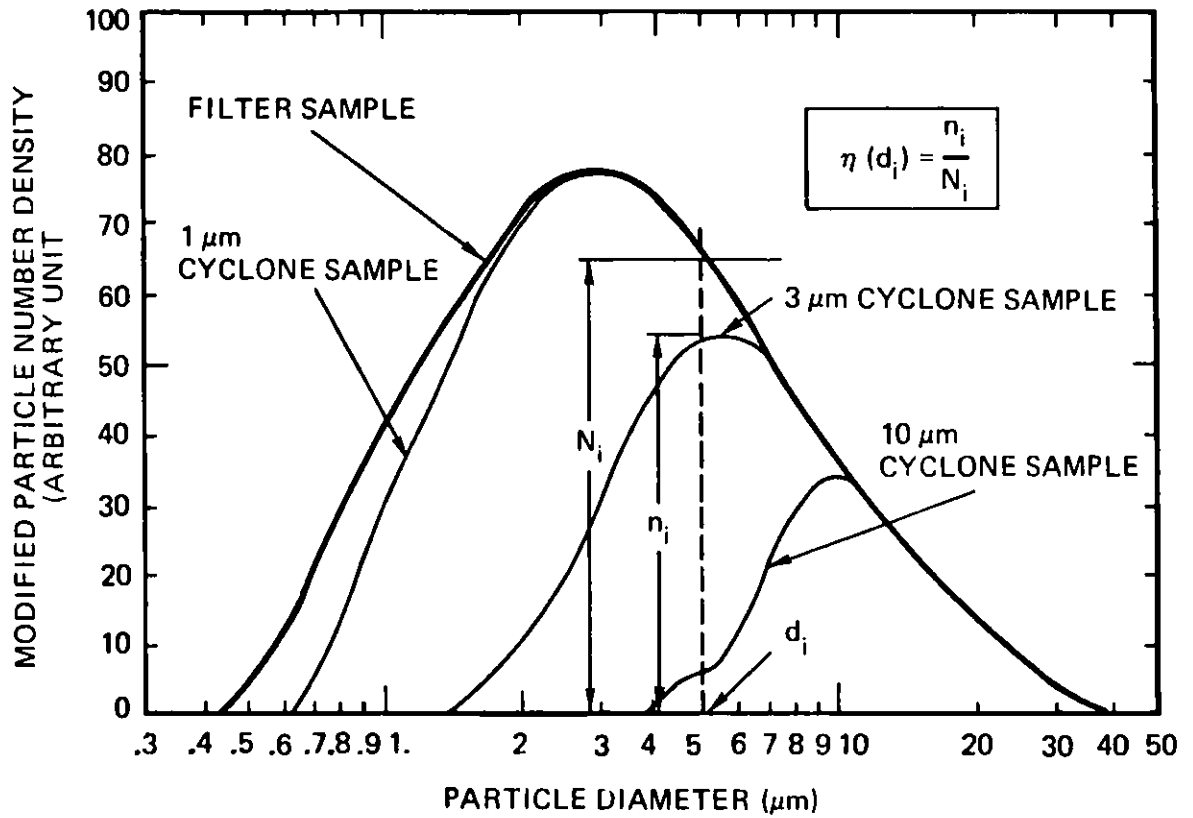


Figure 9. Data reduction procedure for obtaining particle collection efficiency of the cyclones.

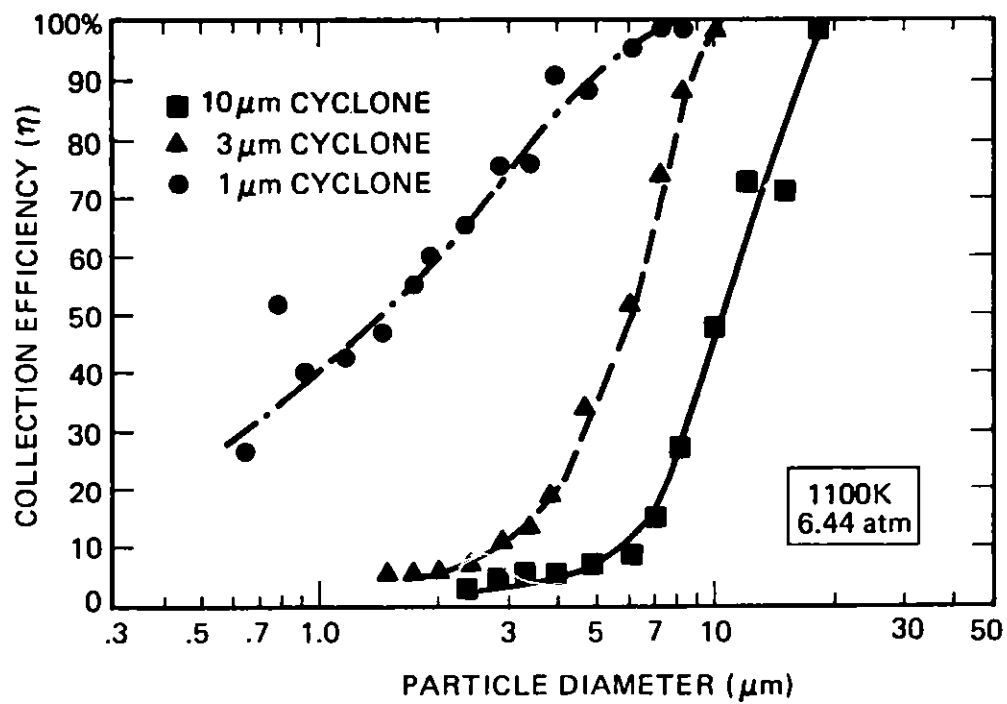


Figure 10. Calibration results of SASS cyclones at 1100 K and 6.44 atm.

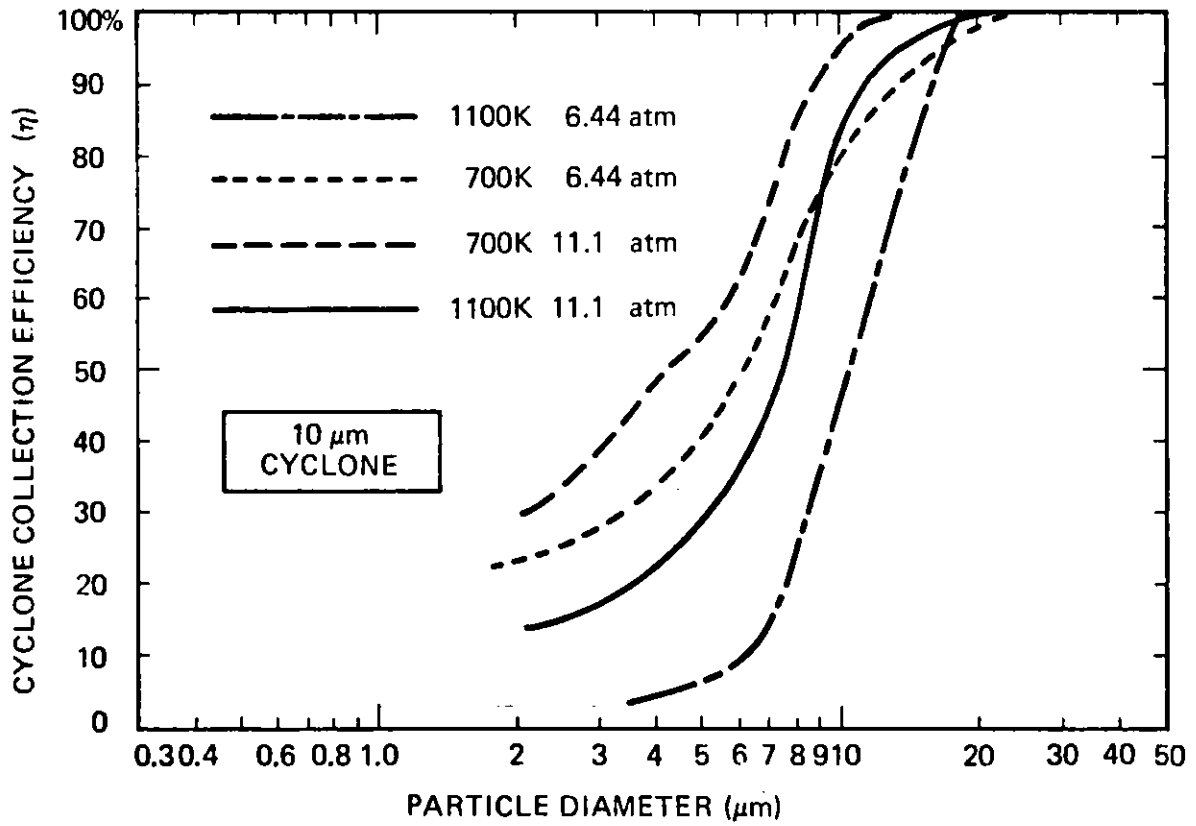


Figure 11. Calibration results of 10  $\mu\text{m}$  cyclone.

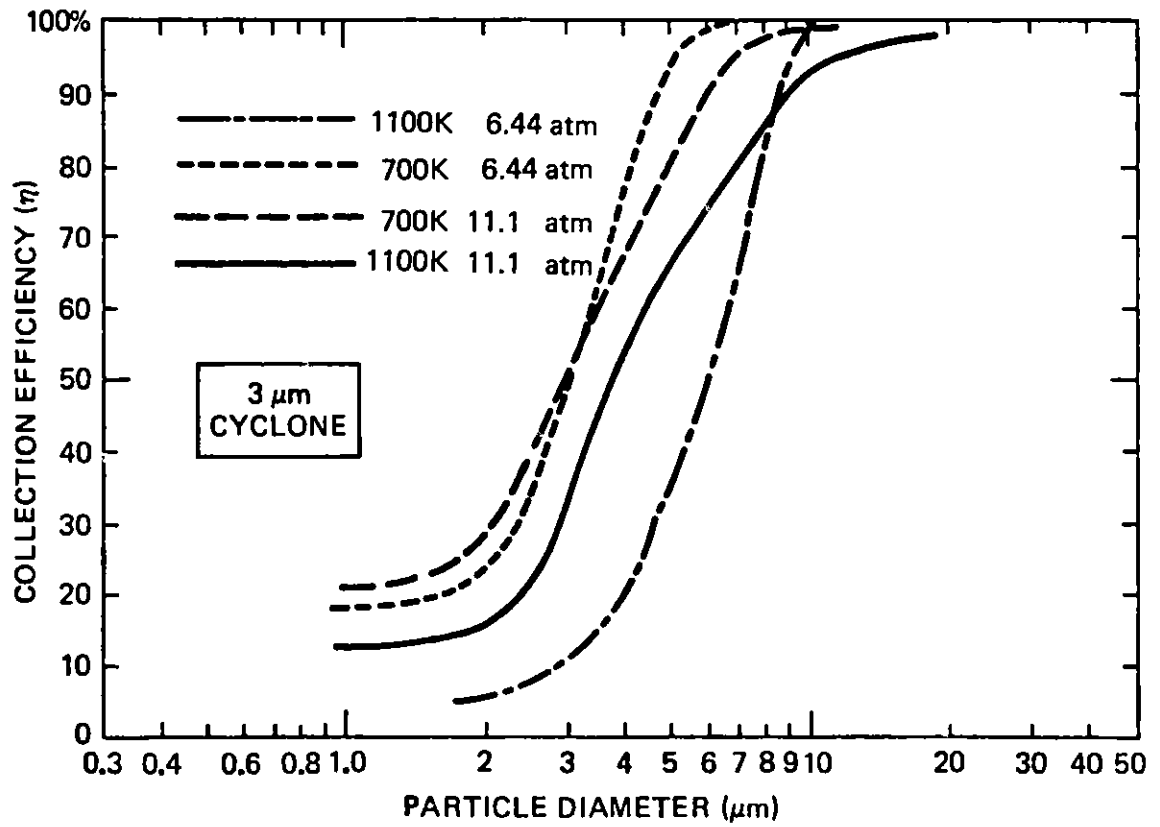


Figure 12. Calibration results of 3  $\mu\text{m}$  cyclone.

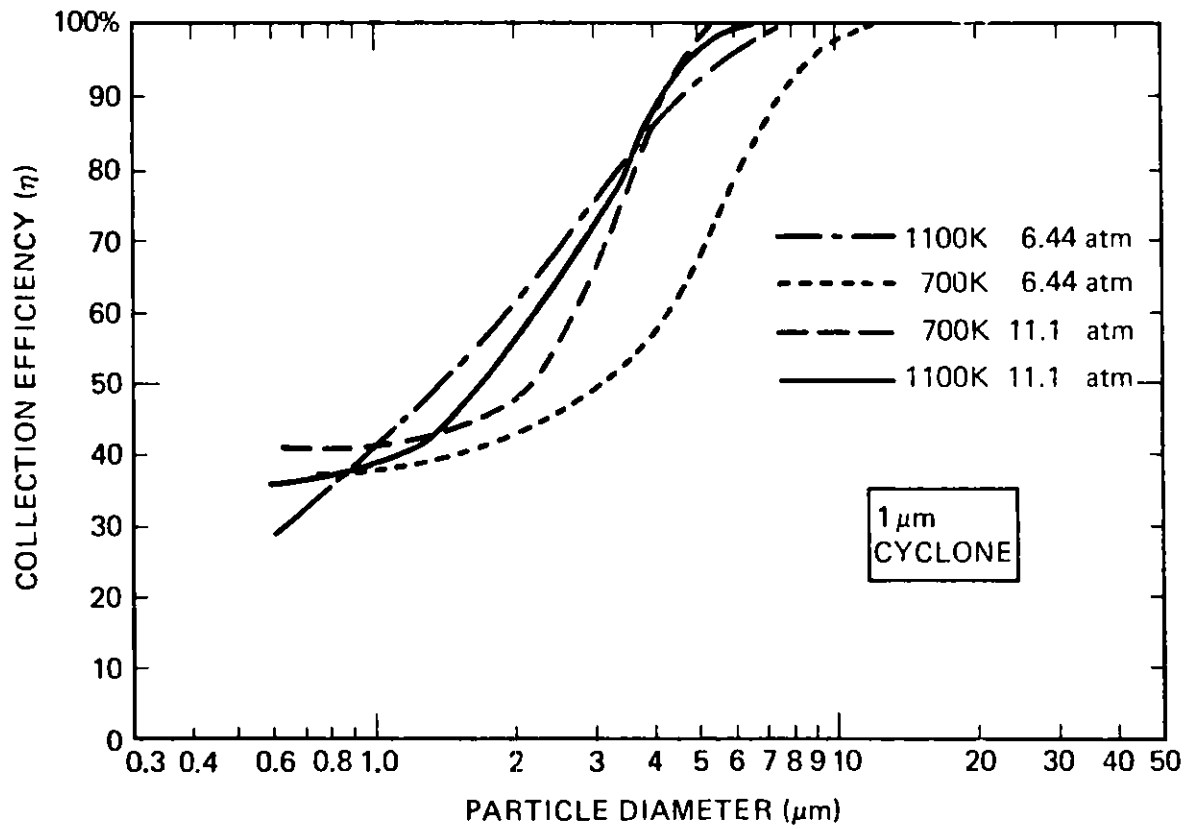


Figure 13. Calibration results of 1  $\mu\text{m}$  cyclone.

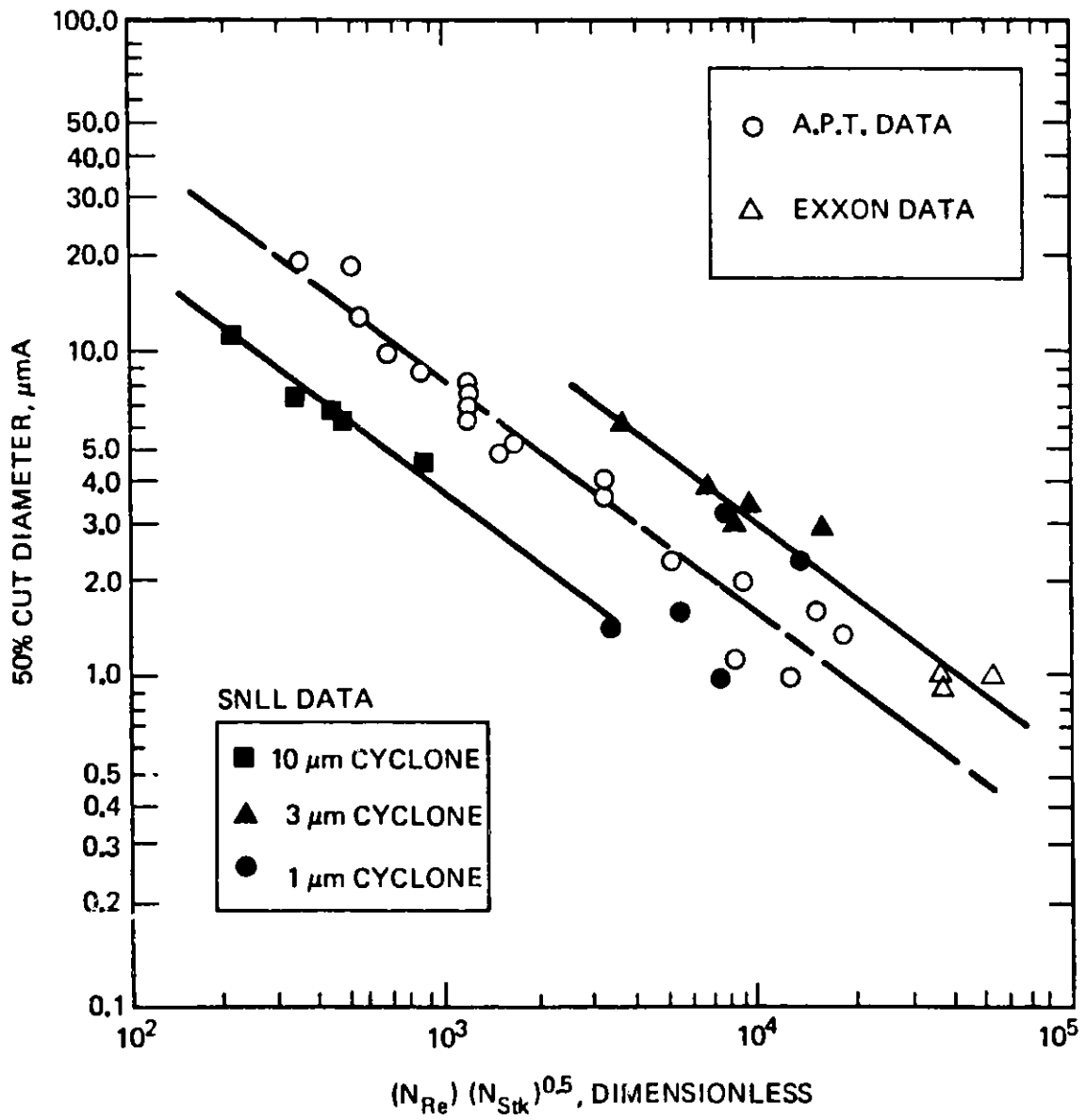


Figure 14. Correlation of cyclone 50% cut-size with respect to  $(N_{Re})(N_{Stk})^{0.5}$ . A.P.T. and Exxon data are duplicated from Reference 5.

PROGRESS AND PERFORMANCE OF ON-LINE ANALYZERS OF COAL

C.M. Spencer  
D.R. Brown  
T. Gozani  
H.Bozorgmanesh  
H. Bernatowicz  
Science Applications, Inc.  
5 Palo Alto Square, Suite 200  
Palo Alto, CA 94304

O.J. Tassicker  
F. Karlson  
Electric Power Research Institute  
3412 Hillview  
Palo Alto, CA 94304

Introduction

Nucoalizers<sup>(1)</sup> are a new family of on-line instruments which can continuously analyze bulk samples of coal for all its major constituents (e.g., H,C,S,N and Cl) calorific value and moisture content. Convenient data displays give current information on the above parameters plus percent ash by weight, slagging coefficients, ash fusion temperature, ferric/dolomite ratio, and other useful parameters.

The need for real-time analysis of coal stems mainly from the large variability in the composition of coal. The constituents of coal differ from region to region, mine to mine, seam to seam, and even from one truck load to another. This variability has significant impacts on the performance of coal preparation facilities and coal fired power plants and on methods used for meeting emissions regulations set by the Environmental Protection Agency.

In the past six years Science Applications, Inc. (SAI), in cooperation with Kennedy Van Saun (KVS, subsidiary of McNally Pittsburgh group), has actively researched, developed and commercialized a family of on-line coal analyzers under the generic trade name NUCOALYZER. Much of the research and development was jointly funded by SAI, KVS, and very significantly by the Electric Power Research Institute (EPRI)<sup>1</sup>. The association with EPRI brought SAI in close contact with power utilities and other potential users of this instrumentation and provided invaluable guidance in its evolution.

This paper describes the past year's progress in the laboratory testing of the most comprehensive Nucoalizer, the CONAC, and the performance of a Nucoalizer-Sulfurmeter in special field tests. Previous papers and presentations provide more detailed background information.<sup>2,3</sup>

Applications of Nucoalizers to Fossil Energy Processes

The near real-time analysis provided by a Nucoalizer can be used in a variety of strategies to optimize efficiency of coal use.



Nucoalizers can be used to monitor coal deliveries and achieve coal uniformity in coal storage and recovery. In a coal cleaning plant, on-line analysis with a Nucoalizer can lead to optimum Btu recovery while meeting specifications for the washed coal.

A Nucoalizer can monitor the blending of different coals to maintain a key constituent such as sulfur below a specified level, or can predict sulfur dioxide emissions, allowing feed forward control to gas scrubbers and precipitators.

The variability in coal feed to the boiler can lead to gross changes in thermodynamic efficiency in combustion. In addition, fouling and slagging incidents due to poor coal quality cause costly boiler shutdowns and maintenance. Nucoalizer monitoring of key constituents and Btu in the coal feed allows operators to adjust boiler parameters for increased efficiency.

#### Principles of the Prompt Gamma Neutron Activation Analysis Technique

Figure 1 illustrates the principles of the PGNA technique. A Californium spontaneous fission source shines energetic neutrons into a bulk sample of material. In materials, such as coal, which contain an appreciable amount of hydrogen, the energetic neutrons collide with and lose energy primarily to the hydrogen nuclei. In this process the neutrons penetrate deeply and are brought into thermal equilibrium with the coal sample. At that point the neutrons are bouncing around inside the material at roughly the speed of sound.

Every time a neutron comes into the proximity of one of the nuclei of the elemental constituents of the coal, there is a probability that the neutron, instead of bouncing off the nuclei, will coalesce with the nucleus. The magnitude of this probability depends primarily on the physical characteristics of the individual nuclei. In particular, it does not depend critically on the chemical environment of the nuclei, or on the samples' temperature or size distribution.

When the neutron and the constituent nuclei fuse, their combined mass is less than the sum of their individual masses. According to Einstein's famous equation, this lost mass shows up as energy in the form of a gamma ray. The exact energy of the gamma ray is a unique characteristic of the nuclei with which the neutron combined. These gamma rays are the signal measured in PGNA. Figure 2 shows these signals from 3 different coal types in the region of the sulfur gamma rays as detected by a high resolution lithium drifted germanium detector.

The gamma ray signal intensity for a particular elemental constituent of the coal depends on the abundance of that element in the coal and on the probability that the particular nucleus and a neutron interact. This latter probability can be increased by increasing the neutron source strength. In Figure 2, it is seen that the signal from iron increases going from the western to eastern coal, as does the sulfur. These signals are proportional to respective elemental abundances.

Two basic non-intrusive configurations have evolved for the Nucoalizer; these are the belt type and a smaller one based on the chute type. The

fundamental difference between them, from a point of view of coal rheology and accuracy, is addressed in the literature<sup>4</sup>. However the availability of either configuration gives the user a flexibility to fit the instrument to his needs.

A schematic of a Nucoalyzer is shown in Figure 3. The instrument is about 25 feet long, stands 14 feet high, and weighs over 10 tons. Coal enters the system through an input hopper and is gravity fed and leveled onto a conveyor belt. A microwave transmission meter monitors the moisture<sup>5</sup> in the coal stream and a mass sensor is used to monitor the mass flow. The coal then enters the shielded nuclear interrogation region where it is radiated by neutrons from the source underneath the belt. The elemental gamma rays are detected in a gamma ray measurement system positioned above the source and coal.

The signals produced in the sensor are processed through an electronics module and fed into a microcomputer, where the elemental abundances in the coal are deduced and output in standard engineering units. This microcomputer is also used for data logging and process control. Depending on the variety of analysed constituents and the complexity of the process control, Nucoalyzers can be designed with various levels of computer-operator interaction; in general they will run unattended for many days. Figure 4 is a photo of a Nucoalyzer-CONAC which incorporates all of the above features.

The size of a peak corresponding to a particular element's gamma ray is measured by the number of detected gamma rays whose energy falls in a narrow region framing the known gamma ray energy. Figures 5 and 6 show the linear relation between this number of gamma rays (also called peak area) and the weight percent of iron and sulfur, as measured by ASTM methods in a variety of American coals. This data was taken on a lithium-drifted germanium detector and shows that the Nucoalyzer has no bias with respect to the origin of the coal and can be calibrated with careful measurements on just a few standard coals.

#### Advantages of the PGNAATechnique

The analysis technique used in the Nucoalyzers eliminates the well-known disadvantages of wet chemical analysis methods as applied to coal: extremely small samples compared to the coal being used, results available only after coal has been burned, and the destruction of the samples so verification is lengthy. The Nucoalyzer has the following advantageous characteristics:

- (a) it performs the measurement directly on the process stream with little or no sampling necessary
- (b) the analysis can be performed on streams of particulate, aggregate, or slurry
- (c) the analysis can be performed on belts, bins, chutes, or pipes
- (d) The system does not have to make contact with the material it measures
- (e) results are available in near real time

### Laboratory Tests of the CONAC

The first CONAC to be constructed is currently undergoing its final laboratory tests before being installed at the TVA Paradise Plant in July, 1982. The CONAC will be installed between the 2000 ton/hour heavy-media coal washing plant and the coal silos. It will process a sidestream of clean coal of about 12 tons/hour in order to demonstrate its new technology in an actual power plant environment.

One of the several tests was to analyze about 40 boxed samples of coal from the Homer City wash plant. These 200 lb or so boxes of coal are grouped into triplets; the first box contains some feed coal, the second contains cleaned coal from the same batch as the feed, and the third contains the associated refuse. Figure 7 shows in a striking way how easily the CONAC can differentiate between these coals; it shows the same part of the germanium detector spectrum for the 3 coals. One can see how the silicon peak at 4.934 MeV dominates the nearby carbon peak in the refuse, and how much smaller it is in the cleaned coal; similarly, one can see that the amount of sulfur and iron has decreased in the clean coal relative to the feed. Table 1 gives the CONAC analyses of three typical triplets for ash, S and Si.

Table 1

#### Conac Analysis of Coal Before and After Washing

<u>Sample</u>	<u>Feed Coal</u>	<u>Cleaned Coal</u>	<u>Refuse</u>
		Ash Wt %	
A	27.00	7.43	45.14
B	27.37	7.67	48.72
C	27.52	7.39	47.60
		Sulfur Wt %	
A	3.42	1.05	5.15
B	3.27	1.12	4.77
C	3.18	1.19	5.22
		Silicon Wt %	
A	6.41	1.63	10.81
B	6.31	1.61	11.82
C	6.66	1.58	11.73

The sulfur results would be available 5 minutes after the coal had passed through the CONAC, the ash and silicon values shortly thereafter. Such swift responses would allow the CONAC to control the adjustments to the heavy media process to maintain specified concentrations of elements in the cleaned coal.

#### Moisture Measurements

Monitoring the moisture content of coal is of great potential importance for coal handling, inventory control, and optimized control in coal drying and combustion. If microwaves with a frequency around 5GHz are passed

through coal they are attenuated, and this attenuation is primarily caused by the water in the coal. A moisture meter has been developed based on this fact; when calibrated for coals from a certain geographical region, it can measure their moisture to within  $\pm 0.5\%$  (absolute).

The calibration is done by completely drying a 20 lb sample, using temperatures below  $110^{\circ}\text{C}$ , then adding small known increments of water and measuring the microwave attenuation through the sample for several different water densities. A calibration curve as shown in Figure 8 results.

#### BTU Calculations

With an accurate measurement of moisture content it is possible to calculate the calorific value of a sample of coal. This is related to the elemental weight percents of carbon, organic hydrogen and, to a lesser extent, to sulfur and nitrogen. There are many slightly different equations to allow calculation of the higher heating value, and we are developing a new one to take advantage of the parameters the CONAC can measure. It is a modified Dulong-Petit equation with coefficients determined by a linear regression on the standard coals used to calibrate the CONAC. Figure 9 shows the excellent agreement between the calculated and measured Btu values of 14 coals.

#### Evaluation of the Detroit Edison Monroe Power Plant Sulfurmeter

The first Nucoalyzer to be used in the field is a sulfurmeter, which uses a high-efficiency, low resolution sodium iodide detector to measure the sulfur and hydrogen content of blended coal at the Detroit Edison Monroe Power Plant.

At this power plant Detroit Edison (DECO) has elected to meet strict state  $\text{SO}_2$  emissions requirements by blending more expensive low sulfur eastern coal with less expensive high sulfur eastern coal. Although coal blending avoids the high initial costs of alternative emission control techniques such as stack gas scrubbing, its long term costs are high because low sulfur coal is increasingly expensive. The costs can be minimized by using only as much of the low sulfur coal as necessary to meet the emissions standards. However, since the variation in the sulfur content of the high and low sulfur coals is large, there is no single optimal blending ratio. Instead, this ratio is a dynamic parameter that can change within minutes.

Knowing the range of each coal's sulfur content allows a blending ratio to be chosen that will ensure that emission levels are not exceeded, but this means more costly low sulfur coal than is necessary. To predict what savings would result from optimizing the blending ratio on the basis of feedback from a Nucoalyzer-Sulfurmeter, Detroit Edison used data on plant operating parameters and the sulfur content and heating value ranges of its targeted coals in a mathematical model<sup>6</sup> to predict the potential savings from dynamic blending. Table 2 summarizes the results of this study.

Table 2

<u>Control of Blending</u>	<u>Percent High Sulfur Coal</u>	<u>Percent Low Sulfur Coal</u>
None (using daily average values)	66%	34%
Nucoalizer (sulfur only)	77.5%	22.5%
Nucoalizer (sulfur plus BTU)	78%	22%

Projected savings range from \$5-15 X 10<sup>6</sup>/year through use of the Sulfur-meter to monitor and control the blending process. The Nucoalizer-Sulfurmeter bought by Detroit Edison for this purpose was installed in the last half of 1980 by the Bechtel Corporation and has been running since its acceptance in March 1981.

Calibration of the Sulfurmeter was done using 200 lb. samples of 9 different U.S. coal types with sulfur contents ranging from 0.4 weight percent to 2.7 Wt%. The accuracy of the calibration in reproducing the known sulfur values is  $\pm 0.02$  Wt% (RMS), which is an entirely suitable accuracy for control of a blending operation.

The evaluation and field testing of this Sulfurmeter were carried out in the following way. The test objective was to compare Sulfurmeter readings to laboratory analyses, both chemical and PNAAs. Special blends of low and high sulfur coal were set up and passed through the usual coal handling system and the Sulfurmeter. As each blend came through the Sulfurmeter its belt was halted, 300 lb samples of coal were scraped from the stationary belt and riffled to produce several small samples which were sent to four laboratories: Bituminous Coal Research Laboratory, Commercial Testing and Engineering Company, DECO Plant Monroe Laboratory, and DECO Research Department Laboratory, for conventional ASTM chemical analyses. The remaining 200 lb samples of this scraped coal were boxed and returned to the belt for re-analysis by the Sulfurmeter. The boxes were then sent to SAI in Sunnyvale, California for PNAAs analysis in the laboratory using a Ge(li) system.

The sulfur content as measured by the Sulfurmeter is compared with that found by chemical analyses, as illustrated in Figure 10. The 45° line would indicate perfect agreement, while the horizontal bars represent the root mean square (RMS) deviation of the separate laboratory chemical determinations. Over the whole range of blends, the agreement is satisfactory. Similar good agreement was found between the Sulfurmeter sulfur values and those measured by the laboratory Ge(li) system.

The dynamic response of the Sulfurmeter to widely varying values in coal sulfur content was also tested. With the cooperation of the Detroit Edison power station staff, some West Virginia 3% S coal, then some 0.7% S. Kentucky coal and blends of the two were passed through the Sulfurmeter. The results of the test over a 12-hour period are shown in Figure 11. For the first five hours, 100% low-sulfur or blends of high- and low-sulfur coals were used. For most of the next 6 hours, 100% high-sulfur coal was analyzed. At about the 6th hour, the plant coal feed was stopped and the Sulfurmeter measured the same coal for approximately an hour; the small deviations in the recorded sulfur content during this time indicate the precision of the instrument

( $\pm 0.04$  wt% S). After the stationary coal was measured, the coal feed was re-started. Subsequent deviations in the measured values indicate variations in the sulfur content of the high-sulfur coal.

A comparison was also made between some silo fill average sulfur values and subsequent sulfur dioxide stack monitor readings. To see if the signature of the various blends could be identified in the SO<sub>2</sub> emissions after the coal had passed through the silos and been burned, printout data from the stack monitor was collected during the course of the week-long sulfurmeter tests.

Figure 12 shows a history of hourly stack monitor SO<sub>2</sub> (in arbitrary units) readings throughout the week of the tests. The breaks in the continuous curve are caused by either instrument self-calibration or malfunction (e.g., middle of second day). The silo fill average sulfur values measured by the sulfurmeter and the fill time and duration are plotted on the same grid. As can be clearly seen from the 100 percent high-sulfur fill on the left, there is about a 6-hour lag time between fill and coal burn as seen in the stack. This 6-hour lag time represents the residence time of the coal in the silos. Using this lag time, noted values of the SO<sub>2</sub> curve can be associated with the sulfur in coal blends. In conclusion, good agreement has been found in various comparisons between the sulfurmeter readings of the sulfur content of coal and chemical analyses of the same coal. Also, a good enough correlation between Sulfurmeter readings and stack monitor readings was observed to allow the Sulfurmeter to make predictions of the SO<sub>2</sub> emissions from the coal.

### Control of Coal Blending

The sulfurmeter microcomputer can run a special interactive blending program in which the coal board operator types in a few parameters, such as anticipated MWatt load for the next 24 hours and starting blend ratio, on a special remote terminal. Then, based on the sulfur values it is measuring and the desired average sulfur value for that day, the program calculates a new blending ratio every 7 minutes during a coal fill and prints it out on the terminal so the operator can set up the new blend as the fill proceeds. If these blending ratios are implemented, the average daily sulfur value will be a fraction under the limits specified by the EPA regulations.

### Conclusion

To summarize, the primary advantages of Nucoalyzers relate to their ability to quickly identify changes in coal composition so that adjustments can be made in a timely manner to accommodate these changes in the process being monitored. Nucoalyzers are the only instruments available that can monitor the coal (for ash, Btu, sulfur, etc.) on-line and provide real-time continuous results. One Nucoalyzer is already working in the field, and by the time of the next Symposium we will have had performance reports on two more.

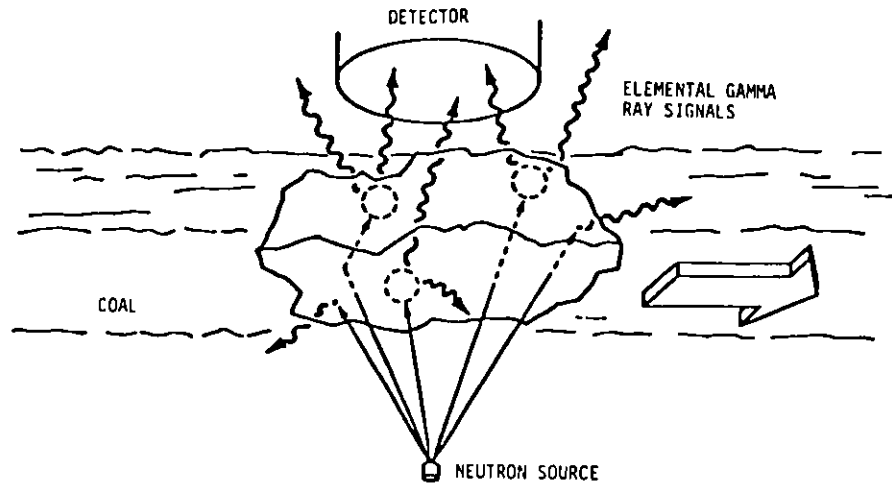


Fig. 1 Coal moving on a conveyor is radiated from below by a fast Neutron Source. The various elements capture thermalized neutrons giving characteristic high energy Gamma Radiation. The Gamma rays are picked up by the Detector and fed to electronic processors.

SECTION OF Ge(Li) GAMMA RAY SPECTRA

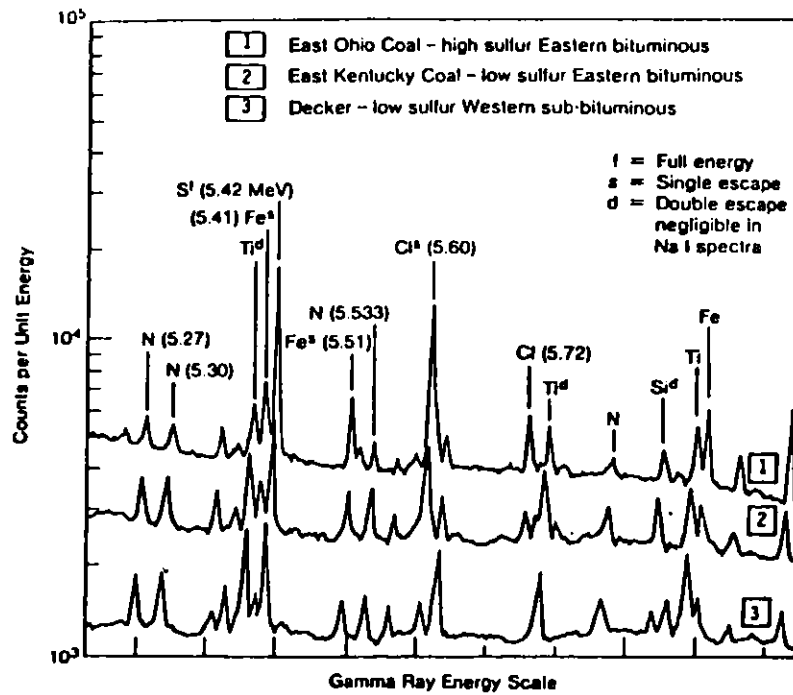


Fig. 2 Portion of the Elemental Gamma Ray Signals for the Different Coal Types. The Signal Strength is Proportional to the Elemental Abundance.

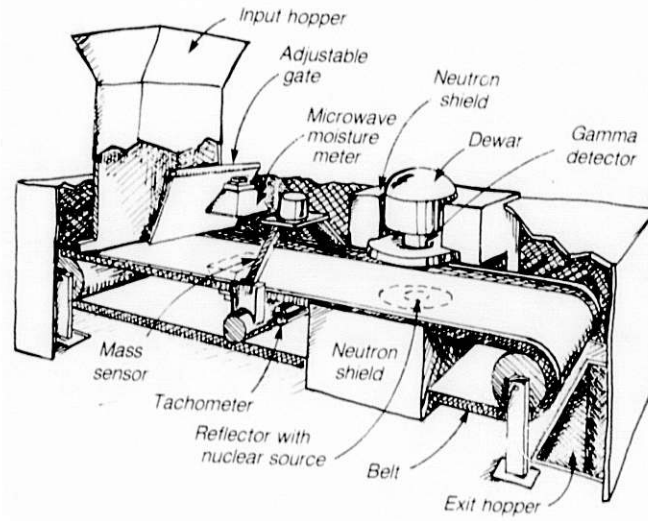


Fig. 3 Schematic of Nucoalyzer-CONAC

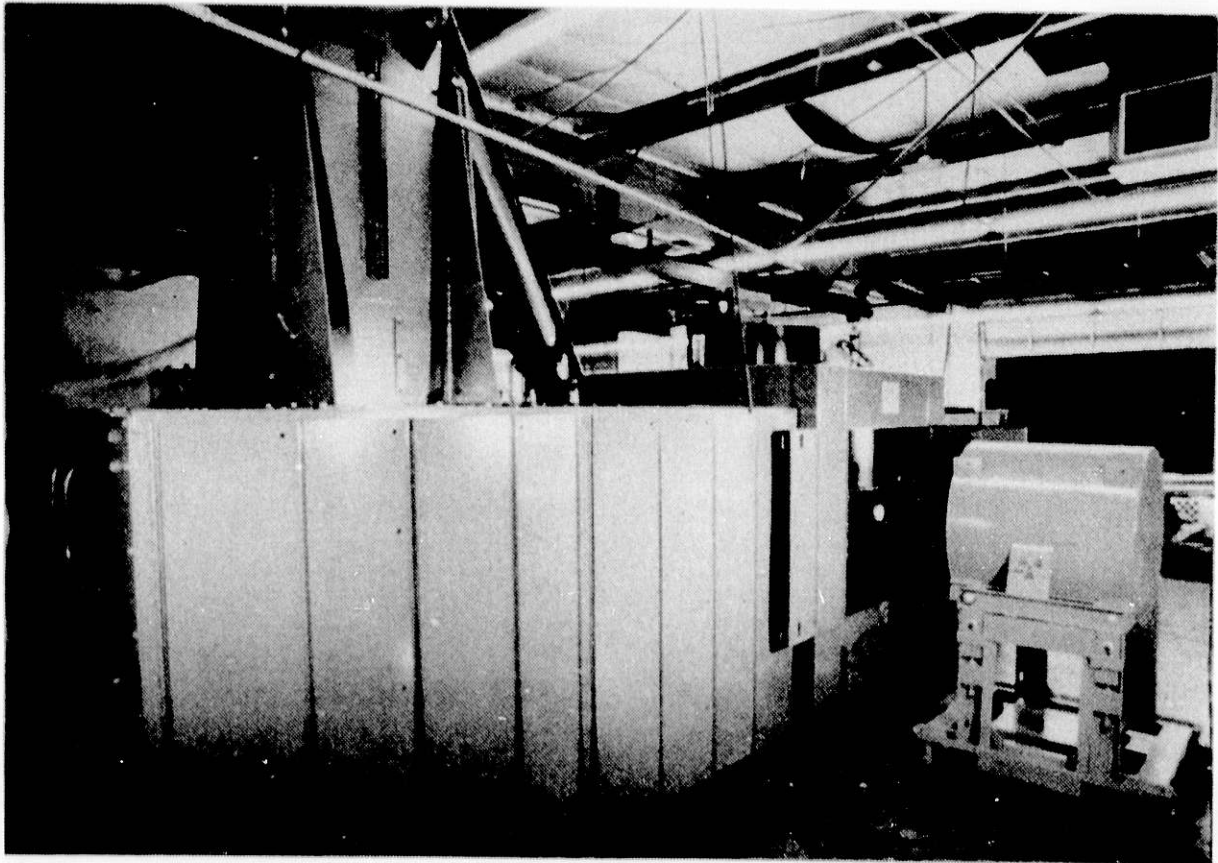


Fig. 4 Belt Conac (Model 110) to be installed at TVA's Paradise Plant Performs On-line Full Elemental Analysis and Calorific Value Determination



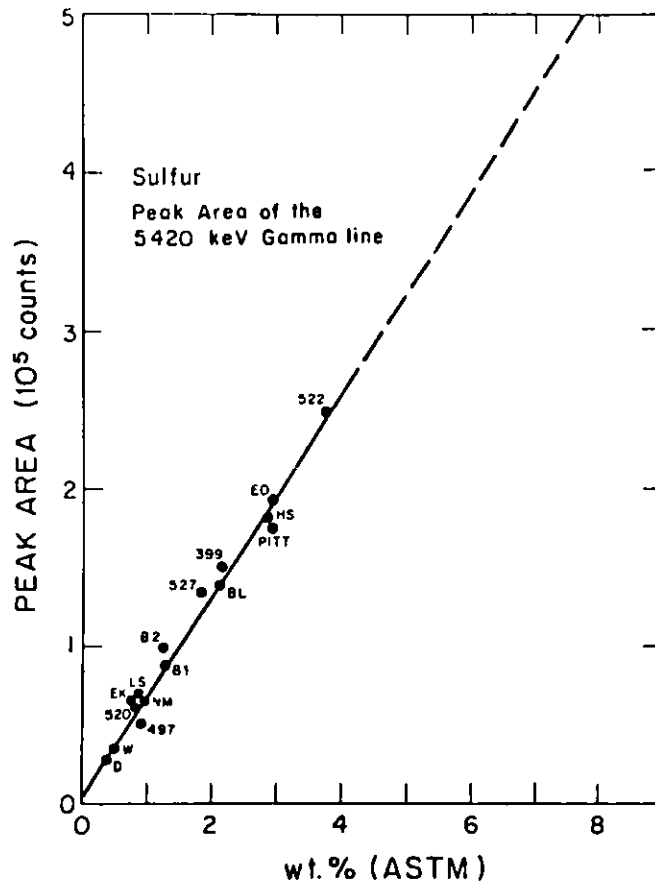


Fig. 5 Calibration curve for sulfur

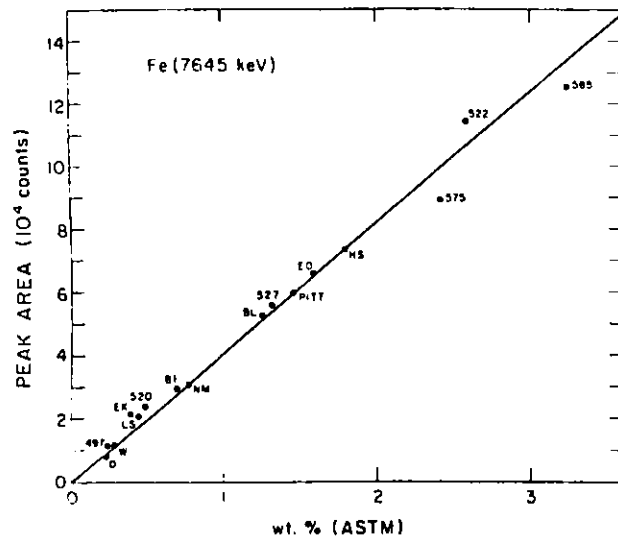


Fig. 6 Calibration Curve for iron

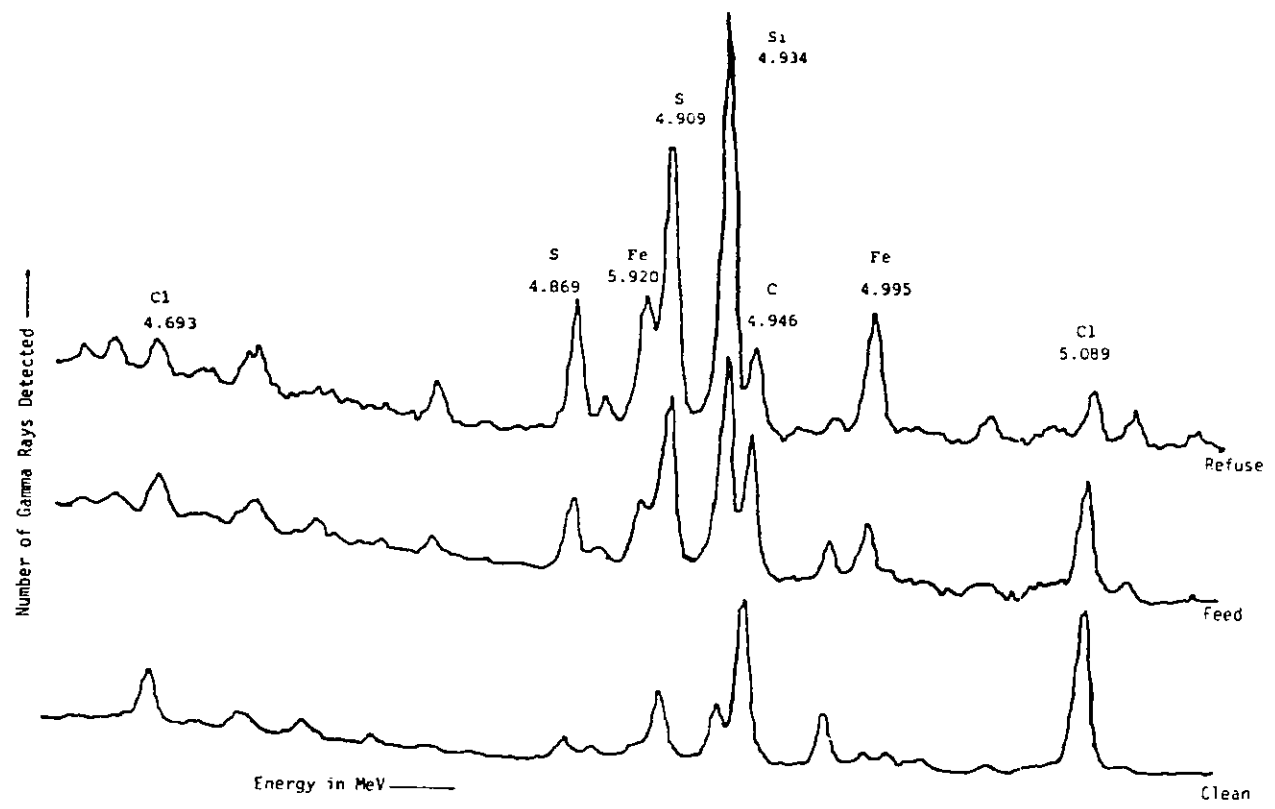


Fig. 7 Comparison of Ge Spectrum for Clean, Feed and Refuse Coals

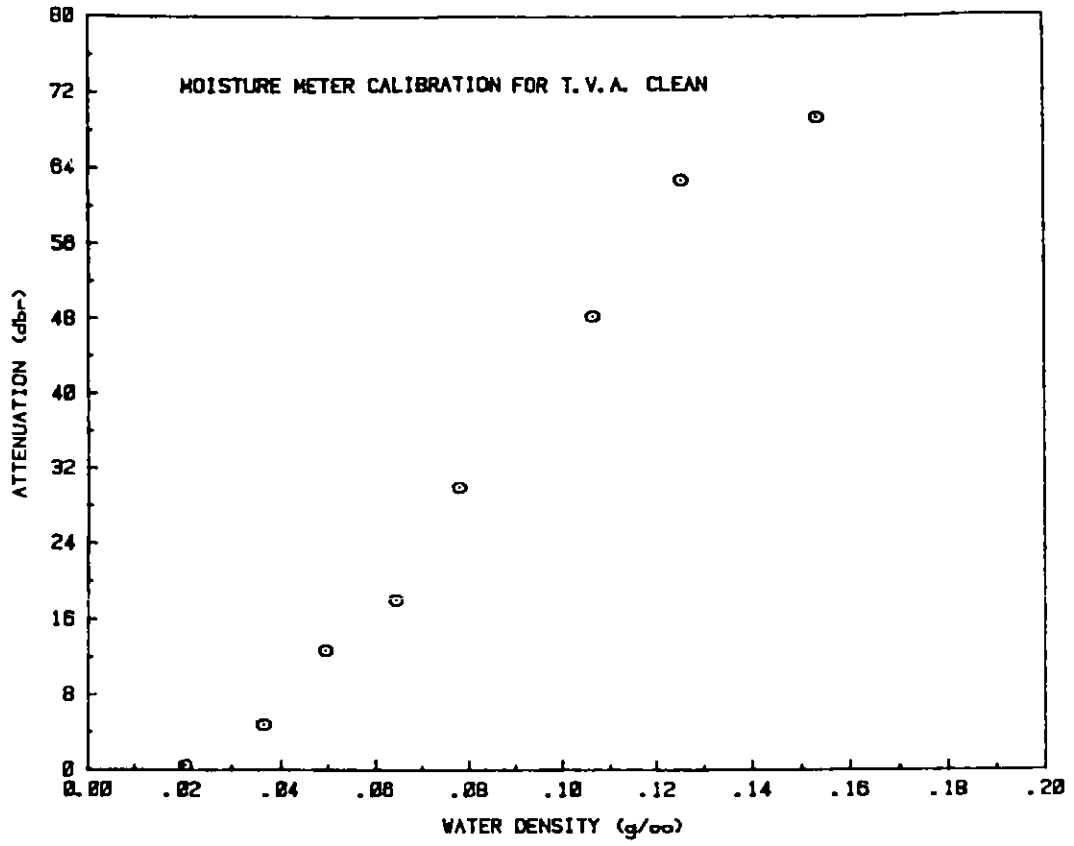


Fig. 8

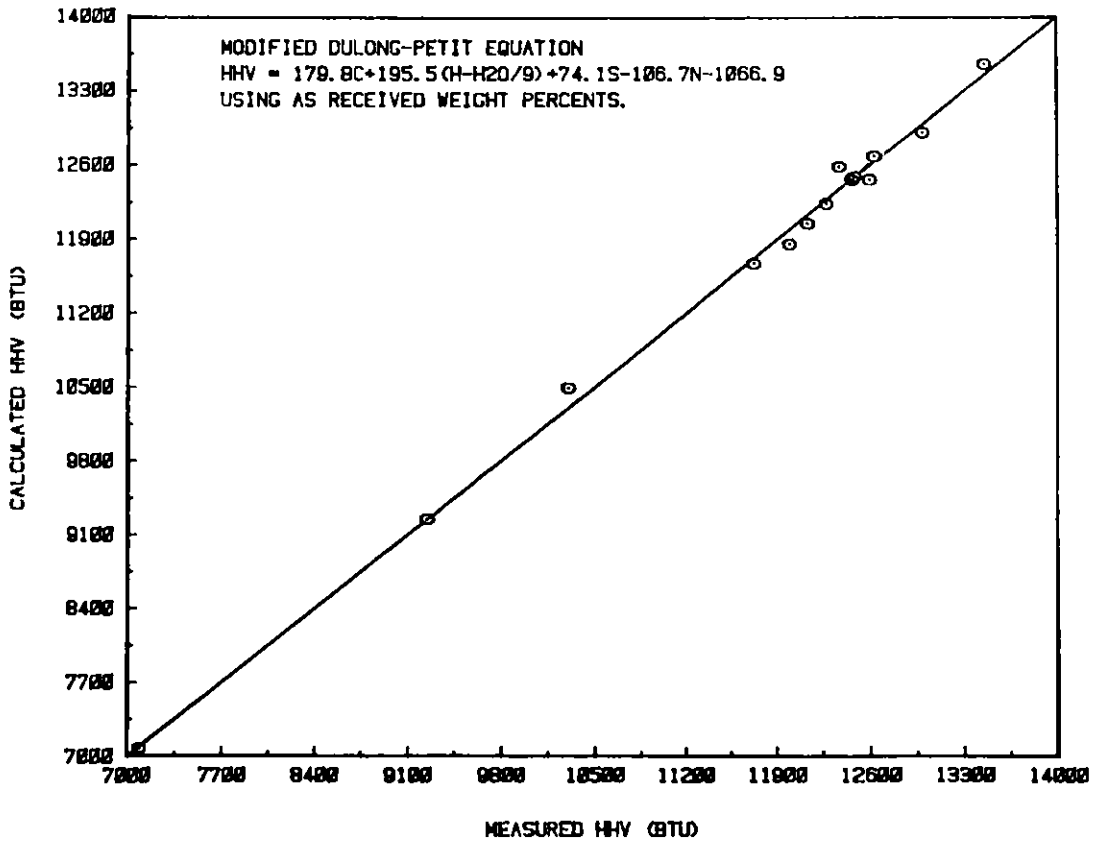


Fig. 9

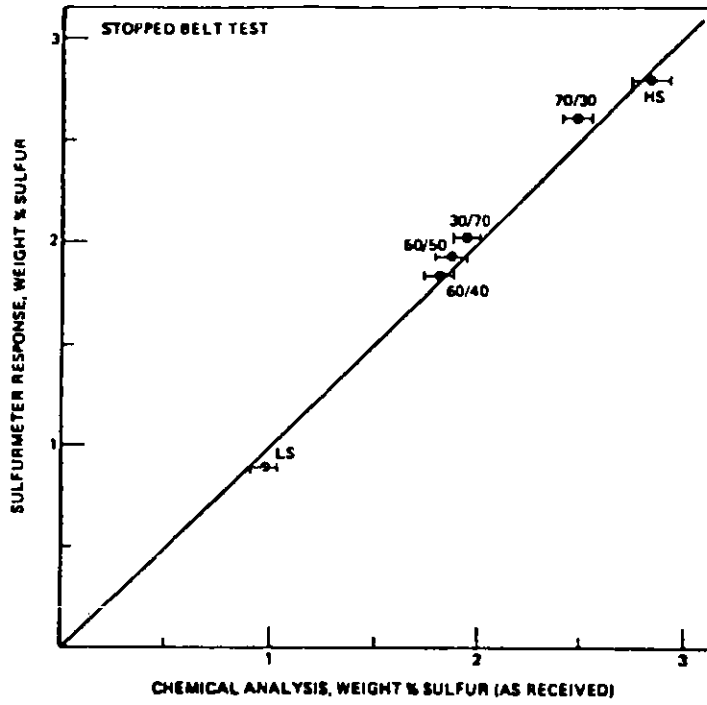


Fig. 10 Comparison between sulfur value measured by Sulfurmeter and chemical analysis on stopped belt samples

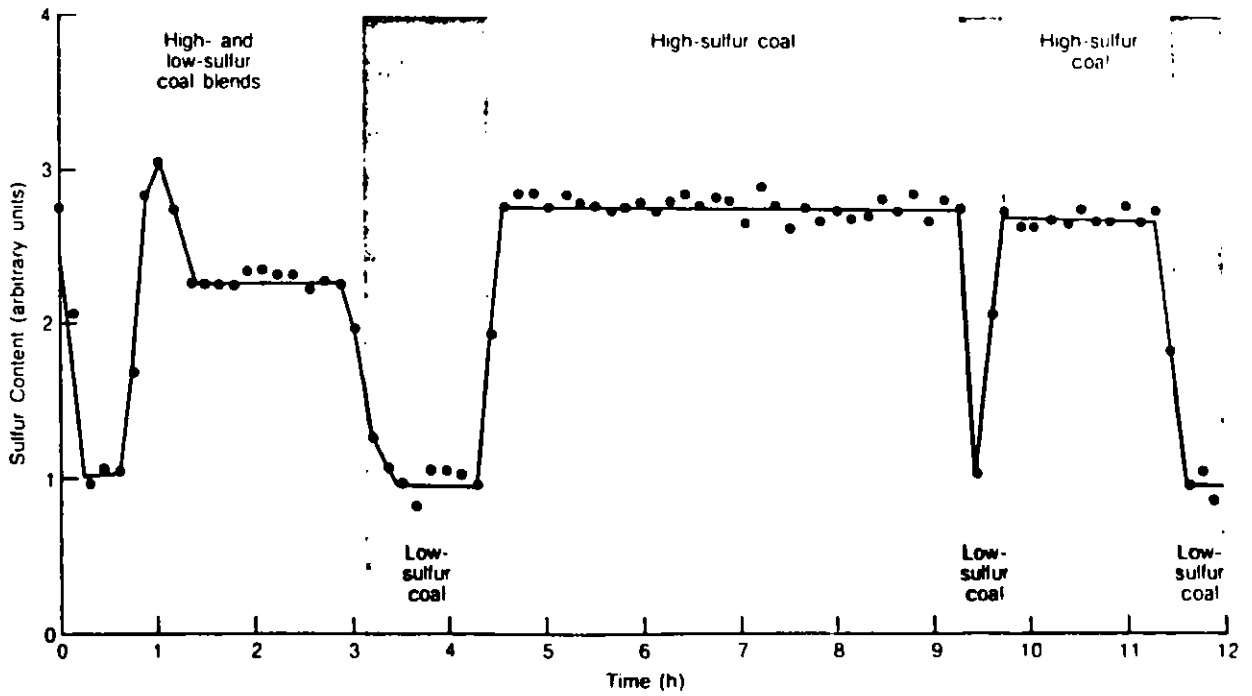
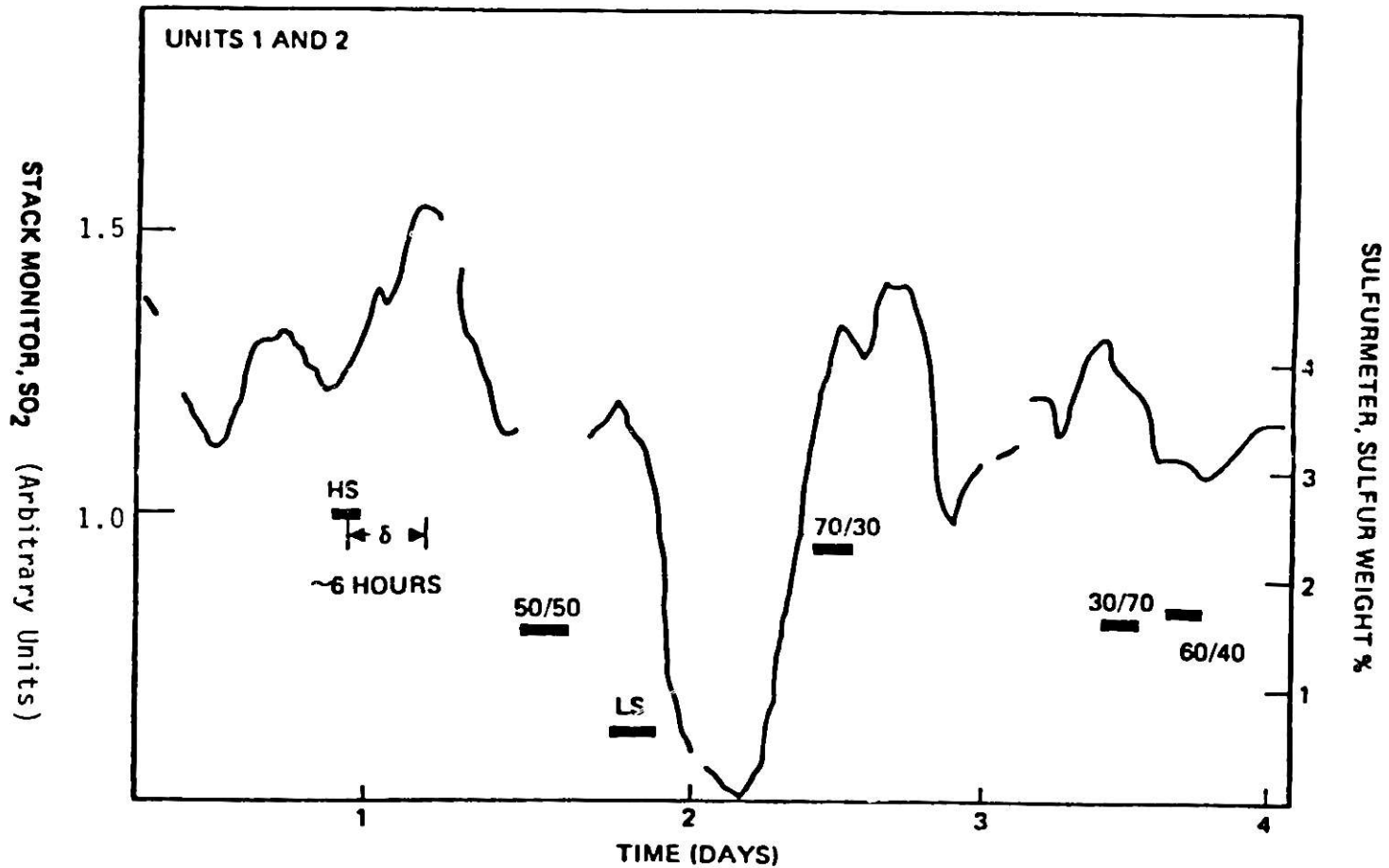


Fig. 11 On-Line Sulfurmeter readings from Detroit Edison's Monroe Power Plant for various coal feeds



**NOTE: THERE IS APPROXIMATELY 6 HOURS LAG TIME BETWEEN SULFURMETER READINGS (FILL) AND STACK READING (BURN).**

Fig. 12 Stack monitor SO<sub>2</sub> reading versus time measured sulfur value for the various fill blends shown

### Acknowledgements

The cooperation of the Detroit Edison Company, including that of many individuals during the conduct of the testing at the Monroe Power Plant, is gratefully acknowledged.

### References

1. T. Gozani et al., "Nuclear Assay of Coal," EPRI FP-989, volumes 1-8; Electric Power Research Institute, Palo Alto, CA.
2. D.R. Brown, T. Gozani and H. Bozorgmanesh, "Nucoalyzer On-Line Nuclear Analysis of Coal," 1980 Coal Technology, Houston, Texas (November 1980).
3. O.J. Tassicker, et al., "Continuous Nuclear Analyzer of Coal for Improved Combustion Control", 1982 American Power Conference, Chicago, IL (April 1982).
4. T. Gozani, R. Hogg and P. Luckie, "Coal Rheology and Its Impact on Nuclear Assay," EPRI FP-989, Volume 7; Electric Power Research Institute, Palo Alto, CA.
5. D.R. Brown, "Coal BTU Measurement Study - Monitoring of Moisture in Coal," EPRI FP-989, Volume 5; Electric Power Research Institute, Palo Alto, CA.
6. P.S. Baur, "Control Coal Quality Through Blending," Power, March 1981.

COAL/STONE MONITORING USING TWO ENERGY GAMMA TRANSMISSION

J S Wykes, G M Croke  
 National Coal Board  
 Mining Research and Development Establishment  
 Ashby Road  
 BURTON UPON TRENT  
 Staffordshire  
 DE15 0QD  
 England  
 Telephone: Burton upon Trent (0283) 216161

Abstract

The principle of using two gamma ray beams of different energies in the analysis of coal/stone mixtures is described. This technique has been developed at the Mining Research and Development Establishment of the UK's National Coal Board in order to monitor run-of-mine coal on a conveyor belt and a prototype device has been built by Marconi Space and Defence Systems Ltd. Problems encountered during this development and the methods used to overcome them are discussed. Finally, experimental results obtained with the prototype device are presented and discussed.

Principle of Method

A method of determining the stone content of a coal/stone mixture consists of measuring the uncollided flux transmitted through the mixture from two gamma ray sources of different energy. As only the uncollided flux is measured, the method is independent of the spatial distribution of the two components in the mixture.

The uncollided gamma flux transmitted through a mixture of two materials a and b is given by

$$I = I^0 \exp[-(\mu^a m^a + \mu^b m^b)]$$

where  $I^0$  is the incident flux,

$I$  is the transmitted flux,

$m$  is the mass loading or mass per unit area,

$\mu$  is the mass absorption coefficient and

the superscripts a and b refer to the two materials.

This may be reduced to

$$I = I^0 \exp[-(\mu - f \Delta\mu)m] \quad (1)$$

where  $m = m^a + m^b$ ,

$$f = m^b/m,$$

$$\mu = \mu^a \text{ and}$$

$$\Delta\mu = \mu^a - \mu^b.$$

Consider now the case of two gamma ray beams of different energies incident on a mixture of coal and stone. In this case, two equations of type (1) apply, viz:

$$I_1 = I_1^0 \exp[-(\mu_1 - f \Delta\mu_1) m]$$

$$I_2 = I_2^0 \exp[-(\mu_2 - f \Delta\mu_2) m]$$

where the subscripts refer to the two different gamma-ray energies and  $f$  is the fraction of stone in the mixture. Denoting the normalised transmitted intensity by  $I^*$  and taking logs, the following relations are obtained:

$$\ln(I_1^*) = -(\mu_1 - f \Delta\mu_1) m$$

$$\ln(I_2^*) = -(\mu_2 - f \Delta\mu_2) m$$

Dividing one of these equations by the other gives the ratio

$$R = \frac{\ln(I_1^*)}{\ln(I_2^*)} = \frac{\mu_1 - f \Delta\mu_1}{\mu_2 - f \Delta\mu_2}$$

which, on re-arrangement gives

$$f = \frac{R \mu_2 - \mu_1}{R \Delta\mu_2 - \Delta\mu_1} \quad (2)$$

Thus an expression for  $f$ , the stone fraction of the mixture, is obtained which is independent both of the spatial distribution of the coal and stone components and of the mass loading in the beam. The mass loading of mineral matter in the beam may be calculated from

$$m = \frac{-\ln(I_1^*)}{\mu_1 - f \Delta\mu_1} = \frac{-\ln(I_2^*)}{\mu_2 - f \Delta\mu_2} \quad (3)$$



For best results, the gamma-ray energies should be chosen such that at one of them the absorption coefficients of the coal and stone are almost equal while at the other, there should be a substantial difference between them. Choosing the energies in this way means that one of the expressions for the mass loading will exhibit only a small dependence on the stone content. It should also be borne in mind that low energy radiation is easily absorbed by minerals and this could limit the maximum mineral loading which can be usefully analysed. At the other end of the energy scale, gamma-ray beams are less readily absorbed in passing through large amounts of mineral and hence the sensitivity to changes in mass loading will be poor. One choice of energies which satisfies all of these constraints is 60keV radiation from  $\text{Am}^{241}$  and 662keV radiation from  $\text{Cs}^{137}$ . At these energies the absorption coefficients are as shown in Table 1.

Table 1

Energy	$\mu_{\text{coal}}$	$\mu_{\text{stone}}$	$\Delta\mu$
keV	<----- m <sup>2</sup> / kg ----->		
60	$19.2 \times 10^{-3}$	$30.2 \times 10^{-3}$	$-11.0 \times 10^{-3}$
662	$8.24 \times 10^{-3}$	$7.69 \times 10^{-3}$	$0.55 \times 10^{-3}$

#### Prototype Device

A schematic diagram of a prototype device operating on the above principle is shown in Figure 1. The detector used is a NaI scintillation crystal viewed by a photomultiplier (PM) tube. The signal from the PM tube is amplified and applied to a single channel analyser (SCA) which spans the photopeak of the radiation. The count-rate from the SCA is directly proportional to the transmitted intensity. The count-rate is normalised to the empty-belt count-rate and the values of  $f$  and  $m$  are calculated by the micro-processor.

The problems encountered during the development of this instrument may be described under the following headings: downscatter and background interference, randomly varying loads and counting losses due to pulse pile-up.

#### Downscatter and Background Interference

Because of the finite resolution of the detectors, the windows set by the single channel analysers also contain a contribution from scattered radiation. In particular, in the case of the SCA spanning the Am photopeak, there may be a significant contribution from radiation from the Cs which has lost much of its energy in passing through the load. A number of measures may be adopted to limit this downscatter but the simplest is perhaps to separate the sources and their associated detectors. In the Coal/Stone Monitor built by Marconi Space and Defence Systems Ltd, the separation between the sources is approximately 0.5m. A third window has also been introduced to further correct for the effect of background radiation.

### Random Load Variations

As the emission of gamma-rays is a random process governed by Poissonian statistics, the measured count-rate will not be exactly the same each time even when there has been no change in the material in the beam. The spread in the values will decrease as the total number of counts used to determine the rate increases so that in order to obtain an accurate value for the count-rate, a large number of counts must be obtained. This restriction also applies to any parameters whose values are calculated using the count-rate; high accuracy can only be obtained when the total number of counts is large. In the usual laboratory situations, the accuracy can be improved by extending the counting period in order to accumulate a larger number of counts. If this technique is applied to situations where significant variations in the absorber can occur during the counting time [such as may take place on a conveyor belt bearing run-of-mine coal], then the results obtained (ie the values of  $f$  and  $m$ ) will be in error. Consider the following simple example where the material in the beam undergoes a step change during the counting time as shown in Figure 2. Let the Cs and Am count-rates for the empty belt be 10000cps. When the mass loading is  $50 \text{ kg m}^{-2}$  these drop to 6715cps and 2908cps respectively. For the period when the mass loading is  $25 \text{ kg m}^{-2}$  the corresponding count-rates are 8195cps and 5393cps. Thus over the full counting period, the mean count-rates are 7455cps for Cs and 4151cps for Am, giving a value for  $R$  of 2.994. Use of relations(2) and (3) gives calculated values for  $m$  and  $f$  of  $36.70 \text{ kg m}^{-2}$  and 0.433 respectively. The true mean values of  $m$  and  $f$  over this period are  $37.5 \text{ kg m}^{-2}$  and 0.5 and these are the values that would be obtained if the counting period was such that the loading was constant during each of two such periods (at  $50 \text{ kg m}^{-2}$  during one and  $25 \text{ kg m}^{-2}$  in the other). This error in  $f$  and  $m$  comes about because the relationship between the transmitted intensity and the mass loading is non-linear whereas the above method is in effect a linear averaging. [This is particularly evident in the case of the stone content where the relative error in  $f$  (13.4%) is more than 6 times as great as that in  $m$  (2.1%). This greater sensitivity of  $f$  to changes in mass loading is due to the fact that  $f$  depends on  $\text{Ln}(T_1^*)$  and on  $\text{Ln}(I_2^*)$  whereas  $m$  is largely dependent only on the latter and this is less sensitive to mass]. In order to apply such an averaging procedure to improve the statistical accuracy, the non-linearities must first be taken out. In the Coal/Stone Monitor, this is achieved by calculating the values of  $f$  and  $m$  in a time which is sufficiently short that significant variations in the load have not taken place. It should be noted that this limits the maximum size of detector which is used (especially its length across the belt) as variations in loading also occur in this dimension. In order to verify that the counting time is sufficiently short, the Coal/Stone Monitor contains a section which monitors the fluctuations in the load and gives an alarm if they are either too large or too fast.

### Pulse Pile-Up Losses

Each gamma photon absorbed in the detector gives rise to a single pulse at the PM tube whose size is directly proportional to the gamma energy (see Figure 3a). If two photons are detected very close together, then the two pulses will appear to the counting system as a single pulse, as shown in Figure 3b. The size of this pulse will be greater than that of either single pulse but less than the sum of the heights. When either of these photons has an energy in one of the energy windows, this pile-up may cause the pulse to be lost to the system. A simple correction for these losses has been included in the Coal/Stone Monitor.

### Experimental Results

The prototype instrument has only been in operation for a short time and effort has so far been concentrated on verifying the principles outlined above. It has been most convenient, from the point of view of handling, to use material other than coal and stone during this verification period. Perspex has been used as a substitute for coal owing to its similar mean atomic number while glass has been used in place of stone. The absorption coefficients of these materials are presented in Table 2. The similarities in the behaviour of the coefficients in coal/stone and perspex/glass can be seen by reference to Table 1.

Table 2

Energy	$\mu_{\text{perspex}}$	$\mu_{\text{glass}}$	$\Delta\mu$
keV	(----- m <sup>2</sup> /kg -----)		
60	$16.3 \times 10^{-3}$	$24.3 \times 10^{-3}$	$-8.0 \times 10^{-3}$
662	$7.27 \times 10^{-3}$	$6.71 \times 10^{-3}$	$0.56 \times 10^{-3}$

A range of measurements has been taken with the instrument covering the mass range of 10 to 190 kgm<sup>-2</sup> and the glass content range of 0.0 to 1.0. A sample of the results obtained is given in Table 3. It can be seen that the value of f obtained is indeed independent of mass loading.

Table 3

Sample of results from Coal/Stone Monitor

Mass loading	f = 0.0		f = 0.5		f = 1.0	
	$\Delta m$	$\Delta f$	$\Delta m$	$\Delta f$	$\Delta m$	$\Delta f$
10	1.4	-4.6			1.3	4.8
30	1.3	-6.4	1.2	-2.2	1.3	1.8
50	1.5	-2.8	1.5	-1.3	1.5	1.0
70	0.7	-0.9			1.5	1.2
90	0.5	0.9	0.3	2.2	1.2	1.0
110	0.2	1.0	0.1	2.6	0.8	1.0
130	0.3	1.0			0.3	0.7
150	-0.3	1.0	0.4	1.7	0.5	0.6
170	-0.2	0.9	-0.6	1.9	-0.5	0.5
190	-0.4	1.0	-1.3	1.8	-0.9	0.5

$$\Delta m = \left\{ \begin{array}{l} m \\ \text{true} \end{array} - \begin{array}{l} m \\ \text{meas} \end{array} \right\} \quad \Delta f = 100 \times \left( \begin{array}{l} f \\ \text{true} \end{array} - \begin{array}{l} f \\ \text{meas} \end{array} \right)$$

In order to test the fluctuation monitor of the instrument, a turntable arrangement was used to provide varying loads to the system. This allows the system to be subjected to step changes in mass loading similar to those discussed above. A sample of the results obtained for step changes varying from  $4 \text{ kgm}^{-2}$  to  $20 \text{ kgm}^{-2}$  of perspex per measurement period can be seen in Table 4. The errors in  $m$  and  $f$  are in agreement with theoretical predictions for these step changes. Larger fluctuations will of course lead to larger errors; unfortunately it is not yet known what size of fluctuations will occur on conveyor belts bearing run-of-mine coal. The next stage of the programme therefore is to evaluate the performance of the system on real conveyor belts.

Table 4

Mean Load		Step Size	$\Delta m$	$\Delta f$
m	f	(perspex)		
24.9	0.593	4.0	-0.1	-0.2
35.0	0.422	8.0	0.4	0.0
45.0	0.328	12.0	1.0	1.0
55.0	0.269	16.0	1.0	1.4
65.0	0.227	20.0	1.3	2.3

$\Delta m$  and  $\Delta f$  defined as for Table 3

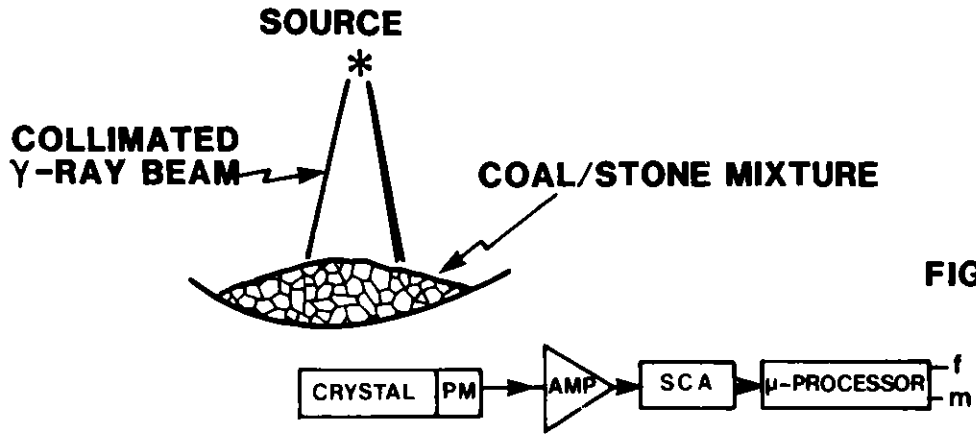


FIGURE 1

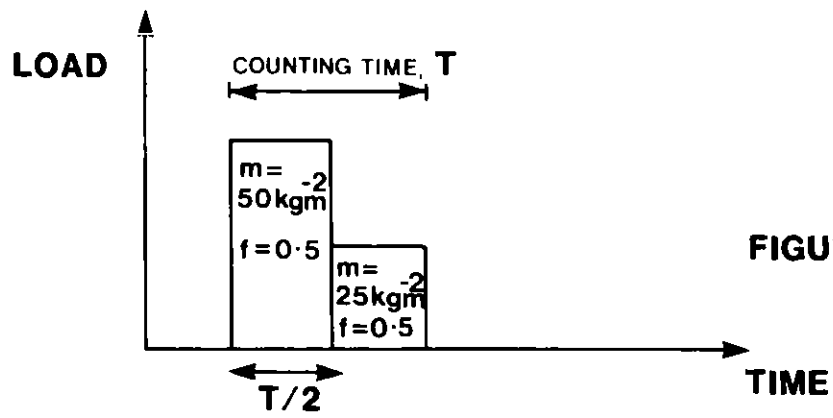


FIGURE 2

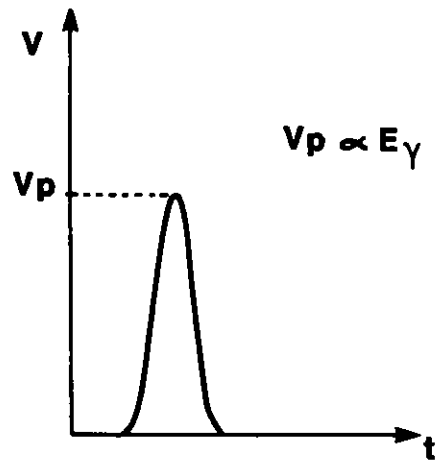
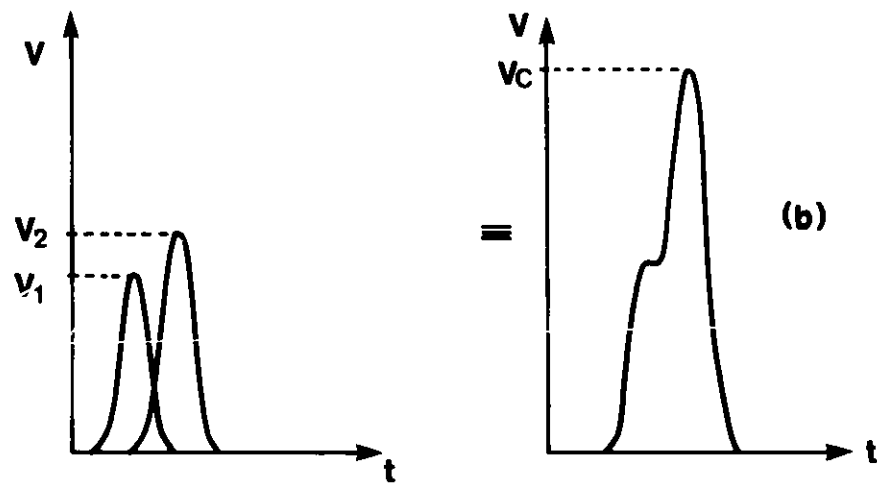


FIGURE 3



$$V_1, V_2 \leq V_c \leq V_1 + V_2$$

RAPID COMPONENT ANALYSIS OF COAL SAMPLES  
BY MEANS OF ALPHA BACKSCATTERING

J. Eddy  
Indiana University

K. G. Porges  
Argonne National Laboratory  
Argonne, Illinois 60439  
312/972-6091 (FTS: 972-6091)

Abstract

Alpha (Rutherford) backscattering has been used to determine the chemical composition of the lunar surface.<sup>1</sup> It involves relatively simple, inexpensive equipment that could be automated, in conjunction with a sample preparation system, to deliver some five sample analyses per hour.

As a method of component analysis, charged particle backscattering is complementary to fluorescent x-ray or Auger electron schemes: the latter provide optimum resolution for nuclear species of large atomic mass, whereas particle scattering offers optimum resolution for low-mass species such as C, O, N, S, and Si, the principle components of coal, ash, and char.

Preliminary results are reported here for a number of representative coal samples; the source used in this work,  $\text{Cm}^{244}$ , has high specific activity and a long lifetime (18 years), yet is readily available. Initial work was based on a considerably wider-than-optimum solid angle, which did not permit resolution of individual ash components. However, the carbon/ash ratio was readily obtainable and Btu values which, in most cases lie within statistical error margins, could be calculated from these measurements.

A stronger source would permit restriction of the solid angle and thus should improve the resolution while reducing the time required per analysis. As indicated by lunar surface data, this should yield a fairly accurate value of sulfur content, one of the original goals of this work. Another possible result would be the Ca, Fe, and heavy element composition.

In comparison to other coal analysis schemes, alpha backscattering produces somewhat primitive results, but also costs less than one percent of typical Ge(Li) capture gamma analysis systems; it necessarily requires some scheme of representative sampling whilst capture gamma analysis can be deployed on-line, scanning the entire coal feedline. Thus, the backscattering scheme could best be used in multiple units, e.g., to ascertain the coal/ash ratio before and after some step in coal conversion or preparation, where the high cost (\$1 M) of on-line systems based on capture gamma analysis would make multiple deployment impractical.

---

<sup>1</sup>A. Turkevich, Science 134, p. 672 (1961).



## 1. Introduction

The work reported here is a preliminary investigation of a cheap, rapid, and convenient determination of the composition of coal. To understand how this particular scheme compares with other "nuclear" schemes, we may consider the standard ASTM chemical analysis of coal: a "proximate" analysis in terms of volatiles, fixed carbon, ash fraction, and moisture can be worked up in about one-half hour; breakdown of the ash fraction into elemental constituents takes considerably longer. The information of principal practical interest, the rank or caloric value, may be measured directly, or calculated from a proximate analysis.

Now the long time required for complete analysis evidently militates against processing a large number of samples, which is needed to avoid sampling error; a secondary problem is the dependence of results on attentiveness and skill of the analyst. Improvement efforts have consequently focused on speed and automation. Over the last four years or so, an elemental analysis scheme based on thermal neutron capture gamma radiation spectrometry has been developed into several systems, one of which was discussed in a preceding paper in this session.<sup>1</sup> These systems scan large samples and thus can process the entire feedstream of a coal utilization plant, eliminating sampling error altogether; most of the information provided in a chemical work-up is provided at relatively short intervals.

Inevitably, however, the equipment is costly and requires attendance by specially trained personnel. This limits its application to situations where complete, on-line analysis offers savings which amortize initial and operating cost. The scheme which we will discuss here aims at providing a proximate analysis only, at considerably lower cost, so as to find use in a variety of situations where proximate analysis is adequate. Like the chemical method, it works with small samples -- however, its high processing rate, in conjunction with potentially fully automated operation, should allow its application on-line with an acceptably small sampling error.

To find a method that seemed likely to provide these features, we started with a survey of available schemes involving nuclear radiation or particles. Some of these, such as fast-neutron inelastic scattering gamma spectroscopy,<sup>2</sup> have had some success in on-line coal analysis but had to be ruled out for reason of cost, complexity, need for highly skilled personnel, and radiation hazard. This likewise eliminated direct scattering analysis with monoenergetic neutron beams. Scattering particle energy analysis also applies, however, to charged particles,<sup>3</sup> and such particles happen to be available from natural alpha sources which eliminates the need for an accelerator, hence, radiation hazard, and simplifies the equipment to the level where it can be readily automated. The chief drawback of this scheme appeared to be that it could not accommodate large samples; however, this could be compensated for by low unit cost and high speed of operation. Thus, a battery of scattering chambers, linked to a common electronic processor, could secure an effective sampling rate that could keep up with a coal feedstream in an on-line application.

Automated sample preparation equipment exists at several laboratories, chiefly for X-ray analysis work (which also can only process small samples). As it happens, fluorescent X-ray analysis works best for elements above the number  $Z = 20$ , while alpha backscatter analysis works best below that number, as discussed further on; it is thus particularly well-suited for the main constituents of coal, principally for carbon itself, which is one of the more difficult cases for thermal neutron capture systems. A completely developed system for elemental analysis based on alpha scattering was used to obtain information on the lunar surface in one of the earlier moon-shots.<sup>4</sup>

## 2. Brief Theoretical Background

The basic relation between the incident energy  $E$  of a particle of mass  $a$ , and the energy  $E'$  of the particle scattered by a target of mass  $A$  at an angle  $\theta$ , is given by:

$$K = (E'/E) = [\text{m} \cos \theta + (1 - \text{m}^2 \sin^2 \theta)^{1/2}]^2 / (1 + \text{m})^2$$

$$= \left( \frac{1 - \text{m}}{1 + \text{m}} \right)^2 [1 + \text{m} \sin^2 \theta + \dots] \quad (1)$$

where  $\text{m} = a/A$ . A plot of Eq. (1) shown in Fig. 1 displays the basic facts relevant to backscattering analysis:

1. Scattered energy varies least with the angle near  $180^\circ$ , hence, to allow a large detector aperture at minimal loss of energy resolution, the system should be arranged for backscattering.
2. Separation  $\Delta E'/E'$  for target atoms of adjacent atomic weight  $\Delta A = 1$  declines with the inverse square of the atomic weight:

$$\Delta E'/E' = [16\Delta A / (A^2 - 16)] [1 - (A^2 - 16) \sin^2 \theta / 4A^2 \dots] \quad (2)$$

where we have put  $a = 4$ , for alpha particles. In practice, one thus finds that adjacent elements are no longer resolved for  $A > 40$  (calcium).

Another relevant parameter is the scattering cross section:

$$(d\sigma/d\Omega) = 2.07 \times 10^{-27} (Z/E)^2 (1 - \text{m}^2)^2 \left[ 1 + \frac{1 + 2\text{m}^2}{2} \sin^2 \theta \dots \right] \quad (3)$$

where  $Z \doteq A/2$  is the atomic number and the energy  $E$  is given in MeV. As the count rate varies with the scattering cross section, Eq. (3) suggests that components of low atomic number are not readily detected; however, other factors that influence the observed count rate contribute an opposing effect, such that the detection efficiency is relatively flat for the lighter elements in practice.<sup>5</sup>

### 3. Experimental Equipment and Procedure

The various factors cited in the introduction, together with theoretical considerations, suggested that an investigation of the practical applicability of alpha backscattering to coal analysis should principally focus on means to achieve a high processing rate: firstly, a geometry that would maximize the count rate; and secondly, a means of data processing that would yield an acceptable statistical error in a minimal counting interval. An additional objective became apparent during the work: testing the reliability of a simple formula determination of caloric value from the backscattering measurements; this included, to some extent, a test of sample variability, hence, sampling error.

The two arrangements shown in Fig. 2 both produce backscattering, the central-source system being capable of a wider overall aperture within a certain limiting angle, whereas the peripheral source arrangement allows a stronger source. Energy degradation limits source plating thickness, hence, the maximum practical source strength varies with source area.

Central-source geometry was first investigated, using an  $\text{Am}^{241}$  source deposited on the tip of a drillrod inserted into a hypodermic stock collimator. The collimator, in turn, passed through an annular surface-barrier alpha detector. Source energy spectra revealed considerable degradation in the shape of a long tail of the alpha peak; scattering spectra likewise showed rather broad and ill-defined features, hence, it became apparent that a peripheral-source geometry was preferable. A new unit was accordingly designed and fabricated, as shown in Fig. 3, and an annular  $\text{Am}^{241}$  source of about 0.1 mCi was deposited on the stainless steel annular region in a plating bath of special design. Results with that source were considerably improved, and a number of coal samples, as well as artificial test samples, were analyzed. Calculations indicated, however, that a further improvement in count rate, needed to achieve practical counting times, would require a source of shorter half-life, given that the specific activity (disintegrations/gram) and thus also the count rate for a given source area and allowable plating thickness vary inversely with the half-life. Another source,  $\text{Cm}^{244}$ , was thus fabricated; with a half-life of 18.1 years, this source allows an improvement by a factor of 24 over  $\text{Am}^{241}$  (half-life = 432 years). A quantity of  $\text{Cm}^{244}$  (which happened to be on hand), produced a source strength of about 3.6 mCi, and this shortened the sample reading time from overnight to  $10^4$  seconds. Calculations indicate that a further increase in source strength by a factor of 30, reducing reading time to 5 minutes, would not degrade the source spectrum to an appreciable extent.

A minor problem, which can be dealt with through careful adjustment of the geometry and passivation of the source, is illustrated in Figs. 4 and 5. These figures show the spectrum obtained with a calcium carbonate sample target. Figure 4 reveals a background resulting from a certain amount of wall-scattering which found its way into the detector, as well as source migration to surfaces directly within view of the detector. Wall effect was eventually eliminated by mounting the source button on a pedestal as depicted in Fig. 3. Source passivation would have required evaporation of a thin

gold layer onto the source for which time and equipment was not available. Figure 5 shows, however, that the combined background can also be dealt with by subtracting the spectrum shown in Fig. 6, measured with a plastic button; the carbon return feature of the plastic background spectrum is first replaced with an extrapolation of the background at higher energies.

These three figures also show a line computed with a smoothing program of least-square type.<sup>6-8</sup> Other features of the information processing scheme are indicated in Fig. 7. The region defined as JBAC serves to normalize background subtraction; spectrum steps are then deconvoluted by stripping and extrapolation from higher to lower pulse-heights. Thus, the relatively narrow region KASH where all elements above Ca are concentrated defines the ash fraction; the concentration of the spectrum here is an advantage, since it makes KASH insensitive to detailed composition. KOXY then serves to define oxygen content and ISUM, carbon content. Known samples, e.g., the calcium carbonate button illustrated in Figs. 4 and 5, were used to confirm this subtraction procedure.

The work with coal samples made use of coal that had been analyzed chemically and was locally available, as well as coal that had been analyzed by ANL by capture gamma spectroscopy. Additional samples were obtained through Sargent and Lundy from local power plants, together with available analyses and caloric values.

As indicated in Table 2, these samples encompass both local and Western mines. Target pills were processed from these coals by grinding to fine consistency and compression in a one-inch diameter die, yielding pills that varied considerably in height after compaction to the same pressure (cf. Table 3). A height gauge was designed to adjust the pedestal so as to equalize target distance from the source.

Spectra for each sample were acquired over  $10^4$  seconds using the  $\text{Cm}^{244}$  source, with repeat runs for confirmation. After processing as indicated, data were printed out in the form shown as an example in Table 4.

#### 4. Results and Discussion

Using the computational procedures described above, total carbon, ash fraction, and oxygen fraction were computed for each sample and compared with analyses insofar as these were available; in addition, the Btu/lb rating was computed and similarly compared. To consider the last-named computation, this involved a brief survey to determine the reliability of such a computation from carbon content alone. A variety of formulae can be found in the literature for caloric computation, making use of carbon, moisture, ash fraction, and even nitrogen and oxygen content.<sup>9</sup>

A large number of analyzed samples for which Btu values were also available<sup>10</sup> were used to establish that, over a broad range (although not, perhaps, for all coals), total carbon is usable as an index of caloric value. Figure 8 is a plot of carbon content versus Btu, which yields a straight line with 0.98 correlation for 72 points (listed in Table 1).

The carbon content of the samples measured by alpha backscattering was determined by plotting ISUM versus carbon from chemical analyses provided with the samples (Fig. 8). A straight line fitted to these points had a correlation of 0.97. Next, the Btu rating of each sample was determined by making use of the slope and intercept found in the survey, shown in Fig. 8. This caloric value was then compared with Btu ratings where those had been determined for samples. With few exceptions, for which further work would be indicated to determine the reliability of the chemical analysis, deviation between these two Btu determinations came to less than 3%, as indicated in Table 5, which is an excerpt of more copious data, only including those measured with the  $\text{Cm}^{244}$  source.

The ash fraction was similarly calibrated by plotting KASH data against proximate analyses available for samples; this is shown in Fig. 10. A correlation of 0.91 indicates more scatter in these results than in the carbon determination. Finally, KOXY was plotted against oxygen content inferred from chemical analyses. Here, correlation was only 0.51, suggesting that background subtraction could perhaps be improved.

To sum up this work, it appears that an alpha source of sufficient strength and a system geometry offering the analysis of a 5-10 gram sample in five minutes can be designed. Data processing techniques based on straight-forward smoothing and spectrum stripping yielded an excellent set of carbon content values and an acceptable set of ash fraction values. The computation of caloric value from this information proved to be, rather surprisingly, highly accurate.

Further work should look into some discrepancies to determine whether the alpha backscatter analysis was at fault, the sample had been contaminated, or the chemical analysis was inaccurate. The latter possibility cannot be discounted, especially for the oxygen data that are obtained by subtraction in the ASTM standard procedure.

Additional work could perhaps refine both the measurement geometry and computation procedure to the point where minor constituents such as sulfur could be analyzed; certainly, there is no reason to believe that such an analysis cannot be done, inasmuch as sulfur is cleanly resolved from its neighboring elements in the backscattered alpha spectrum. Minor technical problems, such as source fabrication and stabilization, would have to be addressed. The next phase would then consider the design or adaptation of an automated sample preparation system if a battery of alpha chambers is to be deployed in an on-line application. The present system, however, would only need minor modifications to be useful in a laboratory where it could eventually be incorporated into a combined analysis procedure offering a higher reliability than available from chemical procedures alone.

### Acknowledgments

The help of Roland Armani and Morris Wahlgren in source fabrication was essential to this work. Thanks are due to E. Lewandowski and the machine shop crew for fabricating and, in part, designing necessary hardware components, and to I. Olson, J. Meadows, and P. Guenther for advice and help in dealing with the computer.

### References

1. D. Brown, T. Gozani, H. Bozorgmanesh, and C. Spencer, "Progress and Performance of On-Line Nuclear Analyzers in Coal," 1982 Symp. on Instrumentation and Control for Fossil Energy Processes, Houston, TX (June 7-9, 1982).
2. T. C. Martin, J. D. Hall, and I. L. Morgan, "An On-Line Nuclear Analysis System," Radioisotope Instruments in Industry and Geophysics, IAEA, Vienna (1966).
3. W. K. Chu, J. W. Mayer, and M. A. Nicolet, "Backscattering Spectrometry," Academic Press, NY (1978).
4. A. Turkevich, "Chemical Analysis of Surfaces by Use of Large-Angle Scattering of Heavy Charged Particles," *Science* 134, p. 672 (1962).
5. J. H. Patteron, A. L. Turkevich, and E. Franzgate, "Analysis of Light Elements by Alpha Backscattering," Radioisotope Instruments in Industry and Geophysics, IAEA, Vienna (1966).
6. A. Savitzky and M. J. E. Golay, "Smoothing and Differentiation of Data by Simplified Least Square Procedures," *J. Anal. Chem.* 36, p. 1627 (1964).
7. V. Barnes, "GASPAN -- An Advanced Computer Code for the Analysis of High-Resolution Gamma Spectra," *IEEE Trans. Nucl. Sci.* NS-15, No. 3 (1968).
8. D. J. Gorman, "A Computer Program for the Smoothing and Differentiation of Data from Multichannel Analyzers," UCRL 19903, Berkeley (1970).
9. L. L. Chyi, Argonne National Laboratory, Internal Memorandum (1980); also, T. K. Subromoriam, "Coal Age Operating Handbook of Preparation" (1975).
10. Illinois State Geological Survey Environmental Geology Notes, Sug. 1974, No. 72.

TABLE I

Sample	Total Carbon	Btu/lb
C-13854	79.94	14362
C-16787	77.72	13794
C-15678	71.49	12952
C-16919	75.43	13280
C-16408	71.21	12990
C-15943	74.53	13392
C-15944	74.92	13517
C-13039	71.28	12927
C-14646	71.70	12829
C-14650	72.73	12951
C-15263	73.24	13102
C-15566	72.33	13042
C-15331	68.23	12387
C-15496	72.06	12996
C-16564	70.61	12920
C-12495	69.98	12466
C-13983	70.76	12736
C-14194	72.28	12973
C-14609	73.20	13137
C-14735	71.18	12724
C-14774	70.31	12485
C-15012	71.86	12873
C-15208	67.18	11973
C-15384	71.94	12997
C-15448	68.88	12390
C-16264	68.99	12480
C-16729	71.23	12728
C-17001	71.57	12947
C-17721	73.49	13324
C-17984	74.20	13276
C-17988	73.46	13087
C-18040	70.27	12456
C-12831	72.16	12895
C-12942	69.91	12621
C-13324	70.76	12779
C-13433	73.33	13060
C-13895	67.84	12303
C-13975	71.16	12729
C-14574	74.72	13480
C-14613	73.42	13027
C-14630	73.72	13162
C-14838	69.49	12465
C-14970	69.25	12419
C-14982	68.57	12255
C-15038	73.76	13005
C-15079	66.24	11900
C-15117	67.44	12074
C-15125	68.68	12220

TABLE I (Contd.)

Sample	Total Carbon	Btu/lb
C-15231	68.09	12222
C-15432	70.58	12438
C-15436	68.97	12442
C-15456	69.23	12274
C-15717	69.11	12449
C-15791	72.92	13008
C-15868	75.13	13290
C-15872	67.70	12109
C-15999	69.49	12470
C-16030	71.96	13140
C-16139	66.25	12050
C-16265	71.79	12810
C-16317	69.97	12400
C-16501	72.06	12980
C-16543	68.71	12380
C-16741	69.53	12455
C-16993	64.57	11562
C-15278	69.87	12630
C-17053	71.06	12850
C-17215	65.30	11908
Lower Freeport	78.82	13964
Western Kentucky	69.41	12746
Ohio	59.61	10855
Belle Ayre	52.52	9086



TABLE II

Origin	Coal Type	Designation	% Total Carbon	Btu/lb	% Ash	% Oxygen	
ANL-K <sup>a</sup>	Western Kentucky	Drum E-17	WK-17	69.41	12746	10.20	7.50 <sup>d</sup>
ANL-K	Western Kentucky	Drum E-20	WK-20	69.41	12746	10.20	7.50 <sup>d</sup>
ANL-K	Lower Freeport	Drum-49	LF-49	78.82	13964	10.17	3.11 <sup>d</sup>
ANL-K	Lower Freeport	Drum-43	LF-43	78.82	13964	10.17	3.11 <sup>d</sup>
ANL-K	Ohio	Drum-16	OH-16	59.61	10855	23.49	4.97 <sup>d</sup>
ANL-K	Ohio	Drum-18	OH-18	59.61	10855	23.49	4.97 <sup>d</sup>
ANL-K	Glen Burn	Drum-A	GB-A	82.16	13399	8.87	2.44 <sup>d</sup>
ANL-K	Glen Burn	Drum-B	GB-B	82.16	13399	8.87	2.44 <sup>d</sup>
S.L. <sup>b</sup>	Western Coal	WC-SL	---	8268-11694	9.03	---	---
ANL <sup>c</sup>	New Mexico (Sub-Bituminous)	NM-04	55.69	8000-11628 (9800)	18.00	9.85	---
ANL	Illinois Bituminous (#10 Mine Peabody Coal Co.)	IB-10	62.94	11304	12.70	8.48	---
ANL	Inland Steel Mine	IN-SM	73.8	13538	6.06	3.0 <sup>d</sup>	---
ANL	Starr Mine (Hi Pyrite)	ST-HP	60.84	11559	14.57	3.5 <sup>d</sup>	---
ANL	North Dakota (Lignite)	ND-LG	45.4-65.94	7443-10810	6.00-18.74	12.90-18.74 <sup>d</sup>	---
ANL	Arkwright Mine (Consol Coal Co.)	AW-02	77.14	13706-14114	7.68-7.91	4.97 <sup>d</sup>	---
S.L.	Seminole Mine (Sample A-Small Lump)	SM-SL	61.54-70.81	10754-12374	6.47-7.44	12.89-14.83 <sup>d</sup>	---
S.L.	Seminole Mine (Sample B-Large Lump)	SM-SL	63.43-72.83	11162-12817	4.39-5.04	12.86-14.77 <sup>d</sup>	---

<sup>a</sup>ANL-K Argonne National Laboratory Coal Instrumentation Group originally obtained from Kennedy Van Saun Corp.

<sup>b</sup>S.L. Sargent Lundy Engineering Company from power plants in the Chicago area.

<sup>c</sup>ANL Argonne National Laboratory Coal Instrumentation Group.

<sup>d</sup>Indicates oxygen determination by difference determination. Two values indicate wet and dry determinations. Value in parentheses indicates an average.

TABLE III

Sample	Thickness (inches)
WK-17-A	0.274
WK-17-B	0.283
WK-20-A	0.294
WK-20-B	0.281
LF-49-A	0.266
LF-49-B	0.251
LF-43-A	0.258
LF-43-B	0.251
OH-16-A	
OH-16-A	0.246
OH-18-A	0.251
OH-18-B	0.252
GB- A A	
GB- A B	Would not hold
GB- B-A	pill SHAPE
GB- B-B	
WC-SL-A	0.271
WC-SL-B	0.257
WC-SL-C	0.278
WC-SL-D	0.273
NM-04-A	0.272
NM-04-B	0.269
IB-10-A	0.277
IB-10-B	0.280
IN-SM-A	0.296
IN-SM-B	0.283
ST-HP-A	0.261
ST-HP-B	0.274
ND-LG-A	0.289
ND-LG-B	0.289
AW-02-A	0.285
AW-02-B	0.282
SM-SL-A	
SM-SL-B	
SM-LL-A	
SM-LL-B	

TABLE IV

<u>IDENTIFICATION</u>	<u>ILW</u>	<u>IUP</u>	<u>JSUM</u>	<u>KSUM</u>	<u>ISUM</u>	<u>FTME</u>	<u>CARBON</u>	<u>BTU/LB</u>	<u>ERR</u>
LF-43-A1	20	70	982	72	910	1.164	81.11	14572	1159
<u>IDENTIFICATION</u>	<u>ILW</u>	<u>IUP</u>	<u>ISUM</u>	<u>KOXY</u>	<u>KASH</u>	<u>FTME</u>	<u>CARBON</u>	<u>BTU/LB</u>	<u>ERR</u>
LF-43-A1	20	70	16529	31	960	1.000	79.61	14301	1137

Table 5. Data Obtained with Cm<sup>244</sup> Source, Including Btu Comparison

Identification	ISUM	KOXY	Ash	Carbon	Btu/lb	Measured Btu/lb	% Error	Measured Ash	Diff.	% Error
WK-17-A2-N	27811	117	11.22	69.74	12505	12746	1.9	10.20	1.02	10.0
WK-17-A2-N	27837	116	11.39	69.80	12517	12746	1.8	10.20	1.19	11.7
WK-20-A1-N	14659	125	10.20	70.45	12634	12746	0.9	10.20	0.0	0.0
WK-20-A1-N	14667	116	9.93	70.49	12641	12746	0.8	10.20	0.27	2.6
WK-20-B1-N	15202	71	12.79	73.11	13118	12746	2.9	10.20	2.59	25.4
WK-20-B1-N	15193	65	13.66	73.06	13110	12746	2.8	10.20	3.46	33.9
WK-20-B2-N	14878	102	11.39	71.52	12829	12746	0.7	10.20	1.19	11.7
WK-20-B2-N	14898	103	12.10	71.62	12847	12746	0.8	10.20	1.90	18.6
WK-20-B2-N	14891	102	12.05	71.58	12841	12746	0.7	10.20	1.85	18.1
WK-20-B3-N	14979	107	10.67	72.02	12919	12746	1.4	10.20	0.47	4.6
WK-20-B3-N	14961	107	11.69	71.93	12903	12746	1.2	10.20	1.49	14.6
WK-20-B1-3 SUM-N	45057	93	11.62	72.21	12955	12746	1.6	10.20	1.42	13.9
WK-20-B1-3 SUM	45052	91	12.84	72.20	12953	12746	1.6	10.20	2.64	25.9
LF-43-A1-N	16529	36	10.05	79.61	14301	13964	2.4	10.17	0.12	1.2
LF-43-A1-N	16512	41	10.28	79.53	14285	13964	2.3	10.17	0.11	1.1
LF-49-A1-N	16565	66	8.86	79.79	14333	13964	2.6	10.17	1.31	12.9
LF-49-A1-N	16535	73	8.48	79.64	14306	13964	2.4	10.17	1.69	16.6
LF-49-B1-N	16406	53	10.85	79.01	14191	13964	1.6	10.17	0.68	6.7
LF-49-B1-N	16392	51	11.59	78.94	14178	13964	1.5	10.17	1.42	14.0
LF-49-B2-N	16368	35	9.30	78.82	14157	13964	1.4	10.17	0.87	8.6
LF-49-B2-N	16377	28	10.11	78.87	14165	13964	1.4	10.17	0.06	0.6
LF-49-B2-3-N	16525	27	11.36	79.59	14297	13964	2.4	10.17	1.19	11.7
LF-49-B3-N	16489	26	12.46	79.42	14265	13964	2.2	10.17	2.29	22.5
LF-49-B4-N	16253	42	11.99	78.26	14055	13964	0.65	10.17	1.82	17.9
LF-49-B4-N	16256	35	12.69	78.27	14057	13964	0.66	10.17	2.52	24.8
IN-SM-B1-N	15381	81	7.57	75.70	13590	13538	0.50	6.06	1.51	24.9
IN-SM-B1-N	15365	83	7.52	75.62	13576	13538	0.4	6.06	1.46	24.1
IN-SM-B2-N	16098	67	5.67	77.50	13916	13538	2.9	6.06	0.39	6.4

Table 5. (cont'd)

Identification	ISUM	KOXY	Ash	Carbon	Btu/lb	Measured		Measured	
						Btu/lb	% Error	Ash	Diff. % Error
IN-SM-B2-N	16077	66	7.06	77.40	13898	13538	2.7	6.06	1.00 16.5
IN-SM-B3-N	15463	86	7.82	74.39	13351	13538	1.4	6.06	1.76 29.0
IN-SM-B3-N	15443	92	8.60	74.29	13333	13538	1.5	6.06	2.54 41.9
IN-SM-B4-N	15368	92	8.18	73.92	13266	13538	2.0	6.06	2.12 35.0
IN-SM-B4-N	15364	88	9.01	73.90	13262	13538	2.0	6.06	2.95 40.1
IN-SM-B5-N	15110	93	7.58	72.66	13036	13538	3.7	6.06	1.52 25.1
IN-SM-B5-N	15109	98	8.44	72.65	13035	13538	3.7	6.06	2.38 39.3
AW-02-B1-N	11596	83	8.45	75.47	13547	14114	4.0	7.91	0.54 6.8
AW-02-B1-N	11595	84	8.08	75.46	13545	14114	4.0	7.91	0.17 2.1
AW-02-B2-N	15847	75	7.18	76.27	13693	14114	3.0	7.91	0.73 9.2
AW-02-B2-N	15852	73	8.28	76.29	13697	14114	3.0	7.91	0.37 4.7
AW-02-A3-N	15910	82	8.74	76.58	13749	14114	2.6	7.91	0.83 10.5
AW-02-A3-N	15898	83	8.65	76.52	13738	14114	2.7	7.91	0.74 9.4
AW-02-A4-N	15739	96	8.26	75.74	13597	14114	3.7	7.91	0.35 4.4
AW-02-A4-N	15756	94	8.30	75.82	13612	14114	3.6	7.91	0.39 4.9
AW-02-A5-N	15823	107	8.38	76.15	13671	14114	3.1	7.91	0.47 5.9
AW-02-A5-N	15815	110	8.56	76.11	13664	14114	3.2	7.91	0.65 8.2
AW-02-A6-N	4017	72	7.77	77.01	13827	14114	2.0	7.91	0.14 2.7
AW-02-A6-N	4043	54	6.64	77.52	13919	14114	1.4	7.91	1.27 16.0
AW-02-A3-6 SUM	51488	96	8.41	76.22	13684	14114	1.1	7.91	0.50 6.3
AW-02-A3-6 SUM	51495	90	8.80	76.23	13686	14114	1.1	7.91	0.89 11.3
OH-18-A1-N	13887	109	13.82	66.66	11946	10855	10.1	23.49	9.67 57.1
OH-18-A1-N	13865	115	14.25	66.56	11927	10855	9.9	23.49	9.24 39.3
OH-16-A2-N	12965	137	15.98	62.14	11125	10855	2.5	23.49	7.51 32.0
OH-16-A2-N	12998	136	15.61	62.31	11154	10855	2.8	23.49	7.88 33.5
OH-16-A3-N	13035	148	15.78	62.49	11187	10855	3.1	23.49	7.71 32.8
OH-16-A3-N	13028	156	15.57	62.45	11181	10855	3.0	23.49	7.92 33.7
OH-16-A4-N	12956	145	15.92	62.10	11117	10855	2.4	23.49	7.57 32.2

Table 5. (cont'd)

Identification	ISUM	KOXY	Ash	Carbon	Btu/lb	Measured		Diff.	% Error	
						Btu/lb	Ash			
IN-SM-B2-N	16077	66	7.06	77.40	13898	13538	2.7	6.06	1.00	16.5
OH-16-A4-N	12970	141	15.65	62.17	11129	10855	2.5	23.49	7.84	33.4
OH-16-A5-N	3417	115	16.40	60.13	10758	10855	0.9	23.49	7.09	30.2
OH-16-A5-N	3431	107	14.56	60.38	10804	10855	0.5	23.49	8.93	38.0
OH-17-A2-5 SUM	42372	141	15.94	62.07	11110	10855	2.3	23.49	7.55	32.1
OH-16-A2-5 SUM	42430	138	16.05	62.15	11126	10855	2.5	23.49	7.44	31.7
WC-SL-A1-N	12510	153	9.12	59.91	10719	11694	8.3	9.03	0.09	1.0
WC-SL-A1-N	12495	154	9.21	59.84	10706	11694	8.4	9.03	0.18	2.0
ST-HP-A1-N	13089	137	15.37	62.75	11235	11559	2.8	14.57	0.80	5.5
ST-HP-A1-N	13087	138	15.35	62.74	11233	11559	2.8	14.57	0.78	5.4
NM-04-A1-N	11671	175	14.34	55.80	9972	9800	1.7	18.00	3.66	20.3
NM-04-A1-N	11666	166	14.58	55.78	9967	9800	1.7	18.00	3.42	19.0
SM-SL-A2-N	14211	113	6.83	68.25	12235	12374	1.1	6.47-7.44	3.42	2.4
SM-SL-A2-N	14203	114	6.97	68.21	12228	12374	1.2	6.47-7.44	3.42	0.4
18-10-A2-N	12812	143	12.80	61.39	10988	11304	2.8	12.70	0.10	0.7
18-10-A2-N	12827	137	12.44	61.47	11002	11304	2.7	12.70	0.26	2.0
ND-LG-A1-N	12634	139	4.23	60.52	10830	10810	0.2	6.00	1.77	29.5
ND-LG-A1-N	12632	142	5.98	60.51	10828	18010	0.17	6.00	0.02	0.33

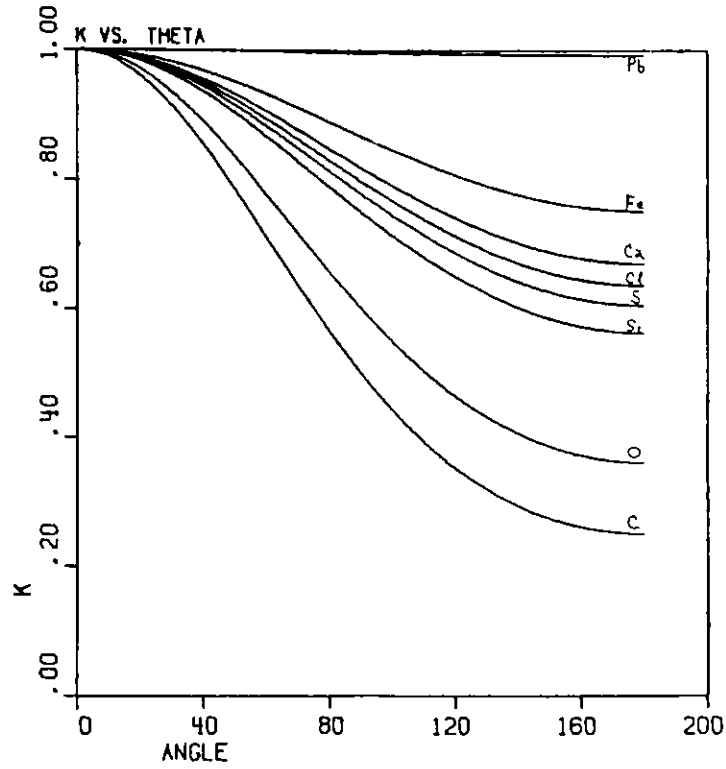


Fig. 1. Scattered to Incident Alpha Particle Energy ratio versus Scattering Angle, for Different Target Atomic Masses

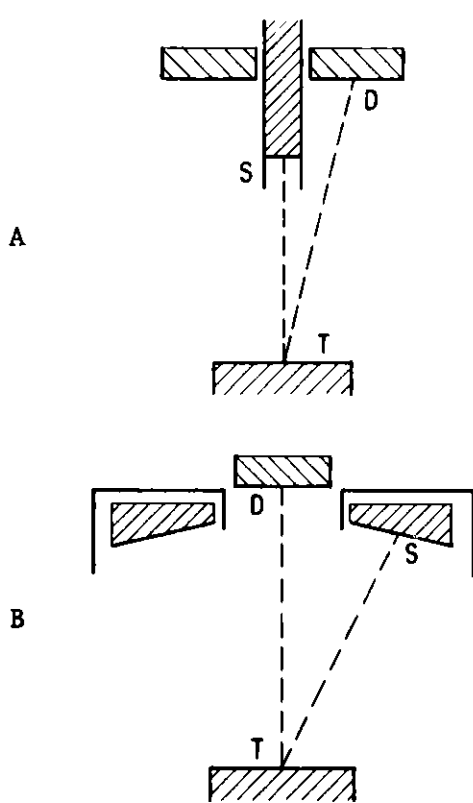


Fig. 2. Backscatter Geometry: (A) Central Source, (B) Peripheral Source. S = Source, D = Detector, T = Target

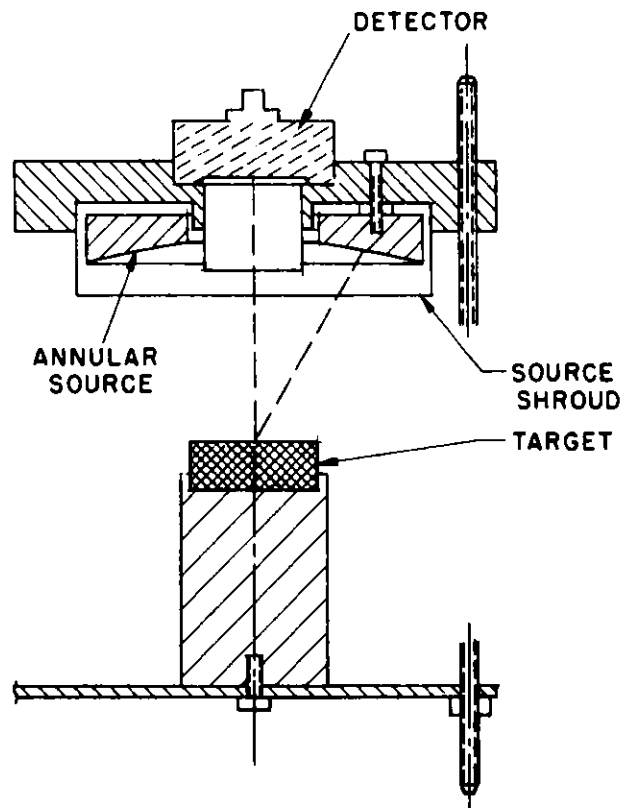


Fig. 3. Final Design of Apparatus Used in These Tests

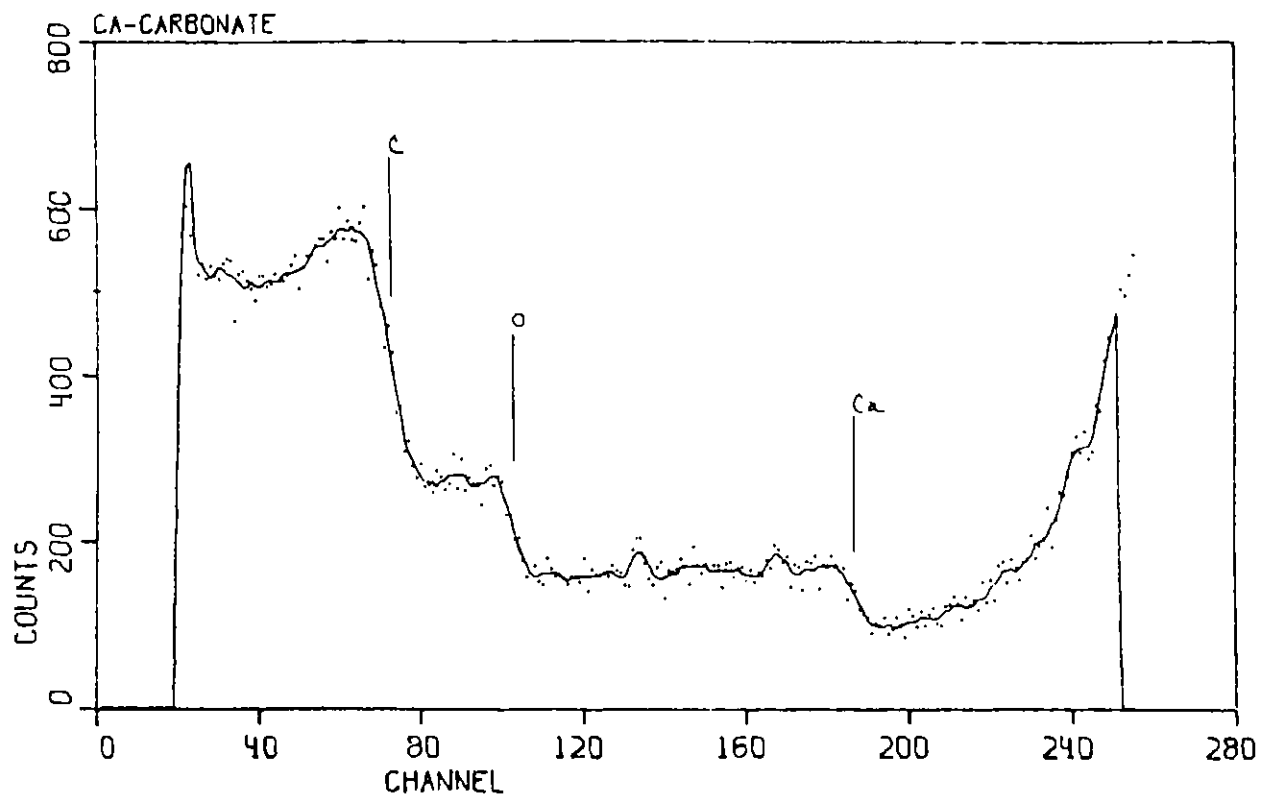


Fig. 4. Calcium Carbonate Spectrum, Unprocessed

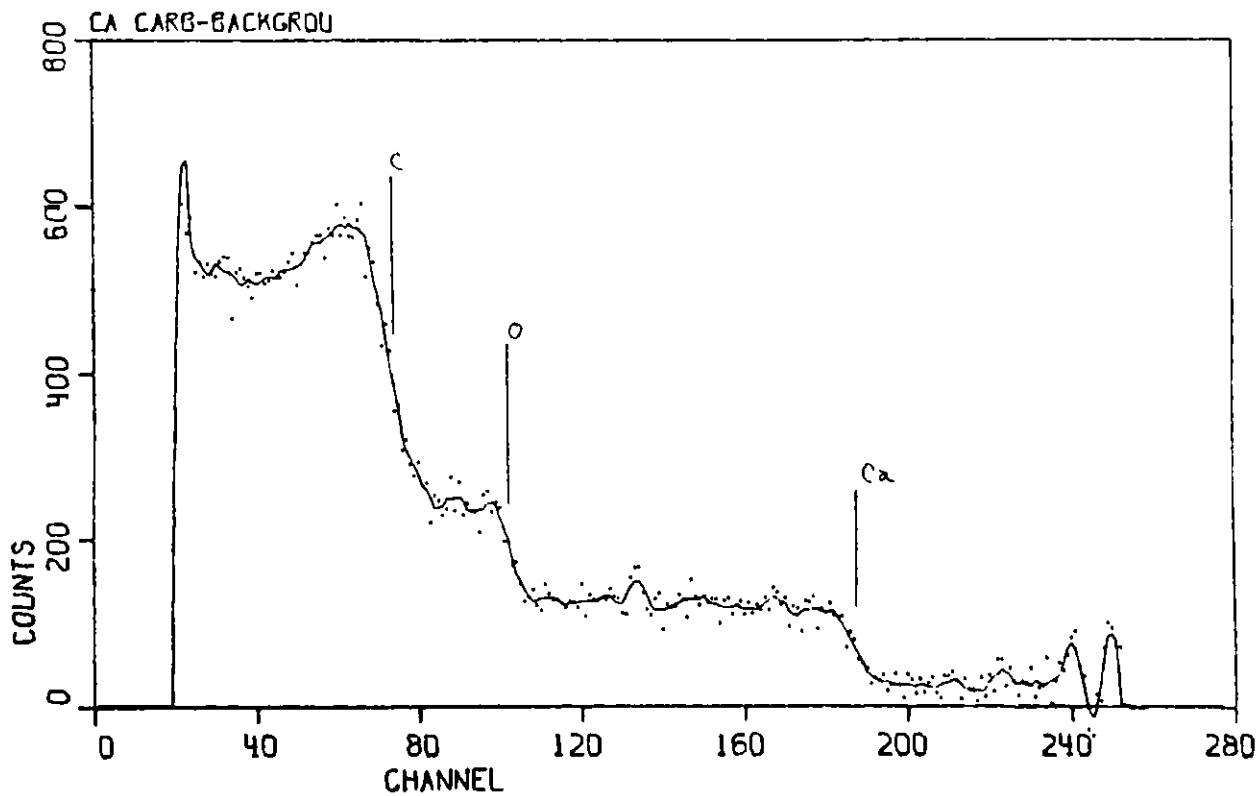


Fig. 5. Calcium Carbonate Spectrum, Background Subtracted



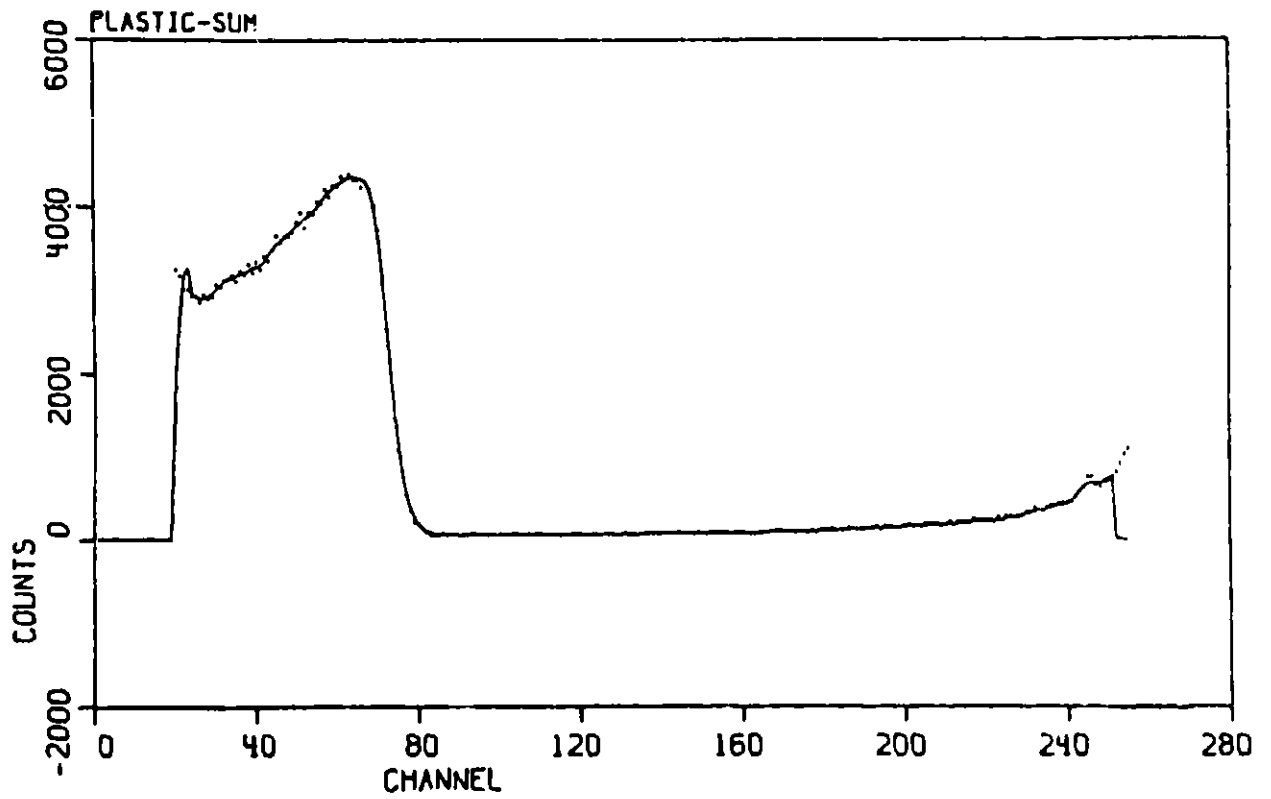


Fig. 6. Plastic Button Scattering Spectrum Used for Background Subtraction

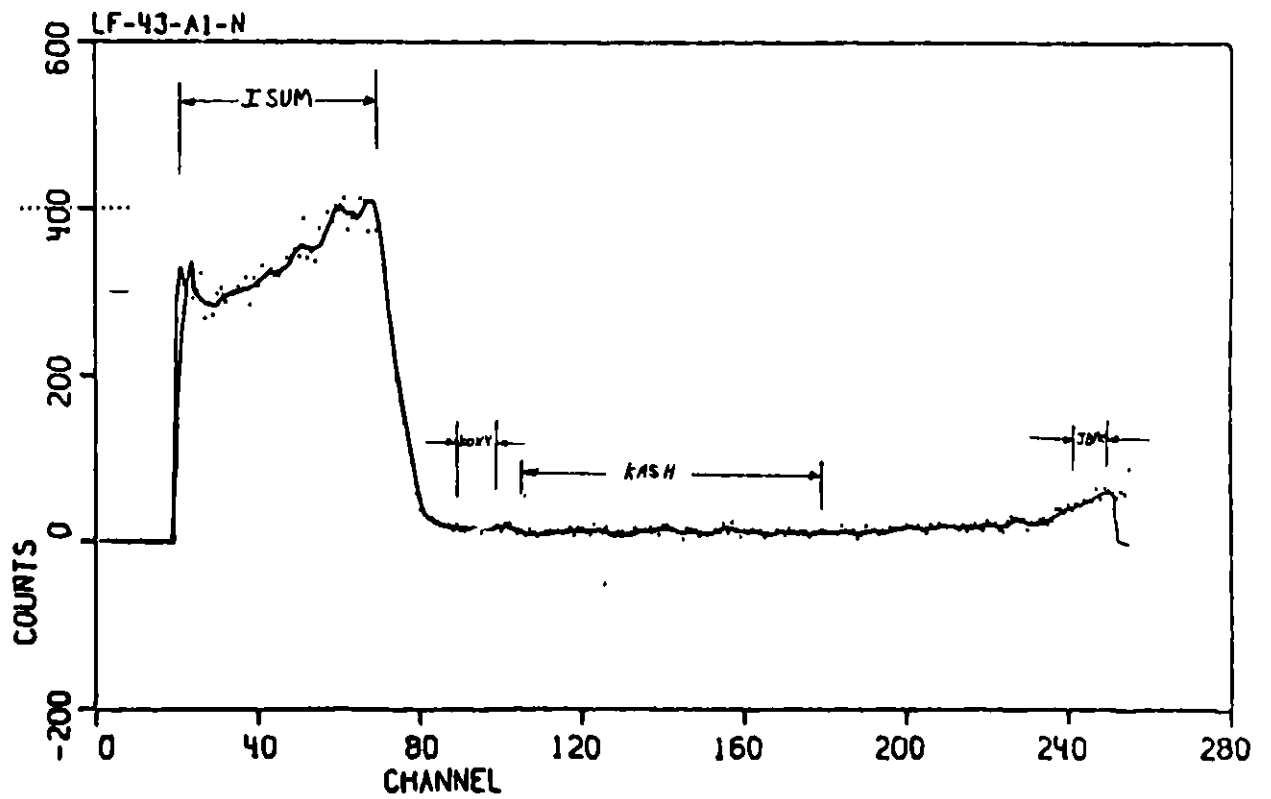


Fig. 7. KASH, KOXY, ISUM, and PAC Regions

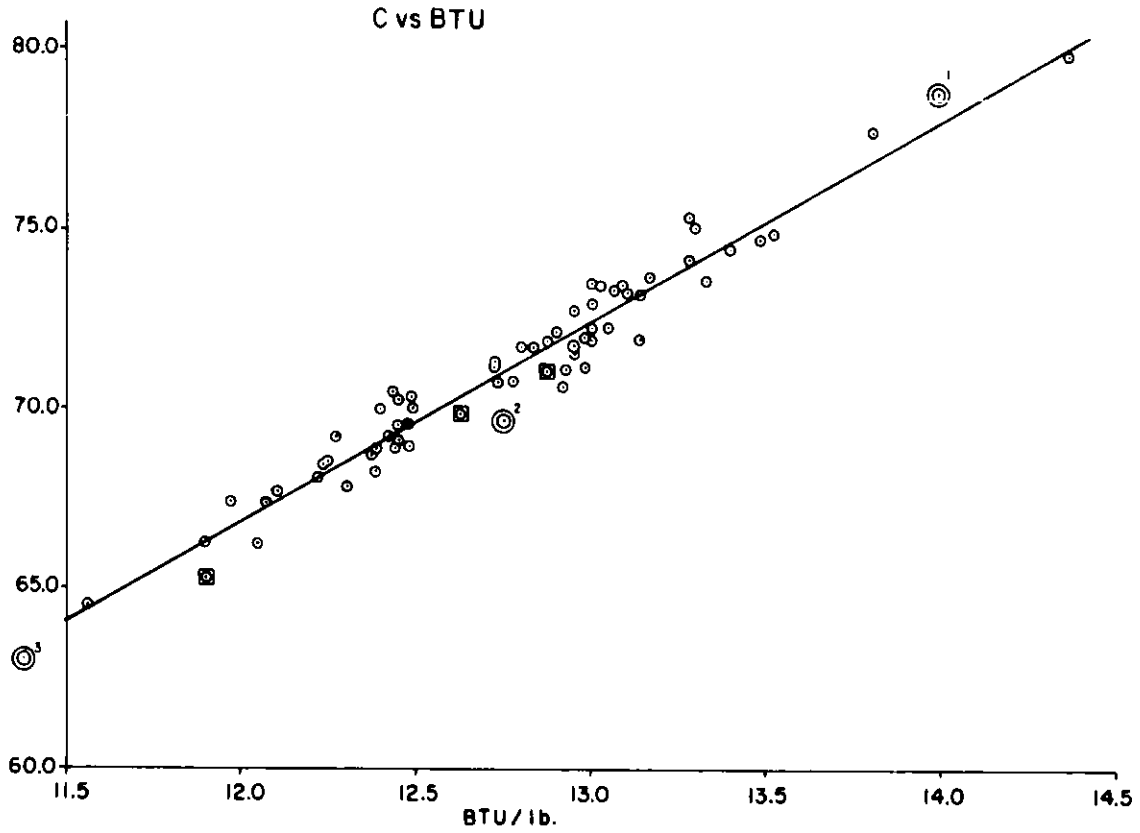


Fig. 8. Coal Carbon Content versus Btu for Coals Listed in Table 1

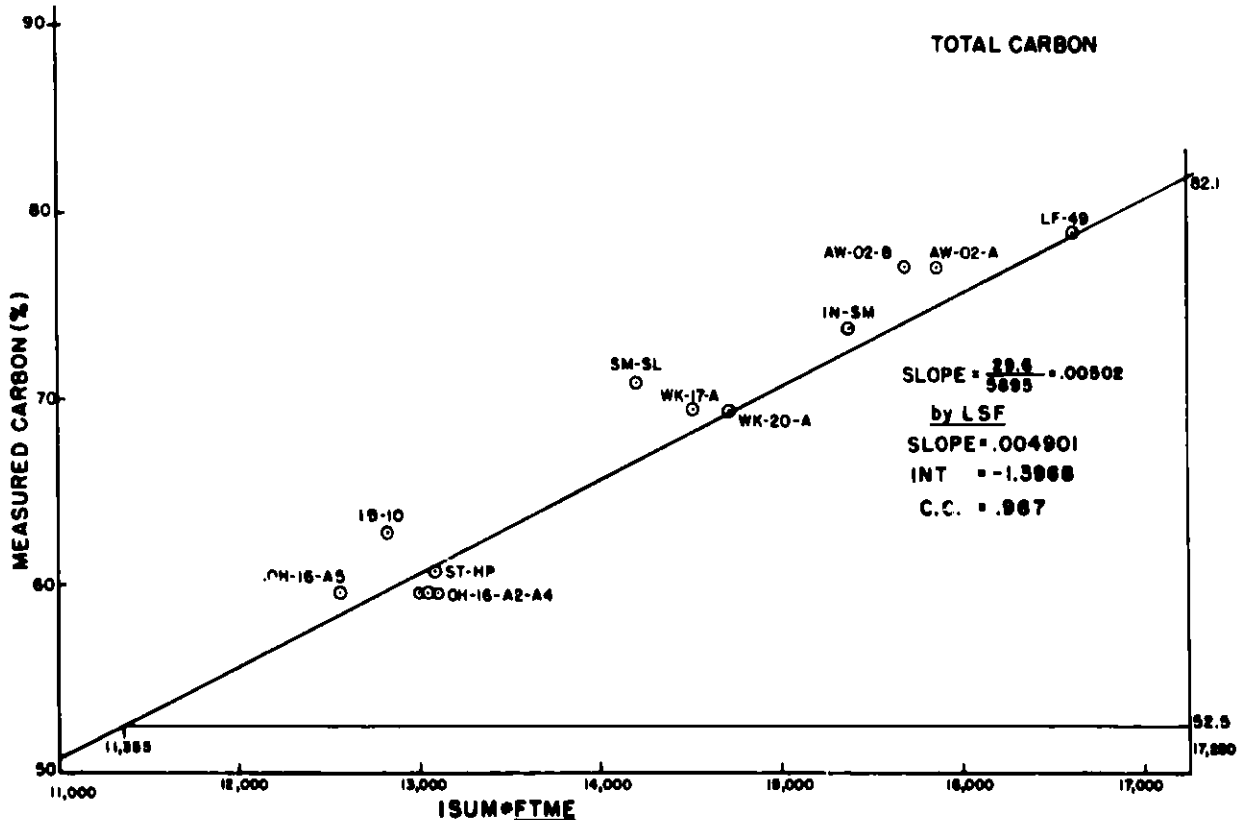


Fig. 9. Measured ISUM Values versus Carbon Content of Samples by Chemical Analysis

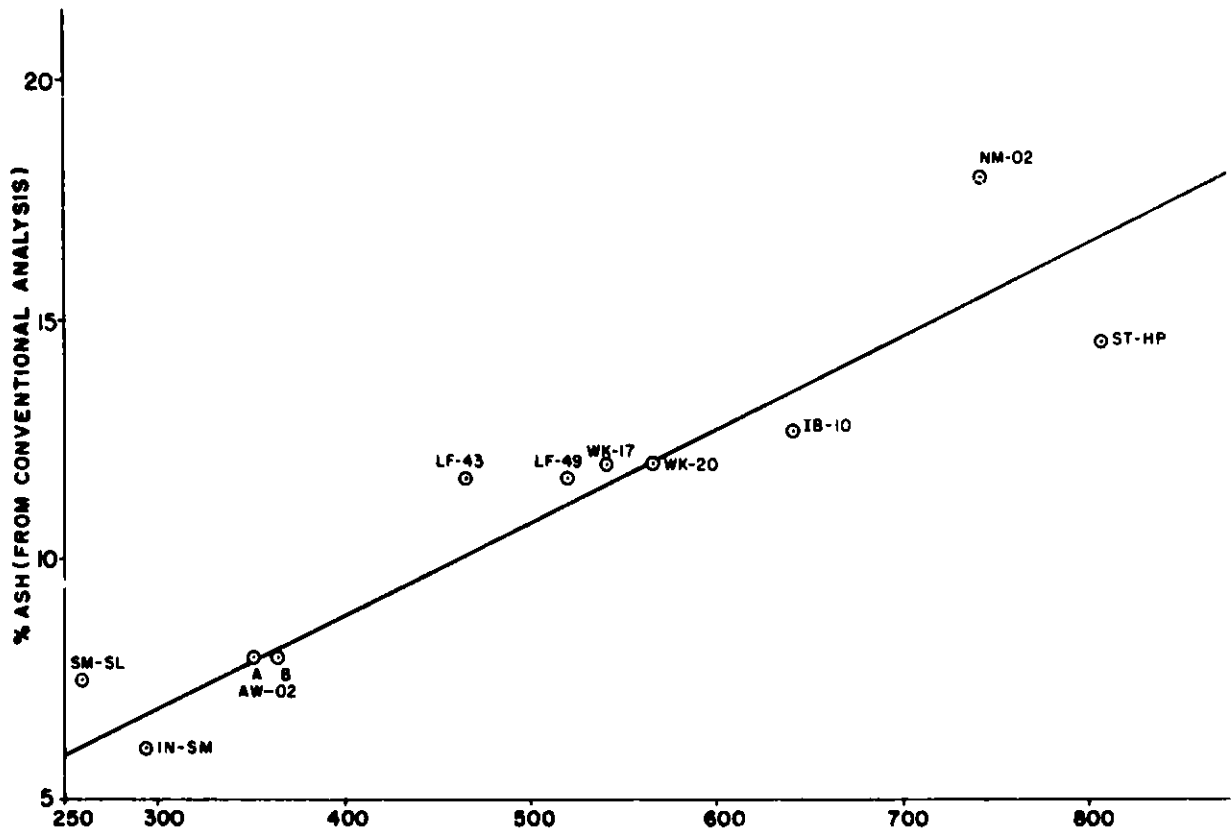


Fig. 10. KASH versus Ash Fraction Values from Chemical Analysis

THE USE OF NATURAL GAMMA RADIATION IN THE COAL MINING INDUSTRY

National Coal Board  
Mining Research and Development Establishment  
Ashby Road  
Stanhope Bretby  
Burton on Trent  
Staffordshire

J S Wykes, I Adsley, L R Cooper

Abstract

The technique of delineating coal seams by the use of natural gamma borehole logging sondes has been known for many years. The principle of the technique is that the gamma fluxes in shales are higher than in coals as the abundance of naturally occurring radionuclides is some twenty times greater in the former.

This paper discusses other applications where the differing natural gamma properties of coals and shales can be used. These are:

- (a) To distinguish between stone (shale) and run-of-mine coal on conveyor belts. A common situation underground is one in which stone from development headings and normal run-of-mine coal have to be batched along the same conveyor system. A natural gamma device capable of distinguishing between such batches of material, and thus allowing suitable mechanical separation, will be described.
- (b) To provide an accurate measurement of roof coal thickness by measuring the natural gamma flux penetrating the roof coal. To illustrate this examples will be given where this technique is used to provide automatic controlled steering of Long Wall Shearers and to provide manually assisted steering of In-seam Heading Machines.

Introduction

Shales contain substantial concentrations of the naturally occurring radionuclides Potassium 40, Thorium 232, and Uranium 238, the latter two radionuclides each giving rise to series which end in stable isotopes of lead. When these radionuclides decay they release gamma rays which propagate through the strata gradually losing energy by scattering processes until they are absorbed; the range of such gamma rays within the strata may be as great as 500 mm. Coals, however, have significantly lower concentrations of these radionuclides and thus the gamma ray flux in coals is correspondingly lower.

This difference in the natural gamma ray flux in the two types of strata has been used for many years as a method of identifying coal seams during borehole logging operations with gamma sensitive sondes. A typical natural gamma borehole log through a coal seam is shown in Figure

1. It may be seen from Figure 1 that when the sonde is in the shale strata the gamma count-rate measured is characteristic of the shale activity, however as the sonde approaches the shale/coal interface there is a gradual reduction in the gamma count-rate as the lower activity coal is sensed until finally when the sonde is well within the coal seam the gamma count-rate is characteristic of the lower gamma activity of the coal.

Other applications where the differing natural gamma properties of shale and coal can be used are suggested by the response of the sonde to the two types of strata. Firstly, the simple situation can be envisaged where it is possible to differentiate between a lump of coal and a lump of shale by measuring the magnitude of the natural gamma flux emanating from the material. Secondly, since the natural gamma flux intensity gradually reduces as the sonde moves from the shale through the shale/coal interface and into the coal, this suggests that it should be possible to determine the amount of coal left in the roof after mining operations by measuring the intensity of the natural gamma flux penetrating the roof coal from the shale overburden.

A consideration of the research and design of working systems for applications of coal/stone monitoring of conveyors and roof coal thickness sensing for coal cutters is given in this paper.

### Coal/Stone Discrimination on Conveyors

#### Requirement for a Coal/Stone Transducer

In the UK there are several mines where it is necessary to use the same conveyor systems to transport both run-of-mine coal and stone (shale) from development headings. It is obviously undesirable to mix these materials and thus the stone is normally batched onto the conveyor belt when it is empty and subsequently mechanically removed at some convenient point. The desire to automate this removal process necessitates the development of a transducer capable of distinguishing between stone and coal on a conveyor belt and a natural gamma transducer capable of performing this task is described below.

#### Evaluation of Method of Natural Gamma Coal/Stone Sensing

The basic problem is to establish that the magnitude of the gamma fluxes from the coal and stone on the belt are sufficiently different as to allow discrimination between the two materials within a reasonable measuring time.

To provide an initial estimate of the magnitudes of these fluxes a laboratory mock-up of a conveyor system was constructed under which was placed a small gamma detector; the detector was shielded from background radiation by lead shields above and below the belt. Samples of coal or shale could be placed on the belt and measurements were taken using mass loadings of  $90 \text{ kg/m}^2$  of both materials.

Using a criterion that the probability of incorrect identification of the material on the belt is less than 1 in  $10^4$  it may be shown that this requires

$$(N_s^{\min})^{1/2} = \frac{4}{1-q} \left[ (2)^{1/2} + (1+q)^{1/2} \right]$$

where  $N_s^{\min}$  is the minimum number of counts needed to meet this condition with shale on the belt and  $q$  is defined as

$q = \frac{N_c}{N_s}$ ,  $q < 1$  where  $N_c(N_s)$  is the mean count per integration interval with coal (shale) on the belt.

In the laboratory the value of  $N_s$  was 16.7 cps and of  $N_c$  was 8.37 giving a  $q$  value of 0.501 and value of  $N_s^{\min}$  of 447 counts. With the small detector used in the laboratory this gives a 'decision time' of 447/16.7 or 27 seconds. The use of a larger detector will obviously reduce the decision time and on the basis of these initial measurements it was decided to design a prototype system with a much shorter response time for further trials.

#### Laboratory and Underground Trials of Prototype System

An intrinsically safe prototype system was constructed by Salford Electrical Instruments Limited (SEI) to a design specification from MRDE. The system employed a large gamma detector shielded by background shields above and below the belt. Gamma events occurring in the detector could be monitored by either a counter-timer or a ratemeter.

Laboratory measurements were taken using the same conveyor mock-up replacing the small detector with the large prototype unit. Mass loadings of 60 kg/m<sup>2</sup> of material were used giving values for  $N_s$  of 283.8 cps and for  $N_c$  of 169.5 cps; this gives a 'q' value of 0.597 and a decision time,  $t$ , of 2.5 seconds. The prototype system employed less shielding around the detector than it had been possible to use with the small laboratory system and consequently higher coal/background levels were experienced resulting in a larger value of  $q$ .

The prototype system was installed underground on a conveyor system at Rawdon Colliery and a series of static tests using known mass loadings of coal and stone were conducted. These results are shown in Figure 2.

Figure 2 indicates the anticipated response of the system, namely that the count-rate for an empty belt or with (inactive) coal on the belt is reasonably constant whereas there is a systematic increase in count-rate with increasing amounts of shale on the belt. If a constant empty belt coal reading is assumed the corresponding  $q$ ,  $N_s^{\min}$  and decision time 't' values to discriminate various amounts of shale on the belt are shown in Table 1.

Table 1

Mass of shale kgm/m <sup>2</sup>	q	Ns <sup>min</sup>	t
10	0.86	-	-
20	0.77	2280	12.30
30	0.72	1500	7.80
40	0.68	1170	5.82
50	0.67	1070	5.14
60	0.66	1000	4.79

The longer decision time (typically about 5 seconds) is due to the higher values of q experienced underground. Although this response time may be too long for some applications this problem may be easily overcome, the simplest solution being to use a larger detector.

#### Comments

This system was a prototype to investigate the possibility of distinguishing stone from coal on conveyors. The activities of shales have a 20% variation and thus it is not expected that there would be any significant variation in the response time of such a system in different situations. The problem of distinguishing coal from sandstone, a more rarely found overburden, is more difficult as sandstone activities are significantly lower than shales but such distinction should still be possible.

The development of a production system is planned.

#### Roof Coal Thickness Sensing

##### Requirement

Unlike the coal/stone differentiator whose potential use would be limited to those mines which handle significant amounts of stone, the requirement for roof coal thickness or horizon sensors is much more general throughout the NCB. The ability to be able to determine, and thus control, the position of coal cutters within a seam is of great importance since it ensures that only coal is mined and also permits a certain thickness of coal to be left above the mining machine in order to support the weaker overlying shale.

### Evaluation of the Method of Roof Coal Thickness Sensing

The main problems associated with a natural gamma method of measuring roof coal thickness are firstly to ascertain that the magnitude of the natural gamma flux penetrating the roof coal is sufficiently great as to allow an accurate estimate of the roof coal thickness to be made within a time adequate for steering control action; and secondly to ensure that the shale activity above the seam is consistent over large areas, ie, that the calibration of any working sensor would be correct over the area of the mine workings.

From the natural gamma logs it would be anticipated that a sensor positioned under a section of roof coal and collimated to collect only gamma rays penetrating the roof coal, should have a monotonically decreasing response with increasing roof coal thickness. Following theoretical modelling of the gamma transport in the coal/shale system, which suggested significant count-rates and ranges of penetration, a series of measurements of the natural gamma count-rate as a function of roof coal thickness was made on several seams. These measurements were made using an Intrinsically Safe gamma counting system comprising a small gamma detector which was shielded such that only gamma rays from the upper half plane, the roof, were detected. Figure 3 shows a typical natural gamma count-rate versus roof coal thickness characteristic from the Five Foot Seam at Bagworth Colliery. During these trials theoretical predictions of the insensitivity of the gamma flux to distance below the roof coal were also confirmed (this allows considerable freedom in positioning the sensor on the coal cutting machine, a freedom not available in gamma backscatter and radar techniques of coal thickness sensing).

Several approaches were used to investigate the consistency of the shale overburden activity. Firstly, some fifty samples of shale overburden were taken during the advance of a face, the area sampled being some 1 km<sup>2</sup>. These samples were analysed for the main radionuclides and the results of these analyses showed that, although there were vertical variations in shale activity, there was less than 5% variation in activity parallel to the seam. Secondly, underground trials conducted on the same seam but in mines some 8 km apart gave identical roof coal thickness versus count-rate characteristics. Thirdly, evidence has gradually accumulated from the natural gamma logs of the same seam but from different boreholes that the variations in activity of a given shale overburden are small even over large distances, ie, tens of kilometres. Finally a survey of activities in five different UK coalfields showed only a 20% variation in characteristics showing that a single sensor would be usable throughout the coalfields.



The main requirement of a working sensor is that it should measure roof coal thickness sufficiently accurately and quickly as to enable the coal cutting machine to be steered within the seam. For a sensing system with a response time  $\tau$  the relative accuracy of coal thickness is given by

$$E(t) = \frac{1}{t} \left( \frac{n}{2\tau} \right) \left( \frac{dn}{dt} \right)^{-1}$$

where  $n$  is the count-rate at coal thickness  $t$  and  $E$  is the estimated error quoted for 95% confidence limits.

From the measured count-rate versus roof coal thickness characteristics evaluation of the above relationship can be used to yield the size of sensor required to achieve a desired level of accuracy within a desired response time.

The most important application for the use of horizon sensors in the UK is on coal shearers. In this situation strips of coal from a face some 200 metres long are successively removed as the machine is advanced. Typical response times to the measurement of roof coal thickness need to be of the order of 8 seconds and the error in the measurement of roof coal thickness should be less than 10% of the actual roof coal thickness. A working sensor to operate on a coal shearer was designed on the basis of these specifications by MRDE and manufactured for the NCB by Salford Electrical Instruments. The size of the sensor required in this instance was a 75 mm diameter x 150 mm long scintillation crystal. The major problem in the design of a working system was to protect this large fragile crystal and its accompanying photomultiplier tube from the harsh pit environment, and a considerable amount of work went into designing suitable shock and vibration protection. The predicted curve of the estimated error in roof coal thickness as a function of roof coal thickness is shown in Figure 4.

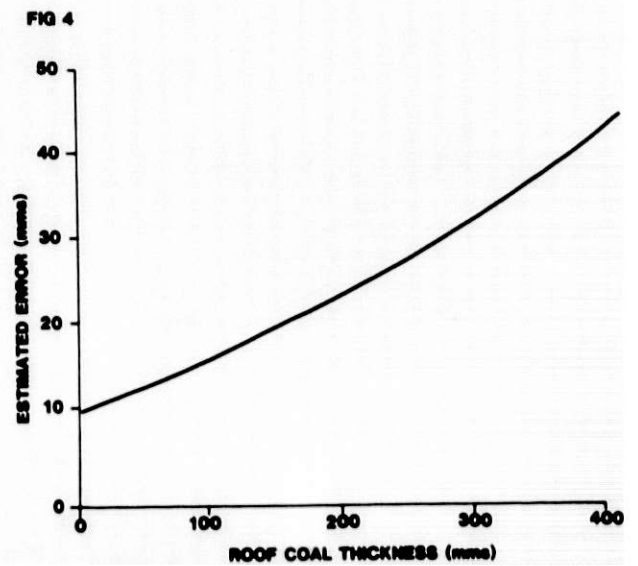
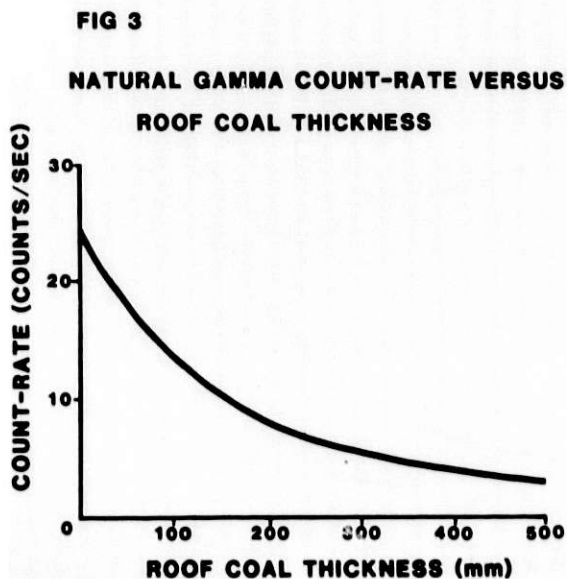
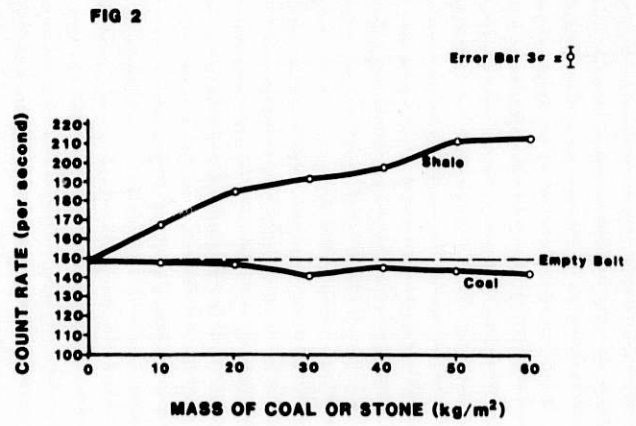
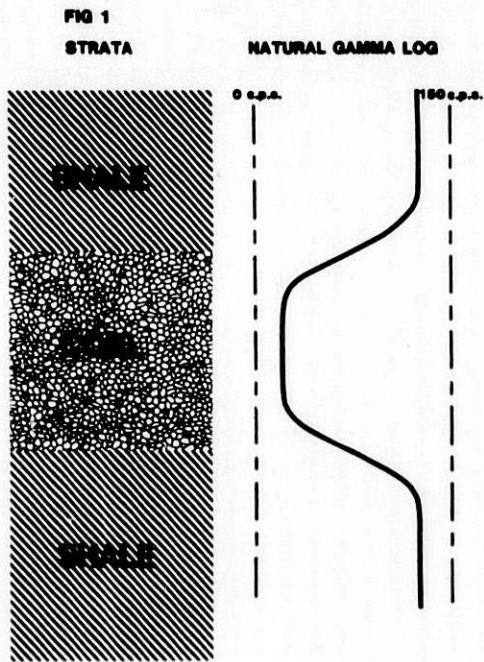
Initial trials of the prototype versions of this system were successful and production versions of the sensor, the Type 801 Natural Radiation Sensor (some two hundred of which have been manufactured to date by SEI) are now in use in the UK and USA and are also being evaluated by the Australian and South African Coal Industries.

The sensor was designed to operate with roof coal thicknesses in the range 0 - 400 mm but field trials have shown that it can operate up to 500 mm. This compares favourably with the only other working system for measuring roof coal thickness, that of gamma backscatter, which has a range of 250 mm.

A second application of horizon sensors on coal cutters is on the In-Seam Miner, this is a machine which extracts a section of the coal seam up to 18 metres wide as it advances. The cutting speed of the machine was significantly slower than that of a shearer and a longer response time of 50 seconds with the use of a smaller detector 37 mm diameter x 50 mm long was sufficient to achieve the same accuracy of roof

coal measurement as that for the shearer (Figure 4). Ten prototype sensor systems for In-seam Miners have thus far been manufactured and a production device based upon this prototype is being designed.

A third application of the use of a natural gamma radiation coal thickness sensor is In-seam Guided Longhole drilling. The requirement to be able to drill long distances in seams in the UK has arisen from the necessity to be able to locate faults ahead of faces and thus be able to adjust mining operations accordingly. Obviously to keep a drill within the seam it is necessary to be able to sense the position of the drill with respect to the seam edges. To achieve this a natural gamma system using a 25 mm x 100 mm detector which may be pumped-up the drill string to the actual drill has been developed. The sensor has a small amount of shielding on one side only which allows the orientation of the sensor to be determined, ie, whether 'roof' or 'floor' thickness is being sensed. The sensor may also be used to determine distance from the seam edge when the drill has left the seam either by reversing the direction of view or by monitoring the overall increase in count-rate as the drill penetrates further into the shale.



INSTRUMENTATION FOR OPTIMIZING AN  
UNDERGROUND COAL GASIFICATION PROCESS

P. W. Seabaugh and R. E. Zielinski  
Monsanto Research Corporation-Mound\*  
Miamisburg, Ohio 45342  
Phone: (513)865-3498  
FTS: 774-3498

Abstract

While the United States has a coal resource base of 6.4 trillion tons only seven percent is presently recoverable by mining. The process of In-Situ Gasification can recover another twenty-eight percent of the vast resource. However, viable technology must be developed for effective in-situ recovery. The key to this technology is an instrumentation system that can optimize and control the process in real-time.

This paper describes an instrumentation system that optimizes the composition of the injection gas, controls the in-situ process and conditions the product gas for maximum utilization. The key elements of this system are Monsanto PRISM<sup>(R)</sup> Systems, a real-time analytical system, and a real-time data acquisition and control system. This system provides for complete automation of the process but can easily be overridden by manual control. The use of this cost effective system can provide process optimization and is an effective element in developing a viable in-situ technology.

Introduction

If the United States is to approach energy self-sufficiency by the year 2000, commercialization of unconventional energy sources must proceed along an expedient path. One of the sources, Underground Coal Gasification (UCG), provides a viable means of supplementing our existing energy sources. The UCG process is directed to those resources that are not amenable to mining; consequently, it will provide energy from a new resource base.

Feasibility of the UCG process has already been demonstrated with several types of coal through various field tests<sup>(1,2,3,4,5)</sup>. An important aspect of the commercialization of the UCG process is the development and implementation of instrumentation and methods for optimizing and controlling the process for specific end uses.

For optimizing control of the process, this instrumentation must have the capabilities of accurately detecting the changing variables from the dynamic reactor and providing on-line analysis to effect timely process changes for control to a target specification, both in regard to process optimization and conditioning the product gas for its end use.

In the past, UCG field tests were minimally instrumentated to provide gas analysis and process monitoring. Only the instrumentation used in the Price-town Field Test approached the sophistication and dependability required for

\*Mound Facility is operated by the Monsanto Research Corporation for the U. S. Department of Energy under contract No. DE-AC04-76-DP00053.

commercial operation<sup>(6,7)</sup>. However, even the instrumentation used at Pricetown requires further refinement prior to its utilization for commercial operation.

To control and monitor a commercial UCG process, an integrated set of analytical and process control instrumentation is proposed. This system which represents an upgrading of the system used at Pricetown utilizes an analytical system and gas sampling system which were proven in an actual field test. Computer-aided design concepts were employed to assure system accuracy and reliability. From an economic viewpoint, PRISM<sup>(R)</sup> separators are used in the product gas conditioning process loop to minimize pumping, compression, and purification costs. PRISM<sup>(R)</sup> units are particularly effective when separation of non-permeates is desirable and when free pressure is available.

For automated process control, an objective, global formalism is proposed to provide the optimum coordination and control of the various elements of the UCG process by allowing for multidimensional control strategies of a multimodule commercial UCG reactor.

### Instrumentation

For a commercial UCG facility, reliable, noncomplex instrumentation is a prime requirement for a safe, consistent, and economical operation. To effect the proper coordination among the various modules, a computer-oriented automated data acquisition and control system is essential for the acquisition, analysis, control, and decision functions. The processes of UCG and surface gasification are similar; however, the changing reactor size and the effective integration of multimodules in the UCG process require a more complex instrumentation system. Simpler versions of this system should be directly applicable to surface gasifiers.

In order to provide appropriate information for a commercial environment, the instrumentation should acquire accurate real-time analytical data, monitor and control process variables (pressure, flows, temperatures), and reduce and analyze the data for decision options in terms of both optimal operations and economics. Many of the attributes were realized with the system approach used in the Pricetown I Field Test<sup>(5,6)</sup>. Details have been presented elsewhere<sup>(6)</sup> and only major features are presented here.

#### A. Analytical System

Timely and accurate analytical data are crucial to the optimization and control of the UCG process. In addition to a mass spectrometer for measuring the standard gas components, a gas chromatograph is used to measure water in real-time. Meaningful water analysis provides the feedback basis for controlling and optimizing the steam/oxygen ratio, for determining influx into the reactor, and for determining the reactor volume by mass balance computations. In gasification processes, the efficiency of oxygen consumption is one of the most important process parameters<sup>(8)</sup>.

For a commercial situation where many reactor modules are to be monitored,

coordinated, and integrated into the process at various stages of development, time-sharing logic is needed for real-time analysis and control. Such an approach was successfully demonstrated at Pricetown where the time-sharing logic was built around a mass spectrometer system, which directed the utilization of the analytical instruments among five different gas streams.

### B. Sample Conditioning System

The key to accurate, continuous on-line gas analysis is a reliable sample conditioning system. An abbreviated schematic of a three-stage cleanup system is shown in Figure 1. As indicated there, the first stage (oven) operates at 350°F where fly ash and heavier organics are removed from the gas. From that point, the gas is transported through heated (375°F) tubing to the second stage oven which is maintained at 200°F for the removal of lighter organics. At this point, the gas is presented to the gas chromatograph for real-time water analysis. Finally at the third stage, condensers are used to lower the dewpoint of the gas to about 43°F in order to protect the mass spectrometer from liquids. Flowtran<sup>(R)</sup> was especially useful in designing the system and fixing the temperatures of the ovens so that the contaminant loading between them would be balanced. The analytical instruments were time-shared among the various gas streams by having the control valves  $V_1$  through  $V_4$  and  $V_{10}$  actuated under the direction of the computer.

### C. Automatic Data Acquisition and Control System

The distributed approach was selected for the data acquisition and control system in order to provide ease of maintenance, to ensure reliability, to reduce the software burden, and to minimize the likelihood of total system failure. The general concept is illustrated in Figure 2. At Pricetown<sup>(7)</sup>, the system was distributed among four microprocessor primary satellite systems. Similarly, the software can also be distributed, allowing for flexibility in algorithms. For example, event driven algorithms were used to minimize the actual collection of data under conditions where the value of a variable remains constant. Such data contain no new information and about a 96% reduction in the number of readings processed can be realized (at Pricetown, about 7 million readings, as opposed to 190 million)<sup>(9)</sup>. This provides the opportunity to reduce both hardware and software costs.

In a commercial operation, distributed process systems can be efficiently utilized to collect and reduce data of the many modules in the process and using statistical techniques as discussed in the following section, the efficiency of the gasification process can be optimized by automatically initiating process changes that maximize the CO/CO<sub>2</sub> ratio. As indicated elsewhere,<sup>(8)</sup> the UCG economics are very sensitive to the rate of oxygen consumption. The general process/control diagram, showing the interrelationship between the process modules and the instrumentation process/control modules is presented in Figure 3.

For a commercial application, the Pricetown system can be simply yet effectively upgraded by having process variables automatically changed to effect optimization by the monitoring of key indicators such as the CO/CO<sub>2</sub> ratio.

### Mathematical Method

To ensure optimum coordination among the various operating systems, some method is needed to objectively monitor and detect changes in the critical process parameters on a timely basis, automatically effect process changes, and control process stability. In addition, the method should be efficient and should be capable of separating statistical effects from chemical and physical effects, particularly since the detection of the onset of real trends will be used as feedback for controlling the process.

The multidimensional nature of the anticipated process control needs for commercial UCG facilities suggests, as one approach, a performance-oriented methodology in which key elements of an absolute performance criterion include magnitude of change, timeliness, false alarm probability (FAP), probability of detection, and alarm resolution<sup>(10,11,12)</sup>. A statement of a performance criterion, stated in general terms, is to detect with probability, P, a critical change of  $\delta_0$  over n process units or composition components. Process parameters such as flow rates, pressures, oxygen usage and product gas components are all amenable to a performance criterion statement directed toward process control based on multiple decision parameters.

For a process operating to a performance criterion, a most powerful, but simple statistic is presented which minimizes the false alarm rates while providing the maximum sensitivity to process variables and effecting optimum process changes.

#### A. Theory

To illustrate the technique, both a one dimensional and a two dimensional example are given. With the assumption

$$d \sim N(\delta, \sigma_d^2)$$

where d denotes the change in some parameter and where the variance  $\sigma_d^2$  is calculated from prior knowledge, the problem is then formulated as that of testing:

$$H_1: \delta = \delta_0 \text{ vs } H_0: \delta = 0.$$

The formulation is presented graphically in Figure 4, where  $\beta$  is the Type-1 error probability of wrongly rejecting the hypothesis  $H_1: \delta = \delta_0$ , under test, that is, failing to detect a critical change; and  $\alpha$  is the Type-2 error probability of wrongly rejecting  $H_0: \delta = 0$ , that is, of sounding a false alarm.

This is the reverse of the Neyman-Pearson theory which holds  $\alpha$  constant; however, the applicability of the theory still holds. The critical value as indicated in Figure 4 for  $\beta = 0.025$  at  $\delta_0 = 3$  mole percent for  $\text{CO}_2$  is given generally by

$$c_\beta = \delta_0 - z_\beta \frac{\sigma}{\delta}$$

and specifically by

$$c_\beta = 3.0 - 1.96(0.52) = 1.98.$$

In other words, a change in the parameter being monitored is considered to have taken place (an alert is sounded) if the change in the CO<sub>2</sub> mole percent exceeds its  $\beta$ -level critical values,  $c_\beta = 1.98$ . The probability of detecting a 3 mole percent change is 0.975.

In a similar way, the  $\beta$ -level most powerful test has been developed for cases where the dimensionality of  $d$  is greater than one. This arises when estimates of  $d_1, d_2, \dots, d_n$  from  $n$  successive time periods for a single control parameter or single estimates  $d_1, d_2, \dots, d_n$  from different control parameters are considered. The problem is formulated as that of testing

where  $H_1: \underline{\delta} = \underline{\delta}_0$  vs  $H_0: \underline{\delta} = 0$

$\underline{\delta} = [\delta_1, \delta_2, \dots, \delta_n]$  is a specific strategy

such that  $\delta = \delta_1 + \delta_2 + \dots + \delta_n$

has the value  $\delta = \delta_0$ . Given the data  $\underline{d}$ , the variance-covariance matrix,  $V$ , and the Gaussian assumption

$$\underline{d} \sim N(\delta, V)$$

the  $\beta$ -level most powerful test has the critical region

$$\{R = \underline{d}: c \leq c_\beta\}$$

where  $c = \underline{\delta}' V^{-1} \underline{d}$

$$\text{and } c_\beta = \mu_c - z_\beta \frac{\sigma_c}{c}$$

with  $\mu_c = \underline{\delta}' V^{-1} \underline{\delta}$  and  $\sigma_c^2 = \underline{\delta}' V^{-1} \underline{\delta}$ .

For the case where  $\beta = 0.025$  and where  $\underline{\delta} = [\delta_{CO}, \delta_{H2}]$

is a specified set of changes such that the sum:

$$\delta = \delta_{CO} + \delta_{H2}$$

has the value  $\delta_0 = 3$  mole percent, the most powerful critical region for the specified strategy  $(\delta_{CO}, \delta_{H2}) = (1.80, 1.20)$  and with  $v_{11} = \frac{\sigma^2}{1} = v_{22} = \frac{\sigma^2}{2} = 0.08$  is shown in Figure 5. In this example the critical region would be applicable for the control strategy where process changes would be made only when the combined CO and H<sub>2</sub> compositional change reached 3 mole percent or greater.

The line AB is the subset of all points such that  $\delta_{CO} + \delta_{H2} = 3.0$ ; the concentric circles indicate the contours for the bivariate normal densities for the strategy being tested. The shaded area to the left lower side of the line CD represents the 0.025 level critical region R.

Although the examples have dealt with compositional changes, the method is equally applicable to any single or combination of process parameters. In



a large commercial plant involving the simultaneous production from several well modules both intra- and intermodule control can be realized with the technique. If the control strategy is to maintain the overall product composition to a target level selected to minimize gas treatment cost by mixing compositions from several modules in a common manifold, then changes in the selected gas components, the flowrates, and the pressures from each module could be detected and monitored by a simple sum statistic and used as feedback to automatically adjust the steam/oxygen ratio, flow or any other variable for maximum efficiency. Virtually any control strategy could be enhanced by this method.

### B. Detailed Calculation

Consider the case where the CO/CO<sub>2</sub> ratio is to be controlled by limiting the total change in the CO and CO<sub>2</sub> composition to 3 mole %; that is,  $\delta_{CO} + \delta_{CO_2} = 3$ . For  $\beta = 0.025$  and the specific strategy  $(\delta_{CO}, \delta_{CO_2}) = (1.80, 1.20)$ , and with the further conditions  $v_{11} = \sigma_{CO}^2 = v_{22} = \sigma_{CO_2}^2 = 0.08$  and  $v_{12} = v_{21} = 0$ , the test statistic becomes:

$$c = \delta_{CO} d_1 / v_{11} + \delta_{CO_2} d_2 / v_{22},$$

and

$$\mu_c = \delta_{CO}^2 / v_{11} + \delta_{CO_2}^2 / v_{22}.$$

From the theory given above, the critical equality  $c = c_\beta$  gives:

$$(1.80/0.08) d_1 + (1.20/0.08) d_2 = \frac{(1.80)^2}{0.08} + \frac{(1.20)^2}{0.08} - 1.96 \sqrt{\frac{(1.80)^2}{0.08} + \frac{(1.20)^2}{0.08}},$$

from which:

$$d_1 + 0.67d_2 = 1.93, \text{ or:}$$

$$1.5d_1 + d_2 = 2.90.$$

The shaded area to the lower left side of the line CD in Figure 5 represents the 0.025 level critical region R, where CO<sub>2</sub> is substituted for H<sub>2</sub>. Any combination of changes in CO and CO<sub>2</sub> values  $(d_{CO}, d_{CO_2})$  beyond this line will trigger an alarm.

### End Use of the Gas Produced by UCG and the Gas Cleanup System

A UCG facility produces a gas which contains CO<sub>2</sub>, CO, H<sub>2</sub>, CH<sub>4</sub>, H<sub>2</sub>S, particulates, tar and water. Surface facilities are needed to remove H<sub>2</sub>S particulates, tar, water and CO<sub>2</sub> and to adjust the H<sub>2</sub>/CO ratio, depending on the end use product.

Figure 6A shows a gas cleanup system for the removal of particulates,

tar and oils. A UCG gas (650°F temperature and 80 psig pressure), coming out of the well bore, passes through a series of three cyclone separators to remove the particulates. The first cyclone removes the particles which are greater than 50 micron in size whereas the second cycle removes the particulates in the 20-50 micron size range, the third cyclone removes the particulates in the 10-20 micron size range. After the particulate removal, the gas stream passes a steam boiler where the temperature of the gas stream is reduced to 250°F and this results in the condensation of tar and oils. This gas can be further processed to remove particular gas constituents as desired. Figure 6B shows a system to remove CO<sub>2</sub> and sulfur from the gases. The carbon dioxide is removed by the improved Benfield process and the sulfur is removed by the Stretford process. As shown in Figure 7, the UCG process can be tailored to provide gas for end uses which include electric power generation or further upgrading for end market use. The CO and H<sub>2</sub> ratios can be changed by the water gas shift reaction as required by further processing steps. Processes for the manufacturer of SNG, methanol, vinyl acetate, acetic anhydride and ethylene glycol are well developed and the process for the manufacture of gasoline via the Mobil M process will soon be commercialized.

A modification using new separation technology is suggested in Figure 8. There the PRISM<sup>(R)</sup> separators are illustrated as means of recovering hydrogen from the purge stream of a methanol or Fischer-Tropsch process. They also could be used in conjunction with a "light" water-gas shift reactor to recover H<sub>2</sub> and return CO at pressure to the shift reactor. In either application the technology offers the potential to optimize a UCG facility by providing the opportunity for trade-offs among pumping, compression and purification costs.

#### Summary

Field tested and off-the-shelf demonstrated technology currently exists to make UCG a commercially viable technology. A new, multidimensional control methodology has been introduced to optimize the control and efficiency of a commercial UCG facility. Also, a new separation technology has been suggested as a modification to the gas conditioning module so that trade-offs among pumping, compression, and purification costs can be balanced to optimize the overall system.

#### Acknowledgements

We thank C. Early and M. Farkas for their discussions.

#### References

1. Burwell, E. L., "The Department of Energy Underground Coal Conversion Program Accomplishments and Strategy," Proceedings of the 6th Underground Coal Conversion Symposium, Shangri-La, OK, July 13-17, 1980.
2. Hill, R. W., C. B. Thorsness, R. J. Cena, W. R. Aiman, and D. R. Stephens, "Results from the Third LLL Underground Coal Gasification Experiment at Hoe Creek," Proceedings of the 6th Underground Coal Conversion Symposium, Shangri-La, OK, July 13-17, 1980.

3. Singleton, A. H., W. L. Noll, and J. M. Allen, "Summary Report of the Rowlins Test I for Gasification of Steeply Dipping Coal Beds," Proceedings of the 6th Underground Coal Conversion Symposium, Shangri-La, OK, July 13-17, 1980.
4. Bartke, T. C., L. Dockter, T. E. Sterner, J. E. Virgona, and L. F. Wojdac, "Status Report on the Hanna III and Hanna IV Underground Coal Gasification Experiments," Proceedings of the 4th Underground Coal Conversion Symposium, Steamboat Springs, CO, July 17-20, 1978.
5. Agarwal, A. K., P. W. Seabaugh, and R. E. Zielinski, "Mass Balance Results for Pricetown I Underground Coal Gasification," Proceedings of the 7th Underground Coal Conversion Symposium, Fallen Leaf Lake, CA, September 8-11, 1981.
6. Agarwal, A. K., R. E. Zielinski, and P. W. Seabaugh, "On-Line Analysis and Sampling of Process and Product Variables for the Pricetown I Underground Coal Gasification Field Test," 1981 Symposium on Instrumentation and Control for Fossil Energy Processes, San Francisco, CA, June 1981.
7. Zielinski, R. E., P. W. Seabaugh, J. W. Martin, and A. J. Liberatore, "Eastern Underground Coal Gasification Process Instrumentation and Data Analysis," Proceedings of the 4th Underground Coal Conversion Symposium, Steamboat Springs, CO, July 17-20, 1978.
8. Bidlack, D. L., "The Economics of Four Options to Utilize Underground Gasification of Kaiparowits Coal to Generate Electricity," Proceedings of the 4th Underground Coal Conversion Symposium, Steamboat Springs, CO, July 17-20, 1978.
9. Walker, W. K., A. F. Ciramella, W. E. Kessling, "Pricetown I Data Acquisition System", Proceedings of the Digital Equipment Computer Users Society, Vol. 6, No. 4, U.S.A., Spring, 1980.
10. Seabaugh, P. W., D. R. Rogers, H. A. Woltermann, F. C. Fushimi, and A. F. Ciramella, "The Controllable Unit Approach to Material Control: Application to a High Through-put Mixed Oxide Process." Mound Facility Report MLM-2532, Vols I & II, Monsanto Research Corporation, Miamisburg, Ohio 45342, January 10, 1980.
11. Duncan, D. B. and H. T. David, "An Evaluation of the Controllable Unit Approach to Material Control and Accounting." Mound Facility Report MLM-2785, Monsanto Research Corporation, Miamisburg, Ohio 45342, 1980.
12. Rudy, C. R., D. B. Armstrong, K. W. Foster, D. R. Rogers, and D. R. Hill, "Controllable Unit Approach: An Application Manual." NUREG/CR-2538, MRC-Mound Report MLM-2881, Monsanto Research Corporation, Miamisburg, Ohio 45342, 1981.

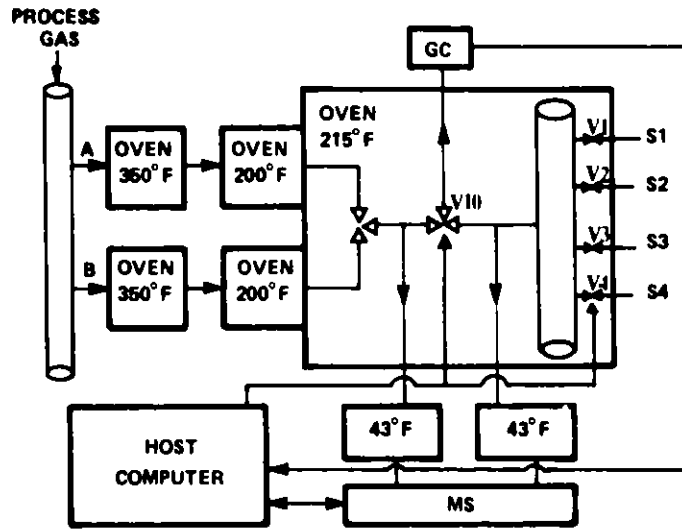


Figure 1. Gas Analysis System

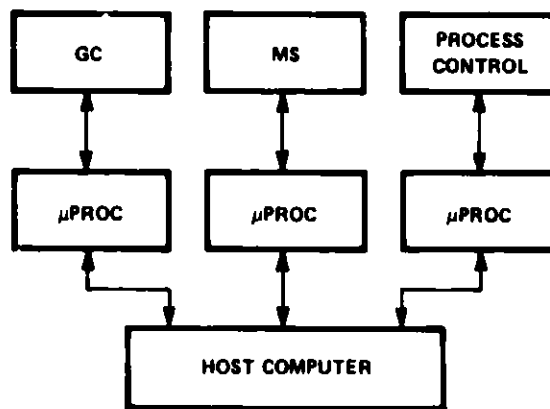


Figure 2. The ADACS is a Distributed System

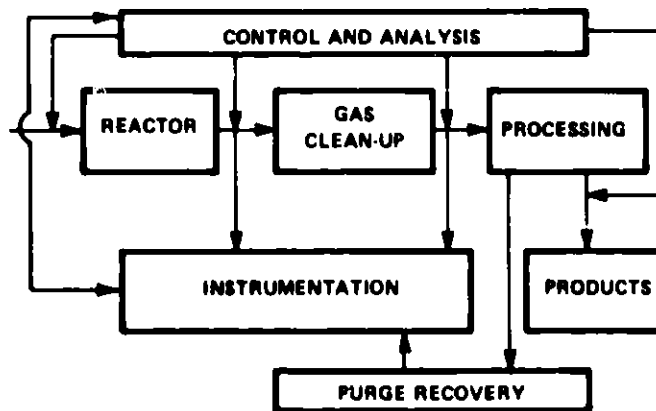


Figure 3. Process/Control Diagram

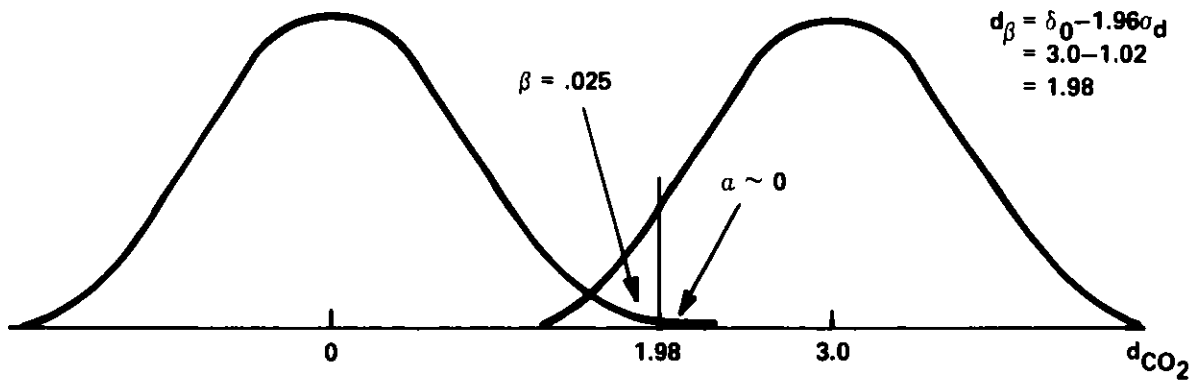


Figure 4. The 0.025-Level Critical Value for Detecting a 3% Change in the Composition of CO<sub>2</sub>

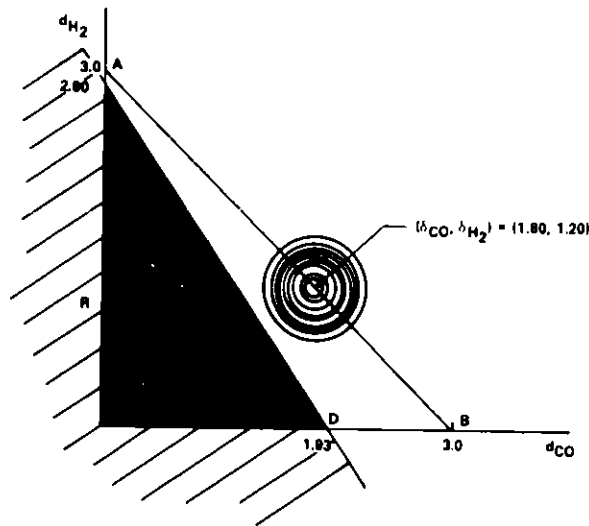


Figure 5. The 0.025-Level Most Powerful Critical Region R, for the Strategy  $(\delta_{CO}, \delta_{H_2}) = (1.80, 1.20)$

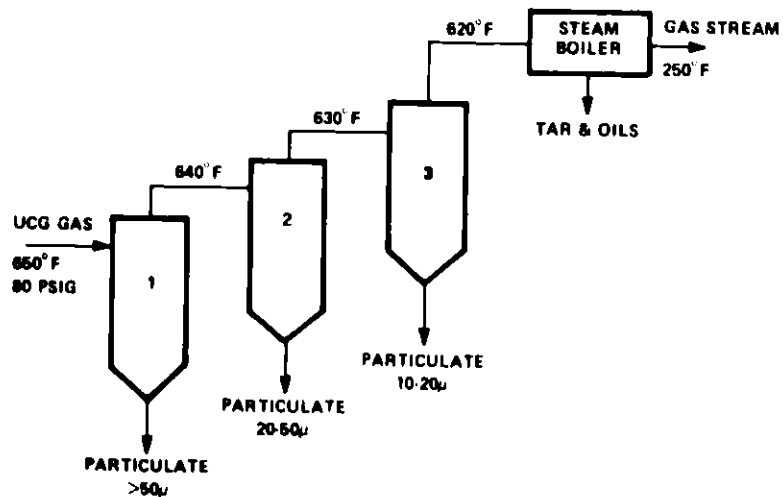


Figure 6a. Gas Clean-Up System – Tar and Particulates

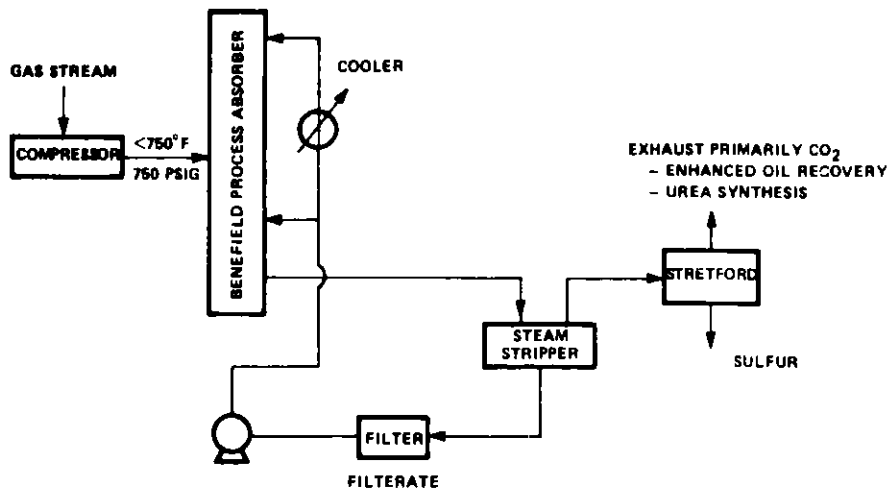


Figure 6b. Gas Clean-Up System – CO<sub>2</sub> and Sulfur

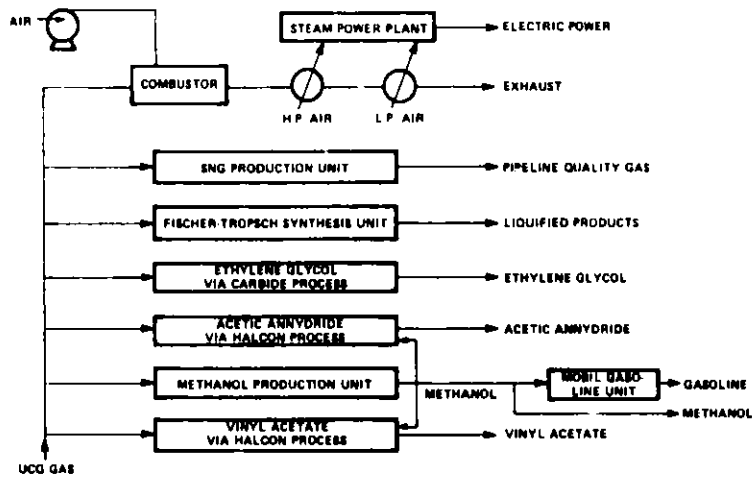


Figure 7. Process Flow Sheet

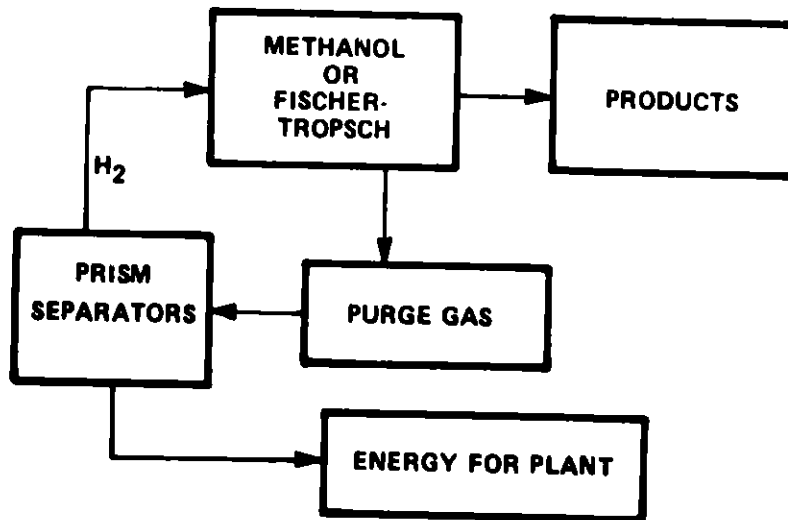


Figure 8. PRISM<sup>®</sup> Supports Optimization Thru Effective Hydrogen Recovery From the Purge Stream

IN SITU RECOVERY OF BITUMEN FROM OIL SANDS -  
LABORATORY PILOT PLANT EXPERIENCE

D.M. Nguyen, T.R. Heidrick  
Alberta Research Council  
Oil Sands Research Department  
11315 - 87th Avenue  
Edmonton, Alberta T6G 2C2  
(403) 467-8861

Abstract

The Alberta Research Council has played a major role in developing the technology of recovering bitumen from Canada's oil sands deposits. Initially a process was developed for oil recovery from mined sands. More recently effort has focused on methods suitable for deposits that are too deep to be profitably mined. The oil must be recovered from these deposits in place (in situ).

To support this in situ recovery research a full range of experimental facilities have been developed. Among these, are physical simulators which allow tests to be done at the high temperatures and pressures characteristic of in situ recovery conditions. Tests run on these simulators provide the data base for development and verification of numerical reservoir models that are used to estimate the field performance of various processes.

Introduction

The major oil sand deposits of Alberta are located within a triangular area cornered in the west by Peace River and in the East by Athabasca and Cold Lake (Figure 1). The bitumen in place is estimated to equal 185 billion cubic meters ( $1.16 \times 10^{12}$  Bbls). Surface mining is expected to recover only a small fraction of this total, the remaining bitumen must be extracted in situ.

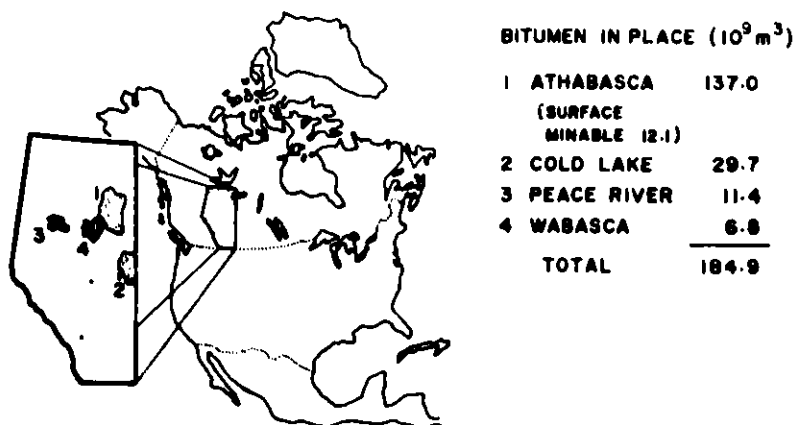


**FIGURE 1: LOCATION AND EXTENT OF MAJOR OIL SAND DEPOSITS  
IN ALBERTA, CANADA (1980)<sup>1</sup>**

The Alberta Research Council has been actively involved in developing the technology to exploit this immense resource since the early 1920's. It has provided support to other government agencies via joint research programs, as well as carried out research on a contract basis for private industry. Through this work, the Alberta Research Council has developed a full range of laboratory piloting facilities dedicated to investigating bitumen recovery techniques from oil sands. Among these are physical simulators.

The important question is: why work with laboratory simulators at all when field pilots provide the ultimate test for any recovery process? The answer is that field pilot operations are expensive and time consuming. Experiments which are properly designed and conducted in physical simulators allow screening of a wide variety of recovery parameters at moderate costs in time and money.

Physical models of a particular process can be scaled, partially scaled or unscaled<sup>2</sup>. Scaled and partially scaled models are designed to simulate field conditions based on the principle of similarity. The unscaled or elemental models on the other hand allow experiments to be performed as close as possible to field conditions on an element of oil sand, representing an elemental volume in the formation. Physical dimensions of the test equipment are the major constraints.

The physical simulators described in this paper are three dimensional elemental models.

### Oil Sand Physical Simulator System

The oil sand simulator system (Figure 2 and 3) consists of three major components: an injection system, a test cell, and a production system. The system is detailed in the following subsections along with a description of the test instruments and the significance of the measurements.

#### Injection System

This is a high pressure and high temperature system which allows steam, gas and solvent to be delivered individually or as a combination to the test bed under controlled flow rates. A schematic flow diagram of all three injection streams is shown in Figure 2. Table 1 gives the system specifications.

Steam Injection. Steam required for process injection and heating sources is produced in a natural gas generator which operates at a constant feed flowrate and at pressure up to 14 MPa. An electric superheater (Figure 2) provides the necessary degree of superheat for accurate flow measurement at the orifice meter shown. The superheater also allows a measure of temperature control at the injection well.

Gas Injection. Gas can be injected at the mixing tee in the manner illustrated in Figure 2. The gas cylinder weight is continuously monitored thus providing a check on the turbine meter flow measurements. Gas is



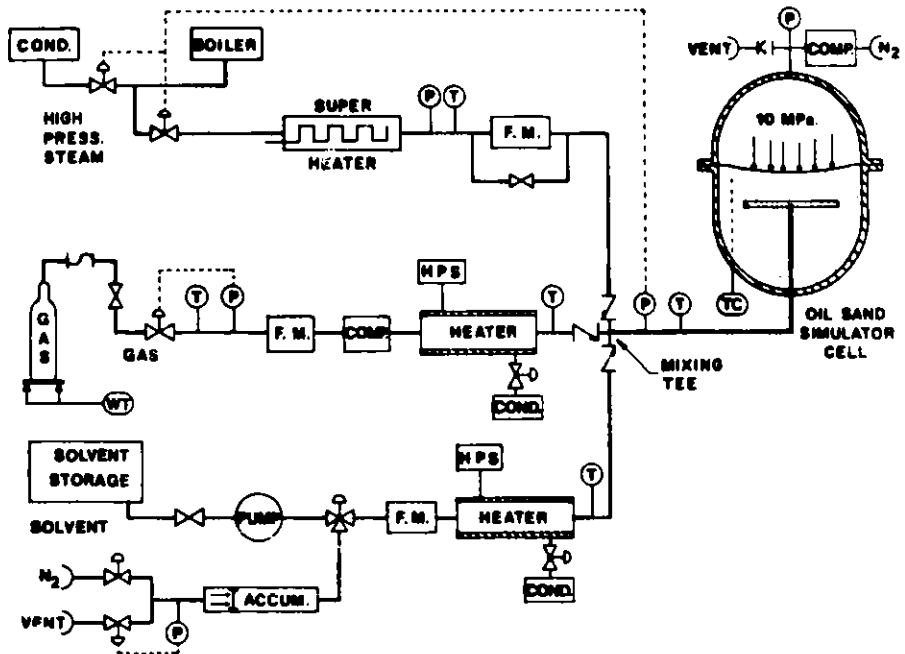


FIGURE 2 : INJECTION SYSTEM FOR 150cm OIL SAND TEST SIMULATOR

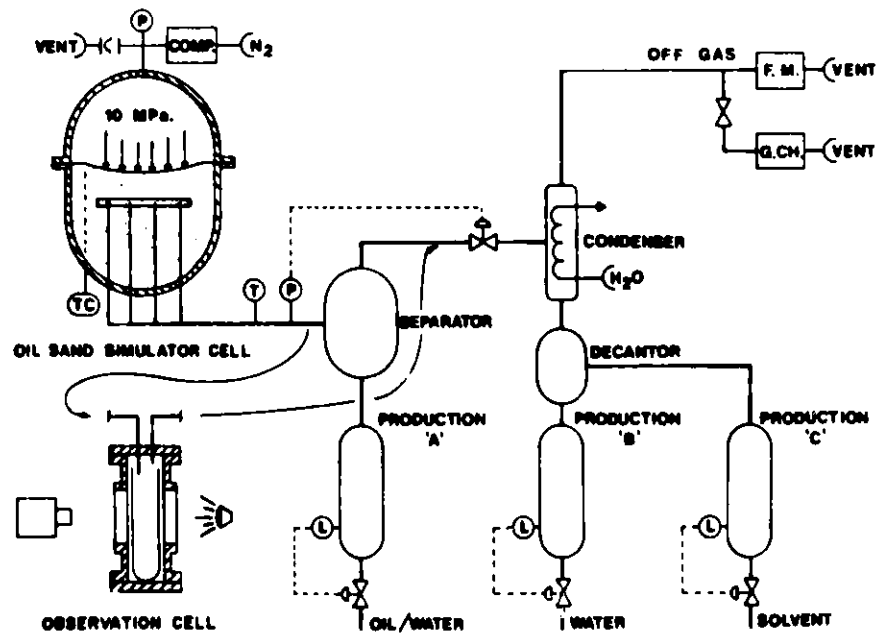


FIGURE 3 : PRODUCTION SYSTEM FOR 150cm OIL SAND TEST SIMULATOR

allowed to expand to a convenient temperature and pressure for flow control, then compressed and heated to the required injection conditions.

Solvent Injection. The solvent feed system, located in a separate location due to the potential fire hazards, consists of a storage tank, a transfer pump and an accumulator (Figure 2). Solvent is transferred to the accumulator in sufficient volume to last for a number of injection cycles. Nitrogen gas pressure is used to drive solvent to the mixing tee through the flow metering shown (orifice or turbine meter). The solvent is heated by a steam heater to injection temperature, immediately upstream of the tee.

Table 1  
Injection System Specifications

	Flow	Pressure	Temperature
STEAM	1-50 kg/hr	13.8 MPa max.	400°C max.
GAS	2-33 l/min. std.	10.3 MPa max.	340°C max.
SOLVENTS	0.1 - 5 kg/hr	10.3 MPa max.	340°C max.

### Production System

Figure 3 represents a flow diagram of the production system. Produced fluids are first separated either in a high pressure gas-liquid separator or in an observation cell. The gaseous portion is then fed through the system pressure control valves. The valves are sized to operate in a split range fashion.

The observation cell allows photographic recording of production fluids being collected under system pressure and temperature. The liquid production obtained in this manner is appropriately cooled to avoid flashing before samples are removed.

Under normal operating conditions, the production fluids are collected using the high pressure gas-liquid separator. The liquid portion is allowed to fill either one of two columns, one of which is shown in Figure 3. The contents of these columns, referred to as Production A, are then flashed to atmospheric pressure before sampling takes place in either small jars or in bulk tank. An earlier set up which used a low pressure separator downstream of the pressure control valve, a design similar to that of field production, resulted in severe plugging problems to the system smaller lines.

Downstream from the pressure control valves, the gaseous portion of the produced fluids is condensed and decanted into a water and a solvent stream, referred to as Production B and C. Each stream is equipped with

its own production columns and sampling containers.

The off-gas flow is continuously monitored with gas meters and, if required, on line gas chromatograph analysis is performed.

### The Test Cell

The heart of the simulator system is a high pressure vessel into which oil sand is packed and maintained under simulated field conditions. Table 2 gives the specifications for three of these vessels. Only the largest vessel, referred to as the 150 cm simulator, is discussed in detail here.

Table 2  
Simulator Test Cell Specifications

	45 cm Simulator	60 cm Simulator	150 cm Simulator
Cell Diameter (approx)	45 cm	60 cm	150 cm
Weight of Oil Sands (approx)	50 kg	200 kg	5000 kg
Design Pressure and Temperature	7.6 MPa @ 316°C	10 MPa @ 345°C	11.4 MPa @ 315°C
Well Configuration	2 well pattern	2 well or 5 well pattern	2 well or 5 well pattern
Turnaround Time	1 week	3 weeks	3 months

Figure 4 shows a typical bed packing arrangement in the 150 cm cell. The overburden pressure existing in deep oil sands formation is simulated by pressurizing the upper part of the test cell with nitrogen gas. The gas and sands are separated by a deformable steel diaphragm which transmits the overburden pressure to the test bed. The various combinations of injection streams described in the previous section are delivered to the test bed via a common injection well. Well configuration can either be a two-well: injector/producer or a five-well: one central injector/four peripheral producers. The wells are inserted from the bottom of the cell to a predetermined height in the bed. Usually a thin layer of clean frac sand is prebuilt into the bed to serve as an initial communication path between wells.

Temperature profiles in the test bed are monitored by inserting a number of thermocouple strings in the bed in the same manner as the wells. Figure 5 shows the location of these thermocouple strings in the 150 cm cell. Up to 95 strings are possible. Each string contains 10 Chromel-Alumel thermocouples spaced 10 cm apart. Figure 6 shows the growth of isotherms in the test bed during a typical thermal stimulation experiment.

Heat losses to ambient air from the cell are calculated using data from a number of thermocouples attached to the inner and outer cell wall.

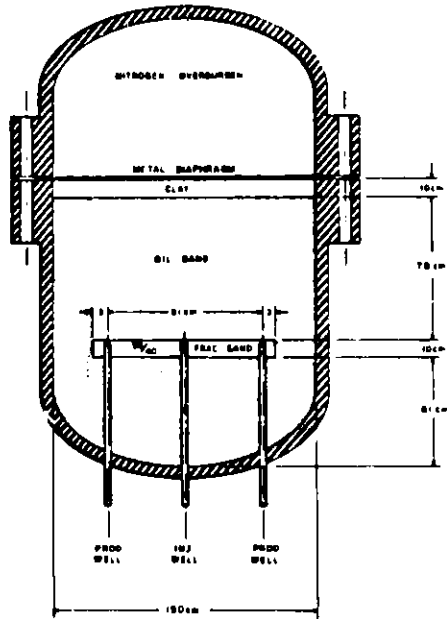


FIGURE 4 150cm OIL SANDS SIMULATOR - BED PACKING ARRANGEMENT

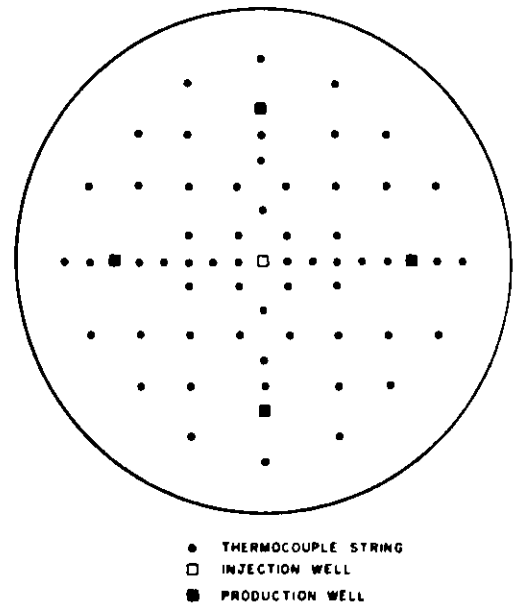


FIGURE 5 THERMOCOUPLE STRING LAYOUT IN SIMULATOR - HORIZONTAL CROSS SECTION

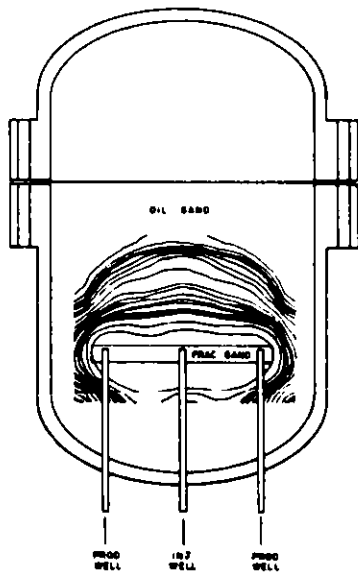


FIGURE 6: GROWTH OF 100°C ISOTHERMS DURING AN EXPERIMENT WITH STEAM INJECTION

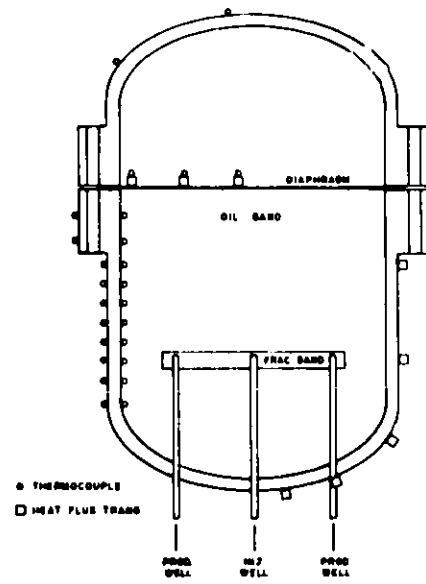


FIGURE 7: LOCATIONS OF THERMOCOUPLES AND HEAT FLUX TRANSDUCERS FOR HEAT LOSS CALCULATIONS

These measurements are complimented by those of the heat flux transducers which are also surface mounted on the cell wall. Figure 7 shows the location of these instruments on the 150 cm cell.

#### Process Control and Data Acquisition

The simulator process control and data acquisition is shown schematically in Figure 8. At present, the central control and data logging system is provided by a Fox 2/10 Foxboro minicomputer. This is a 32K process control computer complete with input interface modules and scanner. Peripherals include hi-speed tape punch and reader, magnetic tape recorder, telewriter and CRT. There is also a direct link to the Amdahl MTS system of the University of Alberta. This inter-computer communication allows data such as test bed temperature to be processed and displayed continuously as isotherms on the CRT.

Work is in progress to link the present system to a newly installed computer which will act as host to the system. Networking with other computers at the Alberta Research Council and the University of Alberta is then possible. Isotherms data such as those shown in Figure 6, in the very near future, can be displayed in animated 3-D format for on line analysis.

#### Test Instrumentation and Data Verification

Table 3 gives a listing of the type of instruments used in the simulator system. The instrument operating ranges and accuracies pertaining to direct measurements are also given. Uncertainties associated with indirect measurements such as orifice meter flow rates are derived from standard regression analysis<sup>3</sup> of all individual contributing measurement accuracies. Typical uncertainty curves for two steam orifice meters are shown in Figure 9.

Complete mass and energy balance are performed after each test. Mass balances on water, gas, solvent and bitumen are based on the following.

$$\text{Initial test bed saturation} + \text{Injected amount} = \\ \text{Produced amount} + \text{Final bed saturation}$$

Injected and produced amounts are calculated from measurements made during the test. Bed saturations are determined from test bed coring.

Energy balance is calculated as follows:

$$\text{Energy input} = \text{Energy in produced fluids} + \text{Energy loss to surrounding} \\ + \text{Energy change in test bed}$$

Energy input and in produced fluids are derived from mass flow, pressure and temperature measurements.

Energy loss to the surrounding is calculated from heat loss measurements on the test cell wall.

Energy change in the test bed is either calculated from the change in heat contents of the different zones within the bed or measured as heat

loss to the surrounding from the end of the test to the time in which the bed returns to its pre-run temperature.

Table 3  
Instrumentation Specifications

Measurement	Manufacturer /Model No.	Range	Accuracy
<b>HEAT FLUX</b>	Hy-Cal Engineering /HI-7-120	Diff. Temp. -46°C + 204°C	Lin. = ± 2% Repeat. = 0.5%
<b>TEMPERATURE</b>			
Test Bed	Type K Chromel/Alumel	-184°C + 1200°C	0.05°C/°C
Cell Wall	Type K Chromel/Alumel	-184°C + 1200°C	0.05°C/°C
Fluid	RTD - Burns Eng. RTD - Rosemount	-10 - 350°C -10 - 350°C	±0.5% of span ±0.5% of span
<b>PRESSURE</b>			
System	Dresser /Ashcroft Digigauge	0 + 2,000 psi	±0.05% of span
Differential	Rosemount /Model-1151 DP	0- 150" H <sub>2</sub> O 0- 40 kPa 0- 750" H <sub>2</sub> O 0-200 kPa 0-2000 psi 0- 10 MPa	±0.2% of span
<b>VOLUME FLOW</b>	FlowTech/Omniflo <sup>™</sup>		±0.2% full range

#### Physical Simulator Versus Field Results

Scaled and partially scaled models have been used extensively in process investigation, strategy development and field-project designs. Good agreement has been reported<sup>4</sup> between field and model results of steam floods.

Elemental models are mostly used to provide data base for development and verification of numerical reservoir models. The latter are in turn employed in estimating field performance of various processes. Striking agreement has been found however between the results from tests performed with one of the Alberta Research Council's simulators and those from the field. This was reported by Redford and McKay<sup>5</sup> and reproduced in Figure 10.

#### Summary

In this paper the physical simulator system developed and operated by the Alberta Research Council are described. The associated instrumentation and control are detailed in the text.

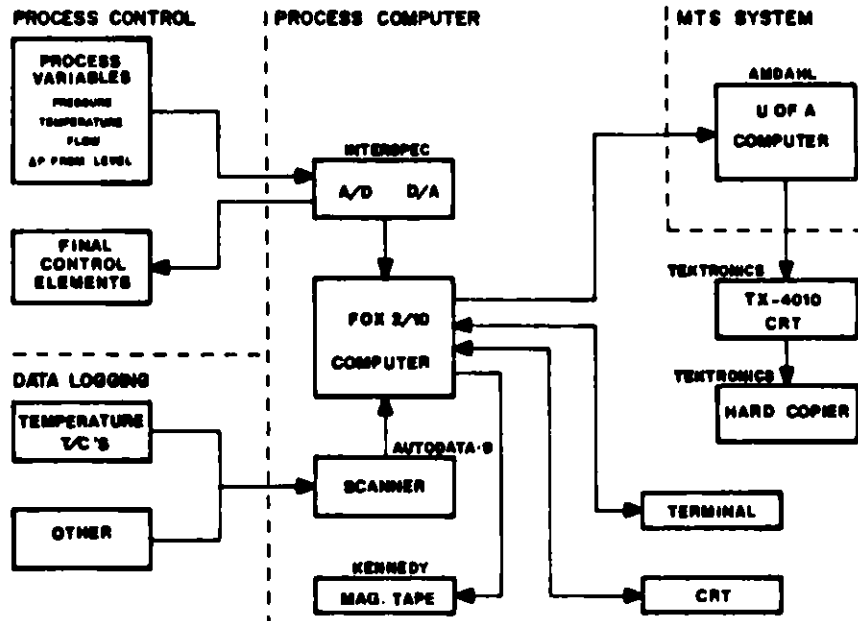


FIGURE 8 : SIMULATOR INSTRUMENTATION, CONTROL & DATA LOGGING

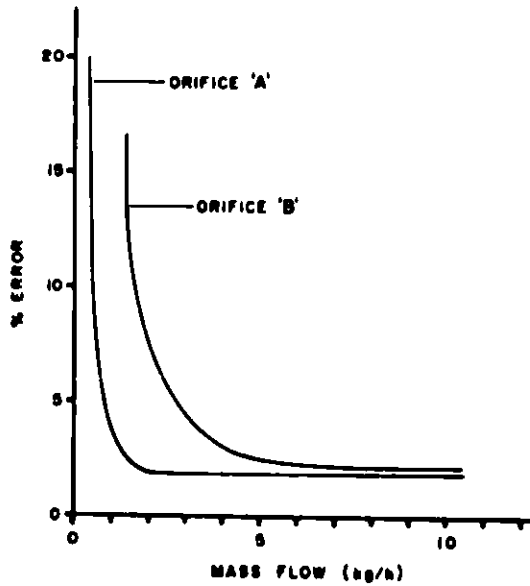


FIGURE 9 : STEAM FLOW ORIFICE UNCERTAINTIES

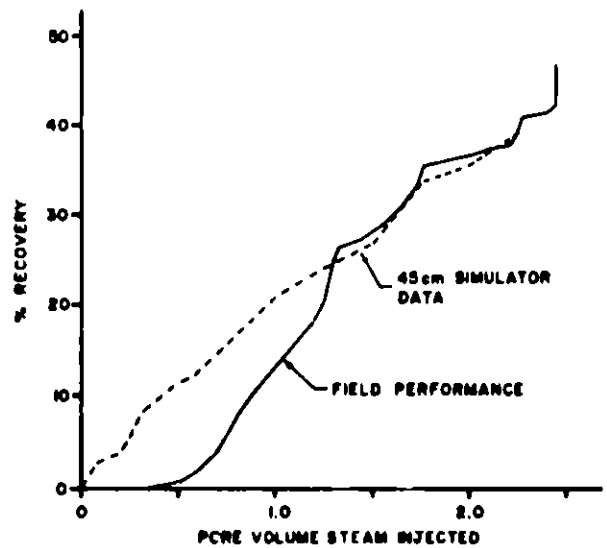


FIGURE 10 : COMPARISON OF FIELD PERFORMANCE AND SIMULATOR RESULTS (REDFORD & MURRAY<sup>6</sup>)

The simulators enable effective screening of bitumen recovery processes from oil sands under highly controlled in situ conditions. Cases in which good agreement have been found between laboratory and field pilot results are highlighted.

#### Acknowledgements

The authors wish to thank the Alberta Oil Sands Technology and Research Authority for funding the construction and development of the simulator system described here. The Authority's permission for publication is also acknowledged.

#### References

1. Energy Resources Conservation Board, "Alberta Reserves of Crude Oil, Gas, Natural Gas Liquids and Sulphur," December 31, 1980.
2. Farouq Ali, S.M. and Redford, D.A. "Physical Modeling of In Situ Recovery Methods for Oil Sands," The Oil Sands of Canada - Venezuela, CIM Special Volume 17 (1974) 319-326.
3. Davies, O.D., "Statistical Methods in Research and Production," Imperial Chemical Industries Limited, Oliver and Boyd, 1961.
4. Burnsell, C.G. and Pitman, G.M., "Performance of Steam Displacement - Kern River Field," J. Pet. Tech. (August, 1975) 997-1004.
5. Redford, D.A. and McKay, A.S., "Hydrocarbon - Steam Process for Recovery of Bitumen from Oil Sands," presented at the Non-Conventional Oil Technology Symposium, Calgary, Alberta, June 20-23, 1980.



MULTIPLE TRACER GAS ANALYZER

James E. Uhl  
Sandia National Laboratories  
In Situ Technologies  
Division 4747  
P.O. Box 5800  
Albuquerque, NM 87185  
505/844-1700

Abstract

A multi-gas tracer system has been designed, built, and used on an explosively fractured oil shale rubble bed. This paper deals exclusively with the hardware, software, and overall operation of the tracer system. This system is a field portable, self-contained unit, which utilizes a mass spectrometer for gas analysis. The unit has a 20 channel sample port capability and is controlled by a desk top computer. The system is configured to provide a dynamic sensitivity range of up to six orders of magnitude. A roots blower is manifolded to the unit to provide continuous flow in all sample lines. The continuous flow process allows representative samples as well as decreasing the time between each measurement. Typical multiplex cycle time to evaluate four unique gases is approximately 12 seconds.

Introduction

Tracer technology provides a method to characterize the active flow through a porous medium. This technology has been applied to the characterization of an explosively expanded in situ oil shale retort. An ideal retort consists of a contained flow region with approximately 20%-40% uniform void and particle sizes.<sup>1,2</sup> Information concerning deviations from these conditions is important in predicting retorting performance; the retorting process is mainly driven by non-uniform flow paths. Therefore the location and magnitude of these preferential air flow channels are important criteria in determining the degree of success in preparing the bed. These beds range in size from 12 m x 12 m x 25 m research retorts<sup>3</sup> to 50 m x 50 m x 80 m commercial scaled units.<sup>4</sup> Thus for tracer research in large-scale porous media systems, many sample points are necessary to insure adequate resolution when flow mapping.

We have developed a 20 channel (i.e., sample locations) tracer system based on the multiplex concept. The application of this concept reduces the number of detector stations necessary to accomplish the retort mapping process. This new tracer system is also multifunctional since any reasonable number of noninterfering tracer gases can be detected simultaneously. This mode of operation significantly reduces the total retort characterization time.

Conventional Systems Capabilities and Limitations

Old flow tracer testing has been an area of active research.<sup>5,6</sup> The instrumentation approach that has been taken for tracer technology has been to rely on the use of systems that are both single channel and single gas.

In other words, each sample line represents essentially a self-contained tracer system with its own detector. The characteristics of the commonly used systems are shown in Table 1.

TABLE 1  
Single Channel Systems

Characteristics	Tracers		
	Helium	Sulfur Hexafluoride	Krypton 85 (Radioactive)
Concentration Std. Air ppm	5	N.D.	N.D.
Density Ref. to Air	0.138	5.32	2.89
Detection System	Leak Detector (Magnetic Spec. Tube)	Packed Column (Electron Capture)	Beta Radiation (Geiger Mueller Tube)
Sensitivity	0.04p atm cc/s (Good)	1ppb (Excellent)	200nCi (Good)
Dynamic Range	1,000,000 (Excellent)	1,000 (Fair)	1,000 (Fair)
Special Precautions	None	None	Yes

(N.D.=non-detectable)

These tracer systems are normally used in a continuous mode of operation, thus the number of detection instruments is equal to the number of points to be simultaneously sampled. Operations in a continuous mode facilitates obtaining the time resolution necessary to accurately define a tracer response pulse. Unfortunately, single channel systems, while appropriate for many applications, have a number of limitations when applied as research tools on large scale systems. These limitations which are enumerated in the following paragraphs have led to the development of a new tracer system.

#### Limitations of Systems

A predominant limitation of the single channel systems for monitoring a tracer gas is the specialized detectors. Tracer response comparisons from gases with different gas densities and adsorbing characteristics cannot be made. The two most common nonradioactive tracer gases, He and SF<sub>6</sub>, are approximately seven times lighter and five times heavier, respectively, than the flow field gas, air. Thus, the density effects of the tracer gases can be significant but the single gas systems cannot evaluate these effects. With respect to the use of adsorbing gases, recent work has indicated that these gases may have the potential for increasing the information gained from a given tracer experiment.<sup>7</sup>

The single gas systems also result in increased testing time. Responses with very long spreads (decay) indicate stagnant flow regions that cause a virtual source effect. Additional tests can be conducted with the conventional systems only after the tracer concentration has reached acceptable background levels; whereas, a different noninterfering tracer gas could be injected at any time.

Finally, the radioactive Kr system has inherent safety problems when sampling a large retort: from one to three curies have been used to permit adequate signal-to-noise ratios. The responses are still far "noisier" than those from other gas systems, where the injection dose is not a limitation. Also, repeat tests have to be minimized, since the material is usually vented to the atmosphere and nonrecoverable.

### Multi-Gas Tracer System

A field-portable, self-contained, and semi-automated tracer system was designed and fabricated to address the multiple problems associated with characterizing a large oil shale retort and to overcome the limitations of conventional systems. The tracer system design criteria to achieve these goals is listed in Table 2. The limitations of the single gas and channel systems are overcome by the ability to sample several tracer gases; the long decay process of one gas to background concentrations does not delay an injection of another gaseous species.

Unlike the conventional systems, this system is also capable of measuring tracer responses from a retort during the burn phase; that is, from a chemical reacting, and possibly explosive gas mixture. This "hot" tracer feature has yet to be tested.

TABLE 2  
Design Criteria

- 1) 20 Sample point channels
- 2) Continuous sample flow
- 3) Multiple (non-radioactive) tracer gases
- 4) Independent injection times
- 5) Multiplex detector
- 6) Short total analysis time
- 7) Sample background correction
- 8) Real time data processing

The method which is used to extract the tracer signal from the retort is shown in Figure 1. A continuous flow, established from the retort sample locations, is periodically sampled and analyzed. This analysis is performed on a small fraction of the extracted volume. This volume reduction is indicated on Figure 1 as the critical pressure reduction which occurs in two stages: the sample and analysis chambers. This reduction is necessary to satisfy the requirements of the mass spectrometer. Figure 2 shows the complete functional block diagram and indicates the degree of system complexity. A detailed explanation of various components and their specific function follows.

#### Sample Line Flow

The gas sample is first transported from the retort via teflon tubing, through the pre-filtration unit to the flow chamber. The pre-filtration unit console consists of eight stations which have two stages of particle filters, air dryer, valving, and mass flow sensors. The purpose of the two stage, five-micron filter is to remove any entrained solid and liquid contaminants from the continuous sample line flow. The refrigerated air dryer

reduces the humidity to an acceptable level before the sample flow is monitored by mass flow transducers. Flow sensors indicate the sample line status (such as plugged, restricted), and also provide qualitative measures of the retort air flow (inferred from the back pressure). The monitoring of this measurement allows retort air flow fluctuations to be observed. Individual valves allow sample line flows to be adjusted to similar values. The predominant air flow through the sample lines is established by a manifold flow chamber and roots blower. The roots blower is capable of obtaining 56.6 l/s (120 scfm) at a pressure of 142 KPa (6 psig). The total flow through the roots blower is measured by another mass flow transducer. This type of transducer was selected because of the relative sensitivity to different species and dynamic range. Adjustment of the total sample flow is obtained by either a pulse width modulated motor controller or by varying the bypass flow around the blower.

### Process Stages

The first stage of the sample process occurs in the sample chamber which is operated at an elevated temperature of 393K (120°C). This minimizes virtual gas sources resulting from condensed water vapor on the chamber surfaces. Furthermore, operating at an elevated temperature maintains the water in the vapor phase which allows it to be reduced through pumping. This approach has the overall effect of reducing the time necessary to bring the water vapor partial pressure to acceptable levels. Total pressure measurements are made with a MHV ion gauge. The baseline or quiescent pressure is typically 2.6  $\mu\text{Pa}$  ( $2 \times 10^{-8}$  torr). This background pressure will reach an equilibrium value of 26  $\mu\text{Pa}$  ( $2 \times 10^{-7}$  torr) after a periodically occurring sampling phase. During the sampling process the pressure in the sample chamber is increased to 0.4 Pa ( $3 \times 10^{-3}$  torr) by the admittance of the sample gas. The integrity of the tracer partial pressure measurement is assured by proper isolation to limit the degree of contamination from previous samples. This isolation was achieved by the greater than four orders of magnitude difference between baseline and sample pressure. The sample chamber is symmetrically configured with 20 electropneumatic valves which are operated individually and in any pre-determined order. The desired input sample pressure is achieved by the pulsed open operation of these valves. This pulse duration time varies due to the individual physical characteristics of the sample valves, hence this pre-determined information is stored in the computer program.

In the second stage of the sampling process the volume of gas to be evaluated is reduced further. This occurs by the pulsed operation of valve  $V_A$  (shown in Fig. 2). This two-stage valve operation brings the sample to the point where it can be leaked to the analyzer section in the molecular flow regime, thereby eliminating mass discrimination that can occur when leaking across a low conductance orifice with a high pressure differential. Once this reduced sample source is isolated in the 3.8 cm (1.5 in.) tee, the evacuation of the main sample chamber is initiated. The measurement gate valve,  $V_D$ , is then opened, exposing the chamber to the 510 l/s turbomolecular pump. During this period the gas analysis is performed by the mass spectrometer. Upon completion, valve  $V_C$  opens for a pre-determined time, thus permitting the rapid evacuation of the tee source. These high pump-down rates are necessary to minimize the sample multiplex time.

Figure 3 shows a systems timing chart for the operation of the valves  $V_A$ ,  $V_C$ ,  $V_D$ , and the sample analysis. The parallel operation of the sample and analysis sections are the determining factor which controls the tracer system multiplex sample time. The pulse widths are mainly controlled by limitations of the mechanical components and the evacuation rates.

### Analyzer

The analysis part of the system consists of a variable leak, ultra high vacuum gauge, mass spectrometer, turbomolecular pump, and valving. This system is also operated at an elevated temperature of 393K (120°C) for the same reasons given before. Total pressure measurements are made with a UHV ion gauge. Background pressure values of  $4 \mu\text{Pa}$  ( $3 \times 10^{-8}$  torr) are typical because the mass spec analyzer is continuously pumped by a 110 l/s turbomolecular unit. The unknown gas sample is metered from the tee source to the mass spectrometer by a manually set leak valve. The dynamic total analysis pressure is typically set for 0.67 mPa ( $5 \times 10^{-6}$  torr) as indicated by the vacuum gauge. A pressure limit of 6.7 mPa ( $5 \times 10^{-5}$  torr) has been selected to insure that nonlinear measurement effects would be minimized. Table 3 contains specifications for the mass spectrometer.

TABLE 3  
Mass Spectrometer Specifications

UTI-100C	
Mass range	1 to 300 AMU
Sensitivity	1mA/torr Faraday cup 300A/torr Electron Multiplier(G=3M)
Amplifier range	.01mA to 1pA
Minimum detectable partial pressure	100pbb
Stability	
1) Peak height ratios	+/- 0.5%/8hrs
2) Peak location	+/- 0.02 AMU/8hrs
3) Peak height stability	+/- 1%/8hrs
Maximum operating pressure	1mTorr
Output signal	0 to 10V(analog)
Computer compatible	

The identification of the tracer ion species requires the mass spec to jump to different peaks. The fragmentation patterns for all the candidate tracer gases were stored prior to testing. The mass spec determines the concentration of the particular gas by measuring its ion current. This ion current, proportional to the species partial pressure, is increased in magnitude by an electron multiplier. Typically a continuous mode of operation is used for the electron multiplier. The output signal of the multiplier is applied to a special amplifier which has a conversion of 1 pA/volt @  $10^{-12}$  scale and is capable of eight orders of magnitude ranging. A tracer response peak is automatically tracked by utilizing a continuously updated set of range information. An estimate of the range selection for the current gas species is made using the previous time step value. Typical sample analysis time for three peaks was approximately 12 s.

Slight variations in sample volume from one cycle to the next are to be expected in a complex mechanical system. Therefore, a correction factor for the tracer data was determined by monitoring a constant nontracer gas component in the flow field, usually argon.

### Combined System

The overall relative system sensitivity was empirically determined by the use of calibration gases. This data, presented in Table 4, includes the effects of mass spec response and turbomolecular pumping speed. One will note that SF<sub>6</sub> is the most sensitive tracer gas. This is due to the mass spec ionization efficiency and density bias of the vacuum pumps. Table 4 can be used to determine the relative amounts of gas that need to be injected to obtain the same output at the detector.

Table 4  
System Gas Sensitivity

SF <sub>6</sub>	1.00	Fr <sub>12</sub>	0.24
Kr	0.02	Fr <sub>13</sub>	0.02
Ne	0.005	Fr <sub>14</sub>	0.04
He	0.01	Fr <sub>22</sub>	0.02

A desk top computer and associated peripherals operating on an IEEE 488 bus provides the control mechanism for the tracer system. The functional capabilities of these units and components are listed in Table 5.

TABLE 5  
Computer System Capabilities

#### Desktop Computer

- (1) 187K RAM
- (2) ROM's
  - (a) Graphics
  - (b) Mass Storage
  - (c) Input/Output
  - (d) Advanced Programming
- (3) 2 Tape units 0.5Mbytes
- (4) 4 I/O Ports
- (5) RS 232

#### Multiprogrammer

- (1) 2K Memory
- (2) Extender Board
- (3) Clock
- (4) 16 Input/Output Slots
- (5) Function Boards
  - (a) 2K RAM
  - (b) 2 Counter/Totalizers
  - (c) D/A 12bits
  - (d) A/D 12bits
  - (e) Digital I/O
  - (f) 7 Relay Cards 16/unit

#### Mass Storage (Floppy Disc)

- (1) 2 Double Side/Double Density 2.36Mbytes

As indicated in the system diagram (Fig. 2), the command flow is as follows:

1. Interactive control and systems management operating program located with computer.
2. A portion of the control program resides in multiprogrammer which hosts the majority of I/O function cards.
3. Mass storage of data is provided by a dual floppy disc unit.
4. Optional outside communication link (RS-232).

The software was written in extended Basic in a menu driven mode. The initial input data block consists of date, time, file name, test location, and test parameters, such as retort pressure drop and input flow. The second block of input parameters includes tracer type, injection points, and monitored sample locations. A programming feature of "user controlled interrupts" permitted injecting the tracers at any time during the test. This was particularly useful for multiple gas injections.

### Calibration

Standard calibration gases are introduced in the sample chamber of the tracer system. These gases are analyzed by the mass spec and their characteristic peaks plus relative amplitude vs. mass filter rod drive voltage are recorded. This information is used to update the ion species library. The amplitude data sampled by a Faraday cup is also used to determine the present electron multiplier gain.

### System Applications

To date, the system has been used in two tracer test series: Laramie Energy Technology Center's (LETC) surface retorts and on Occidental Oil Shale, Inc.'s (Oxy) commercial retorts, 7 and 8. A complete test description and detailed data analysis for the two test series may be found in Ref. 8 and 9, respectively. The goal of the first test was to develop a prediction capability for in situ retort preparation. The data will be used to benchmark existing tracer flow computer codes.<sup>10</sup> The second test was performed on a commercial scale in situ retort to correlate tracer data with thermocouple data obtained during the burn phase.

The LETC test configuration consisted of the 150 ton retort packed with mine-run oil shale. A target cylinder was placed near the top of the retort to provide a known disturbed flow field. The characterization of the permeable bed was accomplished with a nine point sampling matrix. Monitoring of this matrix at two different gas velocities produced information to evaluate both the dispersion of various gases in a porous bed and the wake effects from the target. A sample of the data comparing adsorbing and non-adsorbing tracer effects is shown in Figure 4. One will note the peak delay and longer decay of the adsorbing gas (Fr-22). At first glance the differences in tracer response shown in Figure 4 may not appear great, however, it should be recognized that Fr-22 being higher in molecular weight than He should show both an earlier arrival and less dispersion. The fact that the actual data shows the opposite trend strongly suggests the presence of an adsorption mechanism.

The Oxy test consisted of approximately a 100 sample point network in each retort. Complete tracer characterizations of the retorts were not accomplished, but the interpretation of the obtained data was confirmed by the steam front profile during the retort phase. A comparison of the gas density effects using He and SF<sub>6</sub> tracer gas is shown in Figure 5. As expected, the heavier gas, SF<sub>6</sub>, had a shorter arrival time and faster decay time.

#### Recommendations

Some of the desired improvements and enhancements to the system include:

1. Reducing the multiplex sample time using pulse counting techniques. The ion detector multiplier used for this purpose is a lower resistance channeltron that will operate at a 10 Mhz count rate. A pulse shaping network featuring control over both rise time and amplitude threshold provides discrimination against slow varying noise. This should reduce the cycle time to approximately 7 s. This is an important factor if the system is to be used on experiments with smaller residence times.

2. Increasing the system sensitivity by employing phase-lock and digital signal manipulation techniques. This process involves the amplitude modulation of the ion peak drive voltage. The drive modulation frequency and lock-in amplifier are used to synchronously recover the signal from the electron multiplier. Additional digital signal processing continues to improve the signal to noise ratio. This increase in system performance may be at the expense of an extended measurement time.

#### Summary

The Multiple Gas Tracer System achieved the initial design goals as shown in Table 2. The importance of the multiple gas capability has been demonstrated at the Oxy test, where the system was able to obtain data from a large in situ rubble bed in a timely fashion. The LETC experiments have indicated that the breadth and quality of tracer data that can be obtained using multiple gases with different physical characteristics will allow an assessment of tracer technology as a means to infer the flow field in a porous media to be made.<sup>11</sup>

Possible future applications might take advantage of the "hot" tracer feature of the system to analyze retort gas products during the burn phase. This can aid the understanding of this complex chemical process. Hydrocarbon concentrations can be unfolded from the mass spectrometer data<sup>12</sup> via existing software routines; data up to C<sub>5</sub> are of typical interest for oil shale retorting. This capability would permit monitoring the retort chemical reactions at various locations in the in situ retort.



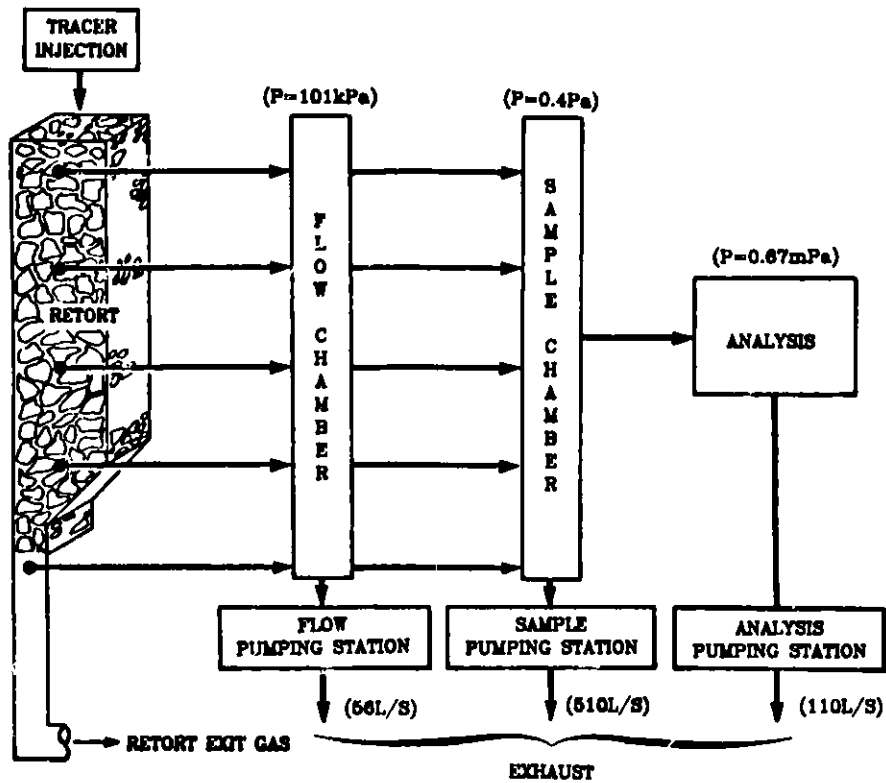


Figure 1. Sample Flow Overview.

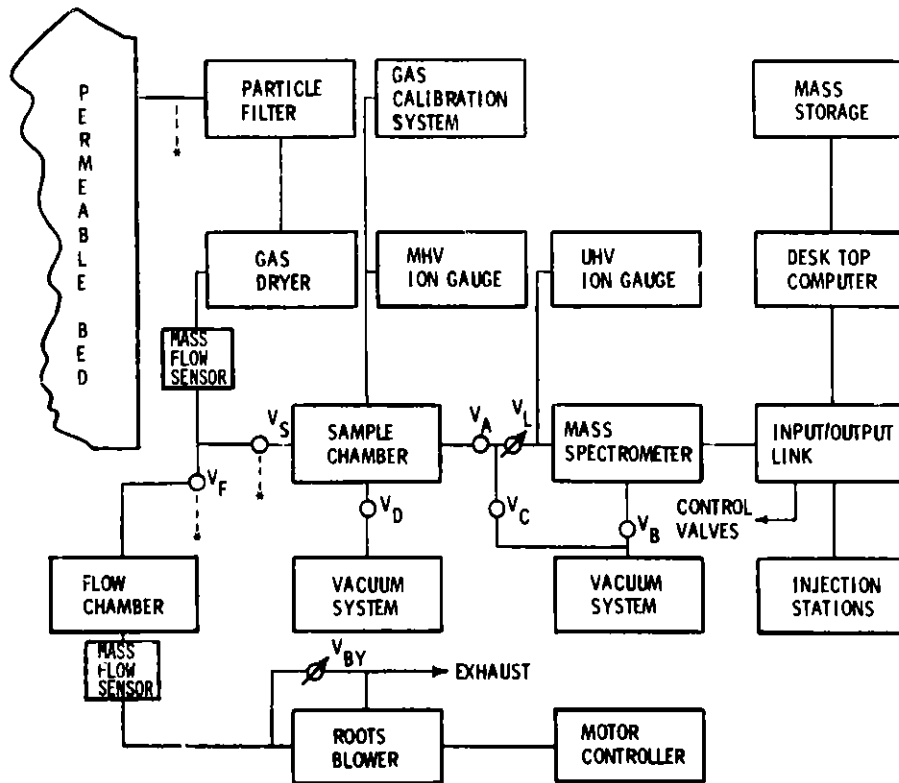


Figure 2. Multiple Tracer Gas Analysis System.

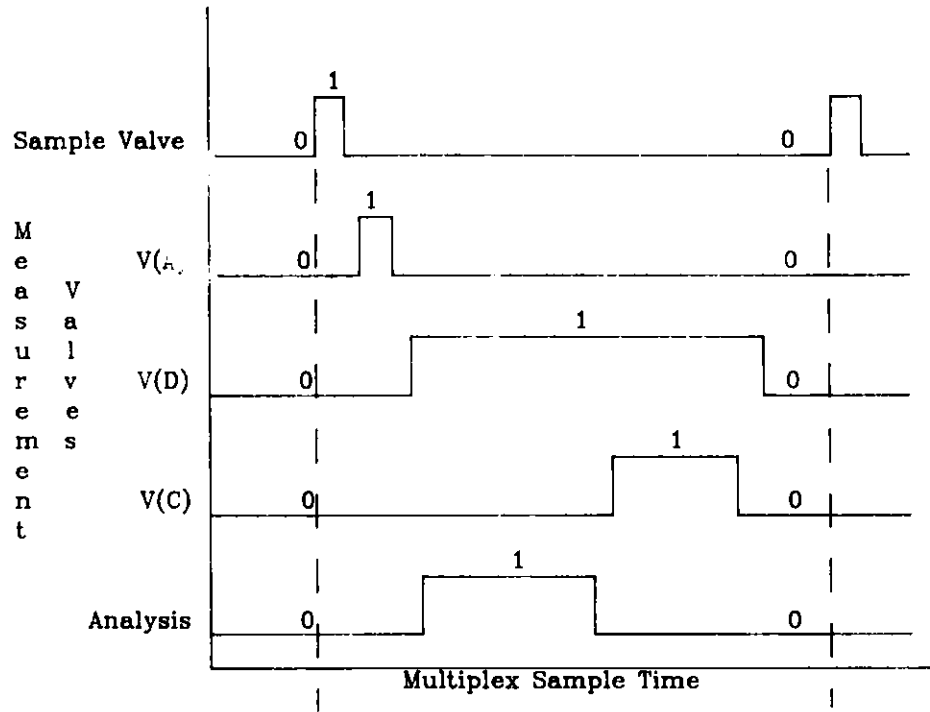


Figure 3. State Diagram of Sampling System; 1 = On, 0 = Off.

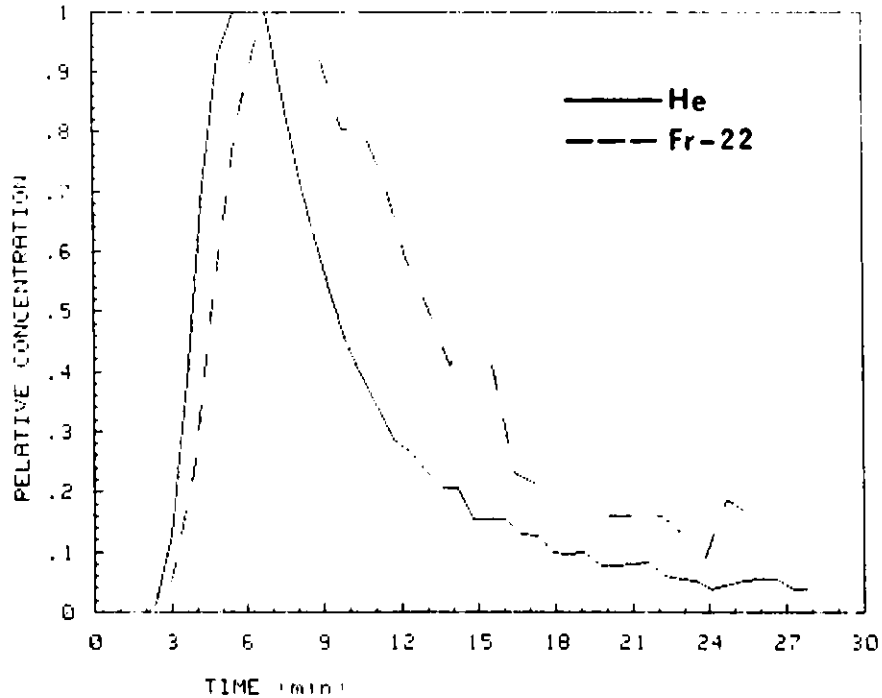


Figure 4. Comparison Between Adsorbing (Fr-22) and Non-Adsorbing He Tracer Gases.

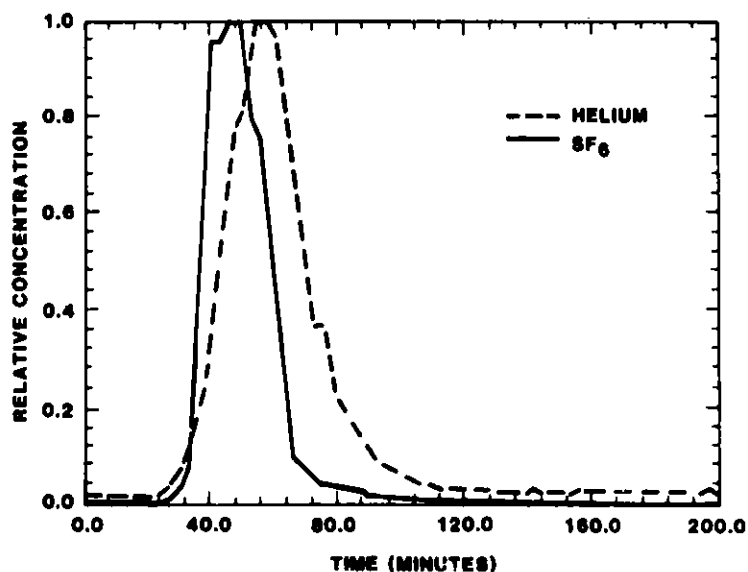


Figure 5. Density Comparisons Between Light (He) and Heavy ( $\text{SF}_6$ ) Tracer Gases.

#### References

1. C. E. Tyner, R. L. Parrish, B. H. Major and J. M. Lekas, "Sandia/Geokinetics Retort 23: A Horizontal In Situ Retorting Experiment," 15th Oil Shale Symposium, Golden, CO (April 28-30, 1982).
2. K. L. Berry, R. L. Hutson, J. S. Sterrett and J. C. Knepper, "Modified In Situ Results of Two Field Retorts," 15th Oil Shale Symposium, Golden, CO (April 28-30, 1982).
3. P. J. Hommert, "Instrumentation and Data Analysis from Occidental's Retorts MR-3 and MR-4," 15th Oil Shale Symposium, Golden, CO (April 28-30, 1982).
4. T. E. Ricketts, "Occidental's Retorts 7 and 8, Rubblization," 15th Oil Shale Symposium, Golden, CO (April 28-30, 1982).
5. T. F. Turner, C. E. Tyner, "In Situ Formation Evaluation Using Tracer and Flow Techniques: DOE Site 12, Rock Springs, WY," 2nd Annual Oil Shale Conversion Conference, Grand Junction, CO (December 6-8, 1978).
6. A. E. Harak, C. Y. Cha, L. Burwell and L. Dockter, "Pressure Drop, Gas Composition, and Gas Velocity Distribution in Simulated, Modified, Vertical Retorting of Oil Shale," Laramie Energy Technology Center report.
7. K. L. Erickson, F. B. Burns, "Non-Adsorbing and Adsorbing Gaseous Tracers for In Situ Characterization of Oil Shale Rubble," to be submitted.
8. T. J. Bartel, J. E. Uhl and R. J. McAniff, "Gas Tracer Tests Performed at LETC's 10 and 150 Ton Surface Retorts," to be published, Sandia National Laboratories Report SAND 82-1333.

9. R. J. McAniff, T. J. Bartel and J. E. Uhl, "Gas Tracer Testing at Occidental Oil Shale, Inc.'s Retorts 7 and 8," to be published, Sandia National Laboratories Report SAND 82-1332.
10. B. J. Travis, "A 3-D Model of Tracer Flow in Rubbled Oil Shale," Jan.-March 1981 Quarterly Report, Explosively Produced Fracture of Oil Shale, Los Alamos National Laboratory Report LA-8956-PR.
11. T. J. Bartel, R. J. McAniff and K. L. Erickson, "Characterizing a Porous Media with Gaseous Tracers," 57th Annual Technical Conference and Exhibition, SPE-11075, New Orleans, LA (September 26-29, 1982).
12. L. F. Monteiro and R. I. Reed, "Mass Spectra and Molecular Structure: Part II - The Analysis of Mixtures," J. Mass Spectrometry and Ion Physics, 2 (1969) pp 265-285.

MEASUREMENT AND EVALUATION OF A SIMULATED  
UNDERGROUND-COAL-GASIFICATION-EXPERIMENT  
BY A MICROPROCESSOR SYSTEM

---

K. Guntermann, G. Suhens, M. Kurth, F.H. Franke  
Institut für Eisenhüttenkunde  
The Aachen University of Technology  
Intzestr. 1, 5100 Aachen  
Federal Republic of Germany  
011-49-241-805834

Abstract

In order to simulate Underground Coal Gasification (UCG), coal blocks of 4 m length and 0.32 m diameter are gasified under pressure-swinging conditions in an autoclave.

The large amount of data needed to adequately characterize this large scale test, and the necessity to process these data during the course of the test, requires the installation of a computer. For the characterization of the process 64 different signals are picked up (i.e. temperatures, gas analyses, mass flows, pressures).

Because the frequency of the pressure change is not controlled by the computer and is subject to variation, the switching times for the pressure-regulating valve must be accurately known. This is accomplished through the use of an interrupt switch, activated each time the valve position changes.

For each measurement-cycle a BASIC-program averages the value of the signals and computes mass and energy balances. A protocol of the balances and the profiles of the temperatures along the coal block are plotted for each cycle.

By this procedure a comprehensive judgement is available during the test so that it is possible to make changes in operating conditions if desired.

The data are transferred to a second computer, where a further detailed evaluation is done.

Introduction

Since 1975 research on Underground Coal Gasification (UCG) has been done at the "Institut für Eisenhüttenkunde". The main work is the simulation of the UCG-process on compact samples which have been cored underground. This has been successfully done in three autoclaves of different sizes.<sup>1</sup>

### Description of the plant

Since June 1980 the large autoclave plant has been operating. It is a special apparatus for simulating the UCG-process in coal samples of 4 m length and 0,32 m diameter under constant pressure and under pressure-swinging conditions.<sup>2</sup> These tests can be carried out at a maximum pressure of 60 bars and can use as gasification agents air, oxygen, hydrogen and steam as well as their suitable mixtures. Figure 1 shows a flow scheme of the plant. It consists of 5 component groups<sup>3</sup>: reactor with piping equipment, gasification agent equipment, product gas incineration equipment heat and massflow measurement, and control and safety systems. The measurement equipment is conventional, i.e., each electrical signal is registered on recording instruments.

The plant has been designed for steady-state pressure as well as for pressure-swinging conditions.

Pressure swinging conditions are achieved by different methods of gas flow control, as shown on figure 2.

Case (a) shows the constant pressure operation; cases b, c and d show different pressure-swinging operating procedures. In case (b) pressure-swinging is done by alternating opening and closing of the inlet and outlet valves. Case (c) is similar to case (b), but has a holding time at the high pressure end where both valves are closed.

Case (d) uses a constant inlet massflow and a cyclic opening and closing of the product gas valve.

For characterizing and balancing the process temperatures are measured at 45 locations in the coal sample, and the temperatures of the inlet and outlet of the reactor and of the product gas are measured. Massflow is measured at three locations. The pressure is registered, and a continuous analysis of the product gas components H<sub>2</sub>, CH<sub>4</sub>, CO, CO<sub>2</sub> and O<sub>2</sub> is made. A schematic of the process measurement system is shown on figure 3.

The measured signals alone cannot describe the process. This is why it is necessary to analyze these data, by balancing or graphically representing the temperatures as a function of position and time. The large amount of data and the calculations in the balances (iterations) requires the installation of a computer.

By using a computer other data processing systems can access and process these data so that it is possible to evaluate all tests systematically.

In seeking the best computer for our cost-to-performance requirements the following functional characteristics were important:

- The computer must be able to work, because of the nearness to the process (dust, dirt, heat) without any external storage, that means an operating system without a floppy disk;
- the memory organization of the Random Access Memory (RAM) should be able to store temporarily a large amount of data for more than 12 hours, without the chance of a disturbance which

stops the program also causing a loss of these data;

- the user program should be stored in an erasable programmable memory (EPROM) so that a maximum reliability of operation is obtained. At the same time changes for adaption of the computer to different operating conditions must be easily practicable;
- the operating system should be able to recognize interrupt requests from the processes and acknowledge them as prioritized interrupts;
- all input/output specifications for data management should be available for analog and digital measurement and control;
- the operation and the hardware configuration of the computer should be so simple that changes in operating conditions can be transferred to the software at any time;
- the system obtained should have been tested and proved under industrial conditions.

Because of these reasons and the infrastructure of the computers at the institute the microprocessor system TM 990 from Texas Instruments was purchased: Figure 4 shows the configuration of the computer systems with their peripheral equipment.

### Hardware

The microprocessor system consists of cover with power pack, temperature control, ventilation, central processing unit (CPU) with two normalized (V 24) interfaces and one parallel interface with 16 individually-controlled interrupt entry points. It also has expansion memory boards for RAM and EPROM, and an analog board with 64 channels for analog-to-digital converting (ADC) as well as 2 for digital-to-analog converting (DAC).

The microcomputer communicates with a terminal (Hazeltine 1520) by one of the serial ports (V 24). The interface of the terminal is connected with a line printer.

The ADC has a bipolar input  $\pm 10$  V direct current. All signals have to be adapted to the system.

The voltage signals of the thermocouples are 45-fold amplified. The signals of the gas analysis, mass flows, and the pressure are currents (0 - 20 mA) and the voltage signals are supplied by an isolation amplifier.

The pressure-swinging conditions are achieved by opening and closing the product gas valve (figure 2d). The switching times must be accurately known for a correct calculation of the mass and energy balances. This is accomplished by an interrupt request activated each time the valve position changes.

## Software

A measurement by a microprocessor system is in general cheaper and more versatile than a conventional one, which is constructed for a certain purpose.<sup>4</sup>

The microprocessor system consists of standard boards. The application of the system is determined by the software and the connected peripherals, so that changes in test assembly can be realized with small wasting of time.

The programming language of the system is BASIC, which is good for all not-time critical processes. BASIC has the advantage that its interpreter consists of an editor so that the computer can be used as a development system. On the other hand it is also possible to use assembler routines to accelerate the data collection.

The coordination of the physical dimensions is done for the gas analysis by calibrating with a gas of known composition, and for the massflows and pressure by reading the values from the registration elements.

The 45-fold amplification of the thermo-voltages is done by a control measurement of a constant voltage source of 50 mV and is corrected by software.

The software development of the system was done under the point of view that anyone can operate the system. The program is organized in an interactive mode and each input command must be authorized by another command before the system accepts it.

It is necessary to abstract the process. Program control of the measurement cycles, which is done by constant pressure tests through the real-time clock of the operating system depending upon the desired interval length, and by the pressure-swinging tests through the interrupt request from the process, starts in a clock frequency of one minute. In this time interval different time conditions start the balancing and the protocolling of the results is done and data transfer to the second computer is made.

There is an influence on the control commands, by calibrating the signals, process setting clock frequencies and breakpoints. For a certain kind of operating conditions (figure 2d) the measurement is described.

The measurement cycle starts when an increase in the pressure is recorded. The inlet mass flows and the pressure are picked up over the whole period. The mass flow analysis and temperature of the gas are measured after the interrupt request of a maximum pressure. Two minutes after maximum pressure the computer picks up the 45 thermo-voltages along the sample and the temperatures at the inlet and outlet of the reactor.

The BASIC-program calculates these voltages by the calibration table (DIN 43710) for Ni-Cr/Ni thermocouples into temperatures and stores them in the data storage (RAM). The signals for the balances are averaged for each measurement cycle and also stored.



After this data processing a balancing of the process is done for each measurement cycle. A protocol of the balance and the temperatures is done in tabulated form and also on a printer plot.

By this procedure at each time of the test the measured signals and criteria for judgement, i.e. heating value, inlet and outlet mass flows, converted steam and coal, are made available and can be used for changing operating conditions.

The RAM of the microprocessor is designed for 16 hours. At this time the data must be transferred. This is done through an interface (V 24) of the microprocessor and a serial data transfer to the computer of the institute (SPC 16/65 General Automation). This is organized by handshaking, because this computer has to work with several processes at the same time. The data rate is 9600 (bit/sec) baud and takes, depending upon load of the computer, about 2 minutes.

There is an alternative connection, in cases of breakdown, to a cartridge. This transfer has a data rate of 2400 baud and takes 1 minute 15 seconds. The time of data transfer can be determined at any time of the test (normally all 12 hours) and takes place after the measurement of the 47 temperatures two minutes after maximum pressure.

All data are stored on the magnetic disk of the SPC 16/65. By FORTRAN-programs a further detailed evaluation is done. Temperatures are recorded, mass- and energy-balances in tabulated form are calculated and a graphic representation of the heating value is made (figure 5). The gas analysis (figure 6) and component and total mass flows are plotted, and also a 3-d plot of the temperatures over the time and along the coal sample is made (figure 7).

This evaluation is done every 12 hours and cumulatively updated to the actual time so that a comprehensive judgement of the process is available at all times. It is possible to make changes in operating conditions and see their results during the test.

The SPC 16/65 is connected to the CYBER 175 of the university. With the help of the program system MIMIC<sup>5</sup> a system of differential equations is solved, which describes the process mathematically.

Here the actual data can be used at any time to examine the model calculations. The model calculations help to find good operating conditions by variation of the process parameters.

#### Acknowledgement

The financial contributions of the "Bundesministerium für Forschung und Technologie" under management of the "Projektleitung nichtnukleare Energieforschung (PLE)" at the "Kernforschungsanlage Jülich (KFA)" made this project possible.

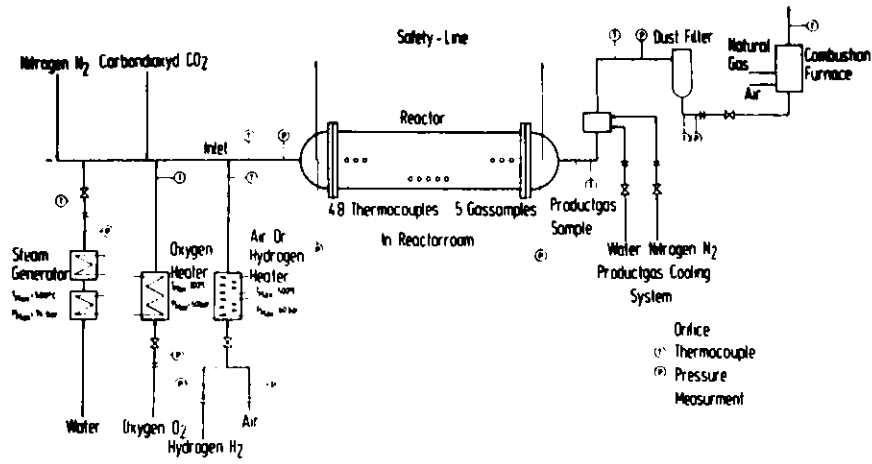


Fig. 1 Flow scheme of the plant

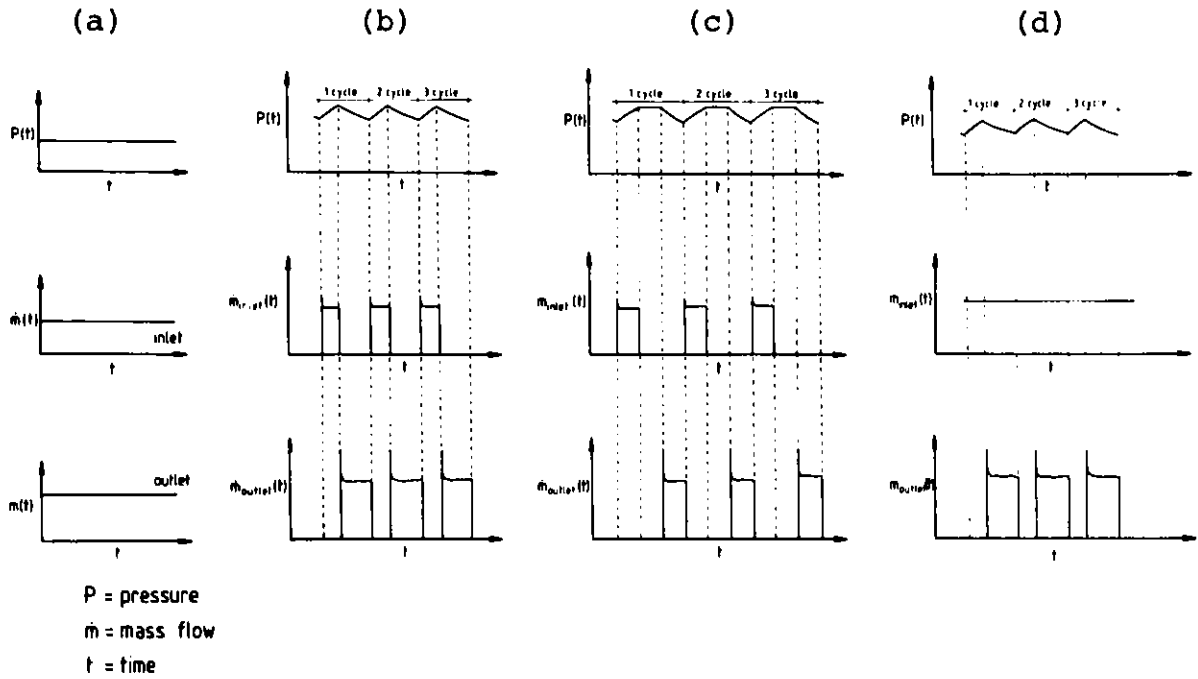


Fig. 2 Operating conditions of the plant

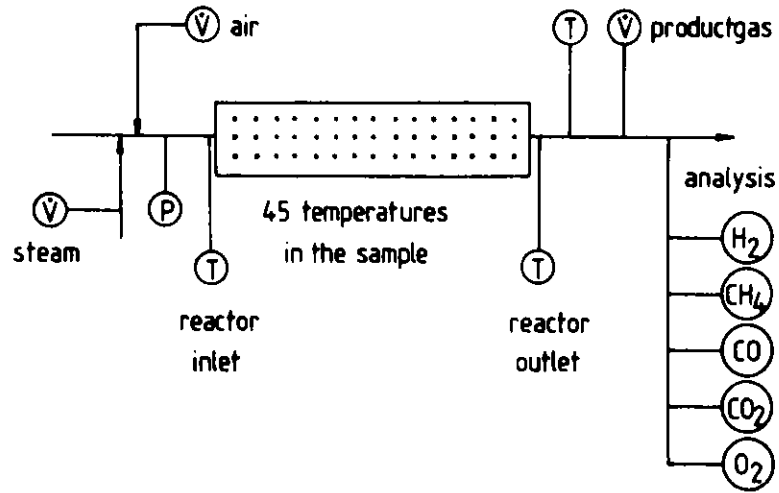


Fig. 3 Measurement signals

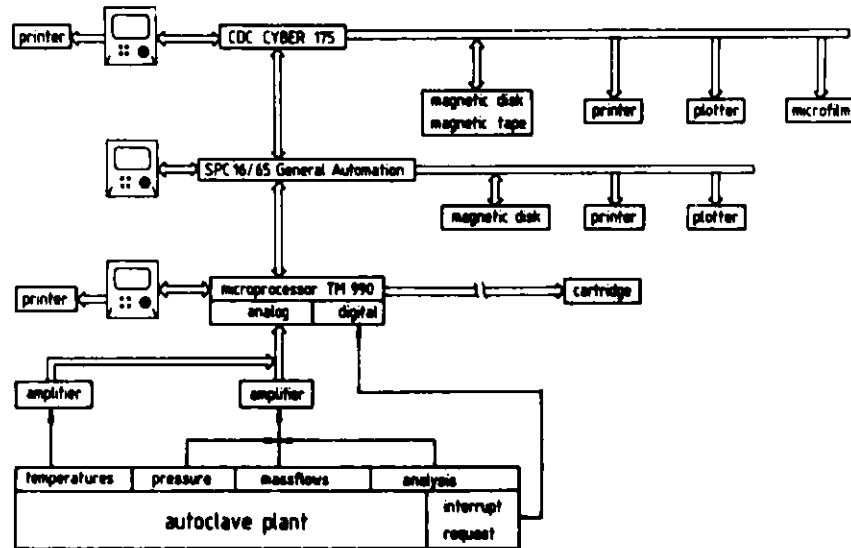


Fig. 4 Configuration of the computer systems

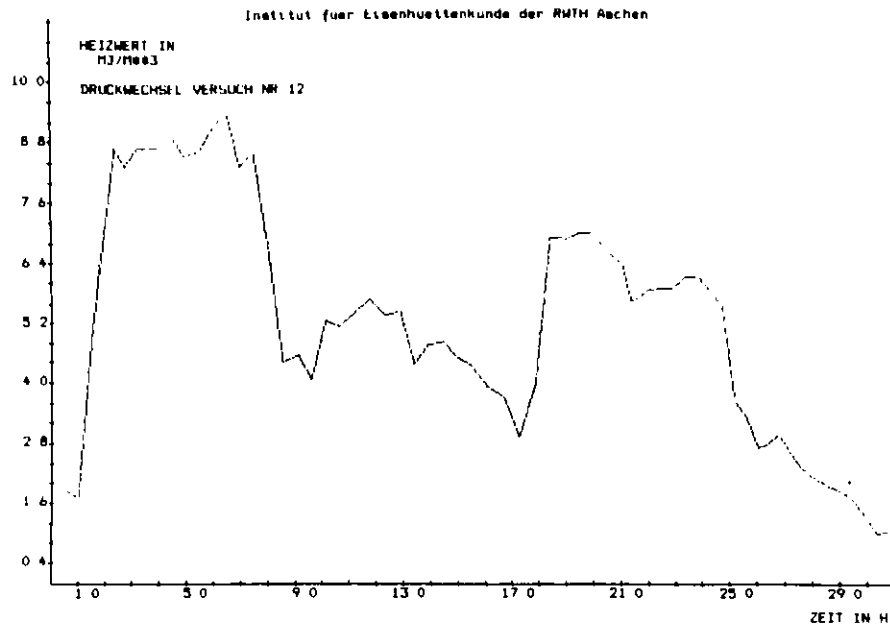


Fig. 5 Heating value of the product gas

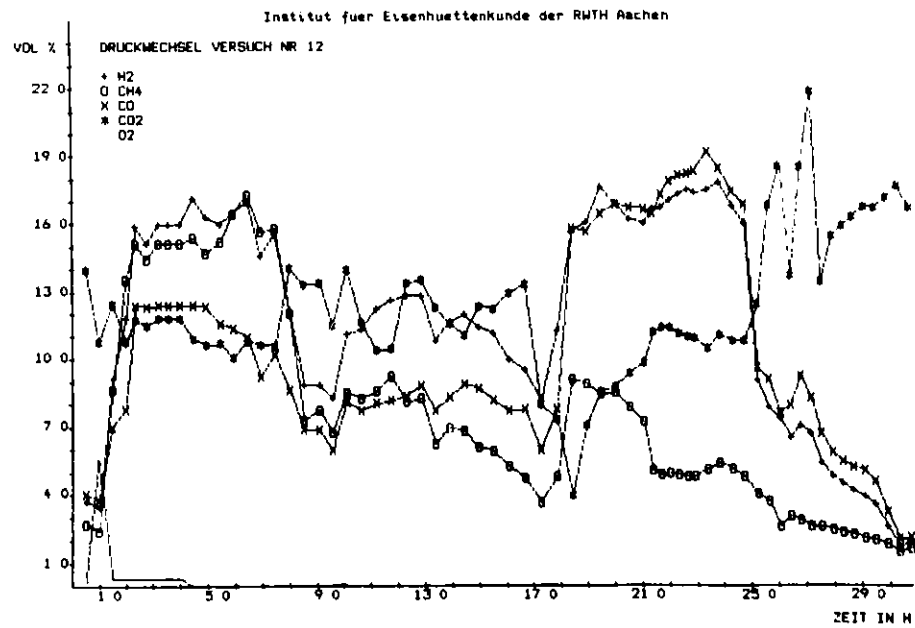


Fig. 6 Gas composition of the product gas

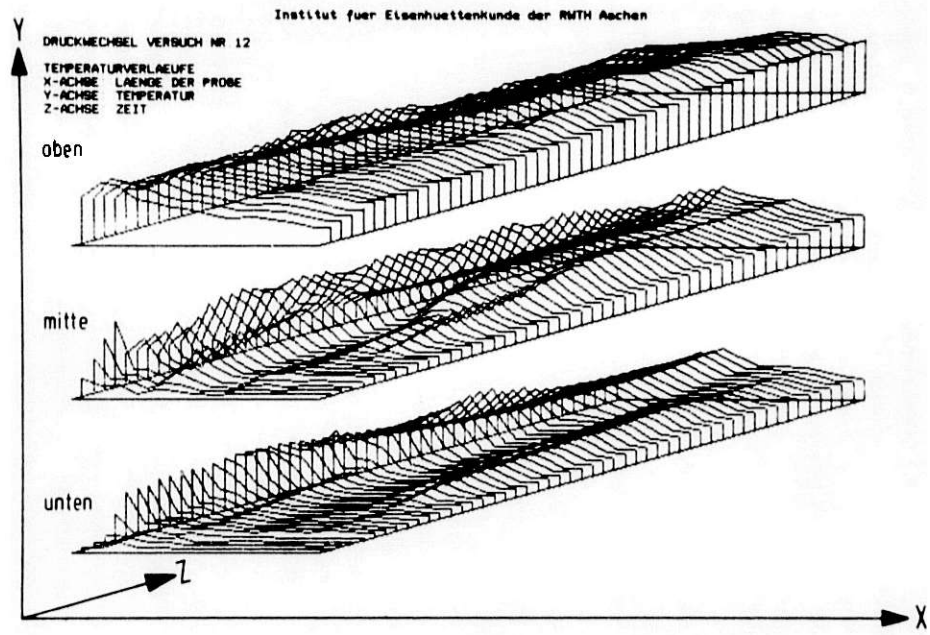


Fig. 7 3-dim. plot of the temperatures in the sample

References

1. W. Wenzel; H.W. Gudenau; M. Mohtadi, "Untertagevergasung tiefliegender Steinkohle", Arch.Eisenhüttenwes. 51 (1980) Nr. 6, S. 249/56.
2. M. Mohtadi; M.J. Paersch; G. Subklew; F.H. Franke, "Druckvergasungsanlage zur Simulation des Untertageprozesses in einem 4 m langen Flözabschnitt", Erdöl und Kohle, Erdgas, Petrochemie 43 (1981), S. 544/48.
3. M. Mohtadi; F.H. Franke; W. Wenzel; H.W. Gudenau; M. Kurth, "A Pilot plant to Simulate In-Situ-Gasification", Proceedings of the Symposium on Instrumentation and Control for Fossil Energy Processes in San Francisco, California, 1981.
4. H.-G. Althoff, "Einsatz von POWER BASIC in Meßdatenerfassung und Verarbeitung", Texas Instruments Deutschland GmbH, Applikationslabor EB 125.
5. CONTROL DATA MIMIC, "A Digital Simulation Language", Reference Manual Control Data Corporation, Publication Number 4461o4oo (1968).

List of Exhibitors

Maureen Derosa  
Amersham Corporation  
2636 South Clearbrook Dr.  
Arlington Heights, IL 60005

Wayne Masnica  
Perkin-Elmer Corp.  
2771 N. Garey Street  
Pomona, CA 91767

Mr. S. Steinberg  
AKI Industries, Inc.  
9000 King Street  
Franklin Park, IL 60131

Herb Kaplan  
SCIEP, Inc.  
193 East Avenue  
Norwalk, CT 06855

Mr. J. Hiett Ives  
Cameron Iron Works, Inc.  
P. O. Box 1212  
Houston, TX 77001

John Sozio  
Taylor Instrument Co.  
95 Ames Street  
Rochester, NY 14601

Douglas F. Butler  
Kamyr Valves, Inc.  
145 Murray Street  
Glen Falls, NY 12801

David Snyder  
Validyne Engineering Corp.  
8626 Wilbur Avenue  
Northridge, CA 91324

Robert Kaufman  
Mogas Industries, Inc.  
P. O. Box 11687  
Houston, TX 77293

Stephen McDonough  
Waters Associates  
34 Maple Street  
Milford, MA 01757

Roy W. Yost  
Perkin-Elmer Corp.  
Main Avenue  
Norwalk, CT 06856

Renate Sielemann  
Carl Zeiss, Inc.  
444 Fifth Avenue  
New York, NY 10018



Amersham Corporation



ARI Industries, Inc.





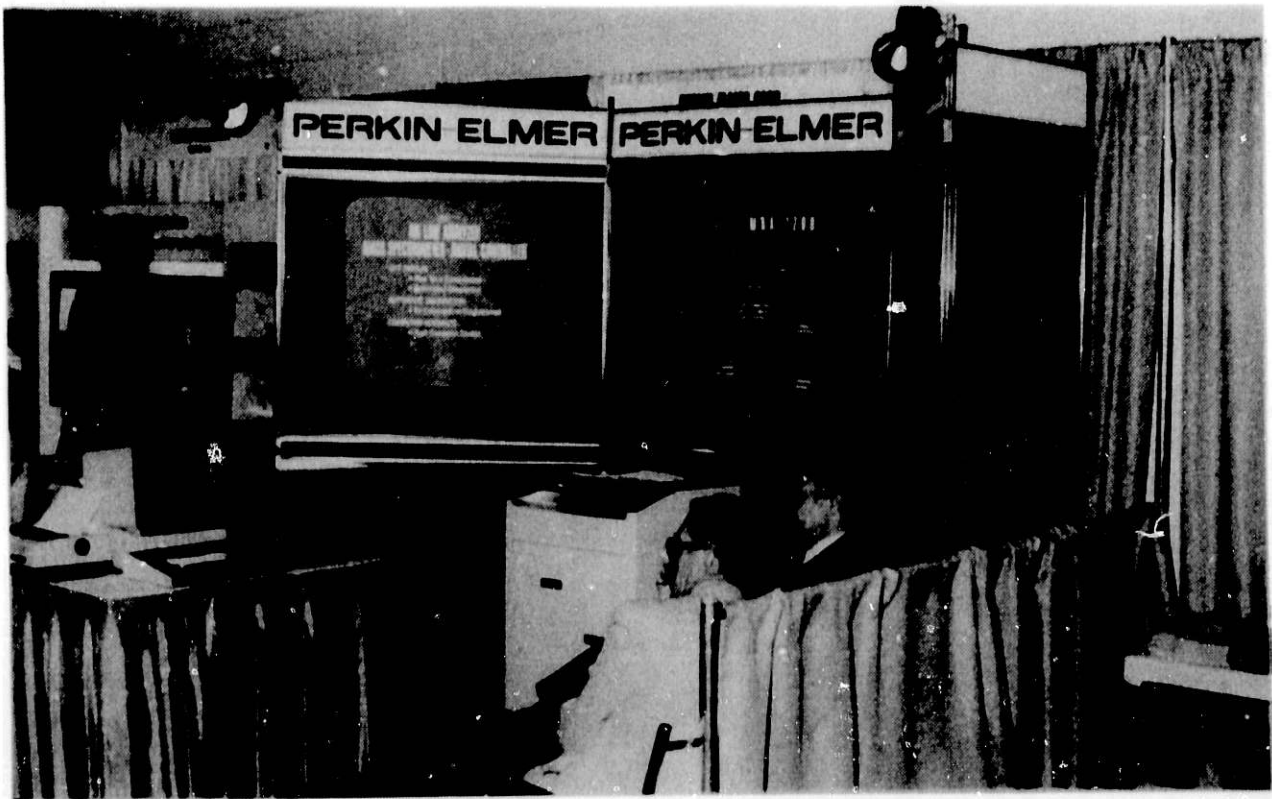
Cameron Iron Works, Inc.



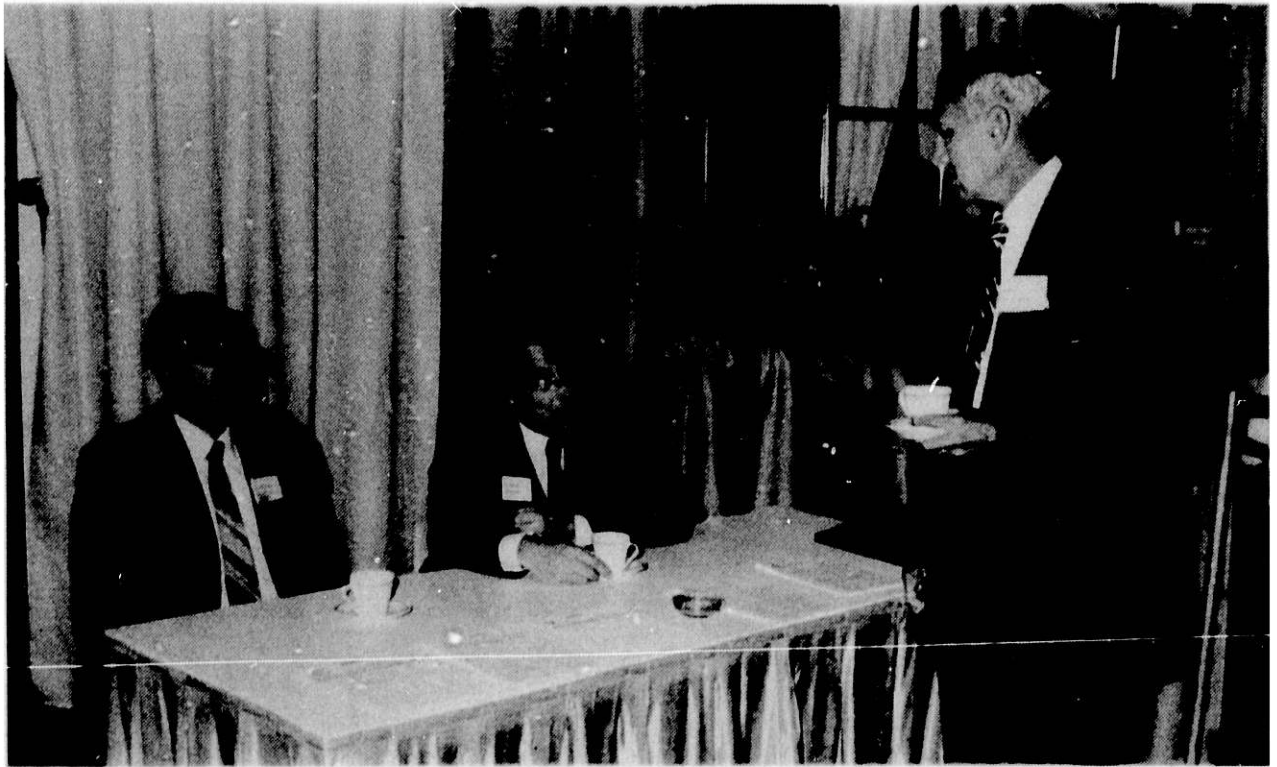
Kamyr Valves, Inc.



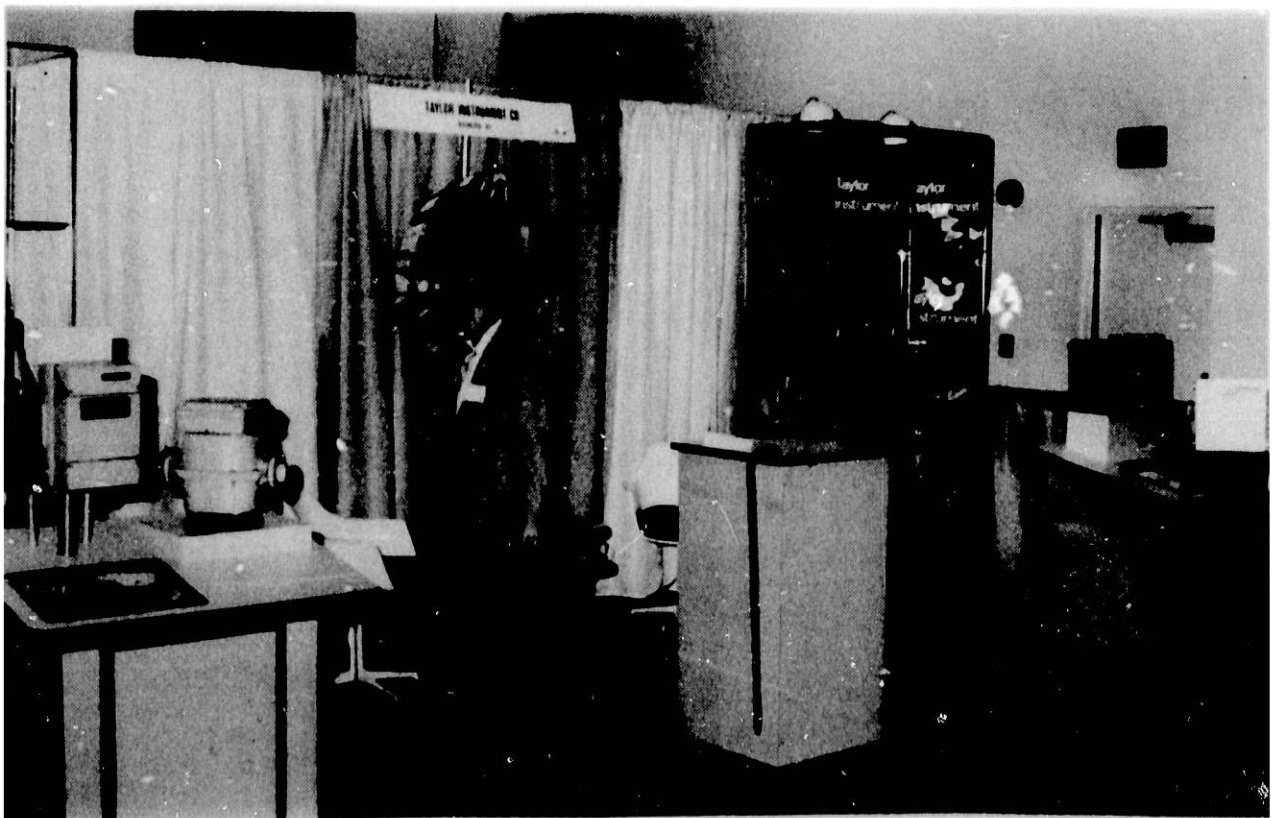
Mogas Industries, Inc.



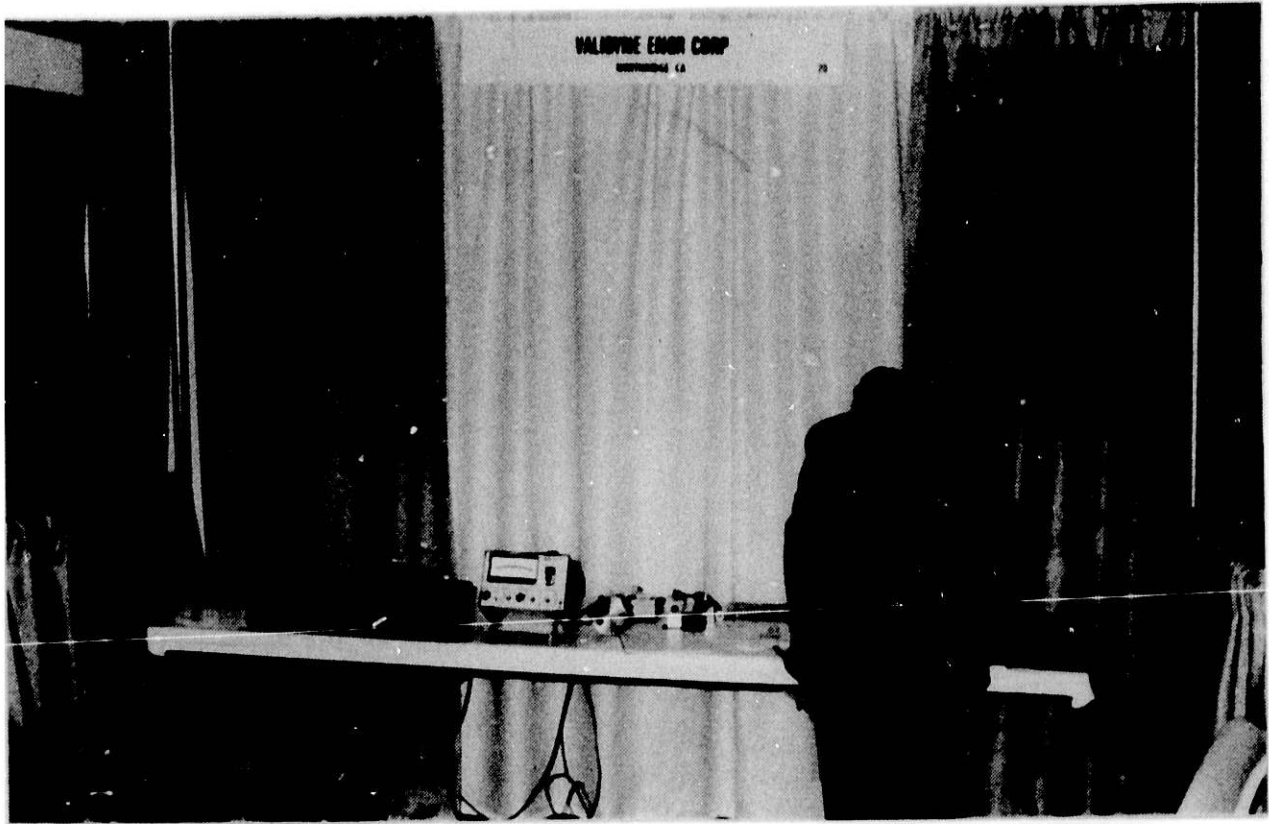
Perkin-Elmer Corp.



SCIEP, Inc.



Taylor Instrument Co.



Validyne Engineering Corp.



Waters Associates



Carl Zeiss, Inc.



Dr. John J. Roberts  
Associate Laboratory Director for  
Energy and Environmental Technology  
Argonne National Laboratory  
Argonne, Illinois



Mr. Donald L. Bauer  
Deputy Assistant Secretary for Fossil Energy  
U.S. Department of Energy  
Washington, D.C.



Dr. James Gary  
Colorado School of Mines  
Golden, Colorado





Mr. John V. Walsh  
Jet Propulsion Laboratory  
Pasadena, California



Judge F. Lee Duggan, Jr., Texas Appellate Court, Houston, Texas



Mr. T. K. Lau, U.S. Department of Energy, Washington, D.C.



Mr. Herb Kaplan  
SCIEP, Inc.  
Norwalk, Connecticut



Mr. Jim McConn  
Former Mayor of Houston  
Houston, Texas



Dr. Nancy M. O'Fallon, Program Manager  
Instrumentation and Control for Fossil Energy  
Argonne National Laboratory  
Argonne, Illinois



Judge F. Lee Duggan, Jr. (Texas Appellate Court); Mr. William R. Miller (Ashland Synthetic Fuels, Inc.) and Mrs. Patricia Miller



Miriam L. Holden and Joan Cooley, Conference Planning and Management,  
Argonne National Laboratory

List of Attendees

Ian Adsley  
National Coal Board, Burton Upon Trent, Staffs, England

Rodney J. Anderson  
Morgantown Energy Technology Center, Morgantown, WV

Thomas L. Atwell  
Gamma-Metrics, San Diego, CA

E. Charles Baetens  
Frumerman Associates, Inc., Pittsburgh, PA

Joseph E. Barbay, Jr.  
Southern Illinois University, Carbondale, IL

Donald L. Bauer  
U.S. Department of Energy, Washington, D.C.

David B. Baxter  
Shell Development Co., Houston, TX

Marvin Beasley  
Mogas Industries, Inc., Houston, TX

Donald G. Beason  
Lawrence Livermore National Laboratory, Livermore, CA

James P. Bobis  
Argonne National Laboratory, Argonne, IL

James A. Bodle  
Kieley & Mueller, Inc., Middletown, NY

Neil Bond  
Ashland Synthetic Fuels, Inc., Ashland, KY

Roger Boos  
Bethlehem Steel Corporation, Bethlehem, PA

Richard Boulay  
Gilbert Associates, Reading, PA

Ronne W. Brower  
EG&G Idaho, Inc., Idaho Falls, ID

James R. Byrd  
Tennessee Valley Authority, Chattanooga, TN

K. R. Carr  
Oak Ridge National Laboratory, Oak Ridge, TN

C. Thomas Carroll  
Foster Wheeler Energy Corporation, Livingston, NJ

S.-G. Chang  
Lawrence Berkeley Laboratory, Berkeley, CA

Eugene V. Clark  
Turbine Metal Technology, Burbank, CA

- Lawrence M. Cohen  
TRW Space & Technology Group, Redondo Beach, CA
- Nancy J. Condon  
MCC Pacific Valves, Long Beach, CA
- Richard L. Conwell  
Gamma-Metrics, San Diego, CA
- Joan S. Cooley  
Argonne National Laboratory, Argonne, IL
- Donald R. Cooper  
Idaho National Engineering Laboratory, Idaho Falls, ID
- Ernesto A. Corte  
Gamma-Metrics, San Diego, CA
- Clayton T. Crowe  
Washington State University, Pullman, WA
- William A. Dark  
Waters Associates, Milford, MA
- Sue Dawson  
Precision Flow Products, Tulsa, OK
- Herbert Deich  
MDH Industries, Monrovia, CA
- Donald M. DeLauder  
West Virginia University, Morgantown, WV
- Delbert W. Devins  
Koppers Process Technologies, Norcross, GA
- Gino J. DiIorio  
Argonne National Laboratory, Argonne, IL
- Ronald R. Dixon  
Babcock & Wilcox, Lynchburg, VA
- Richard W. Doering  
General Atomic Company, San Diego, CA
- Clark V. Dohner  
Electric Power Research Institute, Palo Alto, CA
- R. James Donley  
Struthers Thermo-Flood Corporation, Winfield, KS
- Ezzat D. Doss  
Argonne National Laboratory, Argonne, IL
- Judge F. Lee Duggan, Jr.  
Texas Appellate Court, Houston, TX
- Robert C. Duty  
Illinois State University, Normal, IL
- Jerry L. Edson  
EG&G Idaho, Idaho Falls, ID
- William A. Ellingson  
Argonne National Laboratory, Argonne, IL



Frank T. Finch  
Los Alamos National Laboratory, Los Alamos, NM

F. Don Freeburn  
Morgantown Energy Technology Center, Morgantown, WV

Walter Fuchs  
Pittsburgh Energy Technology Center, Pittsburgh, PA

William Fuller  
Beckman Instruments, Fullerton, CA

Vyt Garnys  
The Australian Mineral Development Laboratories, Australia

James Gary  
Colorado School of Mines, Golden, CO

Guy D. Gimson  
International Coal Refinery Co., Allentown, PA

Peter M. Girling  
International Coal Refinery Co., Allentown, PA

Ira B. Goldberg  
Rockwell International, Thousand Oaks, CA

Nachappa Gopalsami  
Argonne National Laboratory, Argonne, IL

Tsahi Gozani  
Science Applications, Inc., Palo Alto, CA

Terry L. Greenlee  
JAYCOR, San Diego, CA

Klaus Guntermann  
The Aachen University of Technology, Federal Republic of Germany

James J. Guthrie, Jr.  
Ohmart Corporation, Cincinnati, OH

Tetsuo Hadeishi  
Lawrence Berkeley Laboratory, Berkeley, CA

James Clay Hall  
Memphis Light, Gas, & Water, Memphis, TN

E. Newt Hayes  
The Foxboro Company, Foxboro, MA

Floyd C. Henderson  
Fluor Engineers and Constructors, Irvine, CA

Caroline L. Herzenberg  
Argonne National Laboratory, Argonne, IL

Dana Hewitt  
Morgantown Energy Technology Center, Morgantown, WV

J. Robert Hightower  
Oak Ridge National Laboratory, Oak Ridge, TN

- A. G. Hill  
Oklahoma State University, Stillwater, OK
- Guy E. Hines  
Koppers Process Technologies, Norcross, GA
- David F. Hoexter  
Woodward-Clyde Consultants, San Francisco, CA
- Miriam L. Holden  
Argonne National Laboratory, Argonne, IL
- Stefan Jeglinski  
Mississippi State University, Mississippi State, MS
- John D. Jobe  
Shell Development Co., Houston, TX
- June Johansen  
Argonne National Laboratory, Argonne, IL
- Jeffrey P. Jones  
Exxon Company, Baytown, TX
- Latif A. Khan  
Illinois State Geological Survey, Champaign, IL
- Herb Kaplan  
SCIEP, Inc., Norwalk, CT
- H. B. Karplus  
Argonne National Laboratory, Argonne, IL
- Robert Kaufman  
Mogas Industries, Inc., Houston, TX
- Soung S. Kim  
Westinghouse Electric Corp., Madison, PA
- J. Derwin King  
Southwest Research Institute, San Antonio, TX
- Ron Koopman  
Argonne National Laboratory, Argonne, IL
- Herbert R. Lander  
U.S. Air Force, Jet Fuels Division, Dayton, OH
- T. K. Lau  
U.S. Department of Energy-Fossil Energy, Washington, D.C.
- Rene H. Laurens  
Institute of Gas Technology, Chicago, IL
- Swenam R. Lee  
Pittsburgh Energy Technology Center, Pittsburgh, PA
- Leo G. LeSage  
Argonne National Laboratory, Argonne, IL
- Francis E. Levert  
Technology for Energy Corporation, Knoxville, TN

Wen H. Lin  
Argonne National Laboratory, Argonne, IL

James K. Linn  
Sandia National Laboratories, Albuquerque, NM

Robert D. Litt  
Battelle, Columbus Laboratories, Columbus, OH

Paul Longrigg  
Solar Energy Research Institute, Golden, CO

James P. Lucas  
Sandia National Laboratory, Albuquerque, NM

Co Luttik  
Koninklijke/Shell Laboratory, Amsterdam, Holland

Mark Mackinnon  
Kay-Ray, Inc., Arlington Heights, IL

Joseph E. Macko  
Westinghouse Electric, Madison, PA

Herb C. March  
Procon, Inc., Des Plaines, IL

Robert E. Martin  
Jet Propulsion Laboratory, Pasadena, CA

Mahendra P. Mathur  
Pittsburgh Energy Technology Center, Pittsburgh, PA

Jim McConn  
Houston, TX

William R. McIntire  
Dowell, Inc., Tulsa, OK

William R. Miller  
Ashland Synthetic Fuels, Inc., Ashland, KY

Gary Mohr  
Exxon Research and Engineering, Baytown, TX

Frank Mourits  
Saskoil, Regina, Saskatchewan

John E. Mrochek  
Oak Ridge National Laboratory, Oak Ridge, TN

David Murphree  
Mississippi State University, Mississippi State, MS

Thomas E. Murphy  
Taylor Instrument Company, Rochester, NY

D. Nguyen  
Alberta Research Council, Edmonton, Alberta, Canada

Roy O. Nicholson  
Monsanto Research Corp., Washington, D.C.

Nancy M. O'Fallon  
Argonne National Laboratory, Argonne, IL

Emil J. Petrovick  
The Foxboro Company, Foxboro, MA

Robert J. Platt  
Exxon Engineering, Florham Park, NJ

Karl G. Porges  
Argonne National Laboratory, Argonne, IL

James L. Powell  
U.S. Department of Energy, Washington, DC

Paul Raptis  
Argonne National Laboratory, Argonne, IL

John J. Roberts  
Argonne National Laboratory, Argonne, IL

G. W. Robertson  
Preparation Control, Inc., St. Albans, WV

Brad Rogers  
Mountain States Energy, Inc., Butte, MT

Joseph J. Ronchetto  
Lawrence Livermore National Laboratory, Livermore, CA

Toshio Satori  
Hokushin Electric Works, Tokyo, Japan

Ronald A. Scharping  
Argonne National Laboratory, Argonne, IL

Thomas R. Schmidt  
Shell Development Co., Houston, TX

James F. Schooley  
National Bureau of Standards, Washington, DC

Mary Anne H. Scott  
University of Tennessee Space Institute, Tullahoma, TN

Pyrtle W. Seabaugh  
Monsanto Research Corp.-Mound, Miamisburg, OH

George E. Sedgwick  
Alberta Research Council, Edmonton, Alberta, Canada

Patrick Shea  
Stanford University, Stanford, CA

Shuh-Haw Sheen  
Argonne National Laboratory, Argonne, IL

Donald Shegrud  
Continental Disc Corp., Kansas City, MO

G. Kelly Sievers  
Turbine Metal Technology, Burbank, CA

Allan T. Simpson  
Air Products and Chemicals, Allentown, PA

W. Lee Smith  
Micro Motion, Inc., Houston, TX

A. C. Snodgrass  
Houston, TX

Samuel J. Spataro  
Lawrence Livermore National Laboratory, Livermore, CA

Maryanne K. Speciale  
Optical Coating Laboratory, Inc., Santa Rosa, CA

Cherrill M. Spencer  
Science Applications, Inc., Palo Alto, CA

Robert R. Stalnaker  
C. F. Braun and Co., Alhambra, CA

James A. Stares  
Masoneilan Division, McGraw-Edison Co., Norwood, MA

C. Richard Stewart  
Honeywell, Inc., Ft. Washington, PA

Malcolm L. Stitch  
Exxon Research and Engineering Co., Florham Park, NJ

Gerd Suhens  
The Aachen University of Technology, Federal Republic of Germany

Veni Sumaria  
JAYCOR, Woburn, MA

Merve L. Sweeney  
East Kentucky Power Cooperative, Inc., Winchester, KY

J. J. Szakasits  
Shell Development Co., Houston, TX

Frank F. Tao  
Exxon Research and Engineering, Baytown, TX

A. Telfer  
Shell Development Co., Houston, TX

Gordon R. Thompson  
Syncrude Canada Ltd., Edmonton, Alberta, Canada

Jeffrey L. Thompson  
Exxon Research and Engineering Co., Florham Park, NJ

Daniel A. Tichenor  
Sandia National Laboratories, Livermore, CA

Maurice Turgeon  
Catalytic, Inc., Wilsonville, AL

James E. Uhl  
Sandia National Laboratories, Albuquerque, NM

George B. Usnick  
Conoco, Inc., Library, PA

James Henry Vignos  
The Foxboro Co., Foxboro, MA

Michael J. Virr  
Johnston Boiler Company, Ferrysburg, MI

Graham V. Walford  
Gull Engineering, Inc., Oak Ridge, TN

John V. Walsh  
Jet Propulsion Laboratory, Pasadena, CA

James C. F. Wang  
Sandia National Laboratories, Livermore, CA

Eddie S. Washington  
UTSI, Tullahoma, TN

Paul Wellman  
Ashland Synthetic Fuels, Inc., Houston, TX

Chaur S. Wen  
Gulf Research and Development Co., Pittsburgh, PA

James R. Whetstone  
National Bureau of Standards, Washington, DC

Stan J. Wohadlo  
Institute of Gas Technology, Chicago, IL

Charles R. Wright  
Tennessee Valley Authority, Muscle Shoals, AL

Frederick J. Wyant  
Westinghouse Synthetic Fuels Div., Madison, PA

Ronald E. Zielinski  
Monsanto Research Corp.-Mound, Miamisburg, OH

#### Exhibitors

Maureen Derosa  
Amersham Corporation, Arlington Heights, IL

S. Steinberg  
ARI Industries, Inc., Franklin Park, IL

J. Hiett Ives  
Cameron Iron Works, Inc., Houston, TX

Douglas F. Butler  
Kamyr Valves, Inc., Glen Falls, NY

Robert Kaufman  
Mogas Machine Works, Inc., Houston, TX

Roy W. Yost  
Perkin-Elmer Corp., Norwalk, CT

Wayne Masnica  
Perkin-Elmer Corp., Pomona, CA

Herb Kaplan  
SCIEP, Inc., Norwalk, CT

John Sozio  
Taylor Instrument Co., Rochester, NY

David Snyder  
Validyne Engineering Corp., Northridge, CA

Stephen McDonough  
Waters Associates, Milford, MA

Renate Sielemann  
Carl Zeiss, Inc., New York, NY